Transactions of the ASME®

Transactions of the ASME, Journal of Heat Transfer (ISSN 0022-1481) is published quarterly (Feb., May, Aug., Nov.) for $150 per year by The American Society of Mechanical Engineers, 345 East 47th Street, New York, NY 10017. Second class postage paid at New York, NY and additional mailing offices. POSTMASTER: Send address changes to The Journal of Heat Transfer, c/o THE AMERICAN SOCIETY OF MECHANICAL ENGINEERS, 22 Law Drive, Box 2300, Fairfield, NJ 07007-2300.
CHANGES OF ADDRESS must be received at Society headquarters seven weeks before they are to be effective. Please send old label and new address.
PRICES: To members, $27.00, annually; to nonmembers, $150.00.
Add $12.00 for postage to countries outside the United States and Canada.

INDEXED by Applied Mechanics Reviews and Engineering Information, Inc.

Journal of Heat Transfer

Published Quarterly by The American Society of Mechanical Engineers

VOLUME 110 • NUMBER 2 • MAY 1988

ANNOUNCEMENTS

TECHNICAL PAPERS

(Contents continued)

TECHNICAL NOTES

Heat Diffusion in Heterogeneous Bodies Using Heat-Flux-Conserving Basis Functions

A. Haji-Sheikh
Mechanical Engineering Department,
University of Texas at Arlington,
Arlington, TX 76019

The generalized analytical derivation presented here enables one to obtain solutions to the diffusion equation in complex heterogeneous geometries. A new method of constructing basis functions is introduced that preserves the continuity of temperature and heat flux throughout the domain, specifically at the boundary of each inclusion. A set of basis functions produced in this manner can be used in conjunction with the Green's function derived through the Galerkin procedure to produce a useful solution method. A simple geometry is selected for comparison with the finite difference method. Numerical results obtained by this method are in excellent agreement with finite-difference data.

Introduction

A method of finding the temperature distribution in a heterogeneous solid using a new and useful set of basis functions is introduced. An extensive literature search did not reveal any analytical method capable of producing a closed-form temperature solution for a heterogeneous solid with nonorthogonal boundaries, particularly for three-dimensional bodies, that is mathematically valid at every point. Many solutions cited in the literature are for bodies with boundaries orthogonal to coordinate axes, e.g., Chang and Poon (1979), Chester et al. (1984), Clever and Wassel (1985), Horvay et al. (1973), Salt (1983), and Schachinger et al. (1980). Others consider properties to be uniform, utilizing various averaging schemes, e.g., Baker-Jarvis and Inguva (1983), Campo (1982), and Maewal et al. (1976). The existing analytical solutions in multilayered bodies are cumbersome, even for simple geometries, and the method of finding the eigenvalues requires numerical computations. Also, the difference methods cannot always deal effectively with conduction in heterogeneous solids when geometries are three dimensional and the number of inclusions is large. The finite-element and boundary-element methods are useful for the study of conduction in two-dimensional bodies. However, in three-dimensional bodies the number of elements can become too large for the available computational facility.

When the thermal conductivity is discontinuous, e.g., across the phase boundary, the temperature gradient must also be discontinuous. The basis functions introduced here are permitted to have discontinuous gradients across the boundary of each inclusion so that the heat flux is conserved while the temperature field always remains a continuous function of position. These new basis functions will be called Heat-Flux-Conserving basis functions and, for the sake of brevity, will be designated "HFC basis functions" throughout this paper. A solution method that is a linear combination of these basis functions will also satisfy the continuity of the temperature and heat flux across the phase boundary of inclusions. The properties of the HFC basis functions enhance the capability of handling diffusion equations that, to date, resist closed-form solutions or accurate numerical predictions. The HFC basis functions can be extended to a variety of problems that are governed by parabolic and elliptic partial differential equations in other engineering fields such as bioengineering, solid mechanics, field theory, etc. The solution method formulated in this paper is based on the Green's function; hence, it can accommodate linear boundary conditions. The numerical solutions to many partial differential equations with nonlinear boundary conditions can be obtained using the Green's function and solving an integral equation. A numerical procedure for accommodating nonlinear boundary conditions is reported in Villasenor and Squire (1986).

Analysis

The auxiliary equation that defines the Green's function is

$$\nabla \cdot [k(\mathbf{r}) \nabla G(\mathbf{r}, t \,|\mathbf{r}', \tau)] + C(\mathbf{r})\delta(\mathbf{r}-\mathbf{r}')\delta(t-\tau) = C(\mathbf{r})\partial G(\mathbf{r}, t \,|\mathbf{r}', \tau)/\partial t \quad (1)$$

where $C(\mathbf{r}) = \rho(\mathbf{r})C_p(\mathbf{r})$, and the properties $\rho(\mathbf{r})$, $C_p(\mathbf{r})$, and $k(\mathbf{r})$ are position-dependent density, specific heat, and thermal conductivity. The function $G(\mathbf{r}, t \,|\mathbf{r}', \tau)$ is the Green's function (Özişik, 1980) indicating the temperature effect at point $\mathbf{r}$ at time t if there is an impulsive point heat source of strength unity located at point $\mathbf{r}'$ and released at time τ. Equation (1) indicates that the Green's function is symmetric with respect to $\mathbf{r}$ and $\mathbf{r}'$ when $C(\mathbf{r})$ is a constant. Also, the Green's function remains the same if t is replaced by $-\tau$ and τ is replaced by $-t$. It can be demonstrated that the symmetry of the Green's function with respect to $\mathbf{r}$ and $\mathbf{r}'$ holds if a weighting function is included. The weighting function can be defined later. The del operator in equation (1) uses the components of $\mathbf{r}$ (not $\mathbf{r}'$). A del operator ∇_0 is defined that uses the components or $\mathbf{r}'$. If $\mathbf{r}$ is now replaced by $\mathbf{r}'$, $\mathbf{r}'$ by $\mathbf{r}$, t by $-\tau$, and τ by $-t$, equation (1) becomes

$$\nabla_0 \cdot [k(\mathbf{r}) \nabla_0 G(\mathbf{r}', -t \,|\mathbf{r}, -t)] + C(\mathbf{r}')\delta(\mathbf{r}'-\mathbf{r})\delta(\tau-t) = -C(\mathbf{r}')\partial G(\mathbf{r}', -\tau \,|\mathbf{r}, -t)/\partial\tau \quad (2)$$

The diffusion equation using $\mathbf{r}'$ and τ variables is

$$\nabla_0 \cdot [k(\mathbf{r}) \nabla_0 T(\mathbf{r}', \tau)] + g(\mathbf{r}', \tau) = C(\mathbf{r}')\partial T(\mathbf{r}', \tau)/\partial\tau \quad (3)$$

where $g(\mathbf{r}', \tau)$ is the contribution of a distributed volumetric heat source. In order to avoid lengthy mathematical relations, the function $G(\mathbf{r}', -\tau \,|\mathbf{r}, -t)$ will be designated as G. When equation (3) is multiplied by G and equation (2) is multiplied by T and the resulting equations subtracted from each other, the temperature solution is obtained following the integration over $\mathbf{r}'$ space and over τ

$$\rho(\mathbf{r})C_p(\mathbf{r})T(\mathbf{r}, t) = \int_V \rho(\mathbf{r}')C_p(\mathbf{r}')G\,|_{\tau=0}\, T_0(\mathbf{r}')dV'$$

Contributed by the Heat Transfer Division for publication in the JOURNAL OF HEAT TRANSFER. Manuscript received by the Heat Transfer Division April 3, 1987. Keywords: Conduction, Transient and Unsteady Heat Transfer.

$$+\int_{\tau=0}^{t} d\tau \int_V g(\mathbf{r}', \tau) G dV'$$

$$+\int_{\tau=0}^{t} d\tau \int_S k(S')[G\partial T/\partial n - T\partial G/\partial n]_{S'} dS' \quad (4)$$

The algebraic steps leading to this relation are identical to those described by Özisik (1980), except for some modifications to account for the effect of spatially variable properties. The operator $\partial/\partial n$ designates differentiation along the outer normal to the external surface and $T_0(\mathbf{r}')$ is the initial temperature distribution.

The boundary conditions for G in equation (4) are homogeneous and of the same type as the boundary conditions for T. If the boundary conditions for T are also homogeneous, then the term in the square brackets in equation (4) will vanish. An alternate temperature solution for conduction in a heterogeneous solid, but with homogeneous boundary conditions, is (Haji-Sheikh and Mashena, 1987)

$$T = \sum_{n=1}^{N}\sum_{i=1}^{N} \int_V p_{ni} e^{-\gamma_n t} F_n(\mathbf{r}) \rho(\mathbf{r}') C_p(\mathbf{r}') T_0(\mathbf{r}') f_i(\mathbf{r}') dV'$$

$$+\int_0^t \sum_{n=1}^{N}\sum_{i=1}^{N} \int_V p_{ni} e^{-\gamma_n (t-t')} F_n(\mathbf{r}) g(\mathbf{r}', t') f_i(\mathbf{r}') dV' dt' \quad (5)$$

where $\mathbf{r}'$ and t' are dummy variables of integration. A comparison between equations (4) and (5) after t' is replaced by τ reveals the Green's function

$$G = G(\mathbf{r}', -\tau | \mathbf{r}, -t)$$

$$= \sum_{n=1}^{N} \rho(\mathbf{r}) C_p(\mathbf{r}) F_n(\mathbf{r}) \sum_{j=1}^{N} \exp[-\gamma_n (t-\tau)] p_{nj} f_j(\mathbf{r}')$$

$$= \sum_{n=1}^{N}\sum_{j=1}^{N}\sum_{i=1}^{N} d_{ni} p_{nj} \exp[-\gamma_n (t-\tau)] \rho(\mathbf{r}) C_p(\mathbf{r}) f_i(\mathbf{r}) f_j(\mathbf{r}') \quad (6)$$

while

$$F_n(\mathbf{r}) = \sum_{i=1}^{N} d_{ni} f_i(\mathbf{r}) \quad (7)$$

in which d_{ni} is the eigenvector corresponding to the eigenvalue γ_n and $f_i(\mathbf{r})$ is the basis function whose functional value will be defined later. It should be noted that the Green's function G in equations (4) and (6) is $G(\mathbf{r}', -\tau | \mathbf{r}, -t) = G(\mathbf{r}', t | \mathbf{r}, \tau)$. Equation (6) shows that the Green's function is not symmetric in $\mathbf{r}$ and $\mathbf{r}'$. The value of the Green's function $G(\mathbf{r}, t | \mathbf{r}', \tau)$ can be obtained by interchanging the variables $\mathbf{r}$ and $\mathbf{r}'$ in equation (6). An alternate but more elegant procedure is to replace the dummy variable $\mathbf{r}'$ in equation (5) with a new dummy variable ξ and then substituting $T_0 = 0$ and $g(\xi, t') = \rho(\xi) C_p(\xi) \delta(\xi - \mathbf{r}') \delta(t' - \tau)$ in the resulting equation. After performing the integration over ξ and t' the Green's function becomes

$$G(\mathbf{r}, t | \mathbf{r}', \tau) = \sum_{n=1}^{N}\sum_{j=1}^{N}\sum_{i=1}^{N} d_{ni} p_{nj}$$

$$\exp[-\gamma_n (t-\tau)] \rho(\mathbf{r}') C_p(\mathbf{r}') f_i(\mathbf{r}) f_j(\mathbf{r}') \quad (8)$$

Therefore, when the properties are position dependent, the following relation holds:

$$G(\mathbf{r}, t | \mathbf{r}', \tau)/\rho(\mathbf{r}') C_p(\mathbf{r}') = G(\mathbf{r}', -\tau | \mathbf{r}, -t)/\rho(\mathbf{r}) C_p(\mathbf{r}) \quad (9)$$

It should be emphasized that the Green's function appearing in the working equation (4) is provided by equation (6). When the surface temperature is prescribed (boundary conditions of the first kind) the function G vanishes on the external surface. The only term remaining inside the square bracket in equation (4) is $-T\partial G/\partial n$. The derivative $\partial G/\partial n$ using equation (6) requires the calculation of $\partial f_j(\mathbf{r}')/\partial n$ evaluated on the external surface. The function $f_i(\mathbf{r})$ in equation (6) remains unaffected by differentiation and will unconditionally vanish on the external surface. Therefore, when $f_i(\mathbf{r})$ is evaluated on S, the term inside the square bracket in equation (4) appears to become unconditionally zero and as a result equation (4) yields a surface temperature of zero although the actual surface temperature is nonzero. This apparent inconsistency is caused

Nomenclature

a = geometric dimension
a_{ij} = element of matrix **A**, equation (11)
A = matrix
b = geometric dimension
b_{ij} = element of matrix **B**, equation (12)
B = matrix
C_p = specific heat
d_{nj} = coefficients, equation (7)
$\mathbf{d}_n$ = eigenvector containing d_{nj}
D = matrix whose nth row is the vector $\mathbf{d}_n$
f_j = basis functions
$f_{j,i}$ = basis function f_j in ith domain
$f_{j,m}$ = basis function f_j in main domain
f^* = function defined in equation (A2)
F_n = eigenfunction
g = heat generation per unit time and per unit volume
G = Green's function = G($\mathbf{r}'$, $t | \mathbf{r}, \tau$)
H = function in equation (14) defined in equation (14a)
i, j = indices
k = thermal conductivity
k_m = thermal conductivity of main domain
k_i = thermal conductivity of inclusion i
n = index
M = number of surfaces
N = number of eigenvalues
p_{ni} = element of matrix **P**
P = inverse matrix of the transpose of (**B**•**D**)
r = radial coordinate
$\mathbf{r}$ = position vector
$\mathbf{r}'$ = position vector, dummy variable
S = surface
t = time
T = temperature
T_0 = initial temperature distribution
T_s = surface temperature
T^* = auxiliary solution, equation (A1)
V = volume
x, y, z = coordinates
α = thermal diffusivity
α_m = thermal diffusivity of main domain
α_i = thermal diffusivity of inclusion i
γ_n = eigenvalues
δ = delta function
ϵ = criterion
θ = $(T - T_0)/(T_s - T_0)$
ξ = position vector, dummy variable
ρ = density
τ = time, dummy variable
ϕ = boundary function

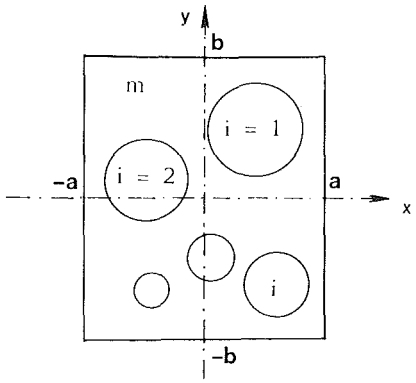

Fig. 1 Schematic of a main region with inclusions for equations (13) and (14)

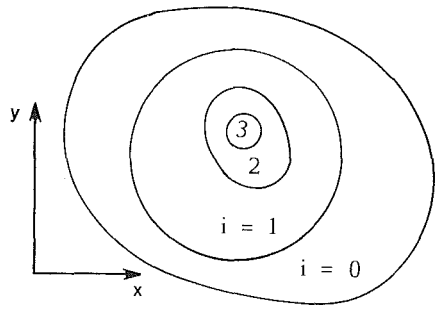

Fig. 2 Schematic of a multilayer region for equations (15) and (16)

by a removable singularity. The procedure for the removal of this singularity is discussed in the Appendix.

The numerical values of γ_n and d_{ni} are obtained from the relation

$$(\mathbf{A}+\gamma_n\mathbf{B})\cdot\mathbf{d}_n=0 \tag{10}$$

in which **A** and **B** are matrices of size $N\times N$ with elements

$$a_{ij}=\int_V f_i\nabla\cdot(k\nabla f_i)dV \tag{11}$$

$$b_{ij}=\int_V \rho C_p f_j f_j dV \tag{12}$$

where $i=1, 2, 3, \ldots$ and $j=1, 2, 3, \ldots$. The solution of equation (10) using equations (11) and (12) results in the values of the eigenvalues and eigenvectors. The eigenvector $\mathbf{d}_n$ has the elements $d_{n1}, d_{n2}, \ldots, d_{nN}$ corresponding to the eigenvalue γ_n. The eigenvectors are needed to solve for the temperature distribution using equations (4) and (6) or equation (5). The matrix **P** with elements p_{nj} in equations (5), (6), and (8) is obtained using the relation $\mathbf{P}=[(\mathbf{B}\cdot\mathbf{D})^t]^{-1}$ (Haji-Sheikh, 1986; Haji-Sheikh and Mashena, 1987).

Heat-Flux-Conserving Basis Functions. As stated earlier, the unique feature of this solution method is the use of a new set of linearly independent, discrete basis functions, which satisfy all homogeneous boundary conditions at the external boundaries. These basis functions also satisfy the continuity of temperature and heat flux at any point where the thermal conductivity is not a continuous function of position. Hence, a new capability is realized for finding the local temperature values in heterogeneous solids with inclusions, as shown in Fig. 1.

In this presentation, the subscript i identifies the material subdomain enclosed in the main region, m denotes the main domain, and $f_{j,m}$ designates the basis function in the absence of any inclusion. The HFC basis function f_j for $j=1, 2, \ldots$ is given by the equation

$$f_j=f_{j,m};\quad \text{in the main domain} \tag{13}$$

and

$$f_j=f_{j,m}+\phi_i H;\quad \text{in the } i\text{th inclusion} \tag{14}$$

The condition $k_m(\partial f_j/\partial n)_m=k_i(\partial f_j/\partial n)_i$ when $\phi_i=0$ at the boundary of inclusion i requires

$$H=[(\nabla f_{j,m}\cdot\nabla\phi_i)\,|_{\phi_i=0}]$$

$$(k_m/k_i-1)/[(\nabla\phi_i\cdot\nabla\phi_i)\,|_{\phi_i=0}] \tag{14a}$$

Any linear combination of the f_j function satisfies the continuity of the temperature and heat flux everywhere on the bondaries of inclusions $i=1$, 2, etc., see Fig. 1; that is, $k_m(\partial T/\partial n)_m=k_i(\partial T/\partial n)_i$ and $(T)_m=(T)_i$ on the boundary of inclusion i. If the main domain is regular, the basis functions $f_{j,m}$ can be selected in the usual manner (Kantorovich and Krylov, 1960). For instance, using the region depicted in Fig. 1, the function $f_{j,m}=(a^2-x^2)(b^2-y^2)x^\mu y^\nu$ vanishes on the outer contour; hence, it satisfies homogeneous boundary conditions of the first kind. The exponents μ and ν are integers selected so that $f_{j,m}$ is a member of a complete set. An ordered set approximating a function is complete if the least square of errors vanishes when the number of members of the set goes to infinity. Procedures for satisfying homogeneous boundary conditions of the second kind (prescribed heat flux) and third kind (convective surface) are reported by Haji-Sheikh and Lakshminarayanan (1987).

Equation (14) is derived for any inclusion whose boundary consists of a single curve, e.g., planes, cylinders, spheres, spheroids, etc. Modifications are possible for the case when the contour of the inclusion consists of sectionally smooth curves, e.g., hemispheres, rectangles, etc. As an illustration, the function ϕ_i for the circular inclusion i can be obtained from the relation $\phi_i=R_i^2-(x-x_i)^2-(y-y_i)^2$ where x_i and y_i are the coordinates of the center of inclusion i and R_i is the radius of that inclusion. This relation satisfies the condition that ϕ_i must vanish on the contour of inclusion i. If the contour of the inclusion is sectionally continuous, the Galerkin procedure may be utilized (Kantorovich and Krylov, 1960) to construct a new ϕ_i. Moreover, in equation (14), it is assumed that there is a perfect contact between the main domain and the inclusions. There are two simple procedures to handle the effect of contact conductance at the boundary of an inclusion. One scheme is to modify equation (14) to account for this effect. The second procedure is to consider a thin low-conductivity layer located along the phase boundary of the inclusion. Generally, when an inclusion is located inside another inclusion, as shown in Fig. 2, or when there are multilayers in a region, equations (13) and (14) can be rewritten as

$$f_j=f_{j,0};\quad \text{in the main domain} \tag{15}$$

and

$$f_j=f_{j,i-1}+\phi_i[(\nabla f_{j,i-1}\cdot\nabla\phi_i)\,|_{\phi_i=0}]$$

$$(k_{i-1}/k_i-1)/[(\nabla\phi_i\cdot\nabla\phi_i)\,|_{\phi_i=0}];\quad \text{in the } i\text{th layer} \tag{16}$$

Here, $f_{j,m}$ is replaced by $f_{j,0}$ and subscripts $i=1, 2, \ldots$ stand for numbers assigned to inclusions in Fig. 2. Equations (15) and (16) satisfy the conservation of heat flux and continuity of temperature between layer $i-1$ and i.

Numerical Example. The numerical example selected for testing the HFC basis functions concerns temperature distribution in concentric cylinders, shown in Fig. 3. This simple geometry is selected because it permits an exact analytic or a finite difference solution and facilitates a comparison of the accuracy of the results obtained with the analytical method using HFC basis functions. It is assumed that the domain under

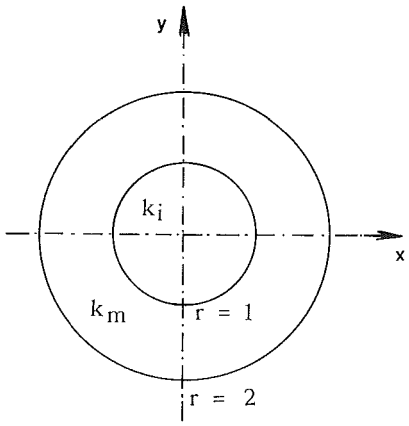

Fig. 3 Concentric cylinders used in the numerical example

consideration consists of two layers. The radius of the outer cylinder is R_m. Both cylinders are intially at a constant temperature T_0 and the surface temperature at $r=R_m$ and $t>0$ is increased to a constant temperature T_s. Because the surface temperature is prescribed, the boundary condition is of the first kind. Assuming the region is isotropic, the basis functions that satisfy the homogeneous boundary conditions of the first kind are selected as $f_{j,m}=(R_m{}^2-r^2)r^{2(j-1)}$. Other complete sets of basis functions that satisfy the homogeneous boundary conditions of the first kind can be used. In general, a set of sine and cosine, Bessel functions, Chebyshev polynomials, etc., may yield more accurate results, but the analytical integrations can become cumbersome. The polynomials that use the Taylor series are usually employed to avoid numerical integrations. The symbolic manipulator, MACSYMA (Symbolics, 1985), is used to perform differentiations and integrations. Equation (13) provides the basis function f_j when $R_1<r<R_m$ and equation (14) yields the function f_j in the subregion whose radius is R_1. Without loss of generality, the radius R_1 is set equal to unity; hence r and R_m (here, $R_m=2$) may be interpreted as dimensionless. The final form of the HFC basis functions used in this example is

$$f_j=(R_m{}^2-r^2)r^{2(j-1)}; \quad \text{in the outer layer (main domain)} \quad (17)$$

$$f_j=(R_m{}^2-r^2)r^{2(j-1)}+(1-r^2)[2j-2(j-1)R_m{}^2](k_m/k_1-1)/2;$$

in the inner layer (18)

It is further assumed that there is no volumetric heat source and the temperature T_s at $r=R_m$ is constant. Since both the initial temperature and the surface temperature are constants, equation (4) or a more convenient form equation (A7) in the Appendix, after replaceing dV' by $2\pi r'$, results in

$$\theta = (T-T_0)/(T_s-T_0)=1-\sum_{n=1}^{N}[F_n(r)\exp(-\gamma_n t)]\sum_{j=1}^{N}p_{nj}$$

$$\int_0^{R_m}\rho(r')C_p(r')f_j(r')2\pi r'dr' \quad (19)$$

The dimensionless $(T-T_0)/(T_s-T_0)$ instead of $(T-T_s)/(T_0-T_s)$, in equation (A7), is used mainly to amplify the error when time t is small, and to demonstrate the limitation of this procedure as well as its advantages.

The dimensionless temperature data at $r=0$ and 1 are presented in Figs. 4 and 5. The point $r=0$ is the central location and $r=1$ corresponds to a point located at the boundary of the inclusion. The abscissas in Figs. 4 and 5, $(\alpha_1 t/R_1^2)$, represent the dimensionless time and the ordinates are the dimensionless temperature appearing on the left-hand side of equation (19). These figures show that the thermal conductivity ratio has a strong influence on the temperature field within

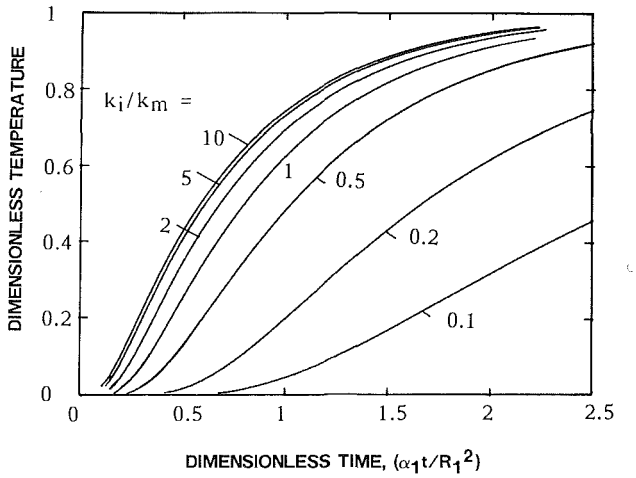

Fig. 4 Dimensionless transient temperature at $r=0$ for different thermal conductivity ratios, $(\rho C_p)_1/(\rho C_p)_m=1$

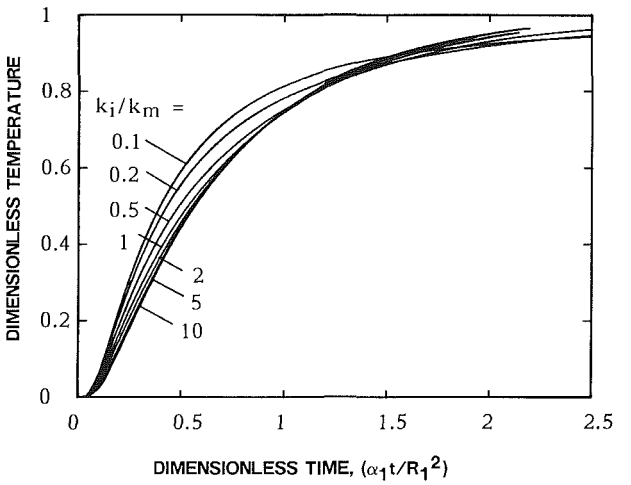

Fig. 5 Dimensionless transient temperature at $r=1$ for different thermal conductivity ratios, $(\rho C_p)_1/(\rho C_p)_m=1$

the inclusion and affects the temperature of the main domain to a lesser extent. As an alternate method of solution and for the purpose of comparison, results using a finite difference scheme were obtained. Although the exact solution is available in Schachinger et al. (1980), the finite-difference (FD) method is used for reasons other than the simplicity of the computational procedure. For this method to be efficient, it must provide better accuracy than one expects from the numerical solutions at a fraction of the computation cost. The spatial step size using an explicit FD solution was $\Delta r/R_1=0.05$. The step size in time varies with α, using a criterion $\Delta t=0.2\Delta r^2/(\alpha)_{\max}$, where $\alpha_{\max}$ represents the larger of α_1 and α_m. Because it is difficult to show graphically the difference between the two solutions in Fig. 4, the temperature solutions for a large range of thermal conductivity ratios using the HFC basis functions and FD are provided in Tables 1 and 2. The representative data are for temperature values at the points $r=0$, 1, and 1.5. In Table 1, the ratio $(\rho C_p)_1/(\rho C_p)_m$ has a unit value while the thermal conductivity ratio changes between 0.1 to 10. The difference between the two solutions is usually small and often negligible. The largest deviation in Table 1 is 0.0033, which appears at a small time, but the agreement improves very rapidly. In general, all entries in Table 1 agree to four digits, except at small time and when $r=0$ and $k_1/k_m<1$. The temperature solution using the HFC basis functions is excellent when the dimensionless temperature is larger than 0.1 even when a small number of basis functions is used. The small-time behavior is similar to that of the exact series solu-

Table 1 Temperature calculation using finite difference and HFC basis functions when $(\rho C_p)_1/(\rho C_p)_m = 1$

k_1/k_m	$\alpha_1 t/R_1^2$	r = 0		r = 1		r = 1.5	
		FD	HFC	FD	HFC	FD	HFC
0.1	1	0.0425	0.0439	0.8150	0.8150	0.9071	0.9073
	1.5	0.1648	0.1677	0.8902	0.8903	0.9484	0.9485
	2	0.3146	0.3176	0.9244	0.9245	0.9657	0.9656
	2.5	0.4533	0.4560	0.9441	0.9442	0.9750	0.9750
	3	0.5692	0.5716	0.9574	0.9574	0.9810	0.9810
0.2	0.5	0.0159	0.0126	0.5573	0.5570	0.7589	0.7589
	1	0.1960	0.1971	0.7834	0.7833	0.8929	0.8930
	1.5	0.4304	0.4319	0.8725	0.8725	0.9396	0.9396
	2	0.6150	0.6163	0.9191	0.9190	0.9623	0.9622
	2.5	0.7437	0.7446	0.9472	0.9472	0.9755	0.9755
	3	0.8301	0.8308	0.9652	0.9652	0.9839	0.9839
0.5	0.5	0.1233	0.1230	0.5068	0.5066	0.7408	0.7407
	1	0.4821	0.4822	0.7530	0.7528	0.8773	0.8773
	1.5	0.7197	0.7198	0.8696	0.8695	0.9359	0.9359
	2	0.8503	0.8503	0.9306	0.9306	0.9659	0.9659
1	0.25	0.0348	0.0347	0.2288	0.2285	0.5602	0.5599
	0.5	0.2462	0.2460	0.4754	0.4752	0.7283	0.7282
	1	0.6233	0.6232	0.7472	0.7471	0.8723	0.8723
	1.5	0.8169	0.8169	0.8773	0.8773	0.9381	0.9381
	2	0.9111	0.9111	0.9405	0.9404	0.9700	0.9700
2	0.25	0.0800	0.0797	0.2062	0.2059	0.5554	0.5553
	0.5	0.3392	0.3390	0.4572	0.4570	0.7195	0.7194
	1	0.6920	0.6919	0.7484	0.7484	0.8714	0.8713
	1.5	0.8573	0.8574	0.8835	0.8835	0.9404	0.9404
	2	0.9339	0.9340	0.9461	0.9461	0.9724	0.9724
5	0.25	0.1299	0.1295	0.1873	0.1870	0.5507	0.5507
	0.5	0.4011	0.4011	0.4474	0.4474	0.7138	0.7137
	1	0.7297	0.7298	0.7508	0.7509	0.8716	0.8716
	1.5	0.8782	0.8783	0.8877	0.8878	0.9421	0.9422
	2	0.9450	0.9452	0.9494	0.9495	0.9739	0.9739
10	0.15	0.0432	0.0424	0.0660	0.0653	0.4175	0.4175
	0.25	0.1508	0.1504	0.1803	0.1800	0.5487	0.5487
	0.5	0.4219	0.4218	0.4448	0.4447	0.7119	0.7119
	1	0.7416	0.7416	0.7519	0.7519	0.8718	0.8718
	1.5	0.8846	0.8847	0.8892	0.8893	0.9428	0.9428
	2	0.9485	0.9485	0.9506	0.9506	0.9744	0.9745

Table 2 Temperature calculation using finite difference and HFC basis functions when $(\rho C_p)_1/(\rho C_p)_m = 2$

k_1/k_m	$\alpha_1 t/R_1^2$	r = 0		r = 1		r = 1.5	
		FD	HFC	FD	HFC	FD	HFC
2	0.25	0.0231	0.0235	0.1613	0.1612	0.5481	0.5476
	0.50	0.1765	0.1759	0.3505	0.3505	0.6873	0.6870
	0.75	0.3441	0.3436	0.4904	0.4904	0.7592	0.7589
	1	0.4827	0.4823	0.5991	0.5991	0.8111	0.8109
	1.25	0.5927	0.5924	0.6845	0.6845	0.8514	0.8513
	1.5	0.6794	0.6792	0.7517	0.7517	0.8830	0.8830
	1.75	0.7477	0.7475	0.8045	0.8045	0.9080	0.9079
	2	0.8014	0.8012	0.8462	0.8462	0.9276	0.9275

tion (large-time solution); hence, its usage for calculating small-time temperatures is inappropriate. For instance, when $k_1/k_m = 0.2$, $\alpha_1 t/R_1^2 = 0.5$, and $N = 10$, Table 1, the HFC method yields a dimensionless temperature value of 0.0126; however, $N = 12$ results in a more accurate value of 0.0152. Table 2 contains a similar comparison but the $(\rho C_p)_1/(\rho C_p)_m$ ratio is selected equal to 2. Generally, when the dimensionless temperature values are larger than 0.1, the FD solutions with the spatial step size $\Delta r/R_1 = 0.05$ also yield nearly four accurate digits. The small step size makes the computation of a FD solution time consuming. In contrast, the analytical solution required 3 s of processing time, when $N = 10$, on a personal computer with an INTEL 80286-10 processor. The number of nodes in FD increases significantly for three-dimensional geometry, resulting in a significant increase in computation time. However, the computation time for the analytical solution depends on the number of basis functions and it is independent of the geometric dimensions. Cognizance should be taken of the fact when $N = 11$, the degree of polynomials in this example is 20 whereas, for a three-dimensional body in the absence of symmetry, the degree of polynomials is only 3.

The testing of the convergence, as the number of eigenvalues N increases, reveals that an accurate solution needs four or five eigenvalues. The accuracy slightly increased for $N = 10$, which is the number of eigenvalues used to produce appropriate entries in Tables 1 and 2. When N, for $k_1/k_m = 0.2$, was increased to above 14, the matrix operations failed to provide the eigenvalues because of the finiteness of the machine's word length. The polynomial-based basis functions become difficult to accommodate when the degree of polynomials is large. The limitation observed in this example is not important for practical applications because the degrees of polynomials are usually small. Purely for theoretical reasons, the appropriate step to circumvent this difficulty is to use another set of basis functions, e.g., sine and cosine, Chebyshev polynomials, etc. However, acceptable solutions for many applications can be obtained using a small number of basis functions. This can be demonstrated by selecting $k_1/k_m = 2$ and $(\rho C_p)_1/(\rho C_p)_m = 1$ and comparing the results with those in Table 1. When $N = 2$, manual computation of a_{ij} and b_{ij} can be carried out easily from equations (11) and (12). Following the evaluation of a_{ij} and b_{ij} equation (10) becomes

$$\left\{ -\begin{bmatrix} 15.5 & 22.333 \\ 22.333 & 84. \end{bmatrix} + \gamma \begin{bmatrix} 9.7917 & 11.354 \\ 11.354 & 17.817 \end{bmatrix} \right\} \begin{bmatrix} d_1 \\ d_2 \end{bmatrix} = 0 \tag{20}$$

The eigenvalues of this matrix equation, $\gamma_1 = 1.5407$ and $\gamma_2 = 11.449$, may be obtained by solving a quadratic equation. For any eigenvalue, one of the d's can be arbitrarily selected, e.g., $d_1 = 1$, and the other d calculated. Once the d's are computed, the eigenfunction is obtained using equation (7) as

$$F_1(r) = f_1 - 0.085593 f_2 \tag{21a}$$

$$F_2(r) = f_1 - 0.89731 f_2 \tag{21b}$$

The temperature solution, equation (19), reduces to

$$\theta = 1 - 0.4258 F_1(r) \exp(-1.5407 \alpha_1 t/R_1^2) + 0.3018 F_2(r) \exp(-11.449 \alpha_1 t/R_1^2) \tag{22}$$

Similarly, a one-term solution yields $\gamma_1 = 15.5/9.7917 = 1.583$ and the temperature solution becomes

$$\theta = 1 - 0.3957 f_1 \exp(-1.583 \alpha_1 t/R_1^2) \tag{23}$$

The numerical values of f_1 and f_2 in equations (21a), (21b), and (23) are obtained from equation (18) when $r < 1$, otherwise equation (17) must be used. The worst agreement between a two-term solution and Table 1 is observed when $r = 0$. This is consistent with the behavior of the Galerkin solutions, which yield their maximum accuracy near the external surface. Equation (22), when $r = 0$ and $N = 2$, yields dimensionless temperatures of 0.0558, 0.6886, and 0.9333 for $\alpha_1 t/R_1^2 = 0.25$, 1, and 2. The corresponding values from Table 1 are 0.0797, 0.6919, and 0.9340. Also, a one-term solution using equation (23) results in the respective dimensionless temperatures of 0.0677, 0.7155, and 0.9416. The corresponding errors for a one-term solution are 15, 3.4 and 0.8 percent. When $N = 2$ these errors become 30, 0.48, and 0.07 percent, in-

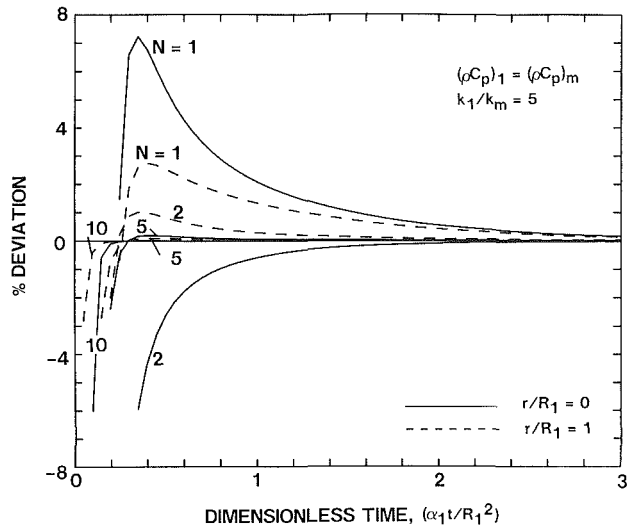

Fig. 6 Percent temperature deviation as a function of dimensionless time at $r/R_1 = 0$ and $r/R_1 = 1$ when $k_1/k_m = 5$ and $(\rho C_p)_1/(\rho C_p)_m = 1$

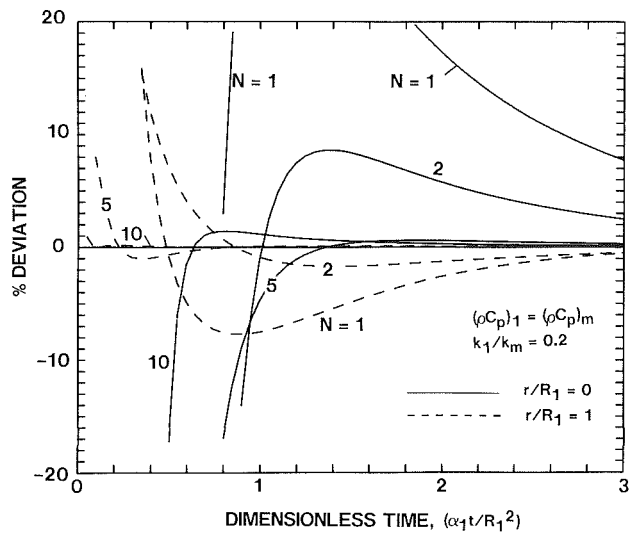

Fig. 7 Percent temperature deviation as a function of dimensionless time at $r/R_1 = 0$ and $r/R_1 = 1$ when $k_1/k_m = 0.2$ and $(\rho C_p)_1/(\rho C_p)_m = 1$

dicating a significant improvement in the large-time solution. The small-time results imply that more than two eigenvalues are needed when the dimensionless temperature is less than 0.1. Also, the percentage error is not a satisfactory means of presenting the errors. For instance, had the dimensionless temperature θ been written as $(T-T_s)/(T_0-T_s)$, the 15 and 30 percent errors would have been reduced to 1.4 and 2.6 percent. Usually, a single-term solution provides a relatively accurate answer for some applications. Indeed the error is quite small, even for a single-term solution, when $k_1/k_m > 1$. This is illustrated in Fig. 6 where the temperature deviation, $(\theta-\theta_r)/\theta_r$, for various 1, 2, 5, and 10 eigenfunctions is plotted as a function of dimensionless time. The dimensionless reference temperature θ_r for computing the deviation is a twelve-term solution for θ. The solid lines correspond to the temperature at $r/R_1 = 0$ and the dash lines are for $r/R_1 = 1$. The temperature deviation for most of the large-time-solution range is below 4 percent and rapidly drops to below 1 percent. Except for a very small time, the temperature deviation of a five-term solution is far below 1 percent. The fast convergence to the correct temperature solution, when $k_1/k_m > 1$, is particularly interesting because the k_1/k_m ratio in many candidate materials such as graphite-reinforced composites and solder balls in substrates of microelectronic chips is also larger than 1. Figure 7 is prepared to show that, when $k_1/k_m < 1$, the deviation of the temperature at $r = 0$ is much larger than those reported in Fig. 6. However, the dash lines corresponding to $r/R_1 = 1$ indicate reasonable accuracy when $N = 2$ or more. When $k_1/k_m < 1$, even the finite difference method required a much finer step size for an acceptable solution. Apparently, whenever the temperature gradient in the neighborhood of a point is rapidly changing direction, more eigenfunctions must be used to obtain an accurate solution at that point. In addition, when there is no other solution, the convergence shown in Figs. 6 and 7 becomes particularly important since it provides an indication of the accuracy of the solution.

A one-, two-, and even a three-term solution for this problem can be carried out without the use of a computer. In fact, the differentiations and integrations leading to the computation of a_{ij} and b_{ij} can be carried out manually with ease. The symbolic manipulator MACSYMA was used to expedite the calculations and to reduce the chance of mathematical errors. In more complex geometries, the numerical computation of a_{ij} and b_{ij} is necessary. In this case, if possible, the use of a large number of basis functions (large N) should be avoided because the number of multi-integrals will become large. In addition, when N is large, the numerical integrations must be carried out to a high degree of accuracy.

Several conclusions can be drawn from this example: (1) Numerical data with equal or better accuracy can be obtained using the HFC basis functions at a fraction of the computation costs of a comparable numerical solution. (2) The accuracy of a large-time solution is generally excellent; however, at small time, the magnitude of the error increases, especially when the temperature gradient changes direction. (3) A small number of basis functions is adequate for many applications.

Comments

Heterogeneous solids are encountered in microelectronic technology, bioengineering, composite materials, and many other engineering applications. A new procedure for solving numerous conduction problems in heterogeneous regions is introduced. This is a flexible procedure that can be used for single or multiple inclusions when dealing with various boundary conditions and that can accommodate a distributed volume heat source. Equation (14) represents a new analytical finding and its full implication is yet to be determined. Among the features that need further investigation are the performance study when the subregions are numerous, e.g., in composite materials, and the ability to deal with discrete volumetric heat sources of infinitesimal size, e.g., in microelectronic devices. Prior experience with this solution method suggests that, for the two applications just mentioned, the utilization of a large number of basis functions may be necessary. However, as demonstrated earlier, only a small number of basis functions is needed for many applications. Whenever there is a need for numerous eigenvalues, the basis functions with polynomial form should be replaced by other basis functions that more rigorously satisfy the linear independency condition, e.g., Chebyshev polynomials. The only advantage of polynomial basis functions is the simplicity of carrying out differentiation and integration.

Acknowledgments

This work is supported by the National Science Foundation Grant MEA 83-12754, and The Mechanical Engineering Department, University of Texas at Arlington.

References

Baker-Jarvis, J., and Inguva, R., 1983, "Heat Conduction in Heterogeneous Materials," ASME JOURNAL OF HEAT TRANSFER, Vol. 107, pp. 39–43.

Campo, A., 1982, "Estimate of the Transient Conduction of Heat in Materials With Linear Thermal Properties Based on the Solution for Constant Properties," *Wärme- und Stoffübertragung*, Vol. 17, pp. 1–9.

Carslaw, H. S., and Jaeger, J. C., 1959, *Conduction of Heat in Solids*, Clarendon Press, Oxford.

Chang, Y. P., and Poon, K. C., 1979, "Three-Dimensional Steady-State Heat Conduction in Cylinders of General Anisotropic Media," ASME JOURNAL OF HEAT TRANSFER, Vol. 101, pp. 548–553.

Chester, W., Bobone, R., and Brocher, E., 1984, "Transient Conduction Through a 2-Layer Medium," *Int. J. Heat Mass Transfer*, Vol. 27, pp. 2167–2170.

Clever, R. M., and Wassel, A. T., 1985, "Three-Dimensional Transient Heat Conduction in a Multilayer Medium," *J. Spacecraft and Rockets*, Vol. 22, pp. 211–214.

Haji-Sheikh, A., 1986, "On Solution of Parabolic Partial Differential Equations Using Galerkin Functions," *Integral Methods in Science and Engineering*, F. R. Payne et al., eds., Hemisphere, Washington, DC, pp. 467–479.

Haji-Sheikh, A., and Lakshminarayanan, R., 1987, "Integral Solution of Diffusion Equation: Part 2—Boundary Conditions of Second and Third Kinds," ASME JOURNAL OF HEAT TRANSFER, Vol. 109, pp. 557–562.

Haji-Sheikh, A., and Mashena, M., 1987, "Integral Solution of Diffusion Equation: Part 1—General Solution," ASME JOURNAL OF HEAT TRANSFER, Vol. 109, pp. 551–556.

Horvay, G., Mani, R., Veluswami, M. A., and Zinsmeister, G. E., 1973, "Transient Heat Conduction in Laminated Composites," ASME JOURNAL OF HEAT TRANSFER, Vol. 95, pp. 309–316.

Kantorovich, L. V., and Krylov, V. I., 1960, *Approximate Methods of Higher Analysis*, Wiley, New York.

Maewal, A., Bache, T. C., and Hegemeier, G. A., 1976, "A Continuum Model for Diffusion in Laminated Composite Media," ASME JOURNAL OF HEAT TRANSFER, Vol. 98, pp. 133–138.

Özişik, M. N., 1980, *Heat Conduction*, Wiley, New York.

Salt, H., 1983, "Transient Conduction in a Two-Dimensional Composite Slab—I. Theoretical Development of Temperature Mode," *Int. J. Heat and Mass Transfer*, Vol. 26, pp. 1611–1616.

Schachinger, E., and Sonnizer, B. Graz, 1980, "General Solution of the Two-Dimensional Heat Equation for Two Concentric Domains of Different Material," *Wärme- und Stoffübertragung*, Vol. 14, pp. 7–13.

SYMBOLICS, Inc., 1985, *Vax Unix Macsyma Reference Manual*, Version 11, Cambridge, MA.

Villsenor, R., and Squire, W., 1986, "Heat Conduction in a Slab With a General Boundary Condition: An Integral Equation Approach," *Integral Methods in Science and Engineering*, F. R., Payne et al., eds., Hemisphere, Washington, DC, pp. 551–562.

APPENDIX

Comments on the Green's Function Solution

When temperature is prescribed on the external surface, there is a singularity associated with using equation (4). It is a simple task to remove this singularity analytically. The procedure to remove the singularity begins by designating the surface temperature in equation (4) as $T_s(\mathbf{r}_s', \tau)$ where $\mathbf{r}_s'$ is the position vector $\mathbf{r}'$ defined at the external surface. Also, the functions $T^*(\mathbf{r}', \tau)$ and $f^*(\mathbf{r}', \tau)$ are defined so that

$$T^*(\mathbf{r}', \tau) = T_s(\mathbf{r}_s', \tau)\,|_{\mathbf{r}_s'=\mathbf{r}'} \tag{A1}$$

and

$$\nabla_0 \cdot [k \nabla_0 T^*(\mathbf{r}', \tau)] = f^*(\mathbf{r}', \tau) \tag{A2}$$

When equation (A2) is multiplied by G and equation (2) multiplied by $T^* = T^*(\mathbf{r}', \tau)$, then, after subtracting the former from the latter, the following relation is obtained:

$$T^* \nabla_0 \cdot (k \nabla_0 G) - G \nabla_0 \cdot (k \nabla_0 T^*)$$

$$T^* C(\mathbf{r}')\delta(\mathbf{r}' - \mathbf{r})\delta(\tau - t) = Gf^* - C(\mathbf{r}')\partial G/\partial \tau \tag{A3}$$

The integration of equation (A3) in τ should be carried out between the limits 0 and $t^* = t + \epsilon$, where ϵ is a small number. Additionally, subsequent to integration $\mathbf{r}'$ over the entire volume, application of the Green's theorem, and some algebraic reduction of terms, the result is

$$-\int_{\tau=0}^{t^*} d\tau \int_V kT_s \partial G/\partial n\,|_{S'}$$

$$dS' = C(\mathbf{r})T^* + \int_V C(\mathbf{r}) \left[\int_{\tau=0}^{t^*} T^*(\partial G/\partial \tau) d\tau \right] dV'$$

$$+ \int_{\tau=0}^{t^*} d\tau \int_V Gf^* dV' \tag{A4}$$

Integrating by parts and then letting ϵ go to zero, the term in the square bracket in equation (A4) becomes

$$\lim_{\epsilon \to 0} \int_{\tau=0}^{t^*} T^*(\partial G/\partial \tau) d\tau = \lim \left[GT^* \Big|_{\tau=0}^{t^*} - \int_{\tau=0}^{t^*} G(\partial T^*/\partial \tau) d\tau \right] = -G\Big|_{\tau=0} T^*(\mathbf{r}, 0)$$

$$- \int_{\tau=0}^{t} G(\partial T^*/\partial \tau) d\tau \Big] \tag{A5}$$

The substitution of equation (A5) in equation (A4) followed by the substitution of the resulting equation in equation (4) and some minor algebraic simplifications will produce the relation

$$C(\mathbf{r})T(\mathbf{r}, t) = C(\mathbf{r})T^*(\mathbf{r}, t) + \int_{\tau=0}^{t} d\tau \int_V G[g(\mathbf{r}', \tau)$$

$$- C(\mathbf{r}')\partial T^*(\mathbf{r}', \tau)/\partial \tau] dV' + \int_V C(\mathbf{r}')G\Big|_{\tau=0} [T_0(\mathbf{r}')$$

$$- T^*(\mathbf{r}', 0)] dV' + \int_{\tau=0}^{t} d\tau \int_V Gf^* dV' \tag{A6}$$

The value of the function $G = G(\mathbf{r}', -\tau\,|\mathbf{r}, -t) = G(\mathbf{r}', t\,|\mathbf{r}, \tau)$ is given by equation (6). If the $T^*(\mathbf{r}, t)$ is the quasi-steady solution, then $f^* = 0$. When both T_s and T_0 are constants and $g = 0$, equation (4) reduces to

$$C(\mathbf{r}) \left[\frac{T(\mathbf{r}, \tau) - T_s}{T_0 - T_s} \right] = \int_V C(\mathbf{r}')G\,|_{\tau=0} dV' \tag{A7}$$

Equation (A7) was used in the numerical example in the main text; see equation (19). Also, equation (A6) suggests various other approximations when the surface temperature has spatial dependence and a quasi-steady solution cannot be produced. The discussion of this and other implications are beyond the scope of this paper.

Steady-State Temperatures in an Infinite Medium Split by a Pair of Coplanar Cracks

Chang Shangchow
Department of Aircraft Engineering,
Northwestern Polytechnical University,
Xian, People's Republic of China

This article presents a study on the steady-state heat conduction in an infinite medium containing two coplanar cracks. Using an integral transform technique, formal temperature solutions have first been worked out for both the fundamental symmetric and antisymmetric cases. The explicit and exact expressions for temperatures are then developed via both the conventional inversion transform approach and an analytical continuation method proposed in this paper. Numerical results prepared from analytic and numerical methods are presented in graphic form for temperatures on the horizontal crack plane and on a plane slant to the cracks. The relative merit of various possible solution methods is also discussed.

Introduction

Real materials necessarily contain various forms of imperfections such as voids, inclusions, impurities, and so on. In many cases, the imperfections can be idealized as cracks, making the heat conduction in cracked solids a problem of engineering significance and the subject of much technical research. To determine the temperature in conductive media with cracks, it is usually necessary to follow two consecutive steps. In the first step we solve the heat conduction problem of the media in their pure form without any imperfections. To take the adiathermal condition, which really dominates on the crack surfaces, into consideration in the second step the problem prescribed by

$$\frac{\partial T}{\partial \bar{n}} = f(\bar{s}) \tag{1}$$

on the crack surfaces is considered. $f(\bar{s})$ is a given function obtained from the first step and can be of an arbitrary form. In the second step the original boundaries of the media under investigation can frequently be regarded as receding to infinity owing to the small crack length and large boundary dimensions.

From the preceding analysis it is seen that the heat conduction problem of cracked media can never be solved completely unless the temperature has been determined over the entire medium and for any form of $f(\bar{s})$ – a situation that has not been reached in previous references.

In the present study we treat an infinite medium with two coplanar cracks whose surfaces are subject to two basic forms of the heat flow function $f(\bar{s})$. Exact formulae for temperatures are obtained through the Mellin transform and integral equation techniques. To provide engineering design and practice with some useful information, a number of numerical results have been worked out using various analytic and numerical techniques. Additionally, it is found that the rather crucial procedure of inverse transform in obtaining the explicit temperature formulae can be bypassed by using a simpler and more direct approach of analytical continuation.

Problem and Fundamental Results

The subject under investigation in this study is an infinite medium containing a pair of symmetric coplanar cracks (see Fig. 1); the desired outcome consists of the temperature solution to the following equation and conditions:

$$\frac{\partial^2 T}{\partial r^2} + \frac{1}{r}\frac{\partial T}{\partial r} + \frac{1}{r^2}\frac{\partial^2 T}{\partial \theta^2} = 0 \tag{2}$$

$$\frac{1}{r}\frac{\partial T}{\partial \theta} = f(t) = \sum_{m=0}^{\infty} A_m t^m,\ t = re^{i\theta},\ \theta = 0,\ \pi,\ a < r < b \tag{3}$$

$$T \to 0, \qquad r \to \infty, \tag{4}$$

where the arbitrary function $f(t)$ is expressed in terms of t^m with sufficient generality. In view of symmetry or antisymmetry with respect to the x and y axes in geometry or temperature we can confine ourselves to finding a solution in the first quadrant region for the fundamental symmetric and antisymmetric cases of $f(t) = 1$ and $f(t) = t$, respectively.

Fundamental Symmetric Case. In this subsection the temperature function $T(r,\theta)$ is to be sought via equations (2), (3), and (4) with $f(t) = 1$ and the additional boundary conditions of

$$\frac{\partial T}{\partial \theta} = 0, \quad \theta = \frac{\pi}{2}, \quad 0 \le r < \infty \tag{5}$$

$$T = 0, \quad \theta = 0, \quad 0 \le r \le a, \quad b \le r < \infty \tag{6}$$

Using the Mellin transform of $T(r,\theta)$

$$\bar{T} = \int_0^{\infty} T r^{s-1} dr$$

in a straightforward manner it is readily seen that the transformed solution $\bar{T}$ satisfying equations (2), (4), and (5) takes the form (Sneddon, 1951)

$$\bar{T} = \frac{A(s)\cos s(\pi/2 - \theta)}{s \cos(s\pi/2)} \tag{7}$$

where the unknown function $A(s)$ should be determined from equations (3) and (6). For this purpose we assume

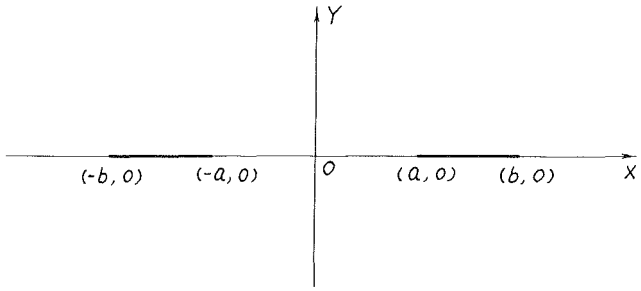

Fig. 1 The infinite medium and the coplanar cracks

Contributed by the Heat Transfer Division for publication in the JOURNAL OF HEAT TRANSFER. Manuscript received by the Heat Transfer Division January 7, 1985. Keywords: Conduction, Numerical Methods.

$$\theta=0,\ T(r,0)=\begin{cases}0, & 0\le r\le a & (8a)\\ \int_a^r p(t^2)dt, & a<r<b & (8b)\\ 0 & b\le r<\infty & (8c)\end{cases}$$

Directly from the above formulae and with

$$\theta=0,\quad \tilde{T}=\frac{A(s)}{s}$$

in mind the following formulae are obtained:

$$\int_a^b p(t^2)\,dt=0 \tag{9}$$

$$A(s)=-\int_a^b t^s p(t^2)\,dt \tag{10}$$

Note that equation (9) is in fact a condition for the single-valuedness of the temperature in a multiconnected geometry. The boundary condition on the crack surfaces (3) provides an inverse transform formula to determine $A(s)$ such that

$$M^{-1}\left[A(s)\tan\frac{s\pi}{2};\ r\right]=r,\quad a<r<b \tag{11}$$

Applying the Faltung theorem for Mellin transform on $A(s)$ $\tan s\pi/2$ in equation (11) together with

$$M^{-1}[A(s);\ r]=\begin{cases}0, & 0\le r\le a & (12a)\\ -tp(t^2), & a<r<b & (12b)\\ 0 & b\le r<\infty, & (12c)\end{cases}$$

and

$$M^{-1}\left[\tan\frac{s\pi}{2};\ r\right]=\begin{cases}-\dfrac{2r}{\pi(1-r^2)}, & r<1 & (13a)\\ \dfrac{2r}{\pi(r^2-1)}, & r>1 & (13b)\end{cases}$$

the following integral equation for the unknown function $p(t^2)$ is reached:

$$\frac{1}{\pi}\int_{a^2}^{b^2}\frac{p(t^2)}{t^2-r^2}\,dt^2=1,\quad a<r<b \tag{14}$$

Following Tricomi (1957), the above equation can be solved under the condition (9) in an ordinary manner and the final result is

$$p(t^2)=\frac{t^2-b^2\mathbf{E}/\mathbf{F}}{\sqrt{(b^2-t^2)(t^2-a^2)}} \tag{15}$$

where $\mathbf{E}=\mathbf{E}(k_0)$, $\mathbf{F}=\mathbf{F}(k_0)$.

Using the Faltung theorem on $\tilde{T}$ and noticing

$$M^{-1}\left[\frac{\cos s(\pi/2-\theta)}{s\cos(s\pi/2)};\ r\right]=\begin{cases}-\dfrac{2}{\pi}\displaystyle\sum_{n=1,3,5,\ldots}^{\infty}\frac{r^n\sin n\theta}{n}, & r<1 & (16a)\\ -1+\dfrac{2}{\pi}\displaystyle\sum_{n=1,3,5,\ldots}^{\infty}\frac{\sin n\theta}{nr^n}, & r>1 & (16b)\end{cases}$$

the formal solution of the temperature $T(r,\theta)$ is then obtained as follows:

$$T(r,\theta)=\begin{cases}\dfrac{2}{\pi}\displaystyle\int_a^b\left[\sum_{n=1,3,5,\ldots}^{\infty}\frac{r^n\sin n\theta}{nt^n}\right]p(t^2)\,dt, & 0\le r\le a & (17a)\\ \displaystyle\int_a^r\left[1-\frac{2}{\pi}\sum_{n=1,3,5,\ldots}^{\infty}\frac{t^n\sin n\theta}{nr^n}\right]p(t^2)dt+\frac{2}{\pi}\int_r^b\left[\sum_{n=1,3,5,\ldots}^{\infty}\frac{r^n\sin n\theta}{nt^n}\right]p(t^2)\,dt, & a<r<b & (17b)\\ \displaystyle\int_a^b\left[1-\frac{2}{\pi}\sum_{n=1,3,5,\ldots}^{\infty}\frac{t^n\sin n\theta}{nr^n}\right]p(t^2)\,dt, & b\le r<\infty & (17c)\end{cases}$$

Nomenclature

a = crack length parameter, Fig. 1
b = crack length parameter, Fig. 1
$\mathbf{E}(k_0)$ = complete elliptic integral of the second kind
$E(\phi,k_0)$ = incomplete elliptic integral of the second kind
$\mathbf{F}(k_0)$ = complete elliptic integral of the first kind
$F(\phi,k_0)$ = incomplete elliptic integral of the first kind
k_0 = $\sqrt{b^2-a^2}/b$
k_1 = $(1-k_0^2/2)/\sqrt{1-k_0^2}$
k_x = coefficient of thermal conductivity in the x direction
k_y = coefficient of thermal conductivity in the y direction
m = positive integer
M^{-1} = inversed Mellin transform operator
n = positive integer
$\tilde{n}$ = coordinate normal to the crack surface
$P_n(k_1)$ = Legendre polynomial of order n
r = radial coordinate in polar coordinates
R_e = real part of a complex quantity
s = transform variable
$\tilde{s}$ = coordinate tangential to the crack surface
t = r coordinate on the crack surface
T = temperature
$\tilde{T}$ = transformed temperature
x, y = rectangular coordinates
z = $x+iy$ = complex variable
$Z(\phi,k)$ = Jacobian zeta function
θ = polar angle in polar coordinates
ϕ = $\sin^{-1}\sqrt{(b^2-r^2)/(b^2-a^2)}$

Fundamental Antisymmetric Case. This case distinguishes itself from the preceding one merely in the boundary conditions on the y axis and the crack surfaces, i.e., in the present case equations (3) and (5) should respectively be rewritten as

$$\frac{1}{r}\frac{\partial T}{\partial \theta}=t, \quad t=re^{i\theta}, \quad \theta=0, \quad a<r<b \tag{18}$$

$$T=0, \quad \theta=\frac{\pi}{2}, \quad 0\le r<\infty \tag{19}$$

Now the solution procedure can be carried out in a manner similar to that for the symmetric case. We first prepare the transformed temperature $\bar{T}$, which satisfies equations (2), (4), and (19) such that

$$\bar{T}=\frac{A_1(s)\sin s(\theta-\pi/2)}{s\sin(s\pi/2)} \tag{20}$$

then express function $A_1(s)$ in terms of function $p_1(t^2)$ in the following form

$$A_1(s)=\int_a^b t^{s+1}p_1(t^2)\,dt \tag{21}$$

with

$$\theta=0,\ T(r,0)=\begin{cases}0, & 0\le r\le a & (22a)\\ \displaystyle\int_a^r t\,p_1(t^2)\,dt, & a<r<b & (22b)\\ 0, & b\le r<\infty & (22c)\end{cases}$$

$$\frac{1}{\pi}\int_{a^2}^{b^2}\frac{p_1(t^2)dt^2}{t^2-r^2}=1, \quad a<r<b \tag{26}$$

The above integral equation should be solved in association with the condition of

$$\int_a^b p_1(t^2)\,dt^2=0 \tag{27}$$

The final result is (Tricomi, 1957)

$$p_1(t^2)=\frac{t^2-(a^2+b^2)/2}{\sqrt{(b^2-t^2)(t^2-a^2)}} \tag{28}$$

Next we use

$$M^{-1}\left[\frac{\sin s(\theta-\pi/2)}{s\sin(s\pi/2)};\,r\right]=$$

$$\begin{cases}\dfrac{2}{\pi}\displaystyle\sum_{n=2,4,6,\ldots}^{\infty}\frac{r^n\sin n\theta}{n}, & r<1 & (29a)\\ 1-\dfrac{2\theta}{\pi}-\dfrac{2}{\pi}\displaystyle\sum_{n=2,4,6,\ldots}^{\infty}\frac{\sin n\theta}{n\,r^n}, & r>1 & (29b)\end{cases}$$

and the Faltung theorem to invert $\bar{T}$ into $T(r,\theta)$. The outcome is presented below:

$$T(r,\theta)=\begin{cases}\dfrac{2}{\pi}\displaystyle\int_a^b tp_1(t^2)\left[\sum_{n=2,4,6,\ldots}^{\infty}\frac{r^n\sin n\theta}{nt^n}\right]dt, & 0\le r\le a & (30a)\\ \displaystyle\int_a^r tp_1(t^2)\left[1-\frac{2\theta}{\pi}-\frac{2}{\pi}\sum_{n=2,4,6,\ldots}^{\infty}\frac{t^n\sin n\theta}{nr^n}\right]dt+\frac{2}{\pi}\int_r^b tp_1(t^2)\left[\sum_{n=2,4,6,\ldots}^{\infty}\frac{r^n\sin n\theta}{nt^n}\right]dt, & a<r<b, & (30b)\\ \displaystyle\int_a^b tp_1(t^2)\left[1-\frac{2\theta}{\pi}-\frac{2}{\pi}\sum_{n=2,4,6,\ldots}^{\infty}\frac{t^n\sin n\theta}{n\,r^n}\right]dt, & b\le r<\infty & (30c)\end{cases}$$

From equation (18) the following equation to determine $p_1(t^2)$ is obtained

$$M^{-1}\left[A_1(s)\cot\frac{s\pi}{2};\,r\right]=r^2, \quad a<r<b \tag{23}$$

Using

$$M^{-1}[A_1(s);r]=\begin{cases}0, & 0\le r\le a & (24a)\\ t^2p_1(t^2), & a<r<b & (24b)\\ 0, & b\le r<\infty & (24c)\end{cases}$$

and

$$M^{-1}\left[\cot\frac{s\pi}{2};\,r\right]=\frac{2r^2}{\pi(1-r^2)} \tag{25}$$

and utilizing the Faltung theorem we obtain

At present the formal solutions for two fundamental cases of heat flow on the crack surfaces have been worked out. The formal solutions still remain to be integrated into explicit forms and this will be done in the following section.

Inversion Procedure

In this section two procedures are presented for obtaining the temperature solutions from the corresponding transformed ones.

Inversion Transform Approach. This is the routine method in the integral transform technique. The inversion transform process is usually a rather crucial one, although we have presented the formal solutions (17*a*, *b*, *c*) and (30*a*, *b*, *c*) in the preceding section. Using the quadrature formulae contained in the Appendix, each term in equations (17*a*, *b*, *c*) and (30*a*, *b*, *c*) can be integrated into closed forms and therefore

$T(r,\theta)$ can be expressed explicitly. The final results are given below:

for $f(t)=1,\ 0\le r\le a,$

$$T(r,\theta)=\sum_{n=1,3,5,\ldots}^{\infty} C_n \frac{r_n}{n}\sin n\theta \tag{31}$$

$$C_n=\frac{1}{b^{n-1}}\left[\frac{1}{(1-k_0^2)^{\frac{n-1}{4}}}P_{\frac{n-3}{2}}(k_1)-\frac{\mathbf{E}}{\mathbf{F}}\cdot\frac{1}{(1-k_0^2)^{\frac{n+1}{4}}}P_{\frac{n-1}{2}}(k_1)\right] \tag{32}$$

with $P_{-1}(k_1)=1.$

for $f(t)=1,\ a<r<b,$

$$T(r,\theta)=\frac{b\mathbf{E}}{\mathbf{F}}F(\phi,k_0)-b\,E(\phi,k_0)+\sum_{n=1,3,5,\ldots}^{\infty}(G_n r^{-n}+H_n r^n)\frac{\sin n\theta}{n} \tag{33}$$

$$G_n=-\frac{2b^{n+1}}{\pi}\left(I_{n+1}-\frac{\mathbf{E}}{\mathbf{F}}I_{n-1}\right),\quad n=1,3,5,\ldots \tag{34}$$

$$I_0=\frac{\pi}{2}-\phi \tag{35a}$$

$$I_2=\left(1-\frac{k_0^2}{2}\right)\left(\frac{\pi}{2}-\phi\right)-\frac{k_0^2}{4}\sin 2\phi \tag{35b}$$

$$I_n=\frac{n-1}{n}\left(2-k_0^2\right)I_{n-2}-\frac{n-2}{n}(1-k_0^2)I_{n-4}-\frac{k_0^2}{2n}\sin 2\phi\,(1-k_0^2\sin^2\phi)^{\frac{n}{2}-1},\quad n=4,6,8,\ldots \tag{35c}$$

$$H_n=\frac{2}{\pi b^{n-1}}\left(J_{n-1}-\frac{\mathbf{E}}{\mathbf{F}}J_{n+1}\right),\quad n=1,3,5,\ldots \tag{36}$$

$$J_0=\phi, \tag{37a}$$

$$J_2=\frac{1}{\sqrt{1-k_0^2}}\tan^{-1}\left(\sqrt{1-k_0^2}\tan\phi\right) \tag{37b}$$

$$J_n=\frac{n-3}{n-2}\frac{2-k_0^2}{1-k_0^2}J_{n-2}-\frac{n-4}{n-2}\frac{1}{1-k_0^2}J_{n-4}-\frac{k_0^2}{2(n-2)(1-k_0^2)}\sin 2\phi\,(1-k_0^2\sin^2\phi)^{1-\frac{n}{2}},\quad n=4,6,8,\ldots, \tag{37c}$$

for $f(t)=1,\ b\le r<\infty,$

$$T(r,\theta)=\sum_{n=1,3,5,\ldots}^{\infty} D_n\frac{\sin n\theta}{nr^n} \tag{38}$$

$$D_n=b^{n+1}\left[\frac{\mathbf{E}}{\mathbf{F}}\left(1-k_0^2\right)^{\frac{n-1}{4}}P_{\frac{n-1}{2}}(k_1)-(1-k_0^2)^{\frac{n+1}{4}}P_{\frac{n+1}{2}}(k_1)\right] \tag{39}$$

for $f(t)=t,\ 0\le r\le a,$

$$T(r,\theta)=\sum_{n=2,4,6,\ldots}^{\infty} L_n\frac{r^n\sin n\theta}{n} \tag{40}$$

$$L_n=\frac{1}{b^{n-2}}\left[\frac{1}{(1-k_0^2)^{\frac{n-2}{4}}}P_{\frac{n}{2}-2}(k_1)-\frac{2-k_0^2}{2(1-k_0^2)^{\frac{n}{4}}}P_{\frac{n}{2}-1}(k_1)\right] \tag{41}$$

for $f(t)=t,\ a<r<b,$

$$T(r,\theta)=\frac{k_0^2b^2}{4}\left(\frac{2\theta}{\pi}-1\right)\sin 2\phi+\sum_{n=2,4,6,\ldots}^{\infty}P_n\frac{\sin n\theta}{n\,r^n}+\sum_{n=2,4,6,\ldots}^{\infty}Q_n\frac{r^n\sin n\theta}{n} \tag{42}$$

$$P_n=-\frac{2b^{n+2}}{\pi}\left(I_{n+2}-\frac{2-k_0^2}{2}I_n\right) \tag{43}$$

$$Q_n=\frac{2}{\pi b^{n-2}}\left(J_{n-2}-\frac{2-k_0^2}{2}J_n\right) \tag{44}$$

for $f(t)=t,\ b\le r<\infty,$

$$T(r,\theta)=\sum_{n=2,4,6,\ldots}^{\infty}\mathrm{M}_n\frac{\sin n\theta}{n\,r^n}, \tag{45}$$

$$\mathrm{M}_n=b^{n+2}\left[\frac{2-k_0^2}{2}(1-k_0^2)^{\frac{n}{4}}P_{\frac{n}{2}}(k_1)-(1-k_0^2)^{\frac{n+2}{4}}P_{\frac{n}{2}+1}(k_1)\right] \tag{46}$$

Analytical Continuation Approach. Consider the case of symmetric heat flow on the crack surfaces. From the boundary condition (3) with $f(t)=1$ and equation (15) it can be obtained that

$$\frac{\partial T}{\partial x}=p(t^2)=\frac{t^2-b^2\mathbf{E}/\mathbf{F}}{\sqrt{(b^2-t^2)(t^2-a^2)}} \tag{47a}$$

$$\frac{\partial T}{\partial y}=1 \tag{47b}$$

The above two formulae are valid on the upper crack surface, i.e., the upward segment of (a, b) on the x axis. On the other hand since

$$Q(z)=\frac{\partial T}{\partial x}-i\frac{\partial T}{\partial y} \tag{48}$$

presents itself as an analytic function in the entire quadrant region under study,[1] from the theory of analytical continuation (Macrobert, 1954) it can be assured that in the quadrant region there is

$$Q(z)=i\left[\frac{z^2-b^2\mathbf{E}/\mathbf{F}}{\sqrt{(z^2-a^2)(z^2-b^2)}}-1\right] \tag{49}$$

Similarly for the case of antisymmetric heat flow we obtain

$$Q(z)=i\left[\frac{z^3-(a^2+b^2)z/2}{\sqrt{(z^2-a^2)(z^2-b^2)}}-z\right] \tag{50}$$

[1] With the possible exception of two small regions around the crack tips.

The temperature functions then can readily be obtained via the integration in

$$T(r,\theta)=\mathrm{Re}\int_0^{re^{i\theta}} Q(z)\,dz \tag{51}$$

Note that both equations (49) and (50) contain the $r^{-1/2}$ type singularity at the crack tips. The integration can again be carried out exactly using the quadrature formulae in the Appendix. Also, since the function $1/\sqrt{(z^2-a^2)\,(z^2-b^2)}$ can be expanded into the following series form:

for $|z|\le a$,

$$\frac{1}{\sqrt{(z^2-a^2)\,(z^2-b^2)}}=$$

$$-\frac{1}{ab}\left(1+\frac{a^2+b^2}{2a^2b^2}\,z^2+\frac{3a^4+2a^2\,b^2+3b^4}{8a^4b^4}\,z^4+\ldots\right) \tag{52a}$$

for $a<|z|<b$,

$$\frac{1}{\sqrt{(z^2-a^2)\,(z^2-b^2)}}=$$

$$\frac{1}{ibz}\left[1+\frac{z^2}{2b^2}+\frac{a^2}{2z^2}+\frac{a^2}{4b^2}+\frac{3}{8}\left(\frac{z^4}{b^4}+\frac{a^4}{z^4}\right)+\ldots\right] \tag{52b}$$

for $b\le|z|$,

$$\frac{1}{\sqrt{(z^2-a^2)\,(z^2-b^2)}}=$$

$$\frac{1}{z^2}\left(1+\frac{a^2+b^2}{2z^2}+\frac{3a^4+2a^2b^2+3b^4}{8z^4}+\ldots\right) \tag{52c}$$

the integrand $Q(z)$ in equation (51) can be put into series form to obtain the following result:

for $f(t)=1,\ 0\le r\le a$,

$$T(r,\theta)=\left(1-\frac{b\mathbf{E}}{a\mathbf{F}}\right)r\sin\theta+\left(1-\frac{a^2+b^2}{2a^2}\cdot\frac{\mathbf{E}}{\mathbf{F}}\right)\frac{r^3\sin 3\theta}{3ab}$$

$$+\left(\frac{a^2+b^2}{2a^2b^2}-\frac{3a^4+2a^2b^2+3b^4}{8a^4b^2}\cdot\frac{\mathbf{E}}{\mathbf{F}}\right)\frac{r^5\sin 5\theta}{5ab}+\ldots \tag{53a}$$

for $f(t)=1,\ a<r<b$,

$$T(r,\theta)=r\sin\theta+\frac{1}{b}\left[\frac{a^2}{2}-\left(1+\frac{a^2}{4b^2}\right)\frac{b^2\mathbf{E}}{\mathbf{F}}\right]\log\frac{r}{a}$$

$$+\frac{1}{2b}\left(1+\frac{a^2}{4b^2}-\frac{\mathbf{E}}{2\mathbf{F}}\right)(r^2\cos 2\theta-a^2)+\ldots \tag{53b}$$

for $f(t)=1,\ b\le r<\infty$,

$$T(r,\theta)=\left(\frac{b^2\mathbf{E}}{\mathbf{F}}-\frac{a^2+b^2}{2}\right)\frac{\sin\theta}{r}+\frac{1}{6}\left[\frac{(a^2+b^2)b^2\mathbf{E}}{\mathbf{F}}\right.$$

$$\left.-\frac{3a^4+2a^2b^2+3b^4}{4}\right]\frac{\sin 3\theta}{r^3}+\ldots \tag{53c}$$

for $f(t)=t,\ 0\le r\le a$,

$$T(r,\theta)=\frac{1}{2}\left(1-\frac{a^2+b^2}{2ab}\right)r^2\sin 2\theta+\left[1-\frac{(a^2+b^2)^2}{4a^2b^2}\right]$$

$$\frac{r^4\sin 4\theta}{4ab}+\frac{a^2+b^2}{4a^3b^3}\left(\frac{1}{3}-\frac{3a^4+2a^2b^2+3b^4}{24a^2b^2}\right)r^6\sin 6\theta+\ldots \tag{54a}$$

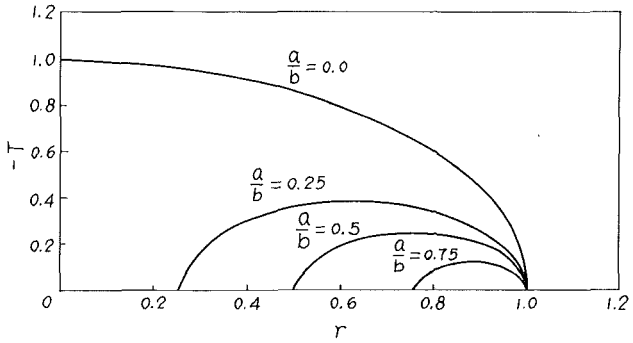

Fig. 2 Steady temperature for fundamental symmetric case ($\theta=0$)

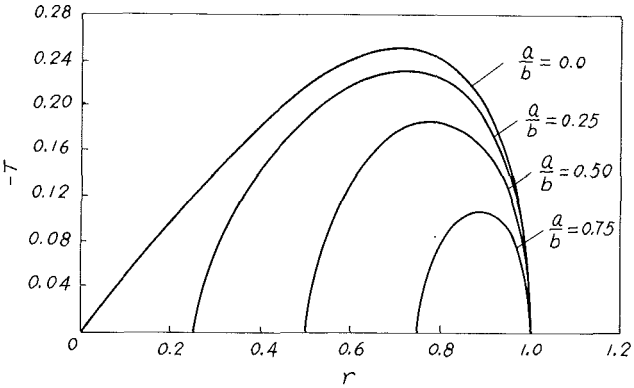

Fig. 3 Steady temperature for fundamental antisymmetric case ($\theta=0$)

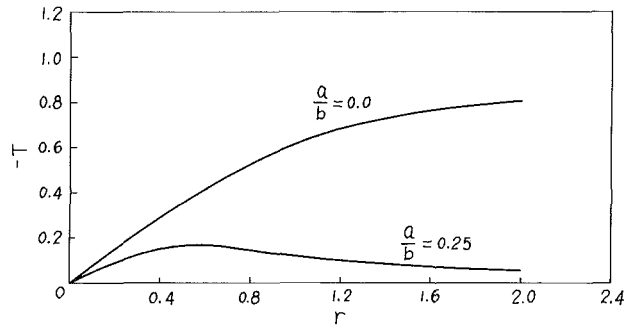

Fig. 4 Steady temperature for fundamental symmetric case ($\theta=\pi/4$)

for $f(t)=t,\ a<r<b$,

$$T(r,\theta)=\frac{1}{2}r^2\sin 2\theta-\left[b^2+\frac{a^2}{4}\left(1+\frac{a^2}{b^2}\right)\right]$$

$$\frac{r\cos\theta-a}{2b}-\frac{a^2(a^2+b^2)}{4b}\left(\frac{1}{a}-\frac{\cos\theta}{r}\right)+\ldots \tag{54b}$$

for $f(t)=t,\ b\le r<\infty$,

$$T(r,\theta)=-\frac{(a^2-b^2)^2}{16}\frac{\sin 2\theta}{r^2}-\frac{(a^2+b^2)\,(a^2-b^2)^2\sin 4\theta}{32r^4}+\ldots \tag{54c}$$

The above formulae for temperatures can be used to obtain exact values in numerical computation. The temperature formulae gained from two inversion approaches have been demonstrated to be in agreement with each other by analysis and numerical evaluation.

Numerical Results and Discussion

Based mainly on equations (31), (33), (38), (40), (42), and

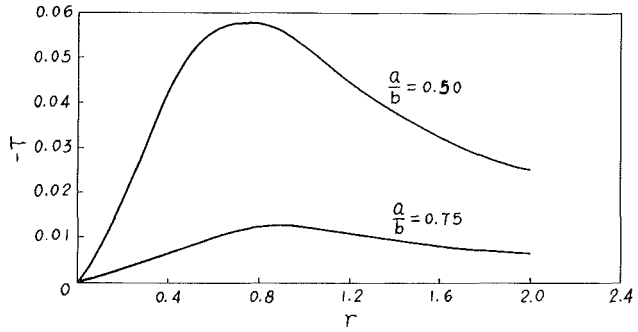

Fig. 5 Steady temperature for fundamental symmetric case ($\theta = \pi/4$)

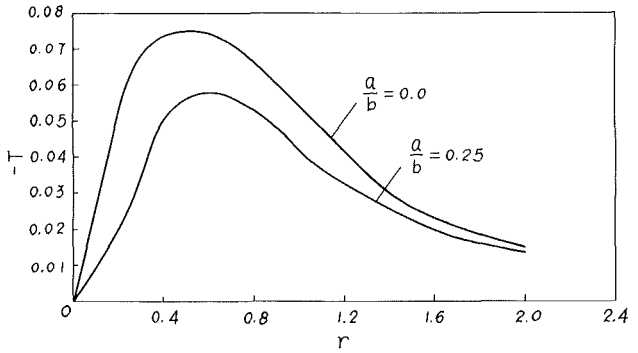

Fig. 6 Steady temperature for fundamental antisymmetric case ($\theta = \pi/4$)

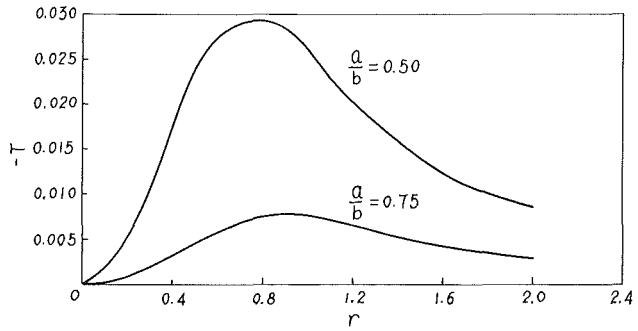

Fig. 7 Steady temperature for fundamental antisymmetric case ($\theta = \pi/4$)

(45), obtained from the inversion approach, numerical results of the temperature solutions are presented in graphic form in this section (see Figs. 2–7) for both the fundamental symmetric and antisymmetric cases.

Figures 2 and 3 show the temperatures on the horizontal (crack) plane for which $\theta = 0$. For this particular plane the temperature solution can be reduced into the following simplified form:

for the fundamental symmetric case,

$$T(r, 0) =$$

$$\begin{cases} 0, & 0 \le r \le a \quad (55a) \\ \dfrac{b\mathbf{E}}{\mathbf{F}} F(\phi, k_0) - bE(\phi, k_0) = -bZ(\phi, k_0), & a < r < b \quad (55b) \\ 0, & b \le r \le \infty \quad (55c) \end{cases}$$

Table 1 Numerical data for fundamental symmetric heat flow ($a/b = 0.5$, $b = 1.0$, $\theta = \pi/4$)

r	s	G	re
0.0	0.0	0.0	0.0
0.2	−0.0187784	−0.0187783	−0.0185709
0.4	−0.0413706	−0.0413478	−0.0408961
0.6	−0.0565011		−0.0565035
0.8	−0.0578618		−0.0579293
1.1	−0.0486244	−0.0482116	−0.0476959
1.2	−0.0445207	−0.0444519	−0.0439601
1.4	−0.0378023	−0.0377997	−0.0373803
1.6	−0.0324943	−0.0324943	−0.0321333
1.8	−0.0283432	−0.0283433	−0.0280282
2.0	−0.0250735	−0.0250736	−0.0247946

s = exact series solution
G = Gauss quadrature
re = rectangular numerical integration

for the fundamental antisymmetric case,

$$T(r, 0) = \begin{cases} 0, & 0 \le r \le a \quad (56a) \\ -\dfrac{1}{2}\sqrt{(b^2 - r^2)(r^2 - a^2)}, & a < r < b \quad (56b) \\ 0, & b \le r < \infty \quad (56c) \end{cases}$$

The numerical evaluation of the above formulae has been carried out either straightforwardly or with use of available mathematical tables in standard reference books (Abramowitz and Stegun, 1966; Byrd and Friedman, 1954).

Note that by the use of equations (55a,b,c) and (56a,b,c) the original mixed boundary condition on $\theta = 0$, $0 \le r < \infty$ (see equations (3) and (6)) can be replaced by a much simpler boundary condition purely in temperature form. The temperature in the medium then can also be obtained by solving an ordinary heat conduction problem whose solution techniques have fully been developed in well-known references (Sneddon, 1951; Carslaw and Jaeger, 1959).

Figures 4–7 depict the temperature distribution on the slant plane of $\theta = \pi/4$. The numerical computation in this situation is rather complicated and we have prepared the numerical data from three different approaches: exact series solution, Gauss quadrature, and rectangular numerical integration. The result is presented in Table 1 for a single case ($f(t) = 1$, $a/b = 0.5$) for comparison and as an example.

Numerical data from the exact series solution have been obtained using the rigorous expressions for temperatures in series form, equations (31)–(54). Highly accurate numerical data can be achieved provided the computation process has been carried out carefully and sufficient terms in series are taken into consideration. In Table 1 the related numerical data having four significant figures are obtained using 4–12 terms in the series. On the other hand, since the series contain some special functions, a specially designed computer program is needed that involves some relatively intricated computations.

Using the transformation $t^2 = (b^2 + a^2)/2 + (b^2 - a^2)\,\epsilon/2$, the integrals in equations (17a, c) can be put into the following form:

$$\int_{-1}^{1} \frac{f(\epsilon)\, d\epsilon}{\sqrt{1 - \epsilon^2}}$$

suitable for Gauss quadrature. The Gauss quadrature is able to give very accurate results. Numerical data presented in Table 1 that are exact to the first four figures have been obtained using merely 5–8 Gauss points in the quadrature and the required computer time was even shorter than that needed in the exact series solution approach.

Adequately precise data have been obtained also by utilizing the most conventional numerical integration technique, the rectangular numerical integration method. This method has the advantage of simplicity but is relatively time consuming on the computer.

However, all computations have been carried out on a microcomputer and all the numerical data obtained from different approaches are in close agreement. These facts manifest the validity of our analytical result as well as its effectiveness in numerical evaluation.

As expected from physical reasoning, temperature variances in the cracked medium depend on the lengths of and the distances between the cracks. Cracks of shorter length with longer distance between them induce a lower temperature on their surfaces and in other places of the medium.

By putting $a = 0$ in the related formulae, the temperature expressions for an infinite medium having a single crack of length $2b$ are obtained. Also, by rewriting the related formulae from the polar coordinates into the rectangular coordinates and then replacing y with $\sqrt{k_x/k_y}y$ we obtain the temperature solutions for an orthotropic infinite medium with two coplanar cracks.

Other kinds of integral transforms can also be used to solve the problem studied in this article. In Chen (1986), Fourier integral transform and triple series equations have been utilized to develop a comprehensive solution to the steady-state temperature in an orthotropic medium with cracks.

Conformal mapping is one of the well-known classic methods in the theory of heat conduction in solids. To use this method to solve the problem, a conformal mapping function should be used to map the quadrant region into a unit circle. The mapping function is not simple whereas the crux of the problem (mixed boundary conditions) remains. To solve the subsequent mixed boundary problem needs the use of dual or triple series technique. On the above basis it seems that the conformal mapping method is not very attractive in solving the problem. Similar arguments could be applied to other classic techniques.

Using suitable computation programs, finite element and other numerical techniques appear feasible to work out the temperature solution. However, it would be very difficult for these techniques to obtain accurate values of temperatures in the crucial region around the crack tips.

Synthesizing the above comments, it seems that this article has solved the problem under study with good accuracy in computation and relative simplicity in analysis.

Acknowledgments

The author is thankful to Mr. B. Chen for his assistance in numerical computation. He also wishes to express his gratitude to Professor K. T. Yang for handling the reviewing process of this paper. This work is supported in part by a research grant from the State Education Commission of China.

References

Abramowitz, M., and Stegun, I. A., 1966, *Handbook of Mathematical Functions*, National Bureau of Standards, Washington, DC.

Byrd, P. F., and Friedman, M. D., 1954, *Handbook of Elliptic Integrals for Engineers and Physicists*, Springer-Verlag, Berlin.

Carslaw, H. S., and Jaeger, J. C., 1959, *Conduction of Heat in Solids*, 2nd ed., Oxford University Press, London.

Chen, B., 1986, "Heat Conduction and Thermal Stresses in Orthotropic Media With Cracks," Master of Engineering Thesis, Northwestern Polytechnical University, Xian, People's Republic of China.

Gradshteyn, I. S., and Ryzhik, I. M., 1980, *Tables of Integrals, Series and Products*, Academic Press, New York.

Macrobert, T. M., 1954, *Functions of a Complex Variable*, Macmillan, London.

Sneddon, I. N., 1951, *Fourier Transforms*, McGraw-Hill, New York.

Tricomi, F. G., 1957, *Integral Equations*, Interscience Publishers, New York.

APPENDIX

The following are some quadrature formulae for integrals in equations (17) and (30) (Gradshteyn and Ryzhik, 1980):

$$\int_a^b \frac{t^m}{\sqrt{(b^2-t^2)\,(t^2-a^2)}}\,dt, \quad m=1,3,5,\ldots \tag{A1}$$

$$\int_a^b \frac{t^m}{\sqrt{(b^2-t^2)\,(t^2-a^2)}}\,dt = \frac{\pi}{2}\, b^{m-1}\,(1-k_0^2)^{\frac{m-1}{4}}\,P_{\frac{m-1}{2}}(k_1)$$

$$\int_a^b \frac{1}{t^m\sqrt{(b^2-t^2)\,(t^2-a^2)}}\,dt, \quad m=1,3,5,\ldots \tag{A2}$$

$$\int_a^b \frac{1}{t^m\sqrt{(b^2-t^2)(t^2-a^2)}}\,dt = \frac{\pi}{2b^{m+1}}\,(1-k_0^2)^{-\frac{m+1}{2}}\,P_{\frac{m+1}{2}}(k_1)$$

$$\int_a^r \frac{t^m}{\sqrt{(b^2-t^2)\,(t^2-a^2)}}\,dt, \quad m=0,1,2,\ldots \tag{A3}$$

$$\int_a^r \frac{t^m}{\sqrt{(b^2-t^2)\,(t^2-a^2)}}\,dt = b^{m-1}\int_\phi^{\frac{\pi}{2}} (1-k_0^2\sin^2\theta)^{\frac{m-1}{2}}\,d\theta = b^{m-1}I_{m-1}$$

with $t^2 = b^2-(b^2-a^2)\sin^2\theta$. The above integral can then be evaluated using equations (35a,b,c).

$$\int_r^b \frac{1}{t^m\sqrt{(b^2-t^2)\,(t^2-a^2)}}\,dt, \quad m=1,3,5,\ldots \tag{A4}$$

$$\int_r^b \frac{1}{t^m\sqrt{(b^2-t^2)\,(t^2-a^2)}}\,dt = \frac{1}{b^{m+1}}\int_0^\phi \frac{1}{(1-k_0^2\sin^2\theta)^{\frac{m+1}{2}}} = \frac{J_{m+1}}{b^{m+1}}$$

The above integral can then be evaluated using equations (37a,b,c).

K. D. Cole
Assistant Professor,
Department of Engineering and
Computer Science,
Trinity College,
Hartford, CT 06106
Assoc. Mem. ASME

J. V. Beck
Professor,
Heat Transfer Group,
Department of Mechanical Engineering,
Michigan State University,
East Lansing, MI 48824
Mem. ASME

Conjugated Heat Transfer From a Hot-Film Probe for Transient Air Flow

A numerical heat transfer model of a flush-mounted hot-film probe is presented for transient air flow. The model geometry involves simultaneous heat flow in both the air and the adjacent slab wall. Two cases are considered, steady laminar flow and laminar flow with a low-frequency oscillating component. In the steady-flow case, the numerical results compare favorably with steady calibration data from the literature. In the unsteady flow case, transfer function results are consistent with literature experimental data. In both cases, agreement with the literature data is obtained by calibrating the numerical model at zero flow.

1 Introduction

A flush-mounted hot-film probe is a thin metal film plated on an electrically insulating substrate such as glass or quartz. The probe is mounted flush with the wall with the hot film perpendicular to the flow. The probe is usually operated with a constant-temperature anemometer circuit. Such probes have been used for measurements of steady shear stress for many years (Brown, 1967; Rubesin et al., 1975). Transient measurements have not been successful for gas flows for two reasons. First, at low frequencies, the storage of heat in the substrate causes a phase lag in the signal (Cook et al., 1986). Second, the frequency response is not adequately known to allow the probe signal to be compensated at these low frequencies.

The subject of this paper is a numerical calculation to characterize the frequency response of a shear stress probe geometry at low frequencies. The numerical method for modeling a constant temperature anemometer is presented in section 2. The transient conjugated heat transfer problem is discussed in section 3. The results are compared with experimental data from the literature in sections 4 and 5. Finally, some conclusions are given.

Previous Work. Several studies have dealt with the effects of unsteady flow on shear-stress probes without substrate heat conduction. Menendez and Ramaprian (1985) have discussed a theory for water flow, which has less severe substrate conduction effects than for air flow. Mao and Hanratty (1985) have examined unsteady flow over a mass-transfer probe. They identify a range of low frequencies for which the transfer to the fluid is quasi-steady, and only at higher frequencies does the flow transient affect the probe transfer function. Mass transfer probes have no substrate effects, but they can only be used with liquids that are electrolytic solutions.

A one-dimensional transient model of a hot-film anemometer was discussed by Bellhouse and Rasmussen (1968). The geometry contained a one-dimensional substrate on one side of the hot film and an oscillating heat transfer coefficient on the other side. The average temperature on the hot film was held constant. Their perturbation solution showed that the response of the probe becomes independent of the frequency at high frequencies. That is, only at low frequency does the heat conduction to the substrate become important.

Brison et al. (1979) examined a two-dimensional model of a hot film on a wedge-shaped substrate. They used a finite element method to examine the transient heat transfer in the wedge geometry heated by a thin film and cooled by a fluid with an oscillating heat transfer coefficient. Their results showed a strong dependence on the Biot number. Specifically, as the Biot number increases, the phase lag between the heat transfer coefficient and the film temperature decreases. Also, the effects of substrate conduction can be minimized for the wedge geometry by placing the hot film as close as possible to the leading edge.

The Bellhouse study and the Brison study each used a spatially uniform, time-varying heat transfer coefficient to simulate the time-varying flow. However, the actual heat transfer coefficient is not spatially uniform—it is large on the hot film and small on the adjacent substrate (Ramadhyani et al., 1985). The present conjugated heat transfer calculation allows the heat transfer to vary over the interface. The input is the time-varying flow itself, and the spatially varying heat transfer coefficient can be calculated as a *result* of the present method.

Geometry. The geometry shown in Fig. 1 contains essential features of a hot-film probe. The two-dimensional geometry applies only to large-aspect-ratio hot films ($b/a \gg 1$). Perfect thermal contact exists among the fluid, the slab, and the hot film. The metal hot film is very thin, so its thermal mass may be neglected. The slab thickness D determines the mass of the slab that is involved with thermal storage. The back wall of the slab, fixed at $T = T_0$, functions as a heat leak to simulate heat losses from actual probes.

For air flow, radiation and natural convection are neglected, viscous dissipation is neglected, and the material properties are constant. The flow used in the model has a linear velocity profile ($u = \beta y_f$), and the temperature distribution in the flow is quasi-steady. The conduction of heat parallel to the wall is also neglected in the fluid flow. These assumptions are appropriate for air flow over a glass substrate, for a small hot film, for a moderate overheat ratio, and for low frequency flow transients. These assumptions are discussed in Cole and Beck (1986).

2 Constant Temperature Hot Film

In this section, the constant temperature anemometer problem is formulated as an inverse problem in heat transfer, and the solution with the exact matching method is outlined.

Inverse Heat Transfer Problem. The usual boundary value problem in heat transfer is to calculate the temperature and heat flux in a domain where all of the boundary and initial conditions are known. This is a *direct* problem in heat

Contributed by the Heat Transfer Division and presented at the National Heat Transfer Conference and Exhibition, Pittsburgh, PA, August 9-12, 1987. Manuscript received by the Heat Transfer Division January 15, 1987. Keywords: Conjugate Heat Transfer, Forced Convection, Transient and Unsteady Heat Transfer.

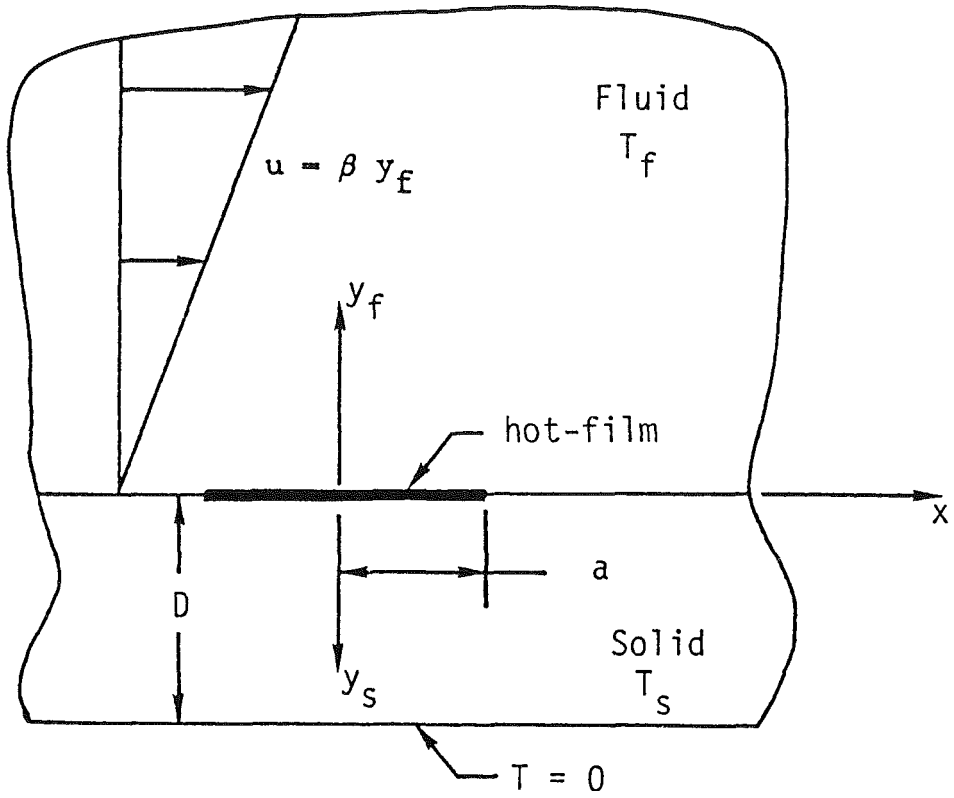

Fig. 1 Slab-wall geometry

transfer. An *inverse* heat transfer problem begins with a constraint condition (such as a temperature condition), and the task is to calculate the boundary or initial condition. The constant-temperature anemometer problem is an inverse heat transfer problem, because given the constraint that T_{av} is constant, the task is to find the hot-film heat flux $p(t)$.

Exact Matching Method. The inverse heat transfer problem is solved by the exact matching method (Beck et al., 1985). The procedure is to estimate $p(t)$ at discrete time steps, given all the geometry information, given the flow, and given all previous values of $p(t)$. The constraint is that the average temperature on the hot film is constant ($T_{av} = T_c$).

The exact matching method is based on a Taylor's series expansion of the hot-film average temperature with respect to the heat flux $p_M = p(t = t_M)$, where M is the time step index. In general, the dimensionless average temperature on the hot film depends on time, on geometry, on the fluid flow described by N_β, and on the heat flux $p(t)$. This dependence can be written $T^+_{av} = T^+_{av}(t^+, D/a, N_\beta, p(t_{M-1}), p_M)$. The parameter p_M has been isolated from $p(t_{M-1})$ to emphasize that the temperature T^+_{av} depends on the heat flux p_M in a continuous manner. The geometric parameter D/a is assumed to be constant in the following analysis.

Because the temperature is a continuous function of p_M, it can be expanded in a Taylor series about an arbitrary value of the hot-film output $\tilde{p}$

$$T^+_{av}(t, N_\beta, p(t_{M-1}), p_M) = T^+_{av}(t, N_\beta, p(t_{M-1}), \tilde{p}) + (p_M - \tilde{p}) \frac{\partial T^+_{av}(t, N_\beta, p(t_{M-1}), p_M)}{\partial p_M}\bigg|_{p_M=\tilde{p}} + \ldots \quad (1)$$

Nomenclature

a = half-length of hot film, m
b = half-width of hot film, m
D = slab-wall depth, m
k = thermal conductivity, W/(m K)
L_j = length of surface element j
M = number of timesteps, or current timestep
N = total number of surface elements
Nu = $2aq_0/(k_f(T_{av} - T_0))$ = Nusselt number
N_β = $k_f/k_s(\beta a^2/\alpha_f)^{1/3}$ = conjugate Peclet number
p = hot-film heat flux, W/m^2
Pe = $\beta a^2/\alpha_f$ = Peclet number
q = heat flux, W/m^2
t^+ = $\alpha_s t/a^2$ = dimensionless time
T^+ = $(T - T_0)k_s/(q_0 a)$ = temperature
u = x-direction velocity, m/s
x = streamwise coordinate, m
y = transverse coordinate, m
α = thermal diffusivity, m^2/s
β = velocity gradient, s^{-1}
ϕ = influence function, K m^2/W
ψ = fundamental solution, K m^2/W
ω = angular frequency, s^{-1}
ω^+ = $\omega D^2/\alpha_s$

Superscripts

f = fluid
s = solid
$+$ = dimensionless variable

Subscripts

av = spatial average on the hot film
f = fluid
k = time index
s = solid
0 = initial or constant value

It turns out that T_{av}^+ is a *linear* function of p_M, so that the second and higher order terms of the Taylor series are exactly zero. The computation of temperature T_{av}^+ is discussed below in section 3.

In the exact matching method, the calculated temperature T_{av}^+ is made exactly equal to the required hot-film temperature T_c^+. Then, equation (1) can be written as

$$T_c^+ = T_{av}^+(t, N_\beta, p(t_{M-1}), \tilde{p}) + [p_M - \tilde{p}]X(t, N_\beta, p(t_{M-1})) \quad (2)$$

where X is the sensitivity coefficient, defined as

$$X(t, N_\beta, p(t_{M-1})) = \frac{\partial T_{av}^+(t, N_\beta, p(t_{M-1}), p_M)}{\partial p_M}\bigg|_{p_M=\tilde{p}} \quad (3)$$

Note that the sensitivity coefficient is not a function of p_M because T_{av}^+ is a *linear* function of p_M. Equation (2) can now be solved for the estimated value p_M

$$p_M = \tilde{p} + [T_c^+ - T_{av}^+(t, N_\beta, p(t_{M-1}), \tilde{p})]/X(t, N_\beta, p(t_{M-1})) \quad (4)$$

The computation procedure at each time step is to choose a value of $\tilde{p}$, calculate the temperature T_{av}^+ and the sensitivity coefficient X, and then calculate p_M from equation (4). Any value can be used for $\tilde{p}$, even zero. Then, the value of M is increased by 1, and the value of p_M at the next time step is calculated, and so on, to calculate the function $p(t)$. The transfer function of the anemometer signal is calculated from $p(t)$.

Sensitivity Coefficient. The sensitivity coefficient X is calculated by a difference equation for temperature at each time step. The temperature T_{av}^+ is calculated twice, once with $\tilde{p}$ and once with a slightly perturbed value of $\tilde{p}$, $(1 + \epsilon)\,\tilde{p}$, where ϵ is a small parameter, perhaps 0.0001. Then the sensitivity coefficient is given by

$$X(t, N_\beta, p(t_{M-1})) = \{T_{av}^+[t, N_\beta, p(t_{M-1}), (1+\epsilon)\tilde{p}] - T_{av}^+[t, N_\beta, p(t_{M-1}), \tilde{p}]\}/\epsilon\tilde{p} \quad (5)$$

3 Average Temperature on the Hot Film

Conjugated Heat Transfer Problem. The average temperature on the hot film is found from a constant-property, conjugated heat transfer problem:

Fluid:

$$\beta(t)y_f \frac{\partial T^f}{\partial x} = \alpha_f \frac{\partial^2 T^f}{\partial y_f^2} \quad (6)$$

Solid:

$$\frac{\partial T^s}{\partial t} = \alpha_s\left(\frac{\partial^2 T^s}{\partial x^2} + \frac{\partial^2 T^s}{\partial y_s^2}\right) \quad (7)$$

The boundary and initial conditions are:

$$T^f(x \to \pm\infty, y_f, t) - T_0 = T^s(x \to \pm\infty, y_s, t) - T_0 = 0 \quad (8a)$$

$$T^s(x, y_s = D, t) - T_0 = 0 \quad (8b)$$

$$T^f(x, y_f \to \infty, t) - T_0 = 0 \quad (8c)$$

$$T^f(x, y_f, t=0) - T_0 = T^s(x, y_s, t=0) - T_0 = 0 \quad (8d)$$

where T_0 is the initial temperature. The matching conditions at the interface between the solid and the fluid are

$$T^f(x, y_f = 0, t) = T^s(x, y_s = 0, t) \quad (9a)$$

$$p(t)P(x) = -k_f \frac{\partial T^f}{\partial y_f}(x, 0, t) - k_s \frac{\partial T^s}{\partial y_s}(x, 0, t) \quad (9b)$$

The heat flux $p(t)$ drives the heat transfer. The term $P(x)$ is a place-keeping dimensionless quantity equal to 1 on the hot film and 0 elsewhere. The task is to calculate the average temperature on the hot film when $p(t)$ and $\beta(t)$ are given.

Unsteady Surface Element Method. The unsteady surface element (USE) method was applied by Cole and Beck (1986) to conjugate heat transfer from a semi-infinite wall. The present work extends the method to the slab-wall geometry. An advantage of the USE method is that only the active interface between the fluid and the solid must be discretized, which reduces the two-dimensional transient problem to a one-dimensional transient problem. The method requires linear partial differential equations (constant property, forced convection). A brief discussion of the numerical method is presented below.

The temperatures in the fluid and the solid are each given by a Duhamel's integral of the unknown interface heat flux and a known "fundamental solution." The fundamental solutions, named ψ^f and ψ^S, are closed-form analytical expressions that are listed in the Appendix. Purely numerical fundamental solutions can be applied to the USE method, but none are considered here.

When the Duhamel's integrals for temperature are substituted into the temperature matching condition, equation (9*a*), a single integral equation results

$$\int_{-\infty}^{\infty}\int_{\lambda=0}^{t} q^f(x', \lambda)\frac{\partial^2\psi^f(x-x', y_f, t-\lambda)}{\partial x'\,\partial t}\,dx'\,d\lambda = \int_{-\infty}^{\infty}\int_{\lambda=0}^{t} q^s(x', \lambda)\frac{\partial^2\psi^s(x-x', y_s, t-\lambda)}{\partial x'\,\partial t}\,dx'\,d\lambda \quad (10)$$

This is the USE equation. Note that each integral can be interpreted as a convolution of a heat flux with a known impulse response to give a temperature. In this view, the ψ functions are step responses.

The USE equation is solved numerically for $q^f(x, t)$ by discretizing the interface into N surface elements, by discretizing over time, and by taking the heat flux to be piecewise constant over each surface element and over each time step. Then the USE equation can be written as a set of matrix equations containing convolution sums over time

$$\sum_{k=1}^{M}(\boldsymbol{\phi}_{M-k+1}^f - \boldsymbol{\phi}_{M-k}^f)\mathbf{q}_k^f = \sum_{k=1}^{M}(\boldsymbol{\phi}_{M-k+1}^s - \boldsymbol{\phi}_{M-k}^s)(p_k\mathbf{P} - \mathbf{q}_k^f) \quad (11)$$

Here $\mathbf{q}_k^s$ has been eliminated with the heat flux matching condition, equation (9*b*). Subscript k is the time index. Vectors $\mathbf{P}$ and $\mathbf{q}_k^f$ are $N \times 1$. Matrix $\boldsymbol{\phi}_k^s$ is $N \times N$ and has components

$$(\boldsymbol{\phi}_k^s)_{ij} = \psi^2(x_i - (x_j - L_j/2), y_s = 0, t_k) - \psi^s(x_i - (x_j + L_j/2), y_s = 0, t_k) \quad (12)$$

where x_j is the coordinate of the center of element j with length L_j. Matrix $\boldsymbol{\phi}_k^f$ is similarly defined. Equation (11) can be solved for the heat fluxes $\mathbf{q}_k^f$, $k = 1, 2$, and so on, by starting with the known initial condition and stepping forward through time. At $t = 0$ the temperature is everywhere zero and all the heat fluxes are identically zero. At $M = 1$ (the first time step), the matrix equation can be solved for $\mathbf{q}_1^f$. Then, at $M = 2$, $\mathbf{q}_2^f$ can be found, and so on up to the desired time step.

After all the heat fluxes have been found, the interface temperature can be found from the right-hand side of equation (11)

$$\mathbf{T}_M = \sum_{k=1}^{M-1}(\boldsymbol{\phi}_{M-k+1}^s - \boldsymbol{\phi}_{M-k}^s)(p_k\mathbf{P} - \mathbf{q}_k^f) + \boldsymbol{\phi}_1^s(p_M\mathbf{P} - \mathbf{q}_M^f) \quad (13)$$

The first term in this expression for $\mathbf{T}_M$ is a convolution sum over all past events. The second term contains the present

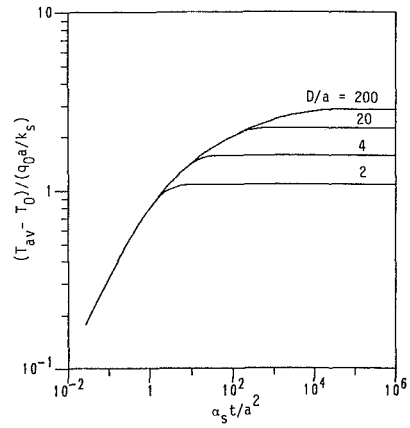

Fig. 2 Spatial average temperature on the hot film at $N_\beta = 0.0724$

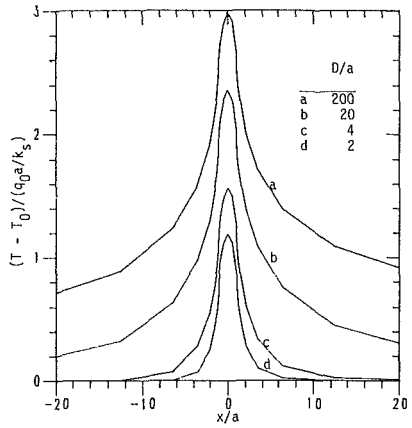

Fig. 3 Steady interface temperature at $N_\beta = 0.0724$

heater output p_M, and this term demonstrates that temperature has a *linear* dependence on p_M. Finally, T_{av} is calculated at each time step with an area-weighted average

$$T_{av}(t, N_\beta, p(t_{M-1}), p_M) = \sum_{j=1}^{n} T_M(x_j) L_j/(2a) \tag{14}$$

where j is summed only over those surface elements on the hot film itself.

Two calculations of T_{av}^+ are required at each time step to find the sensitivity coefficient, but the convolution sum from equation (13) is calculated only once at each time step. This is an important point, as the convolution sum can require a considerable computation effort when M is large.

4 Results—Steady Flow

In this section, interface temperature results are presented for a steady flow with heat transfer due to a step change in the hot-film output flux. The USE method alone is sufficient to obtain these results. The exact matching method is not required because the hot-film heat flux is a known constant. The transient results give the time constant of the anemometer geometry. The steady-state results can be scaled to give the Nusselt number behavior of the constant-temperature hot film in a steady flow.

For a step change in the heat flux, the dimensionless interface temperature depends on two parameters and two variables (Cole and Beck, 1986): $T^+ = T^+(x^+, t^+, N_\beta, D/a)$. For the numerical results presented here, seven surface elements are placed on the hot film itself, and a total of 29 surface elements are placed on the interface. Small elements are placed at the edges of the hot film, and progressively larger elements are symmetrically placed farther from the hot film. The numerical uncertainty of the temperature results are less than 0.3 percent based on studies of the time step size and the surface element size.

Table 1 Simulated calibration data, $2aq_0/(k_f(T_{av} - T_0))$ versus $Pe^{1/3}$, for various air/glass geometries

$Pe^{1/3}$	$D/a=2$	4	20	200
1.414	75.76	55.60	34.86	25.21
3.05	77.85	57.58	37.58	29.47
5.21	80.17	60.24	40.92	34.27
6.56	81.77	61.93	43.06	37.04
8.27	83.80	64.08	45.74	40.32

Transient Results. The initial temperature is everywhere zero, and at $t = 0$ the hot-film heat flux is set to q_0. In Fig. 2 the average hot-film temperature versus time is shown for several values of D/a and for $N_\beta = 0.0724$ ($\beta = 10{,}000\ s^{-1}$ for air flow over glass). The range $0.005 < N_\beta < 0.5$ for $a = 0.25$ represents laminar flow for which natural convection can be neglected.

At early times, Fig. 2 shows that the variation in wall depth D has no effect since all of the curves lie together. As time proceeds, the thinnest wall case becomes steady first, with the others becoming steady in succession, each with a successively higher steady-state temperature. A rough estimate of the time to reach steady state is about D^2/α_s seconds. This estimate applies to the air/glass geometry because the heat transfer to the glass dominates the transient response.

Steady Results. The steady-state results can be calculated with a single large time step. In Fig. 3 the steady interface temperature is shown for several values of D/a for $N_\beta = 0.0724$. The flow direction is from left to right. At $D/a = 200$, the temperature distribution is asymmetric due to the flow—cooler upstream and warmer downstream. However, at $D/a = 2$, the temperature distribution is nearly symmetric around the center of the hot film. This indicates that the flow has a small effect on the interface temperature in the thin wall case. In Table 1, steady Nusselt numbers are listed versus $Pe^{1/3}$ for several values of D/a. These values are a family of simulated calibration curves for steady wall shear stress probes.

Comparison With Steady Experimental Data. Comparisons with two data sets are presented here, Brown (1967) and Rubesin et al. (1975). The data is in the form of Nusselt nubmer versus $Pe^{1/3}$. The strategy for comparing the present work with experimental data has been to match the numerical model with the data at zero flow. This "zero-flow calibration" allows the numerical model to predict the flow behavior of the actual sensors.

The zero-flow Nusselt numbers are found from the experimental data by fitting a straight line to the data and by extrapolating to $Pe^{1/3} = 0$. Then, the D/a value is chosen so that the steady-state average temperature on the heated region at zero flow corresponds to the zero-flow Nusselt number from the experimental data. For Brown, the zero-flow Nusselt number is 47, and the corresponding D/a for the model is 5.8. For Rubesin, the zero-flow Nusselt number is 9.1, and the corresponding value of D/a is 1.84. In Fig. 4 the calibrated USE results are shown with the experimental data. The USE values agree with the experimental data to within 15 percent for the Rubesin data and within 8.6 percent for the Brown data; the agreement is actually very good on the average.

5 Results—Flow With an Oscillating Component

In this section the exact matching method is used to

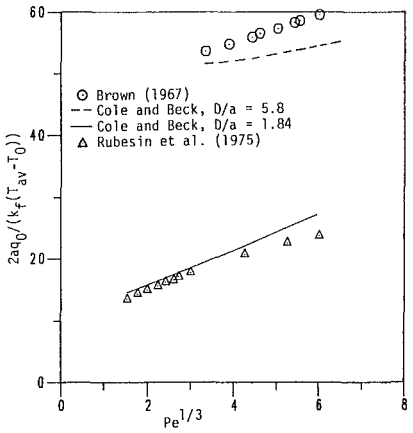

Fig. 4 Steady literature data and calibrated simulation results

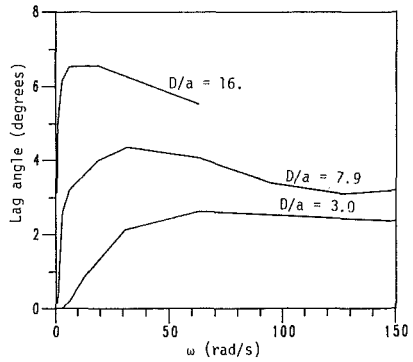

Fig. 5 Phase lag for flow with a 10 percent sinusoidal component for N_β = 0.157

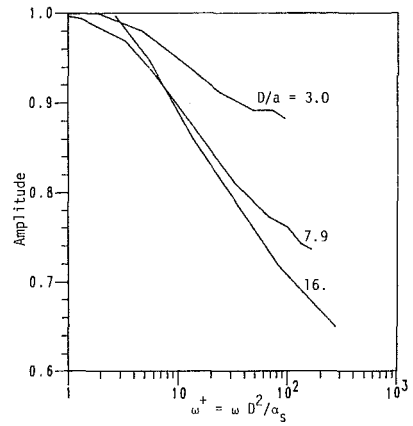

Fig. 6 Normalized amplitude response for flow with a 10 percent sinusoidal component for N_β = 0.157

calculate the hot-film response to unsteady flow. Any time function can be used as an input to the exact matching method—step, ramp, sinusoid, etc. A flow with a ±10 percent oscillating component is used here to find the transfer function of the hot-film model.

Transfer Function. The simulation for flow with an oscillating component is carried out over enough time steps so that any startup transients have died away. The phase and amplitude information is calculated from the $p(t)$ results with a nonlinear estimation program named NLINA that performs a least-squares fit between $p(t)$ and a sinusoid. A minimum of 12 data points is placed within each sinusoidal period (period = $2\pi/\omega$), and an integral number of sinusoidal periods is examined with NLINA in each case. By also examining 24 and 48 data points per sinusoidal period, the uncertainty in the results is estimated to be about 1 deg for the phase lag, and about 1 percent for the amplitude.

Figure 5 is a plot of phase lag (deg) versus frequency for N_β = 0.157 (β_0 = 16860 s^{-1}, a = 0.076 mm, air/glass). As the frequency goes to zero, the phase lag tends to zero, so that the probe signal follows the shear stress. Each value of D/a has a distinct frequency at which the maximum phase lag occurs. Over this range of frequencies, the phase lag is small compared to a complete cycle of 360 deg.

Figure 6 is a plot of normalized response amplitude versus ω^+. The amplitudes are normalized by the steady (ω = 0) response. For $\omega^+ < 1$, the probe follows the flow oscillations without appreciable error. For $\omega^+ > 10$, the amplitude decreases and the decrease occurs faster with the larger D/a. Amplitude attenuation of up to 30 percent is present over these frequencies. This indicates that frequency-dependent effects cannot be neglected for hot-film probes in air flow. That is, steady calibration cannot be used for transient shear-stress measurements at these frequencies.

The frequencies in the simulation are limited to ω^+ = 100 or so because of a practical limit on the number of time steps in the calculation. Many small time steps must be used to calculate higher frequencies. The present version of the USE method uses equal-sized time steps, beginning at a zero-temperature condition. To achieve "steady" oscillating behavior, the time span must be large enough so that the startup transient can decay away. For the Prime 750 computer used for this research, a practical limit of several hours of computer time gives about 600 time steps with 30 surface elements.

Comparison With Unsteady Experimental Data. Cook et al. (1986) studied the frequency response of flush-mounted probes to laminar flow with an oscillating component. Cook reported only phase angle information as a function of frequency. The probe was mounted flush with the surface of a plexiglass flat plate, and the approach flow over the flat plate contained an oscillating component. The phase lag for the probe was found by relating the phase angle of the unsteady wall shear stress (found from laminar theory) to the phase angle of the probe output voltage.

Cook et al. varied the flow oscillation frequency from 3 to 20 Hz, low enough that the fluid-flow thermal transient was always quasi-steady. Thus, the phase lag that they observed in the wall shear stress was due to the substrate heat conduction.

Zero-Flow Calibration. A zero-flow calibration is used to match the simulation geometry with the probe geometry used by Cook et al. In the steady-flow case, the zero-flow Nusselt number was used above to calibrate the simulation geometry. For transient flow, the criterion is the time constant of the probe at zero flow. The time constant for the present work is the time for the probe to respond to a step input of heat flux. The task is to choose the slab-wall thickness, D/a, that gives the same time constant as the probe used by Cook et al.

Cook does not report a time constant for the TSI probe used in his experiments (TSI, Inc., St. Paul, MN). However, geometric information about the probe is available to allow the construction of a detailed thermal model of the TSI probe itself, from which a zero-flow time constant may be estimated. The geometry of the TSI probe and the thermal model for the time constant are shown in Fig. 7. The TSI probe is model number 1237 Au, which is a platinum film plated on a quartz substrate. The quartz substrate is a cylinder mounted in the end of a stainless steel tube.

The thermal model of the probe is a semi-infinite cylinder,

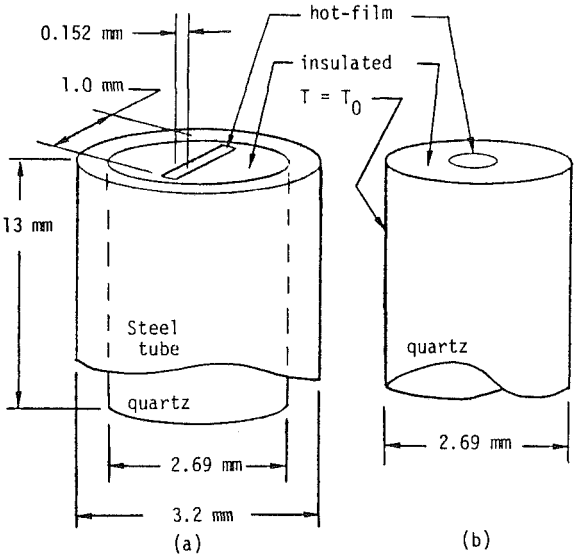

Fig. 7 Geometry of (*a*) the TSI probe and (*b*) the thermal model for the time constant

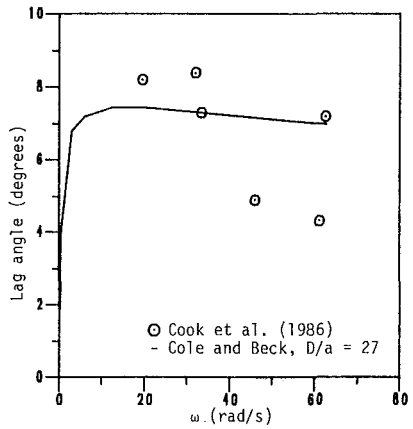

Fig. 8 Phase lag for literature data and simulation results with N_β = 0.0926

heated on the end over a circular region. The heated region has the same area as the hot film on the TSI probe. The region adjacent to the circular heated region is insulated to simulate zero flow. The outside radius of the cylinder is maintained at $T = T_0$ to simulate the heat lost to the steel tube. Initially the temperature is T_0. The time constant is the time for the average temperature on the heated region to reach 99 percent of its steady-state value. This thermal model is only meant to represent an approximate value that would ideally be measured in the laboratory. Also, this thermal model does not include thermal effects of the wall in which the probe is mounted. Many authors have observed that the material in which the probe is mounted affects the probe calibration.

The thermal model for the time constant is analyzed with a Green's function analytical solution. About 20 terms of an infinite series involving Bessel functions are required for four-digit accuracy. For $\alpha_{quartz} = 8.3\ (10^{-7})\ m^2/s$, the time constant for the thermal model is 5.35 s. The same time constant for the slab-wall geometry at zero flow occurs at $D/a = 27$. Again, if unsteady experimental calibration data are available, they should be used to find the probe time constant. Such data could also be used to find the thermal properties of the probe (k_s, α_s).

To be consistent with Cook et al., the phase lag is calculated not from the simulated heat flux signal p, but from $p^{1/2}$, which is proportional to the output voltage of an anemometer circuit. However, there is no difference in the phase lag calcualted from p or calculated from $p^{1/2}$. Figure 8 shows phase lag versus frequency for the experimental data compared to the simulation results for $D/a = 27$ and $N_\beta = 0.0926$ ($\beta_0 = 16860\ s^{-1}$, $a = 0.076$ mm, air/quartz). The simulation results are consistent with the experimental data. Cook et al. report that the experimental data contain an uncertainty of ±3 deg. Thus, the agreement is excellent.

Discussion. The phase lag in the unsteady probe signal is caused by the heat conduction in the probe substrate. Even though the *average* temperature on the hot film is maintained by the anemometer circuit, the steady-state distribution of temperature on the hot film is slightly different for each value of the flow. When the flow changes rapidly, the substrate cannot immediately adjust to a new temperature distribution, so the probe signal lags the flow. The phase lag is a maximum at a frequency where the transient heat conduction penetrates the whole substrate. At higher frequencies, the phase lag decreases because only a thin layer of the substrate is involved with the transient heat transfer.

The zero-flow calibration is different for the steady and unsteady cases because different results are of interest in each case. The steady Nusselt number comes from the steady, or d-c, portion of the probe signal, which depends on the heat leakage from the probe. The phase lag comes from the transient, or a-c, portion of the probe signal, which depends upon the time constant of the probe. The simple slab-wall geometry is useful in each case, but a more elaborate geometry would be needed to satisfy simultaneously both the steady and unsteady calibrations.

6 Summary and Conclusions

A numerical conjugated heat transfer model is presented for the flush-mounted hot-film probe in air flow. The unsteady surface element method is applied in its most efficient form with analytical fundamental solutions. The steady-state results agree with two sets of experimental data from the literature within 15 percent if the numerical model is calibrated for the heat losses that are present in the actual hot-film probes.

The USE method and an inverse heat transfer algorithm are combined to simulate a constant-temperature, flush-mounted, hot-film anemometer. This is the first conjugated heat transfer simulation of this device. Transfer function results are presented for laminar flow with a low-frequency oscillating component. The amplitude response varies dramatically with frequency, which means that steady theory and steady calibrations cannot be used for transient shear stress measurements in gases.

The phase angle response is consistent with literature data if the numerical simulation is calibrated with the probe time constant. An estimate of the probe time constant has been used to demonstrate the procedure. The phase angle response is small (< 8 deg), so that to a first approximation, simple amplitude compensation of transient probe signals may be possible. Further research may lead to compensation of transient probe signals to give transient wall shear stress in gas flows.

Acknowledgments

The research was sponsored in part by the National Science Foundation under Grant No. MEA 81-21499. Computer facilities were provided by the Case Center for Computer-Aided Design at Michigan State University.

References

Beck, J. V., Blackwell, B., and St. Clair, C. R., Jr., 1985, *Inverse Heat Conduction*, Wiley, New York.

Beck, J. V., and Keltner, N. R., 1985, "Green's Function Partitioning Method Applied to Foil Heat Flux Gages," presented at the National Heat Transfer Conference, Denver, CO, Aug. 1985, ASME Paper No. 85-HT-56.

Bellhouse, B. J., and Rasmussen, C. G., 1968, "Low-Frequency Characteristics of Hot-Film Anemometers," *DISA Information*, No. 6, pp. 3-10.

Brison, J. F., Charnay, G., and Comte-Bellot, G., 1979, "Calcul des Transferts Thermiques Entre Film Chaud et Substrat par un Modele a Deux Dimensions: Prevision de la Reponse Dynamique de Sondes Usuelles," *Int. J. Heat Mass Transfer*, Vol. 22, pp. 111-119.

Brown, G. L., 1967, "Theory and Application of Heated Films for Skin Friction Measurement," *Proc. 1967 Heat Transfer and Fluid Mechanics Institute*, Stanford University Press, p. 361.

Cole, K. D., 1986, "Conjugated Heat Transfer With the Unsteady Surface Element Method," Ph.D. Thesis, Mechanical Engineering, Michigan State University, East Lansing, MI.

Cole, K. D., and Beck, J. V., 1986, "Conjugated Heat Transfer From a Strip Heater with the Unsteady Surface Element Method," Paper No. AIAA-86-1242; also *J. of Thermophysics and Heat Transfer*, in press.

Cook, W. J., Giddings, T. A., and Murphy, J. D., 1986, "Response of Hot Element Wall Shear Stress Gages in Laminar Oscillating Flows," AIAA/ASME 4th Fluid Mechanics, Plasma Dynamics and Lasers Conference, May 12-14, *1986, Atlanta, GA*.

Mao, Z. X., and Hanratty, T. J., 1985, "The Use of Scalar Transport Probes to Measure Wall Shear Stress in Flow With Imposed Oscillations," *Experiments in Fluids*, Vol. 3, pp. 129-135.

Menendez, A. N., and Ramaprian, B. R., 1985, "The Use of Flush-Mounted Hot-Film Gages to Measure Skin-Friction in Unsteady Boundary Layers," *J. Fluid Mechanics*, Vol. 161, pp. 139-159.

Ramadhyani, D., Moffatt, D. F., and Incropera, F. P., 1985, "Conjugate Heat Transfer From Small Isothermal Heat Sources Embedded in a Large Substrate," *Int. J. Heat Mass Transfer*, Vol. 28, pp. 1945-1952.

Rubesin, M. W., Okuno, A. F., Mateer, G. G., and Brosh, A., 1975, "A Hot-Wire Surface Gage for Skin Friction and Separation Detection Measurements," NASA TM X-62465, July 1975.

APPENDIX

Fluid Influence Function

The quasi-steady fluid fundamental solution, ψ^f (K m^2/W), is the temperature response in a semi-infinite shear flow due to uniform heat flux (not a specified temperature) over half of the planar boundary. The energy equation is given by equation (1), with initial conditions given by equation (3*d*), and boundary conditions given by equations (3*a*), (3*c*), and also by

$$-k_f \frac{\partial \psi^f(x, y_f=0, t)}{\partial y_f} = \begin{cases} 0 \text{ for } x<0 \text{ and } t<0 \\ 1 \text{ for } x\geq 0 \text{ and } t\geq 0 \end{cases} \quad \text{(A1)}$$

The fluid fundamental solution is given in dimensionless form as (Cole and Beck, 1986)

$$\frac{k_s}{a}\psi_f(x, y_f=0, t) = \frac{9^{1/3}}{\Gamma(2/3)N_\beta}(x/a)^{1/3}H(x)\ H(t) \quad \text{(A2)}$$

where $H(\ )$ is the unit step function and $\Gamma(\ )$ is the gamma function.

Solid Fundamental Solution

The solid fundamental solution is presented in the form of ϕ^s, defined by equation (7), which is the effect of one surface element on the solid. The energy equation for ϕ^s is given by equation (2), with zero initial condition (equation (3*d*)). The boundary conditions are given by equations (3*a*) and (3*c*), and the interface heat flux condition is

$$-k_s \frac{\partial \phi^s(\xi, y_s=0, t^+)}{\partial y_s} = \begin{cases} 1 \text{ for } -1\leq\xi\leq 1;\ t^+\geq 0 \\ 0 \text{ otherwise} \end{cases} \quad \text{(A3)}$$

where $\xi = (x_i - x_j)/(L_j/2)$.

The closed-form analytical expression for ϕ^s is developed from Green's functions, and it is given by (Cole, 1986)

$$\begin{aligned} \phi^s(\xi, y_s=0, t^+) &= I_1(\xi, t_L); && t^+a^2/D^2 \leq B \\ &= I_1(\xi, B) + I_2(\xi, B, t_L); && t^+a^2/D^2 > B \end{aligned} \quad \text{(A4)}$$

where $t_L = t^+(4a^2)/L_j^2$ and where $B = 0.1$ is the dimensionless time-partitioning parameter. The integrals I_1 and I_2 are given by

$$\begin{aligned} I_1(\xi, t_L) &= (L_j/(2k_s))(t_L/\pi)^{1/2}\{\text{erf}[(\xi+1)/(2\sqrt{t_L})] \\ &\quad - \text{erf}[(\xi-1)/(2\sqrt{t_L})]\} + L_j(\xi+1)E_1[(\xi+1)^2/(4t_L)]/(4\pi k_s) \\ &\quad - L_j(\xi-1)E_1[(\xi-1)^2/(4t_L)]/(4\pi k_s) \end{aligned} \quad \text{(A5)}$$

$$I_2(\xi, B, t_L) = \sum_{m=1}^{4} L_j^2/(4k_sD)\left[I_3\left(a_m, \frac{\xi+1}{2}, t_L\right) - I_3\left(a_m, \frac{\xi+1}{2}, B\right) - I_3\left(a_m, \frac{\xi-1}{2}, t_L\right) + I_3\left(a_m, \frac{\xi-1}{2}, B\right)\right] \quad \text{(A6)}$$

and where

$$\begin{aligned} I_3(a_m, r, t_L) &= -\exp(-a_m^2 t_L)[1 - \text{erfc}(r/\sqrt{t_L})]/a_m^2 \\ &\quad - \exp(2a_m r)\text{erfc}(a_m\sqrt{t_L} + r/\sqrt{t_L})/(2a_m^2) \\ &\quad + \exp(-2a_m r)\text{erfc}(a_m\sqrt{t_L} - r/\sqrt{t_L})/(2a_m^2) \end{aligned} \quad \text{(A7)}$$

and $a_m = \pi\ (m - 1/2)/2$. The accuracy for this expression is six significant figures. The functions erf, erfc, and E_1 are the error function, the complementary error function, and the exponential integral, respectively.

Linear Matrix Operator Formalism for Basic Heat Exchanger Thermal Design

A. Pignotti
TECHINT S.A.
1001 Buenos Aires, Argentina

The matrix formalism used for the thermal description of heat exchangers is extended to include streams with variable temperature distributions. In this approach, a heat exchanger is described by a temperature-independent matrix operator, which, acting on the inlet temperature distributions, generates the outlet ones. This formalism is particularly useful for the evaluation of the thermal effectiveness of complex heat exchanger configurations that can be broken into simple constitutive parts, linked to each other by unmixed streams. Applications to crossflow configurations of practical interest are shown.

I Introduction

In the basic thermal analysis of heat exchanger geometries, it is customary to introduce a number of simplifying assumptions, such as: steady state, temperature independence of the heat capacity rates and the heat transfer coefficient, no heat losses, and perfect mixing, or complete lack of mixing, of the fluids involved. As a consequence of these assumptions, the differential equations used to determine the temperature distributions are linear, and so are the equations relating the outlet to the inlet temperatures. It is therefore quite natural to write these relations in matrix form, so that a vector of outlet temperatures is expressed as a product of a 2×2 temperature independent matrix M times a vector of inlet temperatures

$$\begin{bmatrix} t' \\ T' \end{bmatrix} = \begin{bmatrix} M_{11} & M_{12} \\ M_{21} & M_{22} \end{bmatrix} \begin{bmatrix} t \\ T \end{bmatrix}$$

$$= \begin{bmatrix} 1-P(R,\ \mathrm{NTU}) & P(R,\ \mathrm{NTU}) \\ RP(R,\ \mathrm{NTU}) & 1-RP(R,\ \mathrm{NTU}) \end{bmatrix} \begin{bmatrix} t \\ T \end{bmatrix} \tag{1}$$

The matrix M, which, for any given geometry, is a function of the heat capacity rate ratio R, and the number of heat transfer units NTU, is therefore the mathematical entity that describes the heat exchanger thermal behavior.

This scheme was originally proposed by Domingos (1969) for exchangers with one inlet and one outlet perfectly mixed stream for each fluid, and was later extended to exchangers with an arbitrary number of inlet and/or outlet streams (Pignotti, 1984). In this extended version, equation (1) is replaced by

$$\begin{bmatrix} t_1' \\ \cdot \\ \cdot \\ \cdot \\ t_{n'}' \\ T_1' \\ \cdot \\ \cdot \\ \cdot \\ T_{N'}' \end{bmatrix} = \begin{bmatrix} M_{11} & \cdots & M_{1,n+N} \\ \cdot & & \cdot \\ \cdot & & \cdot \\ \cdot & & \cdot \\ M_{n'+N',1} & \cdots & M_{n'+N',n+N} \end{bmatrix} \begin{bmatrix} t_1 \\ \cdot \\ \cdot \\ \cdot \\ t_n \\ T_1 \\ \cdot \\ \cdot \\ \cdot \\ T_N \end{bmatrix} \tag{2}$$

where the multistream exchanger is described by the $(n'+N') \times (n+N)$ rectangular matrix M.

The purpose of the present work is to generalize this treatment to heat exchange processes with unmixed streams, each characterized by a continuous temperature distribution. In this framework, the heat exchanger is described by a matrix operator which, acting on the inlet temperature distributions, generates the outlet ones.

The reason for introducing this matrix operator formalism goes beyond the obvious one, which is the fact that, indeed, inlet and outlet streams are often not perfectly mixed. Given the nature of the approximations already present, the additional one of perfect inlet and outlet stream mixing might seem acceptable. The matrix formalism, however, has been shown to be particularly useful for the description of complex assemblies of heat exchangers, or, equivalently, the analysis of a complex heat exchanger in terms of simpler constitutive parts. In such assemblies or decompositions, it is often found that streams connecting the various elements are not adequately described by the mixed assumption. It is in such cases that the description of the exchanger, or the exchanger part, by the formalism presented here, is most useful.

In sections II–IV the formalism is introduced and illustrated with simple examples.[1] Typical couplings of exchanger components are discussed in section V. With these elements, some complex crossflow configurations are analyzed in sections VI and VII.

II Formalism

We begin our analysis with the case of two inlet and two outlet unmixed streams. Each one is characterized, in principle, by a temperature distribution that is a function of location on the stream cross section. For our purposes, however, it is sufficient to consider a temperature profile that depends on a single transverse coordinate z. A second transverse coordinate does not alter the nature of the problem, and, if needed, may be introduced with no conceptual complications.

For a stream of heat capacity rate c, we define a heat capacity rate density dc/dz, as a function of the z coordinate, and introduce an accumulated heat capacity rate fraction $x(z)$, such that

$$x(z) = (1/c)\int_0^z (dc/dz')dz' \tag{3}$$

with $0 \le x(z) \le 1$. The temperature distribution of each in-

Contributed by the Heat Transfer Division for publication in the JOURNAL OF HEAT TRANSFER. Manuscript received by the Heat Transfer Division April 27, 1987. Keywords: Heat Exchangers, Modeling and Scaling.

[1] A short preliminary account of this matrix operator formalism was included as part of a keynote lecture delivered at the Eighth International Heat Transfer Conference (Pignotti, 1986b).

dividual stream is most conveniently expressed as a function of this variable x, and is denoted $t(x)$ and $T(x)$ for the inlet streams, and $t'(x)$ and $T'(x)$ for the outlet ones. For streams with constant flowrate density over the transverse cross section, the variable x can be interpreted as a dimensionless transverse coordinate, normalized to vary between zero and one. This interpretation is sufficient for all the applications discussed below. The choice of variable is such, however, that, even with nonuniform flow distributions, the average stream temperature is given by

$$t = \int_0^1 t(x)dx \tag{4}$$

The linear relation between the outlet and inlet temperatures can be written, in matrix form, as

$$\begin{bmatrix} t'(x') \\ T'(x') \end{bmatrix} = \int_0^1 \begin{bmatrix} M_{11}(x',x) & M_{12}(x',x) \\ M_{21}(x',x) & M_{22}(x',x) \end{bmatrix} \begin{bmatrix} t(x) \\ T(x) \end{bmatrix} dx \tag{5}$$

Equation (5) can be viewed as the straightforward generalization of the multistream matrix relation (2) to the continuum case, in which the discrete matrix indices have been replaced by the continuous variables x' and x. Alternatively, the matrix M can be seen as an operator that acts on the space of the inlet temperature functions and, upon integration over the x variable, generates the outlet temperature distributions.

Just as in the discrete case, the matrix M has to satisfy constraints that follow from the heat balance equation, and translational invariance in the temperature coordinate (i.e., from the fact that the equations are not affected by a shift of the origin of the temperature scale). These constraints are

$$\int_0^1 M_{11}(x', x)dx' + (1/R)\int_0^1 M_{21}(x', x)dx' = 1 \tag{6a}$$

$$R\int_0^1 M_{12}(x', x)dx' + \int_0^1 M_{22}(x', x)dx' = 1 \tag{6b}$$

$$\int_0^1 M_{11}(x', x)dx + \int_0^1 M_{12}(x', x)dx = 1 \tag{7a}$$

$$\int_0^1 M_{21}(x', x)dx + \int_0^1 M_{22}(x', x)dx = 1 \tag{7b}$$

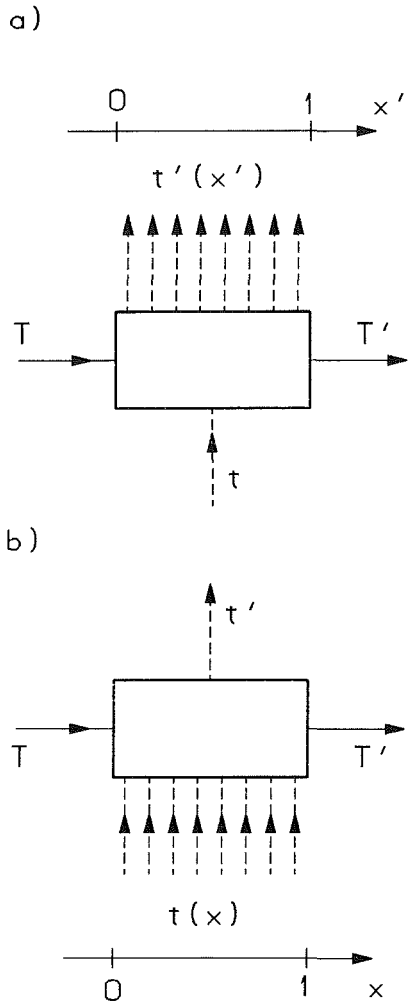

Fig. 1 Special cases in which the inlet and outlet fluid 2 streams are mixed; in addition, inlet fluid 1 is mixed in (a), and outlet fluid 1 in (b)

Finally, given an exchanger described by the matrix M, an exchanger that has the same physical characteristics, but differs from the original one in the inversion of the direction of

Nomenclature

A = heat transfer surface area, m^2
A = thermal matrix of component labeled A
c, C = fluid 1 and fluid 2 heat capacity rates, W/°C
$I_n(\lambda)$ = function defined in equation (34)
M = matrix relating outlet to inlet temperatures
$\hat{M}$ = same as M for a process in which all streams have been reversed
n, n' = inlet and outlet number of streams of fluid 1
N, N' = inlet and outlet number of streams of fluid 2
NTU = UA/c = number of heat transfer units referred to fluid 1
ntu = single-row number of heat transfer units
P = $(t'-t)/(T-t)$ = fluid 1 effectiveness
$p(x)$ = effectiveness density, defined in equation (10)
$\hat{p}(x)$ = effectiveness density of flow-reversed process
R = c/C = fluid 1 heat capacity rate ratio
r = single-row heat capacity rate ratio
t, t' = fluid 1 inlet and outlet temperatures, °C
T, T' = fluid 2 inlet and outlet temperatures, °C
U = overall heat transfer coefficient, W/°C m^2
x = accumulated heat capacity rate fraction
Z = thermal matrix of component labeled Z
z = transverse coordinate in an unmixed stream, m
Δ = quantity defined in equation (28)
η = quantity defined in equation (25)
λ = quantity defined in equation (19)
ρ = quantity defined in equation (18)

Subscripts

a, b = refer to configurations of Figs. 5(*a*) and 5(*b*)
COC = refers to overall cocurrent series connection
COU = refers to overall countercurrent series connection
PAR = refers to parallel connection
4, 6, 8 = refer to four-pass countercrossflow exchangers with 4, 6, and 8 rows

flow of both fluids, is described by a matrix $\hat{M}$ such that (Pignotti, 1985)

$$\begin{aligned}\hat{M}_{11}(x', x) &= M_{11}(x, x')\\ \hat{M}_{12}(x', x) &= M_{21}(x, x')/R\\ \hat{M}_{21}(x', x) &= M_{12}(x, x')R\\ \hat{M}_{22}(x', x) &= M_{22}(x, x')\end{aligned} \tag{8}$$

III Special Cases With Mixed Streams

We often deal with the special case in which one of the fluids, which we choose to be fluid 2, is perfectly mixed in the inlet and outlet streams (but not necessarily inside the exchanger). In this case, some of the dependence of the thermal matrix on the heat capacity rate fraction variables drops out, and equation (5) becomes

$$\begin{bmatrix} t'(x') \\ T' \end{bmatrix} = \int_0^1 \begin{bmatrix} M_{11}(x', x) & M_{12}(x') \\ M_{21}(x) & M_{22} \end{bmatrix} \begin{bmatrix} t(x) \\ T \end{bmatrix} dx \tag{9}$$

If, moreover, the inlet stream of fluid 1 is also mixed, such as sketched in Fig. 1(*a*), i.e., if the inlet temperature t is independent of x, we can define an effectiveness density

$$p(x') = [t'(x') - t]/[T - t] \tag{10}$$

and integrate equation (9) over x, which yields

$$\begin{bmatrix} t'(x') \\ T' \end{bmatrix} = \begin{bmatrix} M_{11}(x') & M_{12}(x') \\ M_{21} & M_{22} \end{bmatrix} \begin{bmatrix} t \\ T \end{bmatrix} = \begin{bmatrix} 1-p(x') & p(x') \\ RP & 1-RP \end{bmatrix} \begin{bmatrix} t \\ T \end{bmatrix} \tag{11}$$

where the total effectiveness P is given by

$$P = \int_0^1 p(x)dx \tag{12}$$

Conversely, if the outlet fluid 1 is mixed, but not the inlet one, as shown in Fig. 1(*b*), we can write

$$\begin{bmatrix} t' \\ T' \end{bmatrix} = \int_0^1 \begin{bmatrix} M_{11}(x) & M_{12} \\ M_{21}(x) & M_{22} \end{bmatrix} \begin{bmatrix} t(x) \\ T \end{bmatrix} dx \tag{13}$$

If, in analogy with equation (11), we define

$$\hat{p}(x) = 1 - M_{11}(x)$$

using equations (6) and (7) we obtain

$$[M(x)] = \begin{bmatrix} 1-\hat{p}(x) & P \\ R\hat{p}(x) & 1-RP \end{bmatrix} \tag{14}$$

with

$$P = \int_0^1 \hat{p}(x)dx \tag{15}$$

Observe that, from equations (8) and (14), it follows that $\hat{M}_{12} = \hat{p}(x)$, i.e., $\hat{p}(x)$ is the effectiveness density of the configuration obtained after reversing both fluids in the exchanger of Fig. 1(*b*).

In summary, equations (11) and (14) exhibit the most general expressions for the matrices that describe the exchangers sketched in Figs. 1(*a*) and 1(*b*), respectively, under the current assumptions.

IV Elementary Example

Consider the elementary crossflow exchanger of Fig. 2, consisting of a single row of tubes, in which fluid 1 is the unmixed out-of-tube fluid, and fluid 2 the perfectly mixed tube fluid. For this exchanger we can write (Braun, 1975; Pignotti and Cordero, 1983)

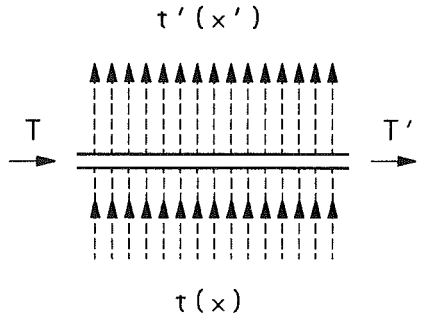

Fig. 2 Single row of tubes in crossflow

$$t'(x') = \rho t(x') + (1-\rho)\exp(-\lambda x')\left[T + \lambda\int_0^{x'} \exp(\lambda x)t(x)dx\right] \tag{16}$$

and

$$T' = \exp(-\lambda)\left[T + \lambda\int_0^1 \exp(\lambda x)t(x)dx\right] \tag{17}$$

with

$$\rho = \exp(-\text{ntu}) \tag{18}$$

and

$$\lambda = r(1-\rho) \tag{19}$$

Here ntu is the single-row number of transfer units, which, in this case, happens to coincide with NTU, the number of transfer units of the whole exchanger. Correspondingly, r is the single-row heat capacity rate ratio.

Equations (16) and (17) can be easily cast into the form of equation (9) setting

$$\begin{aligned} M_{11}(x', x) &= \rho\delta(x'-x) + \lambda(1-\rho)\exp[-\lambda(x'-x)]H(x'-x)\\ M_{12}(x') &= (1-\rho)\exp(-\lambda x')\\ M_{21}(x) &= \lambda\exp[-\lambda(1-x)]\\ M_{22} &= \exp(-\lambda)\end{aligned} \tag{20}$$

where $\delta(x'-x)$ is Dirac's delta function, such that

$$\int_a^b \delta(x'-x)f(x)dx = f(x')$$

provided $a < x' < b$, and $H(x'-x)$ is the step function

$$H(x'-x) = \begin{cases} 1 \text{ for } x' > x, \text{ and} \\ 0 \text{ for } x' < x \end{cases}$$

The above expressions are simplified if the inlet out-of-tube temperature is assumed to be constant, in which case the x integration can be performed explicitly, and we obtain

$$p(x') = (1-\rho)\exp(-\lambda x') \tag{21}$$

and

$$P = [1-\exp(-\lambda)]/R \tag{22}$$

In the same fashion, if the inlet fluid 1 is allowed to be x dependent, but the outlet one is assumed to mix perfectly, equations (13)–(15) apply, and we obtain, after integrating over x'

$$\hat{p}(x) = (1-\rho)\exp[-\lambda(1-x)] \tag{23}$$

P is again given by equation (22).

V Composite Arrangements

The expressions obtained in the previous section can be used as basic building blocks to construct quite elaborate arrangements. In this section, following fairly simple coupling rules (Pignotti, 1986b), we obtain properties of some composite arrangements in terms of those of the constituents.

(A) Series Coupling of Two Exchangers, Overall Parallel Flow Connection, Intermediate Fluid 1 Unmixed. This arrangement, the effectiveness of which we denote by P_{COC}, is sketched in Fig. 3(*a*). For it we can write

$$M_{11} = 1 - P_{COC} = \int_0^1 Z_{11}(x') A_{11}(x')\,dx' + Z_{12}A_{21}$$

where we have denoted by A and Z the thermal matrices corresponding to the lower and upper parts of the diagram. Using the expressions of equations (11) and (14), we obtain

$$P_{COC} = P_A + P_Z - RP_AP_Z - \eta \tag{24}$$

where

$$\eta = \int_0^1 p_A(x)\hat{p}_Z(x)\,dx \tag{25}$$

If the exchanger Z coincides with A, except for the inversion of the direction of flow of both fluids, we have

$$\hat{p}_Z(x) = p_A(x) \quad \text{and} \quad P_Z = P_A \tag{26}$$

so that

$$\begin{aligned} P_{COC} &= 2P_A - RP_A^2 - \eta \\ &= 2P_A - (R+1)P_A^2 - \Delta \end{aligned} \tag{27}$$

with

$$\begin{aligned} \Delta &= (1/2)\int_0^1 \int_0^1 [p_A(x) - p_A(x')]^2 dx\,dx' \\ &= \eta - P_A^2 \geq 0 \end{aligned} \tag{28}$$

This shows that, in such cases, the simplifying assumption of mixing of the intermediate stream, which leads to equation (27) with $\Delta = 0$, is not on the safe side. This is the generalization of a similar result obtained for divided-flow exchangers (Pignotti, 1986a).

(B) Series Coupling of Two Exchangers, Overall Counterflow Connection, Intermediate Fluid 1 Unmixed. For this case, shown in Fig. 3(*b*), we write

$$M_{11} = 1 - P_{COU} = \int_0^1 Z_{11}(x)A_{11}(x)\,dx +$$

$$+ \frac{\int_0^1 Z_{11}(x)A_{12}(x)\,dx \int_0^1 Z_{21}(x)A_{11}(x)\,dx}{1 - \int_0^1 Z_{21}(x)A_{12}(x)\,dx} \tag{29}$$

whence

$$P_{COU} = P_{COC}/(1 - R\eta) \tag{30}$$

Again, when $p_Z(x) = p_A(x)$, we obtain

$$\begin{aligned} P_{COU} &= (2P_A - RP_A^2 - \eta)/(1 - R\eta) = \\ &= [2P_A - (R+1)P_A^2 - \Delta]/[1 - RP_A^2 - R\Delta] \end{aligned} \tag{31}$$

and it is easy to prove that P_{COU} is lower than the effectiveness of a similar assembly with perfect mixing of the intermediate fluid 1, for which equation (31) holds with $\Delta = 0$.

(C) Coupling of Two Exchangers With Fluid 2 in Parallel, Intermediate Fluid 1 Unmixed. For this arrangement, shown in Fig. 3(*c*), we have

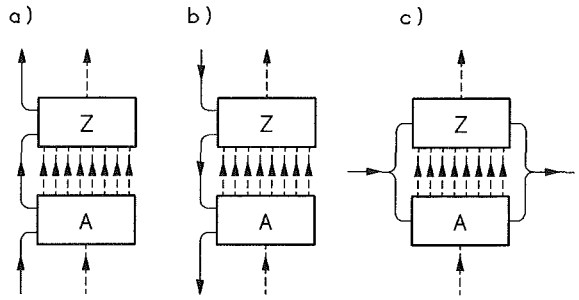

Fig. 3 Examples of composite arrangements with intermediate fluid 1 unmixed: (*a*) series coupling, overall parallel flow; (*b*) series coupling, overall counterflow; (*c*) parallel coupling

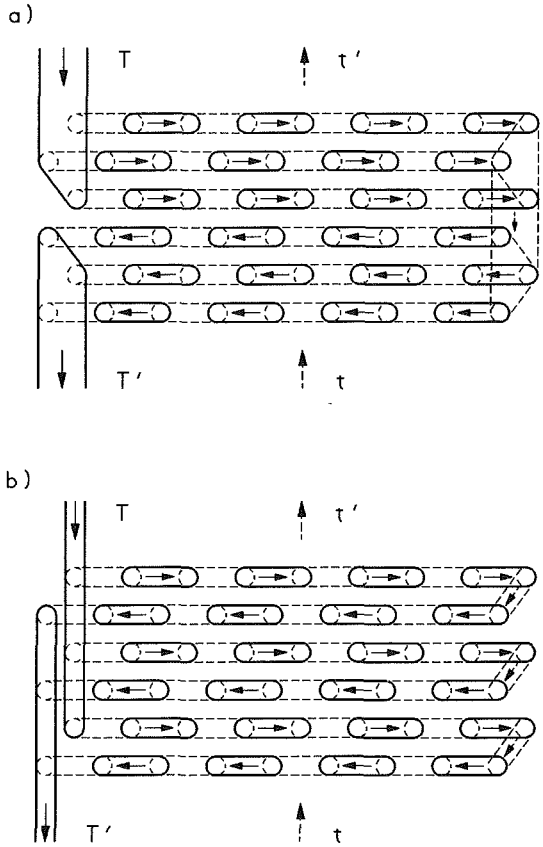

Fig. 4 Cross section of U-tube bundle showing alternative two-pass connections: (*a*) first tube pass through rows 6, 5, and 4, and second pass through rows 3, 2, and 1; (*b*) first tube pass through rows 6, 4, and 2, and second pass through rows 5, 3, and 1

$$1 - P_{PAR} = \int_0^1 Z_{11}(x)A_{11}(x)\,dx = 1 - P_A - P_Z + \eta \tag{32}$$

whence

$$P_{PAR} = P_A + P_Z - \eta \tag{33}$$

VI Other Arrangements

We apply the formalism developed above to the comparative analysis of the two alternative arrangements of Figs. 4(*a*) and 4(*b*), which are made out of the same U-tube bundle. Figures 5(*a*) and 5(*b*) show the corresponding schematic configurations, that, in what follows, we label *a* and *b*, respectively. For both of them, we assume fluid 1 to be unmixed throughout, except for the inlet and outlet streams, which we take as perfectly mixed.

The a configuration is an example of the coupling described in point B of Section V above, in which the components Z and A are single-pass, three-row crossflow exchangers. Therefore, the overall effectiveness is given by equation (31) with (Pignotti, 1986b)

$$P_A = a_0 I_0(\lambda) + a_1 I_1(\lambda) + a_2 I_2(\lambda)$$

$$\eta = a_0^2 I_0(2\lambda) + 2a_0 a_1 I_1(2\lambda) + a_2^2 I_4(2\lambda) + (a_1^2 + 2a_0 a_2) I_2(2\lambda) + 2a_1 a_2 I_3(2\lambda)$$

$$a_0 = 1 - \rho^3$$

$$a_1 = \lambda(1-\rho)^2(1+2\rho)$$

$$a_2 = \lambda^2(1-\rho)^3/2$$

$$\rho = \exp(-\mathrm{NTU}/6)$$

$$\lambda = 3R(1-\rho)$$

$$I_n(\lambda) = \int_0^1 x^n \exp(-\lambda x)\,dx = n![1-(1+\lambda+\ \ldots\ +\lambda^n/n!)\exp(-\lambda)]/\lambda^{n+1} \qquad (34)$$

The analysis of Fig. 5(b) is somewhat more complex because it requires the breakdown of the exchanger into three sections shown in Fig. 6. Each section is a two-pass, two-row counter-crossflow exchanger, and for the whole assembly we can write

$$M_{11} = 1 - P_b = \int_0^1 \int_0^1 Z_{11}(x') M_{11}(x', x) A_{11}(x)\,dx'\,dx \qquad (35)$$

The matrix elements Z_{11}, M_{11}, and A_{11} in the integrand of equation (35), can be obtained from the single-row expressions given in Section IV. The result for the overall effectiveness is

$$P_b = 1 - \rho^2 J_0 - K_1 J_1^2 + K_2 J_2^2 + K_3 J_1 J_2 - K_4 J_3$$

where

$$K_1 = \lambda\beta(1+\rho)/2$$

$$K_2 = \lambda\alpha(1-\rho)/2$$

$$K_3 = \lambda\beta(1-\rho)$$

$$K_4 = \lambda(1-\rho^2)$$

$$\alpha = (1-\rho^2)/(2\gamma)$$

$$\beta = \alpha/X^2$$

$$\gamma = [1+\rho+(1-\rho)/X^2]/2$$

$$X = \exp(\lambda)$$

$$J_0 = 1 + 2\alpha\beta - 2\alpha I_0(\lambda)(1+1/X) + \alpha^2 I_0(2\lambda)(1+1/X^2)$$

$$J_1 = -\alpha + X I_0(\lambda) - \alpha I_0(2\lambda)$$

$$J_2 = -\beta + I_0(\lambda) - \alpha I_0(2\lambda)$$

$$J_3 = \alpha\beta/2 + [1+(\alpha-\beta)\beta/2+\beta]/\lambda + (\beta/2 - 1 - \alpha - 3\beta X/2) I_0(\lambda)/\lambda + \alpha I_0(2\lambda)/\lambda - \alpha I_1(\lambda) + \alpha^2 I_1(2\lambda)$$

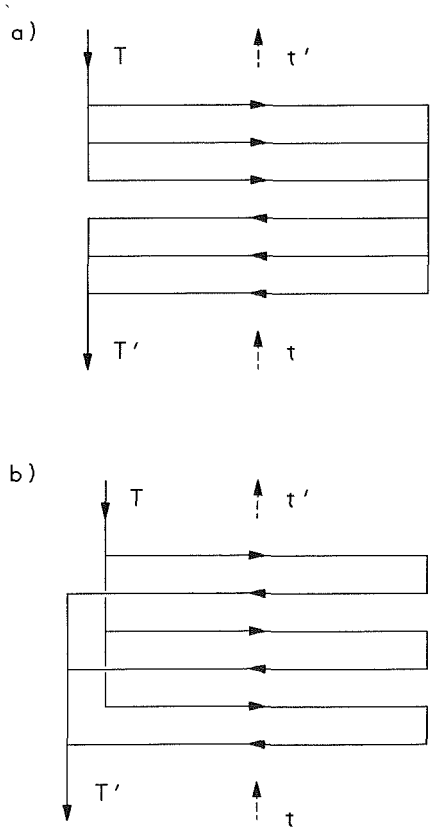

Fig. 5 (a) and (b) Schematic drawings for the geometries of Figs. 4(a) and 4(b), respectively

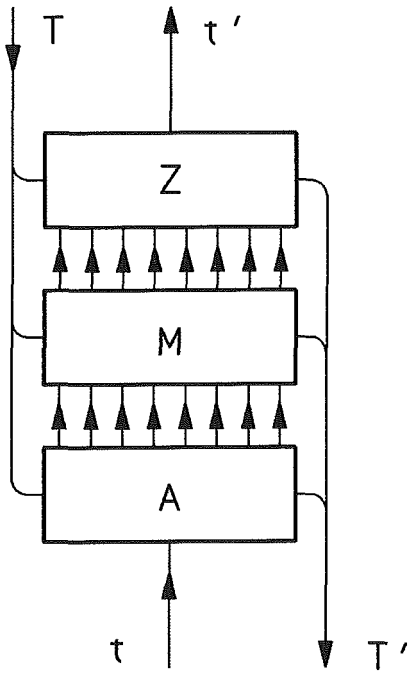

Fig. 6 Diagram showing the geometry of Fig. 5(b) as parallel connection of three exchangers A, M, and Z

Table 1 Effectiveness of the configurations of Figs. 5(a) and 5(b)

	$R=0.2$		$R=0.5$		$R=1.0$		$R=2.0$		$R=5.0$	
NTU	P_a	P_b	P_a	P_b	P_a	P_b	P_a	P_b	P_a	P_b
0.1	0.0943	0.0943	0.0930	0.0930	0.0909	0.0908	0.0868	0.0867	0.0760	0.0758
0.5	0.3802	0.3792	0.3610	0.3588	0.3312	0.3274	0.2794	0.2739	0.1758	0.1701
1.0	0.6025	0.5985	0.5590	0.5502	0.4912	0.4767	0.3784	0.3598	0.1954	0.1818
2.0	0.8241	0.8148	0.7570	0.7336	0.6412	0.6007	0.4482	0.4010	0.1997	0.1740
4.0	0.9571	0.9472	0.8956	0.8546	0.7503	0.6597	0.4828	0.3893	0.2000	0.1583

Here ρ, λ, and $I_n(\lambda)$ coincide with those of configuration *a*, and are given by equations (18), (19), and (34), respectively.

Table 1 shows a comparison of the effectiveness for the two configurations. It is clear that arrangement *a* is preferable, because the effectiveness is consistently higher (24 percent for $R = 2$ and NTU $= 4$). This can be understood from the following argument in which, for concreteness, we take the tube fluid to be the hot one. In configuration *a* the cold fluid first meets the three tubes of the second hot fluid pass, and then meets the hotter tubes of the first pass. In contrast, in configuration *b*, the cold fluid meets alternatingly second-pass and first-pass tube rows. This alternation of hot and not-so-hot fluid is clearly undesirable, and is responsible for the lower effectiveness of this configuration.

It should be pointed out that the numerical results of Table 1 are obtained from the analytical expressions given in this and the previous section, in terms of rational and exponential functions. Even though we use a matrix formalism, no numerical matrix operations, such as multiplications or inversions, are performed. Therefore, there is no reason to expect enhancement of numerical errors beyond those typical of standard computer accuracy. This same comment applies to the numerical results shown in the following section.

VII Extension to Multiple Streams

Just as equation (1) can be generalized to the expression of equation (2) in the case of multiple mixed streams, it is also possible to generalize equation (5) to the case of multiple unmixed streams. The result looks like equation (2), with the following straightforward changes:

- outlet stream temperatures are functions of x'
- inlet stream temperatures are functions of x
- matrix elements are functions of x and x'
- the right-hand side is integrated over x from zero to one.

We illustrate this more general situation analyzing again a six-row countercrossflow exchanger, but this time with four passes on the tube side. Figure 7 shows a cross section of the tube bundle, in which only eight tubes are exhibited in each row, although any even number would do equally well. The tube rows are numbered from 1 to 6 in the order in which the out-of-tube fluid meets them, and the arrangement is such that the inlet tube fluid in the front header is evenly split into twelve tubes: all the tubes in row 6, and half of those in row 5. After mixing in the back header, the tube fluid flows back through the remaining four tubes of row 5, plus all the tubes in row 4, and a similar pattern is followed in rows 3 to 1. Complete lack of mixing of the out-of-tube fluid is assumed throughout the exchanger: neither in the direction of the u axis in Fig. 7, nor in the direction of the tubes, i.e., the normal to the plane of Fig. 7.

The problem of determining analytically the thermal effectiveness of this arrangement looks formidable. We show below, however, that this can be done using the formalism previously developed. But before attempting the calculation, it is sensible to ask what result one should expect. A plausible answer is that, this being a four-pass countercrossflow exchanger with six rows, the effectiveness, which we denote P_6, should be somewhere between P_4 and P_8, which correspond to similar exchangers with the same number of passes and four and eight rows, respectively. This reasoning is by no means rigorous, and we test it below with the exact solution.

The first step in the solution of this problem is to consider the geometry of Fig. 8(*a*), which involves only one vertical "slice," i.e., two columns, of the diagram of Fig. 7. It is clear that R, NTU, and P for this "slice" are equal to those of the whole exchanger, and, therefore, the problems of Figs. 7 and 8(*a*) are equivalent. We further divide the latter into its upper and lower halves, as schematically indicated in Fig. 8(*b*), and realize that the upper part coincides with the lower one, except for the inversion of the direction of flow of the five streams involved (two inlet and three outlet streams for the lower part *A*, and vice versa for the upper part *Z*). The scheme is therefore quite analogous to that of Fig. 3(*b*), except that we now have two intermediate unmixed streams for fluid 1, rather than only one. For the lower half we can write

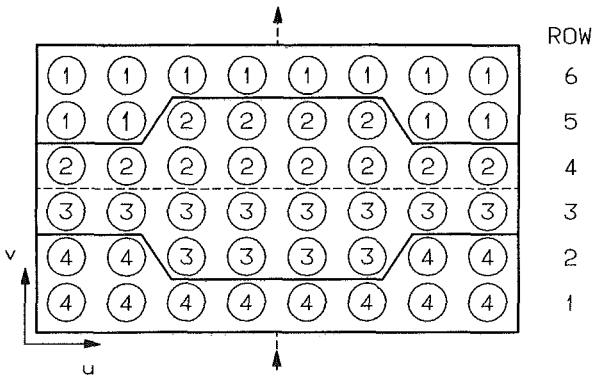

Fig. 7 Cross section of tube bundle with six rows and four passes; numbers inside tube sections identify the pass number

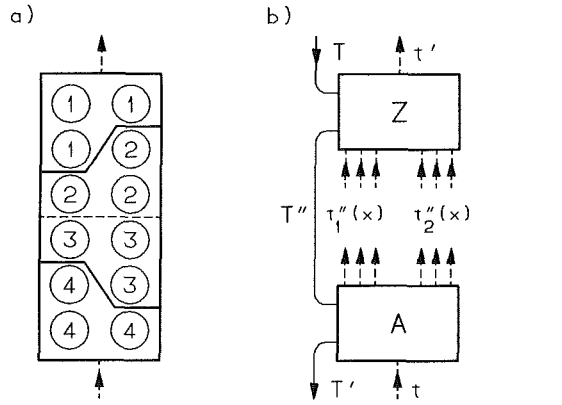

Fig. 8(*a*) Section of the exchanger of Fig. 7 used to calculate the effectiveness; (*b*) analysis of (*a*) in terms of two coupled exchangers with two intermediate unmixed streams for fluid 1

Table 2 Comparison of the effectiveness of four-pass countercrossflow exchangers, with four, six, and eight rows

	$R=0.2$			$R=1.0$			$R=5.0$		
NTU	P_4	P_6	P_8	P_4	P_6	P_8	P_4	P_6	P_8
0.1	0.0943	0.0943	0.0943	0.0909	0.0909	0.0909	0.0761	0.0761	0.0761
0.5	0.3806	0.3805	0.3806	0.3328	0.3326	0.3328	0.1772	0.1770	0.1772
1.0	0.6043	0.6041	0.6044	0.4974	0.4968	0.4976	0.1965	0.1964	0.1965
2.0	0.8293	0.8289	0.8295	0.6578	0.6563	0.6586	0.1998	0.1998	0.1998
4.0	0.9634	0.9631	0.9641	0.7760	0.7752	0.7802	0.2000	0.2000	0.2000

$$\begin{bmatrix} t_1''(x) \\ t_2''(x) \\ T' \end{bmatrix} = \begin{bmatrix} 1-p_1(x) & p_1(x) \\ 1-p_2(x) & p_2(x) \\ RP_A & 1-RP_A \end{bmatrix} \begin{bmatrix} t \\ T'' \end{bmatrix} \quad (36)$$

with

$$P_A = \int_0^1 dx[p_1(x)+p_2(x)]/2 \quad (37)$$

and, for the upper one,

$$\begin{bmatrix} t' \\ T'' \end{bmatrix} = \int_0^1 \begin{bmatrix} [1-p_1(x)]/2 & [1-p_2(x)]/2 & P_A \\ Rp_1(x) & Rp_2(x) & 1-RP_A \end{bmatrix} \begin{bmatrix} t_1''(x) \\ t_2''(x) \\ T \end{bmatrix} dx \quad (38)$$

The same procedure used in Section V(A) leads again to the expression of equation (31), where η is given by

$$\eta = \int_0^1 dx[p_1^2(x)+p_2^2(x)]/2 = (\eta_1+\eta_2)/2 \quad (39)$$

A result of this type could have been guessed because, after all, the difference between two intermediate unmixed streams (as in Fig. 8(*b*)), and a single one (as in Fig. 3(*b*)), is almost semantic. The problem is then essentially solved if the expressions for p_1 and p_2 are found. Careful application of the coupling rules with the building blocks described above leads to

$$p_i(x) = a_i\exp(-\lambda x) + b_i x\exp(-\lambda x) + c_i\exp(\lambda x) + d_i x\exp(\lambda x)$$

where i is either 1 or 2, and

$$\begin{aligned} a_1 &= (1-\rho)[1+\rho-\Omega(1+3\rho)/4] \\ b_1 &= (1-\rho)^2\lambda(1-\Omega/2) \\ c_1 &= \Omega(1+\rho)^2/4 \\ d_1 &= b_2 = 0 \\ a_2 &= (1-\rho)\{1-\Omega[3+\rho+2\lambda(1-\rho)]/4\} \\ c_2 &= \Omega[3+2\rho+3\rho^2+2\lambda(1-\rho^2)]/4 \\ d_2 &= -\Omega\lambda(1-\rho^2)/2 \\ \Omega &= (1-\rho)\exp(-\lambda)N/D \\ \rho &= \exp(-\mathrm{NTU}/6) \\ \lambda &= 1.5R(1-\rho) \\ N &= [1+\lambda(1-\rho)/3]\exp(-\lambda) \\ D &= 1-2\lambda(1-\rho)[(1+\rho)I_0(2\lambda)+\lambda(1-\rho)I_1(2\lambda)]/3 \end{aligned}$$

Hence

$$\begin{aligned} P_A &= [(a_1+a_2)I_0(\lambda)+b_1I_1(\lambda)+(c_1+c_2)I_0(-\lambda) \\ &\quad + d_2I_1(-\lambda)]/2 \\ \eta_i &= a_i^2I_0(2\lambda)+2a_ib_iI_1(2\lambda)+b_i^2I_2(2\lambda) \\ &\quad + c_i^2I_0(-2\lambda)+2c_id_iI_1(-2\lambda)+d_i^2I_2(-2\lambda) \\ &\quad + 2a_ic_i+a_id_i+b_ic_i+2b_id_i/3 \end{aligned}$$

P_6 is then obtained using equation (31) for P_{COU} and equation (39).

Table 2 shows a comparison of P_4, P_6, and P_8, for several values of R and NTU. The values of P_4 and P_8 are computed following a more conventional approach (Pignotti and Cordero, 1983). Contrary to the expectations stated above, P_6 does not turn out to be bracketed between the other two values but, rather, is smaller than both of them. The effect is, however, quite small, and the calculation shows that using P_4 in place of P_6 is a good approximation.

VIII Conclusions

The matrix operator formalism presented here is the natural tool to deal with unmixed streams in the thermal description of heat exchangers, under commonly used simplifying assumptions. In conjunction with symmetry properties and coupling rules, it is of great value in obtaining analytical solutions for the effectiveness of quite elaborate configurations. Because of the approximations that underlie this treatment, these solutions are not the ultimate answer to the problem of thermal design. They can be used, however, to unveil some mechanisms that are certainly present, and would be less apparent in a purely numerical approach.

Acknowledgments

The author is indebted to Dr. Ramesh K. Shah for suggesting possible applications, and providing sustained encouragement during the course of this work. The work was supported in part by a CONICET-NSF Cooperative Science Program.

References

Braun, B., 1975, "Wärmeübergang in Temperaturverlauf in Querstrom-Rohrbündeln bei beliebiger Schaltung der Rohrreihen," *Forsch. Ing-Wes.*, Vol. 41, pp. 181–191.

Domingos, J. D., 1969, "Analysis of Complex Assemblies of Heat Exchangers," *International Journal of Heat and Mass Transfer*, Vol. 12, pp. 537–548.

Pignotti, A., 1984, "Matrix Formalism for Complex Heat Exchangers," ASME Journal of Heat Transfer, Vol. 106, pp. 352–360.

Pignotti, A., 1985, "Flow-Reversal Symmetry in a Convective Heat Exchange Model," *Journal of Mathematical Physics*, Vol. 26, pp. 1860–1862.

Pignotti, A., 1986a, "Effectiveness of Series Assemblies of Divided-Flow Heat Exchangers," ASME Journal of Heat Transfer, Vol. 18, pp. 141–146.

Pignotti, A., 1986b, "Analytical Techniques for Basic Thermal Design of Complex Heat Exchanger Configurations," *Proceedings of the Eighth International Heat Transfer Conference*, C. L. Tien et al., eds., Hemisphere, Washington, DC, Vol. 1, pp. 249–256.

Pignotti, A., and Cordero, G., 1983, "Mean Temperature Difference in Multipass Crossflow," ASME Journal of Heat Transfer, Vol. 105, pp. 584–591.

S. Ahmad

B. Linnhoff

R. Smith

Department of Chemical Engineering,
UMIST,
Manchester, England

Design of Multipass Heat Exchangers: an Alternative Approach

Multipass heat exchangers are often designed according to the rule of thumb $F_T \geq 0.75$. *This criterion can give rise to poor designs. It is the slope* $(\partial F_T/\partial P)_R$ *that is important, not just the absolute value of* F_T. *Furthermore, in multishell arrangements, the number of shells required is usually evaluated by trial and error. This paper introduces an approach based on a new parameter that is an alternative to* F_T *factors. The method is fully compatible with established design practice, takes account of the* F_T *slope, and evaluates the number of shells* explicitly *in multishell cases.*

1 Introduction

One of the most common types of shell-and-tube exchanger is the 1-2 design (1 shell pass-2 tube passes). Because the flow arrangement involves part countercurrent and part cocurrent flow, the effective temperature difference for heat exchange is reduced compared with a purely countercurrent device. This is accounted for in design by the introduction of the F_T factor into the basic heat exchanger design equation, as discussed by Bowman et al. (1940)

$$Q = UA\Delta T_{LM} F_T \quad \text{where } 0 < F_T < 1 \tag{1}$$

The F_T correction factor is usually correlated in terms of two dimensionless ratios, the thermal effectiveness of the exchanger (P) and the ratio of the two heat capacity flow rates (R).

At the early stages of design, engineers need to be able to screen alternative designs before going forward to more detailed calculations. These alternatives include not only different types of exchanger, but also in the case of 1-2 designs, multiple shell arrangements forced by unacceptably low values of F_T. If multiple shells are required then the most common practice is to adopt a trial-and-error approach in which the number of shells in series is progressively increased until a satisfactory value of F_T is obtained for each shell.

This paper describes an alternative approach to the design of 1-2 exchangers, particularly useful in the early stages of design, which does not rely directly on F_T factors. The approach is fully compatible with established design procedures and offers two distinct advantages:

(*i*) It generates better designs than those based on traditional rules of thumb for specifying minimum permissible F_T be avoiding uncertain areas of the F_T chart more effectively.

(*ii*) For multishell arrangements, the number of shells does not need to be evaluated by trial and error but can by evaluated explicitly.

2 F_T Correction Factors

Graphical and analytical correlations exist for F_T based on a number of assumptions concerning the heat transfer in a 1-2 exchanger (see Bowman et al., 1940). Important among these are that the streams assume constant heat capacity flow rates and that the overall heat transfer coefficients remains fixed. The correlations are then normally expressed in the form

$$F_T = f(R, P) \tag{2}$$

where

$$R = CP_H/CP_C = (T_{Co} - T_{Ci})/(T_{Hi} - T_{Ho}) \tag{3}$$

and

$$P = (T_{Hi} - T_{Ho})/(T_{Hi} - T_{Ci}) \tag{4}$$

Some designers use the alternative definitions

$$R' = CP_C/CP_H = (T_{Hi} - T_{Ho})/(T_{Co} - T_{Ci}) \tag{3a}$$

and

$$P' = (T_{Co} - T_{Ci})/(T_{Hi} - T_{Ci}) \tag{4a}$$

instead of R and P. Whichever of the two conventions is adopted is immaterial in determining the value of F_T for given exchanger profiles. This results because

$$R' = 1/R, \quad P' = RP$$

and

$$F_T(R, P) = F_T(1/R, RP) = F_T(R', P') = F_T(1/R', R'P')$$

Three basic situations can be encountered when using 1-2 exchangers (Fig. 1):

(*a*) We have a temperature approach. This situation is straightforward to design for using a single 1-2 shell.

(*b*) We have a small temperature cross. This situation is usually straightforward to design for and again can probably be accommodated in a single shell.

(*c*) We have a large temperature cross. Local reversal of heat flow may be encountered, which is wasteful in heat transfer area. The design might even become infeasible.

One basic question therefore remains: How much temperature cross can we tolerate before encountering reversal of heat flow or infeasibility? Clearly, infeasible exchanger designs return $F_T \leq 0$, but having $F_T > 0$ is not enough to make a design practical. A commonly used rule of thumb requires $F_T \geq 0.75$ for the design to be considered practical as discussed by Kern (1950).

However, the use of the criterion $F_T \geq 0.75$ for 1-2 exchangers is only a rule of thumb and can lead to poor designs if not used with caution.

The fact that designs using values of F_T less than 0.75 are unacceptable is not solely due to the inefficiency of the chosen configuration. Bell (1984) has pointed out that the whole method is only approximate since it is based on certain simplifying assumptions. Any violation of the simplifying assumptions will tend to have a particularly significant effect in areas of the F_T chart where slopes are particularly steep. For example, in an exchanger with a close temperature approach, bundle and baffle bypassing not accounted for in the approach can result in an exchanger that is not just inefficient but is thermodynamically infeasible. Any uncertainties or inac-

Contributed by the Heat Transfer Division for publication in the JOURNAL OF HEAT TRANSFER. Manuscript received by the Heat Transfer Division February 23, 1987. Keywords: Heat Exchangers, Modeling and Scaling.

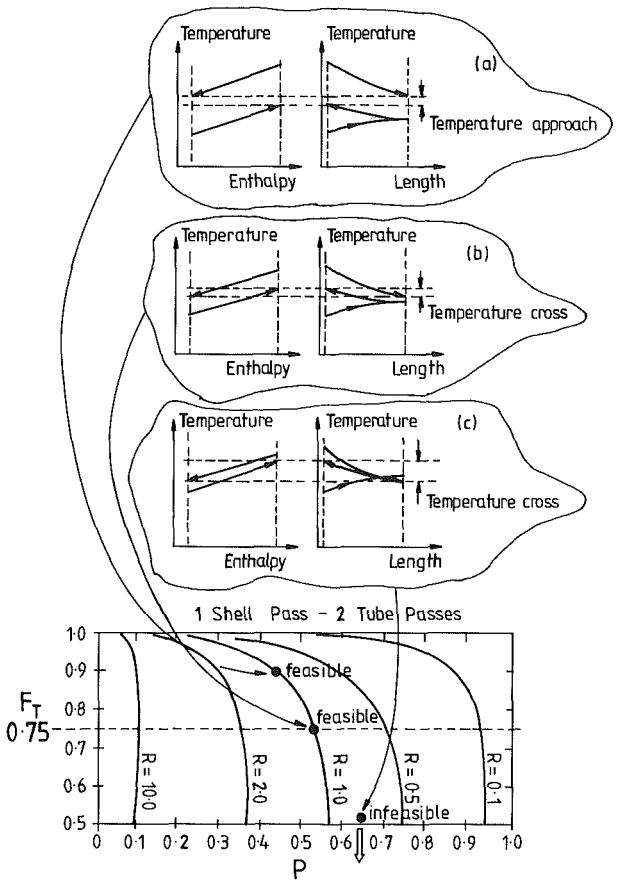

Fig. 1 Three basic temperature situations can be encountered when using 1-2 exchangers

curacies in design data also have a more significant effect when slopes are steep.

Consequently, if we are to be confident in a design, we should avoid those parts of the F_T chart where slopes are steep, irrespective of $F_T \geq 0.75$. These considerations have been acknowledged previously in qualitative form by Taborek (1979, 1983b) and Liu et al. (1985), but they do not appear to be widely practiced. This is probably because no easily interpreted rules of thumb are available.

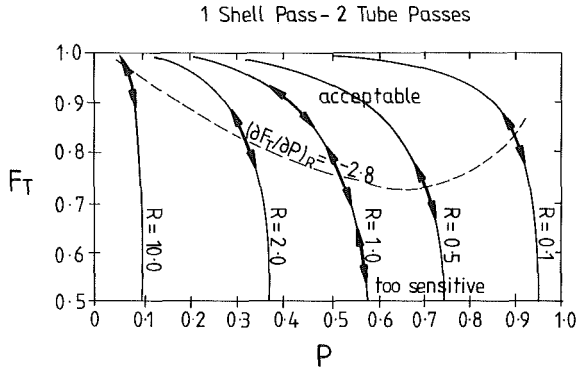

Fig. 2 A line of constant slope can be defined to separate regions of preferred design from regions of unacceptable design

These arguments can be made quantitative by introducing a line of constant slope, that is

$$(\partial F_T/\partial P)_R = \text{const}$$

The expression for $(\partial F_T/\partial P)_R$ for 1-2 design has been derived by Mitson (1984) as

$$(\partial F_T/\partial P)_R = [F_T/P(1-P)] - [(1-P)F_T^2/\sqrt{2}P][\beta/(2-P\beta) - \alpha/(2-P\alpha)] \quad (5)$$

where $\alpha = 2-\sqrt{2}$ and $\beta = 2+\sqrt{2}$.

A line of constant slope that follows the same slope as the point $F_T = 0.75$ at $R = 1$ has $(\partial F_T/\partial P)_R = -2.8$, and is illustrated in Fig. 2. Design can be carried out with far greater confidence above the line of constant slope irrespective of $F_T \geq 0.75$. The line of constant slope shown in Fig. 2 was chosen simply to be in line with current acceptable design practice. More conservative design would require a line of less steep slope, say for example $(\partial F_T/\partial P)_R = -1$. The value of the slope to be tolerated is at the discretion of the designer, similar to the lowest value of the F_T correction factor in the tradi-

Nomenclature

A = heat exchange area, m^2
CP_C = heat capacity flow rate of cold stream, kW/°C
CP_H = heat capacity flow rate of hot stream, kW/°C
F_T = logarithmic mean temperature difference correction factor
N = number of 1-2 shells in series
P = heat exchanger thermal effectiveness, equation (4)
P_{max} = maximum (asymptotic) value of P, equation (7)
$P_{1,2}$ = thermal effectiveness for a single 1-2 shell
$P_{1,2max}$ = maximum (asymptotic) value of $P_{1,2}$, equation (7)
$P_{N,2N}$ = overall thermal effectiveness for N 1-2 shells in series
Q = exchanger heat duty, kW
R = heat capacity flow-rate ratio, equation (3)
T's = inlet and outlet temperatures to an exchanger, °C
T_{Ci} = cold stream inlet temperature, °C
T_{Co} = cold stream outlet temperature, °C
T_{Hi} = hot stream inlet temperature, °C
T_{Ho} = hot stream outlet temperature, °C
ΔT_1 = temperature difference at exchanger hot end, °C
ΔT_C = cold stream temperature change, °C
ΔT_H = hot stream temperature change, °C
ΔT_{LM} = logarithmic mean temperature difference, °C
U = overall exchanger heat transfer coefficient, kW/m^2°C
X_P = Ratio of actual to maximum thermal effectiveness in a single 1-2 exchanger, equation (7)
$(\partial F_T/\partial P)_R$ = slope of F_T line against P for a given value of R on the F_T chart

tional approach. The slope becomes a particularly important consideration when 1-2 exchangers are to be used in situations in which the overall heat transfer coefficient varies appreciably over the length of the exchanger (see Bannerot and Mahajan, 1978).

3 A Simple Design Criterion

Although the constant slope criterion outlined in the previous section is an effective means of avoiding undesirable areas of the F_T chart, it is rather complex to evaluate and use. A simpler approach, which retains the essential advantages of the constant slope approach, is possible and will now be developed.

This alternative approach is based upon the observation that for any value of R there is a maximum asymptotic value for P, say P_{max}, which is given as F_T tends to $-\infty$. This represents the limit of thermal effectiveness in feasible 1-2 exchanger design for given heat capacity flow rates. An expression for P_{max} has been stated by Taborek (1983a) and also derived by Mitson (1984); it takes the form

$$P_{max} = 2/(R + 1 + \sqrt{R^2 + 1}) \tag{6}$$

A 1-2 exchanger designed for $P = P_{max}$ will not be feasible. However, exchangers with $P < P_{max}$ will be feasible. We can define a practical design to be limited to some fraction of P_{max} according to

$$P = X_P P_{max}, \quad \text{where } 0 < X_P < 1 \tag{7}$$

and X_P is a constant defined by the designer.

A typical profile for equation (7) with $X_P = 0.9$ is shown in Fig. 3 and compared with the line of constant slope for $(\partial F_T/\partial P)_R = -2.8$. It can be seen that the line $X_P = \text{const}$ follows the same basic profile as the line of constant slope.

In fact, the relationship between the slope $(\partial F_T/\partial P)_R$ and the parameter X_P can be expressed concisely (Fig. 4). To obtain the simple mapping between the constant slope and constant X_P criteria, $P = X_P P_{max} = 2X_P/(R + 1 + \sqrt{R^2 + 1})$ is substituted into the expression for $(\partial F_T/\partial P)_R$. In practice, the slope of the line $R = 1$ on F_T charts can be taken as a reasonable median from which to obtain X_P values against $(\partial F_T/\partial P)_R$. In summary, two competing criteria have been developed for exchanger design that are equally good. The constant X_P approach is simpler to use than the constant slope approach. However, we have only considered designs that require single 1-2 shells. Once designs that require multiple shells are considered, the constant X_P approach shows even more significant advantages over the constant slope approach.

4 Design with Multiple 1-2 Shells

Designers often encounter situations where the F_T is too low or the F_T slope too large. If this happens, they may be forced to consider either different types of shell or multipe shell arrangements (Fig. 5). The present paper will concentrate on multiple shell arrangements of the 1-2 type. The profiles shown in Fig. 5 could in principle be achieved either by two 1-2 shells in series or a single 2-4 shell. These two arrangements will be considered equivalent in design terms, displaying the same temperature profiles. Various ways of evaluating design situation that require multiple 1-2 shells in series will now be explored.

(a) Traditional Design Practice. Traditionally, the designer would approach a problem requiring multiple shells by trail and error. The design begins by assuming a number of shells, usually one in the first instance, and the F_T is evaluated. If the F_T is not acceptable then the number of shells in series is progressively increased until a satisfactory value for F_T is obtained for each shell. The task is simplified by having subcharts that evaluate the performance of the overall unit for arrangements of 2, 3, 4, etc., shells in series (see Bowman et

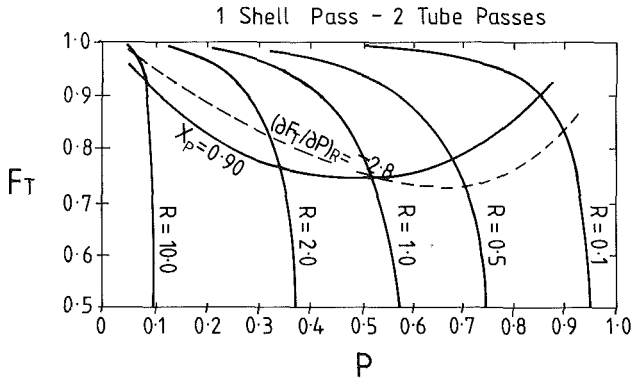

Fig. 3 A line of constant slope can be closely approximated by a line of constant X_P

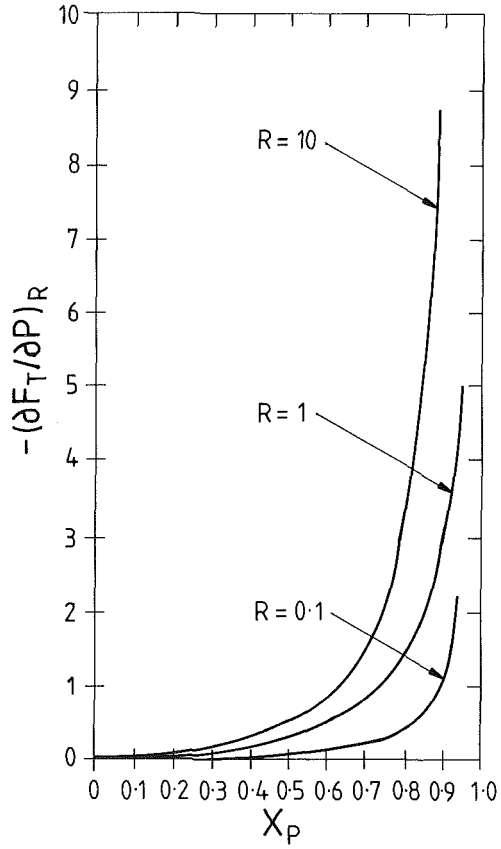

Fig. 4 The relationship between lines of constant slope and parameter X_P can be determined knowing the value of R

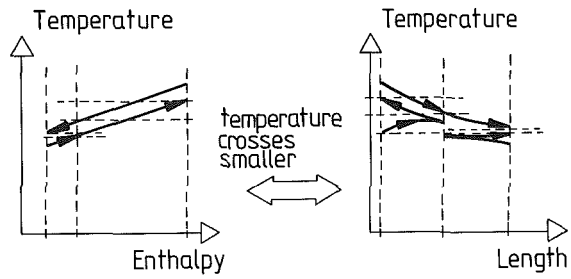

Fig. 5 Two 1-2 shells in series or a single 2-4 shell

al., 1940). We emphasize again that achieving minimum F_T may not be sufficient to achieve a satisfactory slope.

The traditional approach can be demonstrated using a simple example. A hot stream is to be cooled from 410°C to 110°C by exchange with a cold stream being heated from 0°C to 360°C, using 1-2 shells. For the problem overall $R=1.2$ and $P=0.73$. Try one shell initially and the problem is infeasible.

Adding another shell in series does not solve the problem since F_T is still infeasible. Three shells return a feasible $F_T=0.65$ against the appropriate chart for three shells. This F_T is too low and yet another shell is required. For four shells $F_T=0.8$ against the corresponding chart. This looks to be a reasonable solution to the problem as far as $F_T \geq 0.75$ is concerned, leaving for the moment F_T slope considerations.

Although this basic approach is the one most commonly used to determine the minimum number of 1-2 shells in series, trial and error is in fact not needed. Various ways of tackling this will now be explored.

(b) Simple Stepping-Off. The simplest method for multishell design is "stepping-off" as discussed by Bell (1983) and Liu et al. (1985). The method is illustrated in Fig. 6. Starting at the final cold stream temperature we project across horizontally to the hot stream, then vertically down to the cold stream and so on. Each step then corresponds to one shell. The basis of this method is to terminate each shell such that the outlet temperature of the hot stream equals the outlet temperature of the cold stream, giving zero temperature cross. This is often conservative in design because, in practice, some degree of temperature cross in each shell can usually be tolerated. Therefore, fewer shells are often required than suggested by this method.

One important point that should be understood about simple stepping-off is that each shell will have the same F_T. This results from:

(1) R being constant as a result of heat capacity flow rates being constant.

(2) P being constant for all shells as a result of each step being geometrically similar.

Since both R and P are constant for each step then F_T must also be constant.

Recognizing that this method gives constant F_T in each shell and is conservative in not allowing any temperature cross, a simple modification to the technique can allow us to step-off for any prespecified F_T.

(c) Stepping-Off With Prespecified F_T. Rather than stepping-off as shown in Fig. 6, we could step-off with a temperature cross as shown in Fig. 7. Providing the same geometry is maintained for each step, then F_T must remain

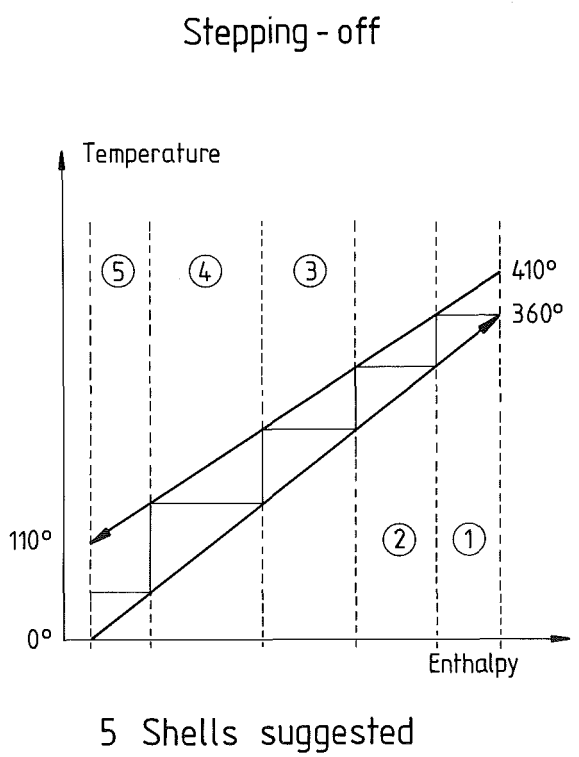

Fig. 6 The simplest method for multishell design is "stepping-off" (with no temperature cross allowed)

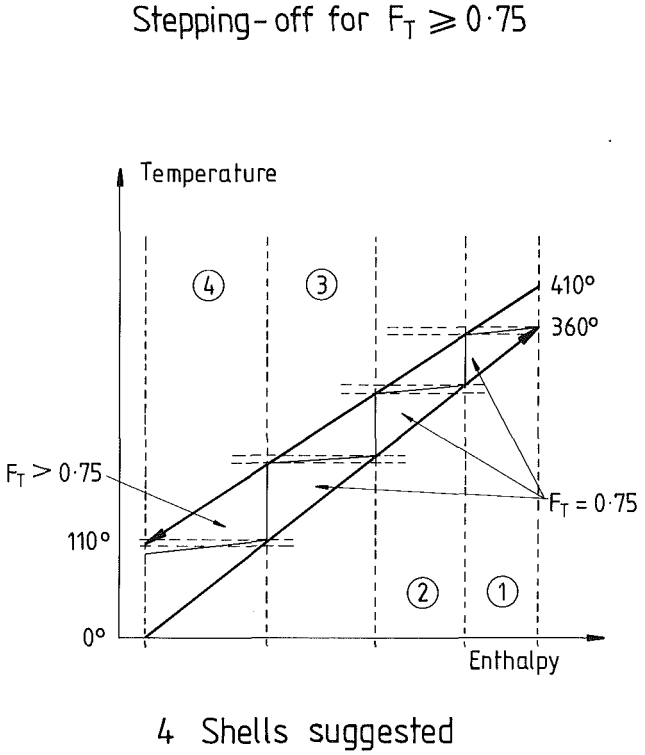

Fig. 7 Stepping-off can also be performed for temperature cross to achieve a prespecified value of F_T in each 1-2 shell

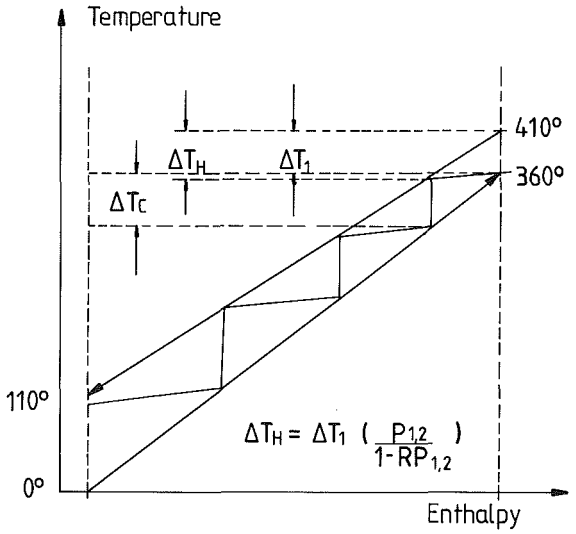

Fig. 8 The slope of the first step is given by ΔT_1, R, and $P_{1,2}$ (which depends on X_P). Continuing to step-off with the same slope will determine the number of shells required to satisfy a given value of X_P

constant in each shell. The designer can then step-off with a specified F_T as follows.

The unknown temperatures for the first step, T_{Ho} and T_{Ci}, can be calculated from R, F_T, T_{Hi}, and T_{Co} using equations (2), (3), and (4). This then establishes the step slope and the remainder of the problem can be stepped-off with the same slope as shown in Fig. 7. (Note that the slope referred to here in stepping-off is fundamentally different from the slope of $(\partial F_T/\partial P)_R$ discussed earlier.)

It makes no difference whether the F_T for stepping-off is chosen on the basis of traditional rules of thumb, such as $F_T \geq 0.75$, or a chosen value for $(\partial F_T/\partial P)_R$, because F_T is constant for each step in either case. However, we have yet another possibility for a stepping-off criterion, that is, a chosen value for X_P. As we will see, this offers definite advantages over $(\partial F_T/\partial P)_R = \text{const}$.

(d) Stepping-Off With Specified X_P. The temperature span covered by a single 1-2 shell will determine its value of P. Next, we know that $P_{\max}$ for each shell is determined fully by the ratio of heat capacity flow rates, R, in equation (6).

Introducing X_P, say $X_P = 0.9$, will fix P through equation (7). The value of P so chosen in each shell, $P_{1,2}$, is sufficient information to place the steps. The size of the first step is easily deduced by reference to Fig. 8.

$P_{1,2}$ for a given step-size is defined by

$$P_{1,2} = \Delta T_H/(\Delta T_1 + \Delta T_C) \tag{8}$$

Since $R = \Delta T_C/\Delta T_H$, then equation (8) gives

$$P_{1,2} = \Delta T_H/\Delta T_1 + R\Delta T_H) \tag{9}$$

which can be rearranged to

$$\Delta T_H = \Delta T_1[P_{1,2}/(1 - RP_{1,2})] \tag{10}$$

Since $P_{1,2}$ is determined fully from R and X_P, equations (6) and (7), the step slope given by ΔT_H ultimately depends only on the designer's choice of X_P.

To complete the design we carry on stepping-off with the same step slope. Keeping the same step slope ensures the same X_P, the same $(\partial F_T/\partial P)_R$, and the same F_T in each shell.

Figure 9 shows the example introduced earlier with the steps completed for $X_P = 0.9$. This corresponds to $F_T \geq 0.75$ in each shell and the problem requires four shells, but now ensuring that uncertain areas of the F_T chart according to $X_P = 0.9$ have been avoided. If a more conservative value of X_P is chosen, say $X_P = 0.8$, then the step slope will be different, resulting in a different number of shells to solve the problem.

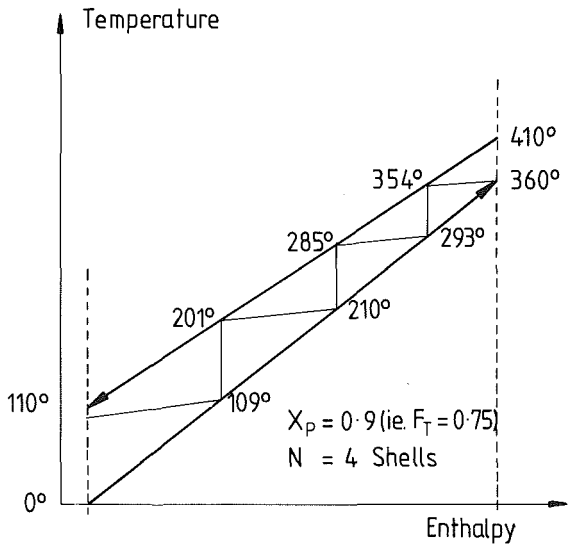

Fig. 9 Stepping-off to meet a given value of X_P is consistent with achieving the corresponding value of F_T

5 An Analytical Procedure

It is possible to transform the graphical stepping-off procedure into a more convenient analytical equivalent by making use of the expression of Bowman (1936). This relates the overall P for N shells in series of 1-2 design, $P_{N,2N}$, with the individual P for each shell, $P_{1,2}$, and is of the form:

$$P_{N,2N} = f(R, P_{1,2}, N) \tag{11}$$

If we apply equation (7), the definition of X_P, to this unit overall then

$$P_{N,2N} = f(R, X_P\ P_{1,2\max}, N) \tag{12}$$

Recognizing from equation (6) that $P_{1,2\max}$ is only a function of R, then

$$P_{N,2N} = f(R, X_P, N) \tag{13}$$

If we invert this function we can evaluate N directly

$$N = f^{-1}(R, P_{N,2N}, X_P) \tag{14}$$

Details of the derivation have been given by Ahmad (1985) and the final expression is

$R \neq 1$:

$$N = \ln[(1 - RP_{N,2N})/(1 - P_{N,2N})]/\ln W \tag{15}$$

where

$$W = (R + 1 + \sqrt{R^2 + 1} - 2RX_P)/(R + 1 + \sqrt{R^2 + 1} - 2X_P) \tag{16}$$

$R = 1$:

$$N = (P_{N,2N}/1 - P_{N,2N})(1 + (\sqrt{2}/2) - X_P)/X_P \tag{17}$$

Equations (15)-(17) return a value of N that satisfies precisely a chosen value of X_P throughout the series of 1-2 shells. Taking the number of shells to be the next largest integer above N will result in X_P becoming marginally improved (decreased) over the originally specified value. These expressions evaluate explicitly the minimum number of 1-2 shells required and, at the same time, ensure that each shell in the design satisfies the

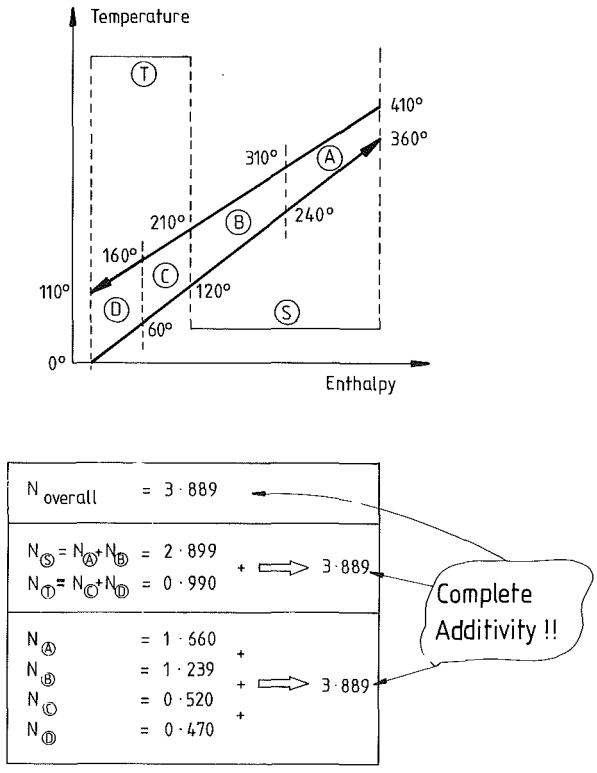

Fig. 10 No matter how we divide the problem into sections, there is complete additivity among the parts in determining the overall number of shells

required F_T slope criterion given by the specification for X_P. Applying this analytical approach to the problem in Fig. 9 with $X_P = 0.9$ we obtain the answer that 3.9 shells are required (four shells in practice).

The expressions given above for the number of shells are simple and straightforward to use. F_T slope requirements for each individual shell are observed through the definition of the X_P parameter. The reason the method is so straightforward is that we no longer include F_T explicitly in the analysis. For a given problem R is fixed and, X_P having been specified, F_T has also been specified implicitly but is not used directly.

The authors believe that the introduction of the X_P parameter both simplifies and improves procedures for the design of heat exchangers:

(*i*) Better designs are generated than those based on traditional rules of thumb, such as $F_T \geq 0.75$, because uncertain areas of the F_T chart are avoided more effectively.

(*ii*) For multishell arrangements the number of shells can be evaluated explicitly, requiring neither trial and error nor graphic constructions.

(*iii*) For evaluating the number of 1-2 shells in series, recourse to F_T charts is no longer necessary.

6 Additivity—an Important Property

Now that we have the inversion

$$N = f^{-1}(T\text{'s, desirable } F_T)$$

$$= f^{-1}(T\text{'s}, X_P) \tag{18}$$

one further most important property can be demonstrated. Consider again the example introduced earlier. If, instead of solving the overall problem for the number of shells, we solve the problem in parts and add up the parts, will we always get the same result?

This is demonstrated in Fig. 10. The problem overall requires 3.889 shells. If we divide the problem arbitrarily into two parts, S, and T as shown, then part S requires 2.899 and part T requires 0.990 giving a total of precisely 3.889. It does not matter how many sections we divide the problem into and how big the sections are, we always get identically the same result provided we work in fractional shells. When the problem is divided into four arbitrary parts A, B, C, and D, adding up the individual shell requirements gives precisely 3.889 again.

Concerning consistency between F_T charts and the Bowman equations we have now established the theoretical link between the number of shells N and F_T via the parameter X_P. We are told that for a given F_T (as specified by R and X_P) the number of shells is additive over any arbitrary number of sections over the exchanger profile so long as we maintain the same F_T in each section. Additivity in these charts has always existed but probably gone unnoticed because: (*i*) F_T charts could not be constructed for fractional values of N and (*ii*) The inversion $N = f^{-1}(T\text{'s}, F_T)$ has not been expressed previously.

The additive property takes on fundamental practical significance when complex problems are addressed where heat capacity flow rates and overall heat transfer coefficients are not constant. In this context, there exists no additivity in the traditional approach that would allow the overall problem to be decomposed into meaningful subproblems. Faced with a complex problem the designer has no recourse at present by to resort to the use of detailed computer models. Development of the current approach may lead either to a reduction in the need for detailed computer models or at least to better initialization for the computer models. This is being explored in current research.

On a different subject, additivity also allows the prediction of the minimum number of shells required for the heat exchanger network of an entire process ahead of design, allowing predesign optimization to be carried out (Linnhoff and Ahmad, 1986).

7 Conclusions

The following points can be made concerning the X_P parameter approach as introduced in this paper. For 1-2 shells in general:

- significantly better exchanger designs than those based on rules of thumb for minimum F_T, such as $F_T \geq 0.75$;
- similarly good designs as those based directly on constant F_T slope.

A new criterion for 1-2 exchanger feasibility has been proposed that does not relate to F_T. Instead it is based on the limiting 1-2 exchanger effectiveness, that is, $P_{\max}$.

In the case of multishell arrangements we have shown that different F_T criteria can be interpreted as variations of stepping-off. The X_P parameter approach is also represented as a modification of stepping-off. Next, it has been shown that the X_P parameter is ideally suited to obtaining a simple expression determining explicitly the minimum number of 1-2 shells in series for multishell designs. This alters the traditional design approach for multishell arrangements.

It should be borne in mind, however, that any results at this level of exchanger design based on minimum F_T, F_T slope, or X_P are still subject to detailed evaluation. Given that any of these F_T-based results are really initializations, we do not need to be absolutely precise. More importantly, design practice requires speed and simplicity at this stage of design. The X_P parameter approach achieves fast evaluation at remarkable reliability.

Acknowledgments

The authors would like to thank their colleague, Dr. G. T. Polley, for useful criticism and help in the preparation of this paper, and the Journal referees for their useful comments.

References

Ahmad, S., 1985, "Heat Exchanger Networks: Cost Tradeoffs in Energy and Capital," Ph.D. Thesis, University of Manchester Institute of Science and Technology, United Kingdom.

Bannerot, R. B., and Mahajan, K. K., 1978, "The Caloric Temperature Factor for a 1-2 Heat Exchanger With an Overall Heat Transfer Coefficient Varying Linearly With Tube Side Temperature," *AIChE Symp. Series*, Vol. 74, No. 171, p. 61.

Bell, K. J., 1983, *Heat Exchanger Design Handbook*, Vol. 3, Hemisphere Publishing Corporation, Washington, D. C.

Bowman, R. A., 1936, "Mean Temperature Difference Correction in Multipass Exchangers," *Ind. Eng. Chem.*, Vol. 28, p. 541.

Bowman, R. A., Mueller, A. C., and Nagle, W. M., 1940, "Mean Temperature Difference in Design," *Trans. ASME*, Vol. 62, p. 283.

Kern, D. Q., 1950, *Process Heat Transfer*, McGraw-Hill, New York.

Linnhoff, B., and Ahmad, S., 1986, "SUPERTARGETING, or the Optimisation of Heat Exchanger Networks Prior to Design," World Congress III of Chemical Engineering, Tokyo, Japan.

Liu, Y. A., Pehler, F. A., and Cahela, D. R., 1985, "Studies in Chemical Process Design and Synthesis. Part VII: Systematic Synthesis of Multipass Heat Exchanger Networks," *AIChE Journal*, Vol. 31, p. 487.

Mitson, R. J., 1984, "Number of Shells Versus Number of Units in Heat Exchanger Network Design," M.Sc. Dissertation, University of Manchester Institute of Science and Technology, United Kingdom.

Taborek, J., 1979, "Evolution of Heat Exchanger Design Techniques," *Heat Transfer Eng.*, Vol. 1, p. 15.

Taborek, J., 1983a, *Heat Exchanger Design Handbook*, Vol. 1, Hemisphere Publishing Corporation, Washington, D. C.

Taborek, J., 1983b, *Heat Exchanger Design Handbook*, Vol. 3, Hemisphere Publishing Corporation, Washington, D. C.

Numerical Analysis of Laminar Forced Convection in the Entrance Region of Tubes With Longitudinal Internal Fins

I. M. Rustum
Graduate Student.

H. M. Soliman
Associate Professor.
Mem. ASME

Department of Mechanical Engineering,
University of Manitoba,
Winnipeg, Manitoba,
Canada R3T 2N2

Steady, laminar, forced convection heat transfer in the thermal entrance region of internally finned tubes is investigated numerically for the case of fully developed hydrodynamics using the (H1) and (T) thermal boundary conditions. Results are presented for 16 geometries including the local Nusselt number and developing length corresponding to each boundary condition. These results indicate that internal finning influences the thermal development in a complicated way, which makes it inappropriate to extend the smooth tube results to internally finned tubes on a hydraulic diameter basis.

Introduction

Previous theoretical investigations of laminar fluid flow and heat transfer in internally finned tubes have been predominantly concerned with forced convection in the fully developed region. These include studies of the velocity distribution and friction factor (Hu and Chang, 1973; Nandakumar and Masliyah, 1975; Soliman and Feingold, 1977) and the temperature distribution and Nusselt number for the conditions of uniform heat input axially with uniform wall temperature circumferentially (Masliyah and Nandakumar, 1976; Soliman and Feingold, 1978), uniform heat input axially and circumferentially (Hu and Chang, 1973), and uniform wall temperature axially and circumferentially (Soliman et al., 1980). Other effects such as the influence of fin conductance (Soliman, 1981) and mixed free and forced convection in the vertical orientation (Prakash and Patankar, 1981) were investigated in recent studies.

Due to the relevance of internally finned tubes to compact heat exchangers, it is necessary to produce results in the developing region. Only one investigation was reported (Prakash and Liu, 1985) in which simultaneous development of velocities and temperature was studied theoretically. In the present investigation, a theoretical study is conducted for forced convective heat transfer in the developing region of internally finned tubes with fully developed hydrodynamics. The theoretical results presented in this paper should define the limiting values of the heat transfer parameters as Grashof number (which is a measure of free convection) decreases to a certain critical value.

Analytical Formulation

The geometry under consideration (shown in Fig. 1) is that of a circular tube with a variable number of straight longitudinal fins evenly distributed around the inner circumference of the tube. Fins are assumed to be of negligible thickness with sides oriented radially within the tube cross section. The assumption of zero fin thickness helps in eliminating one of the geometric variables and it is motivated by earlier results (Masliyah and Nandakumar, 1976; Soliman et al., 1980), which showed significant fin-thickness effects on heat transfer only for large numbers of long fins.

This analysis is applicable to steady, laminar, forced convection flow of incompressible, Newtonian fluids with constant properties. Axial conduction and viscous dissipation within the fluid are assumed negligible. The flow is assumed to be fully developed hydrodynamically but developing thermally. Heat transfer results are sought for the two limiting boundary conditions of uniform heat input axially with uniform wall (tube and fins) temperature cross-sectionally and uniform wall temperature axially and cross-sectionally, classified by Shah and London (1978) as the (H1) and (T) boundary conditions, respectively. The uniformity of fin temperature in the radial direction for both boundary conditions implies negligible thermal resistance in the fins, which was found in an earlier analysis by Soliman et al. (1980) to be a reasonable assumption for a wide range of applications. Due to geometric symmetry of the flow domain (see Fig. 1), solutions of the governing equations are necessary only within $0 \le r \le r_i$ and $0 \le \theta \le \alpha$.

Momentum Equation. Introducing the dimensionless quantities $U = u/[(r_i^2/\mu)(-dp/dx)]$ and $R = r/r_i$, the applicable momentum equation takes the form

$$\frac{1}{R}\frac{\partial}{\partial R}\left(R\frac{\partial U}{\partial R}\right) + \frac{1}{R^2}\frac{\partial^2 U}{\partial \theta^2} = -1 \qquad (1)$$

In order to establish a well-defined boundary condition at the tube centerline, the transformation $U' = U \cdot R$ was introduced. The final form of the momentum equation is then

$$\frac{1}{R}\frac{\partial^2 U'}{\partial R^2} - \frac{1}{R^2}\frac{\partial U'}{\partial R} + \frac{1}{R^3}\left(U' + \frac{\partial^2 U'}{\partial \theta^2}\right) = -1 \qquad (2)$$

Equation (2) is subject to the following boundary conditions:

$$U' = 0 \quad \text{at} \quad R = 0, \quad R = 1,\ 0 \le \theta \le \alpha, \quad \text{and} \quad (1-H) \le R \le 1,\ \theta = 0 \qquad (3a)$$

$$\frac{\partial U'}{\partial \theta} = 0 \quad \text{at} \quad 0 < R < (1-H),\ \theta = 0, \quad \text{and} \quad 0 < R < 1,\ \theta = \alpha \qquad (3b)$$

The following definitions were adopted for the friction factor f and Reynolds number Re (which use the inside tube diameter D_i as the characteristic dimension):

$$f = D_i(-dp/dx)/(2\rho u_b^2) \qquad (4)$$

and

$$\mathrm{Re} = \rho\, u_b D_i/\mu \qquad (5)$$

Consequently, the product $f\mathrm{Re}$ can be reduced to this dimensionless form

$$f\mathrm{Re} = 2/U_b \qquad (6)$$

Contributed by the Heat Transfer Division for publication in the JOURNAL OF HEAT TRANSFER. Manuscript received by the Heat Transfer Division January 6, 1987. Keywords: Finned Surfaces, Forced Convection, Numerical Methods.

It is clear from the above equations that the product fRe is dependent only on the geometric parameters M and H.

Energy Equation: (H1) Boundary Condition. Introducing the dimensionless axial coordinate $X^+ = x/(D_i \text{ Re Pr})$ and defining $T' = T \cdot R$, where $T = (t - t_i)/(qD_i/k)$, the energy equation for the (H1) boundary condition can be reduced to this dimensionless form

$$R\frac{\partial^2 T'}{\partial R^2} - \frac{\partial T'}{\partial R} + \frac{1}{R}\left(T' + \frac{\partial^2 T'}{\partial \theta^2}\right) = (f\text{Re}/8)U'\frac{\partial T'}{\partial X^+} \tag{7}$$

At inlet ($X^+ = 0$), equation (7) is subject to the initial condition $T' = 0$, while for $X^+ > 0$ these boundary conditions apply

$$T' = 0 \quad \text{at} \quad R = 0 \tag{8a}$$

$$T' = T_w \quad \text{at} \quad R = 1,\ 0 \le \theta \le \alpha \tag{8b}$$

$$T' = T_w \cdot R \quad \text{at} \quad (1 - H) \le R \le 1,\ \theta = 0 \tag{8c}$$

$$\frac{\partial T'}{\partial \theta} = 0 \quad \text{at} \quad 0 < R < (1 - H),\ \theta = 0, \quad \text{and} \quad 0 < R < 1,\ \theta = \alpha \tag{8d}$$

The parameter T_w in equations (8b) and (8c) is the dimensionless wall temperature, which is a function of X^+; however, its value is not known a priori. The method used for determining T_w at each axial location X^+ is similar to the one used by Prakash and Liu (1985). The circumferentially averaged values of the heat transfer coefficient $h_{x,H1}$ and Nusselt number $\text{Nu}_{x,H1}$ at any axial location are defined by

$$h_{x,H1} = q/(t_w - t_b) \tag{9a}$$

and

$$\text{Nu}_{x,H1} = h_{x,H1} D_i/k \tag{9b}$$

Nondimensionalizing, equation (9b) takes the form

$$\text{Nu}_{x,H1} = 1/(T_w - T_b) \tag{10}$$

Energy Equation: (T) Boundary Condition. Introducing the dimensionless quantities $T' = T \cdot R$ and $T = (t - t_w)/(t_i - t_w)$ we find that the dimensionless energy equation for the (T) boundary condition is identical to equation (7). At $X^+ = 0$, the initial condition is given by $T' = R$ within the fluid and $T' = 0$ at the solid boundaries. For $X^+ > 0$ the applicable boundary conditions are

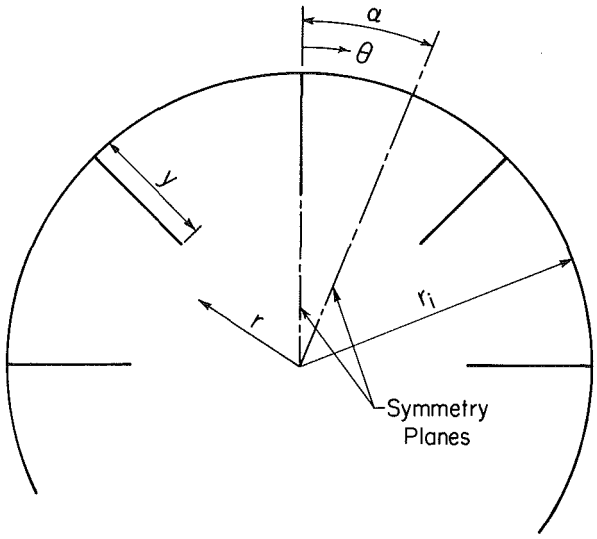

Fig. 1 Geometry and coordinate system

$$T' = 0 \quad \text{at} \quad R = 0, \quad R = 1,\ 0 \le \theta \le \alpha, \quad \text{and} \quad (1 - H) \le R \le 1,\ \theta = 0 \tag{11a}$$

$$\frac{\partial T'}{\partial \theta} = 0 \quad \text{at} \quad 0 < R < (1 - H),\ \theta = 0, \quad \text{and} \quad 0 < R < 1,\ \theta = \alpha \tag{11b}$$

The circumferentially averaged value of Nusselt number at any axial location can still be calculated from definitions (9a) and (9b). The local average heat flux q (based on the unfinned surface area of the tube), which appears in (9a), was calculated by summing all heat inputs from the solid boundaries (tube wall and fin sides) and dividing the sum by (πD_i).

Solution Procedure

Solutions for the temperature distribution in the fully developed and developing regions were obtained numerically using the finite difference method. Second-order central differences were used for the derivatives in the R and θ directions and backward differences were used for derivatives in the X^+ direction. The resulting systems of linear algebraic equations were solved using the Gauss-Seidel method with overrelaxation factors ranging from 1.90 to 1.99.

The solution domain in the R, θ, and X^+ directions was

Nomenclature

D_i = inside diameter of tube $= 2r_i$
f = friction factor, equation (4)
H = relative fin height $= y/r_i$
k = thermal conductivity
L^+_{H1} = dimensionless entrance length for the (H1) condition
L^+_T = dimensionless entrance length for the (T) condition
M = number of fins
$\text{Nu}_{x,H1}$ = local Nusselt number for the (H1) condition
$\text{Nu}_{x,T}$ = local Nusselt number for the (T) condition
p = pressure
Pr = Prandtl number
q = mean heat flux based on inside diameter
R = dimensionless radial coordinate $= r/r_i$
r = radial coordinate
r_i = inside radius of tube
Re = Reynolds number, equation (5)
T = dimensionless temperature
T_b = dimensionless bulk temperature
T_w = dimensionless wall temperature
t = temperature
t_b = bulk temperature
t_i = inlet temperature
t_w = wall temperature
U = dimensionless velocity
U_b = dimensionless mean velocity
u = velocity
u_b = mean velocity
x = axial coordinate
X^+ = dimensionless axial coordinate
y = fin height
α = half the angle between two consecutive fins $= \pi/M$
θ = angular coordinate
μ = viscosity
ρ = density

discretized by an uneven three-dimensional mesh. At any cross section, higher concentrations of mesh points were used near the solid boundary (tube wall and fin side), under the fin tip, and near the tube centerline due to the steep gradients at these locations. Smaller subdivisions are needed near $R=0$ because the radial gradients of U' and T' do not approach zero at the centerline as the gradients of U and T do. Similarly, in the X^+ direction, very small values of ΔX^+ were used near the beginning of heating, increasing gradually in the flow direction. The decision about the mesh size in the R and θ directions was guided by the accuracy of the results in the fully developed region. Solutions were obtained for a number of extreme geometries using different mesh sizes and based on these results, it was decided to use a 35×20 mesh throughout the solution domain for all tube geometries as a reasonable compromise between accuracy and computer time.

Solutions were progressed in the X^+ direction for both the (H1) and (T) boundary conditions until the local Nusselt number reached 1.05 times the respective fully developed value. The magnitude of X^+ at this location was taken as an estimate of the thermal entrance length L^+. The decision about the mesh size in the X^+ direction was guided mainly by the accuracy of the results for the smooth tube case. After considerable experimentation it was decided to use the following distribution of axial stations for all tube geometries: 10 stations with $\Delta X^+ = 0.5\times10^{-6}$ followed by 10 stations with $\Delta X^+ = 0.5\times10^{-5}$, then ΔX^+ was increased gradually so that ΔX^+ at a particular station was 1.05 times ΔX^+ of the previous station until ΔX^+ reached the value 0.5×10^{-3}, which was kept constant for the remainder of the entrance length. Values of Nu_x obtained with this mesh for the smooth tube case were in excellent agreement with the analytical results reported by Shah and London (1978). Also, our values of $L^+_{H1}=0.0442$ and $L^+_T=0.0357$ for smooth tubes agree well with 0.0437 and 0.0344, respectively (Shah and London, 1978). Trials with finer mesh sizes in the X^+ direction using selected finned tube geometries resulted in higher computation time without significant changes in the Nu_x and L^+ values.

Results and Discussion

The geometric range covered in this investigation includes the smooth tube and finned tubes with combinations of the following geometric parameters:

H = 0.2, 0.4, 0.6, and 0.8

M = 4, 8, 16, and 24

Developing Heat Transfer: (H1) Boundary Condition. Figures 2 to 5 show the development of the local Nusselt number $Nu_{x,H1}$ over the region $10^{-4}<X^+<L^+_{H1}$ for $M=4$, 8, 16, and 24, respectively. In each figure, the influence of fin height is illustrated by showing results for $H=0$ (smooth tube), 0.2, 0.4, 0.6, and 0.8. The inside tube diameter is used as the characteristic dimension in $Nu_{x,H1}$ and X^+, rather than the hydraulic diameter, in order to show the enhancement caused by internal finning in a definite manner.

For all geometries, $Nu_{x,H1}$ follows the expected behavior of monotonic decrease along the developing region down to the fully developed value. An interesting feature of the results in Figs. 2 to 5 is that all finned tubes appear to have approximately the same rate of decrease as $Nu_{x,H1}$ with respect to X^+ near the beginning of heating and this rate is approximately equal to the rate for smooth tubes. However, sharp changes in this rate occur later in the developing region and this is particularly noticeable for large numbers ($M=16$ and 24) of medium-height fins ($H=0.4$ and 0.6). Naturally, this behavior is expected to have some effects on the L^+_{H1} results to be presented later. In an attempt to explain this behavior, the temperature development at some cross-sectional locations was studied. For smooth tubes, it was found that (T_w-T) increases monotonically in the axial direction for all radial locations within the tube cross section. On the other hand, for some internally finned tubes (e.g., $M=24$ and $H=0.6$), (T_w-T) was found to increase monotonically at some locations within the core ($R=0.2$) while at other locations within the bays formed by the fins ($R=0.7$), (T_w-T) starts out increasing, reaches a maximum, and then drops toward the fully developed value. This unconventional manner of temperature development is probably caused by the complex velocity distribution (Soliman and Feingold, 1977) and the irregular shape of the wall-fluid interface where heat transfer takes place. Interestingly, for $M=24$ and $H=0.8$ the form of temperature development was found to be similar to smooth tubes, which is consistent with the $Nu_{x,H1}$ behavior for this geometry shown in Fig. 5. The $Nu_{x,H1}$ results of Prakash and Liu (1985) for simultaneous development of velocities and temperature showed trends quite similar to those in Figs. 2 to 5.

Table 1 provides values of the entrance length L^+_{H1} for the whole range of finned tube geometries considered in this investigation. These results contain maxima and minima that are not easy to explain, but which can be attributed to the complicated way by which the geometry influences the velocity distribution and in turn the temperature and local Nusselt number developments. Two important observations can be made from the results in Table 1:

1 The value of L^+_{H1} for some finned tube geometries exceeds

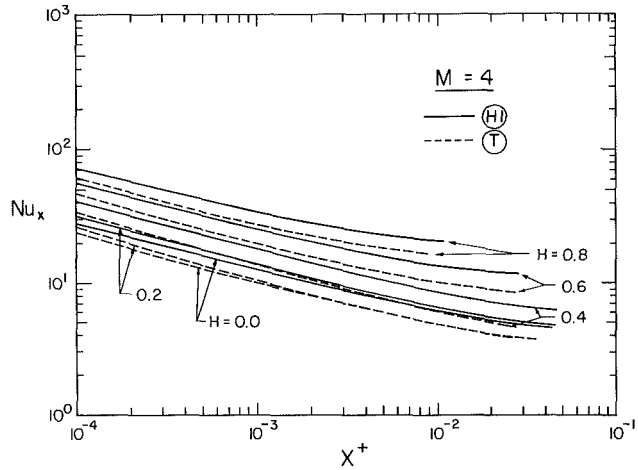

Fig. 2 $Nu_{x,H1}$ and $Nu_{x,T}$ for $M=4$

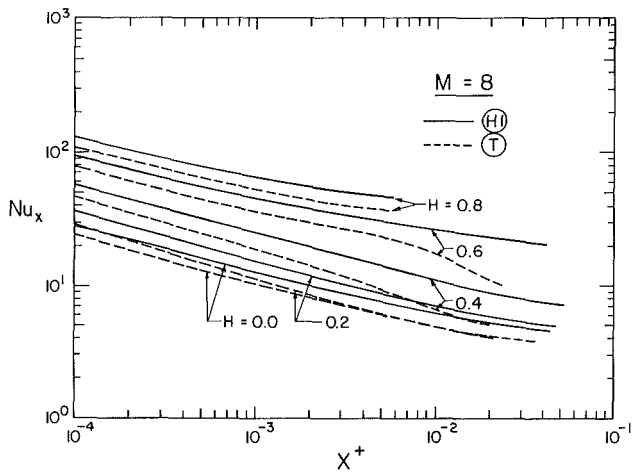

Fig. 3 $Nu_{x,H1}$ and $Nu_{x,T}$ for $M=8$

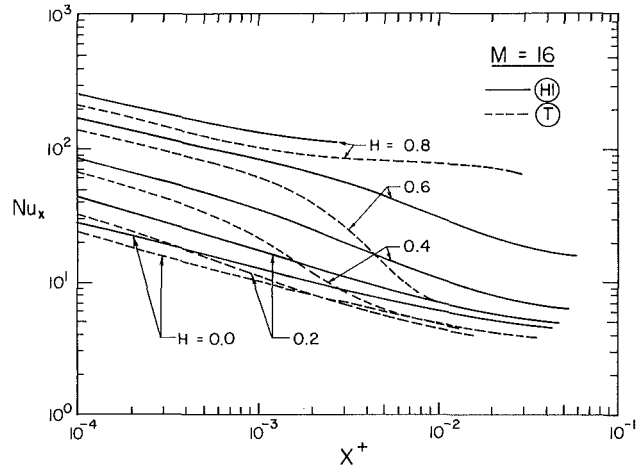

Fig. 4 $Nu_{x,H1}$ and $Nu_{x,T}$ for $M = 16$

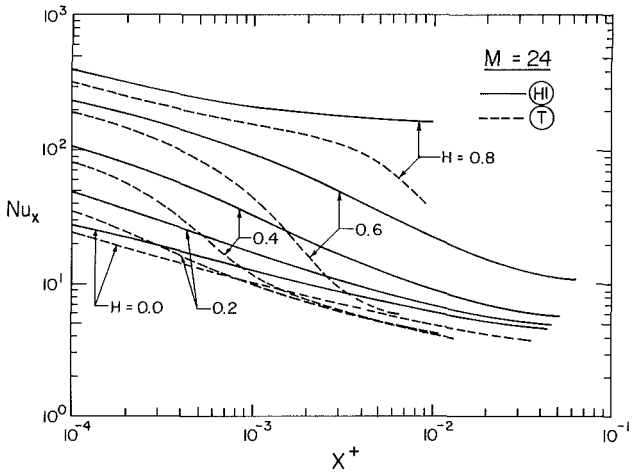

Fig. 5 $Nu_{x,H1}$ and $Nu_{x,T}$ for $M = 24$

the value for smooth tubes, which is contrary to some expectations.

2 The assumption that the entrance length for finned tubes based on the hydraulic diameter may be equated to the entrance length for smooth tubes appears to be invalid.

Both of the above observations, as well as the existence of local maxima and minima, are consistent with the trends in the results of Prakash and Liu (1985). In terms of magnitudes, the present results for $H = 0.6$ are 45.7 to 51.4 percent lower than the predictions of Prakash and Liu; however, their flow situation is different from ours.

Developing Heat Transfer: (T) Boundary Condition. The present results of $Nu_{x,T}$ are shown in Figs. 2 to 5 and values of L_T^+ are listed in Table 2. For all geometries considered, the value of $Nu_{x,T}$ is lower than the corresponding $Nu_{x,H1}$ at the same X^+. Also, $Nu_{x,T}$ shows an irregular rate of development along X^+ as was noted for the (H1) case. This irregular rate of development is reflected in the L_T^+ results, which contain local maxima and minima similar to the L_{H1}^+ results. For $H = 0.6$, the present results of L_T^+ are 44.1 to 77.4 percent lower than those of Prakash and Liu (1985).

Establishing general trends from the present results was found to be a difficult task. For example, values of L_T^+ are generally lower than L_{H1}^+; however, for the case $M = 16$ and $H = 0.8$, L_T^+ is more than 10 times L_{H1}^+. Also, the ratio L_{H1}^+/L_T^+ varies significantly among different geometries. While it is unfortunate that simple but accurate correlations cannot be developed for $Nu_{x,H1}$, $Nu_{x,T}$, L_{H1}^+, and L_T^+, the results are useful in their present form and should serve as a warning against extending smooth tube results to other geometries on a hydraulic diameter basis.

Table 1 Values of L_{H1}^+

H	$M=4$	8	16	24
0.2	0.0451	0.0462	0.0475	0.0466
0.4	0.0458	0.0524	0.0544	0.0518
0.6	0.0287	0.0412	0.0596	0.0630
0.8	0.0109	0.00588	0.00275	0.0102

Table 2 Values of L_T^+

H	$M=4$	8	16	24
0.2	0.0259	0.0209	0.0157	0.0131
0.4	0.0255	0.0197	0.0128	0.0107
0.6	0.0274	0.0234	0.00929	0.00649
0.8	0.00882	0.00551	0.0296	0.00925

Concluding Remarks

In the entrance region of internally finned tubes, the local Nusselt number for both boundary conditions exhibited some unconventional behavior. At very low values of X^+, the rate of decrease of local Nusselt number for all finned tube geometries was found to be almost equal to that of smooth tubes. However, sharp changes occurred in this rate later in the developing region, which resulted in unexpected trends in the magnitudes of the entrance length. This behavior is attributed to the fact that internal finning influences the velocity distribution and results in a complex geometry for the wall-fluid interface (where heat transfer takes place), which may cause the form of temperature development to be different from that of smooth tubes.

It must be emphasized that all the present results correspond to pure forced convection, i.e., flows with low Grashof number. Free convective currents superimposed on the main flow may have substantial effects on the heat transfer characteristics.

Acknowledgments

Financial assistance provided by the Natural Sciences and Engineering Research Council of Canada is gratefully acknowledged.

References

Hu, M. H., and Chang, Y. P., 1973, "Optimization of Finned Tubes for Heat Transfer in Laminar Flow," ASME JOURNAL OF HEAT TRANSFER, Vol. 95, pp. 332-338.

Masliyah, J. H., and Nandakumar, K., 1976, "Heat Transfer in Internally Finned Tubes," ASME JOURNAL OF HEAT TRANSFER, Vol. 98, pp. 257-261.

Nandakumar, K., and Masliyah, J. H., 1975, "Fully Developed Viscous Flow in Internally Finned Tubes," *The Chemical Engineering Journal*, Vol. 10, pp. 113-120.

Prakash, C., and Patankar, S. V., 1981, "Combined Free and Forced Convection in Vertical Tubes With Radial Internal Fins," ASME JOURNAL OF HEAT TRANSFER, Vol. 103, pp. 566-572.

Prakash, C., and Liu, Y. D., 1985, "Analysis of Laminar Flow and Heat Transfer in the Entrance Region of an Internally Finned Circular Duct," ASME JOURNAL OF HEAT TRANSFER, Vol. 107, pp. 84-91.

Shah, R. K., and London, A. L., 1978, *Laminar Flow Forced Convection in Ducts*, Academic Press, New York.

Soliman, H. M., and Feingold, A., 1977, "Analysis of Fully Developed Laminar Flow in Internally Finned Tubes," *The Chemical Engineering Journal*, Vol. 14, pp. 119-128.

Soliman, H. M., and Feingold, A., 1978, "Analysis of Heat Transfer in Internally Finned Tubes Under Laminar Flow Conditions," *Proceedings, 6th International Heat Transfer Conference*, Vol. 2, pp. 571-576.

Soliman, H. M., Chau, T. S., and Trupp, A. C., 1980, "Analysis of Laminar Heat Transfer in Internally Finned Tubes With Uniform Outside Wall Temperature," ASME JOURNAL OF HEAT TRANSFER, Vol. 102, pp. 598-604.

Soliman, H. M., 1981, "The Effect of Fin Conductance on Laminar Heat Transfer Characteristics of Internally Finned Tubes," *The Canadian Journal of Chemical Engineering*, Vol. 59, pp. 251-256.

Variable Property Effects of Fully Developed Laminar Flow in Concentric Annuli

H. Herwig

K. Klemp

Institut fur Thermo und Fluiddynamik,
Ruhr Universitat,
Bochum, Federal Republic of Germany

By means of a linear perturbation theory, the influences of density, viscosity, thermal conductivity, and specific heat capacity, all varying with temperature, are taken into account. The wall heat flux is assumed to be constant at the inner and outer wall, with an arbitrary ratio between these two. Even for variable properties the problem can be reduced to solving a set of ordinary differential equations with three parameters: heat flux ratio, diameter ratio, and Prandtl number. Skin friction and heat transfer results are given for specific numbers of the parameters, including the limiting cases of pipe and channel flows.

1 Introduction

There are several ways of incorporating variable property effects into flow and heat transfer calculations. A straightforward manner is to introduce the complete temperature and pressure dependence of all physical properties into the basic equations. As a consequence the solution is complicated by nonlinearities and a coupling of the momentum and energy equations. Moreover the results are valid only for a specific set of boundary conditions.

Often, however, it is sufficient to account for variable property effects only approximately. That is why approximate concepts like "property ratio method" and "reference temperature method" are in wide use (see for example Kays and Crawford, 1980, and a detailed description of these methods in section 2.5 below). These methods provide a correction for the corresponding constant property results and are thus easy to apply. Both are empirical methods developed for standard cases like pipe and boundary layer flows. A theoretical background is needed to decide whether these methods can be extended to more complex flows such as annular flows, for example.

This theoretical background is given by an asymptotic perturbation approach to the problem. By means of a regular perturbation technique the correction functions provided by the property ratio method and the reference temperature method, respectively, can be deduced analytically.

Based on these results it turns out that we cannot recommend these methods for more complex flows but instead propose to account for variable property effects by more suitable correction formulae. They are provided by the perturbation technique described in the following section.

2 Asymptotic Analysis

The basic idea is to expand the physical properties involved in a Taylor series. With a subsequent expansion of all dependent variables of the problem, a hierarchy of equations can be established with the lowest order or basic flow being that for constant properties. Higher order equations describe a perturbation of this basic flow according to the linear or nonlinear deviations triggered by the ascending terms of the property Taylor series expansion.

For convenience this procedure will be applied in five steps in subsections 2.1–2.5. A general description can be found in Herwig (1986) or a more detailed one in Herwig (1985a). The method itself is well established and applied to various flow situations; see for example Matting (1964) for stagnation point flow or Carey and Mollendorf (1980) for free convection flows.

2.1 Basic Equations. The basic equations are nondimensionalized according to Table 1 and include all physical properties as variable quantities. Neglecting viscous dissipation and axial heat conduction the equations for internal flows in ducts read

$$\frac{\partial}{\partial x}(\rho u)+\frac{1}{r}\frac{\partial}{\partial r}(\rho r v)=0 \tag{1}$$

$$\rho\left(u\frac{\partial u}{\partial x}+v\frac{\partial u}{\partial r}\right)=-\frac{\partial p}{\partial x}+\frac{1}{r}\frac{\partial}{\partial x}\left(r\eta\frac{\partial u}{\partial r}\right) \tag{2}$$

$$0=-\frac{\partial p}{\partial r} \tag{3}$$

$$\rho\left(u\frac{\partial h}{\partial x}+v\frac{\partial h}{\partial r}\right)=\frac{1}{\mathrm{Pr}_\infty}\frac{1}{r}\frac{\partial}{\partial r}\left(r\frac{\lambda}{c_p}\frac{\partial h}{\partial r}\right) \tag{4}$$

The energy equation is given in terms of enthalpy, which is related to the temperature by

$$h=\int_0^T c_p\,dT \tag{5}$$

The reference state (subscript ∞) along with the coordinate system is shown in Fig. 1. It is the isothermal hydrodynamically fully developed oncoming flow. After a thermal adjustment region the hydrodynamically and thermally fully developed state, which is the scope of this study, is reached.

The boundary conditions hold on the wall of the inner (R_i) and outer (R_o) cylinder

Inner:

$$r=R_i:\quad u=v=0,\quad \frac{\partial h}{\partial r}=-\frac{c_{pi}}{\lambda_i}q_i \tag{6a}$$

Outer:

$$r=R_o:\quad u=v=0,\quad \frac{\partial h}{\partial r}=\frac{c_{po}}{\lambda_o}q_o \tag{6b}$$

Here $q_k\,(k=i,\,o)$ is the dimensionless wall heat flux; $q_k\equiv q_k^*\,d_h^*/2\lambda_\infty^*\,T_\infty^*$ ($q_k>0$ if heat is added to the fluid).

With regard to the solution procedure the integral formulae of the continuity and energy equation may be provided

$$\dot m\equiv\frac{\dot m^*}{\rho_\infty^* U_\infty^* A^*}=\int_{R_i}^{R_o}\rho u r\,dr=\frac{1-R^2}{(1-R)^2} \tag{7}$$

$$h_B\equiv\frac{h_B^*-h_\infty^*}{h_\infty^*}=\int_{R_i}^{R_o}\rho u h r\,dr=\frac{2q_o(1+Rq)}{\mathrm{Pr}_\infty(1+R)}x \tag{8}$$

Contributed by the Heat Transfer Division for publication in the JOURNAL OF HEAT TRANSFER. Manuscript received by the Heat Transfer Division January 29, 1987. Keywords: Forced Convection, Modeling and Scaling.

Table 1 Nondimensional quantities; all starred quantities are dimensional

x	r	u	v	p	$\tilde{p}$
$x^*/(\mathrm{Re}_\infty d_h^*/2)$	$r^*/(d_h^*/2)$	u^*/U_∞^*	$v^*/U_\infty^* \mathrm{Re}_\infty$	$\dfrac{p^*-p_\infty^*}{\rho_\infty^* U_\infty^{*2}}$	$\dfrac{p^*-p_\infty^*}{p_\infty^*}$

T	h	ρ	η	λ	c_p
$(T^*-T_\infty^*)/T_\infty^*$	$(h^*-h_\infty^*)/h_\infty^*$	ρ^*/ρ_∞^*	η^*/η_∞^*	$\lambda^*/\lambda_\infty^*$	$c_p^*/c_{p\infty}^*$

$$\mathrm{Re}_\infty = \frac{\rho_\infty^* U_\infty^* d_h^*/2}{\eta_\infty^*} \qquad \mathrm{Pr}_\infty = \frac{\eta_\infty^* c_{p\infty}^*}{\lambda_\infty^*}$$

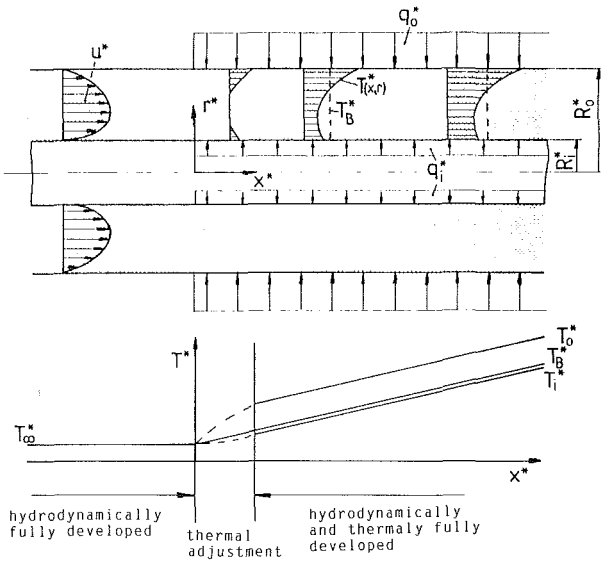

Fig. 1 Flow situation under consideration; the temperature distribution shown holds for constant properties

with the definitions

$$R \equiv \frac{R_i^*}{R_o^*} \quad \text{(ratio of radii)} \tag{9}$$

$$q \equiv \frac{q_i^*}{q_o^*} \quad \text{(ratio of wall heat fluxes)} \tag{10}$$

Together with the Prandtl number we thus have a three-parameter problem in Pr_∞, q, and R for each set of temperature and pressure-dependent physical properties.

2.2 Perturbation Formulae. We start with a Taylor series expansion of all physical properties α (ρ^*/ρ_∞^*, η^*/η_∞^*, $\lambda^*/\lambda_\infty^*$, and $c_p^*/c_{p\infty}^*$):

$$\alpha = 1 + K_\alpha\, T + \tilde{K}_\alpha \tilde{p} + \ldots \tag{11}$$

where

$$K_\alpha = \left(\frac{T^* \partial \alpha^*}{\alpha^* \partial T^*}\right)_\infty \qquad \tilde{K}_\alpha = \left(\frac{p^* \partial \alpha^*}{\alpha^* \partial p^*}\right)_\infty \tag{12}$$

The pressure dependence of all properties is extremely small and will be neglected for that reason. As far as gases are concerned, that means a restriction to small Mach numbers, however.

Since viscous dissipation is not involved, the only reason for a nonisothermal flow field is the heat flux across the walls, which means asymptotically that T is of the order of $0(|q_i| + |q_o|)$.

We introduce the perturbation parameter

$$\epsilon = (|q_i| + |q_o|)\ \mathrm{sign}(q_o) \tag{13}$$

The sign-function in equation (13) is necessary because otherwise the results for $q<0$ would not be unique. Its definition is: sign $(q_o) = -1$ for $q_o < 0$ and sign $(q_o) = +1$ for $q_o \geq 0$.

Equation (11) can be rewritten

$$\alpha = 1 + \epsilon\, K_\alpha \bar{T} + 0(\epsilon^2); \quad \bar{T} = T/\epsilon \tag{14}$$

The Taylor series truncated after the linear term is an asymptotic approximation for $\epsilon \to 0$. The reduced temperature $\bar{T} \equiv T/\epsilon$ is of order 0(1) for $\epsilon \to 0$, since T itself is of order $0(\epsilon)$.

Nomenclature

A = cross-section area
c_p = specific heat at constant pressure
c_f = skin friction coefficient, equation (36)
d_h = hydraulic diameter, $d_h^* = 2R_o^*(1-R)$
f_ρ, f_η = influence functions, equation (40)
h = specific enthalpy
K_α = dimensionless fluid property, equation (12)
$n_{\alpha k}$ = exponents, equation (44)
Nu = Nusselt number, equation (41)
p = pressure
Pr = Prandtl number, see Table 1
q_k = wall heat flux
q = ratio of wall heat fluxes, equation (10)
r = radial coordinate
R_k = radius, $k = i, o$
R = ratio of radii, equation (9)
Re = Reynolds number, see Table 1
T = temperature
u, v = velocity components
U_∞ = mean velocity at reference conditions
x = axial coordinate
α = physical property
ϵ = perturbation parameter, equation (13)
η = viscosity
λ = thermal conductivity
ρ = density
τ = shear stress
τ_w = combined wall shear stresses, equation (35)

Subscripts

B = bulk
cp = constant property
i = at the inner wall
k = i or o
o = at the outer wall
w = at the wall
α = referred to property α
∞ = reference conditions
0 = zero order

Neglecting the pressure dependence is a nonasymptotic approximation justified in the light of practical applications.

The perturbation parameter ϵ is assumed to be small, thus justifying a truncation of the series after the linear term. What follows therefore is a linear theory valid for $\epsilon \to 0$ with an error of order $0(\epsilon^2)$ asymptotically.

With all physical properties according to equation (14) the problem under consideration now is an eight-parameter problem (Pr_∞, q, R, ϵ, K_ρ, K_η, K_λ, K_c) described by partial differential equations that are nonlinear and mutually coupled.

The problem can be reduced drastically by applying the following perturbation expansion of the dependent variables. A three-parameter set of ordinary linear differential equations is left, which can be solved sequentially.

Later on it turns out that the Prandtl number dependence can be extracted from the problem so that only a two-parameter problem in q and R is left.

The adequate expansions are

$$u = u_0 + \epsilon[K_\rho (u_\rho - u_0 \bar{h}_B) + K_\eta u_\eta] + 0(\epsilon^2) \tag{15a}$$

$$v = v_0 + \epsilon[K_\rho (v_\rho - v_0 \bar{h}_B) + K_\eta v_\eta] + 0(\epsilon^2) \tag{15b}$$

$$\frac{dp}{dx} = \frac{dp_0}{dx} + \epsilon\left[K_\rho\left(\frac{dp_\rho}{dx} - \frac{dp_0}{dx}\bar{h}_B\right) + K_\eta\left(\frac{dp_\eta}{dx} + \frac{dp_0}{dx}\bar{h}_B\right)\right] + 0(\epsilon^2) \tag{15c}$$

$$\bar{h} \equiv \frac{h}{\epsilon} = \bar{h}_B + \bar{h}_0 + \epsilon[K_\rho \bar{h}_\rho + K_\eta \bar{h}_\eta + (K_c - K_\lambda)\cdot(\bar{h}_c + \bar{h}_0 \bar{h}_B + \bar{h}_0^2)] + 0(\epsilon^2) \tag{15d}$$

In equation (15) all u_j and $\bar{h}_j$ are functions of r alone. The only x-dependent function is $\bar{h}_B = h_B/\epsilon$ with h_B according to equation (8). The temperature $\bar{T}$ can be expanded like $\bar{h}$ in equation (15*d*), with

$$\bar{T}_j = \bar{h}_j,\ j = 0, B, \rho, \eta, \lambda \quad \text{and} \quad \bar{T}_c = \bar{h}_c - \bar{T}_0^2/2 \tag{15e}$$

according to equation (5).

Reduced quantities are also introduced for the wall heat fluxes q_k

$$\bar{q}_i = \frac{q_i}{\epsilon}; \qquad \bar{q}_o = \frac{q_o}{\epsilon} \tag{16}$$

2.3 Zero and First-Order Equations; Solutions. The expansion formulae (15) along with the Taylor series expansions (14), inserted into the basic equations (1)–(8), provide the ordinary differential equations for u_j and $\bar{h}_j$. With $\bar{h}_B' = 2\bar{q}_o \cdot (1 + Rq)/\mathrm{Pr}_\infty (1 + R)$ (see equation (8)), they read (a prime menas the derivative with respect to r; except $p_j' = dp_j/dx$):

Zero order (constant properties):

$$(r v_0)' = 0 \tag{17}$$

$$v_0 u_0' = -p_0' + \frac{1}{r}(r u_0')' \tag{18}$$

$$u_0 \bar{h}_B' + v_0 \bar{h}_0' = \frac{1}{r\,\mathrm{Pr}_\infty}(r \bar{h}_0')' \tag{19}$$

with the associated boundary conditions

$$r = R_i: \quad u_0 = v_0 = \bar{h}_0' + \bar{q}_i = 0 \tag{20a}$$

$$r = R_o: \quad u_0 = v_0 = \bar{h}_0' - \bar{q}_0 = 0 \tag{20b}$$

First order (variable property influence) associated with K_ρ:

$$(r v_\rho)' = 0 \tag{21}$$

$$v_\rho u_0' = -p_\rho' + \frac{1}{r}(r u_\rho')' + u_0^2 \bar{h}_B' \tag{22}$$

$$u_\rho \bar{h}_B' + v_\rho \bar{h}_o' = \frac{1}{r\,\mathrm{Pr}_\infty}(r \bar{h}_\rho')' - u_0 \bar{h}_0 \bar{h}_B' \tag{23}$$

associated with K_η:

$$(r v_\eta)' = 0 \tag{24}$$

$$v_\eta u_0' = -p_\eta' + \frac{1}{r}(r u_\eta')' + \frac{1}{r}(r \bar{h}_0 u_0')' \tag{25}$$

$$u_\eta \bar{h}_B' + v_\eta \bar{h}_0' = \frac{1}{r\,\mathrm{Pr}_\infty}(r \bar{h}_\eta')' \tag{26}$$

associated with K_c (and K_λ):

$$\frac{1}{r}(r \bar{h}_c')' = -\bar{h}_o'^2 \tag{27}$$

$$\bar{h}_\lambda = -\bar{h}_c \tag{28}$$

with the associated boundary conditions

$$r = R_i: u_\rho = v_\rho = u_\eta = v_\eta = \bar{h}_\rho' = \bar{h}_\eta' = 0$$

$$\bar{h}_c' = -\bar{h}_\lambda' = -\bar{h}_0 (\bar{q}_i + 2\bar{h}_0') \tag{29a}$$

$$r = R_o: u_\rho = v_\rho = u_\eta = v_\eta = \bar{h}_\rho' = \bar{h}_\eta' = 0$$

$$\bar{h}_c' = -\bar{h}_\lambda' = \bar{h}_0 (\bar{q}_0 - 2\bar{h}_0') \tag{29b}$$

Inserting the perturbation formulae into the integral equations (7) and (8) we get six integral conditions for u_j and $\bar{h}_j$. The equation for $\bar{h}_\rho$, e.g., reads

$$\int_{R_i}^{R_o} (u_0 \bar{h}_0^2 + u_\rho \bar{h}_0 + u_0 \bar{h}_\rho) r\, dr = 0 \tag{30}$$

The solutions of equations (17)–(29) can be found analytically, although the expressions become increasingly complicated. That is why only the zero-order results are given analytically, and those of the first order are provided numerically.

Zero-Order Solutions. The constant property results are well known for specific thermal boundary conditions (see, e.g., Kays and Crawford, 1980). The general result (parameters: q, R) reads, with $\bar{r} = r(1 - R)$

$$u_0 = -\frac{1}{4}\frac{dp_0}{dx}\left[r^2 + A \ln \bar{r} - \frac{1}{(1-R)^2}\right]; \quad v_0 = 0 \tag{31}$$

$$\frac{dp_0}{dx} = -\frac{8(1-R)^2 \ln R}{(1-R^2)\ln R + 1 - R^2} \tag{32}$$

$$\bar{h}_0 = B\left[\left(\frac{r^4}{4} + r^2(A \ln \bar{r} - C)\right)D - I_1 \ln \bar{r} + I_2\right] \tag{33}$$

The auxiliary functions A–D and I_1, I_2 are

$$A = \frac{1+R}{(1-R)\ln R}, \quad B = -\frac{1}{8}\frac{dp_0}{dx}\frac{\bar{q}_o}{(1+R)}$$

$$C = \frac{1 - R + \ln R}{(1-R)^2 \ln R}, \quad D = 1 + Rq$$

$$I_1 = \frac{R(R^3(1 - \ln R) - R - q(\ln R - R^2 + 1))}{(1-R)^4 \ln R}$$

$$I_2 = \frac{\ln R}{(1-R^4)\ln R + (1-R^2)^2}(D\, I_{21} - I_1 I_{22})$$

$$I_{21} = \frac{21(1-R^8)(\ln R)^2 + 50(1-R^2)(1-R^6)\ln R + 27(1-R^2)^3(1-R^2)}{72(1-R)^4 \ln R}$$

$$I_{22} = \frac{R^2 \ln R(4 - 7R^2 + 4R^2 \ln R) + 4(1-R^2)^2 + 3 \ln R}{4 \ln R} \tag{34}$$

It is important to note that $\bar{h}_B$ (see equation (8)) is the only Pr-dependent zero-order function.

The enthalpy $\bar{h}_0$, equation (33), has been achieved by superposition of two basic solutions: one with $\bar{q}_i$ and an adiabatic outer wall and the other with $\bar{q}_0$ and an adiabatic inner wall.

Pipe and channel flow are special cases of the general solution with respect to the parameter R ($R \to 0$: pipe flow, $R \to 1$: channel flow).

First-Order Solutions. The numerical solution of equations (21)–(29) is straightforward using Runge–Kutta integration and shooting techniques for the initial/boundary value problem when necessary. It turns out that the Prandtl number dependence can be extracted from the solution procedure and appears explicitly in the results. As with the zero-order equations, a two-parameter set (q, R) of results is sufficient.

Although the first-order energy equations are linear like the zero-order equation, a superposition of two basic solutions, each of them with adiabatic boundary conditions on one wall, is not possible. This is prevented by nonlinearities of zero-order terms in the nonhomogeneous part of the first-order equations or the integral conditions, like the term $\bar{h}_0'^2$ in equation (27) or $u_0\bar{h}_0^2$ in the integral condition (30).

The quantities needed further on are the first-order pressure gradients p_j' and wall enthalpies $\bar{h}_j$ at the outer and inner wall, respectively. For three values of q and six values of R the numerical results are provided in Table 2. The three thermal boundary conditions under consideration are: $q=0 (q_i=0;\ q_o\neq 0)$, $q=1$ $(q_i=q_o)$, and $q=\infty$ $(q_i\neq 0;\ q_o=0)$. For later use not the pressure gradients p_j' themselves but some functions of these quantities, called f_ρ and f_η, defined below, are listed in Table 2.

A characteristic feature of some of the functions given in Table 2 is the steep gradient in the limit $R \to 0$ (vanishing inner cylinder). To demonstrate this behavior, the function $f_\rho \mathrm{Pr}_\infty$ (first row for each q in Table 2) is shown in Fig. 2 for the three-parameter values of q.

2.4 Skin Friction and Heat Transfer Formulae. So far the reference state lies in the isothermal region as shown in Fig. 1. The perturbation expansions equation (15) show, however, that the only x-dependent quantity is the bulk enthalpy $\bar{h}_B(x)$. That is why a very important change in the reference state is possible. With $x=0$ all variable property results are referred to

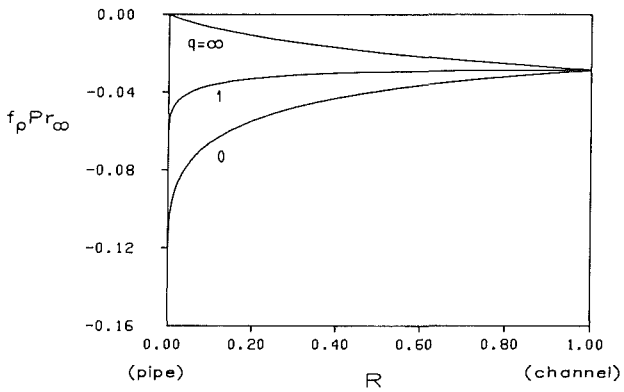

Fig. 2 First-order function $f_\rho \mathrm{Pr}_\infty$, see equation (40)

Table 2 First-order numerical results, f_ρ and f_η defined in equation (40); $\bar{h}_\lambda = -\bar{h}_c$; all quantities at the wall

q	R	0.0	0.1	0.2	0.4	0.6	0.8	1.0
	$f_\rho \cdot \mathrm{Pr}_B$	−0.1667	−0.0658	−0.0544	−0.0428	−0.0363	−0.0318	−0.0286
	f_η	0.2500	0.1330	0.1151	0.0942	0.0810	0.0715	0.0643
	$\bar{h}_{0o}$	0.4583	0.4137	0.4096	0.4017	0.3922	0.3819	0.3715
0	$\bar{h}_{\rho o}$	$-0.0715 + 0.0269/\mathrm{Pr}_B$	$-0.0534 + 0.0087/\mathrm{Pr}_B$	$-0.0494 + 0.0061/\mathrm{Pr}_B$	$-0.0425 + 0.0033/\mathrm{Pr}_B$	$-0.0366 + 0.0019/\mathrm{Pr}_B$	$-0.0316 + 0.0011/\mathrm{Pr}_B$	$-0.0275 + 0.0006/\mathrm{Pr}_B$
	$\bar{h}_{\eta o}$	0.0313	0.0304	0.0293	0.0263	0.0232	0.0203	0.0178
	$\bar{h}_{co}$	−0.1587	−0.1257	−0.1209	−0.1125	−0.1044	−0.0967	−0.0900
	$f_\rho \cdot \mathrm{Pr}_B$	−0.0833	−0.0362	−0.0327	−0.0300	−0.0290	−0.0287	−0.0286
	f_η	0.1250	0.0731	0.0690	0.0659	0.0648	0.0644	0.0643
	$\bar{h}_{0i}$	-	−0.0322	0.0113	0.0604	0.0889	0.1079	0.1214
	$\bar{h}_{0o}$	0.2292	0.1952	0.1835	0.1687	0.1480	0.1338	0.1214
	$\bar{h}_{\rho i}$	-	$0.0026 - 0.0003/\mathrm{Pr}_B$	$0.0018 - 0.0001/\mathrm{Pr}_B$	$0.0005 + 0.0002/\mathrm{Pr}_B$	$-0.0007 + 0.0003/\mathrm{Pr}_B$	$-0.0017 + 0.0005/\mathrm{Pr}_B$	$-0.0025 + 0.0006/\mathrm{Pr}_B$
1	$\bar{h}_{\rho o}$	$-0.0179 + 0.0067/\mathrm{Pr}_B$	$-0.0114 + 0.0024/\mathrm{Pr}_B$	$-0.0093 + 0.0019/\mathrm{Pr}_B$	$-0.0065 + 0.0013/\mathrm{Pr}_B$	$-0.0047 + 0.0010/\mathrm{Pr}_B$	$-0.0035 + 0.0008/\mathrm{Pr}_B$	$-0.0025 + 0.0006/\mathrm{Pr}_B$
	$\bar{h}_{\eta i}$	-	−0.0017	−0.0013	−0.0006	0.0001	0.0006	0.0012
	$\bar{h}_{\eta o}$	0.0078	0.0062	0.0051	0.0039	0.0025	0.0017	0.0012
	$\bar{h}_{ci}$	-	0.0046	0.0036	−0.0002	−0.0038	−0.0068	−0.0093
	$\bar{h}_{co}$	−0.0396	−0.0280	−0.0243	−0.0189	−0.0149	−0.0118	−0.0093
	$f_\rho \cdot \mathrm{Pr}_B$	0.0	−0.0066	−0.0109	−0.0171	−0.0218	−0.0255	−0.0286
	f_η	0.0	0.0133	0.0230	0.0377	0.0486	0.0572	0.0643
	$\bar{h}_{0i}$	-	0.1680	0.2353	0.3038	0.3383	0.3585	0.3715
∞	$\bar{h}_{\rho i}$	-	$-0.0016 - 0.0001/\mathrm{Pr}_B$	$-0.0048 - 0.0002/\mathrm{Pr}_B$	$-0.0119 - 0.0002/\mathrm{Pr}_B$	$-0.0182 - 0.0000/\mathrm{Pr}_B$	$-0.0234 + 0.0003/\mathrm{Pr}_B$	$-0.0275 + 0.0006/\mathrm{Pr}_B$
	$\bar{h}_{\eta i}$	-	0.0011	0.0032	0.0078	0.0119	0.0152	0.0178
	$\bar{h}_{ci}$	-	−0.0153	−0.0313	−0.0551	−0.0709	−0.0818	−0.0900

the local (fictitious) isothermal state at the (local) bulk temperature which from now on is the reference state indicated by the subscript B.

(a) *Skin Friction.* We restrict ourselves to a general skin friction formula including both walls (corresponding expressions for the inner and outer walls separately are possible).

With the wall shear stress at the inner and outer wall, τ_i^* and τ_o^*, respectively, we define

$$\tau_w^* = \frac{\tau_i^* R_i^* + \tau_o^* R_o^*}{R_i^* + R_o^*} \tag{35}$$

and a skin friction coefficient

$$c_f = \frac{2\tau_w^*}{\rho_B^* U_B^{*2}} \tag{36}$$

From a momentum balance in the x direction we get

$$c_f \mathrm{Re}_B = -2\,\frac{1-R}{1+R}\,\frac{d}{dx}\int_{R_i}^{R_o} (p+\rho\,u^2) r\,dr \tag{37}$$

For constant properties (index cp) this leads to ($' \hat{=} d/dx$):

$$(c_f\,\mathrm{Re}_B)_{cp} = -p_0' \tag{38}$$

combining equations (37) and (38) and inserting the perturbation expansions for p, ρ, and u, we get the final result

$$\frac{c_f\,\mathrm{Re}_B}{(c_f \mathrm{Re}_B)_{cp}} = 1 + \epsilon[K_\rho f_\rho + K_\eta f_\eta] + 0(\epsilon^2) \tag{39}$$

with

$$f_\rho \equiv \frac{p_\rho'}{p_0'} - 2\,\frac{1-R}{1+R}\,\frac{\bar{h}_B'}{p_0'}\int_{R_i}^{R_o} u_0^2\, r\,dr \tag{40a}$$

$$f_\eta \equiv \frac{p_\eta'}{p_0'} \tag{40b}$$

listed in Table 2.

(b) *Heat Transfer.* The heat transfer results will be given for the inner and outer wall by the corresponding Nusselt numbers Nu_i and Nu_o, defined as

$$\mathrm{Nu}_k = \frac{q_k^* d_h^*}{(T_k^* - T_B^*)\lambda_B^*} = 2\,\frac{\tilde{q}_k}{\bar{T}_k} \qquad k = i,\ o \tag{41}$$

The constant property value is $\mathrm{Nu}_{kcp} = 2\tilde{q}_k/\bar{h}_{ok}$ (see equation (16)) so that we get the final result

$$\frac{\mathrm{Nu}_k}{\mathrm{Nu}_{kcp}} = 1 - \epsilon\Big[K_\rho\,\frac{\bar{h}_{\rho k}}{\bar{h}_{0k}} + K_\eta\,\frac{\bar{h}_{\eta k}}{\bar{h}_{0k}} + K_c\Big(\frac{\bar{h}_{ck}}{\bar{h}_{0k}} + \bar{h}_{0k} - \frac{1}{2}\Big) - K_\lambda\Big(\frac{\bar{h}_{ck}}{\bar{h}_{0k}} + \bar{h}_{0k}\Big)\Big] + 0(\epsilon^2) \qquad k = i,\ o \tag{42}$$

with $\bar{h}_{\rho k}$, $\bar{h}_{\eta k}$, $\bar{h}_{ck}$, and the corresponding value $\bar{h}_{0k}$ listed in Table 2.

It should be pointed out that in certain flow situations $\bar{h}_{0k}$ may become zero (in Table 2 for example: $\bar{h}_{0i} = 0$ for $q = 1$ and R close to 0.2). As a consequence Nu_{kcp} is infinite and should not be used, since it is a misleading concept (at least in these extreme cases). The heat transfer result in terms of wall temperature should be used instead. According to equations (15d) and (15e) it reads

$$\bar{T}_k = \bar{h}_{0k} + \epsilon[K_\rho \bar{h}_{\rho k} + K_\eta \bar{h}_{\eta k} + K_c(\bar{h}_{ck} + \bar{h}_{0k}^2 - 1/2\ \bar{h}_{0k}) - K_\lambda(\bar{h}_{ck} + \bar{h}_{0k}^2)] + 0(\epsilon^2) \qquad k = i,\ o \tag{43}$$

2.5 Property Ratio and Reference Temperature Formulae

(a) *Property Ratio Method.* This method originated as an empirical way to account for variable property influence and was developed for simple flow situations like pipe and channel flows.

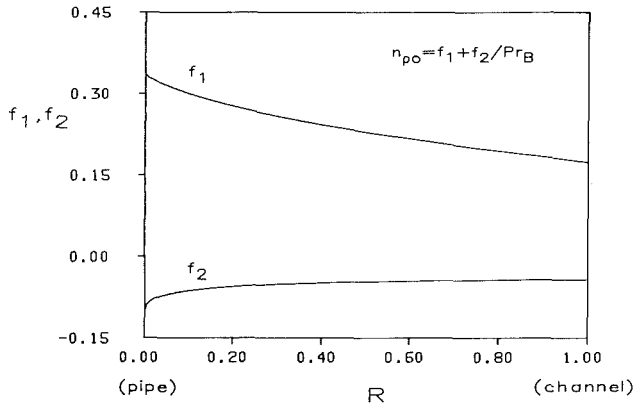

Fig. 3 Exponent $n_{\rho o}$ for $q = 1$

The constant property results are multiplied by a power of some pertinent property (or properties) evaluated at two different temperatures. For pipe flow these temperatures usually are the bulk and the wall temperature. The unknown power (or powers) were determined empirically in the past (see, e.g., Kays and Crawford, 1980).

By means of the perturbation technique described in this study they can be determined analytically and so this method itself now is analytic in character. It turns out that the linear (first-order) asymptotic results are exactly what is covered by the property ratio method, so that this method is linear by nature.

A complete correction formula for the Nusselt number for example reads

$$\frac{\mathrm{Nu}_k}{\mathrm{Nu}_{kcp}} = \rho_k^{n_{\rho k}}\ \ \eta_k^{n_{\eta k}}\ \ \lambda_k^{n_{\lambda k}}\ \ c_{pk}^{n_{ck}}; \quad k = i,\ o \tag{44}$$

For the general property α holds (see equation (14))

$$\alpha_k^{n_{\alpha k}} = \Big[\frac{\alpha_k^*}{\alpha_B^*}\Big]^{n_{\alpha k}} = 1 + n_{\alpha k}\epsilon\, K_\alpha \bar{T}_{0k} + 0(\epsilon^2) \tag{45}$$

so that equation (44) compared to the asymptotic result, equation (42), gives for $n_{\rho k}$, for example

$$n_{\rho k} = -\frac{\bar{h}_{\rho k}}{\bar{h}_{0k}\bar{T}_{0k}} = -\frac{\bar{h}_{\rho k}}{\bar{h}_{0k}^2} \tag{46}$$

Equivalent expressions hold for $n_{\eta k}$, $n_{\lambda k}$ and n_{ck}. All exponents have the denominator $\bar{h}_{0k}^2$, which may become zero (see discussion after equation (42)) for certain (q, R) combinations, with the result of infinite values of $n_{\alpha k}$. Nothing dramatic happens physically in these cases (note that $\alpha_k \to 1$ in these cases, so that (44) is still an order 0(1) function) but unbounded values of the exponent are not acceptable.

For this reason and since there is no trend toward a unifying functional behavior of the exponents, we recommend use of the correction in terms of equation (42) or (43).

Nevertheless, it is possible to determine the values of $n_{\alpha k}$ analytically. In Fig. 3 one example is given for $n_{\rho o}$ with $q = 1$ ($q_i = q_o$). From Herwig (1985a) we know the limiting values:

pipe flow ($R = 0$): $\quad n_\rho = 0.340 - 0.128\ \mathrm{Pr}_B^{-1}$

channel flow ($R = 1$): $\quad n_\rho = 0.173 - 0.043\ \mathrm{Pr}_B^{-1}$

Figure 3 shows that the Prandtl number dependence again can be separated from the solution procedure with the result of the functional form $n_{\rho o} = f_1(q, R) + f_2(q, R)\mathrm{Pr}_B^{-1}$.

(b) *Reference Temerpature Method.* In this empirical method a temperature T_r^* is specified at which the properties appearing in the dimensionless groups of the problem should

Table 3 K_α values of some fluids (Gersten and Herwig, 1984)

	Air			Water			Oil (Shell Voluta 919)				Liquid sodium		
T_∞/K	293 (20°C)	473 (200°C)	773 (500°C)	273 (0°C)	293 (20°C)	343 (70°C)	273 (0°C)	293 (20°C)	343 (70°C)	473 (200°C)	673 (400°C)	873 (600°C)
Pr_∞	0.74	0.68	0.70	13.2	7.0	2.5	1303	412	81	7.2×10^{-3}	5.6×10^{-3}	4.9×10^{-3}
K_ρ	−1.0	−1.0	−1.0	0.010	−0.057	−0.205	−0.215	−0.234	−0.286	−0.124	−0.189	−0.262
K_η	0.733	0.695	0.626	−8.791	−7.142	−4.749	−19.97	−14.72	−8.414	−0.918	−0.933	−0.941
K_λ	0.906	0.820	0.747	1.008	0.825	0.493	−0.153	−0.166	−0.199	−0.310	−0.459	−0.618
K_c	−0.303	0.116	0.179	−0.188	−0.053	0.045	0.567	0.5837	0.622	−0.149	−0.133	−0.055

be evaluated to get the variable property results by constant property formulae.

This method is similar to the property ratio method in that all asymptotically linear effects are expressed by certain empirical numbers. Defining

$$T_r^* = T_B^* + J(T_k^* - T_B^*) \tag{47}$$

the factor J must be determined either empirically or analytically by comparison with the asymptotic results. This may be done by a procedure similar to the one described in the previous section. Again we recommend use of the correction expressions of subsection 2.4 instead.

3 Discussion

There are three important features of our systematic approach to the variable property flow:

1 The final results are universal in the sense that they hold for all fluids. For example, there is no need to distinguish between liquids and gases, as is usually done when the property ratio method is applied (see, for example, Kays and Crawford, 1980).

2 All physical information is extracted from the basic equations and there is no need to have recourse to empirical information as was necessary in the past.

3 In the final equations the influence of the physical properties can be checked separately. For fluids with one or more properties being constant the corresponding K_α values are zero. Some K_α values that are properties of a particular fluid are given in Table 3.

Comparing the asymptotic results with empirical data from the heat transfer literature shows a very good agreement. For the special case of pipe flow a detailed comparison is made in Herwig (1985b).

For pipe flow many empirical data are available. For example, Kays and Perkins (1973) provide a property ratio formula that they recommend for liquids. It reads

$$\frac{c_f \mathrm{Re}_B}{(c_f \mathrm{Re}_B)_{cp}} = \left[\frac{\eta_w^*}{\eta_B^*}\right]^n, \quad \begin{matrix} n = 0.50 \text{ (cooling)}, \\ n = 0.58 \text{ (heating)}' \end{matrix}$$

$$\frac{\mathrm{Nu}}{\mathrm{Nu}_{cp}} = \left[\frac{\eta_w^*}{\eta_B^*}\right]^{-0.14} \tag{48}$$

The formulae show that viscosity is assumed to have the dominating influence. That means $\rho^* = \text{const}$, $\lambda^* = \text{const}$, and $c_p^* = \text{const}$ so that our results written in the property ratio form for the circular pipe flow reduce to

$$\frac{c_f \mathrm{Re}_B}{(c_f \mathrm{Re}_B)_{cp}} = \left[\frac{\eta_w^*}{\eta_B^*}\right]^{0.545}; \quad \frac{\mathrm{Nu}}{\mathrm{Nu}_{cp}} = \left[\frac{\eta_w^*}{\eta_B^*}\right]^{-0.149} \tag{49}$$

The exponents deduced analytically are very close to the empirical exponents of equation (48). The exponents in equation (49) for the channel flow with the boundary condition $q = 1$ would be 0.529 and −0.079, respectively. Annular flows between the limiting pipe and channel flows have exponents from 0.545 to 0.529 and −0.149 to −0.079.

In the introduction we claimed that a theoretical background is needed to find the limitations of the empirical methods. From this theoretical background, provided by the perturbation approach, we can conclude, for example, that it is a misleading concept to distinguish between cooling and heating as is done in equation (48). The constant exponents in the property ratio method are uniquely related to the first order (linear) results of the perturbation approach, compare equation (46), and so they are one number. To the next order, $0(\epsilon^2)$, the exponent is a linear function of ϵ. Figure 4 is a sketch of this situation. The perturbation parameter, equation (13), for pipe flow reduces to $\epsilon = q_o$. Approximating the linear func-

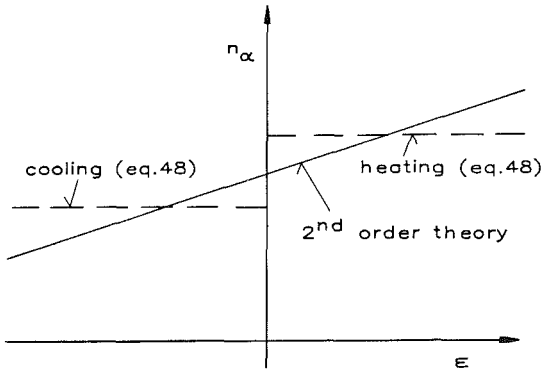

Fig. 4 Property ratio exponents for pipe flow

tion for n_α by constants makes sense only in a specific ϵ interval. This obviously was given in the experimental design from which the results in equation (48) were taken. But these results are not valid for general application.

References

Carey, V. C., and Mollendorf, J. C., 1980, "Variable Viscosity Effects in Several Natural Convection Flows," *Int. J. Heat Mass Transfer*, Vol. 23, pp. 95–109.

Gersten, K., and Herwig, H., 1984, "Impuls- und Waermeuebertragung bei variablen Stoffwerten fuer die laminare Plattenstroemung," *Waerme- und Stofuebertragung*, Vol. 18, pp. 25–35.

Herwig, H., 1985a, "Asymptotische Theorie zur Erfassung des Einflusses variabler Stoffwerte auf Impuls- und Waermeuebertragung," *VDI-Fortschrittsberichte*, Vol. 7, No. 93, VDI-Verlag Duesseldorf.

Herwig, H., 1985b, "The Effect of Variable Properties on Momentum and Heat Transfer in a Tube With Constant Heat Flux Across the Wall," *Int. J. Heat Mass Transfer*, Vol. 28, pp. 423–431.

Herwig, H., 1986, "A Regular Perturbation Procedure to Account for Variable Property Effects in Momentum and Heat Transfer," *ZAMM*, Vol. 66, pp. T 217–T 218.

Kays, W. M., and Perkins, H. C., 1973, "Forced Convection. Internal Flow in Ducts," *Handbook of Heat Transfer*, W. M. Roshenow, ed., McGraw-Hill, New York.

Kays, W. M., and Crawford, M. E., 1980, *Convective Heat and Mass Transfer*, McGraw-Hill, New York.

Matting, F. W., 1964, "General Solution of the Laminar Compressible Boundary Layer in the Stagnation Region of Blunt Bodies in Axisymmetric Flow," NASA TN D-2234.

Heat Transfer and Friction Characteristics in Rectangular Channels With Rib Turbulators

J. C. Han
Associate Professor,
Department of Mechanical Engineering,
Texas A&M University,
College Station, TX 77843
Mem. ASME

The effect of the channel aspect ratio on the distribution of the local heat transfer coefficient in rectangular channels with two opposite ribbed walls (to simulate turbine airfoil cooling passages) was determined for a Reynolds number range of 10,000 to 60,000. The channel width-to-height ratios (W/H, *ribs on side* W) *were 1/4, 1/2, 1, 2, and 4. The test channels were heated by passing current through thin, stainless steel foils instrumented with thermocouples. The local heat transfer coefficients on the ribbed side wall and on the smooth side wall of each test channel from the channel entrance to the fully developed regions were measured for two rib spacings* (P/e = *10 and 20*). *The rib angle-of-attack was kept at 90 deg. The local data in the fully developed region were averaged and correlated, based on the heat transfer and friction similarity laws developed for ribbed channels, to cover the ranges of channel aspect ratio, rib spacing, rib height, and Reynolds number. The results compare well with the published data for flow in a square channel with two opposite ribbed walls. The correlations can be used in the design of turbine airfoil cooling passages.*

Introduction

In advanced gas turbine blades and vanes, turbulence promoters (rib turbulators) are cast onto two opposite walls of internal cooling passages to enhance the heat transfer to the cooling air. Figure 1(*a*) is a sketch of an internally cooled turbine airfoil. The internal cooling passages can be approximately modeled as rectangular channels with a pair of opposite walls with rib turbulators, as shown in Fig. 1(*b*). Han et al. (1984, 1985) investigated systematically the effects of the rib pitch, rib height, and rib angle of attack on the average heat transfer and the average pressure drop for the fully developed turbulent flow in a uniformly heated, straight, square channel with two opposite rib-roughened walls. These average heat transfer and friction results in the fully developed region are applied primarily for a long square channel with two opposite rib-roughened walls. The configurations of the internal cooling passages of turbine airfoils are nearly rectangular, however, and are relatively short (typically, $L/D = 10 \sim 15$). The technical literature contains no information on the distributions of the local heat transfer coefficient in short rectangular channels with two opposite rib-roughened walls. The local heat transfer distributions in such channels are important to engineers for the design of effectively cooled turbine airfoils that are not susceptible to structural failure from uneven metal temperature distribution.

The present investigation aimed at determining the effect of the channel aspect ratio on the distributions of the local heat transfer coefficient in rectangular channels with two opposite rib-roughened walls for a Reynolds number range of 10,000 to 60,000. The channel width-to-height ratios (W/H) were 1/4, 1/2, 1, 2, and 4. The channel length-to-hydraulic diameter ratios (L/D) were 10 to 15. In order to obtain the local heat transfer coefficients, the test channels were heated uniformly by passing current through 0.025 mm (0.001 in.) thick, stainless steel foils and were instrumented with 180 thermocouples. In each channel, the brass ribs with a square cross section were glued periodically to the top and bottom walls of the foil-heated channel so that the ribs on opposite walls (the channel width, w, side) were all parallel with an angle of attack of 90 deg. The rib height-to-hydraulic diameter ratios (e/D) were 0.047 and 0.078, whereas the rib pitch-to-height ratios (P/e) were 10 and 20. The distribution of the local heat transfer coefficient on the smooth side (side H) and on the ribbed side (side W) walls from the channel entrance to the fully developed region were measured. For the results of ribbed channels to be useful for designers, the local data in the fully developed region ($X/D > 3$) were averaged and correlated, based on the heat transfer and friction similarity laws, to cover the ranges of channel aspect ratio, rib spacing, rib height, and Reynolds number. First, the rough channel analysis is developed. Then experimental results are presented and discussed, and the semi-empirical correlations are obtained.

Additional information on the present investigation may be found in Han et al. (1986), and Han and Park (1988).

Ribbed Channel Analysis

Analytical methods for predicting the friction factors and the heat transfer coefficients for turbulent flow over rib-roughened surfaces are not available because of the complex flow, such as separation, reattachment, and recirculation, created by periodic rib roughness elements. Thus heat transfer designers still depend on the semi-empirical correlations over a wide range of rib geometry for the friction and heat transfer calculations. Those semi-empirical correlations for the friction factors and the heat transfer coefficients are derived from the law of the wall similarity for flow over rough surfaces.

The similarity law concept was first developed by Nikuradse (1950), who applied it successfully to correlate the friction data for fully developed turbulent flow in tubes with sand roughness. Based on a heat–momentum transfer analogy, Dipprey and Sabersky (1963) developed the heat transfer similarity law for fully developed turbulent flow in tubes with sand roughness, which is complementary to Nikuradse's friciton similarity law. Webb et al. (1971) extended the friction and heat transfer similarity laws to correlate the friction and heat transfer data for turbulent flow in tubes with periodic rib roughness elements. The similarity laws were employed to correlate rib-roughened friction and heat transfer data for flow in annuli by Dalle Donne and Meyer (1977), for flow between parallel plates by Han et al. (1978), for flow in tubes by Gee and Webb (1980) and by Sethumadhavan and Raja Rao (1983), and for flow in square channels by Han et al. (1985).

Contributed by the Heat Transfer Division for publication in the JOURNAL OF HEAT TRANSFER. Manuscript received by the Heat Transfer Division December 22, 1986. Keywords: Finned Surfaces, Forced Convection.

According to the concept of Nikuradse (1950) and Dipprey and Sabersky (1963), the laws of the wall in fully developed turbulent flow can be expressed by the velocity and temperature profiles normal to the rough surface as

$$u^+ = 2.5 \ln (y/e) + R(e^+) \quad (1)$$

$$T^+ = 2.5 \ln (y/e) + G(e^+, \text{Pr}) \quad (2)$$

where u^+ and T^+ are the dimensionless velocity and temperature at a distance y from the rough wall, e is the height of the ribs of the roughness, and $R(e^+)$ and $G(e^+, \text{Pr})$ are the dimensionless velocity and temperature at the tip of the ribs, i.e., at the point $y = e$. Integrating equations (1) and (2) over y in the cross section of a tube (to obtain the dimensionless average velocity $\bar{u}^+$ and the dimensionless average temperature $\bar{T}^+$, respectively) and combining with the definitions of the dimensionless average velocity, $\bar{u}^+ = (2/f)^{1/2}$, and the dimensionless average temperature, $\bar{T}^+ = (f/2)^{1/2}/\text{St}$, gives the friction and heat transfer similarity laws as

$$R(e^+) = (2/f)^{1/2} + 2.5 \ln (2\, e/D) + 3.75 \quad (3)$$

$$G(e^+, \text{Pr}) = R(e^+) + [f/(2\text{St}) - 1]/(f/2)^{1/2} \quad (4)$$

Equations (3) and (4) imply that the friction (f) and the heat transfer (St) data for any geometrically similar roughness family (i.e., any e/D ratio) may be correlated by the roughness functions, $R(e^+)$ and $G(e^+, \text{Pr})$, respectively. A family of repeated-rib rougheners is defined as geometrically similar if the rib pitch, rib shape, and rib angle of attack are not varied. In order to correlate the friction and heat transfer data for geometrically nonsimilar repeated-rib rougheners, the roughness functions may be expressed by

$$R = \phi_1(e^+, P/e, \alpha, \text{shape}, \ldots) \quad (5)$$

$$G = \phi_2(e^+, \text{Pr}, P/e, \alpha, \text{shape}, \ldots) \quad (6)$$

The law of the wall shown in equations (1) and (2) should also be applied for fully developed turbulent flow in rectangular channels, with different channel aspect ratios (W/H), with repeated-rib rougheners. Integrations of equations (1) and (2) over y in the cross section of a rectangular channel give

$$\bar{u}^+ = 2.5 \ln(\delta/e) + R(e^+) - 2.5 \quad (7)$$

$$\bar{T}^+ = 2.5 \ln(\delta/e) + G(e^+, \text{Pr}) - 2.5 \quad (8)$$

where δ is the distance between the ribbed wall and the position of zero shear stress. The length δ can be related to channel dimension by

$$\delta = (1/2)H = [(H + W)/4W]D \quad (9)$$

Using the definition of the dimensionless average velocity, $\bar{u}^+ = (2/f)^{1/2}$, the dimensionless average temperature, $\bar{T}^+ = (f/2)^{1/2}/\text{St}$, and the length δ from equation (9) with equations (7) and (8), respectively, the friction and heat transfer similarity laws in rectangular channels with four-sided ribbed walls can be expressed by

$$R(e^+) = (2/f)^{1/2} + 2.5 \ln\{(2e/D)[2W/(W + H)]\} + 2.5 \quad (10)$$

along with equation (4).

The R and G can be experimentally determined (or correlated) by measuring f and St for fully developed turbulent flow in rectangular channels (given W/H) with four-sided, geometrically similar, ribbed walls (given e/D). For geometrically nonsimilar ribbed channels, the R and G can be expressed as those in equations (5) and (6), respectively.

Nomenclature

A = heat transfer surface area (smooth foil on each wall)
a = plenum height
b = plenum width
CR = contraction ratio between plenum and test channel = $ab/(WH)$
D = channel hydraulic diameter = $2WH/(W + H)$
e = rib height
e^+ = roughness Reynolds number = $(e/D)\text{Re}(f/2)^{1/2}$
f = friction factor for four-sided ribbed channel
f_s = friction factor for four-sided smooth channel
$\bar{f}$ = average friction factor in a channel with two opposite ribbed walls
$f(FD)$ = fully developed smooth tube friction factor
g_c = conversion factor
G = mass flux = $\rho \bar{V}$; also heat transfer roughness function
$\bar{G}$ = average heat transfer roughness function
h = heat transfer coefficients
H = flow channel height
K = thermal conductivity of air
ΔL = channel length for frictional pressure drop measurement
L = test channel length
ℓ = plenum length
LHS = left-hand side wall
Nu = Nusselt number = hD/K
Nu(FD) = fully developed smooth tube Nusselt number
Nu_r = the ribbed-side-wall centerline-average Nusselt number for flow in a channel with two opposite ribbed walls
Nu_s = the smooth-side-wall centerline-average Nusselt number for flow in a channel with two opposite ribbed walls
ΔP = pressure drop across the test section
P = rib pitch
Pr = Prandtl number of air
q = local net heat transfer rate from the foil to the cooling air
R = friction roughness function
Re = Reynolds number = GD/μ
RHS = right-hand side wall
St = Stanton number = Nu/(Re Pr), for flow in a channel with four-sided ribbed channel
St_r = the ribbed-side-wall centerline-average Stanton number for flow in a channel with two opposite ribbed walls
St_s = the smooth-side-wall centerline-average Stanton number for flow in a channel with two opposite ribbed walls
ST(FD) = fully developed smooth tube Stanton number
$\overline{\text{St}}$ = the average of the centerline-average Stanton numbers for flow in a channel with two opposite ribbed walls
T_b = bulk mean temperature of air
T_w = local wall temperature
$\bar{V}$ = average velocity of air
W = flow channel width
W/H = channel aspect ratio, ribs on side W
X = axial distance from heated test channel
α = rib angle of attack
δ = distance between the ribbed wall and the position of zero shear stress
μ = average viscosity of air
ρ = average density of air

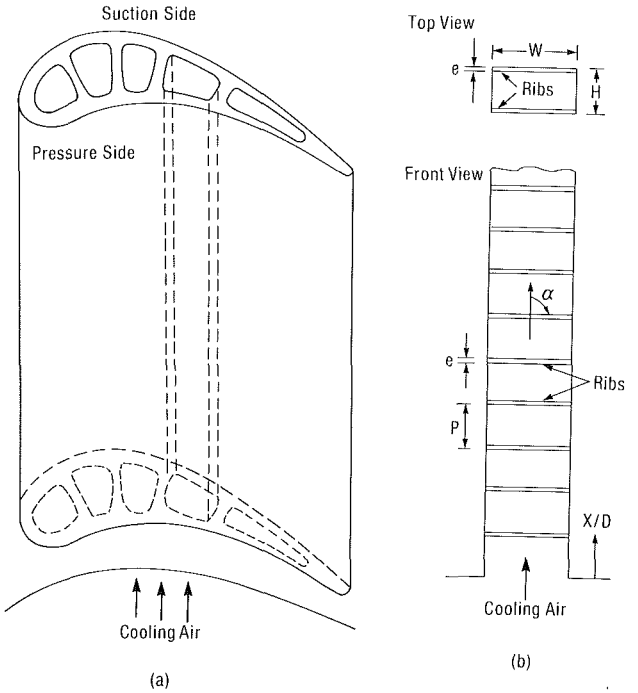

Fig. 1 *(a)* **Sketch of an internally cooled turbine airfoil; (*b*) rectangular channel with a pair of opposite ribbed walls**

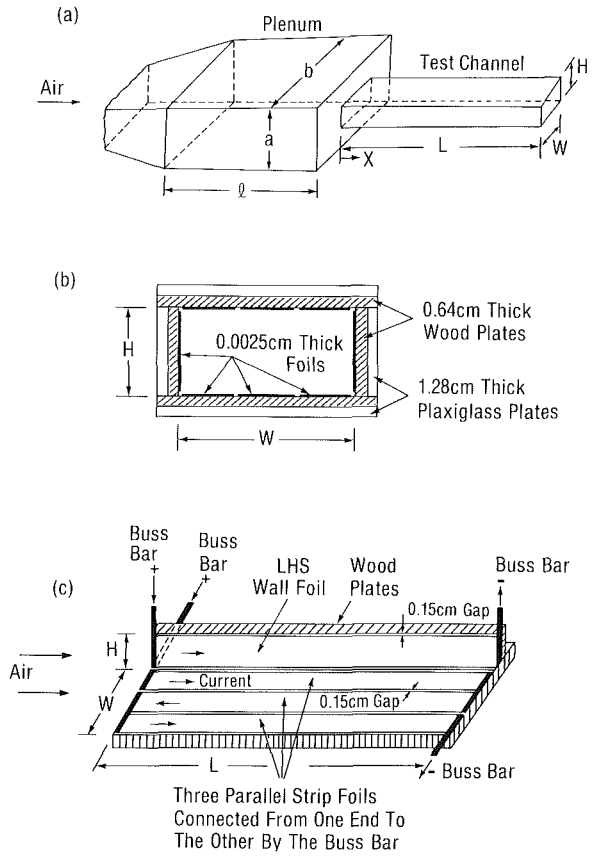

Fig. 2 *(a)* **Sketch of the test channels and the plenums; (*b*) test channel cross section; (c) distributions of electrical foil heaters**

This study concerns turbulent flow in rectangular channels with two opposite, instead of four-sided, ribbed walls. Han (1984) suggested that the average friction factor $\bar{f}$ for flow in this kind of channel could be found from

$$\bar{f} = (H f_s + W f)/(H + W) \tag{11}$$

which gives the average friction factor as a weighted average of the four-sided smooth channel friction factor f_s and the four-sided ribbed channel friction factor f. These friction factors are weighted by the smooth wall height H and the ribbed wall width W, respectively. Equation (11) can be rearranged as

$$f = \bar{f} + (H/W)(\bar{f} - f_s) \tag{12}$$

By inserting the expression for f from equation (12) into equation (10), the roughness function R of the present study can be written as

$$R(e^+) = \{2/[\bar{f} + (H/W)(\bar{f} - f_s)]\}^{1/2} + 2.5 \ln\{(2e/D)[2W/(W+H)]\} + 2.5 \tag{13}$$

where f_s can be approximately calculated from the Blasius equation for smooth circular tubes (Han, 1984) as

$$f_s = f(FD) = 0.046\,\mathrm{Re}^{-0.2} \tag{14}$$

Equation (13) implies that the friction roughness function R of the present study can be experimentally determined (or correlated) by measuring the average friction factor ($\bar{f}$) for fully developed ($X/D > 3$) turbulent flow in rectangular channels (given W/H) with two opposite, geometrically similar, ribbed walls (given e/D), and by combining with the f_s calculated from equation (14).

Similarly, in order to apply equation (4), the heat transfer similarity law, for flow in rectangular channels with two opposite ribbed walls of the present study (for $X/D > 3$), the friction factor (f) is replaced by equation (12), and the Stanton number (St) replaced by the Stanton number on the ribbed side wall (St_r). It is assumed that the ribbed side wall Stanton number has a constant value for either two opposite or four-sided ribbed channels (i.e., $\mathrm{St} \cong \mathrm{St}_r$). The heat transfer roughness function G of the present study can then be determined by

$$G(e^+, \mathrm{Pr}) = R(e^+) + \{[\bar{f} + (H/W)(\bar{f} - f_s)]/(2\mathrm{St}_r) - 1\}/\{[\bar{f} + (H/W)(\bar{f} - f_s)]/2\}^{1/2} \tag{15}$$

The roughness functions, $R(e^+)$ in equation (13) and $G(e^+, \mathrm{Pr})$ in equation (15), can also be extended to correlate the effects of geometrically nonsimilar parameters, P/e, α, . . . , as expressed in equations (5) and (6). One of the objectives of the present investigation is to determine correlations for R and G for flow in rectangular channels with rib turbulators.

Based on the abovementioned analysis, there appear to be two approaches to obtain the roughness functions R and G. The first approach is experimentally correlating R and G from equations (10) and (4) by measuring f and St for flow in rectangular channels (given W/H) with four-sided ribbed walls (given e/D, P/e, . . .). The second approach is correlating R and G from equations (13) and (15) by measuring $\bar{f}$ and St_r for flow in rectangular channels (given W/H) with a pair of opposite ribbed walls (given e/D, P/e, . . .) and incorporating equation (14). The present study uses the second approach to correlate R and G, because the results can be directly applied for the design of turbine airfoil cooling passages.

Experimental Program

Foil Heated Test Channel. Three rectangular channels were constructed. The square channel had a 5.1 cm × 5.1 cm (2 in. × 2 in.) cross section. Rectangular channel I and rectangular channel II had cross sections of 10.2 cm × 5.1 cm (4 in. × 2 in.) and 10.2 cm × 2.55 cm (4 in. × 1 in.), respectively. A Plexiglas plenum was connected to the inlet of the test channel to provide a sudden entrance condition. The sketch and dimensions of the test channels and the associated plenum are shown in Fig. 2(*a*) and Table 1.

Table 1 Dimensions of the test channels and plenums (cm)

	W	H	W/H	D	L	b	a	CR	ℓ
Square Channel	5.1	5.1	1	5.1	127.5	15.3	15.3	9	15D
Rectangular Channel I	10.2	5.1	2	6.8	127.5	30.6	15.3	9	15D
Rectangular Channel II	10.2	2.55	4	4.08	127.4	30.6	15.3	18	25D

Table 2 Rib geometries in each test channel (cm)

	W/H	e	e/D	P/e	α	Re x 10^{-3}
Square Channel	1	0.24	0.047	10 20	90°	10 30 60
Rectangular Channel I	2	0.32	0.047	10 20	90°	10 30 60
Rectangular Channel II	4	0.32	0.078	10 20	90°	10 30 60
Rectangular Channel IA	1/2	0.32	0.047	10 20	90°	10 30 60
Rectangular Channel IIA	1/4	0.32	0.078	10 20	90°	10 30 60

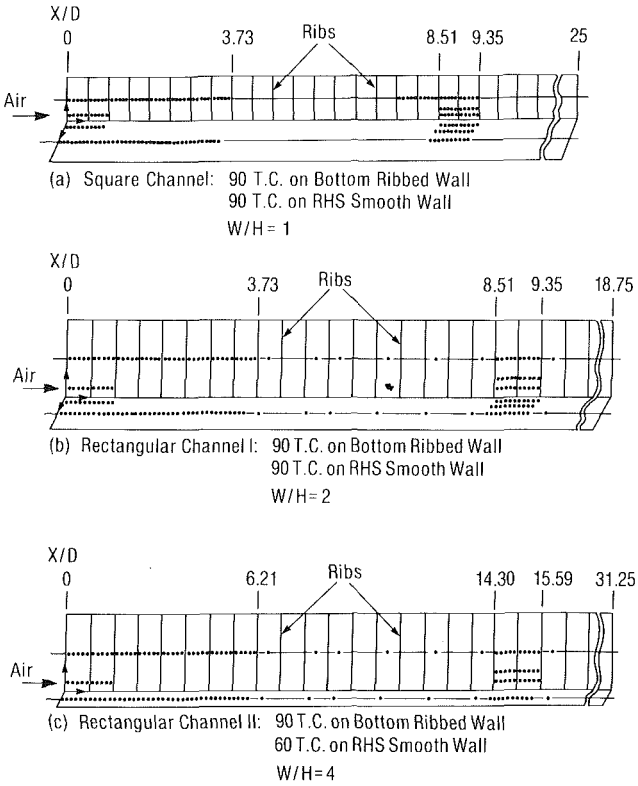

Fig. 3 Detailed thermocouple locations in each test channel

Each wall of the test channel was made of nonconductive material. The nonconductive wall was constructed by the combination of a 0.64 cm (0.25 in.) thick wood board and a 1.28 cm (0.5 in.) thick, Plexiglas plate. Then, the 0.0025 cm (0.001 in.) thick, stainless steel foils were cemented to the inner face (wood-board surface) of each wall, controlled individually by a variac transformer, for controllable electrical heating to the test channel. The cross section of the test channel and the distributions of electrical foil heaters are sketched in Fig. 2(*b*) and Fig. 2(*c*).

For ribbed channel tests, brass ribs with a square cross section were glued periodically in-line on the top and bottom walls of the foil-heated channels in a required distribution. The thin layer of glue (less than 0.01 cm thick) provides electrical isolation (but thermal conduction) from foil to brass ribs. Additionally, the rectangular channel I ($W/H=2$, ribs on side W) and the rectangular channel II ($W/H=4$, ribs on side W) were modified to be the rectangular channel IA ($W/H=1/2$, ribs on side W) and the rectangular channel IIA ($W/H=1/4$, ribs on side W), respectively, simply by moving ribs from the top and bottom walls to the right and left-hand side walls of the channels. The rib geometries for each test channel are shown in Table 2.

The typical thermocouple locations in each test channel are shown in Fig. 3. Each channel had 180, 36 gauge, copper-constantan thermocouples in strategic locations to measure the local surface temperature. Ninety of these thermocouples were placed on the bottom ribbed wall (channel width side), and the other ninety on the right-hand side smooth wall (channel height side). Sixty of each ninety thermocouples were placed along the centerline of the ribbed and the smooth walls. Twenty of the remaining thirty thermocouples were distributed in the fully developed region, along the spanwise direction of each wall, as shown in Fig. 3. A Fluke 2280A Data Logger and a TI PC were used for temperature readings and data storage.

In each test channel, six pressure taps along the top ribbed wall and six along the left-hand side smooth wall were used for the static pressure drop measurements. A pressure tap was alos located at the plenum to check the static pressure of air entering the test channel. A Dywer Microtector with accuracy up to 0.0025 cm (0.001 in.) water was used for pressure drop measurements in the test channel.

Data Reduction. The local heat transfer coefficient was calculated from the local net heat transfer rate per unit surface area from the foil (wall) to the cooling air, the local foil (wall) temperature, and the local bulk mean air temperature as

$$h = q/[A(T_w - T_b)] \tag{16}$$

Equation (16) was used for the ribbed side wall and the smooth side wall heat transfer coefficient calculations. The local net heat transfer rate was the electrical power generated from the foil minus the heat loss to the outside of the test channel. The electrical power generated from the foil was determined from the measured foil resistance and the current through the foil on each plate. The effect of the local foil temperature on the local foil resistance was estimated to be very small and negligible in calculations. The electrical power was also checked with the measured voltage drop across the foil on each plate. In order to place the results on a common basis, the heat transfer area used in equation (16) was always that of a smooth foil on each wall. The foil provided a nearly uniform heat flux on each wall of the test channel. The maximum heat loss from the ribbed side wall and the smooth side wall was estimated to be less than 3 and 5 percent, respectively, for Reynolds numbers greater than 10,000. The net heat flux (q/A) level was varied from about 950 to 2500 W/m^2 (300 to 800 Btu/hr-ft^2) depending on the test conditions.

The local wall temperatures used in equation (16) were read from the thermocouple output. The bulk mean air temperatures entering and leaving the test channel were measured by thermocouples. The local bulk mean air temperature used in equation (16) was calculated, assuming a linear air temperature rise along the flow channel. The total net heat transfer rate from the test channel to the cooling air

agreed well with the cooling air enthalpy rise along the test channel. The inlet bulk mean air temperature was 24° to 29°C (75° to 85°F) depending on the test conditions.

The local Nusselt number of the present study was normalized by the Nusselt number for fully developed turbulent flow in smooth circular tubes correlated by McAdams as

$$\mathrm{Nu}/\mathrm{Nu}(FD) = (hD/K)/[0.023\ \mathrm{Re}^{0.8}\mathrm{Pr}^{0.4}] \quad (17)$$

The maximum uncertainty in the Nusselt number was estimated to be less than 8 percent for Reynolds numbers larger than 10,000 by using the uncertainty estimation method of Kline and McClintock (1953).

The pressure drop across the test channel was measured by a microtector. In fully developed channel flow, the average friction factor was calculated from the average pressure drop across the flow channel and the mass flow rate of the air as

$$\bar{f} = \Delta P/\{4(\Delta L/D)[G^2/(2\rho g_c)]\} \quad (18)$$

The average friction factor of the present investigation was based on the isothermal conditions (tests without heating). The maximum uncertainty in the average friction factor was estimated to be less than 9 percent for Reynolds numbers greater than 10,000.

The average friction factor of the present study was normalized by the friction factor for fully developed turbulent flow in smooth circular tubes ($10^4 < \mathrm{Re} < 10^6$) proposed by Blasius as

$$\bar{f}/f(FD) = \bar{f}/[0.046\ \mathrm{Re}^{-0.2}] \quad (19)$$

Experimental Results and Discussion

The friction factor and the heat transfer coefficient in the smooth channels are given in Han et al. (1986). The maximum deviation of the friction factor from the Blasius equation is 12 percent, and that of the Nusselt number from the McAdams correlation is 10 percent.

The test results for the ribbed channels are presented here. Thirty sets of local heat transfer data were obtained (five W/H ratios, two P/e ratios, and three Reynolds numbers). The detailed raw data for all test runs are given in Han et al. (1986). Only the most representative results are presented here. The local heat transfer results are presented as the axial distributions of a normalized Nusselt number ratio, $\mathrm{Nu}/\mathrm{Nu}(FD)$, as given in equation (17). For the transverse ribs ($\alpha = 90$ deg) of the present study, the variations of the local heat transfer coefficient in the lateral direction in the fully developed region were very small. Therefore, only the local Nusselt number ratios along the centerlines of the ribbed side and the smooth side walls are presented. These centerline Nusselt number ratios are not evenly distributed. In regions of interest, such as the entrance and the fully developed, the local Nusselt number was determined at up to five stations every rib pitch along axial line for the case of $P/e = 10$ (or ten stations for the case of $P/e = 20$). In regions between the entrance and the fully developed, the local Nusselt number was determined at only one station every rib pitch.

Local Heat Transfer Coefficient

Effect of Rib Spacing. Typical results to illustrate the effect of rib spacing on the centerline heat transfer coefficients on both the ribbed side wall and the smooth side wall of the square and rectangular channel I are shown in Fig. 4 for $\mathrm{Re} = 30{,}000$. The results show that the local Nusselt number ratios on the right-hand side (RHS) smooth wall of the ribbed channels decrease sharply with increasing distance for both P/e ratios. These are similar to the four-sided smooth channel results, except that the former have some small fluctuations and about 20–60 percent higher values than the latter because of the influence of the adjacent periodic ribs. The local

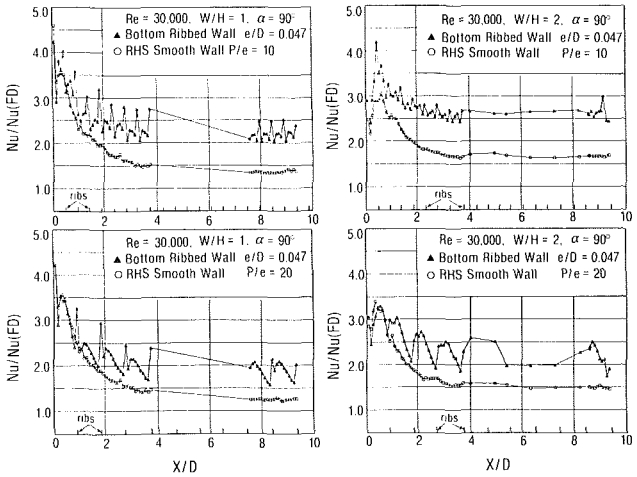

Fig. 4 Effect of rib spacing on the centerline heat transfer distributions

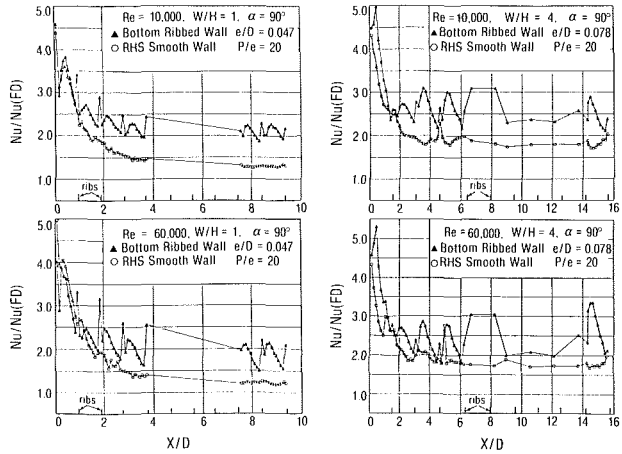

Fig. 5 Effect of Reynolds number on the centerline heat transfer distributions

Nusselt number ratios on the ribbed side wall have larger fluctuations, however, and decrease slowly with increasing distance, settling into a periodic pattern just after the first few ribs ($X/D > 3.0$). For $P/e = 10$, heat transfer coefficients increase after the flow separates from the ribs, decrease after flow reattachment on the surface (about 4 rib heights downstream from separation), and increase again before the flow hits the next rib.

For $P/e = 20$, similar heat transfer patterns are observed, except that the heat transfer coefficients are 10–20 percent lower than those of $P/e = 10$ because of wider rib spacing, creating thicker boundary layer thickness after flow reattachment between ribs. Periodic distribution of the local heat transfer between ribs is obtained after $X/D > 3$. At $X/D < 1.0$, for both $P/e = 10$ and 20, the Nusselt number ratios on the ribbed side and the smooth side walls are about the same; at $X/D > 1.0$, the ribbed side wall Nusselt number ratios gradually depart from the smooth wall values and are up to two times higher at the downstream fully developed region.

Effect of Reynolds Number. Typical results to demonstrate the effect of Reynolds number on the centerline heat transfer coefficient of the square and rectangular channel II are shown in Fig. 5 for the case of $P/e = 20$. The Nusselt number ratios for $\mathrm{Re} = 10{,}000$ and 60,000 shown in Fig. 5 have the same trend as those for $\mathrm{Re} = 30{,}000$ shown in Fig. 4. Flow tends to reattach more quickly for $\mathrm{Re} = 60{,}000$, about 2 rib heights downstream from separation, than for $\mathrm{Re} = 10{,}000$, about 6 rib heights downstream from separation. Therefore,

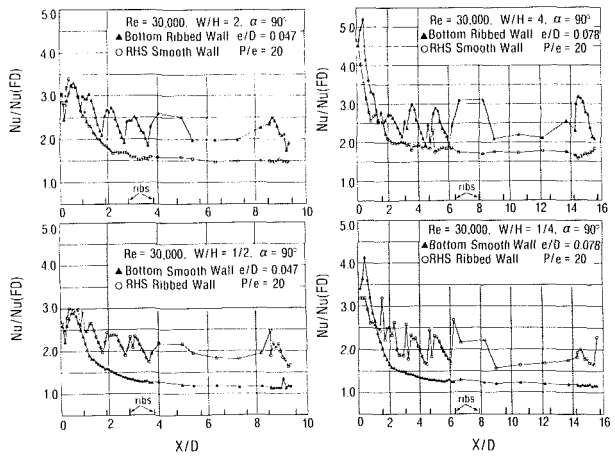

Fig. 6 Effect of channel aspect ratio on the centerline heat transfer distributions

the Nusselt number ratio decreases slightly with increasing Reynolds number.

Effect of Channel Aspect Ratio. Typical results showing the effect of channel aspect ratio on the centerline heat transfer coefficient are shown in Fig. 6 for the case of $P/e = 20$ and Re = 30,000. The Nusselt number ratios on the ribbed side and the smooth side walls show the same trend for different channel aspect ratios, but the local Nusselt number ratios in larger aspect ratio channels ($W/H = 2$ or 4) are higher than those in the smaller aspect ratio channels ($W/H = 1/2$ or 1/4). For the same rib geometry (e/D and P/e) and the same flow condition (Re), the larger aspect ratio channels have wider ribbed side walls and narrower smooth side walls that result in a higher heat transfer coefficient; the smaller aspect ratio channels have narrower ribbed side walls and wider smooth side walls, and therefore the heat transfer coefficient is reduced.

Centerline Average Heat Transfer and Friction Data. To develop the heat transfer and friction correlations, the average heat transfer coefficient and friction factor are required. Based on the local heat transfer and pressure distribution, it was found that the Nusselt number has a periodic distribution and the friction factor has a constant value in the region where $X/D > 3$. Therefore, the heat transfer and pressure data in the region with $X/D > 3$ in each channel were used to determine average Nusselt number and the average friction factor. The present study bases the average Nusselt (or Stanton) numbers on the smooth side wall and on the ribbed side wall on the average values of the centerline Nusselt (or Stanton) number between $X/D = 2.9$–3.7 and $X/D = 8.5$–9.4 for both the square channel and rectangular channel I. The average Nusselt (or Stanton) numbers are the average values of the Nusselt (or Stanton) numbers between $X/D = 4.8$–6.2 and $X/D = 14.2$–15.6 for rectangular channel II.

Typical results showing the effect of Reynolds number and P/e ratio on the normalized Nusselt number and the normalized friction factor are plotted in Figs. 7–9 for all channels studied. As expected, the average heat transfer ratios on both the ribbed side and the smooth side walls decrease slightly with increasing Reynolds number for all channels, whereas the average friction factor ratios increase with Reynolds number. The results also show that, for a given Reynolds number, both the average heat transfer and friction factor ratios decrease with increasing P/e ratio for all channels. Typical results illustrating the effect of the channel aspect ratio on the average heat transfer and friction ratios are included in Figs. 8 and 9. Again the results show that the average Nusselt number and

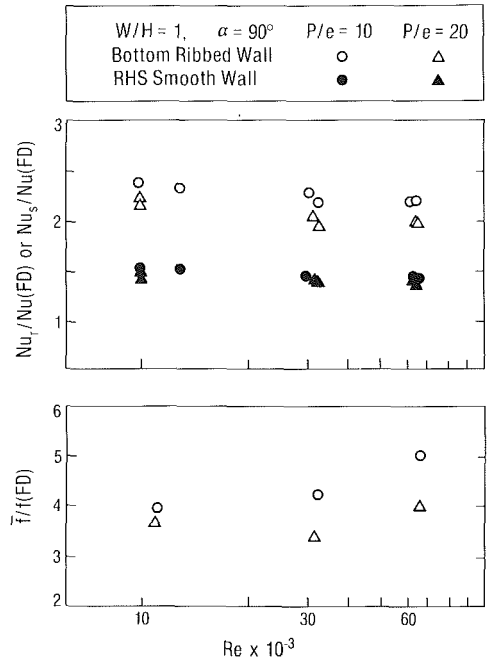

Fig. 7 Heat transfer and friction versus Re for square channel

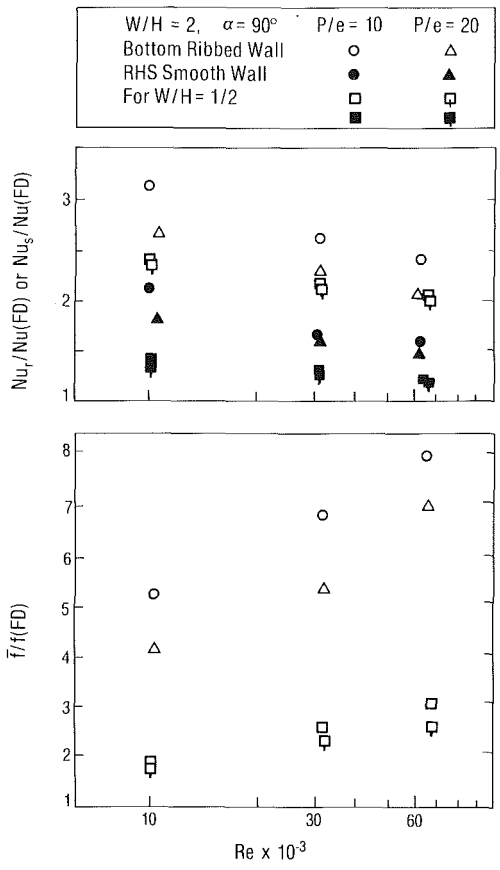

Fig. 8 Heat transfer and friction versus Re for rectangular channel I

the average friction factor ratios increase with increasing channel aspect ratio from 1/2 to 2, and from 1/4 to 4, respectively.

Heat Transfer Performance Comparison. One of the performance evaluation criteria was to compare the increased heat transfer, $[St_r/St(FD)]/[\bar{f}/f(FD)]^{1/3}$ or $[\bar{St}/St(FD)]/[\bar{f}/f(FD)]^{1/3}$, for the same surface area and pumping power.

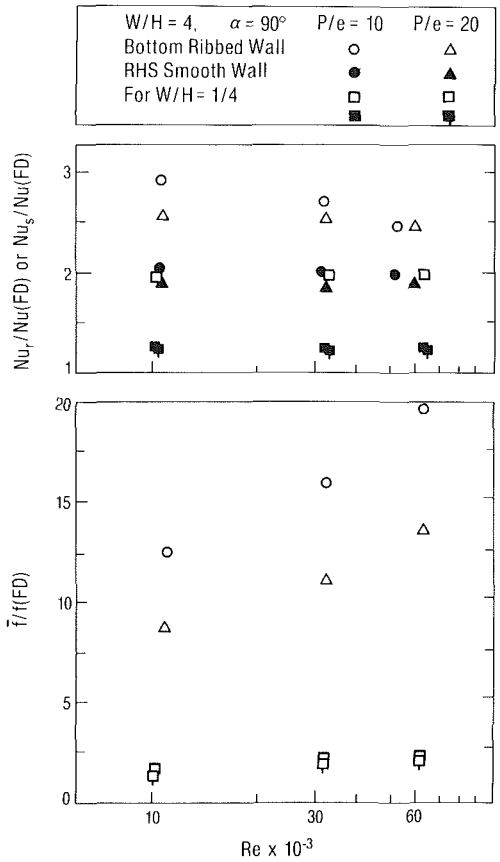

Fig. 9 Heat transfer and friction versus Re for rectangular channel II

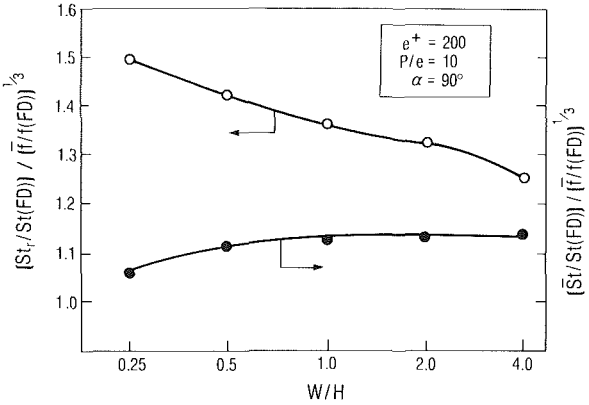

Fig. 10 Increased heat transfer for a constant pumping power

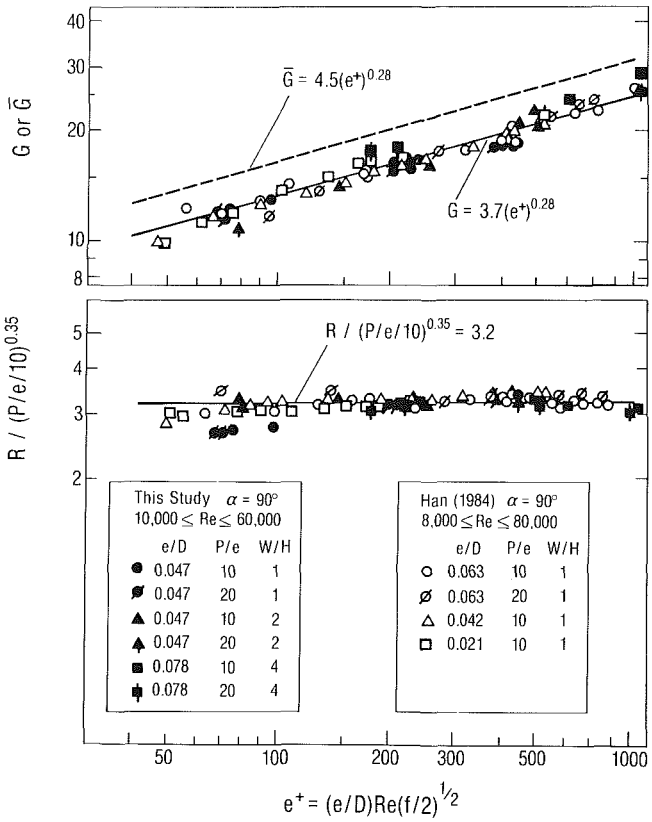

Fig. 11 Friction and heat transfer correlations

Typical results to demonstrate the effect of channel aspect ratio on the increased heat transfer for a constant pumping power are shown in Fig. 10 for $e^+ = 200$ and $P/e = 10$. The increased ribbed side wall heat transfer for a constant pumping power, $[St_r/St(FD)]/[\bar{f}/f(FD)]^{1/3}$, decreases from 1.5 to 1.25 when the channel aspect ratio (W/H, ribs on side W) increases from 1/4 to 4. The increased average heat transfer, $[\overline{St}/St(FD)]/[\bar{f}/f(FD)]^{1/3}$, increases from 1.06 to 1.13, however, when the W/H ratio changes from 1/4 to 4.

Friction and Heat Transfer Correlations. Based on the ribbed channel analysis discussed earlier, the wall similarity laws were employed to correlate the friction and heat transfer data for fully developed turbulent flow in rectangular channels with two opposite ribbed walls of the present study. According to the friction similarity law derived in equation (13), the measured average friction factor ($\bar{f}$), the channel aspect ratio (W/H), the rib height-to-hydraulic diameter ratio (e/D), and the Reynolds number could be correlated with the friction roughness function $R(e^+)$. The geometrically nonsimilar parameter, the ratio P/e, could also be taken into account. A plot of $R/(P/e/10)^{0.35}$ versus roughness Reynolds number e^+ is shown in Fig. 11. The published friction data by Han (1984) for fully developed turbulent flow in a square channel ($W/H = 1$) with two opposite ribbed walls, and with values of e/D, P/e, and Re similar to those of the present study, were correlated by using equation (13) and also included in Fig. 11. Figure 11 shows that the present friction results compare well with the published data. The correlation of the friction roughness function R shown in Fig. 11 can be written as

$$R = 3.2((P/e)/10)^{0.35} \quad \text{for } e^+ \geq 50 \tag{20}$$

The deviation of equation (20) is ±6 percent for 95 percent of the data shown in Fig. 11. Note that R in equaton (20) is independent of e^+. This implies that the average friction factor is almost independent of Reynolds number (i.e., in the fully rough region with $e^+ \geq 50$). After R is determined experimentally from equation (20), the average friction factor ($\bar{f}$) can be predicted by combining equations (13), (14), and (20) for a given rib geometry (e/D, P/e), channel aspect ratio (W/H), and Reynolds number. Equation (20) is valid for $0.021 \leq e/D \leq 0.078$, $10 \leq P/e \leq 20$, $1 \leq W/H \leq 4$, and $8000 \leq \text{Re} \leq 80{,}000$.

According to the heat transfer similarity law derived in equation (15), the measured centerline-average Stanton number (converted from centerline-average Nusselt number) on the ribbed side wall St_r, the average friction factor $\bar{f}$, the channel aspect ratio W/H, and R could be correlated with the heat transfer roughness function $G(e^+, \text{Pr})$. The effect of the P/e ratio on the $G(e^+, \text{Pr})$ is negligible. A plot of G versus e^+ is also shown in Fig. 11. Again, the published heat transfer data by Han (1984) were correlated by using equation (15) and

included in Fig. 11. The present heat transfer results compare well with the published data. For a Prandtl number of 0.703 of the present study, the correlation of G shown in Fig. 11 can be represented by

$$G = 3.7(e^+)^{0.28} \quad \text{for } e^+ \geq 50 \tag{21}$$

The deviation of equation (21) is ± 8 percent for 95 percent of the data shown in Fig. 11. After G is correlated experimentally from equation (21), the ribbed-side-wall centerline-average Stanton number (St_r) can be predicted by combining equations (13), (14), (20), (15), and (21) for a given e/D, P/e, W/H, and Re. Equation (21) is valid for $0.021 \leq e/D \leq 0.078$, $10 \leq P/e \leq 20$, $1 \leq W/H \leq 4$, and $8000 \leq \text{Re} \leq 80{,}000$.

Since both the smooth-side-wall centerline-average Stanton number (St_s) and the ribbed-side-wall centerline-average Stanton number (St_r) were measured, the average Stanton number ($\overline{St}$) between the smooth side and the ribbed side walls was obtained. Assuming that equation (15) can be used to correlate the average heat transfer data by replacing G and St_r by $\bar{G}$ and $\overline{St}$, the correlation of the $\bar{G}$ shown in Fig. 11 can be expressed by

$$\bar{G} = 4.5(e^+)^{0.28} \quad \text{for } e^+ \geq 50 \tag{22}$$

The deviation of equation (22) is ± 10 percent. If G, $\bar{G}$, R, and $\bar{f}$ are known for a given e/D, P/e, W/H, and Re, the ribbed-side-wall centerline-average Stanton number St_r and the average Stanton number $\overline{St}$ can be predicted, respectively, from equation (15), and from the same equation (15) by replacing G and St_r by $\bar{G}$ and $\overline{St}$. After determining St_r and $\overline{St}$ from correlations, the smooth-side-wall centerline-average Stanton number St_s can be found by

$$St_s = \overline{St} + (W/H)(\overline{St} - St_r). \tag{23}$$

Concluding Remarks

The effect of the channel aspect ratio on the distributions of the local heat transfer coefficient in rectangular channels with two opposite rib-roughened walls have been investigated. The main findings of the study are:

1 For all test channels, the local Nusselt number becomes uniformly periodic between ribs in the axial direction after several ribs from the channel entrance ($X/D > 3$).

2 The local Nusselt number on the ribbed side wall is about two to three times higher than the four-sided smooth channel values, depending on the e/D, P/e, W/H, and Re. The local Nusselt number on the smooth side wall is also enhanced about 20–50 percent because of the influence of the adjacent periodic ribs.

3 The local (and the average) ribbed-side-wall Nusselt number ratio decreases with increasing rib spacing or Reynolds number and increases with increasing rib height or channel aspect ratio, for a constant Reynolds number.

4 The increased ribbed-side-wall heat transfer in a smaller aspect ratio channel is higher than that in a larger aspect ratio channel, for a constant pumping power. But, the increased average heat transfer is slightly lower, under the same pumping power conditions.

5 Based on the ribbed channel analysis, the correlations for the friction factor and the Stanton number are obtained. Those friction and heat transfer data compare very well with the published data. The correlations are valid for $e^+ \geq 50$, $0.021 \leq e/D \leq 0.078$, $10 \leq P/e \leq 20$, $1 \leq W/H \leq 4$, and $8000 \leq \text{Re} \leq 80{,}000$. The correlations can be used in the design of turbine airfoil cooling passages.

Acknowledgments

This work was funded through Mr. Curtis Walker at the U.S. Army Propulsion Laboratory and monitored by Mr. Robert Boyle at the NASA-Lewis Research Center under Contract No. NAS 3-24227. Additional support was provided by NSF Grant MEA-8205234. Their support is greatly appreciated. Experimental data were taken by Dr. J. S. Park, Mr. M. Y. Ibrahim, and Mr. C. K. Lei, all of Texas A & M University.

References

Dalle Donne, M., and Meyer, L., 1977, "Turbulent Convective Heat Transfer From Rough Surfaces With Two-Dimensional Rectangular Ribs," *Int. J. Heat Mass Transfer*, Vol. 20, pp. 582–620.

Dipprey, D. F., and Sabersky, R. H., 1963, "Heat and Momentum Transfer in Smooth and Rough Tubes in Various Prandtl Number," *Int. J. Heat Mass Transfer*, Vol. 6, pp. 329–353.

Gee, D. L., and Webb, R. L., 1980, "Forced Convection Heat Transfer in Helically Rib-Roughened Tubes," *Int. J. Heat Mass Transfer*, Vol. 23, pp. 1127–1136.

Han, J. C., 1984, "Heat Transfer and Friction in Channels with Two Opposite Rib-Roughened Walls," ASME JOURNAL OF HEAT TRANSFER, Vol. 106, No. 4, pp. 774–781.

Han, J. C., Glicksman, L. R., and Rohsenow, W. M., 1978, "An Investigation of Heat Transfer and Friction for Rib-Roughened Surfaces," *Int. J. Heat Mass Transfer*, Vol. 21, pp. 1143–1156.

Han, J. C., Park, J. S., and Lei, C. K., 1985, "Heat Transfer Enhancement in Channels With Turbulence Promoters," ASME *Journal of Engineering for Gas Turbines and Power*, Vol. 107, pp. 628–635.

Han, J. C., Park, J. S., and Ibrahim, M. Y., 1986, "Measurement of Heat Transfer and Pressure Drop in Rectangular Channels With Turbulence Promoters," NASA Contractor Report 4015; AVSCOM Technical Report 86-C-25, pp. 1–197.

Han, J. C., and Park, J. S., 1988, "Developing Heat Transfer in Rectangular Channels With Rib Turbulators," *Int. J. Heat Mass Transfer*, Vol. 31, No. 1, pp. 183–195.

Kline, S. J., and McClintock, F. A., 1953, "Describing Uncertainties in Single-Sample Experiments," *Mechanical Engineering*, Vol. 75, pp. 3–8.

Nikuradse, J., 1950, "Laws for Flow in Rough Pipes," NACA TM 1292.

Sethumadhavan, R., and Raja Rao, M., 1983, "Turbulent Flow Heat Transfer and Fluid Friction in Helical-Wire-Coil-Inserted Tubes," *Int. J. Heat Mass Transfer*, Vol. 26, pp. 1833–1844.

Webb, R. L., Eckert, E. R. G., and Goldstein, R. J., 1971, "Heat Transfer and Friction in Tubes With Repeated-Rib Roughness," *Int. J. Heat Mass Transfer*, Vol. 14, pp. 601–617.

S. Garimella
Affiliate Member,
Battelle Columbus Laboratories,
Columbus, OH 43201

D. E. Richards
Assistant Professor.
Assoc. Member

R. N. Christensen
Associate Professor.

Mechanical and Nuclear Engineering
Graduate Programs,
Department of Mechanical Engineering,
The Ohio State University,
Columbus, OH 43210

Experimental Investigation of Heat Transfer in Coiled Annular Ducts

Forced convection heat transfer in coiled annular ducts was investigated experimentally. Average heat transfer coefficients were obtained for both laminar and transition flows. Two coiling diameters and two annulus radius ratios were used in the study. The data were correlated with Dean number and Reynolds number separately and compared with the available studies of coiled circular tubes and straight annular ducts. It was found that coiling augments the heat transfer coefficients above the values for a straight annulus especially in the laminar region. However, the augmentation is less than would be expected for a coiled circular tube. The augmentation decreases as the flow enters the transition region.

Introduction

Coiled tube-in-tube heat exchangers are used extensively in HVAC applications because they provide a large surface area per unit volume. Design of these exchangers requires knowledge of heat transfer coefficients for coiled circular tubes and for coiled annular ducts. Correlations for predicting heat transfer in coiled circular tubes are available in the literature; however, no work has been reported on coiled annular ducts. This paper presents the results of an experimental study of forced convection heat transfer in coiled annular ducts. A cross section of this duct is shown in Fig. 1 where the duct inner and outer diameter are d_i and d_o, respectively, and D is the coiling diameter. The experiments were performed using a coiled tube-in-tube heat exchanger with water as the heat transfer medium.

The literature is conspicuously devoid of studies on forced convection heat transfer in coiled annular ducts. Thus, discussion of the related forced convection literature will be divided into two categories: flow inside coiled circular tubes and flow inside straight annular ducts.

A recent paper by Yao and Berger [1] provides a comprehensive review and some insight into flow in coiled ducts. When a fluid flows in a coiled duct, a centrifugal force is generated due to the curvature. This force is proportional to the square of the axial velocity, which varies across the cross section. The centrifugal force is small at the wall where the viscous forces dominate. The interaction between the centrifugal and viscous forces produces secondary flow loops, which result in enhanced heat transfer when compared with a straight tube.

Early theoretical studies on flow in curved tubes were performed by Dean [2, 3] who attempted to determine the deviation of the velocity profile from the Poiseuille flow pattern by solving the Navier-Stokes equations. From dynamic similarity considerations, he demonstrated that curvature produces a secondary flow. He also introduced a dimensionless grouping, the Dean number, which characterizes flow in coiled tubes. The Dean number represents the ratio of the square root of the product of the inertia and centrifugal forces to the viscous force and can be written as

$$\mathrm{De} = \mathrm{Re}\ \delta^{1/2} \tag{1}$$

where Re is the Reynolds number based on hydraulic diameter and δ is the ratio of the duct hydraulic diameter to the coiling diameter, d_h/D. Berger et al. [4] present a good discussion of the many variations in the definition of Dean number.

The criterion for transition from laminar to turbulent flow was established by Ito [5-7] who experimentally measured laminar and turbulent friction coefficients. Ito's transition criterion can be represented by the relation

$$\mathrm{Re}_{\mathrm{critical}} = 2 \times 10^4 (\delta)^{0.32} \tag{2}$$

A Nusselt number correlation was developed by Mori and Nakayama [8] for heat transfer in the laminar flow regime with the uniform heat flux boundary condition. The correlation was based on a theoretical analysis combined with experiments using air as the working fluid. For Prandtl numbers greater than one, the following expression was obtained:

$$\frac{\mathrm{Nu}_c}{\mathrm{Nu}_s} = \frac{0.1979\ \mathrm{De}^{1/2}}{\xi\left[1+\frac{37.05}{\xi}\left[\frac{1}{40}-\frac{17}{120}\,\xi+\left(\frac{1}{10\xi}+\frac{13}{30}\right)\frac{1}{10\mathrm{Pr}}\right]\mathrm{De}^{-1/2}\right]} \tag{3}$$

where

$$\xi = \frac{2}{11}\left[1+\sqrt{\left(1+\frac{77}{4}\,\frac{1}{\mathrm{Pr}^2}\right)}\right] \tag{4}$$

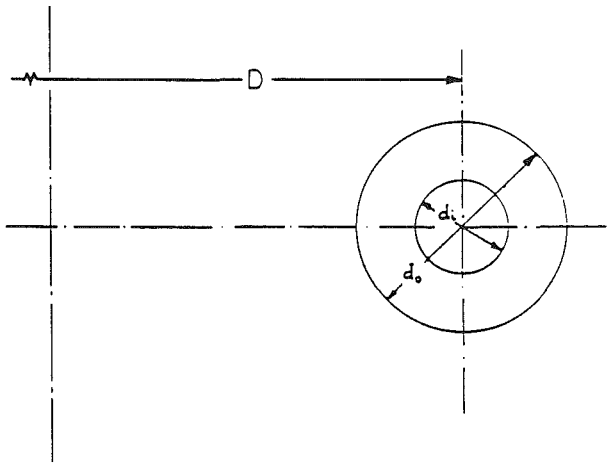

Fig. 1 The coiled annulus

Contributed by the Heat Transfer Division and presented at the ASME Winter Annual Meeting, New Orleans, Louisiana, December 1984. Manuscript received by the Heat Transfer Division May 28, 1986. Keywords: Forced Convection, Rotating Flows.

Pr = Prandtl number; Nu_c = Nusselt number for coiled tubes; Nu_s = Nusselt number for straight tubes.

Turbulent heat transfer has been studied by Seban and McLaughlin [9] using two coils with $1/\delta = 17$ and 104 in which the fluid was heated by passing a current through the tube wall. The data were correlated by

$$NuPr^{-0.4} = 0.023Re^{0.85}(\delta)^{0.1} \quad (5)$$

Similar studies were conducted by Rogers and Mayhew [10], who used water flowing through steam-heated tubes ($1/\delta$ = 10.8, 13.3, and 20.12). Ito's criterion for transition was also validated in these experiments.

In a straight annular duct, the inner and outer surface each have a different Nusselt number. Different combinations of constant-surface-temperature and constant-heat-flux boundary conditions can be imposed on these surfaces. Lundberg et al. [11] have solved all the combinations of this problem for the laminar flow case. Analytical approaches to this problem use the linearity of the energy equation and superposition to build asymmetric heating solutions from the two fundamental solutions: outer wall heated with the inner insulated and inner wall heated with the outer insulated. The most comprehensive study on heat transfer in the turbulent flow regime was done by Kays and Leung [12]. They combined an experimental study with analytical derivations to obtain solutions for radius ratios between 0.0 and 1.0, Prandtl numbers between 0.0 and 1000, and Reynolds numbers above 10^4. As for the laminar flow case, these constant heat flux solutions can be used to obtain the more general results.

In the transition region for straight annular ducts, work on fluid friction has been used to predict critical Reynolds numbers. Walker et al. [13] studied fluid friction for the laminar, transition, and lower turbulent ranges of flow of water in annular ducts. They argued that since the shear stresses on the inner and outer surfaces of the annulus are different, the corresponding friction factors will be different. Therefore, the friction factors can be correlated with Reynolds numbers based on two different hydraulic radii

$$Re_{h1} = \frac{r_m^2 - r_i^2}{2r_i} \quad (6)$$

$$Re_{h2} = \frac{r_o^2 - r_m^2}{2r_o} \quad (7)$$

where r_m is the radius of the maximum velocity or zero shear and r_i and r_o are the inner and outer radii, respectively. When the inner radius is made vanishingly small, Re_{h1} loses significance. Therefore, they use Re_{h2} as the basis for correlation. In addition, r_m is calculated for the entire range of Reynolds numbers assuming laminar flow. The bulk average linear velocity is taken over the entire annular section between the outer and inner radii. The critical Reynolds numbers so calculated were found to be approximately linear functions of the radius ratio.

The foregoing discussion has shown that past studies have addressed flow and heat transfer in curved circular tubes and straight annular ducts separately. The present study investigates the effet of coiling on forced convection heat transfer in an annular duct. Attention is also directed to the transition flow regime, a subject which has been studied by few investigators.

Experimental Apparatus and Procedures

Figure 2 presents a schematic overview of the experimental test facility. Two independent loops, an open city water loop and a closed water loop were used. The closed loop conveyed hot water through one side of the heat exchanger (1) being tested. Four banks of resistance heaters (2) provided heating of this loop on demand up to a total capacity of 34 kW. City water passed through the other side of the exchanger and served as the coolant. Any additional cooling required in the closed loop was accomplished using an auxiliary cooling bay fed by a separate open city water loop (3). Water cooled to the

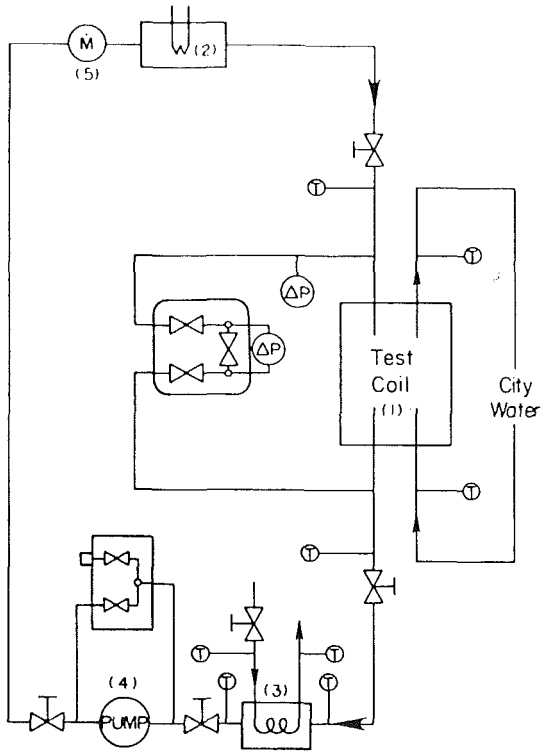

Fig. 2 Test loop schematic

Nomenclature

A = heat transfer surface area, m^2
C_p = specific heat, J/kg•K
d = tube diameter, m
D = coiling diameter, m
De = Dean number = $Re\delta^{1/2}$
h = heat transfer coefficient, W/m^2•K
k = thermal conductivity, W/m•K
Nu = Nusselt number = $h\,d_h/k$
Pr = Prandtl number = ν/α
Q = heat loss/gain, W
q = heat flux, W/m^2
r^* = annulus radius ratio = d_i/d_o
Re = Reynolds number = Vd_h/ν
T = temperature, °C
U = overall heat transfer coefficient, W/m^2 K
V = axial flow velocity, m/s
α = thermal diffusivity, m^2/s
δ = coiling ratio = $(d_o - d_i)/D$
Δ = change in a variable
ϵ = fractional error in a variable
ν = kinematic viscosity, m^2/s
ξ = augmentation term, curved-tube transfer
ρ = density, kg/m^3

Subscripts

c = coiled
h = hydraulic
i = inner
in = inlet
LM = log-mean
m = mean
o = outer
out = outer
s = shell side, straight
t = tube side

city water inlet temperature entered a magnetically driven gear pump (Series 200 Micropump) (4) controlled by a variac, which drives the closed loop. Flow rate in the closed loop was measured with a Flow Technology turbine meter (5) connected to a modulated carrier RF pickoff. The closed-loop circuit is completed when water from the pump returns to the heaters. The loop was pressurized to prevent boiling and was pressure tested to withstand up to 100 bars. Venting was provided by a relief valve located at the highest elevation in the loop.

Inlet and outlet temperatures of both streams of the heat exchangers were measured by TYPE T thermocouples rated to meet the ANSI special limits of error, i.e., 0.5°C or 0.4 percent (whichever is greater). To determine the temperature profile along the length of the coil, TYPE T thermocouple wires with ANSI standard limits of error were taped to the outer surface of the coils using a high thermal conductivity silicone paste (OMEGATHERM 201) to ensure good thermal contact.

An Analog Devices MACSYM 350 computer was used for control and data acquisition. The control algorithm maintained the water temperatures at the heat exchanger inlet at specified levels. Fluctuation in the specified level was ±5 percent. The computer also recorded the temperatures, pressures, and flow rates at specified time intervals. When steady state was attained, the control algorithm changed sampling rates while recording ten sets of data over a specified time interval. These ten sets were then averaged on-line, with the actual "data set" consisting of the average value and standard deviation for each variable.

Two different heat exchanger coils were used in the experiments: Coil 1 and Coil 2. Schematic drawings of these coils with dimensions are presented in Figs. 3 and 4. Both tube-in-tube coils were fabricated from 316 stainless steel. To preserve concentricity of the annular shell-side cross section, a spacer wire was twisted around the inner tube. Coil 1 was 45.72 m long and had two coiling diameters: an inner diameter of 0.45 m and an outer diameter of 0.51 m. The average coiling diameter D = 0.48 m was used for calculations. The spacer wire had a diameter of 1.07 mm and a pitch of 1 wrap per 0.36 m. Coil 2 was 31.70 m long and coiled around a diameter of 0.36 m. The spacer wire for this coil had a diameter of 2.41 mm and a pitch of one wrap per 0.2 m. Both coils were wrapped with a 25-mm-thick fiberglass insulation layer on the inside and outside. In addition, the cylindrical cavity in the coil was completely filled with loosely packed insulating material. Some sample test runs showed negligible heat loss to the ambient.

The experiments were designed so that shell-side heat transfer coefficients could be calculated using measured overall heat transfer coefficients and predicted tube-side heat transfer coefficients. The tube side mass flow rate was maintained constant while the shell-side flow rate was varied. In another set of experiments, the shell-side flow rate was maintained constant while the tube side flow rate was varied. The procedure outlined above was used to generate heat transfer data for the Reynolds number range $1000 \leq \mathrm{Re} \leq 9500$ and Prandtl number range of $2 \leq \mathrm{Pr} \leq 8$. The variation in Prandtl number was obtained by using different water inlet temperatures for different test runs.

Analysis of Experiments

In the following discussion, it will be assumed that the closed water loop passes through the shell side and city water passes through the tube side of the heat exchanger. In addition, the properties of each stream are assumed constant and evaluated at the average bulk temperatures. Due to the relatively small temperature difference between the two streams, viscosity variation from the bulk to wall surface temperature was assumed to be insignificant.

Heat loss from the shell side can be evaluated from

$$Q = \dot{m}_s (T_{in} - T_{out}) C_{ps} \tag{8}$$

where Q = heat loss; $\dot{m}_s$ = shell-side flow rate; T_{in_s} = shell-side inlet temperature; T_{out_s} = shell-side outlet temperature; C_{p_s} = shell-side specific heat. Solving a heat balance applied to the tube side for mass flow rate yields

$$\dot{m}_t = \frac{Q}{C_{pt}(T_{out_t} - T_{in_t})} \tag{9}$$

where $\dot{m}_t$ = tube-side flow rate; C_{pt} = tube-side specific heat; T_{out_t} = tube-side outlet temperature; T_{in_t} = tube-side inlet temperature.

The overall heat transfer can also be evaluated using

$$Q = U A \Delta T_{LM} \tag{10}$$

where Q = heat transfer evaluated using equation (8); U = overall heat transfer coefficient, A = area on which the heat transfer coefficients are based; ΔT_{LM} = log-mean-temperature difference:

$$\Delta T_{LM} = \frac{(T_{in_s} - T_{out_t}) - (T_{out_s} - T_{in_t})}{\ln \dfrac{T_{in_s} - T_{out_t}}{T_{out_s} - T_{in_t}}} \tag{11}$$

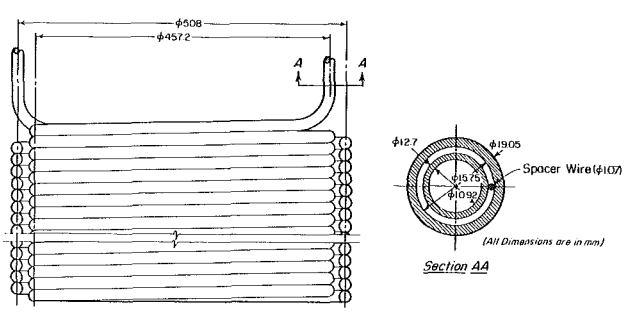

Fig. 3 Coil 1 schematic

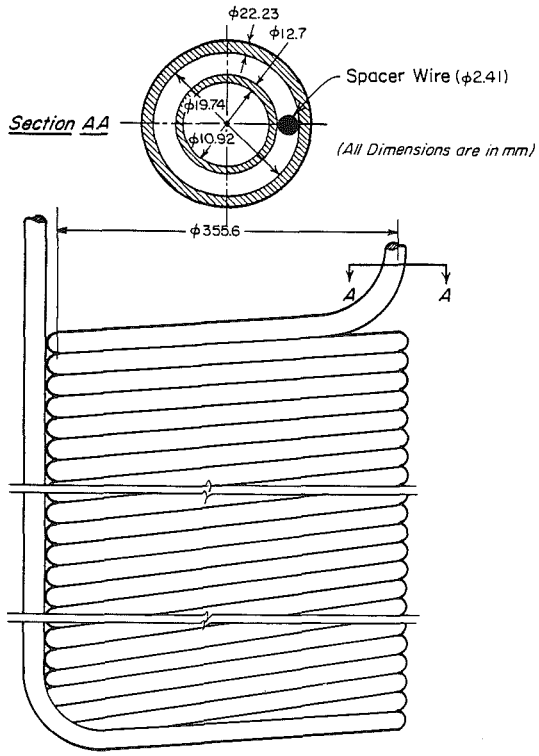

Fig. 4 Coil 2 schematic

When the overall coefficient is based on the outer surface of the inner tube, U is defined as

$$U = \left[\frac{1}{h_{io}} + R_{th} + \frac{1}{h_o}\right]^{-1} \tag{12}$$

where h_{io} = tube-side heat transfer coefficient, referred to the outer diameter; h_o = shell-side heat transfer coefficient; R_{th} = thermal resistance of the tube wall. Fouling resistances on both sides of the tube-wall have been neglected. This is a valid assumption because the tubes were new. The heat transfer area is given by

$$A = \pi d_i L \tag{13}$$

where L is the length of the heat exchanger and d_i is the outer diameter of the inner tube. Once U was calculated, h_o was obtained using h evaluated from equation (3), or equation (5) as required. When the flow rate in one stream was much lower than in the other, the experimental results indicated that the temperature attained an asymptotic profile after the first few coils (Fig. 5). A flat temperature profile region is unreliable for heat transfer calculations because the temperature differences between the streams approach the magnitude of the error bands of the thermocouples. Thus, only the portion of the heat exchanger with nonasymptotic temperature profiles was used.

Direct temperature measurements of the shell-side fluid temperatures were made only at the inlet and outlet of the coil. Since outside tube wall temperatures were also measured at these locations, an average temperature drop between the tube wall surface and shell-side fluid temperatures was estimated using outside tube wall temperatures and this average temperature drop (which was always below 1°C). Once the shell-side temperature at L was calculated the corresponding tube-side temperature was obtained from an energy balance.

To study the variation of average U values with heat exchanger length, an average U value was calculated between the inlet and each thermocouple location. Some typical profiles which represent the entire range of mass flow rates are presented in Fig. 6. Although the influence of the entrance length is apparent in the first section, it is almost imperceptible at length L. For points that are one thermocouple location upstream or downstream of the length L, the deviation in U is less than 4 percent. This value was used as the fully developed value. The effective exchanger lengths were chosen as 11.5 m for Coil 1 and 11.2 m for Coil 2. These lengths were kept constant for all runs.

The shell-side Nusselt number was calculated using $(d_o - d_i)$ as the characteristic length. This is appropriate because a calculation of the flow cross-sectional area and the wetted perimeter with the wire insert included showed that there was only 5 percent change from the true annulus values.

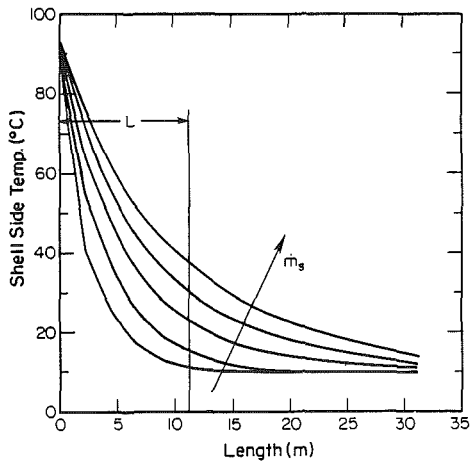

Fig. 5 Typical shell-side temperature profiles, $T_{in,shell}$ = 95°C

The uncertainty in the mass flow rates used for the calculations was ±0.15 percent. Temperatures were accurate up to ±1.5 percent. From the tolerances in the heat exchanger dimensions, it was estimated that the uncertainty in the area used for the heat transfer calculations was approximately 2.0 percent. Tube-side heat transfer coefficients were taken from various sources in the literature as discussed earlier. A conservative estimate of the error in this quantity is ±30 percent. Also, due to turbulent flow on the tube side, heat transfer coefficients on this side were typically about three times higher than shell-side heat transfer coefficients. Any errors in h_i would thus not significantly affect the values obtained for h_o. All the abovementioned uncertainties were combined using a propagation of uncertainties approach and the uncertainty in the shell-side Nusselt numbers was estimated to be 11 percent.

Comparison With Past Studies

The results from the experiments in the present study are compared with the available correlations for straight concentric annuli and curved circular tubes. This comparison demonstrates the influence of Reynolds number (Re), Dean number (De), Prandtl number (Pr), annulus radius ratio (r^*), and coiling ratio (δ) on Nusselt number. Heat transfer in the

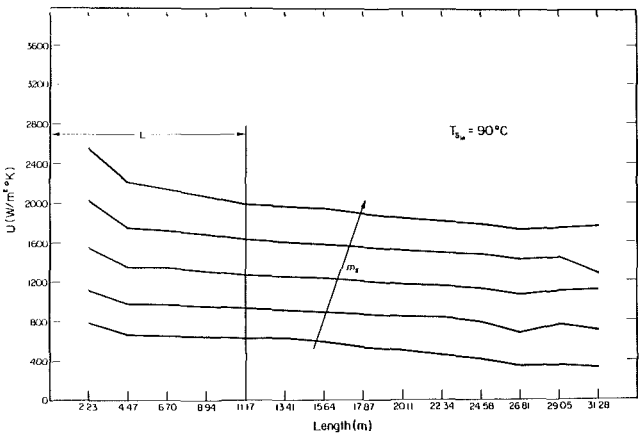

Fig. 6 Typical overall heat transfer coefficient profiles

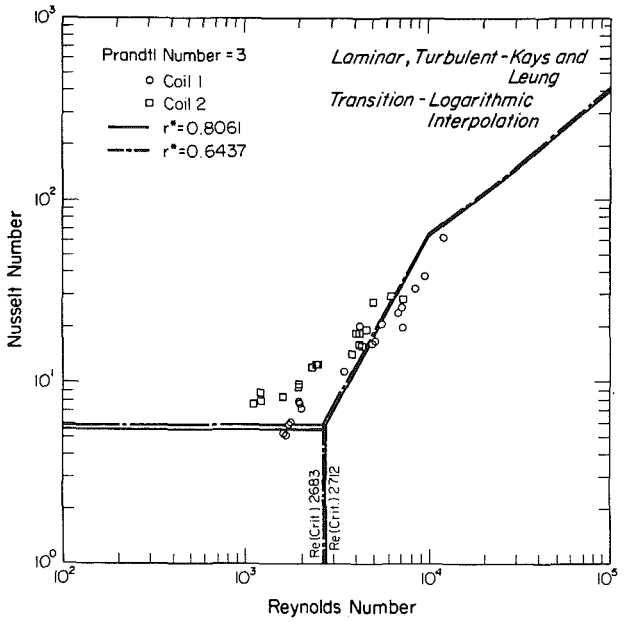

Fig. 7 Present study compared with straight concentric annulus literature

annulus was also influenced by the presence of the twisted wire insert. Any deviation from, for example, the case of a straight annular duct is due to a combination of both the curvature and the wire insert. In view of the lack of a systemized data base for the effects of wire inserts in curved and straight annular ducts, the approach used here is to recognize that the wire insert influences the flow, but to concentrate mainly on the parameters representing curvature δ, and the annular cross section r^*. A qualitative discussion of how the insert may influence the flow is presented later.

Since Prandtl number has a demonstrated effect on laminar and turbulent heat transfer in coiled ducts, see equations (3) and (5), the data should be separated into groups so that the scatter due to the Prandtl number effect does not obscure the influence of other variables. Therefore, the data were divided into three groups according to Prandtl number: $2 \leq Pr \leq 4$, $4 \leq Pr \leq 6$, and $6 \leq Pr \leq 8$. Corresponding correlations from the literature were evaluated at Prandtl numbers of 3, 5, and 7 respectively, and presented in the appropriate figures.

In accordance with existing correlations, the comparison with straight annular ducts is based on Reynolds number (Figs. 7 to 9), while that with curved tubes is based on Dean number (Figs. 10 to 12). It was expected that plots based on Dean number would demonstrate the effect of r^*, while plots based on Reynolds number would demonstrate the effect of the coiling ratio δ. At the very outset, it should be noted that very little can be inferred about the influence of r^* because the two values used in the study, 0.81 and 0.64, were not very different from each other.

In Figs. 7 to 9, the laminar and turbulent portions of the curve are from the data of Lundberg et al. [11] and Kays and Leung [12]. Because of the lack of information in the literature on the transition region for straight annular ducts, a logarithmic interpolation between the laminar and turbulent

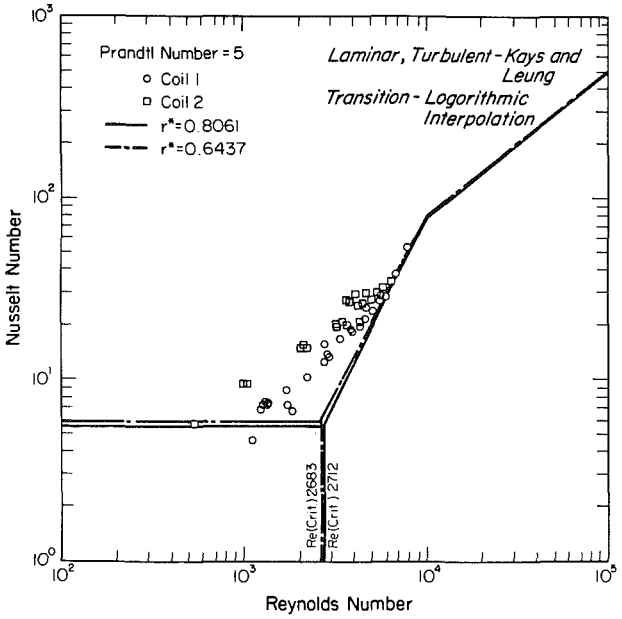

Fig. 8 Present study compared with straight concentric annulus literature

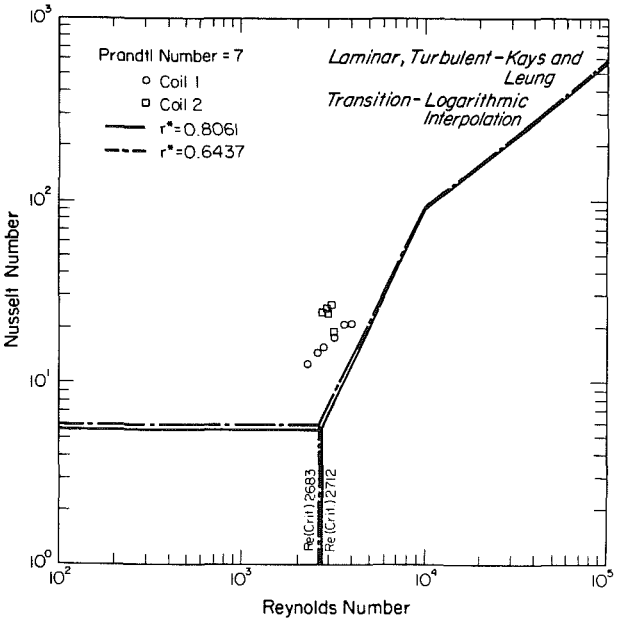

Fig. 9 Present study compared with straight concentric annulus literature

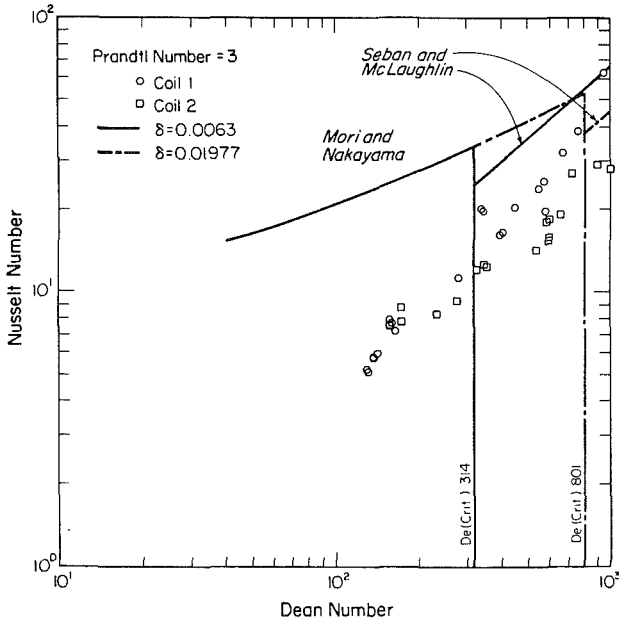

Fig. 10 Present study compared with curved tube literature

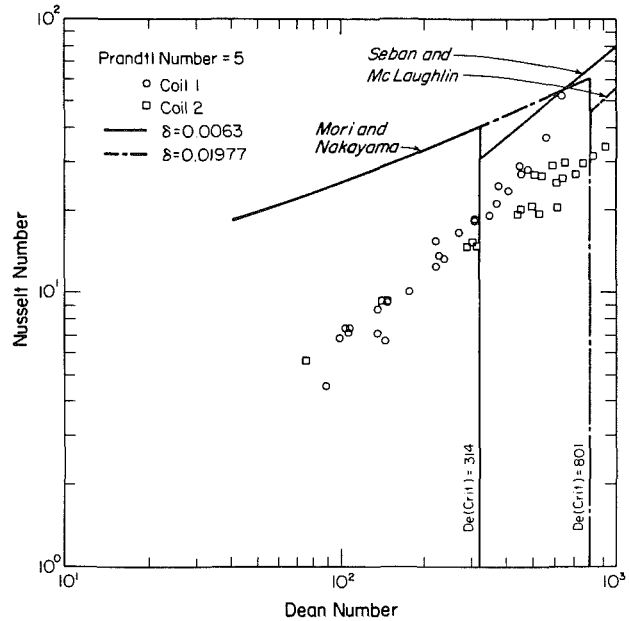

Fig. 11 Present study compared with curved tube literature

regimes was chosen to represent this region. The critical Reynolds numbers were calculated from the curves by Walker et al. [13], with the appropriate adjustments for the difference in hydraulic diameter (equation (7)).

As shown in Figs. 7–9, the Nusselt numbers for coil 2, δ = 0.02, are greater than those for coil 1, δ = 0.006. Also, in all three curves, the experimental Nusselt numbers are significantly higher than the predicted values for a straight annulus with the exception of some points at Pr = 3. The augmentation is greater in the laminar regime than at higher Reynolds numbers. These trends agree with the curved circular duct literature; Mori and Nakayama [8] showed significant augmentation in curved tubes which increased with the degree of coiling and Seban and McLaughlin [9] showed almost no augmentation in curved tubes for turbulent flow. Thus, it is only reasonable to expect a decreasing augmentation as the flow conditions approach the turbulent region.

The data were also compared with curved tube literature (Figs. 10–12) to determine the difference between augmentation in an annular duct and a circular tube. Mori and Nakayama's correlation, equation (3), for the laminar regime and Seban and McLaughlin's empirical correlation, equation (5), for the turbulent region are shown on these figures for comparison. The transition point is chosen according to Ito's criterion, equation (2), for curved tubes.

Figures 10–12 show that Nusselt numbers in a curved annulus are significantly lower than those in a circular tube at all Prandtl numbers. In addition, data points for Coil 1 and Coil 2 can no longer be clearly distinguished from each other as was the case in Figs. 7–9. Data points from both coils collapse to a single curve in the laminar region. This indicates that the Dean number is an appropriate parameter to correlate heat transfer in a curved annular duct. The scatter is greater in the transition regime than in the laminar region. This is to be expected because Dean number, which represents secondary flows and augmentation, is an accepted nondimensional number primarily for the laminar regime. Hence, the transition points for Coil 2, which were higher in Figs. 7–9, are lower than points for Coil 1 in these figures. This indicates that the coiling ratio δ is less important than the Dean number would indicate. Figure 11 also shows that there is a steeper rise in Nusselt numbers beyond a Dean number of about 320 for Coil 1. This might be an indication of the occurrence of transition around this point. However, a definite statement about this cannot be made without further investigation.

The augmentation due to curvature (Nu_c/Nu_s) in an annulus is compared with that in a circular tube in Figs. 13–15. For the annulus, transition Reynolds numbers were calculated using equation (7). For the circular tube case, critical Reynolds numbers were calculated using equation (2). The corresponding Dean numbers for both geometries were obtained using equation (1). As in the earlier comparisons, these figures demonstrate that augmentation in an annular duct is less than that in a circular tube in the laminar regime. They also show that correlating the data with Dean number results in the points from both coils collapsing together on the same general curve in the laminar regime. A more significant feature of these curves, however, is the sharp change in augmentation at higher Dean numbers. Figure 14 shows a steep decrease in augmentation beyond a Dean number of around 250 for the coil with δ = 0.006 and beyond 400 for the coil with δ = 0.02. This trend indicates the onset of transition with augmentation levels decreasing from the large laminar values to almost negligible values in turbulent flow. It is also evident that transition is delayed at higher coiling ratios, which agrees with curved circular tube results [5].

Figures 13, 14, and 15 indicate that transition occurs over a range of Dean numbers, not at a unique point. Although the exact values of the upper and lower critical Dean numbers cannot be determined, it appears that they have different values. These values need to be identified more clearly in future work. These figures also show that the slope of the data points in the transition region is steeper at higher Prandtl numbers. This is to be expected, because laminar augmentation is greater at higher Prandtl numbers, whereas turbulent augmentation is independent of Prandtl number.

The geometry of the double-pipe heat exchangers used in this study provides only an approximation to the theoretical curved annulus. While maintaining concentricity in the annulus, the spacer also leads to swirl in the flow and interruptions in the secondary flow loops.

The effects of a twisted wire insert on heat transfer in a straight annulus with a grooved inner tube have been investigated by Kemeny and Cyphers [14]. Bergles [15] provides a comprehensive survey of the effects of various insert geometries (including the abovementioned case) on heat

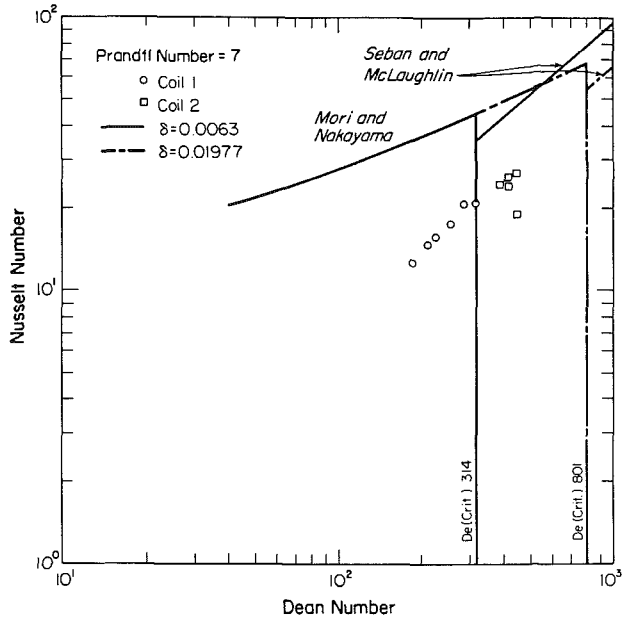

Fig. 12 Present study compared with curved tube literature

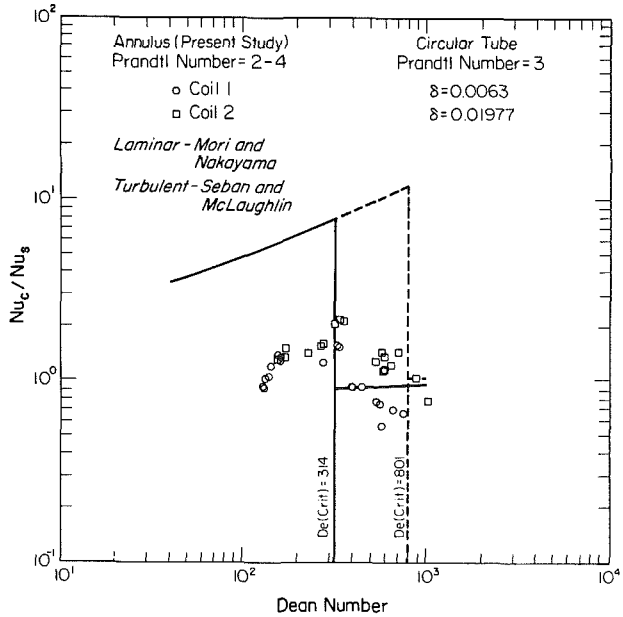

Fig. 13 Comparison of Nu_c/Nu_s for annular ducts and circular tubes

transfer in straight tubes and annular ducts. It appears from these investigations that the parameter most important in characterizing the effects of various inserts is the pitch/diameter ratio and in the case of protrusions on the tube surface, it is the spacing/height ratio. This leads to the conclusion that for the present case, the appropriate parameter would be the pitch/diameter ratio of the spacer wire. According to these investigators, there seems to be an optimum value of about 20 for this parameter, beyond which the swirl introduced is not sufficient to augment the heat transfer for most geometries. Spacer wires used in this study have pitch/diameter ratios of 336 for Coil 1 and 83 for Coil 2. Therefore any influence on the primary heat transfer mechanism can safely be neglected.

Secondary flow loops, however, might be inhibited to some extent by the spacer. The consequent decrease in the stabilizing effects of curvature would tend to bring about transition from laminar flow at lower Dean numbers than in a curved annular duct without a spacer. Figures 13–15 tend to substantiate this argument. A slight decrease in heat transfer would also result from the inhibition of the secondary flow loops.

In summary, it is impossible quantitatively to separate out the effect of the wire insert. A coiled tube-in-tube heat exchanger without the wire insert would have had an eccentric annular flow passage, which would also have been impossible to quantify. It is our considered opinion that the data do provide useful information about heat transfer in a coiled annular duct with a wire insert. These results should provide the designer with a useful correlation for a practical geometry.

Curved Annulus Heat Transfer Correlations

In the foregoing discussion, an attempt was made to compare the experimental data with past studies with the objective of identifying the parameters which influence heat transfer. Some qualitative insight was also obtained about the relative significance of these parameters. It is now possible to consolidate these influences into numerical formulae at least for the more significant variables. Thus, it is required to determine the constant and the exponents in the expression

$$\mathrm{Nu} = a\mathrm{Re}^{m}\mathrm{Pr}^{n}\delta^{p}r^{*q} \tag{14}$$

A suitable combination of m and p could yield a correlation in terms of the Dean number. Multivariate regression analysis was used to fit the data to equation (14).

At first, Re and δ were combined as De and a fit was attempted for Nu versus De and Pr. The data sets for each coil were fit separately to find out whether the dependence on these variables was similar. The fits obtained were as follows:

Coil 1: ($\delta = 0.0063$)

$$\mathrm{Nu} = 0.012\ \mathrm{De}^{1.11}\mathrm{Pr}^{0.61} \tag{15}$$

Coil 2: ($\delta = 0.01977$)

$$\mathrm{Nu} = 0.080\ \mathrm{De}^{0.756}\mathrm{Pr}^{0.58} \tag{16}$$

Equations (15) and (16) correlate the data within +22 and −26 percent, respectively. The exponents for Pr are almost equal in both cases and thus, an exponent of about 0.6 seems to suffice over a range of coiling ratios. Because the exponents for De are significantly different in each case, the Dean number has not accounted for the difference in coiling ratios in the two cases. However, as has been shown in Figs. 10–12, the Dean number represented the augmentation effects in both coils and resulted in the experimental data points collapsing around a single curve for the laminar regime. Therefore, this difference in the exponents might be due to the augmentation phenomena being different at the higher Reynolds numbers, i.e., in the transition region.

To investigate this further, data sets for each coil were divided into two parts. The demarcation point was chosen at De = 350 around which Figs. 7 to 9 show a change in slope and a divergence between points for the two coils. The choice of the transition Dean number did not significantly influence the correlations obtained from these two groups because there were very few data points between De = 300 and 400. A fit of the form Nu versus Re, Pr, and δ was now attempted. The ad hoc assumption about the validity of Dean number was not made and exponents for Re and δ were found separately. For the low Re group, the data were correlated to within +22 and −16 percent by

$$\mathrm{Nu} = 0.027\mathrm{Re}^{0.94}\mathrm{Pr}^{0.69}\delta^{0.48} \tag{17}$$

Re and δ can now be combined as a Dean number to yield

$$\mathrm{Nu} = 0.027\mathrm{De}^{0.94}\mathrm{Pr}^{0.69}\delta^{0.01} \tag{18}$$

This shows that the Dean number does indeed represent the heat transfer in laminar flow. The exponent for Pr is higher in equation (18) than in equations (15) and (16). The higher value

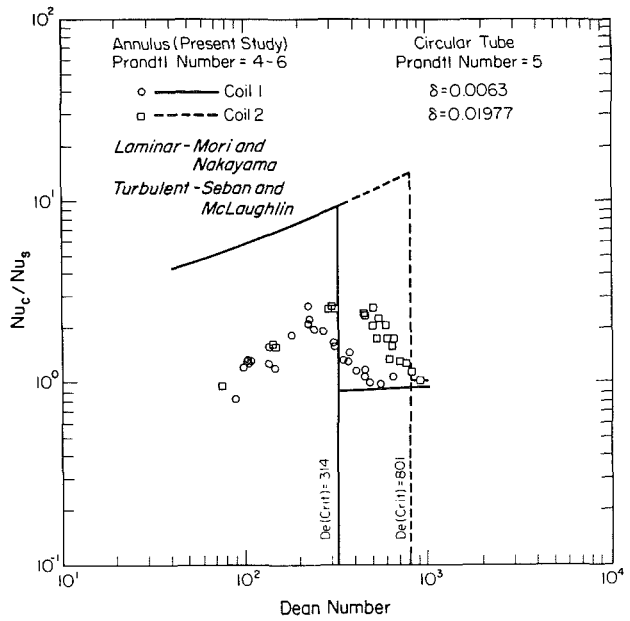

Fig. 14 Comparison of $\mathrm{Nu_c/Nu_s}$ for annular ducts and circular tubes

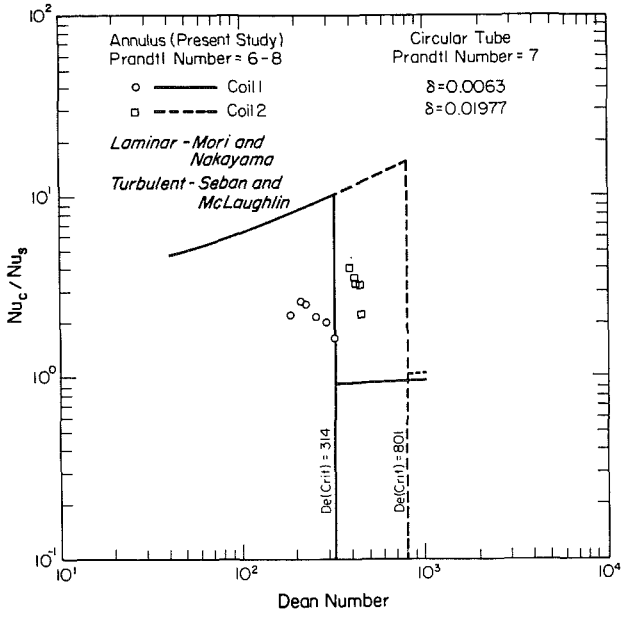

Fig. 15 Comparison of $\mathrm{Nu_c/Nu_s}$ for annular ducts and circular tubes

accounts for the increased augmentation in the laminar regime.

In the transition region, the equation obtained was

$$\mathrm{Nu} = 0.0018\mathrm{Re}^{1.13}\mathrm{Pr}^{0.65}\delta^{0.22} \tag{19}$$

Equation (19) correlated the data to within +27 and −24 percent. The higher scatter is justified because the transition phenomenon is unstable and poorly predictable. A better fit might be obtained with a second-order curve. However, the inherent uncertainty in this region does not warrant such higher order fits. The higher exponent for Re is to be expected because of the steep rise in Nusselt number during transition in any flow configuration when Nu shifts to the turbulent values. The lower exponent for δ is also in accordance with the previous discussion, which showed a decreasing dependence on coiling at increasing Reynolds numbers. It was mentioned above that no qualitative information could be obtained about the influence of r^* on Nu due to the magnitudes being almost equal for both coils. The same problem was encountered in attempts to correlate r^* with Nu.

Conclusions and Recommendations for Further Study

Heat transfer in coiled annular ducts in the laminar-transition flow regimes was investigated. A combination of the effects of curvature, the annular cross section, and the wire insert within have been observed. The most significant conclusion that can be drawn from this study is that the introduction of curvature in a concentric annulus in the presence of a twisted wire insert leads to heat transfer augmentation.

Although it was not possible to differentiate between the effects of curvature and the wire insert, a significant part of the augmentation can be attributed to the introduction of curvature because the Nusselt numbers in the laminar regime have been correlated with the Dean number, a parameter that governs flow in curved tubes.

Augmentation in the laminar flow regime was found to be higher than in the transition regime. It was noticed that there is a tendency for the transition to set in around a Dean number of 300–375. The precise location can be determined only after further investigation; and even then, it might not be a unique point. Dean number was demonstrated to be one of the governing factors for heat transfer in the laminar regime, while the importance of the coiling ratio decreases in the transition region.

The predictions from this study are limited in the range of application due to the restricted variation in the geometric parameters. Future studies should aim at broadening this range by using more coiling ratios and annulus radius ratios. The low laminar regime and the highly turbulent regime should be investigated to complement this study. The specific effect of the twisted wire insert on the heat transfer deserves further attention. Finally, the hydrodynamic aspects of the problem should be investigated by conducting pressure drop measurements.

References

1 Yao, L. S., and Berger, S. A., "Flow in Heated Curved Pipes," *Journal of Fluid Mechanics*, Vol. 88, No. 2, 1978, pp. 339–354.

2 Dean, W. R., "Note on the Motion of Fluids in a Curved Pipe," *The London, Edinburgh, and Dublin Philosophical Magazine and Journal of Science*, Vol. 4, 1927, pp. 208–223.

3 Dean, W. R., "The Stream-Line Motion of Fluid in a Curved Pipe," *The London, Edinburgh, and Dublin Philosophical Magazine and Journal of Science*, Vol. 5, 1928, pp. 673–693.

4 Berger, S. A., Talbot, L., and Yao, L. S., "Flow in Curved Pipes," *Annual Review of Fluid Mechanics*, Vol. 15, 1983, pp. 461–512.

5 Ito, H., "Theory on Laminar Flows Through Curved Pipes of Elliptic and Rectangular Cross-Sections," *Reports of the Institute of High Speed Mechanics*, Tohoku University, Vol. 1, 1951, pp. 1–16.

6 Ito, H., "Friction Factors for Turbulent Flow in Curved Pipes," *Transactions of ASME*, Vol. D81, 1959, pp. 123–134.

7 Ito, H., "Laminar Flow in Curved Pipes," *Z. Agnew. Math. Mech.*, Vol. 49, 1969, pp. 653–663.

8 Mori, Y., and Nakayama, W., "Study on Forced Convective Heat Transfer in Curved Pipes," *International Journal of Heat and Mass Transfer*, Vol. 8, 1965, pp. 67–82.

9 Seban, R. A., and McLaughlin, E. F., "Heat Transfer in Tube Coils With Laminar and Turbulent Flow," *International Journal of Heat and Mass Transfer*, Vol. 6, 1963, pp. 387–395.

10 Rogers, G. F. C., and Mayhew, Y. R., "Heat Transfer and Pressure Loss in Helically Coiled Tubes With Turbulent Flow," *International Journal of Heat and Mass Transfer*, Vol. 7, 1964, pp. 1207–1216.

11 Lundberg, R. E., McCuen, P. A., and Reynolds, W. L., "Heat Transfer in Annular Passages—Hydrodynamically Developed Flow With Arbitrarily Prescribed Wall Temperatures or Heat Fluxes," *International Journal of Heat and Mass Transfer*, Vol. 6, 1963, pp. 495–529.

12 Kays, W. M., and Leung, E. Y., "Heat Transfer in Annular Passages—Hydrodynamically Developed Turbulent Flow With Arbitrarily Prescribed Heat Flux," *International Journal of Heat and Mass Transfer*, Vol. 6, 1963, pp. 537–557.

13 Walker, J. E., Whan, G. A., and Rothfus, R. R., "Fluid Friction in Noncircular Ducts," *AIChE Journal*, Vol. 3, 1957, pp. 484–489.

14 Kemeny, G. A., and Cyphers, J. A., "Heat Transfer and Pressure Drop in an Annular Gap With Surface Spoilers," ASME JOURNAL OF HEAT TRANSFER, Vol. 83, 1961, pp. 189–198.

15 Bergles, A. E., "Survey and Evaluation of Techniques to Augment Convective Heat and Mass Transfer," *Progress in Heat and Mass Transfer*, Vol. 1, G. Griguil and E. Hahne, eds., Pergamon Press, New York, 1969, pp. 331–424.

Analysis of Combined Buoyancy Effects of Thermal and Mass Diffusion on Laminar Forced Convection Heat Transfer in a Vertical Tube

T. F. Lin
Assoc. Mem. ASME

C. J. Chang[1]

W. M. Yan

Department of Mechanical Engineering,
National Chiao Tung University,
Hsinchu, Taiwan

This study investigates the role of vaporization of a thin liquid film on the tube wall in laminar mixed convection flows under the combined buoyancy effects of thermal and mass diffusion. Major nondimensional groups identified are Gr_T, Gr_M, Re, Pr, Sc, and ϕ. Results are specifically presented for an air–water system under various conditions. The effects of the liquid film temperature, the Reynolds number, and the relative humidity of the moist air in the ambient on the momentum, heat, and mass transfer in the flow are examined in great detail.

Introduction

Situations often arise in which the combined buoyancy forces of heat and mass transfer, resulting from the simultaneous presence of differences in temperature and variations in concentration, have rather significant influences on the heat transfer of a flowing gas mixture in many engineering systems and natural environments. Windy-day evaporation and vaporization of mist and fog, distillation of a volatile component from a mixture with nonvolatiles, the process of evaporative cooling for waste heat disposal, and cooling of a high-temperature surface by coating it with a phase-change material are just some prominent examples of processes in which mass transfer operations are accompanied by the transfer of heat.

A vast amount of work, both theoretical and experimental, exists in the literature to study the effects of buoyancy forces on forced convection channel flows, as is evident in a recent review by Petukhov et al. (1982). Only those relevant to the present work are briefly reviewed here. Sparrow and Gregg (1959) established a quantitative criterion for distinguishing the conditions under which the effects of natural convection may be neglected in heat transfer and shear stress calculations for flow over a vertical plate. Carter and Gill (1964) studied the influences of suction and blowing on heat and momentum transfer rates in mixed convection flows, reporting that suction creates steeper transverse temperature gradients and accentuates buoyancy effects in vertical flows, while injection flattens temperature profiles and thus decreases the influence of buoyancy on the velocity field.

Combined heat and mass transfer from a vertical flat plate in natural convection flows has been the subject of many papers (Bottemanne, 1971; Gill et al., 1965; Mather et al., 1957; Saville and Churchill, 1970; Somers, 1956; Soundalgekar and Ganesan, 1981). Recently, natural convection in a vertical plate channel within which the buoyancy force reverses its sign was studied by Lee et al. (1982). The effects of combined buoyancy forces of heat and mass diffusion on the natural convection flows in a vertical open tube were examined by the present authors (Chang et al., 1986). As far as pure forced convection flows are concerned, simultaneous energy and mass transfer in a laminar boundary layer flow over a flat surface was also well treated (Chow and Chung, 1983; Hanna, 1965; Manganaro and Hanna, 1970). For mixed convection, Santarelli and Foraboschi (1973) examined the effects of natural convection on reaction and heat transfer parameters for a laminar fluid flow undergoing a chemical reaction.

Despite its importance, the combined buoyancy effects of thermal and mass diffusion on forced convection channel flows have not been adequately studied. In the present study, the system to be investigated is a long, vertical, open-ended tube with a thin liquid water film on the inner surface of the tube, which is maintained at a uniform temperature T_w, higher than the ambient temperature T_o. The flow of moist air, initially stationary, in the tube is initiated by a mechanical device such as a blower or fan as well as by the combined buoyancy forces due to differences in temperature and in concentration of water vapor between the liquid film and the ambient. Leaving the unsteady part of the problem out for future study, we will focus on the theoretical study of the effects of the coupled thermal and mass diffusion on steady developments of the velocity, temperature, and concentration fields in the flow of the dry air–water vapor mixture. Particular attention is paid to the investigation of the extent of the energy transport through mass diffusion, a latent energy exchange process, in comparison with that through thermal diffusion, a sensible energy transport process.

Analysis

As a preliminary attempt to study mass diffusion effects, the liquid film on the tube's inside surface is assumed to be extremely thin so that it can be regarded as a boundary condition for heat and mass transfer; the film is stationary and at the same uniform temperature as the tube wall T_w. In reality, the liquid film is finite in thickness. The film could be moving upward or downward, and the shape of the liquid–gas interface could be quite complex. As a result, the momentum, heat, and mass transfer in the film should also be analyzed with the interfacial phenomena appropriately treated. This would, however, greatly complicate the analysis and make the theoretical work formidable. The influences of the finite

[1]Current address: Department of Mechanical Engineering, University of California, Berkeley, CA 94720.

Contributed by the Heat Transfer Division and presented at the ASME Winter Annual Meeting, Miami Beach, Florida, November 1985. Manuscript received by the Heat Transfer Division October 6, 1986. Keywords: Evaporation, Mixed Convection.

liquid film on the heat transfer may not be properly assessed without help from the experimental study that will be conducted shortly.

The formulation for the problem to be presented is rather brief with the complete details being available in the previous study (Lin and Chang, 1985). By introducing the Boussinesq approximation (the concentration of water vapor in the mixture being very low and the temperature nonuniformity in the system being small), the steady laminar mixed convection flow of moist air in a vertical tube resulting from the combined buoyancy effects of thermal and mass diffusion can be described by the basic equations, in dimensionless form, as:

Continuity equation

$$\frac{\partial(\eta U)}{\partial \xi}+\frac{\partial(\eta V)}{\partial \eta}=0 \tag{1}$$

Axial-momentum equation

$$U\frac{\partial U}{\partial \xi}+V\frac{\partial U}{\partial \eta}=-\frac{dp}{d\xi}+2\left(\frac{\mathrm{Gr}_T}{\mathrm{Re}}\theta+\frac{\mathrm{Gr}_M}{\mathrm{Re}}W\right)+\frac{1}{\eta}\frac{\partial}{\partial \eta}\left(\eta\frac{\partial U}{\partial \eta}\right) \tag{2}$$

Energy equation

$$U\frac{\partial \theta}{\partial \xi}+V\frac{\partial \theta}{\partial \eta}=\frac{1}{\mathrm{Pr}}\frac{1}{\eta}\frac{\partial}{\partial \eta}\left(\eta\frac{\partial \theta}{\partial \eta}\right)+\frac{A}{\mathrm{Sc}}\frac{\partial \theta}{\partial \eta}\frac{\partial W}{\partial \eta} \tag{3}$$

Equation of continuity for water vapor

$$U\frac{\partial W}{\partial \xi}+V\frac{\partial W}{\partial \eta}=\frac{1}{\mathrm{Sc}}\frac{1}{\eta}\frac{\partial}{\partial \eta}\left(\eta\frac{\partial W}{\partial \eta}\right) \tag{4}$$

In nondimensionalizing the governing equations, the following dimensionless variables were introduced:

$$\xi=2x/(R\cdot\mathrm{Re}),\qquad \eta=r/R$$
$$U=u/u_o,\qquad V=vR/\nu$$
$$\theta=(T-T_o)/(T_w-T_o),\qquad W=(w_1-w_o)/(w_r-w_o) \tag{5}$$
$$P=p_m/(\rho u_o^2),\qquad \mathrm{Gr}_T=g(T_w-T_o)R^3/(T_o\nu^2)$$
$$\mathrm{Gr}_M=g(M_2/M_1-1)\cdot(w_r-w_o)R^3/\nu^2$$

Here w_r is the saturated mass fraction of water vapor at T_w and p_o, Gr_T, and Gr_M are, respectively, the Grashof numbers for heat transfer and mass transfer.

In writing the above equations, we have introduced the concept of motion pressure or pressure defect (Gebhart and Mahajan, 1982)

$$p_m=p-p_o \tag{6}$$

Notice that p_m is frequently referred to as the dynamic pressure; p_o satisfies

$$dp_o/dx=-\rho_o g \tag{7}$$

Also, it is assumed that the level of water vapor concentration is low and the moist air is an ideal gas mixture of dry air and water vapor. This results in

$$(\rho_o-\rho)/\rho=(T-T_o)/T_o+(M_2/M_1-1)(w_1-w_o) \tag{8}$$

Moreover, by assuming the moist air–liquid film interface to be in thermodynamic equilibrium, the interfacial mass fraction of water vapor can be calculated by the equation

$$w_w=p_wM_1/[p_wM_1+(p-p_w)M_2] \tag{9}$$

It is worth noting that the mixture pressure p varies with x, and so does w_w. This prohibits us from taking w_w as a reference scale in the nondimensionalization process. Instead w_r is employed.

To facilitate the analysis, the usual boundary layer approximations are invoked, that is, the axial diffusion of momentum, heat, and mass are neglected. In addition, the thermophysical properties of the mixture are taken to be constant and are evaluated by the 1/3 rule. This special way of evaluating the properties is found to be appropriate for the

Nomenclature

A = $[(c_{p1}-c_{p2})/c_p](w_r-w_o)$
c_p = specific heat
d = tube diameter
D = mass diffusivity
g = gravitational acceleration
Gr_M = Grashof number (mass transfer) = $g(M_2/M_1-1)(w_r-w_o)R^3/\nu^2$
Gr_T = Grashof number (heat transfer) = $g(T_w-T_o)R^3/(T_o\nu^2)$
h_{fg} = latent heat of vaporization
h_M = local mass transfer coefficient
J = total number of grid points in the radial direction
k = thermal conductivity
M = molecular weight
M_r = nondimensional film evaporation rate, equation (26)
Nu_l = local Nusselt number (latent heat), equation (17)
Nu_s = local Nusselt number (sensible heat), equation (16)
Nu_x = overall local Nusselt number, equation (14)
n = number of iteration
n_1 = absolute mass flux of water vapor
p = mixture pressure
P = dimensionless motion pressure = $p_m/(\rho u_o^2)$
Pe = Peclet number = Re•Pr
p_m = motion pressure, equation (6)
Pr = Prandtl number = ν/α
p_w = partial pressure of water vapor at interface
Q = total heat transfer rate
Q_o = total heat transfer rate without liquid water film
q'' = interfacial energy flux flowing into air stream
r = radial coordinate
R = tube radius
Re = Reynolds number = u_od/ν
S = parameter, equation (18)
Sc = Schmidt number = ν/D
Sh_x = local Sherwood number, equation (22)
T = temperature
u = axial velocity
u_o = inlet velocity
U = dimensionless axial velocity = u/u_o
v = radial velocity
V = dimensionless radial velocity = vR/ν
V_w = dimensionless interfacial velocity of mixture, equation (11)
w_1 = mass fraction of water vapor
W = dimensionless mass fraction of water vapor = $(w_1-w_o)/(w_r-w_o)$
w_r = saturated mass fraction of water vapor at T_w and p_o
x = axial coordinate
α = thermal diffusivity
η = dimensionless radial coordinate = r/R
θ = dimensionless temperature = $(T-T_o)/(T_w-T_o)$
ν = kinematic viscosity
ξ = dimensionless axial coordinate = $2x/(R\cdot\mathrm{Re})$
ρ = density
ϕ = relative humidity of air in the ambient

Subscripts

1 = of water vapor
2 = of air
b = bulk quantity
o = at ambient condition
w = condition at interface

analysis of combined heat and mass transfer problems (Chow and Chung, 1983; Hubbard et al., 1975). The complete details on the evaluation of properties are given in the Appendix.

The governing equations are subjected to the following boundary conditions:

$$\xi=0,\quad U=1,\quad \theta=0,\quad W=0,\quad P=0,$$
$$\eta=0,\quad \partial U/\partial\eta=0,\quad \partial\theta/\partial\eta=0,\quad \partial W/\partial\eta=0,$$
$$\eta=1,\quad U=0,\quad V=V_w,\quad \theta=1, \tag{10}$$
$$W=(w_w-w_o)/(w_r-w_o)$$

By noticing that the air–water interface is semipermeable, that is, the solubility of air in water is negligibly small and air is stationary at the interface, the velocity of the mixture at the interface can be evaluated by

$$V_w=-\frac{w_r-w_o}{1-w_w}\cdot\frac{1}{\mathrm{Sc}}\cdot\frac{\partial W}{\partial\eta}\bigg|_{\eta=1} \tag{11}$$

One constraint to be satisfied in the analysis of a steady channel flow is the overall mass balance at every axial location

$$\int_0^1 U\cdot\eta d\eta=\frac{1}{2}-\int_0^\xi V_w d\xi \tag{12}$$

Energy transport from the tube wall to the fluid in the presence of mass transfer depends on two related factors: the fluid temperature gradient at the wall, resulting in sensible heat transfer, and the rate of mass transfer, resulting in latent heat transfer (Eckert and Drake, 1972; Manganaro and Hanna, 1970). The total heat flux from the wall can then be expressed as

$$q''=q_s''+q_l''=k\frac{\partial T}{\partial r}\bigg|_{r=R}+\frac{\rho D h_{fg}}{1-w_w}\frac{\partial w_1}{\partial r}\bigg|_{r=R} \tag{13}$$

The local Nusselt number, defined as

$$\mathrm{Nu}_x=\frac{h\cdot 2R}{k}=\frac{q''}{k(T_w-T_b)/2R} \tag{14}$$

can be written as

$$\mathrm{Nu}_x=\mathrm{Nu}_s+\mathrm{Nu}_l \tag{15}$$

where

$$\mathrm{Nu}_s=\frac{2}{1-\theta_b}\cdot\frac{\partial\theta}{\partial\eta}\bigg|_{\eta=1} \tag{16}$$

$$\mathrm{Nu}_l=\frac{2S}{(1-\theta_b)\cdot(1-w_w)}\cdot\frac{\partial W}{\partial\eta}\bigg|_{\eta=1} \tag{17}$$

Here S signifies the importance of energy transport through species diffusion relative to that through thermal diffusion

$$S=\rho D h_{fg}\cdot(w_r-w_o)/k\cdot(T_w-T_o) \tag{18}$$

The fraction of energy transport through mass diffusion alone q_l''/q'' is a parameter of interest and is connected with the Nusselt numbers by the equation

$$\frac{q_l''}{q''}=\frac{\rho D h_{fg}}{1-w_w}\frac{\partial w_1}{\partial r}\bigg|_{r=R}/q''=\mathrm{Nu}_l/\mathrm{Nu}_x \tag{19}$$

The mass flux flowing into the air stream at the interface is given as

$$n_1=\frac{\rho D}{1-w_w}\cdot\frac{\partial w_1}{\partial r}\bigg|_{r=R} \tag{20}$$

For a low mass transfer rate at the interface, which happens to be the case in the present study, a mass transfer coefficient h_M can be defined as

$$n_1\cdot(1-w_w)=\rho h_M\cdot(w_w-w_b) \tag{21}$$

The local Sherwood number then becomes

$$\mathrm{Sh}_x=\frac{h_M\cdot d}{D}=2\left(\frac{w_r-w_o}{w_w-w_b}\right)\cdot\frac{\partial W}{\partial\eta}\bigg|_{\eta=1} \tag{22}$$

Solution Method

Because the flow under consideration is a boundary-layer type, the solution for equations (1)–(4) can be marched in the downstream direction. A fully implicit numerical scheme in which the axial convection is approximated by the upstream difference and the radial convection and diffusion terms by the central difference is employed to transform the governing equations into finite-difference equations. Each system of the finite-difference equations forms a tridiagonal matrix, which can be efficiently solved by the Thomas algorithm (Patankar, 1980). For a given condition, a brief outline of the solution procedures is given as follows:

1 Specify a Reynolds number Re.

2 For any axial location, guess $(dP/d\xi)$ and solve the finite-difference forms of equations (1)–(4) for U, θ, and W.

3 Integrate the continuity equation numerically to find V

$$V=-\frac{1}{\eta}\frac{\partial}{\partial\xi}\int_0^\eta U\cdot\eta d\eta \tag{23}$$

4 Check the satisfaction of the overall conservation of mass, equation (12). If the right-hand side of equation (12) agrees with the left-hand side to the extent that

$$\left|\int_0^1 U\cdot\eta d\eta-\left(\frac{1}{2}-\int_0^\xi V_w d\xi\right)\right|<10^{-4} \tag{24}$$

then test the convergence of the velocity, temperature, and concentration fields. If the total mean-square errors for the velocity, temperature, and concentration between two consecutive iterations satisfy the criterion

$$\sum_{j=1}^{J}[(U_{i,j}^n-U_{i,j}^{n-1})^2+(\theta_{i,j}^n-\theta_{i,j}^{n-1})^2+(W_{i,j}^n-W_{i,j}^{n-1})^2]<10^{-3} \tag{25}$$

the solution for the current axial location is complete. Now if equation (25) is not met, repeatedly solve the finite-difference equations for U, θ, and W, and use equation (23) to get V until the condition specified in equation (25) is fulfilled. If equation (24) is not satisfied, guess a new $(dP/d\xi)$ and repeat procedures (2)–(4) for the current axial location.

5 Procedures (2)–(4) are applied successively to every axial location from the tube entrance to the downstream region where the flow is fully developed.

To obtain enhanced accuracy in the numerical computation, grids are chosen to be uniform in the radial direction but nonuniform in the axial direction to account for the drastic variations of velocity, temperature, and concentration in the near-entrance region. The first axial interval $\Delta\xi_1$ is taken to be from 10^{-3} to 10^{-4} and every subsequent interval is enlarged by 10 percent over its previous one, i.e., $\Delta\xi_i=1.10\cdot\Delta\xi_{i-1}$. Several grid sizes are tested and a comparison of the results among these computations is given in Table 1. It is noted that the differences in the local Nusselt number for the computations by using 47 × 41 and 94 × 81 grids are always less than 2 percent, and the accuracy of the results for various grid arrangements gets better for large ξ. Accordingly, the computation for the 47 × 41 grid is sufficient to understand the heat and mass characteristics in the flow.

Table 1 Comparison of local Nusselt numbers Nu_x for various grid arrangements for case III

ξ	94×81	94×41	47×81	47×41	47×21
0.00331	69.53	69.28	68.53	68.82	71.20
0.00949	47.20	46.82	46.31	46.35	46.45
0.02138	35.46	35.41	35.14	35.13	35.16
0.09835	23.75	23.73	23.81	23.79	23.77
0.22225	20.72	20.71	20.77	20.76	20.74

Table 2 Comparison of local Nusselt numbers Nu_s with the solutions from Zeldin and Schmidt (1972) for $Gr_T/Re = 30$ and $Gr_M/Re = 0$

x/Pe	Present results (47 × 41 grid)	Nu_s from Zeldin and Schmidt	Percentage difference
0.002849	10.25	10.29	0.39
0.00410	8.101	7.789	−3.99
0.01099	6.912	6.648	−3.97
0.02564	5.661	5.451	−3.85
0.04762	5.083	4.910	−3.52
0.1026	4.581	4.688	2.30
0.2308	3.953	4.039	2.13

Table 3 Values of major parameters for various cases

Case	Re	T_w	ϕ	Pr	Sc	Gr_T	Gr_M	S
I	2000	60°C	50 percent	0.7	0.58	4495	2504	8.25
II	2000	60°C	80 percent	0.7	0.58	4495	2416	7.80
III	2000	40°C	50 percent	0.7	0.59	2563	909	5.49
IV	2000	40°C	80 percent	0.7	0.59	2563	808	4.88
V	2000	21°C	50 percent	0.7	0.60	149	219	23.58
VI	2000	21°C	80 percent	0.7	0.60	149	102	11.03
VII	500	80°C	50 percent	0.7	0.58	5949	6122	14.22
VIII	500	40°C	50 percent	0.7	0.59	2563	909	5.49

To check further the adequacy of the numerical scheme described above for the present study, the results for the limiting case of forced convection flows in a vertical tube influenced by the buoyancy force of thermal diffusion alone were obtained. In Table 2 the present predictions are compared with the results of Zeldin and Schmidt (1972). The percentage differences between these two predictions are within 4 percent. This again indicates that the 47 × 41 grid is appropriate for the present study.

Results and Discussion

In this study, the calculations are specifically performed for moist air flowing in the tube, a situation widely found in engineering systems. Other mixtures can be analyzed similarly. It should be recognized herein that not all the values for the nondimensional groups appearing in the analysis, i.e., Pr, Sc, Gr_T, etc., can be arbitrarily assigned. In fact, they are interdependent for a given mixture under certain specific conditions. Hence for a specified mixture it is not proper to vary Pr, Sc, Gr_T, or Gr_M independently to study their individual effects. Instead the physical parameters – the wall temperature, the relative humidity of the ambient air, and the inlet Reynolds number – are picked as the independent variables. In light of practical situations, the following conditions are selected in the computations: Unsaturated moist air with relative humidity of 50 percent or 80 percent at 20°C and 1 atm enters a long vertical tube of 2-cm diameter from the bottom end by the combined action of certain external force as well as the buoyancy forces of heat and mass diffusion, and the tube wall is assumed to be at a uniform temperature ranging from 20.1°C to 80°C. All the nondimensional parameters can then be evaluated except the inlet Reynolds number, which should be specified separately. Results are obtained for several cases indicated in Table 3.

Shown in Fig. 1 is the development of dimensionless axial velocity in the flow. It is clearly seen that in Figs. 1(*a*), 1(*b*), and 1(*c*), the velocity profiles develop gradually from the uniform distributions at the inlet to the parabolic ones in the fully developed region, a situation normally found in laminar tube flows without mass addition. But the mass flow rate keeps increasing as the air moves downstream owing to the evaporation of water vapor into the air stream from the liquid film. The velocity profiles are not distorted by the buoyancy forces. This is readily explained by the fact that the parameters

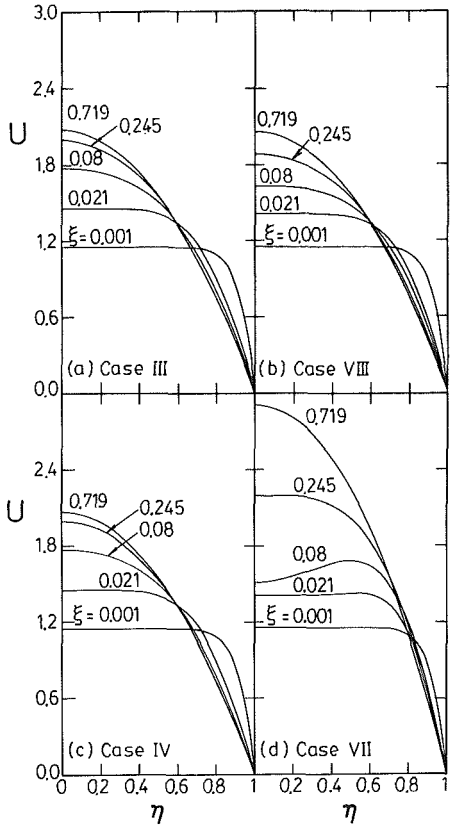

Fig. 1 Developments of dimensionless axial velocity profiles: (*a*) Re = 2000, $T_o = 20°C$, $T_w = 40°C$, $\phi = 50$ percent; (*b*) Re = 500; (*c*) Re = 2000, $\phi = 80$ percent; (*d*) Re = 500, $T_w = 80°C$, $\phi = 50$ percent

Gr_T/Re and Gr_M/Re for these cases are small. When the buoyancy effects get larger at higher T_w (Fig. 1*d*), the velocity profile gradually becomes distorted at certain axial locations. The distortion fades away as the air moves further downstream. This confirms the results of other studies (Zeldin and Schmidt, 1972; Hebchi and Acharya, 1986) in which no mass transfer is considered. It is also noticed in Fig. 1(*d*) that a rise in T_w would result in higher axial velocity U, in conformity with a greater amount of water vapor evaporating into the air for higher T_w and a larger buoyancy force through thermal diffusion. Change of ϕ, however, is found to have very slight effects on the development of U (Figs. 1*a* and 1*c*).

The developments of dimensionless temperature and mass-fraction profiles are shown in Figs. 2 and 3, respectively. It is interesting to observe that both θ and W develop in a very similar fashion. Careful inspection, however, discloses that the mass-fraction boundary layers develop a little more rapidly than the temperature boundary layers do. This is simply due to the fact that Pr is slightly larger than Sc in the flow. It is noteworthy that because of the small pressure defect in the flow, w_w is almost equal to w_r, and hence W is very close to unity at the interface of air and the liquid film. In a parametric study it was observed that the developments of θ and W are rather insensitive to the variations of Re, T_w, and ϕ. Although not clear in the results presented in Figs. 3(*a*) and 3(*b*), it is found in numerical results that temperature gradient at $\eta = 1$ is a little steeper for the case with $T_w = 40°C$. This is in congruence with the results obtained by Carter and Gill (1964) that larger evaporation in conjunction with higher T_w causes the temperature profiles to become flattened.

The distributions of motion pressure in the flow are given in Fig. 4. It is clear from this plot that for low T_w and high Re (cases III and V) the motion pressure is always negative and decreases with ξ, similar to that in pure forced convection

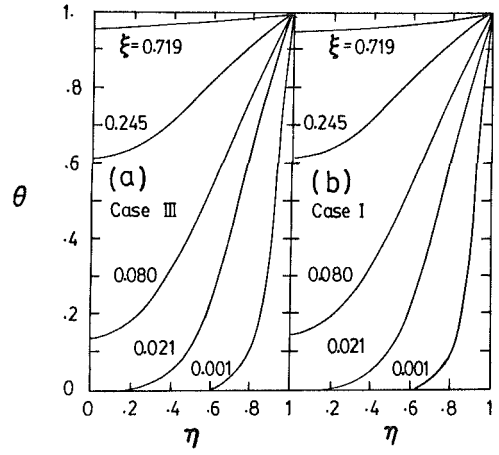

Fig. 2 Developments of dimensionless temperature profiles: (*a*) Re = 2000, $T_o = 20°C$, $T_w = 40°C$, $\phi = 50$ percent; (*b*) $T_w = 60°C$

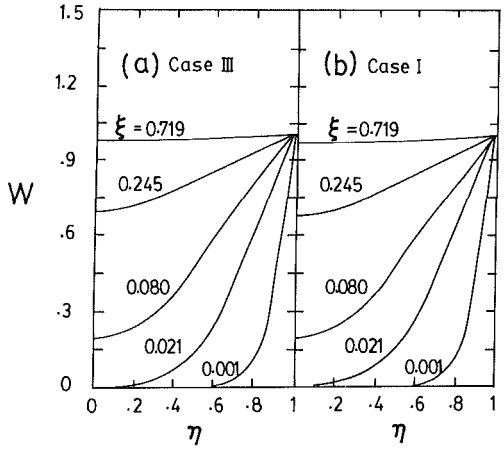

Fig. 3 Developments of dimensionless mass-fraction profiles: (*a*) Re = 2000, $T_o = 20°C$, $T_w = 40°C$, $\phi = 50$ percent; (*b*) $T_w = 60°C$

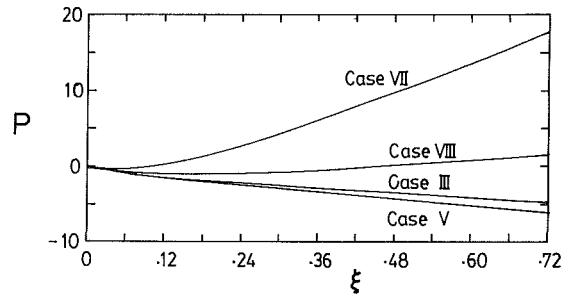

Fig. 4 Dimensionless motion pressure distributions along the tube: Case III—Re = 2000, $T_o = 20°C$, $T_w = 40°C$, $\phi = 50$ percent; Case V—$T_w = 21°C$; Case VII—Re = 500, $T_w = 80°C$; Case VIII—Re = 500, $T_w = 40°C$

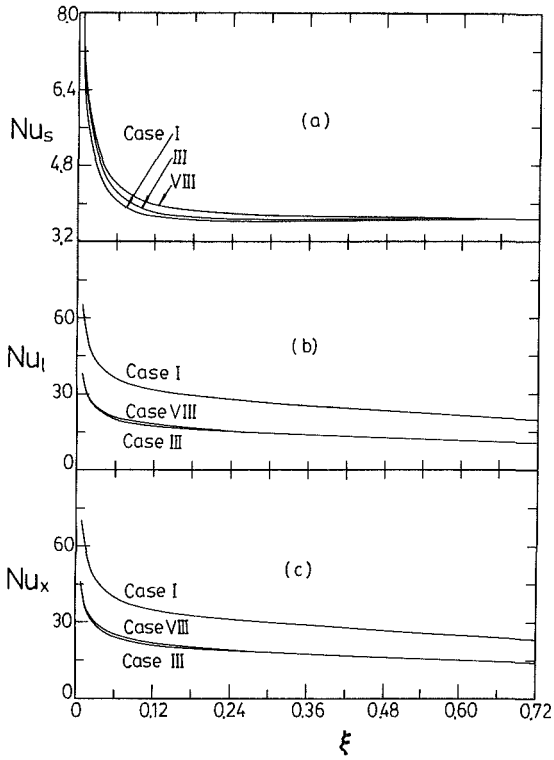

Fig. 5 Local Nusselt number for: (*a*) sensible heat; (*b*) latent heat; (*c*) overall along the tube; Case I—Re = 2000, $T_o = 20°C$, $T_w = 60°C$, $\phi = 50$ percent; Case III—$T_w = 40°C$; Case VIII—Re = 500, $T_w = 40°C$

flows. The buoyancy effects are weak. For high T_w and low Re in cases VII and VIII (high Gr_T/Re and Gr_M/Re), the motion pressure first decreases and stays negative, and then increases and becomes positive as the fluid goes downstream: an adverse pressure gradient. This can be understood by realizing that the mixed convection in the tube is closer to forced convection flow for higher Re and lower T_w. On the other hand, buoyancy effects are significant for low Re and high T_w. The increase in the pressure in the flow direction for these cases is derived from the fact that the frictional force is overwhelmed by the positive buoyancy forces.

To study the relative contributions of heat transfer through sensible and latent heat exchanges in the flow, both Nu_s and Nu_l are presented in Figs. 5(*a*) and 5(*b*). A slightly larger Nu_s is found for the flow with lower T_w in the entry portion of the tube. This is a direct consequence of the findings by Carter and Gill (1964): Larger water vapor evaporation associated with high T_w causes the temperature profiles to become flattened which then results in less sensible heat transfer. In the fully developed region ($\xi > 0.7$) no difference in Nu_s is observed for various cases in Fig. 5(*a*). In fact, Nu_s converges to a single constant value of 3.665 for all cases studied in the region where the fully developed conditions prevail, a value frequently found for forced convection heat transfer in laminar tube flows. According to the temperature and concentration profiles shown in Figs. 2 and 3, heat and mass transfer in the fully developed region is rather insignificant with the mixture nearly saturated, i.e., ϕ is close to 100 percent. Also noted is the much longer developing length, as compared with that without mass addition, due to the film vaporization.

An opposite trend is noticed for Nu_l in Fig. 5(*b*), i.e., the flow with $T_w = 60°C$ shows a higher value for Nu_l. This again is brought about by the larger latent heat transport in connection with the larger liquid film evaporation for higher T_w. It becomes apparent, by comparing the magnitudes of Nu_s and Nu_l, that heat transfer resulting from latent heat exchange is much more effective.

The influence of Re on the heat transfer is also of interest. Comparing cases III and VIII in Fig. 5(*a*) shows that the sensible heat transfer is better for the flow with lower Re owing to the larger buoyancy effect (higher Gr_T/Re and Gr_M/Re). But the difference in Nu_l is unnoticeable under different Re. This is because the latent heat transport is mainly determined by the parameter S in equation (17), which depends mainly on T_w irrespective of Re, as evident in Table 3. It was also found in separate computations that the effect of ϕ on Nu_s is small.

Although the influences of ϕ on the developments of velocity, temperature, and concentration, as noted above, are

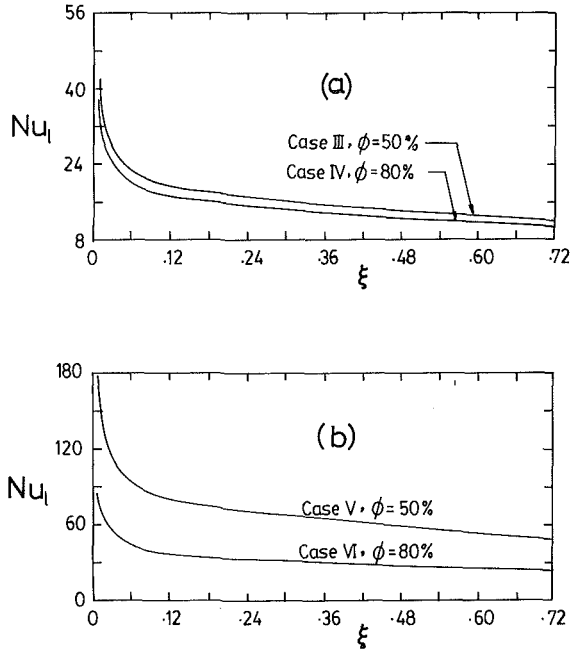

Fig. 6 Local Nusselt number (latent heat): (a) $T_w = 40°C$; (b) $T_w = 21°C$ at different ambient humidity with Re = 2000

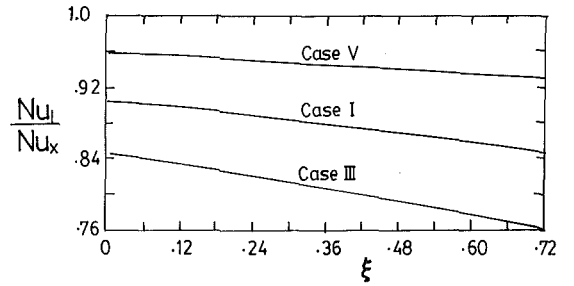

Fig. 7 The fractions of latent heat transport distribution along the tube: Case I—Re = 2000, $T_o = 20°C$, $T_w = 60°C$, $\phi = 50$ percent; Case III—$T_w = 40°C$; Case V—$T_w = 21°C$

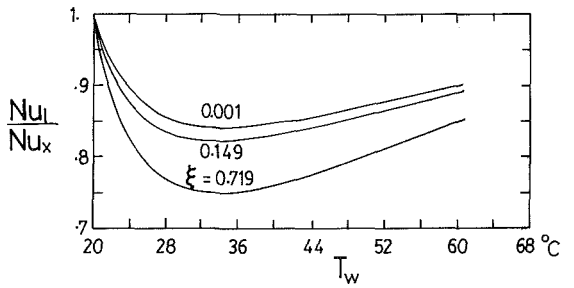

Fig. 8 The fractions of latent heat transport distribution at various wall temperatures with Re = 2000 and $\phi = 50$ percent

rather insignificant, its effect on the transport of latent heat cannot be ignored. This is readily understandable by recognizing that the latent heat exchange associated with the liquid film evaporation is very large, and thus a slight increase in the film evaporation by lowering ϕ can cause a substantial increase in the latent heat exchange. This is demonstrated in Fig. 6(*a*). Besides, the influence of ϕ on Nu_l is more pronounced for the flow with lower T_w, Fig. 6(*b*). This obviously indicates that the vaporization of the liquid film is substantially reduced, relative to the original evaporation rate, for a fixed amount of increase in ϕ for the flow with low T_w, wherein the

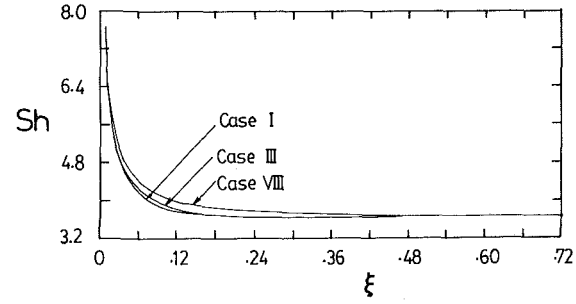

Fig. 9 Local Sherwood number along the tube: Case I—Re = 2000, $T_o = 20°C$, $T_w = 60°C$, $\phi = 50$ percent; Case III—$T_w = 40°C$; Case VIII—Re = 500, $T_w = 40°C$

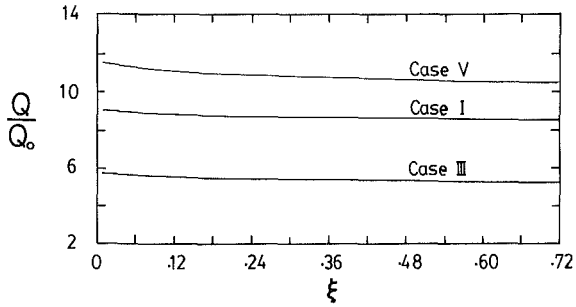

Fig. 10 Effect of system temperatures on the total heat transfer rate: Case I—Re = 2000, $T_o = 20°C$, $T_w = 60°C$, $\phi = 50$ percent; Case III—$T_w = 40°C$; Case V—$T_w = 21°C$

driving potential for mass transfer (Gr_M) is smaller. This becomes apparent if the change in Gr_M with T_w is checked, as given in Table 3.

It is physically important to be aware of the portion of the energy that is transported by mass transfer alone. To this end, the variations of Nu_l/Nu_x ($= q_l''/q''$) are shown in Fig. 7 for several cases. In congruence with the earlier discussion, the energy transfer in the flow is dominated by the exchange of latent heat. In the meantime, it is noted in this plot that the latent heat exchange is more effective for the flows with high or low T_w. To elucidate this phenomenon, we have to examine the parameter S defined in equation (18), a dominant factor for mass transfer Nusselt number, for each flow. Since a rise in T_w causes an increase in w_r, a slight decrease in h_{fg}, and meanwhile an increase in $(T_w - T_o)$, as a consequence S is not a monotonically increasing or decreasing function of T_w. As a matter of fact, it is found in this study that S decreases with increasing T_w for $T_w < 34°C$, and the reverse is true for $T_w > 34°C$. This is more clearly illustrated in Fig. 8. Also clearly seen in Fig. 7 is the transfer of latent heat becoming more prominent in the initial portion of the tube. This is simply due to the entrance effect for mass transfer.

The variations of local Sherwood number Sh_x, shown in Fig. 9, resemble those of Nu_s in Fig. 5(*a*). Similarly, Sh_x asymptotically reaches a constant value of 3.66 in all cases.

To illustrate the effectiveness of latent heat transfer through mass diffusion, the total heat transfer rate from the tube to the moist air with the presence of the liquid film on the tube's inside surface is compared with the result for the situation in which the liquid film is absent. The results for Q/Q_o are given in Fig. 10. Q_o represents the total heat transfer rate under the same condition for each case except for no liquid film on the inside surface of the tube. The tremendous capacity of energy transport through mass diffusion is demonstrated by noting that Q/Q_o can be as large as 11 for $T_w = 21°C$.

The amount of water vapor added to the flow due to film evaporation is important in improving our understanding on

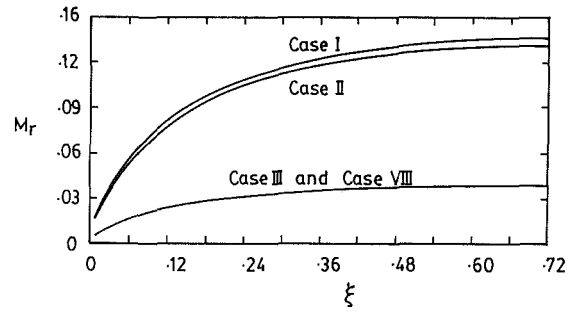

Fig. 11 Effects of various parameters on the mass flow rate due to film vaporization: Case I—Re = 2000, $T_o = 20°C$, $T_w = 60°C$, $\phi = 50$ percent; Case II—$\phi = 80$ percent, Case III—$T_w = 40°C$; Case VIII—Re = 500, $T_w = 40°C$

the mass transfer effects. To this end, a nondimensional flow rate resulting from the film evaporation is introduced

$$M_r = \frac{\text{evaporating mass flow rate}}{\text{inlet mass flow rate}}$$

$$= \left| \int_0^x \rho v_w 2\pi R dx \right| / \rho U_o \pi R^2 \tag{26}$$

In dimensionless variables

$$M_r = \left| 2 \int_0^\xi V_w d\xi \right| \tag{27}$$

The distributions of M_r for various cases are presented in Fig. 11. Large film vaporization is observed for a system with a high T_w. The mass addition to the flow is mainly dependent on T_w, with the effect of ϕ being slight and the effect of Re unnoticeable.

Concluding Remarks

The nature of laminar mixed convection flows in a vertical tube under the simultaneous influences of the combined buoyancy effects of thermal and mass diffusion has been studied, particularly for air-water systems. The effects of the liquid film temperature, the Reynolds number of the flow, and the relative humidity of the moist air in the ambient on the transfer of momentum, heat, and species in the flow were examined in great detail. What follows is a brief summary of the major results:

1 Heat transfer in the flow is dominated by the transport of latent heat in association with the vaporization of the liquid film.

2 An increase in ϕ results in a slight decrease in Nu_l when $(T_w - T_o)$ is large, while the decrease in Nu_l is rather substantial when $(T_w - T_o)$ is very small.

3 There exists a wall temperature T_w at which Nu_l/Nu_s is at a minimum. Up to this wall temperature, an increase in T_w leads to a decrease in Nu_l/Nu_x; above it, the relation is reversed.

4 A higher T_w results in a larger V_w in the entry region, which, in turn, causes the temperature profiles to become flattened and thus gives a lower value for Nu_s.

It is recognized herein that the results presented above are based on a number of assumptions made in the study. To test the validity of the assumptions, further research must be pursued. One important point requiring further study is to investigate the influences of a liquid film with finite thickness in which the temperature is no longer uniform and the fluid in the film is flowing.

Additionally, it is also realized that when the system operates at high temperatures, the use of the Boussinesq approximation (constant thermophysical properties except the density in the buoyancy term and linearization of the buoyancy force variations with temperature and concentration) is simply inappropriate. This becomes a serious problem, especially for an air-water system, for the reason that the water vapor contained in the mixture could be in significant amounts when the mixture is at a high temperature.

Acknowledgments

The authors wish to acknowledge the financial support of this work by National Science Council of Taiwan, Republic of China.

References

Bottemanne, F. A., 1971, "Theoretical Solution of Simultaneous Heat and Mass Transfer by Free Convection About a Vertical Flat Plate," *Appl. Sci. Res.*, Vol. 25, pp. 137–149.

Carter, L. F., and Gill, W. N., 1964, "Asymptotic Solution for Combined Free and Forced Convection in Vertical and Horizontal Conduits With Uniform Suction and Blowing," *AIChE J.*, Vol. 10, pp. 330–339.

Chang, C. J., Lin, T. F., and Yan, W. M., 1986, "Natural Convection Flows in a Vertical Open Tube Resulting From Combined Buoyancy Effects of Thermal and Mass Diffusion," *Int. J. Heat Mass Transfer*, Vol. 29, pp. 1543–1552.

Chow, L. C., and Chung, J. N., 1983, "Evaporation of Water Into a Laminar Stream of Air and Superheated Steam," *Int. J. Heat Mass Transfer*, Vol. 26, pp. 373–380.

Eckert, E. R. G., and Drake, R. M., Jr., 1972, *Analysis of Heat and Mass Transfer*, McGraw-Hill, New York, Chaps. 20 and 22.

Fujii, T., Kato, Y., and Mihara, K., 1977, "Expressions of Transport and Thermodynamic Properties of Air, Steam and Water," Sei San Ka Gaku Ken Kyu Jo, Report No. 66, Kyu Shu University, Kyu Shu, Japan.

Gebhart, B., and Mahajan, R. L., 1982, "Instability and Transition in Buoyancy-Induced Flows," *Adv. in Appl. Mech.*, Vol. 22, Academic Press, New York, pp. 231–315.

Gill, W. N., Casal, E. D., and Zeh, D. W., 1965, "Binary Diffusion and Heat Transfer in Laminar Free Convection Boundary Layers on a Vertical Plate," *Int. J. Heat Mass Transfer*, Vol. 8, pp. 1135–1151.

Hanna, O. T., 1965, "Diffusion in the Laminar Boundary Layer With a Variable Density," *AIChE J.*, Vol. 11, pp. 706–712.

Hebchi, S., and Acharya, S., 1986, "Laminar Mixed Convection in a Symmetrically or Asymmetrically Heated Vertical Channel," *Numerical Heat Transfer*, Vol. 9, pp. 605–618.

Hubbard, G. L., Denny, V. E., and Mills, A. F., 1975, "Droplet Evaporation: Effects of Transients and Variable Properties," *Int. J. Heat Mass Transfer*, Vol. 18, pp. 1003–1008.

Lee, T. S., Parikh, R. G., Acrivos, A., and Bershader, D., 1982, "Natural Convection in a Vertical Channel With Opposing Buoyancy Forces," *Int. J. Heat Mass Transfer*, Vol. 25, pp. 499–511.

Lin, T. F., and Chang, C. J., 1985, "Analysis of Combined Buoyancy Effects of Thermal and Mass Diffusion on Laminar Forced Convection Heat Transfer in a Vertical Tube," ASME Winter Annual Meeting, Miami, FL, HTD-Vol. 53, pp. 71–78.

Manganaro, J. L., and Hanna, O. T., 1970, "Simultaneous Energy and Mass Transfer in the Laminar Boundary With Large Mass Transfer Rates Toward the Surface," *AIChE J.*, Vol. 16, pp. 204–211.

Mathers, W. G., Madden, A. J., Jr., and Piret, E. L., 1957, "Simultaneous Heat and Mass Transfer in Free Convection," *Ind. Eng. Chem.*, Vol. 49, pp. 961–968.

Patankar, S. V., 1980, "Numerical Heat Transfer and Fluid Flow," Hemisphere/McGraw-Hill, New York, Chap. 6.

Petukhov, B. S., Polyakov, A. F., and Martynenko, O. G., 1982, "Buoyancy Effect on Heat Transfer in Forced Channel Flows," Keynote Paper, *7th Int. Heat Transfer Conf.*, Munich, Federal Republic of Germany, pp. 343–362.

Santarelli, F., and Foraboschi, F. P., 1973, "Heat Transfer in Mixed Laminar Convection in a Reacting Fluid," *Chem. Eng. J.*, Vol. 6, pp. 59–68.

Saville, D. A., and Churchill, S. W., 1970, "Simultaneous Heat and Mass Transfer in Free Convection Boundary Layers," *AIChE J.*, Vol. 16, pp. 268–273.

Somers, E. V., 1956, "Theoretical Considerations of Combined Thermal and Mass Transfer From a Vertical Flat Plate," ASME *Journal of Applied Mechanics.*, Vol. 23, pp. 295–301.

Soundalgekar, V. M., and Ganesan, P., 1981, "Finite-Difference Analysis of Transient Free Convection With Mass Transfer on an Isothermal Vertical Flat Plate," *Int. J. Eng. Sci.*, Vol. 19, pp. 757–770.

Sparrow, E. M., and Gregg, J. L., 1959, "Buoyancy Effects in Forced Convection Flow and Heat Transfer," ASME *Journal of Applied Mechanics*, Vol. 26, pp. 133–134.

Zeldin, B., and Schmidt, F. W., 1972, "Developing Flow With Combined Forced-Free Convection in an Isothermal Vertical Tube," ASME JOURNAL OF HEAT TRANSFER, Vol. 94, pp. 211–223.

APPENDIX

Evaluation of Thermophysical Properties

The thermophysical properties of a binary mixture undoubtedly depend on the mixture temperature and the concentration of each component. To simplify the analyses, the properties are often considered to be constant with the reference temperature and concentration being appropriately selected. Chow and Chung (1983) have shown that the constant-property approximation using the 1/3 rule yields accurate results for the prediction of the evaporation rate of water into the air stream. In the numerical study of the droplet evaporation Hubbard et al. (1975) compare the solutions using various reference-property schemes with those for variable properties and show that best agreement is obtained by using the 1/3 rule. Although the problems they solved are not quite the same as the present study, it gives us confidence in using the 1/3 rule to solve this problem. In this study all the thermophysical properties are evaluated at the reference temperature T and concentration w given as

$$T = T_w - \frac{1}{3}(T_w - T_o) \tag{28}$$

$$w = w_r - \frac{1}{3}(w_r - w_o) \tag{29}$$

The properties of air, water vapor, and their mixture are calculated by the following formulae (Fujii et al., 1977):

Air: component 2

$$\mu_2 = 1.4888 \times 10^{-6} \cdot T^{1.5}/(118 + T) \quad \text{(kg/m•s)} \tag{30}$$

$$k_2 = (1.195 \times 10^{-3} \cdot T^{1.6})/(118 + T) \quad \text{(W/m•k)} \tag{31}$$

$$c_{p2} = (1 + 2.5 \times 10^{-10} \cdot T^3) \times 10^3 \quad \text{(J/kg•k)} \tag{32}$$

Water Vapor: component 1

$$\mu_1 = [8.02 + 0.04(T - 273.16)] \times 10^{-6} \quad \text{(kg/m•s)} \tag{33}$$

$$k_1 = [1.87 + 1.65 \times 10^{-3}(T - 273.16)^{9/7} + 5.7 \times 10^{-13}(T - 273.16)^{5.1}] \times 10^{-2} \quad \text{(W/m•k)} \tag{34}$$

$$c_{p1} = 1.863 \times 10^3 + 1.65 \times 10^{-3}(T - 273.16)^{2.5} + 1.2 \times 10^{-18}(T - 273.16)^{8.5} \quad \text{(J/kg•k)} \tag{35}$$

Mixtures (air + water vapor):

$$\rho = \frac{21.955}{[1.8(T - 273.26) + 491.69] \cdot \left(\frac{w_1}{M_1} + \frac{1 - w_1}{M_2}\right)} \quad \text{(kg/m}^3\text{)} \tag{36}$$

$$\mu = \frac{\mu_1}{1 + 0.1727\left(1 + 1.1259\sqrt{\frac{\mu_1}{\mu_2}}\right)^2 \cdot \frac{1 - w_1}{w_1}} + \frac{\mu_2}{1 + 0.3520\left(1 + 0.8882\sqrt{\frac{\mu_2}{\mu_1}}\right)^2 \cdot \frac{w_1}{1 - w_1}} \quad \text{(kg/m•s)} \tag{37}$$

$$k = \frac{k_1}{1 + A_{12}(y_2/y_1)} + \frac{k_2}{1 + A_{21}(y_1/y_2)} \quad \text{(W/m•k)} \tag{38}$$

where

$$A_{ij} = \frac{1}{4}\left\{1 + \left[\frac{i}{j}\left(\frac{M_j}{M_i}\right)^{0.75} \frac{1 + S_i/T}{1 + S_j/T}\right]^{0.5}\right\}^2 \frac{1 + S_{ij}/T}{1 + S_i/T}$$

y_1, y_2 = mole fractions of components 1 and 2

$S_1 = 559.5, \quad S_2 = 115.5, \quad S_{ij} = 0.733\sqrt{S_i S_j}$

$$c_p = c_{p1} w_1 + c_{p2}(1 - w_1) \quad \text{(J/kg•k)} \tag{39}$$

$$D = 8.07 \times 10^{-10} \times T^{1.833} \quad \text{(m}^2\text{/s)} \tag{40}$$

In the above equations the units for temperature and pressure are degrees Kelvin and bars, respectively.

An Experimental Study on Natural Convection Heat Transfer in an Inclined Square Enclosure Containing Internal Energy Sources

Jae-Heon Lee
Department of Mechanical Engineering,
College of Engineering,
Hanyang University,
Seoul, 133 Korea

R. J. Goldstein
Department of Mechanical Engineering,
University of Minnesota,
Minneapolis, MN 55455
Fellow ASME

An experiment was carried out to study two-dimensional laminar natural convection within an inclined square enclosure containing fluid with internal energy sources bounded by four rigid planes of constant equal temperature. Inclination angles, from the horizontal, of 0, 15, 30, and 45 deg for Rayleigh numbers from 1.0×10^4 to 1.5×10^5 were studied. At inclined angles of 0 and 15 deg, there are two extreme values of temperature and temperature gradient within the fluid, while there is only one at 30 and 45 deg. Local and average Nusselt numbers are obtained on all four walls. As the inclination angle increases, the average Nusselt number increases on the right (upper) and bottom walls, decreases on the left (lower) wall and stays almost constant on the top wall.

1. Introduction

Thermal convection in a fluid with internal energy sources is of major interest in nuclear reactor safety analysis (Baker et al., 1976 a, b) as well as in geophysics (Runcorn, 1962) and astrophysics (Tritton, 1975; Bethe, 1968). In addition, engineering processes in fluids with chemical reactions or microwave heating are common today. A number of studies have been conducted on convection in fluids with internal energy sources. Kulacki and Goldstein (1972) measured heat transfer from a plane layer containing internal energy sources with equal boundary temperatures. Goldstein and Kudo (1982) measured the temperature distribution in a similar system with a free surface boundary. Recently, Kawara et al. (1984) have measured velocity and temperature fluctuations in turbulent natural convection in a horizontal fluid layer heated with uniform volumetric energy sources. Jahn and Reineke (1974) reported the characteristics of flow and heat transfer within a horizontal semicircular enclosure and a horizontal rectangular enclosure. Emara and Kulacki (1979) numerically analyzed thermal convection with uniform volumetric energy sources in a confined fluid with insulated side and bottom walls and rigid top wall or free top surface; Nusselt numbers and average temperature profiles within the fluid were in good agreement with experimental data. Beukema and Bruin (1983) developed a model of three-dimensional natural convection in a confined porous medium with internal heat generation and applied their theory to the storage process of agricultural products. Recently Acharya and Goldstein (1985) gave a numerical solution of natural convection in an externally heated square box containing uniformly distributed internal energy sources.

Natural convection in inclined enclosures also has been the subject of numerous investigations during past decades. Early work in this problem has been presented systematically by Hart (1971). Ozoe and Churchill have contributed to this area since 1974. Ozoe and Churchill (1983) computed the three-dimensional velocity and temperature fields for a cellular element with aspect ratio of 7 in a rectangular enclosure heated from below. Recently Goldstein and Wang (1984) studied thermal instability and heat transfer by natural convection in an inclined rectangular water layer using an interferometer.

The purpose of the present work is to investigate the temperature distribution and the heat transfer rate for an inclined square geometry with uniform energy sources within it. The convecting fluid is distilled water with NaCl added to raise the electrical conductivity. The salinity of the water is less than 0.01 molar so that the thermophysical properties are close to those of pure water. A Mach-Zehnder interferometer is employed to measure the temperature distribution within the water bounded by four rigid isothermal planes maintained at the same temperature T_w. A 60 Hz alternating current is passed from one silver-plated copper plate to the opposing one through water (resistance about 220 Ω) to provide a relatively uniform internal energy source.

The Rayleigh number Ra is appropriately defined in terms of the volumetric rate of internal energy dissipation and the maximum temperature difference that would occur in the one-dimensional layer with pure conduction heat transfer, and the corresponding characteristic length $L/2$ of the region with unstable temperature gradient. This definition is the same as that of Kulacki and Goldstein (1972)

$$\mathrm{Ra}=\frac{g\beta}{\alpha\nu}\left(\frac{L}{2}\right)^3\frac{(HL^2)}{8k} \tag{1}$$

where g, β, α, ν, L, H, and k are gravitational acceleration, thermal expansion coefficient, thermal diffusivity, kinematic viscosity, length of enclosure wall, volumetric energy source, and thermal conductivity of the fluid, respectively.

2. Experimental Apparatus and Procedure

The natural convection apparatus shown schematically in Fig. 1 was reconstructed from the one used by Kulacki and Goldstein (1972). Most of the parts are the same, but two side walls that acted as electrodes were modified. To maintain these at the same temperature as the upper and lower walls, cooling water tubes were soldered to the back of the electrode walls. Eight thermocouple wells were drilled in each of the four plates within 0.038 cm of the surface in contact with the

Contributed by the Heat Transfer Division for publication in the JOURNAL OF HEAT TRANSFER. Manuscript received by the Heat Transfer Division August 14, 1986. Keywords: Enclosure Flows, Natural Convection.

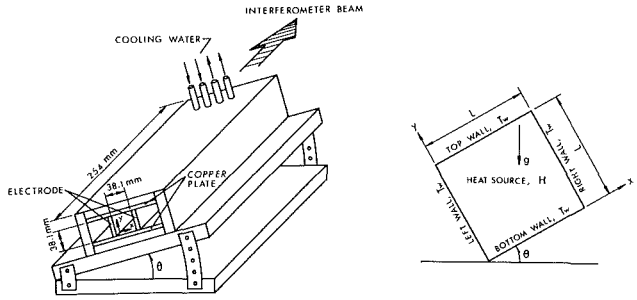

Fig. 1 Schematic of experimental apparatus and two-dimensional section of the enclosure

test fluid. Cooling water of temperature T_w is supplied to the channels and pipes from a bath with a pumping capacity large enough to supply both the upper and lower channelled plates and the tubes on the back of the side plates. The convection chamber has 3.81 cm square cross section; the length of the chamber is 25.4 cm. To confine the test fluid, two optical windows 32 mm thick are mounted at each end of the chamber (i.e., 25.4 cm apart). The optical windows are essentially adiabatic and are ground to a 1/4 wavelength flatness on both sides. The chamber can be inclined from the horizontal using a simple tilt mechanism. The range of inclined angle θ (see Fig. 1) is limited to 0–45 deg. Constant alternating current voltage applied across the electrode walls is 20 V or less and the total power dissipation is 1.5 W or less, where clear steady-state interferograms were desired. Above 1.5 W of consumed power, an electrochemical reaction occurs near the vertical symmetric line of the chamber. This reaction produces a swaying white sediment of salt which interferes with the interferometer beam.

Before each experimental run, the interferometer is adjusted to its infinite fringe mode so that isotherms can be observed. To ensure steady state, 4 hours elapse after the current is turned on before interferograms are recorded. Five interferograms are taken in series, usually an infinite-fringe and four wedge-fringe patterns. The infinite-fringe interferograms are used to observe the temperature distributions and to deduce the flow patterns. For the wedge-fringe results, the fringe line nearest a wall is adjusted parallel to the wall. To evaluate the heat transfer rate along the lower halves of left and right walls, for example, a wedge-fringe interferogram that had been adjusted parallel to the bottom wall is used. Other experimental procedures are almost the same as those described in Kulacki and Goldstein (1972).

The combined uncertainties in the thermophysical properties, geometric factors, and wattmeter readings cause an experimental uncertainty of 4-5 percent in Rayleigh number. There was a half fringe, at most, in the enclosure before applying the electric current to electrodes. There is also a slight error when extrapolating to the location of the wall to obtain the temperature gradient from wedge-fringe patterns. The uncertainty in the local Nusselt number is 3-4 percent.

3. Results and Discussion

The experimental Rayleigh numbers employed are approximately 1.0×10^4, 5.0×10^4, 1.0×10^5, and 1.5×10^5, which are provided by 0.09 W, 0.45 W, 0.9 W, and 1.35 W, respectively, in total power input to the test fluid. For each Rayleigh number, the inclined angles are selected as 0, 15, 30 and 45 deg.

The discussion includes the positions of maximum temperature and the flow characteristics, which can be analyzed from the distribution of isotherms from the infinite-fringe interferogram. The discussion on the rate of heat transfer is based on the wedge-fringe results.

3-1. Maximum Temperature and Flow Characteristics. Sixteen sets of isotherms are shown in Fig. 2. Natural convection shifts the isotherms toward the top wall so that the position of maximum temperature is higher than for pure conduction. Even at $\mathrm{Ra}=1.0\times10^4$, the influence of natural convection is observed except in the lower portion of the enclosure.

It can be seen from the isotherms for θ of 30 and 45 deg and $\mathrm{Ra}\geq5.0\times10^4$ that there is only one maximum of temperature near the top corner of the enclosure. From this, we deduce that the flow in the enclosure with $\theta\geq30$ deg consists of a pair of strong counterrotating convective rolls as depicted in Fig. 3(*a*). The hot interior fluid from the rolls starts to move upward along the line parallel to the gravity vector, which divides the whole cross-section approximately in half. These two hot flows arrive at almost the same position near the top wall, yielding a single position of maximum temperature. The flows then divide and move downward separately along the cold side walls. Further confirmation of the flow pattern came from observation of the motion of the small particles suspended in the fluid.

In the horizontal enclosure at $\mathrm{Ra}\geq5.0\times10^4$ there are two extreme values of temperature in the fluid and two extreme values of the temperature gradient on the top wall. Since the isotherms are concave upward at the center of the top wall, cold fluid moves downward here. Similar observations had been presented in the interferometric study by Farhadieh and Tank in (1974). This distribution implies that there is another pair of counter rotating rolls smaller in size near the upper-center portion of the enclosure. Figure 3(*b*) shows schematically the flow pattern deduced from the interferogram in this case. These secondary rolls make the upward hot interior flows separate some distance from the top wall. Consequently, there are two apparent "impingement" points on the top wall. For an inclined angle of 15 deg, the pat-

Nomenclature

g = gravitational acceleration
H = energy source per unit time and volume
k = thermal conductivity
L = width (and height) of enclosure, 38.1 mm in present study
Nu = local Nusselt number, equation (2)
$\overline{\mathrm{Nu}}$ = average Nusselt number, equation (3)
Nu^+ = modified local Nusselt number, equation (4)
$\overline{\mathrm{Nu}}^+$ = modified average Nusselt number, equation (5)
q_{conv} = local heat transfer rate with convection
$q_{\mathrm{2D,\ cond}}$ = local heat transfer rate for two-dimensional conduction-only
Ra = Rayleigh number, equation (1)
T = temperature
T_W = wall temperature (all four walls)
x, y = Cartesian coordinates, Fig. (1)
α = thermal diffusivity of fluid
β = thermal expansion coefficient of fluid
θ = inclined angle, Fig. (1)
ν = kinematic viscosity of fluid

Subscripts

B = bottom wall
L = left wall
R = right wall
T = top wall

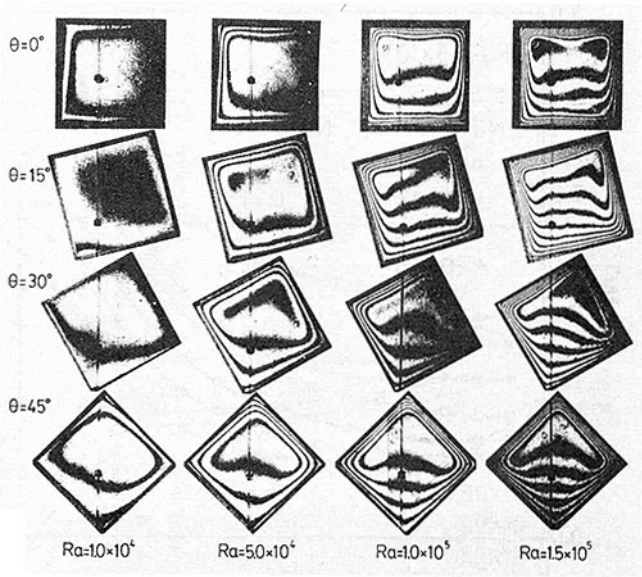

Fig. 2 Experimental isotherms

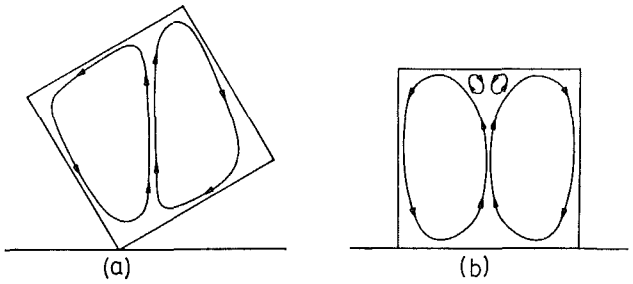

Fig. 3 Flow patterns deduced from interferograms: (*a*) a pair of strong counter-rotating rolls for inclined enclosure; (*b*) two pairs of counter-rotating rolls for horizontal enclosure

tern of isotherms is similar to that for 30 deg inclination, but characteristics of the temperature field found in a horizontal enclosure still remain.

The shift in the location of maximum temperature and the value of it in the enclosure are interesting results in the present investigation. The relative values of maximum temperature difference compared to those that occur if heat transfer were two-dimensional and conduction-only are listed in Table 1. The maximum temperature difference in the two-dimensional conduction mode is 0.589371 times that for the one-dimensional conduction mode, $HL^2/(8k)$, which would occur if two opposing walls were adiabatic rather than isothermal. The values in the table are all less than unity, and decrease as the Rayleigh number increases. Stronger convective motion in the fluid at higher Rayleigh number causes the higher heat transfer coefficient at the cold walls, lowering the peak fluid temperature. The rate of maximum temperature rise is not proportional to the rate of volumetric energy input to the fluid. The peak temperature is essentially independent of the inclined angle.

The positions of maximum temperature are determined from the infinite-fringe interferograms. When the enclosure is inclined at 30 and 45 deg, the positions are at $x/L=0.75$ and $y/L=0.75$ for $\mathrm{Ra}=1.0\times10^4$. The position moves continuously toward the upper top corner as the Rayleigh number increases and reaches $x/L=0.85$ and $y/L=0.85$ at $\mathrm{Ra}=1.0\times10^5$.

3-2 Heat Transfer. Heat transfer rates are evaluated from wedge-fringe interferograms. Among the interferograms

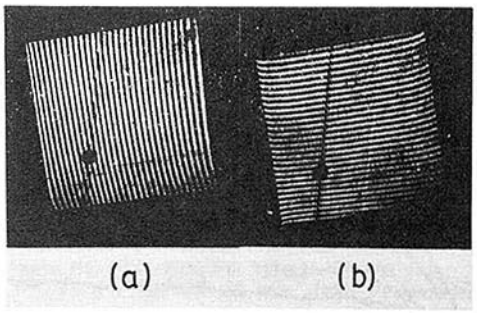

Fig. 4 Interferograms taken from finite-fringe mode, $\mathrm{Ra}=1.0\times10^4$, $\theta=15$ deg: (*a*) for evaluation of temperature gradients on upper halves of top and bottom wall; (*b*) for evaluation of temperature gradients on upper halves of left and right wall

Table 1 The ratio of maximum temperature difference in convection to that in two-dimensional conduction-only

Ra	$\theta=0$ deg	$\theta=15$ deg	$\theta=30$ deg	$\theta=45$ deg
1.0×10^4	0.656	0.658	0.660	0.660
5.0×10^4	0.497	0.498	0.497	0.497
1.0×10^5	0.435	0.437	0.436	0.436
1.5×10^5	0.401	0.404	0.396	0.397

taken, a pair of fringe distributions is shown in Figs. 4(*a*) and 4(*b*) when $\mathrm{Ra}=1.0\times10^4$ and $\theta=15$ deg; these are read to evaluate temperature gradients on the upper halves of top and bottom wall, and on upper halves of left and right wall, respectively. The local and average Nusselt number, Nu and $\overline{\mathrm{Nu}}$, are defined using the half layer width, $L/2$, as the characteristic temperature. For example, in the x direction

$$\mathrm{Nu}=\left[\frac{|\partial T|}{|\partial x|}_{\mathrm{wall}}\cdot\frac{L}{2}\right]/[HL^2/(8k)] \tag{2}$$

$$\overline{\mathrm{Nu}}=(1/L)\int_0^L \mathrm{Nu}\,dx \tag{3}$$

There are four kinds of local Nusselt numbers: Nu_L, Nu_R, Nu_B, and Nu_T, corresponding to the left, right, bottom, and top wall, respectively. These subscripts are also used to differentiate values of Nu. From a heat balance, one expects that the sum of the $\overline{\mathrm{Nu}}$ on the four walls should be four. This was applied to check the reliability of the experimental results.

Several plots of the local Nusselt number distribution along each wall are given in Fig. 5 for $\mathrm{Ra}=1.0\times10^5$ and $\theta=15$ deg. The values are compared with Nu, which would result in a two-dimensional conduction-only mode. Along the top wall, Nu_T is greater than that by conduction only. The reverse is true along the bottom wall. The values of Nu along the left and right walls become smaller in the lower portion and greater in the upper portion of the enclosure than those for conduction-only. Two maxima in Nu_T can be seen in Fig. 5; these are caused by the flow pattern that would include some of the characteristics of the flow pattern within a horizontal enclosure.

A comparison of the local heat transfer rate with convection q_{conv}, to that which would occur with only two-dimensional conduction, $q_{\mathrm{2D,\,cond}}$, is useful in investigating the influence of natural convection. To describe this ratio of relative heat transfer rate, we define a modified local Nusselt number Nu^+ as

$$\mathrm{Nu}^+ = q_{\mathrm{conv}}/q_{\mathrm{2D,\,cond}} = \mathrm{Nu}\cdot\pi^2\Big/\left\{16\sum_{n=0}^{\infty}\{\sin\{(2n+1)\pi x/L\}\cdot\tanh\{(2n+1)\pi/2\}(2n+1)^2\}\right\} \tag{4}$$

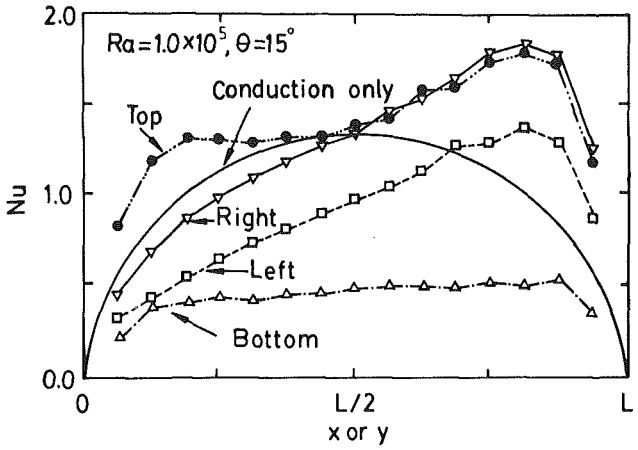

Fig. 5 Nusselt number distributions on each wall: $Ra = 1.0 = 10^5$, $\theta = 15$ deg

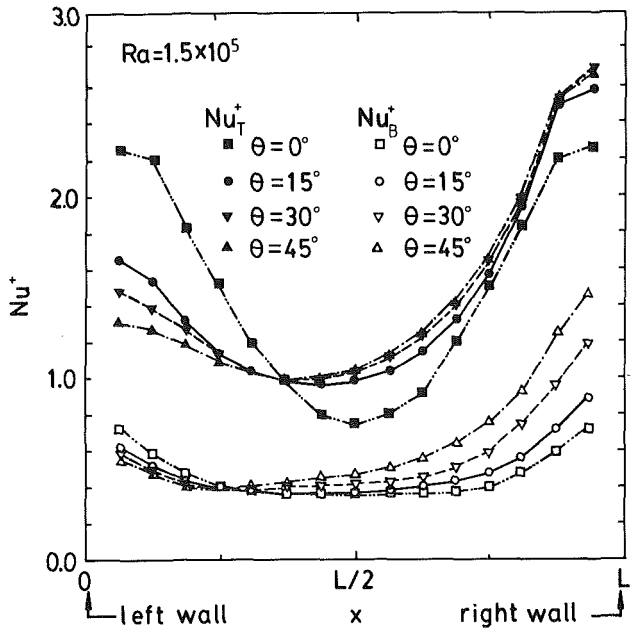

Fig. 6 Nu^+ distributions on the top and bottom walls: $Ra = 1.5 \times 10^5$

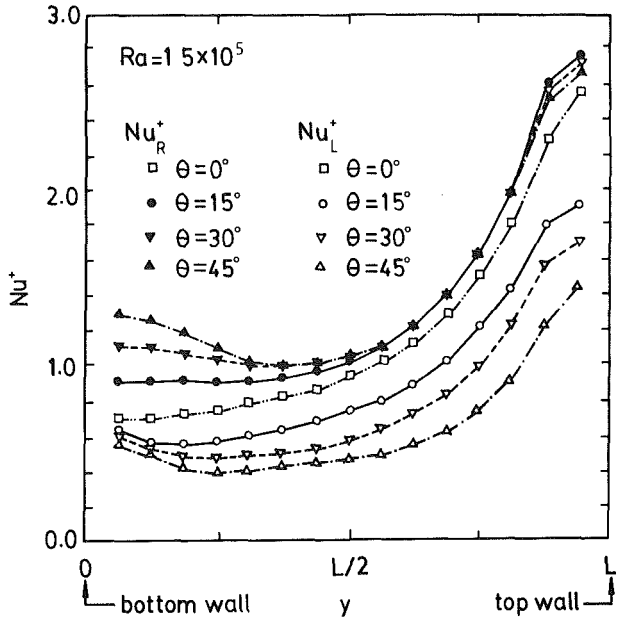

Fig. 7 Nu^+ distributions on the left and right walls: $Ra = 1.5 \times 10^5$

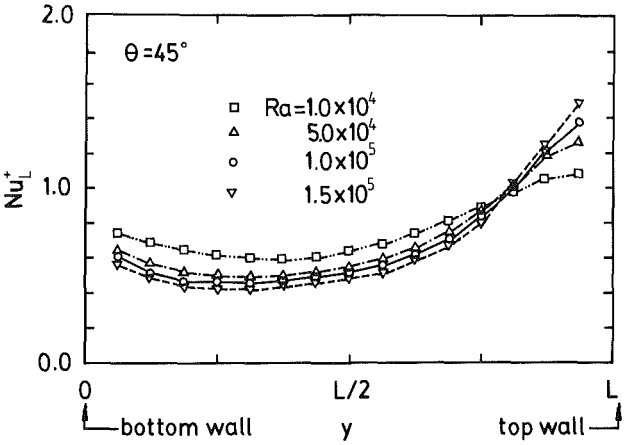

Fig. 8 Influence of Rayleigh number on Nu_L^+ at $\theta = 45$ deg

The modified average Nusselt number $\overline{Nu}^+$ defined by

$$\overline{Nu}^+ = \left\{\int_0^L q_{conv}\,dx\right\} \Big/ \left\{\int_0^L q_{2D,\,cond}\,dx\right\} \tag{5}$$

has the same value as $\overline{Nu}$. It is worth noting that Nu, from equation (2), is related to the absolute magnitude of the heat transfer rate while Nu^+, from equation (4), is the heat transfer relative to that by two-dimensional conduction. At $Ra = 1.5 \times 10^5$, Nu^+ distributions are shown for the top and bottom walls in Fig. 6, and for the left and right walls in Fig. 7. The distinctive minimum in Nu_T^+ (Fig. 6) at $\theta = 0$ deg is caused by the aforementioned pair of counter-rotating rolls. Nu_B^+ (Fig. 6) near the right wall is greater at larger inclined angle while Nu_L^+ (Fig. 7) near the top wall is larger at smaller inclined angle. The values of Nu_T^+ (Fig. 6) near the right wall and Nu_R^+(Fig. 7) near the top wall do not vary greatly with inclined angle.

To investigate the variation of Nu^+ with Rayleigh number, Nu_L^+ at $\theta = 45$ deg was selected; results are presented in Fig. 8. Although Nu_L increases monotonically with y (compare Fig. 5 for $\theta = 15$ deg), Nu_L^+ has a minimum. As the Rayleigh number increases, the values of Nu_L^+ decrease near the bottom wall and increase near the top wall. This indicates that the stronger convective flow at higher Rayleigh number within the inclined enclosure causes a steeper change in the heat transfer rate along the left wall.

The variation of $\overline{Nu}$ with inclined angle and Rayleigh number is shown in Fig. 9. The line of $\overline{Nu} = 1$ that corresponds to the two-dimensional conduction-only mode is drawn for comparison. For every Rayleigh number employed, as the inclined angle increases from $\theta = 0$ deg the magnitude of $\overline{Nu}$ increases on the right and bottom walls, decreases on the left wall, and stays almost constant on the top wall. As the Rayleigh number increases $\overline{Nu}$ increases, with $\overline{Nu} > 1$, on the top and right walls, and decreases, with $\overline{Nu} < 1$, on the bottom and left walls.

4. Summary

The natural convection in an inclined square enclosure containing internal energy sources has been investigated experimentally. Quantities obtained include temperature distribution and local average heat transfer rates. Interferograms were obtained using water of very low salinity for a square enclosure of 38.1 mm × 38.1 mm. Through the observation of isotherms for $Ra \geq 5.0 \times 10^4$, one can deduce

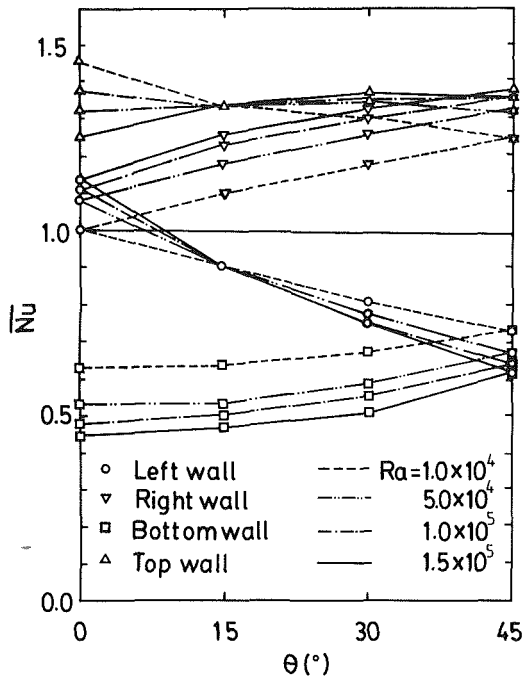

Fig. 9 Effect of inclined angle on $\overline{Nu}$ of each wall for various Rayleigh numbers

that there are two sets of counter-rotating rolls within the horizontal enclosure while there is one set of rolls within the inclined enclosure for θ of 30 and 45 deg.

In the presence of natural convection within the inclined enclosure, the average heat transfer rates on the top and right walls are higher than those for the two-dimensional convection-only mode. The reverse is true on the bottom and left walls for the higher angles of inclination.

The relative maximum temperature in the fluid decreased from the conduction-only value due to natural convection. The maximum temperature occurs near the upper top corners of the inclined enclosure. When $\theta \geq 30$ deg, the position of maximum temperature stays near $x/L = y/L = 0.85$ for $Ra \geq 1.0 \times 10^5$.

Acknowledgment

The authors wish to acknowledge the support from the US National Science Foundation and the Korean Science and Engineering Foundation (KOSEF) through the post-doctoral training program at the University of Minnesota.

References

Acharya, S., and Goldstein, R. J., 1985, "Natural Convection in an Externally Heated Vertical or Inclined Square Box Containing Internal Energy Source," ASME JOURNAL OF HEAT TRANSFER, Vol. 107, pp. 855–866.

Baker, L., Jr., Faw, R. E., and Kulacki, R. A., 1976a, "Postaccidental Heat Removal—Part I: Heat Transfer Within an Internally Heated Nonboiling Liquid Layer," *Nuc. Sci. Engrg.*, Vol. 66, pp. 223–230.

Baker, L. Jr., Faw, R. E., and Kulacki, R. A., 1976b, "Postaccidental Heat Transfer From an Internally Heated Liquid to a Melting Solid," *Nuc. Sci. Engrg.*, Vol. 66, pp. 231–238.

Bethe, H. A., 1968, "Energy Production in Stars," *Science*, Vol. 161, pp. 541–547.

Beukema, K. J., and Burin, S., 1983, "Three-Dimensional Natural Convection in a Confined Porous Medium With Internal Heat Generation," *Int. J. Heat Mass Trans.*, Vol. 26, No. 3, pp. 451–458.

Emara, A. A., and Kulacki, F. A., 1979, "A Numerical Investigation of Thermal Convection in a Heat-Generating Fluid Layer," ASME Paper No. 79-HT-103.

Farhadieh, R., and Tankin, R. S., 1974, "Interferometric Study of Two-Dimensional Benard Convection Cells," *J. of Fluid Mech.*, Vol. 66, pp. 739–752.

Goldstein, R. J., and Kudo, K., 1982, "Convection in a Horizontal Fluid Layer Having a Shear-Free Upper Surface and Uniform Volumetric Energy Source," *Proc. 7th Int. Heat Trans. Conf.*, U. Grigul et al., eds., Hemisphere Publishing Corp., Washington, DC, Vol. 2, pp. 129–134.

Goldstein, R. J., and Wang, Q.-J., 1984, "An Interferometric Study of the Natural Convection in an Inclined Water," *Int. J. Heat Mass Trans.*, Vol. 27, No. 9, pp. 1145–1453.

Hart, J. E., 1971, "Stability of the Flow in a Differentially Heated Inclined Box," *J. of Fluid Mech*, Vol. 47, pp. 547–576.

Jahn, M., and Reinke, H. H., 1974, "Free Convection Heat Transfer With Internal Heat Sources Calculations and Measurements," *Proc. 5th Int. Heat Trans. Conf.*, Tokyo, Japan, Paper No. NC2.8, pp. 74–78.

Kawara, Z., Morishima, N., Kikuchi, Y., and Michiyoshi, I., 1984, "Turbulent Natural Convection in a Horizontal Fluid Layer With Internal Heat Generations," *Proc. 21st Nat. Heat Trans. Symp. Japan*, pp. 355–357.

Kulacki, F. A., and Goldstein, R. J., 1972, "Thermal Convection in a Horizontal Fluid Layer With Uniform Volumetric Energy Sources," *J. of Fluid Mech.*, Vol. 55, pp. 271–287.

Ozoe, H., Fujii, K., Lior, N., and Churchill, S. W., 1983, "Long Rolls Generated by Natural Convection in an Inclined Rectangular Enclosure," *Int. J. Heat Mass Trans.*, Vol. 26, No. 10, pp. 1427–1438.

Runcorn, S. K., 1962, "Convection Current in the Earth's Mantle," *Nature*, Vol. 195, pp. 1248–1249.

Tritton, D. J., 1975, "Internally Driven Heat Convection in the Atmosphere of Venus and in the Laboratory," *Nature*, Vol. 257, pp. 110–112.

Natural Convection in an Inclined Rectangular Cavity With Different Thermal Boundary Conditions at the Top Plate

T. G. Karayiannis[1]
Research Fellow.

J. D. Tarasuk
Professor.

Faculty of Engineering Science,
The University of Western Ontario,
London, Ontario, N6A 5B9 Canada

Natural convection inside a rectangular cavity with different temperature boundary conditions on the cold top plate was studied using a Mach-Zehnder interferometer for $\theta = 15$, 45, and 60 deg to the horizontal. At $\theta = 60$ deg coupling with external forced convection and non-coupled heat transfer from a cavity with an isothermal top plate was studied. In all experiments the bottom hot plate was isothermal. The Rayleigh number Ra was varied from subcritical to 6×10^5 and the cavity aspect ratio AR_x, from 6.68 to 33.4. The Reynolds number of the external forced flow Re_{dh} was constant and approximately equal to 5.8×10^4. It was found that for $Ra \lesssim 3 \times 10^4$ the differing thermal boundary conditions at the top plate did not affect the local or average heat transfer rates from the cavity. For $Ra \gtrsim 3 \times 10^4$ coupling at the top plate compared to the non-coupled case resulted not only in a reduction in the variation of the local heat transfer rates at the cold plate, but also in a significant reduction in the variation of the average transfer rates from hot and cold plates of the cavity. Forced convection at the top plate as compared to natural convection resulted only in a small reduction in the heat transfer coefficient at the cold plate. Correlation equations for coupled and noncoupled average heat transfer rates are presented.

Introduction

Excellent reviews by Schinkel (1980) and Catton (1978) on natural convective heat transfer from cavities of general orientation are already available and will not be repeated here. A summary of the frequently referenced heat transfer relations for vertical, horizontal, and inclined cavities is given by Karayiannis (1986).

An understanding of the dependence of the heat transfer rates on the average parameters cannot be complete unless knowledge of the flow behavior inside the cavity is available. For this reason a number of researchers (Birikh et al., 1968; Gershuni and Zhukhovitskii 1969; De Graaf and Van der Held, 1953; Hart, 1971; Liang and Acrivos, 1970; Clever and Busse, 1977; Ruth et al., 1980; Ozoe et al., 1974; Ozoe et al., 1975; Ozoe et al., 1977; Linthorst et al., 1981) have investigated the stability and the flow patterns inside a cavity both experimentally and theoretically.

A literature review revealed that most of the researchers have considered cavities with isothermal hot bottom and cold top plates. Different thermal boundary conditions at the hot plate and their effect on heat transfer rates from the cavity have been investigated among others by Schinkel (1980), Chao et al. (1981), and MacGregor and Emery (1969). The effect of differing thermal boundary conditions at the cold plate on heat transfer rates from the cavity has received less attention. Saidi and Tarasuk (1986) reported an interferometric investigation of convective heat transfer in an air-filled horizontal cavity for $8.85 \leq AR_x \leq 35.4$ and $10^3 < \mathrm{Ra} < 3.27 \times 10^5$. The hot plate was isothermal and the top transparent plate was cooled by natural or forced convection. Although increased cooling rates were observed as the external Re increased, the $\overline{\mathrm{Nu}}_h$–Ra relation was not reported to depend on the external flow conditions for the range studied.

Sparrow and Prakash (1981) studied numerically the coupling of internal and external natural convective heat transfer. This was done for a vertical square cavity ($AR_x = 1.0$) in the range $7 \times 10^2 < \mathrm{Ra} < 7 \times 10^6$ and $\mathrm{Pr} = 0.7$ (air). The hot plate was isothermal and the cold plate was cooled by an external natural convection boundary layer flow. The case of the isothermal hot and cold plates (noncoupled heat transfer) was included for direct comparison. They report that if $(T_h - T_a)$ for the coupled problem were equal to $(T_h - T_c)$ for the non-coupled problem the $\overline{\mathrm{Nu}}_h$ values for the former case would only be about 60 percent of those of the latter case for $\mathrm{Ra} > 7 \times 10^3$ with slightly smaller deviations at lower Ra numbers. To the authors' knowledge there is no information for coupled flows for an inclined rectangular cavity. This paper is an extension of an earlier report by the same authors (Karayiannis and Tarasuk, 1985). In the above paper the average heat transfer results reported were only for the condition of external natural convection and for $5 \times 10^4 < \mathrm{Ra} < 6 \times 10^5$ and $\theta = 15$ and 60 deg.

Definition of the Problem

A schematic of the air layer indicating the boundary conditions examined in this investigation is shown in Fig. 1. The hot plate of the cavity is at uniform temperature, $T_h = \text{const}$. Three different boundary conditions can exist on the top plate, namely:

(*a*) Coupled internal and external heat transfer.
  (*i*) External natural convection (case *a*1), $T_c = T_c(x)$
  (*ii*) External forced convection (case *a*2), $T_c = T_c(x)$
(*b*) Non-coupled convective heat transfer; the standard problem
  (*i*) Cold plate at uniform temperature (case *b*.1)
  $T_c = \text{const}$.

The upper and lower end walls at $x = 0$ and $x = H$ and the side walls at $z = 0$ and $z = W$ (W being the width normal to the

[1]Current address: Thermo-Fluids Engineering Research Centre, The City University, Northampton Square, London, EC1V 0HB, United Kingdom.

Contributed by the Heat Transfer Division for publication in the JOURNAL OF HEAT TRANSFER. Manuscript received by the Heat Transfer Division May 5, 1986. Keywords: Enclosure Flows, Natural Convection.

plane of the figure) complete the cavity. The angle of inclination θ is measured from the horizontal. The aspect ratio AR_x of the cavity is defined as the ratio of its length H to the spacing between the plates L. Similarly AR_z can be defined as the ratio of the width W to the spacing between the plates. For the range of aspect ratios studied, $6.68 \le AR_x \le 33.4$ and $7.2 \le AR_z \le 36.0$, AR_z was found to have only an insignificant effect on heat transfer rates from the cavity (Catton, 1978; Karayiannis, 1986; ElSherbiny et al., 1982).

Experimental Apparatus and Procedure

The experimental cavity, originally designed by Saidi (1983), had to be adaptable to changes in the aspect ratio, the Ra number, and the angle of inclination. The hot plate was made of copper 45.72 cm wide, 42.42 cm long, and 1.27 cm thick. Two aluminum plates, 0.635 cm thick each, were fastened to it. A teflon plate was attached to the lower aluminum plate to minimize heat losses. The hot plate assembly could be moved and thus changes in the plate spacing (changes in AR_x and Ra) were possible. The surface temperature of the copper plate was measured by means of 24 copper-constantan thermocouples. Readings from these thermocouples indicated an isothermal condition at the hot plate. The maximum to minimum temperature variation over the surface was <1 percent.

Two different cold plates were used: For the study of coupled convective heat transfer the cold plate was an assembly of two polycarbonate plastic (lexan) plates 45.72 cm wide, 42.42 cm long, and 0.952 cm in total thickness. Thermocouples were placed in grooves made on the lower 0.635 cm plate and extended to the top and bottom surface of the cold plate through 0.0762 cm holes. They provided temperature readings at 15 locations for each top and bottom surface of the cold plate. For the study of non-coupled convective heat transfer, for which an insothermal top plate was required, the lexan plate was replaced by an aluminum plate of equal length and width and 1.27 cm thick. The bottom surface temperature of the aluminum plate was measured with 15 thermocouples, which were inserted through 0.175-cm-dia holes that reached to 0.0762 cm from the bottom surface. A 6-cm-thick honeycomb, placed on the aluminum top surface, destroyed the external natural convective boundary layer that can form when the temperature of the cold plate rises above ambient. This helped establish isothermal conditions at the aluminum bottom surface. The maximum to minimum temperature variation on the aluminum plate bottom surface was <2.5 percent.

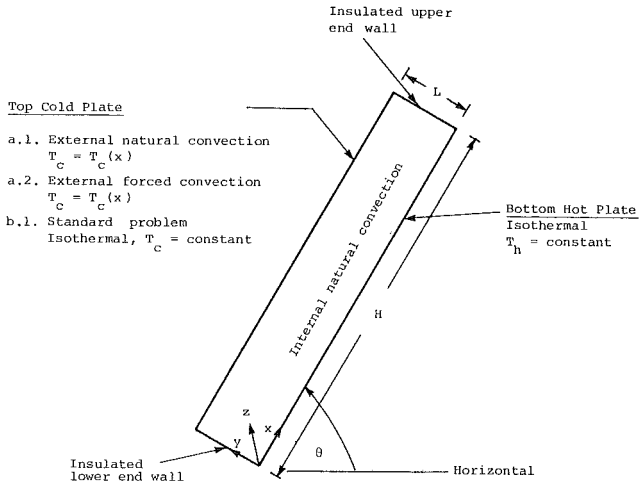

Fig. 1 Schematic of the cavity indicating boundary conditions

The side boundaries of the cavity at $x=0$ and $x=H$ (see Fig. 1) were constructed from an assembly of teflon plates 2.54 cm in total thickness. A 0.635 cm thick aluminum plate was fastened on the outside for rigidity. The other two opposing boundaries of the enclosure were made of 1.27-cm-thick transparent perspex (Plexiglas). These extended above the cavity and formed the side walls of a low-speed wind tunnel. The cavity was positioned in such a way that its top plate formed part of the lower wall of the wind tunnel.

The wind tunnel had a working section with a rectangular (30.5 cm × 45.7 cm) cross section. The velocity of air in the wind tunnel was kept constant at $V_m \simeq 2.5$ m/s for all the experiments with forced convection at the top plate of the cavity. This corresponds to turbulent flow with $\mathrm{Re}_{dh} \simeq 5.8 \times 10^4$, where Re_{dh} is the Reynolds number based on the hydraulic diameter ($dh = 36.58$ cm) of the wind tunnel working section. Due to the small length/dh ratio of the wind tunnel, the flow was not fully developed. Particular care was, however, taken to ensure uniform flow in the wind tunnel working section. Changes in the angle of inclination of the cavity were made possible by tilting the working section of the wind tunnel. Optical windows 15.24 cm in diameter and 2.54 thick were inserted in circular holes made in the perspex side walls of the wind tunnel working section and allowed the use of a Mach-

Nomenclature

AR_x = cavity aspect ratio $= H/L$
AR_z = cavity aspect ratio $= W/L$
dh = hydraulic diameter of wind tunnel test section
g = acceleration due to gravity
h_x = local convective coefficient
H = air cavity length
k = thermal conductivity
L = spacing between plates
Nu_x = local Nusselt number: equation (1)
Nu_{xh} = local Nusselt number at the hot plate
Nu_{xc} = local Nusselt number at the cold plate
$\overline{\mathrm{Nu}}$ = average Nusselt number: equation (2)
$\overline{\mathrm{Nu}}_h$ = average Nusselt number at the hot plate
$\overline{\mathrm{Nu}}_c$ = average Nusselt number at the cold plate
Ra = Rayleigh number: equation (3)
Ra_c = critical Rayleigh number
Re = Reynolds number
T = temperature
T^* = nondimensional temperature $= (T - T_{cb})/(T_h - T_{cb})$
y^* = nondimensional coordinate $= y/L$
α = thermal diffusivity
β = coefficient of volumetric expansion
θ = angle of inclination from horizontal
ν = kinematic viscosity

Subscripts

a = ambient measured above cold plate
c = cold plate
cb = bottom surface of cold plate
$cb\ av$ = average at the bottom surface of the cold plate
dh = based on the hydraulic diameter of the wind tunnel
h = hot plate
$h\ av$ = average at the hot plate
m = for cavity: calculated at $(T_h + T_{cb})/2$; for wind tunnel: measured at the center of the wind tunnel cross section

Zehnder long path difference interferometer (Karayiannis, 1985).

The experimental facility described above was subjected to a number of tests to substantiate experimental accuracy and reproducibility. The critical Ra number for convection to start was measured for $\theta = 60$ deg and found to be 3440. Agreement with the accepted value of 3416 given by the relation $\mathrm{Ra}_c(\theta) = 1708/\cos\theta$ reported by Gershuni and Zhukhovitskii is within 0.7 percent. Earlier, Saidi and Tarasuk (1986), using the same experimental facility, reported the critical Ra number for a horizontal cavity to be 1717, which agrees within 0.5 percent with the accepted value of 1708. Results from experiments performed for the same conditions at different times (up to 2 h difference) indicated that the Nu number was reproducible to within ± 1.5 percent.

The aspect ratio AR_x was varied from 6.68 to 33.4 and the angle of inclination was 15, 45, and 60 deg to the horizontal. Infinite interferograms provided a direct temperature field visualization since fringes represented isotherms. Finite interferograms were used for quantitative analysis.

Temperature profiles across the air layer at 14 locations were obtained from the finite interferograms. The temperature gradient with respect to y was then calculated at both the hot and cold plates and the local Nusselt number was obtained according to

$$\mathrm{Nu}_x = \frac{h_x L}{k_m} = \frac{k_w}{k_m}\frac{dT^*}{dy^*}\bigg|_{\text{wall}} \tag{1}$$

where k_w is the thermal conductivity of air evaluated at either the hot or the cold plate and k_m is the thermal conductivity of air evaluated at $(T_h + T_{cb})/2.0$. The average Nusselt number can then be found by

$$\overline{\mathrm{Nu}} = \int_0^1 \mathrm{Nu}_x d(x/H) \tag{2}$$

The maximum uncertainty in the calculation at the $\overline{\mathrm{Nu}}$ number at the hot plate was estimated to be 4.9 percent. For the $\overline{\mathrm{Nu}}$ number at the cold plate it was estimated to be 8 percent due to the additional error introduced by refraction (Karayiannis, 1986). Since the top plate temperature was not uniform, division of the cavity into four constant-temperature-difference regions was necessary for the evaluation of the air properties and the Rayleigh number, which is defined by

$$\mathrm{Ra} = \frac{g\beta L^3 (T_h - T_{cb})}{\nu\alpha} \tag{3}$$

The Ra number reported in this paper is the average of the four values calculated for each constant-temperature-difference region of the 42.42-cm-long cavity.

Experimental Results and Discussion

Temperature Distribution Inside the Cavity. In the conductive regime, $\mathrm{Ra} < 1708/\cos\theta$, the flow inside the cavity is a two-dimensional circulation with the streamlines (and isotherms, Karayiannis, 1986) parallel to the bounding surfaces except in the corner regions of the cavity. Heat is transferred by molecular conduction (dT/dy = constant across the air layer and $\mathrm{Nu}_x \simeq 1.0$) except in the corner regions where convective heat transport occurs due to the turning of the fluid.

As the Rayleigh number is increased beyond the critical value Ra_c, convection inside the cavity becomes increasingly important. Thermal boundary layers begin to grow on the hot and cold plates of the cavity. Following the onset of convection, the flow inside an air-filled cavity at $\theta < 70°\mathrm{C}$ can consist, depending on AR_x, of longitudinal rolls (rolls with their axis in the x direction) superimposed on the two-dimensional circulation (Gershuni and Zhukhovitskii, 1969; Hart, 1971; Clever and Busse, 1977; Ruth et al., 1980). In addition to molecular conduction (and radiation), laminar natural convection begins to contribute to the total heat transport from the hot to the cold plate of the cavity. The above changes are manifested by the changes in the isotherm patterns inside the cavity.

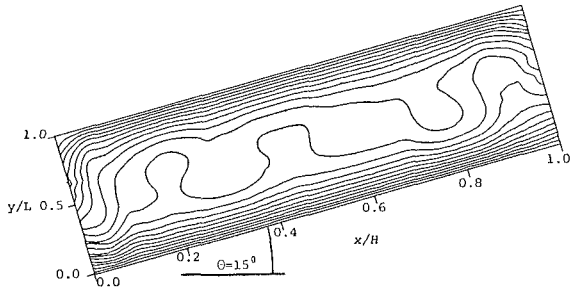

Fig. 2 Temperature contour plot: $\mathrm{Ra} = 1.843 \times 10^4$, $T_{h\ av} = 49.55°\mathrm{C}$, $T_{cb\ av} = 33.83°\mathrm{C}$, $AR_x = 16.7$, $T_a = 24.8°\mathrm{C}$; natural convection on top plate (0.05 T^* isotherms)

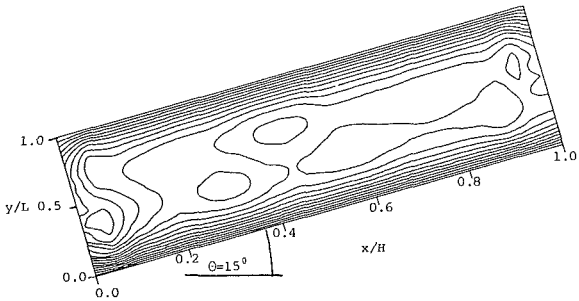

Fig. 3 Temperature contour plot: $\mathrm{Ra} = 1.13 \times 10^5$, $T_{h\ av} = 89.01°\mathrm{C}$, $T_{cb\ av} = 47.86°\mathrm{C}$, $AR_x = 11.13$, $T_a = 24.5°\mathrm{C}$; natural convection on top plate (0.05 T^* isotherms)

For all the angles studied, the flow inside the cavity began to exhibit unsteadiness when the aspect ratio was reduced from 33.4 to 16.7 ($\mathrm{Ra} > 5 \times 10^3$). This was indicated by the fluctuating fringes of infinite interferograms. The unsteadiness was mostly confined to the core region of the air layer. The fringes near the walls were fairly stable even at significantly higher Ra numbers.

Figure 2 shows a temperature contour plot for $\theta = 15$ deg, $AR_x = 16.7$, and $\mathrm{Ra} = 1.843 \times 10^4$. This is similar to the pattern obtained for $\theta = 0$ deg by Schinkel and Hoogendoorn (1978) and Samuels and Churchill (1967) using an interferometric and a numerical technique, respectively. For a similar isotherm configuration, in a water-filled horizontal cavity, Farhadieh and Tankin (1974) used a dye and observed rolls or cells (Bernard cells). In the inclined cavity the rolls are superimposed on a weak two-dimensional circulation. Cold fluid breaks away from the outer edges of the cold plate thermal boundary and moves down to the hot plate. This occurs at locations where the isotherms are concave upward. The fluid is heated as it moves laterally along the hot plate boundary and rises upward where the isotherms are concave downward so that the circulation in the core becomes a closed cell with the axis in the z direction.

The flow and isotherm patterns described above persisted up to $\mathrm{Ra} \lesssim 2.7 \times 10^4$. At higher Ra numbers more violent unsteadiness was observed. Thermals were observed to break away from the outer regions of the hot boundary layer. These either diffused in the core region or reached the cold boundary layer (Fig. 3). Similar activity occurred at the cold boundary

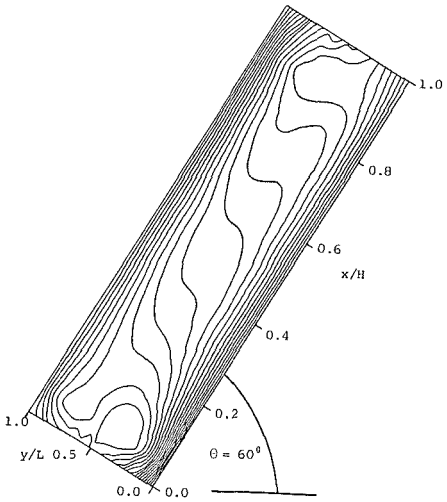

Fig. 4 Temperature contour plot: Ra = 1.129 × 10^5, $T_{h\ av}$ = 89.89°C, $T_{cb\ av}$ = 48.27°C, AR_x = 11.13, T_a = 26.7°C; natural convection on top plate (0.05 T^* isotherms)

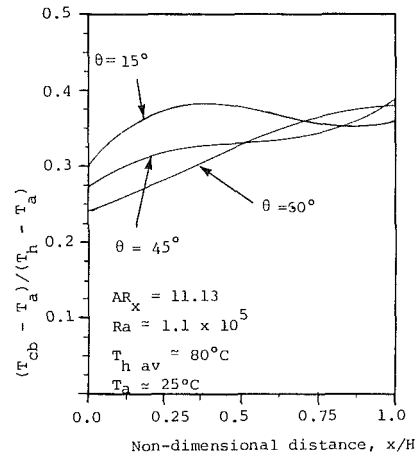

Fig. 5 Temperature distribution along the bottom of the cold plate at different angles of inclination; natural convection on top plate

layer. No other changes in the temperature and flow fields were observed as the aspect ratio was reduced or as the Ra number was increased other than an increase in the unsteadiness of the flow and the frequency of the appearance of thermals.

Examination of the isotherm patterns at $\theta = 45$ deg, $AR_x = 16.7$, $\mathrm{Ra} < 3 \times 10^4$ indicated the existence of unstable rotational motion about the z axis in the core region of the air layer. This, however, did not have the consistency of the rotational motion described earlier for $\theta = 15$ deg ($\mathrm{Ra} < 2.7 \times 10^4$). As the Ra number increases, the unsteadiness in the core region increases and thermals also appear. This unsteady mixing process increases the isothermality of the core region. Randall et al. (1979) described a similar large-scale mixing in the core of the air layer and attributed it to "eddies" breaking away from the outer edges of the boundary layers. De Graaf and Van der Held (1953) reported that for 30 deg $< \theta <$ 60 deg the air layer was turbulent after transition, i.e., for $\mathrm{Ra} > \mathrm{Ra}_c(\theta)$. Unstable mixing, however, might have given the impression of turbulence in the flow visualization with smoke reported by De Graff and Van der Held. Reducing the aspect ratio to $AR_x = 11.13$, 8.35, and 6.68 ($\mathrm{Ra} > 3 \times 10^4$) resulted in no other changes in the isotherm patterns and flow structure. Schinkel (1980) in his flow visualization experiments reported unstable large vortices at $AR_x = 7.0$, $\mathrm{Ra} = 2 \times 10^5$, and $\theta = 40$ deg, which is in agreement with the present deductions made from the study of the interference patterns mentioned above.

Observations of the interference patterns indicated that the flow patterns for $\theta = 60$ deg are similar to the previously described flow patterns for $\theta = 45$ deg. At low Ra numbers the flow can consist of longitudinal rolls superimposed on the two-dimensional circulation. As the Ra number increases the flow becomes unstable and finally consists of vortices and thermals ($\mathrm{Ra} > 3 \times 10^4$) superimposed again on the two-dimensional circulation, which becomes the main mode of heat transport. No other changes occur for $AR_x < 11.13$, $\mathrm{Ra} > 2 \times 10^4$.

Schinkel and Hoogendoorn (1978) reported that for $\theta < 30$ deg the interferograms look like the interferograms for the horizontal orientation and for $\theta > 50$ deg like the interferograms for vertical orientation. This observation agrees with the results of the present study. As mentioned earlier the interferograms at $\theta = 15$ deg were similar to the interferograms obtained for the horizontal orientation. The interferograms at $\theta = 45$ deg resembled mostly the interferograms of the vertical orientation, although similarities to the isotherm patterns of the horizontal orientation were not absent. The isotherm patterns of Fig. 4 have a clear resemblance to the isotherm patterns for $\theta = 90$ deg reported by Schinkel and Hoogendoorn (1978).

Examination of the isotherms of Fig. 4 indicates that at some locations in the cavity, e.g., at $0.03 < x/H < 0.15$, the temperature gradient dT^*/dy^* changes from negative at the hot plate to positive and then negative again at the cold plate. Where the gradient is positive, heat is transferred toward the hot plate. This phenomenon is called "temperature reversal" and is fully explained by Karayiannis (1986). It is caused by (*a*) the high velocities of the circulating flow and (*b*) instabilities in the flow. Temperature reversal was first found to appear at:

$\theta = 15$ deg, $\mathrm{Ra} = 1.834 \times 10^4$ or $\mathrm{Ra} = 10.40\ \mathrm{Ra}_c(15\ \mathrm{deg})$, $AR_x = 16.7$

$\theta = 45$ deg, $\mathrm{Ra} = 1.320 \times 10^4$ or $\mathrm{Ra} = 5.46\ \mathrm{Ra}_c(45\ \mathrm{deg})$, $AR_x = 16.7$

$\theta = 60$ deg, $\mathrm{Ra} = 1.213 \times 10^4$ or $\mathrm{Ra} = 3.50\ \mathrm{Ra}_c(60\ \mathrm{deg})$, $AR_x = 16.7$

As the angle of inclination from the horizontal increases, temperature reversal occurs at the decreasing value of Ra number. This is because the velocity of the circulating fluid at any Ra number increases with increasing angle of inclination.

Temperature Distribution on the Cold Plate. The temperature distribution on the cold plate in the coupled heat transfer case is the result of thermal interaction and the relative strengths of the internal and external heat transfer processes. In the conductive regime the distribution of T_c was similar for all the angles studied. T_c was uniform for most of the length of the cavity, except at the upper end, i.e., at $x \approx H$, where it was higher. The reason for this is the uniform local heat transfer rate ($\mathrm{Nu}_x \simeq 1.0$) for most of the length of the cavity in the conductive regime. This predominates over the external heat transfer rate, which decreases with distance x from the lower end wall. At the upper end, fluid that has been heated at the hot plate turns and travels to the cold plate. This accounts for the higher temperature of the cold plate at the upper end.

When convection inside the cavity occurs the temperature of the cold plate was found to vary with distance x from the end walls. The variation was found to increase with increasing angle of inclination. This is seen in Fig. 5, which shows the nondimensional temperature of the bottom surface of the cold plate obtained from thermocouples plotted against the nondimensional distance x/H for all angles studied and for similar Ra numbers and equal aspect ratios. The reason for this is the increasing dominance of the two-dimensional boundary layer circulation as the angle of inclination increases. The variation in the temperature of the cold plate was also found to increase

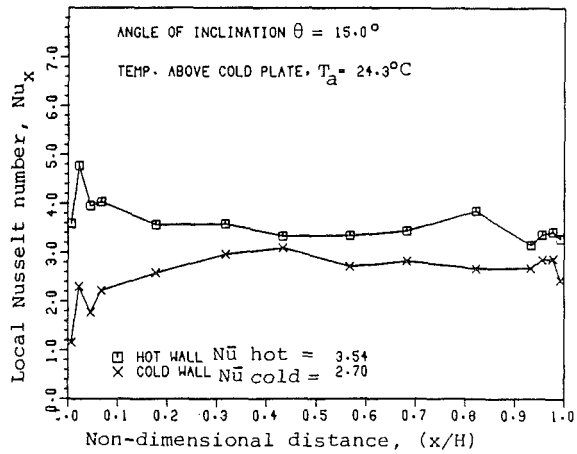

Fig. 6 Local Nusselt number in the cavity: $Ra = 3.176 \times 10^4$, $T_{h\,av} = 88.63°C$, $T_{cb\,av} = 48.89°C$, $AR_x = 16.7$; natural convection on top plate

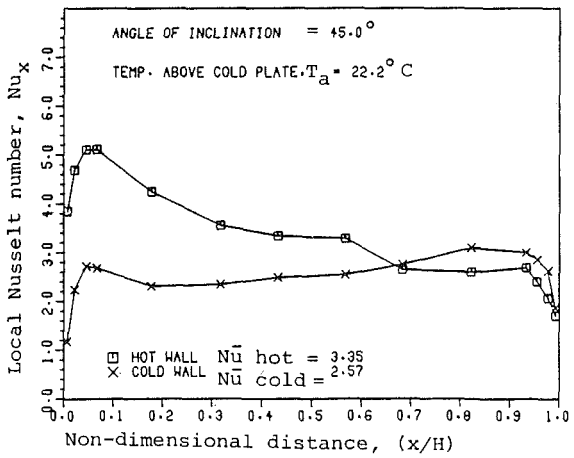

Fig. 7 Local Nusselt number in the cavity: $Ra = 1.175 \times 10^5$, $T_{h\,av} = 39.09°C$, $T_{cb\,av} = 27.60°C$, $AR_x = 8.35$; natural convection on top plate

strongly with decreasing aspect ratio and very moderately with increasing Ra number. At $\theta = 60$ deg, comparison of the temperature distribution on the cold plate with natural and forced convection at the cold plate led to the conclusion that, for a constant hot plate temperature, forced convection ($Re_{dh} \simeq 5.8 \times 10^4$) results in an increased rate of cooling and thus lower cold plate temperature. However, the variation of the temperature on the cold plate with distance x is the same for both conditions (Karayiannis, 1986).

Local Heat Transfer Rates. The local heat transfer rate Nu_x, calculated according to equation (1), was found to depend strongly on AR_x, Ra, θ, and distance x from the end walls. Increasing Ra and θ and reducing AR_x resulted in an increase in the dependence of Nu_x on distance x.

For $\theta = 15$ deg and $AR_x = 33.4$, i.e., $Ra < 3.8 \times 10^3$, the Nu_x number was independent of x and was mostly uniform for the entire length of the cavity. This indicates that there is no thickening of the thermal boundary layers at the two plates with distance x. When the aspect ratio was reduced to $AR_x = 16.7$ the "starting" and "departure" corners (Eckert and Carlson, 1961) become well defined. However, the Nu_x number remained independent of distance x for most of the length of the cavity up to $Ra \lesssim 2 \times 10^4$. At $Ra \gtrsim 2 \times 10^4$ a weak dependence on x become obvious. This is seen in Fig. 6 at $Ra = 3.176 \times 10^4$. Maximum and minimum values in the Nu_x number were observed, e.g., at $x/H \approx 0.8$ (Fig. 6) a local maximum occurs. This is in agreement with the observations of Schinkel and Hoogendoorn (1978) and is attributed to thermal instabilities. For $AR_x = 11.13$, 8.35, and 6.68, i.e., $Ra > 2 \times 10^4$, the Nu_x number remained weakly dependent on distance x from the end walls.

With the cavity inclined at $\theta = 45$ deg starting and deparature corners were well defined at $AR_x = 33.4$, $Ra < 4.3 \times 10^3$. However, the Nu_x number was still uniform in the central region of the cavity. As was the case for $\theta = 15$ deg the thermal boundaries at the two plates did not grow in thickness with distance x even when the apsect ratio was reduced to $AR_x = 16.7$, i.e., $8 \times 10^3 < Ra < 3 \times 10^4$. As a consequence only a weak dependence of Nu_x on x was exhibited in this range. However, reducing the aspect ratio further ($Ra > 3 \times 10^4$) resulted in a significant dependence of Nu_x on distance x. This is seen in Fig. 7, which shows the local heat transfer rates at $\theta = 45$ deg, $AR_x = 8.35$, $Ra = 1.175 \times 10^5$.

With the cavity inclined at $\theta = 60$ deg the dependence of Nu_x on distance x was stronger at all Ra numbers. Local maxima and minima in the Nu_x values persisted up to $\theta = 60$ deg. These become less pronounced and frequent as the angle from the horizontal was increased. Brooks and Probert (1972) for a cavity of general orientation reported that maximum Nu_x at the starting corner of the hot plate occurred at $x/H \sim 0.05$. In this study maximum Nu_x at the hot plate was found to occur between $0.0225 \leq x/H \leq 0.1725$.

Effect of Different Boundary Conditions at the Top Plate on Heat Transfer Rates (the Coupling Effect). As seen in Fig. 7, the variation of the local heat transfer rate with distance x at the cold plate, Nu_{xc}, was less than the variation of the local heat transfer rate at the hot plate Nu_{xh}. This is in agreement with the findings of Sparrow and Prakash (1981). This difference in the Nu_x dependence on distance x becomes more pronounced as the angle from the horizontal increases, and the results for $\theta = 60$ deg confirm this. The reason for this difference is the opposite direction of the internal and external flow at the cold plate. As mentioned in the introduction, the case of non-coupled heat transfer was also studied at $\theta = 60$ deg. Figures 8 and 9 show the local heat transfer rates at $\theta = 60$ deg, $AR_x = 8.35$, $Ra \simeq 2.0 \times 10^5$ for coupled and non-coupled conditions at the cold plate respectively. The variation of Nu_{xc} for the coupled case is seen to be less than the variation of Nu_{xc} for the noncoupled case.

Figure 10 shows the average heat transfer rates at the hot ($\overline{Nu}_h$) plate for the three different boundary conditions at the top plate studied at $\theta = 60$ deg. The solid lines through the data represent empirical best fits. As seen in the figure, the average heat transfer rates for the coupled case are lower, indicating that coupling with external natural or forced convection results not only in a reduction in the variation of the local heat transfer rate with distance x, but also in a reduction in the $\overline{Nu}$ number ($\overline{Nu}_h$ and $\overline{Nu}_c$). This coupling effect, however, does not occur at $Ra \lesssim 3 \times 10^4$. $\overline{Nu}_x$ and $\overline{Nu}$ values in this lower range of Ra number are not affected by the thermal boundary conditions at the top plate of the cavity. The reason for this is the different heat transfer processes that prevail inside the cavity at lower Ra numbers, i.e., the existence of longitudinal rolls and the dominance of molecular conduction across the air layer. Heat transfer by the formation of longitudinal rolls and molecular conduction is basically x independent and thus the coupling effect is very weak.

At higher Ra numbers heat is transferred primarily by the boundary layers that form on the hot and cold plates. A smaller amount is transferred by rotational motion and thermal diffusion (thermals) across the air layer. Coupling at the top plate affects mostly the component of heat transferred by the boundary layer circulation, and since this component increases as the Ra number is increased (or the aspect ratio is

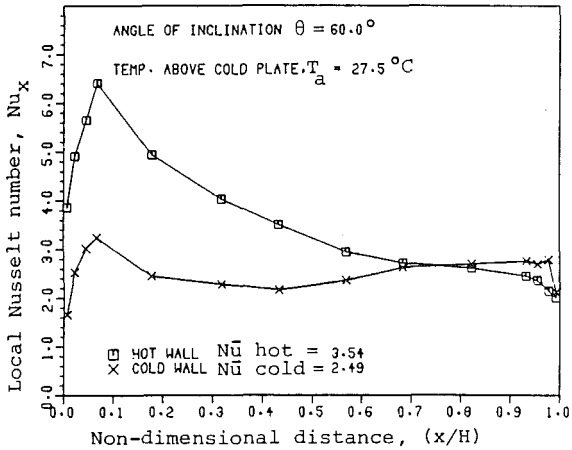

Fig. 8 Local Nusselt number in the cavity: $Ra = 2.225 \times 10^5$, $T_{h\,av} = 70.55°C$, $T_{cb\,av} = 41.43°C$, $AR_x = 8.35$; natural convection on top plate

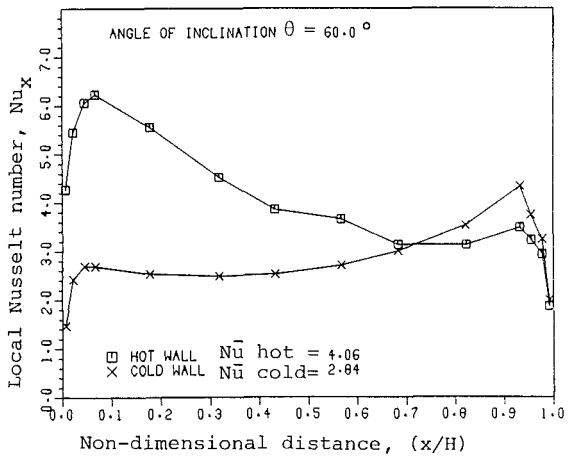

Fig. 9 Local Nusselt number in the cavity: $Ra = 1.941 \times 10^5$, $T_{h\,av} = 70.5°C$, $T_{cb\,av} = 44.89°C$, $AR_x = 8.35$; isothermal top plate

decreased) the effect of coupling becomes more pronounced at high Ra numbers. The ratio

$$\frac{\overline{Nu}_h(\text{case } a.1)}{\overline{Nu}_h(\text{case } b.1)}$$

decreases from about one at $Ra \simeq 3 \times 10^4$ to 0.75 at $Ra = 6 \times 10^5$. In the numerical solution of Sparrow and Prakash (1981) the flow inside the cavity consisted of a stable two-dimensional circulation, which did not change in the range studied. The external natural convection boundary layer was also stable and two-dimensional. The stability of the whole system and the uniformity of the flow inside the cavity account for the approximately constant value of the above ratio obtained by Sparrow and Prakash. As the resistance R_c of the cold plate is reduced, an increase in the coupling effect is to be expected, since the interaction of the internal and external thermal processes becomes more effective. Also as the angle of inclination is increased the coupling effect will increase. This is because the strength of the two-dimensional circulation inside the cavity and the strength of the opposing external boundary layer flow increase as θ approaches 90 deg. Sparrow and Prakash considered R_c to be zero, i.e., heat flux and temperature were assumed continuous at the cold plate. In addition, their cavity was vertical. These reasons account for the smaller value of 0.6 obtained for the ratio $\overline{Nu}_h$ (case $a.1$)/$\overline{Nu}_h$(case $b.1$) by Sparrow and Prakash as compared to the present result.

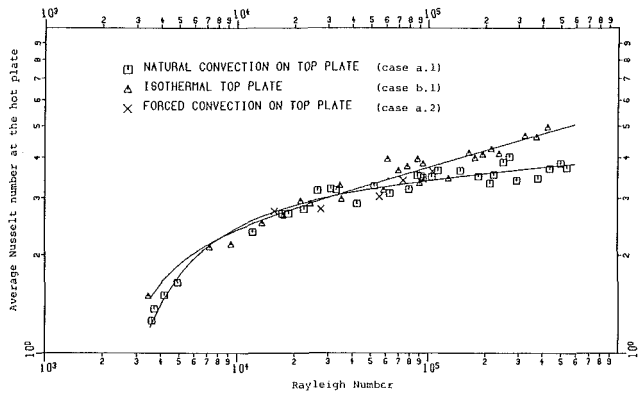

Fig. 10 Average Nusselt number at the hot plate versus Rayleigh number for $\theta = 60$ deg

The condition of forced convection at the top plate when compared to the isothermal condition at the same Ra number resulted in a similar effect on heat transfer rates as the condition of natural convection discussed above with only some small additional reduction in the variation of Nu_{xc} and the value of $\overline{Nu}_c$. The results of Saidi and Tarasuk (1986) indicate that the effect of forced convection as compared to the effect of natural convection on $\overline{Nu}_h$ is the same for $Re_{dh} < 5.3 \times 10^4$.

Average Heat Transfer Rates. The average Nusselt number was obtained by numerical integration of the local values according to equation (2). The dependence of the $\overline{Nu}$ number on Ra number and θ was found to be a complex one. At all angles studied, the dependence of $\overline{Nu}$ on Ra decreases as Ra increases, i.e., the slope of the $\overline{Nu}$-Ra curve decreases. This is attributed to changes in the flow patterns and mode of heat transfer inside the cavity that occur as the Ra number increases from the critical value. At high Ra numbers ($Ra \gtrsim 2 \times 10^4$) the $\overline{Nu}$ number dependence on Ra becomes constant, because no further changes in the flow patterns and mode of the heat transfer occur. A monotonic drop in the Nu number was found at any Ra number as θ increases. However, the dependence of $\overline{Nu}$ on θ at different Ra numbers was not constant, but was found to decrease as the Ra number increases This is in agreement with De Graaf and Van der Held (1953). The average Nusselt number at the cold plate $\overline{Nu}_c$ was found to be smaller than the average number at the hot plate $\overline{Nu}_h$. The difference in $\overline{Nu}_h$ and $\overline{Nu}_c$ varied from approximately 0 to 30 percent. This was mostly attributed to losses from the end walls (Karayiannis, 1986; Brooks and Probert, 1972).

The complex dependence of Nu_h on θ and Ra precludes the use of simple scaling law, such as the replacement of Ra by Ra cos θ in the relationship for a horizontal cavity. Different mathematical models were examined before the final correlating equations were obtained. The effect of the aspect ratio ($6.68 \leq AR_x \leq 33.4$) was not included. Changes in the aspect ratio were made possible by varying the space between the two plates L. This resulted in a simultaneous change in the Ra number, which is proportional to L^3. Therefore, the separate effect of AR_x and Ra on $\overline{Nu}_h$ could not be studied. Literature review reveals that in this range of AR_x the aspect ratio effect is very small. Randall et al. (1979) studied a range $9 < AR_x < 36$ for 45 deg $< \theta <$ 90 deg. They reported no effect of the aspect ratio on the $\overline{Nu}$ number. Meyer et al. (1982) combined their results with the results of Randall et al. only to conclude again that the aspect ratio has no effect on $\overline{Nu}_h$ for $AR_x \geq 9$. Hart (1973) for a slightly inclined cavity reported that the aspect ratio can be neglected if $AR_x > 10$. Schinkel (1980) reports that for $\theta = 50$ deg the Nu_h number does not depend on aspect ratio for $AR_x > 7.0$. Statistical modeling also

indicated that the parameter $\widetilde{AR}_x$ could be eliminated from the correlating equations. For a given θ the $\overline{\mathrm{Nu}}_h$ number is quite satisfactorily expressed as a function of Ra number only.

The following correlating equations for the average heat transfer rate from the hot plate $\overline{\mathrm{Nu}}_h$ were obtained:

Coupling with natural and forced convection:

$\theta = 0$ deg (data by Saidi, 1983)

$$\overline{\mathrm{Nu}}_h = 5.087 - \frac{0.043\mathrm{Ra}^{0.493}}{1+\frac{\mathrm{Ra}}{8\times10^3}} - \frac{0.0390\mathrm{Ra}^{0.277}}{1+\frac{\mathrm{Ra}^{1.6}}{5\times10^4}} \quad (4)$$

$\theta = 15$ deg (coupling with natural convection)

$$\overline{\mathrm{Nu}}_h = 0.882 - \frac{0.066\mathrm{Ra}^{0.640}}{1+\frac{\mathrm{Ra}^{1.5}}{2\times10^4}} + \frac{0.947\mathrm{Ra}^{0.098}}{1+\frac{2\times10^4}{\mathrm{Ra}^2}} \quad (5)$$

$\theta = 45$ deg (coupling with natural convection)

$$\overline{\mathrm{Nu}}_h = 2.416 - \frac{0.052\mathrm{Ra}^{0.653}}{1+\frac{\mathrm{Ra}^{1.4}}{2\times10^4}} + \frac{0.450\mathrm{Ra}^{0.095}}{1+\frac{2\times10^4}{\mathrm{Ra}^2}} \quad (6)$$

$\theta = 60$ deg (coupling with natural convection)

$$\overline{\mathrm{Nu}}_h = 1.238 - \frac{0.197\mathrm{Ra}^{0.803}}{1+\frac{\mathrm{Ra}^{1.75}}{2\times10^4}} + \frac{0.830\mathrm{Ra}^{0.086}}{1+\frac{2\times10^4}{\mathrm{Ra}^2}} \quad (7)$$

$\theta = 60$ deg (non-coupled case)

$$\overline{\mathrm{Nu}}_h = -0.310 - \frac{15.462\mathrm{Ra}^{0.335}}{1+\frac{\mathrm{Ra}^2}{3\times10^4}} + \frac{0.647\mathrm{Ra}^{0.159}}{1+\frac{\mathrm{Ra}^2}{3\times10^4}} \quad (8)$$

The coefficient of determination of the above equations was between 86.6 and 96.2 percent. The standard deviation of the data about the regression line varied from 0.1742 to 0.3327. Equations (4)–(8) correlate the data for $\mathrm{Ra}_c(\theta) < \mathrm{Ra} < 6\times10^5$ and $6.68 \le AR_x \le 33.4$. Extrapolation to higher Ra numbers is not recommended. This is because possible changes in the flow patterns at $\mathrm{Ra} > 6\times10^5$ (i.e., appearance of turbulence) could result in changes in the dependence of $\overline{\mathrm{Nu}}_h$ on Ra. Also use of the equations for cavities of $AR_x < 7$ is not recommended since the aspect ratio (not included in the above equations) is important at low aspect ratios. Linear interpolation for any angle in the range $0 \text{ deg} < \theta < 60$ deg is possible. Equation (4) was obtained by correlating data by Saidi (1983). The equation provided by Saidi and Tarasuk (1986) does not allow for the varying dependence of $\overline{\mathrm{Nu}}_h$ on Ra.

Comparison of Present Results With Results of Earlier Investigators. To the best of the authors' knowledge no information is available in the literature on heat transfer rates from an inclined cavity with coupled heat transfer at the cold plate. In Figs. (11)–(13) the present results are compared with the results of earlier investigations on inclined cavities with isothermal hot and cold plates. The varying dependence of the $\overline{\mathrm{Nu}}_h$ number on Ra number mentioned in the preceding section is also expressed by the correlating equations of De Graaf and Van der Held (1953) and Hollands et al. (1976). At low Ra numbers the average heat transfer rates obtained in this study (including the results for the noncoupled case) were higher than the results of earlier investigations. As seen in Figs. (11)–(13) this disagreement is very small at $\theta = 15$ deg but increases as the angle of inclination from the horizontal increases. At high Ra numbers the present results for coupling with external natural convection were found to be lower than the results of earlier investigators. This is due to the coupling effect at the cold plate. Exception to this were the results for the isothermal top plate. At high Ra numbers the $\overline{\mathrm{Nu}}_h$ numbers obtained in this case were in good agreement with the results of earlier investigators.

The results of Hollands et al. (1976) were obtained by measuring the heat flux at the center of the enclosure at $AR_x = 44$. The end effects were not included and $\overline{\mathrm{Nu}}_h$ was considered to be equal to Nu_{xh} at $x/H = 0.5$. Therefore, although frequently referenced, the equations of Hollands et al. can on-

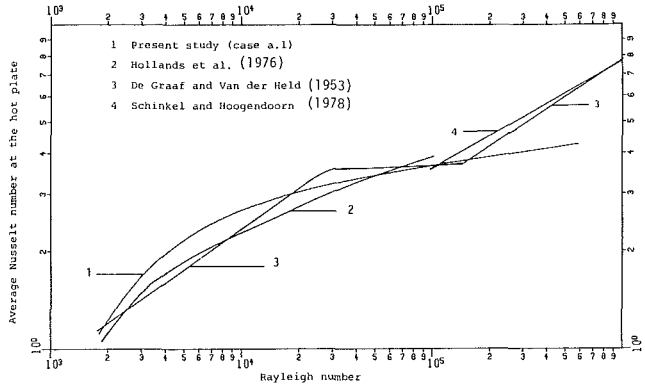

Fig. 11 Comparison of the present results of earlier investigations for $\theta = 15$ deg

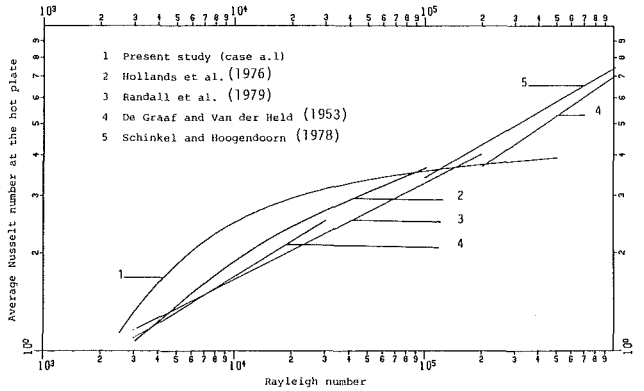

Fig. 12 Comparison of the present results with the results of earlier investigations for $\theta = 45$ deg

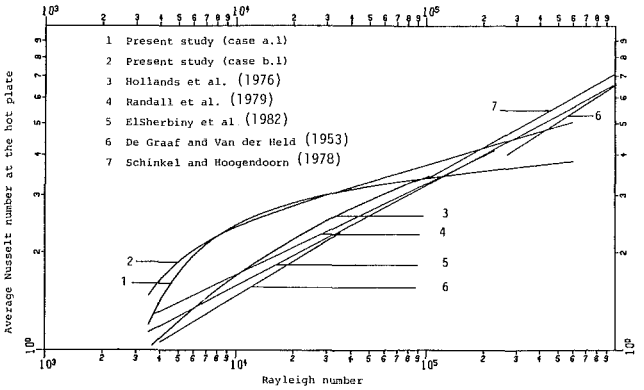

Fig. 13 Comparison of the present results with the results of earlier investigations for $\theta = 60$ deg

ly be applied to cavities of high aspect ratio. The assumption $\overline{Nu}_h = Nu_{xh}$ at $x/H = 0.5$ was checked in the present study for $\theta = 60$ deg (case *b*1), $AR_x = 16.7$, and $AR_x = 11.13$ (i.e., $Ra < 1 \times 10^5$). This was found to be valid only for $AR_x = 16.7$. For $AR_x = 11.13$ $\overline{Nu}_{xh}$ at the center was always lower (5–17 percent) than $\overline{Nu}_h$. The correlation of ElSherbiny et al. (1982) in Fig. 13 was plotted for the present range of aspect ratio.

Conclusions

A Mach-Zehnder interferometer was utilized in the study of coupled and non-coupled convective heat transfer from an inclined rectangular cavity. For Ra numbers below the critical value gaseous molecular conduction across the cavity predominates. The isotherms are parallel to the bounding surfaces except near the corners, where convection contributes to the total heat transport. As the Ra number is increased the convective contribution increases. At high Ra numbers ($Ra \geq 2 \times 10^4$) heat is transferred by boundary layer circulation, rotational motion, and thermal diffusion.

Under coupled conditions the temperature of the cold plate was found to vary with distance x from the end walls. The variation was found to increase with increasing θ and decreasing AR_x. The Ra number had only a moderate effect on the cold plate temperature variation.

When compared to the non-coupled case, coupling of external and internal convection flows at the top plate of the cavity resulted not only in a reduction in the variation of Nu_{xc} with distance x but also in reduction in $\overline{Nu}_h$ and $\overline{Nu}_c$ for the range $Ra \gtrsim 3 \times 10^4$. For $Ra \lesssim 3 \times 10^4$ the thermal boundary conditions at the top plate did not affect the local or average heat transfer rates from the cavity. The ratio $\overline{Nu}_h$ (coupled)/$\overline{Nu}_h$ (non coupled) was found to decrease from 1.0 at $Ra \simeq 3 \times 10^4$ to 0.75 at $Ra = 6 \times 10^5$. The effect of coupling with external forced convection when compared to coupling with external natural convection at the same Ra number was limited to a small reduction in the variation of $\overline{Nu}_{xc}$ and the value of $\overline{Nu}_c$.

The local heat transfer rate was found to depend strongly on AR_x, Ra, θ, and distance x from the end walls. The dependence of Nu_x on x increased with increasing Ra and θ and decreasing AR_x. The dependence of $\overline{Nu}_h$ on Ra and θ was found to be a complex one. Correlation equations for $\overline{Nu}_h$ were developed for both coupled ($\theta = 0$, 15, 45, 60 deg) and non-coupled ($\theta = 60$ deg) convective heat transfer from the cavity. These are applicable in the range $Ra_c(\theta) < Ra < 6 \times 10^5$ and $7 \leq AR_x \leq 33$.

Acknowledgments

This research was supported in part by the National Science and Engineering Research Council of Canada.

References

Birikh, R. V., Gershuni, G. Z., Zhukhovitskii, E. M., and Rudakov, R. N., 1968, "Hydrodynamic and Thermal Stability of a Steady Convective Flow," *Journal of Applied Mathematics and Mechanics*, Vol. 32, No. 2, pp. 256–263.

Brooks, R. G., and Probert, S. D., 1972, "Heat Transfer Between Parallel Walls," *Journal Mechanical Engineering Science*, Vol. 14, No. 2, pp. 107–127.

Catton, I., 1978, "Natural Convection in Enclosures," *Proceedings of the 6th International Heat Transfer Conference*, Toronto, pp. 13–30.

Chao, P., Ozoe, H., and Churchill, S. W., 1981, "The Effect of a Non-uniform Surface Temperature on Laminar Natural Convection in a Rectangular Enclosure," *Chem. Eng. Commun.*, Vol. 19, pp. 245–254.

Clever, R. M., and Busse, F. H., 1977, "Instabilities of Longitudinal Convection Rolls in an Inclined Layer," *Journal of Fluid Mechanics*, Vol. 81, pp. 107–127.

De Graaf, J. G. A., and Van Der Held, E. F. M., 1953, "The Relation Between the Heat Transfer and the Convection Phenomena in Enclosed Plane Air Layers," *Applied Scientific Research*, Vol. 3, pp. 393–409.

Eckert, E. R. G., and Carlson, W. O., 1961, "Natural Convection in an Air Layer Enclosed Between Two Vertical Plates With Different Temperatures," *International Journal of Heat and Mass Transfer*, Vol. 2, pp. 106–120.

ElSherbiny, S. M., Raithby, G. D., and Hollands, K. G. T., 1982, "Heat Transfer by Natural Convection Across Vertical and Inclined Air Layers," ASME JOURNAL OF HEAT TRANSFER, Vol. 104, pp. 96–102.

Farhadieh, R., and Tankin, R. S., 1974, "Interferometric Study of Two-Dimensional Bernard Convection Cells," *Journal of Fluid Mechanics*, Vol. 66, pp. 49–68.

Gershuni, G. Z., and Zhukhovitskii, E. M., 1969, "Stability of Plane-Parallel Convective Motion With Respect to Spatial Perturbations," *Journal of Applied Mathematics and Mechanics*, Vol. 33, No. 5, pp. 855–860.

Hart, J. E., 1971, "Stability of the Flow in a Differentially Heated Inclined Box," *Journal of Fluid Mechanics*, Vol. 47, part 3, pp. 547–676.

Hart, J. E., 1973, "A Note on the Structure of Thermal Convection in a Slightly Slanted Slot," *International Journal of Heat and Mass Transfer*, Vol. 16, pp. 741–753.

Hollands, K. G. T., Unny, T. E., Raithby, G. D., and Konicek, L., 1976, "Free Convective Heat Transfer Across Inclined Air Layers," ASME JOURNAL OF HEAT TRANSFER, Vol. 98, pp. 189–193.

Karayiannis, T. G., and Tarasuk, J. D., 1985, "Influence of Temperature Characteristics of the Upper Surface on Heat Transfer in a Solar Collector," *Transactions of CSME*, Vol. 9, No. 1.

Karayiannis, T. G., 1986, "An Interferometric Study of Coupled and Non-coupled Convective Heat Transfer From an Inclined Rectangular Cavity," Ph.D. Thesis, University of Western Ontario, London, Ontario, Canada.

Liang, S. F., and Acrivos, A., 1970, "Stability of Buoyancy-Driven Convection in a Tilted Slot," *International Journal of Heat and Mass Transfer*, Vol. 13, pp. 449–458.

Linthorst, S. J. M., Schinkel, W. M. M., and Hoogendoorn, C. J., 1981, "Flow Structure With Natural Convection in Inclined Air-Filled Enclosures," ASME JOURNAL OF HEAT TRANSFER, Vol. 103, pp. 535–539.

MacGregor, R. K., and Emery, A. F., 1969, "Free Convection Through Vertical Plane Layers—Moderate and High Prandtl Number Fluids," ASME JOURNAL OF HEAT TRANSFER, Vol. 91, pp. 391–403.

Meyer, B. A., Mitchell, J. W., and El-Wakil, M. M., 1982, "The Effect of Thermal Wall Properties on Natural Convection in Inclined Rectangular Cells," ASME JOURNAL OF HEAT TRANSFER, Vol. 104, pp. 111–117.

Ozoe, H., Sayama, H., and Churchill, S. W., 1974, "Natural Convection in an Inclined Square Channel," *International Journal of Heat and Mass Transfer*, Vol. 17, pp. 401–406.

Ozoe, H., Sayama, H., and Churchill, S. W., 1977, "Natural Convection Patterns in a Long Inclined Rectangular Box Heated From Below—Part I, Three-Dimensional Photography," *International Journal of Heat and Mass Transfer*, Vol. 20, pp. 123–129.

Randall, K. R., Mitchell, J. W., and El-Wakil, M. M., 1979, "Natural Convection Heat Transfer Characteristics of Flat Plate Enclosures," ASME JOURNAL OF HEAT TRANSFER, Vol. 101, pp. 120–125.

Ruth, D. W., Raithby, G. D., and Hollands, K. G. T., 1980, "On the Secondary Instability in Inclined Air Layers," *Journal of Fluid Mechanics*, Vol. 96, part 3, pp. 481–492.

Saidi, N. N., 1983, "An Interferometric Study of Coupled Convective Heat Transfer in a Horizontal Flat Plate Enclosure," Ph.D. Thesis, University of Western Ontario, London, Ontario, Canada.

Saidi, N. N., and Tarasuk, J. D., 1986, "Evaluation of Natural Convection Heat Transfer Coefficients in and Over an Enclosure by Mach-Zehnder Interferometry," *Proceedings of the 8th International Heat Transfer Conference*, San Francisco, Vol. 2, pp. 513–518.

Samuels, M. R., and Churchill, S. W., 1967, "Stability of a Fluid in a Rectangular Region Heated From Below," *AIChE Journal*, Vol. 13, No. 1, pp. 77–85.

Schinkel, W. M. M., and Hoogendoorn, C. J., 1978, "An Interferometric Study of Local Heat Transfer by Natural convection in Inclined Air Filled Enclosures," *Proceedings of the 6th International Heat Transfer Conference*, Toronto, Paper No. 18, Vol. 6, pp. 287–292.

Schinkel, W. M. M., 1980, "Natural Convection in Inclined Air-Filled Enclosures," *Dutch Efficiency Bureau-Pijnacket*.

Sparrow, E. M., and Prakash, C., 1981, "Interaction Between Internal Natural Convection in an Enclosure and an External Natural Convection Boundary-Layer Flow," *International Journal of Heat and Mass Transfer*, Vol. 24, No. 5, pp. 895–907.

Measurements in the Transition Vortex Flow Regime of Mixed Convection Above a Horizontal Heated Plate

S. S. Moharreri

B. F. Armaly
Fellow ASME

T. S. Chen
Fellow ASME

Department of Mechanical and Aerospace Engineering,
University of Missouri—Rolla,
Rolla, MO 65401

Experimental results covering the transition vortex flow regime of mixed convection over a heated, horizontal flat plate are presented. A criterion for the onset of vortex instability as a function of critical Reynolds and Grashof numbers was established with the aid of a flow visualization technique. The three-dimensional nature of this flow regime was documented through both velocity and temperature measurements using laser-Doppler and hot/cold-wire anemometers, respectively. A higher buoyancy force, through a higher plate temperature or a larger downstream distance, and/or a lower free-stream velocity, intensifies the strength of the vortices. Velocity and temperature profiles through vortex peaks and valleys are reported to quantify the behavior of these vortices. It has been found from these measurements that the two-dimensional laminar mixed convection flow changes into a transitional three-dimensional vortex flow in a relatively short distance from the leading edge of the plate. The vortex three-dimensional flow continues to intensify as the buoyancy force increases and then develops into a two-dimensional fully turbulent flow at the end of the transition regime. These findings place an upper limit on the applicability of the two-dimensional, laminar boundary layer flow analysis for mixed convection over a heated horizontal flat plate.

Introduction

The problem of thermal instability in boundary layer flows over isothermally heated horizontal flat plates has been examined by many investigators in recent years. It is now well recognized that buoyancy forces contribute a great deal to changing the characteristics of forced convective heat transfer. The effects of the buoyancy force may become pronounced when the flow velocity is low and the temperature difference between the plate and the free stream is large. Contrary to the problems of mixed convective heat transfer along a vertical flat plate (see, for example, Merkin, 1969; Lloyd and Sparrow, 1970; Wilks, 1973; Ramachandran et al., 1985; etc.), a vertical cylinder (see, for example, Chen and Mucoglu, 1975; Lee et al., 1986; etc.), a horizontal cylinder (see, for example, Mucoglu and Chen, 1977; Badr, 1984; etc.), and a concave wall (see, for example, Tani, 1962; McCormack et al., 1970; Kamotani et al., 1985; etc.), the horizontal flat plate geometry has received less attention. Owing to heating from below in this latter geometry, the flow becomes unstable and longitudinal vortices develop within the boundary layer to cause the flow to become three-dimensional, thus making the complete measurements of velocity and temperature fields at any cross section tedious and very time consuming. Wang (1982) reported on the heat transfer measurements for horizontal flat plate geometry and established the domains of pure forced, mixed, and pure free convection regimes.

For a given free-stream velocity and plate-to-free stream temperature difference, the incipience of vortex rolls or instability can be detected within the laminar boundary layer at a critical distance downstream of the leading edge of the plate. That critical distance is considered to be the beginning of the transition from the laminar mixed convection regime to the turbulent flow regime for a given free-stream velocity and plate-to-free-stream temperature difference. The two-dimensional laminar flow solution will not be valid in this transition regime owing to the three-dimensional nature of the vortex flow. The transition occurs at a much smaller Reynolds number than that predicted and measured for the onset of the wave instability (i.e., $Re_{xc} = 10^5$) for this flow. The presence of these vortices had been noticed in previous works on flows over horizontal plates heated from below and over concave walls. Vortex rolls appearing on a heated flat plate and a concave wall, although similar in nature, are induced by different forces. Vortices on the heated flat plate are due to buoyancy forces, whereas centrifugal forces are the cause for the vortices in flow over the concave wall. An analogy between these two phenomena was demonstrated in a study by Goertler (1959), which stated that the presence of any forces that have components perpendicular to the flow direction and to the surface can cause such a vortex instability. The criterion as to when such an instability occurs in laminar mixed convection boundary layer flow over a heated, horizontal flat plate has not been properly established, and thus the range of applicability of the two-dimensional laminar mixed convection solution for horizontal flat plates (e.g., Sparrow and Minkowycz, 1962; Chen et al., 1977; Ramachandran et al., 1983; etc.) has not been determined.

The onset of vortex instability in laminar mixed convection boundary layer flow above a heated horizontal flat plate has been examined theoretically by Wu and Cheng (1976) and Moutsoglou et al. (1981), and experimentally by Wang (1982) and by Hayashi et al. (1977) for air, and Gilpin et al. (1978) and Imura et al. (1978) for water. Moutsoglou et al. (1981) pointed out that the results of Wu and Cheng (1976) are incorrect because, in addition to a slight numerical error, they neglected the buoyancy force effect in the mainflow that was used to examine the vortex instability of that flow. It is, however, interesting to note that the results of Wu and Cheng (1976) are in better agreement with the measurements of

Contributed by the Heat Transfer Division for publication in the JOURNAL OF HEAT TRANSFER. Manuscript received by the Heat Transfer Division July 22, 1986. Keywords: Mixed Convection, Turbulence.

Wang (1982) and Hayashi et al. (1977) than those of Moutsoglou et al. (1981). Mixed convection flow in parallel-plate water channels was studied experimentally by Osborne and Incropera (1985a, 1985b). McCormack et al. (1970) and Kamotani et al. (1985) reported results on the effect of heating on Goertler vortices for flow over concave walls. The analysis of Moutsoglou et al. (1981) predicted a much earlier onset of vortices than what has been observed experimentally by the authors in this study and by Hayashi et al. (1977).

The above survey demonstrates the need for more quantitative measurements, particularly the velocity and temperature distributions, in the vortex flow regime of mixed convection. Such measurements have not been reported previously, and this has motivated the present study.

Experimental Apparatus and Procedure

The experiment was performed in an existing low-turbulence, open circuit air tunnel. The tunnel has a relatively long damping inlet box (1.22 m long), a smooth converging nozzle with a contraction ratio of 9:1, a test section, and a smooth diverging diffuser. Plastic honeycomb material (10.2 cm thick) and a section of plastic straws (22.2 cm thick), along with several wire screens, were used in the inlet and exit sections to straighten the flow and to reduce the turbulence level in the test section. The free-stream turbulence intensity as measured by the laser-Doppler velocimeter was less than 0.2 percent. A variable speed fan was used at the diffuser end to provide air velocities of 15 to 64 cm/s through the test section. The heated aluminum plate (30 cm wide, equivalent to the width of the test section of the air tunnel, 104 cm long, and 1.58 cm thick) could be maintained at any desired temperature between 25°C and 85°C without harming the plexiglass walls of the test section. The uniformity of the heated plate temperature was maintained to within 0.1°C by using rheostats to control individually the energy input to the various heating pads that are placed below the plate. The LDV measurements of the average velocity was repeatable to within 1 percent. Details of the air tunnel and the isothermally heated test plate assembly have been described by Ramachandran (1983) and by Ramachandran et al. (1985).

The velocities at any desired location were measured by a single-channel laser-Doppler velocimeter (LDV) using a counter as the Doppler signal processor. Glycerin smoke particles, resulting from the immersion of a 100-W heating element into a glycerine container, were mixed with the inlet air to provide the scattering centers for the LDV. The LDV was mounted on a three-dimensional traversing system capable of placing the measuring volume of the LDV at any x, y, z location in the flow within accuracies of 0.05, 0.003, and 0.05 mm, respectively. Velocity and temperature profiles in the boundary layer were measured for several free-stream velocities and plate temperatures. Temperature measurements were performed by utilizing a single cold wire boundary layer probe. The probe was calibrated frequently to ensure accurate measurements. The uncertainty associated with the temperature measurements is approximately 0.1°C and that with the velocity measurements is about one percent. The estimated experimental uncertainty in the reported Nusselt number is between 8 and 10 percent and that in the reported friction factor is between 5 and 8 percent, which are mainly due to uncertainties in determining the gradients at the wall. Rapid data acquisition and reduction for measurements of both velocity and temperature were performed with the aid of a microcomputer through the proper analog-to-digital converter and software (see Ramachandran, 1983, and Moharreri, 1986).

Flow visualizations were conducted to detect the onset of vortex instability and to examine the resulting three-dimensional nature of the flow. They were carried out by using a 15-W collimated white light beam (2.5 cm in diameter) that shone through the flow field containing small glycerin particles as light scattering centers. The light beam illuminated a y-z plane of the flow field. The glycerin particles were generated in the same manner as described earlier for the velocity measurements by the laser-Doppler velocimeter, except that a much higher concentration was used for flow visualizations. The flow visualization also helped in selecting the locations where the velocity and the temperature profiles were finally measured.

Experimental Results and Discussion

The uniformity of the flow velocity upstream and at the leading edge of the plate was confirmed by a series of measurements in both the y (measured from the surface of the plate) and the z directions. Two-dimensional, uniform laminar flow existed at the leading edge of the plate for the range of the velocities encountered in this experiment. The boundary layer flow above the plate without heating was examined by measuring velocity profiles for various free-stream velocities and streamwise locations. These measurements agree very well (less than 2 percent error) with the Blasius velocity profile, thus validating the performance of the wind tunnel and its instrumentation.

A series of photographs depicting segments from flow visualizations at various axial locations is shown in Fig. 1. Each photograph was taken from a location downstream of the collimated light beam, which crossed the width of the test section and exposed the flow characteristics in the spanwise direction at a given axial location. The darker regions in these photographs correspond to regions with lower scattering particle densities, which resulted from the secondary flow induced by the vortex. The changes in the sequence of flow patterns can clearly be seen from Fig. 1 as follows:

1 A region of two-dimensional laminar forced convection flow at small downstream distances.

Nomenclature

$C_{fx} = (2\nu/u_\infty^2)(\partial u/\partial y)_{y=0}$ = local friction factor
C_{fo} = local friction factor for pure forced convection
g = gravitational acceleration
$\mathrm{Gr}_x = g\beta(T_w - T_\infty)x^3/\nu^2$ = local Grashof number
Gr_{xc} = critical Grashof number
$\mathrm{Nu}_x = [-x/(T_w - T_\infty)](\partial T/\partial y)_{y=0}$ = local Nusselt number
Nu_o = local Nusselt number for pure forced convection
Pr = Prandtl number
$\mathrm{Re}_x = u_\infty x/\nu$ = local Reynolds number
Re_{xc} = critical Reynolds number
T = fluid temperature
$T_f = (T_w + T_\infty)/2$ = film temperature
T_w = wall temperature
T_∞ = free-stream temperature
u,v,w = axial, normal, and spanwise components of the local velocity, respectively
u_∞ = free-stream velocity
x, y, z = axial, normal, and spanwise coordinates, respectively
$\beta = 1/T_f$ = volumetric coefficient of thermal expansion
$\eta = y(u_\infty/\nu x)^{1/2}$ = pseudo-similarity variable
ν = kinematic viscosity
$\xi = \mathrm{Gr}_x/\mathrm{Re}_x^{2.5}$ = buoyancy parameter

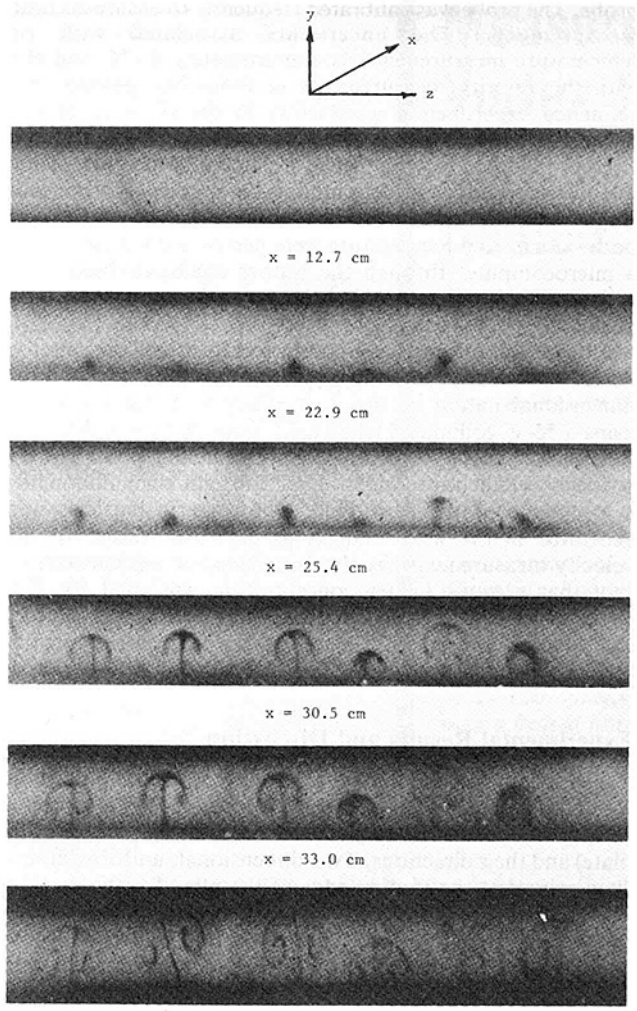

Fig. 1 Incipience and growth of vortex rolls in convective flow above a heated, horizontal flat plate ($u_\infty = 34$ cm/s, $T_W - T_\infty = 30°C$)

2 The onset of vortices at a critical downstream distance (first appearance of stationary cavitylike spots, spaced across the span of the heated surface, thus forming a three-dimensional flow).

3 A region where well-defined, stable, laminar vortices are present in pairs (pairs of vortices whose axes are in the streamwise direction, one rolling clockwise and another counterclockwise with a plumelike flow in the center).

4 An unstable vortex region consisting of several cells that were created from the growth of the individual vortices. Downstream of this region, the cells start mixing with each other in a random fashion and the flow develops slowly into a two-dimensional, fully developed turbulent flow.

It has been predicted by Turner (1960) and observed by Imura et al. (1978) in similar experiments with water that after the breakup of these vortex cells, which is accompanied by a sudden increase in the thermal boundary layer thickness, a two-dimensional region much like the "fully developed turbulent free convection" regime appears. Unfortunately, in this study, due to the length limitations of the test plate the fully developed, two-dimensional turbulent flow regime was not observed.

As noted earlier, for the mixed convective flow, a laminar two-dimensional flow region was observed upstream from the onset point of the vortex rolls. The length of this two-dimensional region is decreased by either increasing the temperature difference between the plate and the free stream or by decreasing the free-stream velocity (i.e., increasing the buoyancy force). The measured results in that region deviate only very slightly from the Blasius solution because the buoyancy parameter is very small (i.e., $\xi < 0.005$). The results in that region agree with the corresponding predictions of laminar mixed convection of Ramachandran et al. (1983). Flow visualization was used to detect and determine the first onset point of the vortex rolls for different free-stream velocities and plate temperatures. These streamwise locations for the onset of vortex rolls under different conditions were correlated in terms of critical Reynolds numbers Re_{xc}, and critical Grashof numbers Gr_{xc}, as shown in Fig. 2. It is noted that the critical downstream location x_c, where the onset of vortex instability was observed, could be reproduced to within 1 cm in the experiment. The thermophysical properties used in determing the critical Reynolds and Grashof numbers were evaluated at the average film temperature, $T_f = (T_w + T_\infty)/2$. A comparison with available analytical results and experimental data is including in Fig. 2. The present experimental results for air can be correlated by the equation

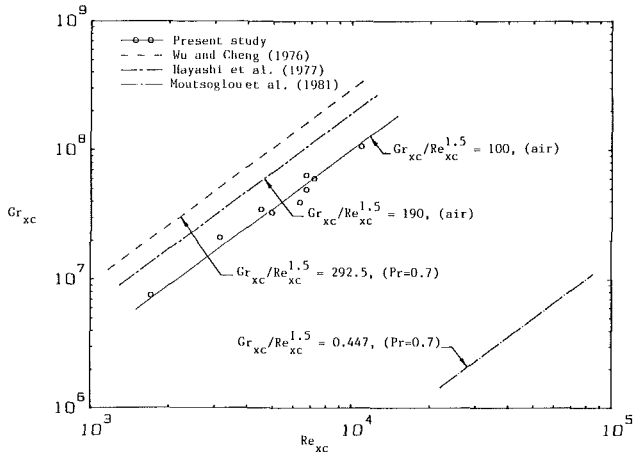

Fig. 2 Critical Grashof and Reynolds numbers for the onset of vortex instability

$$\mathrm{Gr}_{xc}/\mathrm{Re}_{xc}^{1.5} = 100 \tag{1}$$

with some scattering (± 20 percent). The experimental results of Hayashi et al. (1977) for air that were correlated by

$$\mathrm{Gr}_{xc}/\mathrm{Re}_{xc}^{1.5} = 192 \tag{2}$$

are also presented in the figure. The results of Wang (1982) correlated well with equation (2). It should be noted that both Wang (1982) and Hayashi et al. (1977) used heat flux measurements as a means of establishing the transition (the heat flux increased above the laminar flow domain at transition). The authors, on the other hand, used velocity measurements and flow visualization to establish that transition. The latter method is more sensitive and thus the result in equation (1) should be more accurate than those reported by Wang (1982) and by Hayashi et al. (1977) in equation 2. The experimental results of Gilpin et al. (1978) for water were correlated by a similar relation with a constant that varied between 46 and 110 when free-stream properties were used and between 30 and 200 when the film properties were used in the correlation.

The analytical prediction of vortex instability by Wu and Cheng (1976) gives $\mathrm{Gr}_{xc}/\mathrm{Re}_{xc}^{1.5} = 292.5$ for Pr = 0.7, whereas that by Moutsoglou et al. (1981) gives $\mathrm{Gr}_{xc}/\mathrm{Re}_{xc}^{1.5} = 0.447$. As mentioned earlier, Moutsoglou et al. (1981) indicated that the results of Wu and Cheng (1976) are incorrect because they neglected the buoyancy force, the driving force for the vortex

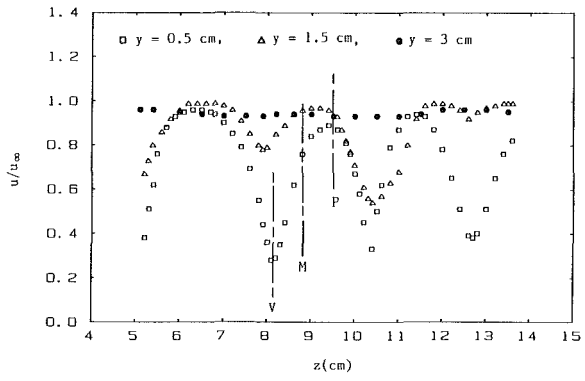

Fig. 3 Spanwise distributions of the streamwise velocity component ($x = 29.5$ cm, $T_w - T_\infty = 30°C$, $u_\infty = 34$ cm/s)

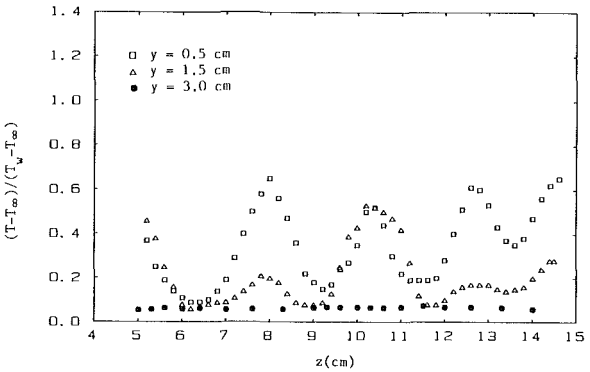

Fig. 4 Spanwise temperature distributions ($x = 29.5$ cm, $T_w - T_\infty = 30°C$, $u_\infty = 34$ cm/s)

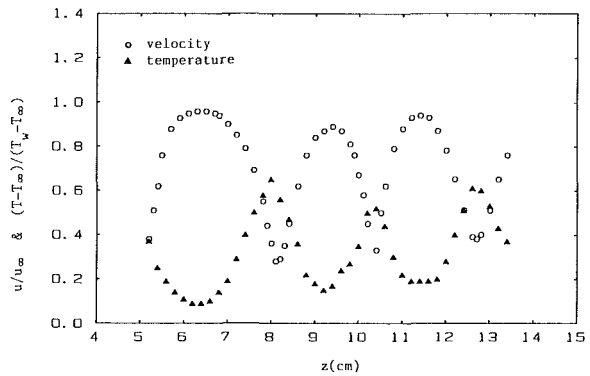

Fig. 5 Spanwise distributions of the streamwise velocity component and the temperature ($u_\infty = 34$ cm/s, $T_w - T_\infty = 30°C$, $x = 29.5$ cm, $y = 0.5$ cm)

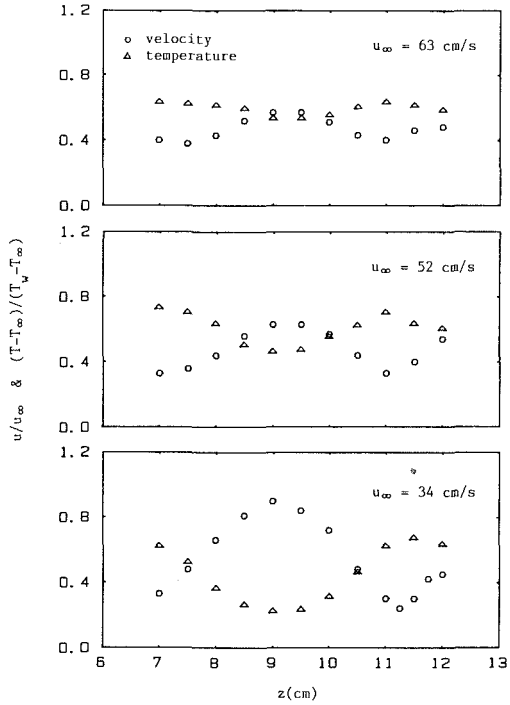

Fig. 6 Spanwise distributions of the streamwise velocity component and the temperature ($T_w - T_\infty = 10°C$, $x = 77.9$ cm, $y = 0.5$ cm)

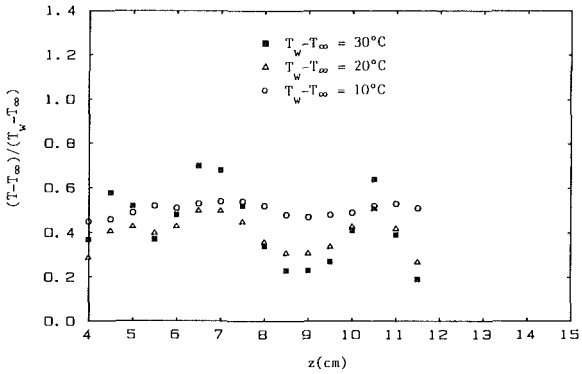

Fig. 7 Spanwise temperature distributions ($x = 24.5$ cm, $y = 0.5$ cm, $u_\infty = 34$ cm/s)

instability, in the mainflow, in addition to some numerical errors. It is, however, interesting to note that the results of Wu and Cheng (1976) are in better agreement with the measurements than the results of Moutsoglou et al. (1981).

Flow visualizations revealed the starting point of vortex rolls and the growth of these vortices downstream from the starting point, as was shown in Fig. 1. Velocity and temperature measurements were also made to quantify the behavior of these vortices. From the spanwise measurements at various heights above the plate, it was found that both the streamwise velocity and the temperature exhibit some peaks and valleys that are repeated almost periodically in the spanwise direction corresponding to the vortices that appeared in the flow. The behavior of the spanwise velocity and temperature variations at a given streamwise location x, for different y distances above the heated surface, are shown respectively in Figs. 3 and 4. As can be seen from these figures, the differences in magnitude between the peaks and the valleys for the streamwise velocity and the temperature are higher close to the surface and that difference diminishes gradually as the free stream is approached. It is also interesting to note that the streamwise velocity inside the boundary layer (i.e., at 1/6 the boundary layer thickness from the wall) can be almost equal to the free-stream velocity at the peak value as shown in Fig. 3. A similar statement can be made with reference to the temperature as shown in Fig. 4. It should also be noted that even for the highest wall temperature case (60°C), the free stream was uniform and its turbulence intensity was less than 0.2 percent. When the spanwise variation of the streamwise velocity develops a peak (highest value) the spanwise temperature variation develops a valley (lowest value), and vice versa, as illustrated in Fig. 5. In addition, the streamwise velocity component develops a valley (lowest value) at the location where the vertical velocity component is a maximum, i.e., at the plume part of the vortex. Also, as the strength of the vortex increases (i.e., a smaller u_∞ or a larger $T_w - T_\infty$), the differences between the maximum and minimum of the

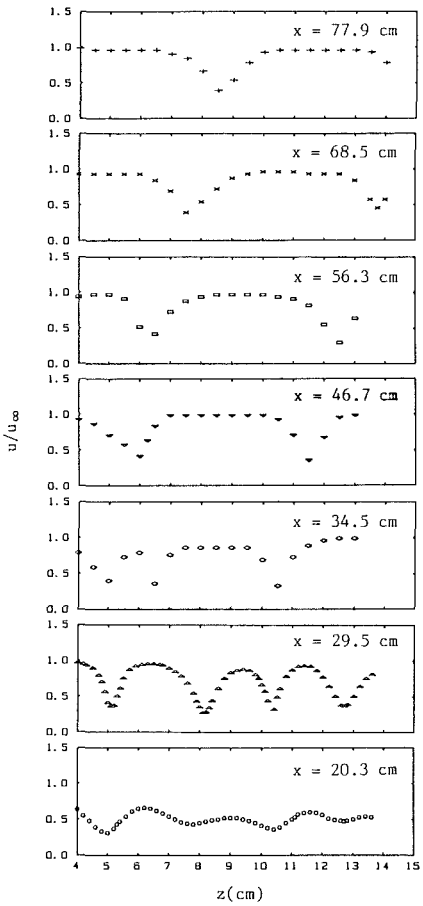

Fig. 8 Spanwise distributions of the streamwise velocity component at various axial locations ($u_\infty = 34$ cm/s, $T_w - T_\infty = 30°C$, $y = 0.5$ cm)

spanwise variation of the streamwise velocity and of the temperature increase as shown in Figs. 6 and 7.

The average distance between two vortices (peaks or valleys) appears to be independent of the free-stream velocity and the plate temperature. This can be observed from Figs. 6 and 7. Although the spacing between the vortices remains relatively unaffected by the different free-stream velocities (Fig. 6), the amplitude of the vortices decreases as the free-stream velocity increases. This is due to the fact that as the free-stream velocity increases, the boundary layer thickness and the buoyancy parameter decrease, thus developing a smaller vortex. Figure 7 illustrates the effect of different levels of heating on the strength of the vortices. It is clear from this figure that vortices gain strength as the temperature difference between the plate and the free stream, $(T_w - T_\infty)$, is increased. Different levels of heating, however, did not change the spacing between the vortices noticeably, as long as they were in the stable vortex flow regime and the vortices did not start to meander. The spacing between the vortices also seems to be independent of the downstream coordinate as long as the measurements are confined to the stable transition regime (regime of stable vortices). This is clearly demonstrated in Fig. 8 for the streamwise locations of $x = 20.3$ cm and 29.5 cm. A similar study of vortex flow on a concave wall (Kamotani et al., 1985) provided similar results regarding the spacing between the vortices as not being a function of the free-stream velocity, plate temperature, and downstream location for the stable vortex flow regime.

As the strength of the vortices intensifies (due to either a smaller free-stream velocity, a larger downstream distance, or a higher level of heating), they become unstable (moving sideways and swaying) and start to combine, causing the appearance of a smaller number of larger vortices. This behavior indicates the start of a second transition regime from the stable three-dimensional vortex flow toward a two-dimensional fully turbulent flow. Such a flow development can be observed from Fig. 8, which illustrates how the stable three-dimensional vortex flow will develop into a two-dimensional fully turbulent flow as the distance increases downstream. The experimental apparatus, however, did not permit an in-depth exploration of the two-dimensional turbulent flow regime.

Streamwise velocity and temperature distributions across the boundary layer were measured at various axial and spanwise locations. These distributions at the various axial locations for spanwise locations corresponding to the peak and the valley of a vortex are shown in Figs. 9 and 10 for the case with a free-stream velocity of $u_\infty = 63$ cm/s and a temperature difference of $(T_w - T_\infty) = 30°C$. These spanwise locations have already been identified as P and V in Fig. 3 for a given vortex. The profiles at the middle section M (between the peak and the valley) of the vortex are not shown in these figures, in order better to illustrate the behaviors at the vortex peak and the valley. It is noted that the solid lines in Figs. 9 and 10 are for the pure forced convection case. At the smallest downstream location of $x = 15.4$ cm, the spanwise velocity and temperature distributions indicate the existence of a two-dimensional, laminar forced convection regime (i.e., no vortices). The axial velocity and temperature profiles at that station, $x = 15.4$ cm, compare very well with the predicted laminar, two-dimensional, mixed convection results of Ramachandran et al. (1983) under small buoyancy forces. The results in this regime deviate only very slightly from the Blasius laminar boundary layer results. In the stable vortex flow regime, the velocity and temperature profiles at the middle section of the vortex always fall between those at the peak and valley sections and are generally close to the pure forced convection profiles. This is illustrated in Fig. 11 for the velocity distributions at $x = 61$ cm, with $u_\infty = 34$ cm/s and $(T_w - T_\infty) = 9°C$. In addition, before the vortices start to meander (e.g., $x < 60$ cm for $u_\infty = 63$ cm/s and $(T_w - T_\infty) = 30°C$, Fig. 9), the velocity distributions at the valley section of the vortex are below the predictions of laminar forced convection boundary layer flow and the reverse is true at the peak section of the vortex as shown in Figs. 9 and 11. The vortex flow brings low axial velocity fluid from the vicinity of the wall upward, where the vortex flow is upward, causing the streamwise velocity to decrease. Similarly, the vortex flow brings high axial velocity fluid from the free stream downward, where the vortex flow is downward, causing the streamwise velocity to increase. The valley section of the vortex corresponds to the center of the plume that is forming that vortex, and thus has higher temperature as shown in Fig. 10.

The velocity and temperature distributions at both a vortex peak ($z = 9.5$ cm) and a vortex valley ($z = 8$ cm), similar to those shown in Figs. 9 and 10, were used to determine the velocity and the temperature gradients at the wall. These gradients were then used to estimate the local friction coefficient C_{fx}, and the local Nusselt number Nu_x, as defined in the nomenclature. It should be noted that the gradient of either the velocity or the temperature at the wall for the peak and most of the valley positions is always equal to or larger than the predicted laminar boundary layer value. This causes the Nusselt number and the friction coefficient in the vortex flow regime to always be equal to or larger than the laminar boundary layer value. The velocity and the temperature gradients, however, at a vortex peak (temperature valley) are always larger than those measured at a vortex valley (temperature peak). This is due to the lower vertical velocity components that exist at vortex peak (spanwise temperature valley) locations. The higher vertical velocity at vortex valley

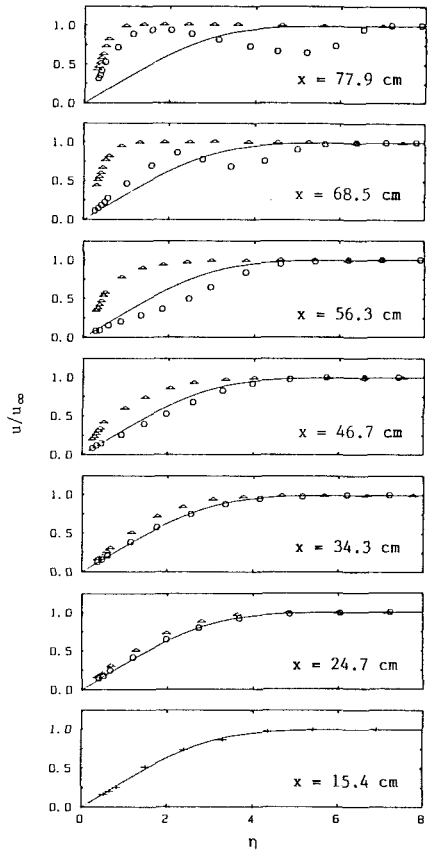

Fig. 9 Velocity profile at various axial locations ($u_\infty = 63$ cm/s, $T_w - T_\infty = 30°C$; △ vortex peak, ○ vortex valley, + no vortex)

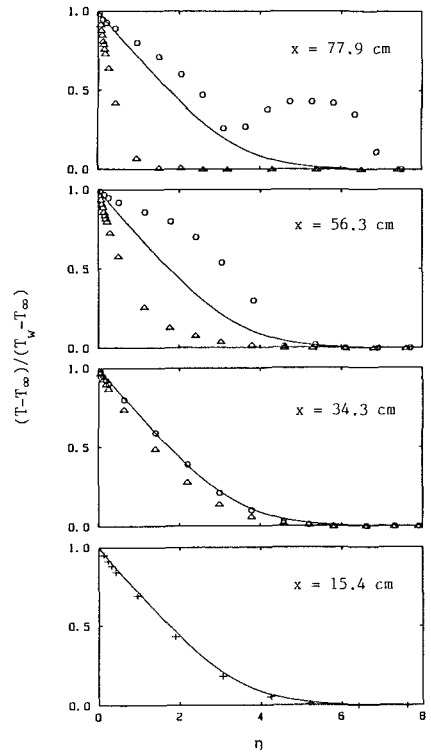

Fig. 10 Temperature profiles at various axial locations ($u_\infty = 63$ cm/s, $T_w - T_\infty = 30°C$; △ vortex peak, ○ vortex valley, + no vortex)

(spanwise temperature peak) promotes mixing and thus lowers the gradients. Thus, a larger Nusselt number and a larger wall friction factor will result at the vortex peak (spanwise

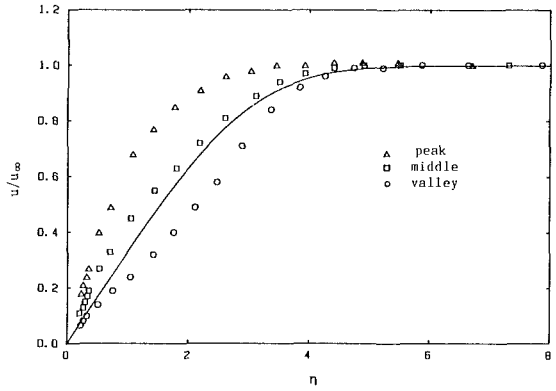

Fig. 11 Velocity profiles ($u_\infty = 34$ cm/s, $T_W - T_\infty = 9°C$, $x = 61$ cm)

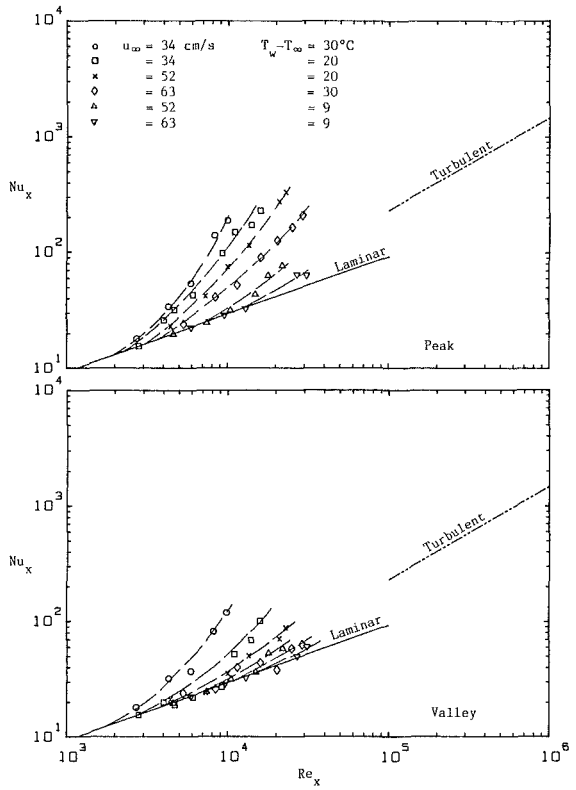

Fig. 12 Local Nusselt numbers corresponding to vortex peak and valley

temperature valley) locations. As mentioned earlier, the experimental uncertainty in the measured Nusselt numbers is estimated to be between 8 and 10 percent, which results mainly from the uncertainty in determining the temperature gradient at the wall. Figure 12 shows the local Nusselt number results, which are compared with those for the laminar forced convection and the fully turbulent forced convection (Kays and Crawford, 1980). The Nusselt number curves for mixed convection start to deviate from the laminar pure forced convection line at a lower Reynolds number than the value of $Re_x = 10^5$ which is normally considered as the critical transition Reynolds number for forced convective flow. This deviation is due to the secondary vortex flow, which develops on the heated plate. The point at which this deviation starts corresponds to the point where the secondary vortex flow develops on the heated plate, causing the heat transfer to increase.

Figures 13 and 14 illustrate, respectively, the ratios of the measured local Nusselt number Nu_x and the local friction fac-

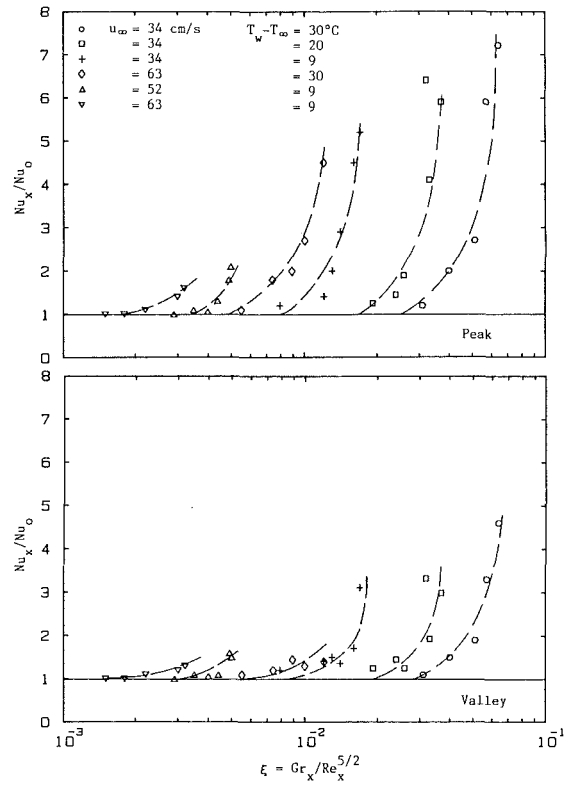

Fig. 13 Local Nusselt number ratio as a function of buoyancy parameter

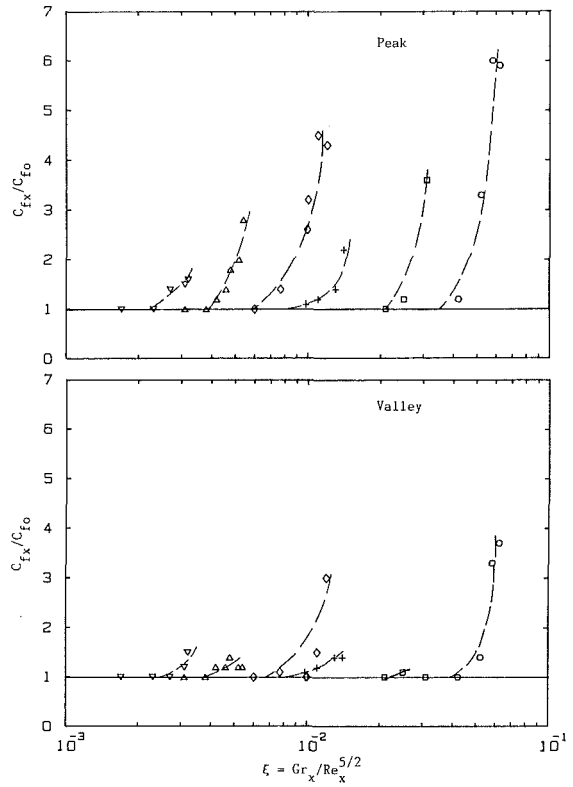

Fig. 14 Local friction factor ratio as a function of buoyancy parameter (notations are the same as in Fig. 13)

tor C_{fx} to their respective pure forced convection values Nu_o and C_{fo} as functions of the buoyancy parameter $\xi = Gr_x/Re_x^{5/2}$. It is clear from these figures that deviations from the two-dimensional laminar forced convection values (for which $Nu_x/Nu_o = C_{fx}/C_{fo} = 1$) occur at a very small value of the buoyancy parameter ξ, where a three-dimensional vortex flow regime starts to develop, which eventually becomes unstable as the value of ξ becomes larger. The fact that the curves in Figs. 13 and 14 do not collapse into a single curve indicates that the buoyancy parameter ξ is not particularly suitable for correlating the results in the three-dimensional vortex flow regime. A comparison between Figs. 13 and 14 reveals that both the local Nusselt number and the local friction factor experience similar effects (i.e., increase) when the vortex flow develops in the transition regime.

Conclusions

A criterion for the onset of vortex instability, the start of the transition from two-dimensional laminar flow to three-dimensional vortex flow, in mixed convection air flow above an isothermally heated horizontal flat plate was established. The vortex flow regime starts with a stable laminar flow region where vortices develop and grow gradually, and ends with an unstable flow region where vortices mix together and collapse to form a two-dimensional turbulent flow regime. The vortex flow behavior in the stable flow regime was quantified by measurements of temperature and velocity distributions. The secondary vortex flow causes a rapid increase in both the Nusselt number and the friction factor. The spanwise distributions of the streamwise velocity and temperature at the peak and the valley of a vortex differ significantly from each other, and also differ from the pure forced convection solution. In the stable vortex flow regime, the distance between two vortices appears to be independent of the free-stream velocity, temperature difference, and downstream location, with both the velocity and the temperature exhibiting similar behavior in the spanwise direction. The difference between the maximum and the minimum streamwise velocity at a given point in the vortex increases as the plate temperature increases or as the free-stream velocity decreases. The spanwise temperature variation develops a peak (i.e., a maximum) when the streamwise velocity in the spanwise direction develops a valley (i.e., a minimum).

Acknowledgments

The study reported in this paper was supported in part by grants from the National Science Foundation (NSF MEA 81-11673 and NSF MEA 83-00785).

References

Badr, H. M., 1984, "Laminar Combined Convection From a Horizontal Cylinder-Parallel and Contra Flow Regimes," *International Journal of Heat and Mass Transfer*, Vol. 27, pp. 15-27.

Chen, T. S., and Mucoglu, A., 1975, "Buoyancy Effects on Forced Convection Along a Vertical Cylinder," ASME JOURNAL OF HEAT TRANSFER, Vol. 97, pp. 198-203.

Chen, T. S., Sparrow, E. M., and Mucoglu, A., 1977, "Mixed Convection in Boundary Layer Flow on a Horizontal Plate," ASME JOURNAL OF HEAT TRANSFER, Vol. 99, pp. 66-71.

Gilpin, R. R., Imura, H., and Cheng, K. C., 1978, "Experiments on the Onset of Longitudinal Vortices in Horizontal Blasius Flow Heated From Below," ASME JOURNAL OF HEAT TRANSFER, Vol. 100, pp. 71-77.

Goertler, H., 1959, "Über eine Analogie zwischen den Instabilitaten Laminarer Grenzchichtstromungen an Konkaven Wanden und an Erwarmten Wanden," *Ingr. Arc*, Vol. 23, pp. 71-78.

Hayashi, Y., Takimoto, A., and Hori, K., 1977, "Heat Transfer in Laminar, Mixed Convection Flow Over a Horizontal Flat Plate" [in Japanese], *Proceedings of the 14th Japan Heat Transfer Symposium*, pp. 4-6.

Imura, H., Gilpin, R. R., and Cheng, K. C., 1978, "An Experimental Investigation of Heat Transfer and Buoyancy Induced Transition From Laminar Forced Convection to Turbulent Free Convection Over a Horizontal Isothermally Heated Plate," ASME JOURNAL OF HEAT TRANSFER, Vol. 100, pp. 429-434.

Kamotani, Y., Lin, J. K., and Ostrach, S., 1985, "Effect of Destabilizing Heating on Goertler Vortices," ASME JOURNAL OF HEAT TRANSFER, Vol. 107, pp. 877-882.

Kays, W. M., and Crawford, M. E., 1980, *Convective Heat and Mass Transfer*, 2nd ed., McGraw-Hill, New York.

Lee, S. L., Chen, T. S., and Armaly, B. F., 1986, "Mixed Convection Along Isothermal Vertical Cylinders and Needles," *Proceedings of the 8th International Heat Transfer Conference*, Paper No. NM21.

Lloyd, J. R., and Sparrow, E. M., 1970, "Combined Forced and Free Convection Flow on Vertical Surfaces," *International Journal of Heat and Mass Transfer*, Vol. 13, pp. 434–438.

McCormack, P. D., Welker, H., and Kelleher, M., 1970, "Taylor-Goertler Vortices and Their Effect on Heat Transfer," ASME JOURNAL OF HEAT TRANSFER, Vol. 92, pp. 101–112.

Merkin, J. H., 1969, "The Effect of Buoyancy on the Boundary Layer Flow Over a Semi-infinite Vertical Flat Plate in a Uniform Free Stream," *Journal of Fluid Mechanics*, Vol. 35, pp. 439–450.

Moharreri, S. S., 1986, "Laser-Doppler and Hot-Wire Measurements in Convective Flows," Master's Thesis, University of Missouri, Rolla, MO.

Moutsoglou, A., Chen, T. S., and Cheng, K. C., 1981, "Vortex Instability of Mixed Convection Flow over a Horizontal Flat Plate," ASME JOURNAL OF HEAT TRANSFER, Vol. 103, pp. 257–261.

Mucoglu, A., and Chen, T. S., 1977, "Analysis of Combined Forced and Free Convection Across a Horizontal Cylinder," *Canadian Journal of Chemical Engineering*, Vol. 55, pp. 265–271.

Osborne, D. G., and Incropera, F. P., 1985a, "Laminar, Mixed Convection Heat Transfer for Flow Between Horizontal Parallel Plates With Asymmetric Heating," *International Journal of Heat and Mass Transfer*, Vol. 28, pp. 207–217.

Osborne, D. G., and Incropera, F. P., 1985b, "Experimental Study of Mixed Convection Heat Transfer for Transitional and Turbulent Flow Between Horizontal, Parallel Plates," *International Journal of Heat and Mass Transfer*, Vol. 28, pp. 1337–1344.

Ramachandran, N., 1983, "Measurements, and Predictions of Laminar Mixed Convection From Flat Surfaces," Master's Thesis, University of Missouri, Rolla, MO.

Ramachandran, N., Armaly, B. F., and Chen, T. S., 1983, "Mixed Convection Over a Horizontal Heated Flat Plate," ASME JOURNAL OF HEAT TRANSFER, Vol. 105, pp. 420–423.

Ramachandran, N., Armaly, B. F., and Chen, T. S., 1985, "Measurements and Predictions of Laminar Mixed Convection Flow Adjacent to a Vertical Surface," ASME JOURNAL OF HEAT TRANSFER, Vol. 107, pp. 636–641.

Sparrow, E. M., and Minkowycz, W. J., 1962, "Buoyancy Effects on Horizontal Boundary-Layer Flow and Heat Transfer," *International Journal of Heat and Mass Transfer*, Vol. 5, pp. 505–511.

Tani, I., 1962, "Production of Longitudinal Vortices in the Boundary Layer Along a Concave Wall," *Journal of Geophysics Research*, Vol. 67, pp. 3075–3080.

Turner, J. S., 1960, "A Comparison Between Buoyant Vortex Rings and Vortex Pairs," *Journal of Fluid Mechanics*, Vol. 7, pp. 419–433.

Wang, X. A., 1982, "An Experimental Study of Mixed, Forced, and Free Convection Heat Transfer From a Horizontal Flat Plate to Air," ASME JOURNAL OF HEAT TRANSFER, Vol. 104, pp. 139–144.

Wilks, G., 1973, "Combined Forced and Free Convection Flow on Vertical Surfaces," *International Journal of Heat and Mass Transfer*, Vol. 16, pp. 1958–1964.

Wu, R. S., and Cheng, K. C., 1976, "Thermal Instability of Blasius Flow Along Horizontal Plates," *International Journal of Heat and Mass Transfer*, Vol. 19, pp. 907–913.

Experimental Investigation of Laminar Mixed Convection in Tubes With Longitudinal Internal Fins

I. M. Rustum
Graduate Student.

H. M. Soliman
Associate Professor.
Mem. ASME

Department of Mechanical Engineering,
University of Manitoba,
Winnipeg, Manitoba, Canada R3T 2N2

Experiments were performed to study the pressure drop and heat transfer characteristics for laminar flow in a smooth tube and four tubes with internal longitudinal fins, with emphasis on showing how the experimental results relate to previous analytical predictions. Measured quantities include the fully developed friction factor, local and fully developed Nusselt numbers. Good agreements were obtained between the friction factor results and previous analytical predictions, and between Nusselt number results for the smooth tube and previous experiments. Free convection is shown to have a strong influence on heat transfer in finned tubes and the results approach the forced-convection predictions as Rayleigh number decreases. Internal fins appear to retard the onset of significant free convective currents; however, once initiated, a faster rate of heat transfer enhancement occurs compared to the smooth tube. An empirical correlation of fully developed Nusselt number is presented taking into account the influences of tube geometry.

Introduction

An interesting feature of the literature on laminar flow and heat transfer in internally finned tubes is that there has been very little (if any) correlation between experimental and analytical results. The purpose of this paper is to report that results of a detailed experiment on the laminar pressure drop and heat transfer characteristics of internally finned tubes, and more importantly, to relate these results to those reported in analytical studies.

Previous experiments on the laminar side include the extensive one by Watkinson et al. (1975), where eighteen tubes with straight and spiral fins and two smooth tubes were tested using oil as the working fluid. The boundary condition of uniform wall temperature axially and circumferentially was imposed by condensing steam on the outer surface. Measurements of the overall friction factor and Nusselt number were made across 2.44-m heated sections. These results provided useful information on the degree of enhancement by finned tubes over smooth tube conditions and the influence of tube geometry on performance. However, these results could not be compared with the available analytical studies for the following two reasons: (1) The experiments contain, unavoidably, effects of mixed free and forced convection, while all analytical studies assumed pure forced convection, and (2) the measured overall friction and Nusselt numbers correspond to developing and fully developed regions of the test sections, while most of the previous analytical studies were limited to the fully developed region. Similar experimental investigations where the overall performance of internally finned tubes was studied under laminar flow conditions were reported by Hilding and Coogan (1964), and Heeren and Wegscheider (1967).

The first results of local Nusselt number in the developing region of internally finned tubes appear to be those reported by Marner and Bergles (1978). Limited data were presented for one electrically heated tube using water ($4 < Pr < 7$) and ethylene glycol ($40 < Pr < 100$) as test fluids. Based on their results, Marner and Bergles (1978) concluded that Prandtl number has a strong influence on heat transfer. They also noted a large discrepancy between their experimental results and the analytical predictions of Nusselt number for fully developed flow with constant heat flux. However, the possible influence of free convection was not considered in this study and the values of Grashof number were not reported.

In turbulent flow, the situation is different in terms of analytical-experimental correlation. Patankar et al. (1979) produced analytical predictions for fully developed forced convection in internally finned tubes, which were found to be in reasonable agreement with the experimental data. Keeping in mind that for turbulent flow the entrance lengths are very short and free convection does not have a strong influence on heat transfer, the agreement between data and analysis is not surprising. Unfortunately, the entrance and free convective effects can be very significant for laminar flow and must be taken into consideration.

The objective of this experiment is to generate data for the fully developed friction factor, as well as developing and fully developed Nusselt numbers for a group of internally finned tubes using the boundary condition of uniform heat input axially. A strong emphasis is placed on the effects of geometry and free convection on the heat transfer results. Comparisons are made between different measured quantities and their respective analytical predictions whenever possible.

Experimental

Experimental Setup. A closed-loop test facility (shown schematically in Fig. 1) was designed and constructed using distilled water as the working fluid. Controllable amounts of water were circulated through the system by a centrifugal pump with a bypass line. Measurements of the bulk temperature were made upstream of the test section and in the mixing chamber downstream of the test section using copper-constantan thermocouples. Five horizontal test sections were used, each consisting of a hydrodynamic entrance length and a heated length where predetermined amounts of a-c electric power were supplied. Following the test section, the water was cooled in one or two double-pipe, counterflow heat exchangers using city water as a heat sink. The flow rate of the

Contributed by the Heat Transfer Division for publication in the JOURNAL OF HEAT TRANSFER. Manuscript received by the Heat Transfer Division January 6, 1987. Keywords: Finned Surfaces, Mixed Convection.

Table 1 Detailed dimensions of test tubes

Tube number	1	9	10	13	14
Outside diameter D_o, mm	21.3	12.7	9.53	9.53	15.9
Inside diameter, D_i, mm	15.9	10.3	8.0	7.04	13.9
Fin height y, mm	—	1.28	1.27	1.15	1.50
Number of fins M	—	10	16	10	10
Relative fin height H	—	0.248	0.318	0.325	0.216
Flow area A_f, mm^2	198.6	73.6	40.6	29.9	137.0
Surface area A_s, mm^2/mm	50.0	54.0	60.0	35.2	67.3
Hydraulic diameter D_h, mm	15.9	5.45	2.71	3.39	8.15

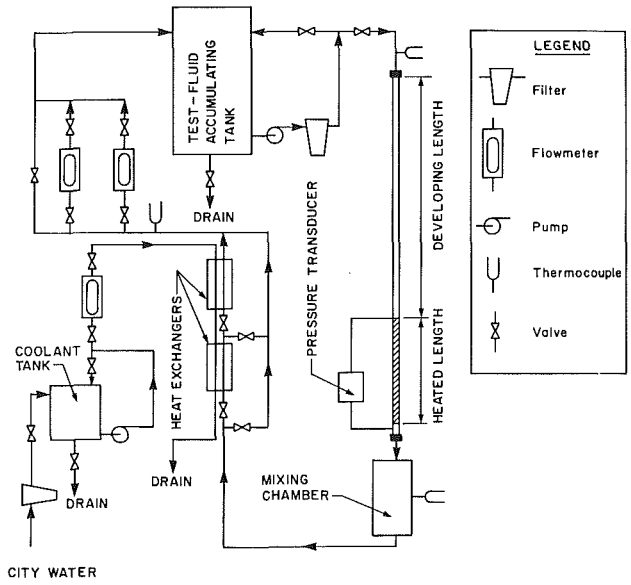

Fig. 1 Schematic diagram of experimental setup

test fluid was measured by two variable-area type flowmeters with overlapping ranges (0-18 cm^3/s and 0-70 cm^3/s) before returning to the accumulating tank.

Test Section. Four copper tubes with internal longitudinal fins, supplied by the Forge-Fin Division of Noranda Metal Industries, and one smooth copper tube were used in this investigation. Geometric details of these tubes are listed in Table 1. The tube numbering suggested by the manufacturer is used for the finned tubes, while the smooth tube is called tube 1. The two major geometric parameters influencing the laminar performance of finned tubes are the number of fins M and the relative fin height H (Nandakumar and Masliyah, 1975; Soliman and Feingold, 1977). Tubes 9, 13, and 14 have the same M but different H, while tubes 10 and 13 have approximately the same H but different M.

The test section for all finned tubes was 3.2 m long, of which the first 2.2 m constituted the hydrodynamic entry length. Pressure drop measurements were made by a pressure transducer with adjustable span across the remaining 1.0 − m length of the test section, of which 0.875 m constituted the heated section. For the smooth tube, the total length of the test section was 5.65 m with the first 3.4 m used for hydrodynamic development and the remaining 2.25 m for the heated section.

Heating was supplied by insulated electric resistance wiring (0.81 − mm diameter and 2.08 ohm/m) wrapped tightly around the tube in two parallel lines to decrease the overall resistance. Input power was regulated by a power variac and measured by a digital wattmeter. The outside wall temperature in the heated section was measured at 23 axial stations with two (24 gage) copper-constantan thermocouples attached at the top and bottom of each station. A small axial distance of 20 mm separated the wall thermocouples at the beginning of the heated section, increasing to 50 mm toward the end. All test sections were covered by a 50-mm layer of fiberglass insulation to minimize heat losses. The different measuring devices (flowmeters, wall and bulk thermocouples, wattmeter, and pressure transducer) were calibrated prior to the beginning of testing.

Procedure and Data Reduction. For each tube, the testing began by isothermal pressure drop runs at increasing Reynolds numbers until the transition from laminar to turbulent flow occurred. These tests provided data for the fully developed

Nomenclature

A_f = flow area
A_s = inner surface area per unit length
c_p = specific heat
D_h = hydraulic diameter $= 4A_f/A_s$
D_i = inside diameter of tube
D_o = outside diameter of tube
f = friction factor, equation (1)
G = mass flux
g = gravitational acceleration
Gr = Grashof number, equation (5)
H = relative fin height $= 2y/D_i$
k = thermal conductivity
L = distance between pressure taps
M = number of fins
Nu_{fd} = fully developed Nusselt number
Nu_o = fully developed Nusselt number for pure forced convection
Nu_x = local Nusselt number, equation (6)
Pr = Prandtl number, equation (4)
q_e = input heat flux
Ra = Rayleigh number, equation (3)
Ra_c = critical Rayleigh number
Ra_m = Rayleigh number at mean bulk temperature
Re = Reynolds number, equation (2)
Re_c = critical Reynolds number
Re_m = Reynolds number at mean bulk temperature
T_{b_x} = bulk temperature at location x
T_{wi_x} = inner wall temperature at location x
x = distance from beginning of heating
X^+ = dimensionless distance, equation (7)
y = fin height
β = half-fin angle
Δp = pressure drop
μ = viscosity
ν = kinematic viscosity
ρ = density

Table 2 Ranges of operating conditions

Tube number	Mass flux G, kg/m^2•s	Input heat flux q_e, kW/m^2	Critical Reynolds number Re_c	Mean Reynolds number Re_m	Mean Rayleigh number $Ra_m \times 10^{-6}$	Mean Prandtl number Pr_m
1	6.6–59.7	0.44–17.8	—	325–1600	1.88–74.8	3.4–6.0
9	17.8–57.7	1.77–24.7	1530	215–920	0.61–16.6	4.3–6.2
10	32.2–80.7	2.27–13.6	1300	360–940	0.47–4.3	3.4–4.8
13	43.8–56.1	2.58–12.9	600	420–600	0.27–2.5	3.5–4.9
14	16.7–61.4	1.31–31.4	2130	280–1360	1.70–73.5	4.0–5.6

friction factor f and the critical Reynolds number for laminar-turbulent transition Re_c. The friction factor and Reynolds number were calculated, respectively, from the following definitions using the inside diameter as the characteristic dimension:

$$f = \rho D_i (\Delta P/L)/(2G^2) \tag{1}$$

and

$$\mathrm{Re} = GD_i/\mu \tag{2}$$

where ρ, D_i, Δp, L, G, and μ are the density, inside diameter, pressure drop, distance between pressure taps, mass flux, and dynamic viscosity, respectively.

Following the isothermal pressure drop tests, heat transfer tests were conducted. For each test section, three to six mass fluxes were selected within the laminar range thus providing a test range for Re. At each mass flux several test runs were conducted corresponding to different input powers to the heated section, thus providing a test range of Rayleigh number Ra for each Re. Rayleigh number is defined by

$$\mathrm{Ra} = \mathrm{Pr} \cdot \mathrm{Gr} \tag{3}$$

where

$$\mathrm{Pr} = \mu c_p/k \tag{4}$$

$$\mathrm{Gr} = g\beta q_e D_i^4/(\nu^2 k) \tag{5}$$

and g, β, q_e, c_p, k, and ν are the gravitational acceleration, coefficient of thermal expansion, input heat flux based on the inside diameter, specific heat, thermal conductivity, and kinematic viscosity, respectively. The ranges of operating conditions for the five test sections are listed in Table 2. For each test run, values of Re, Ra, and Pr changed along the heated section because of increasing bulk temperature. The mean values Re_m, Ra_m, and Pr_m listed in Table 2 were calculated for each test run from equations (2), (3), and (4), respectively, using fluid properties corresponding to the mean bulk temperature.

For each test run, operation continued until steady-state conditions were reached, at which time all readings of wall and bulk thermocouples, flowmeters, and wattmeter were recorded. An overall heat balance was performed by comparing the electrical power input with the rate of heat gain by the test fluid. Only runs with a heat balance error within ±10 percent were accepted; in fact 90 percent of the recorded runs had heat balance errors within ±5 percent. For the acceptance runs, calculations were made of the local Nusselt number Nu_x at all axial stations where wall temperature measurement was made. Definitions of Nu_x and the dimensionless axial distance along the heated section X^+ are given by

$$\mathrm{Nu}_x = q_e D_i/[k(T_{wi_x} - T_{b_x})] \tag{6}$$

and

$$X^+ = x/(D_i \mathrm{Re}\,\mathrm{Pr}) \tag{7}$$

where x, T_{b_x}, and T_{wi_x} are the axial distance from the beginning of heating, local bulk temperature, and local inside wall temperature, respectively. The local bulk temperatures were calculated based on linear change between the measured inlet and outlet bulk temperatures. The local inside wall temperature at any station was calculated by first averaging the two measured outside wall temperatures (which were very close in value) and then assuming one-dimensional radial conduction through the tube wall.

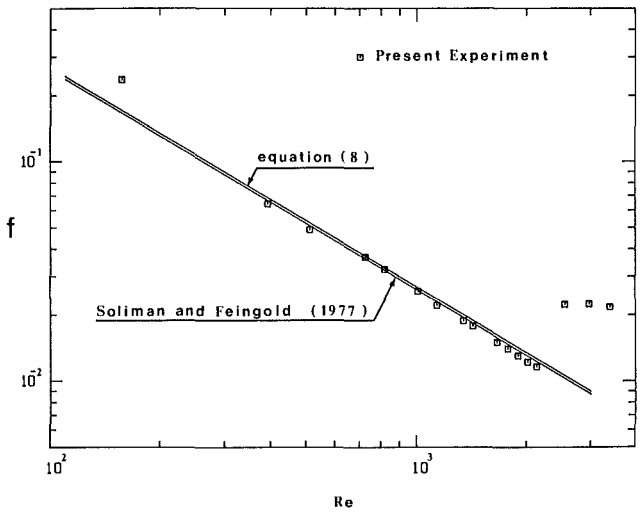

Fig. 2 Fully developed friction factors for tube 14

An uncertainty analysis was performed (Holman, 1978) from which it was determined that the uncertainties for the major parameters calculated during data conversion are as follows: Friction factors are within ± 8 percent, Reynolds numbers are within ± 4 percent, and Rayleigh and Nusselt numbers are within ± 15 percent. Further details about the experimental investigation were documented by Rustum (1984).

Results and Discussion

Fully Developed Friction Factor. A sample of our fully developed friction-factor results is shown in Fig. 2. These results for tube 14 show f decreasing with increasing Re in the laminar region until the critical Reynolds number $Re_c = 2130$ is reached where a sudden jump occurs in the value of f. This sudden jump is attributed to the laminar-turbulent transition. Within the laminar region, the friction factor results for each tube were found to conform closely to the relation $f\mathrm{Re} = C$, where the constant C is dependent on tube geometry. This behavior is consistent with the predictions of previous analytical investigations.

The analytical predictions of Nandakumar and Masliyah (1975) and Soliman and Feingold (1977) are shown in Fig. 2 along with the experimental data. Nandakumar and Masliyah (1975) solved the momentum equation for fully developed laminar flow in tubes with straight internal fins using the finite element technique. The fins were chosen to be of triangular shape, each subtending an angle 2β at the tube centerline. For the range $0.1 \le H \le 0.2$, $6 \le M \le 24$, and 3 deg $\le \beta \le 12$ deg,

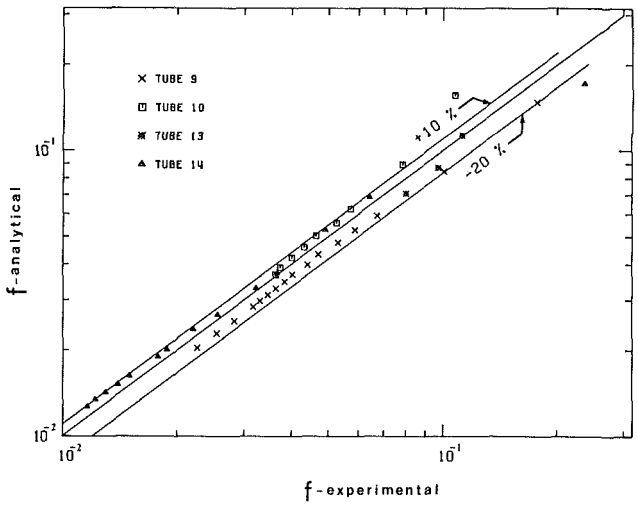

Fig. 3 Values of f compared with Nandakumar and Masliyah (1975)

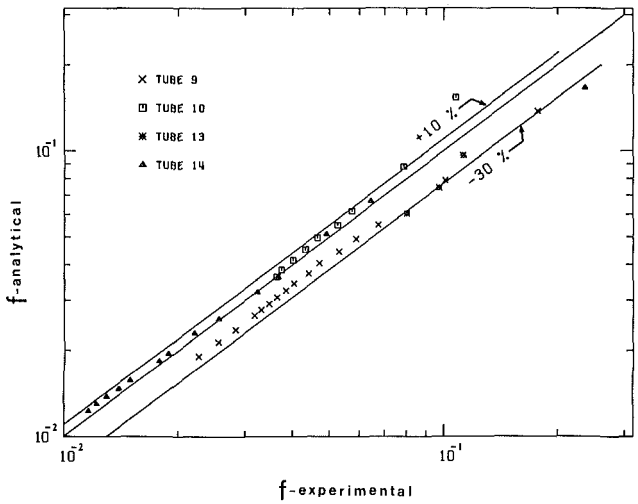

Fig. 4 Values of f compared with Soliman and Feingold (1977)

they correlated their numerical results by the following equation:

$$f\mathrm{Re} = 16.287(D_i/D_h)^{0.8} - 0.5077(D_i/D_h)^2$$

$$-0.049(D_i/D_h)^2[1-\exp\{40\pi H/(MH+2\pi)\}] \quad (8)$$

Soliman and Feingold (1977) developed a series solution for the momentum equation during fully developed laminar flow in tubes with straight internal fins. They assumed a trapezoidal shape for the fins, each subtending an angle 2β at the tube centerline. The value of fRe was found to be a function of M, H, and β and results were reported for a wide range of these geometric parameters. In the present comparisons, the results of Soliman and Feingold (1977) corresponding to $\beta = 3$ deg were used. Figure 2 shows excellent agreement between the data of tube 14 and the predictions of these two analytical studies.

Comparisons between the experimental values of f for all finned tubes and the analytical predictions of Nandakumar and Masliyah (1975) and Soliman and Feingold (1977) at the same Re are shown in Figs. 3 and 4, respectively. These figures show that the analytical predictions of Nandukumar and Masliyah (1975) are mostly -20 to $+10$ percent off the experimental values, while the predictions of Soliman and Feingold (1977) are -30 to $+10$ percent off the experimental values. Both comparisons are quite satisfactory, which enhances our confidence in the predictions as well as the present experimental results.

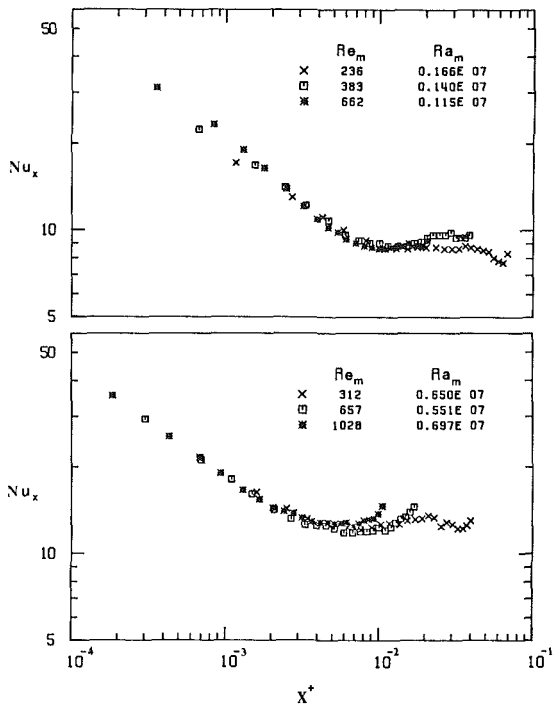

Fig. 5 Influence of Re_m on Nu_x for tubes 9 and 14

Local Heat Transfer. Values of Nu_x at different axial locations X^+ were calculated using definitions (6) and (7). The influence of Reynolds number on the local Nusselt number was explored first by comparing test runs with approximately the same Ra_m but different Re_m. For all tubes, it was found that Re_m has practically no influence on Nu_x throughout the heated section. A sample of these results is shown in Fig. 5.

On the other hand, Rayleigh number was found to have a strong effect on the local heat transfer in all test sections as illustrated by Figs. 6–8. These results emphasize the influence of the free convective currents on the heat transfer characteristics of all test tubes. In Figs. 6–8, the results based on a recent numerical study by Rustum and Soliman (1988) for the case of pure forced convection are shown. Since these numerical results of the local Nusselt number Nu_x and the fully developed Nusselt number Nu_o are both for the case of pure forced convection (i.e., $\mathrm{Ra}_m = 0$), these numerical values should serve as a lower bound for the present experimental results, which correspond to $\mathrm{Ra}_m > 0$.

For a given value of Ra_m, Figs. 6–8 show that Nu_x decreases as X^+ increases in the thermally developing region until the flow reaches the fully developed region, where Nusselt number remains approximately constant with X^+. This behavior is particularly evident at low values of Ra_m. At very high values of Ra_m there appears to be a slight gradual increase in Nu_x along the fully developed region, which is attributed to the change in fluid properties (particularly μ) as a result of heating. In tube 14 for example, the run corresponding to $\mathrm{Ra}_m = 0.735 \times 10^8$ had a change in the local Rayleigh number from 0.376×10^8 at the beginning of heating to 0.112×10^9 at the end of heating, mainly due to the continuous decrease in μ along the heated section. In the analytical investigations of mixed convection inside ducts where a constant value of Nusselt number is normally predicted in the fully developed region, it was always assumed that all properties remained constant in the flow direction.

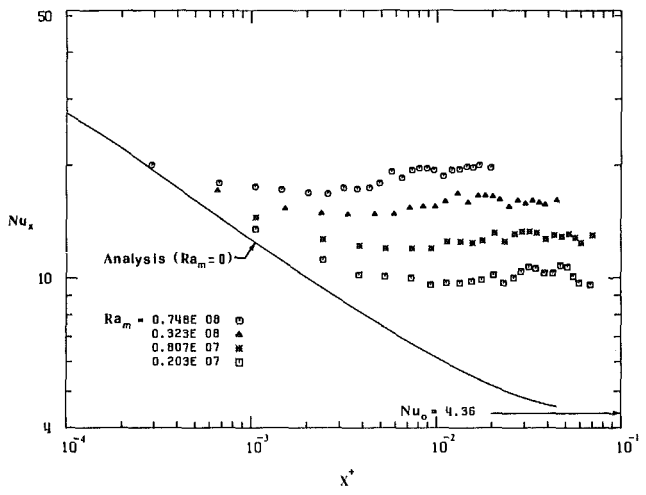

Fig. 6 Influence of Ra_m on Nu_x for tube 1

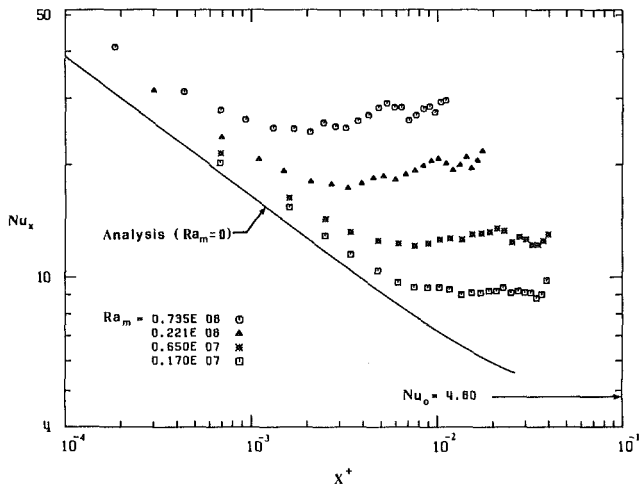

Fig. 8 Influence of Ra_m on Nu_x for tube 14

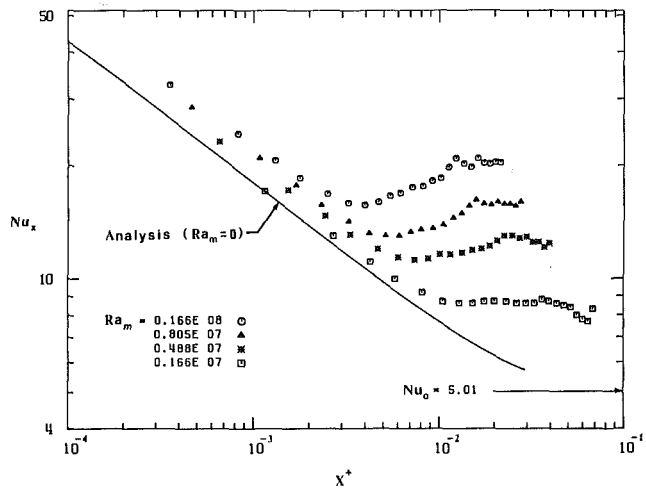

Fig. 7 Influence of Ra_m on Nu_x for tube 9

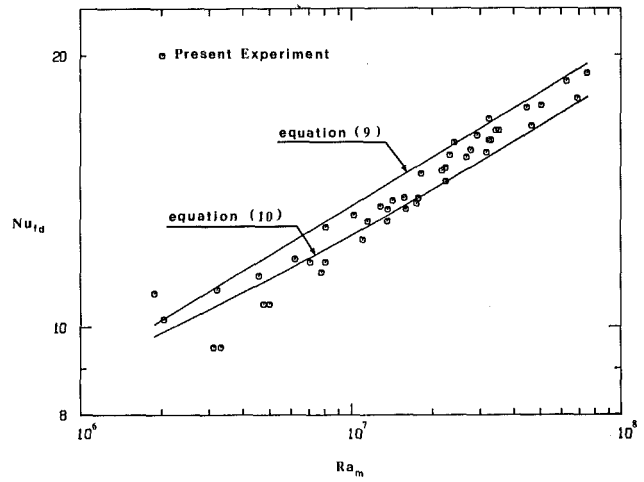

Fig. 9 Fully developed Nusselt numbers for tube 1

Figures 6–8 also show that as Ra_m decreases, the experimental values of Nu_x approach the analytical values for pure forced convection, thus indicating the success of the study by Rustum and Soliman (1988) in defining a lower bound for $Ra_m = 0$. For all test tubes, the influence of Ra_m is much more pronounced in the fully developed region than in the developing region. Another important feature of the results is the influence of free convection on the length of the thermally developing region. It is clear from Figs. 6–8 that the entrance length for any test tube decreases as Ra_m increases. With free convective currents superimposed on the main axial flow, the entrance lengths can be seen to be substantially smaller than the analytical predictions for pure forced convection.

Fully Developed Nusselt Number. Values of Nu_{fd} were obtained for all test runs by calculating the length-mean average of the Nu_x values in the fully developed region. This procedure was adopted in order to even out the influences of experimental scatter and property variations in the flow direction. In most cases (see Figs. 6–8), the heated length between the seventh wall-temperature-measuring station and the end of heating was in the fully developed region.

In order to enhance our confidence in the results, comparison was made between our results for the smooth tube and those of previous experiments. Ede (1961) and Petukhov and Polyakov (1967) conducted experiments similar to the present one using water as the test fluid, uniform heating axially, and similar Re_m and Ra_m ranges. In the fully developed region, Ede (1961) correlated his results by

$$Nu_{fd}/Nu_o = 1 + 0.0322\,(Ra_m/Nu_{fd})^{0.3} \tag{9}$$

where $Nu_o = 4.36$ is the fully developed Nusselt number for pure forced convection. Later, Petukhov and Polyakov (1967) correlated their Nu_{fd} results by

$$Nu_{fd}/Nu_o = [1 + (Ra_m/Ra_c)^4]^{0.045} \tag{10}$$

where $Ra_c = 0.18 \times 10^5$ is the critical Rayleigh number at which Nu_{fd} starts deviating from Nu_o. Comparisons between the present experimental results and the predictions of equations (9) and (10) are shown in Fig. 9. For the present range of Ra_m, Fig. 9 shows that the predictions of equations (9) and (10) are quite close and the present experimental data fall mostly between the two predictions. Accordingly, it is fair to conclude that the present data correlate well with previous experiments.

Although correlations (9) and (10) appear to be different, they do have some common features. Both correlations predict free convection to be insignificant (i.e., $Nu_{fd} = Nu_o$) up to a certain Rayleigh number, after which Nu_{fd} increases significantly with Ra_m. Examination of our data for finned tubes revealed that these characteristics remain valid except that the value of Ra_m at which free convection becomes significant and the rate of change of Nu_{fd} with Ra_m vary from

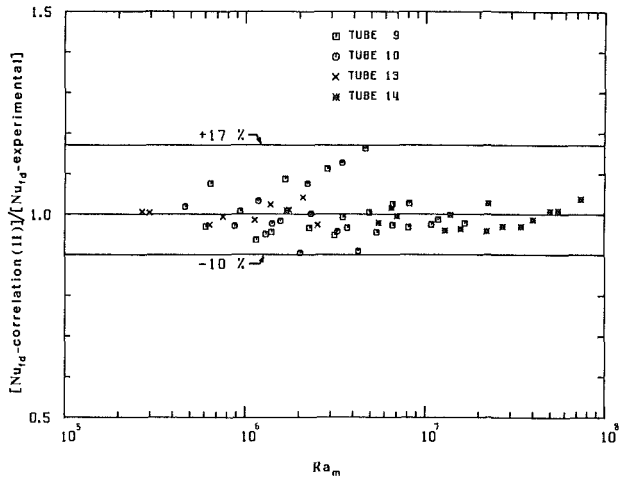

Fig. 10 Comparison between data and correlation (11)

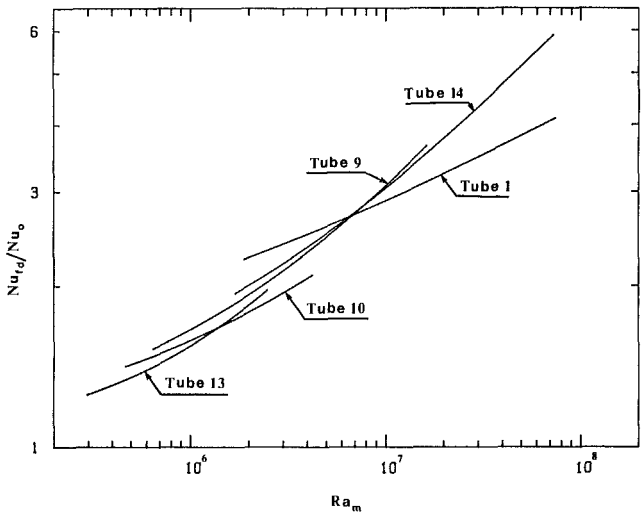

Fig. 11 Effect of tube geometry on heat transfer enhancement

Table 3 Coefficients C_1 and C_2 in equation (11)

Tube number	H	M	Nu_o	$C_1 \times 10^{-6}$	C_2
1	—	—	4.36	0.80	0.25
9	0.248	10	5.01	2.33	0.50
10	0.318	16	4.90	3.45	0.44
13	0.325	10	5.53	2.63	0.63
14	0.216	10	4.80	1.98	0.44

one tube to the other depending on geometry. A simple correlation allowing for the effects of geometry can be written as

$$\mathrm{Nu}_{fd}/\mathrm{Nu}_o = 1 + (\mathrm{Ra}_m/C_1)^{C_2} \qquad (11)$$

where C_1 and C_2 are geometry-dependent coefficients.

A standard computer program based on the least-squares method was used to obtain the values of C_1 and C_2 that provided the best fit between equation (11) and the experimental data of each tube. The resulting values of C_1 and C_2 are listed in Table 3, along with values of Nu_o obtained for each tube based on the analysis of Rustum and Soliman (1988). Figure 10 illustrates the success of equation (11) in correlating the data of finned tubes, which is reflected by the minimum scatter in the figure. It must be pointed out however that correlation (11) is empirical and thus, it is recommended only for geometric and operating ranges similar to those listed in Tables 1 and 2.

An interesting feature of the results in Table 3 is that values of C_1 and C_2 for all internally finned tubes exceeded their respective value for the smooth tube. This means that free convection begins to be significant for finned tubes at higher values of Ra_m than for the smooth tube but the rate of increase of Nu_{fd} with respect to Ra_m is higher for finned tubes than for the smooth tube. Also, for the same M, we note that both C_1 and C_2 increase as H increases. These trends are consistent with the results of recent analytical investigations by Prakash and Patankar (1981), who studied mixed convection in vertical tubes with internal radial fins, and by Mirza and Soliman (1985), who studied mixed convection in the simplified geometry of horizontal tubes with two vertically oriented internal fins. Comparing the results for tubes 10 and 13 we find that at approximately the same H, C_1 increases and C_2 decreases as M increases. Of course, these trends are based on the limited number of tube geometries tested here and further analytical and experimental investigations are necessary to fully determine the influence of internal finning on mixed convection inside horizontal tubes.

The effects of geometry are further illustrated in Fig. 11 using equation (11) with the appropriate values of C_1 and C_2 from Table 3. Since the free convective effects start early in the smooth tube, the value of $(\mathrm{Nu}_{fd}/\mathrm{Nu}_o)$ is higher for the smooth tube than for all finned tubes up to Ra_m of about 5×10^6. Beyond this value of Rayleigh number a reversal of trend is apparent in Fig. 11. Keeping in mind that Nu_o for any finned tube is higher than Nu_o for the smooth tube, it can be concluded that internally finned tubes are capable of significant heat transfer enhancement over smooth tube conditions, particularly at high Rayleigh numbers.

Concluding Remarks

The main objective of this paper is to clarify the apparent discrepancy between analytical and experimental results of laminar pressure drop and heat transfer in internally finned tubes. This was done by generating experimental results of fully developed friction factors, local and fully developed Nusselt numbers using four internally finned tubes and one smooth tube. The friction factor results are in excellent agreement with the analytical predictions.

Two important features were illustrated by the heat transfer results; these are the strong influence of free convection and the dependence of the free-convective effect on tube geometry. For all tubes, the experimental results approach the analytical predictions for pure forced convection as Rayleigh number decreases. To our best knowledge, only limited analytical studies of mixed convection in horizontal internally finned tubes were reported (Mirza and Soliman, 1985) and further studies are needed. The present results indicate that as Ra_m increases, Nu_{fd} increases and the thermal entrance length decreases.

The influence of tube geometry on Nu_{fd} was explored and it was concluded that for all finned tubes, the enhancement in Nu_{fd} due to free convection starts at higher values of Ra_m than for the smooth tube. However, once free convection becomes significant, the rate of increase of Nu_{fd} with respect to Ra_m is higher for finned tubes than for smooth tubes. An empirical correlation of Nu_{fd} was developed with geometry-dependent coefficients and shown to agree with the data with minimum scatter. This correlation is recommended only within geometric and operational ranges tested. Finally, it must be noted that since one test fluid (water) was used in the present experiment, no definite statements can be made on the possible influences of Prandtl number.

Acknowledgments

Financial assistance provided by the Natural Sciences and Engineering Research Council of Canada is gratefully acknowledged.

References

Ede, A. J., 1961, "The Heat Transfer Coefficient for Flow in a Pipe," *Int. J. Heat Mass Transfer*, Vol. 4, pp. 105–110.

Heeren, H., and Wegscheider, J. J., 1967, "Internally Finned Tubes—A Design Tool to Improve Condenser Performance," ASME Paper No. 67-WA/CT-2.

Hilding, W. E., and Coogan, C. H., 1964, "Heat Transfer and Pressure Loss Measurements in Internally Finned Tubes," presented at the ASME National Heat Transfer Conference, *Symposium on Air-Cooled Heat Exchangers*, pp. 57–85.

Holman, J. P., 1978, Experimental Methods for Engineers, McGraw-Hill, New York.

Marner, W. J., and Bergles, A. E., 1978, "Augmentation of Tubeside Laminar Flow Heat Transfer by Means of Twisted-Tape Inserts, Static-Mixer Inserts, and Internally Finned Tubes," *Proceedings, 6th International Heat Transfer Conference*, Vol. 2, pp. 583–588.

Mirza, S., and Soliman, H. M., 1985, "The Influence of Internal Fins on Mixed Convection Inside Horizontal Tubes," *Int. Comm. Heat Mass Transfer*, Vol. 12, pp. 191–200.

Nandakumar, K., and Masliyah, J. H., 1975, "Fully Developed Viscous Flow in Internally Finned Tubes," *The Chemical Engineering Journal*, Vol. 10, pp. 113–120.

Patankar, S. V., Ivanovic, M., and Sparrow, E. M., 1979, "Analysis of Turbulent Flow and Heat Transfer in Internally Finned Tubes and Annuli," ASME JOURNAL OF HEAT TRANSFER, Vol. 101, pp. 29–37.

Petukhov, B. S., and Polyakov, A. F., 1967, "Effect of Free Convection on Heat Transfer During Forced Flow in a Horizontal Pipe," *Teplofizika Vysokikh Temperatur*, Vol. 5, pp. 384–387.

Prakash, C., and Patankar, S. V., 1981, "Combined Free and Forced Convection in Vertical Tubes With Radial Internal Fins," ASME JOURNAL OF HEAT TRANSFER, Vol. 103, pp. 566–572.

Rustum, I. M., 1984, "Experimental Investigation of Laminar Heat Transfer in the Thermal Entrance Region of Internally Finned Tubes," M.Sc. Thesis, University of Manitoba, Winnipeg, Canada.

Rustum, I. M., and Soliman, H. M., 1988, "Numerical Analysis of Laminar Forced Convection in the Entrance Region of Tubes With Longitudinal Internal Fins," ASME JOURNAL OF HEAT TRANSFER, this issue.

Soliman, H. M., and Feingold, A., 1977, "Analysis of Fully Developed Laminar Flow in Longitudinal Internally Finned Tubes," *The Chemical Engineering Journal*, Vol. 14, pp. 119–128.

Soliman, H. M., and Feingold, A., 1978, "Analysis of Heat Transfer in Internally Finned Tubes Under Laminar Flow Conditions," *Proceedings, 6th International Heat Transfer Conference*, Vol. 2, pp. 571–576.

Watkinson, A. P., Miletti, D. L., and Kubanek, G. R., 1975, "Heat Transfer and Pressure Drop of Internally Finned Tubes in Laminar Oil Flow," ASME Paper No. 75-HT-11.

N. Ramachandran[1]
Assoc. Mem. ASME

T. S. Chen
Professor.
Fellow ASME

B. F. Armaly
Professor.
Fellow ASME

Department of Mechanical and Aerospace Engineering,
University of Missouri—Rolla,
Rolla, MO 65401

Mixed Convection in Stagnation Flows Adjacent to Vertical Surfaces

Laminar mixed convection in two-dimensional stagnation flows around heated surfaces is analyzed for both cases of an arbitrary wall temperature and arbitrary surface heat flux variations. The two-dimensional Navier-Stokes equations and the energy equation governing the flow and thermal fields are reduced to a dimensionless form by appropriate transformations and the resulting system of ordinary differential equations is solved in the buoyancy assisting and opposing regions. Numerical results are obtained for the special cases for which locally similar solutions exist as a function of the buoyancy parameter. Local wall shear stress and heat transfer rates as well as velocity and temperature distributions are presented. It is found that the local Nusselt number and wall shear stress increase as the value of the buoyancy parameter increases in the buoyancy assisting flow region. A reverse flow region develops in the buoyancy opposing flow region, and dual solutions are found to exist in that flow regime for a certain range of the buoyancy parameter.

Introduction

In pure forced convection, two-dimensional stagnation flow refers to the flow in the neighborhood of a stagnation line that results from a two-dimensional flow impinging on a surface at right angle and flowing thereafter symmetrically about the stagnation line. Mixed convection in stagnation flows becomes important when the buoyancy forces, due to the temperature difference between the wall and the free stream, become high and thereby modify the flow and the thermal fields significantly. In such flows, the flow and thermal fields are no longer symmetric with respect to the stagnation line. In addition, the local heat transfer rate and the local shear stress can be significantly enhanced or diminished in comparison to the pure forced convection case.

The two-dimensional stagnation flow was first studied by Hiemenz (1911), who developed an exact solution to the governing Navier-Stokes equations. Exact similar solutions for the thermal field were later reported by Eckert (1942). His studies treated the momentum and energy equations as uncoupled and hence did not account for the buoyancy effects on the flow field. Also, no experimental work has been reported in this area. In the present investigation, a general analysis of mixed convection in stagnation flows is carried out for an arbitrary variation of the surface temperature or the surface heat flux condition. Numerical results are reported for cases where a global similarity solution and locally similar solutions exist.

Analysis

Consider a two-dimensional stagnation flow normal to a heated surface, as shown in Fig. 1. The flow in the neighborhood of the stagnation line has the same characteristics irrespective of the shape of the body. This flow is often referred to as the Hiemenz flow. The flow is symmetric about the y-z plane and the flow field away from the heated surface can be expressed by (see Schlichting, 1979)

$$u_\infty = ax; \quad v_\infty = -ay; \quad T = T_\infty \tag{1}$$

and

$$p = p_o - \rho a^2 x^2/2 \tag{2}$$

where p_o is the stagnation pressure, p is the pressure in the flow field, and the constant a in equations (1) and (2) is directly proportional to the free-stream velocity far from the body (U_∞) and inversely proportional to a characteristic length of the body. Thus $a = \kappa U_\infty/L$, where the constant of proportionality κ depends on the exact shape of the body. In the formulation of the problem, the surface is assumed to be either at a temperature $T_w(x)$ or be subjected to a heat flux $q_w(x)$, both of which are arbitrary functions of x. The governing two-dimensional Navier-Stokes equations and the energy equation, written in conventional notations, are

$$u_x + v_y = 0 \tag{3}$$

$$uu_x + vu_y = -\frac{1}{\rho}p_x + \nu(u_{xx} + u_{yy}) \pm g\beta(T - T_\infty) \tag{4}$$

$$uv_x + vv_y = -\frac{1}{\rho}p_y + \nu(v_{xx} + v_{yy}) \tag{5}$$

$$uT_x + vT_y = \alpha(T_{xx} + T_{yy}) \tag{6}$$

with the boundary conditions

$$u = v = 0; \quad T = T_w(x) \text{ or } -k(\partial T/\partial y)_{y=0} = q_w(x) \text{ at } y = 0$$

$$u \to u_\infty; \quad v \to v_\infty; \quad T \to T_\infty \text{ as } y \to \infty \tag{7}$$

In writing equation (4) the Boussinesq approximation is used to account for the density variation in the temperature stratified flow field. Also, the last term on the right-hand side

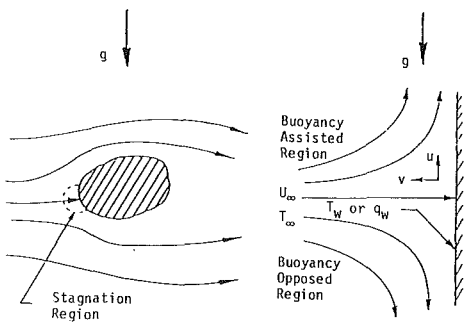

Fig. 1 The flow geometry

[1] Presently at USRA, NASA/MSFC, Huntsville, AL 35806.

Contributed by the Heat Transfer Division for publication in the JOURNAL OF HEAT TRANSFER. Manuscript received by the Heat Transfer Division March 19, 1987. Keywords: Mixed Convection.

of equation (4) represents the influence of the thermal buoyancy force on the flow field, with the plus and minus signs pertaining, respectively, to the buoyancy assisting and the buoyancy opposing flow regions. Figure 1 illustrates such a flow field for a vertical, heated surface with the upper half of the flow field being assisted and the lower half of the flow field being opposed by the buoyancy force. The reverse trend will occur if the plate is cooled below the ambient temperature. The reported results are thus true for both the heated and cooled surface conditions when the appropriate (assisting and opposing) flow regions are selected.

Following the analysis given by Schlichting (1979), equations (4) and (5) can be transformed to yield a single ordinary differential equation

$$\nu f''' + ff'' - f'^2 = -a^2 \mp g\beta(T - T_\infty)/x \tag{8}$$

where

$$u = xf'(y) \text{ and } v = -f(y) \tag{9}$$

and the pressure gradient is given as

$$(p_o - p)/\rho = a^2x^2/2 + v^2/2 - \nu v_y \mp g\beta(T - T_\infty)x \tag{10}$$

It should be noted that the assumption $v = -f(y)$, which is valid for the forced convection case (Hiemenz flow), is assumed to be also valid for mixed convection flow, which is considered in this study. This assumption is required for developing the proposed locally similar solutions, but its validity and accuracy need experimental or other type of verification. It is also to be noted that the minus and plus signs in equation (8) and (10) now correspond to the buoyancy assisting and opposing regions, respectively. Further simplification of the governing equations and the boundary conditions can be achieved by introducing into equations (6)-(8) different transformation variables appropriate for the two surface heating conditions mentioned earlier. These transformations are the same as those presented by Sparrow et al. (1959) in their numerical investigation of mixed convection in boundary layer flows and utilized later by Gunness and Gebhart (1965) and Merkin (1969) to examine laminar mixed convection adjacent to heated surfaces. It should be pointed out, however, that these transformations are applied in this study to the Navier-Stokes equations rather than to the boundary layer equations as was done in the previous studies.

Case 1: Arbitrary Surface Temperature, $T_w(x)$. For this case the following transformation variables are used:

$$\eta = y(u_\infty/\nu x)^{1/2} = y(a/\nu)^{1/2}; \quad \xi = \xi(x) \tag{11}$$

and

$$F(\xi, \eta) = f(y)(\nu a)^{-1/2}; \ \theta(\xi, \eta) = (T - T_\infty)/(T_w - T_\infty) \tag{12}$$

The transformed momentum and energy equations are

$$F''' + FF'' - (F')^2 = -1 \mp [g\beta(T_w - T_\infty)/(a^2x)]\theta \tag{13}$$

$$\theta''/\mathrm{Pr} + F\theta' = [x(dT_w/dx)F'\theta - \alpha\theta(d^2T_w/dx^2)/a]/(T_w - T_\infty) \tag{14}$$

where the prime stands for differentiation with respect to η. It is evident from equation (14) that separation of variables is possible and hence locally similar solutions exist only if

$$d^2T_w/dx^2 = 0 \tag{15}$$

which for a power law variation implies

$$T_w - T_\infty = bx^n; \quad n = 0 \text{ or } 1 \tag{16}$$

where b is a constant. An examination of equations (13) and (14) reveals that the buoyancy parameter, $\xi = g\beta(T_w - T_\infty)/(a^2x)$, is inversely proportional to x for the case of $n = 0$ and is equal to a constant $g\beta b/a^2$ for the case of $n = 1$. In particular, for the case of $n = 1$ and $b = a^2/g\beta$, that constant becomes equal to unity and that case will be referred to as the self-similar case for linear variation of wall temperature. It should be pointed out, however, that since the constant b and the constant a are independent of each other, the condition of $b = a^2/g\beta$ is only one of the numerous possible linear temperature boundary conditions that could be imposed on the wall, i.e., it is a subset of the general case of $n = 1$ where $\xi = g\beta b/a^2$ and for the self-similar case $\xi = 1$. The momentum and energy equations (13) and (14) and boundary conditions along with the restriction of equation (16) can be written as

$$F''' + FF'' - (F')^2 = -1 \mp \xi\theta \tag{17}$$

$$\theta''/\mathrm{Pr} + F\theta' - nF'\theta = 0 \tag{18}$$

$$F(\xi, 0) = F'(\xi, 0) = 0; \quad \theta(\xi, 0) = 1$$

$$F'(\xi, \infty) = 1; \quad \theta(\xi, \infty) = 0 \tag{19}$$

where the buoyancy parameter ξ can be expressed as

Nomenclature

a, b = constants
C_{fx} = local friction factor
$f(y)$ = function of y, equation (9)
$F(\xi, \eta)$ = transformation variable, equation (12)
g = gravitational acceleration
Gr_x = local Grashof number = $g\beta(T_w - T_\infty)x^3/\nu^2$
Gr_x^* = modified local Grashof number = $g\beta q_w x^4/k\nu^2$
n = constant exponent, equations (16) and (28)
h = local heat transfer coefficient
k = thermal conductivity
Nu_x = local Nusselt number = hx/k
p = pressure
p_o = stagnation pressure
Pr = Prandtl number
q = local heat flux
Re_x = local Reynolds number = $u_\infty x/\nu$
T = fluid temperature
u, v = streamwise and normal velocity components
x, y = streamwise and normal coordinates
α = thermal diffusivity
β = coefficient of volumetric thermal expansion
η = transformation variable, equation (11)
θ, ϕ, Φ = dimensionless temperature
κ = proportionality constant
ν = kinematic viscosity
ξ = buoyancy parameter (Case 1), $\mathrm{Gr}_x/\mathrm{Re}_x^2$, equation (20)
ξ^* = buoyancy parameter (Case 2), $\mathrm{Gr}_x^*/\mathrm{Re}_x^{5/2}$, equation (32)
ρ = density

Subscripts

w = condition at the wall
x = differentiation with respect to x
y = differentiation with respect to y
∞ = condition away from the surface

$$\xi = \mathrm{Gr}_x/\mathrm{Re}_x^2 \tag{20}$$

with

$$\mathrm{Gr}_x = g\beta(T_w - T_\infty)x^3/\nu^2, \quad \mathrm{Re}_x = u_\infty x/\nu \tag{21}$$

where $u_\infty = ax$ as in equation (1). The minus and plus signs in equation (17) pertain to the buoyancy assisting and opposing regions, respectively. The physical quantities of interest are the friction factor (i.e., the local wall shear stress) and the local Nusselt number (i.e., the heat transfer rate). They are given by

$$C_{fx}\mathrm{Re}_x^{1/2} = 2F''(\xi, 0) \tag{22}$$

and

$$\mathrm{Nu}_x\mathrm{Re}_x^{-1/2} = -\theta'(\xi, 0) \tag{23}$$

Case 2: Arbitrary Surface Heat Flux, $q_w(x)$. For this case the same η and $F(\xi^*, \eta)$ transformation variables, as given by equation (11), are used. However, the dimensionless temperature is now selected as

$$\phi(\xi^*, \eta) = (T - T_\infty)(u_\infty x/\nu)^{1/2}/(q_w x/k) \tag{24}$$

The transformed momentum and energy equations become equivalent to

$$F''' + FF'' - (F')^2 = -1 \mp [(g\beta q_w/a^2 k)/\mathrm{Re}_x^{1/2}]\phi \tag{25}$$

$$\phi''/\mathrm{Pr} + F\phi' = [x(dq_w/dx)F'\phi - \alpha\phi(d^2q_w/dx^2)/a]/q_w \tag{26}$$

Again, as in Case 1, the separation of variables in equation (26) is possible (i.e., locally similar solutions exist) only if

$$d^2q_w/dx^2 = 0 \tag{27}$$

which for a power law variation implies

$$q_w = cx^n; \quad n = 0 \text{ or } 1 \tag{28}$$

where c is a constant. The momentum and energy equations (25) and (26) and the corresponding boundary conditions along with the restriction of equation (28) can be written as

$$F''' + FF'' - (F')^2 = -1 \mp \xi^*\phi \tag{29}$$

$$\phi''/\mathrm{Pr} + F\phi' - nF'\phi = 0 \tag{30}$$

$$F(\xi^*, 0) = F'(\xi^*, 0) = 0; \quad \phi'(\xi^*, 0) = -1$$

$$F'(\xi^*, \infty) = 1; \quad \phi(\xi^*, \infty) = 0 \tag{31}$$

where ξ^* is the buoyancy parameter for this case and is given by

$$\xi^* = \mathrm{Gr}_x^*/\mathrm{Re}_x^{5/2} \tag{32}$$

with

$$\mathrm{Gr}_x^* = g\beta q_w x^4/k\nu^2 \text{ and } \mathrm{Re}_x = u_\infty x/\nu \tag{33}$$

Equations (25)-(32) reveal that the buoyancy parameter, $\xi^* = (g\beta q_w/a^2k)/\mathrm{Re}_x^{1/2}$, is inversely proportional to x when $n = 0$ and is independent of x and equal to $\xi^* = c[(g^2\beta^2\nu)/a^5k^2]^{1/2}$ when $n = 1$. In particular, when $c = [a^5k^2/(g^2\beta^2\nu)]^{1/2}$ along with $n = 1$, the buoyancy parameter becomes equal to unity (i.e., $\xi^* = 1$), and this case will be referred to as the self-similar case for the linear wall heat flux. Similar to the earlier discussion for case 1, this condition is only one of the many different linear wall heat flux cases that could be imposed and for that reason it will be treated as a subset of the general case of $n = 1$ with $\xi^* = 1$. As mentioned earlier, the minus and plus signs in equation (29) pertain to the buoyancy assisting and opposing regions, respectively. The quantities of interest are the local wall shear stress and the local heat transfer rate. They are given by

$$C_{fx}\mathrm{Re}_x^{1/2} = 2F''(\xi^*, 0) \tag{34}$$

and

$$\mathrm{Nu}_x\mathrm{Re}_x^{-1/2} = 1/\phi(\xi^*, 0) \tag{35}$$

Numerical solutions to the set of equations (17)-(19) for the specified wall temperature case and to the set of equations (29)-(31) for the specified wall heat flux case were obtained for both the $n = 0$ case (uniform wall temperature and uniform wall heat flux) and the $n = 1$ case (linear variation of the wall temperature or the surface heat flux with the streamwise coordinate x), for both the buoyancy assisting and opposing flow regions.

Results and Discussion

The sets of nonlinear ordinary differential equations and the boundary conditions, equations (17)-(19) and (29)-(31), were solved by the fourth-order Runge-Kutta integration scheme along with the Nachtsheim-Swigert shooting technique for the following cases: Case 1, specified wall temperature, and Case 2, specified wall heat flux. Initial values for $F''(\xi, 0)$, $\theta'(\xi, 0)$ for case 1 and $F''(\xi^*, 0)$, $\phi(\xi^*, 0)$ for Case 2 were guessed so that integration of the governing equations yielded solutions that satisfied the boundary conditions asymptotically. The Prandtl number used in all the computations of the locally similar solutions was 0.7 (air).

It should be pointed out that all of the results that are presented in this study are valid only in the small region around the stagnation line, and are not applicable outside that region. Thus an increase in the buoyancy parameter should be interpreted as being due mainly to increase in the temperature difference between the wall and the ambient and/or due to an increase in the wall heat flux, rather than being caused by an increase in the axial distance. Another important point is the fact that this study is limited to only laminar flow conditions and assumes that laminar flow exists throughout the range of the buoyancy parameter presented. The criterion for transition from laminar to turbulent flow needs to be established from experimental observations, which are not available at this time, and these observations will then establish the range of applicability of the results that are presented here. For this reason, the present results should be used, in the absence of experimental data, with caution in estimating the local wall shear stress and the local heat transfer rate for this geometry and flow conditions.

The self-similar cases that were discussed earlier for $n = 1$ with $b = a^2/g\beta$ for linear wall temperature and for $c = [a^5k^2/(g^2\beta^2\nu)]^{1/2}$ for linear wall heat flux were examined for both buoyancy assisting and buoyancy opposing flows in the Prandtl number range $0.7 \le \mathrm{Pr} \le 100$. Results for the local friction factor and the local Nusselt number, $F''(0)$, $-\theta'(0)$ for Case 1 and $F''(0)$, $1/\phi(0)$ for Case 2, respectively, are given in Table 1 and Table 2. As the Prandtl number increases, the thermal boundary layer thickness decreases, resulting in higher values of the local Nusselt number. The reverse trend is seen for the local friction factor, which decreases as the Prandtl number increases. The aforementioned trends are observed for both the buoyancy assisting and opposing situations with the latter case having lower Nusselt numbers and friction factors than the former case. In Table 2, results for $\mathrm{Pr} = 0.7$ for the buoyancy opposing flow case are not listed because the self-similar solution does not exist for this particular case when $\xi^* = 1$. In fact, self-similar buoyancy opposing solutions do not exist for $\mathrm{Pr} = 0.7$ when $\xi^* > 0.975$, as will be discussed later.

The local wall shear stress and the local heat transfer results for the specified wall temperature case, Case 1, are presented in Figs. 2 and 3, respectively, for both the buoyancy assisting and buoyancy opposing flow regions. These figures include results for both the $n = 0$ and the $n = 1$ cases. For the buoyancy

Table 1 Local friction factors and Nusselt numbers for the self-similar cases of linear variation of wall temperature

	Buoyancy assisting flow		Buoyancy opposing flow	
Pr	$F''(0)$	$-\theta'(0)$	$F''(0)$	$-\theta'(0)$
0.7	1.7063	0.7641	0.6917	0.6332
7	1.5179	1.7224	0.9235	1.5403
20	1.4485	2.4576	1.0031	2.2683
40	1.4101	3.1011	1.0459	2.9054
60	1.3903	3.5514	1.0677	3.3527
80	1.3774	3.9095	1.0817	3.7089
100	1.3680	4.2116	1.0918	4.0097

Table 2 Local friction factors and Nusselt numbers for the self-similar cases of linear variation of surface heat flux

	Buoyancy assisting flow		Buoyancy opposing flow	
Pr	$F''(0)$	$1/\phi(0)$	$F''(0)$	$1/\phi(0)$
0.7	1.8339	0.7776	—	—
7	1.4037	1.6912	1.0408	1.5839
20	1.3237	2.4074	1.1359	2.3279
40	1.2919	3.0402	1.1710	2.9755
60	1.2785	3.4850	1.1853	3.4277
80	1.2708	3.8395	1.1934	3.7871
100	1.2658	4.1391	1.1987	4.0901

assisting region, computations were carried out from $\xi = 0$ (no buoyancy effect) to $\xi = 10$. As the buoyancy parameter increases, both the wall shear stress and the local heat transfer rate increase, this increase being substantial in comparison to the no-buoyancy effect (forced convection) value. This is similar to other mixed convection results and it is due to the increased velocity caused by the assisting buoyancy forces. The wall shear stress for the $n = 0$ case is slightly larger than the corresponding value for the $n = 1$ case at the same value of the buoyancy parameter and the reverse trend is true for the local Nusselt number. This is in agreement with other laminar convective heat transfer studies.

For the buoyancy opposing flow region, as the buoyancy parameter increases, the adverse pressure gradient increases, which causes the flow to separate and eventually to reverse. Since the exact Navier–Stokes equations are solved, this flow reversal can be numerically simulated and can be seen in the velocity distributions that are discussed and presented later in this section. The opposing buoyancy force decreases the velocity near the wall and causes the local wall shear stress and the local heat transfer rate to decrease with increasing value of the buoyancy parameter. In the buoyancy opposing flow region, solutions do not exist beyond some critical value of the buoyancy parameter (solutions exist for $\xi < 1.884$ with $n = 0$ and for $\xi < 2.203$ with $n = 1$), and dual solutions exist for some range of the buoyancy parameters (dual solutions exist when $1.67 < \xi < 1.884$ for $n = 0$ and when $1.9 < \xi < 2.203$ for $n = 1$). As the buoyancy parameter increases, the wall shear stress decreases and becomes equal to zero at $\xi = 1.71$ for $n = 0$ and at $\xi = 1.96$ for $n = 1$. The boundary layer separates at that point, and for larger buoyancy parameters, the opposing buoyancy force causes the flow to reverse and the wall shear stress to become negative. Thus, a critical buoyancy parameter is reached, as mentioned above, where $d\theta'(\xi, 0)/d\xi$ approaches minus infinity and beyond which solutions do not exist. A decrease in the buoyancy parameter from that critical value develops a dual solution, which continues until the wall shear stress in that reverse flow region reaches a minimum value.

The existence of dual solutions in mixed convection boundary layer flow was pointed out by Hoog et al. (1984) and also by Afzal et al. (1984). Such conditions for two-dimensional stagnation flow has not been reported in the literature. As discussed by Afzal et al. (1984), it seems plausible that depending on the manner in which the temperature field is imposed, one or the other dual solutions could be approached after different adjustment phases, causing the solution in the neighborhood of the separation region to be dual.

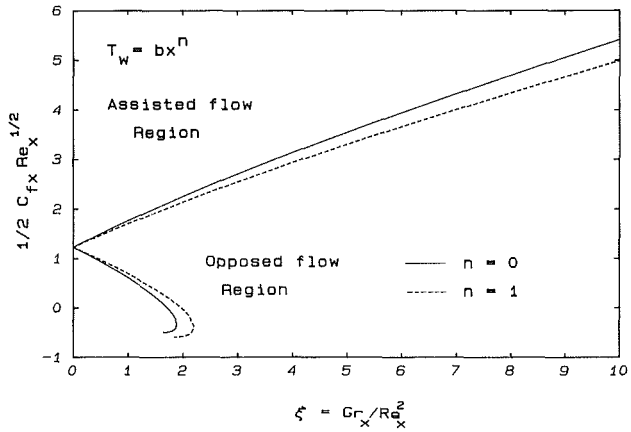

Fig. 2 Local wall shear stress results, Case 1

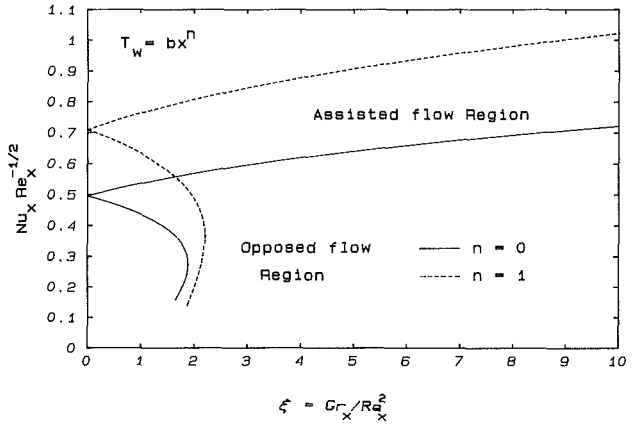

Fig. 3 Local Nusselt number results, Case 1

The local wall shear stress and the local heat transfer results for the specified wall heat flux case, Case 2, are presented in Figs. 4 and 5, respectively, for the buoyancy assisting and the buoyancy opposing regions, for both $n = 0$ and $n = 1$. The behavior and the trends for Case 2 are similar to those that were discussed earlier for Case 1. In the buoyancy opposing flow region, solutions do not exist beyond some critical value of the buoyancy parameter (solutions exist for $\xi^* < 0.61$ when $n = 0$ and for $\xi^* < 0.975$ when $n = 1$), and dual solutions exist for some range of the buoyancy parameter (dual solutions exist when $0.25 < \xi^* < 0.61$ for $n = 0$ and when $0.3 < \xi^* < 0.975$ for $n = 1$). For this case, the wall shear stress becomes equal to zero at the critical buoyancy parameter of $\xi^* = 0.61$ for $n = 0$ and at $\xi^* = 0.975$ for $n = 1$. This behavior is different from that observed for Case 1, where solutions exist for larger buoyancy parameters than the one identifying the zero wall shear stress or the start of the reverse flow region. In the present case, Case 2, the reverse flow region occurs only in the dual solution domain. The solution is again terminated when the wall shear stress in the reversed flow region reaches a minimum value.

A comparison of the results reveals that for both the $n = 0$ (uniform wall temperature or uniform wall heat flux) and $n = 1$ (linear wall temperature or linear wall heat flux) cases, the local Nusselt numbers are higher in Case 2 (specified wall heat flux) than in Case 1 (specified wall temperature) in the buoyancy assisted region. The reverse trend is true in the buoyancy opposed region. These trends are similar to those observed in boundary layer flow calculations of mixed convection where the uniform surface heat flux yields higher heat transfer rates than the uniform surface temperature case in the

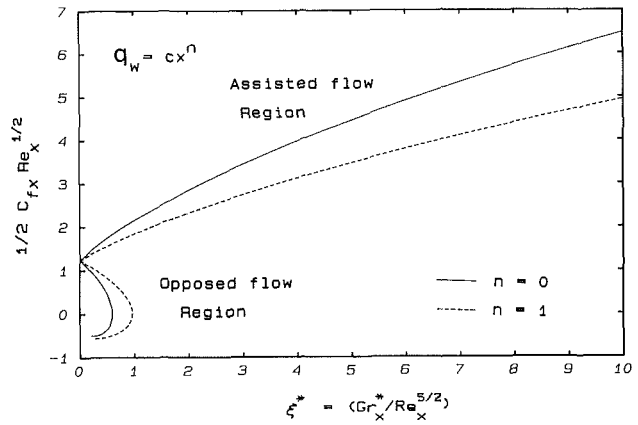

Fig. 4 Local wall shear stress results, Case 2

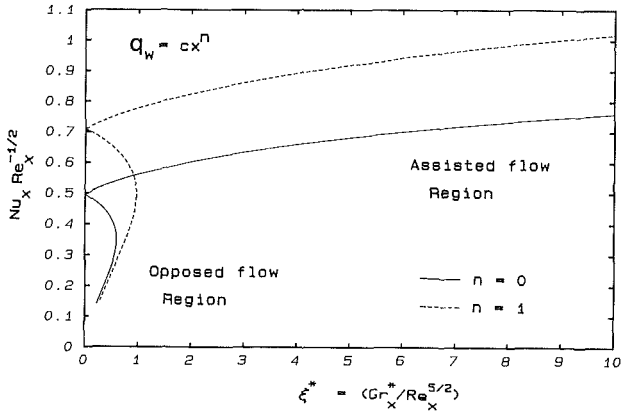

Fig. 5 Local Nusselt number results, Case 2

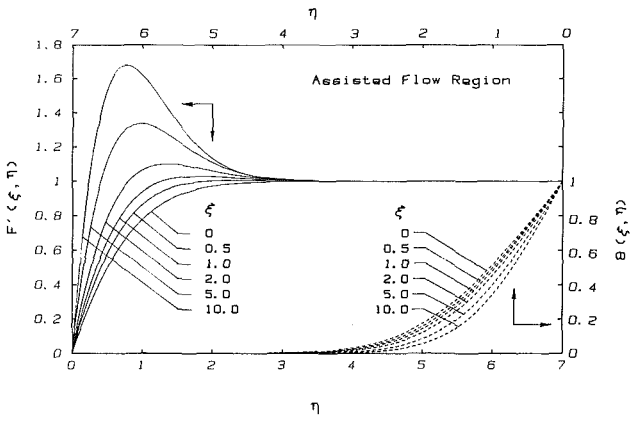

Fig. 6 Velocity and temperature distributions in the buoyancy assisting region, Case 1, $n = 0$

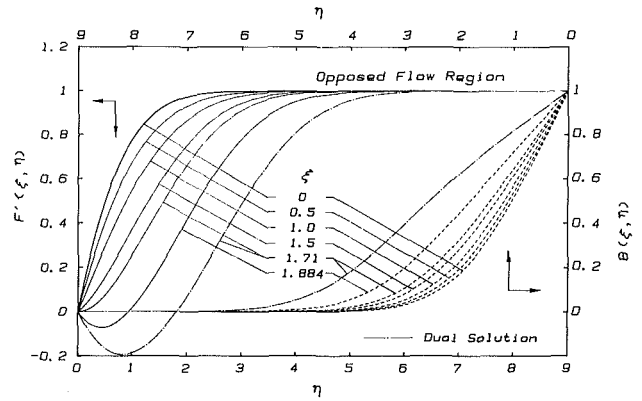

Fig. 7 Velocity and temperature distributions in the buoyancy opposing region, Case 1, $n = 0$

buoyancy assisting region. A reverse trend is observed in the buoyancy opposing flow region.

Representative velocity and temperature profiles for the buoyancy assisting region of Case 1 with $n = 0$ are shown in Fig. 6. Significant velocity overshoot beyond the free-stream value is observed at higher values of the buoyancy parameter. Augmented wall shear stress and local heat transfer rate are evident from the increased velocity and temperature gradients at the wall as the value of the buoyancy parameter is increased. The velocity and temperature distributions for the buoyancy opposing region for Case 1 with $n = 0$ are presented in Fig. 7. It can be seen from that figure that the velocity and the temperature gradients at the wall decrease as the buoyancy parameter increases, causing a decrease in the wall shear stress and in the surface heat transfer rate. Also, flow separation (characterized by zero wall shear stress) occurs when $\xi = 1.71$. Further increase in the value of the buoyancy parameter causes the flow to reverse until $\xi = 1.884$ when $d\theta'(\xi, 0)/d\xi$ approaches minus infinity. A sample of the dual solutions is also shown in Fig. 7 for $\xi = 1.71$.

Conclusion

The Navier–Stokes and the energy equations (not the boundary layer equations) are solved for the two-dimensional, buoyancy-affected, stagnation flow that develops adjacent to a vertical heated surface. Locally similar solutions are found to exist for the boundary condition of uniform wall temperature or uniform surface heat flux ($n = 0$) and also for the boundary condition where the wall temperature or the wall heat flux varies linearly with the streamwise coordinate ($n = 1$). Results are presented for both the buoyancy assisting and the buoyancy opposing flow regions. Similar to other mixed convection studies, the local wall shear stress and the local wall heat flux increase with increasing buoyancy parameter in the buoyancy assisting flow regime, and the reverse trend is true for the buoyancy opposing flow regime. A reversed flow region is predicted in the buoyancy opposing flow regime, in addition to a dual solution for some range of the buoyancy parameter. Solutions do not exist for buoyancy parameters that are larger than a specified critical value in the buoyancy opposing flow regime.

Acknowledgments

This study was supported in part by Grant No. MEA 83-00785 from the National Science Foundation.

References

Afzal, N., and Hussain, T., 1984, "Mixed Convection Over a Horizontal Plate," ASME JOURNAL OF HEAT TRANSFER, Vol. 106, pp. 240–241.

Eckert, E. R. G., 1942, "Die Berechnung des Wärmeüberganges in der laminaren Grenzschicht umströmter Körper," *VDI Forschungsheft*, p. 416.

Gunness, R. C., and Gebhart, B., 1965, "Combined Forced and Natural Convection Flow for the Wedge Geometry," *International Journal of Heat and Mass Transfer*, Vol. 8, pp. 43–53.

Hoog, F. R., Laminger, B., and Weiss, R., 1984, "A Numerical Study of Similarity Solutions for Combined Forced and Free Convection," *ACTA Mechanica*, Vol. 51, pp. 139–149.

Hiemenz, K., 1911, "Dei Grenzschicht an einem in den gleichförmigen Flüssigkeitsstrom eingetauchten geraden Kreiszylinder," *Dingl. Polytech. Journal*, Vol. 32, pp. 321–410.

Merkin, J. H., 1969, "The Effect of Buoyancy Forces on the Boundary Layer Flow over a Semi-infinite Vertical Flat Plate in a Uniform Free Stream," *Journal of Fluid Mechanics*, Vol. 35, pp. 439–450.

Schlichting, H., 1979, *Boundary Layer Theory*, McGraw-Hill, New York.

Sparrow, E. M., Eichorn, R., and Gregg, J. L., 1959, "Combined Forced and Free Convection in a Boundary Layer Flow," *Physics of Fluids*, Vol. 2, pp. 319–328.

Non-Darcian Convection in Cylindrical Packed Beds

M. L. Hunt
Research Assistant.

C. L. Tien
A. Martin Berlin Professor.
Fellow ASME

Department of Mechanical Engineering,
University of California,
Berkeley, CA 94720

Non-Darcian transport describes the nonuniform flow and thermal anomalies often found in flow through packed beds. These effects include the high-flow-rate inertial pressure loss, near-wall porosity variation, solid-boundary shear, and thermal dispersion. Inclusion of these effects significantly alters the velocity and temperature profiles from those predicted by models using uniform or Darcian flow. In this paper, the non-Darcian formulation is used to predict the heat transfer rates for cylindrical packed beds such as chemical reactors. Traditional analyses of chemical reactors assume slug flow and must include a temperature-slip boundary condition to predict the measured temperature profiles. The present analysis predicts similar temperature variations by allowing the velocity and diffusivity to vary across the bed. The results agree with experimental data for chemical reactors and do not depend on the extensive experimental relations needed in conventional reactor models.

Introduction

This paper examines momentum and thermal transport in chemical reactors with inert packing. Many experimental and theoretical results, such as those of Wakao and Kaguei (1982), Froment and Bischaff (1979), Li and Finlayson (1977), and Schlunder (1978), predict heat transfer rates for these nonreacting systems. However, most of these reactor studies assume slug flow and uniform conductivity throughout the bed. Consequently, the analyses rely on empirical temperature-slip heat transfer coefficients to incorporate the steep temperature gradient observed near the walls. These slug-flow analyses are based solely on empirical relations and generally are limited to fully developed flow in specific reactor sizes. With proper experimental data, they agree quite well with measurements. However, when the results are applied to reacting beds, the temperature-slip predictions often do not agree with experimental data.

This work reconsiders the chemical reactor problem for inert beds; however, the analysis is based on the volume-averaged governing equations that include the non-Darcian effects as discussed in Vafai and Tien (1981) and Tien and Hunt (1987). These effects describe the nonuniform flow phenomena observed at large Reynolds numbers or through bounded porous media. The governing non-Darcian momentum equation equates the pressure gradient across the bed to a sum of the Darcian resistance caused by viscous drag along the solid particles, the high-flow-rate inertial pressure loss, and the viscous resistance from the solid boundary. The inclusion of the last term requires that the velocity be zero at the bounding surface. Due to the variation in packing next to the solid surface, the porosity in the momentum equation varies as shown in the measurements by Benenati and Brosilow (1962) and by Roblee et al. (1958). Chandrasekhara and Vortmeyer (1979), Vafai (1984), and Vortmeyer and Schuster (1983) analyzed this porosity variation and demonstrated how it results in flow channeling close to the solid surface. The present work predicts similar velocity profiles; however, the thermal analysis differs by including transport due to thermal dispersion. The dispersive flux is caused by mixing as the fluid moves around the solid particles. Unlike traditional chemical reactor studies, the porosity, velocity, and effective diffusivity vary with distance from the wall.

Using the non-Darcian analysis with the wall-temperature boundary condition, as opposed to the traditional temperature-slip condition, the governing equations are numerically integrated. The resulting velocity and temperature profiles are shown to agree with existing data from chemical reactor studies. This analysis predicts the fully developed temperature-slip and local-bulk-temperature heat transfer coefficients, and determines the entrance lengths required for the flow to become fully developed. These results demonstrate the applicability of the non-Darcian analysis and the physical phenomena controlling transport in chemical reactors.

Contributed by the Heat Transfer Division and presented at the ASME/JSME Joint Thermal Engineering Conference, Honolulu, Hawaii, March 22–27, 1987. Manuscript received by the Heat Transfer Division June 15, 1987. Keywords: Packed and Fluidized Beds, Porous Media.

Analytical Formulation

Flow parameters in porous media, such as velocity and temperature, are often determined by averaging the local quantities over some representative area (Slattery, 1978; Whitaker, 1969). For one-dimensional creeping flows, the velocity is determined by averaging over the total cross-sectional area of the flow. However, for high flow velocities, the velocity profile is often quite irregular and local velocity measurements fluctuate from the average value, as indicated by the measurements of Lerou and Froment (1977) and Vortmeyer and Schuster (1983). Furthermore, if the flow occurs adjacent to a solid surface, the local near-wall velocity is much higher than that found in the far field. To account for these variations, the velocity is averaged within a small local volume instead of over the cross-sectional area. Slattery (1978) and Whitaker (1969) showed that this local averaging incorporates both global flow variations and local intrapore transport. For a cylindrical geometry, a toroid represents the averaging volume so that the velocity is constant along any circumferential element. To insure that the average quantity is meaningful, the overall geometry, such as the tube diameter, must be significantly larger than the length corresponding to the particle or pore size. Furthermore, the averaging volume must be small enough to minimize any gradients within the volume.

The steady volume-averaged continuity and momentum equations for forced convection in a porous medium, from the work of Vafai and Tien (1981) and Vafai (1984), are

$$\nabla \cdot \langle \mathbf{u} \rangle = 0 \tag{1}$$

$$\frac{\rho}{\epsilon^2} \langle \mathbf{u} \cdot \nabla \mathbf{u} \rangle = -\nabla \langle P \rangle - \frac{\mu}{K} \langle \mathbf{u} \rangle - kC |\langle \mathbf{u} \rangle| \langle \mathbf{u} \rangle \pm \frac{\mu}{\epsilon} \nabla^2 \langle \mathbf{u} \rangle \tag{2}$$

where $\langle\ \rangle$ represents a volume-averaged quantity, $\mathbf{u}$ and P are the local velocity and pressure, ρ and μ are the fluid density

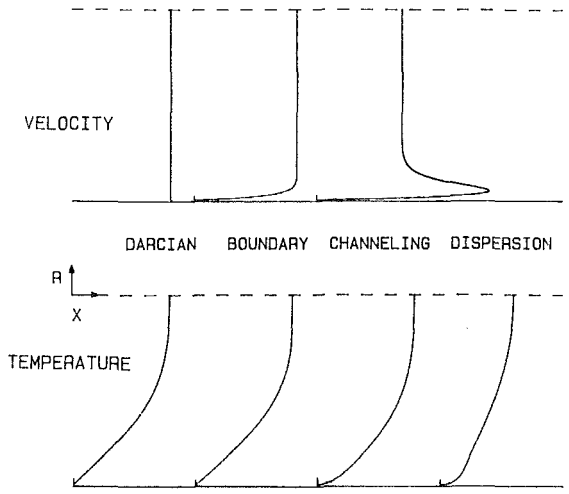

Fig. 1 Velocity and temperature profiles in a cylindrical tube resulting from the inclusion of various non-Darcian effects

and viscosity, ϵ is the porosity, and K and C are the permeability and inertial coefficient, parameters dependent on porosity and particle diameter. The momentum equation contains terms similar to those found in the Navier–Stokes equations, along with the flow resistance terms inherent to porous media studies. The first two terms on the right-hand side represent, respectively, the pressure drop and the viscous drag caused by the porous medium (Slattery, 1977; Whitaker, 1969). If these two terms are isolated from the other terms, the equation would reduce to Darcy's law yielding the uniform velocity approximation often used in chemical reactor studies. The third term is the Ergun term, which accounts for high-flow-rate inertial pressure losses (Ergun, 1952). The fourth term on the right side of the equation, the boundary effect, accounts for the shear stress along the solid boundaries and is significant in the near-wall region (Vafai and Tien, 1981). The term on the left-hand side is the convective term and usually is neglected except in the entrance region of the flow (Vafai and Tien, 1981). The Darcian and inertial terms contain the empirical coefficients K and C, which are given by the relations developed by Ergun (1952) for flow in a packed bed

$$K = \frac{d^2\epsilon^3}{150(1-\epsilon)^2} \tag{3}$$

$$C = \frac{1.75(1-\epsilon)}{d\epsilon^3} \tag{4}$$

Both of these quantities depend on the porosity of the bed. The porosity in a packed bed varies with distance from the wall, from a maximum of one at the solid boundary decreasing to the free-stream value ϵ_∞ after a few particle diameters (Benenati and Brosilow, 1962; Roblee et al., 1958). Since the porosity varies, the coefficients K and C also vary with distance from the wall.

The inclusion of the variable porosity and the no-slip boundary condition dramatically alters the Darcian velocity profile. Figure 1 depicts the Darcian profile along with the velocity profile due to the viscous, wall-shear force and the nonhomogeneous effect. The boundary profile demonstrates that with the inclusion of the viscous shear force, the no-slip boundary condition is satisfied. The nonhomogeneous effect with the no-slip boundary condition causes the velocity profile to peak near the solid surface, resulting in the channeling profile.

The volume-averaged, steady energy equation for porous media is (Tien and Hunt, 1987; Carbonell and Whitaker, 1984)

$$\rho c_p \langle \mathbf{u} \rangle \cdot \nabla \langle T \rangle = \nabla \cdot (k_e \nabla \langle T \rangle) \tag{5}$$

where ρ and c_p are the fluid density and heat capacity, and k_e is the effective conductivity composed of a sum of the stagnant and dispersion conductivities, $k_e = k_o + k_d$. The stagnant conductivity k_o is a function of porosity and the conductivities of the fluid and solid, and thus accounts for the molecular conduction between the phases. Its bulk value is determined from various empirical models, such as presented in Froment and Bischaff (1979) and Wakao and Kaguei (1982). However, the local stagnant conductivity also varies with distance from the wall. At the solid boundaries the porosity is one, and conduction occurs only through the fluid phase. Farther from the wall as the porosity decreases, the stagnant conductivity increases to the bulk value. This type of homogeneous conductivity model assumes a small, local temperature difference between the fluid and solid phases.

Nomenclature

a, b = coefficients used in porosity variation
C = inertial coefficient
c_p = specific heat at constant pressure
D_t = tube diameter
d = particle diameter
f = coefficient in momentum equation $= K_\infty/d^2$
G = mass flow rate
h = heat transfer coefficient
K = permeability
k = thermal conductivity
k_r = uniform radial conductivity
L_e = entrance length
l = mixing length
Nu_b = bulk temperature Nusselt number $= h_b D_t/k_f$
Nu_s = temperature-slip Nusselt number $= h_b d/k_f$
P = pressure
Pe = Peclet number $= u_D d/\alpha_f$
Pr = Prandtl number $= \nu/\alpha_f$
R = dimensionless length $= r/d$
R_t = dimensionless tube radius $= D_t/2d$
r = radial direction
Re = Reynolds number $= u_D d/\nu$
Re_c = inertial Reynolds number $= u_D K_\infty C_\infty/\nu$
Re_a = average Reynolds number $= u_a d/\nu$
T = temperature
U = dimensionless velocity $= u/u_D$
U_a = dimensionless average velocity
u = streamwise velocity
u_D = Darcian velocity $= -(K/\mu)dP/dx$
X = dimensionless length $= x/(dPe)$
x = streamwise direction
α_f = thermal diffusivity $= k_f/\rho c_p$
γ = coefficient in dispersion diffusivity
ϵ = porosity
Θ = dimensionless temperature
μ = dynamic viscosity
ν = kinematic viscosity
ρ = density

Subscripts and Superscripts

a = average
b = bulk
D = Darcian
d = dispersion
e = effective
f = fluid
i = initial
o = stagnant
s = slip
t = tube inner wall
w = wall
∞ = infinity

The effective conductivity also includes thermal transport due to dispersion. Dispersion results from the mixing of local fluid streams as the fluid follows tortuous paths around the solid particles. If a temperature gradient exists across the solid particles, the mixing of the fluid streams yields a net transport of heat. Therefore the process is assumed to be macroscopically diffusive and dependent on the temperature gradient. Since the fluid mixes within a length scale l, with an average velocity u, the dispersion conductivity is assumed to follow the relationship (Carbonell and Whitaker, 1984; Tien and Hunt, 1987)

$$k_d = \rho\, c_p\, u\, l\, \gamma \tag{6}$$

where γ is a constant dependent on the type of porous medium. Its value is determined from experimental studies as outlined in Wakao and Kaguei (1982) and Wen and Fan (1975).

Shown in Fig. 1, along with the velocity profiles, are the corresponding temperature profiles resulting from the inclusion of the various non-Darcian terms. The first temperature profile for Darcian or slug flow varies almost linearly near the wall. The temperature profile that results when the no-slip boundary condition is included appears similar to the Darcian profile. However, the temperature gradient at the wall is actually smaller than for the Darcian flow due to the decreased momentum transport near the solid boundary. For variable porosity, the momentum transport near the wall is large, increasing the temperature gradient and yielding a higher heat transfer rate. If dispersion is included with the variable porosity, the temperature gradient at the wall remains quite severe, but in the bulk region dispersion mixes the fluid resulting in a more uniform temperature variation across the tube.

Problem Description and Formulation

The problem investigated in this paper involves the configuration and flow conditions similar to those found in chemical reactor studies. A fluid of constant temperature enters a cylindrical reactor filled with a porous medium. The reactor walls are either heated or cooled to a constant temperature different from the inlet conditions. The purpose of this study and other chemical reactor studies is to determine the heat transfer rate between the walls and the fluid-solid system and the local temperature within the reactor. The results from these nonreacting studies are used to estimate the cooling rate needed for catalytic packed-bed reactors.

In contrast to the approach used in the present analysis, most chemical reactor studies assume a constant velocity as determined from the flow rate and reactor size. The resulting two-dimensional energy equation neglecting axial conduction, as given by Froment and Bischaff (1979), Li and Finlayson (1977), and Wakao and Kaguei (1982), is

$$G\, c_p \frac{\partial T}{\partial x} = \frac{k_r}{r} \frac{\partial}{\partial r}\left(r \frac{\partial T}{\partial r}\right) \tag{7}$$

where r is the direction perpendicular to the flow, x is along the flow direction, G is the flow rate within the reactor, and k_r is an effective radial conductivity. This radial conductivity k_r is different from the effective conductivity k_e discussed in the previous section; its value is assumed to be constant throughout the reactor and represents a sum of the bulk stagnant conductivity and the dispersion conductivity based on the average flow velocity.

With the appropriate boundary conditions, equaton (7) is readily integrable. Using a constant-wall-temperature boundary condition

$$T = T_w \text{ at } r = D_t/2 \tag{8}$$

the resulting temperature profile varies almost linearly near the wall, as shown in the Darcian temperature profile in Fig. 1. However, measured temperature profiles in chemical reactors indicate a very steep temperature gradient near the wall with a relatively mild gradient in the central region as demonstrated in the experiments of Kunii et al. (1968), Lerou and Froment (1977), Plautz and Johnstone (1955), and Yagi and Wakao (1959). In order to retain the slug-flow assumption, chemical reactor analyses have replaced the constant-wall-temperature boundary condition with a temperature-slip heat transfer coefficient boundary condition

$$k_r \frac{\partial T}{\partial r}\bigg|_t = h_s (T_w - T_t) \tag{9}$$

where the t location represents a position just within the reactor tube wall, and h_s is the temperature-jump heat transfer coefficient. The quantities h_s and k_r are determined from measured profiles within the reactor and the bulk temperatures at the bed exit. Using this jump boundary condition and the experimental values of k_r and h_s, the solution to the slug flow equation (7) corresponds with measured profiles as shown in Plautz and Johnstone (1955) and Yagi and Wakao (1959). This type of analysis requires extensive experimental investigations and is valid only after certain entrance lengths (Li and Finlayson, 1977; Wakao and Kaguei, 1982).

The present investigation re-examines the chemical reactor problem; however, the analysis is based on the volume-averaged non-Darcian approach. The analysis assumes a porosity variation and utilizes empirical models for the effective conductivity. However, the analysis does not use the temperature-slip boundary condition, but instead allows the velocity and conductivity to vary.

The governing equations (1), (2), and (5) are nondimensionalized by introducing the following variables:

$$u_D = -\frac{K_\infty}{\mu}\frac{d\langle P\rangle}{dx},\quad U = \frac{\langle u\rangle}{u_D},\quad R = \frac{r}{d}$$

$$\mathrm{Re} = \frac{u_D d}{\nu},\quad \mathrm{Re}_c = \frac{K_\infty C_\infty u_D}{\nu},\quad f = \frac{K_\infty}{d^2} \tag{10}$$

$$\mathrm{Pe} = \mathrm{PrRe},\quad X = \frac{x}{d\mathrm{Pe}},\quad \Theta = \frac{\langle T\rangle - \langle T_w\rangle}{\langle T_i\rangle - \langle T_w\rangle}$$

where ∞ represents the bulk porous medium value and i is the inlet flow condition. The parameter f relates the permeability to the particle size, and is determined from the porosity using equation (3). The momentum and energy equations are

$$0 = 1 - \frac{K_\infty}{K} U - \frac{C}{C_\infty}\mathrm{Re}_c\, U^2 + \frac{\epsilon_\infty}{\epsilon}\frac{f}{R}\frac{\partial}{\partial R}\left(R\frac{\partial U}{\partial R}\right) \tag{11}$$

$$U\frac{\partial \Theta}{\partial X} = \frac{1}{R}\frac{\partial}{\partial R}\left(\frac{k_e}{k_f} R \frac{\partial \Theta}{\partial R}\right) \tag{12}$$

with the boundary conditions

$$\Theta = 1 \text{ at } X = 0 \tag{13}$$

$$\Theta = 0 \text{ at } R = R_t,\ \frac{\partial \Theta}{\partial R} = 0 \text{ at } R = 0 \tag{14}$$

and total flow constraint

$$\int_0^{R_t} U\, R\, dR = 1/2\, R_t^2\, U_a \tag{15}$$

The average velocity U_a in the reactor is determined by rearranging the Ergun relation (Ergun, 1952)

$$U_a = [-1 + (1 + 4\,\mathrm{Re}_c)^{1/2}]/(2\,\mathrm{Re}_c) \tag{16}$$

and the average Reynolds number Re_a is defined as $\mathrm{Re}_a = \mathrm{Re}U_a$. Since the inertial forces decrease the velocity

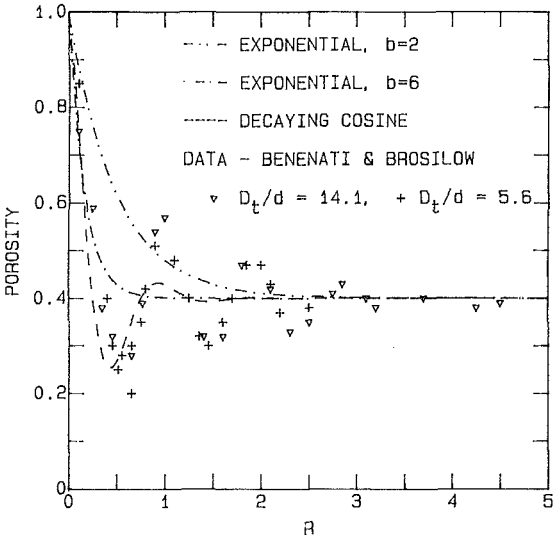

Fig. 2 Porosity as a function of radial position within a packed cylindrical bed

from the Darcian value, the average velocity is always less than the Darcian velocity and hence U_a is always less than one.

From Vafai and Tien (1981), the hydraulic entrance region is important only for downstream distances smaller than $K_\infty u_D/\nu$, and therefore the convective term is neglected in the present analysis. However, the inertial or Ergun force is present throughout the flow and is important whenever Re_c is greater than one. Since the Peclet number is greater than one, axial conduction is also not included.

Before the momentum and energy equations are solved, an appropriate variation must be chosen to represent the porosity close to the wall. To determine the variation, the measurements of Benenati and Brosilow (1962) are considered. Figure 2 shows the data from two different-sized reactors filled with perfectly spherical particles. The data demonstrate that the porosity is one at the wall and decreases to a minimum at the first half diameter. The porosity continues to oscillate around the free-stream value for approximately five particle diameters.

The porosity variation is often approximated by a simple exponential as used in the studies by Chandresekhara and Vortmeyer (1979), Vafai (1984), and Vortmeyer and Schuster (1983)

$$\epsilon = \epsilon_\infty [1 + a \exp(-b\, R)] \tag{17}$$

where the value of a is chosen so that the porosity at the wall is one, and b is chosen to approximate the porosity decay. Figure 2 also shows the variation for different values of b. In calculations by these researchers the value of b is chosen to be about 2 or 3, averaging the peak and the valley. However, a value of b of about 6 more closely reflects the near wall variation. The figure also includes a decaying-cosine porosity profile, which incorporates the oscillations after one particle diameter.

The stagnant conductivity k_o varies with distance from the wall, from the fluid conductivity to the bulk stagnant conductivity. Thus it depends on the choice of parameters in the porosity variation, equation (17), and on the value of bulk stagnant conductivity. The dynamic or dispersion conductivity k_d incorporates the additional thermal transport due to the radial mixing between the solid particles. This quantity is proportional to a product of the mixing length, local velocity and a constant γ. From numerous experimental packed-bed studies, the dispersion relation has been verified for both heat and mass transfer using a particle diameter for the mixing length and a value of γ equal to 0.1 (Wen and Fan, 1975). However, these studies do not examine the region of porosity variation. In the near-wall region the velocity and the mixing length vary affecting the dispersion relation. The present analysis recognizes that adjacent to the solid surface transport is due only to molecular conduction, and in the bulk region the transport is determined by the established semi-empirical relations. Therefore in the dispersion relation, the velocity increases from zero as determined by the momentum equation and the mixing length increases from zero to a value of d one diameter from the surface. Thus the effective conductivity as a function of radial position R equals

$$\frac{k_e}{k_f}(R) = \frac{k_d}{k_f} + \frac{k_o}{k_f} = \gamma\, \mathrm{Pe}\, \frac{l(R)}{d}\, U(R) + \frac{k_o}{k_f}\,[1 + a' \exp(-bR)] \tag{18}$$

where b has the value used in the porosity variation, and a' is chosen so that k_e/k_f equals one at the wall as the velocity U approaches zero. The variation of the mixing length is then

$$\frac{l(R)}{d} = R_t - R, \text{ for } R_t - R \le 1 \tag{19}$$

Results

To determine the velocity and temperature profiles, the momentum and energy equations are integrated numerically using a finite difference scheme. Two different grid sizes are used in the calculations, with a finer grid used near the wall to account for the steep velocity and temperature gradients. The momentum equation is a nonlinear ordinary differential equation with variable coefficients due to the variation in porosity. The numerical formulation, based on central differences, linearizes the inertial term, and iterates the calculations until the solution converges. The formulation of the energy equation uses a marching scheme based on upwind differences in the flow direction and an implicit-central-difference scheme for the radial direction. Since the conductivity varies with radial direction, the model calculates the interface conductivity by using the harmonic-mean conductivity as opposed to an arithmetic average (Patankar, 1980). The numerical method is verified by calculating the slug flow solution, and by varying the grid spacing. The downstream temperature profiles are also checked to ensure that the temperature profile reaches a fully developed state. For most calculations approximately 300 points are used in the main flow and another 300 points near the wall.

Using the three porosity profiles shown in Fig. 2, the momentum equation is integrated for the flow conditions corresponding to the experiment of Price (1968). Price measured the outlet velocity for air flow in a packed bed of highly spherical particles by placing a honeycomb mesh over the exit plane. He then used a pitot tube to measure the average velocity in each of the flow compartments. Without this flow partitioning, the viscous shear forces along the exit wall slow the fluid, diffusing the high-velocity region into the center and reducing the peak (Chandrasekhara and Vortmeyer, 1979). Experiments by Schwartz and Smith (1953) and Schertz and Bischoff (1969) made without the honeycomb arrangement show a broad, short, inwardly skewed peak. However, Price's measurements (1968) indicate a narrow sharp peak near the wall as shown in Fig. 3. Also shown are the calculated profiles for each of the different porosity variations. The profile corresponding to $b = 2$ lies well below the velocity in the center of the bed, and contains a peak that is much too broad. The other two profiles lie closer to the mainstream velocity, and if averaged over similar ring elements, fall quite close to the average experimental profile by Price. The oscillating profile presents a large dip located approximately one half particle diameter from the wall due to the dip in the porosity variation.

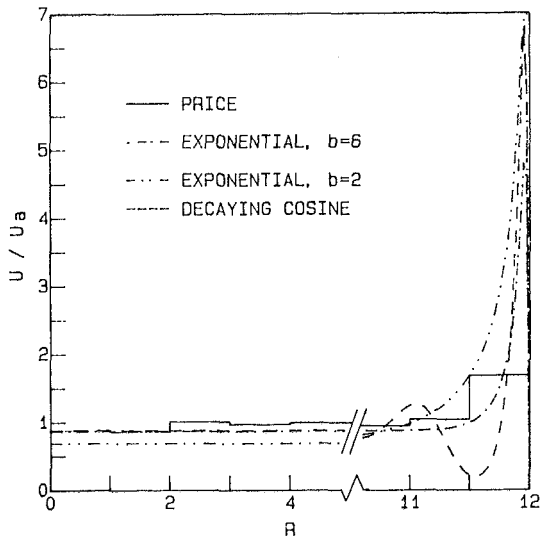

Fig. 3 Velocity profiles as a function of radial position with the numerical calculations based on different porosity variations; $Re_a = 4000$, $\epsilon_\infty = 0.40$, $d = 1.27$ cm, $K_\infty = 1.9 \times 10^{-7}$ m^2, $C_\infty = 1300$ m^{-1}

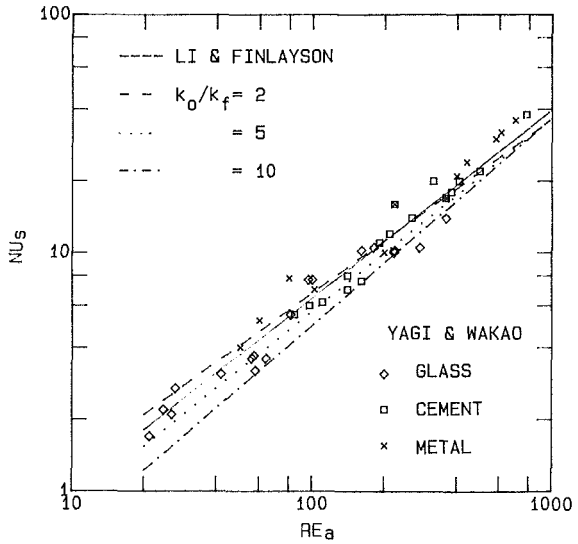

Fig. 5 Temperature-slip Nusselt numbers for fully developed flows at various ratios of stagnant to fluid conductivities; $\epsilon_\infty = 0.40$, $R_t = 10$

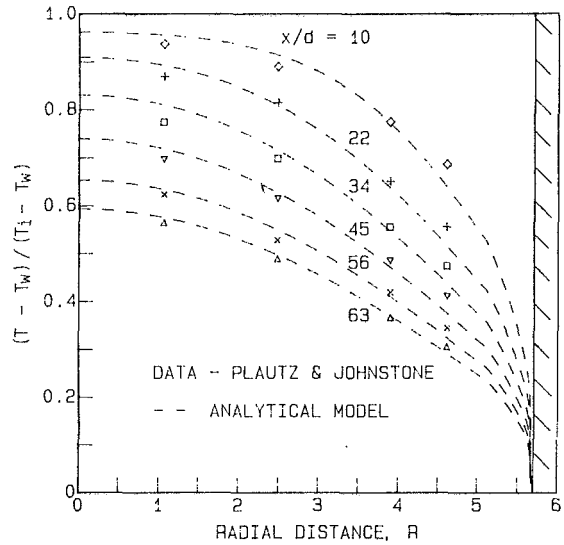

Fig. 4 Numerically calculated temperature profiles within a packed bed for different radial and axial locations; $Re_a = 1000$, $\epsilon_\infty = 0.38$, $b = 6$, $d = 1.9$ cm, $K_\infty = 4.3 \times 10^{-7}$ m^2, $C_\infty = 860$ m^{-1}, $R_t/d = 5.68$

This is not demonstrated in the measured profile due to the relatively large size of the honeycomb spacing.

The velocity profiles indicate the importance of the region within the first half-particle. The approximate variation should account for the rapid porosity change with either a sharp exponential decrease, $b = 6$, or with a decaying cosine. The oscillating profile is probably the correct porosity variation for highly spherical packings; however, if the spheres are slightly irregular, the packing becomes tighter and the oscillatory nature of the porosity variation is not apparent (Benenati and Brosilow, 1962; Roblee et al., 1958). A steep exponential, such as $b = 8$, is a good approximation for packings of irregular or variable sized particles.

To demonstrate the adequacy of the thermal model, the momentum and energy equations are integrated for the flow conditions corresponding to the experimental measurements in air by Plautz and Johnstone (1955). Figure 4 compares calculated temperature profiles with the measured quantities at various downstream locations. The numerical calculations use the measured inlet temperatures given by the authors instead of a uniform inlet condition. Since the particles are not perfectly spherical, the analysis also assumes an exponential variation in porosity from one at the wall to 0.38 in the center, with the exponential parameter $b = 6$. The figure demonstrates both the large temperature gradient near the wall, which in a typical reactor analysis would be incorporated through an experimental heat transfer coefficient, and the relatively mild temperature variation in the bulk of the flow.

To verify the steep temperature gradient near the wall, numerical computations are used to predict the temperature-slip heat transfer coefficient. Using the fully developed bulk and centerline temperatures as suggested by the analysis of Li and Finlayson (1977), it is possible to compute the temperature-slip heat transfer coefficient. Li and Finlayson correlated the data of Yagi and Wakao (1959) and Kunii et al. (1968) for air flow through spherical particles with average Reynolds numbers between 20 and 7000 and reactor sizes, D_t/d, from 3 to 20. Figure 5 compares the slip Nusselt number, $Nu_s = h_s d/k_f$, versus the average Reynolds number for the Li and Finlayson correlation, the data from Yagi and Wakao, and the predicted results from the numerical calculations. The data from Kunii et al. are not included since the reactor diameters are only a few times larger than the particle size, and probably are not valid for volume-averaging analysis. The calculations are based on three different ratios of stagnant to fluid conductivity, k_o/k_f. For low flow rates, the numerical calculations vary slightly with the highest Nusselt numbers corresponding to the largest conductivity ratio. However, at high flow rates the effect of the solid conductivity is minimal, and the heat transfer from the wall appears independent of solid phase conductivity. This is due to the large mixing or dispersion, which overwhelms any molecular transport. The data by Yagi and Wakao are for a number of different materials, as shown in the figure. Their data fall together with no distinction between conductivity materials over the entire range of Reynolds numbers. However, the scatter of the measurements appears to be approximately equal in magnitude to the difference between the calculated results for various conductivities.

The Nusselt number can also be defined using the bulk temperature and the following definition of the heat transfer coefficient:

$$h_b(T_b - T_w) = \left(k_e \frac{\partial T}{\partial r}\right)\Big|_w \tag{20}$$

Using this local heat transfer coefficient, and noting that the effective conductivity at the wall is equal to the fluid conductivity, the bulk-temperature Nusselt number is defined as

$$\mathrm{Nu}_b = \frac{h_b D_t}{k_f} = \frac{2R_t}{\Theta_b}\frac{\partial \Theta_b}{\partial R}\Big|_w \tag{21}$$

Figure 6 shows the variation in this Nusselt number for two different flow rates, and for different ratios of solid to fluid conductivity. For the higher flow rate, the entrance region is longer and the relative variation in Nusselt number for the conductivity ratios is not as significant as for the lower flow rate. The approximate entrance length L_e can be determined by the following relation:

$$L_e = \frac{x}{d}\frac{1}{\mathrm{Pe}}\frac{1}{U_a}\left(\frac{d}{R}\right)^2\left(\frac{k_e}{k_f}\right) \tag{22}$$

which is obtained by balancing the average convective and conductive transport. At some distance downstream, x/d, the flow is fully developed if L_e is greater than 0.2. This result is similar to that given in Li and Finlayson (1977).

The asymptotic, bulk heat transfer coefficients, like those shown in Fig. 6, can be compared to the fully developed one-dimensional heat transfer coefficient defined by Li and Finlayson. This one-dimensional analysis equates the gradient in the fully developed bulk temperature to the temperature difference between the wall and the local bulk temperature

$$Gc_p \frac{dT_b}{dx} = \frac{4}{D_t} h_b(T_b - T_w) \tag{23}$$

Figure 7 compares this one-dimensional correlation with the calculated bulk-temperature Nusselt numbers, $\mathrm{Nu}_b = h_b D_t/k_f$, for various stagnant conductivity ratios. Again as in Fig. 6, as the Reynolds number increases, the variation between the results for varying conductivity ratios decreases due to the large dispersion effect.

Similar results are obtained for packed beds of cylindrical particles as also shown in Fig. 7. The difference between the packed spheres and cylinders is the lower bulk porosity and the larger near-wall porosity gradient for the packed cylinders (Roblee et al., 1958). The porosity is assumed to vary from one to a value of 0.3 with an exponential coefficient $b = 8$. Using these assumptions for the porosity, the numerical calculations for fully developed bulk Nusselt numbers correspond to the correlation for packed cylinders by Li and Finlayson.

Conclusion

This analysis demonstrates the importance of the non-Darcian effects in modeling high-Reynolds-number flows in chemical reactors. Traditional inert-packed-bed analyses have relied on temperature-slip boundary conditions to predict experimental data. The temperature-slip coefficients are then used to estimate the heat transfer in reacting beds with limited success. The present results show that with the incorporation of the non-Darcian terms, a theoretical model can be established that predicts experimental heat transfer measurements without relying on temperature-slip boundary conditions. This non-Darcian analysis successfully models inert reactors and can be extended for use in reacting beds and other geometric configurations.

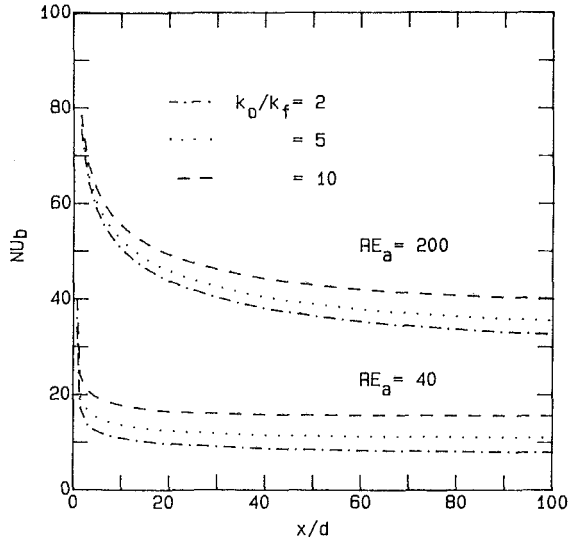

Fig. 6 Bulk-temperature Nusselt numbers for different conductivity ratios; $\epsilon_\infty = 0.40$, $R_t = 10$

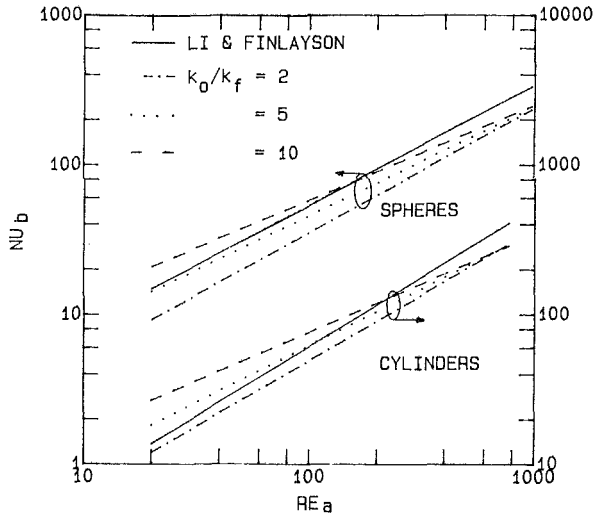

Fig. 7 Fully developed bulk-temperature Nusselt numbers for packed spheres: $R_t = 10$, $\epsilon_\infty = 0.40$; and packed cylinders: $\epsilon_\infty = 0.30$

References

Benenati, R. F., and Brosilow, C. B., 1962, "Void Fraction Distribution in Beds of Spheres," *AIChE J.*, Vol. 8, pp. 359–361.

Carbonell, R. G., and Whitaker, S., 1984, "Heat and Mass Transfer in Porous Media," in: *Fundamentals of Transport Phenomena in Porous Media*, J. Bear and M. Y. Corapcioglu, eds., NATO ASI Series.

Chandrasekhara, B. C., and Vortmeyer, D., 1979, "Flow Model for Velocity Distribution in Fixed Porous Beds Under Isothermal Conditions," *Warme- und Stoffubertragung*, Vol. 12, pp. 100–111.

Ergun, S., 1952, "Fluid Flow Through Packed Columns," *Chem. Eng. Prog.*, Vol. 48, pp. 89–94.

Froment, G. F., and Bischaff, K. B., 1979, *Chemical Reactor Analysis and Design*, Wiley, New York.

Kunii, D., Suzuki, M., and Ono, N., 1968, "Heat Transfer From Wall Surface to Packed Beds at High Reynolds Number," *J. Chem. Eng. Japan*, Vol. 1, pp. 21–26.

Lerou, J. J., and Froment, G. F., 1977, "Velocity, Temperature and Conversion Profiles in Fixed Bed Catalytic Reactors," *Chem. Eng. Sci.*, Vol. 32, pp. 853–861.

Li, C. H., and Finlayson, B. A., 1977, "Heat Transfer in Packed Beds—A Reevaluation," *Chem. Eng. Sci.*, Vol. 32, pp. 1055–1066.

Patankar, S., 1980, *Numerical Heat Transfer and Fluid Flow*, Hemisphere, New York.

Plautz, D. A., and Johnstone, H. F., 1955, "Heat and Mass Transfer in Packed Beds," *AIChE J.*, Vol. 1, pp. 193–199.

Price, J., 1968, "The Distribution of Fluid Velocities for Randomly Packed Beds of Spheres," *Mech. Chem. Eng. Trans.*, Vol. 7, pp. 7–14.

Roblee, L. H. S., Baird, R. M., and Tierney, J. W., 1958, "Radial Porosity Variations in Packed Beds," *AIChE J.*, Vol. 4, pp. 460–464.

Schlunder, E. U., 1978, "Transport Phenomena in Packed Bed Reactors," *Chem. Reaction Engineering Reviews—Houston*, V. W. Weekmann, ed., A.C.S. Symp. Ser., No. 72, pp. 110–161.

Schertz, W. W., and Bischoff, K. B., 1969, "Thermal and Material Transport in Non-isothermal Packed Beds," *AIChE J.*, Vol. 15, pp. 597–603.

Schwartz, C. E., and Smith, J. M., 1953, "Flow Distribution in Packed Beds," *Ind. Eng. Chem.*, Vol. 45, pp. 1209–1218.

Slattery, J. C., 1978, *Momentum, Energy and Mass Transfer in Continua*, Kreiger Press, New York.

Tien, C. L., and Hunt, M. L., 1987, "Boundary-Layer Flow and Heat Transfer in Porous Beds," *Chem. Eng. Proc.*, Vol. 21, pp. 53–63.

Vafai, K., 1984, "Convective Flow and Heat Transfer in Variable-Porosity Media," *J. Fluid Mech.*, Vol. 147, pp. 233–259.

Vafai, K., and Tien, C. L., 1981, "Boundary and Inertia Effects on Flow and Heat Transfer in Porous Media," *Int. J. Heat Mass Transfer*, Vol. 24, pp. 195–203.

Vortmeyer, D., and Schuster, J., 1983, "Evaluation of Steady Flow Profiles in Rectangular and Circular Packed Beds," *Chem. Eng. Sci.*, Vol. 38, pp. 1691–1699.

Wakao, N., and Kaguei, S., 1982, *Heat and Mass Transfer in Packed Beds*, Gordon and Breach Science Publishers, New York.

Wen, C. Y., and Fan, L. T., 1975, *Models for Flow Systems and Chemical Reactors*, Marcel Dekker, New York.

Whitaker, S., 1969, "Advances in Theory of Fluid Motion in Porous Media," *Ind. Eng. Chem.*, Vol. 61, pp. 14–28.

Yagi, S., and Wakao, N., 1959, "Heat and Mass Transfer From Wall to Fluid in Packed Beds," *AIChE J.*, Vol. 5, pp. 79–85.

Heat Transfer in a Countercurrent, Gas-Solid, Packed Column

E. Saatdjian
CNRS Laboratoire d'Aérothermique,
Meudon, France

J. F. Large
Université de Technologie
de Compiègne,
Compiègne, France

A theoretical model has been used, in conjunction with pressure drop and solid holdup data, to predict correctly the thermal efficiency of a countercurrent, gas-solid, packed heat exchanger. In the model, the ideal efficiency is multiplied by a ratio of particles in contact with the gas to the total amount of particles in the packed section. The Ergun equation is used to obtain both an effective packing porosity and the number of particles in contact with the gas. The results show that the model correctly gives the efficiency versus gas velocity curve for different packing heights and solids mass fluxes. The calculated and experimental velocities for which exchanger efficiency is a maximum are also in agreement.

Introduction

Packed columns are used in several unit operations where a liquid phase and a gas phase flow countercurrently. Gas absorption, humidification operations, and distillation are probably the best known applications. The packing is almost always introduced into the column in a random way and helps to increase the transfer contact area without prohibitively increasing pressure drop (Treybal, 1968).

In general, a plug-flow velocity profile is assumed valid in modeling the transport phenomena of these processes; however, when the column-to-packing diameter ratio is small, the velocity near the column walls can be sufficiently high, due to the increased void fraction in this region, that it modifies the reactor performance considerably (Fahien and Stankovic, 1979). In the literature, considerable experimental work has been published on the different flow regimes, pressure drops, residence time distributions, and holdup in these reactors (Satterfield, 1975).

Countercurrent gas-solid operations have been studied much less than their gas-liquid counterparts; Zenz and Othmer (1960) have reviewed the early results obtained experimentally with this operation. Recent interest on new coal gasification processes has changed this since pulverized coal transport usually involves countercurrent gas-solid flow. Arastoopour and Gidaspow (1979) solved four different sets of hydrodynamic equations numerically in order to predict solid particle flow reversal. As gas velocity is increased, the particle flow becomes unstable, pressure drop begins to increase, and a flooding regime, similar to the one encountered in gas-liquid flow, is observed.

A packed column in countercurrent gas-solid flow has been used as a heat exchanger by Large et al. (1981); the hydrodynamics and the heat transfer were both studied experimentally. These authors observed that, as the gas velocity is increased, the solid particles in the packed zone shift from a homogeneous, full contact regime to a radially segregated type of flow where the particles trickle down the reactor near the tube walls while the gas flows upward mainly near the tube center. Heat transfer data by these authors show that, as the gas velocity is increased, the exchanger efficiency passes through a maximum value and decreases thereafter. The exchanger performance is also closely linked to the initial solid distributor (Large et al., 1983). Saatdjian and Large (1985) explained this behavior by formulating a model where holdup and pressure drop measurements were used to determine the fraction of solids in the packed section that are in contact with the gas phase; their first results were in good agreement with experimental data. The Ergun equation (1952) was used to determine both an effective porosity and this fraction.

Here, this last model is again used to compare model predictions to experimental results in this column. The influence of packing height, solid mass flux, and gas velocity are studied in more detail. As will be seen below, the model is a useful tool in scaling up this operation.

Theoretical Analysis

The analysis used here has been previously published (Saatdjian and Large, 1985) and will only be reviewed briefly. Heat balances for the gas and solid phases in the packed column are

$$\frac{dT_s}{dx} = \frac{6h}{d_s \rho_s C_{ps} v_s} (T_s - T_g) \tag{1}$$

$$\lambda_g \epsilon A_R \frac{d^2 T_g}{dx^2} + \rho_g v_g \epsilon A_R C_{pg} \frac{dT_g}{dx} + \frac{h W_s A_R A_s dx}{\rho_s v_s V_p} (T_g - T_s) = 0 \tag{2}$$

In these equations, the x direction is considered positive from the bottom of the packed section upward; the heat transfer to the packing from external means or by conduction and the heat losses from the column have been neglected. Furthermore radiation transfer has also been neglected because the temperatures used in this study are below 600 K.

Defining the heat exchanger efficiency as

$$\eta' = \frac{T_s(x=0) - T_s(x=l)}{T_g(x=0) - T_s(x=l)} \tag{3}$$

the analytical solution can be easily obtained if the axial conduction term in (2) is neglected. This hypothesis is valid because the flow Peclet number is above 10,000.

$$\eta' = \frac{C_1(1 - e^{-C_2 l})}{1 - C_1 e^{-C_2 l}} \quad \text{if } C_1 \neq 1 \tag{4}$$

$$\eta' = \frac{l}{l + C_3} \quad \text{if } C_1 = 1 \tag{5}$$

where

$$C_1 = \frac{\rho_g v_g \epsilon C_{pg}}{W_s C_{ps}}; \qquad C_2 = \frac{6h}{d_s \rho_s v_s C_{ps}} \left(\frac{1}{C_1} - 1\right);$$

$$C_3 = \frac{\rho_s v_s d_s C_{ps}}{6h}$$

However, in writing and solving these equations, we assumed

Contributed by the Heat Transfer Division for publication in the JOURNAL OF HEAT TRANSFER. Manuscript received by the Heat Transfer Division October 30, 1986. Keywords: Heat Exchangers, Modeling and Scaling, Packed and Fluidized Beds.

that all the particles in the packed section are in contact with the gas. In Saatdjian and Large (1985), we suggested that η' should be multiplied by a ratio of the number of particles in the packed section in contact with the gas to the total number of particles in the packed section. In mathematical form, this ratio can be written as

$$\eta = \eta' \frac{(1-\epsilon_s)}{\beta} \tag{6}$$

where β is the experimentally measured holdup. Below, a method for determining $(1-\epsilon_s)$ is presented.

The experimentally measured pressure drop per unit packing length can be decomposed into two terms: a first contribution due to the packing and a second due to the solid flux

$$\left(\frac{\Delta P}{x}\right)_{\text{total}} = \left(\frac{\Delta P}{x}\right)_o + \left(\frac{\Delta P}{x}\right)_s \tag{7}$$

From measurements with no solid flow the first term can be deduced. This pressure drop depends on the way the packing is introduced into the column. Applying the Ergun equation

$$\frac{\epsilon_{eff}^3}{1-\epsilon_{eff}} = \frac{\rho_g v_g^2}{a_p (\Delta P/x)_o}\left[1.75 + \frac{150(1-\epsilon_{eff})}{\text{Re}_p}\right] \tag{8}$$

an effective porosity ϵ_{eff} can be deduced.

Finally, the fraction of solids in contact with the gas $(1-\epsilon_s)$ is obtained by re-applying the Ergun equation to the pressure drop due to the solids

$$\frac{\epsilon_s^3}{1-\epsilon_s} = \frac{\rho_g (v_g/\epsilon_{eff})^2}{d_s (\Delta P/x)_s}\left[1.75 + \frac{150(1-\epsilon_s)}{\text{Re}_s}\right] \tag{9}$$

Experimental Procedure

In order to compare the theory presented above to the available experimental data on the performance of a countercurrent packed bed heat exchanger, a series of experiments on a small 0.114 m i.d. column (Fig. 1) was undertaken. After filling the column with Pall-15 rings, introduced one by one in a random way, the pressure drop in the packed section was measured for gas velocities between 0 and 4 m/s and no solid flux. The air velocity was measured with both a calibrated diaphragm and a pitot tube. The pressure drop in the packed region was measured with inclined manometers.

Afterward, for a fixed solid flux, the pressure drop and holdup were measured as a function of gas velocity for different packing heights. The final runs consisted of measuring the holdup as a function of the solid flux for zero gas velocity. The pressure drop per unit packing length is plotted versus gas velocity for different solid fluxes (Fig. 3) and the solid holdup as a function of W_s, the solid mass flux, is given in Fig. 4.

The heat transfer data we obtained on the 0.32 m i.d. column (Fig. 2). In this setup, the air is preheated to about 600 K before entering the column. The pressure drops are again measured with inclined manometers; thermocouples were used to record temperatures. The only parameter necessary for our analysis that cannot be measured in this column is the solid holdup.

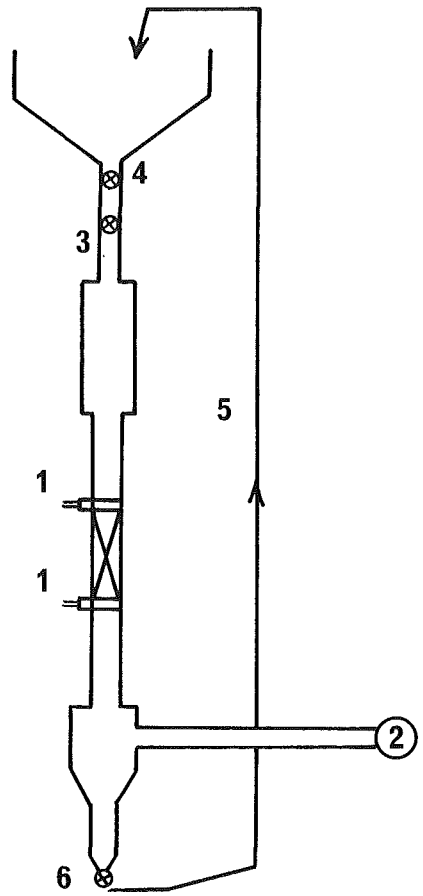

Fig. 1 View of the column used for hydrodynamic measurements: (1) guillotine valves; (2) ventilator; (3) solid input regulation valve; (4) stop valve; (5) solid elevator; (6) solid exit regulation valve

The solid phase consisted of sand particles of 205 μm mean diameter. The metallic Pall-15 rings are thin, open cylinders 15 mm long and with a diameter at the base of also 15 mm. The ceramic rings are 25 mm long. A sketch of these rings can be found in Treybal (1968).

At low gas velocities, the experimental data are accurate and easily reproduced. For identical conditions, the solid holdup

Nomenclature

a_p = specific packing length, m
A_R = reactor cross-sectional area, m^2
A_s = surface area of a solid particle, m^2
C_{ps}, C_{pg} = solids and gas heat capacity, J/kg/K
d_s, d_p = solid particle and packing diameters, m
h = gas–solid heat transfer coefficient, W/m^2/K
l = length of packed zone, m
Re_s, Re_p = Reynolds numbers for the particles and the packing
T_g, T_s = gas and solid temperatures, K
v_g = gas velocity, m/s
v_s = solid trickle velocity, m/s
V_p = volume of one particle, m^3
W_s = solid mass flux, kg/m^2/s
x = vertical coordinate, m
$\Delta P/x$ = pressure drop per unit length, kg/m^2/s^2
β = volumetric fraction occupied by the solid particles in the packed zone
ϵ = porosity in packed zone
ϵ_{eff} = effective porosity in the packed zone
η', η = ideal and real thermal efficiencies of the heat exchanger
λ_g = gas thermal conductivity, W/m/K
μ_g = gas viscosity, kg/m/s
ρ_g, ρ_s = gas and solid densities, kg/m^3
ϕ = column diameter, m

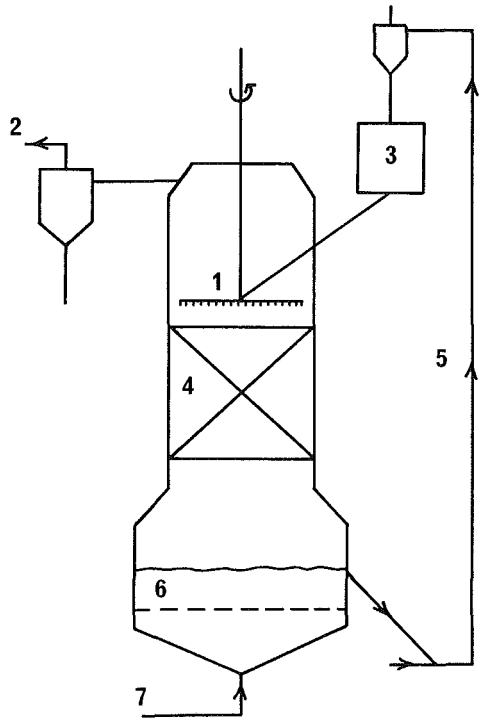

Fig. 2 View of column for heat-exchanger efficiency measurements: (1) solid distributor; (2) vent; (3) sand cooler; (4) packing; (5) solid elevator; (6) fluidized gas distributor; (7) hot gas

can vary by no more than 5 percent. At higher velocities, when a segregated regime is fully established, pressure fluctuations are observed. It must be noted that the holdup was measured by opening the guillotine valves after the system had been shut down and collecting the particles trapped in the packed region. On several occasions, the static holdup, i.e., the sand particles trapped inside the rings, was measured. This implied taking out all of the rings from the column and re-inserting them for the next run. Since they are inserted randomly, the fact that they are not in the exact same location can influence the results somewhat. A 15 percent overall accuracy estimate is not unrealistic.

Results and Discussion

The experimental results for heat transfer in this heat exchanger are given in Tibourtine (1981) and were obtained in the 0.32 m i.d. column filled with either metallic Pall-15 or ceramic Pall-25 rings. The experimental efficiency as a function of gas velocity for the Pall-25 rings is plotted in Figs. 5 and 6. In the first figure, the influence of packing height is examined, while in the second, the variation with solid flux is shown. All the results show that there is a gas velocity for which the heat exchanger efficiency is a maximum. Qualitatively, this is a result of a transition from a full contact (or almost) to a radially segregated regime. These two figures are given without their corresponding theoretical prediction because we were unable to use ceramic Pall-25 rings in the small column. It is well known that for scale-up, a column/packing ratio higher than 8 is necessary. Otherwise, the increased void fraction effects at the column inside diameter would be appreciable. On Fig. 5 it can be seen that increasing the packing height l results in an improved efficiency; nevertheless, above $l = 0.4$ m, no further improvement is noticed.

The obtained results on the small column are summarized in Tables 1–4. The first three columns give the experimentally determined gas velocity, the pressure drop per unit packing height, and the solid holdup. In the fourth column, the expected solid volumetric fraction at 250°C is tabulated. The experimental heat transfer data were obtained at this gas temperature so the holdup had to be predicted at these conditions. We obtained this value by applying the following

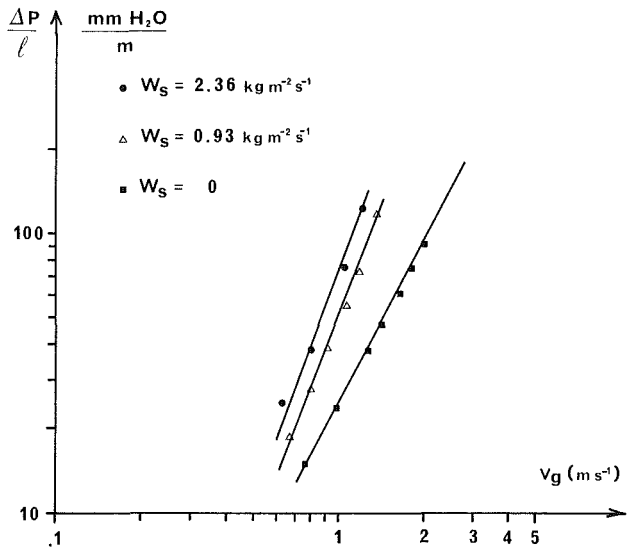

Fig. 3 Total pressure drop per unit packing height versus gas velocity influence of solid flux

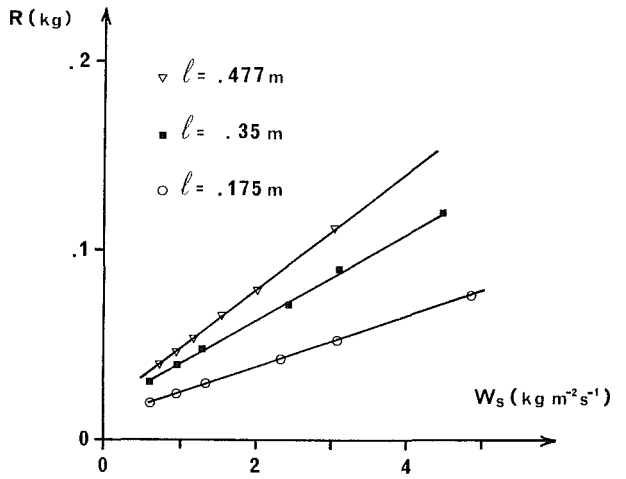

Fig. 4 Solid holdup in the packed region versus mass flux; $v_g = 0$

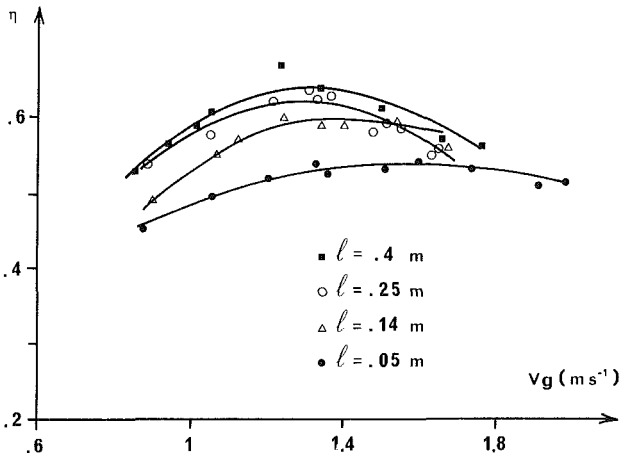

Fig. 5 Measured thermal efficiency in the packed region versus gas velocity; influence of packing height; Pall-25 rings

Table 1 Results for $W_s = 0.93$ kg/m^{2}s and $z = 0.477$ m

v_g	$\frac{\Delta P}{z}$	R	$\beta_{250°C}$	v_s	C_1	C_2	η'	$(1-\epsilon_s)$	η
(m/s)	pa/m	(gms)		(m/s)		m^{-1}			
0.533	120	108	0.0075	0.0473	0.36	112.5	0.36	0.0075	0.36
0.656	178	130	0.00765	0.0464	.444	81	.444	0.0076	.444
0.75	232	148	0.00854	0.04152	0.508	69.98	0.508	0.0078	0.467
0.817	282	170	0.00953	0.0372	0.5534	65	0.5534	0.0084	0.488
0.908	371	218	0.01163	0.03052	0.615	61.53	0.615	0.0098	0.521
1.009	550	370	0.018	0.0197	0.6834	70.55	0.6834	0.014	0.532
1.108	790	496	0.024	0.01479	0.7505	67.43	0.7505	0.0188	0.588
1.202	1080	691	0.03283	0.0108	0.814	63.4	0.814	0.023	0.583

Table 2 Results for $W_s = 0.93$ kg/m^{2}s and $z = 0.175$ m

v_g	$\frac{\Delta P}{z}$	R	$\beta_{250°C}$	v_s	C_1	C_2	η'	$(1-\epsilon_s)$	η
(m/s)	pa/m	(gms)		(m/s)		m^{-1}			
0.661	171.4	52	0.00923	0.0385	0.445	97.18	0.445	0.0073	0.352
0.794	285.7	96	0.01485	0.0239	0.5348	109.19	0.5348	0.0102	0.367
0.919	400	126	0.01876	0.01892	0.6187	97.72	0.6187	0.0113	0.373
1.067	600	167	0.02426	0.01463	0.7183	80.42	0.7183	0.0138	0.4086
1.189	771.4	189	0.02714	0.01308	0.8	57.34	0.8	0.0148	0.4363
1.437	985.7	193	0.02766	0.01283	0.9674	7.88	0.9567	0.0119	0.4127

Table 3 Results for $W_s = 0.93$ kg/m^{2}s and $z = 0.35$ m

v_g	$\frac{\Delta P}{z}$	R	$\beta_{250°C}$	v_s	C_1	C_2	η'	$(1-\epsilon_s)$	η
(m/s)	pa/m	(gms)		(m/s)		m^{-1}			
0.67	186	59	0.00782	0.0513	0.453	70.6	0.453	0.007	0.405
0.79	270	83	0.00922	0.0433	0.534	60.46	0.534	0.008	0.451
0.92	390	136	0.01245	0.032	0.622	57	0.622	0.01	0.4918
1.06	540	191	0.0158	0.0253	0.717	46.8	0.717	0.0115	0.522
1.18	540	236	0.01854	0.02153	0.798	35.3	0.798	0.013	0.56
1.45	1100	360	0.0261	0.0153	0.981	3.8	0.974	0.0135	0.504
1.55	900	282	0.02134	0.0268	1.048	−5.16	0.992	0.007	0.3256

Table 4 Results for $W_s = 1.33$ kg/m^{2}s and $z = 0.35$ m

v_g	$\frac{\Delta P}{z}$	R	$\beta_{250°C}$	v_s	C_1	C_2	η'	$(1-\epsilon_s)$	η
(m/s)	pa/m	(gms)		(m/s)		m^{-1}			
0.631	187	141.5	0.0104	0.04876	0.2984	144.7	0.2984	0.01	0.287
0.808	307	178.2	0.01263	0.04018	0.382	120.8	0.382	0.0104	0.3145
1.04	597	316	0.02104	0.02413	0.492	128.4	0.492	0.0144	0.337
1.212	968	486	0.02723	0.01864	0.5732	119.84	0.5732	0.0193	0.404
1.435	852	442	0.0287	0.0177	0.6787	80.32	0.6787	0.0086	0.206

reasoning to our room temperature measurements on the small column: The particles in the packed section are slowed down by both the packing and the countercurrent gas flow. The holdup due to the packing can be determined from experiments with no gas flow and is assumed to be temperature independent. The holdup due to the gas flow is temperature dependent since the gas density, and thus the upward force, varies within T. This term was multiplied by the density ratio

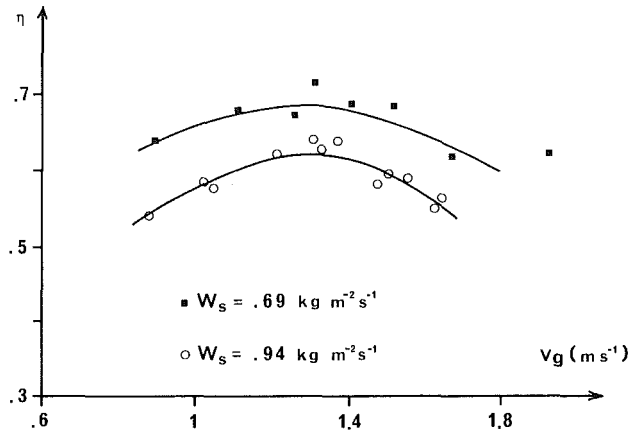

Fig. 6 Measured thermal efficiency in the packed region versus gas velocity; influence of solid mass flux; Pall-25 rings

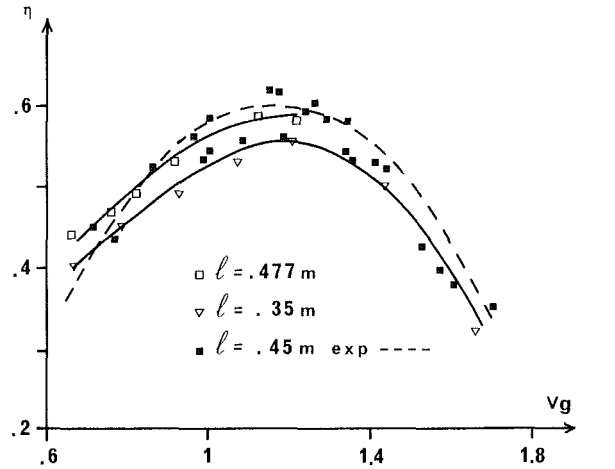

Fig. 7 Comparison of measured and theoretical efficiencies; $W_s = 0.93$ kg/m^2/s; Pall-15 rings

between 250°C and 20°C. The solid trickle velocity v_s and the values of C_1, C_2, and η' in equation (4) are next given. In almost all cases, the value of η' is equal to the value of C_1; the reason for this is that the product $C_2 l$ is in all cases very high, see equation (4). The tabulated values of C_2 were obtained by using the conduction solution (Nu = 2) for the heat transfer coefficient h. If a semi-empirical relationship of the type $\mathrm{Nu} = 2 + a\mathrm{Re}^{0.5}$ were used, an even higher value for C_2 would be obtained. This means that for the experimental conditions used here, the exact value of h, above the conduction regime solution, is of little importance. The last two columns in these tables give the calculated values of $(1-\epsilon_s)$ and η. For low gas velocities, below 1 m/s, the $(1-\epsilon_s)$ values are practically equal to the $\beta_{250°C}$ experimental values. This would mean that the solid particles are suspended uniformly in the packed section. As the gas velocity increases, the value of $(1-\epsilon_s)$ becomes smaller than the $\beta_{250°C}$ value. The real exchanger efficiency η obtained with equation (6) also becomes much smaller than the η' value.

Theoretical and experimental results are compared in Fig. 7 where the efficiency is plotted versus gas velocity. The two theoretical curves were obtained with packing heights of 0.350 m and 0.477 m while the experimental data were obtained for 0.45 m. It is interesting to note that increasing the packing height above 0.4 m also results in no heat transfer gain, a result previously obtained experimentally. Figures 8 and 9 are theoretical predictions of efficiency as a function of packing length and solid flux. The shape of these curves is to be com-

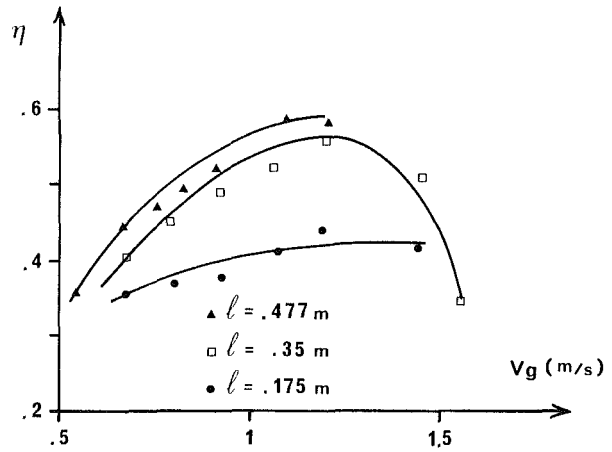

Fig. 8 Theoretical efficiency versus gas velocity; influence of packing height; Pall-15 rings

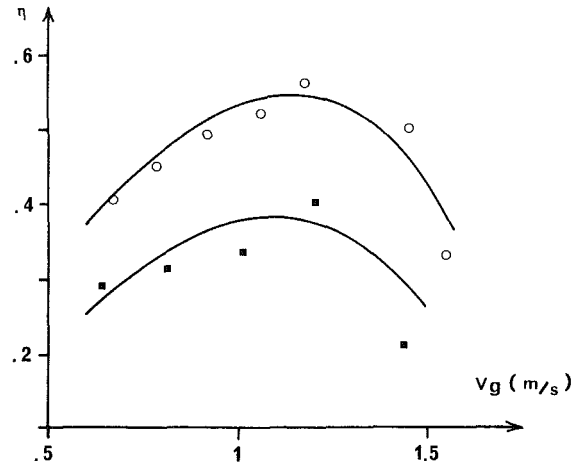

Fig. 9 Theoretical efficiency versus gas velocity; influence of solid mass flux; Pall-15 rings

pared to that of Figs. 5 and 6. For packed section lengths below 0.175 m, the efficiency curves are flatter since the radially segregated regime appears at higher gas velocities.

A last point concerning the way in which the solid particles are initially suspended into the flow merits a discussion. In a previous work (Large et al., 1983), different solid distributors were compared and it was found that the highest heat-exchanger efficiency was obtained for the distributor that provoked the highest pressure drop in the packed zone. This point is easily explained, qualitatively, using the above analysis. If the pressure drop is higher for given gas velocity and solid flux, the pressure drop due to the solids in equation (7) is thus obviously higher and the ratio $(1-\epsilon_s)/\beta$ will increase, thus increasing the efficiency.

Conclusions

A model for scale-up of countercurrent, gas–solid heat transfer in a packed column has been formulated. The model uses only pressure drop and holdup experimental measurements at room temperature and has proved that it successfully predicts the exchanger efficiency. In particular, the fact that the efficiency passes by a maximum value as gas velocity is increased is well represented. The influences of solid flux and packing height are also in qualitative agreement with experimental data obtained using a different packing.

References

Arastoopour, H., and Gidaspow, D., 1979, "Vertical Countercurrent Solids Gas Flow," *Chem. Eng. Sci.*, Vol. 34, pp. 1063–1066.

Ergun, S., 1952, "Flow Through Packed Columns," *Chem. Eng. Progr.*, Vol. 48, p. 89.

Fahien, R. W., and Stankovic, I. M., 1979, "An Equation for the Velocity Profile in Packed Columns," *Chem. Eng. Sci.*, Vol. 34, pp. 1350–1354.

Large, J. F., et al., 1981, "Hydrodynamics of the Raining Packed Bed Gas–Solids Heat Exchangers," *Chem. Eng. J.*, Vol. 22, pp. 95–100.

Large, J. F., Guigon, P., and Saatdjian, E., 1983, "Multistaging and Solids Distributor Effects in a Raining Packed Bed Exchanger," *Proc. 4th International Conference on Fluidization*, Kashikojima, Japan.

Saatdjian, E., and Large, J. F., 1985, "Heat Transfer Simulation in a Raining Packed Bed Exchanger," *Chem. Eng. Sci.*, Vol. 40, No. 5, p. 693–697.

Satterfield, C., 1975, "Trickle-Bed Reactors," *AIChE J.*, Vol. 21, No. 2, pp. 209–228.

Tibourtine, M., 1981, "Hydrodynamique et Transfert Thermique dans un échangeur garni à pluie de particules," Thèse de Docteur Ingénieur, Université de Technologie de Compiègne, France.

Treybal, R. E., 1968, *Mass Transfer Operations*, McGraw-Hill, New York.

Zenz, F. A. and Othmer, D., 1960, *Fluidization and Fluid Particle Systems*, Reinhold, New York.

Mixed Convective Heat Transfer From a Heated Horizontal Plate in a Porous Medium Near an Impermeable Surface

P. H. Oosthuizen
Department of Mechanical Engineering,
Queen's University,
Kingston, Ontario, K7L 3N6 Canada

Two-dimensional flow over a horizontal plate in a saturated porous medium mounted near an impervious adiabatic horizontal surface and subjected to a horizontal forced flow has been numerically investigated. The plate is heated to a uniform temperature that is higher than the temperature of the flowing fluid. The conditions considered are such that the buoyancy forces have an effect on the flow and, therefore, on the heat transfer rate from the plate. The full governing equations, written in dimensionless form, have been solved for a range of values of the governing parameters using the finite element method. The heat transfer rate from the plate is influenced both by the dimensionless depth of the plate below the surface and the importance of the buoyancy forces, the latter having been characterized by a parameter which is equal to the ratio of the Darcy-Rayleigh number to Peclet number. The conditions under which these parameters have a negligible effect on the heat transfer rate are discussed.

Introduction

Two-dimensional flow over a horizontal plate embedded in a saturated porous medium near an impervious adiabatic horizontal surface with a horizontal forced flow over it has been considered, the flow situation thus being as shown in Fig. 1. The plate is assumed to be heated to a uniform temperature T_H', which is higher than the temperature of the flowing fluid T_0'. The conditions considered are such that the buoyancy forces arising from the temperature differences have an effect on the flow and on the heat transfer rate from the plate despite the presence of the forced velocity, i.e., mixed convection has been considered. It should also be noted that the conditions considered are such that the boundary layer assumptions will not generally be applicable.

There have been a number of previous studies of mixed convective heat transfer from flat plates embedded in a porous medium, summaries of previous work in this area being given by, for example, Joshi and Gebhart (1985), Cheng (1977), and Chandrasekhara and Namboodiri (1985). Almost all of these studies have, however, assumed that the component of the buoyancy force parallel to the plate surface is dominant and most of the studies have been based on the use of the boundary layer approximations. Essentially all of the studies have also been concerned with a plate in an infinite surrounding medium. In the geometry considered in the present study, only the buoyancy force component normal to the plate surface exists and the impermeable surface above the plate influences the flow and heat transfer rate. In this respect, the flow situation considered here differs from that dealt with in available studies.

One of the more important applications of the present work is in the prediction of heat transfer from objects buried relatively near the surface with a horizontal groundwater flow over them.

Governing Equations and Solution Procedure

The flow is assumed to be two dimensional and steady and the usual Darcy model is adopted. The fluid velocity well upstream of the plate is assumed uniform and the plate is assumed to be at a higher temperature than the oncoming fluid so that the buoyancy forces are always vertically upward.

Using these assumptions, the governing equations are

$$\frac{\partial u'}{\partial x'}+\frac{\partial v'}{\partial y'}=0 \tag{1}$$

$$\frac{\partial p'}{\partial x'}=-\frac{\mu_f u'}{K} \tag{2}$$

$$\frac{\partial p'}{\partial y'}=-\frac{\mu_f v'}{K}-\beta_g \rho_f (T'-T_0') \tag{3}$$

$$u'\frac{\partial T'}{\partial x'}+v'\frac{\partial T'}{\partial y'}=\left(\frac{k}{\rho_f C_f}\right)\left(\frac{\partial^2 T'}{\partial x'^2}+\frac{\partial^2 T'}{\partial y'^2}\right) \tag{4}$$

The prime (′) is used to denote dimensional quantities and the symbols have their conventional meaning. The subscript f denotes fluid properties, the temperature T_0' of the flowing fluid being used as the reference temperature.

The solution has been obtained by introducing the stream function and defining the following dimensionless variables:

$$\begin{aligned}\theta &= (T'-T_0')/(T_H'-T_0')\\ x &= x'/L', \qquad y=y'/L'\\ \psi &= \text{stream function}/u_0'L'\end{aligned} \tag{5}$$

In terms of these variables, the governing equations are

$$\frac{\partial^2 \psi}{\partial x^2}+\frac{\partial^2 \psi}{\partial y^2}=-B\frac{\partial \theta}{\partial x} \tag{6}$$

$$\frac{\partial \psi}{\partial y}\frac{\partial \theta}{\partial x}-\frac{\partial \psi}{\partial x}\frac{\partial \theta}{\partial y}=\left(\frac{\partial^2 \theta}{\partial x^2}+\frac{\partial^2 \theta}{\partial y^2}\right)/P \tag{7}$$

where

$$B=\frac{\beta g K \rho_f (T_H'-T_0')}{\mu_f u_0'}=\mathrm{Ra}^*/P \tag{8}$$

and

$$P=\frac{\rho_f u_0' L' C_f}{k} \tag{9}$$

where Ra* is the Darcy-Rayleigh number based on L', i.e.,

Contributed by the Heat Transfer Division and presented at the AIAA/ASME Thermophysics and Heat Transfer Conference, Boston, Massachusetts, August 1986. Manuscript received by the Heat Transfer Division July 9, 1986. Keywords: Mixed Convection, Numerical Methods, Porous Media.

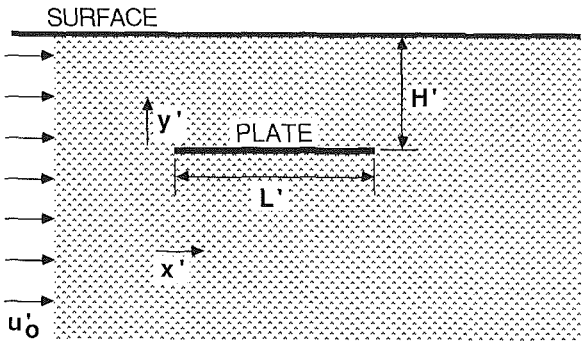

Fig. 1 Flow situation considered

$$\mathrm{Ra}^* = \beta g \rho_f (T'_H - T'_0)/\mu_f \alpha \tag{10}$$

where α is the equivalent thermal diffusivity of the porous medium. The boundary conditions on the solution are:

(*i*) On the surface of the plate:

$$\theta = 1, \qquad \psi = \text{const}$$

(*ii*) At the surface, i.e., at $y = 0$:

$$\psi = 0, \qquad \frac{\partial \theta}{\partial y} = 0$$

(*iii*) At large distances ahead of the plate:

$$\psi \to y, \qquad \theta \to 0$$

(*iv*) At large depths below the surface:

$$\psi \to y, \qquad \theta \to 0$$

In addition, it has been assumed that at large distances downstream of the plate, the x-wise gradients of the stream function and temperature become negligibly small.

Since the flow upstream of the plate is influenced by the presence of the plate due to the buoyancy forces, the stream function on the plate is not directly known. In order to calculate conditions at the plate surface, it has therefore been noted that for any closed surface in the flow, the tangential pressure gradient integrated around the surface must be zero. This is, of course, equivalent to noting that there is no vorticity generated in the flow except by the action of the buoyancy forces. In the present study, since a flat plate is being considered, this requirement is equivalent to

$$\left(\int_0^L \frac{\partial p'}{\partial x'} dx'\right)_{\substack{\text{upper} \\ \text{surface}}} = \left(\int_L^0 \frac{\partial p'}{\partial x'} dx'\right)_{\substack{\text{lower} \\ \text{surface}}} \tag{11}$$

which is equivalent to

$$\left(\int_0^1 \frac{\partial \psi}{\partial y} dx\right)_{\substack{\text{upper} \\ \text{surface}}} = \left(\int_1^0 \frac{\partial \psi}{\partial y} dx'\right)_{\substack{\text{lower} \\ \text{surface}}} \tag{12}$$

This condition allows the stream function at the plate surface to be determined.

The governing equations, subject to the boundary conditions discussed, have been solved using the finite element method, the Galerkin method being used to obtain the required equations. Simple linear triangular elements were used. The solution procedure has been successfully used in a number of other studies of convective heat transfer, e.g., see Oosthuizen and Paul (1986, 1987a, 1987b). A very fine grid spacing was used near the leading and trailing edges of the plate. Calculations were undertaken with several different element distributions and numbers of elements to ensure that the results presented here are essentially grid independent. The results presented were obtained with roughly 700 elements nonuniformly distributed over the solution domain. The boundary conditions well ahead of the plate, well below the plate, and well downstream of the plate were, of course, applied at finite distances from the plate. The actual distances used depended on the conditions being considered but calculations with different distances were undertaken to ensure that the results are essentially independent of the distance chosen.

Results

The solution has, as parameters:

(*i*) the dimensionless depth H of the plate below the surface;

(*ii*) the forced flow parameter Pe, which is, of course, a Peclet number based on the plate length and equivalent thermal diffusivity of the medium;

(*iii*) the buoyancy parameter B, which acts basically as a measure of the importance of the buoyancy forces on the flow.

Solutions have been obtained here for values of the forced flow parameter Pe between 0 and 300 and values of B between 0 and approximately 8 for H values of 0.25, 0.35, 0.5, and 0.75.

The concern in the present study is the mean heat transfer rate from the plate. It must be stressed that this mean heat transfer rate includes the effects of the heat transfer from both the upper and lower surfaces of the plate, the heat transfer

Nomenclature

a = function of H and P, see equation (15)
B = buoyancy parameter, see equation (8)
c_f = specific heat of fluid
g = gravitational acceleration
H' = depth of plate below surface
H = H'/L'
K = permeability
k = effective conductivity of porous medium
L' = length of plate
$\overline{\mathrm{Nu}}$ = mean Nusselt number based on L'
$\overline{\mathrm{Nu}_0}$ = mean Nusselt number for $B = 0$
Pe = Peclet number, see equation (9)
p' = pressure
Ra^* = Darcy–Rayleigh number
T' = temperature
T'_H = plate temperature
T'_0 = temperature of incoming fluid
u' = velocity in x direction
u'_0 = uniform velocity of flow upstream of plate
v' = velocity in y direction
x' = coordinate in horizontal direction
x = x'/L'
y' = coordinate in vertical direction
y = y'/L'
β = coefficient of thermal expansion of fluid
θ = dimensionless temperature, see equation (5)
μ_f = viscosity of fluid
ρ_f = density of fluid
ψ = dimensionless stream function, see equation (5)

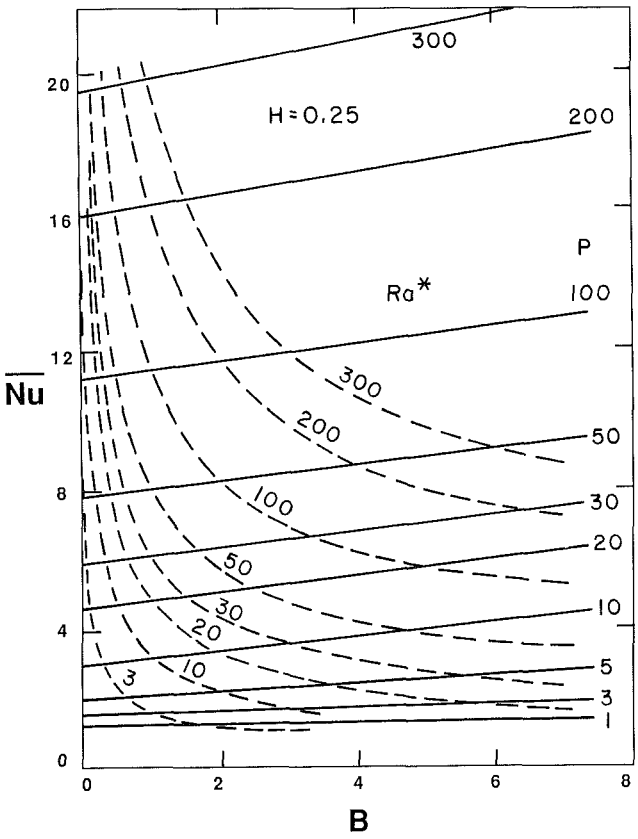

Fig. 2 Variation of mean Nusselt number with B and Pe for $H = 0.25$

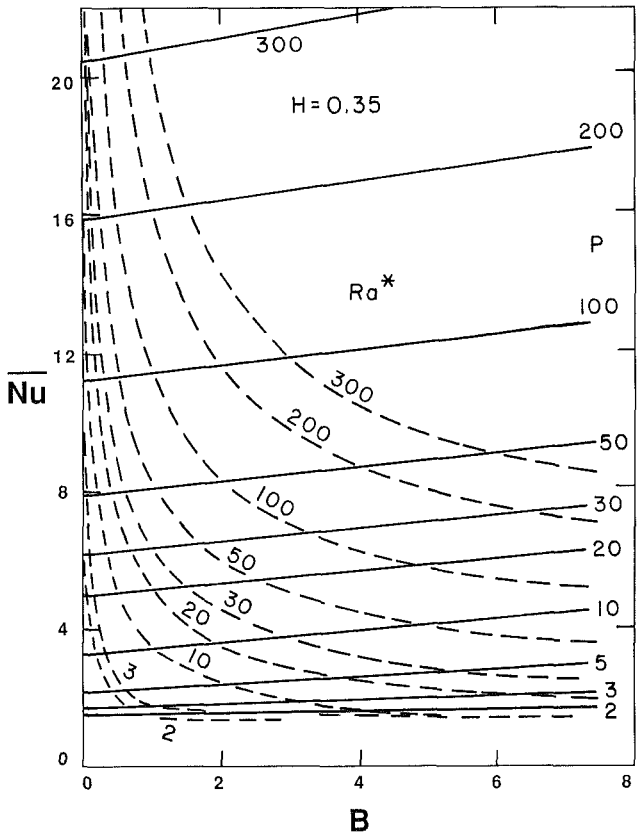

Fig. 3 Variation of mean Nusselt number with B and Pe for $H = 0.35$

rates from these two surfaces differing both because of the presence of the impermeable adiabatic surface above the top of the plate and because of the effects of the buoyancy forces. The variations of the mean Nusselt number with the buoyancy parameter for various values of Pe is shown in Fig. 2, 3, and 4 for H values of 0.25, 0.35, and 0.75. Since, for any values of B and Pe, the Rayleigh number can be determined, lines of constant Rayleigh number are also shown as the dotted curves in these figures.

Attention will first be directed to the results for $B = 0$, i.e., to the case where the buoyancy force is negligible. In this case the velocity field is undisturbed by the presence of the plate or the surface. The variation of the mean Nusselt number with Pe for various values of H for this case is shown in Fig. 5. At the larger values of Pe the results for all of the H values considered converge and become equal to those given by the boundary layer solution for forced convective flow over a flat plate, i.e., by Bejan (1984)

$$\overline{Nu}_0 = 1.13 Pe^{-0.5}$$

In this situation, of course, the temperature changes are all confined to a boundary layer adjacent to the plate that is small compared to the distance between the upper surface of the plate and the bounding impermeable surface and the presence of this impermeable surface has no effect on the heat transfer rate. The agreement of the present results with the boundary layer result at larger values of Pe provides one validation of the solution procedure.

As Pe decreases, the results diverge from the boundary layer result due both to the fact that the longitudinal temperature gradients become comparable to the normal temperature gradients so that the boundary layer approximations are not

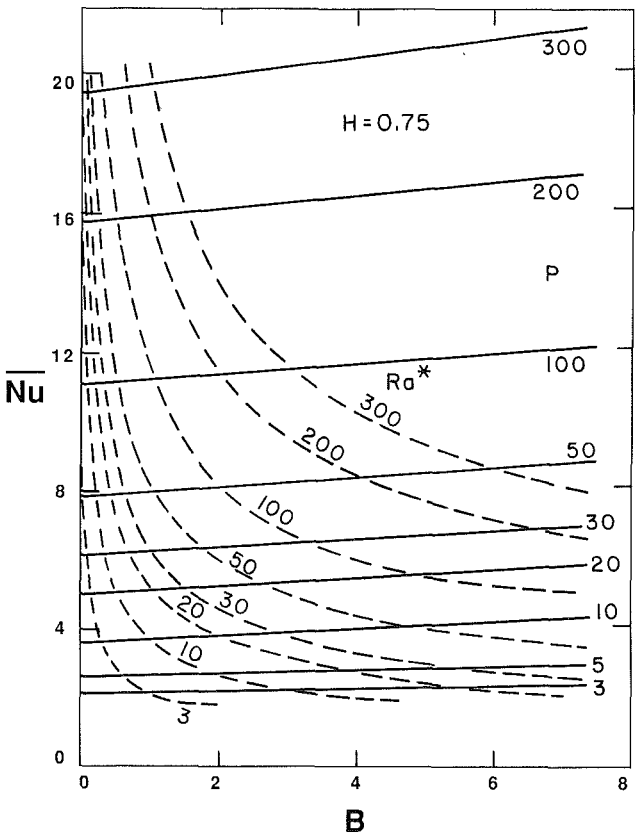

Fig. 4 Variation of mean Nusselt number with B and Pe for $H = 0.75$

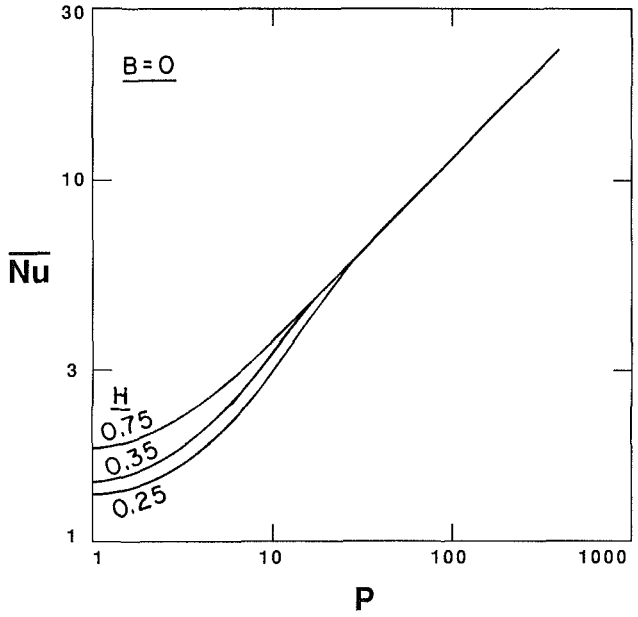

Fig. 5 Mean Nusselt number variation for purely forced convection

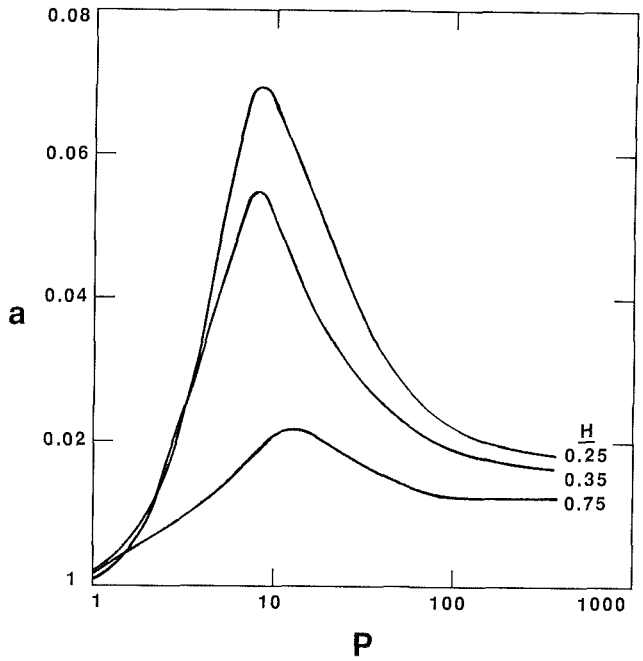

Fig. 6 Variation of buoyancy effect parameter *a* with *H* and Pe

valid, i.e., the boundary layer thickness is comparable to the plate length, and due to the fact that at the smaller values of H considered, the temperature changes produced by the presence of the plate have spread to the impermeable surface near the upper surface of the plate. Since the impermeable surface is adiabatic, this latter effect produces a reduction in the mean heat transfer rate for the upper surface as compared to that on the lower surface. At very small values of Pe, when the boundary layer thickness is much greater than the plate size, the plate behaves like a point heat source and the Nusselt number becomes dependent only on the depth below the surface H. The results of all of these effects on the mean heat transfer rates from the entire plate will be seen in Fig. 5. At lower Pe values, the heat transfer rates for the different H values considered diverge from each other, being lowest for $H=0.25$ and highest for $H=0.75$. The results for $H=0.75$ are little affected by the presence of the impermeable surface except at very small values of Pe. As a result, the mean heat transfer rates for this value of H lie above those predicted by the boundary layer result at smaller values of Pe. At $H=0.25$ and $H=0.35$, however, the impermeable surface has a significant influence on the results and the mean heat transfer rates tend to lie below those predicted by the boundary layer result. Since the boundary layer thickness will be related to $L\mathrm{Pe}^{-0.5}$, it is to be expected that the impermeable surface will start to influence the mean heat transfer results when $H\mathrm{Pe}^{-0.5}$ falls below a certain value. Based on the results presented in Fig. 5, it is therefore concluded that the effects of the impermeable surface become negligible approximately when

$$\mathrm{Pe} > 2/H^2 \tag{14}$$

However, when H gets above about 0.5, the effect of the surface starts to occur at such low values of P that this result, based as it is partly on the boundary layer approximations, become increasingly inaccurate.

Turning next to a consideration of the effects of the buoyancy forces on the mean heat transfer rates it will be noted from Figs. 2, 3, and 4, that at a given value of Pe for any given H, Nu varies approximately linearly with B, i.e., $(\overline{\mathrm{Nu}} - \overline{\mathrm{Nu}}_0)$ is proportional to B, $\overline{\mathrm{Nu}}_0$ being the value of $\overline{\mathrm{Nu}}$ at $B=0$ for the particular values of H and Pe considered. From this it follows that approximately

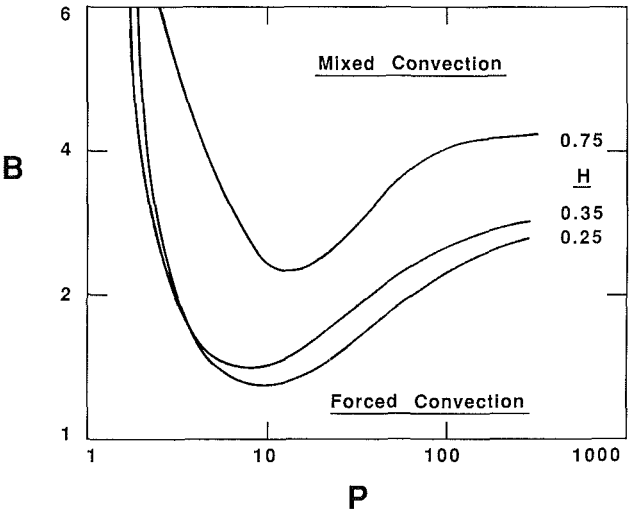

Fig. 7 Variation of the value of *B* at the "beginning" of the mixed convection region with Pe for various values of *H*

$$\overline{\mathrm{Nu}}/\overline{\mathrm{Nu}}_0 = 1 + aB \tag{15}$$

where a is a function of H and Pe. The variation of a with Pe for the various values of H considered is shown in Fig. 6. It will be seen that as $\mathrm{Pe}\to 0$, $a\to 0$ basically because as $\mathrm{Pe}\to 0$ for a finite value of B the Rayleigh number $\mathrm{Ra}^*\to 0$ so the buoyancy force effect becomes negligible. It will also be seen that the a variation shows a maximum at all values of H considered at Pe values of about 10, the peak value increasing over the range of values considered with decreasing H. At larger Pe values, a then tends to drop toward an approximately constant value at large values of Pe. It will further be noted from these results that, at all values of H considered, the presence of the adiabatic impermeable surface seems to have a significant effect on the mean heat transfer rates. This is, of course, in contrast to the results of $B=0$ for which the effects of the surface were very nearly negligible for H above about 0.5, as discussed earlier, i.e., surface effects are more significant in the mixed

convection region than in the purely forced convection region due to the fact that the upward motion induced by the buoyancy forces in the leading edge region is inhibited by the presence of the surface. The temperature gradients near the leading edge of the plate cause the flow ahead of the plate to rise, this effect increasing with increasing B. Because the flow rises ahead of the plate, the presence of the free surface causes the mean velocity over the top of the plate to be higher than it would be if the buoyancy forces were negligible. This causes the heat transfer rate on the upper surface of the plate to be higher than it would be in purely forced convective flow. This is also, of course, the reason why the effects of the surface are more significant in the mixed convection region than in the purely forced convection region. At larger values of Pe, as the boundary layer region is approached, the upstream effects of the plate decreases causing a to decrease.

The mixed convection region is assumed to start at the lowest value of B at which the mean Nusselt number becomes 5 percent greater than the mean Nusselt number under the same conditions in purely forced convection, i.e., when $\overline{Nu}/\overline{Nu}_0 = 1.05$. It follows from equation (15) that this region is entered when

$$B > 0.05/a \tag{16}$$

The variation of this value of B with Pe for various values of H is shown in Fig. 7. This again shows that buoyancy force effects occur at lower values of B as the plate approaches the surface, i.e., as H is decreased.

Conclusions

The results of the present study indicate that:

(*i*) in purely forced convection, the effects of the impermeable adiabatic surface on the heat transfer rates become negligible when

$$\mathrm{Pe} > 2/H^2$$

(*ii*) in purely forced convection, if the presence of the surface is important, it causes a reduction in the heat transfer rate from the upper surface compared to what would exist with an infinite environment;

(*iii*) in the combined convection region, the buoyancy forces cause the flow to rise ahead of the plate and the presence of the surface then causes the heat transfer rate on the upper surface of the plate to be increased;

(*iv*) the mean Nusselt number for any given values of H and Pe varies linearly with B in the mixed convective region;

(*v*) The results given in Fig. 7 can be used to determine when the mixed convection region is entered.

Acknowledgments

This work was supported by the Natural Sciences and Engineering Research Council of Canada.

References

Chandrasekhara, E. C., and Namboodiri, B. P. M. S., 1985, "Influence of Variable Permeability on Combined Free and Forced Convection About Inclined Surfaces in Porous Media," *Int. J. Heat Mass Transfer*, Vol. 28, pp. 199–206.

Cheng, P., 1977, "Combined Free and Forced Convection Flow About Inclined Surfaces in Porous Media," *Int. J. Heat Mass Transfer*, Vol. 20, pp. 807–814.

Joshi, Y., and Gebhart, B., 1985, "Mixed Convection in Porous Media Adjacent to a Vertical Uniform Heat Flux Surface," *Int. J. Heat Mass Transfer*, Vol. 28, No. 9, pp. 1783–1786.

Oosthuizen, P. H., and Paul, J. T., 1986, "Natural Convective Heat Transfer Across a Liquid-Filled Cavity," *Proceedings of the 8th International Heat Transfer Conference*, San Francisco, CA, Vol. 4, pp. 1527–1532.

Oosthuizen, P. H., and Paul, J. T., 1987a, "Effect of Cap Shape on Free Convective Heat Transfer Across a Cavity," *Proceedings of the 1987 ASME/JSME Thermal Engineering Joint Conference*, Honolulu, HI, Vol. 2, pp. 221–226.

Oosthuizen, P. H., and Paul, J. T., 1987b, "Natural Convective Flow in a Square Cavity Partly Filled With a Porous Medium," *Proceedings of the 1987 ASME/JSME Thermal Engineering Joint Conference*, Honolulu, HI, Vol. 2, pp. 407–412.

V. Prasad
Department of Mechanical Engineering,
Columbia University,
New York, NY 10027
Mem. ASME

F.-C. Lai[1]

F. A. Kulacki[2]
Mem. ASME

Department of Mechanical and
Aerospace Engineering,
University of Delaware,
Newark, DE 19716

Mixed Convection in Horizontal Porous Layers Heated From Below

Numerical studies are reported for steady, mixed convection in two-dimensional horizontal porous layers with localized heating from below. The interaction mechanism between the forced flow and the buoyant effects is examined for wide ranges of Rayleigh number Ra and Peclet number Pe*. The external flow significantly perturbs the buoyancy-induced temperature and flow fields when Pe* is increased beyond unity. For a fixed Peclet number, an increase in Rayleigh number produces multicellular recirculating flows in a domain close to the heat source. This enhances heat transfer by free convection. However, for a fixed Ra*, an increase in forced flow or Peclet number does not necessarily increase the heat transfer rate. Hence, there exists a critical Peclet number as a function of Ra* for which the overall Nusselt number is minimum. The heat transfer is, generally, dominated by the buoyant flows for Pe* < 1 whereas the contribution of free convection is small for Pe* > 10 when Ra* ≤ 10.*

Introduction

An understanding of the basic properties of convection in a horizontal porous layer heated from below is important from both a theoretical and an applied point of view. Convective instability is a widespread phenomenon, numerous examples of which have been noted in geophysical and engineering situations. Theoretically, convection driven by an adverse temperature gradient is one of the simplest types of hydrodynamic stability, and considerable progress has been made in its study. Not only the researchers have investigated the criteria for onset of convection and the local and overall heat transfer rates, but they have also examined the stability of fluid flow, the cell structure, and its oscillatory behavior under various conditions. In recent years, attempts have also been made to characterize the effects of the thermal boundary conditions, the thermophysical property variation, the layer width-to-height ratio, the superposed fluid layers, and the layered porous media with direction-dependent permeability, etc. Extensive reviews of these studies have been presented by Combarnous and Bories (1975), Cheng (1978), Prasad et al. (1985), and Catton (1985).

A related problem of practical interest is when a finite heat source is located on the bottom of the horizontal porous layer that extends beyond the edges of the heated segment. This situation may be encountered in several geothermal areas, which consist of troughs of volcanic debris or some other form of heat source. Thus, the model region considered is a locally heated long trough of porous medium. Also, the recent motivation to study the convection from a localized heat source has come from the efforts to identify a geologic repository for the storage of nuclear wastes.

Several attempts have been made to study the buoyancy-induced flow and heat transfer in a horizontal porous layer with localized heating from below by Elder (1967a, b), Horne and O'Sullivan (1974, 1978), and Prasad and Kulacki (1985, 1986). Interesting features of the growth of convective cells, the inversion in temperature gradient, and the extent of the significantly influenced thermoconvective domain as functions of the size and strength of the heat source have been reported. Recently, El-Khatib and Prasad (1986) have extended these studies to examine the effects of the linear thermal stratification caused by an external temperature gradient.

The present study considers the buoyancy effects produced by a finite heat source on the bottom of a horizontal porous layer through which a fluid is flowing because of an external pressure gradient. The geometry considered is a two-dimensional, saturated porous layer bounded by an isothermally cooled, impermeable horizontal wall on the top and an insulated, impermeable wall at the bottom with a finite, isothermal heat source. The interaction mechanism of free and forced convection has been numerically examined for wide ranges of Rayleigh and Peclet numbers when the length of the heated segment is equal to the height of the layer. The effect of the externally induced flow on multicellular recirculating flows, observed in the case of natural convection, has also been investigated.

Formulation and Numerical Method

Consider the flow of an incompressible, constant-property, Boussinesq fluid through an isotropic, homogeneous porous medium bounded by two impermeable, horizontal walls. A finite heat source of length d, at a constant temperature T_h, is located on the bottom surface, which is otherwise adiabatic. The top surface is assumed to be isothermally cooled at T_c (Fig. 1). On the upstream side, the fluid at a constant temperature T_c is considered to be flowing with an uniform velocity U far away from the leading edge of the heat source. In the porous medium, Darcy's law is assumed to hold, and the viscous drag (Brinkman model) and inertia terms in the equations of motion are neglected assuming that the Darcy number and the particle Reynolds number for the porous matrix are small. Owing to the last assumption, velocity slip at the bounding walls is permitted.

With these assumptions, the conservation equations for mass, momentum, and energy (Prasad and Kulacki, 1984) for steady, two-dimensional flow through porous medium can be written in stream function-temperature form as

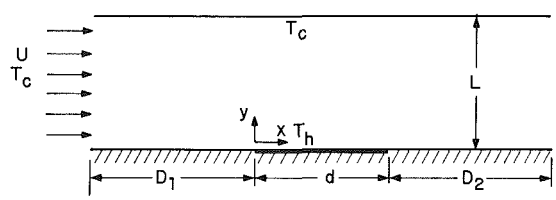

Fig. 1 Two-dimensional horizontal porous layer with a finite, isothermal heat source of width, $d = L$, coordinate system and boundary conditions

[1]Present address: B-120 Engineering Research Center, Colorado State University, Fort Collins, CO 80523.

[2]Present address: Office of the Dean, College of Engineering, Colorado State University, Fort Collins, CO 80523.

Contributed by the Heat Transfer Division for publication in the JOURNAL OF HEAT TRANSFER. Manuscript received by the Heat Transfer Division March 7, 1987. Keywords: Mixed Convection, Porous Media.

$$\frac{\partial^2\psi}{\partial X^2}+\frac{\partial^2\psi}{\partial Y^2}=\frac{\mathrm{Ra}^*}{\mathrm{Pe}^*}\frac{\partial\theta}{\partial X} \tag{1}$$

$$\frac{\partial\psi}{\partial X}\frac{\partial\theta}{\partial Y}-\frac{\partial\psi}{\partial Y}\frac{\partial\theta}{\partial X}=\frac{1}{\mathrm{Pe}^*}\left(\frac{\partial^2\theta}{\partial X^2}+\frac{\partial^2\theta}{\partial Y^2}\right) \tag{2}$$

The governing dimensionless parameters are thus

$$\mathrm{Ra}^*=g\,\beta\,KL(T_h-T_c)/\nu\alpha \qquad \text{(Rayleigh number)} \tag{3}$$

and

$$\mathrm{Pe}^*=UL/\alpha \qquad \text{(Peclet number)} \tag{4}$$

Here, the significance of buoyancy term is governed by the ratio of Rayleigh and Peclet or Grashof and Reynolds numbers ($\mathrm{Ra}^*/\mathrm{Pe}^* = \mathrm{Gr}^*/\mathrm{Re}$).

The relevant hydrodynamic and thermal boundary conditions on the bounding surfaces are straightforward, and are given by

$$Y=0,\quad \psi=0 \qquad \begin{cases} \partial\theta/\partial Y=0 & -X_1\le X>0 \\ \theta=1 & 0\le X\le H \\ \partial\theta/\partial Y=0 & H<X<X_2+H \end{cases} \tag{5}$$

$$Y=1,\quad \psi=-1,\quad \theta=0 \tag{6}$$

Since the x direction velocity far away from the heat source on the upstream side has been assumed to be a constant and the fluid is cold, one may write

$$X=-X_1,\quad u=U \text{---}> \psi=-Y,\quad \theta=0 \tag{7}$$

While satisfying this condition, it has to be ascertained that X_1 is large enough that the buoyancy effects do not penetrate to the upstream end, $x = -D_1$.

The assumption of downstream boundary conditions is not easy. For the present calculations, it has been assumed that

$$X=H+X_2,\quad \partial\psi/\partial X=0,\quad \partial\theta/\partial X=0 \tag{8}$$

which is based on the fact that far away from the heat source, $X_2 \gg H$, the flow will become, once again, parallel after releasing a large fraction of thermal energy on the top wall. The axial conduction will, then, be almost negligible.

Finite-difference equations are derived from equations (1) and (2) by integration over finite area elements following a procedure outlined by Gosman et al. (1969). The successive substitution formulas derived in this way by employing upwind differences for convective terms in the energy equation satisfy the convergence criterion, and are quite stable under many circumstances (Roache, 1982). For solving the system of algebraic equations thus obtained, the Gauss-Seidel point iterative method is used, which makes use of the new values as soon as they are available. To make the iterative convergence faster, the temperature is overrelaxed. A suitable value of the overrelaxation parameter is between 1.3 and 1.6. A detailed account of the numerical scheme used here has been presented by Prasad elsewhere (1983, 1986).

As discussed earlier, the lengths of the unheated section, X_1 and X_2, are of considerable importance to the present computations. Hence, several trial runs were made for various combinations of Ra^* and Pe^* to select proper values X_1 and X_2. Based on these results, X_1 and X_2 are generally taken as 4 and 5, respectively, when $H = 1$ and $\mathrm{Ra}^* < 500$. This makes the length of the bottom wall 10 times larger than the height, in the computational domain. For higher Rayleigh number calculations, $(X_1 + H + X_2)$ has been taken as 15.

Various combinations of uniform and nonuniform grid fields have been used to select one that would yield reasonably accurate results and yet require less CPU time. It has been observed that the use of varying grids with fine mesh near the horizontal walls is advantageous and more reasonable owing to sharp temperature gradients and significant changes in the magnitude and direction of velocities near the boundaries. Furthermore, to predict large-scale variations in u and v accurately in a region close to the heat source, very fine grids are needed in the x direction. Since the computational domain is quite large in the x direction and we can't afford to use very

Nomenclature

D_1 = distance before the heat source, m
D_2 = distance after the heat source, m
d = length of heat source, m
g = acceleration due to gravity, m/s^2
Gr^* = Grashof number $= g\beta KL(T_h - T_c)/\nu^2$
H = dimensionless length of heat source $= d/L$
$\bar{h}$ = average heat transfer coefficient, W/m^2-K
h_x = local heat transfer coefficient on the bounding surface, W/m^2-K
K = permeability of saturated porous medium, m^2
k = effective thermal conductivity of porous medium, W/m-K
L = height of porous layer, m
$\overline{\mathrm{Nu}}$ = overall Nusselt number based on layer height $= \bar{h}\,L/k$
Nu_x = local Nusselt number $= h_xL/k$
Pe^* = Peclet number $= UL/\alpha$
Pr^* = Prandtl number $= \nu/\alpha$
Q = heat transfer rate, W
Re = Reynolds number $= UL/\nu$
Ra^* = Rayleigh number based on cavity width $= g\,\beta\,KL(T_h - T_c)/\nu\alpha$
T = temperature, K
u = fluid velocity in x direction, m/s
u' = dimensionless velocity in x direction $= u/U = -(\partial\psi/\partial Y)$
U = velocity in x direction due to forced flow, m/s
v = fluid velocity in y direction, m/s
v' = dimensionless velocity in y direction $= v/U = (\partial\psi/\partial X)$
y, y = Cartesian coordinates, m/s
X = dimensionless distance on x axis $= x/L$
Y = dimensionless distance on y axis $= y/L$
X_1 = dimensionless distance before the heat source (in computational domain) $= D_1/L$
X_2 = dimensionless distance after the heat source (in computational domain) $= D_2/L$
α = thermal diffusivity of porous medium, m^2/s
β = isobaric coefficient of thermal expansion of fluid, K^{-1}
θ = dimensionless temperature $= (T - T_c)/(T_h - T_c)$
ν = kinematic viscosity, m^2/s
ψ = dimensionless stream function

Subscripts

c = cooled wall
fc = forced convection
h = heated wall
max = maximum
nc = natural convection
x = local value on the bounding wall

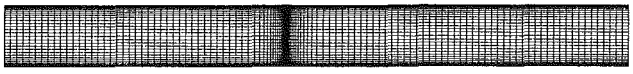

Fig. 2 121 × 31 grid distribution for the present computations

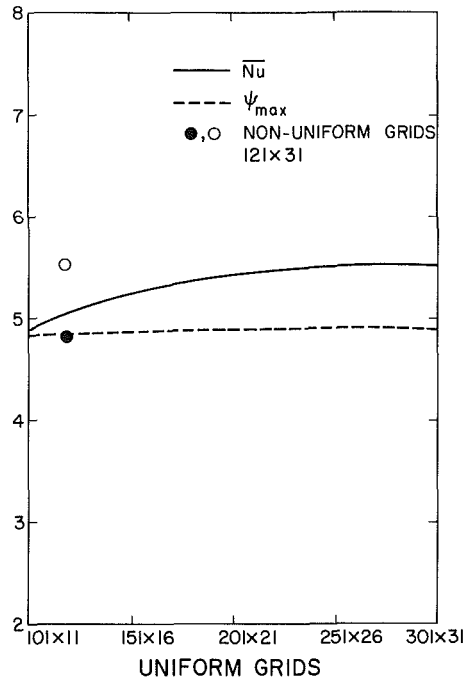

Fig. 3 Effect of grid size on numerical results

small Δx everywhere, nonuniform grids (in the x direction) are generally used for the length of the heated segment. Hence, the grid fields are symmetric about $x = 0.5d$ and $y = 0.5L$ with very fine mesh close to the bounding walls and the center of the heated segment, i.e., $x = 0.5d$ (Fig. 2). A grid field of 121 × 31 mesh has been used when both the Rayleigh and Peclet numbers are low; otherwise a 171 × 31 mesh is employed. For trial runs, these grid fields predicted heat transfer results within 3 percent of the asymptotic values. For example, a 301 × 31 uniform grid field produces $\overline{Nu}$ and ψ_{max} only 1.3 and 2 percent higher than that obtained by using a 121 × 31 nonuniform mesh for Ra* = 100 and Pe* = 10 (Fig. 3).

A variation of 10^{-4} or less in both θ and ψ at all nodes in the domain is used as the iterative convergence criterion for the present computations. This usually requires 800 to 2000 iterations for the present range of parameters. Since the diffusion of buoyancy effects takes longer to penetrate into the upstream flow, larger number of iterations are required to achieve convergence when the Rayleigh number is high.

Another difficulty associated with the present computations is that when the Peclet number is low and the Rayleigh number is high, the contribution of the source term in equation (1) is large. This also reduces the contribution of convection as compared to conduction (equation (2)); hence, a large portion of the flow upstream of the heat source is influenced by buoyancy effects (to be discussed later) so that boundary condition (7) becomes unrealistic. Also, the downstream condition (8) limits the range of Rayleigh and Peclet numbers suitable for the present computational domain. This has restricted the range of parameters to $1 \le Ra^* \le 500$ and $0.01 \le Pe^* \le 50$, for which the results could be obtained with the desired accuracy.

To check the accuracy of results reported here further, an energy balance has been employed that compares the energy lost by the heat source to the heat removed on the cold wall plus the energy being carried away by the fluid at the downstream end. Mathematically

Table 1 Selected values of overall Nusselt number $\overline{Nu}$

Ra*/Pe*	0.01	0.1	0.5	1.0	5	10	50
1	1.934	1.969	1.982	2.025	2.804	3.816	8.382
10	2.007	2.014	2.057	2.093	2.926	3.942	8.431
100	5.670	5.669	5.658	5.623	5.077	5.494	8.932
500		12.633	12.401	12.367	11.338	9.986	11.009
fc				2.010	2.792	3.803	8.376
fc (Vertical Plate)+					2.523	3.568	7.977

+ Boundary Layer solution for forced convection on an isothermal horizontal surface (Cheng, 1977).

$$\int_0^H -\frac{\partial\theta}{\partial Y}\bigg|_{Y=0} dX = \int_{X_1}^{H+X_2} -\frac{\partial\theta}{\partial Y}\bigg|_{Y=1} dX + \int_0^1 u'\theta\bigg|_{X=X+H_2} dY \tag{9}$$

For a large number of these calculations the energy balance is satisfied within 1 percent. However, to keep the computational cost low, the results for low Ra* and high Pe* have been accepted even if the variation is up to 4 percent.

Although the upwind difference is known to cause false diffusion, this effect is of small order in the present computations. This can be seen from an estimation of the ratio of false diffusion to true diffusion (Gosman et al., 1969)

$$\epsilon = 0.36(Vh/\alpha)\sin 2\phi \tag{10}$$

where V is the velocity, h is the grid size, and ϕ is the angle that the streamline makes with the coordinate system. With the nonuniform grids used in this study, where V is large (near the walls and near the center line of heat source), h and $\sin 2\phi$ are very small. This always leads to $\epsilon \ll 1$.

The overall accuracy of the numerical scheme and negligible effects of false diffusion can also be ascertained by comparing the forced convection results with the boundary layer solutions for a flat plate (Cheng, 1977). The predicted heat transfer rate for Pe* = 50 is only 4.8 percent higher than Cheng's solution (Table 1).

Results and Discussion

Heat transfer results have been obtained for Ra* = 1, 10, 100, and 500, and $0.01 \le Pe^* \le 50$ when the width of the heat source is equal to the height of the horizontal porous layer, i.e., $d = L$. To present the decreasing influence of the externally induced flow or the relatively increasing strength of the buoyancy, the isotherms and streamlines for Ra* = 10 and Pe* = 10, 5, 1, 0.5, and 0.1 are presented in Figs. 4(*a–e*). When the Peclet number is high, the perturbation in the flow field by buoyancy is negligible (Fig. 4*a*), and the flow is almost uniform. The vertical velocity v is, thus, zero (Fig. 5). This indicates that the contribution of the buoyancy term in equation (1) is very small when Gr*/Re (or Ra*/Pe*) is of the order of unity. The isotherms further indicate that the upstream diffusion of thermal energy is small. The heat transfer is thus dominated by forced convection.

The local Nusselt number on the bottom surface

$$Nu_x = h_x L/k = -\partial\theta/\partial Y \text{ at the wall} \tag{11}$$

is very high at the leading edge of the heat source, $x = 0$, and decreases greatly with an increase in x (Fig. 6*a*). It reaches a minimum slightly before the trailing edge of the heated segment, and then increases by a small amount with x until $x = d$. The local Nusselt number on the upper surface is very small when $x < 0$ (Fig. 6*b*), again indicating that the diffusion of energy in upstream flow is minimal. However, the heat

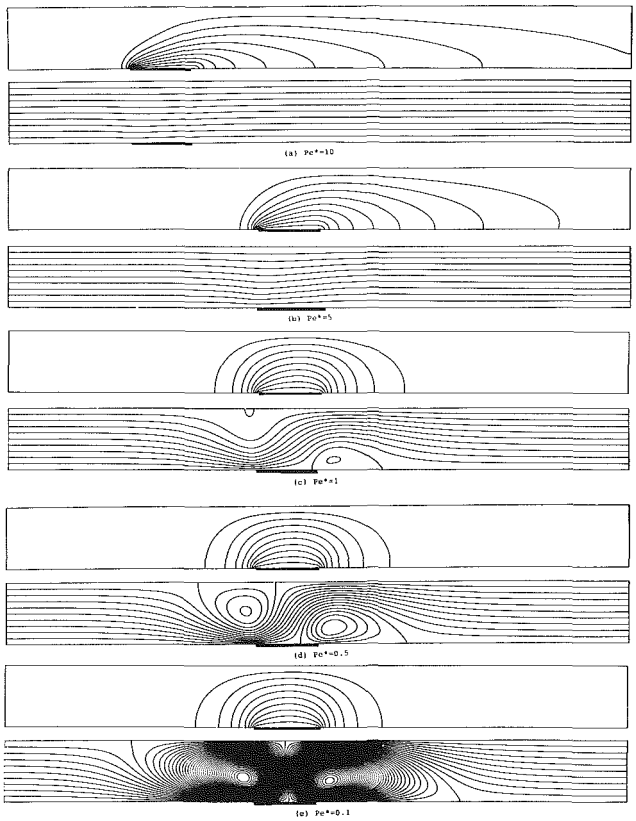

Fig. 4 Isotherms and streamlines for Ra* = 10 ($\Delta\theta$ = 0.1, $\Delta\psi$ = 0.1), (*a*) Pe* = 10, (*b*) Pe* = 5, (*c*) Pe* = 1, (*d*) Pe* = 0.5, and (*e*) Pe* = 0.1

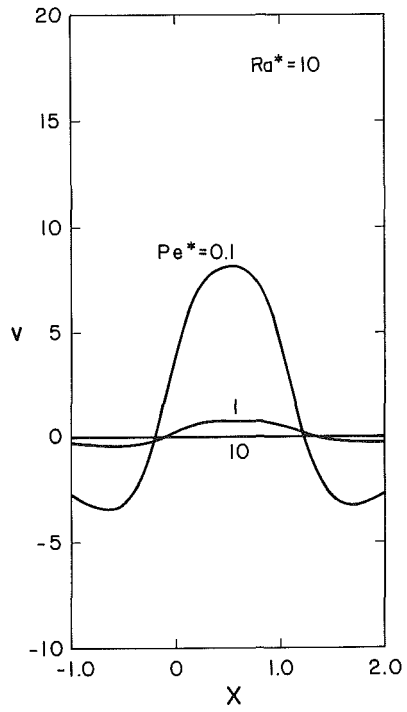

Fig. 5 Vertical velocity at the midheight for Pe* = 0.1, 1, and 10

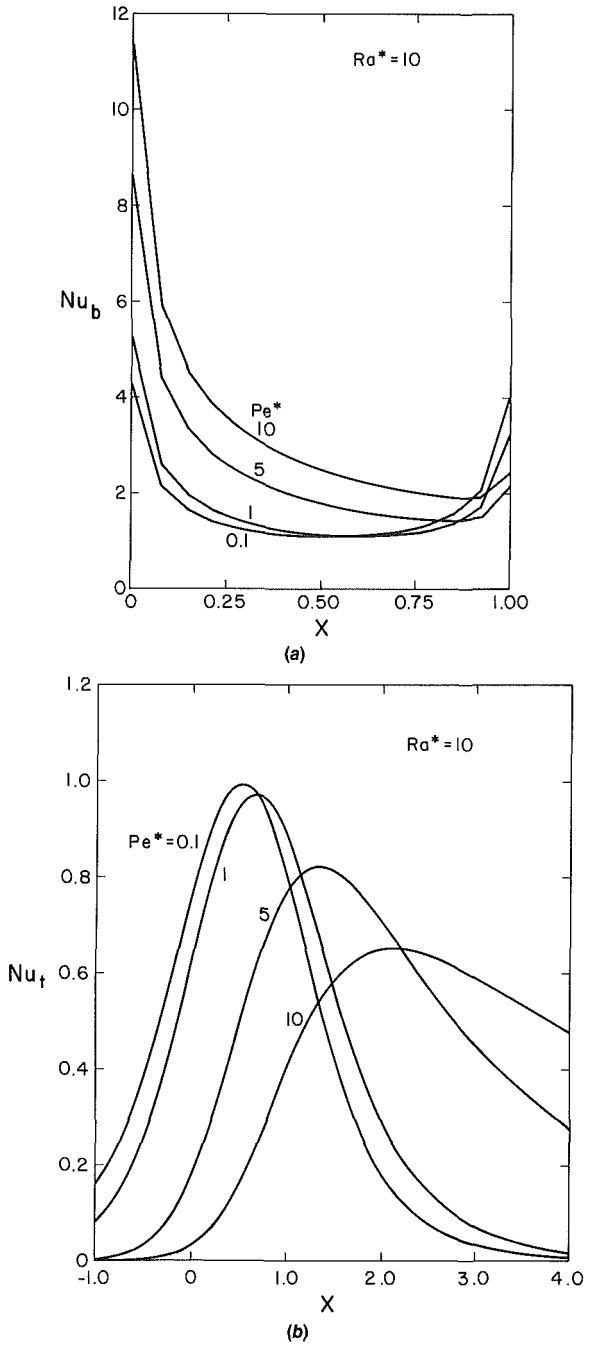

Fig. 6 Local Nusselt number on the bounding surfaces for Pe* = 0.1, 1, 5, and 10: (*a*) heated segment and (*b*) upper surface

transfer rate increases with x until it reaches a peak at $x \simeq 2d$, beyond which it monotonically decreases. The reason for $(\mathrm{Nu}_x)_{\max}$ existing at a location far beyond $x = d$ is that the convective transport of energy in the y direction is slow since the $(v\partial T/\partial y)$ term in the energy equation (2) is relatively small. As a result, the energy continues to be removed for a large distance beyond $x = d$ before the medium cools down.

A decrease in Peclet number to 5 results in a perturbed velocity field, particularly near the leading edge of the heat source (Fig. 4*b*). The disturbance in streamline patterns is, however, highly localized and the velocity field away from the heat source is largely unaffected. The temperature field is modified accordingly; thermal diffusion in the upstream flow has increased whereas the energy transport on the downstream side has decreased. Consequently, the upward convection has been enhanced.

Although the distribution of local heat flux on the heated segment for Pe* = 5 is qualitatively similar to that observed for Pe* = 10 (Fig. 6*a*), the area under this curve has decreased. Indeed, the heat transfer by forced convection has substantially decreased and the transport of energy by free

convection has increased. However, the enhancement in Q_{nc} is much smaller than the reduction in Q_{fc}.

The local Nusselt number Nu_x on the top surface is now significant for $x < 0$ (Fig. 6*b*), and is maximum at $x \simeq 1.3d$. This peak value of Nu_x for $Pe^* = 5$ is larger than that for $Pe^* = 10$. As a result, the energy is removed on the top surface over a shorter distance beyond $x = d$.

When $Pe^* = 1$ and $Ra^* = 10$, convection of energy in the downstream flow is reduced substantially (see isotherms in Fig. 4*c*), and the transport of energy by diffusion is enhanced. The isotherms get clustered in a region close to the heated segment increasing heat removal on the top surface directly above the heat source. The velocity field is, thus, significantly modified in the heated region. Consequently, the streamlines in a region adjacent to the leading edge are skewed to bring the flowing fluid closer to the heat source, producing a region of very small horizontal velocity in the upper layers (Fig. 4*c*). The fluid then gets heated and moves upward because of buoyancy effects. The streamlines in a region close to the trailing edge, thus, shift upward, producing a region of recirculating flow in the lower portion of the porous layer. The vertical velocity at the midheight is, thus, negative when $x < 0$ and $x > d$, and positive for $0 < x < d$ (Fig. 5). The (relative) enhancement in buoyancy effects is now discernible.

Furthermore, due to shear, the nature of the convective cells (recirculation) is opposite to the main flow (Fig. 4*c*). Also, the recirculation near the trailing edge is observed to be stronger than that near the leading edge. This asymmetry in the production of counterrotating convective cells is a result of the unidirectional forced flow.

The decrease in Pe^* to unity significantly alters the local Nusselt number distribution (Fig. 6*a*). Nu_x is now minimum at $x \simeq 0.6d$, and starts increasing with x beyond that. It should be noted that Nu_x at $x = d$ is now close to that at $x = 0$, the leading edge. Evidently, the increase in heat transfer rate in the later part of the heated segment is caused by the recirculating flows. However, the increase in Q_{nc} is still not large enough to compensate for the decrease in Q_{fc}, and hence, the overall heat transfer rate for $Pe^* = 1$ is lower than that for $Pe^* = 5$ and 10 (Table 1). The corresponding change in the local heat flux on the top surface can be observed in Fig. 4(*b*) where the increasing effects of diffusion and buoyancy on the upstream flow and the reduced effects of forced convection on the downstream side are clearly exhibited. A large fraction of energy is now removed in a portion of the upper surface directly above the heat source.

Any further decrease in the Peclet number makes the temperature field nearly symmetric and the recirculating flows stronger (Figs. 4*d*, *e*). However, the two counterrotating convective cells are not identical unless the externally induced flow is very weak so that the buoyancy effects dominate the convective flows and heat transfer. In the present case, such a situation is achieved at $Pe^* = 0.1$. The vertical velocity v at the midheight directly above the heat source, is positive with a very large peak value at $x \simeq 0.5$ whereas away from the heat source, it is negative because of the recirculating flows (Fig. 5). Qualitatively, the nature of the secondary cells (Fig. 4*e*) looks similar to what has been observed for buoyancy-induced flow in the horizontal porous cavities of large aspect ratios with localized heating from below, and adiabatic side walls (Prasad and Kulacki, 1985, 1986). However, because of the externally induced flow, the left cell is shifted upward and the right cell is moved downward, and a layer of upward-moving fluid exists between the two convective cells.

The local Nusselt number has further decreased in the first half of the heated segment owing to the reduced effects of forced convection (Fig. 6*a*). However, Nu_x in the second half of the heated portion is substantially increased. This enhancement in heat transfer due to the buoyancy effects compensates for the reduction in the forced convection heat transfer and

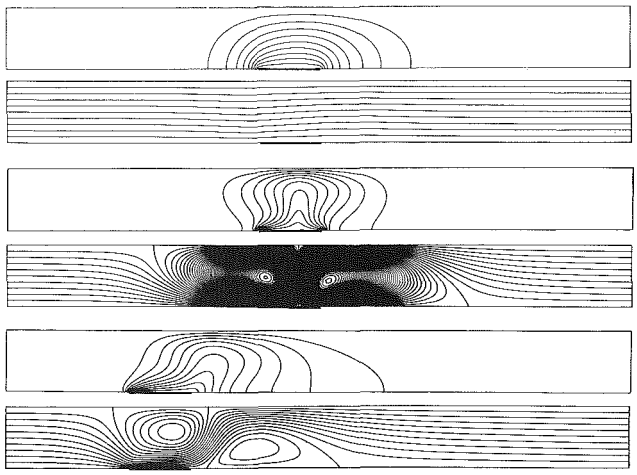

Fig. 7 Isotherms and streamlines for ($\Delta\theta = 0.1$, $\Delta\psi = 0.1$), (*a*) $Pe^* = 1$, $Ra^* = 1$, (*b*) $Pe^* = 1$, $Ra^* = 100$, and (*c*) $Pe^* = 5$, $Ra^* = 100$

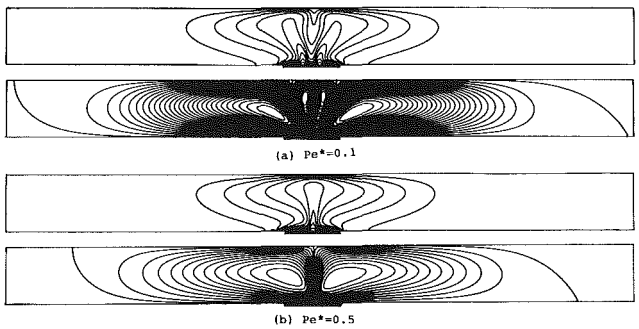

Fig. 8 Isotherms and streamlines for $Ra^* = 500$ ($\Delta\theta = 0.1$), (*a*) $Pe^* = 0.1$ ($\Delta\psi = 5$) and (*b*) $Pe^* = 0.5$ ($\Delta\psi = 2.5$). Note that the externally induced parallel flow is not shown in these plots because $\Delta\psi > 1$.

results in an overall Nusselt number almost independent of the Peclet nubmer for $Pe^* < 1$. Indeed, the heat transfer rate reduces by only 3.8 percent when the Peclet number decreases from 1 to 0.1 for $Ra^* = 10$. Consequently, Nu_x on the top surface is largest at a location close to $x = 0.5d$, and the distribution of local heat flux is almost symmetric for $Pe^* < 1$. Moreover, the plots for θ, ψ, v, and Nu_x (Figs. 4*e*, 5, and 6) clearly indicate that $Ra^* = 10$ and $Pe^* = 0.1$ is a situation where the buoyancy effects dominate and the heat transfer by forced convection is almost negligible.

To examine further the interaction mechanism between free and forced convection, the isotherms and streamlines for $Ra^* = 1$, 100, and 500 are presented in Figs. 7 and 8. When $Ra^* = 1$ and $Pe^* = 1$, the temperature field is almost symmetric (Fig. 7*a*). This is primarily because the buoyancy force is very small, but the forced flow is not strong enough to produce large convective effects. Hence, the velocity field is largely unaffected. An increase in Ra^* to 10 does not disturb the basic nature of the temperature field, but shifts the isotherms closer to the heat source. The recirculating flows near the edges are now visible (Fig. 4*c*). When Ra^* is increased to 100, the temperature field is observed to be greatly modified (Fig. 7*b*). A plume is produced over the heated segment. Thermal diffusion in the lower half of the porous layer has decreased whereas that in the upper portion has increased owing to the increased vertical velocity and the recirculation. This has resulted in a temperature field in which an inversion in temperature gradient, $\partial T/\partial y$, is possible (Figs. 7*b* and 8*a*). Such inversion in the vertical temperature gradient has already been reported for the case of natural convection in horizontal

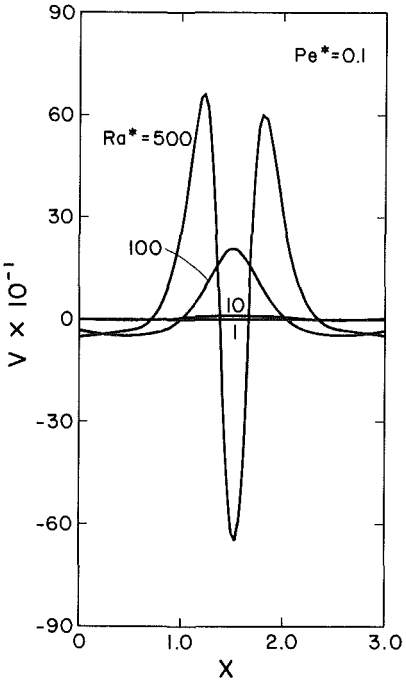

Fig. 9 Vertical velocity at the midheight for Ra* = 1, 10, 100, and 500

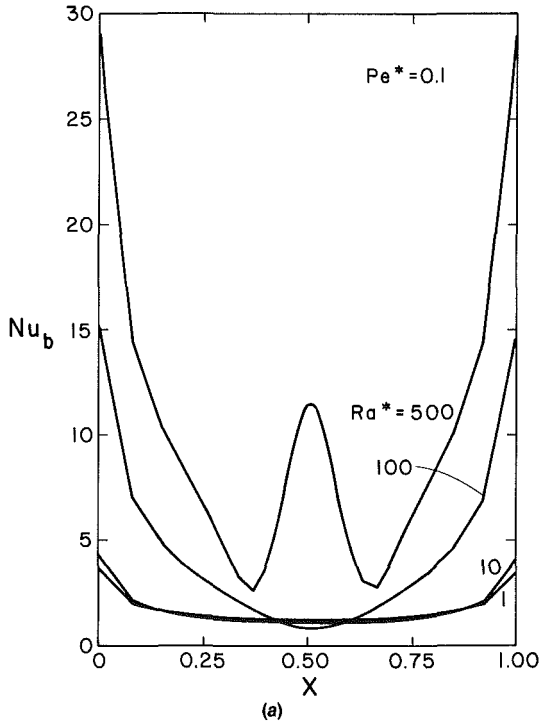

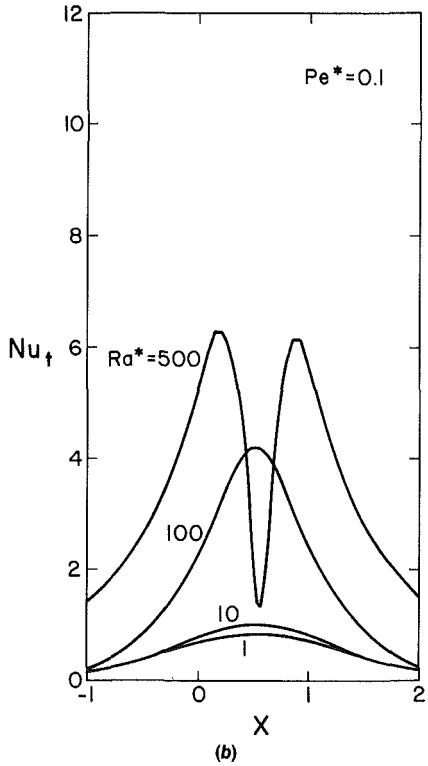

Fig. 10 Local Nusselt number on the horizontal surfaces for Ra* = 1, 10, 100, and 500: (a) heated segment and (b) upper surface

porous layers with localized heating from below (Elder, 1967a, b; Horne and O'Sullivan, 1974, 1978; Prasad and Kulacki, 1985, 1986).

Another interesting aspect of buoyancy effects is exhibited by the isotherms and streamlines for Ra* = 500 (Fig. 8). These plots indicate that more than one pair of secondary cells may appear at high Ra* and low Pe*. For Ra* = 500, this occurs when the Peclet number is reduced below 0.5. As a result of the reduced strength of external flow, the main cells have been shifted outward and two counterrotating, thin cells have been produced in the central portion of the heated segments (Fig. 6*a*). This results in highly complex velocity and temperature distributions in a region directly above the heat source. An inverted thermal plume now exists at the center of the heat source, $x = 0.5d$.

This feature of the multicellular flow behavior has not been observed for pure natural convection in the horizontal cavity. The results of Elder, Horne, and O'Sullivan, and Prasad and Kulacki indicate that the flow is bicellular as long as $H < 2$. It seems that the production of two pairs of convective cells in the present case ($H = 1$), is a direct consequence of the forced flow, however small it is. Indeed, the heat transfer near the leading edge of the heat source is aided by the external flow, which results in a sharp density gradient and causes the fluid to move up much earlier than that observed in the case of natural convection ($U = 0$). Consequently, a pair of thin cells are produced in $0.2d < x < 0.8d$ (Fig. 8*a*).

Other interesting features of the modifications in the temperature and flow fields are exhibited in Fig. 7(*b*), when both the Rayleigh and Peclet numbers are large. The nice, symmetric-looking plume produced at Ra* = 100 and Pe* $\simeq$ 1 is skewed toward the downstream when the Peclet number is increased to 5. This is because of the increased velocity in the x direction. The enhanced (forced) convective effects, also, change the nature of the recirculation. The upstream cell is now observed to be stronger than the downstream one which is opposite to that observed for Ra* = 1 and 10. In fact, the streamlines obtained for Ra* = 100 and Pe* < 10 indicate that the flow field first gets perturbed near the leading edge. Obviously, the convective cell on the upstream side is strengthened first. It may, thus, be concluded that the region for perturbation in the velocity field with an increase in buoyancy largely depends on the Rayleigh number itself. As a consequence, the relative strength of the convective cells is also a function of the buoyancy parameter Ra*, although the appearance of these cells is always governed by Gr*/Re.

The production of recirculating cells and an increase in v with the buoyant force Ra* are further demonstrated in Fig. 9, which shows that the enhancement in vertical velocity with Rayleigh number is substantial. For example, the peak velocity v_{max} for Ra* = 100 is about 25 times larger than that for Ra* = 10. Also, consistent with the multicellular flow pattern

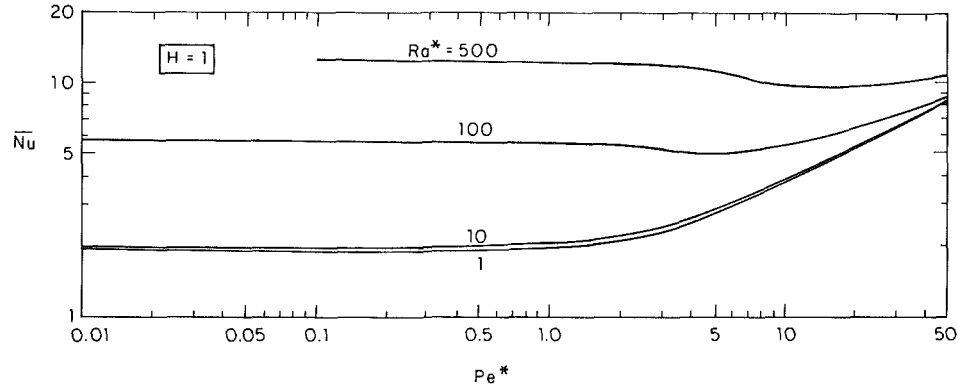

Fig. 11 Overall Nusselt number for mixed convection in horizontal porous layer with a finite heat source at the bottom

observed in Fig. 8*a*, the velocity distribution for Ra* = 500 indicates two positive and one negative peaks.

The variation in local heat transfer rate Nu_x with Ra* is reported in Figs. 10(*a*, *b*). Since Gr*/Re is large for each of these curves (Fig. 10*a*), the distribution of Nu_x is symmetric about $x = 0.5d$. However, the enhancement in overall heat transfer is small for Rayleigh number increasing up to 10, beyond which the heat transfer rate increases substantially with the Rayleigh number.

The effect of the additional pair of convective cells (Ra* = 500) on the enhancement in local heat transfer rate is clearly demonstrated in Fig. 10(*a*). On the top surface, a large fraction of energy is removed in a portion directly above the heat source. However, Nu_x is distributed over a large area beyond $0 < x < d$ primarily due to the recirculating flows (Fig. 10*b*).

Overall Heat Transfer

To present the overall heat transfer rate, an average Nusselt number has been obtained as

$$\overline{Nu} = \bar{h}\, L/k = -\int_0^1 \partial\theta/\partial Y(Y=0)dX \tag{12}$$

For a fixed Peclet number, $\overline{Nu}$ always increases with the buoyancy parameter Ra*. However, the rate of increase in $\overline{Nu}$ with Ra* strongly depends on both Ra* and Pe*. The lower the Peclet number and the higher the Rayleigh number, the larger is the rate of increase in $\overline{Nu}$ (Fig. 11, Table 1).

The variation in overall Nusselt number with Peclet number is, however, not straightforward. When Ra* $\leq$ 1, the overall heat transfer rate remains almost constant up to Pe* $\leq$ 1 beyond which it increases monotonically with the Peclet number (Fig. 11). However, contrary to our intuition, this behavior is altered when the Rayleigh number is high. Indeed, the Nusselt number for Ra* = 100 decreases when the Peclet number is increased beyond unity. It reaches a minimum at Pe* $\leq$ 5 before it starts increasing with the Peclet number. A much larger reduction in Nu is observed when the Rayleigh number is 500. The overall heat transfer rate decreases by about 24 percent when the Peclet number is increased from 0.1 to 19 for Ra* = 500 (Fig. 11). This is consistent with our earlier discussion of the combined effects of externally induced flow and buoyancy on the temperature and flow fields. A recent experimental study of mixed convection in a horizontal porous annulus also supports this observation (Vanover and Kulacki, 1987).

From Fig. 11, it can now be easily concluded that for Pe* < 1, the Nusselt number is almost independent of the forced flow, i.e.,

$$\overline{Nu} = f(Ra^*), \text{ for a fixed } H \text{ and } Pe^* < 1 \tag{13}$$

This situation characterizes the dominant buoyant effects and negligible forced convection. It should also be noted that the additional pair of convective cells in the case of Ra* = 500 and Pe* = 0.1 has very small effect on the overall heat transfer rate; $\overline{Nu}$ increases by only 1.9 percent when the Peclet number is reduced from 0.5 to 0.1.

At lower Rayleigh numbers, the externally induced flow enhances the heat transfer, and the Nusselt number increases monotonically with the Peclet number when Pe* > 1. The slope of the Nusselt number curve, thus, increases from 0 to 0.5, a value reported for the forced convection (Cheng, 1977), e.g., the slope is 0.49 for $10 \leq Pe^* \leq 50$ when Ra* = 1 (Fig. 11). Similar behavior is demonstrated by the Nusselt number curve for Ra* = 10. Indeed, the two curves are very close to each other for Pe* > 20, which clearly indicates that the forced convection dominates when Ra $\leq$ 10 and Pe* > 20. However, much larger Peclet numbers are required for these curves to attain a slope of 0.5 when the Rayleigh number is high.

Finally, the overall Nusselt number for high Peclet number and low Rayleigh number may be compared with that obtained for forced convection and also, with the boundary layer solutions of Cheng (1977), for forced convection on an impermeable, isothermal horizontal surface. Table 1 shows that the predicted values of Nusselt number for Ra* = 1 are in close agreement (within 1 percent) with the forced convection results. The difference, however, increases with the Rayleigh number.

Furthermore, the flat plate solution for Pe* = 5 (Cheng, 1977) predicts a Nusselt number 9.6 percent lower than that obtained here for forced convection in a bounded horizontal layer. The difference between the two values of $\overline{Nu}$, however, reduces to 4.8 percent at Pe* = 50. A larger variation at a lower Peclet number may thus be attributed to a combined effect of the boundary layer approximations in Cheng's solution and the presence of a cold top surface in the present configuration.

To the authors' knowledge, no study has been reported in the literature with which to compare the present results directly. It may, however, be noted that Cheng (1977), and Hsu and Cheng (1980) have provided the asymptotes for free and forced convection, and the criteria for their relative strength. No such generalized correlations could be obtained in the present case due to the lack of sufficient data. Nevertheless, the bounds have been presented in terms of their significant contributions.

Conclusion

Two-dimensional, steady mixed convection in a horizontal porous layer has been numerically studied for the case when a finite isothermal heat source is located on the bottom surface.

The governing parameters are the Rayleigh number, the Peclet number, and the size of the heat source. The computational results show that an increase in Rayleigh number perturbs the externally induced flow field, and produces bicellular recirculating flows in a region close to the heat source. The recirculation exists together with the main flow. At high Rayleigh numbers, the flow field is (almost) diagonally symmetric whereas the temperature field, the vertical velocity, the local Nusselt number are all symmetric about a vertical plane at $x = 0.5d$. Two pairs of convective cells are produced when the Rayleigh number is high and the Peclet number is low. A plumelike temperature field appears at high Rayleigh numbers, which is then drifted toward the downstream with an increase in the Peclet number. The extent of diffusion of energy in the upstream and downstream flows depends on the relative strength of free and forced convection.

The overall heat transfer rate always increases with the Rayleigh number, but the effect of the Peclet number is not straightforward. There exists a critical Peclet number as a function of Ra* for which the heat transfer rate is minimum. Any increase in Pe* beyond this value enhances the contribution of forced convection, whereas if the Peclet number is decreased, the free convective effects increase. When $Pe^* < 1$, the heat transfer is dominated by buoyancy and the contribution of forced convection is negligible. At high Peclet numbers, the ln(Nu)-versus-ln(Pe*) curve attains a slope of 0.5, a value reported for the forced convection. For $Ra^* \leq 10$, this is achieved when $Pe^* > 10$.

Acknowledgments

The support of this work by the Department of Mechanical Engineering, Columbia University, and the U.S. Nuclear Regulatory Commission under Contract NRC-04-84-126 to the University of Delaware is appreciated.

References

Catton, I., 1985, "Natural Convection Heat Transfer in Porous Media," in: *Natural Convection: Fundamentals and Applications*, Hemisphere, New York.

Cheng, P., 1977, "Similarity Solutions for Mixed Convection From Horizontal Impermeable Surfaces in Saturated Porous Media," *International Journal of Heat and Mass Transfer*, Vol. 20, pp. 893–898.

Cheng, P., 1987, "Heat Transfer in Geothermal Systems," *Advances in Heat Transfer*, Vol. 14, pp. 1–105.

Combarnous, M. A., and Bories, S. A., 1975, "Hydrothermal Convection in Saturated Porous Media," *Advances in Hydroscience*, Vol. 10, pp. 231–307.

Elder, J. W., 1967a, "Steady Free Convection in a Porous Medium Heated From Below," *Journal of Fluid Mechanics*, Vol. 27, pp. 29–48.

Elder, J. W., 1967b, "Transient Convection in a Porous Medium," *Journal of Fluid Mechanics*, Vol. 27, pp. 609–623.

El-Khatib, G., and Prasad, V., 1986, "Effects of Stratification on Thermal Convection in Horizontal Porous Layers With Localized Heating From Below," *Natural Convection in Porous Media*, ASME HTD-Vol. 56, pp. 61–68; ASME JOURNAL OF HEAT TRANSFER, Vol. 109, 1987, pp. 683–687.

Gosman, A. D., Pun, W. M., Runchal, A. K., Spalding, D. B., and Wolfshtein, M., 1969, *Heat and Mass Transfer in Recirculating Flows*, Academic Press, New York.

Horne, R. N., and O'Sullivan, M. J., 1974, "Oscillatory Convection in a Porous Medium Heated From Below," *Journal of Fluid Mechanics*, Vol. 66, pp. 339–352.

Horne, R. N., and O'Sullivan, M. J., 1978, "Convection in a Porous Medium Heated From Below: The Effect of Temperature Dependent Viscosity and Thermal Expansion Coefficient," ASME JOURNAL OF HEAT TRANSFER, Vol. 100, pp. 448–452.

Hsu, C. T., and Cheng, P., 1980, "Vortex Instability of Mixed Convective Flow in a Semi-infinite Porous Medium Bounded by a Horizontal Surface," *International Journal of Heat and Mass Transfer*, Vol. 23, pp. 789–798.

Prasad, V., 1983, "Natural Convection in Porous Media—An Experimental and Numerical Study for Vertical Annular and Rectangular Enclosures," Ph. D. Dissertation, University of Delaware, Newark, DE.

Prasad, V., 1986, "Numerical Study of Natural Convection in a Vertical, Porous Annulus with Constant Heat Flux on the Inner Wall," *International Journal of Heat and Mass Transfer*, Vol. 29, pp. 841–853.

Prasad, V., and Kulacki, F. A., 1984, "Convective Heat Transfer in a Rectangular Porous Cavity—Effect of Aspect Ratio on Flow Structure and Heat Transfer," ASME JOURNAL OF HEAT TRANSFER, Vol. 106, pp. 158–165.

Prasad, V., and Kulacki, F. A., 1985, "Natural Convection in Horizontal Porous Layers With Localized Heating from Below," *Heat Transfer in Porous Media and Particular Flows*, ASME HTD-Vol. 46, pp. 199–207; ASME JOURNAL OF HEAT TRANSFER, Vol. 109, 1987, pp. 795–798.

Prasad, V., and Kulacki, F. A., 1986, "Effects of the Size of Heat Source on Natural Convection in Horizontal Porous Layers Heated From Below," *Heat Transfer 1986*, Vol. 5, Hemisphere, New York, pp. 2677–2682.

Prasad, V., Kulacki, F. A., and Keyhani, M., 1985, "Natural Convection in Porous Media," *Journal of Fluid Mechanics*, Vol. 150, pp. 89–119.

Roache, P. J., 1982, *Computational Fluid Dynamics*, Hermosa Publishers, New York.

Vanover, D. E., and Kulacki, F. A., 1987, "Experimental Study of Mixed Convection in a Horizontal Porous Annulus," presented at the ASME Winter Annual Meeting, Boston, MA, ASME HTD-Vol. 84, pp. 61–66.

Onset of Finger Convection in a Horizontal Porous Layer Underlying a Fluid Layer

F. Chen

C. F. Chen

Department of Aerospace and Mechanical Engineering, University of Arizona, Tucson, AZ 85721

In the directional solidification of concentrated alloys, the frozen solid region is separated from the melt region by a mushy zone consisting of dendrites immersed in the melt. Simultaneous occurrence of temperature and solute gradients through the melt and mushy zones may be conducive to the occurrence of salt-finger convection, which may in turn cause adverse effects such as channel segregation. We have considered the problem of the onset of finger convection in a porous layer underlying a fluid layer using linear stability analysis. The eigenvalue problem is solved by a shooting method. As a check on the method of solution and the associated computer program, we first consider the thermal convection problem. In this process, it is discovered that at low depth ratios $\hat{d}$ *(the ratio of the fluid layer depth to the porous layer depth), the marginal stability curve is bimodal. At small* $\hat{d}$*, the long-wave branch is the most unstable and the convection is dominated by the porous layer. At large* $\hat{d}$*, the short-wave branch is the most unstable and the convection is dominated by the fluid layer, with a convection pattern consisting of square cells in the fluid layer. In the salt-finger case with a given thermal Rayleigh number* $Ra_m = 50$*, as the depth ratio* $\hat{d}$ *is increased from zero, the critical salt Rayleigh number* Ra_{sm} *first decreases, reaches a minimum, and then increases. The system is more stable at* $\hat{d} > 0.2$ *than at* $\hat{d} = 0$*. This rather unusual behavior is again due to the fact that at small* $\hat{d}$*, convection is dominated by the porous layer and, at large* $\hat{d}$*, convection is dominated by the fluid layer. However, in the latter case, the convection pattern in the fluid layer consists of a number of high aspect ratio cells.*

1 Introduction

In the directional solidification of concentrated alloys, when the mold is cooled from below, the solid frozen region at the bottom is separated from the liquid region above by a mushy zone consisting of dendrites immersed in the melt. In the theoretical and computational considerations of the mushy zone, it is regarded as a porous layer with variable permeability (Hills et al., 1983; Maples and Poirier, 1984). Through the mushy zone and part of the melt region, the temperature and the concentration of the component that has a higher melting point both increase upward. This simultaneous increase in the temperature and concentration is the situation in which finger convection is likely to occur. In actual castings and laboratory experiments with NH_4Cl–H_2O, channel segregation or freckles have been observed to form (Copley et al., 1970; Sample and Hellawell, 1984). It has been suggested by Copley et al. (1970) that these may be the result of finger convection. A more detailed review of the channel segregation phenomenon has been given recently by Glicksman et al. (1986), in which the effect of double-diffusive convection on the interaction of flows with a crystal-melt interface is clearly and concisely discussed. In this paper, we study the hydrodynamic problem of the onset of finger convection in a porous layer of constant porosity underlying a fluid layer.

The onset of salt-finger convection in a porous layer has been considered by Nield (1968) and Taunton et al. (1972). It is known, however, that when a porous layer is underlying a fluid layer, the critical condition for the onset of thermal convection when the system is being heated from below is considerably different from that for a porous layer alone. Sun (1973) was the first to consider such a problem, and he used a shooting method to solve the linear stability equations. The results show that the critical Rayleigh number in the porous layer, Ra_m, decreases continuously as the thickness of the fluid layer is increased. He further considered the effect of volumetric heat generation in the porous layer. He also performed experiments to verify his predictions. Nield (1977) formulated the problem with surface-tension effects at a deformable upper surface included. He obtained asymptotic solutions for small wavenumbers for a constant-heat-flux boundary condition. Somerton and Catton (1982) departed from the formulations used by Sun and Nield by including the Brinkman term in the Darcy equation for the porous layer. They solved the problem of a volumetrically heated porous layer underlying a fluid layer by the Galerkin method. More recently, Taslim et al. (1985) and Pillatsis et al. (1986) considered the convective stability of a porous layer sandwiched between two fluid layers. Their method of solution involved the use of rapidly convergent power series, and results have been obtained for $\hat{d}$ up to 0.1.

In this paper, we consider the additional effect of a salinity gradient. We first formulate the linear stability equations for a porous layer underlying a fluid layer with temperature and salinity gradients existing in both layers. The eigenvalue problem is then solved by a shooting method. To validate our method of solution and the associated computer program, we first compare our results with those of Sun (1973) for the thermal convection case. We then present the results for the onset of salt-finger convection.

2 Governing Equations

We consider a porous layer of thickness d_m underlying a fluid layer of thickness d. The top of the fluid layer and the bottom of the porous layer are bounded by rigid walls which are kept at different constant temperatures and salinities. For the salt-finger case, the temperature and salinity at the bottom boundary are lower than those at the upper boundary. A

Contributed by the Heat Transfer Division and presented at the 2nd ASME-JSME Joint Thermal Engineering Conference, Honolulu, Hawaii, March 1987. Manuscript received by the Heat Transfer Division December 22, 1986. Keywords: Double Diffusion Systems, Phase-Change Phenomena, Porous Media.

Cartesian coordinate system is chosen with the origin at the interface between the porous and fluid layers and the z axis vertically upward. The continuity, momentum, energy, and concentration equations for the fluid layer are, respectively,

$$\nabla \cdot \mathbf{u} = 0 \tag{1}$$

$$\rho_0\left[\frac{\partial \mathbf{u}}{\partial t} + \mathbf{u}\cdot\nabla\mathbf{u}\right] = -\nabla P + \mu\nabla^2\mathbf{u} - \rho_0 g[1-\alpha(T-T_0) + \beta(S-S_0)]\mathbf{k} \tag{2}$$

$$(\rho_0 C_p)_f\left[\frac{\partial T}{\partial t} + \mathbf{u}\cdot\nabla T\right] = k_f\nabla^2 T \tag{3}$$

$$\frac{\partial S}{\partial t} + \mathbf{u}\cdot\nabla S = D_f\nabla^2 S \tag{4}$$

The same equations for the porous layer are

$$\nabla \cdot \mathbf{u}_m = 0 \tag{5}$$

$$\frac{\rho_0}{\phi}\frac{\partial \mathbf{u}_m}{\partial t} = -\nabla P_m - \frac{\mu}{K}\mathbf{u}_m - \rho_0 g[1-\alpha(T_m-T_0) + \beta(S_m-S_0)]\mathbf{k} \tag{6}$$

$$(\rho_0 C_p)^*\frac{\partial T_m}{\partial t} + (\rho_0 C_p)_f\mathbf{u}_m\cdot\nabla T_m = k^*\nabla^2 T_m \tag{7}$$

$$\phi\frac{\partial S_m}{\partial t} + \mathbf{u}_m\cdot\nabla S_m = D_m\nabla^2 S_m \tag{8}$$

It is noted that the nonlinear term has been neglected in the momentum equation for the porous layer, and the effects of cross diffusion are neglected. In both sets of equations, the Boussinesq approximation has been applied. The boundary conditions are that at the upper boundary $z=d$, $T=T_u$, $S=S_u$, and all velocity components vanish; at the lower boundary, $z=-d_m$, $T=T_\ell$, $S=S_\ell$, and the vertical components of the velocity vanish. At the interface ($z=0$), T, S, heat flux, salt flux, and the normal stress must be continuous. Since in the Darcy equation there are no viscous stresses, continuity of shear stress across the interface cannot be enforced. We apply the condition proposed by Beavers and Joseph (1967) in which the slip in the tangential velocity is proportional to the vertical gradient of the tangential velocity in the fluid.

The steady basic state is quiescent; the eight equations reduce to the diffusion equations for temperature and salinity in the fluid and porous layers. Applying the boundary condition that the temperature, salinity, heat flux, and salt flux must be continuous through the interface, we obtain the solution

$$\left.\begin{aligned}\bar{T} &= T_0 + (T_u - T_0)z/d\\ \bar{S} &= S_0 + (S_u - S_0)z/d\end{aligned}\right\} 0 \le z \le d \tag{9}$$

and

$$\left.\begin{aligned}\bar{T}_m &= T_0 + (T_0 - T_l)z/d_m\\ \bar{S}_m &= S_0 + (S_0 - S_l)z/d_m\end{aligned}\right\} -d_m \le z \le 0 \tag{10}$$

where the values at the interface are

$$T_0 = (k^* dT_l + k_f d_m T_u)/(k^* d + k_f d_m) \tag{11}$$

$$S_0 = (\mathcal{D}_m dS_l + \mathcal{D}_f d_m S_u)/(\mathcal{D}_m d + \mathcal{D}_f d_m) \tag{12}$$

The pressure is hydrostatic and need not be presented here.

2.1 Small Perturbation Equations and Boundary Conditions. The governing equations are linearized in the usual manner. To render the equations nondimensional, we choose separate length scales for the fluid layers and the porous layers so that both layers are of unit depth, as was done by Nield (1977). In this manner, the detailed flow fields in both the fluid and the porous layer can be clearly discerned for all depth ratios. For the fluid layer, we choose the characteristic length to be d, time to be d^2/λ_f, velocity to be ν/d, temperature to be $(T_u - T_0)\,\nu/\lambda_f$, and salinity to be $(S_u - S_0)\,\nu/D_f$. For the porous layers, we choose d_m, d_m^2/λ_m, ν/d_m, $(T_0 - T_l)\,\nu/\lambda_m$, and $(S_0 - S_l)\,\nu/D_m$ for the corresponding characteristic quantities.

The nondimensional equations, written in the same symbols for dimensional quantities, are

Nomenclature

a, a_m = wavenumber in fluid and porous layers
C_p = specific heat of fluid at constant pressure
d, d_m = thickness of fluid and porous layers
$\hat{d}$ = depth ratio $= d/d_m$
D_f, D_m = mass diffusivity in fluid and porous layers
$\mathcal{D}_f$, $\mathcal{D}_m$ = $\rho_0 C_p D_f$, $\rho_0 C_p D_m$
f = planar function of normal mode expansion in fluid layer
g = gravity constant
G_m = $(\rho C_p)^*/(\rho C_p)_f$, $(\ )^* = \phi(\ )_f + (1-\phi)(\ )_m$
k_f, k_m = thermal conductivity in fluid layer and porous material
k^* = $\phi k_f + (1-\phi)k_m$
$\mathbf{k}$ = unit vector in z direction
K = permeability
Le, Le_m = Lewis numbers D_f/λ_f, D_m/λ_m
P = pressure
Pr = Prandtl number $= \nu/\lambda$
Ra, Ra_s = Rayleigh numbers of the fluid layer, equation (19)
Ra_m, Ra_{sm} = Rayleigh numbers of the porous layer, equation (20)
S = salinity
$\mathcal{S}$ = normalized dimensionless salinity
T = temperature
t = time
$\mathbf{u}$ = velocity vector $= (u, v, w)$
W = normalized dimensionless vertical velocity
w = vertical component of velocity
α = $-\rho_0^{-1}(\partial\rho/\partial T)$
$\hat{\alpha}$ = Beavers–Joseph constant
β = $\rho_0^{-1}(\partial\rho/\partial S)$
δ = Darcy number $= \sqrt{K}/d_m$
γ_T, γ_S = $(T_u - T_0)/(T_0 - T_\ell)$, $(S_u - S_0)/(S_0 - S_\ell)$
ϵ_T, ϵ_S = λ_f/λ_m, D_f/D_m
θ = normalized dimensionless temperature
λ_f, λ_m = thermal diffusivity of fluid and porous layers
μ, ν = dynamic and kinematic viscosities
ρ = density of fluid
σ, σ_m = complex growth rate in fluid and porous layers
ϕ = porosity

Subscripts

f, m = fluid and porous layers
l, u = lower and upper boundaries
0 = interface

$$\left(\frac{1}{\mathrm{Pr}}\frac{\partial}{\partial t}-\nabla^2\right)\nabla^2 w=R\nabla_2^2 T-R_S\nabla_2^2 S \tag{13}$$

$$\frac{\partial T}{\partial t}+w=\nabla^2 T \tag{14}$$

$$\frac{1}{\mathrm{Le}}\frac{\partial S}{\partial t}+w=\nabla^2 S \tag{15}$$

$$\left(\frac{\delta^2}{\phi}\frac{1}{\mathrm{Pr}_m}\frac{\partial}{\partial t}+1\right)\nabla^2 w_m=\mathrm{Ra}_m\nabla_2^2 T_m-\mathrm{Ra}_{sm}\nabla_2^2 S_m \tag{16}$$

$$G_m\frac{\partial T_m}{\partial t}+w_m=\nabla^2 T_m \tag{17}$$

$$\frac{\phi}{\mathrm{Le}_m}\frac{\partial S_m}{\partial t}+w_m=\nabla^2 S_m \tag{18}$$

It is noted that all variables are perturbation quantities and $\nabla_2^2=\partial^2/\partial x^2+\partial^2/\partial y^2$. With the chosen nondimensional scaling, the buoyancy terms on the right-hand side of the momentum equations are directly proportional to the Rayleigh numbers. For the fluid layer, the Rayleigh numbers are defined as

$$\begin{aligned}\mathrm{Ra}&=g\alpha(T_u-T_0)d^3/(\nu\lambda_f)\\ \mathrm{Ra}_S&=g\beta(S_u-S_0)d^3/(\nu D_f)\end{aligned} \tag{19}$$

For the porous layer, the Rayleigh numbers are defined in terms of the permeability K

$$\begin{aligned}\mathrm{Ra}_m&=g\alpha(T_0-T_l)d_m K/(\nu\lambda_m)=R\hat{d}^{-4}(\delta\epsilon_T)^2\\ \mathrm{Ra}_{sm}&=g\beta(S_0-S_l)d_m K/(\nu D_m)=\mathrm{Ra}_S\hat{d}^{-4}(\delta\epsilon_S)^2\end{aligned} \tag{20}$$

The boundary conditions at the top and bottom walls are

$$\begin{aligned}w(1)=T(1)=S(1)=\frac{\partial w(1)}{\partial z}&=w_m(-1)\\ &=T_m(-1)=S_m(-1)=0\end{aligned} \tag{21}$$

and those at the interface $z=0$ are the continuity of velocity, temperature, salinity, heat flux, salt flux, and the normal stress

$$w=\hat{d}w_m,\ \gamma_T T=\epsilon_T T_m,\ \gamma_S S=\epsilon_S S_m \tag{22}$$

$$\frac{\partial T}{\partial z}=\epsilon_T\frac{\partial T_m}{\partial z_m},\ \frac{\partial S}{\partial z}=\epsilon_S\frac{\partial S_m}{\partial z_m} \tag{23}$$

$$\left(-\nabla_2^2+\frac{\partial^2}{\partial z^2}\right)\frac{\partial w}{\partial z}=\hat{d}^4\,\delta^{-2}\frac{\partial w_m}{\partial z_m} \tag{24}$$

In addition, the Beavers-Joseph (1967) condition must be satisfied at the interface

$$\frac{\partial^2 w}{\partial z^2}=\hat{\alpha}\hat{d}\delta^{-1}\left(\frac{\partial w}{\partial z}-\hat{d}^2\frac{\partial w_m}{\partial z_m}\right) \tag{25}$$

in which $\hat{\alpha}$ is a constant approximately equal to 0.1 as determined experimentally by Beavers and Joseph (1967). This condition has been supported experimentally and theoretically by Neale and Nader (1974), Beavers et al. (1974), and Nield (1983). We remark here that the solution is quite insensitive to $\hat{\alpha}$. Results obtained for $\hat{\alpha}=0.1$ and 1 are practically the same.

2.2 Normal Mode Analysis. We apply the normal mode expansion on the dependent variables as follows:

$$(w,\ T,\ S)=[W(z),\ \theta(z),\ \mathbb{S}(z)]\,f(x,\ y)e^{\sigma t}$$

where

$$\nabla_2^2 f+a^2 f=0$$

and similarly for the variables in the porous layer. The separation constants a and a_m are nondimensional horizontal wavenumbers. Since the dimensional horizontal wavenumber must be the same for the fluid and porous layers if matching of solutions in the two layers is to be possible, we must have $a/d=a_m/d_m$ and hence $\hat{d}=a/a_m$. The growth factors σ and σ_m are generally complex.

We denote the differential operators d/dz and d/dz_m by D and D_p, respectively, and apply the normal mode expansion in the equations and boundary conditions as shown below:

$$D^4 W-\left(2a^2+\frac{\sigma}{\mathrm{Pr}}\right)D^2 W+\left(a^2\frac{\sigma}{\mathrm{Pr}}+a^4\right)W=$$

$$a^2\mathrm{Ra}\theta-a^2\mathrm{Ra}_S\mathbb{S} \tag{26}$$

$$D^2\theta-(a^2+\sigma)\theta=W \tag{27}$$

$$D^2\mathbb{S}-\left(a^2+\frac{\sigma}{\mathrm{Le}_f}\right)\mathbb{S}=W \tag{28}$$

$$\left(1+\frac{\delta^2\sigma_m}{\phi\mathrm{Pr}_m}\right)(D_p^2-a_m^2)W_m=-a_m^2\,\mathrm{Ra}_m\theta_m+a_m^2\,\mathrm{Ra}_{sm}\mathbb{S}_m \tag{29}$$

$$D_p^2\theta_m-(a_m^2+\sigma_m G_m)\theta_m=W_m \tag{30}$$

$$D_p^2\mathbb{S}_m-\left(a_m^2+\frac{\phi\sigma_m}{\mathrm{Le}_m}\right)\mathbb{S}_m=W_m \tag{31}$$

The boundary conditions are

$$\begin{aligned}W(1)=\theta(1)=\mathbb{S}(1)=DW(1)&=W_m(-1)\\ &=\theta_m(-1)=\mathbb{S}_m(-1)=0\end{aligned} \tag{32}$$

At the interface $z=0$

$$W=\hat{d}W_m,\ \gamma_T\theta=\epsilon_T\theta_m,\ \gamma_S S=\epsilon_S S_m \tag{33}$$

$$D\theta=\epsilon_T D_p\theta_m,\ D\mathbb{S}=\epsilon_S D_p\mathbb{S}_m \tag{34}$$

$$-D^3 W+a^2 DW=\hat{d}^4\delta^{-2}D_p W_m \tag{35}$$

$$D^2 W=\hat{\alpha}\hat{d}\delta^{-1}(DW-\hat{d}^2 D_p W_m) \tag{36}$$

It is known that the principle of exchange of instabilities holds for salt-finger convection in pure fluid layer or a porous layer. It is reasonable to assume that, for the present situation, the principle also holds, and the onset of instability is in the form of steady convection. In the following calculations, σ and σ_m are set to zero identically, and the solution no longer depends on the Prandtl number.

The eigenvalue problem consists of an eighth-order ODE in the fluid layer and a sixth-order ODE in the porous layer, with 14 boundary conditions. For the salt-finger case, temperature is stabilizing and salt is destabilizing. We may regard Ra, Ra_m, $\hat{d}$, δ, and all properties of the fluid and the porous medium as given, and we seek the eigenvalues Ra_{sm} (and Ra_S) for given a_m (and a).

3 Method of Solution

A fourth-order Runge-Kutta (Forsythe et al., 1977) shooting method is applied to solve these ordinary differential equations with the relevant boundary conditions. Shooting starts at the interface and ends at the top and the bottom boundaries. For each shooting process, 14 initial conditions are needed at the interface, 7 of these are known and the other 7 must be guessed. A so-called unit disturbance method (see, for example, Sparrow et al., 1964) is applied here for the initial guesses. The method consists of setting one of the guesses to be unity and the others to be zero and carrying out the shooting for as many times as the number of initial guesses. After shooting seven times, we obtain an array of boundary values at the top and the bottom walls: $W(1)$, $\theta(1)$, $\mathbb{S}(1)$, $DW(1)$, $W_m(-1)$, $\theta_m(-1)$, and $\mathbb{S}_m(-1)$. They are not necessarily equal to zero as the boundary condition requires. However, a linear combination of the initial guesses should yield a solution which satisfies the boundary condition.

Table 1 Comparison of critical conditions for the thermal convection case; $\epsilon_T = 0.7$, $\delta = 0.002$, $\hat{\alpha} = 0.1$

	Present study		Sun (1973, Table 3.5)	
$\hat{d}$	$-\mathrm{Ra}_m$	a_m	$-\mathrm{Ra}_m$	a_m
0.001	39.422	3.14	39.426	3.14
0.01	36.702	3.02	37.951	3.10
0.04	24.772	2.35	26.331	2.50
0.10	19.093	2.14	18.197	2.20
0.11	14.294	23.41	17.284	2.20
0.12	10.242	21.60	16.370	2.20
0.13	7.535	20.05	15.426	2.20
0.33	0.2069	8.29	–	–
0.5	0.0410	5.55	–	–
1.0	0.0027	2.82	–	–

Hence, we obtain a seven-by-seven determinant that involves all the parameters, in particular, Ra_{sm}, a_m, Ra_m, and $\hat{d}$. Setting this determinant to zero, the eigenvalue Ra_{sm} can be obtained by bisection algebra for a chosen wavenumber a_m. In the present computation scheme, it usually takes 10 to 15 bisections to reach the zero value of the determinant. By definition, the zero value is reached when the value of the determinant is less than 10^{-35} of the original value.

It is noted here that the shooting method fails when the differential equations become too stiff (Antar, 1976). In the present case, the stiffness of the equations is related to $\hat{d}$; the larger the $\hat{d}$, the stiffer the equations. Using the fourth-order integration subroutine, the present method can successfully handle problems of depth ratios up to 1.5. For larger values of $\hat{d}$ the stability of the system is controlled by the fluid layer, as discussed below. It would then be more efficient to reformulate the problem by defining a new depth ratio as d_m/d.

Having obtained the eigenvalue Ra_{sm}, we proceed to compute the eigenfunctions W, θ, and S in the fluid layer and W_m, θ_m, and S_m in the porous layer. This is accomplished by determining the coefficients of the linear combinations of the initial unit disturbances using the system of seven homogeneous algebraic equations previously obtained. The seven coefficients are determined to within an arbitrary constant. With these coefficients known, we can then start with the "correct" initial conditions and integrate across the layers to obtain the vertical velocity, temperature, and salinity perturbations. All these perturbation quantities are determined to within an arbitrary constant.

4 Results and Discussion

We first check our calculation procedure and associated computer program by comparing the results of pure thermal convection with the results of Sun (1973). In this process, we have uncovered some interesting aspects heretofore overlooked by the previous investigators. We then present the results for the salt-finger case.

4.1 Thermal Convection Case. In his Ph.D. thesis, Sun (1973) considered the onset of thermal convection in a two-layer system. He presented results of calculations for depth ratios $\hat{d}$ from 0.001 to 0.15 for $\epsilon_T = 0.7$, $\delta = 0.002$, and $\hat{\alpha} = 0.1$. Using the same values of these parameters, we have computed the results for $\hat{d}$ up to 1.0. The results for $d \le 0.15$ are compared in Table 1. We note here that in the present case with heating from below, the Rayleigh number as defined in equation (20) is negative. It can be seen that for $\hat{d} \le 0.10$, the agreement is quite good. Beyond that depth ratio, the bimodal nature of the marginal stability curve was overlooked by Sun; therefore, his results are incorrect.

For subsequent calculations, we have used a slightly different $\delta = 0.003$, which corresponds to a 3-cm layer of 3-mm-dia glass beads. The marginal stability curves at a number of depth ratios are shown in Fig. 1. For small depth ratios ≤ 0.14, the marginal stability curves are bimodal, exhibiting two relative minima. For $\hat{d} < 0.13$, the long-wave branch is the most unstable, whereas for $\hat{d} \ge 0.13$, the short-wave branch is the most unstable. At higher $\hat{d}$, the relative minimum in the long-wave region disappears. Since Sun (1973) constructed the marginal stability curve only in a small range of wavenumbers in the neighborhood of the long-wave critical point, he missed this interesting facet of the problem. The precipitous drop of the critical Ra_m with increasing $\hat{d}$ and the rapid change of the critical wavenumber are shown in Fig. 2. The kink in the Ra_m curve at $\hat{d} = 0.12$ corresponds to the sudden jump from one mode to another. The wavelength decreased almost tenfold at that point.

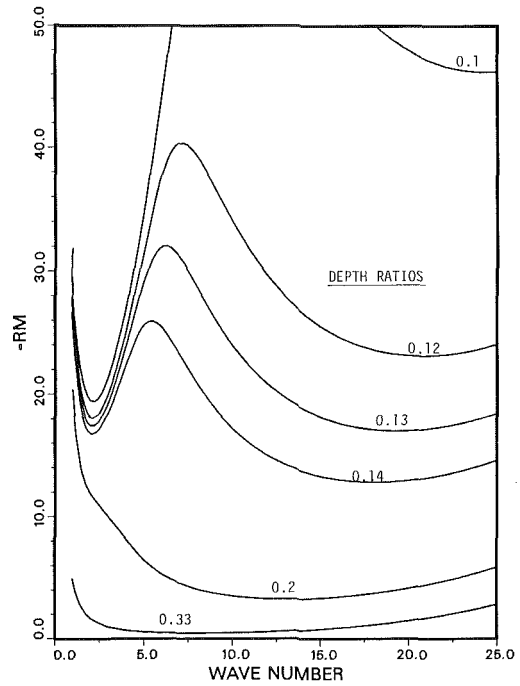

Fig. 1 Marginal stability curves for the thermal convection case

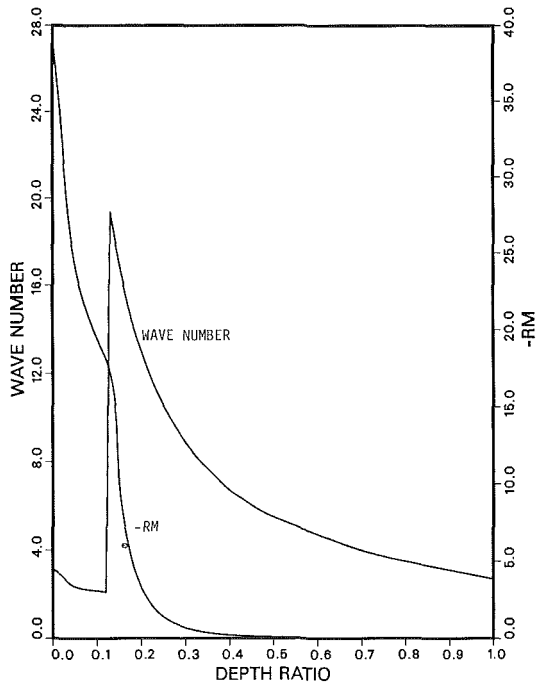

Fig. 2 Variation of critical Ra_m and a_m with $\hat{d}$ for the thermal convection case

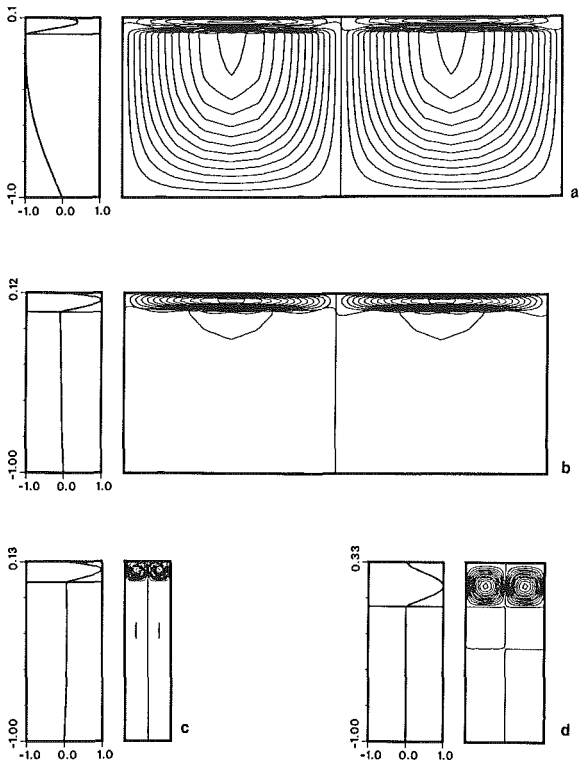

Fig. 3 Streamline pattern and W for the thermal convection case: (*a*) $\hat{d}=0.1$; (*b*) $\hat{d}=0.12$; (*c*) $\hat{d}=0.13$; (*d*) $\hat{d}=0.33$

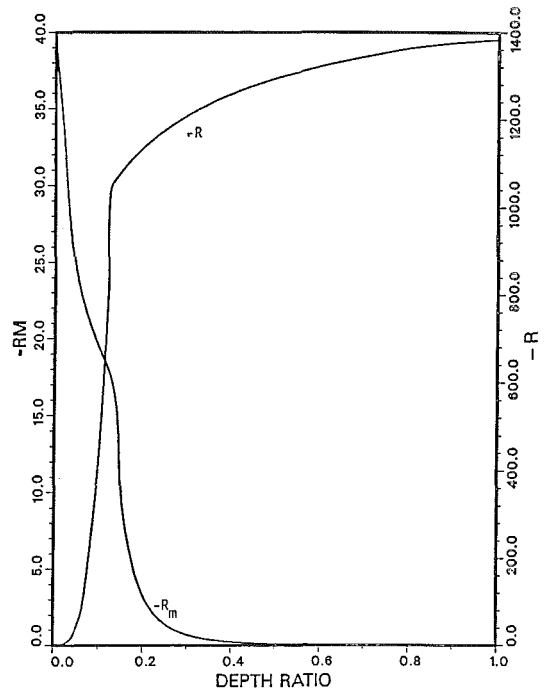

Fig. 4 The critical thermal Rayleigh numbers for the porous and fluid layers

In an effort to understand the cause for such a modal change, we present the eigenfunction W together with the streamline patterns for four depth ratios in Fig. 3. For each of the cases presented, the value of W has been normalized so that its maximum magnitude is 1.0, and it is shown on the left of the figure. The porous layer extends from 0 to -1 in the vertical direction, and the fluid layer extends from 0 to $\hat{d}$. The width of the streamline plot is the critical wavelength. It is seen that for $\hat{d}=0.10$, the convection pattern is dominated by the porous layer, with each convection cell having a width of the same order of magnitude as the porous layer depth. At $d=0.13$, the convection is now dominated by the fluid layer and the dramatic reduction of the critical wavelength is clearly evident. For $0.13 \leq \hat{d}$, the convection is dominated by the fluid layer; the convection cells in the fluid layer are nearly square, with the circulation in the porous layer diminishing in strength. For $\hat{d} \geq 0.5$, the velocity in the porous layer is essentially zero. The modal change at $\hat{d}=0.13$ is the result of switching from a porous layer-dominated circulation to a fluid layer-dominated circulation.

Physically, as $\hat{d}$ increases, the Rayleigh number of the fluid layer increases as d_f^3, and it quickly exceeds the critical value and convection ensues. From equation (2), the critical value of $-\mathrm{Ra}$ corresponding to the critical value of $-\mathrm{Ra}_m$ can be calculated, and these two critical Rayleigh numbers are shown in functions of $\hat{d}$ in Fig. 4. The fluid layer Rayleigh number increases sharply to approximately 1100 and then continues to increase at a much smaller rate. It is known that for a Bernard problem with a fixed and a free boundary, the critical Rayleigh number is 1100. The porous interface behaves more like a free boundary than a fixed one.

4.2 Salt-Finger Case. For the salt-finger case, the initial temperature distribution is stabilizing. We seek the critical salt Rayleigh number that will cause the onset convection. In all results reported here, we assume that the value of the initial stabilizing Ra_m is 50. This is a reasonable assumption for a laboratory system consisting of 3-mm glass beads and salt solution of small concentration. Other property values needed for the calculation are assumed to be $\delta=0.003$, $\epsilon_T=0.7$, $\epsilon_S=3.75$, $\gamma_T=\hat{d}/\epsilon_T$, and $\gamma_S=\hat{d}/\epsilon_S$. These values are for salt-water solutions with 3-mm glass beads as the solid matrix.

The marginal stability curves for a number of depth ratios are shown in Fig. 5(*a*). It is seen that the curves for $\hat{d}=10^{-4}$ and 10^{-2} are almost indistinguishable from each other and the critical salt Rayleigh number ($\mathrm{Ra}_{sm}=88.91$) is very close to the value $\mathrm{Ra}_m+4\pi^2$ predicted by Nield (1968) for a porous layer. As $\hat{d}$ is increased to 0.1, the curve moves downward, as expected, and results in a lower critical Ra_{sm}. However, as $\hat{d}$ is increased to 0.5, the state actually becomes more stable as the marginal stability curve moves upward. For the two higher depth ratios, $\hat{d}=1.0$ and 1.5, the results are nearly the same as the one for $\hat{d}=0.5$.

Ever mindful of the possible bimodal nature of the marginal stability curves, we have extended our calculations to $a_m=20$ for $\hat{d}=0.2$ and 1.0, as shown in Fig. 5(*b*). Although the marginal stability curve is bimodal, the local minimum at the high wavenumber branch is at a much larger Rayleigh number than the one at the low wavenumber branch. This situation remains the same for all depth ratios considered.

The critical salt Rayleigh number Ra_{sm} and wavenumber a_m for depth ratios from 0.01 to 0.5 are presented in Table 2. These results are graphically displayed in Fig. 6. It can be seen that there is a critical depth ratio $\hat{d}=0.044$ that gives the lowest Ra_{sm} of 83.42. For $\hat{d}>0.5$, Ra_{sm} is almost constant $\simeq 104$. The wavenumber exhibits the same behavior, being the smallest at the critical depth of 0.044, and approaches a nearly constant value of 4.4 for $\hat{d}>0.5$.

In order to understand this phenomenon, we examine the eigenfunction W and the streamline patterns for four depth ratios, as shown in Fig. 7. Up to a depth ratio of $\hat{d}=0.05$, Fig. 7(*a*), the convection is dominated by the motion in the porous layer and the convection cell is nearly square in the combined layers. However, at $\hat{d}=0.1$, Fig. 7(*b*), a small cell appears in the fluid layer. At $\hat{d}=0.4$, Fig. 7(*c*), there are two cells in the fluid layer and the circulation strength in the porous layer is

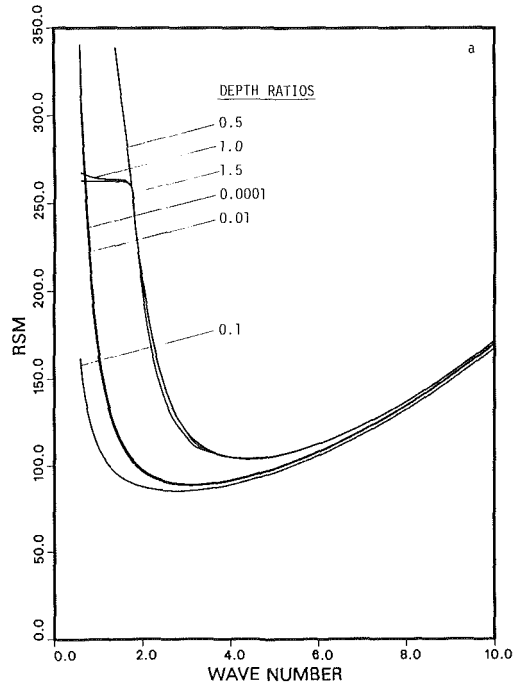

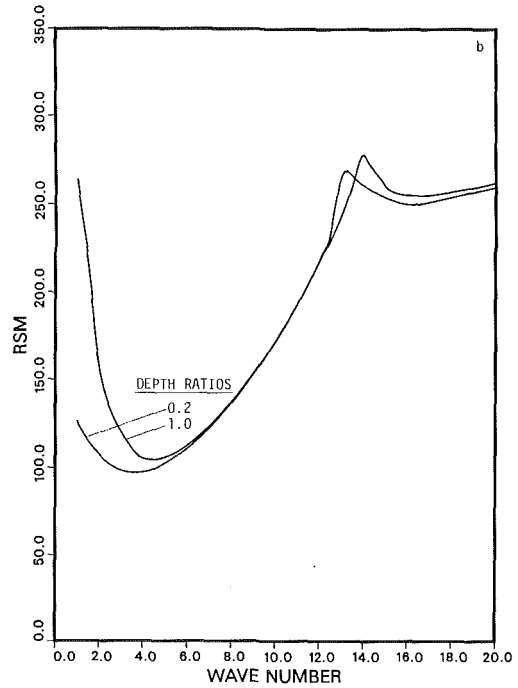

Fig. 5 Marginal stability curves for the salt-finger case: (*a*) wavenumber to 10; (*b*) wavenumber to 20

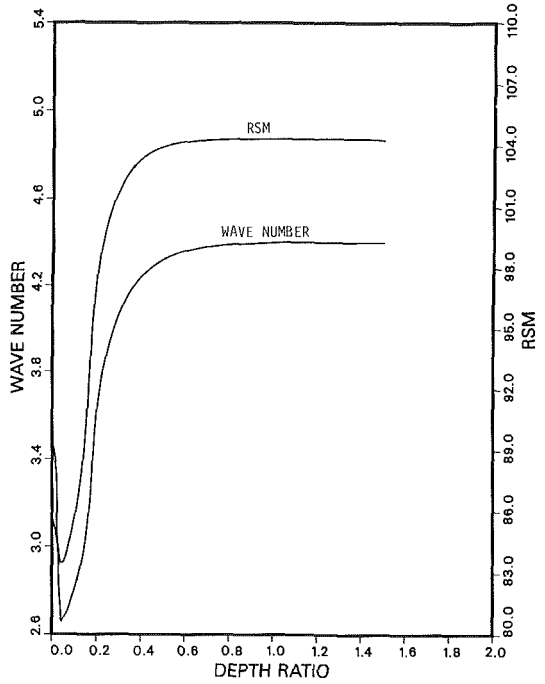

Fig. 6 Variation of critical Ra_{sm} and a_m with $\hat{d}$ for the salt-finger case; $Ra_m = 50$ and $\delta = 0.003$

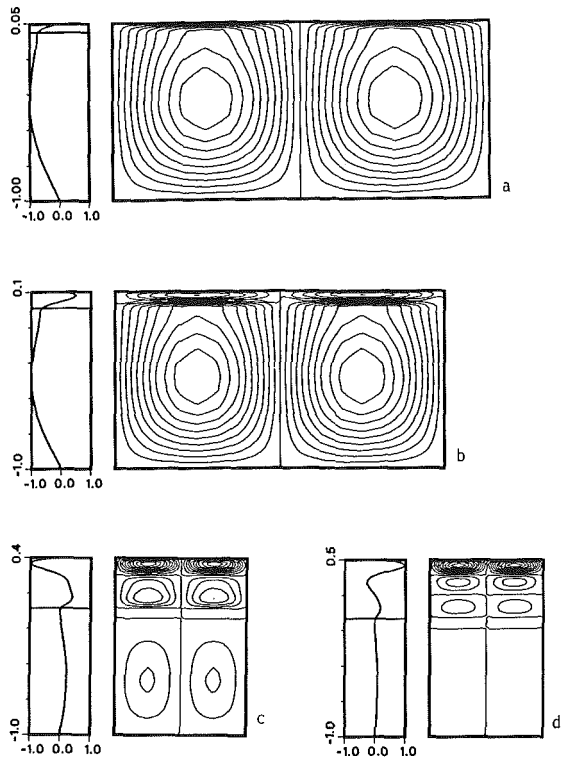

Fig. 7 Streamline pattern and *W* for the salt-finger case with $Ra_m = 50$ and $\delta = 0.003$: (*a*) $\hat{d} = 0.05$; (*b*) $\hat{d} = 0.1$; (*c*) $\hat{d} = 0.4$; (*d*) $\hat{d} = 0.5$

Table 2 Critical conditions for the salt-finger case with $Ra_m = 50$

$\hat{d}$	a_m	Ra_{sm}	$\hat{d}$	a_m	Ra_{sm}
0.01	3.1	88.91	0.10	2.8	85.59
0.042	2.7	83.43	0.20	3.6	97.23
0.044	2.7	83.42	0.40	4.3	103.37
0.05	2.7	83.48	0.50	4.3	103.96

$\delta = 0.003$, $\epsilon_T = 0.7$, $\epsilon_S = 3.75$, $\gamma_T = \hat{d}/\epsilon_T$, $\gamma_S = \hat{d}/\epsilon_S$.

diminishing. Eventually, at $\hat{d} = 0.5$, Fig. 7(*d*), there are three high aspect ratio cells in the fluid layer and the vertical velocity in the porous layer is essentially zero.

From the flow patterns, it may be concluded that the existence of the critical depth ratio for the minimum critical Ra_{sm} is related to the switching of the convection dominated by the porous layer to that dominated by the fluid layer. In contrast to the thermal convection case in which single-cell

convection prevailed in the fluid layer-dominated convection regime, multicell convection prevailed in the salt-finger case. It is this multicell configuration which rendered the entire system more stable. This conclusion awaits the confirmation of experimental results.

5 Conclusions

For the thermal convection case, the critical $|\mathrm{Ra}_m|$ decreases precipitously with increasing depth ratio. The marginal stability curve is bimodal for small depth ratios. For the example case calculated, if $\hat{d}<0.12$, the long-wave branch is the most unstable and the convection is dominated by the porous layer. For $\hat{d}>0.12$, the short-wave branch is the most unstable and the convection is dominated by the fluid layer.

For the salt-finger case with $\mathrm{Ra}_m=50$ and other property values appropriate for salt-water solutions with 3-mm glass beads as the solid matrix as specified in Section 4.2, there exists a critical depth ratio ($\hat{d}=0.044$) below which the critical Ra_{sm} decreases with increasing $\hat{d}$ and above which the critical Ra_{sm} increases with increasing $\hat{d}$. For $\hat{d}\geq 0.2$, the combined system is more stable than the porous layer alone. The critical depth phenomenon is also related to the switching of porous layer-dominated convection to the fluid layer-dominated convection. But, in this case, the convection pattern in the fluid layer consists of a number of wide and flat cells, which rendered the flow more stable. This last effect awaits experimental confirmation.

Acknowledgments

This research was supported by the National Science Foundation through Grant MEA 82-06087 and by NASA through Grant NAG-3-723, for which we are grateful.

References

Antar, B. N., 1976, "On the Solution of Two-Point Linear Differential Eigenvalue Problems," *J. Computational Phys.*, Vol. 20, pp. 208–219.

Beavers, G. S., and Joseph, D. D., 1967, "Boundary Conditions at a Naturally Permeable Wall," *J. Fluid Mech.*, Vol. 30, pp. 197–207.

Beavers, G. S., Sparrow, E. M., and Masha, B. A., 1974, "Boundary Condition at a Porous Surface Which Bounds a Fluid Flow," *AIChE J.*, Vol. 20, pp. 596–597.

Copley, S. M., Giamei, A. F., Johnson, S. M., and Hornbecker, M. F., 1970, "The Origin of Freckles in Unidirectionally Solidified Castings," *Metall. Trans.*, Vol. 1, pp. 2193–2204.

Forsythe, G. E., Malcolm, M. A., and Moler, C. B., 1977, *Computer Methods for Mathematical Computations*, Prentice-Hall Press, New Jersey.

Glicksman, M. E., Coriell, S. R., and McFadden, G. B., 1986, "Interaction of Flows With Crystal-Melt Interface," *Ann. Rev. Fluid Mech.*, Vol. 18, pp. 307–335.

Hills, R. N., Loper, D. E., and Roberts, P. H., 1983, "A Thermodynamically Consistent Model of the Mushy Zone," *Q. J. Mech. Appl. Math.*, Vol. 36, pp. 505–539.

Maples, A. L., and Poirier, D. R., 1984, "Convection in the Two-Phase Zone of Solidifying Alloys," *Metall. Trans. B.*, Vol. 15, pp. 163–172.

Neale, G., and Nader, W., 1974, "Practical Significance of Brinkman's Extension of Darcy's Law: Coupled Parallel Flows Within a Channel and a Bounding Porous Medium," *Can. J. Chem. Eng.*, Vol. 52, pp. 475–478.

Nield, D. A., 1968, "Onset of Thermohaline Convection in a Porous Medium," *Water Resources Res.*, Vol. 4, pp. 553–560.

Nield, D. A., 1977, "Onset of Convection in a Fluid Layer Overlying a Layer of a Porous Medium," *J. Fluid Mech.*, Vol. 81, pp. 513–522.

Nield, D. A., 1983, "The Boundary Correction for the Rayleigh–Darcy Problem: Limitations of the Brinkman Equation," *J. Fluid Mech.*, Vol. 128, pp. 37–46.

Pillatsis, G., Derjani, G., Taslim, M. E., and Narusawa, U., 1986, "Effects of Boundary Conditions on Thermal Instability of Superposed Porous and Fluid Layers," presented at the 4th AIAA/ASME Heat Transfer and Thermophysics Conference, June.

Sample, A. K., and Hellawell, A., 1984, "The Mechanism of Formation and Prevention of Channel Segregation During Alloy Solidification," *Metall. Trans. A*, Vol. 15, pp. 2163–2173.

Somerton, C. W., and Catton, I., 1982, "On the Thermal Instability of Superposed Porous and Fluid Layers," ASME JOURNAL OF HEAT TRANSFER, Vol. 104, pp. 160–165.

Sparrow, E. M., Munro, W. D., and Jonsson, V. K., 1964, "Instability of Flow Between Rotating Cylinders: the Wide-Gap Problem," *J. Fluid Mech.*, Vol. 20, pp. 35–46.

Sun, W. J., 1973, "Convective Instability in Superposed Porous and Free Layers," Ph.D. Dissertation, University of Minnesota, Minneapolis, MN.

Taslim, M. E., Narusawa, U., and Pillatsis, G., 1985, "Convective Stability of a Fluid-Saturated Porous Layer Sandwiched Between Two Fluid Layers," ASME Paper No. 85-HT-29.

Taunton, J. W., Lightfoot, E. N., and Green, T., 1972, "Thermohaline Instability and Salt Fingers in a Porous Medium," *Phys. of Fluid*, Vol. 15, pp. 748–753.

Developing Laminar Mixed Convection With Solidification in a Vertical Channel

W. D. Bennon

F. P. Incropera

School of Mechanical Engineering,
Purdue University,
W. Lafayette, IN 47907

Solidification of both high and low Prandtl number fluids (n-octadecane and aluminum) is considered for downward, mixed convection in the entrance region between vertical parallel plates symmetrically cooled below the fusion temperature. A continuum model is used to formulate a set of steady, two-dimensional partial differential equations, which include the influences of both axial diffusion and thermal buoyancy. The equations are solved using a fully elliptic, control-volume-based finite-difference scheme. Results reveal that, for a given phase change system, conditions are uniquely determined by a Grashof-to-Reynolds number ratio, Gr/Re, a Peclet number Pe, and a characteristic dimensionless temperature. Limiting cases involving both large and small values of Pe have been considered, and the effect of Gr/Re on thermally induced flow reversal in the fluid core has been determined.

Introduction

The analysis of discrete phase change in the presence of forced fluid motion has received considerable attention during the past two decades, and the subject has been recently reviewed by Cheung and Epstein (1984). Problems which involve *external* forced flows include spacecraft heat shield ablation, the melting of large polar ice masses, and cutting operations involving the impingement of hot liquid or gaseous jets on solid workpieces. Applications involving *internal* forced flows include the freezing of heat exchanger working fluids, the formation of ice layers in domestic water supply lines, and solidification within nozzles of industrial metal casting operations.

The analysis of internal solidification is complicated by the strong coupling that exists between the confined fluid core and the solidified layer. In the early work of Zerkle and Sunderland (1968), which concerned steady, laminar flow in a circular tube, freezing was imposed on an isothermal fluid in hydrodynamically fully developed flow. Thermal buoyancy and axial conduction were neglected, and the liquid core velocity profile was assumed to be parabolic throughout the chill region. With an appropriate coordinate transformation, the problem could then be reduced to the classical Graetz problem without solidification. However, the model significantly underpredicted experimental results for water, suggesting that thermal buoyancy effects were important. The model was subsequently applied to flow between parallel plates (Lee and Zerkle, 1969) and extended to accommodate an externally imposed convective boundary condition (Cheng and Wong, 1977).

Ozisik and Mulligan (1969) used a slug flow approximation in the liquid core to analyze transient solidification in an isothermal circular tube. However, thermal buoyancy and axial conduction were neglected, and to permit the assumption of quasi-steady, unidirectional conduction in the solid layer, variations of solid layer thickness with time and axial position were also neglected. Comparisons of predictions with the data of Zerkle and Sunderland (1968) were generally favorable, although heat transfer rates were still underpredicted.

Combined thermal and hydrodynamic development during transient solidification in an isothermal tube has been analyzed by Hwang and Sheu (1976). Axial conduction and thermal buoyancy were again neglected, quasi-steady approximations were invoked, and axial variations in solid layer thickness were presumed small. Hence, except for inclusion of a flow constriction parameter in the axial pressure gradient term, conservation equations for the liquid core reduced to those of the combined entry region problem without solidification. To minimize the influence of thermal buoyancy, experiments with water were conducted using a tube diameter that was approximately four times smaller than that used by Zerkle and Sunderland. The significant reduction in experimental heat transfer rates and the improved agreement with predictions suggested that the Zerkle and Sunderland data were significantly influenced by mixed convection phenomena.

More recently, Toda et al. (1986) analyzed transient solidification in an isothermal tube using a finite-difference scheme. Liquid core velocity profiles were computed and axial conduction was considered, but the effects of thermal buoyancy were again neglected.

In each of the foregoing analyses, simplifying assumptions severely limit the range of applicability of the results. For example, axial conduction in the fluid core may be important when Peclet numbers are small. Similarly, the neglect of axial conduction in the solidified layer may be inappropriate for systems exhibiting rapid axial solid layer growth. In addition, thermal buoyancy can significantly influence solidification for superheated liquids and/or small mass flow rates. Hence, the significance of axial conduction and thermal buoyancy depends on the phase change system and the external boundary conditions. Furthermore, due to local variations in core fluid velocities and temperatures, the influence of these phenomena depends on axial position.

In this study, solidification of a pure substance is considered for downward, mixed convection between vertical parallel plates symmetrically cooled below the fusion temperature. Contrary to previous investigations, attention is focused on solidification in the entry region of systems exhibiting rapid axial solid layer growth. In addition, the effects of both axial conduction and assisting thermal buoyancy are delineated through appropriate selections of fluid Prandtl numbers, entry liquid superheats, and imposed mass flow rates.

Mathematical Model

Solidification of a pure phase change material is considered within a vertical, two-dimensional parallel plate channel of aspect ratio $L/W=2$ (Fig. 1). Initially, the entire channel

Contributed by the Heat Transfer Division and presented at the National Heat Transfer Conference and Exhibition, Pittsburgh, Pennsylvania, August 9-12, 1987. Manuscript received by the Heat Transfer Division April 9, 1987. Keywords: Mixed Convection, Phase-Change Phenomena.

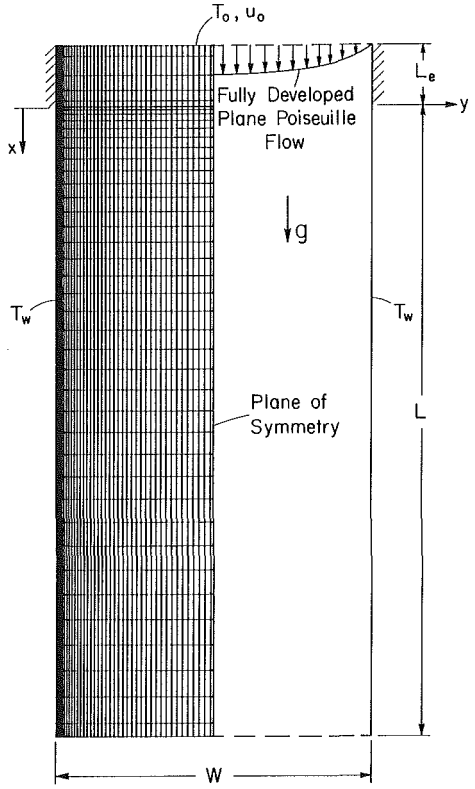

Fig. 1 Model schematic and coordinate system

$(-L_e \le x \le L)$ is insulated and superheated liquid at a uniform temperature T_o enters at $x = -L_e$ with a fully developed parabolic velocity profile characterized by a mean velocity u_o. At time $t = 0$, both vertical boundaries $(0 \le x \le L)$ are brought to a temperature T_w, which is below the fusion temperature T_f. Although the subsequent solidification process is transient, it is the final, steady-state conditions that are considered in the calculations of this study.

Steady-state conditions are governed by conservation equations for mass, momentum, and energy, which may be expressed in continuum form as

$$\nabla \cdot (\rho \mathbf{V}) = 0 \tag{1}$$

$$\nabla \cdot (\rho \mathbf{V} u) = \nabla \cdot (\mu \nabla u) - \frac{\partial P}{\partial x} - \rho g \beta_T (T - T_o) \tag{2}$$

$$\nabla \cdot (\rho \mathbf{V} v) = \nabla \cdot (\mu \nabla v) - \frac{\partial P}{\partial y} \tag{3}$$

$$\nabla \cdot (\rho \mathbf{V} h) = \nabla \cdot \left(\frac{k}{c_s} \nabla h\right) + \nabla \cdot \left(\frac{k}{c_s} \nabla (h_s - h)\right) \tag{4}$$

Each of the phase enthalpies is defined by an expression of the form

$$h_k = \int_0^T c_k dT + h_k^0 \tag{5}$$

and the Fourier diffusion flux $k \nabla T$ is separated into two components to eliminate temperature as an explicit dependent variable. Except for the buoyancy force appearing in the x-momentum equation, the continuum density ρ is assumed constant, and continuum enthalpy and thermal conductivity are defined as

$$h = h_s + f_l (h_l - h_s) \tag{6}$$

$$k = k_s + f_l (k_l - k_s) \tag{7}$$

Thermophysical properties of each phase are also assumed constant, and the continuum viscosity μ is expressed as the harmonic mean of the phase viscosities, in the limit as $\mu_s \to \infty$. That is

$$\mu = \frac{\mu_l}{f_l} \tag{8}$$

Phase enthalpies defined by equation (5) are related to temperature by the expressions

$$h_s = c_s T \tag{9}$$

$$h_l = c_l T + \{(c_s - c_l) T_f + h_f\} \tag{10}$$

where h_f is the latent heat of fusion. Hence, from equilibrium thermodynamic considerations, the liquid mass fraction may be expressed as

$$f_l = \begin{cases} 0 & ; \quad h \le c_s T_f \\ (h - c_s T_f)/h_f & ; c_s T_f < h < (c_s T_f + h_f) \\ 1 & ; \quad h \ge (c_s T_f + h_f) \end{cases} \tag{11}$$

The assumption of constant phase specific heats and ther-

Nomenclature

c = specific heat
D_h = hydraulic diameter = $2W$
f = mass fraction
g = gravitational acceleration
Gr = Grashof number = $g\beta_T(T_o - T_f)D_h^3/\nu_l^2$
h = enthalpy
h^0 = enthalpy evaluated at $T = 0$
h_f = latent heat of fusion
k = thermal conductivity
k^* = thermal conductivity ratio = k_s/k_l
L = axial length of chill region
L_e = axial length of unchilled entry region
P = pressure (isotropic stress component)
P^* = dimensionless pressure = $P/\rho u_o^2$
Pe = Peclet number = RePr
Pr = Prandtl number
q = heat flux
q^* = dimensionless heat flux = $qD_h/k_s(T_f - T_w)$
Re = Reynolds number = $u_o D_h/\nu_l$
T = temperature
T^* = dimensionless temperature = $(T - T_w)/(T_o - T_w)$
u, v = velocity components
u^*, v^* = dimensionless velocity components; $u^* = u/u_o$; $v^* = vD_h/\alpha_l$
$\mathbf{V}$ = velocity vector
W = plate spacing
x, y = Cartesian coordinates
x^*, y^* = dimensionless coordinates; $x^* = x/\mathrm{Pe}D_h$; $y^* = y/D_h$
α = thermal diffusivity
β_T = thermal expansion coefficient
θ = dimensionless temperature = $(T_f - T)/(T_o - T_f)$
μ = dynamic viscosity
ν = kinematic viscosity = μ/ρ
ρ = density
ψ = stream function

Subscripts

f = fusion
k = phase designation
l = liquid
o = entry
r = reference
s = solid
w = chilled wall

mal conductivities is a computational simplification suitable for solidification over moderate temperature ranges. No general restrictions are, however, associated with these properties. While the viscosity of the liquid phase μ_l is assumed constant, this assumption should not be confused with constant viscosity assumptions often invoked in multiple region solutions. The continuum viscosity defined by equation (8) is not constant by virtue of variations in the liquid mass fraction. Variations in continuum viscosity accommodate the constitutive transformation from the liquid ($f_l = 1$) to solid ($f_l \approx 0$) states. While often criticized for smearing discrete phase transition, the viscosity behavior implied by equation (8) is, in fact, similar to that of empirical liquid viscosity data near the fusion temperature. Furthermore, for situations where quantitative viscosity data are available, alternate descriptions of continuum viscosity could be readily accommodated within the framework of the present model.

Difficulties arise when attempts are made to cast equations (1)-(4) into a meaningful dimensionless form. For example, the variation of solid layer thickness and flow cross-sectional area with axial position precludes the identification of meaningful length and velocity scales. Depending on the choice of these scales, alternative dimensionless forms may be obtained. Nevertheless, for the purpose of generalization and interpretation, it is useful to present results in dimensionless form. Omitting details of the nondimensionalization procedure, it can be verified that, using the variables x^*, y^*, u^*, v^*, P^*, and θ defined in the nomenclature, the present problem is characterized by five dimensionless parameters. The parameters, which depend on the phase change system (Pr, k^*) and on externally imposed conditions (Gr/Re, Pe, θ_w), were chosen because of their ability to collapse predictions corresponding to high Peclet numbers.

While the parameters Gr/Re, Pe, and θ_w permit the generalization of the present results and reduce the high Peclet number *n*-octadecane results to a two-parameter dependence, they do not provide a convenient means for physical interpretation. The difficulty centers on the fact that the independent variation of any of the three physical (dimensional) parameters T_o, T_w, and u_o causes variations in *two* dimensionless parameters. For example, the influence of entry liquid superheat is not uniquely characterized by Gr/Re since changes in T_o influence both Gr and θ_w. Similarly, the influence of entry mass flow rate is not uniquely characterized by Pe since changes in u_o also influence Gr/Re.

Solution Methodology and Model Validation

Since each of the continuum equations (1)-(4) is valid throughout the entire solution domain, explicit consideration need not be given to *internal* boundaries between the solid and liquid phases. The need for moving numerical grids and/or coordinate mapping, as well as the prescription of interfacial boundary conditions, is therefore eliminated. As with conventional single-phase analyses, consideration need only be given to *externally* imposed boundary conditions.

An elliptic, control-volume-based, finite-difference scheme (Patankar, 1981) has been used to solve the continuum equations. The sequence of numerical operations is identical to that used to solve conventional single-phase problems. Coupling that exists between the energy and momentum equations is accommodated through iteration and underrelaxation. Within the iterative scheme, equations (6) and (9)-(11) provide necessary descriptions of temperature fields for the evaluation of buoyancy source terms, as well as liquid mass fraction distributions for the evaluation of continuum viscosity, thermal conductivity, and solid-liquid interface position. Supplementary numerical calculations performed on grids ranging from 22×22 to 52×52 suggested that satisfactory grid independence could be achieved using a biased 42×42 grid (Fig. 1). The predicted solid-liquid interface position for the finer 52×52 grid deviated less than 5 percent from those for the 42×42 grid. The adiabatic entry length L_e was selected to be $L/10$ for both high and low Prandtl number fluids. Calculations performed for larger entry regions revealed only minor changes (<3.5 percent) in global parameters such as total solidified mass and cold wall heat extraction. Computations were carried out on a Cyber 205 super computer, requiring 1000-2000 CPU seconds for high Prandtl number runs and up to 5000 CPU seconds for low Prandtl numbers.

Table 1 Thermophysical property data for *n*-octadecane and aluminum

	n-Octadecane	Aluminum
Fusion Temperature, T_f (K)	300.65	933.52
Latent Heat of Fusion, h_f (J/kg)	2.44×10^5	3.95×10^5
Mean Density, ρ (kg/m^3)	776.5	2542.5
Solid Specific Heat, c_s (J/kg K)	2150.0	1076.0
Liquid Specific Heat, c_l (J/kg K)	2180.0	1080.0
Solid Thermal Conductivity, k_s (W/m K)	0.358	238.00
Liquid Thermal Conductivity, k_l (W/m K)	0.152	94.03
Dynamic Liquid Viscosity, μ_l (kg/m s)	3.9×10^{-3}	1.3×10^{-3}
Thermal Expansion Coefficient, β_T (1/K)	8.5×10^{-4}	1.2×10^{-4}
Prandtl Number, Pr	55.9	0.015
Thermal Conductivity Ratio, k^*	2.36	2.53

The continuum formulation and numerical procedures have been verified through comparisons with exact, one-dimensional Neumann solutions. Using a uniform grid and a fixed numerical time step, predictions of interface location and phase temperature distributions were within 10 percent of the exact solution for a wide range of phase Stefan numbers and thermal diffusivities. For prescribed conditions, however, the numerical time step and grid could be adjusted to provide predictions that were indistinguishable from the exact solution. Further verification of the formulation for diffusion-dominated situations was achieved through agreement with reported two-dimensional solidification results (Shamsundar and Sparrow, 1975).

The ability of the formulation to accommodate buoyancy-driven flows accurately was verified through comparison with the deVahl Davis (1983) benchmark solution for single-phase thermally induced natural convection in a square cavity. For a 42×42 grid, a Prandtl number of 0.71, and Rayleigh numbers up to 10^6, predictions of average Nusselt numbers were within 2 percent of the benchmark solution.

Results

Calculations were performed for both large (*n*-octadecane) and small (aluminum) Prandtl number fluids. Thermophysical properties used for each system are listed in Table 1.

Calculations for *n*-octadecane (Pr = 55.9) were performed for values of Gr/Re ranging from 500 to 8000, Peclet numbers ranging from 2800 to 11,200, and values of θ_w between 50 and 200. For a fixed temperature ratio θ_w, however, solidification behavior was found to be independent of Peclet number. For example, for Gr/Re = 2000, $\theta_w = 100$, and Peclet numbers spanning the range 2800-11,200, solid-liquid interface profiles were nearly indistinguishable and variations in total solidified mass were less than 3 percent. At large Peclet numbers, liquid core axial diffusion is negligible and significant axial temperature gradients are confined to the solidified

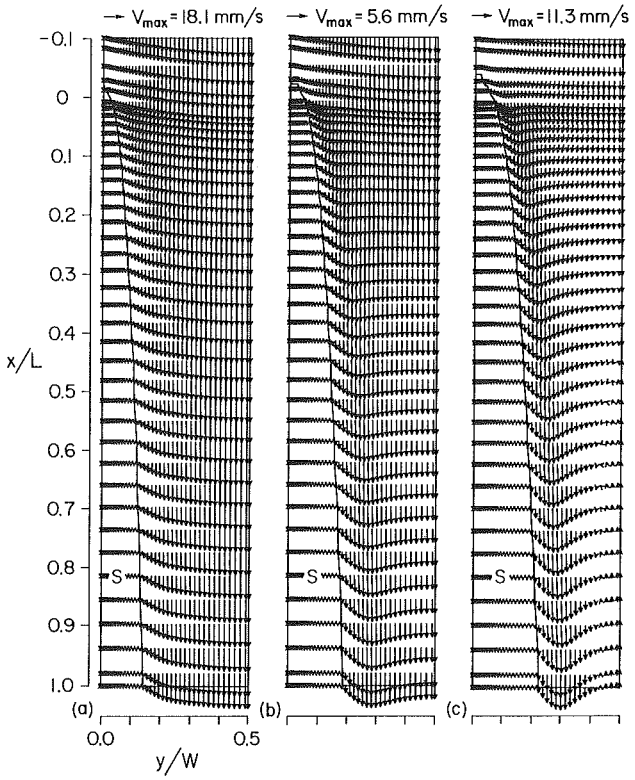

Fig. 2 Influence of Gr/Re on the velocity field and solid-liquid interface for *n*-octadecane ($\theta_W = 100$): (*a*) Gr/Re = 500, (*b*) Gr/Re = 2000, (*c*) Gr/Re = 8000

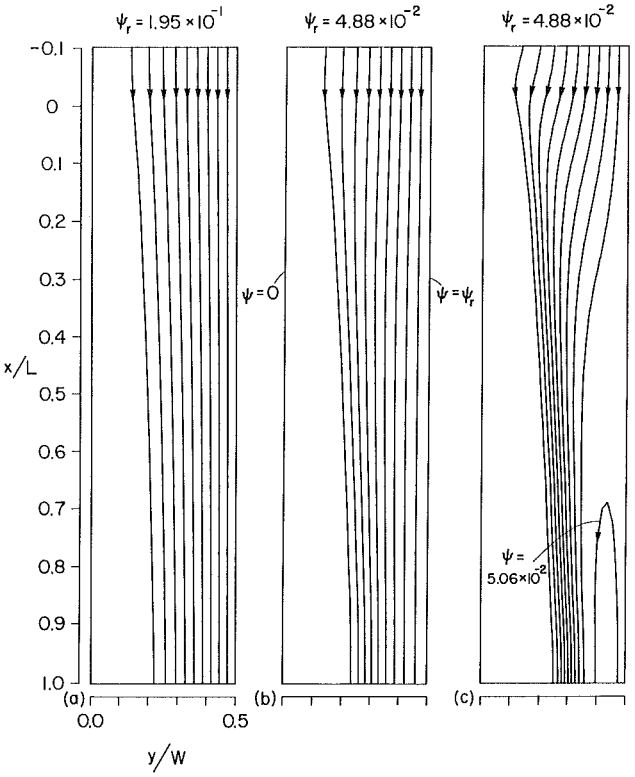

Fig. 3 Influence of Gr/Re on streamlines for *n*-octadecane ($\theta_W = 100$): (*a*) Gr/Re = 500, (*b*) Gr/Re = 2000, (*c*) Gr/Re = 8000

layer. The range of θ_w was chosen to insure rapid axial growth of the solid layer.

Figures 2 and 3 illustrate velocity fields and streamlines for $\theta_w = 100$ and Gr/Re = 500, 2000, and 8000. Solid-liquid interface profiles shown in Fig. 2 represent lines of constant $f_l = 0.5$. For Gr/Re = 500, the influence of thermal buoyancy is small and energy transport in the fluid core is dominated by forced convection. Fluid acceleration near the solid-liquid interface, which accompanies the flow constriction, leads to a gradual "flattening" of the entry parabolic velocity profile. Since the flow is steady, streamlines coincide with the flow field pathlines and illustrate the converging trajectory of fluid particles as they proceed through the channel (Fig. 3*a*).

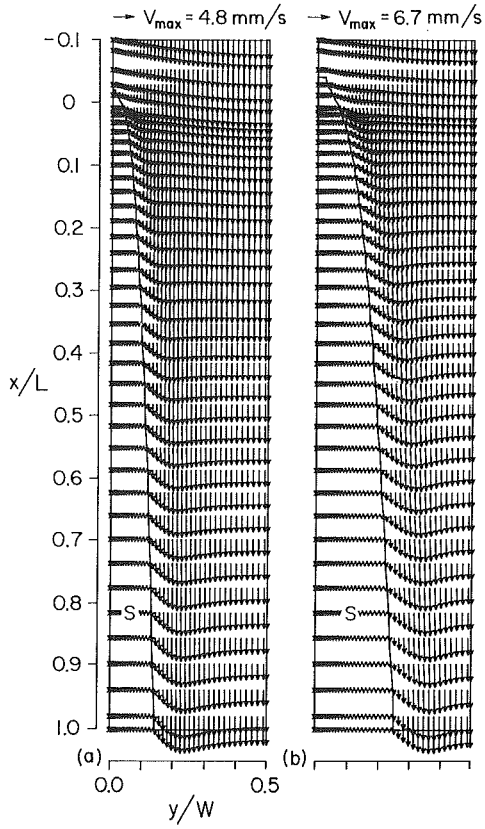

Fig. 4 Influence of θ_W on velocity field and solid-liquid interface for *n*-octadecane (Gr/Re = 2000): (*a*) $\theta_W = 50$, (*b*) $\theta_W = 200$

The influence of assisting thermal buoyancy becomes evident for Gr/Re = 2000. Although the solidification-induced flow constriction tends to accelerate the fluid core, buoyancy-induced fluid acceleration near the solid-liquid interface and the constraint of mass conservation result in the establishment of a W-shaped exit velocity profile (Fig. 2*b*). The increased density of streamlines near the solid-liquid interface (Fig. 3*b*) illustrates the influence that assisting thermal buoyancy has on channeling flow in this region. As Fig. 2 indicates, increasing Gr/Re with θ_w held constant also increases the solid layer thickness. Physically, such behavior could be achieved by decreasing the mass flow rate (decreasing Re) or increasing $(T_o - T_f)$ and $(T_f - T_w)$ by equal amounts.

For Gr/Re = 8000 (Figs. 2*c* and 3*c*), the imposed entry mass flow rate is no longer sufficient to feed strong buoyancy-induced flows. Consequently, *flow reversal* is established with *inflow* at the channel *exit*. While flow reversal has recently been discerned for single-phase, mixed convection in a vertical channel (Aung and Worku, 1986), to the authors' knowledge, the present results represent the first prediction of such behavior in the presence of solidification. As with single-phase mixed convection, Gr/Re is the primary parameter that governs the onset of flow reversal. Since the present results assume the channel exit ($x = L$) to be an outflow boundary, the onset of flow reversal, shown in Figs. 2(*c*) and 3(*c*), represents a limit beyond which meaningful solutions cannot be ob-

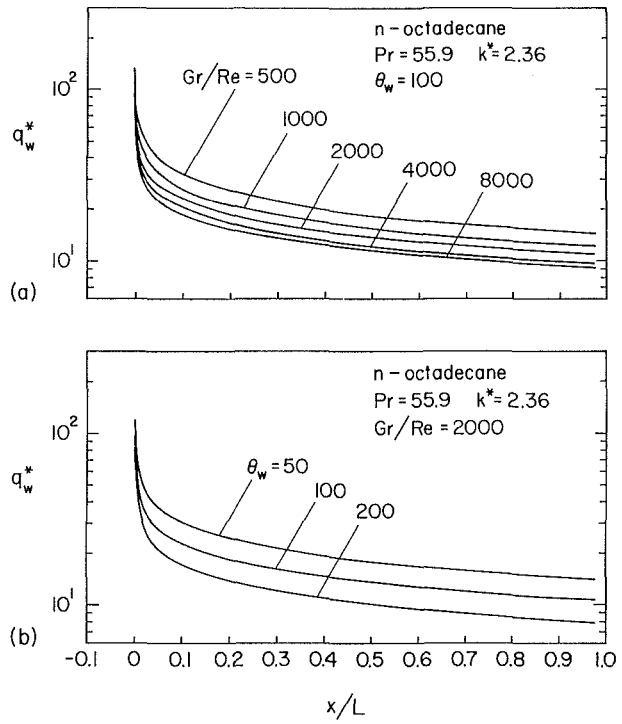

Fig. 5 Dimensionless chilled wall heat extraction flux for *n*-octadecane: (a) influence of Gr/Re, (b) influence of θ_w

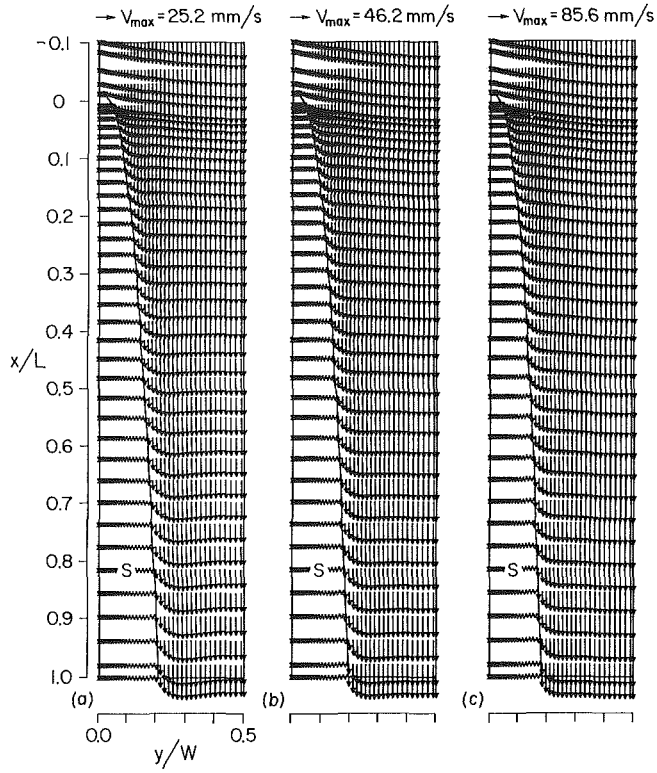

Fig. 6 Influence of Peclet number on the velocity field and solid-liquid interface for aluminum (Gr/Re = 10,000, $\theta_w = 0.5$): (a) Pe = 37.5, (b) Pe = 75.0, (c) Pe = 150.0

tained. For this reason, consideration has not been given to conditions for which Gr/Re > 8000.

Figure 4 illustrates the effect of θ_w on the velocity field and solid layer profile for a fixed Gr/Re ratio of 2000. With Gr/Re held constant, $(T_o - T_f)$ is fixed and increases in θ_w are associated with increases in $(T_f - T_w)$. Consequently, there is a significant increase in the solid layer thickness with increasing θ_w. However, since the liquid core remains in contact with solid at the fusion temperature, the change in θ_w has little effect on the velocity field, which retains the characteristic W-shaped profile associated with Gr/Re = 2000. Hence, it is the value of Gr/Re, which controls the relative influence of thermally induced and forced fluid motion, that has the dominant influence on the velocity field.

Figure 5(*a*) illustrates the influence of Gr/Re on the dimensionless chilled wall heat extraction flux, q_w^*. For a prescribed set of conditions, the heat flux distribution is similar to that of the classical Graetz problem exhibiting, for example, the rapid decay corresponding to a thermal entrance region. For a fixed temperature ratio θ_w, an increase in Gr/Re results in an increase in the solid layer thickness and hence a decline in dimensionless wall heat fluxes. Due to an increase in the solid layer thickness, which also accompanies an increase in θ_w, q_w^* also declines as θ_w increases (Fig. 5*b*).

In order to obtain solidification behavior comparable to results presented for *n*-octadecane, calculations for aluminum (Pr = 0.015) were performed for $\theta_w = 0.5$, values of Gr/Re ranging from 10,000 to 20,000, and Peclet numbers ranging from 37.5 to 150. Contrary to predictions for the high Prandtl number *n*-octadecane, results for aluminum were not independent of the Peclet number. Hence, for a fixed value of θ_w, results depended on both Gr/Re and Pe.

Figures 6 and 7 illustrate the influence of Peclet number on the velocity field, solid layer profile, and isotherms for Gr/Re = 10,000 and $\theta_w = 0.5$. Isotherms shown in Fig. 7 represent lines of constant $T^* = (T - T_w)/(T_o - T_w)$, with T^* equal to 0 and 1 at the chilled wall and channel entrance, respectively. All isotherms are plotted in increments of $\Delta T^* = 0.1$. As shown in Fig. 6, an increase in Pe causes a slight reduction in

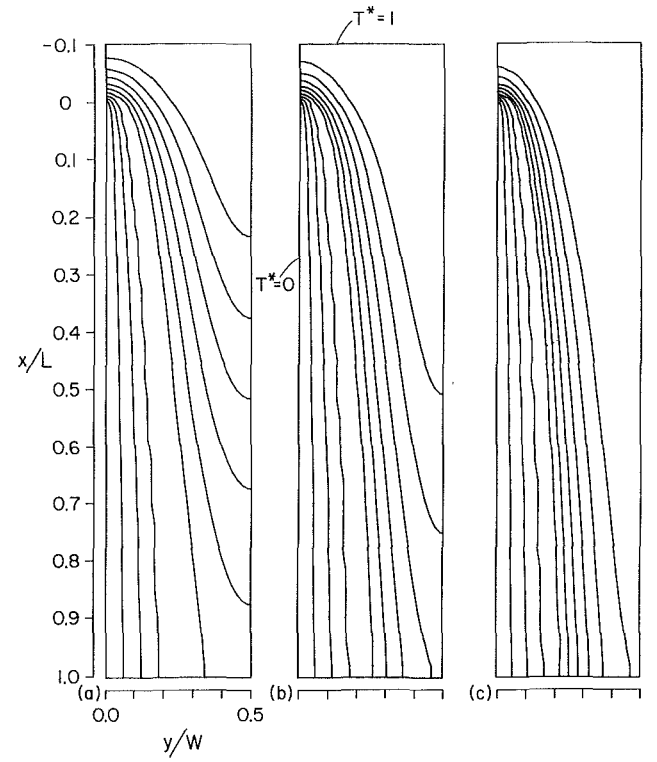

Fig. 7 Influence of Peclet number on isotherms for aluminum (Gr/Re = 10,000, $\theta_w = 0.5$): (a) Pe = 37.5, (b) Pe = 75.0, (c) Pe = 150.0

the thickness of the solidified layer, as well as a "flattening" of the velocity profiles. The influence of thermal buoyancy on liquid core velocity profiles becomes more pronounced at low Peclet numbers.

While axial diffusion in the liquid core was essentially

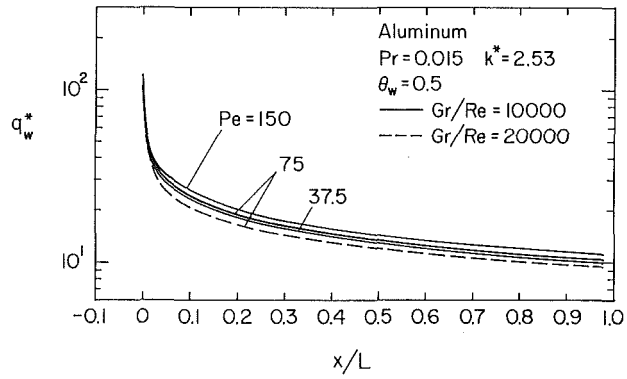

Fig. 8 Dimensionless chilled wall heat extraction flux for aluminum

nonexistent for the high Peclet number *n*-octadecane, Fig. 7 illustrates its significance for low Peclet number conditions. While the isotherms of Fig. 7 suggest that the effects of axial diffusion decrease with increasing Pe, axial temperature gradients remain significant for Pe = 150. It is noteworthy that there is significant *precooling*, as well as some solidification, of the liquid upstream of the chilled region due to axial conduction effects.

While not graphically illustrated, the influence of Gr/Re on velocity fields and solid layer profiles for aluminum were similar in nature to those presented in Fig. 2 for *n*-octadecane. Exit velocity profiles for aluminum at Gr/Re = 20,000 and Pe = 75 resembled the W-shaped profiles observed for *n*-octadecane at Gr/Re = 2000 (Fig. 2*b*). Flow reversal would, therefore, be expected for aluminum for Gr/Re values sufficiently in excess of 20,000.

Dimensionless heat flux distributions for aluminum (Fig. 8) indicate a weak dependence on Peclet number. With increasing Peclet number (increasing Re) the thickness of the solidified layer decreases, causing an increase in q_w^*. In addition, as for the *n*-octadecane results, an increase in Gr/Re for a fixed θ_w causes a decline in q_w^*.

Conclusions

Although laminar, mixed convection flow in a vertical parallel-plate channel has been extensively considered, the permuted, yet important, problem of flow with solidification has received comparatively little attention. In the present study a continuum model, which includes axial diffusion and thermal buoyancy, has been used to investigate solidification for both large and small Prandtl number fluids. In general, steady-state behavior was found to depend on values of the dimensionless groups Gr/Re, Pe, and θ_w.

For phase change systems characterized by large Prandtl numbers (for example, *n*-octadecane), Peclet numbers were sufficiently large to render the effects of axial diffusion negligible. Hence, for such systems, the influence of Peclet number was negligible and solidification behavior reduced to a dependence on only Gr/Re and θ_w. However, phase change systems characterized by small Prandtl numbers (for example, aluminum) and correspondingly small Peclet numbers were significantly influenced by axial diffusion and retained a Peclet number dependence.

As for single-phase mixed convection problems, the parameter Gr/Re was found to characterize the relative effects of thermally induced and forced fluid motions. While forced convection dominated conditions were predicted for small values of Gr/Re, strong mixed convection behavior became evident with increasing Gr/Re. Effects were manifested by first a flattening of the velocity profile, the subsequent appearance of a W-shaped profile, and finally the onset of flow reversal. Flow reversal resulted from inability of the imposed entry mass flowrate to sustain the strong acceleration due to assisting buoyancy forces near the solid/liquid interface. An increase in Gr/Re also caused an increase in the solid layer thickness and, hence, a reduction in the wall heat flux.

Acknowledgments

One of us (W. D. B.) is grateful for support of the Aluminum Company of America under a continuing education grant. Support for a portion of the work has been provided by the National Science Foundation under Grant CBT 83-16580.

References

Aung, W., and Worku, G., 1986, "Developing Flow and Flow Reversal in a Vertical Channel With Asymmetric Wall Temperatures," ASME JOURNAL OF HEAT TRANSFER, Vol. 108, pp. 299-304.

Aung, W., and Worku, G., 1986, "Theory of Fully Developed, Combined Convection Including Flow Reversal," ASME JOURNAL OF HEAT TRANSFER, Vol. 108, pp. 485-488.

Cheng, K. C., and Wong, Sum-Lok, 1977, "Liquid Solidification in a Convectively-Cooled Parallel-Plate Channel," *Canadian Journal of Chemical Engineering*, Vol. 55, pp. 149-155.

Cheung, F. B., and Epstein, M., 1984, "Solidification and Melting in Fluid Flow," *Advances in Transport Processes*, A. S. Mujumdar and R. A. Mashelkar, eds., Wiley Eastern Limited, New Delhi, Vol. 3, pp. 35-117.

deVahl Davis, G., 1983, "Natural Convection of Air in a Square Cavity: A Benchmark Numerical Solution," *Int. J. Num. Methods Fluids*, Vol. 3, pp. 249-264.

Hwang, G. J., and Sheu, Ja-Pung, 1976, "Liquid Solidification in Combined Hydrodynamic and Thermal Entrance Region of a Circular Tube," *Canadian Journal of Chemical Engineering*, Vol. 54, pp. 66-71.

Lee, D. G., and Zerkle, R. D., 1969, "The Effect of Liquid Solidification in a Parallel Plate Channel Upon Laminar-Flow Heat Transfer and Pressure Drop," ASME JOURNAL OF HEAT TRANSFER, Vol. 91, pp. 583-585.

Ozisik, M. N., and Mulligan, J. C., 1969, "Transient Freezing of Liquids in Forced Flow Inside Circular Tubes," ASME JOURNAL OF HEAT TRANSFER, Vol. 91, pp. 385-390.

Patankar, S. V., 1981, "A Calculation Procedure for Two-Dimensional Elliptic Situations," *Numerical Heat Transfer*, Vol. 4, pp. 409-425.

Shamsundar, N., and Sparrow, E. M., 1975, "Analysis of Multidimensional Conduction Phase Change Via the Enthalpy Model," ASME JOURNAL OF HEAT TRANSFER, Vol. 97, pp. 333-340.

Toda, S., Sugiyama, H., Owada, H., Kurokawa, M., and Hori, Y., 1986, "Laminar Flow Heat Transfer in a Tube With Internal Solidification," *Proceedings 8th International Heat Transfer Conference*, C. L. Tien et al., eds., Hemisphere, Washington, DC, Vol. 4, pp. 1745-1750.

Zerkle, R. D., and Sunderland, J. E., 1968, "The Effect of Liquid Solidification in a Tube Upon Laminar-Flow Heat Transfer and Pressure Drop," ASME JOURNAL OF HEAT TRANSFER, Vol. 90, pp. 183-190.

C. P. Grigoropoulos[1]

R. H. Buckholz[2]

Columbia University,
Department of Mechanical Engineering,
New York, NY 10027

G. A. Domoto

Xerox, Webster Research Center,
Mechanical Engineering Sciences Laboratory,
North Tarrytown, NY 10591

An Experimental Study on Laser Annealing of Thin Silicon Layers

A laser annealing technique directed toward producing single crystalline silicon on substrates is studied. In this paper the laser-induced melting of thin silicon films is studied experimentally. Direct heating of thin silicon layers on substrates is shown to produce a variety of different silicon melting patterns. A systematic study of these phase change phenomena has been performed. The important parameters are: (1) the laser beam power, (2) the laser beam intensity distribution, and (3) the speed of the translating silicon layer. Unstable silicon phase boundaries break up to form regions where solid and melt silicon coexist. Complicated silicon phase boundary patterns are shown. The experimental results showed the occurrence of organized patterns of alternating solid and liquid silicon stripes for two-dimensional heating distributions. Finally, temperature fields for the experimental operating conditions are calculated using an enthalpy model.

I Introduction

Research objectives in the area of solid state electronics call for higher device performance and improved circuit packing density. New techniques are being introduced to overcome the present limitations of the conventional semiconductor material processing methods. Trends in this technology are toward smaller-sized and three-dimensional circuit devices. It is of fundamental interest to produce single-crystal, thin silicon layers on amorphous insulators. One of the most promising innovations toward this goal is the laser annealing technique (Hess et al., 1983).

The most commonly used method to grow silicon layers is chemical vapor deposition (CVD). In this method, the constituents of a vapor phase, diluted with an inert gas, react at a hot surface to deposit a solid silicon film. The material obtained in this way has a definite crystalline structure; however, it presents imperfections, in the form of grain boundaries. These grain boundaries act as barriers to the movement of charge carriers across junctions. Thus, the value of this polycrystalline as an electronic device fabrication material is significantly reduced. This structure has been improved by the method of laser recrystallization.

In this study the experimental results from a laser annealing technique are presented and discussed. The laser annealing technique has application to three-dimensional large-scale integrated circuits. There has recently been a significant effort to produce electronic quality silicon-on-insulator. Several different methods have been used to improve the quality of the silicon layer.

This paper describes a method whereby a laser annealing procedure is applied to polysilicon that has been deposited on a silicon-oxide layer. The authors' approach and interpretation to these experimental results is from a conductive heat transfer point of view.

The central issue is the effective control of the associated solidification process. The need to understand the solidification for thin layers of silicon has sparked a number of experimental efforts. Lemons and Bosch (1982) directly observed the melting of thin silicon films. They used continuous wave (CW) argon laser beams. The molten silicon spot was viewed using three different methods: (1) the emitted light, (2) the reflected light, and (3) the transmitted light. They showed that both the solid and liquid silicon phases would coexist in a heated spot for a range of laser power. They observed numerous solid-silicon filaments that penetrated into the molten silicon pool. These silicon filaments formed fixed phase patterns within the silicon melt. The filaments are believed to be solid since their emissivity matches the surrounding hot solid silicon emissivity. A HeNe laser beam was also used to determine the phase of the heated silicon. The HeNe laser light was transmitted through the silicon filaments. This light transmission would be reduced for opaque liquid silicon. This result also suggests the filaments were solid silicon. These lamellae were identical when viewed from above the silicon layer or through the transparent substrate. This indicated that the solid filaments were continuous through the entire silicon film thickness. To explain the occurrence of these solid inclusions these investigators suggested two possible models: (1) Impurities could be present in the system; the most probable impurity is oxygen acquired either from the ambient or from the substrate; impurities could segregate into the liquid silicon and lower its melting point, thus triggering the mechanism of constitutional supercooling; (2) phase separation in pure silicon melt. The authors did not elaborate on this second explanation.

Coexisting solid and liquid silicon phases were also observed by Hawkins and Biegelsen (1983). In their studies no impurities could be detected by an Auger analysis. They demonstrated that the formation of lamellae is in fact an intrinsic characteristic of radiatively induced thin silicon film melting. When the silicon melts it reflects more light. Thus, the neighboring solid silicon absorbs more heat relative to the melt. In the microscopic picture this appears as the unusual phenomenon of superheated solid lamellae coexisting with supercooled liquid. These lamellae initially occur at random spots within the molten silicon. These spots tend to move dynamically and coalesce into larger regions. Hawkins and Biegelsen used CO_2 laser irradiation to melt 0.6-μm-thick polysilicon films on glass substrates. They found that partial melting begins in the form of liquid lamellae; these lamellae have a minimum diameter of about 3 μm. As the laser power is increased, the molten pool expands in size. Solid inclusions persist in the liquid region. These structures are continuous through the thickness of the silicon layer. When the laser power exceeds a certain limit, the melt zone becomes uniformly liquid. Aligned and alternating liquid and solid stripes of silicon were also observed under continuous wave laser heating of thin silicon films on quartz substrates.

[1]Present address: Department of Mechanical Engineering, University of Washington, Seattle, WA 98195.

[2]Present address: Salomon Brothers Inc., Special Projects Group, One New York Plaza, New York, NY 10004.

Contributed by the Heat Transfer Division for publication in the JOURNAL OF HEAT TRANSFER. Manuscript received by the Heat Transfer Division September 9, 1986. Keywords: Laser Processing, Materials Processing and Manufacturing Processes, Phase-Change Phenomena.

In this study an experimental apparatus was built for direct in-situ microscopic observations of the melting process. The laser beam parameters are varied and the resulting effects on the silicon phase change are studied.

The difficulty in measuring the temperature at these microscopic length scales should be recognized. There are only a few reported temperature measurements corresponding to laser annealing experiments. Sedwick (1981) measured the maximum temperature during CW annealing by using a modified optical micropyrometer. The range of these measurements was 1025–1410°C and the estimated accuracy a few tens of degrees. Lemons and Bosch (1982) measured the emitted light from melted silicon. They analyzed the power spectra of the emitted light to determine the temperatures. The silicon spot diameter was approximately 200 μm. The single temperature value they assigned to the spectral data—an accuracy of ± 50°C—indicates all the temperatures in the measured region. The experiments mentioned represent the extent of published temperature measurements. It is not within the scope of this paper to measure the silicon layer temperature distribution. However, such data would be a valuable tool for the processing of materials on a microscopic scale.

Experiments are presented for the melting of silicon by laser beams having circular Gaussian intensity distribution profiles. To study the propagation of straight phase boundaries, the laser beam shape is modified. To accomplish this a cylindrical lens is used to produce narrow, elliptic heating profiles.

II Description of the Experimental Apparatus

The experimental setup is shown in Fig. 1. A Lexel (model 95-4) 4 W argon laser is used to heat the silicon. This laser operates on the fundamental mode (i.e., TEM_{00}). The laser beam has a Gaussian intensity distribution. The power level is set externally by adjusting the current through the plasma tube. The maximum nominal power obtained around the $\lambda = 0.5145$ μm (green) line is 2.3 W. The laser beam $1/e^2$ irradiance diameter at the transmitter mirror is 1.3 mm (per manufacturer's specifications). The full angle of beam divergence is 0.6 mrad.

The laser beam is focused using a symmetric convex glass lens. The measured paraxial focal length of this spherical lens is 110 mm. Elliptic beams with high aspect ratios can be obtained by placing a plano-cylindrical lens after the spherical lens. The measured focal length of this lens is 77 mm.

The laser beam is directed toward the silicon sample that is fixed to a translation stage. The translation stage is moved in one direction by a piezoelectric motor controlled through a command module. Either a manual control or a minicomputer is used. The travel of the motor spindle is 50 mm. The maximum constant translation speed is 2 mm/s. Both the translation speed and the position of the stage are measured using a laser interferometer system.

The experiments were performed on silicon samples provided by Biegelsen (Hawkins and Biegelsen, 1983). These

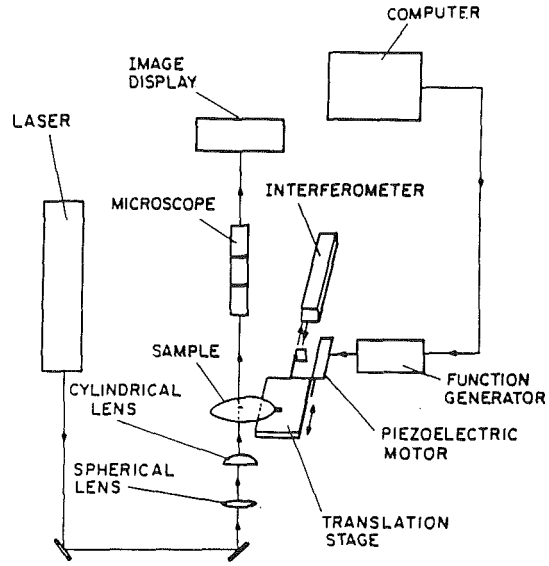

Fig. 1 Sketch of the experimental setup. Silicon sample is positioned on the translation stage. Transmitted light is viewed through the microscope.

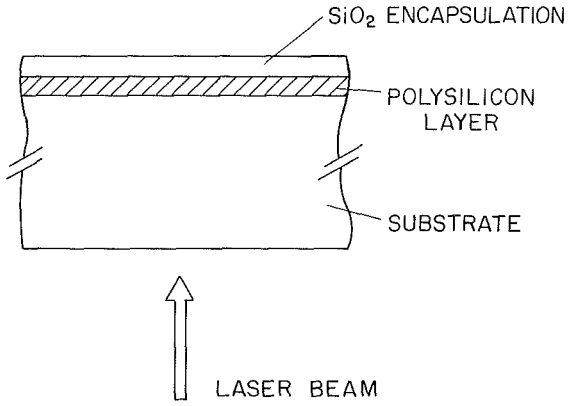

Fig. 2 Sketch of the silicon sample that was processed. A 0.5-μm-thick silicon layer is shown to be deposited on a thick silicon-oxide layer. The deposited polysilicon layer is then covered with a 0.5-μm-thick glass layer.

samples were prepared on 0.5-mm-thick bulk, fused silica wafers. These samples are 3 in. in diameter. Polysilicon layers, 0.5 μm thick, were deposited by CVD on the substrates. An encapsulating SiO_2 layer, 0.5 μm thick, was placed on top of the polysilicon.

In this experiment the laser beam is directed toward the silicon layer through the transparent glass substrate. A sketch of the silicon sample cross section is shown in Fig. 2. A portion of the incident light is reflected by the silicon surface. Another fraction of light is transmitted through the thickness

Nomenclature

d = light absorption depth
k = extinction coefficient
n = real part of refractive index
n^* = complex refractive index
P = incident laser power at the sample surface
Q_0 = averaged peak intensity over the $1/e$ irradiance width in the y direction
r = Gaussian beam $1/e$ irradiance half-width
R = reflectance in the direction normal to the sample surface
s = molten spot width
t = time
T = absolute temperature
V = sample translation speed
α = absorption coefficient
δ = uncertainty estimate
λ = laser light wavelength

Subscripts

l = liquid silicon
s = solid silicon
x = coordinate in the direction of motion
y = coordinate in the direction normal to motion

of the silicon layer. The remaining light is absorbed within the silicon. The transmitted light is observed using a microscope that is placed directly above the silicon sample. The transmitted light intensity is attenuated using a yellow sharp cutoff Schott glass filter. Alternatively it is possible to see the molten silicon spot using a reflected light method. An incandescent tungsten light source is used to reflect light from the silicon surface. These observations are recorded on 35 mm photographic films.

The experimental apparatus is mounted on an optical table. The positions of the optical components are individually adjusted using micrometers. The vertical distances between the central planes of the two lenses and the level of the table are measured. This information is used in thin lens calculations to estimate the shape of the light intensity distribution. The accuracy of these calculations depends on both the alignment of the optical system and the validity of the thin lens approximations.

III Experimental Results

To compare the experimental observations with theoretical results, it is necessary for the laser power, the silicon translation speed, and the laser beam diameter to be known. The laser beam power is decreased at each of the optical components shown in Fig. 1. When the cylindrical lens is used, the effective power at the silicon surface is 57 percent of the initial laser beam power at the laser exit. Table 1 shows the uncertainty estimates associated with the various measurements.

There are two factors that relate the effect of changing the laser beam intensity distribution. The first is the laser beam radius for the circular beam shape. The parameter chosen to quantify this effect is the beam $1/e$ irradiance radius r. The effect of changing this parameter over a range 17–65 μm is studied. The second factor is the laser beam cross-sectional shape. Experiments were done for both elliptically shaped laser beams and for circular cross-sectional laser beams.

Table 1 Uncertainty in the measured variables. Q_0 is the averaged peak intensity over the $1/e$ irradiance width in the y direction.

Beam 1/e radii		$Q_0 \times 10^6$	Uncertainties		
r_x(μm)	r_y(μm)	(W/m²)	δr_x(%)	δr_y(%)	δQ_0(%)
17	133	1.36	5.5	2.6	10.7
	119	1.52		2.9	7.6
	105	1.72		3.3	7.3
	93	1.95		3.8	6.9
19	131	1.27	13.9	2.6	14.3
	116	1.43		3.0	14.5
	103	1.62		3.4	14.1
	90	1.85		4.0	13.6
22	128	1.03	16.8	2.7	22.5
	114	1.25		3.1	16.7
	100	1.43		3.6	16.3
	87	1.65		4.2	15.8
26	126	0.96	16.5	2.7	24.1
	111	1.08		3.1	16.4
	97	1.24		3.6	16.0
	84	1.43		4.2	15.4
31	123	0.82	15.1	2.8	22.6
	108	0.93		3.2	15.2
	94	1.07		3.7	14.7
	81	1.25		4.4	14.2

III.1 Circular Beams. In this sequence of experiments the maximum laser power available was used. The position of the spherical lens was initially adjusted so that the silicon sample intercepted the laser beam at its focal waist. The $1/e$ irradiance radius of the beam at the focal waist is about 17 μm. In this case, a "keyhole" in the silicon layer that extended to the glass substrate was produced. This keyhole pattern is shown in Fig. 3(a). The laser beam radius was increased by translating the spherical lens along the axis of the laser beam. Consequently, the peak power intensity was reduced and the beam radius was increased to 20 μm. The molten silicon spot appeared round. A photograph of the transmitted light is shown in Fig. 3(b). The bright spot in this figure corresponds to a completely melted silicon region.

The silicon phase boundary for the melt region became irregular as the laser beam diameter was further increased to 50 μm. Bright filaments were observed to originate from ripples along the phase change boundary. These filaments appeared to propagate into the liquid region; the solid filaments formed stable patterns within the liquid phase. A photograph of the transmitted light is shown in Fig. 3(c). The solidification patterns shown persisted for several minutes. These patterns can adjust their shape in response to slight variations of the incident laser power. Melt silicon exhibits a metallike behavior; it absorbs laser light within a thin surface layer. The liquid silicon complex refractive index as a function of the light wavelength has been measured by Shvarev et al. (1975). At the $\lambda = 0.5145$ μm wavelength this refractive index is

$$n_l^* = n(1 + ik) = 2.2 + i4.4$$

The absorption depth in liquid silicon therefore is

$$d_l = \frac{\lambda}{4\pi nk} = 0.0093 \ \mu\text{m}$$

The absorption coefficient, α_s, and the normal incidence reflectance, R_s, for solid silicon as functions of temperature have been measured by Jellison and Modine (1983)

$$\alpha_s = 6.28 \cdot \exp(T/433) \cdot 10^3 \quad (\text{cm}^{-1}) \qquad 300 < T < 1000 \text{ K}$$

$$R_s = 0.382 + 5.0 \times 10^{-5}(T - 300)$$

At $T = 1000$ K, well below the melting temperature of 1685 K, the above expressions give an absorption depth $d_s = 0.158$ μm. At the silicon melting temperature, the solid silicon transmissivity is larger than the liquid silicon transmissivity. The bright inclusions are therefore solid silicon that is coexisting with the liquid phase.

The laser beam radius was further increased to roughly 55 μm, Fig. 3(d). More solid material formations appeared in the melt region. Three different types of silicon phase pattern are identified. First, a rather randomly oriented filament growth pattern is observed. Secondly, the solid filaments are seen to coalesce into larger regions and form a partial-arc structure. These partial-arc structures are consistently observed. In another type of pattern, the solid filaments divide into smaller round disks. A typical disk diameter is about 5 μm. The fraction of melt silicon in the heated spot decreased when the beam radius was increased to 60 μm, Fig. 3(e). The end of partial melting was found to occur for a beam radius of 65 μm, Fig. 3(f). For this beam radius the heated silicon spot was almost completely solid.

In another series of experiments, the laser beam diameter was varied. Different sample translation speeds were studied. Molten silicon spot diameters were measured from photographic pictures. Data are given in Table 2. As expected, the molten silicon spot size is reduced when the translation speed is increased. Nevertheless, the shape remains nearly circular.

It is interesting to note that the molten spot appears uniformly liquid for $r \sim 40$ μm and for zero translation speed.

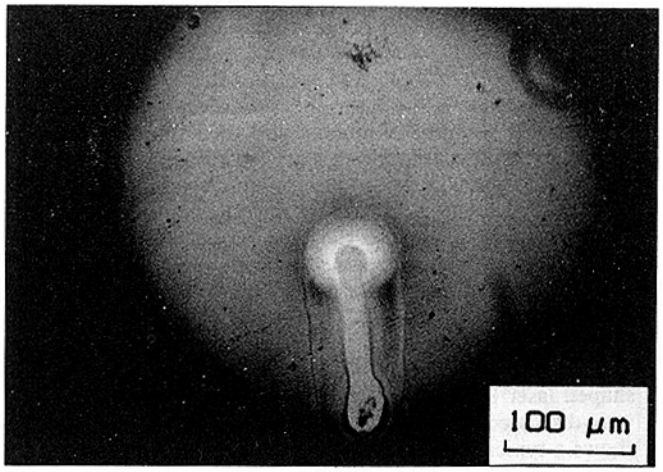

Fig. 3(a) Photograph of the "keyhole" that appeared on the polysilicon surface during heating. In this case the silicon sample translation speed was zero. The laser beam radius was 17μm and the laser power was 1.6 W.

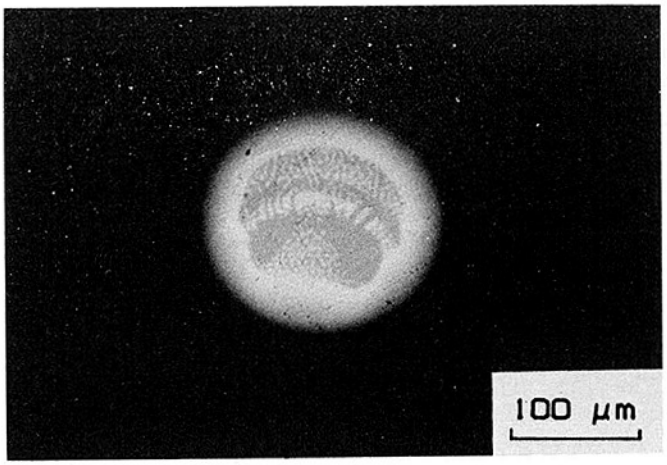

Fig. 3(d) Photograph of a polysilicon layer during melting. A circular laser beam having power $P = 1.6$ W and $1/e$ irradiance radius of 55 μm was used.

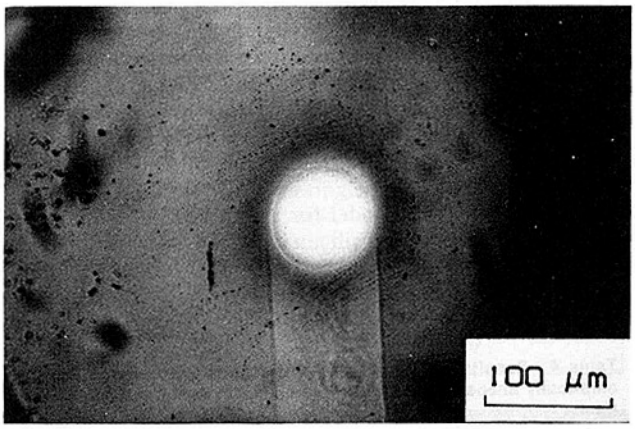

Fig. 3(b) Photograph of a polysilicon layer during melting. A circular laser beam having power $P = 1.6$ W and a $1/e$ irradiance radius of 20 μm was used.

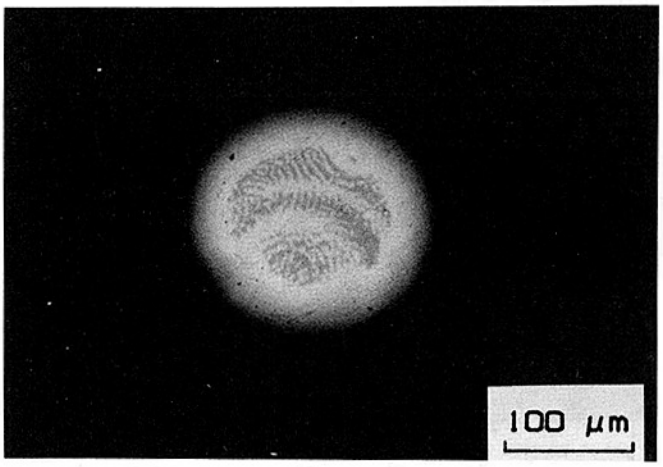

Fig. 3(e) Photograph of a polysilicon layer during melting. A circular laser beam having power $P = 1.6$ W and $1/e$ irradiance radius of 60 μm was used.

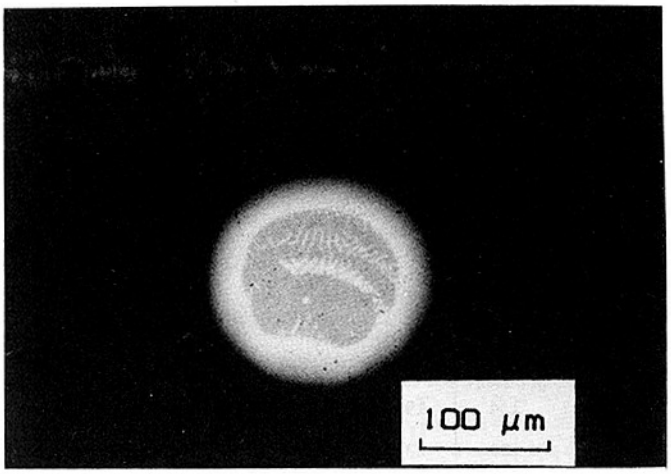

Fig. 3(c) Photograph of a polysilicon layer during melting. A circular laser beam having power $P = 1.6$ W and $1/e$ irradiance radius of 50 μm was used.

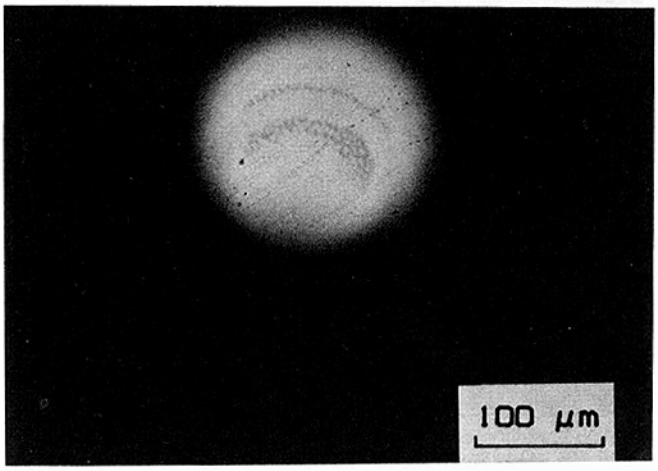

Fig. 3(f) Photograph of a polysilicon layer during melting. A circular laser beam having power $P = 1.6$ W and $1/e$ irradiance radius of 65 μm was studied. Note the decrease in the amount of solid filaments contained in the silicon melt.

When the silicon layer is translated, the once entirely molten silicon spot now is described as a "mushy region." The solid and melt phases coexist in the heated spot. Solid filaments quickly move inward from the phase boundary.

III.2 Elliptic Beams. The application of elliptic Gaussian beams to thin silicon layer melting is now considered. A cylindrical lens is used to make a nearly one-dimensional laser heating source. In these experiments, the maximum laser

Table 2 Results for the silicon phase state are summarized for the circular laser beams of Gaussian intensity distribution. Results are shown for five radii of the laser beam, for two different laser beam powers, and for four values of the silicon layer translation speed.

r(μm)	P(W)	V(mm/sec) 0	1	2	4±0.08
17	1.6	72 keyhole	80	78	75
	1.1	63	55	52	49
20	1.6	90	83	80	76
	1.1	55	50	48	44
29	1.6	110	100	95	81
	1.1	68	57	55	53
39	1.6	113	99 mushy	84 mushy	no melting
	1.1	70	54 mushy	53 mushy	no melting
50	1.6	120	80 mushy	no melting	no melting
	1.1	50 mushy	no melting	no melting	no melting

Table 3 Results for the silicon phase state are summarized for elliptically shaped laser beams of Gaussian intensity distribution. The results are for the case where the silicon layer is stationary. Description of the silicon phase is given for a range of elliptical beam cross sections.

Beam 1/e radii		Spot dimensions		Description
r_x(μm)	r_y(μm)	s_x(μm)	s_y(μm)	
17	133	10	192	mushy
	119	19	185	clear
	105	22	177	clear
	93	27	165	clear
19	131	10	185	clear
	116	19	189	clear
	103	17	173	clear
	90	27	162	clear
22	128	19	173	mushy
	114	23	162	wavy interface
	100	27	165	wavy interface
	87	34	150	clear
26	126	23	148	mushy
	111	29	150	mushy
	97	35	146	mushy
	84	54	135	clear

power incident on the sample surface was 1.3 W. The $1/e$ irradiance width in the direction of laser beam motion is $2r_x$. This distance was varied by adjusting the axial position of the cylindrical lens. Experiments were performed for four different silicon layer translational speeds.

The results for zero translational speed and for a range of laser beam dimensions are shown in Table 3. Both the laser beam dimensions and the silicon spot dimensions are shown. Mushy conditions correspond to a result where both liquid and solid phases are observed to coexist. Clear conditions correspond to an entirely melted spot of silicon. The wavy interface description is used for the condition where the phase boundary is continually melting and then resolidifying. This generates the appearance of a wavy interface. A solid filament begins to form at the silicon phase boundary. However, before that solid filament penetrates far into the liquid melt the solid filament changes back to the melt phase. Results from the same elliptically shaped beam at speeds equal to 2.0 mm/s, 0.1 mm/s, and 4.0 mm/s are shown in Tables 4, 5, and 6, respectively.

Typical transmitted light photographs of silicon phase patterns are shown in Figs. 4(a) and 4(b) for the elliptically shaped laser beam. These results exhibit all the features that were discussed earlier for the circular laser beam. Figure 4(a) shows a typical molten spot configuration for a translational speed of 2 mm/s, $r_x \sim 17$ μm and $r_y \sim 93$ μm. In this example, the melting conditions allow a stable phase boundary. This observation is made based on the uniform brightness of the transmitted light near the maximum power region of the laser beam. Figure 4(b) shows the silicon phase pattern for an elliptically shaped laser beam ($r_x \sim 24$ μm and $r_y \sim 113$ μm) and a sample translation speed of 2 mm/s. In this case, the phase boundary was unstable and partial melting was observed.

Figures 4(c) and 4(d) show higher magnification reflection micrographs of elliptic molten spots. In Fig. 4(c), the occurrence of randomly oriented dark inclusions is observed in the liquid silicon region. The liquid silicon reflects twice as much light as the solid silicon. Therefore, the solid inclusions appear dark in contrast to the neighboring bright liquid region.

An enthalpy-based model for the three-dimensional, transient heat transfer in thin silicon layers on glass substrates was given by Grigoropoulos et al. (1986). This model was used to calculate the temperature fields associated with the experimen-

Table 4 Results for the silicon phase state are summarized for the elliptically shaped laser beam. The silicon layer translation speed is 2 mm/s.

Beam 1/e radii		Spot dimensions		Description
r_x(μm)	r_y(μm)	s_x(μm)	s_y(μm)	
17	133	5	154	mushy
	119	13	135	clear
	105	15	173	clear
	93	16	154	clear
19	131	7	154	mushy
	116	15	177	mushy
	103	17	173	clear
	90	29	150	clear
22	128	-	-	no melting
	114	19	155	wavy interface
	100	23	153	wavy interface
	87	31	151	wavy interface
26	126	-	-	no melting
	111	27	135	mushy
	97	30	132	mushy
	84	46	127	mushy

Table 5 Results for the silicon phase state are summarized for the elliptically shaped laser beam. The silicon layer translation speed is 0.1 mm/s.

Beam 1/e radii		Spot dimensions		Description
r_x(μm)	r_y(μm)	s_x(μm)	s_y(μm)	
24	102	8	133	mushy
20	99	15	135	mushy
18	96	16	142	clear
17.5	94	25	162	clear
17	93	23	160	clear
18	91	23	158	clear
19	90	19	156	clear
22	87	33	152	clear
26	84	46	133	mushy

Table 6 Results for the silicon phase state are summarized for the elliptically shaped laser beam. The silicon layer translation speed is 4 mm/s.

Beam 1/e radii		Spot dimensions		Description
r_x(μm)	r_y(μm)	s_x(μm)	s_y(μm)	
17	93	14	143	wavy interface
19	90	18	152	wavy interface
22	87	19	125	mushy
26	84	30	100	mushy

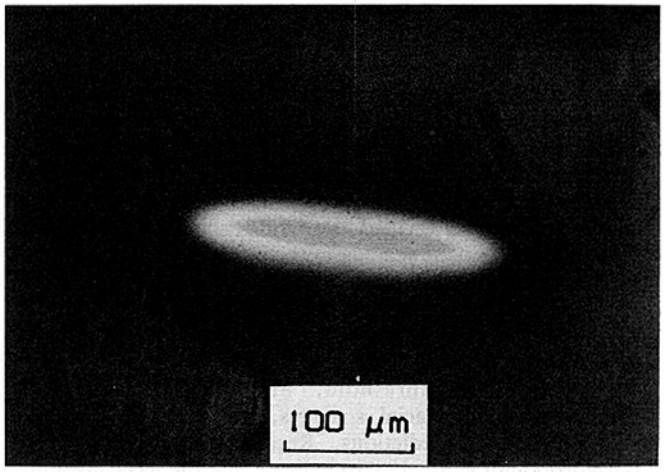

Fig. 4(a) Photograph of a polysilicon layer during melting. An elliptically shaped beam of power $P = 1.3$ W was used. The operating conditions were $V = 2.0$ mm/s, $r_x \sim 17$ μm, $r_y \sim 93$ μm.

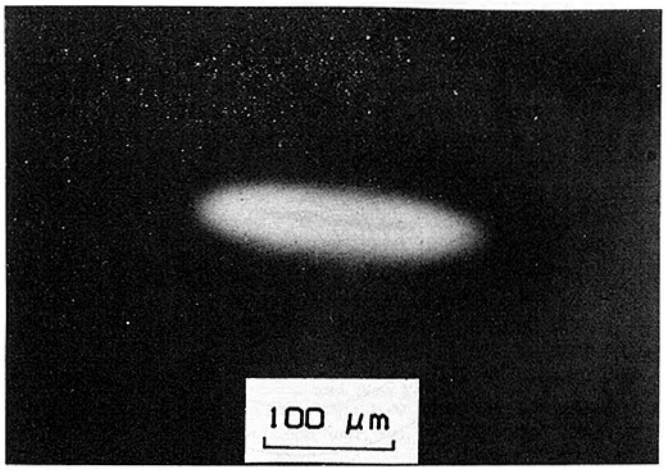

Fig. 4(b) Photograph of a polysilicon layer during melting. An elliptically shaped beam of power $P = 1.3$ W was used. The operating conditions were $V = 2$ mm/s, $r_x \sim 24$ μm, $r_y \sim 113$ μm.

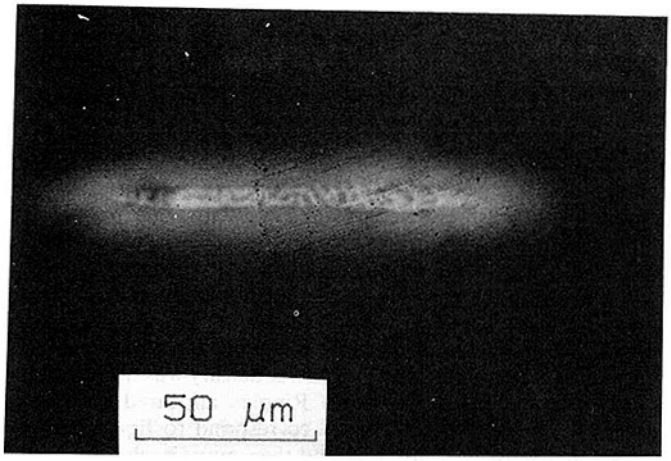

Fig. 4(c) Photograph of reflected light from a silicon surface during laser melting of the polysilicon layer. The translational speed was zero. The power was 1.3 W. and $r_x \sim 29$ μm, $r_y \sim 120$ μm.

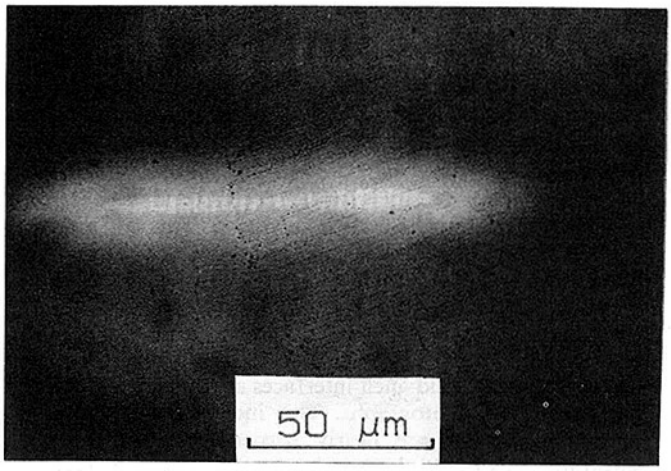

Fig. 4(d) Photograph of reflected light from a silicon surface during laser melting of the polysilicon layer. The translational speed was 0.01 mm/s. A striped pattern having a wavelength of approximately 5 μm is observed.

tal data. Temperature fields were calculated for a laser power of 1.6 W. The polysilicon layer was 0.5 μm thick and the glass substrate is 500 μm thick. The silicon layer is bounded by a 0.5 μm thick encapsulating glass layer. Thin film optics are incorporated into the solution to account for interference effects. The $1/e$ radius of the laser beam was 30 μm. The isotherms on the silicon layer are shown in Fig. 5. The melting temperature for the polysilicon is 1412°C. In this figure, the radius of the isotherm identifying the solidification interface is about 80 μm. The isotherms in the glass substrate are shown in Fig. 6.

IV Discussion

In the experiments, two basic types of heating intensity

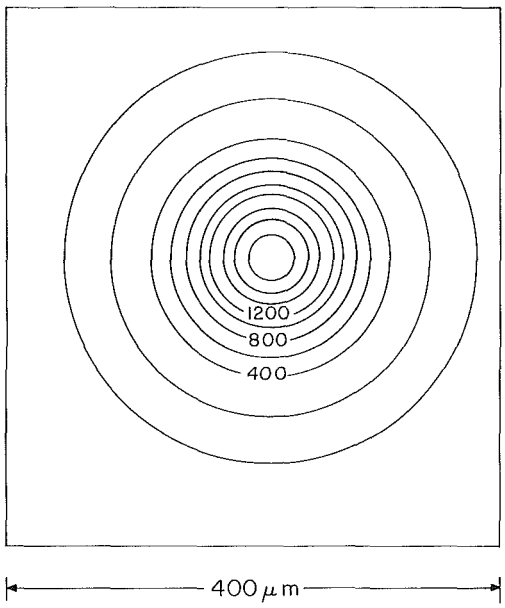

Fig. 5 Isotherms in the polysilicon layer generated by a 1.6 W heating source. The 1/e irradiance radius of the circular heating source is 30 μm. The time $t = 2.2$ ms.

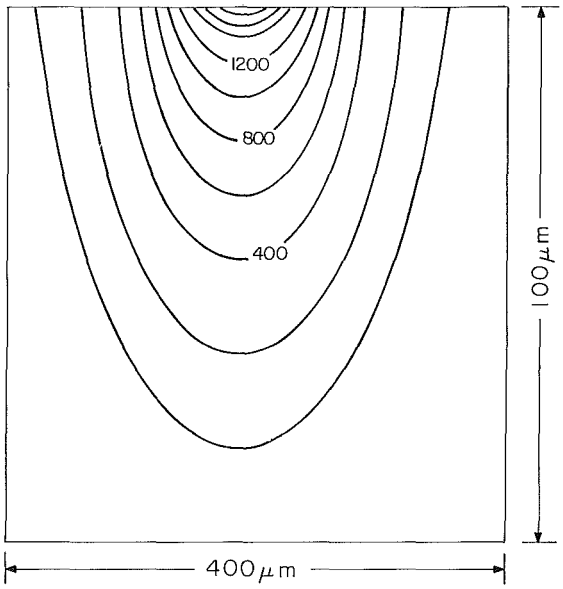

Fig. 6 Isotherms in the glass substrate for 1.6 W circular heating source having a 30 μm 1/e irradiance radius. The time $t = 2.2$ ms.

distributions were used: (*i*) Gaussian circular spots, and (*ii*) narrow elliptic beams. Both beam geometries can be used for material processing. The circular Gaussian beam produces a two-dimensional temperature distribution in the silicon layer. The elliptic beam geometry provides a more—but not entirely—one-dimensional phase boundary and temperature field. In the case of circular laser beams it was found that small beam sizes and higher beam concentrations produce stable melting conditions. The power density was decreased by increasing the laser spot size. Ripples appeared along the phase boundary. These ripples correspond to liquid protrusions that grow into the solid and then move back toward the initial location of the phase boundary. This wavy phase boundary pattern appears to have a characteristic wavenumber. This operating condition corresponds to the neutral stability condition.

When the laser beam size was increased (i.e., a decrease in heating density), the boundary ripples grew into the melt. In many cases these solid filaments broke apart and formed solid inclusions in the melt. This breaking apart occurred during the rapid growth of the solid filament. The rapid growth of solid filaments suggests that they are growing into an undercooled liquid. The power density is further decreased and the fraction of solid material in the melt is increased. This experimental trend is observed until the heated spot solidifies completely. It is important to note that solid filament growth originates from the phase boundary at the onset of coexisting silicon phases. A characteristic wavelength having a spacing of about 6 μm can be observed along the outer solid–melt interface. It must also be noted that the solid–melt interfaces are distinct and sharply outlined in the photographs. This indicates that the phase boundary surfaces are nearly perpendicular to the glass substrate. This result also can be argued using a surface free energy balance.

The mechanism of solid silicon formation in the melt is determined by conductive heat transfer. The possibility of a thermocapillary flow on the silicon free surface is suppressed by the encapsulating glass layer. In the absence of such coverings thermocapillary flows are expected. Benard convection type of flow also is excluded. This is due to the small silicon layer thickness. The basic dimensionless number, the Rayleigh number, is of the order of 10^{-9}.

An alternative to analyzing the individual microstructural details of the phase coexistence is to adopt a continuum phase approach. The silicon phase at any point is divided between solid and melt. The division can be assigned by the local enthalpy of the silicon layer. This approach is directed toward modeling the experimentally observed conditions where solid islands occur in the liquid melt. However, this method does not take into account the specific details of the observed phase boundary patterns and cannot explain the physical origin of phase coexistence.

The experiments with the circular Gaussian beams established a basis for understanding and explaining the origin of phase coexistence. Phase boundaries were observed to become unstable when the heating density was decreased. This result is consistent with the stability models given by Grigoropoulos et al. (1987a, 1987b). Experiments with narrow, elliptic-shaped laser beams showed that nearly straight phase boundaries are stable at high heating power densities. The heating density then was reduced by spreading out the laser beam in the direction perpendicular to the scanning motion. As in the case of circular spots, solid fingers originated from the phase boundary and penetrated into the liquid region. In some cases this penetration extended through the width of the molten silicon region and divided the liquid pool into rectangular cells. A characteristic spacing of the boundary instabilities can be identified. This spacing is on the order of 4–6 μm. It should be pointed out that these spacings do not correlate with the $\lambda = 0.5145$ μm laser light wavelength.

The power threshold for instability can be traced in the experiments. This threshold, and also the observed characterisitic interfacial spacings, are compared with the stability theory predictions. Results of this comparison (Grigoropoulos et al., 1987b) indicate that the basic instability mechanism is the abrupt silicon surface reflectivity increase when melting occurs. In the neighborhood of phase boundaries, the solid silicon absorbs twice as much heat as the adjacent liquid material. Thus, there exists a strong tendency toward solid superheating and liquid supercooling. This cannot be resolved by further reduction of the liquid pool, because in this case the difference in the absorbed heat by the two adjacent phases would be increased. Consequently, the tendency toward superheating and supercooling would be enhanced. Depending upon the heating source characteristics, these physical conditions may lead to phase boundary instability and subsequent formation of solid inclusions within the liquid region.

Acknowledgments

The authors express their gratitude to Dr. Juris Pirvics of Xerox, WRC, MES, for supporting this work. They also thank Dr. David Biegelsen of Xerox, PARC, for providing the polysilicon samples for the experiments.

References

Bosch, M. A., and Lemons, R. A., 1981, "Laser Induced Melt Dynamics of Si and Silica," *Physical Review Letters*, Vol. 47, No. 16, pp. 1151–1158.

Grigoropoulos, C. P., Buckholz, R. H., and Domoto, G. A., 1986, "A Heat Transfer Algorithm for the Laser Induced Melting and Recrystallization of Thin Silicon Layers," *Journal of Applied Physics*, Vol. 60, No. 7, pp. 2304–2309.

Grigoropoulos, C. P., Buckholz, R. H., and Domoto, G. A., 1987a, "A Thermal Instability in the Laser-Driven Melting and Recrystallization of Thin Silicon Films on Glass Substrates," ASME JOURNAL OF HEAT TRANSFER, Vol. 109, pp. 841–847.

Grigoropoulos, C. P., Buckholz, R. H., and Domoto, G. A., 1987b, "Stability of Phase Boundaries on Thin Silicon Layers With Glass Substrates," *Journal of Applied Physics*, Vol. 62, No. 2, pp. 474–480.

Hawkins, W. G., and Biegelsen, D. K., 1983, "Origin of Lamellae in Radiatively Melted Silicon Films," *Applied Physics Letters*, Vol. 42, No. 4, pp. 358–360.

Hess, L. D., et al., 1983, "Application of Laser Annealing in IC Fabrication," *MRS Proceedings: Laser–Solid Interactions and Transient Processing of Materials*, J. Narayan, W. L. Brown, and R. A. Lemons, eds., North Holland, New York, Vol. 13, pp. 337–348.

Jellison, G. E., and Modine, F. A., 1983, "Optical Functions of Silicon Between 1.7 and 4.7 eV at Elevated Temperatures," *Physical Review B*, Vol. 27, No. 12, pp. 7466–7472.

Lemons, R. A., and Bosch, M. A., 1982 "Microscopy of Si Films During Laser Melting," *Applied Physics Letters*, Vol. 40, No. 8, pp. 703–706.

Sedwick, T. O., 1981, "A Simple Optical Pyrometer for in-situ Temperature Measurement During CW Laser Annealing," *MRS Proceedings: Laser and E-Beam Solid Interactions and Materials Processing*, J. F. Gibbons, L. D. Hess, and T. W. Sigmon, eds., North Holland, New York, Vol. 1, pp. 147–153.

Shvarev, K. M., Baum, B. A., and Gel'd, P. V., 1975, "Optical Properties of Liquid Silicon," *Soviet Physics Solid State*, Vol. 16, No. 11, pp. 2111–2112.

Thermal Analysis of Laser-Assisted Thermoplastic-Matrix Composite Tape Consolidation

E. P. Beyeler[1]

S. I. Güçeri

Thermal Engineering and Advanced Manufacturing Group,
Department of Mechanical Engineering,
Center for Composite Materials,
University of Delaware,
Newark, DE 19716

A novel approach to producing composite parts using thermoplastic-matrix tapes is described. A thermal analysis is presented for the case of focused heat sources such as lasers for melting and consolidating the prepregs in a continuous manufacturing process. A numerical grid generation method is employed to account for the complex geometry of the solution domain. Heat transfer is modeled using an orthotropic domain made of two-dimensional, continuous fiber anisotropic laminates. Heat of crystallization melting/solidification are included in the form of a heat generation term. The temperature distributions and thermal histories in the laminated composites are presented for varying consolidation speeds. The effects of preheating the consolidated laminate are investigated and the overall feasibility of the proposed process is discussed.

Introduction

With the development of high-temperature, advanced thermoplastic resins, a need for a better understanding of the fundamentals of thermoplastic-matrix composite materials processing techniques has gained importance. Various prepregs are readily available, including the tape form made of continuous fibers imbedded in a thermoplastic-resin matrix. Thermoplastic-matrix composites offer several advantages, such as fracture toughness and unlimited shelf life, but most importantly open the possibility of combining consolidation and tape laydown in a one-step process, avoiding the curing steps that are necessary with thermosetting materials. Laser-assisted thermoplastic tape consolidation is an example of such a one-step process and its conceptual description is shown in Fig. 1. It can be seen that the heat input generates melting of the matrix resin of the incoming tape and the already-consolidated layers at around contact region. The tape is consolidated through a melting and diffusion process under the pressure of the consolidation roller. The solidification of the material occurs as a result of heat removal from the melt region as the consolidated laminate moves on. The cooling rate of the material, and consequently its degree of crystallinity and the performance of the finished product, are highly dependent on the tape speed and the nature of the thermal boundary conditions. Therefore, a complete understanding of the thermal history and the relevant operational parameters is needed to develop this new technology successfully.

Essentially all processing techniques that are developed for thermoplastic matrix composites involve melting/solidification, and it is a well-established fact that the resulting material properties, such as crystallinity, and the performance characteristics depend heavily on the thermal history of the laminate, as shown by many investigators, including Seferis (1984), Seferis and Velisaris (1986), and Blundell et al. (1985). The thermal analysis of a tape consolidation process requires the determination of temperature fields around the consolidation region and temperature histories of the consolidated laminate. This information is necessary, for example, to determine the maximum allowable heat input that will give maximum layup speeds without degrading the material by exposing it to temperatures that are higher than allowable limits as has been reported for APC-2[1] (Aromatic Polymer Composite) tapes by Grove and Short (1984).

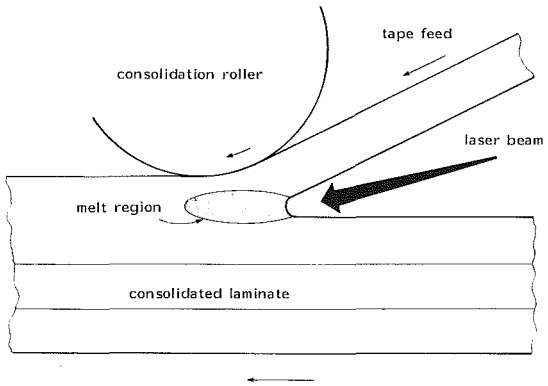

Fig. 1 General configuration of laser-assisted thermoplastic-matrix composite tape consolidation

The influences of the thermal history of the matrix resin on its microstructure have been reported by Blundell et al. (1985), Blundell and Osborn (1985), and Blundell and Wilmouth (1986). In the case of a composite tape with unidirectional, continuous fibers of high thermal conductivity (such as carbon) and low thermal conductivity matrix (such as a polymeric resin), the heat transfer phenomena are highly anisotropic. Studies on conduction heat transfer in anisotropic medium can be found in the literature. Özisik (1979) gives a general presentation of the theoretical aspects of anisotropic heat transfer. McWhorter and Sadd (1980) investigated heat conduction on a disk for different anisotropic configurations. The thermal response of anisotropic structures, such as embedded plates with different fiber orientation, was studied by Projahn and Beer (1981) using a numerical mapping technique similar to the one used in the present study. An analytical solution for a thin anisotropic plate with mixed boundary conditions was developed by Huang and Chang (1984). An exact solution for heat conduction in heterogeneous materials, in this case inclusions, was obtained by Baker-Jarvis and Inguva (1985). Hatta and Taya (1986) used Eshelby's method to solve a similar problem. Transient heat conduction was studied analytically by Nomura and Chou (1986) for composite materials sub-

[1]Currently with E.I. duPont de Nemours & Co., Inc., Wilmington, DE 19898.

Contributed by the Heat Transfer Division for publication in the JOURNAL OF HEAT TRANSFER. Manuscript received by the Heat Transfer Division March 19, 1987. Keywords: Laser Processing, Materials Processing and Manufacturing Processes, Numerical Methods.

[1]APC-2 tape is a composite prepreg manufactured by Imperial Chemical Industries, United Kingdom.

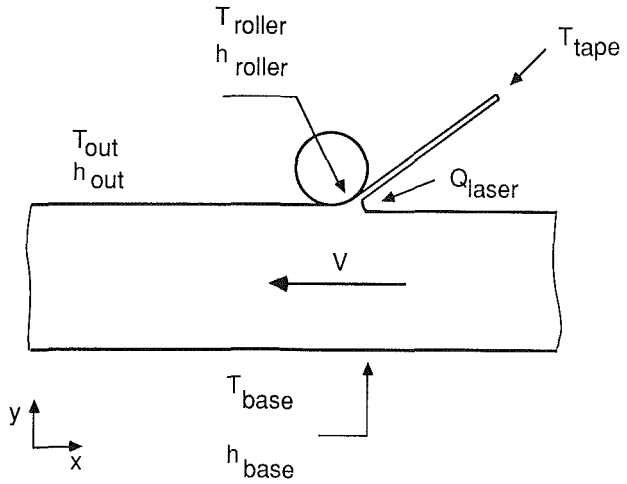

Fig. 2 Nomenclature and boundary conditions for the thermal analysis of tape consolidation

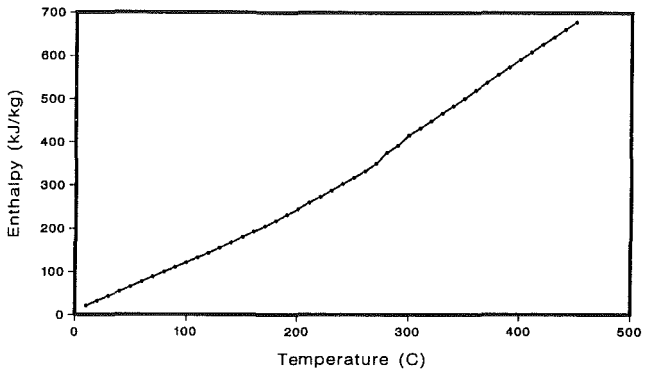

Fig. 3 Variation of enthalpy with temperature for APC-2 prepreg tape (Blundell and Willmouth, 1986)

jected to oscillating temperature fields. A finite difference solution of transient heat conduction with temperature-dependent thermal properties is proposed for plastic plates by Katayama et al. (1971).

The present paper reports on studies for the thermal analysis of the thermoplastic-matrix composite tape consolidation process. Analytical models are presented to predict the temperature distribution and resulting cooling rates and are solved using a numerical technique. One of the primary objectives of this phase of the study is to identify the dominant processing parameters, and establish their influence on the microstructure.

Thermal Analysis

The thermal analysis of the tape consolidation process is based on an anisotropic heat conduction model. The nomenclature and the boundary conditions for the present analysis are depicted in Fig. 2. The objective of the analysis is to develop a computational procedure to be able to predict the temperature distributions in the presence of tape motion. The working material is considered to be an anisotropic, two-dimensional medium. The incoming tape is assumed to be at a uniform temperature that can be varied to investigate the effects of preheating. The elliptic nature of the diffusion equations requires that the complete boundaries and the boundary conditions be defined enclosing the solution domain. This necessitates the implementation of pseudoboundaries for the laminated composite and the incoming tape. These boundaries are chosen at a sufficient distance from the consolidation point and in the transverse direction to the laminate and the incoming tape as shown in Fig. 2. For the ends of the laminated region, a gradient type boundary condition becomes applicable. This, in the presence of laminate motion, indicates that the primary transport mode at these locations is one of laminate motion rather than thermal diffusion. Considering the low thermal conductivity in cross-ply direction and the relatively high rate of motion, this assumption can easily be justified. In addition, considering that sufficient time has elapsed between two tape lays, it is assumed that all the heat from the previous tape lay has dissipated. This assumption is not a restrictive one and can be readily removed if the complete description of part configuration and the tape lay sequence is available. In a moving domain, for an anisotropic material, an Eulerian approach to the temperature distribution yields

$$v_x \frac{\partial T}{\partial x} + v_y \frac{\partial T}{\partial y} = \frac{1}{\rho c}\left[k_{11}\frac{\partial^2 T}{\partial x^2} + 2k_{12}\frac{\partial^2 T}{\partial x \partial y} + k_{22}\frac{\partial^2 T}{\partial x^2}\right] + \frac{\dot{U}}{c} \quad (1)$$

Note that, even though from a Lagrangian approach the problem is one of transient type, in a continuous processing it can be formulated as a asteady-state-type problem since at every instant, the temperature distribution would remain unchanged with respect to a fixed coordinate system as long as the boundary conditions are kept steady. In this formulation, the convective-like terms of the left-hand side account for the motion of the tape and the consolidated laminate. The velocity terms v_x and v_y represent the local material velocities with respect to the Cartesian coordinates. A further addition to the models used by McWhorter and Sadd (1980), Sottos and Güçeri (1986), and Farraye and Güçeri (1985) is the introduction of a heat generation term U to account for the heat release or heat absorption effects due to the complex solidification/melting that occurs during consolidation. For thermoplastic materials during solidification or melting, latent heat is released over a range of temperature in a highly irregular fashion due to the effects of crystallization. Figure 3 shows the variation of enthalpy with respect to temperature that is produced from data obtained by Blundell and Willmouth (1986). In the present work the complex ther-

Nomenclature

c = heat capacity, J/kg•°C
h = heat convection coefficient, W/m²•°C
k = conductivity, W/m•°C
q = heat flux, W/m²
T_w = surface temperature
T_∞ = ambient temperature
T_g = glass transition temperature
T_{melt} = melt temperature
U = heat generation, J/m³
v = velocity, m/s
x, y = Cartesian coordinates, m
ξ, η = computational coordinates
ρ = density, kg/m³
θ = angle between fiber direction and x axis

Subscripts

L = parallel to fiber direction
T = transverse to fiber direction

modynamic behavior of the material is modeled by assuming a linear variation of the specific heat between T_{melt} and T_g, and including in a heat generation term the remaining heat loss or heat gain, to stay in agreement with the enthalpy variations with temperature according to the data by Blundell and Willmouth (1986). Defining θ as the angle between the fiber and the x axis, the elements of the thermal conductivity tensor are obtained from the conductivity values along and transverse fiber directions in the following manner:

$$k_{11} = k_L \cos^2\theta + k_T \sin^2\theta$$
$$k_{22} = k_L \sin^2\theta + k_T \cos^2\theta \quad (2)$$
$$k_{12} = k_L \cos\theta \sin\theta - k_T \sin\theta \cos\theta$$

To proceed with the numerical solution, the tape is subjected to boundary conditions of various kinds as illustrated in Fig. 2. A general expression to account for all these conditions can be written as

$$(q_x \mathbf{i} + q_y \mathbf{j}) \cdot \mathbf{n} = q_i - h\,[T_\infty - T_w] \quad (3)$$

with

$$q_x = -k_{11}\frac{\partial T}{\partial x} - k_{12}\frac{\partial T}{\partial y}$$

$$q_y = -k_{12}\frac{\partial T}{\partial x} - k_{22}\frac{\partial T}{\partial y}$$

The laser heating is approximated by considering a concentrated heat flux at the surface of the tape and the laminate, since it was reported by Tung et al. (1987) that the surface of APC-2 absorbs the energy of a 10.6 μm laser wavelength beam in its entirety. This wavelength corresponds to that of a CO_2 laser, which was used in the experimental study (Beyeler, 1987).

Solution Procedure

The geometric complexity of the problem that is combined with the different boundary conditions suggests the use of a mapping technique. A body-fitted coordinate system with numerical grid generation is chosen as a suitable approach for the present problem because it offers the degree of flexibility to account for the varying shapes and the boundary conditions of the physical domain. This technique combines the geometric flexibility of finite element methods with the simplicity of the finite-difference approaches. The details of this transformation technique have been presented by many investigators including Thompson (1982, 1981) Häuser and Taylor (1986), and Güçeri (1988). Recent applications of this technique cover a wide range of thermal-fluid problems including melting/solidification (Beyeler et al., 1987), heat transfer in anisotropic domains (Farraye and Güçeri, 1985), free surface flows (Trafford et al., 1986) and thermal and residual stresses (Sottos and Güçeri, 1986), all of which exist in an actual consolidation process.

Unlike for other transformation techniques, in numerical grid generation the relations between the physical coordinates and the computational coordinates themselves are given in the form of differential equations. A curvilinear mesh is then generated on the physical domain using these grid generators in such a way that the physical boundaries of the shape coincide with the curvilinear coordinates. For the current study, an elliptic grid generation is chosen due to its inherent smoothness and ability to allow for grid concentration where greater accuracy is needed. For a transformation into a Cartesian domain, the equations relating the physical and computational coordinates are given as

$$\frac{\partial^2 \xi}{\partial x^2} + \frac{\partial^2 \xi}{\partial y^2} = P \quad (4a)$$

$$\frac{\partial^2 \eta}{\partial x^2} + \frac{\partial^2 \eta}{\partial y^2} = Q \quad (4b)$$

These can be inverted to make the physical coordinates (x, y) dependent variables, which results in

$$\alpha\frac{\partial^2 x}{\partial \xi^2} + 2\beta\frac{\partial^2 x}{\partial \xi \partial \eta} + \gamma\frac{\partial^2 x}{\partial \eta^2} + J^2\left[P\frac{\partial x}{\partial \xi} + Q\frac{\partial x}{\partial \eta}\right] = 0$$
$$\alpha\frac{\partial^2 y}{\partial \xi^2} + 2\beta\frac{\partial^2 y}{\partial \xi \partial \eta} + \gamma\frac{\partial^2 y}{\partial \eta^2} + J^2\left[P\frac{\partial y}{\partial \xi} + Q\frac{\partial y}{\partial \eta}\right] = 0 \quad (5)$$

where

$$\alpha = \frac{\partial^2 x}{\partial \eta^2} + \frac{\partial^2 y}{\partial \eta^2}, \quad \beta = -\frac{\partial x}{\partial \xi}\frac{\partial x}{\partial \eta} - \frac{\partial y}{\partial \xi}\frac{\partial y}{\partial \eta},$$
$$\gamma = \frac{\partial^2 x}{\partial \xi^2} + \frac{\partial^2 y}{\partial \xi^2}, \quad J = \frac{\partial x}{\partial \xi}\frac{\partial y}{\partial \eta} - \frac{\partial y}{\partial \xi}\frac{\partial x}{\partial \eta}$$

The P and Q terms are the grid control functions and are used to regulate the distribution of the grid points over the domain, for example concerning them toward specified lines or points. In the current analysis, both P and Q will be used to concentrate coordinate lines toward the surface of the laminate, where the temperature gradients are steeper.

The next step in numerical grid generation is the transformation of the governing equations. Applying the mapping expressions given by equations (5a) and (5b), the governing equation becomes

$$\left[k_{11}a_{xx} + k_{22}a_{yy} + 2k_{12}a_{xy} - \rho c J\left(v_x\frac{\partial y}{\partial \eta} - v_y\frac{\partial x}{\partial \eta}\right)\right]\frac{\partial T}{\partial \xi}$$
$$+\left[k_{11}b_{xx} + k_{22}b_{yy} + 2k_{12}b_{xy} - \rho c J\left(v_x\frac{\partial y}{\partial \xi} - v_y\frac{\partial x}{\partial \xi}\right)\right]\frac{\partial T}{\partial \eta}$$
$$+[k_{11}c_{xx} + k_{22}c_{yy} + 2k_{12}c_{xy}]\frac{\partial^2 T}{\partial \xi^2} + [k_{11}d_{xx} + k_{22}d_{yy}$$
$$+2k_{12}d_{xy}]\frac{\partial^2 T}{\partial \eta^2} + [k_{11}e_{xx} + k_{22}e_{yy} + 2k_{12}e_{xy}]$$
$$\frac{\partial^2 T}{\partial \xi \partial \eta} + \frac{\dot{U}}{c} = 0 \quad (6)$$

where the expressions of the different coefficients can be found in the appendix. Applying the same transformation on equation (3) yields a different expression for each of the four sides of the rectangular computational domain shown in Fig. 4. Only the expressions for sides 1 and 2, respectively, are presented, noting that the expressions for sides 3 and 4, respectively, can be obtained by switching the sign of the left-hand term

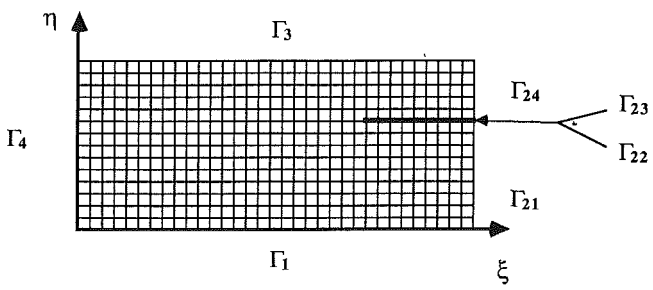

Fig. 4 The configuration for the boundary-fitted coordinate system computational grid, and identification of various boundary sections

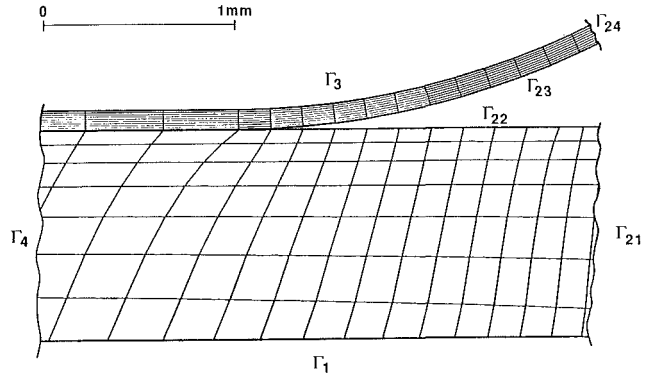

Fig. 5 Section of the composite grid used for the numerical analysis. Note that the figure depicts only the region that is close to the consolidation zone, whereas the full mesh extends in the downstream direction

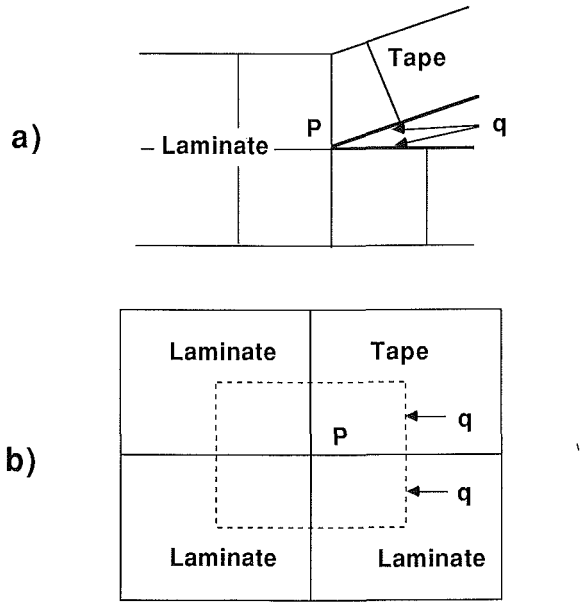

Fig. 6 Numerical treatment of consolidation point singularity and the identification of the control volume in: (*a*) physical domain; (*b*) computational domain

$$A\frac{\partial T}{\partial \xi}+B\frac{\partial T}{\partial \eta}=-J\sqrt{\gamma}[-q+h(T_\infty-T_w)]$$

$$A=-k_{11}\frac{\partial y}{\partial \xi}\frac{\partial y}{\partial \eta}+k_{12}\left[\frac{\partial x}{\partial \eta}\frac{\partial y}{\partial \xi}+\frac{\partial y}{\partial \eta}\frac{\partial x}{\partial \xi}\right]-k_{22}\frac{\partial x}{\partial \xi}\frac{\partial x}{\partial \eta} \tag{7a}$$

$$B=k_{11}\left[\frac{\partial y}{\partial \xi}\right]^2-2\,k_{12}\frac{\partial y}{\partial \xi}\frac{\partial x}{\partial \xi}+k_{22}\left[\frac{\partial x}{\partial \xi}\right]^2$$

$$C\frac{\partial T}{\partial \xi}+D\frac{\partial T}{\partial \eta}=J\sqrt{\alpha}[-q+h\,(T_\infty-T_W)]$$

$$C=k_{11}\left[\frac{\partial y}{\partial \eta}\right]^2-2\,k_{12}\frac{\partial y}{\partial \eta}\frac{\partial x}{\partial \eta}+k_{22}\left[\frac{\partial x}{\partial \eta}\right]^2 \tag{7b}$$

$$D=-k_{11}\frac{\partial y}{\partial \xi}\frac{\partial y}{\partial \eta}+k_{12}\left[\frac{\partial x}{\partial \eta}\frac{\partial y}{\partial \xi}+\frac{\partial y}{\partial \eta}\frac{\partial x}{\partial \xi}\right]-k_{22}\frac{\partial x}{\partial \xi}\frac{\partial x}{\partial \eta}$$

Table 1 Boundary conditions

T_{base}, °C	h_{base}, W/M^2	T_{base}, °C	T_{roller}, °C	h_{roller}, W/m^2	T_{out}, °C	h_{out}, W/m^2
20	1000	20	20	500	20	5

These expressions are then discretized in the computational domain using central differencing for the diffusion terms. For the velocity-induced heat transfer terms a technique inspired from the upwind differencing scheme was used. Most of the materials that are considered in this type of manufacturing have thermal conductivities of fiber and matrix that vary approximately by a factor of ten. At the consolidation speeds considered, the heat transfer is fiber dominated; therefore heat flows primarily in a direction parallel to the laminate motion. The situation is then analogous to that of a fluid particle in a laminar flow whose thermal behavior is dependent on the thermal history upstream or upwind. Additional information on the numerical approach is presented by Beyeler (1987).

Results

The first step of the solution technique is to define the geometry of the physical domain and generate a mesh well suited to both the geometric and thermal aspects of the problem. Several mesh configurations have been tried to represent most accurately all the parameters of the process (Beyeler and Güçeri, 1986). The mesh configuration chosen to analyze the tape layup problem is a composite grid that enables splitting of the computational domain along the lines of the laminate and the new tape layer. Portions of the top (tape) and bottom (laminate) mesh are shown in Fig. 5. The top and bottom mesh contain in their entirety, respectively, 60 × 10 and 60 × 20 nodes and are shown here in the area where consolidation is performed. The correspondence between computational and physical domains is indicated for all boundaries in Fig. 4. The large length-to-width ratio of the problem geometry prevents us from showing the entire mesh with enough accuracy. With the chosen configuration it is clear that the η coordinate lines are parallel to the fiber direction and the constant ξ lines are perpendicular to the fiber direction.

The temperature distribution is computed at every node of the mesh using a second-order central differencing technique along with the boundary conditions described in Table 1. The energy from the laser beam is assumed to be distributed evenly on the tape and the laminate. Heat flux continuity is applied on the overlapping boundary of the top and bottom grids. The consolidation point P, where the tape and laminate meet, is treated differently from the others since central differencing could not have been applied due to the geometric singularity depicted in Fig. 6. The contact point P represents a common computational node, which is shared by the laminate and the tape. It is also exposed to the laser heating. Therefore, a control volume approach was used to solve for temperature at this location, based on the schematic of Fig. 6.

Temperature profiles along the laminate are obtained for different consolidation speeds, laser heat input, and laminate thicknesses. The processing conditions are chosen such that both the tape and the laminate are raised above the melt temperature T_m. The material properties used are those reported by Grove and Short (1984), Cattanagh and Cogswell (1985), and Blundell and Willmouth (1986) for APC-2, with 60 percent fiber volume fraction, i.e., k_L = 6.0 W/m•°C, k_T = 0.72 W/m•°C, and ρ = 1.56 g/cm^3.

Temperature profiles along the length of a 5-mm-thick laminate, which corresponds to 40 plies for a ply thickness of 0.125 mm, are presented in Fig. 7(*a*) for v = 0.01 m/s, q = 600,000 W/m^2 (equivalent to q = 15.4 W for a 0.635 cm wide

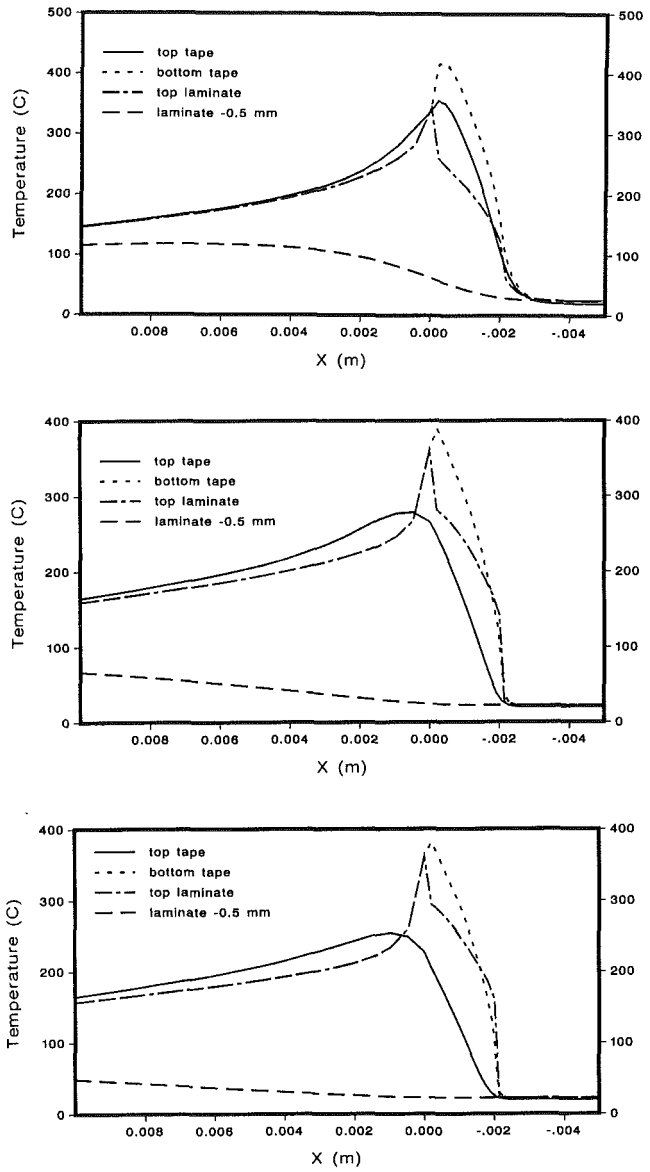

Fig. 7 Temperature profiles along laminate length for a 5-mm-thick laminate at various consolidation speeds and heating rates: (*a*) v = 0.01 m/s, q = 600000 W/m^2; (*b*) v = 0.05 m/s, q = 1500000 W/m^2; (*c*) v = 0.08 m/s, q = 1900000 W/m^2

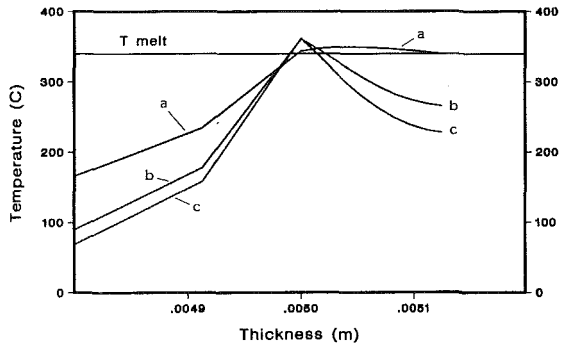

Fig. 8 Temperature profiles in the transverse laminate direction at x = 0.0. Note that the region above the T_{melt} indicates molten state for the polymeric matrix, with the slowest consolidation speed (*a*) indicating essentially a meltthrough; (*a*) v = 0.01 m/s, q = 600000 W/m^2; (*b*) v = 0.05 m/s, q = 1500000 W/m^2; (*c*) v = 0.08 m/s, q = 1900000 W/m^2

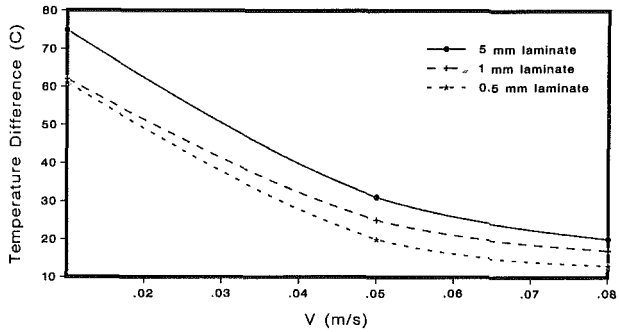

Fig. 9 Difference between maximum tape and laminate temperatures with no preheating of the laminate

tape, i.e., a single tow). At this consolidation speed, the tape is raised to a significantly higher temperature than the laminate and the temperature along the tape exceeds the recommended processing window for PEEK. In the laminate, at 0.5 mm from the surface of the laminate (exposed to the laser heat source), the temperature rises slowly to about 110°C. Raising the tape speed to v = 0.05 m/s and increasing the heat input to 1,500,000 W/m^2 (38.1 W), the differences between tape and laminate maximum temperatures are significantly decreased as shown in Fig. 7(*b*). For v = 0.08 m/s, as shown in Fig. 7(*c*), the temperatures for the top surface of the laminate and the bottom surface of the tape (both exposed directly to the laser beam) are similar to the previous case but the temperature of the rest of the laminate remains close to the initial temperature. At such speeds, heat transfer is fiber dominated and very little diffusion occurs through the low conductance matrix material. The progression of heat needed to melt the tape increases at a smaller rate than the tape speed and, for the same length of tape consolidated, less energy is used for consolidation at higher speeds than at slower speeds.

Different observations can be made if the thickness of the laminate is changed. When consolidation is performed on a 1 mm thick laminate, the temperature of the laminate rises significantly faster and at higher temperatures since there is less material through which the heat can diffuse. It was observed that for a thinner laminate (0.5 mm) the temperature rises above T_g halfway through the thickness for v = 0.01 m/s; however the laminate cools down very rapidly causing an almost amorphous microstructure. Overall the variations seen for different laminate thicknesses are small as most of the relevant heat transfer occurs in the top two plies, which corresponds to a depth of 0.25 mm.

To evaluate the extent of melting in the material, temperature profiles at the consolidation point were studied. Figure 8 shows profiles through the entire thickness at the x value corresponding to the consolidation point for various heat inputs and consolidation speeds. The local characteristic of heat transfer is apparent, indicating poor thermal diffusion in the cross-ply direction. It can be observed in this figure that the melt pool obtained at the consolidation point (y = 0.005 m) is a strong function of the consolidation speed and the heat input as would be expected. A too-narrow melt pool would indicate that a higher laser beam itensity or a lower speed is needed to obtain satisfactory consolidation. This figure also shows that an additional problem can be encountered at low speeds, i.e., the melt-through of the tape feed if the combination of the consolidation speed and the heat input falls outside the operational window causing excessive, localized heat input. To avoid such a problem a different distribution of laser energy between the tape and laminate can be suggested. The compensating effects of the increase in velocity and an increase in heat input upon temperature distribution are also apparent.

It can be seen from Fig. 9 that there exists a significant dif-

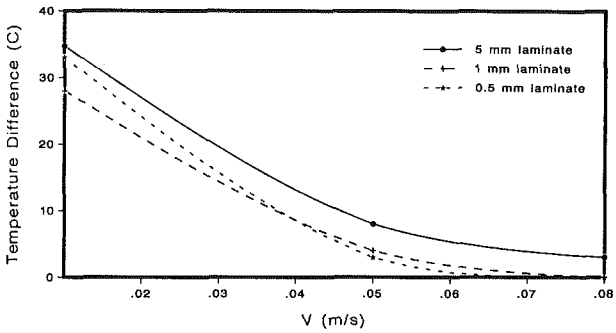

Fig. 10 Difference between maximum tape and laminate temperatures with incoming laminate preheated at 150°C

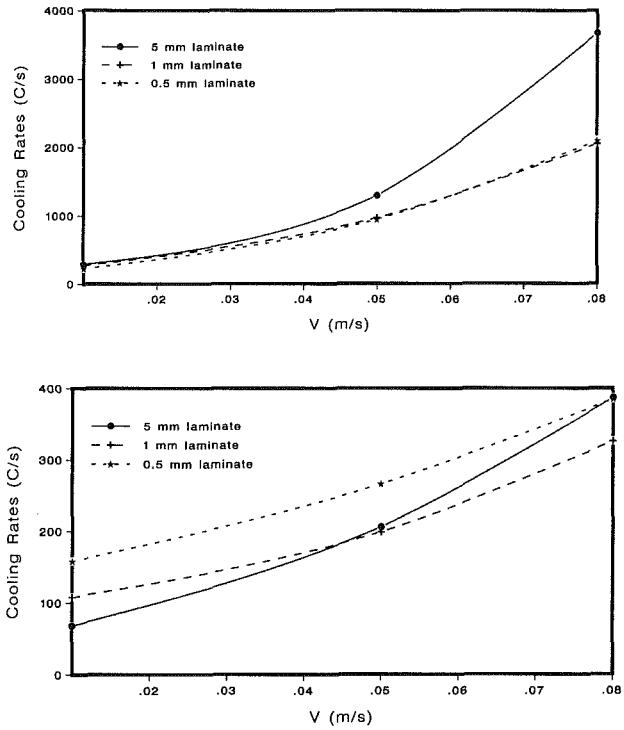

Fig. 11 Cooling rates during consolidation: (*a*) no preheating; (*b*) preheating at 150°C

ference between maximum temperatures in the tape and laminate, especially for slow tape consolidation speeds, for the heating configuration presented. From Fig. 6 it is clear that the laminate only reaches the melt temperature when put in contact with the tape, which might not insure proper bonding as early experimental results seem to indicate.

By preheating the laminate before consolidation, it can be expected that the laser heat input can be significantly decreased, thus resulting in smoother temperature gradients both along the laminate length and across its thickness. To see this effect, the thermal behavior of the material was investigated on a laminate preheated at 150°C before consolidation. The amount of laser heat required to obtain melting for tape and laminate was reduced, respectively, to q = 12.7 W, 35.6 W, 45.7 W, for v = 0.01 m/s, v = 0.05 m/s, v = 0.08 m/s. The gap between the maximum temperature of the tape and the laminate, shown in Fig. 10, is reduced by about 50 percent at v = 0.01 m/s and v = 0.05 m/s, and disappears at v = 0.08 m/s. But the most significant difference is in the cooling rates, as shown in Fig. 11, which decreased sufficiently to allow crystallization potentially to occur during consolidation for v = 0.01 m/s. Seferis (1984) has shown that PEEK crystallization occurs for cooling rates less than 160°C/s. But a different behavior of PEEK matrix in APC-2 was observed by Blundell and Osborn (1985), who suggested an ideal cooling rate of 700°C/min (11.6°C/s) and that above 2000°C/min (33.3°C/s) only the amorphous phase can be found. Therefore, it is clear from Fig. 11 that consolidation at high speeds, under the previously described process conditions, generates sharp temperature gradients and very fast cooling, therefore potentially producing essentially an amorphous material.

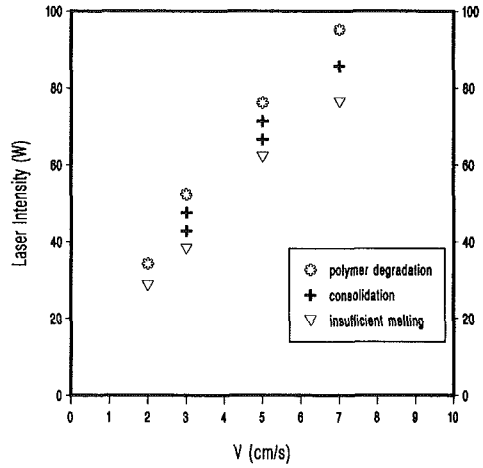

Fig. 12 Numerically generated process window for APC-2, which is bounded by the polymer degradation and insufficient consolidation limits corresponding to various consolidation speeds

Furthermore, the model can be used to generate a process window, as shown in Fig. 12. The results presented used the thermophysical data for APC-2 and correspond to a laser beam energy distribution on a 1 mm length of tape and 2 mm length of laminate. The limits of the window were defined as follows: If less than 90 percent of a ply thickness of matrix was melted in the transverse direction, melting was considered to be insufficient; on the other hand if the maximum temperature of the tape or laminate reached 550°C, it was considered that significant polymer degradation had occurred, as was observed by Biggs (1987). It appears from the data points presented in Fig. 12 that for consolidation speeds below 3 cm/s little or no consolidation can be achieved for the proposed process configuration.

Due to a lack of comparable work available in the literature, the accuracy of the method is tested by refining the mesh in the areas where temperature gradients are the highest, namely around the consolidation point. The variations between the temperature results presented here and those obtained with the most refined mesh (175 × 20 and 175 × 10) did not exceed 5 percent. Since the computational model relied on experimental measurements of thermal properties that do not have similar accuracies, these results were considered to be satisfactory.

Conclusions

A novel manufacturing method for thermoplastic-matrix composites is described and a model was presented to study heat transfer during continuous processing, using laser assisted tape consolidation. Availability of such a model is expected to form the bridging between the processing, microstructure, material performance, which are very strongly coupled in the case of composite materials, thus allowing for process optimization. Numerical results as well as experimental results have shown a very small processing window for laser consolidation of APC-2 at speeds below 5 cm/s (Beyeler, 1987), indicating the need for an insight into the heat transfer process to achieve optimum process conditions that can be

provided through such a model. The influence of velocity on the nature of the heat transfer in the anisotropic medium was demonstrated for a specific laser energy distribution. Cooling rates were estimated and shown to fall in the amorphous range for the PEEK matrix, suggesting the use of a preheating or postannealing process if higher degrees of crystallinity are desired. The study presented in this paper is not restricted to laser heating processes and can be applied to other techniques such as infrared heating or even to some welding applications.

Acknowledgments

The authors wish to acknowledge the support by the NSF ERC Program, Office of Cross-Disciplinary Research, and the CCM Industrial Sponsors.

References

Baker-Jarvis, J., and Inguva, R., 1985, "Heat Conduction in Heterogeneous Materials," ASME JOURNAL OF HEAT TRANSFER, Vol. 107, pp. 39–43.

Beyeler, E., 1987, "Melting and Solidification in Processing and Applications to Thermoplastic Matrix Composites Manufacturing," Ph.D. Dissertation, University of Delaware, Newark, DE.

Beyeler, E., Güçeri, S. I., and Yost, B., 1986, "Two Dimensional Solidification in Irregularly Shaped Domains," submitted to ASME JOURNAL OF HEAT TRANSFER.

Beyeler, E., and Güçeri, S. I., 1986, "Laser Assisted Thermoplastic Tape Consolidation," American Society for Composites First Conference on Composite Materials, Dayton, OH.

Biggs, L., 1987, "Laser Processing of Poly-Ether-Ether-Ketone," Senior Thesis, University of Delaware, Newark, DE.

Blundell, D. J., Chalmers, J. M., Mackenzie, M. W., and Gaskin, W. F., 1985, "Crystalline Morphology of the Matrix of Peek-Carbon Fiber Aromatic Polymer Composites, I. Assessment of Crystallinity," *SAMPE Quarterly*, Vol. 16, No. 4, pp. 22–30.

Blundell, D. J., and Osborn, B. N., 1985, "Crystalline Morphology of the Matrix of Peek-Carbon Fiber Aromatic Polymer Composites, II. Crystallization Behavior," *SAMPE Quarterly*, Vol. 17, No. 1, pp. 1–6.

Blundell, D. J., and Willmouth, F. M., 1986, "Crystalline Morphology of the Matrix of Peek-Carbon Fiber Aromatic Polymer Composites," *SAMPE Quarterly*, Vol. 17, No. 2, pp. 50–57.

Cattanach, J. B., and Cogswell, F. N., 1985, "Processing With Aromatic Polymer Composites," in: *Developoments in Reinforced Plastics*, G. Pritchard, ed., Applied Science Publishers, New York.

Farraye, E. A., and Güçeri, S. I., 1985, "Computational Investigation of Transient Heat Conduction in Composite Structures," CAE Report-4/85, University of Delaware, Newark, DE.

Grove, S., and Short, D., 1984, "Heat Transfer in APC Fabrication," Final Report for I.C.I. PLC Petrochemicals and Plastics Division, Wilton, DE.

Güçeri, S. I., 1988, "Finite Difference Methods in Polymer Processing," in: *Fundamentals of Computer Modeling for Polymer Processing*, C. L. Tucker, ed., Hanser Publishers, to be published.

Hatta, H., and Taya, M., 1986, "Equivalent Inclusion Method for Steady State Heat Conduction in Composites," *Int. J. Engng. Sci.*, Vol. 24, No. 7, pp. 1159–1162.

Häuser, J., and Taylor, C., 1986, *Numerical Grid Generation in Computational Fluid Dynamics*, Pineridge Press, Swansea, United Kingdom.

Huang, S. C., and Chang, Y. P., 1984, "Anisotropic Heat Conduction With Mixed Boundary Conditions," ASME JOURNAL OF HEAT TRANSFER, Vol. 106, pp. 646–648.

Katayama, K., Hattori, M., Okada, M., and Kotake, S., 1971, "Numerical Method of Transient Heat Conduction With Temperature Dependent Thermal Properties," *Bulletin of the JSME*, Vol. 15, pp. 1394–1401.

McWhorter, J. C., and Sadd, M. H., 1980, "Numerical Anisotropic Heat Conduction Using Boundary-Fitted Coordinate Systems," ASME JOURNAL OF HEAT TRANSFER, Vol. 102, pp. 308–311.

Nomura, S., and Chou, T. W., 1986, "Heat Conduction in Composite Materials Due to Oscillating Temperature Fields," *International Journal of Engineering Science*, Vol. 24, No. 5, pp. 643–647.

Özişik, M. N., 1979, *Heat Conduction*, Wiley Interscience, New York.

Projahn, U., Rieger, H., and Beer, H., 1981, "Heat Conduction in Anisotropic Composites of Arbitrary Shape (A Numerical Analysis)," *Wärme- und Stoffübertragung*, Vol. 15, pp. 223–232.

Sottos, N. R., and Güçeri, S. I., 1986, "Residual and Transient Thermal Stresses in Laminar Orthotropic Composites," in: *Numerical Grid Generation in Computational Fluid Dynamics*, J. Häuser and C. Taylor, eds., Pineridge Press, Swansea, United Kingdom, pp. 741–754.

Seferis, J. C., 1984, "Polyetheretherketone (PEEK) A Matrix Semicrystalline Polymer for High Performance Composites," National Academy of Athens, Greece.

Seferis, J. C., and Velisaris, C. N., 1986, "Modeling-Processing-Structure Relationships of Polyetheretherketone (PEEK) Based Composites," *31st International Sampe Symposium Proceedings*, pp. 1236–1252.

Thompson, J. F., 1982, *Numerical Grid Generation*, Elsevier, New York.

Thompson, J. F., 1983, "A Survey of Grid Generation Techniques in Computational Fluid Dynamics," AIAA 21st Aerospace Sciences Meeting, Paper No. AIAA-83-0447.

Trafford, D. L., Güçeri, S. I., and Crochet, M. J., 1986, "A Numerical Grid Generation Approach to the Injection Molding Problem, *Numerical Methods in Industrial Forming*, Göteborg, Sweden.

Tung, C. M., Gnanamuthu, D. S., Moores, R. J., and Leung, C. J., 1987, "Effect of Laser Radiation on the Rapid Processing of Graphite Reinforced Composites," *32nd International SAMPE Symposium and Exhibition, Advanced Materials Technology 87*, Vol. 32, pp. 476–483.

APPENDIX

$$a_{xx}=\frac{\partial^2 y}{\partial\xi\partial\eta}\frac{\partial y}{\partial\eta}-\frac{\partial^2 y}{\partial\eta^2}\frac{\partial y}{\partial\xi}-\frac{1}{J}\frac{\partial J}{\partial\xi}\left[\frac{\partial y}{\partial\eta}\right]^2+\frac{1}{J}\frac{\partial J}{\partial\eta}\frac{\partial y}{\partial\xi}\frac{\partial y}{\partial\eta}$$

$$b_{xx}=\frac{\partial^2 y}{\partial\xi\partial\eta}\frac{\partial y}{\partial\xi}-\frac{\partial^2 y}{\partial\xi^2}\frac{\partial y}{\partial\eta}+\frac{1}{J}\frac{\partial J}{\partial\xi}\frac{\partial y}{\partial\xi}\frac{\partial y}{\partial\eta}-\frac{1}{J}\frac{\partial J}{\partial n}\left[\frac{\partial y}{\partial\xi}\right]^2$$

$$c_{xx}=\left[\frac{\partial y}{\partial\eta}\right]^2\quad d_{xx}=\left[\frac{\partial y}{\partial\xi}\right]^2\quad e_{xx}=-2\frac{\partial y}{\partial\xi}\frac{\partial y}{\partial\eta}$$

$$a_{yy}=\frac{\partial^2 x}{\partial\xi\partial\eta}\frac{\partial x}{\partial\eta}-\frac{\partial^2 x}{\partial\eta^2}\frac{\partial x}{\partial\xi}-\frac{1}{J}\frac{\partial J}{\partial\xi}\left[\frac{\partial x}{\partial\eta}\right]^2+\frac{1}{J}\frac{\partial J}{\partial\eta}\frac{\partial x}{\partial\xi}\frac{\partial x}{\partial\eta}$$

$$b_{yy}=\frac{\partial^2 x}{\partial\xi\partial\eta}\frac{\partial x}{\partial\xi}-\frac{\partial^2 x}{\partial\xi^2}\frac{\partial x}{\partial\eta}+\frac{1}{J}\frac{\partial J}{\partial\xi}\frac{\partial x}{\partial\xi}\frac{\partial x}{\partial\eta}-\frac{1}{J}\frac{\partial J}{\partial\eta}\left[\frac{\partial x}{\partial\xi}\right]^2$$

$$c_{yy}=\left[\frac{\partial x}{\partial\eta}\right]^2\quad d_{yy}=\left[\frac{\partial x}{\partial\xi}\right]^2\quad e_{yy}=-2\frac{\partial x}{\partial\xi}\frac{\partial x}{\partial\eta}$$

$$a_{xy}=-\frac{\partial^2 y}{\partial\xi\partial\eta}\frac{\partial x}{\partial\eta}+\frac{\partial^2 y}{\partial\eta^2}\frac{\partial x}{\partial\xi}+\frac{1}{J}\frac{\partial J}{\partial\xi}\frac{\partial x}{\partial\eta}\frac{\partial y}{\partial\eta}-\frac{1}{J}\frac{\partial J}{\partial\eta}\frac{\partial x}{\partial\xi}\frac{\partial y}{\partial\eta}$$

$$b_{xy}=-\frac{\partial^2 y}{\partial\xi\partial\eta}\frac{\partial x}{\partial\xi}+\frac{\partial^2 y}{\partial\xi^2}\frac{\partial x}{\partial\eta}-\frac{1}{J}\frac{\partial J}{\partial\xi}\frac{\partial y}{\partial\eta}\frac{\partial x}{\partial\eta}+\frac{1}{J}\frac{\partial J}{\partial\eta}\frac{\partial y}{\partial\xi}\frac{\partial x}{\partial\xi}$$

$$c_{xy}=-\frac{\partial x}{\partial\eta}\frac{\partial y}{\partial\eta}\quad d_{xy}=-\frac{\partial x}{\partial\xi}\frac{\partial y}{\partial\xi}\quad e_{xy}=\frac{\partial x}{\partial\xi}\frac{\partial y}{\partial\eta}+\frac{\partial x}{\partial\eta}\frac{\partial y}{\partial\xi}$$

A Diffusion Flame Adjacent to a Partially Saturated Porous Slab: Funicular State

M. Kaviany

Y. Tao

Department of Mechanical Engineering and Applied Mechanics, The University of Michigan, Ann Arbor, MI 48109

The burning on the surface of a porous slab initially fully saturated with liquid fuel, and during the period where the liquid phase is continuous, is studied in order to determine the effects of the surface saturation, relative permeability, and vapor flow rate on the critical time. The critical time is defined as the time at which for the first time the surface saturation becomes zero, i.e., the first dry patches appear. The experimental and predicted results are in good agreement. The results show that unlike forced convection drying, the surface saturation does not influence the mass transfer rate significantly. Also, for the range of absolute permeabilities considered, the critical time is proportional to the absolute permeability.

1 Introduction

When the surface of a porous slab that is completely saturated (saturation is defined as the fraction of the voids occupied by the liquid) with a liquid fuel is ignited, the surface saturation gradually decreases, and after an elapsed time, dry patches appear on the surface. The time of the first appearance of dry patches is called the critical time. The period marked by the onset of surface evaportion and the critical time is called the funicular state (due to the continuity of the liquid phase throughout the slab). This period is followed by the pendular state (discontinuous liquid phase), which is associated with a noticeable reduction in the evaporation rate.

The burning of gaseous fuel flowing through porous slabs has been sutdied experimentally and analytically by Liu et al. (1982), where it was shown that the gas radiation contribution to heat transfer is rather significant. The effect of finite rate chemical reactions has been studied by Chen and T'ien (1984). Their results show that inclusion of this effect results in a decrease in the predicted total heat transfer rate. Burning of *n*-heptane liquid on the surface of metallic, porous, circular cylinders was considered by Abdel-Khalik et al. (1974, 1975), as a model for burning of droplets. The liquid and the porous cylinder was cooled in order to avoid boiling inside the cylinder. Attempts were made to keep the surface fully covered with a film of the liquid fuel. Since the fuel was forced to the surface by a pump, the capillary pressure was not required for the flow and, therefore, the surface could indeed have had a saturation of unity. It was found that radiation heat transfer to the fuel surface was significant. The burning of liquid fuel on the surfaces of metallic and ceramic wicks has been investigated experimentally and analytically by Kim et al. (1971, 1974), Ahmed and Faeth (1977), and Groff and Faeth (1978), where the steady-state analytical treatments are based on the presence of a planar liquid film on the wick surface. Since the experimental and predicted results are in good agreement, it appears that the presence of a nonplanar surface (because the surface is only partially saturated), which is required for the flow of liquid to the surface due to capillary action, does not influence the mass transfer rate. This contrasts with forced convection drying results, which show that surface saturation affects the mass transfer rate significantly (Plumb et al., 1985; Kaviany and Mittal, 1986). One major difference between drying and burning is that in the former the heat supplied to the surface is nearly independent of the mass transfer, while in the latter the heat and mass transfer are strongly coupled.

Multiphase transport though porous media has been treated by Chen and Whitaker (1986) and Udell (1985), among others. These formulations include the effects of the presence of noncondensibles on vapor diffusion, which reduces the rate of molecular diffusion of the vapor. This diffusion, which is usually related to the molecular diffusion in plain media and the porous media tortuosity, has been discussed by Smith (1986), among others.

In this study, the burning of a porous slab made of sintered stainless steel, initially saturated with ethanol, is treated experimentally and analytically. Figure 1 gives a schematic of the system. The one-dimensional analysis is based on the simplifying assumptions of (*a*) prescribed constant burning rate, and (*b*) negligible gravity effect on the liquid flow. The effects of internal vapor generation and convection, surface saturation, and liquid subcooling on the critical time are examined.

2 Analysis

In the following one-dimensional transient analysis the variables are nondimensionalized using the scales given in Table 1(*a*). Whenever the quantities appear in both dimensional and dimensionless forms, asterisks indicate that quantities are dimensional. The governing equations for thermal energy and saturation, which are found by proper reduction of the equations given by Whitaker (1977), are

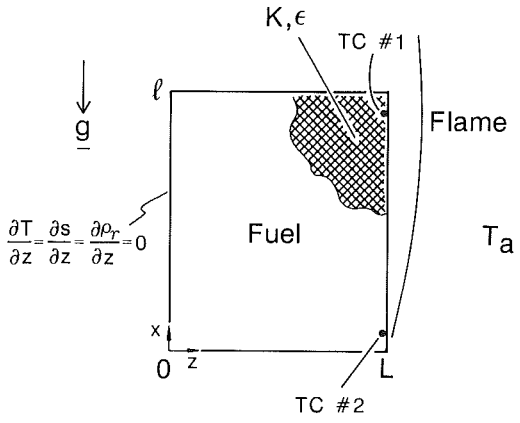

Fig. 1 Schematic of the problem

Contributed by the Heat Transfer Division for publication in the JOURNAL OF HEAT TRANSFER. Manuscript received by the Heat Transfer Division February 3, 1987. Keywords: Combustion, Fire/Flames, Natural Convection.

$$\frac{\partial}{\partial z}\left(k_e \frac{\partial T}{\partial z}\right) - \mathrm{Pe}\, sK_{r\beta} \frac{df}{ds} \frac{\partial s}{\partial z} \frac{\partial T}{\partial z} + i_{fg}\left\{-\epsilon \frac{\partial}{\partial t}(1-s)\rho_\gamma + \frac{R_\gamma \mathrm{Pe}}{\mu_\gamma} \frac{\partial}{\partial z}\left[(1-s)\rho_\gamma K_{r\gamma} T \frac{\partial \rho_\gamma}{\partial z} + (1-s)K_{r\gamma}\rho_\gamma^2 \frac{\partial T}{\partial z}\right]\right\} = [(1-\epsilon)(\rho c)_a + \epsilon s + \epsilon(1-s)(\rho c)_\gamma] \frac{\partial T}{\partial t} \quad (1)$$

$$-\mathrm{Pe} \frac{\partial}{\partial z}\left(sK_{r\beta} \frac{df}{ds} \frac{\partial s}{\partial z}\right) + \frac{R_\gamma \mathrm{Pe}}{\mu_\gamma} \frac{\partial}{\partial z}\left[(1-s)\rho_\gamma K_{r\gamma} T \frac{\partial \rho_\gamma}{\partial z} + (1-s)K_{r\gamma}\rho_\gamma^2 \frac{\partial T}{\partial z}\right] = \epsilon(1-\rho_\gamma) \frac{\partial s}{\partial t} + \epsilon \frac{\partial}{\partial t}(1-s)\rho_\gamma \quad (2)$$

where in equation (1) the vapor convection term has been neglected. Perfect gas behavior has been assumed for the vapor. The effect of gravity on liquid flow appears in the x-direction momentum equation as $g\rho_\beta^* (K/\epsilon)^{1/2} L/\sigma$ and is the ratio of the gravity force per unit volume to the gradient of the capillary pressure. In general, for large permeabilities the capillary pressure is negligible compared to the gravity force (Schulenberg and Muller, 1987) and for very low permeabilities the gravity force is negligible. For simplicity, equation (2) is written for a one-dimensional flow flowing perpendicular to the direction of gravity. As will be shown, the magnitude of the permeability encountered in the experiment is not small enough completely to justify this assumption; however, this one-dimensional model describes the general behavior of the wick fairly well. The effect of noncondensibles on the vapor diffusion is also neglected. However, this is not easily justifiable, especially when the liquid is initially subcooled and the vapor pressure gradient near the burning surface is rather large. By neglecting the resistance to vapor flow due to the presence of noncondensibles, a significant inward vapor flow and consequent condensation occur and, therefore, the predicted critical time will be much shorter than that expected. In order to account for this resistance properly the composition of the noncondensibles in the block after the onset of combustion and the effective diffusion coefficient must be relatively accurately known. Due to lack of sufficient available data, the inclusion of this resistance was not attempted. The initial conditions are uniform temperature T_i and complete saturation. The boundary conditions are (*a*) zero gradients at $z=0$, and (*b*) for $t>0$ the surface temperature is at T_{sat} and the liquid mass flow rate is that given by the approximate integral solution based on steady-state behavior, namely (Kim et al., 1974)

$$\dot{m}''_\beta = \mathrm{Pe}\, sK_{r\beta} \frac{df}{ds} \frac{\partial s}{\partial z} = \mu_a \mathrm{Pr}_\beta HG \quad \text{at } z=1 \quad (3)$$

where in general the mass flow rate decreases with the distance from the leading edge. Equation (3) is the integrated value over the length of the wick (in the direction of gravity) and the parameters in equation (3) are

$$H = \left[\frac{g}{\nu_{\gamma,1}^{*2}} \frac{i_{fg}}{c_a T_a} \left(\frac{\rho_a}{\rho_{\gamma,1}}\right)^4 \frac{L^4}{l}\right]^{1/4}$$

$$G = \left[\frac{B\ln(1+B)}{\mathrm{Pr}}\right]^{1/2} \left\{\frac{6(B+\tau)(1-F_f^{2/3})+\tau}{25(B+1)\left[\mathrm{Pr}+\frac{5}{6}(B+1)\right]}\right\}^{1/4}$$

$$F_f = \frac{B+1}{B} \frac{r}{r+1} \quad \text{and} \quad \mathrm{Pr}_\beta = \mu_\beta c_\beta / k_{a\beta} \quad (4)$$

Equation (3) is based on the assumption that all the heat supplied to wall by the flame is consumed by evaporation, i.e., if the slab is subcooled, the heat supplied to the slab cannot be determined using this formulation. Determination of the heat transferred to a subcooled slab requires the conjugated porous slab-flame formulation, which was not attempted. The energy equation given above was solved to estimate the rate of heat transfer to the slab for slightly subcooled slabs. This required heat is

$$q_{in} = -k_e \frac{\partial T}{\partial z} \quad \text{at } z=1$$

The vapor flow rate (used in equation (2)) is

Nomenclature

B = mass transfer potential
c = specific heat capacity, J/kg-K
C_e = effective specific heat capacity, J/kg-k
f = saturation function in the capillary pressure equation, equation (7)
F_f = defined in equation (4)
i_{fg} = heat of evaporation, J/kg
g = gravitational constant, m^2/s
G, H = defined in equation (4)
k = thermal conductivity, W/m-K
K = permeability, m^2
$K_{r\beta}$ = liquid phase relative permeability
$K_{r\gamma}$ = gas phase relative permeability
L = block length, m
l = block height, m
$\dot{m}''$ = mass flux, kg/m^2-s
$\dot{m}$ = mass flow rate, kg/s
M = molecular weight, kg/kg-mole
p = pressure, N/m^2
Pe = Peclet number $= \epsilon\sigma(K/\epsilon)^{1/2}/\alpha\mu$
Pr = Prandtl number for gas phase
Pr_β = Prandtl number for liquid phase
q_{in} = inward heat flux, W/m^2
Q = heat flow rate, W
R_γ = gas constant for vapor, J/kg-K
s = saturation ϵ_β/ϵ
S = $(s-s_{im})/(1-s_{im})$
t = time, s
T = temperature, K
w = block width, m
x, z = coordinate axes, m
α = thermal diffusivity $= k_e/(\rho c)_\beta$, m^2/s
ϵ = porosity
μ = viscosity, kg/m-s
ρ = density, kg/m^3
σ = surface tension, N/m

Superscripts

* = dimensional
$\bar{}$ = average

Subscripts

1 = evaluated at the surface
a = ambient
c = capillary, or critical
e = effective
im = immobile liquid saturation
0 = reference, same as saturation
sat = saturation
sc = subcooled
β = liquid phase
γ = vapor phase
σ = solid phase

Table 1(*a*) Dimensionless variables

z	t	u_β	u_γ	T	s	ρ_γ	p_γ
$\frac{z^*}{L}$	$\frac{t\alpha_\beta^*}{L^2}$	$\frac{u_\beta^* L}{\alpha_\beta}$	$\frac{u_\gamma^* L}{\alpha_\beta}$	$\frac{T^*}{T_0}$	$\frac{\epsilon_\beta}{\epsilon}$	$\frac{\rho_\gamma^*}{\rho_\beta^*}$	$\frac{p_\gamma^*(K/\epsilon)^{1/2}}{\sigma}$

Table 1(*b*) Dimensionless parameters

Porous medium–fluid					Fluid, solid properties							
Dynamic			Static	p_γ-reduction	R_γ	b	μ_γ	c_σ	c_σ	ρ_σ	i_{fg}	$k_{\sigma-\gamma}$
Pe	$K_{r\beta}$	$K_{r\gamma}$	f	a								
$\frac{\epsilon\sigma(K\epsilon)^{1/2}}{\alpha_\beta\mu_\beta^*}$	s^3	$(1-s)^3$		$\frac{\sigma}{\rho_\beta^* R_\gamma^* T_0 (K/\epsilon)^{1/2}}$	$\frac{\rho_\beta^* R_\gamma^* T_0 (K/\epsilon)^{1/2}}{\sigma}$	$\frac{i_{fg}^*}{R_\gamma^* T_0^*}$	$\frac{\mu_\gamma^*}{\mu_\beta^*}$	$\frac{c_\gamma^*}{c_\beta^*}$	$\frac{c_\sigma^*}{c_\beta^*}$	$\frac{\rho_\sigma^*}{\rho_\beta^*}$	$\frac{i_{fg}^*}{c_\beta^* T_0^*}$	$\frac{k_{\sigma-\gamma}^*}{k_{\sigma-\beta}^*}$

Table 2 Example of grid size selection

Δz	Δt	t_c
1/20	4×10^{-6}	0.4343
1/30		0.4443
1/40		0.4496

$$\dot{m}_\gamma'' = -\mathrm{Pe}\, K_{r\gamma} \frac{R_\gamma}{\mu_\gamma}(1-s)\left(T\rho_\gamma \frac{\partial \rho_\gamma}{\partial z} + \rho_\gamma^2 \frac{\partial T}{\partial z}\right) \tag{5}$$

The constitutive equations used are (Udell, 1985)

$$P_\gamma = R_\gamma P_\gamma T = P_{\mathrm{sat}} \exp\left[\frac{af}{T} - b\left(\frac{1}{T} - 1\right)\right] \tag{6}$$

$$P_\gamma^* - P_\beta^* = P_c^* = \frac{\sigma}{(K/\epsilon)^{1/2}}\,[1.42(1-s) - 2.12(1-s)^2 + 1.26(1-s)^3] = f\frac{\sigma}{(K/\epsilon)^{1/2}} \tag{7}$$

where

$$S = \frac{1-s_{im}}{1-s_{im}}, \quad \frac{df}{dS} = \frac{1}{1-s_{im}}\frac{df}{ds}$$

The immobile saturation s_{im} was estimated as 0.05. The effective thermal conductivity was taken as (Udell and Fitch, 1985)

$$k_e^* = k_{\sigma\gamma}^* + s^{1/2}(k_{\sigma\beta}^* - k_{\sigma\gamma}^*) \tag{8}$$

The solid–gas and solid–liquid thermal conductivities were determined by volume averaging. The relative permeability for the porous medium used in the experiment was measured and these approximations were adapted

$$K_{r\beta} = s^3, \quad K_{r\gamma} = (1-s)^3 \tag{9}$$

The dimensionless parameters are given in Table 1(*b*). Equations (1) and (2), subject to the previously mentioned conditions, were solved using the approximate explicit finite-difference formulation. The grid size and time step size were chosen based on stability and convergence. Progressively smaller Δz and Δt were chosen until the result no longer changed significantly. The critical time is defined as the time at which the surface saturation becomes zero. This occurs as the resistance to the liquid flow increases (because the saturation decreases) and the required saturation gradient (for a given mass flow rate) becomes very large. It should be noted that the presence of the critical time does not require a prescribed liquid flow rate [an example of this is reported for a drying process (Kaviany and Mittal, 1986)]. Table 2 gives an example for the selection of Δz and Δt. A grid size of 1/40 and $\Delta t = 4\times10^{-6}$ were used. The overall mass and energy balances were examined and found satisfactory (to less than 1 percent).

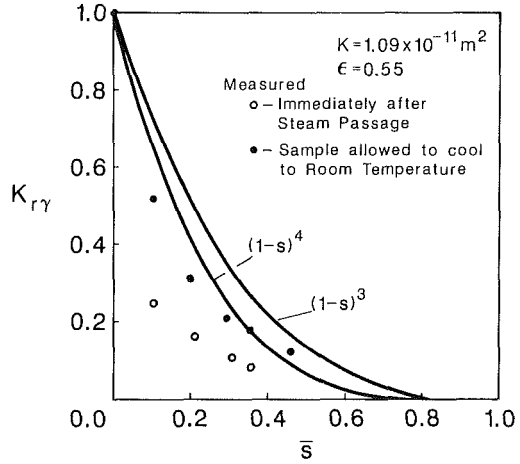

Fig. 2 Variation of relative permeability with respect to saturation

3 Experiment

A sintered stainless steel (316) porous block $0.0432\times0.0438\times0.0446$ m (for $L\times l\times w$), made by ASTRO MET ASSOCIATES (Cincinnati, OH), was used; the porosity was measured and found to be 0.55. The absolute permeability was measured using the modified Darcy's law (Kaviany and Mittal, 1986), which includes the second-order effect. It was found that the absolute peremeability is 1.09×10^{-11} m^2 and the factor F in the second-order term is 1.5×10^{-4}, which is rather insignificant for the range of velocity encountered. The relative permeability was measured by passing steam through the porous medium. The steam condensed in the medium and the saturation was then measured. Then, the relative permeability was measured by passing air through this partially saturated medium. Details of the measurement are similar to those described in Kaviany and Mittal (1986). The results are shown in Fig. 2. The relative permeability measured immediately after condensation was different than that measured after allowing the block to cool to room temperature. This can be attributed to the redistribution of the liquid in the porous medium due to a decrease in temperature and the corresponding changes in the density, viscosity, and surface tension. For the room temperature data the approximate representation by $(1-s)^3$ overestimates $K_{r\gamma}$ for $s<0.6$ but appears to be reasonable for $s>0.6$. It should be noted that since the contact angles of water and ethanol (for the solid surface used) are different, the topology of the liquid distribution within the solid matrix for the same average saturation will not be the same for the two fluids (Dullien, 1979). Therefore, the relative permeability would also be different.

Thermocouples were placed in various locations inside and around the block, including two on the burning surface, one

Table 3(*a*) Numerical values

Solid					Liquid					Vapor			
L,	ρ^*_σ,	c^*_σ,	K,	ϵ	ρ^*_β,	c^*_β,	μ^*_β,	$k^*_{\sigma-\beta}$,	α^*_β,	μ^*_γ,	c^*_γ,	R^*_γ,	i^*_{fg},
m	kg/m^3	J/kg-K	m^2		kg/m^3	J/kg-K	Pa•s	W/m-k	m^2/s	Pa•s	J/kg-K	J/kg-K	J/kg
0.043	8,328	470	1.09×10^{-11}	0.55	770	2,452	5×10^{-4}	6.40	3.4×10^{-6}	1.1×10^{-5}	1,430	180.5	8.8×10^5

Table 3(*b*) Numerical values

Medium			Ambient	Dimensionless parameters								
σ,	$k^*_{\sigma-\gamma}$,	T_{sat},	T_a,	Pe	$R_\gamma=\frac{1}{a}$	P_0	b	μ_γ	c_γ	ρ_σ	c_σ	i_{fg}	$k_{\sigma-\gamma}$
N/m	W/m-K	K	K										
0.018	6.31	351.5	297	14.3	1.2×10^4	25	13.9	0.022	0.583	10.7	0.191	1.02	0.988

Table 3(*c*) Parameters[1] for the surface mass transfer rate (ethanol)

M, kg/kg-mole	Δh, MJ/kg-mole	B	r	τ	Pr	Pr_β
46.07	1.278	3.41	0.111	0.044	0.73	0.192

[1]From Ahmed and Faeth (1977).

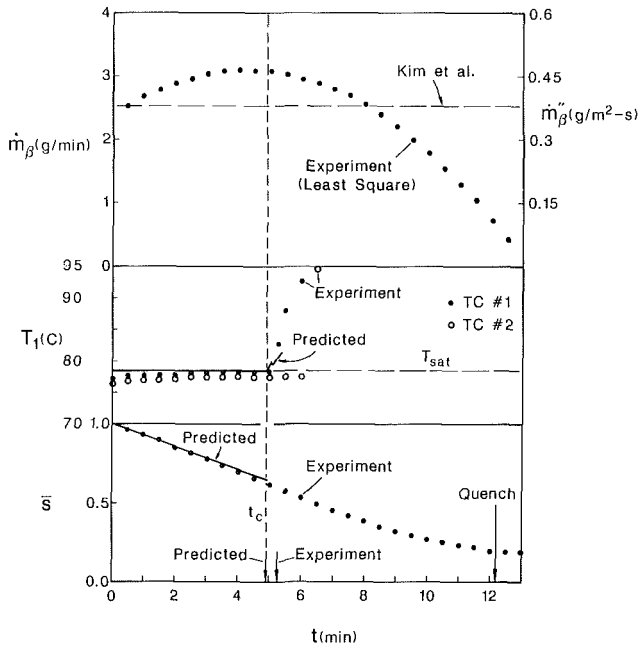

Fig. 3 Variations of mass flow rate, surface temperatures, and average saturation with respect to time; the critical time and the quench time are also marked

on top (shown in Fig. 1 as TC #1), and one at the bottom (TC #2). The block was tightly placed in an aluminum casing with only one side open. The thickness of the casing was about 1 mm. The choice of aluminum was made based on the relative inertness to the fuel and ease of machining. However, the heat flowing through it can be significant and could be as large as that through the porous medium. A separate test made using aluminum foil to wrap the porous medium resulted in a similar mass flow rate; therefore the influence of the casing was thought to be negligible. The burning side was surrounded by an aluminum plate of 15×15 cm (except for the burning surface). The entire assembly was wrapped in insulation and then placed on top of a scale for mass transfer rate measurement.

In order to ensure the minimum subcooling of the porous slab, prior to the start of the combustion, boiling fuel was poured onto it while the entire assembly was being heated on a hot plate (so that the solid matrix was also near the saturation temperature). Then the assembly was removed from the hot plate and the surface was ignited.

The magnitudes of the various parameters appearing in the analysis are given in Tables 3(*a*), 3(*b*), and 3(*c*).

4 Results and Discussion

The time of the appearance of the first dry patches (i.e., the critical time) corresponds to the moment at which, for a demand for the liquid flow to the surface, due to a significant decrease in the surface saturation the resistance to the liquid flow is so large that the saturation gradient at the surface must become very large. Figure 3 shows the experimental and predicted results for the mass flow rate, surface temperature, and average saturation. The prescribed mass flow rate (from Kim et al., 1974) is smaller than that measured. This could be due to the approximate nature of the results and also the assumption of negligible radiation heat transfer. Note that for the fuel used, the ratio of heat of evaporation to the enthalpy of reaction is 1/35, i.e., only a small amount of heat is returned to the surface for evaporation. The maximum mass transfer rate is about 20 percent higher than the approximate prediction. The results show that prior to t_c the decrease in the surface saturation does not adversely affect the mass flow. This is in contrast to the results for forced convection drying (Plumb et al., 1985; Kaviany, 1987; Kaviany and Mittal, 1986). Observation of the flame, directly and with a holographic interferometer, shows that the flame is laminar over the entire length of the burning surface. The average flame standoff distance was about 3 mm and the small-scale characteristic length $(K/\epsilon)^{1/2}$ for the porous medium used is 0.0044 mm. Therefore, the effect of the surface roughness on the flame hydrodynamics is expected to be negligible. Therefore, the hydrodynamics of the flame is nearly similar to that for a completely liquid-covered surface. However, the heat transferred to the exposed solid matrix will be indirectly transferred to the liquid surface. The exposed solid matrix may have temperatures higher than the saturation temperature, i.e., at and near the surface solid and liquid phases are

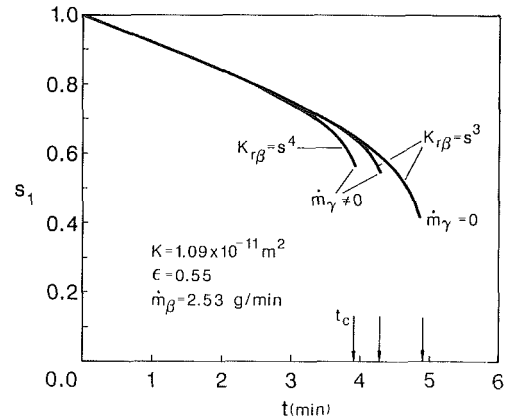

Fig. 4 Variation of the surface saturation with respect to time for two different relative permeabilities; the effect of vapor flow rate is also shown

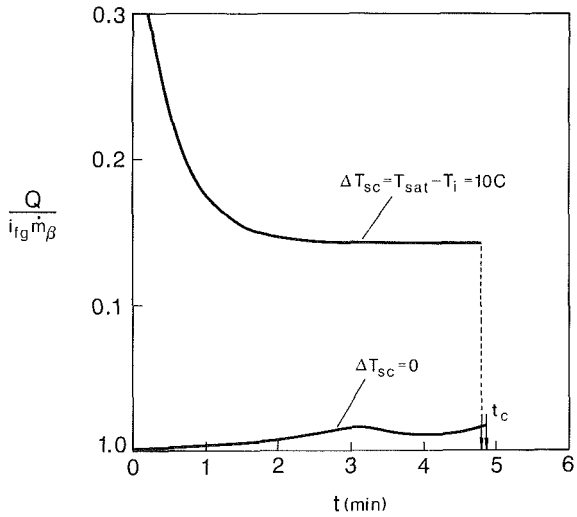

Fig. 5 Amount of heat flowing into the block for two different values of the initial subcooling

not in equilibrium. Therefore, the multidimensional heat transfer through the porous medium (along with local nonequilibrium) must be analyzed for estimate of the total rate of heat transfer to the liquid phase. Also, due to the nonplanar geometry of the surface, the liquid surface area of a partially saturated surface is larger than that for a planar surface with the same saturation. These interesting aspects of surface mass transfer from partially liquid covered surfaces have not yet been studied in detail.

The results in Fig. 3 show that the experimental and predicted values of the critical time are in good agreement and almost immediately after t_c, the surface temperature rises very rapidly above the saturation value. Since for the permeability encountered the gravity field influences the liquid flow, the upper portion of the block dries out first, as shown in Fig. 3. The one-dimensional analysis does lead to a reasonable estimate of t_c, but cannot be applied to strongly gravity-influenced systems, where the x-direction momentum equation must be solved simultaneously.

Figure 4 shows variation of the surface saturation with respect to time to the critical time. The effects of the relative permeability and the inward flow of vapor are examined. Even though the initial temperature distribution is uniform at T_{sat}, the combined effect of internal evaporation and condensation results in a very small depression of the temperature inside the block. This gives rise to a gradient of vapor pressure, forcing

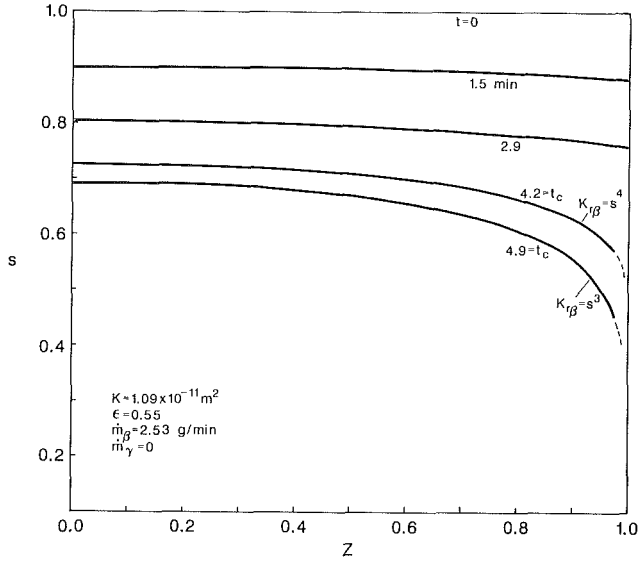

Fig. 6 Distribution of the saturation for several elapsed times; the effect of the relative permeability on the distribution is also shown

the flow of the vapor inward. This flow (relative permeability) must be supplied by extra surface evaporation. The result is faster drying of the surface, as found from the results shown in Fig. 4. The effect of the magnitude of resistance on the liquid flow is also shown for two different resistances. As mentioned earlier, the required surface saturation gradient, which becomes very large at t_c, is proportional to this resistance and as the resistance increases the critical time decreases.

Since it is assumed that all of the heat transferred to the wall is consumed by evaporation, the analysis is valid for a uniform initial temperature distribution with the magnitude corresponding to the saturation state. Assuming that the surface liquid flow rate is not affected by the block subcooling (note that the surface is always at T_{sat}), then the amount of heat flowing into the block can be determined by solving the energy equation. In steady-state processes, the effect of fuel subcooling is assessed through the magnitude of $c_e\Delta T_{sc}^*/i_{fg}$, where c_e is the effective specific heat capacity and $\Delta T_{sc}^* = T_{sat}^* - T_i^*$. At $\Delta T_{sc}^* = 10°C$ this is less than 3 percent for the system considered. However, for this transient experiment, the rate of heat transfer needed to heat the block from the initial subcooled temperature to the saturation temperature can be rather large in the early stages. This normalized heat flow rate is shown in Fig. 5 for ΔT_{sc}^* equal to 0 and 10°C. As was mentioned before, even for $\Delta T_{sc} = 0$, the temperature is slightly depressed, due to internal evaporation-condensation and therefore, there is a small amount of heat flowing into the block. For $\Delta T_{sc}^* = 10°C$, initially a substantial amount of heat flows into the block. Note that the heat transferred from the flame to the block is only a small fraction of the heat released by combustion and therefore the mass transfer rate is not expected to be significantly different than that for the case $\Delta T_{sc} = 0$. However, as expected (and observed experimentally), $\dot{m}_\beta$ is slightly smaller for $\Delta T_{sc} > 0$. It should also be noted that since the Peclet number is relatively large, adjacent to the surface the temperature gradient is rather large and therefore the heat flow into the block is rather small. As a result the energy required for raising the temperature of the block can be rather substantial.

Figure 6 shows the saturation distribution for different elapsed times and for two different relative permeabilities. As expected, the lower resistance results in a larger t_c. The rather extreme gradients occurring near the surface lead to discontinuity of the liquid flow (appearance of dry patches).

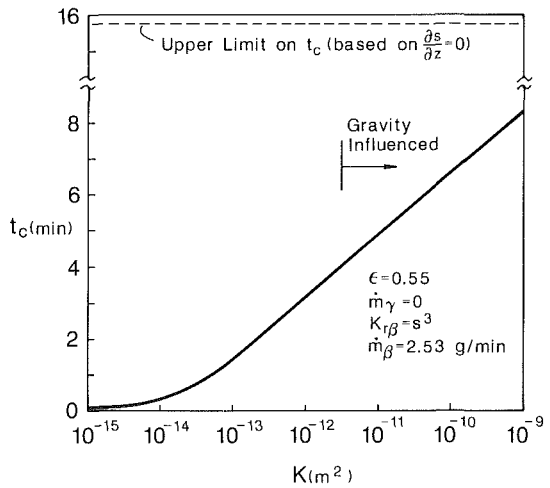

Fig. 7 Effect of the absolute permeability on the critical time; the upper limit on t_c, corresponding to a zero saturation gradient, is also shown

Figure 7 shows the effect of the magnitude of the absolute permeability on the critical time. For the ideal case of zero resistance to the liquid flow, i.e., zero saturation gradient, the critical time is simply the initial liquid content divided by the mass flow rate. This upper limit on t_c is also shown in the figure. Examination of Fig. 3 shows that the flame quenches before this limit is reached (and the mass flow rate is not constant). Figure 7 also shows that the critical time is proportional to the logarithm of absolute permeability for $K>10^{-13}$ m^2. This is not quite evident from the saturation equation.

Examination of equation (3) shows that using equation (9), we have

$$s^4 \frac{df}{ds}\frac{\partial s}{\partial z}=\frac{\mu_a \,\mathrm{Pr}_\beta HG}{\mathrm{Pe}}=\frac{\dot{m}''_\beta}{\mathrm{Pe}}$$

Since $\dot{m}''_\beta$ is taken as a constant, for a given saturation as Pe increases the magnitude of $\partial s/\partial z$ decreases, i.e., the critical time is delayed. The results shown in Fig. 7 suggest that

$$t_c = A + C \log \mathrm{Pe}$$

where C and A depend on the solid matrix and fuel properties.

5 Summary

Within the limits imposed by the various assumptions made in the analysis, including the lack of the influence of gravity in the one-dimensional model, the following conclusions are drawn:

(*a*) The surface saturation does not significantly influence the mass transfer rate. This is in contrast with the available results for forced convection mass transfer from partially liquid-covered surfaces, where a significant dependence on the surface saturation exists.

(*b*) Although the inward vapor flow rate is significant, the resistance of the noncondensible to this flow must be taken into account, otherwise inclusion of this mass flow results in unreasonably small values for the critical time.

(*c*) Observations also show that the mass transfer rate is not significantly reduced when the slab is initially subcooled. This suggests that the interaction between the subcooled slab and the flame results in additional heat transfer to the slab.

Acknowledgments

Mr. J. Rogers and Miss S. Yohn have contributed to the project, for which we are grateful. We are also grateful to the reviewers for their constructive comments. The financial support of the Institute of Science and Technology, The University of Michigan, is appreciated.

References

Abdel-Khalik, S., Tamaru, T., and El-Walik, M. M., 1974. "An Experimental and Analytical Determination of Heat and Mass Transfer in a Diffusion Flame," in: *Heat Transfer in Flames*, Script Book, publisher, pp. 365–374.

Abdel, Khalik, S. Tamaru, T., and El-Walik, M. M., 1975, "An Experimental and Analytical Determination of Heat and Mass Transfer in a Diffusion Flame Around a Simulated Fuel Drop," *Proceedings of the 15th (International) Symposium on Combustion*, Combustion Institute, pp. 389–399.

Ahmed, T., and Faeth, G. M., 1977. "An Investigation of the Laminar Over Fire Region Along Upright Surfaces," ASME Paper No. 77-HT-68.

Chen, C. H., and T'ien, J. S., 1984, "Fire Plume Along Vertical Surfaces: Effects of Finite-Rate Chemical Reaction," ASME JOURNAL OF HEAT TRANSFER, Vol. 106, pp. 713–720.

Chen, S., and Whitaker, S., 1986, "Moisture Distribution During the Constant Rate Drying Period for Unconsolidated Porous Media. Failure of the Diffusion Theory," *Drying '86*, Vol. 1, A. S. Majumdar, ed., Hemisphere, Washington, DC, pp. 39–48.

Groff, E. G., and Faeth, G. M., 1978, "Laminar Combustion of Vertical Free-Standing Fuel Surfaces," *Combustion and Flame*, Vol. 32, pp. 139–150.

Dullien, F. A. L., 1979, *Porous Media, Fluid Transport and Pore Structure*, Academic Press, New York, pp. 257–262.

Kaviany, M., and Mittal, M., 1987, "Funicular State in Drying of a Porous Slab," *Int. J. Heat Mass Transfer*, Vol. 30, pp. 1407–1418.

Kaviany, M., 1987, "Forced Convection Heat and Mass Transfer From a Partially Liquid Covered Surface," submitted to *J. Fluid Mechanics*.

Kim, J. S., de Ris, J., and Kroesser, F. W., 1971, "Laminar Free-Convective Burning of Fuel Surface," *13th Symposium (International) on Combustion*, The Combustion Institute, pp. 949–961.

Kim, J. S., de Ris, and Kroesser, F. W., 1974, "Laminar Burning Between Parallel Fuel Surfaces," *Int. J. Heat Mass Transfer*, Vol. 17, pp. 439–451.

Liu, V. F., Yang, K. T., and Lloyd, J. R., 1982, "Elliptic Field Calculations of a Laminar Diffusion Flame Adjacent to a Vertical Flat Plate Burner," *Int. J. Heat Mass Transfer*, Vol. 25, pp. 863–869.

Plumb, O. A., Spolek, G. E., and Olmstead. B. A., 1985, "Heat and Mass Transfer in Wood Drying," *Int. J. Heat Mass Transfer*, Vol. 28, pp. 1669–1678.

Schulenberg, T., and Muller, U., 1987, "An Improved Model for Two-Phase Flow Through Beds of Coarse Particles," *Int. J. Multiphase Flow*, Vol. 13, pp. 87–89.

Smith, D. M., 1986, "Restricted Diffusion Through Pores With Periodic Constrictions," *AIChE J.*, Vol. 32, pp. 1039–1042.

Udell, K. S., 1985, "Heat Transfer in Porous Media Considering Phase Change and Capillarity—The Heat Pipe Effect," *Int. J. Heat Mass Transfer*, Vol. 28, pp. 485–495.

Udell, K. S., and Fitch, J. S., 1985, "Heat and Mass Transfer in Capillary Porous Media Considering Evaporation, Condensation and Noncondensible Gas Effects," in: *Heat Transfer in Porous Media and Particulate Flows*, ASME HTD-Vol. 46, pp. 103–110.

Whitaker, S., 1977, "Simultaneous Heat, Mass and Momentum Transfer in Porous Media: A Theory of Drying," *Advances in Heat Transfer*, Vol. 13, pp. 119–203.

I. S. Wichman

H. R. Baum[1]

Department of Mechanical Engineering,
Michigan State University,
East Lansing, MI 48824-1226

An Integral Analysis of Two Simple Model Problems of Wind-Aided Flame Spread

The method of integral analysis is applied to two simple model problems closely related to the general wind-aided flame spread problem. The analysis of the two models strongly suggests approximating the general problem as a steady-state process in the pyrolysis zone and as an unsteady process in the preheat zone ahead of it.

Introduction

This paper is concerned with an investigation of the equations of wind aided flame spread. We use integral methods (Schlichting, 1979) to analyze *two* simple model problems that characterize their overall fluid-dynamic and heat-transfer behavior. The integral solutions presented in sections 2 and 3 suggest an approximation for the general equations that will greatly facilitate their approximate solution. This study only motivates the approximation; the actual solution is the subject of a later study.

In the first model problem the velocity field for the impulsively started semi-infinite flat plate is examined. Two cases are considered: (*i*) no transverse blowing at the surface and (*ii*) transverse blowing in the region $0 \le \hat{x} \le \hat{x}_p$ (see Fig. 1). The boundary layer equations for case (*i*) were analyzed first by Stewartson (1951, 1960); the recent numerical study of Tadros and Kirkhope (1978) confirms the validity of his theoretical predictions. Stewartson (1951) shows for an impulsive starting velocity $\hat{U}$ that the streamwise velocity is independent of $\hat{x}$ when $\hat{t} < \hat{x}/\hat{U}$, i.e., $\hat{u}$ is given in this region by the Rayleigh solution. The point $\hat{t} = \hat{x}/\hat{U}$ is described as an essential singularity, through which the transition from the initial Rayleigh solution to the laminar Blasius boundary layer solution occurs. For $\hat{t} > \hat{x}/\hat{U}$ Stewartson shows that the velocity field depends on *both* $\hat{x}$ and $\hat{t}$. However, in this regime the $\hat{t}$ dependence decays exponentially as $\hat{t} \to \infty$, leaving the steady Blasius boundary layer as the long-time solution. In sum, the initial Rayleigh solution with no $\hat{x}$ dependence settles into an $\hat{x}$-dependent but time-independent Blasius solution. To support these predictions, Stewartson (1951) analyzes two simple models: (*i*) the linearized Oseen version of the boundary layer equations, and (*ii*) an integral model that assumes the velocity distribution $\hat{u}/\hat{U} = \sin(\pi\hat{z}/2\hat{\delta})$, $0 \le \hat{z} \le \hat{\delta}$. For (*i*), $\hat{u}$ is independent of $\hat{x}$ when $\hat{t} < \hat{x}/\hat{U}$ giving, as before, the Rayleigh solution; $\hat{u}$ is *always* independent of $\hat{t}$ when $\hat{t} > \hat{x}/\hat{U}$. The location $\hat{x} = \hat{U}\hat{t}$ specifies the instantaneous extent of influence of the leading edge. For (*ii*), the respective regions of $\hat{x}$ and $\hat{t}$ independence are $\hat{t} < 2.65\ (\hat{x}/\hat{U})$ and $\hat{t} > 2.65\ (\hat{x}/\hat{U})$. By combining the predictions of these two separate models, it is clear that $\hat{u}$ is given initially by the Rayleigh solution, which is independent of $\hat{x}$. Then, at $\hat{t} = \hat{x}/\hat{U}$, the effect of the leading edge is first felt at the outer edge of the boundary layer, where the Oseen approximation is most nearly valid. The influence of this signal subsequently propagates toward the plate until, at $\hat{t} = 2.65\ (\hat{x}/\hat{U})$, $\hat{x}$ has replaced $\hat{t}$ as the dominant timelike coordinate. The velocity field is thereafter described by the steady Blasius boundary layer solution. For the integral analysis of Section 2.1, the assumed streamwise velocity profile is given by the error function; the location of the $\hat{t}$-to-$\hat{x}$ transition is given by $\hat{t} = (1/(\sqrt{2}-1))\hat{x}/\hat{U} = 2.41\ \hat{x}/\hat{U}$, which lies *between* the limits of Stewartson's (1951) Oseen-flow and sine-function models. The integral analysis of Section 2.1 is then extended in Section 2.2 to describe the velocity field when there is blowing *only in the pyrolysis zone*, $0 \le \hat{x} \le \hat{x}_p$ (see Fig. 1). The steady problem with blowing along the entire downstream interface, varying as $\hat{x}^{-1/2}$, is discussed in Schlichting (1979). Our integral analysis shows that the flow in the pyrolysis region is *steady*, while in the preheat region $\hat{x} > \hat{x}_p$ it is *unsteady*.

The second model problem examined here is the impulsively started constant temperature plate, with unequal gas and plate temperatures and no chemical reactions in the gas. This model describes the procedure for calculating the Schvab-Zeldovich coupling functions for the full wind-aided flame spread problem. The equations for the coupling functions also contain no reaction terms, although the boundary conditions are more complicated. The effects of blowing are not addressed in this model, so that the gas velocities used in the convective terms are those of Section 2.1.

Previous theoretical studies of wind-aided flame spread relevant to this study are those of Carrier et al. (1980, 1983), for flame spread over noncharring (1980) and charring (1983) fuels. In these analyses the Oseen flow linearization was employed, enabling the gas and fuel phase conservation equations to be reduced, along the interface, to a complicated set of integral equations that were integrated numerically; this procedure was first utilized by Sirignano (1974) for the opposed-flow flame spread problem. For an extensive discussion of other theoretical approaches, as well as previous ex-

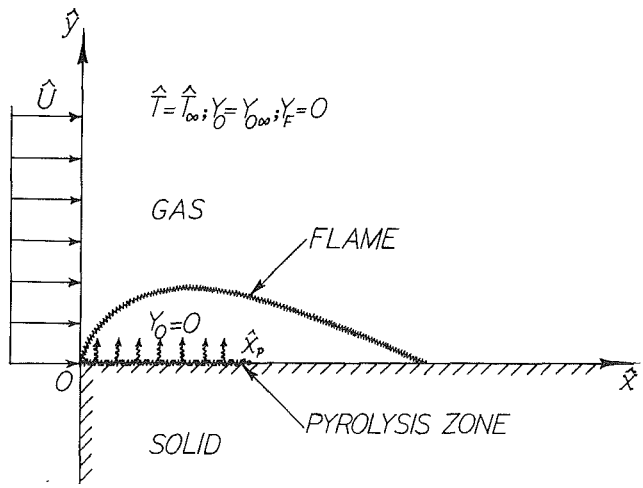

Fig. 1 Physical configuration for wind-aided flame spread. Shown are the flame sheet, where the chemical reaction occurs, and the pyrolysis zone, $0 \le \hat{x} \le \hat{x}_p$. No pyrolysis occurs in the preheat zone, $\hat{x} > \hat{x}_p$.

[1]Center for Fire Research, National Bureau of Standards, Gaithersburg, MD 20899.

Contributed by the Heat Transfer Division for publication in the JOURNAL OF HEAT TRANSFER. Manuscript received by the Heat Transfer Division December 17, 1986. Keywords: Combustion, Fire/Flames, Mixed Convection.

perimental studies, the reader is referred to the reviews of Fernandez-Pello (1984) and Fernandez-Pello and Hirano (1983).

We note that the flame spread problem as posed here and elsewhere (Carrier et al., 1980, 1983; Fernandez-Pello, 1984) is not general, in that flames do not necessarily originate at the leading edge of the combustible solid. If the flame originates downstream, the solution will be nonsimilar; furthermore, the elliptical behavior near the tip of the flame zone could then not be neglected, since conduction in the streamwise direction would affect upstream flame spread. However, none of these effects need to be addressed if we restrict ourselves to flames originating at $\hat{x}=0$.

2 Integral Analysis of Mass and Momentum Equations for the Impulsively Started Flat Plate

The coordinate system is attached to the leading edge, and a uniform flow of gas across the plate begins at $\hat{t}=0$. The nondimensional mass and momentum equations for a zero-pressure-gradient time-dependent boundary layer flow are

$$\frac{\partial \rho}{\partial t}+\frac{\partial(\rho u)}{\partial x}+\frac{\partial(\rho v)}{\partial y}=0 \tag{1}$$

$$\rho\frac{\partial u}{\partial t}+\rho u\frac{\partial u}{\partial x}+\rho v\frac{\partial u}{\partial y}=\frac{\partial}{\partial y}\left(\mu\frac{\partial u}{\partial y}\right) \tag{2}$$

Here, length, time, and velocity are nondimensionalized with $\hat{L}$, $\hat{t}_0$, and $\hat{U}$, respectively, where $\hat{U}=\hat{L}/\hat{t}_0$. The dynamic viscosity is nondimensionalized with its ambient value. Equations (1) and (2) are reduced to incompressible form by the time-dependent Howarth transformation

$$\left.\begin{aligned} z&=\int_0^y \rho dy \\ w&=\rho v+\int_0^y \frac{\partial \rho}{\partial t}dy+u\int_0^y \frac{\partial \rho}{\partial x}dy \end{aligned}\right\} \tag{3}$$

With the additional assumption $\rho\mu=1$, one obtains

$$\frac{\partial u}{\partial x}+\frac{\partial w}{\partial z}=0 \tag{4}$$

and

$$\frac{\partial u}{\partial t}+u\frac{\partial u}{\partial x}+w\frac{\partial u}{\partial z}=\frac{\partial^2 u}{\partial z^2} \tag{5}$$

Equations (4) and (5) are now solved when there is no blowing at the surface and when there is blowing only in the pyrolysis zone, $0\le x\le x_p$.

2.1 No Blowing Along the Surface. The boundary conditions in this case are $u=w=0$ at $z=0$ and $u=1$ at $z=\infty$. Equations (4) and (5) are integrated from $z=0$ to $z=\infty$ and combined, using the conditions $w(0)=w(\infty)=0$. Into this combined integral momentum equation one substitutes

$$u=\operatorname{erf}\eta \tag{6}$$

where

$$\eta=\frac{z}{\Delta(x,\,t)} \tag{7}$$

Note that equation (6) satisfies both the initial and boundary conditions on u *and* the momentum equation at the surface and that the quantity $\Delta(x,\,t)$ is a measure of the boundary-layer thickness. It is found by solving the equation

$$\frac{\partial \Delta}{\partial t}+(\sqrt{2}-1)\frac{\partial \Delta}{\partial x}=\frac{2}{\Delta} \tag{8}$$

We substitute

$$\Delta=\sqrt{x}f(\xi) \tag{9}$$

where

$$\xi=x/t \tag{10}$$

so that equation (8) reduces to

$$\xi[\sqrt{2}-1-\xi]\,f'+\frac{(\sqrt{2}-1)}{2}f=\frac{2}{f} \tag{11}$$

which has a singularity at $\xi=\sqrt{2}-1$.[2] We note here that it is *not* necessary to define equations (9) and (10) in order to solve equation (8). By simply introducing $\Gamma=\Delta^2/2$ as the new dependent variable, it can be solved instead by the method of characteristics. When the two conditions, $\Delta(x,\,0)=0$ for $x\ge 0$, and $\Delta(x,\,t)$ *continuous* across the singular characteristic $x=(\sqrt{2}-1)t$, are applied, the solutions for u are given by equations (14) and (17).

The solution of equation (11) is

$$f^2=\frac{4}{\sqrt{2}-1}+C\left[\frac{\xi-(\sqrt{2}-1)}{\xi}\right]\operatorname{sgn}\{\xi-(\sqrt{2}-1)\} \tag{12}$$

where C is the constant of integration. Because of the singularity, this equation must be analyzed separately in the two regions $0\le\xi\le\sqrt{2}-1$, and $\xi>\sqrt{2}-1$.

[2] Equations (7), (9), and (10) are closely related to the similarity variables for the time dependent boundary layer equations, $\mu=z/\sqrt{x}$, $\xi=x/t$. In these variables equation (7) is simply $\eta=\mu/f(\xi)$. By defining the stream function $\psi=\sqrt{x}\,h(\xi,\,\mu)$ such that $u=\partial\psi/\partial z$ and $w=-\partial\psi/\partial x$, equation (5) becomes $h_{\mu\mu\mu}+hh_{\mu\mu}/2=\xi h_{\mu\xi}(h_\mu-\xi)-\xi h_\xi h_{\mu\mu}$; note that $u=h_\mu$ and $w=x^{-1/2}[(\mu/2)h_\mu-h/2-\xi h_\xi]$. By then substituting $u=\operatorname{erf}\eta$ into the equation for h and integrating from $\mu=0$ to $\mu=\infty$ one obtains equation (11).

Nomenclature

M_0 = measure of the blowing velocity, see equation (18)
Nu = Nusselt number
Pr = Prandtl number $=\hat{\mu}\hat{c}_p/\hat{\lambda}=\hat{\nu}/\hat{\alpha}$
Re_x = Reynolds number $=\hat{\rho}_\infty\hat{U}\hat{x}/\hat{\mu}_\infty=x$
t = time
T = temperature
u = streamwise velocity
U = streamwise velocity at leading edge and in the far field
v = transverse velocity
w = transverse mass flux
x = streamwise coordinate
y = transverse coordinate
z = transverse Howarth coordinate
α = thermal diffusion coefficient; $\hat{\alpha}=\hat{\lambda}/\hat{\rho}\hat{c}_p$
δ_0 = displacement thickness
$\Delta/\sqrt{\pi}$ = boundary-layer thickness, when $M_0=0$
η = z/Δ
Θ = nondimensional temperature $=T_f-1$
λ = thermal conductivity
μ = gas viscosity; similarity coordinate $=z/\sqrt{x}$
ν = kinematic viscosity
ξ = similarity coordinate $=x/t$
ρ = density

Subscripts

p = pyrolysis
∞ = ambient conditions

When $0 \le \xi < \sqrt{2}-1$, sgn $\{\bullet\} = -1$, and a bounded solution is possible only when $C = 0$. Thus

$$f = \frac{2}{\sqrt{\sqrt{2}-1}}, \quad 0 \le \xi < \sqrt{2}-1 \tag{13}$$

which gives

$$u = \operatorname{erf}\left(\frac{z}{2\sqrt{x}}\sqrt{\sqrt{2}-1}\right), \quad 0 \le \xi < \sqrt{2}-1 \tag{14}$$

In this region the solution approximates the steady Blasius boundary layer. The surface friction coefficient is obtained from equations (6), (7), and (14) by reintroducing dimensional variables and using $\hat{\tau} = \hat{\mu}[\partial \hat{u}/\partial \hat{y}]_{\hat{y}=0} = \hat{\rho}\hat{\mu}[\partial \hat{u}/\partial \hat{z}]_{\hat{z}=0}$. Thus

$$C_f(x) = \frac{0.726}{\sqrt{\mathrm{Re}_x}} \tag{15}$$

where $\mathrm{Re}_x = \hat{\rho}_\infty \hat{U}\hat{x}/\hat{\mu}_\infty$ is the streamwise Reynolds number. Comparison of equation (15) with the exact result of Blasius boundary-layer theory, $C_f = 0.664/\sqrt{\mathrm{Re}_x}$, indicates an overestimate of C_f by 9.4 percent. The nondimensional displacement thickness is given by $\delta_0 = \int_0^\infty (1-u)dz = \Delta/\sqrt{\pi}$. Resubstitution of dimensional quantities gives $\hat{\delta}_0/\hat{x} = 1.7533/\sqrt{\mathrm{Re}_x}$, which differs from the exact result, $\hat{\delta}_0/\hat{x} = 1.7208/\sqrt{\mathrm{Re}_x}$, by less than 2 percent.

When $\xi > \sqrt{2}-1$, sgn $\{\bullet\} = 1$. Far enough downstream of the origin, the influence of the leading edge must vanish, i.e., equation (5) must reduce to $u_t = u_{zz}$, whose solution is $u = \operatorname{erf}(z/2\sqrt{t})$. Comparison with equations (6), (7), and (12) requires $C = -4/(\sqrt{2}-1)$, whereby

$$f = \frac{2}{\sqrt{\xi}}, \quad \xi > \sqrt{2}-1 \tag{16}$$

Thus

$$u = \operatorname{erf}\left(\frac{z}{2\sqrt{t}}\right), \quad \xi > \sqrt{2}-1 \tag{17}$$

giving the *Rayleigh solution* for an infinite plate in the region $\xi > \sqrt{2}-1$.

Therefore, when there is no blowing, a steady-state solution that approximates the Blasius boundary layer is obtained in the upstream region, $0 \le \xi < \sqrt{2}-1$, while the transient Rayleigh solution for the impulsively started plate problem is obtained in the downstream region, $\xi > \sqrt{2}-1$. The dividing line, $x = (\sqrt{2}-1)t$, locates the instantaneous extent of influence of the leading edge. Because streamwise diffusion is neglected in the boundary layer approximation, this influence occurs in $x < (\sqrt{2}-1)t$ only through the convective acceleration term. The local acceleration there is negligible by comparison. Downstream of the dividing line, the influence of the leading edge vanishes, requiring the formation of a balance between the transient and diffusive terms in the momentum equation. At $\xi = \sqrt{2}-1$, the two solutions for u are continuous. However, the streamwise derivatives are discontinuous; in the steady boundary layer, $\partial u/\partial x = -(\eta/\sqrt{\pi x})\exp(-\eta^2)$, while $\partial u/\partial x = 0$ in the transient boundary layer.

We note that $u = \operatorname{erf}\eta$ is the solution of the *Rayleigh problem* (Stewartson, 1951), obtained from equation (5) by neglecting the second convective term, $w\partial u/\partial z$, and by applying the Oseen linearization, $u\partial u/\partial x \to \partial u/\partial x$, to the first. One finds $\eta = z/2\sqrt{t}$ in the region $\xi > 1$, which is exactly the result predicted by equation (17) in $\xi > \sqrt{2}-1$, and $\eta = z/2\sqrt{x}$ in the region $\xi < 1$, which should be compared with the predictions of equation (14), obtained in $\xi < \sqrt{2}-1$. The instantaneous extent of influence of the leading edge for the Rayleigh problem is clearly $\xi = 1$. We recall that the integral analysis of Stewartson gives $\xi = 1/2.65 = 0.3774$ as the streamwise extent of influence of the leading edge. This differs from the value $\xi = \sqrt{2}-1$, found here, by 8.9 percent. Consequently, the integral analysis of this section is in both qualitative and quantitative agreement with the analysis of Stewartson (1951); the changeover from t to x as principle independent variable occurs *between* the limits discussed by Stewartson, since $0.3774 < \sqrt{2}-1 < 1$. The use of error functions for the velocity distribution is clearly a compromise between the Oseen problem, whose exact solution is given by error functions, and the sine-function integral model of Stewartson (1951).

2.2 Blowing in the Pyrolysis Zone. It is assumed that the mass blowing rate in the pyrolysis zone (see Fig. 1) is given by

$$w(x, 0, t) = w_0(x, t) = \begin{cases} \dfrac{M_0}{\sqrt{x}}, & 0 \le x < x_p \\ 0, & x > x_p \end{cases} \tag{18}$$

This form for w_0 is commonly used when self-similar solutions of the boundary layer equations are sought (Williams, 1965). The assumed streamwise velocity distribution is

$$u = 1 - \frac{\operatorname{erfc}[\eta - g(\xi)]}{\operatorname{erfc}[-g(\xi)]} \tag{19}$$

Note that u satisfies the initial and boundary conditions imposed on equation (5). The function $g(\xi)$ is chosen to satisfy equation (5) at $z = 0$; thus

$$g(\xi) = \begin{cases} \dfrac{M_0}{\sqrt{x}}\dfrac{\Delta(x, t)}{2}, & 0 \le x < x_p \\ 0, & x > x_p \end{cases} \tag{20}$$

Note that g is constant when Δ is given by equation (14).

In this study it is assumed that the pyrolysis zone length, ξ_p, is less than $\sqrt{2}-1$. Since the pyrolysis front does not propagate downstream faster than the average streamwise boundary-layer velocity u_{avg}, this assumption is justifiable when $u_{\mathrm{avg}} < \sqrt{2}-1$. For the velocity field of equations (6) and (7), which is approximately the same as that of equation (19), $u_{\mathrm{avg}} = \delta_0^{-1}\int_0^{\delta_0} u dz = \pi^{-1/2}\int_0^{\pi^{-1/2}} \operatorname{erf} x dx = 0.3025 < \sqrt{2}-1$.

The solution in $0 \le \xi < \xi_p$ is found by integrating equation (5) over z, using equations (9), (18), (19), and (20). This produces a nonlinear first-order ordinary differential equation for $f(\xi)$, which has a singularity at $\xi = 0$. The simplest nonsingular solution is $f_0 = \text{const}$, given by

$$f_0^2 = 4\left\{\frac{\sqrt{\pi}g(1+\operatorname{erf} g) + e^{-g^2}}{\sqrt{2}\dfrac{1+\operatorname{erf}\sqrt{2}g}{1+\operatorname{erf} g} - e^{-g^2}}\right\}, \quad 0 \le \xi < \xi_p \tag{21}$$

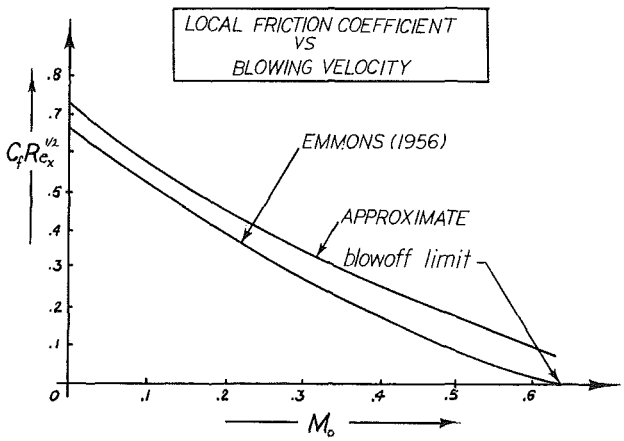

Fig. 2 Plot of the skin friction coefficient $C_f\ \mathrm{Re}_x^{1/2}$ versus the nondimensional mass blowing rate M_0

where $g = M_0 f_0/2$ [see equations (9) and (20)].

In $\xi_p \le \xi < \sqrt{2}-1$, $\text{sgn}\{\bullet\} = -1$, and the solution for f is obtained from equation (12) (with $\text{sgn}\{\bullet\} = -1$) by evaluating C at ξ_p, where $f = f_0$. When $\xi \ge \sqrt{2}-1$, f is given by equation (16). Therefore the velocity field over the entire range of ξ is given by

$$u = 1 - \frac{\text{erfc}\left[\dfrac{z}{\sqrt{x f_0}} - \dfrac{M_0 f_0}{2}\right]}{\text{erfc}\left[-\dfrac{M_0 f_0}{2}\right]}, \qquad 0 \le \xi < \xi_p$$

$$u = \text{erf}\left[\frac{z}{\sqrt{x}\left[\dfrac{4}{\sqrt{2}-1} + \dfrac{\xi_p}{\xi}\dfrac{\sqrt{2}-1-\xi}{\sqrt{2}-1-\xi_p}\left({f_0}^2 - \dfrac{4}{\sqrt{2}-1}\right)\right]^{1/2}}\right],$$

$$\xi_p \le \xi < \sqrt{2}-1$$

$$u = \text{erf}\left[\frac{z}{2\sqrt{t}}\right], \qquad \xi > \sqrt{2}-1 \tag{22}$$

Note that the *pyrolysis zone is in the steady state*, while the preheat zone, $\xi > \xi_p$, contains the *transient effects of preheating*. Note also that the velocities are continuous across $\xi = \sqrt{2}-1$, but discontinuous across the pyrolysis front, where the transition to zero blowing occurs. This discontinuity is $0(M_0 f_0)$ as $M_0 f_0 \to 0$.

A plot of the nondimensional mass blowing rate M_0 versus the skin friction coefficient $C_f\sqrt{\text{Re}_x}$ is shown in Fig. 2. This plot compares the approximate results obtained in the pyrolysis zone with the exact predictions of boundary layer theory (Emmons, 1956). The percentage difference between the exact and the approximate results is seen to increase as the blowing velocity increases. It is apparent that the approximate analysis does not produce a blowoff limit.

3 Impulsively Started Plate With Unequal Gas and Plate Temperatures

Consider a solid, stationary plate and a nonreacting, stationary gas, both with initial temperature $T = 1$. At $t = 0$, and starting at the upstream edge, gas with temperature $T_f > 1$ is blown across the surface, whose temperature remains constant. Because of the boundary layer assumption there is no streamwise diffusion of heat; therefore, a discontinuity in T propagates downstream with velocity $dx/dt = 1$. When $x > t$ the solution is $T = 1$. By defining $\Theta = T_f - T$, and applying the Howarth transformation of equations (3), the compressible boundary layer form of the energy equation reduces to

$$\frac{\partial \Theta}{\partial t} + u\frac{\partial \Theta}{\partial x} + w\frac{\partial \Theta}{\partial z} = \frac{1}{\text{Pr}}\frac{\partial^2 \Theta}{\partial z^2} \tag{23}$$

The initial and boundary conditions are $\Theta(x, z, 0) = 0$, $\Theta(0, z, t) = T_f - 1$, $\Theta(x, 0, t) = T_f - 1$ and $\Theta(x, \infty, t) = 0$. Now assume [compare with equation (6)]

$$\Theta = [T_f - 1]\text{erfc}\left[\frac{z}{A(x, t)}\right] \tag{24}$$

where

$$A(x, t) = \sqrt{x}a(\xi) \tag{25}$$

which satisfies the initial and boundary conditions, as well as equation (23) at $z = 0$. Integration of equation (23) over z, use of $w(0) = w(\infty) = 0$, followed by substitution of equations (6), (7), (24), and (25), gives

$$\xi\left[\frac{a}{\sqrt{f^2 + a^2}} - \xi\right]a' + \xi f'\left[\frac{f}{\sqrt{f^2 + a^2}} - 1\right] + \frac{\sqrt{f^2 + a^2} - f}{2} - \frac{2}{a\text{Pr}} = 0 \tag{26}$$

Note that when $f = a$ and $\text{Pr} = 1$ this reduces to equation (11).

Because of the similarity in the equations for u [equation (5) with no blowing] and Θ [equation (23)], solutions are obtained here for Θ in the steady convective-diffusive boundary layer region, $0 < \xi < \sqrt{2}-1$, and in the unsteady transient-diffusive region, $\sqrt{2}-1 < \xi < 1$. In the first region f is constant and is given by equation (13); therefore the simplest solution of equation (26) that is bounded at the singular point $\xi = 0$ is $a = \text{const.}$, obtained by solving the quartic equation $[\sqrt{f^2 + a^2} - f]/2 = 2/(a\text{Pr})$. Since the Reynolds analogy requires that the thermal and velocity boundary layers be identical when $\text{Pr} = 1$, the proper root gives $\lim_{\text{Pr}\to 1} a = f$. Thus

$$a = \frac{1}{\sqrt{\text{Pr}}}\left[\sqrt{A} + \sqrt{-A + \sqrt{4A^2 + 16}}\right] \tag{27}$$

where

$$A = \left(\frac{\text{Pr}f^2}{2} + \sqrt{\frac{\text{Pr}^2 f^4}{4} + \frac{64}{27}}\right)^{1/3} + \left(\frac{\text{Pr}f^2}{2} - \sqrt{\frac{\text{Pr}^2 f^4}{4} + \frac{64}{27}}\right)^{1/3} \tag{28}$$

An estimate for the accuracy of these results is obtained by calculating the streamwise Nusselt number and comparing with the boundary layer calculation. In the nondimensional variables used here, Nu_x is defined as

$$\text{Nu}_x = \frac{x}{T_f - 1}\left(\frac{\partial T}{\partial z}\right)_{z=0} = \frac{2}{a}\sqrt{\frac{x}{\pi}} = \frac{2}{\sqrt{\pi}}\frac{\sqrt{\text{Re}_x}}{a} \tag{29}$$

Using $\text{Pr} = 3/4$ gives $\text{Nu}_x = 0.326\sqrt{\text{Re}_x}$, which differs from the exact value $\text{Nu}_x = 0.302\sqrt{\text{Re}_x}$ (Schlichting, 1979) by 8.2 percent. When $\text{Pr} = 1$ this formulation gives $\text{Nu}_x = 0.363\sqrt{\text{Re}_x}$, which overestimates the exact result, $\text{Nu}_x = 0.332\sqrt{\text{Re}_x}$, by 9.3 percent.

In the transient region, $\sqrt{2}-1 < \xi < 1$, one puts $f = 2/\sqrt{\xi}$ into equation (26). The solution for a is then $a(\xi) = 2/\sqrt{\text{Pr}\xi}$, which gives the Rayleigh solution for Θ. Along the line $\xi = \sqrt{2}-1$ the solutions are continuous *only when Pr = 1*. For $\text{Pr} = 3/4$, the steady boundary layer solution at $\xi = \sqrt{2}-1$ gives $\Theta = (T_f - 1)\,\text{erfc}\,(0.449\, z/\sqrt{t})$, while the downstream solution gives $\Theta = (T_f - 1)\text{erfc}(0.433 z/\sqrt{t})$. As the Prandtl number decreases the discontinuity increases.

When the velocity field with blowing is employed in the convective terms of equation (23), the pyrolysis (blowing) region will be steady, while the downstream (preheat) region will be unsteady. The discontinuity of Θ for $\text{Pr} \ne 1$ will remain. The assumed solution for Θ must resemble equation (19).

4 Discussion and Conclusions

The solution for the velocity field of Section 2 can be used without modification in the governing equations for the general wind-aided flame spread model, because for zero pressure gradient boundary layer flows the calculation of the velocity field is decoupled from the calculation of the species and temperature fields. The comparisons between the exact Blasius solution and the integral solutions in Section 2.1 show good agreement, although better agreement for C_f (2.7 percent as opposed to 9.4 percent) can be obtained by using simple polynomials instead of the error function (Schlichting, 1979). However, this does not diminish the validity of the results in Sections 2.1 and 2.2, where it is shown that the error function velocity profile of equation (6) is the *exact* solution of

equation (5) under the Oseen linearization, which is itself a very useful approximation in the study of wind-aided flame spread. From Fig. 2 one observes that the accuracy of the integral approximation decreases as the blowing rate increases. Note, however, that the accuracy of the boundary layer assumptions *also* worsens as the blowing rate increases. Blowoff is not obtained for the integral analysis of Section 2.2 because $\partial u/\partial z > 0$ is forced by the chosen velocity profile of equation (19).

For the solution of the general problem it is the temperature field that presents the most difficulty, because the equations in the solid and the gas are coupled through the interface boundary conditions. When radiation is neglected the general equations of wind-aided flame spread can be solved in terms of the similarity coordinates $\xi = x/t$ and $\mu = z/\sqrt{x}$ (Carrier et al., 1980), although the blowing velocity must then have an inverse square root dependence on x [see equation (18)]. By additionally employing the Oseen linearization for the gas flow field, this procedure led finally to a complicated set of integral equations that were solved numerically (Carrier et al., 1980, 1983). In the simplified model of Section 3, none of these complications are addressed. Good agreement for $\Pr = 3/4$ is obtained between the heat transfer model analyzed here with integral methods, and the exact results of boundary layer theory. The spatial and temporal coordinate dependence of the temperature is dictated by, and across $\xi = \sqrt{2} - 1$ is identical to, that for the velocity field, i.e., it is steady for $\xi < \sqrt{2} - 1$, unsteady for $\xi > \sqrt{2} - 1$.

Thus, the principal result of this investigation is that the velocity field for the impulsively started plate with or without blowing, and the temperature field for the impulsively started plate with unequal gas and plate temperatures, both exhibit steady-state behavior in the pyrolysis zone ($0 \le x \le x_p$) and transient behavior in the preheat zone ($x > x_p$). We note that this is an approximate result, subject to the limitations of integral analysis, which often very successfully extracts global behavior while sacrificing local rigor. As emphasized by Stewartson (1951), the transition from spatial to temporal dependence is *not stepwise*, but rather is continuous, with the influence of ξ on the velocity field dying out as $\exp(-0.03/\xi^3)$ as $\xi \to 0$. This theoretically predicted exponential decay is confirmed by the finite-element analysis of Tadros and Kirkhope (1978) who also show that for $t/x \simeq 3$ (i.e., $\xi \simeq 0.333$) the initial Rayleigh solution has settled into the Blasius solution. We believe that the neglect of such local behavior is justifiable when the purpose of the analysis is to extract the correct overall behavior and to develop useful predictive formulas, while minimizing computational and calculational effort.

Consequently, for wind-aided flame spread the problem in the pyrolysis zone $0 \le x \le x_p$ can be viewed as a steady-state Blasius boundary layer with blowing, while the problem in the preheat zone, $x > x_p$, can be assumed transient and to contain no streamwise (x) coordinate dependence. This suggested to the authors that instead of performing an integral analysis, the assumption of a steady state in the pyrolysis zone and a transient response in the preheat zone would be made from the outset. When the Oseen flow assumption is employed the mass, momentum, species, and energy equations can be solved *exactly* in each zone, and then matched across the transition line. We note that the Oseen linearization is a very good approximation for flow-assisted flame spread, since the flame is generally well outside the velocity boundary layer.

Acknowledgments

Support provided for the first author by an NRC postdoctoral research fellowship during 1983–1985 is greatly appreciated. Partial support of the first author has also been provided by USDA grant No. 86-FSTY-9-90192.

References

Carrier, G. F., Fendell, F. E., and Feldman, P. S., 1980, "Wind-Aided Flame Spread Along a Horizontal Fuel Slab," *Combustion Science and Technology*, Vol. 23, pp. 41–78.

Carrier, G. F., Fendell, F. E., and Fink, S., 1983, "Towards Wind-Aided Flame Spread Along a Horizontal Charring Slab: the Steady-Flow Problem," *Combustion Science and Technology*, Vol. 32, pp. 161–209.

Emmons, H. R., 1956, "The Film Combustion of Liquid Fuel," *Zeitschrift fur Angewandte Mathematik und Mechanik*, Vol. 36(2), pp. 60–71.

Fernandez-Pello, A. C., 1984, "Flame Spread Modeling," *Combustion Science and Technology*, Vol. 39, pp. 119–134.

Fernandez-Pello, A. C., and Hirano, T., 1983, "Controlling Mechanisms of Flame Spread," *Combustion Science and Technology*, Vol. 32, pp. 1–31.

Schlichting, H., 1979, *Boundary-Layer Theory*, McGraw-Hill, New York.

Sirignano, W. A., 1974, "Theory of Flame Spread Above Solids," *Acta Astronautica*, Vol. 1, pp. 1285–1299.

Stewartson, K., 1951, "On the Impulsive Motion of a Flat Plate in a Viscous Fluid," *Quarterly Journal of Mechanics and Applied Mathematics*, Vol. IV, Pt. 2, pp. 182–198.

Stewartson, K., 1960, "The Theory of Unsteady Boundary Layers," *Advances in Applied Mechanics*, Vol. 6, Academic Press, New York, pp. 1–37.

Tadros, R. N., and Kirkhope, J., 1978, "Unsteady Boundary Layer Over an Impulsively Started Flat Plate Using Finite Elements," *Computers and Fluids*, Vol. 6, pp. 285–292.

Experiments for the Determination of Convective Diffusion Heat/Mass Transfer to Burner Rig Test Targets Comparable in Size to Jet Stream Diameter

G. J. Santoro

S. A. Gökoğlu

NASA Lewis Research Center,
Cleveland, OH 44135

The application of a recently formulated vapor transport theory to predict deposition rates of corrosive salts from alkali-seeded combustion gases of a small-capacity, high-velocity, atmospheric-pressure burner rig was hampered by the relatively large dimensions of the cylindrical deposit collector compared to the diameter of the combustion gas stream. The relative dimensions led to a highly nonadiabatic combustion gas flow around the collector and necessitated two series of experiments. In the first series, mass transfer coefficients were determined by utilizing the naphthalene sublimation technique. The second series of experiments determined the dilution effect on the sodium species concentrations due to the entrainment of ambient air. This second series involved the measurement of the temperature variation along the surface of the collector under steady-state conditions. Vapor deposition rates were determined exploiting this information and the results were found to compare favorably with experimentally obtained rates.

Introduction

Accelerated blade and vane failures can occur in the hot section of gas turbine engines due to the deposition of corrosive salts resulting from trace impurities in the combustion gases (hot corrosion). This problem prompted the investigation of the deposition rates occurring on internally air-cooled, inert, cylindrical collectors in the cross stream of the combustion products of a small-capacity, high-velocity, atmospheric-pressure burner rig seeded with sodium salts (Santoro et al., 1984; Santoro et al., 1985; Gökoğlu, 1984).

Our intention was to compare the measured vapor transport deposition rates with a recently formulated comprehensive chemically frozen boundary layer (CFBL) vapor transport theory (Rosner et al., 1979; Gökoğlu et al., 1984). The original procedure for introducing the contaminant into the burner rig consisted of air atomization of various sodium salt solutions into the combustor. This resulted in inertial impaction of solution droplets onto the collector, precluding our intended comparison. To insure that the sodium species were entirely in the vapor phase in the combustor, a new procedure was adopted that involved physically mixing a solution of sodium acetate in ethanol with Jet A-1 fuel in the cavity of the fuel nozzle and spraying this mixture through the fuel nozzle into the combustor. However, dimensional restraints of the experimental setup required additional information because the size of the deposition collector was large (1.90 cm diameter by 1.27 cm high cylinder) relative to the 2.54 cm diameter of the combustion gas jet stream. The minimum size of the collector is dictated by its internal air cooling feature, which allows the collector temperature to be controlled anywhere from beyond the dew point temperature of sodium sulfate down to 500°C while maintaining a constant fuel-to-air ratio (constant flame temperature and chemistry of the sodium species vapors). Were the collector totally immersed in the jet stream (a "perfect" cylinder in crossflow situation), the mass transfer coefficient would be readily calculable and the local dopant species concentration would be equal to that in the burner exit nozzle. The dimensional relationship however results in a highly nonadiabatic combustion gas flow and a nonuniform mainstream gas concentration around the collector due to the entrainment of ambient air (see Fig. 1). Consequently the local thermodynamic and transport properties become angle dependent. This angular dependency necessitated additional experiments to provide the mass transfer coefficient and the dilution effect of the dopant species in the mainstream as input to the CFBL theory.

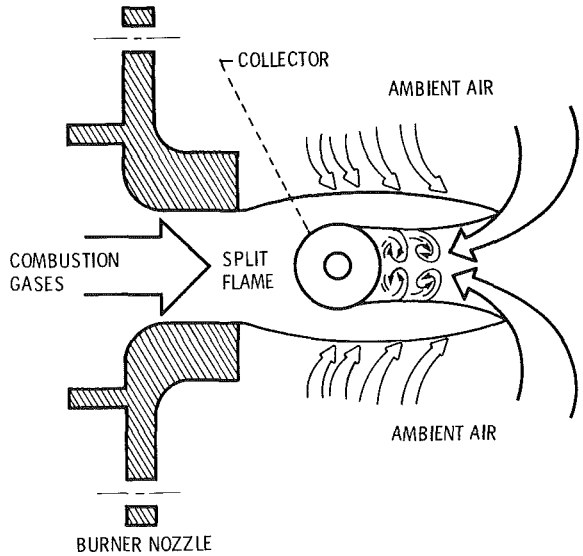

Fig. 1 Schematic of burner rig and collector configuration showing ambient air entrainment; relative positions and dimensions reflect real experimental setup

[1] Case Western Reserve University, Department of Mechanical and Aerospace Engineering, Cleveland, OH 44106; NASA Resident Research Associate; Mem. ASME.

Contributed by the Heat Transfer Division and presented at the ASME Winter Annual Meeting, Anaheim, California, December 1986. Manuscript received by the Heat Transfer Division September 5, 1986. Keywords: Combustion, Condensation, Forced Convection.

A series of experiments to determine the mass transfer coefficient was performed utilizing the naphthalene sublimation technique. The dilution effect was ascertained by measuring the temperature variation along the surface of the collector under steady-state conditions. The discharge coefficient of the burner exit nozzle was also determined to provide values of the jet approach velocities, i.e., to obtain accurate Reynolds numbers. Finally, vapor deposition rates were measured and their values compared with those predicted by the CFBL theory. The analytical techniques employed in this application of the theory, utilizing the transport parameters derived from the experiments presented here, have been reported in detail elsewhere (Gökoğlu and Santoro, 1987) and are only outlined in this report for completeness. The predicted vapor deposition rates compared favorably with measured rates.

Experimental Procedures

Discharge Coefficient of the Burner Exit Nozzle. The correct calculation of the jet approach velocities and, therefore, the Reynolds numbers requires values for the discharge coefficient of the burner exit nozzle. These values were experimentally determined as a function of Reynolds number by measuring the differences between the stagnation and barometric pressures. A pitot tube and sensitive differential pressure (± 2 psid) transducer were used for these measurements. Ambient pressure was recorded using a 0–20 psia transducer. The windward stagnation point of the collector was 1.27 cm from the burner exit nozzle. Therefore, the leading surface of the collector was well within the core of the jet (isentropic zone of the flame), i.e., the free-stream approach velocity and temperature did not change in this region. These experiments were carried out at ambient temperatures (as opposed to flame temperatures) so that one can apply the isentropic jet expansion relationships more confidently. Hence, the free-stream velocities inferred from Δp measurements were the same at both the burner exit and the cylinder locations. The jet airstream temperature was measured with a sonic temperature probe. The pitot probe and the sonic temperature probe were attached one above the other on the vertical axis of a three-axis remotely controlled slide mechanism. Figure 1 shows the relative dimensional configuration of the burner nozzle used in all the testing reported here. Equivalent aerodynamic conditions at flame temperature (i.e., the same Reynolds number) required mass flow velocities of about 7 g/s under ambient temperature conditions, the lower sensitivity limit of our pressure difference measurements.

Naphthalene Sublimation From Cylindrical Targets. Two sets of naphthalene sublimation experiments were conducted, one set in which the entire cast naphthalene target cylinder was exposed to the flow (full-cylinder experiments) and another set in which all but a predetermined angular segment of the surface of the target cylinder was covered by cellophane tape. The exposed segment faced the jet stream (segmented cylinder experiments). In both series of experiments the cast naphthalene cylinders were enclosed in a small insulated tunnel attached to the exit nozzle of the burner so as to maintain near equal temperature between the jet stream and the ambient air (within 0.5°C). The full-cylinder tests provided the data to determine the perimeter-averaged mass transfer coefficient, while the segmented cylinder tests yielded data to obtain the angular dependence of the mass transfer coefficient by varying the angle of the exposed surface segment.

Sublimation Cylinder Construction. The construction particulars and rigid tolerances duplicated those used by Sparrow et al. (1984), except the overall dimensions were scaled to our requirements. The components include the target element, the upper and lower guard sections that flank the target element and are themselves flanked by aluminum sections, and a base section for attachment to the rig. The entire assembly is held together by a center rod screwed into the base and fastened on top with a knurled nut. The overall length was intended to represent an infinitely long cylinder with respect to the jet airstream diameter from the burner rig. The cast target element dimensions duplicated those of the collectors employed in the deposition runs. Each guard element provided a naphthalene surface 1.90 cm high by 1.90 cm in diameter. The function of the guard elements was to eliminate the effects of axial interactions as discussed by Sparrow et al. (1984).

Naphthalene Casting Procedures. A casting procedure described by Sparrow et al. (1984) was followed to produce the naphthalene target and guard elements. A cylindrical brass sleeve was slipped over the respective element to serve as the outer boundary and create a mold cavity. Molten naphthalene was then poured into the cavity through a small hole in the upper face of the element, the pouring operation being facilitated by the use of a funnel. The air displaced from the cavity escaped through a second hole, also equipped with a funnel. Once the naphthalene had solidified, the element was readily separated from the sleeve by applying pressure from below. The inner surface of the sleeve had been lapped to a mirror finish and the finish of the exposed surface of the naphthalene was of comparable quality. Each completed cast cylinder was

Nomenclature

A = area
D = (Fick) diffusion coefficient
DC = discharge coefficient
d = diameter
$F\{\text{turb}\}$ = function describing mainstream turbulence
j = deposition rate
j'' = mass (deposition) flux
L = characteristic length (diameter of cylindrical collector)
l = length
M = molecular weight
Ma = Mach number = $U_\infty/U_{\text{sonic}}$
m = mass flowrate = ρUA
Nu = mass transfer Nusselt (Sherwood) number
Nu_θ = local (θ-dependent) Nusselt number
P = pressure
R = universal gas constant
Re = Reynolds number
Sc = Schmidt number = $\mu/(\rho D)$
T = absolute temperature
U = velocity
γ = ratio of heat capacity at constant pressure to heat capacity at constant volume
θ = angle from the windward stagnation point
μ = dynamic viscosity of gas
ρ = density of gas
ω = mass fraction of transported species
$\bar{\ }$ = averaged quantity
$\{\ \}$ = function of argument inside parenthesis

Subscripts

amb = ambient conditions
e = local outer edge of boundary layer
eff = effective
l = leeward stagnation point
o = windward stagnation point
w = at the surface (wall)
∞ = upstream infinity

placed in its own storage container designed to minimize the inner air space and thus limit the loss of naphthalene by sublimation during storage.

Sublimation Testing Procedure. Each test run was initiated with freshly cast naphthalene sections. The assembled cylinder was removed from its storage container immediately prior to insertion into a 20.3 cm diameter by 43.2 cm long insulated tunnel, which was attached to the exit nozzle of the burner. The cylinder was secured to a shaft extending through the wall of the tunnel, thus positioning the cylinder so that its target element was in the same position with respect to the burner nozzle as the collector would be in the deposition runs. Then the cast cylinder was shrouded by an outer concentric tube. The tunnel access door was fastened shut for the remainder of the operation and the desired airflow rate established. When the temperature of the air jet stream and ambient air in the tunnel was equilibrated, the shroud was lowered, thereby exposing the naphthalene to the airflow. Equilibrium was considered established when the reading of a precision thermometer in the combustor of the burner was within 0.5°C of that of an identical thermometer located in the tunnel. The smallest scale reading of these thermometers was 0.2°C. The length of time the naphthalene was exposed to the airflow was limited so that the recession of the diameter of the target element would not exceed about 0.3 percent of the initial diameter, an amount which can be neglected. Thus the initial diameter was taken as the characteristic dimension in subsequent calculations. To accommodate this restriction, the interval of exposure varied from about 5 min for high flow rates (approximately 21 g/s) and temperatures (approximately 25°C) to about 30 min for low flow rates (approximately 7 g/s) and temperatures (approximately 19°C).

The amount of mass transfer was determined by differencing the weighings made of the target section before and after the run. These weighings utilized an electronic balance with a smallest scale reading of 10^{-5} g. Prior to actual sublimation testing, handling and storage weight losses of the target element were found to be within the precision of the balance; this includes the time spent within the shroud of maximum airflow and run time interval.

The testing procedures for the segmented cylinder experiments were equivalent to the full-cylinder experiments except that prior to the initial weighing, the target section was carefully taped so as to expose only a windward angular segment of naphthalene surface. The exposed surface was centered on the stagnation point. The precise arc length of the exposed naphthalene was determined by carefully measuring its chord length with a caliper, where

$$l_{\text{arc}} = \frac{\pi d}{180 \text{ deg}} \sin^{-1}\left(\frac{l_{\text{chord}}}{d}\right) \quad (1)$$

The reproductibility of the data was segment angle dependent, being better for large angles. There were two contributing factors for this dependency. First, less weight loss could be permitted to occur at the smaller angles and still maintain the allowable radial thinning of the target. The second factor was due to the perturbation of the boundary layer flow around the target by the ends of the tape (at the tape end–naphthalene junctions). At the stagnation point we estimated the boundary layer thickness for a Reynolds number of 1.5×10^4 to be about a factor of five times the thickness of the tape (approximately 70 μm). This factor increases as a function of distance from the stagnation point because of the increasing thickness of the boundary layer. Thus, both the percentage of surface naphthalene affected by the tape edge perturbation, and the percentage of the boundary layer perturbed, decreased with increase in the angle of the exposed naphthalene segment. We found we could gather acceptable data at segment angles of $\geq$ 40 deg.

Angular Variation of Collector Surface Temperature. The entrainment of ambient air around the relatively large deposition collector resulted in cooling of the mainstream temperature and dilution of the sodium dopant species concentrations. An indirect approach was taken to determine the angular variation of the dopant species concentration. Experiments were performed to measure the angular variation of collector surface temperatures. The collectors were fabricated of materials with different thermal conductivities and exposed to different combustion gas temperatures under steady-state conditions at different Reynolds numbers. When the normalized collector surface temperatures were plotted against angle for the burner operating range of interest, a "universal" curve emerged. The curve was independent of collector material, Reynolds number, and approach gas temperature. We then assumed that the mainstream had the same normalized temperature distribution and that this distribution reflected the dopant species concentrations relative to their concentrations as they left the burner exit nozzle.

Surface temperature variation was measured for both Pt–20 percent Rh collectors, normally utilized in the deposition runs, and alumina collectors of identical dimensions. The positions of the collectors with respect to the exit nozzle of the burner were identical to the position of the deposition collectors in the deposition runs. The internal cooling air feature of the collector was not utilized. The collector temperature was sensed by a thermocouple embedded in the wall. The angular position of the thermocoupled collector was varied with respect to the direction of the jet stream by rotating the shaft supporting the collector.

A typical run consisted of setting the collector at the zero angle, allowing the burner to come to thermal equilibrium at the desired burner pressure and fuel/air flows, measuring the combustion gas temperature with a sonic temperature probe, swinging the burner into position to heat the collector, recording the steady-state collector temperature, rotating the collector to the next angle, recording its steady-state temperature, continuing this procedure for all angles from 0 to 180 deg in both directions, swinging the burner out of the heat position and finally rechecking the combustion gas temperature. The burner parameters were then changed (new mass flow and gas temperature) for the start of another run. In this way angular temperature variation data were gathered for Reynolds numbers from 1.4×10^4 to 1.8×10^4 and gas temperatures from 1700 to 2000 K on both the metallic and ceramic collectors.

Vapor Phase Deposition. The deposition runs were conducted as described by Santoro et al. (1985), except for the method used to inject the sodium salt solutions into the combustor. In order to eliminate the deposition of molten droplets as occurred in the previous method, i.e., to insure that the sodium species are entirely vaporized in the combustor, a dilute solution of sodium acetate in ethanol was pumped into the fuel nozzle cavity to be mixed there with the jet A-1 fuel. The mixture of fuel and sodium acetate–alcohol solution was sprayed through the fuel nozzle, mixed with swirling preheated air (140°C) and burned. The volume flow ratio of alcohol to fuel was 0.05. The salt–alcohol solution flow rate was determined by a graduated cylinder reservoir.

Some of the sodium fed into the burner deposited as acetate on the inner walls of the burner liner (5.08 cm dia) at its cooled end. Also a negligibly small amount was found as sodium sulfate on the hot end of the liner and on the throat of the exit nozzle. From chemical analyses of the deposit on the liner,[2] we estimated that about 25 percent of the total sodium injected was extracted from the combustion gases, yielding a

[2]The method of analysis was the inductively coupled plasma atomic emission spectrometry.

corrected typical sodium concentration of 5 ppm with respect to the air mass flow of 25 g/s. Other typical operating parameters are: 30 min run times, Mach number 0.3 (Δp = 1 psig across the burner exit nozzle), Reynolds number 1.7 × 10^4, fuel-to-air mass flowrate ratio of 0.035, and combustion gas temperature of 1800 K. In all cases the Pt–20 percent Rh cylindrical collectors were 1.90 cm diameter by 1.27 cm high. The collector temperature was varied from 600 to 900°C by means of its internal air impingement cooling feature. The deposit on the collector in all cases was essentially sodium sulfate resulting from the excess presence of sulfur impurity available in the fuel (0.02 to 0.06 percent). The amount of deposit was determined both by weight change and by chemical analyses (see footnote 2). Frequent cleaning of the combustor liner insured that salt deposit buildup would not become so thick as to shed the deposit back into the combustion gases.

Reduction of Data and Experimental Results

Discharge Coefficient Data Reduction and Results. The discharge coefficient of the burner exit nozzle is defined as the ratio of the effective area of the jet nozzle through which gas with a uniform velocity profile passes to the geometric area, i.e.,

$$DC = \frac{A_{\text{eff}}}{A_{\text{nozzle}}} \tag{2}$$

The isentropic jet expansion relationship can be applied at ambient conditions to obtain the jet exit velocity

$$U_\infty = U_{\text{sonic}} \left\{ \left[\left(1 + \frac{\Delta P}{P_\infty} \right)^{\frac{(\gamma-1)}{\gamma}} - 1 \right] \frac{2}{\gamma - 1} \right\}^{1/2} \tag{3}$$

where $\Delta P = P_o - P_\infty$ and $U_{\text{sonic}} = (\gamma RT/M)^{1/2}$. For a known gas mass flow rate m, using the ideal gas law, the effective nozzle area is

$$A_{\text{eff}} = \frac{RT_\infty}{P_\infty M} \frac{\dot{m}}{U_\infty} \tag{4}$$

We measured ΔP, P_∞, and m under ambient conditions and at equivalent aerodynamic conditions of interest at flame temperatures (same Reynolds numbers). Measuring ΔP instead of P_o greatly reduced the experimental uncertainty as confirmed by an error analysis.

Figure 2 is a plot of the discharge coefficient as a function of Reynolds number. Data were accumulated at Reynolds numbers well above the range of immediate interest to the problem. Note that only in this figure the Reynolds numbers are given with respect to the diameter of the throat of the burner exit nozzle.

Sublimation Data Reduction and Results. In the sublimation experiments the mass transfer coefficient was not affected by the entrainment of ambient air as its temperature and the temperature of the jet stream were kept to within 0.5°C. Thus the sublimation of naphthalene from the target cylinder was dependent on the jet stream temperature.

The measured naphthalene weight change data from both the full and the segmented sublimation runs were reduced to their respective dimensionless average mass transfer coefficients as follows. In the basic mass flux equation

$$j'' = \frac{\rho D}{L} \cdot \overline{\text{Nu}} \cdot \omega_w \tag{5}$$

The following substitutions are made: $\omega_w = (P_{\text{naph}}/P_\infty) \cdot (M_{\text{naph}}/M)$, $D = \mu/(\rho \text{Sc})$, and $L = d$ where P_{naph} is the vapor pressure of naphthalene at the prevailing temperature, M_{naph} is the molecular weight of naphthalene, and M is the mean molecular weight of gas. Multiplying through by A, the area of exposed naphthalene, and rearranging yields

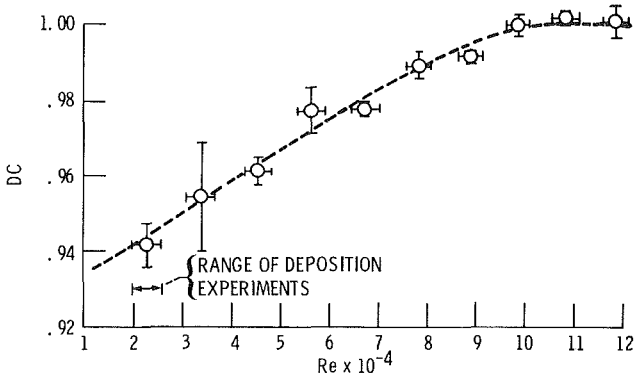

Fig. 2 Burner exit nozzle discharge coefficient as a function of Reynolds number based on nozzle diameter

$$\overline{\text{Nu}} = \frac{(j)(\text{Sc})(P_\infty)(\bar{M})(d)}{(A)(\mu)(P_{\text{naph}})(M_{\text{naph}})} \tag{6}$$

where $(A)(j'') = j$ is the measured target weight change rate. In addition to j, the barometric pressure and ambient temperatures were recorded. P_{naph} was obtained from the published tables (Ambrose et al., 1975; Camin and Rossini, 1955; Sogin, 1958; Vargaftik, 1975) at the measured ambient temperature.

The segmented cylinder naphthalene sublimation data collected within the Reynolds range of the deposition experiments allowed the determination of the effect of mainstream turbulence. The details were presented by Gökoğlu and Santoro (1987). Within this Reynolds number range, it was found that mainstream turbulence did not affect heat and/or mass transfer rates.

The experimental mass transfer coefficients were compared to correlations for cylinder-in-crossflow situations. Two correlations were used: the correlation by Whitaker (1976) for the full cylinder

$$\overline{\text{Nu}} = (0.4\ \text{Re}^{1/2} + 0.06\ \text{Re}^{2/3})\text{Sc}^{0.38} \tag{7}$$

and the modified stagnation point Nusselt number describing the stagnation point region for the segmented cylinder (Gökoğlu and Santoro, 1987)

$$\overline{\text{Nu}}_\theta = \text{Nu}_o \left\{ 1 - \frac{1}{4} \left(\frac{\theta}{\left(\frac{\pi}{2}\right)} \right)^3 \right\} \qquad 0 \le \theta \le \frac{\pi}{2} \tag{8}$$

where

$$\text{Nu}_o = 1.14\ \text{Re}^{1/2}\text{Sc}^{0.35} \tag{9}$$

Recall from the experimental procedure section that the angular dependence of the mass transfer was derived from segmented cylinder sublimation experiments where arc lengths of the exposed naphthalene were expressed by their subtended angles. What was actually measured then was the average mass transfer over the angles of the exposed naphthalene. Thus the equation representing the angular relationship

$$\text{Nu}_\theta = \text{Nu}_o \left[1 - \left(\frac{\theta}{\left(\frac{\pi}{2}\right)} \right)^3 \right] \qquad 0 \le \theta \le \frac{\pi}{2} \tag{10}$$

must be integrated to yield the average values encompassing the segments of exposed naphthalene for comparison with the

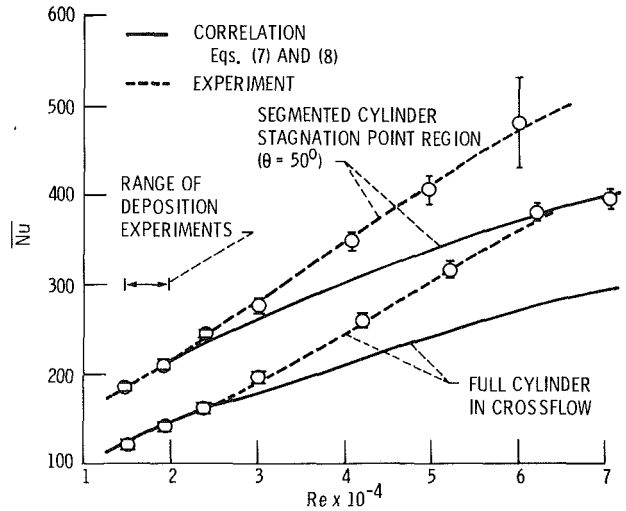

Fig. 3 Full and segmented (θ = 50 deg) cylinder mass transfer Nusselt number as a function of Reynolds number (based on cylinder diameter)

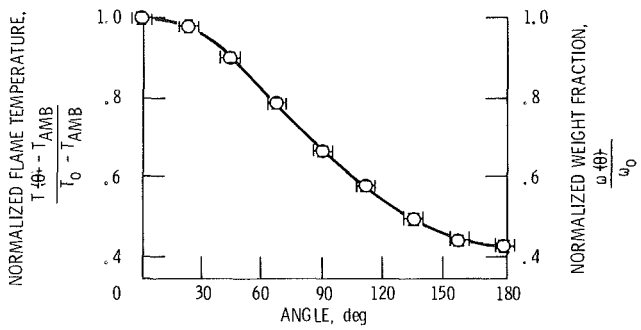

Fig. 4 Mainstream temperature and species mass fraction distribution around the collector as obtained from surface temperature measurement of collectors made of different materials for the range of operation of burner rig

experimental data. The integration of equation (10) is equation (8).

The quality of data from full-cylinder tests is better than from segmented cylinder tests because of the influence of the tape on the boundary layer flow as explained earlier. In fact the full-cylinder data were so reproducible that the uncertainty was entirely due to the precision of the naphthalene temperature measurements. Figure 3 represents experimental results from some of the sublimation runs, where the mass transfer Nusselt number is given as a function of Reynods number for full and segmented (θ = 50 deg) cylinders. Also shown are the correlation equations (7) and (8). In the Reynolds number range of the deposition experiments ($1.5 \times 10^4 \leq \mathrm{Re} \leq 2.0 \times 10^4$), the correlation and experimental data are in agreement, i.e., the "perfect" cylinder in crossflow assumption is applicable here in spite of the relatively large collector dimensions with respect to the jet stream diameter. Thus the aerodynamic structure inside the boundary layer was not altered by the entrainment phenomenon around the collector. At higher Reynolds numbers, F(turb) given by

$$F(\text{turb}) = \frac{\overline{\text{Nu}}\ (\text{experimental})}{\overline{\text{Nu}}\ (\text{correlation})} \tag{11}$$

becomes greater than unity as indicated by the divergence of the experimental and correlation curves.

Angular Temperature Data Reduction and Results. From the angular surface temperature measurements on metallic and ceramic cylinders exposed to the combustion gases of the burner rig, a normalized surface temperature distribution was derived that, within the burner operating range of interest, was found to be independent of combustion gas temperature, Reynolds number, or collector conductivity. We assumed the same distribution describes the gas temperature variation around the collector, i.e.,

$$\left[\frac{T\{\theta\} - T_l}{T_0 - T_l}\right]_{\text{collector}} = \left[\frac{T\{\theta\} - T_l}{T_0 - T_l}\right]_{\text{gas}} \tag{12}$$

With the sonic temperature probe we also measured the leeward (T_l) and windward (T_o) stagnation point gas temperatures. The leeward stagnation point gas temperature was determined by positioning the sonic temperature probe at various distances downstream of the collector along the centerline and extrapolating their values to the leeward stagnation point. The measurement of $T(\theta)$ (gas) in equation (12) was calculated at each angle. A properly reduced gas temperature distribution was in turn generated from the calculated $T(\theta)$ (gas) values and set equal to the properly reduced mass fraction distribution of the sodium species via the heat/mass transfer analogy, assuming turbulent mixing

$$\left[\frac{T\{\theta\} - T_{\text{amb}}}{T_0 - T_{\text{amb}}}\right]_{\text{gas}} = \left[\frac{\omega_e\{\theta\}}{\omega_o}\right] \tag{13}$$

Equation (13) is plotted against θ in Fig. 4.

Deposition Rate Data Reduction and Results. The experimental data gleaned from the testing described in this report have provided all the information required to apply the CFBL vapor transport theory to the deposition rate data from our burner rig experiments. The analytical technique developed for this purpose has already been reported by Gökoğlu and Santoro (1987) and includes the multicomponent nature of the problem by considering the dominant sodium carrying species and the thermal diffusion and variable property effects due to steep temperature gradients. In general, the procedure consisted of integrating the local mass transfer (deposition) flux equation with each term within the equation expressed by its angle and/or temperature dependency

$$\bar{j}''_w = \frac{1}{2\pi L}\int_0^{2\pi} \rho_e\{T_e\{\theta\}\} \cdot D_e\{T_e\{\theta\}\} \cdot \mathrm{Nu}(\theta, T_e\{\theta\}) \cdot \omega_e\{\theta\} \cdot d\theta \equiv \frac{1}{L} \cdot \overline{(\rho_e D_e \mathrm{Nu}_\theta \omega_e)} \tag{14}$$

Notice that an approach directed at obtaining the isolated effective mainstream concentrations ω_e, and the isolated effective Nusselt number Nu_θ, etc., would not give the correct total deposition rate as the average of the product is not equal to the product of the averages, i.e.,

$$\frac{1}{L} \cdot \overline{(\rho_e \cdot D_e \cdot \mathrm{Nu}_\theta \cdot \omega_e)}^{\theta} \neq \frac{1}{L} \cdot \bar{\rho}_e \cdot \bar{D}_e \cdot \bar{\mathrm{Nu}}_\theta \cdot \bar{\omega}_e$$

The predicted deposition rates derived from the analytical technique described by Gökoğlu and Santoro (1987) are compared with the experimental rates in Fig. 5. The experimental data were reduced to the following set of conditions: Ma_∞ = 0.3, Re = 1.74×10^4, fuel-to-airflow rate = 0.035, T_o = 1800 K. The predicted band refers to 30 percent (lower curve) and 20 percent (higher curve) of total sodium fed into the system lost on the wall of the burner liner (estimated at 25 percent). The reduced net sodium concentration for Fig. 5 is about 5 ppm with respect to the combustion gases. Excellent agreement is found between theory and experiment for the plateau region. The disagreement above the melting point of

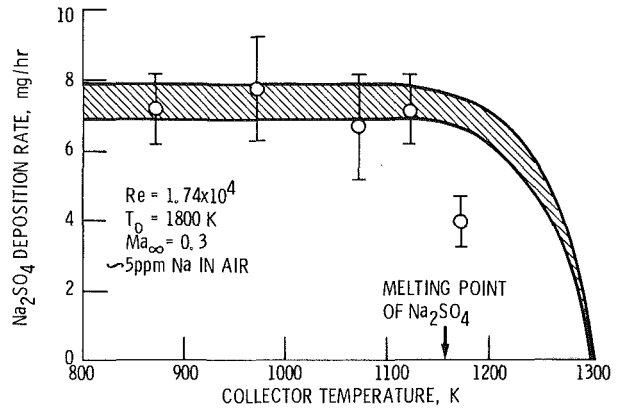

Fig. 5 Comparison of predicted and experimental sodium sulfate deposition rates for high-velocity burner rig

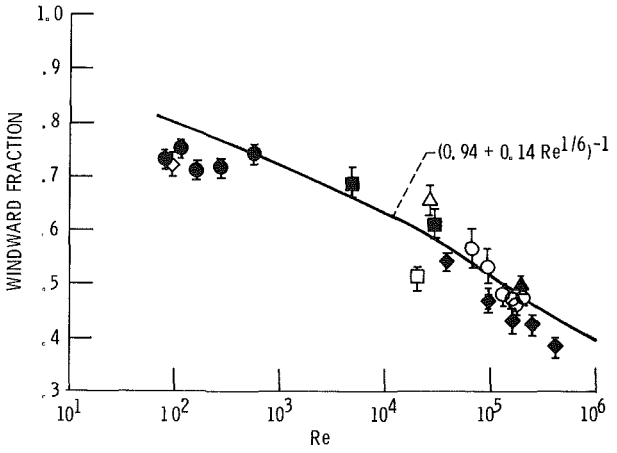

Fig. 6 Modification of figure by Gökoğlu and Rosner (1983): The symbols represent polar integration of experimental heat/mass transfer data from eight sources as in the original figure, but the curve was generated from equations (7) and (8) of this report

sodium sulfate (884°C) has been found to be due to shear-driven molten deposit layer runoff from the smooth collector surface (Santoro et al., 1984; Rosner et al., 1983; Rosner and Nagarajan, 1987) resulting in lower experimental values.

Experimental data available in the literature describing the Reynolds number dependence of the angular variation of the heat/mass transfer coefficient around cylinders in crossflow was utilized by Gökoğlu and Rosner (1983) to obtain the windward fraction ($-\pi/2 \le \theta \le \pi/2$) of the total heat/mass transferred to the cylinders (see Fig. 6). The error bars in the figure indicate the uncertainty in the polar integration of experimental data and the different symbols represent the scatter of data from different sources. The curve is based on the ratio of windward section averaged mass transfer using equation (8) to perimeter averaged mass transfer using equation (7); i.e.,

$$\text{Windward fraction} \cong \frac{1.14\ \mathrm{Re}^{1/2}(0.75)(A/2)}{(0.4\ \mathrm{Re}^{1/2} + 0.06\ \mathrm{Re}^{2/3})(A)} \simeq (0.94 + 0.14\ \mathrm{Re}^{1/6})^{-1} \quad (15)$$

Equation (15) assumes that the effect of Sc on the ratio is negligible. This modification of the original figure affirms the suitability of the cubic decline relationship describing the angular dependence of mass transfer coefficient on the windward surface of a cylinder (equation (12)) to represent experimental heat/mass transfer data. However, we do not have an ideal cylinder in crossflow in our experiments. Just as the total amount of deposit is affected by the dilution of the mainstream dopants due to the entrainment of ambient air, so is the distribution of the deposit on the surface of the target. The dilution causes the leeward ($\pi/2 \le \theta \le 3\pi/2$) mainstream concentration to be less than the windward concentration; therefore an even higher percentage of the total deposit should be collected on the windward surface. For our experimental setup the windward fraction is calculated to be 83 percent of the total deposit, a significant increase above the 65 percent value for the ideal crossflow situation given in Fig. 6.

Concluding Remarks

Vapor deposition rates were experimentally determined on an internally air-impingement-cooled cylindrical collector located in the crossflow of the sodium-seeded combustion gases of a small-capacity, high-velocity burner rig. However, the dimensions of the collector, by virtue of its internal cooling feature, were comparable to (although less than) the diameter of the jet stream of the burner, causing entrainment of ambient air resulting in a highly nonadiabatic gas flow around the collector. To predict the vapor deposition rates for comparison with the test data gathered from this setup, experiments were required to determine the angular variation of both the mass transfer coefficient and the concentration of the sodium species in the gases around the collector. These experiments have been described in detail. The predicted deposition rates were found to be in excellent agreement with experiment. Thus the CFBL vapor deposition theory has been successfully applied to a nonidealized experimental arrangement, which incorporated the high velocity gas flows characteristic of gas turbine engines.

Additional information resulting from these experiments includes the following findings: (*a*) The aerodynamic boundary layer structure was not affected by the entrainment phenomenon; (*b*) the mainstream turbulence factor was unity within the Reynolds number range of the deposition test parameters; (*c*) the mainstream turbulence factor could be represented by a single curve for both segmented and full cylinder data; (*d*) the cubic decline relationship expressing the angle dependence of the mass transfer coefficient proved suitable for our data and the experimental data of other authors; (*e*) it is predicted that not only the amount of deposit but the deposit distribution on the collector should be significantly altered by the dilution of the mainstream sodium species; therefore, the windward fraction of the deposit should be larger on our cylinders than on cylindrical targets totally immersed in the combustion gases.

Acknowledgments

The authors take pleasure in expressing their appreciation to Professor E. M. Sparrow of the University of Minnesota, Department of Mechanical Engineering, for providing us with detailed information on the construction and experimental procedures of the naphthalene sublimation cylinder.

References

Ambrose, D., Lawrenson, I. J., and Sproke, C. H., 1975, "The Vapor Pressure of Naphthalene," *Journal of Chemical Thermodynamics*, Vol. 7, No. 12, pp. 1173–1176.

Camin, D. L., and Rossini, F. D., 1955, "Physical Properties of 14 American Petroleum Institute Research Hydrocarbons, C_9 to C_{15}," *Journal of Physical Chemistry*, Vol. 59, No. 11, pp. 1173–1179.

Gökoğlu, S. A., and Rosner, D. E., 1983, "Windward Fraction of the Total Mass or Heat Transport for Flow Past a Circular Cylinder," *Aerosol Science and Technology*, Vol. 2, No. 4, pp. 543–544.

Gökoğlu, S. A., 1984a, "Experimental Verification of Vapor Deposition Model in Mach 0.3 Burner Rigs," *Turbine Engine Hot Section Technology 1984*, NASA CP-2339, pp. 110–121.

Gökoğlu, S. A., Chen, B. K., and Rosner, D. E., 1984b, "Computer Program for the Calculation of Multicomponent Convective Diffusion Deposition Rates From Chemically Frozen Boundary Layer Theory," NASA CR-168329.

Gökoğlu, S. A., and Santoro, G. J., 1988, "Determination of Convective Diffusion Heat/Mass Transfer Rates to Burner Rig Test Targets Comparable in Size to Cross-Stream Jet Diameter," ASME JOURNAL OF HEAT TRANSFER, Vol. 110, this issue.

Rosner, D. E., et al., 1979, "Chemically Frozen Multicomponent Boundary Layer Theory of Salt and/or Ash Deposition Rates From Combustion Gases," *Combustion Science and Technology*, Vol. 20, No. 3/4, pp. 87–106.

Rosner, D. E., Güneş, D., and Nazih-Amous, N., 1983, "Aerodynamically Driven Condensate Layer Thickness Distributions on Isothermal Cylindrical Surfaces," *Chemical Engineering Communications*, Vol. 24, No. 4–6, pp. 275–287.

Rosner, D. E., and Nagarajan, R., 1988, "Vapor Deposition and Condensate Flow on Combustion Turbine Blades: Theoretical Model to Predict/Understand Some Corrosion Rate Consequences of Molten Alkali Sulfate Deposition in the Field or Laboratory," *Int. J. Turbo, Jet Engines*, in press.

Santoro, G. J., et al., 1984, "Experimental and Theoretical Deposition Rates From Salt-Seeded Combustion Gases of a Mach 0.3 Burner Rig," NASA TP-2225.

Santoro, G. J., et al., 1985, "Deposition of Na_2SO_4 From Salt-Seeded Combustion Gases of a High Velocity Burner Rig," *High Temperature Corrosion in Energy Systems*, M. F. Rothman, ed., TMS-AIME Publications, pp. 417–434.

Sogin, H. H., 1958, "Sublimation From Disks to Air Streams Flowing Normal to Their Surfaces," *Transactions of the ASME*, Vol. 80, pp. 61–67.

Sparrow, E. M., Stahl, T. J., and Traub, P., 1984, "Heat Transfer Adjacent to the Attached End of a Cylinder in Crossflow," *International Journal of Heat and Mass Transfer*, Vol. 27, No. 2, pp. 233–242.

Vargaftik, N. B., 1975, *Tables on the Thermophysical Properties of Liquids and Gases*, 2nd ed., Wiley, New York, p. 359.

Whitaker, S., 1976, *Elementary Heat Transfer Analysis*, Pergamon Press, Oxford.

Determination of Convective Diffusion Heat/Mass Transfer Rates to Burner Rig Test Targets Comparable in Size to Cross-Stream Jet Diameter

S. A. Gökoğlu[1]

G. J. Santoro

NASA Lewis Research Center
Cleveland, OH 44135

Two sets of supplementary experiments have been performed to be able to predict the convective diffusion heat/mass transfer rates to a cylindrical target whose height and diameter are comparable to, but less than, the diameter of the circular cross-stream jet, thereby simulating the same geometric configuration as a typical burner rig test specimen located in the cross stream of the combustor exit nozzle. The first set exploits the naphthalene sublimation technique to determine the heat/mass transfer coefficient under isothermal conditions for various flow rates (Reynolds numbers). The second set, conducted at various combustion temperatures and Reynolds numbers, utilizes the temperature variation along the surface of the abovementioned target under steady-state conditions to estimate the effect of cooling (dilution) due to the entrainment of stagnant room temperature air. The experimental information, combined with an analytical treatment, is used to predict high-temperature, high-velocity corrosive salt vapor deposition rates in burner rigs on collectors that are geometrically the same. The agreement with preliminary data obtained from Na_2SO_4 vapor deposition experiments is found to be excellent.

Introduction

Trace amounts of impurities in hot gas flow systems can lead to the deposition of corrosive salts (i.e., sodium sulfate) on cold surfaces, severely deteriorating system performance. The objective of the "hot" corrosion research at NASA Lewis Research Center is to predict hot section component life, specifically for combustion turbine engine applications. For this purpose less expensive (cf. full-scale engine testing) high-velocity–high-temperature (and high-pressure) burner rigs, nominally operating at Mach 0.3, were built to measure deposition rates of sodium sulfate on inert, internally cooled, cylindrical collectors located in the cross stream of Na-salt-doped combustion gases. The purpose of internal cooling (by air impingement) was to control the collector surface temperature independently of combustion gas and prevailing dew point temperatures. The results of the previous work were reported in detail in Santoro et al. (1984) and Santoro et al. (1985).

The corrosive deposits are formed primarily by the vapor transport of precursors (e.g., NaOH, Na, Na_2SO_4, etc. in the case of Na_2SO_4 deposition) across the boundary layer. A comprehensive, chemically frozen boundary layer vapor transport theory has been recently formulated to predict deposition rates (Rosner et al., 1979; Gökoğlu et al., 1984). However, because the theory was designed for simpler geometric configurations, the complicated aerodynamic conditions prevailing in the burner rig deposition tests necessitated further experimentally determined parameters to be provided to the theory to gain quantitative predictive capabilities.

Because of the internal air cooling feature, the collector diameter has to be relatively large with respect to the burner nozzle throat diameter. The collector diameter was 1.90 cm (with a height of 1.27 cm and a wall thickness of 0.32 cm) and the throat diameter was 2.54 cm. This dimensional relationship facilitates ambient air entrainment and penetration into the hot gases around the collector, causing significant cooling of the mainstream and dilution of precursor contaminants. If it were a "perfect" cylinder in a crossflow situation where the collector was totally immersed in the jet stream, then the mass transfer coefficients would be readily calculable using the verified correlations in the literature (Zukauskas, 1972; Achenbach, 1975; Churchill and Bernstein, 1977; Peller et al., 1984). Furthermore, the contaminant concentrations in the mainstream would be ideally equal to those in the burner exit nozzle. Similarly, if the collector diameter were much larger than the jet stream diameter, then the available literature on impinging jets (Martin, 1977; Sparrow and Alhomoud, 1984) could be exploited. The predictions for these "idealized" cases would then be limited only to the determination of the mainstream turbulence effect (Kestin, 1966; Lowery and Vachon, 1975; Yardi and Sukhatme, 1978; Gorla and Nemeth, 1982; Simoneau et al., 1984; Fairweather et al., 1984). However, in our present system where the collector and jet stream diameters are comparable in size, the full utilization of such information and the straightforward application of the previously formulated vapor deposition theory were hindered by the geometric constraints, as shown in Fig. 1. Therefore, supplementary experiments were performed as explained in detail in Santoro and Gökoğlu (1988). The data provided by these experiments were used, as described below, to determine (*a*) the discharge coefficient of the burner exit nozzle by exploiting isentropic jet expansions, (*b*) the mass transfer coefficient and the mainstream turbulence effect pertaining to the burner rig test configuration by exploiting the naphthalene sublimation technique (Sparrow et al., 1984; Mairzale and Mayle, 1984; Goldstein and Karni, 1984), and (*c*) the entrained ambient air cooling and dilution effect by exploiting the effective jet impingement cooling concepts (Striegl and

[1]Present address: Case Western Reserve University, Department of Mechanical and Aerospace Engineering, Cleveland, OH 44106; NASA Resident Research Associate.

Contributed by the Heat Transfer Division and presented at the 31st International Gas Turbine Conference and Exhibit, Düsseldorf, Federal Republic of Germany, June 8–12, 1986. Manuscript received by the Heat Transfer Division March 3, 1987. Keywords: Forced Convection, Mass Transfer.

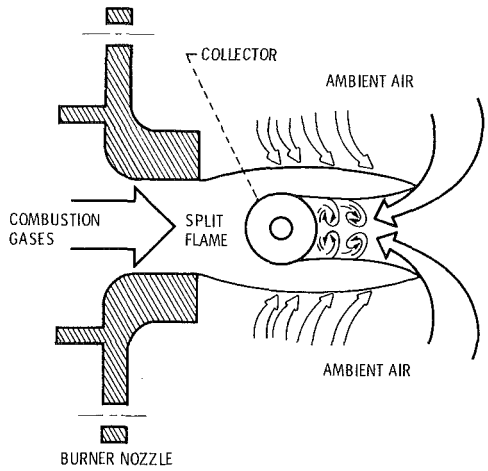

Fig. 1 Schematic of burner rig and collector configuration showing ambient air entrainment

Diller, 1984a, 1984b; Hollworth and Gero, 1984; Hollworth and Wilson, 1984). The adaptation of the vapor deposition theory by further analytical treatment, combined with the additional experimental information, enabled us to predict deposition rates quantitatively under burner rig operating conditions. Comparison of sodium sulfate deposition rate predictions with preliminary experiments gave excellent agreement.

Problem Definition and Approach

For a cylindrical collector in crossflow with the nomenclature given in Fig. 2, the local mass transfer (deposition) flux of a trace ($\omega_\infty \ll 1$, 1–10 ppm Na in our case) species at the surface can be given by

$$j''_w = \frac{\rho_e D_e}{L} \cdot \mathrm{Nu}_e \cdot (\omega_e - \omega_w) \tag{1}$$

In equation (1) we deliberately neglected the thermal diffusion (Soret) effect for simplicity, although we do include it for our rigorous predictions (Rosner et al., 1979; Gökoğlu et al., 1984). The surface mass fraction of the species ω_w is derived from surface reaction (or "sticking") rate constants or equilibrium vapor pressures prevailing at the surface temperature. However, again for the sake of simplicity,

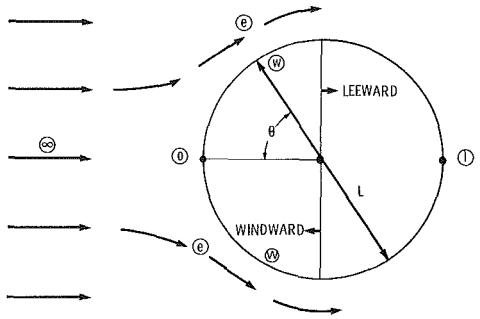

Fig. 2 Station nomenclature for the cylindrical collector

although with no loss of generality, we will also assume that $\omega_w \ll \omega_e$ is our discussions below.

In an ideal cylinder in a crossflow situation the collector would be small enough to be totally immersed in the combustion gases such that the angular mass fraction of the dopant species in the mainstream around the collector ω_e would be constant and equal to that in the burner exit gases ω_∞. Similarly, the mainstream total temperature T_e would be the same as the total jet temperature T_o of the approach stream. The fact that our collector diameter is comparable to, but less than, the jet diameter, causing the efficient entrainment of ambient air, gives rise to a highly nonadiabatic flow and a nonuniform concentration mainstream. In turn, the local thermodynamic and transport properties become angle dependent. Moreover, the entrainment and mixing taking place in the mainstream may be strong enough, eventually, to influence the boundary layer aerodynamic structure to cause the mass transfer Nusselt (Sherwood) number Nu_e to have an angle dependence other than its customary cubic relationship (Martinelli et al., 1943) obtained in "perfect" cylinder in crossflow studies. Therefore, the average deposition flux on the collector is given by

$$\overline{j''_w} = \frac{1}{2\pi L}\int_0^{2\pi} \rho_e(T_e(\theta)) \cdot D_e(T_e(\theta)) \cdot \mathrm{Nu}_e(\theta, T_e(\theta)) \cdot \omega_e(\theta) \cdot d\theta \equiv \frac{1}{L} \cdot \overline{(\rho_e D_e \mathrm{Nu}_e \omega_e)} \tag{2}$$

Note that the perimeter-averaged product is not the same as the product of the individual perimeter-averaged quantities.

Nomenclature

A = area
d = diameter
D = (Fick) diffusion coefficient
DC = discharge coefficient
$F(\mathrm{turb})$ = function describing mainstream turbulence
j'' = mass (deposition) flux
L = characteristic length (diameter of cylindrical collector)
$\dot{m}$ = mass flowrate = (ρUA)
M = molecular weight of gas
Ma = Mach number = $U_\infty / U_{\mathrm{sonic}}$
n = exponent of Schmidt number
Nu = mass transfer Nusselt (Sherwood) number
Nu_e = local (θ-dependent) Nusselt number
p = pressure
R = universal gas constant
Re = Reynolds number
Sc = Schmidt number = $\mu/(\rho D)$
T = absolute temperature
U = velocity
γ = ratio of heat capacity at constant pressure to heat capacity at constant volume
Δ = difference operator
θ = angle from the windward stagnation point
μ = dynamic viscosity of gas
ρ = density of gas
ω = mass fraction of transported species

Subscripts and Symbols

amb = ambient conditions
e = local outer edge of boundary layer around the collector
eff = effective
l = leeward stagnation point
lam = laminar mainstream
o = windward stagnation point
w = at the surface (wall)
∞ = upstream infinity
$-$ = averaged quantity
$(\ )$ = function of argument inside parenthesis

Therefore, an approach directed at obtaining the isolated effective mainstream concentration ω_e ($\approx \omega_e - \omega_w$), and the isolated effective Nusselt number Nu_e, etc., via properly designed experiments and then taking their product would not give the correct total deposition rate. Cognizant of the difficulty involved in determining the angular variation of the local, ω_e, T_e, and Nu_e, we have taken a path that would give a reasonable engineering prediction of total deposition rates on our collectors, minimizing the error within the constraints of our experimental facilities.

Discharge Coefficient of Burner Exit Nozzle. For our burner rig test conditions at flame temperatures of 1500 to 2000 K and at Mach numbers of about 0.3, the Reynolds number range of interest is determined to be between 1.5 and 2.0×10^4. Experiments under equivalent aerodynamic conditions require carefully determined Reynolds numbers that depend on jet approach velocities U_∞. For the correct calculation of U_∞, therefore, first the discharge coefficient of the burner exit nozzle was experimentally determined as a function of Reynolds number by measuring the stagnation pressure of the jet stream at ambient temperature for known mass flow rates of air (Santoro and Gökoğlu, 1988).

$F\{\mathrm{turb}\}$ Factor and Mass Transfer Nusselt Number. In equations (1) and (2), Nu_e actually includes the effect of mainstream turbulence on convective diffusion mass transport; i.e., it can be expressed as

$$\mathrm{Nu}_e = F\{\mathrm{turb}\}\,\mathrm{Nu}_{e,\,\mathrm{lam}} \tag{3}$$

where $\mathrm{Nu}_{e,\mathrm{lam}}$ is the Nusselt number for the laminar mainstream and the effect of mainstream turbulence is factored out as $F\{\mathrm{turb}\}$. Stagnation point region naphthalene sublimation experiments (Santoro and Gökoğlu, 1988) for which $\mathrm{Nu}_{o,\mathrm{lam}}$ can be theoretically calculated were used to determine $F\{\mathrm{turb}\}$ at various Reynolds numbers.

For the Reynolds number range of interest about 65 percent of the total deposit is collected on the windward surface ($-\pi/2 \le \theta \le \pi/2$) of ideal cylinders in crossflow (Gökoğlu and Rosner, 1983). In our situation, because the leeward ($\pi/2 \le \theta \le 3\pi/2$) mainstream concentration of the species is less than the windward concentration due to dilution, an even higher percentage of the total deposit will be collected on the windward surface of our collectors. Therefore, we divide our analysis into two parts; (*a*) the windward section: the primary region that is treated more rigorously by more direct experimental information, and (*b*) the leeward section: the secondary region for which some justifiable rational estimations were made. Geometric symmetry allows us below to deal only with angles for which $0 \le \theta \le \pi$.

For the windward section, after determining that for the Re range of interest $F\{\mathrm{turb}\}$ is unity, we experimentally verified the traditional Nusselt number angular dependence, i.e.,

$$\mathrm{Nu}_e\{\theta\} = \mathrm{Nu}_o\left\{1 - \left[\frac{\theta}{(\pi/2)}\right]^3\right\}, \qquad 0 \le \theta \le \frac{\pi}{2} \tag{4}$$

by using the naphthalene sublimation technique and by exposing different angular fractions ($\theta = \pi/9,\ \pi/6,\ \pi/4,\ \pi/3$) of the naphthalene cast cylinders of the same dimensions as collectors. The details of the experimental technique and procedure are given by Santoro and Gökoğlu (1988).

For the leeward section, the angular dependence of the Nusselt number is obtained via an indirect approach. Because exposing certain angular fractions of the naphthalene surface is technically more difficult and subject to greater experimental error, we did full cylinder naphthalene sublimation experiments to determine the perimeter averaged Nusselt number Nu. For the Re range of interest, the full cylinder experimental data agreed perfectly with the correlation of Whitaker (1975) indicating that the boundary layer aerodynamic structure is not actually affected by mainstream entrainment phenomena, and that correlations for "perfect" cylinders in crossflow to obtain the mass transfer coefficient apply even to cylinders of our dimensions. The leeward section Nu_e angular distribution inferred from the Whitaker correlation gave a leeward stagnation point Nusselt number Nu_l, which is in very good agreement with the reported literature values (Yardi and Sukhatme, 1978; Richardson, 1963).

Note that the sublimation technique is an essential feature of our approach, as opposed to many other heat or mass deposition techniques, to determine the mass transfer Nusselt number and its angular variation. The reasons are twofold: (*a*) The direction of mass transfer (from surface to mainstream) enables us to exploit the zero mainstream mass fraction of the species ($\omega_e = 0$) as one of our boundary condition regardless of the presence of the entrainment phenomenon (mainstream dilution effect), and (*b*) the experiments were run under ambient conditions such that the entrained ambient air did not affect the mainstream temperature (mainstream cooling effect). Therefore, an isolated study of Nu_e independent of mainstream entrainment consequences was possible.

Cooling and Dilution Effects Due to Entrainment. The approach taken to determine the angular variation of the mainstream cooling effect was to measure the angular variation of the surface temperature of collectors made of different materials at different Re and T_∞. Independent of whether the collector was high-thermal-conductivity platinum–20 percent rhodium or low-thermal-conductivity alumina ceramic, and irrespective of Re and T_∞ within the burner operation range of interest, when the normalized collector surface temperature, $(T\{\theta\} - T_l)/(T_o - T_l)$, was plotted against angle, a "universal" curve emerged. We then assumed that the mainstream had the same normalized temperature distribution and derived the mainstream $T\{\theta\}$ after measuring the hot gas temperatures for T_o and T_l.

Because the collector thickness was small compared with its diameter, heat conduction is basically along the circumference (one-dimensional). The Biot numbers calculated for the metallic Pt-20 percent Rh collectors were typically around 0.5 (and larger for ceramic collectors). Since ΔT between the gas windward and leeward stagnation temperatures were typically around 850 K, we were able to measure ΔT around 250 K between the metallic collector windward and leeward stagnation temperatures (and larger for ceramic collectors).

In our analysis the mainstream temperature distribution is described by $T\{\theta\}$ for the windward section. However, for the leeward section of secondary importance an effective temperature $T_{l,\,\mathrm{eff}}$ is used, which is obtained from the integral average of the gas temperature distribution over the leeward section. The dilution effect is derived via the heat/mass transfer analogy.

The overall approach described in this section provides the rationale for evaluation of the integral given by equation (2) to predict total collector deposition rates to within reasonable engineering accuracy.

Implementation and Results

Discharge Coefficient of Burner Exit Nozzle. The discharge coefficient of burner exit nozzle is defined as the ratio of the effective area of the jet nozzle through which gas with a uniform velocity profile passes to the geometric nozzle area, i.e.,

$$DC = \frac{A_{\mathrm{eff}}}{A_{\mathrm{nozzle}}} \tag{5}$$

The true jet exit velocity at ambient conditions can be obtained from the isentropic jet expansion relationship, i.e.,

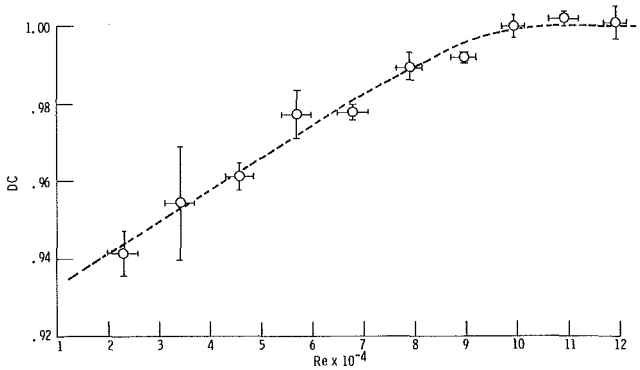

Fig. 3 Burner exit nozzle discharge coefficient as a function of Reynolds number based on nozzle diameter

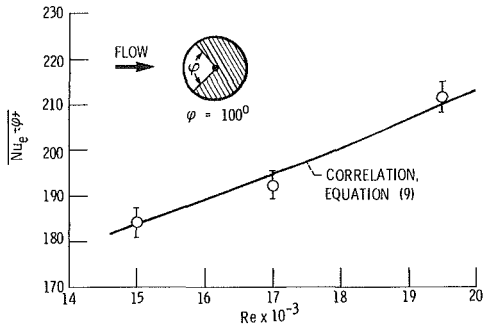

Fig. 4 Stagnation point region mass transfer Nusselt number obtained by the naphthalene sublimation technique as a function of Reynolds number (based on collector diameter) for the range of interest

$$U_\infty = U_{\text{sonic}}\left\{\left[\left(1+\frac{\Delta p}{p_\infty}\right)^{(\gamma-1)/\gamma}-1\right]\frac{2}{\gamma-1}\right\}^{1/2} \tag{6}$$

where $\Delta p = p_o - p_\infty$ and $U_{\text{sonic}} = (\gamma RT/M)^{1/2}$. However, for a known gas mass flowrate $\dot{m}$, using the ideal gas law, the effective nozzle area is given by

$$A_{\text{eff}} = \frac{RT_\infty}{p_\infty M}\frac{\dot{m}}{U_\infty} \tag{7}$$

We, therefore, used air at ambient conditions and measured Δp and p_∞ for each $\dot{m}$. The direct measurement of Δp instead of p_o greatly reduces the experimental uncertainty involved (cf. equation (6)) in determining U_∞. The Reynolds number based on nozzle diameter is then calculated from

$$\text{Re} = \frac{(\dot{m}/DC)d_{\text{nozzle}}}{\mu} \tag{8}$$

A plot of DC versus Re is shown in Fig. 3, where the error bars indicate the experimental scatter. Note that equivalent aerodynamic conditions of interest at flame temperatures (the same Re) are only the lower end of Fig. 3 ($2.0\times10^4 \le \text{Re} \le 2.7\times10^4$ where Re is based on the nozzle throat diameter) since we were limited by the lowest possible air mass flow rate at ambient conditions.

$F\{\text{turb}\}$ Factor and Mass Transfer Nusselt Number. The Nusselt number averaged over some windward angle θ can be obtained from equation (4) as

$$\overline{\text{Nu}_e} = \text{Nu}_o\left\{1-\frac{1}{4}\left[\frac{\theta}{(\pi/2)}\right]^3\right\}, \qquad 0\le\theta\le\frac{\pi}{2} \tag{9}$$

where the stagnation point Nusselt number Nu_o is given by (Kays and Crawford, 1980)

$$\text{Nu}_o = F\{\text{turb}\}\,(1.14)\text{Re}^{1/2}\text{Sc}^n \tag{10}$$

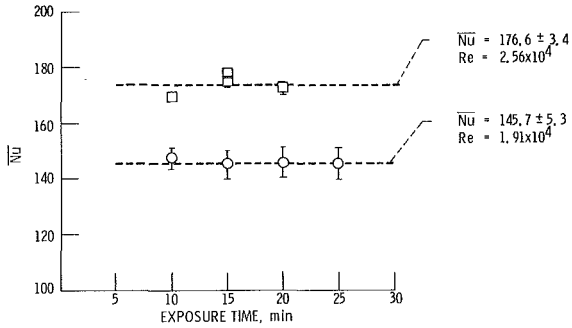

Fig. 5 Full cylinder mass transfer Nusselt number obtained by the naphthalene sublimation technique as a function of time of exposure to flow (duration of experiment) showing linearity of naphthalene weight loss; the circles and squares are reproducible experimental values; error bars indicate uncertainty in naphthalene surface temperature measurement

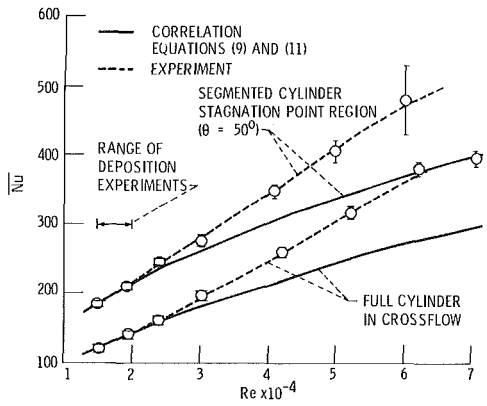

Fig. 6 Full and segmented cylinder mass transfer Nusselt number as a function of Reynolds number (based on cylinder diameter)

The exponent of the Schmidt number, n, varies between 1/3 and 0.4 in the literature (Churchill and Bernstein, 1977; Whitaker, 1975; Kays and Crawford, 1980). Our experiments, shown in Fig. 4 and run for the Re range of interest ($\text{Re} = 1.5$ to 2.0×10^4) where the angle of exposed naphthalene surface was about $\theta = 5\pi/18$ (~ 50 deg), indicate that (*a*) $F\{\text{turb}\}$ is unity, (*b*) the cubic relationship in equations (4) and (9) is a satisfactory description of the angle dependence of Nu_e, and (*c*) experiments are within ± 3 percent of the theoretical values (equation (9)) if $n = 0.35$, consistent with the literature values. The details explaining the experimental scatter as well as the calculation of the experimental Nusselt numbers using the naphthalene vapor pressure values reported in the literature (Camin and Rossini, 1955; Vargaftik, 1975; Sogin, 1958; Ambrose et al., 1975) are given by Santoro and Gökoğlu (1988).

The experimental perimeter-averaged mass transfer Nusselt numbers for fully exposed naphthalene cast cylinders were compared to the Whitaker correlation given by

$$\overline{\text{Nu}}_{\text{lam}} = (0.4\,\text{Re}^{1/2} + 0.06\,\text{Re}^{2/3})\text{Sc}^n \tag{11}$$

In the Re range of interest, the best agreement is obtained again within ± 3 percent if $n = 0.38$ ($F\{\text{turb}\}$ is unity), also consistent with the literature. The full cylinder naphthalene sublimation experiments at ambient conditions verified the applicability of the Whitaker correlation for cylinders with our dimensions.

Both the segmented (partially exposed) and full cylinder naphthalene sublimation experiments were extended to higher mass flow rates outside the Re range of interest. As shown in Figs. 5 and 6, the quality of data for full cylinders is better at higher Re than segmented cylinders, because full cylinder experiments are more straightforward and do not involve careful

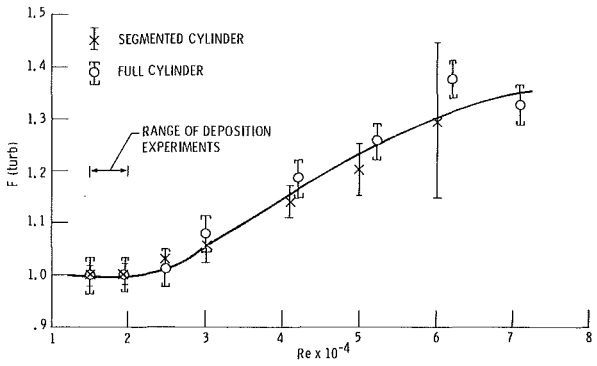

Fig. 7 Mainstream turbulence factor $F\{\text{turb}\}$ as a function of Reynolds number (based on cylinder diameter) for the burner rig experiments

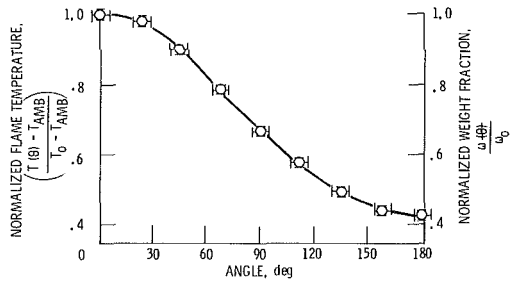

Fig. 8 Mainstream temperature distribution around the collector as obtained from surface temperature measurements of collectors made of different materials for the range of operating conditions of the burner rig

covering of the unexposed portion by taping (see details in Santoro and Gökoğlu, 1988). In fact, the full cylinder experimental data were so reproducible that the uncertainty was entirely due to the precision of the naphthalene surface temperature measurement, as indicated by the error bars in Fig. 5. The circles and squares in Fig. 5 are actual full cylinder Nusselt numbers experimentally determined as a function of exposure time of naphthalene surface to flow (duration of experiment), showing the linearity of naphthalene weight loss with time. As a part of the characterization of our burner rigs in their full operation range, we also determined the $F\{\text{turb}\}$ factor by taking the ratio of Nusselt numbers determined experimentally to the ones obtained from correlations. As shown in Fig. 7, both segmented and full cylinder data give $F\{\text{turb}\}$ factors that could be described by a single curve within experimental accuracy. (Note again that the scatter of data for segmented cylinders is larger at higher Reynolds numbers.) This observation is supporting evidence for the fact that $F\{\text{turb}\}$ is angle independent around the cylinder and can factored out from $\text{Nu}_{e,\text{lam}}$ for our setup. However, since $F\{\text{turb}\}$ is unity for our interest range, it will be dropped from our treatment below.

A consistency check for the windward section between equation (9) obtained from equation (4) and the Whitaker correlation (equation (11)) for full cylinders shows that for equal Schmidt number exponents n, the laminar portion (proportional to $\text{Re}^{1/2}$) of the Whitaker correlation can indeed be derived from equation (9) with the same coefficient, 0.4. The same type of check for the leeward section can be inversely applied to the Whitaker correlation, which has an explicit $\text{Re}^{2/3}$ term different from the Froessling (1958) relation to account for the increasing importance of the wake region. Therefore, if one assumes the same cubic decline relationship as in equation (9) for the leeward section of the cylinder corresponding to turbulent separated flow proportional to $\text{Re}^{2/3}$ (a reasonable assumption for $\text{Re} < \sim 10^5$) (Giedt, 1957), the leeward stagnation point Nusselt number $\overline{\text{Nu}}_l$ can be derived from equation (11) (again for equal n) giving

$$\text{Nu}_l = 0.160\,\text{Re}^{2/3}\text{Sc}^n \tag{12}$$

The coefficient 0.160 is consistent with the correlation of Richardson (1968), which proposes 0.171, and the experiments of Yardi and Sukhatme (1978), which suggest 0.153 as the premultiplier of $\text{Re}^{2/3}$. Therefore, based on the above analyses, which are further supported by our own experiments given in Figs. 4 and 5, we take equation (4) for the windward section, and

$$\text{Nu}_e\{\theta\} = \text{Nu}_l\{1 - [(\pi-\theta)/(\pi/2)]^3\}, \qquad \frac{\pi}{2} \le \theta \le \pi \tag{13}$$

for the leeward section. Note that equations (4) and (13) assume that the flow separates at $\theta = \pi/2$.

Cooling and Dilution Effects Due to Entrainment. Angular dependence of the cooling and dilution effect due to entrainment is obtained by the method described in section 2(*c*). The resulting curve is shown in Fig. 8, which is well fitted by two simple parabolas:

$$\frac{T_e\{\theta\} - T_{\text{amb}}}{T_o - T_{\text{amb}}} = \frac{\omega_e\{\theta\}}{\omega_o} = 1 - 0.33\left[\frac{\theta}{(\pi/2)}\right]^2, \qquad 0 \le \theta \le \frac{\pi}{2} \tag{14}$$

$$\frac{T_e\{\theta\} - T_{\text{amb}}}{T_o - T_{\text{amb}}} = \frac{\omega_e\{\theta\}}{\omega_o} = \left[1 - \left(\frac{\theta}{\pi}\right)\right]^2 + 0.42, \qquad \frac{\pi}{2} \le \theta \le \pi \tag{15}$$

$T_{l,\text{eff}}$ and $\omega_{l,\text{eff}}$ derived from equation (15) for the leeward section are then given by

$$T_{l,\text{eff}} = 0.50(T_o + T_{\text{amb}}), \qquad \omega_{l,\text{eff}} = 0.50\omega_o \tag{16}$$

Prediction of Deposition Rates. The temperature dependencies of the thermodynamic and transport properties pertaining to air and Na-carrier species (i.e., Na, NaOH, Na_2SO_4, etc.) for the windward section will be described by simple power laws (Martinelli et al., 1943; Gökoğlu and Rosner, 1984a)

$$\rho_e\{\theta\} = \rho_o[T_e\{\theta\}/T_o]^{-1}, \qquad 0 \le \theta \le \frac{\pi}{2} \tag{17}$$

$$D_e\{\theta\} = D_o[T_e\{\theta\}/T_o]^{1.70}, \qquad 0 \le \theta \le \frac{\pi}{2} \tag{18}$$

$$\mu_e\{\theta\} = \mu_o[T_e\{\theta\}/T_o]^{0.70}, \qquad 0 \le \theta \le \frac{\pi}{2} \tag{19}$$

Consequently, the Schmidt number becomes temperature independent and for a fixed mass flow rate

$$\text{Nu}_e\{T_e\{\theta\}\} = \text{Nu}_e\{T_o\}[T_e\{\theta\}/T_o]^{-0.35}, \qquad 0 \le \theta \le \frac{\pi}{2} \tag{20}$$

If the local temperature and angular effects for the Nusselt number are mutually exclusive and can be factored out, i.e.,

$$\text{Nu}_e\{\theta, T_e\{\theta\}\} = \text{Nu}_o[T_e\{\theta\}/T_o]^{-0.35}\left\{1 - \left[\frac{\theta}{(\pi/2)}\right]^3\right\}, \qquad 0 \le \theta \le \frac{\pi}{2} \tag{21}$$

then equations (17), (18), (21), and (14), can be substituted in equation (2) to give

$$\bar{j}''_w(\quad \text{windward} \quad) = \frac{j''_o}{(\pi/2)} \int_0^{\pi/2} \left\{1 - 0.33\left[1 - \left(\frac{T_{\text{amb}}}{T_o}\right)\right]\left[\frac{\theta}{(\pi/2)}\right]^2\right\}^{0.35} \times \left\{1 - \left[\frac{\theta}{(\pi/2)}\right]^3\right\}\left\{1 - 0.33\left[\frac{\theta}{(\pi/2)}\right]^2\right\} d\theta \qquad (22)$$

Approximating the bracket with the exponent by the first term of its Taylor series expansion and using the fact that $T_{\text{amb}}/T_o \leq 0.2$, equation (22) can now be easily integrated to obtain the average deposition flux on the windward surface of the collector

$$\bar{j}''_w(\text{windward}) = (0.68) j''_o \qquad (23)$$

Because the leeward effective temperature $T_{l,\text{eff}}$, and mass fraction $\omega_{l,\text{eff}}$, are constant, after substituting equation (13) into equation (2), the average deposition flux for the leeward section is obtained from a straightforward integration of equation (2)

$$\bar{j}''_w(\quad \text{leeward} \quad) = (0.75) j''_l(T_{l,\text{eff}}) = (0.75) \frac{\rho(T_{l,\text{eff}}) D(T_{l,\text{eff}})}{L} \text{Nu}_l(T_{l,\text{eff}}) \omega_{l,\text{eff}} \qquad (24)$$

Note that if one assumed no entrainment effect for the windward section and perfect turbulent mixing for the leeward section (i.e., a step function for the temperature distribution given by T_o for the windward and by $T_{l,\text{eff}}$ for the leeward section), then equation (23) would also read as

$$\bar{j}''_w(\quad \text{windward} \quad) = (0.75) j''_o \qquad (25)$$

Equations (23) and (24) can now be used for each of the Na-carrier species like Na, NaOH, Na_2SO_4, etc. (multicomponent transport) to calculate the total elemental Na flux to the collector surface, which can then be converted into equivalent Na_2SO_4 deposition rates. Because sodium is in trace amounts, sulfur (from jet A-1 fuel) and oxygen (left over after combustion) are excessively available to form sodium sulfate.

Comparison of Theory and Experiment. For the burner rig deposition experiments Na-acetate dissolved in alcohol is used as the Na source. The Na-acetate/alcohol solution is mixed with jet A-1 fuel in the fuel nozzle cavity and sprayed into the combustor through the fuel nozzle to assure the complete vaporization and chemical equilibrium of Na-carrier species. However, some of the Na fed into the system deposits on the inner wall of the cool end of the burner liner after the fuel and the alcohol burn away. From chemical analyses we currently estimate that about 25 percent of the total Na added is lost on the liner wall with a maximum uncertainty of ±5 percent (see Santoro and Gökoğlu, 1988) and, therefore, the Na concentration in the burner exit combustion gases is effectively so much less. Direct measurement of Na concentration in the combustion effluent gases will be done in situ by the Na-emission spectrometry technique in the near future. The collector located 5/8 in. from the burner nozzle is rotated with a velocity much smaller than the jet stream velocity to keep the surface temperature constant and uniform.

Predictions made as described above, including also the thermal (Soret) diffusion effect (only about 2 to 3 percent in our case), are compared with the experimental deposition rates as shown in Fig. 9. All the experiments were run under the following conditions: $\text{Ma}_\infty = 0.3$, $\text{Re} = 1.74 \times 10^4$, fuel-to-air flow rate ratio = 0.035, $T_o = 1800$ K. The prediction band

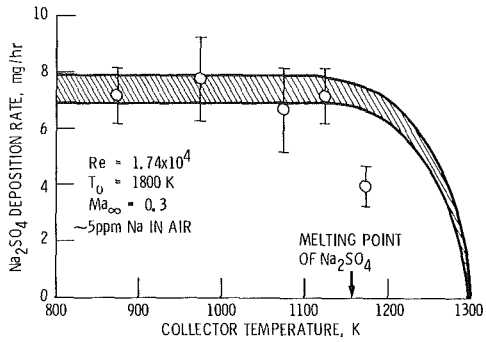

Fig. 9 Comparison of predicted and experimental sodium sulfate deposition rates for burner rigs

refers to 30 percent (lower curve) and 20 percent (higher curve) loss of total Na fed into the system on the burner wall (estimated at 25 percent, resulting in a net 5 ppm sodium concentration with respect to the combustion air). Excellent agreement is found between theory and experiment for the plateau region. The disagreement above the melting point of Na_2SO_4 (884°C) is due to shear-driven molten deposit layer runoff from the smooth collector surface (Santoro et al., 1984; Rosner et al., 1983) resulting in lower experimental values. It should be noted that about 83 percent of the total deposition is predicted to occur on the windward surface of the collector, justifying our original premise that the windward section should be treated more carefully.

The chemical equilibrium calculations for the conditions prevailing in the leeward section ($\omega_{l,\text{eff}} = 0.50\ \omega_o = \sim 2.5$ ppm Na in air, $T_{l,\text{eff}} = 0.50\ (T_o + T_{\text{amb}}) = \sim 1050$ K, $p = 1$ atm) using the NASA CEC code (Gordon and McBride, 1971) indicate that the gas stream is supersaturated (supersaturation ratio $= 9 \times 10^2$) and Na_2SO_4 particles should condense. If the homogeneous kinetics is indeed fast enough for nucleation (based on the estimates given in Rosner et al., 1979, the critical supersaturation ratio is expected to be larger than 10^3 for these conditions), then the submicron particles formed would be transported by thermophoresis (Gökoglu and Rosner, 1984b, 1985, 1986). However, since the gas stream is cool in the leeward section and the gas stream-to-collector surface temperature contrast, T_w/T_e, is not sufficient, one would hardly expect any deposition on the leeward surface by thermophoresis.

A simple experiment was designed to check whether there was any mainstream condensation. For that purpose an inert segmented collector 20 deg on each side of the leeward stagnation point (the rest of the cylinder being made of silicon nitride ceramic) is used to measure leeward stagnation point region deposition rates. Deposition was indeed observed on the segmented collector and the measured rates agreed well with what was expected from multicomponent vapor deposition rates described above, indicating that no condensation took place in the gas stream. It should be noted that even if condensation had taken place, our predicted deposition rate would have been in error by a maximum of 20 percent.

Conclusions

Convective diffusion mass transfer (deposition) rates to cylindrical burner rig test targets comparable in size to cross-stream jet diameter have been determined. The previously developed chemically frozen boundary layer multicomponent vapor deposition theory (Rosner et al., 1979; Gökoğlu et al., 1984), which was designed for simpler geometries, has been adapted and extended to handle the geometric constraints of the experimental burner rig setup properly. The information available in the literature for "perfect" cylinders in crossflow, where the target diameter would be much smaller than the jet-

stream diameter, and for impinging jets, where the target dimensions would be much larger than the jet thickness, has been exploited to guide our approach to deal with the intermediate case of comparable target and jet diameters. Supplementary experimental data provided the necessary information which, when combined with further analytical treatment, gave the theory the pursued quantitative predictive capability.

The first set of supplementary experiments utilized the naphthalene sublimation technique under isothermal conditions for both full and segmented (partially exposed) cylinders of the same dimensions as burner rig collectors to obtain the angular variation of the mass transfer coefficient on the windward and leeward surfaces. The second set of supplementary experiments determined the angular variation of the concentration of precursor species (dilution effect) and temperature (cooling effect) caused by the entrainment of the ambient air due to the relatively large size of the collector.

The predictions of the theory after its extension to these nonidealized arrangements were found to be in excellent agreement with the experimental sodium sulfate deposition rates within experimental uncertainty.

Although the application is presented for a specific setup in this paper, the extension/generalization of the methodology, limited by the accuracy and/or availability of $F\{\text{turb}\}$, is certainly possible. For example, the methodology developed here in conjunction with the data in the Sparrow and Alhomoud (1984) paper can be applied to the heat/mass transfer problems at circular cylinders for various target-to-nozzle distances, target-to-nozzle diameter ratios, offset and nonoffset target positions, etc.

References

Achenbach, E., 1975, "Total and Local Heat Transfer From a Smooth Circular Cylinder in Cross-Flow at High Reynolds Number," *Int. J. Heat Mass Transfer*, Vol. 18, pp. 1387–1396.

Ambrose, D., Lawrenson, I. J., and Sprake, C. H. S., 1975, "The Vapor Pressure of Naphthalene," *J. Chem. Thermodynamics*, Vol. 7, pp. 1173–1176.

Camin, D. L., and Rossini, F. D., 1955, "Physical Properties of Fourteen American Petroleum Institute Research Hydrocarbons, C_9 to C_{15}," *J. Phys. Chem.*, Vol. 59, pp. 1173–1179.

Churchill, S. W., and Bernstein, M., 1977, "A Correlating Equation for Forced Convection From Gases and Liquids to a Circular Cylinder in Crossflow," ASME JOURNAL OF HEAT TRANSFER, Vol. 99, 1977, pp. 300–306.

Fairweather, M., Kilham, J. K., and Mohebi-Ashtiani, A., 1984, "Stagnation Point Heat Transfer From Turbulent Methane–Air Flames," *Combust. Sci. Technol.*, Vol. 35, pp. 225–238.

Froessling, N., 1958, "Evaporation, Heat Transfer, and Velocity Distribution in Two-Dimensional and Rotationally Symmetrical Laminar Boundary-Layer Flow," NACA TM-1432.

Giedt, W. H., 1957, *Principles of Engineering Heat Transfer*, D. Van Nostrand Co., New York.

Gökoğlu, S. A., Chen, B. K., and Rosner, D. E., 1984, "Computer Program for the Calculation of Multicomponent Convective Diffusion Deposition Rates From Chemically Frozen Boundary Layer Theory," NASA CR-168329.

Gökoğlu, S. A., and Rosner, D. E., 1983, "Windward Fraction of the Total Mass or Heat Transport for Flow Past a Circular Cylinder," *Aerosol Sci. Technol.*, Vol. 2, No. 4, pp. 543–544.

Gökoğlu, S. A., and Rosner, D. E., 1984a, "Engineering Correlations of Variable-Property Effects on Laminar Forced Convection Mass Transfer for Dilute Vapor Species and Small Particles in Air," NASA CR-168322.

Gökoğlu, S. A., and Rosner, D. E., 1984b, "Correlation of Thermophoretically-Modified Small Particle Diffusional Deposition Rates in Forced Convection Systems With Variable Properties, Transpiration Cooling and/or Viscous Dissipation," *Int. J. Heat Mass Transfer*, Vol. 27, No. 5, pp. 639–645.

Gökoğlu, S. A., and Rosner, D. E., 1985, "Thermophoretically-Enhanced Mass Transport Rates to Solid and Transpiration-Cooled Walls Across Turbulent (Law-of-the-Wall) Boundary Layers," *Ind. Eng. Chem. Fundam.*, Vol. 24, No. 2, pp. 208–214.

Gökoğlu, S. A., and Rosner, D. E., 1986, "Thermophoretically-Augmented Forced Convection Mass Transfer Rates to Solid Walls Across Non-isothermal Laminar Boundary Layers," *AIAA J.*, Vol. 24, pp.

Goldstein, R. J., and Karni, J., 1984, "The Effect of a Wall Boundary Layer on Local Mass Transfer From a Cylinder in a Crossflow," ASME JOURNAL OF HEAT TRANSFER, Vol. 106, pp. 260–267.

Gordon, S., and McBride, B. J., 1971, "Computer Program for Calculation of Complex Chemical Equilibrium Compositions, Rocket Performance, Incident and Reflected Shocks, and Chapman-Jouget Detonations," NASA SP-273.

Gorla, R. S. R., and Nemeth, N., 1982, "Effects of Free-Stream Turbulence Intensity and Integral Length Scale on Heat Transfer From a Circular Cylinder in Crossflow," *7th International Heat Transfer Conference*, Munich, Federal Republic of Germany, pp. 153–158.

Hollworth, B. R., and Gero, L. R., 1984, "Entrainment Effects on Impingement Heat Transfer. Part II: Local Transfer Measurements," ASME-AIChE 22nd National Heat Transfer Conference, Niagara Falls, New York, ASME Paper No. 84-HT-20.

Hollworth, B. R., and Wilson, S. I., 1984, "Entrainment Effects on Impingement Heat Transfer: Part I—Measurements of Heated Jet Velocity and Temperature Distributions and Recovery Temperatures on Target Surface," ASME JOURNAL OF HEAT TRANSFER, Vol. 106, pp. 797–803.

Kays, W. M., and Crawford, M. E., 1980, *Convective Heat and Mass Transfer*, 2nd ed., McGraw-Hill, New York.

Kestin, J., 1966, "The Effect of Free-Stream Turbulence on Heat Transfer Rates," *Adv. Heat Transfer*, Vol. 3, pp. 1–32.

Lowery, G. W., and Vachon, R. I., 1975, "The Effect of Turbulence on Heat Transfer From Heated Cylinders," *Int. J. Heat Mass Transfer*, Vol. 18, pp. 1229–1242.

Martin, H., 1977, "Heat and Mass Transfer Between Impinging Gas Jets and Solid Surfaces," *Adv. Heat Transfer*, Vol. 13, pp. 1–60.

Martinelli, R. C., Guibert, A. G., Morrin, E. H., and Boelter, L. M. K., 1943, "An Investigation of Aircraft Heaters VIII—A Simplified Method for the Calculation of the Unit Thermal Conductance Over Wings," NACA Wartime Report, ARR WR-W-14.

Marziale, M. L., and Mayle, R. E., 1984, "Effect of an Oscillating Flow Direction on Leading Edge Heat Transfer," *Journal Engineering Gas Turbines Power*, Vol. 106, pp. 222–228.

Peller, H., Lippig, V., Straub, D., and Waibel, R., 1984, "Thermofluiddynamic Experiments With a Heated and Rotating Circular Cylinder in Crossflow, Part 1: Subcritical Heat Transfer Measurements," *Exp. Fluids*, Vol. 2, pp. 113–120.

Richardson, P. D., 1963, "Heat and Mass Transfer in Turbulent Separated Flows," *Chem. Eng. Sci.*, Vol. 18, pp. 149–155.

Rosner, D. E., Chen, B. K., Fryburg, G. C., and Kohl, F. J., 1979, "Chemically Frozen Multicomponent Boundary Layer Theory of Salt and/or Ash Deposition Rates From Combustion Gases," *Combust. Sci. Technol.*, Vol. 20, No. 3/4, pp. 87–106.

Rosner, D. E., Güneş, D., and Nazih-Anous, N., 1983, "Aerodynamically Driven Condensate Layer Thickness Distributions on Isothermal Cylindrical Surfaces," *Chem. Eng. Commun.*, Vol. 24, pp. 275–287.

Santoro, G. J., and Gökoğlu, S. A., 1988, "Experiments for the Determination of Convective Diffusion Heat/Mass Transfer Rates to Burner Rig Test Targets Comparable in Size to Cross-Stream Jet Diameter," ASME JOURNAL OF HEAT TRANSFER, this issue.

Santoro, G. J., Gökoğlu, S. A., Kohl., F. J., Sterns, C. A., and Rosner, D. E., 1984, "Deposition of Na_2SO_4 From Salt-Seeded Combustion Gases of a High Velocity Burner Rig," NASA TM-83751.

Santoro, G. J., Kohl., F. J., Stearns, C. A., Gökoğlu, S. A., and Rosner, D. E., 1984, "Experimental and Theoretical Deposition Rates From Salt-Seeded Combustion Gases of a Mach 0.3 Burner Rig," NASA TP-2225.

Simoneau, R. J., Morehouse, K. A., VanFossen, G. J., and Behning, F. P., 1984, "Effect of a Rotor Wake on Heat Transfer From a Circular Cylinder," NASA TM-83613.

Sogin, H. H., 1958, "Sublimation From Disks to Air Streams Flowing Normal to Their Surfaces," *Trans. ASME*, Vol. 80, pp. 61–69.

Sparrow, E. M., and Alhomoud, A., 1984, "Impingement Heat Transfer at a Circular Cylinder Due to an Offset or Non-offset Slot Jet," *Int. J. Heat Mass Transfer*, Vol. 27, No. 12, pp. 2297–2306.

Sparrow, E. M., Stahl, T. J., and Traub, P., 1984, "Heat Transfer Adjacent to the Attached End of a Cylinder in Crossflow," *Int. J. Heat Mass Transfer*, Vol. 27, No. 2, pp. 233–242.

Striegl, S. A., and Diller, T. E., 1984a, "The Effect of Entrainment Temperature on Jet Impingement Heat Transfer," ASME JOURNAL OF HEAT TRANSFER, Vol. 106, pp. 27–33.

Striegl, S. A., and Diller, T. E., 1984b, "An Analysis of the Effect of Entrainment Temperature on Jet Impingement Heat Transfer," ASME JOURNAL OF HEAT TRANSFER, Vol. 106, pp. 804–810.

Vargaftik, N. B., 1975, *Tables on the Thermophysical Properties of Liquids and Gases*, 2nd ed., Wiley, New York, p. 359.

Whitaker, S., 1975, *Elementary Heat Transfer Analysis*, Pergamon Press, New York.

Yardi, N. R., and Sukhatme, S. P., 1978, "Effects of Turbulence Intensity and Integral Length Scale of a Turbulent Free Stream on Forced Convection Heat Transfer From a Circular Cylinder in Cross Flow," *6th International Heat Transfer Conference*, Toronto, Canada, Vol. 5, pp. 347–352.

Zukauskas, A., 1972, "Heat Transfer From Tubes in Crossflow," *Advances in Heat Transfer*, Vol 8, pp. 93–160.

A Continuous Exchange Factor Method for Radiative Exchange in Enclosures With Participating Media

M. H. N. Naraghi
Department of Mechanical Engineering,
Manhattan College,
Riverdale, NY 10471

B. T. F. Chung
Department of Mechanical Engineering,
The University of Akron,
Akron, OH 44325

B. Litkouhi
Department of Mechanical Engineering,
Manhattan College,
Riverdale, NY 10471

A continuous exchange factor method for the analysis of radiative exchange in gray enclosures with absorbing-emitting and isotropically scattering media and diffuse surfaces is developed. In this method two types of exchange function are defined: the direct exchange function and the total exchange function. Certain integral equations relating total exchange functions to direct exchange functions are developed. These integral equations are solved using a Gaussian quadrature integration method. The results obtained based on the present approach are found to be more accurate than those of the zonal method. Unlike the zonal method, in the present approach, there is no need for evaluation of multiple integrations for calculating direct exchange factors.

Introduction

The problem of radiative exchange in enclosures with absorbing-emitting and scattering media has received considerable attention for many years due to its significant engineering applications, such as heat transfer in combustion chambers and furnaces. To date, numerous techniques have been available to deal with this problem. Among these techniques, the zone method developed by Hottel and co-workers (1958, 1963, 1967) is the most versatile method. Later, Noble (1975) and Naraghi and Chung (1985) used completely different approaches to obtain explicit formulations for total exchange areas in terms of direct exchange areas. The major drawback in using the zone method is the evaluation of direct exchange areas, which can be an extremely tedious task. To avoid this difficulty, Larsen and Howell (1985) proposed an alternative scheme in which the exchange factors are determined experimentally.

This work presents a continuous version of the zonal method in which two types of exchange functions are introduced. They are direct exchange functions, such as $\overline{dss}(\mathbf{r}_i, \mathbf{r}_j)$, $\overline{dsg}(\mathbf{r}_i, \mathbf{r}_j)$, $\overline{dgs}(\mathbf{r}_i, \mathbf{r}_j)$, and $\overline{dgg}(\mathbf{r}_i, \mathbf{r}_j)$. The stochastic approach developed earlier by Naraghi and Chung (1986) is further extended to analyze radiative exchange in gray enclosures with absorbing-emitting and isotropically scattering media. Based on this approach a number of integral equations for total exchange functions in terms of the direct exchange functions are obtained. The Gaussian quadrature method is used to discretize the aforementioned integral equations. Consequently, four explicit formulations are obtained for the discretized total exchange function in terms of the discretized direct exchange functions. Since a continuous formulation (nonisothermal gas and surface assumption) is used and an accurate integration method is applied in the present method, it would yield results that are more accurate than those of the zonal method. In the zonal method, for an enclosure consisting of N_g gas and N_s surface zones, at least $N_g^2/2$ double volume, $N_g N_s$ volume-surface, and $N_s^2/2$ double surface integrations have to be evaluated. The direct exchange factors in the present formulation are between two differential surfaces and/or volumes; the evaluation of these exchange factors does not require any integration. Hence, substantial computational effort can be saved using the present approach.

Contributed by the Heat Transfer Division and presented at the National Heat Transfer Conference, Pittsburgh, PA, August 1987. Manuscript received by the Heat Transfer Division April 13, 1987. Keywords: Modeling and Scaling, Radiation, Radiation Interactions.

Analysis

Consider the enclosure shown in Fig. 1. The surfaces of the enclosure are opaque and diffuse, and the medium is isotropically scattering.

The objective here is to determine the radiative exchange between differential surfaces ds_i and gas differential volumes dv_j. The direct exchange function (factor) between two differential areas $\overline{dss}(\mathbf{r}_i, \mathbf{r}_j)$ is defined as the fraction of energy that is emitted from a differential surface at position $\mathbf{r}_i$ and reaches another differential area at position $\mathbf{r}_j$ by direct radiation; it is given by

$$\overline{dss}\ (\mathbf{r}_i, \mathbf{r}_j) = \frac{\cos\theta_i \cos\theta_j dA_j \tau(\mathbf{r}_i - \mathbf{r}_j)}{\pi |\mathbf{r}_i - \mathbf{r}_j|^2}$$

The direct exchange function between a differential area and a differential volume $\overline{dsg}(\mathbf{r}_i, \mathbf{r}_j)$ is the fraction of energy that is emitted from the differential area at position $\mathbf{r}_i$ and reaches the differential volume located at the position $\mathbf{r}_j$ by direct radiation; it is given by

$$\overline{dsg}\ (\mathbf{r}_i, \mathbf{r}_j) = \frac{k_t dv_j \cos\theta_i \tau(\mathbf{r}_i - \mathbf{r}_j)}{\pi |\mathbf{r}_i - \mathbf{r}_j|^2}$$

Similarly, the direct exchange function between two differential volumes $\overline{dgg}(\mathbf{r}_i, \mathbf{r}_j)$ is defined as the fraction of energy that is emitted from the differential volume (differential gas zone) at position $\mathbf{r}_i$ and reaches differential volume at the position $\mathbf{r}_j$ by direct radiation; it is given by

$$\overline{dgg}(\mathbf{r}_i, \mathbf{r}_j) = \frac{k_t dv_j \tau(\mathbf{r}_i - \mathbf{r}_j)}{4\pi |\mathbf{r}_i - \mathbf{r}_j|^2}$$

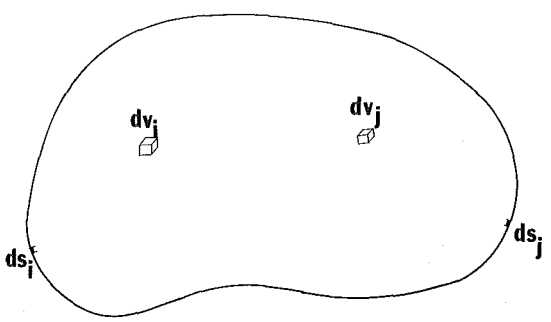

Fig. 1 An enclosure with differential surfaces and differential gas volumes

In general, the direct exchange function between two differential zones $\overline{dzz}(\mathbf{r}_i, \mathbf{r}_j)$ is the fraction of energy that is emitted from a differential zone at position $\mathbf{r}_i$ and reaches a differential zone at position $\mathbf{r}_j$ by direct radiation.

Next, the total exchange functions (factors) between two differential zones are defined. The total exchange function between two differential zones $\overline{DZZ}(\mathbf{r}_i, \mathbf{r}_j)$ is the fraction of energy that is emitted from a differential zone at position $\mathbf{r}_i$ and reaches another differential zone at position $\mathbf{r}_j$ by direct radiation and multiple reflection and scattering from surfaces and gas, respectively. Here, a number of integral equations will be derived for the total exchange functions, $\overline{DSS}(\mathbf{r}_i, \mathbf{r}_j)$, $\overline{DSG}(\mathbf{r}_i, \mathbf{r}_j)$, $\overline{DGS}(\mathbf{r}_i, \mathbf{r}_j)$, and $\overline{DGG}(\mathbf{r}_i, \mathbf{r}_j)$, in terms of the direct exchange functions, $\overline{dss}(\mathbf{r}_i, \mathbf{r}_j)$, $\overline{dsg}(\mathbf{r}_i, \mathbf{r}_j)$, $\overline{dgs}(\mathbf{r}_i, \mathbf{r}_j)$, and $\overline{dgg}(\mathbf{r}_i, \mathbf{r}_j)$.

First, radiation exchange between two differential gas volumes dv_i and dv_j, allowing only gas scattering, is considered (see Fig. 2). The term $p_{gg}(\mathbf{r}_i, \mathbf{r}_j)$ is considered to define the probability that radiation reaches differential gas volume dv_j at $\mathbf{r}_j$ having been emitted from differential gas volume dv_i at $\mathbf{r}_i$, allowing multiple scattering but excluding wall reflection. Then, based on the stochastic approach described by Naraghi and Chung (1986) we obtain

$$p_{gg}(\mathbf{r}_i, \mathbf{r}_j) = \overline{dgg}(\mathbf{r}_i, \mathbf{r}_j) + \int_v \overline{dgg}(\mathbf{r}_i, \mathbf{r}_{k_1})\omega_0 \overline{dgg}(\mathbf{r}_{k_1}, \mathbf{r}_j)$$

$$+ \int_v \int_v \overline{dgg}(\mathbf{r}_i, \mathbf{r}_{k_1})\omega_0 \overline{dgg}(\mathbf{r}_{k_1}, \mathbf{r}_{k_2})\omega_0 \overline{dgg}(\mathbf{r}_{k_2}, \mathbf{r}_j) + \ldots .$$

This expression involves the evaluation of an infinite series consisting of multiple integrations and it can be reduced into the following implicit formulation:

$$p_{gg}(\mathbf{r}_i, \mathbf{r}_j) = \overline{dgg}(\mathbf{r}_i, \mathbf{r}_j) + \int_v \overline{dgg}(\mathbf{r}_i, \mathbf{r}_k)\omega_0 p_{gg}(\mathbf{r}_k, \mathbf{r}_j) \qquad (1)$$

Next consideration is given to the term $p_{ss}(\mathbf{r}_i, \mathbf{r}_j)$, which is the probability that radiation reaches differential surface ds_j having been emitted from differential surface ds_i, allowing multiple scattering but excluding wall reflections (see Fig. 3). This probability is given by

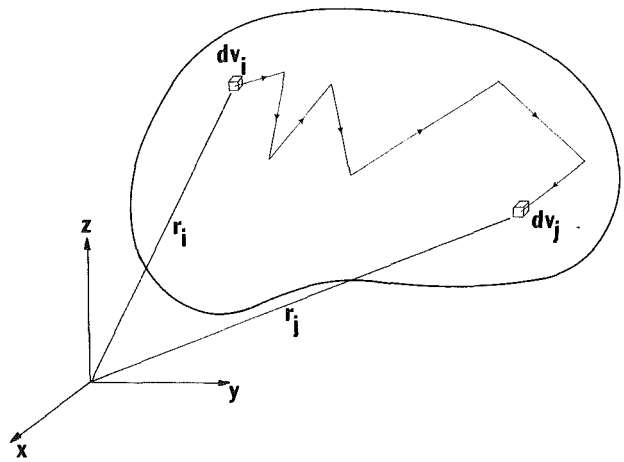

Fig. 2 A possible route that the radiative energy bundle could travel between two differential gas volumes (no wall reflection, allowing gas scattering)

$$p_{ss}(\mathbf{r}_i, \mathbf{r}_j) = \overline{dss}(\mathbf{r}_i, \mathbf{r}_j) + \int_v \overline{dsg}(\mathbf{r}_i, \mathbf{r}_k)\omega_0 \overline{dgs}(\mathbf{r}_k, \mathbf{r}_j)$$

$$+ \int_v \int_v \overline{dsg}(\mathbf{r}_i, \mathbf{r}_k)\omega_0 p_{gg}(\mathbf{r}_k, \mathbf{r}_l)\omega_0 \overline{dgs}(\mathbf{r}_l, \mathbf{r}_j) \qquad (2)$$

The continuous total exchange function $\overline{DSS}(\mathbf{r}_i, \mathbf{r}_j)$ can be written in terms of the following infinite series:

$$\overline{DSS}(\mathbf{r}_i, \mathbf{r}_j) = p_{ss}(\mathbf{r}_i, \mathbf{r}_j)\alpha + \int_s p_{ss}(\mathbf{r}_i, \mathbf{r}_{k_1})\rho p_{ss}(\mathbf{r}_{k_1}, \mathbf{r}_j)\alpha$$

$$+ \int_s \int_s p_{ss}(\mathbf{r}_i, \mathbf{r}_{k_1})\rho p_{ss}(\mathbf{r}_{k_1}, \mathbf{r}_{k_2})\rho p_{ss}(\mathbf{r}_{k_2}, \mathbf{r}_j)\alpha + \ldots$$

Nomenclature

$\overline{dgg}(\mathbf{r}_i, \mathbf{r}_j)$ = direct exchange function between gases
$\overline{DGG}(\mathbf{r}_i, \mathbf{r}_j)$ = total exchange function between gases
$\overline{dgs}(\mathbf{r}_i, \mathbf{r}_j)$ = direct exchange function between gas and surface
$\overline{DGS}(\mathbf{r}_i, \mathbf{r}_j)$ = total exchange function between gas and surface
$\overline{dsg}(\mathbf{r}_i, \mathbf{r}_j)$ = direct exchange function between surface and gas
$\overline{DSG}(\mathbf{r}_i, \mathbf{r}_j)$ = total exchange function between surface and gas
$\overline{dss}(\mathbf{r}_i, \mathbf{r}_j)$ = direct exchange function between surfaces
$\overline{DSS}(\mathbf{r}_i, \mathbf{r}_j)$ = total exchange function between surfaces
I = $[\delta_{i,j}]$ = identity matrix
k_a = absorption coefficient
k_s = scattering coefficient
k_t = extinction coefficient
N_g = number of discrete points in gas
N_s = number of discrete points on surface
$p_{gg}(\mathbf{r}_i, \mathbf{r}_j)$ = probability that radiation reaches a differential gas volume at $\mathbf{r}_j$ having been emitted from a differential gas volume at $\mathbf{r}_i$, allowing multiple scattering
$p_{gs}(\mathbf{r}_i, \mathbf{r}_j)$ = probability that radiation reaches a differential surface at $\mathbf{r}_j$ having been emitted from a differential gas at $\mathbf{r}_i$, allowing multiple scattering but excluding wall reflection
$p_{sg}(\mathbf{r}_i, \mathbf{r}_j)$ = probability that radiation reaches differential gas volume at $\mathbf{r}_j$ having been emitted from a differential surface at $\mathbf{r}_i$, allowing multiple scattering but excluding wall reflection
$p_{ss}(\mathbf{r}_i, \mathbf{r}_j)$ = probability that radiation reaches differential surface at $\mathbf{r}_j$ having been emitted from a differential surface at $\mathbf{r}_i$, allowing multiple scattering but excluding wall reflection
P_{xy} = $[p_{xy}(\mathbf{r}_i, \mathbf{r}_j)]$, where x and y can take either s or g
$\mathbf{r}_j$ = position vector
w_i = Gaussian quadrature weight factor
W = $[w_i\delta_{i,j}]$
α = absorptivity
ϵ = emissivity
θ_i = angle between normal to dA_i and connecting line between position $\mathbf{r}_i$ and $\mathbf{r}_j$
ρ = reflectivity
$\tau(\mathbf{r})$ = transmittance along path $\mathbf{r}$
τ_0 = optical thickness
ω_0 = k_s/k_t = albedo for scattering

Subscripts

g = designates gas
s = designates surface

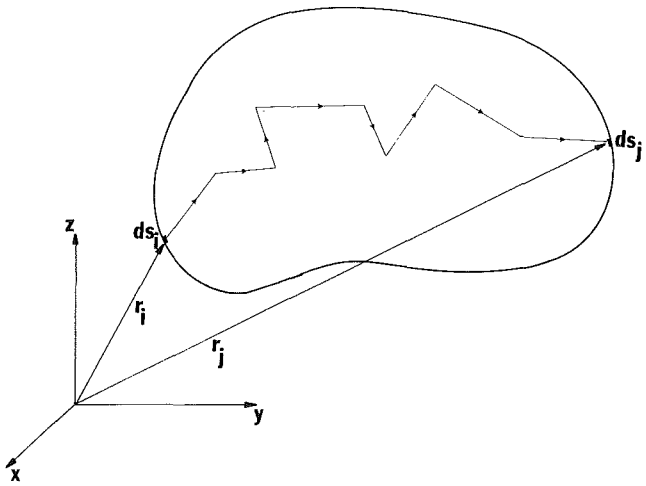

Fig. 3 A possible route that the radiative energy bundle could travel between two differential surface (no wall reflection, allowing gas scattering)

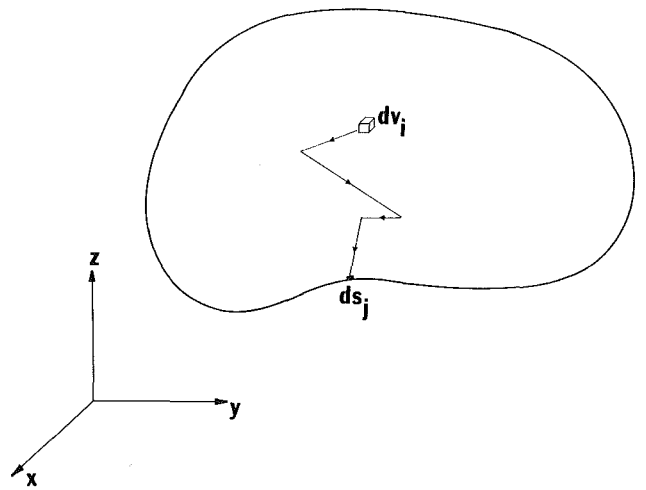

Fig. 4 A possible route that radiative energy bundle could travel between a differential surface and a differential gas volume (no wall reflection, allowing gas scattering)

The first term of the above infinite series corresponds to the probability that radiation is absorbed by ds_j having been emitted from ds_i, allowing multiple scattering but excluding wall reflections. The second term represents the same probability as the first term including one intermediate reflection from other surfaces. Similarly, the third and the rest of the terms represent the same probability as the first term including two and more intermediate reflections. The above infinite series can be reduced to

$$\overline{DSS}\ (\mathbf{r}_i, \mathbf{r}_j) = p_{ss}(\mathbf{r}_i, \mathbf{r}_j)\alpha + \int_s p_{ss}(\mathbf{r}_i, \mathbf{r}_k)\rho\overline{DSS}\ (\mathbf{r}_k, \mathbf{r}_j) \tag{3}$$

Equation (3) gives the total exchange functions between surfaces $\overline{DSS}(\mathbf{r}_i, \mathbf{r}_j)$ of the enclosure. Next, equations for the total exchange functions between gases $\overline{DGG}(\mathbf{r}_i, \mathbf{r}_j)$ will be derived.

Let $p_{gs}(\mathbf{r}_i, \mathbf{r}_j)$ be the probability that radiation reaches a differential surface located at r_j, having been emitted from a differential gas located at r_i, allowing multiple scattering (see Fig. 4). Thus

$$p_{gs}(\mathbf{r}_i, \mathbf{r}_j) = \overline{dgs}\ (\mathbf{r}_i, \mathbf{r}_j) + \int_v \overline{dgg}(\mathbf{r}_i, \mathbf{r}_{k_1})\omega_0\overline{dgs}\ (\mathbf{r}_{k_1}, \mathbf{r}_j)$$

$$+ \int_v \int_v \overline{dgg}(\mathbf{r}_i, \mathbf{r}_{k_1})\omega_0\overline{dgg}(\mathbf{r}_{k_1}, \mathbf{r}_{k_2})\omega_0\overline{dgs}\ (\mathbf{r}_{k_2}, \mathbf{r}_j) + \ldots$$

The first, second, third, . . . terms on the right-hand side of the above equation represent the probability that radiation reaches ds_j by direct radiation, one scattering, two scatterings, . . . respectively. The above infinite series can be reduced to

$$p_{gs}(\mathbf{r}_i, \mathbf{r}_j) = \overline{dgs}\ (\mathbf{r}_i, \mathbf{r}_j) + \int_v \overline{dgg}(\mathbf{r}_i, \mathbf{r}_k)\omega_0 p_{gs}(\mathbf{r}_k, \mathbf{r}_j) \tag{4}$$

A similar equation for $p_{sg}(\mathbf{r}_i, \mathbf{r}_j)$ can be derived, and is of the form

$$p_{sg}(\mathbf{r}_i, \mathbf{r}_j) = \overline{dsg}\ (r_i, \mathbf{r}_j) + \int_v p_{sg}(\mathbf{r}_i, \mathbf{r}_k)\omega_0\overline{dgg}(\mathbf{r}_k, \mathbf{r}_j) \tag{5}$$

The total exchange function between two gas zones is described by the following equation:

$$\overline{DGG}(\mathbf{r}_i, \mathbf{r}_j) = \Big[p_{gg}(\mathbf{r}_i, \mathbf{r}_j) + \int_s p_{gs}(\mathbf{r}_i, \mathbf{r}_{k_1})\rho p_{sg}(\mathbf{r}_{k_1}, \mathbf{r}_j)$$

$$+ \int_s \int_s p_{gs}(\mathbf{r}_i, \mathbf{r}_{k_1})\rho\overline{DSS}\ (\mathbf{r}_{k_1}, \mathbf{r}_{k_2})\rho/\alpha p_{sg}(\mathbf{r}_{k_2}, \mathbf{r}_j)\Big](1-\omega_0) \tag{6}$$

The total exchange functions between surfaces and gas $\overline{DGS}(\mathbf{r}_i, \mathbf{r}_j)$ and $\overline{DSG}(\mathbf{r}_i, \mathbf{r}_j)$ can be represented by the following equations:

$$\overline{DGS}(\mathbf{r}_i, \mathbf{r}_j) = p_{gs}(\mathbf{r}_i, \mathbf{r}_j)\alpha + \int_s p_{gs}(\mathbf{r}_i, \mathbf{r}_k)\rho\overline{DSS}\ (\mathbf{r}_k, \mathbf{r}_j) \tag{7}$$

and

$$\overline{DSG}(\mathbf{r}_i, \mathbf{r}_j) = \Big[p_{sg}(\mathbf{r}_i, \mathbf{r}_j) + \int_s \overline{DSS}\ (\mathbf{r}_i, \mathbf{r}_k)\rho/\alpha p_{sg}(\mathbf{r}_k, \mathbf{r}_j)\Big] \cdot (1-\omega_0) \tag{8}$$

Equations (1)–(8) have to be solved simultaneously in order to obtain the total exchange functions (factors). Solving these equations analytically is difficult; hence, a numerical integration method will be used here to discretize the integral equations.

Based on the Gaussian quadrature integration scheme, the discretized form of equation (1) becomes

$$P_{gg} = \overline{dgg} + \overline{dgg}\omega_0 W_g P_{gg}$$

where P_{gg} is a matrix with elements $p_{gg}(\mathbf{r}_i, \mathbf{r}_j)$ and $\mathbf{r}_i$ and $\mathbf{r}_j$ are discretized positions in the gas, $\overline{dgg} = [\overline{dg_i g_j}]$ is the matrix of discretized direct exchange factor functions between points in the gas, and $W_g = [w_i\delta_{ij}]$ is the diagonal matrix of Gaussian quadrature weight factors for integration over the gas volume. The above equation can be solved for P_{gg}, which yields

$$P_{gg} = [I - \overline{dgg}\omega_0 W_g]^{-1}\overline{dgg} \tag{9}$$

Similarly the discretized forms of equations (2) and (3), respectively, become

$$P_{ss} = \overline{dss} + \overline{dsg}\ \omega_0 W_g \overline{dgs} + \overline{dsg}\ \omega_0 W_g P_{gg}\omega_0 W_g \overline{dgs} \tag{10}$$

and

$$\overline{DSS} = P_{ss}\alpha + P_{ss}\rho W_s \overline{DSS} \tag{11}$$

where P_{ss} is a matrix with elements $p_{ss}(\mathbf{r}_i, \mathbf{r}_j)$ and $\mathbf{r}_i$ and $\mathbf{r}_j$ are discretized positions on the surface, $\overline{dsg} = [\overline{ds_i g_j}]$ is a matrix of discretized direct exchange functions between points on the surface and points in the gas, $\overline{dgs} = [\overline{dg_i s_j}]$ is a matrix of discretized direct exchange functions between points in the gas and points on the surface, and $W_s = [w_i\delta_{ij}]$ is a diagonal matrix of Gaussian quadrature weight factors for integration

over the surface. Substituting for P_{gg} from equation (9) into equation (10) and substituting P_{ss} into equation (11) yields, after algebraic simplification

$$\overline{DSS} = [I - \{\overline{dss} + \overline{dsg}\omega_0 W_g [I - \overline{dgg}\omega_0 W_g]^{-1}\overline{dgs}\}\rho W_s]^{-1} \cdot \{\overline{dss} + \overline{dsg}\ \omega_0 W_g [I - \overline{dgg}\omega_0 W_g]^{-1}\overline{dgs}\}\alpha \quad (12)$$

The right-hand side of the above equation consists of discretized direct exchange function matrices $\overline{dss}$, $\overline{dsg}$, $\overline{dgg}$, and $\overline{dgs}$, and the Gaussian quadrature weight factor diagonal matrices W_g and W_s. When W_g and W_s become identity matrices, equation (12) becomes identical to the formulation obtained independently by Noble (1975) and Naraghi and Chung (1985). The formulation given by equation (12) has two advantages over the existing zonal method. Firstly, the direct exchange functions (factors) in the present formulation are between points in the gas and/or on the surface of the enclosure; hence, there is no need for evaluating multiple integrals to obtain the direct exchange factors here. Secondly, in the present method the gas and surface are nonisothermal and an accurate integration scheme, i.e., the Gaussian quadrature method, is used to discretize the integral equations. Hence, the present approach will provide results which are more accurate than those of the zonal method.

Next, the numerical integration method is applied to equations (4)–(6). The resulting discretized forms of the aforementioned equations accordingly are

$$P_{gs} = \overline{dgs} + \overline{dgg}\omega_0 W_g P_{gs} \quad (13)$$

$$P_{sg} = \overline{dsg} + P_{sg}\omega_0 W_g \overline{dgg} \quad (14)$$

and

$$\overline{DGG} = [P_{gg} + P_{gs}\rho W_s P_{sg} + P_{gs}\rho W_s \overline{DSS}\ \rho/\alpha P_{sg}](1-\omega_0) \quad (15)$$

From equations (13) and (14), P_{gs} and P_{sg} are determined and are given by

$$P_{gs} = [I - \overline{dgg}\omega_0 W_g]^{-1}\overline{dgs}$$

and

$$P_{sg} = \overline{dsg}\ [I - \omega_0 W_g \overline{dgg}]^{-1}$$

Substituting P_{gg}, P_{gs}, P_{sg}, and $\overline{DSS}$ into equation (15) gives, after algebraic simplifications

$$\overline{DGG} = [I - \overline{dgg}\omega_0 W_g]^{-1}\overline{dgg}(1-\omega_0) + [I - \overline{dgg}\omega_0 W_g]^{-1} \cdot \overline{dgs}\ \rho W_s [I - \{\overline{dss} + \overline{dsg}\omega_0 W_g [I - \overline{dgg}\omega_0 W_g]^{-1}\overline{dgs}\}\rho W_s]^{-1} \cdot \overline{dsg}\ [I - \omega_0 W_g \overline{dgg}]^{-1}(1-\omega_0) \quad (16)$$

The above equation can be used to evaluate the discretized total exchange functions between gases. As in equation (12), the right-hand side of equation (16) consists of discretized direct exchange function matrices $\overline{dss}$, $\overline{dsg}$, $\overline{dgg}$, and $\overline{dgs}$, and the Gaussian quadrature weight factor diagonal matrices W_g and W_s.

Finally, equations (7) and (8) are discretized to obtain $\overline{DGS}$ and $\overline{DSG}$, the discretized total exchange functions between gas and surface. For equation (7) we obtain

$$\overline{DGS} = P_{gs}\alpha + P_{gs}\rho W_s \overline{DSS}$$

Substituting P_{gs} and $\overline{DSS}$ into the above equation from (13) and (12), respectively, we obtain

$$\overline{DGS} = [I - \overline{dgg}\omega_0 W_g]^{-1}\overline{dgs} \cdot [I - \rho W_s \{\overline{dss} + \overline{dsg}\ \omega_0 W_g [I - \overline{dgg}\omega_0 W_g]^{-1}\overline{dgs}\}]^{-1}\alpha \quad (17)$$

Similarly, for equation (8) can be written in the form of

$$\overline{DSG} = [P_{sg} + \overline{DSS}\rho/\alpha P_{sg}](1-\omega_0)$$

Substituting for P_{sg} and $\overline{DSS}$ into the above equation from equations (14) and (12), respectively, yields

$$\overline{DSG} = [I - \{\overline{dss} + \overline{dsg}\ \omega_0 W_g [I - \overline{dgg}\omega_0 W_g]^{-1}\overline{dgs}\}\rho W_s]^{-1} \cdot \overline{dsg}\ [I - \omega_0 W_g \overline{dgg}]^{-1}(1-\omega_0) \quad (18)$$

The total exchange functions obtained based on the present formulation satisfy the following two conditions:

$$\int_s \overline{DSS}\ (\mathbf{r}_i, \mathbf{r}_j) + \int_v \overline{DSG}(\mathbf{r}_i, \mathbf{r}_j) = 1 \quad (19)$$

and

$$\int_s \overline{DSG}(\mathbf{r}_i, \mathbf{r}_j) + \int_v \overline{DGG}(\mathbf{r}_i, \mathbf{r}_j) = 1 \quad (20)$$

Equations (19) and (20) imply that the energy emitted from any differential source (differential surface or volume) will finally be absorbed by another point in the gas or on the surface of the same enclosure. When the discretized functions are used, equations (19) and (20), respectively, become

$$\sum_{j=1}^{N_s} w_j \overline{DS_i S_j} + \sum_{j=1}^{N_g} w_j \overline{DS_i G_j} = 1 \quad (21)$$

and

$$\sum_{j=1}^{N_s} w_j \overline{DG_i S_j} + \sum_{j=1}^{N_g} w_j \overline{DG_i G_j} = 1 \quad (22)$$

Once the total exchange functions are determined, the heat flux and temperatures of the gas and the surface can be related to each other through the following equations:

$$q_s''(\mathbf{r}_i) = \epsilon\sigma T_s(\mathbf{r}_i)^4 - \int_s \overline{DSS}\ (\mathbf{r}_j, \mathbf{r}_i)\epsilon\sigma T_s(\mathbf{r}_j)^4 - \int_v \overline{DGS}(\mathbf{r}_j, \mathbf{r}_i)4k_t(1-\omega_0)\sigma T_g(\mathbf{r}_j)^4 \quad (23)$$

and

$$q_g'''(\mathbf{r}_i) = 4k_t(1-\omega_0)\sigma T_g(\mathbf{r}_i)^4 - \int_s \overline{DSG}(\mathbf{r}_j, \mathbf{r}_i)\epsilon\sigma T_s(\mathbf{r}_j)^4 - \int_v \overline{DGG}(\mathbf{r}_j, \mathbf{r}_i)4k_t(1-\omega_0)\sigma T_g(\mathbf{r}_j)^4 \quad (24)$$

The discretized forms of the above equations are given by

$$q_{s_i}'' = \epsilon\sigma T_{s_i}^4 - \sum_{j=1}^{N_s} w_j \overline{DS_j S_i}\epsilon\sigma T_{s_j}^4 - \sum_{j=1}^{N_g} w_j \overline{DG_j S_i}4k_t(1-\omega_0)\sigma T_{g_j}^4 \quad (25)$$

and

$$q_{g_i}''' = 4k_t(1-\omega_0)\sigma T_{g_i}^4 - \sum_{j=1}^{N_s} w_j \overline{DS_j G_i}\epsilon\sigma T_{s_j}^4 - \sum_{j=1}^{N_g} w_j \overline{DG_j G_i}4k_t(1-\omega_0)\sigma T_{g_j}^4 \quad (26)$$

In summary, equations (12), (16), (17), and (18) can be used to evaluate the discretized total exchange function matrices $\overline{DSS}$, $\overline{DSS}$, $\overline{DGS}$, and $\overline{DSG}$, respectively. These equations are explicit, and are in terms of the discretized exchange function matrices $\overline{dss}$, $\overline{dgg}$, $\overline{dgs}$, and $\overline{dsg}$. Elements of $\overline{dss}$, $\overline{dsg}$, $\overline{dgs}$, and $\overline{dsg}$ are direct exchange factors between differential surfaces and differential volumes located at a number of discrete points. Evaluating these matrices is quite simple and does not

require any integration. Once the discretized total exchange functions are determined, equations (25) and (26) can be used to relate temperature and heat fluxes in the enclosure.

It will be shown in the next section that the numerical results based on the present formulation are more accurate than the results based on the zonal method (Hottel and Sarofim, 1967; Noble, 1975; Naraghi and Chung, 1985).

Application and Results

To demonstrate the advantages of the present approach over the zonal method, two gray and infinitely long parallel plates (surfaces 1 and 2) with an absorbing-emitting and isotropically scattering medium between them are considered. The optical thickness between the plates is $\tau_0 = k_t L = 1$; the albedo for scattering is $\omega_0 = 0.5$, and the emissivities of the surfaces are $\epsilon_1 = 0.3$ and $\epsilon_2 = 0.7$. The direct exchange areas for the zonal method are calculated based on the formulations given by Hottel and Sarofim (1967). The total exchange areas between surfaces 1 and 2 are calculated based on the present approach (equation (12)) and the zonal method (Noble, 1975; Naraghi and Chung, 1985). The total exchange area $\overline{S_i S_j}$ is proportional to the fraction of energy that is emitted from surface s_i and absorbed by surface s_j by direct radiation, multiple reflections, and scattering from surfaces and gas, respectively. The resulting total exchange factors are given in Table 1. The parameter n in this table indicates the number of points of the Gaussian quadrature method used in equation (12) and also the number of gas zones in the zonal method. It is obvious that as n increases more accurate results are obtained in both methods, the present approach and the zonal method. However, for values of n larger than a certain value, the resulting total exchange factor remains unchanged, which corresponds to the exact solution.

It can be seen from Table 1 that for $n > 11$, the resulting total exchange factors do not change as n is increased. Hence,

$$\overline{SS} = \begin{bmatrix} 0.01662 & 0.07579 \\ 0.07579 & 0.10805 \end{bmatrix}$$

corresponds to the exact solution accurate up to five significant figures for the total exchange factors (areas) between the two parallel surfaces. In order to obtain results as accurate as the above results using the zonal method, the gas must be subdivided into at least 44 gas zones (see Table 1). As can be seen from Table 1, for a given n, the present approach yields more accurate results than the zonal method with the exception of the case for $n = 2$. It should also be noted the value of n represents the size of matrices involved in the calculations and that smaller values of n require less computational time.

The resulting total exchange factors obtained from equa-

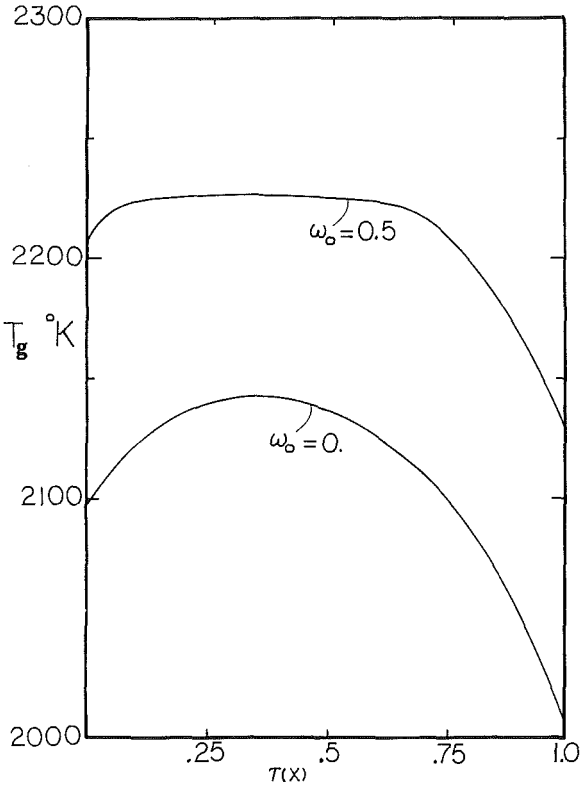

Fig. 5 Temperature distribution for an isotropically scattering medium with internal heat generation $q_g''' = 1$ W/m^2 bounded by two surfaces with emissivities $\epsilon_1 = 0.3$ and $\epsilon_2 = 0.7$

Table 1 Comparison between total exchange factors (areas): present approach and zonal method

	Continuous Exchange Factor Method, Equation (12)						Zonal Method					
n	S_1S_1	Percent Error	S_1S_2	Percent Error	S_2S_2	Percent Error	S_1S_1	Percent Error	S_1S_2	Percent Error	S_2S_2	Percent Error
2	0.01559	6.20	0.07478	1.33	0.10264	5.01	0.01578	5.05	0.07666	1.15	0.10469	3.11
3	0.01639	1.38	0.07554	0.33	0.10682	1.14	0.01620	2.53	0.07617	0.50	0.10631	1.61
4	0.01655	0.42	0.07570	0.12	0.10764	0.38	0.01637	1.50	0.07600	0.28	0.10700	0.97
5	0.01659	0.18	0.07575	0.05	0.10788	0.16	0.01645	1.02	0.07592	0.17	0.10734	0.66
6	0.01661	0.06	0.07577	0.03	0.10797	0.07	0.01650	0.72	0.07588	0.12	0.10755	0.46
7	0.01662	0.00	0.07578	0.01	0.10801	0.04	0.01653	0.54	0.07586	0.09	0.10767	0.35
8	0.01662	0.00	0.07578	0.01	0.10803	0.02	0.01655	0.42	0.07584	0.07	0.10776	0.27
9	0.01662	0.00	0.07578	0.01	0.10804	0.01	0.01657	0.30	0.07583	0.05	0.10782	0.21
10	0.01662	0.00	0.07578	0.01	0.10805	0.00	0.01658	0.24	0.07582	0.04	0.10786	0.18
11	0.01662	0.00	0.07579	0.00	0.10805	0.00	0.01659	0.18	0.07581	0.03	0.10789	0.15
12	0.01662	0.00	0.07579	0.00	0.10805	0.00	0.01659	0.18	0.07581	0.03	0.10792	0.12
13	0.01662	0.00	0.07579	0.00	0.10805	0.00	0.01660	0.12	0.07581	0.03	0.10794	0.10
20							0.01661	0.06	0.07580	0.01	0.10800	0.05
30							0.01662	0.00	0.07579	0.00	0.10803	0.02
40							0.01662	0.00	0.07579	0.00	0.10804	0.01
43							0.01662	0.00	0.07579	0.00	0.10804	0.01
44							0.01662	0.00	0.07579	0.00	0.10805	0.00
90							0.01662	0.00	0.07579	0.00	0.10805	0.00

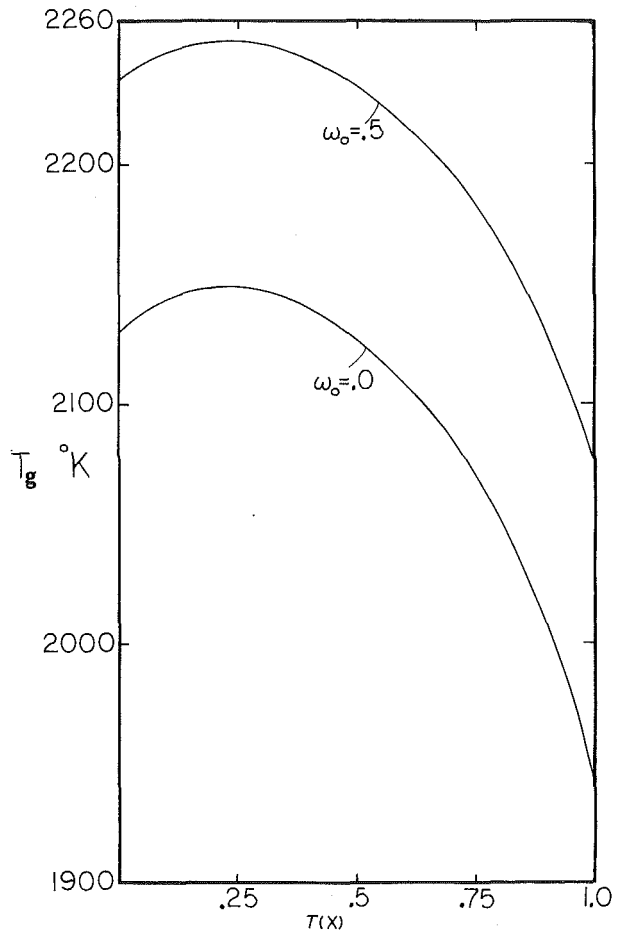

Fig. 6 Temperature distribution for an isotropically scattering medium with internal heat generation q_g'' = 1 W/m^2 bounded by two surfaces with emissivities ϵ_1 = 0.1 and ϵ_2 = 0.9

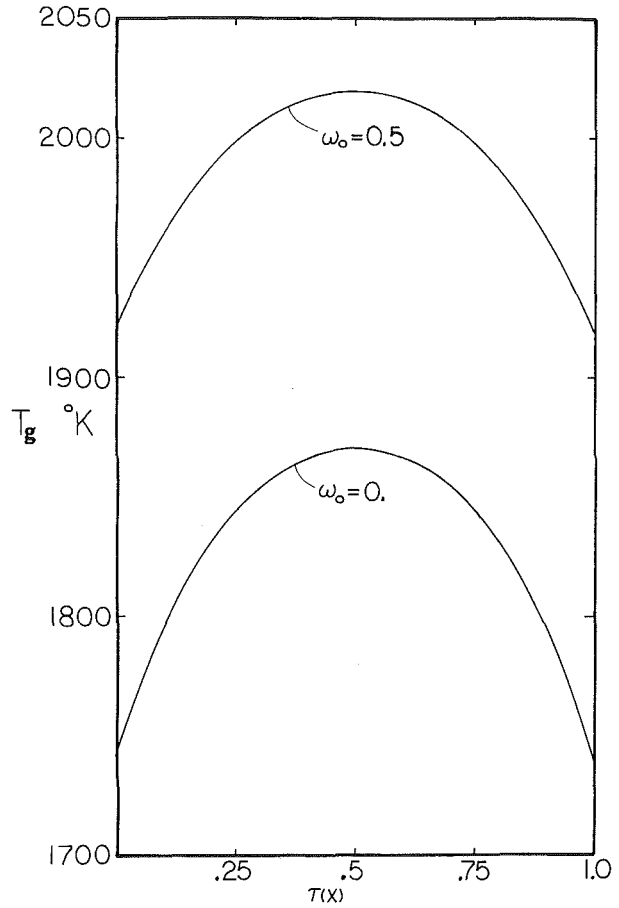

Fig. 7 Temperature distribution for an isotropically scattering medium with internal heat generation q_g'' = 1 W/m^2 bounded by two surfaces with emissivities ϵ_1 = ϵ_2 = 1

tions (12) and (16)–(18) satisfy equation (22), which can be used as a check for the accuracy of the results.

As another example, consider the above problem in which the medium between the two plates generates heat at a rate of q_g'' = 1 W/cm^2. Equations (12), (16)–(18), (25) and (26) are used to evaluate the gas temperature distribution. Figure 5 shows the gas temperature distribution versus $\tau_0(x)$ and albedo for scattering ω_0 = 0. and 0.5. The results shown in Fig. 5 are obtained based on a ten-point Gaussian quadrature method. These results are the same as those obtained based on the zonal method; however, in the zonal method the medium must be subdivided into at least 40 equally spaced gas zones in order to obtain identical results accurate up to five significant figures. The relative difference between the temperature distribution of the ten-point Gaussian quadrature method and the zonal method with ten equally spaced zones is at most 1 percent. Similarly, Fig. 6 shows the gas temperature distribution versus $\tau_0(x) = k_t x$ when ϵ_1 = 0.3 and ϵ_2 = 0.7 when albedo for scattering ω_0 = 0 and 0.5. It can be noticed from Figs. 5 and 6 that the gas temperature gradient is larger close to the surface with the larger emissivity and the point corresponding to the maximum temperature is closer to the surface with smaller emissivity. Finally, Fig. 7 shows the same results as Figs. 5 and 6 when the surfaces are black. As can be seen from this figure, the point of maximum temperature is midway between the two surfaces, which is due to the symmetric condition of the problem.

The problem considered here is one dimensional, in which the location of discrete nodal points of the Gaussian quadrature can be easily determined. In complex multidimensional geometries, however, local coordinate system are chosen in which the Gaussian quadrature nodal points are specified. It should also be noted that the improvement of the accuracy of the present approach over the zonal method will be more noticeable in the multidimensional enclosures than the one-dimensional problem considered here. This follows from the fact that, in the one-dimensional problem, a single integration is performed, while multidimensional problems involve multiple integrations.

Conclusion

A new formulation for the analysis of radiative exchange in gray enclosures with absorbing-emitting and isotropically scattering media is developed. This method is based on the continuous exchange factor (function). Two types of exchange functions are defined; direct and total exchange functions. The stochastic approach developed earlier by Naraghi and Chung (1986) is used to develop a number of integral equations that relate direct and total exchange functions. The Gaussian quadrature integration method is used to discretize the integral equations, and explicit matrix formulations are derived for the discretized total exchange function matrices in terms of discretized direct exchange function matrices, surfaces and gas properties, and the Gaussian quadrature weight factors.

It is shown that the total exchange factors obtained based on the present approach are more accurate than those obtained based on the zonal method. The direct exchange factors used in the present approach are between differential surfaces and/or volumes. Evaluating these exchange factors does not require any integration. In contrast, in the zonal method, the

direct exchange areas are between finite surfaces and/or volumes and evaluating these integrals requires up to six integrations.

The accuracy of the present approach is due to the nonisothermal gas and surface assumptions and the use of the Gaussian quadrature method for discretization of the gas volume and the surface area. In contrast, in the zonal method, the gas and surface zones are assumed isothermal and locations and sizes are chosen arbitrarily.

The present approach is also used to determine the gas temperature distribution. The resulting temperature distributions agree with the results obtained based on the zonal method.

Acknowledgment

The support of the National Science Foundation to the first two authors under the grant No. MEA-8314478 is gratefully acknowledged.

References

Hottel, H. C., and Cohen, E. S., 1958, "Radiant Heat Exchange in a Gas-Filled Enclosure: Allowance of Non-uniformity of Gas Temperature," *AIChE Journal*, Vol. 4, No. 1, pp. 3–14.

Hottel, H. C., and Sarofim, A. F., 1963, "Gaseous Radiation With Temperature Gradient—Allowance for Isotropic Scatter," *Research in Heat Transfer*, pp. 139–150.

Hottel, H. C., and Sarofim, A. F., 1967, *Radiative Transfer*, McGraw-Hill, New York.

Larsen, M. E., and Howell, J. R., 1985, "The Exchange Factor Method: An Alternative Basis for Zonal Analysis of Radiating Enclosures," ASME JOURNAL OF HEAT TRANSFER, Vol. 107, pp. 936–942.

Naraghi, M. H. N., and Chung, B. T. F., 1985, "A Unified Matrix Formulation for the Zone Method: A Stochastic Approach," *International Journal of Heat and Mass Transfer*, Vol. 28, No. 1, pp. 245–251.

Naraghi, M. H. N., and Chung, B. T. F., 1986, "Radiative Exchange in Enclosures With Non-isothermal Diffuse Surfaces and Thermally Transparent Medium," presented at the Joint AIAA/ASME Thermophysics and Heat Transfer Conference, Boston, MA, June 2–4, Paper No. 86-HT-30.

Noble, J. J., 1975, "The Zone Method: Explicit Matrix Relations for Total Exchange Areas," *International Journal of Heat and Mass Transfer*, Vol. 18, pp. 261–269.

G. Flamant

T. Menigault

D. Schwander

Institut de Science et de Génie des Matériaux et Procédés, Centre National de Recherche Scientifique, BP.5, 66120, Odeillo, France

Combined Heat Transfer in a Semitransparent Multilayer Packed Bed

Combined radiative, conductive, and forced convective heat transfer through a packed bed composed of two spectrally dissimilar slabs of particles is analyzed on the basis of the two-flux model. Taking into account the variation of absorption and scattering of the layers in the visible and infrared spectral ranges, the selectivity of such a system is proved theoretically. Experiments are run using a bed composed of glass and silicon carbide particles as a solar absorber for gas heating. Good agreement is shown in the comparison of predictions with experimental data.

Introduction

Many industrial or new processes are concerned with radiative heat transfer in absorbing and scattering media. For example, practical engineering situations are: gases containing particulates (Buckius, 1982; Grosshandler et al., 1982); fibrous insulation, (Tong and Tien, 1983; Tong et al., 1983; Sacadura et al., 1986); chemical reactors or heat exchangers as packed or fluidized beds (Brewster and Tien, 1982a; Flamant, 1986); coal combustors, (Phillips and Eustis, 1985); and high-temperature solar absorbers (Flamant, 1982). Generally, constant values of particle diameter and medium porosity are assumed for calculations, but real situations are often concerned with nonhomogeneous mixtures of particles or multiple particle concentration systems. Recently, Buckius (1986) discussed the radiative properties of polydispersed clouds of particles, and radiative transfer in spectrally dissimilar adjacent media was studied by Im and Ahluwalia (1981). The variation in radiative properties of two adjacent particle layers may be used to modify the temperature profile in a packed bed. This concept was formulated by Flamant et al. (1987).

Let us consider two slabs composed of particles whose scattering and absorption coefficients are different in two spectral ranges, for example, solar range ($0.2 < \lambda \leq 1.5\ \mu$m) and infrared range ($1.5 < \lambda < 20\ \mu$m). Two absorption and scattering coefficients must be defined (a_s, a_r, σ_s', σ_r', respectively) for both slabs. Let us suppose that slab 1, situated above slab 2 and exposed to concentrated solar radiation, is transparent in the solar band but absorbent in the infrared band. If slab 2 absorbs solar radiation, its temperature increases but the backward IR emission is absorbed by slab 1. Therefore the temperature distribution exhibits a maximum inside the bed. To explain this phenomenon a qualitative comparison of two situations is shown in Fig. 1. Solar flux and temperature distributions are shown for a bed composed of solar absorbent particles and a two-slab packed bed defined by previous properties. The main difference is the surface temperature reduction and consequently a large decrease in infrared emission losses.

Since one of our objectives is gas heating using solar energy, air is supposed to flow through the packed bed. To simulate the heat transfer in such a system, radiative, conductive, and convective heat transfer must be taken into account. Because of the mathematical complexity of the exact problem formulation, particularly the radiative transfer, we chose the two-flux model accounting for anisotropic scattering (Brewster, 1985). This approximation validity has been discussed by Brewster and Tien (1982). In the previous study, the two-flux model predictions are compared with those of exact radiative transfer theory to determine the influence of optical depth and scattering anisotropy. The main conclusion is that single scattering anisotropy is the prime cause of the two-flux model inaccuracy, whereas the model predictions are in good agreement with exact theory, even for large optical depth ($\tau \sim 100$), when the phase function is quasi-isotropic. Notice that for a thick slab of randomly oriented particles, a quasi-isotropic distribution of scattered intensity exists inside the medium (Chan and Tien, 1974).

Analysis

A schematic representation of the system is shown in Fig. 2. The model main assumptions are: steady-state conditions; one-dimensional plane parallel slabs; each slab is composed of identical isotropic spherical particles; the fluid is incompressible and nonabsorbent. The conductive heat transfer in the fluid may be neglected in comparison with the convective heat transfer; two spectral bands are considered: solar band

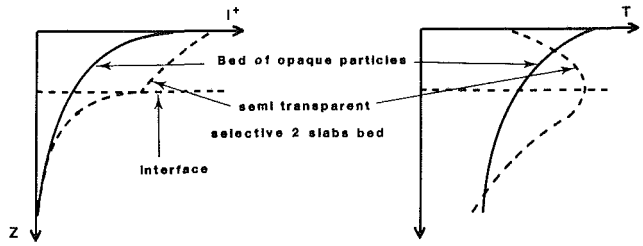

Fig. 1 Comparison of the typical flux and temperature profiles inside a bed of opaque particles and a semitransparent selective two-layer packed bed

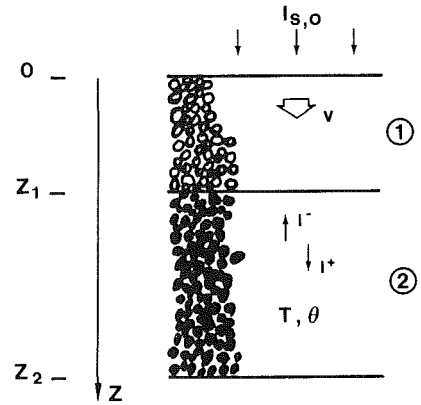

Fig. 2 Scheme of the physical model

Contributed by the Heat Transfer Division for publication in the JOURNAL OF HEAT TRANSFER. Manuscript received by the Heat Transfer Division January 23, 1987. Keywords: Forced Convection, Radiation, Radiation Interactions.

(subscript s), 0.2 μm $< \lambda <$ 1.5 μm, and infrared band (subscript r), $\lambda >$ 1.5 μm. The infrared emission in the solar band is neglected.

Accounting for conduction, convection, and radiation, the six governing equations of transfer for a slab i are (I is the radiant heat flux):

$$1/2\ (dI_s^+/dZ) = -(a_{s,i} + B_s\sigma'_{s,i})I_s^+ + B_s\sigma'_{s,i}I_s^- \quad (1)$$

$$1/2\ (dI_s^-/dZ) = (a_{s,i} + B_s\sigma'_{s,i})I_s^- - B_s\sigma'_{s,i}I_s^+ \quad (2)$$

$$1/2\ (dI_r^+/dZ) = -(a_{r,i} + B_r\sigma'_{r,i})I_r^+ + B_r\sigma'_{r,i}I_r^- + a_{r,i}\sigma T^4 \quad (3)$$

$$1/2\ (dI_r^-/dZ) = -(a_{r,i} + B_r\sigma'_{r,i})I_r^- - B_r\sigma'_{r,i}I_r^+ - a_{r,i}\sigma T^4 \quad (4)$$

$$\rho_f C_f \xi_i v(d\theta/dZ) = [6(1-\xi_i)/d_i]h_i(T-\theta) \quad (5)$$

$$(1-\xi_i)\lambda_i^*(T)(d^2T/dZ^2) + 2a_{s,i}(I_s^+ + I_s^-) + 2a_{r,i}(I_r^+ + I_r^-) = [6(1-\xi_i)/d_i]h_i(T-\theta) + 4a_{r,i}\sigma T^4 \quad (6)$$

B_s and B_r are the back-scatter fraction in the solar and infrared bands, defined as

$$B = 1/2 \int_0^1 \int_{-1}^0 p(\mu, \mu')d\mu' d\mu \quad (7)$$

where $p(\mu,\mu')$ is the scattering phase function.

T and θ are the particle and gas temperatures; ξ, v, and d are the mean values of a related to glass in each band and accounting for the bed porosity (equation (9)). The values of back-

The equivalent thermal conductivity $\lambda_i^*(T)$, and the gas-solid heat exchange coefficient h_i, are defined according to Baddour and Yoon (1960) and Donnadieu (1961), respectively.

Assuming a monodispersion of opaque spherical particles, the scattering and absorption coefficients can be expressed as (Siegel and Howel, 1972)

$$\sigma'_i = 1.5(1-\epsilon_i)(1-\xi_i)/d_i \quad (8)$$

$$a_i = 1.5\ \epsilon_i(1-\xi_i)/d_i \quad (9)$$

The boundary conditions are written considering a material diffuse reflectance R, which is a property of the interface are not an effective property of the slab.

$R_{s,i}^-(R_{r,j}^-)$ and $R_{s,i}^+$ $(R_{r,i}^+)$ are the reflectances for the radiant flux coming from medium i in the upward direction (Z and $\mu < 0$) and in the downward direction (Z and $\mu > 0$), respectively.

In order to be thermodynamically consistent, the following relation must be respected:

$$n_i^2(1-R_i^+) = n_{i+1}^2(1-R_{i+1}^-) \quad (10)$$

where n_i is the refractive index of slab i; for the particle layer $n_i = 1$ is assumed.

Formulation of the Boundary Conditions

Surface of the bed, $Z=0$: Assuming a constant flux density $I_{s,0}$ at the surface, we have

$$\left.\begin{aligned} &I_{s,1}^+(Z=0) = (1-R_{s,0}^+)I_{s,0} + R_{s,1}^-I_{s,1}^-(Z=0) \\ &I_{r,1}^+(Z=0) = R_{r,1}^-\ I_r^-\ \ (Z=0) \\ &\theta(Z=0) = \theta_0\ \ (\theta_0 = 293\text{ K for calculations}) \end{aligned}\right\} \quad (11)$$

Boundary between slab 1 and slab 2, $Z = Z_1$: Each equation is written for $Z = Z_1$, but the subscript is omitted for clarity

$$\left.\begin{aligned} &I_{s,2}^+ = (1-R_{s,1}^+)I_{s,1}^+ + R_{s,2}^-I_{s,2}^- \\ &I_{s,1}^- = (1-R_{s,2}^-)I_{s,2}^- + R_{s,1}^+I_{s,1}^+ \end{aligned}\right\} \quad (12)$$

and two similar equations for the infrared fluxes

$$\left.\begin{aligned} &T_1 = T_2 \\ &\text{and} \\ &\theta_1 = \theta_2 \end{aligned}\right\} \quad (13)$$

For temperatures T and θ, two other conditions are necessary. They are obtained by writing both energy equations for gas and solid in slab 1 and slab 2 at $Z = Z_1$. The mathematical formulation will not be developed here to save space

Bottom of bed, $Z = Z_1 + Z_2$:

$$\left.\begin{aligned} &I_{s,2}^+ = 0 \\ &I_{s,2}^- = 0 \\ &I_{r,2}^+ - I_{r,2}^- = 0 \\ &dT/dZ = d\theta/dZ = 0 \end{aligned}\right\} \quad (14)$$

The numerical solution of previous equations is derived from Patankar's (1980) computation method.

Theoretical Results

Glass beads and silicon carbide particles were selected to compose slab 1 and slab 2. The estimated values of the properties are listed in Table 1.

For glass beads (slab 1) a_s and a_r were chosen according to the mean values of a related to glass in each band and accounting for the bed porosity (equation (9)). The values of back-scatter fractions B_s and B_r were proposed by Brewster and Tien (1982); for transparent spheres of real refractive index $n = 1.5$: $B_s = 0.265$; for specularly reflecting spheres: $B_r = 0.667$.

For silicon carbide particles (slab 2) the absorption and scat-

Nomenclature

a = absorption coefficient
B = diffuse back scatter fraction
C = specific heat
d = particle diameter
h = gas-solid heat transfer coefficient
I = radiant heat flux
K = extinction coefficient = $a+\sigma'$
n = refractive index
p = scattering phase function
R = hemispherical reflectance
T = solid temperature
v = gas average velocity in the axial direction
Z = bed coordinate
α = polar angle of slab
ϵ = emissivity
θ = gas temperature
λ = wavelength of radiation or thermal conductivity
μ = cos α
ξ = porosity
ρ = density
σ = Stefan-Boltzmann constant
σ' = scattering coefficient
ω = scattering albedo = $\sigma'/(a+\sigma')$

Subscripts

i = related to medium i (0: air, 1: glass, 2: silicon carbide)
f = fluid
p = particle
r = infrared spectrum
s = solar spectrum

Superscripts

$*$ = effective quantity
$+$ = forward direction ($Z > 0$)
$-$ = backward direction ($Z < 0$)

Table 1 Properties of slab 1 and 2 for calculations (in addition $R_{s,0} = 0.05$)

slab	$d(10^{-3}\text{m})$	ξ	a_s, m^{-1}	a_r, m^{-1}	σ_s', m^{-1}	σ_r', m^{-1}	B_s	B_r	R_s^+	R_r	R_s^-	R_r^-
1	2	0.45	15	700	85	100	0.265	0.667	0.2	0.1	0.05	0.05
2	2	0.45	220	250	55	500	0.5	0.5			0.2	0.1

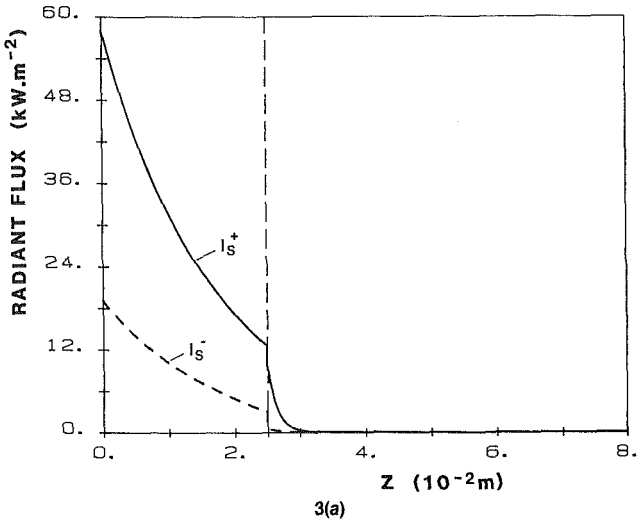

3(a)

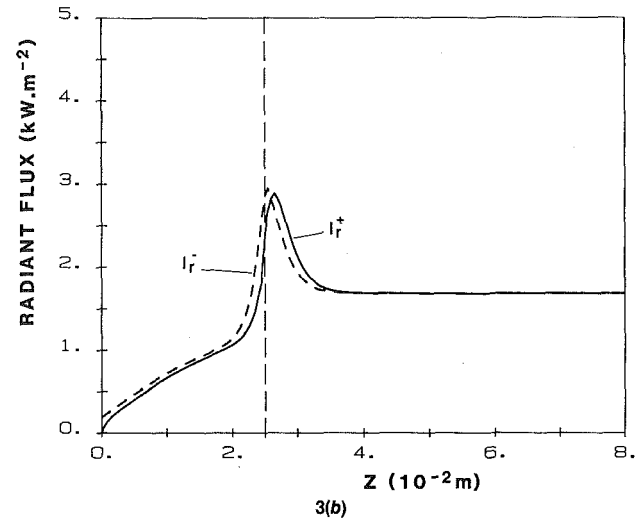

3(b)

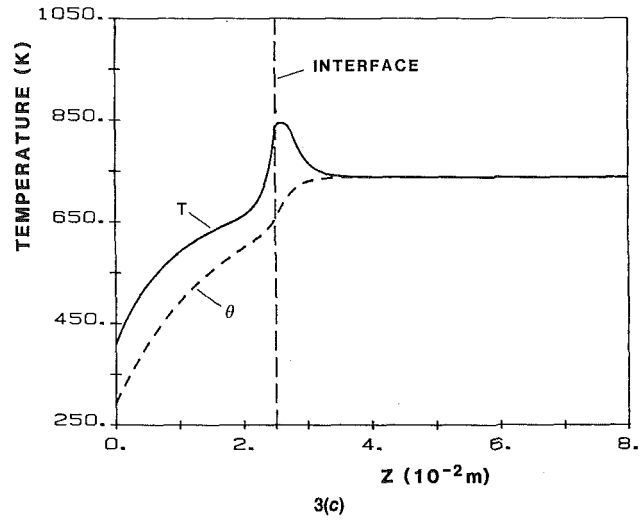

3(c)

Fig. 3 (a) Solar radiant flux profiles; (b) infrared flux profiles; (c) solid and gas temperature distributions versus bed depth; for model parameters see Table 1; $I_{s,0} = 600\ \text{kW}\cdot\text{m}^{-2}$, $\theta_0 = 293$ K

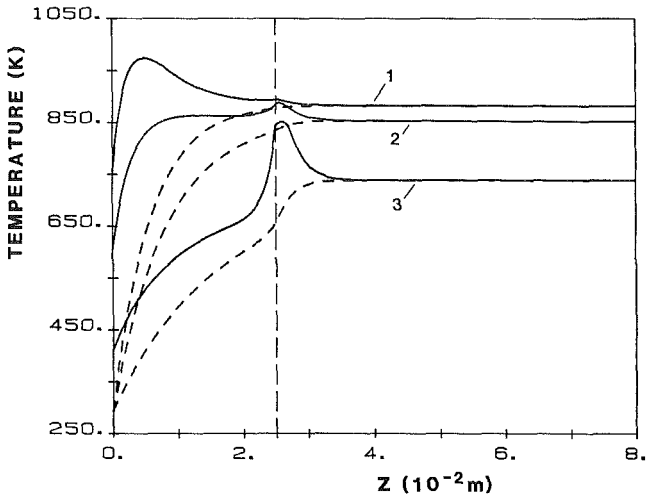

Fig. 4 Solid temperature distribution versus bed depth and slab 1 albedo; $K_{s,1} = 100\ \text{m}^{-1}$; (1) $\omega_{s,1} = 0.15$; (2) $\omega_{s,1} = 0.5$; (3) $\omega_{s,1} = 0.85$

tering coefficients were calculated according to relations (8) and (9) assuming $\epsilon_s = 0.8$ and $\epsilon_r = 0.9$. But the infrared scattering coefficient (σ_r') was overestimated by comparison with relation (8) to take into account the experimental results of Chen and Churchill (1963). The back-scatter fractions are related to diffuse reflecting large spheres (with $n = 1$).

A large uncertainty exists about the values of the reflectance R. An estimation was obtained assuming that the interface diffuse reflectance is equal to the particle reflectance. The latter values were based on Touloukian and Dewitt (1972) data.

Solar radiant fluxes, infrared fluxes, and temperature profiles are shown on Figs. 3(*a*), 3(*b*), and 3(*c*) for $Z_1 = 2.5 \times 10^{-2}$ m and $Z_2 = 5.5 \times 10^{-2}$ m. A very sharp decrease of solar flux is observed at the boundary between the two slabs because the extinction coefficient increases from $K_{s,1} = 100\ \text{m}^{-1}$ to $K_{s,2} = 275\ \text{m}^{-1}$. The infrared radiant fluxes and the temperatures distributions present a maximum at $Z = Z_1$. This observation is in agreement with the expected system behavior. The backward IR emission of slab is absorbed by slab 1, thus the surface temperature is low and the particle temperature is maximal inside the bed.

The ratio of scattering to extinction is defined by the scattering albedo ω. The solid temperature distribution is given as a function of $\omega_{s,1}$ in Fig. 4. To compute these curves, the values $K_{s,1} = 100\ \text{m}^{-1}$ was selected, and $a_{s,1}$ and $\sigma_{s,1}$ were modified to obtain $\omega_{s,1} = 0.15$ (curve 1), $\omega_{s,1} = 0.5$ (curve 2), $\omega_{s,1} = 0.85$ (curve 3). It should be pointed out that the temperature profiles are very sensitive to the albedo $\omega_{s,1}$. When the albedo rises from 0.15 to 0.85, the surface temperature decreases by about 300°C. Since the fraction of solar radiation absorbed by the slab decreases, the gas outlet temperature is reduced at the same time. But notice that these observations are related to ideal cases: The albedo is supposed to be independent of slab 1 reflectance and $a_{r,1}$ does not vary with temperature. The relation between ω and R is known for non-participating media and for complete extinction of radiation at $Z = Z_1$ (Brewster and Tien, 1982), but in the present work this relation cannot be used.

Experimental and Discussion

A scheme of the experimental device is shown in Fig. 5. This

receiver is set at the focus of a 6.5 kW solar concentrator described by Arnaud et al. (1982).

The particles are put inside a 80 mm i.d. alumina tube placed in a stainless steel shell. Cold air is introduced at the upper part of the bed between the irradiated surface of the bed and the transparent window. The 6-mm-thick window transmissivity in the solar band was determined by Pierrot (1987): $\tau_s = 0.94$.

Temperatures are measured using six bare K thermocouples placed inside the bed and two pyrometers. The latter are alumina-shielded thermocouples indicating the inlet and outlet gas temperatures. A mobile optical fiber is used to evaluate the solar radiation extinction through the beds of particules in the forward direction. The silica fiber (core diameter 400 μm) is connected to a silicon photodiode and a position gage to measure the solar intensity and the depth.

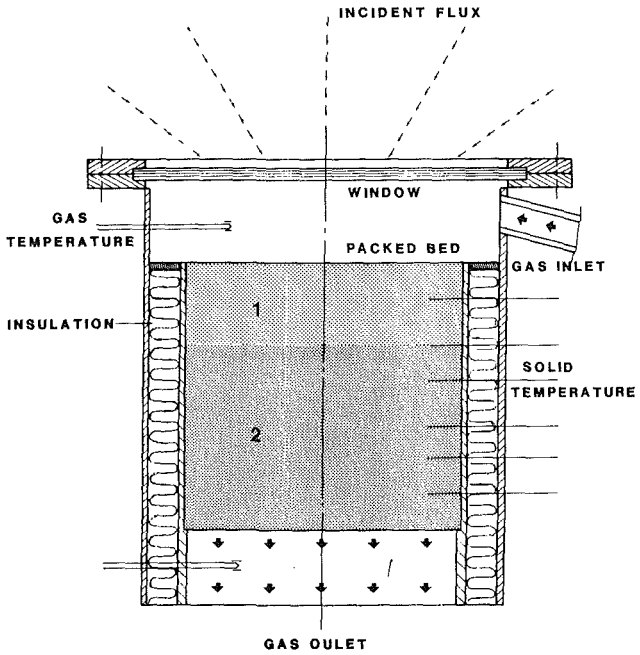

Fig. 5 Scheme of the experimental setup

Extinction versus bed depth is shown in Figs. 6(*a*) and 6(*b*) for glass beads ($d = 2 \times 10^{-3}$ m) and nonspherical silicon carbide particles ($d = 2.36\ 10^{-3}$ m), respectively. Concerning glass, the comparisons of theoretical and experimental profiles are satisfactory for $K = 100\ m^{-1}$, but the results related to SiC particles are not in agreement. The main difference is observed near the bed surface ($Z/d < 2$), where the theoretical and experimental curve concavities are inverted. This suggests that the extinction coefficient varies a lot through the first particle layers (one or two diameter depth). Since the extinction coefficient and the porosity are related by equations (8) and (9), we showed previously, (Flamant, 1985) that experimental and theoretical results may be fitted taking into account the bed vodage variation near the surface. We don't introduce this variation for comparing the results about the two-slab bed because the large decrease of solar intensity between the surface and the slab 2 interface (see Fig. 3*a*) reduces the influence of this parameter on the temperature profile.

Hot experiments were run with a two-layer packed bed composed of glass beads (slab 1) and silicon carbide particles (slab

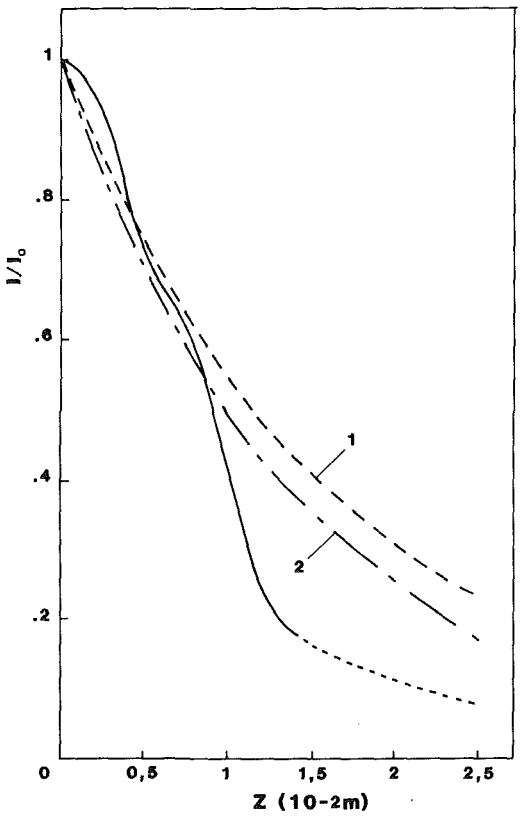

6(*a*)

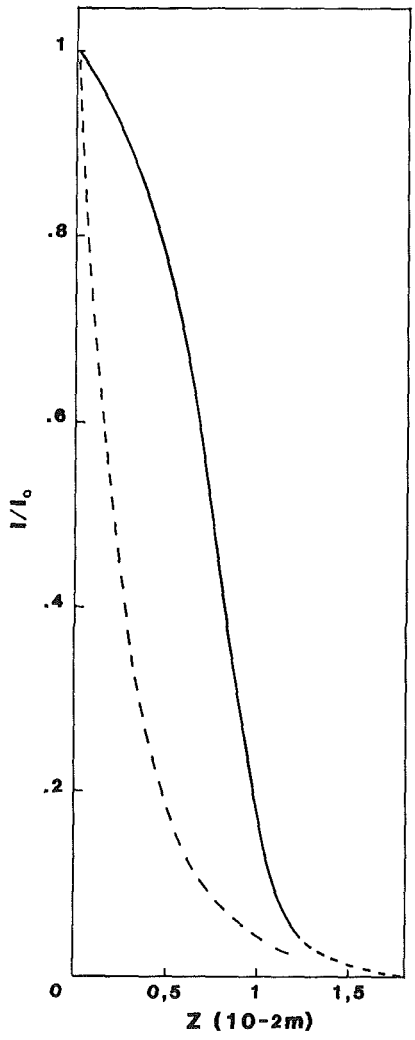

6(*b*)

Fig. 6 Comparison between theoretical and experimental solar flux distribution; 6(*a*) glass beads: $K = 100\ m^{-1}$; (1) $a_s = 15\ m^{-1}$; (2) $a_s = 20\ m^{-1}$; 6(*b*): silicon carbide particles; $K = 195\ m^{-1}$; $a_s = 155\ m^{-1}$, $\sigma_s' = 40\ m^{-1}$, solid line: experimental

Table 2 Properties of slab 1 and 2 for comparison of theoretical and experimental results

Slab	d	ξ	a_s	a_r	σ_s'	σ_r'
1	2	0.42	15	700	85	100
2	2.36	0.54	155	175	40	500

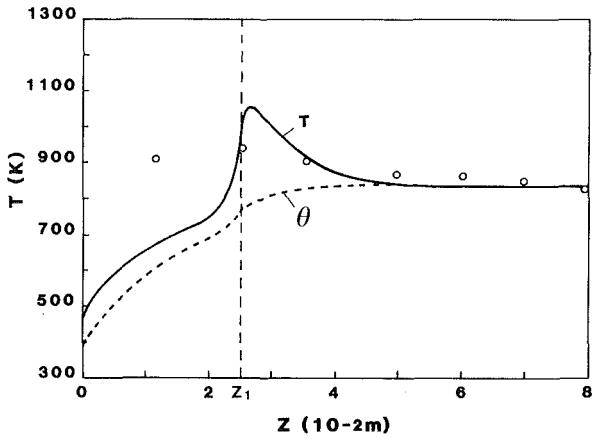

Fig. 7 Comparison between theoretical and experimental temperature profiles (for parameters see Table 2)

2). The depth and the diameter are $Z_1 = 25$ mm, $d_1 = 2$ mm and $Z_2 = 55$ mm, $d_2 = 2.36$ mm, respectively. Experimental results are shown on Fig. 7 (mean solar intensity on the bed surface: 600 kW • m^{-2}) and compared with the theoretical profiles. The numerical simulation parameters are listed on Table 2. The slab 1 properties are not changed (same values in Tables 1 and 2). For slab 2, a_s, a_r, and σ_s' are estimated according to equations (8) and (9), accounting for the measured values of bed voidage. The reflectivities are the same. The gas inlet temperature corresponds to the measured one.

The influence of the window on the bed temperature distribution is analyzed as follows. The window spectral emissivity (ϵ_λ) is a function of wavelengths up to $\lambda = 4$ μm, then $\epsilon_\lambda \simeq 1$. Taking into account the spectral distribution of the bed surface emitted radiation (Planck function) the infrared window transmissivity (τ_w) was calculated versus surface temperature (T_0). At temperatures ranging from 300 to 500 K, τ_w is lower than 0.1. Finally, at low temperatures, the radiant exchange between the slab 1 glass particles and the window may be neglected if $T_0 \simeq T_w$. The thermocouple indications are questionable: Are the measurements related to gas, solid, or intermediate temperature? The latter solution is the more likely, but the heat exchange between the thermocouples and the particles by conduction and radiation are dominant if the temperature difference between the fluid and the solid is small. Inside the bed this condition is respected and the thermocouple is, to a first approximation, at thermal equilibrium with the particles. Consequently we assume that measured temperatures are the solid ones.

Figure 7 shows a good agreement between the experimental and the theoretical data. The difference about gas outlet temperature is less than 10 K and the temperature distribution is fitted except inside slab 1 where the thermocouple is irradiated by the solar flux. The location of the maximal temperature is not measured with precision because the uncertainty concerning the thermocouple depth is about 0.5 mm, and the gradient in this zone is very sharp.

In conclusion, this study shows that a selected temperature profile should be obtained using semitransparent multilayer packed beds. The two-flux model based computing analysis of combined heat transfer in a semitransparent two-layer packed bed prove to be well adapted to predict the solid temperature distribution. The radiative transfer is analyzed using a two-band approach to take into account the variation of absorption and scattering coefficients with wavelength. The spectral selectivity of such a system is demonstrated for slab 1, in which the infrared-to-solar absorption coefficient ratio ranges from 10 to 50. This value is obtained for glass beads. Concerning the temperature distribution, the slab 1 scattering albedo in the solar band is a key parameter. The previous demonstration deals with a two-layer, two-band model, but the approach should be extended to n-layer, n-band systems.

References

Arnaud, G., Flamant, G., Olalde, G., and Robert, J. F., 1981, "Les fours solaires de recherche du L.E.S. d'Odeillo," *Entropie*, 97, pp. 139–146.

Baddour, R. T., and Yoon, C. Y., 1960, "Local Radial Effective Conductivity and Wall Effect in Packed Beds," *Chem. Engng. Prog. Symp. Series*, No. 32, p. 35.

Brewster, M. Q., 1985, "High Temperature Solids/Gas Interactions," ASME/AIChE National Heat Transfer Conference, Denver, CO, Aug. 2-3.

Brewster, M. Q., and Tien, C. L., 1982a, "Radiative Transfer in Packed Fluidized Beds: Dependent Versus Independent Scattering," ASME JOURNAL OF HEAT TRANSFER, Vol. 104, pp. 573-579.

Brewster, M. Q., and Tien, C. L., 1982b, "Examination of the Two Flux Model for Radiative Transfer in Particular Systems," *Int. J. Heat Mass Transfer*, Vol. 25, No. 12, pp. 1905-1907.

Buckius, R. O., 1982, "The Effect of Molecular Gas Absorption on Radiative Heat Transfer With Scattering," ASME JOURNAL OF HEAT TRANSFER, Vol. 104, pp. 580-586.

Buckius, R. O., 1986, "Radiative Transfer in Scattering Media: Real Property Contribution," *Proc. of the 8th Int. Heat Transfer Conf.*, C. L. Tien, V. P. Carey, and J. K. Fernell, eds., Vol. 1, pp. 141-150.

Chan, C. K., and Tien, C. L., 1974, "Radiative Transfer in Packed Spheres," ASME JOURNAL OF HEAT TRANSFER, Vol. 96, pp. 52-58.

Chen, J. C., and Churchill, S. W., 1963, "Radiant Heat Transfer in Packed Beds," *AIChE J.*, Vol. 9, No. 1, p. 35.

Donnadieu, G., 1961, "Transmission de chaleur dans les milieux granulaires. Etude du lit fixe et du lit fluidise," *Revue de l'Institut Francais du Petrole*, Vol. 16, No. 11, pp. 1330-1357.

Flamant, G., 1982, "Theoretical and Experimental Study of Radiant Heat Transfer in a Solar Fluidized Bed Reactor," *AIChE J.*, Vol. 28, No. 4, pp. 529-535.

Flamant, G., 1985, "Transferts de chaleur couplés dans les lits fluidisés à haute température. Application à la conversion de l'énergie solaire," Thesis No. 93, I.N.P., Toulouse, March.

Flamant, G., 1986, "Combined Radiative and Conductive Transient Heat Transfer Between a Wall and a Fluidized Bed," *Proc. of the 8th Int. Heat Transfer Conf.*, C. L. Tien, V. P. Carey, and J. K. Fernell, eds., Vol. 2, pp. 809-814.

Flamant, G., Menigault, T., and Olalde, G., 1987, "Nouveau dispositif d'absorption selective de l'énergie solaire concentré par des lits de particules," *C. R. Acad. Sci.*, Paris, Vol. 304, Series II, No. 13, pp. 689-694.

Grosshandler, W. L., and Monteiro, S. L. P., 1982, "Attenuation of Thermal Radiation by Pulverized Coal and Char," ASME JOURNAL OF HEAT TRANSFER, Vol. 104, pp. 587-593.

Im, K. H., and Ahluwalia, R. K., 1981, "Radiative Transfer in Spectrally Dissimilar Absorbing-Emitting-Scattering Adjacent Media," 16th Thermophys. Conf., Palo Alto, CA, June 23.

Patankar, S. V., 1980, *Numerical Heat Transfer and Fluid Flow*, Series in Computational Methods in Mechanics and Thermal Sciences, McGraw-Hill, New York.

Phillips, J. N., and Eustis, R. H., 1985, "Performance of Radiant Waste Heat Boilers for Coal Gasification Using Diffusion Approximation," XVII I.C.H.M.T. Symposium on High Temperature Heat Exchangers, Dubrovnik, Yugoslavia, Aug. 26-30.

Pierrot, A., 1987, "Contribution ` l'étude des transferts de chaleur à haute température dans les milieux alvéolaires," Thesis, Perpignan University, May.

Sacadura, J. F., Uny, G., and Venet, A., 1986, "Models and Experiments for Radiation Estimation of Absorbing, Emitting and Anisotropically Scattering Media," *Proc. of the 8th Int. Heat Transfer Conf.*, C. L. Tien, V. P. Carey, and J. K. Fernell, eds., Vol. 2, pp. 565-570.

Siegel, R., and Howel, J. R., 1972, *Thermal Radiation Heat Transfer*, McGraw-Hill, New York.

Tong, T. W., and Tien, C. L., 1983, "Radiative Heat Transfer in Fibrous Insulation – Part I: Analytical Study," ASME JOURNAL OF HEAT TRANSFER, Vol. 105, pp. 70-75.

Tong, T. W., Yang, Q. S., and Tien, C. L., 1983, "Radiative Heat Transfer in Fibrous Insulations – Part II: Experimental Study," ASME JOURNAL OF HEAT TRANSFER, Vol. 105, pp. 76-81.

Touloukian, K. S., and De Witt, O. P., 1972, "Thermal Radiative Properties, Nonmetallic Solids," *Thermophysical Properties of Matter*, TPRC Data series, Vol. 8, IFI/Plenum, New York.

Analysis of Combined Conductive-Radiative Heat Transfer in a Two-Dimensional Rectangular Enclosure With a Gray Medium

W. W. Yuen

E. E. Takara

Department of Mechanical and Environmental Engineering, University of California at Santa Barbara, Santa Barbara, CA 93106

Combined conductive-radiative heat transfer in a two-dimensional enclosure is considered. The numerical procedure is based on a combination of two previous techniques that have been demonstrated to be successful for a two-dimensional pure radiation problem and a one-dimensional combined conductive-radiative heat transfer problem, respectively. Both temperature profile and heat transfer distributions are generated efficiently and accurately. Numerical data are presented to serve as benchmark solutions for two-dimensional combined conductive-radiative heat transfer. The accuracy of two commonly used approximation procedures for multidimensional combined conductive-radiative heat transfer is assessed. The additive solution, which is effective in generating approximation to one-dimensional combined conductive-radiative heat transfer, appears to be an acceptable empirical approach in estimating heat transfer in the present two-dimensional problem. The diffusion approximation, on the other hand, is shown to be generally inaccurate. For all optical thicknesses and conduction-radiation parameters considered (including the optically thick limit), the diffusion approximation is shown to yield significant errors in both the temperature and heat flux predictions.

1 Introduction

Combined conductive-radiative heat transfer in a multidimensional enclosure is a problem of considerable practical importance. Until now, most of the reported work in this area has been confined to either combined conduction-radiation in a one-dimensional planar system (Viskanta and Grosh, 1962; Einstein, 1963; Yuen and Wong, 1980) or pure radiation in multidimensional systems (Glatt and Olfe, 1973; Modest, 1975; Ratzel and Howell, 1982; Yeun and Wong, 1984). A series of recent works by Howell et al. (1982, 1984, 1985) appears to contain the only reported solutions in the literature that deal with the combined conductive-radiative heat transfer in a system with multidimensional geometry.

Fundamentally, the difficulty associated with multidimensional combined conductive-radiative heat transfer lies in its extreme mathematical complexity. The energy balance equation is a highly nonlinear partial differential integral equation. While exact analytical solutions are practically impossible to obtain, numerical solutions are difficult and time consuming. Numerical results presented by Razzaque et al. (1984), for example, are mainly those with moderate or large values of the conduction-radiation parameter ($N_1 \geq 0.05$). For cases with low values of the conduction-radiation parameter, the authors noted that "the method requires a substantial amount of computer time to achieve convergence."

In a recent series of works by Yuen et al. (1984a, 1984b, 1985), a numerical technique was developed for two-dimensional pure radiation problems. Utilizing tabulated values of a class of generalized exponential integral function, $S_n(x)$, numerical results were generated accurately and efficiently (cpu time on an 11/780 Vax computer for a typical two-dimensional pure radiation calculation is less than 1 min). In another work on one-dimensional combined conductive-radiative heat transfer (Yuen and Wong, 1980), an iterative procedure, in which the blackbody emissive power is not required to satisfy the no-slip condition at the boundary, was shown to be effective in solving the highly nonlinear differential integral governing equation. The objective of the present work is to demonstrate that the same numerical technique and iteration procedure are also effective in analyzing two-dimensional combined conductive-radiative heat transfer problems. Based on numerical results, the general characteristics of two-dimensional combined conductive-radiative heat transfer are discussed.

It is important to note that due to the mathematical complexity associated with radiation, some approximate procedures are probably necessary for analysis of combined conductive-radiative heat transfer in practical engineering systems. Until now, development of such approximation methods has been difficult because of the lack of an available numerical "benchmark" solution. As is illustrated in the later sections, numerical results generated in the present work are accurate. In addition to illustrating the important physics of combined conductive-radiative heat transfer, these results can serve as a valuable basis for such development. Specifically, the additive solution, which has been shown to be quite accurate for one-dimensional combined conductive-radiative heat transfer (Einstein, 1963; Yuen and Wong, 1980), is demonstrated to be also an accurate empirical procedure to determine two-dimensional combined conductive-radiative heat transfer. The diffusion approximation, which is still one of the common techniques utilized by industries in estimating the effect of radiative heat transfer in practical engineering systems, is shown to be highly inaccurate for two-dimensional problems. For all optical thicknesses and conduction-radiation parameters considered, the diffusion approximation is shown to yield significant errors in both the temperature and heat flux predictions.

Contributed by the Heat Transfer Division for publication in the JOURNAL OF HEAT TRANSFER. Manuscript received by the Heat Transfer Division April 21, 1986. Keywords: Conduction, Radiation, Radiation Interactions.

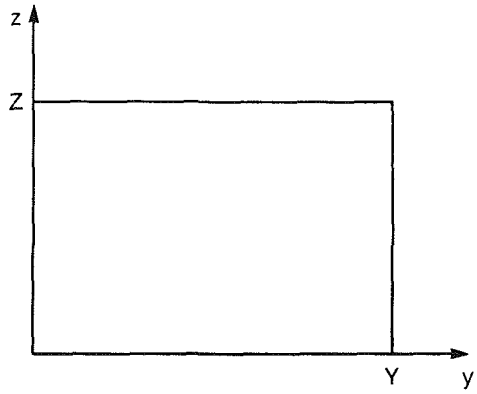

Fig. 1 Geometry and coordinate system for the two-dimensional enclosure

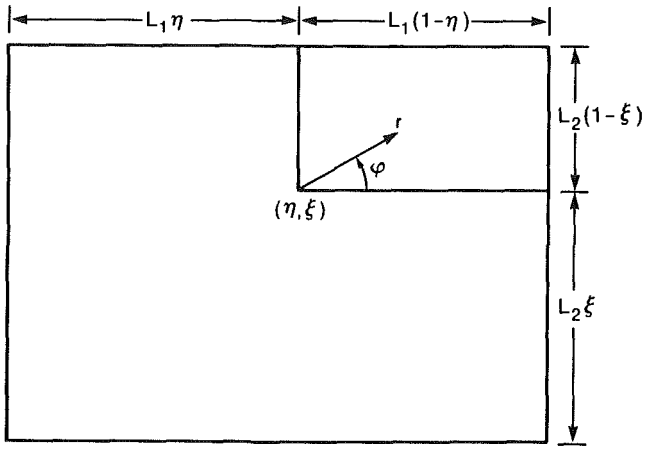

Fig. 2 Domain of integration and the "polar" coordinate used in equation (5)

2 Mathematical Formulation

2(a) Basic Equations. Consider a rectangular enclosure with an associated coordinate system as shown in Fig. 1. The governing equation for combined conductive-radiative heat transfer is well known. For an enclosure with black walls and a nonscattering medium with constant properties and no internal heat generation, it can be written as

$$\frac{4N_1}{L_1^2}\frac{\partial^2\vartheta}{\partial\eta^2}+\frac{4N_1}{L_2^2}\frac{\partial^2\vartheta}{\partial\zeta^2}+L_1L_2\int_0^1\int_0^1 F(\eta',\zeta')\frac{S_1(d_0)}{d_0}\,d\eta'\,d\zeta' = 4F-L_1L_2(1-\vartheta_2^4)\zeta\int_0^1\frac{S_2(d_1)}{d_1^2}\,d\eta' \tag{1}$$

where

$$d_0=[L_1^2(\eta-\eta')^2+L_2^2(\zeta-\zeta')^2]^{1/2} \tag{2a}$$

$$d_1=[L_1^2(\eta-\eta')^2+L_2^2\zeta^2]^{1/2} \tag{2b}$$

$$\vartheta=\frac{T}{T_1},\quad F=\vartheta^4-\vartheta_2^4 \tag{2c}$$

$$N_1=\frac{ka}{4\sigma T_1^3} \tag{2d}$$

$$L_1=aY,\quad L_2=aZ \tag{2e}$$

$$\eta=\frac{y}{Y},\quad \zeta=\frac{z}{Z} \tag{2f}$$

with $\vartheta_2=T_2/T_1$ and T_1 and T_2 being the temperature of the lower wall and the remaining boundary, respectively. N_1 is the familiar conduction-radiation parameter with k and a being the thermal conductivity and absorption coefficient of he medium, respectively. The functions $S_1(x)$ and $S_2(x)$ belong to a class of generalized exponential integral function defined by

$$S_n(x)=\frac{2}{\pi}\int_1^\infty\frac{e^{-xt}dt}{t^n(t^2-1)^{1/2}} \tag{3}$$

This function has been studied extensively and applied successfully to solutions of two-dimensional pure radiation problems in previous works by Yuen et al. (1984a, 1984b, 1985). The boundary conditions for equation (1) are

$$\begin{aligned}\vartheta(\eta,0)&=1.0\\ \vartheta(\eta,1)&=\vartheta_2\\ \vartheta(0,\zeta)&=\vartheta_2\\ \vartheta(1,\zeta)&=\vartheta_2\end{aligned} \tag{4}$$

Nomenclature

- a = absorption coefficient
- $A_{m,n,i,j}$ = coefficient defined by equation (9)
- $B_{i,j}$ = coefficient defined by equation (9)
- d_0 = optical distance, equation (2a)
- d_1 = optical distance, equation (2b)
- F = dimensionless emissive power, equation (2c)
- k = thermal conductivity
- L_1 = optical thickness in the y direction, equation (2e)
- L_2 = optical thickness in the z direction, equation (2e)
- N_1 = conduction-radiation parameter, equation (2d)
- q_a = heat flux calculated by the additive solution, equation (10)
- q_r = heat flux calculated by a pure radiation analysis
- r = radial coordinate, Fig. 2
- S_n = general exponential integral function, equation (3)
- T_1 = temperature of the hot lower wall
- T_2 = temperature of the cold wall
- y = coordinate, Fig. 1
- Y = dimension of the enclosure, Fig. 1
- z = coordinate, Fig. 1
- Z = dimension of the enclosure, Fig. 1
- β_c = dimensionless temperature gradient calculated by a pure conduction analysis
- ζ = dimensionless coordinate in the z direction, equation (2f)
- η = dimensionless coordinate in the y direction, equation (2f)
- ϑ = dimensionless temperature, equation (2c)
- ϑ_2 = T_2/T_1
- σ = Stefan-Boltzmann constant
- φ = angular coordinate, Fig. 2
- φ_1 = angle parameter, equation (6a)
- φ_2 = angle parameter, equation (6b)

As in previous analyses for two-dimensional pure radiation problems utilized by Yuen et al. (1984a, 1984b, 1985), the integrals appearing in equation (1) are reformulated, for convenience, in terms of a "polar" coordinate as shown in Fig. 2. Equation (1) becomes

$$\frac{4N_1}{L_1^2}\frac{\partial^2\vartheta}{\partial\eta^2}+\frac{4N_1}{L_2^2}\frac{\partial^2\vartheta}{\partial\zeta^2}+\iint_{(r,\varphi)}F\left(\eta+\frac{r}{L_1}\cos\varphi,\ \zeta+\frac{r}{L_2}\sin\varphi\right)S_1(r)drd\varphi \tag{5}$$

$$=4F-(1-\vartheta_2^4)\int_{\varphi_1}^{\varphi_2}S_2(L_2\zeta\sec\varphi)d\varphi$$

with

$$\varphi_1=\tan^{-1}\frac{L_1\eta}{L_2\zeta} \tag{6a}$$

$$\varphi_2=\tan^{-1}\frac{L_1(1-\eta)}{L_2\zeta} \tag{6b}$$

2(*b*) Numerical Procedure. Solutions to equation (5) are generated numerically by finite difference. Specifically, the medium is first divided into an $M_1\times M_2$ interior grid such that the coordinate of each interior grid point is given by

$$\eta_i=i\,\delta\eta,\qquad i=1,\ldots,M_1 \tag{7a}$$

$$\delta\eta=\frac{1}{M_1+1}$$

$$\zeta_j=j\,\delta\zeta,\qquad j=1,\ldots,M_2 \tag{7b}$$

$$\delta\zeta=\frac{1}{M_2+1}$$

Equation (5) is then evaluated at the $M_1\times M_2$ grid points to generate a set of M_1M_2 equations for the M_1M_2 unknown temperatures and emissive powers.

Based on a usual Taylor-series expansion of the dimensionless temperature ϑ, the conduction term in equation (5) can be written as

$$\frac{4N_1}{L_1^2}\frac{\partial^2\vartheta}{\partial\eta^2}+\frac{4N_1}{L_2^2}\frac{\partial^2\vartheta}{\partial\zeta^2}=\frac{4N_1}{L_1^2}\frac{\vartheta_{i-1,j}+\vartheta_{i+1,j}-2\vartheta_{i,j}}{\delta\eta^2}+\frac{4N_1}{L_2^2}\frac{\vartheta_{i,j-1}+\vartheta_{i,j+1}-2\vartheta_{i,j}}{\delta\zeta^2} \tag{8}$$

Utilizing a linearized distribution of F within each rectangular element as in Yuen and Ho (1985), the radiation term becomes

$$\iint_{(r,\varphi)}F(\eta_i+\frac{r}{L_1}\cos\varphi,\ \zeta_j+\frac{r}{L_2}\sin\varphi)S_1(r)drd\varphi+(1-\vartheta_2^4)\int_{\varphi'}^{\varphi_2}S_2(L_2\zeta_j\sec\varphi)d\varphi \tag{9}$$

$$=\sum_{m,n=1}^{m,n=M}A_{i,j,m,n}F_{m,n}+B_{i,j}$$

The coefficients $B_{i,j}$ and $A_{i,j,m,n}$ are identical to those generated in the appendix of the previous work (Yuen and Ho, 1985). They are, in general, functions of geometry only and can be readily evaluated based on tabulated values of $S_n(x)$. A set of coefficients, similar to $A_{i,j,m,n}$, must also be tabulated for the evaluation of radiative heat flux. For a typical calculation ($L_1=L_2=1$, $M_1=M_2=10$), the cpu time required for the evaluation of these coefficients is less than 3 min on a 11/780 Vax computer.

Note that in the development of equation (9), the value of F at the boundary is generated by linear interpolation of its values at the two closest grid points in the direction normal to the boundary. It thus does not satisfy the no-slip temperature boundary condition. Since the function F has, in general, a much steeper gradient near the boundary than the function ϑ, a linear approximation for F that does not satisfy the temperature boundary condition yields a better approximation of the radiative contribution to the energy balance. Numerical experiments show that this greatly increases the accuracy of the result, particularly for cases with relatively large grid sizes.

Numerical solutions to equation (5) are generated by iteration. In contrast to many existing works on combined conductive-radiative heat transfer, the present work utilizes different iteration procedures depending on the value of the conduction-radiation parameter. In the limit of large N_1, the conduction term is expected to have the most significant influence on the temperature distribution. Solutions are generated by a conductive iteration in which, at each step of the iteration, the radiative term is evaluated using the temperature distribution calculated at the previous iteration step and considered as a source term. The new temperature distribution is then determined by a matrix inversion of the conduction term. In the limit of small N_1, on the other hand, the effect of radiation is expected to dominate. The emissive power distribution is determined by a radiative iteration in which the conduction term is evaluated using the emissive power determined by the previous iterative step and considered as a source term. The new emissive power distribution is generated by a matrix inversion of the radiative term. For all cases considered, one or both of the above iteration techniques are effective in generating numerical solutions efficiently. For cases with

Table 1 Maximum value of Δ_φ, Δ_{q_η}, and Δ_{q_ζ} in percent along the horizontal and vertical centerlines between the 11 × 11 and 21 × 21 calculations for a square enclosure with various values of L_1 and N_1

$L_1 = L_2$		N_1 = 1.0	0.1	0.01	0.001
0.1	Δ_φ	0.16	0.16	0.14	0.09
	Δ_{q_η}	1.57	1.40	0.64	0.61
	Δ_{q_ζ}	3.88	2.36	0.43	0.33
0.5	Δ_φ	0.15	0.12	0.06	0.42
	Δ_{q_η}	1.47	1.26	1.95	0.82
	Δ_{q_ζ}	3.12	0.76	1.12	0.50
1.0	Δ_φ	0.15	0.09	0.19	0.35
	Δ_{q_η}	1.38	2.05	2.40	1.07
	Δ_{q_ζ}	2.61	1.07	1.53	0.64
2.0	Δ_φ	0.12	0.05	0.12	0.14
	Δ_{q_η}	1.29	2.61	1.95	1.44
	Δ_{q_ζ}	2.17	1.28	1.99	0.89
5.0	Δ_φ	0.11	0.06	0.55	0.53
	Δ_{q_η}	2.88	3.40	4.77	4.90
	Δ_{q_ζ}	2.88	3.40	6.12	3.67

Table 2(a) $\varphi(0.5, \zeta)$ and $q_\zeta(0.5, \zeta)$ for square enclosures with $L_1 = L_2 = 0.1$ and various values of N_1

N_1	ζ = 1.0	0.7	0.5	0.3	0.0
1.0	φ = 0.500	0.560	0.625	0.733	1.000
	q_ζ = 7.473	10.795	17.369	28.074	41.144
0.1	φ = 0.500	0.561	0.626	0.733	1.000
	q_ζ = 1.100	1.542	2.305	3.503	4.932
0.01	φ = 0.500	0.567	0.633	0.738	1.000
	q_ζ = 0.462	0.616	0.798	1.046	1.311
0.001	φ = 0.500	0.615	0.680	0.766	1.000
	q_ζ = 0.398	0.524	0.648	0.801	0.949

Table 2(b) $\varphi(0.5, \zeta)$ and $q_\zeta(0.5, \zeta)$ for square enclosures with $L_1 = L_2 = 1.0$ and various values of N_1

N_1	ζ = 1.0	0.7	0.5	0.3	0.0
1.0	φ = 0.500	0.564	0.630	0.737	1.000
	q_ζ = 0.927	1.352	2.112	3.315	4.701
0.1	φ = 0.500	0.589	0.661	0.763	1.000
	q_ζ = 0.289	0.430	0.609	0.860	1.083
0.01	φ = 0.500	0.653	0.726	0.807	1.000
	q_ζ = 0.222	0.344	0.463	0.610	0.730
0.001	φ = 0.500	0.685	0.736	0.794	1.000
	q_ζ = 0.226	0.322	0.423	0.556	0.722

Table 2(c) $\varphi(0.5, \zeta)$ and $q_\zeta(0.5, \zeta)$ for square enclosures with $L_1 = L_2 = 5.0$ and various values of N_1

N_1	ζ = 1.0	0.7	0.5	0.3	0.0
1.0	φ = 0.500	0.567	0.640	0.755	1.000
	q_ζ = 0.173	0.298	0.514	0.858	1.034
0.1	φ = 0.500	0.585	0.689	0.834	1.000
	q_ζ = 0.039	0.130	0.257	0.408	0.253
0.01	φ = 0.500	0.658	0.732	0.814	1.000
	q_ζ = 0.068	0.111	0.165	0.245	0.388
0.001	φ = 0.500	0.665	0.738	0.817	1.000
	q_ζ = 0.071	0.110	0.161	0.238	0.380

$\vartheta_2 = 0.5$ and $L_1 = L_2 = 1.0$, for example, the conductive iteration is effective in generating solutions with $N_1 \geq 0.02$ while the radiative iteration is effective when $N_1 \leq 0.01$. Using pretabulated values for the coefficients $A_{i,j,m,n}$ and $B_{i,j}$, each iterative calculation requires less than 3 min of cpu time on an 11/780 Vax computer.

Table 2(d) $\varphi(\eta, 0.5)$, $q_\eta(\eta, 0.5)$, and $q_\zeta(\eta, 0.5)$ for square enclosures with $L_1 = L_2 = 0.1$ and various values of N_1

N_1	η = 0.6	0.8	1.0
1.0	φ = 0.620	0.577	0.500
	q_ζ = 16.819	11.800	0.395
	q_η = 4.347	12.619	16.839
0.1	φ = 0.621	0.578	0.500
	q_ζ = 2.241	1.668	0.395
	q_η = 0.494	1.431	1.919
0.01	φ = 0.628	0.583	0.500
	q_ζ = 0.783	0.655	0.395
	q_η = 0.109	0.312	0.427
0.001	φ = 0.674	0.620	0.500
	q_ζ = 0.638	0.554	0.395
	q_η = 0.070	0.200	0.277

Table 2(e) $\varphi(\eta, 0.5)$, $q_\eta(\eta, 0.5)$, and $q_\zeta(\eta, 0.5)$ for square enclosures with $L_1 = L_2 = 1.0$ and various values of N_1

N_1	η = 0.6	0.8	1.0
1.0	φ = 0.624	0.580	0.500
	q_ζ = 2.050	1.489	0.238
	q_η = 0.491	1.422	1.898
0.1	φ = 0.654	0.603	0.500
	q_ζ = 0.595	0.478	0.240
	q_η = 0.107	0.305	0.404
0.01	φ = 0.721	0.669	0.500
	q_ζ = 0.454	0.381	0.245
	q_η = 0.070	0.195	0.250
0.001	φ = 0.733	0.711	0.500
	q_ζ = 0.416	0.357	0.242
	q_η = 0.059	0.171	0.243

3 Results and Discussion

3(a) Numerical Accuracy. Numerical results show that except for regions near the two lower corners at which the boundary condition is singular, solutions converge rapidly. To

Table 2(f) $\varphi(\eta, 0.5)$, $q_\eta(\eta, 0.5)$, and $q_\zeta(\eta, 0.5)$ for square enclosures with $L_1 = L_2 = 5.0$ and various values of N_1

N_1	$\eta = 0.6$	0.8	1.0
1.0	$\varphi = 0.634$	0.586	0.500
	$q_\zeta = 0.496$	0.344	0.039
	$q_\eta = 0.125$	0.344	0.418
0.1	$\varphi = 0.681$	0.614	0.500
	$q_\zeta = 0.245$	0.164	0.048
	$q_\eta = 0.059$	0.137	0.113
0.01	$\varphi = 0.728$	0.692	0.500
	$q_\zeta = 0.161$	0.129	0.061
	$q_\eta = 0.034$	0.099	0.149
0.001	$\varphi = 0.734$	0.700	0.500
	$q_\zeta = 0.158$	0.128	0.063
	$q_\eta = 0.032$	0.095	0.153

illustrate the numerical accuracy, predictions of the dimensionless temperature and heat fluxes along the vertical and horizontal centerline, ($\eta = 0.5$, ζ) and (η, $\zeta = 0.5$), for a square enclosure ($L_1 = L_2$) generated by an 11×11 calculation ($\delta\eta = \delta\zeta = 0.1$) are compared with those generated by a 21×21 calculation ($\delta\eta = \delta\zeta = 0.05$). As a quantitative indicator of the accuracy of the calculation, the relative error of a parameter f (which can be either φ, q_η, or q_ζ) is introduced as

$$\Delta_f = \frac{f_{11\times 11} - f_{21\times 21}}{f_{11\times 11}} \tag{10}$$

The maximum values of Δ_φ, $\Delta_{q\zeta}$, and $\Delta_{q\eta}$ along the two center lines for different optical thicknesses and conduction-radiation parameters are tabulated and presented in Table 1. The dimensionless temperature φ is accurate to within 1 percent for all cases while somewhat higher errors (5 and 6 percent, respectively) are observed for q_η and q_ζ. The accuracy of the solution improves as N_1 decreases. For the pure radiation results, φ, q_η, and q_ζ are all accurate (in the whole enclosure including regions near the two corners) to within 1 percent. Physically, these results indicate that radiative transfer is not very sensitive to the localized temperature distribution. Accurate solution can be generated with a relatively "coarse" 11×11 grid. Because of its relative accuracy, the present numerical data can serve as reference "benchmark" solutions for future development of approximation techniques for multidimensional combined mode heat transfer. They are presented in Tables 2(*a–f*).

For enclosures with L_2/L_1 less than one, numerical experiments show that results generated by an 11×11 calculation are of the same order of accuracy as those presented in Tables 2(*a–f*). For cases with L_2/L_1 greater than one, additional grid points in the vertical direction are required because a larger fraction of the enclosed medium is away from the heating surface. In general, results with a relative accuracy of 5 percent can be obtained provided the dimensionless grid size in the direction of smaller optical thickness is taken to be 0.1 or less and the optical distance between grid points in the two direction are equal (i.e., $L_1\delta\eta = L_2\delta\zeta$).

Table 3 Nondimensional heat flux distribution at different walls with $L_1 = L_2 = 1.0$

Nondimensional position η	Bottom(hot) wall nondimensional heat flux $N_1 = 1.0$	$N_1 = 0.1$	$N_1 = 0.01$	$N_1 = 0.001$	$N_1 = 0$
0.1	11.019	1.817	0.888	0.792	0.778
0.3	5.615	1.195	0.758	0.736	0.729
0.5	4.701	1.083	0.730	0.722	0.716
Nondimensional position ζ	Side(cold) wall nondimensional heat flux $N_1 = 1.0$	$N_1 = 0.1$	$N_1 = 0.01$	$N_1 = 0.001$	$N_1 = 0$
0.1	10.250	1.452	0.581	0.494	0.487
0.3	3.918	0.698	0.373	0.345	0.344
0.5	1.898	0.404	0.250	0.243	0.244
0.7	0.917	0.233	0.163	0.168	0.170
0.9	0.308	0.110	0.096	0.108	0.112
Nondimensional position η	Top(cold) wall nondimensional heat flux $N_1 = 1.0$	$N_1 = 0.1$	$N_1 = 0.01$	$N_1 = 0.001$	$N_1 = 0$
0.1	0.373	0.176	0.163	0.175	0.178
0.3	0.778	0.260	0.207	0.213	0.216
0.5	0.927	0.289	0.222	0.228	0.228
	Total nondimensional heat fluxes $N_1 = 1.0$	$N_1 = 0.1$	$N_1 = 0.01$	$N_1 = 0.001$	$N_1 = 0$
Bottom wall	3.157	0.649	0.398	0.379	0.375
Side wall	2.824	0.518	0.289	0.274	0.274
Top wall	0.316	0.114	0.095	0.099	0.101
% error	0.54	2.52	3.54	1.63	0.00

To demonstrate the heat transfer characteristics and to illustrate further the accuracy of the numerical results, heat flux distributions at the bottom, top, and side boundaries, together with the overall energy balance for enclosures with L_1, $L_2 = 1.0$, 0.5, are presented in Tables 3, 4, and 5. It can be readily observed that in all cases overall energy balance is achieved to within 4 percent. In general, the accuracy of the heat flux prediction is equivalent to a similar pure-conduction calculation utilizing an 11×11 grid. Indeed, it is interesting to note that the general overall accuracy of the computation appears to depend on the finite difference approximation of the conduction term. The radiative term, based on the present formulation, is extremely accurate. Additional numerical data for both temperature and heat flux distribution (with L_1, $L_2 = 0.1$, 0.5, 1.0, 2.0, 5.0 and $N_1 = 0$, 0.001, 0.01, 0.1, 1.0, 10.0) are presented elsewhere (Takara, 1987).

For a square enclosure with $L_1 = L_2 = 1.0$, the centerline temperature and heat flux distribution presented in Tables 2(*a–f*) are essentially identical to the graphic results presented by Razzaque et all. (1984). This agreement supports the accuracy of the present calculation. The centerline heat flux generated by the P-3 approximation (Ratzel and Howell, 1982) differs significantly from the present results. This demonstrates the uncertain accuracy of the P-3 approximation.

3(*b*) Accuracy of the Diffusion Approximation. Because

Table 4 Nondimensional heat flux distribution at different walls with $L_1 = 1.0$ and $L_2 = 0.5$

Nondimensional position η	Bottom(hot) wall nondimensional heat flux $N_1 = 1.0$	$N_1 = 0.1$	$N_1 = 0.01$	$N_1 = 0.001$	$N_1 = 0$
0.1	14.042	2.128	0.934	0.812	0.797
0.3	6.363	1.309	0.807	0.765	0.757
0.5	5.494	1.210	0.786	0.754	0.746
Nondimensional position ζ	Side(cold) wall nondimensional heat flux $N_1 = 1.0$	$N_1 = 0.1$	$N_1 = 0.01$	$N_1 = 0.001$	$N_1 = 0$
0.1	13.889	1.848	0.653	0.536	0.524
0.3	7.223	1.093	0.484	0.430	0.426
0.5	4.098	0.711	0.373	0.348	0.349
0.7	2.214	0.458	0.285	0.279	0.282
0.9	0.796	0.249	0.202	0.213	0.220
Nondimensional position η	Top(cold) wall nondimensional heat flux $N_1 = 1.0$	$N_1 = 0.1$	$N_1 = 0.01$	$N_1 = 0.001$	$N_1 = 0$
0.1	1.556	0.461	0.353	0.348	0.349
0.3	3.309	0.743	0.481	0.455	0.453
0.5	3.819	0.827	0.521	0.489	0.486
	Total nondimensional heat fluxes $N_1 = 1.0$	$N_1 = 0.1$	$N_1 = 0.01$	$N_1 = 0.001$	$N_1 = 0$
Bottom wall	3.748	0.723	0.420	0.391	0.387
Side wall	2.419	0.396	0.196	0.181	0.181
Top wall	1.319	0.317	0.216	0.207	0.207
% error	0.25	1.28	1.99	1.13	0.10

Table 5 Nondimensional heat flux distribution at different walls with $L_1 = 0.5$ and $L_2 = 1.0$

Nondimensional position η	Bottom(hot) wall nondimensional heat flux $N_1 = 1.0$	$N_1 = 0.1$	$N_1 = 0.01$	$N_1 = 0.001$	$N_1 = 0$
0.1	21.278	2.896	1.000	0.864	0.836
0.3	10.576	1.779	0.898	0.826	0.809
0.5	8.772	1.587	0.871	0.816	0.802
Nondimensional position ζ	Side(cold) wall nondimensional heat flux $N_1 = 1.0$	$N_1 = 0.1$	$N_1 = 0.01$	$N_1 = 0.001$	$N_1 = 0$
0.1	11.681	1.532	0.520	0.410	0.405
0.3	2.708	0.481	0.253	0.227	0.228
0.5	0.824	0.200	0.134	0.128	0.130
0.7	0.268	0.093	0.073	0.075	0.077
0.9	0.077	0.040	0.038	0.042	0.045
Nondimensional position η	Top(cold) wall nondimensional heat flux $N_1 = 1.0$	$N_1 = 0.1$	$N_1 = 0.01$	$N_1 = 0.001$	$N_1 = 0$
0.1	0.098	0.082	0.083	0.092	0.097
0.3	0.143	0.098	0.094	0.101	0.105
0.5	0.159	0.103	0.098	0.104	0.108
	Total nondimensional heat fluxes $N_1 = 1.0$	$N_1 = 0.1$	$N_1 = 0.01$	$N_1 = 0.001$	$N_1 = 0$
Bottom wall	2.983	0.483	0.230	0.210	0.205
Side wall	2.946	0.455	0.199	0.180	0.180
Top wall	0.032	0.023	0.023	0.024	0.026
% error	0.58	0.57	3.71	2.86	0.03

of the mathematical complexity of radiation, the diffusion approximation (Deisler, 1964) is still a common approximation procedure utilized by most practicing engineers in assessing the importance of radiation in actual multidimensional engineering systems. It is interesting to note, however, that, except for one-dimensional planar systems, the relative accuracy of the diffusion approximation has never been demonstrated quantitatively. The present numerical results are now used to assess the accuracy of the diffusion approximation for two-dimensional combined conduction-radiation problems.

Using an 11×11 grid, numerical results are generated for the same set of values for L_1, L_2, and N_1 based on the diffusion approximation. A complete set of numerical data is presented elsewhere (Takara, 1987). Using an expression similar to equation (10) (with $f_{21\times21}$ replaced by f_{dif}), the minimum and maximum values of Δ_φ, Δ_{q_η} and Δ_{q_ζ} for various square enclosures are presented in Table 6. Since the diffusion approximation always predicts a correct φ at the boundary, the minimum Δ_φ is calculated only for the interior points along the two centerlines. It is apparent that while the diffusion approximation is moderately successful in predicting the interior temperature distributions φ (less than 17 percent maximum relative error), it is uniformly inaccurate in predicting heat transfer. The validity of many existing practical engineering calculations utilizing the diffusion approximation for the radiative heat transfer effect is thus highly uncertain.

3(c) Accuracy of the Additive Solution. In one-dimensional combined conductive-radiative heat transfer

Table 6 Maximum (minimum) value of Δ_φ, Δ_{q_η}, and Δ_{q_ζ} in percent along the horizontal and vertical centerlines between the numerical results and the diffusion approximation and an 11 x 11 grid for a square enclosure with various values of L_1 and N_1

$L_1 = L_2$		$N_1 = 1.0$	0.1	0.01	0.001
0.1	Δ_φ	6.20(1.29)	15.02(5.06)	16.30(5.38)	9.67(2.13)
	Δ_{q_η}	60.01(59.98)	57.43(56.56)	531.69(516.30)	871.27(836.27)
	Δ_{q_ζ}	100.00(60.27)	100.00(3.60)	387.37(86.88)	563.32(100.00)
0.5	Δ_φ	5.98(1.18)	12.60(4.03)	7.11(0.27)	10.19(0.01)
	Δ_{q_η}	62.31(62.22)	3.32(1.97)	85.48(81.68)	111.24(102.78)
	Δ_{q_ζ}	100.00(63.04)	100.00(9.01)	100.00(5.68)	100.00(0.25)
1.0	Δ_φ	5.52(1.00)	9.23(2.72)	4.81(0.04)	10.06(0.21)
	Δ_{q_η}	64.60(64.49)	27.66(27.61)	5.36(0.97)	14.08(6.79)
	Δ_{q_ζ}	100.00(65.23)	100.00(32.66)	100.00(12.51)	100.00(12.47)
2.0	Δ_φ	4.62(0.83)	5.64(2.08)	7.34(0.64)	10.14(0.18)
	Δ_{q_η}	67.93(67.01)	53.37(44.72)	38.90(38.50)	39.84(32.86)
	Δ_{q_ζ}	100.00(67.42)	100.00(47.68)	100.00(46.48)	100.00(44.37)
5.0	Δ_φ	3.25(0.94)	7.19(0.64)	6.55(0.26)	8.15(0.08)
	Δ_{q_η}	72.11(67.78)	73.77(46.96)	64.70(59.64)	66.12(58.51)
	Δ_{q_ζ}	100.00(66.78)	100.00(34.27)	100.00(63.64)	100.00(62.98)

Table 7 Maximum (minimum) value of Δ_φ, Δ_{q_η}, and Δ_{q_ζ} in percent along the horizontal and vertical centerlines between the numerical results and the additive solution with an 11×11 grid for a square enclosure with various values of L_1 and N_1

$L_1 = L_2$		$N_1 = 1.0$	0.1	0.01	0.001
0.1	Δ_{q_η}	0.02(0.01)	0.20(0.10)	0.87(0.42)	1.24(0.40)
	Δ_{q_ζ}	0.48(0.00)	0.48(0.00)	0.64(0.01)	0.69(0.09)
0.5	Δ_{q_η}	0.33(0.08)	2.11(0.42)	4.95(0.35)	1.77(1.06)
	Δ_{q_ζ}	0.73(0.03)	1.75(0.02)	2.79(0.77)	1.08(0.38)
1.0	Δ_{q_η}	1.04(0.20)	5.78(1.39)	10.60(4.32)	1.11(0.85)
	Δ_{q_ζ}	1.38(0.27)	4.30(0.46)	6.22(0.19)	1.19(0.08)
2.0	Δ_{q_η}	2.73(0.47)	14.66(3.37)	4.41(3.54)	0.88(0.50)
	Δ_{q_ζ}	10.26(0.50)	19.31(0.95)	5.62(0.05)	1.07(0.00)
5.0	Δ_{q_η}	16.12(0.38)	65.04(7.58)	5.50(2.02)	0.65(0.16)
	Δ_{q_ζ}	60.46(0.71)	119.18(0.23)	7.05(0.06)	0.99(0.00)

analysis, it is well know that the additive solution generated by separate independent analyses of the two transfer processes is an accurate approximation (within 10 percent) to the total heat transfer (Einstein, 1963; Yuen and Wong, 1980). For the present two-dimensional problem, an additive solution for the heat transfer can be written as

$$q_a = 4N_1\beta_c + q_r \tag{11}$$

where β_c is the appropriate temperature gradient calculated from a pure conduction analysis and q_r is the radiative flux generated by a pure radiation analysis of the same enclosure. Utilizing numerical results generated from an 11×11 pure conduction analysis ($\delta\eta = \delta\zeta = 0.1$) and results of a pure radiation analysis presented in a previous work (Yuen and Wong, 1984), the maximum and minimum values of Δ_{q_η} and Δ_{q_ζ} for various square enclosures are tabulated and presented in Table 7. The additive approximation appears to be a reasonable estimate for both components of the heat flux over the whole enclosure. Physically, this result suggests that for the estimate of heat transfer, the interaction between conduction and radiation can be considered as sufficiently weak that each process acts almost independently. It is important to note, however, that the additive solution cannot be used to predict the temperature profile.

4 Conclusions

Results of a two-dimensional combined conductive-radiative heat transfer analysis are presented. Based on a numerical technique developed previously for a two-dimensional analysis of radiative transfer and an iteration procedure utilized for a previous one-dimensional combined conductive-radiative analysis, numerical results are generated accurately and efficiently. Numerical data for temperature and heat flux distributions are presented.

Based on numerical results, the accuracy of two commonly used approximation methods for radiative transfer is assessed. The diffusion approximation is shown to be uniformly inaccurate for two-dimensional combined conduction radiation problems. For all optical thicknesses and conduction-radiation parameters considered (including the optically thick limit), the diffusion approximation is shown to yield significant errors in both the temperature and heat flux predictions. The additive solution, on the other hand, appears to be an effective empirical approach in estimating heat transfer. The success of the additive solution suggests that in multidimensional combined conduction-radiation problems, the interaction between radiation and conduction can be considered as sufficiently weak that the two processes contribute independently to the total heat transfer.

References

Deisler, R. G., 1964, "Diffusion Approximation for Thermal Radiation in Gases With Jump Boundary Condition," ASME JOURNAL OF HEAT TRANSFER, Vol. 86, No. 2, pp. 240-246.

Einstein, T. H., 1963, "Radiant Heat Transfer to Absorbing Gases Enclosed Between Parallel Flat Plates With Flow and Conduction," NASA TR R-154.

Glatt, L., and Olfe, D. B., 1973, "Radiative Equilibrium of a Gray Medium in a Rectangular Enclosure," *Journal of Quantitative Spectroscopy and Radiative Transfer*, Vol. 13, p. 881.

Larsen, M. E., and Howell, J. R., 1985, "The Exchange Factor Method: An Alternative Basis for Zonal Analysis of Radiating Enclosure," ASME JOURNAL OF HEAT TRANSFER, Vol. 107, No. 4, pp. 936-942.

Modest, M. F., 1975, "Radiative Equilibrium of a Gray Medium in a Rectangular Enclosure Bounded by Gray Walls," *Journal of Quantitative Spectroscopy and Radiative Transfer*, Vol. 15, p. 445.

Ratzel, A. C., and Howell, J. R., 1982, "Two-Dimensional Radiation in Absorbing-Emitting-Scattering Media Using the P-N Approximation," ASME Paper No. 82-HT-19.

Ratzel, A. C., and Howell, J. R., 1982, "Two-Dimensional Energy Transfer in Radiatively Participating Media With Conduction by the P-N Approximation," *Proceedings of the Seventh International Heat Transfer Conference*, Vol. R14, pp. 535-540.

Razzaque, M. M., Howell, J. R., and Klein, D. E., 1984, "Coupled Radiative and Conductive Heat Transfer in a Two-Dimensional Rectangular Enclosure With Gray Participating Media Using Finite Elements," ASME JOURNAL OF HEAT TRANSFER, Vol. 106, pp. 613-619.

Takara, E., 1987, "Two-Dimensional Combined Conductive Radiative Heat Transfer," M. S. Thesis, University of California, Santa Barbara, in preparation.

Viskanta, R., and Grosh, R. J., 1962, "Heat Transfer by Simultaneous Conduction and Radiation in an Absorbing Medium," ASME JOURNAL OF HEAT TRANSFER, Vol. 84, pp. 63-72.

Yuen, W. W., and Wong, L. W., 1980, "Heat Transfer by Conduction and Radiation in a One-Dimensional Abosrbing, Emitting and Anisotropically Scattering Medium," ASME JOURNAL OF HEAT TRANSFER, Vol. 102, pp. 303-307.

Yuen, W. W., and Wong, L. W., 1984, "Analysis of Radiative Equilibrium in a Rectangular Enclosure With Gray Medium," ASME JOURNAL OF HEAT TRANSFER, Vol. 106, pp. 433-440.

Yuen, W. W., 1984, "Analysis of Radiative Equilibrium in a Rectangular Enclosure With Gray Medium: Cases With Diffusely Reflecting Surfaces and Heat Flux Boundary Conditions," presented at the 1984 ASME Winter Annual Meeting, New Orleans, LA, Dec.

Yuen, W. W., and Ho, C. F., 1985, "Analysis of Two-Dimensional Radiative Heat Transfer in a Gray Medium With Internal Heat Generation," *International Journal of Heat and Mass Transfer*, Vol. 28, No. 1, pp. 17-23.

R. L. Judd
Professor,
McMaster University,
Department of Mechanical Engineering,
Hamilton, Ontario, L8S 4L7, Canada

On Nucleation Site Interaction

Introduction

The ultimate goal of nucleate boiling heat transfer research is to be able to incorporate the surface characteristics in the relationships that predict boiling heat transfer rate. Much effort has been devoted to this goal but until very recently, most of the research has been directed toward specific tasks such as determining the interrelationship between heat flux and surface superheat for a particular material, with less of the research being directed toward understanding the nucleate boiling phenomena. Yet if the underlying mechanisms were better understood, it would be possible to predict the rate of boiling heat transfer a priori and to design and manufacture boiling heat transfer surfaces to specification. More importantly, the ability to predict boiling conditions from the surface characteristics would enable the performance of the boiling heat transfer surfaces to be optimized.

Accordingly, a probabilistic approach to relating boiling heat transfer rate to the surface characteristics has been pursued. Given the number of nucleation sites randomly distributed over a boiling surface, the active site density could be predicted if relationships were known for the probability of nucleation at the sites, and once the active site density was known, the bubble flux density and boiling heat transfer rate could be predicted in the manner outlined in Shoukri and Judd [1]. The problem of relating boiling heat transfer rate to the boiling surface characteristics then becomes a matter of determining the probability relations, which depend on the interaction of the processes of bubble nucleation at adjacent sites.

Despite the fact that Gaertner [2] claimed to have proven that clustering around nucleation sites was an illusion because the nucleation sites were randomly distributed over the boiling surface, Sultan [3] found that the clustering effect was indeed real since the bubble flux density was nonuniformly distributed over the boiling surface even though the nucleation sites were randomly distributed. The observation of clustering suggested interaction between the nucleation sites and in a subsequent investigation, Sultan and Judd [4] demonstrated that such interaction actually occurred by doing cross-correlation function analysis on the signals arising from the nucleation processes occurring at adjacent nucleation sites. However, the information obtained from this investigation was not in an appropriate form to generate probability relationships and so another investigation of a different nature was contrived.

Experimental Investigation

Calka [5] and Calka and Judd [6] undertook an experimental investigation in which boiling was observed from beneath a transparent heater surface. The time that elapsed between the commencement of bubble formation at pairs of adjacent nucleation sites was measured using photo-optical techniques in the manner described in the reference and the values obtained were stored in computer memory. The measuring process was repeated continuously under the control of the computer and when sufficient measurements had been obtained to assure that the distribution of the measurements was no longer changing with time, histograms were generated. These histograms had the general form of a gamma distribution $\Gamma(\bar{\tau}, \nu)$ where $\bar{\tau}$ is the mean value of the sample of elapsed time values and ν is a numerical parameter known as the shape coefficient that determines the particular gamma distribution. The shape of the histograms was dependent upon the separation between the pair of adjacent nucleation sites. Accordingly, the experimental results were fitted with the gamma distribution, using a visual technique that involved subjective judgment of the goodness of fit, thereby enabling values of $\bar{\tau}$ and ν corresponding to the best fit for each pair of adjacent nucleation sites to be determined.

The relationship observed between the shape coefficient of the gamma distribution that best fitted the data ν and the dimensionless separation distance $S/\bar{D}_b$ can be seen in Fig. 1. High-speed motion picture analysis afforded an explanation of the form of the relationship. For $\nu > 1$, which occurred for $0.5 < S/\bar{D}_b < 1.0$, formation of a bubble at the initiating site promoted the formation of a bubble at the adjacent site as the result of "site seeding"; for $\nu < 1$, which occurred for $1.0 < S/\bar{D}_b < 3.0$, formation of a bubble at the initiating site inhibited the formation of a bubble at the adjacent site, most likely as the result of "site deactivation." Both of these phenomena have been reported in Eddington and Kenning [7] and Judd and Lavdas [8]. For $\nu \simeq 1$, which occurred for $S/\bar{D}_b > 3.0$, there was no interaction between the nucleation phenomena occurring at the adjacent sites. From this research, it was concluded that the active site distribution and the bubble flux density are determined by the bubble nucleation process occurring at the continually active nucleation sites on the surface, which are capable of affecting bubble nucleation at the surrounding intermittently active nucleation sites.

Knowles [9] repeated this investigation using the same apparatus but a different transparent heater surface, because Calka's surface had broken at the end of his investigation after several high-speed motion pictures had been taken. In keeping with the previous experiment, dichloromethane was boiled on the glass surface, which was coated with a ½ wavelength thickness of stannic oxide enabling heat to be generated. The heat transfer surface had dimensions of 50 mm

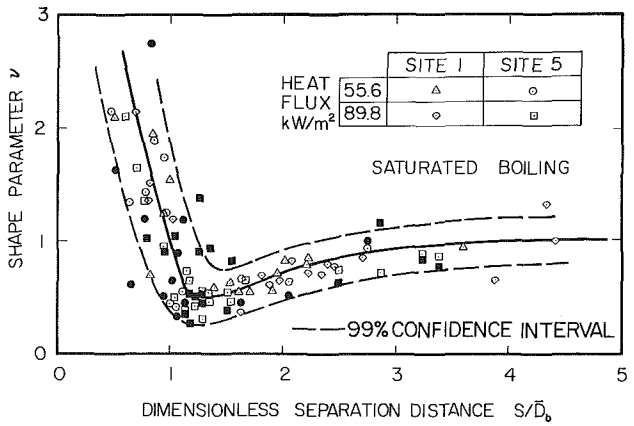

Fig. 1 Variation of shape parameter with dimensionless separation distance from Calka's investigation

Contributed by the Heat Transfer Division for publication in the JOURNAL OF HEAT TRANSFER. Manuscript received by the Heat Transfer Division October 10, 1985. Keywords: Building Heat Transfer, Modeling and Scaling.

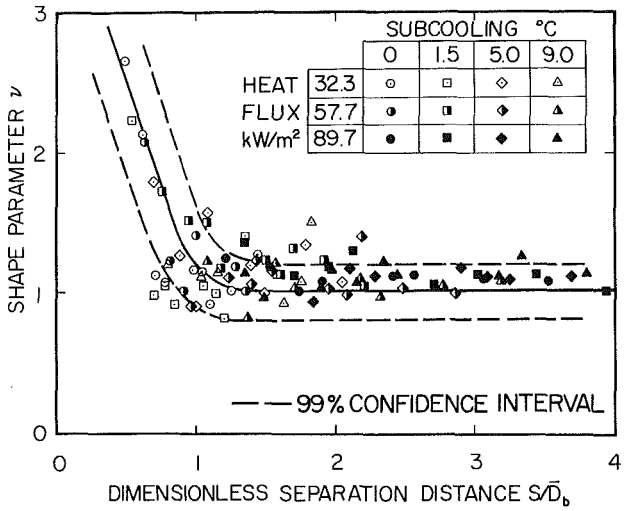

Fig. 2 Variation of shape parameter with dimensionless separation distance from Knowles' investigation

by 33 mm and it was assumed that heat was generated uniformly over it because this assumption had been shown to be satisfactory in Judd [10]. The lower part of the heat transfer surface, which was coated with a ¼ wavelength thickness of antireflective coating, was exposed to the air. More details concerning the heat transfer surface can be found in Voutsinos [11].

Data Acquisition

A data acquisition system (DECLAB 11/03 laboratory computer and appropriate software) was employed to gather and store the data. Voltage signals generated by the activity at each of the pair of adjacent nucleation sites under investigation were directed to the two Schmitt triggers in the computer's programmable real time clock unit. The setting of the threshold levels of the Schmitt triggers was very important for the accuracy of the elapsed time measurement because of the necessity of minimizing spurious interrupts. For this reason, the level of both Schmitt triggers was set as close to the base signal levels corresponding to boiling inactivity as possible and both were set to trigger on voltage rising (positive slope).

As explained above, Calka and Judd [6] found that the gamma distribution correlated the time elapsed between the formation of bubbles at adjacent nucleation sites. In order to fit the present data with the gamma distribution, a modified version of Calka's [5] program GAMFIT was used. Using the techniques of nonlinear optimization, the modified program varied the two parameters that determine the gamma distribution (mean value $\bar{\tau}$ and shape coefficient ν) incrementally in order to minimize the χ^2 value based upon the differences between the predicted and measured distributions. The modified version of program GAMFIT was tested on Calka's [5] data prior to being used in the present investigation, yielding the darkened symbols that appear in Fig. 1. Except for a small amount of additional scatter, there is no real difference in the results obtained inasmuch as a statistical test performed upon the two sets of values indicated that there was no reason to favor either one over the other.

Similar levels of heat flux were investigated in Calka's [5] and Knowles' [9] experiments at saturated boiling conditions, although the saturation pressure levels were somewhat different and in addition, Knowles investigated four levels of subcooling as well. All of the interrelationships between bubble nucleation phenomena at adjacent sites were investigated, one pair of active sites at a time. When all pairs had been so examined, the boiling conditions were changed, and after steady state was re-established, the whole procedure was repeated again.

Results and Analysis

Figure 2, which presents the results of Knowles' [9] investigation, is significantly different from Fig. 1, which presents the results of Calka's [5] investigation. The most prominent difference is the fact that, while according to the results of both investigators, promotion of bubble nucleation occurred in the region $0.5 < S/\bar{D}_b < 1.0$ where $\nu \geq 1$, inhibition of bubble nucleation in the region $1.0 < S/\bar{D}_b < 3.0$ was absent in Knowles' [9] investigation where $\nu \simeq 1$, although it was present in Calka's investigation where $\nu \leq 1$. The reason for the difference is not immediately apparent inasmuch as the surfaces were ostensibly the same. However, while the exact service history is not known, Calka's surface had been in use for many hundreds of hours, whereas Knowles' surface had been in use for only a relatively short period of time. The difference was manifest in the way in which the two surfaces responded to an increase in heat flux. Calka's surface boiled easily in that a small increase in heat flux led to an immediate increase in the number of active nucleation sites to accommodate it. On the other hand, Knowles' surface was difficult to boil and initially it had to be heated for over a week before any stable nucleation sites were formed. This behavior is not unusual for oxide coated glass boiling surfaces in which nucleation sites have to be developed because the surface is essentially smooth to begin with, but this particular surface seemed more difficult to break in than most. The difficulty experienced with breaking in this surface suggests that at the times that the surfaces were tested, the surface characteristics were considerably different. In fact as it turned out, Calka's [5] surface had approximately twice as many potentially active nucleation sites as Knowles' [9] surface and the nearest neighboring distances were considerably less, as will be discussed later.

Interpretation of Results

The difference in the behavior of the two boiling surfaces is associated with the distribution of the nucleation sites on the surfaces. The model being proposed envisages a random distribution of nucleation sites comprised of a small number of continually active nucleation sites surrounded by a large number of intermittently active nucleation sites. The continually active nucleation sites are capable of trapping a vapor residue that will form the nucleus of the next bubble whenever a bubble departs, whereas the intermittently active nucleation

Nomenclature

$\bar{D}_b$ = average bubble departure diameter
h = heat transfer coefficient
N/A = active site density
P_{sat} = saturation pressure
q'' = heat flux
$\bar{R}_b$ = average bubble departure radius
s = shortest spacing between nucleation sites
S = spacing between nucleation sites
T_{sat} = saturation temperature
T_w = wall temperature
ν = shape parameter of the gamma distribution
$\bar{\tau}$ = mean value of the gamma distribution

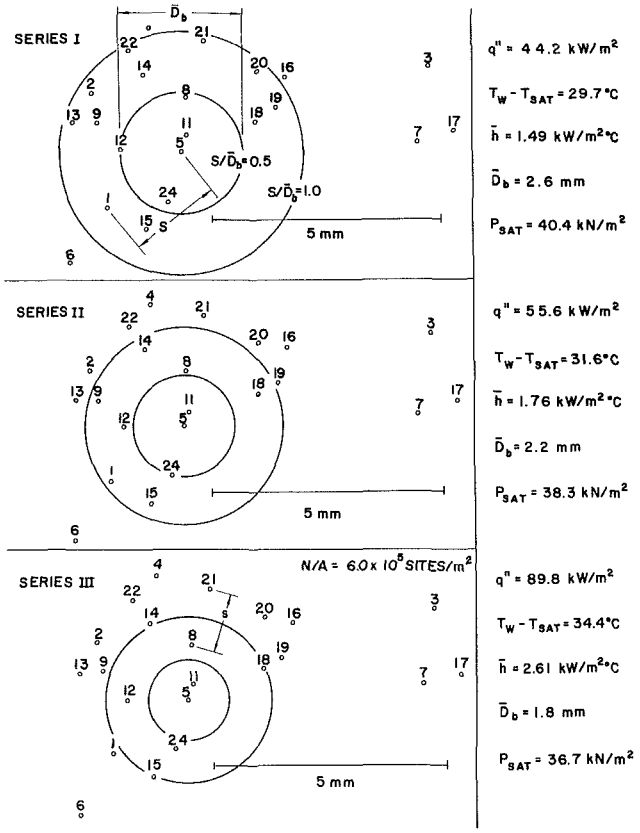

Fig. 3 Site map from Calka's investigation

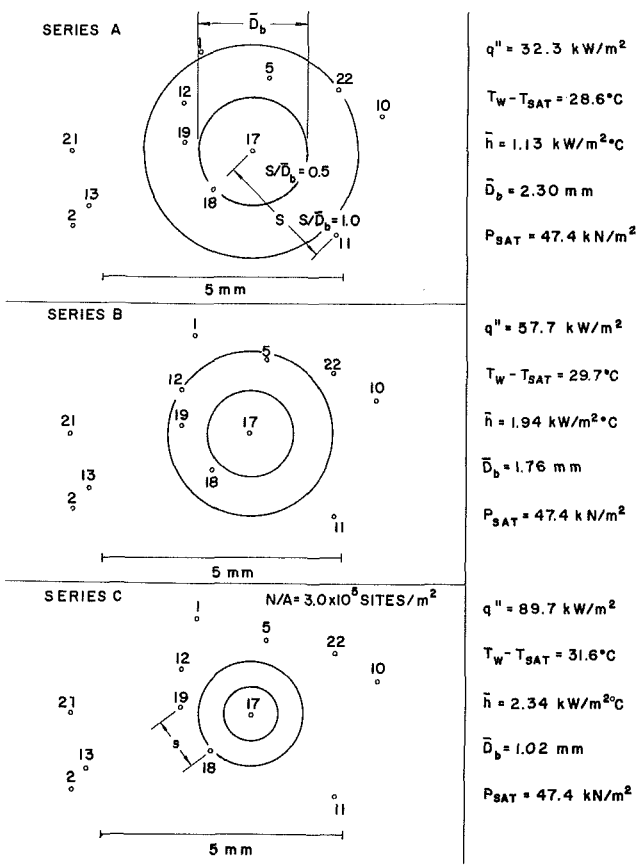

Fig. 4 Site map from Knowles' investigation

sites are capable of emitting only a single bubble whenever a nucleus is deposited in them. Bankoff [12] established the existence of such nucleation sites when he identified four different types of cavity: those that are always vapor filled, those from which vapor can be displaced by liquid, those from which liquid can be displaced by vapor, and those that are always liquid filled. The continually active nucleation sites and the intermittently active nucleation sites correspond to the first and second categories, respectively. The conditions that must be satisfied in order for a bubble to be nucleated at a continually active nucleation site and the frequency at which bubbles will be nucleated will depend upon the properties of the liquid, the effective cavity radius, and the level of superheat in accordance with traditional nucleation theory. However, the nucleation of a bubble at an intermittently active nucleation site depends upon deposition of vapor by a bubble that formed at a adjacent site as the result of being covered and "dried out" by evaporation of the microlayer that formed beneath it. Bubble emission at these sites depends upon "seeding" because any vapor residue would be swept out of the cavity by the liquid that replaced the bubble that grew from the deposited nucleus when it departed.

Figures 3 and 4 show the site maps for the regions surrounding two particularly stable continually active nucleation sites (site #5 on Calka's [5] boiling surface and site #17 on Knowles' [9] surface). Each of the points on the surfaces is an active nucleation site inasmuch as bubble nucleation was observed at the particular location at some time during the investigation but continuous bubble emission occurred only at site #5 and site #17, respectively (with the possible exception of site #1 on Calka's surface, which might have been a continually active nucleation site as well). By inspection, it is apparent that there are approximately twice as many active nucleation sites on Calka's [5] boiling surface as there are on Knowles' [9] boiling surface in the regions surrounding the continually active nucleation sites.

As Calka and Judd [6] reported, the radius of a bubble at departure would sometimes grow as large as twice the average departure diameter. Subsequently, bubbles would be formed at sites that had been seeded between $S/\bar{D}_b = 0.5$ and $S/\bar{D}_b = 1.0$ and these sites, which would have otherwise been inactive, would be temporarily activated and emit one bubble ($\nu > 1$). About one bubble in ten would grow much larger, presumably as the result of energy accumulation in the vicinity of the continually active nucleation site after a relatively long period of inactivity at the surrounding sites. Some of the surrounding sites lying farther out ($S/\bar{D}_b > 1.0$) would be seeded and it is the subsequent nucleation of bubbles at these sites that accounts for the differences reported by Calka and Knowles.

Depending upon the spacing between the sites, as will be explained below, bubble emission could be delayed by the formation of bubbles at adjacent sites. When the separation between the sites was great enough that bubbles forming at the sites inside of the circle $S/\bar{D}_b = 1.0$ were able to cover few of the sites outside of the circle, which is the situation that existed on Knowles' surface, then the time that would elapse from the formation of a bubble at the continually active nucleation site to the formation of a bubble at any of the surrounding nucleation sites would most often be a random event ($\nu = 1$). Because of the sparse active site population and the relatively large separation distances, there would be little interaction. When the separation between the sites was small enough that bubbles forming at the sites inside of the circle $S/\bar{D}_b = 1.0$ were able to cover many of the sites outside of the circle, which is the situation that existed on Calka's surface, then nucleation from any site that had not yet emitted a bubble after having been seeded could be delayed while it was being covered ($\nu < 1$). Any bubble subsequently emitted by such a site would form from the nucleus left by the bubble that had covered it last and not from the nucleus deposited by the bubble that had formed at the

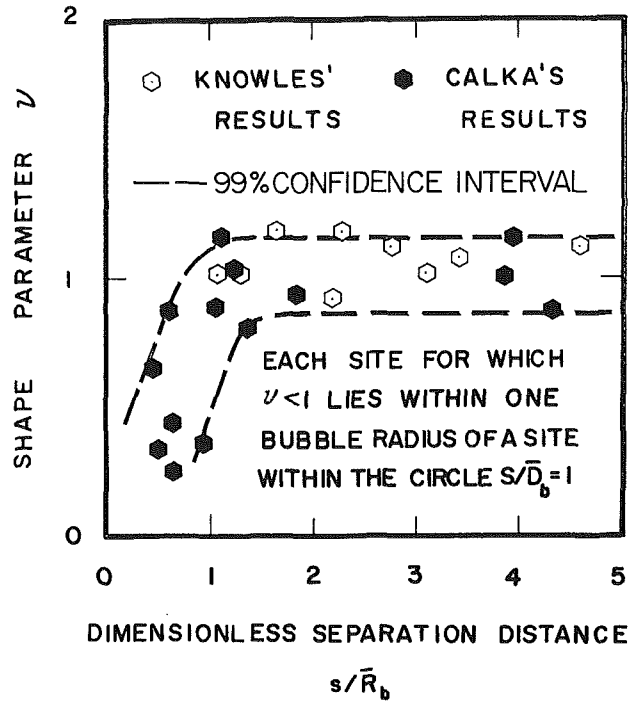

Fig. 5 Interaction of nucleation phenomena at sites inside and outside of the circle $S/\bar{D}_b = 1.0$

continually active nucleation site. Because of the dense active site population and the relatively small separation distances, considerable interaction could occur. Such interaction was much more likely to have happened in Calka's experiment than in Knowles' experiment because the site density was twice as great and the number of sites lying between the circles $S/\bar{D}_b = 0.5$ and $S/\bar{D}_b = 1.0$ that are essential for this sort of interaction to occur were twice as numerous.

Figure 5 shows a correlation between the shape parameter ν pertaining to the probability density distributions obtained at the sites outside of the circle $S/D_b = 1.0$ with the dimensionless separation distance s/R_b where s is the shortest distance between the site in question and the nearest site within the circle. It is apparent that for those sites on Calka's surface where the inhibitive effect was observed ($\nu < 1$), the dimensionless separation distance s/R_b is less than unity, whereas for those sites on Knowles' and Calka's surfaces where independence of the nucleation phenomena occurring at the sites was observed ($\nu = 1$), the dimensionless separation distance s/R_b is greater than unity. This correlation supports the explanation given above.

Concluding Remarks

Further investigation is required to confirm the mechanism of nucleation site interaction identified in this paper. An investigation is planned in which the research apparatus will be modified so that high-speed motion pictures can be taken simultaneously with the measurement of elapsed time between the nucleation of bubbles at adjacent sites. The conditions under which the extra large bubbles form will be of particular interest in the future investigation.

Acknowledgments

The author wishes to acknowledge the contribution of the late Scott Knowles, an undergraduate student in the Department of Mechanical Engineering. He was extremely talented and his promise was great.

References

1 Shoukri, M., and Judd, R. L., "On the Influence of Surface Conditions in Nucleate Boiling—the Concept of Bubble Flux Density," ASME JOURNAL OF HEAT TRANSFER, Vol. 100, No. 4, 1978, pp. 618-623.

2 Gaertner, R. F., "Distribution of Active Sites in the Nucleate Boiling of Liquids," *Chemical Engineering Progress Symposium Series*, Vol. 59, No. 41, 1963, pp. 52-61.

3 Sultan, M., and Judd, R. L., "Spatial Distribution of Active Sites and Bubble Flux Density," ASME JOURNAL OF HEAT TRANSFER, Vol. 100, No. 1, 1978, pp. 56-62.

4 Sultan, M., and Judd, R. L., "Interaction of the Nucleation Phenomena at Adjacent Sites in Nucleate Boiling," ASME JOURNAL OF HEAT TRANSFER, Vol. 105, No. 1, 1983, pp. 3-9.

5 Calka, A., "Some Aspects of the Interaction Among Nucleation Sites During Saturated Nucleate Boiling," M. Eng. Thesis, Mech. Eng. Dept., McMaster University, Hamilton, Ontario, Canada, 1984.

6 Calka, A., and Judd, R. L., "Some Aspects of the Interaction Among Nucleation Sites During Saturated Nucleate Boiling," *International Journal of Heat and Mass Transfer*, Vol. 28, No. 12, 1985, pp. 2331-2342.

7 Eddington, R. I., and Kenning, D. B. R., "The Prediction of Flow Boiling Bubble Populations From Gas Bubble Nucleation Experiments," *Proceedings of the Sixth International Heat Transfer Conference*, Toronto, Canada, Vol. 1, 1978, pp. 275-279.

8 Judd, R. L., and Lavdas, C. H., "The Nature of Nucleation Site Interaction," ASME JOURNAL OF HEAT TRANSFER, Vol. 102, No. 3, 1980, pp. 461-464.

9 Knowles, S., "Interaction Between Bubble Emission Phenomena at Adjacent Nucleation Sites," unpublished research, Mech. Eng. Dept., McMaster University, 1984.

10 Judd, R. L., "Influence of Acceleration on Subcooled Nucleate Boiling," Ph.D. Thesis, Mech. Eng. Dept., University of Michigan, Ann Arbor, MI, 1968.

11 Voutsinos, C. M., "Laser Interferometric Investigation of the Microlayer Evaporation for Various Levels of Subcooling and Heat Flux," M. Eng. Thesis, Mech. Eng. Dept., McMaster University, Hamilton, Ontario, Canada, 1976.

12 Bankoff, S. G., "Entrapment of Gas in the Spreading of a Liquid Over a Rough Surface," *AIChE Journal*, Vol. 4, No. 1, 1958, pp. 24-26.

Influences of Subcooling on Burnout of Horizontal Cylindrical Heaters

Y. Elkassabgi
Graduate Student.
Student Mem. ASME

J. H. Lienhard
Professor.
Fellow ASME

Heat Transfer/Phase Change Laboratory,
Mechanical Engineering Department,
University of Houston,
Houston, TX 77004

The peak pool boiling heat flux is observed on horizontal cylindrical heaters in acetone, Freon-113, methanol, and isopropanol over ranges of subcooling from zero to 130°C. Photographs, and the data themselves, revealed that there are three distinct burnout mechanisms at different levels of subcooling. Three interpretive models provide the basis for accurate correlations of the present data, and data from the literature, in each of the three regimes. Burnout is dictated by condensation on the walls of the vapor jets and columns at low subcooling. In the intermediate regime, burnout is limited by natural convection, which becomes very effective as vapor near the heater reduces boundary layer resistance. Burnout in the high-subcooling regime is independent of the level of subcooling, and is limited by the process of molecular effusion.

Introduction

The problem of predicting the peak pool boiling (or "burnout") heat flux q_{max} in subcooled liquids has received intermittent attention for over 30 years; yet it remains essentially unresolved. Perhaps work has been less intense than in other areas of boiling because, strictly speaking, true steady pool boiling cannot be subcooled. The boiled liquid in a stagnant pool will eventually warm to the saturation temperature.

However, since a heater in a large bath can operate in quasi-static subcooled boiling for a long time, subcooled burnout is important in the short term. Furthermore, if cool liquid is replenished, either by slow fluid motion or a cooling process in the bath, a condition very close to pool boiling can be maintained indefinitely. Finally, since subcooled behavior is important in flow boiling, an understanding of the zero velocity limit is a part of a general understanding of burnout in flow boiling.

Kutateladze (1951) first looked at the subcooled boiling burnout heat flux $q_{max,sub}$, and argued that since some fraction of the heat had to go to warming the liquid to its boiling point before boiling could occur, one could represent $q_{max,sub}$ as

$$\frac{q_{max,sub}}{q_{max}} = \text{const} \cdot \text{Ja} \tag{1}$$

where the Jakob number

$$\text{Ja} \equiv \rho_f c_p \Delta T_{sub} / \rho_g h_{fg} \tag{2}$$

$\Delta T_{sub} \equiv$ the liquid subcooling $= (T_{sat} - T_{bath})$; and $q_{max} \equiv$ the saturated peak heat flux.

Kutateladze and Schneiderman (before 1953) measured $q_{max,sub}$ on horizontal cylinders. Their limited data in water, ethanol, and iso-octane suggested that $q_{max,sub}$ varied in direct proportion to Ja and thus to ΔT_{sub}; but they also suggested that the constant in equation (1) should contain the factor $(\rho_f/\rho_g)^{0.077}$ to account for the "recirculation of unheated subcooled liquid." The maximum subcoolings that they observed were 64°C in water, 120°C in ethanol, and 76°C in iso-octane. They did their measurements on graphite rods, whose diameters they failed to report.

Zuber et al. (1963) suggested in 1961 that subcooling would augment burnout by condensing a fraction of the departing vapor on the walls of the jets through which it flowed. This meant that additional vapor would have to be generated at a heater surface before Helmholtz instability caused burnout. The amount of vapor condensed must then be established by a process of transient heat conduction in the moving liquid-vapor interface. Thus they obtained a correlation that explicitly displays the familiar formula for transient conduction into a semi-infinite medium

$$\frac{q_{max,sub}}{q_{max}} = 1 + \text{const} \frac{2k\Delta T_{sub}}{q_{max}\sqrt{\pi\tau\alpha}} \tag{3}$$

where τ was Zuber's approximate lifetime of the vapor jets

$$\tau = \frac{\pi\sqrt{2\pi}}{3}\left(\frac{\sigma}{g(\rho_f - \rho_g)}\right)^{1/2}\left(\frac{\rho_g^2}{g(\rho_f - \rho_g)\sigma}\right)^{1/4} \tag{4}$$

The Zuber–Tribus–Westwater mechanism remains the most probable one for subcooled burnout; however it has not succeeded in providing very good correlation of the existing subcooled data.

Ivey and Morris (1962) (see also Ivey and Morris, 1966) provided the following modification of Kutateladze and Schneiderman's correlation:

$$\frac{q_{max,sub}}{q_{max}} = 1 + 0.1\left(\frac{\rho_g}{\rho_f}\right)^{1/4} \text{Ja} \tag{5}$$

Equation (5) correlated the data of Kutateladze, and their own data for horizontal wires 1.22 to 2.67 mm in diameter in water, in the range $0 < \Delta T_{sub} \leq 72$°C. The correlation was only

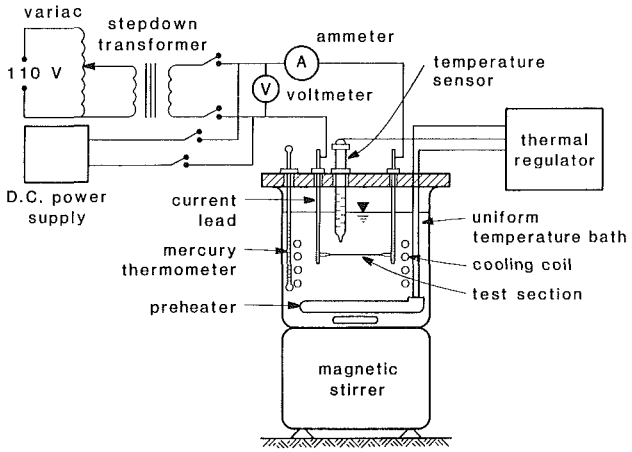

Fig. 1 Schematic representation of the experimental apparatus

Contributed by the Heat Transfer Division and presented at the 2nd ASME-JSME Joint Thermal Engineering Conference, Honolulu, Hawaii, March 1987. Manuscript received by the Heat Transfer Division October 27, 1986. Keywords: Boiling.

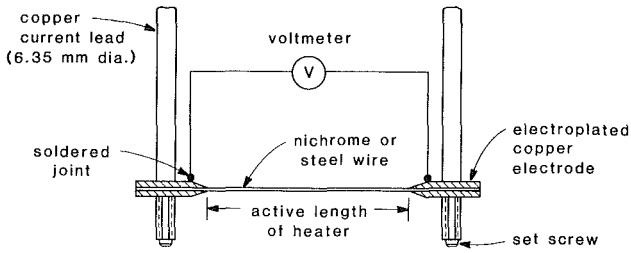

Fig. 2 Detail of the heater mounting

accurate within ±25 percent, and failed to represent data for other geometries.

Thus, by 1966, it had been established that $q_{max,sub}$ varied more or less as ΔT_{sub}, at least when ΔT_{sub} was not too great. However, the influence of both geometry and geometric scale had not been clarified at all. Furthermore, the fact that the thermal conductivity had to enter the process (as indicated by Zuber et al., 1963) was still an important neglected consideration.

Our objective here is to produce an expanded set of $q_{max,sub}$ data for a given geometry (the horizontal cylinder); to look for different regimes of subcooled burnout; and finally to provide either burnout predictions or at least conceptual models for correlating the results over a range of fluids and geometric scales.

Experiment and Results

Figure 1 shows the relatively conventional apparatus that we used to measure q_{max} on cylindrical electric resistance heaters ranging from 0.80 to 1.54 mm in diameter. Four liquids – isopropanol, acetone, methanol, and Freon-113 – were boiled at atmospheric pressure. The heaters were mounted as shown in Fig. 2.

In each case, the bath was either preheated or cooled, and thoroughly mixed, to a predetermined temperature. An array of thermocouples in the liquid was used to confirm that this procedure yielded a uniform bath temperature within 1/2°C prior to burnout. The mixing and heating (or cooling) were then stopped for about half a minute which was enough to guarantee that gross fluid motion (as evidenced by bubble motion) had damped out. The heater was then rapidly powered up to about 90 percent of q_{max}. Then it was brought to burnout over another 15 to 30 s, which was slow enough to guarantee that boiling remained quasi-static.

A total of 631 such observations were made with approximately equal numbers of observations in each fluid, and only two or three observations were made on any one heating element. The heating elements were all nichrome with the exception of four observations made on steel heaters in Freon-113. Figure 2 shows the mounting of the heater elements. Tapered copper electrodes were electroplated on the ends of each wire to eliminate any end effects. Each wire was inspected for any flaws, washed with detergent soap, rinsed in water, and finally rinsed with the fluid to be boiled, before it was installed.

To obtain the very highest levels of subcooling, we immersed the test container in a bath of isopropanol mixed with dry ice instead of the control scheme shown in Fig. 1.

More complete details of the experiment, and complete tabulations of the data, are given by Elkassabgi (1986). The probable error of the resulting $q_{max,sub}$ data was within 3.6 percent.

Extensive still and motion pictures were also taken for each of the fluids and at the different levels of subcooling.

The results of the experiment are plotted in Figs. 3–6. In these plots, $q_{max,sub}$ has been normalized by the saturated burnout heat flux predicted by Sun and Lienhard (1970)

Nomenclature

A, $A_{cond.}$ = area; area of vapor jets on which condensation occurs
A_{jet}, A_{heater} = cross-sectional area of the vapor jets; area of the heater per escaping vapor jet
a, b, c = undetermined constants
c_p = specific heat at constant pressure for the boiled liquid
g = acceleration of gravity
h_{fg} = latent heat of vaporization
Ja = volumetric Jakob number $= \rho_f c_p \Delta T_{sub}/\rho_g h_{fg}$
k = thermal conductivity
Nu = Nusselt number defined in equation (26)
Pe = an effective Peclet number, defined in equation (20)
Pr = Prandtl number $= \nu/\alpha$
q, q_{max}, $q_{max,sub}$ = boiling heat flux; saturated peak pool boiling heat flux; q_{max} in subcooled boiling
$q_{max_{Sun}}$, q_{max_Z} = predicted q_{max} for horizontal cylinders; Zuber's estimate of q_{max} (see equations (6) and (8))
$q_{cond.}$ = heat flux conducted from the vapor jet interface to the surrounding subcooled liquid, expressed on a per-unit-heater-area basis
$q_{mol.eff.}$ = molecular effusion limited q (see equation (28))
R = radius of a horizontal cylindrical heater
R_{eff} = effective radius, defined in equation (23)
R_{gas} = ideal gas constant on a mass basis
R' = $R[\rho_f - \rho_g)/\sigma]^{1/2}$
Ra = Rayleigh number defined in equation (27)
t = time
T, T_{sat}, T_{bath} = temperature, saturated liquid temperature, actual temperature of surrounding liquid
u_g, $\bar{u}_g$ = Helmholtz unstable velocity in a vapor jet; an average vapor velocity defined by equation (16)
α = thermal diffusivity of the boiled liquid
β = volumetric coefficient of thermal expansion
ΔT_{sub} = saturation temperature minus the liquid bath temperature
θ = retreating contact angle
λ_d, λ_H = most susceptible Taylor unstable wavelength, critical Helmholtz wavelength
ν = kinematic viscosity
ρ_f, ρ_g = saturated liquid and vapor densities
σ = surface tension
τ = characteristic duration of transient heat conduction (for which different estimates are given in the paper)
ϕ = fraction of limiting q (see equation (29))
χ = dimensionless group defined in equation (32)

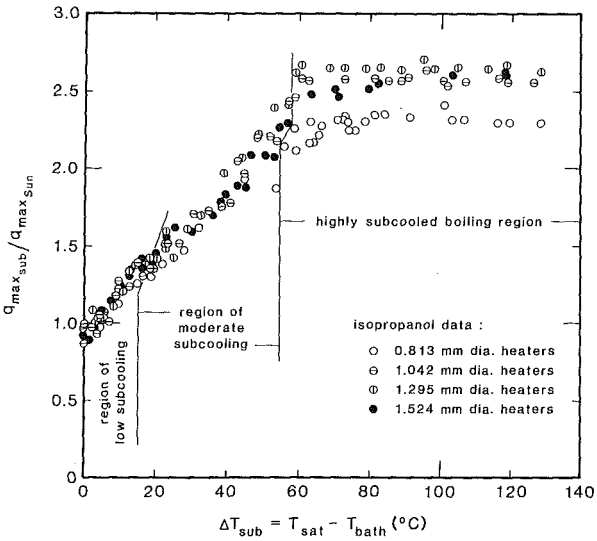

Fig. 3 The effect of liquid subcooling on the peak heat flux, for heaters of various sizes in isopropanol

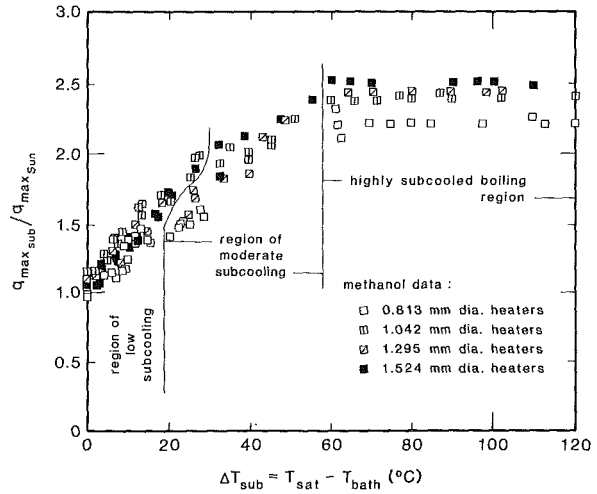

Fig. 4 The effect of liquid subcooling on the peak heat flux, for heaters of various sizes in methanol

$$q_{\max_{Sun}} = q_{\max_Z}[0.89 + 2.27\exp(-3.44\sqrt{R'})] \quad (6)$$

where R' is the Laplace number based on the cylinder radius R

$$R' \equiv R[g(\rho_f - \rho_g)/\sigma]^{1/2} \quad (7)$$

and $q_{\max_Z}$ is Zuber's estimate of the peak heat flux on a horizontal flat plate

$$q_{\max_Z} = \frac{\pi}{24}\rho_g^{1/2} h_{fg}[g\sigma(\rho_f - \rho_g)]^{1/4} \quad (8)$$

The purpose of using the hydrodynamic prediction of q_{max} to reduce the data on an otherwise dimensional plot is to make it feasible to put data for different wire sizes on the same graph. While we do not claim that equation (6) presents the correct accounting for geometric scale at high subcooling, this normalization nevertheless makes it possible for us to see, at this preliminary stage, three identifiable regimes of boiling behavior near $q_{max,sub}$, as ΔT_{sub} is increased.

The three regimes of subcooled burnout behavior become more sharply evident in photographs made at heat fluxes near burnout. Indeed the photographs make it clearer than do the data alone that a middle region must be identified. Figures 7(*a–d*) are typical photographs showing saturated boiling and the three subcooled regimes, just below the peak heat flux. In the "region of low subcooling" some of the familiar jets-and-columns behavior of saturated boiling is preserved, although

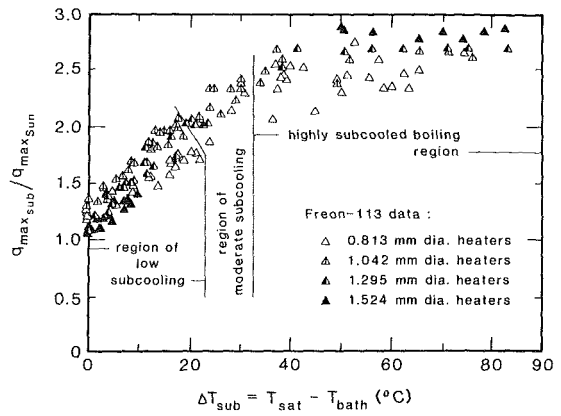

Fig. 5 The effect of liquid subcooling on the peak heat flux, for heaters of various sizes in Freon-113

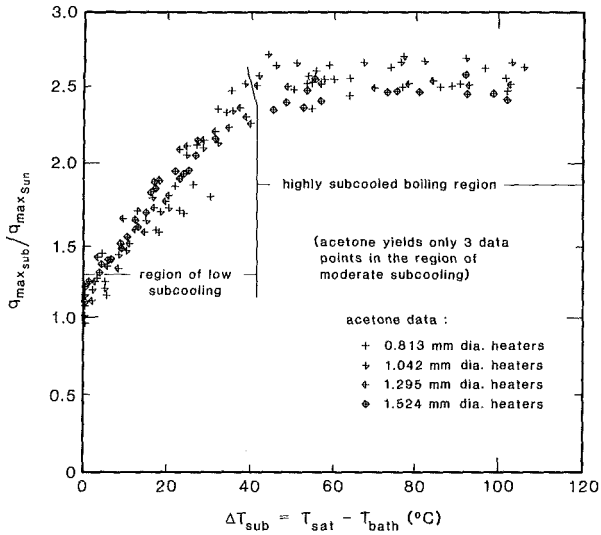

Fig. 6 The effect of liquid subcooling on the peak heat flux, for heaters of various sizes in acetone

the jets diminish slightly in size. In the "region of intermediate subcooling" the jets give way to fairly large bubbles that continue to condense away after they depart from the wire.

The most dramatic surprise awaits us in the "region of high subcooling." Here two unexpected things occur: The burnout heat flux reaches a ceiling that is independent of ΔT_{sub}, and the bubble departure pattern takes on the appearance of saturated *film* boiling. At high superheats, very small bubbles leave the wire and rise, without condensing, in what must be a thin sheet of liquid that has been heated all the way to T_{sat} by the wire. We have delineated this region by developing complete sets of data at the highest subcoolings while other investigators have only provided a few points.

Our task is now to determine what factors dictate burnout in each of these three regimes and to do what we can about developing predictions of the peak heat flux in each case.

Heat Transfer Models

The Region of Low Subcooling. The mechanism for burnout in the region of low subcooling is the same Helmholtz instability process that occurs in saturated boiling. However when the liquid is subcooled, more vapor must be supplied to the escaping jets to make up that portion that condenses on the jet walls before burnout occurs.

This is the essence of the Zuber et al. mechanism. Like Zuber et al., we note that it is necessary to add to q_{max} the transient heat flux from the saturated interface of the vapor jets to the surrounding subcooled liquid. The *average* transient

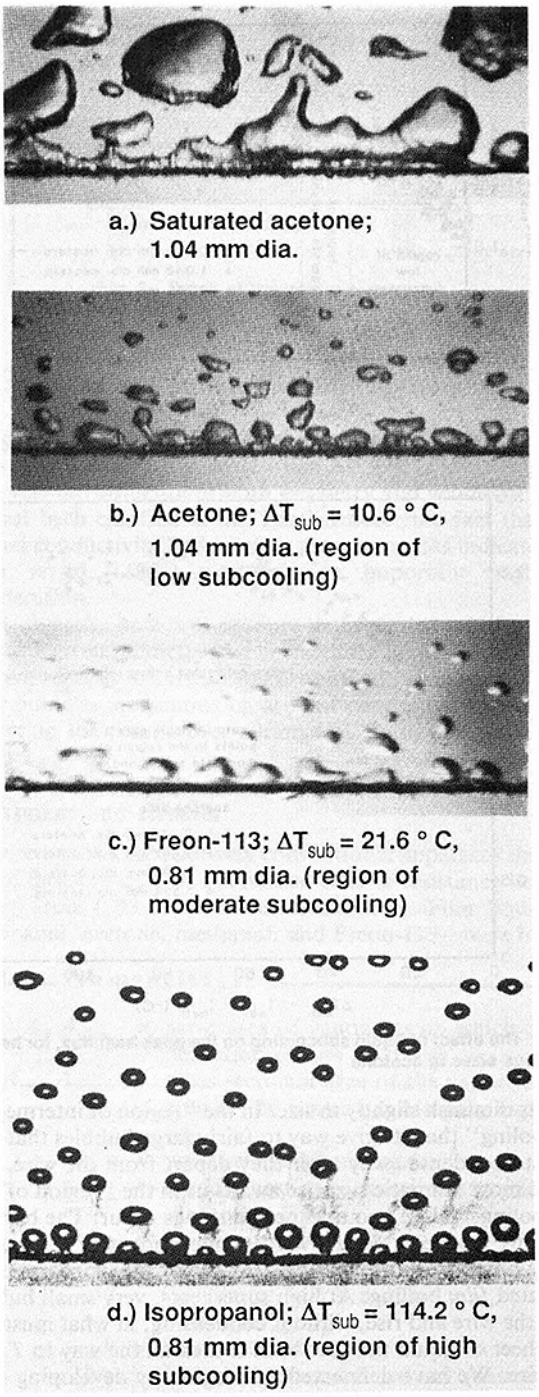

Fig. 7 Typical photographs of nucleate boiling just below the peak heat flux, in each of the regimes of subcooling

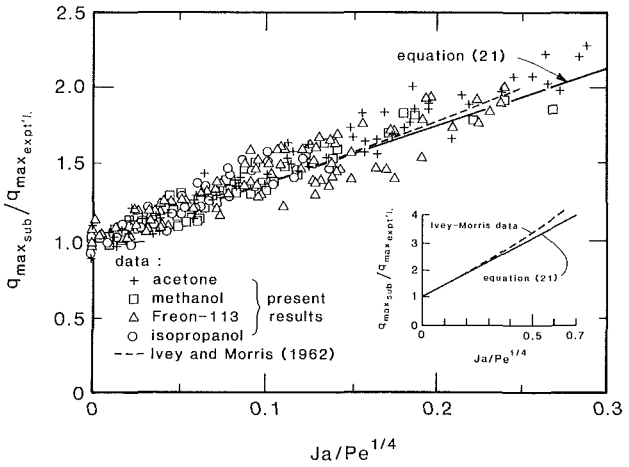

Fig. 8 Correlation of $q_{max,sub}$ data in the region of low subcooling in accordance with equation (21)

conduction is well known. Here we express it as a flux per unit area of the *heater*

$$q_{\text{cond.}} \equiv \frac{2k\Delta T_{\text{sub}}}{\sqrt{\pi\alpha\tau}} \cdot \frac{A_{\text{cond.}}}{A_{\text{heater}}} \tag{9}$$

where $A_{\text{cond.}}$ is the jet surface on which the condensation process takes place. Unfortunately, Zuber's estimate of the duration of conduction (τ given by equation (4)) gives values on the order of 1 ms, while the motion pictures give jet lifetimes on the order of 100 ms. We therefore seek a more reasonable strategy, not for estimating τ, but for setting its functional form.

The duration of survival of a vapor jet must stand in proportion to the ratio of the Taylor wavelength λ_d (which sets the size of the jet configuration) to the Helmholtz unstable vapor velocity[1] u_g. Using the Helmholtz velocity

$$u_g = (2\pi\sigma/\rho_g\lambda_H)^{1/2} \propto (2\pi\sigma/\rho_g\lambda_d)^{1/2} \tag{10}$$

where the Helmholtz unstable wavelength λ_H for all but very small cylinders must stand in proportion to the most susceptible Taylor wavelength λ_d, for reasons of dimensional consistency. The Taylor wavelength is

$$\lambda_d = 2\pi\sqrt{3}[\sigma/g(\rho_f - \rho_g)]^{1/2} \tag{11}$$

It follows that

$$\tau = \frac{\lambda_d}{u_g} \propto \frac{\rho_g^{1/2}\sigma^{1/4}}{[g(\rho_f - \rho_g)]^{3/4}} \tag{12}$$

which is identical in form to equation (4), but it does not have the restricted coefficient of proportionality in it.

The subcooled peak heat flux can then be written in the following variation of equation (3):

$$\frac{q_{\text{max,sub}}}{q_{\text{max}}} = 1 + \frac{q_{\text{cond.}}}{q_{\text{max}}} \cdot \frac{A_{\text{cond.}}}{A_{\text{heater}}} \tag{13}$$

where

$$A_{\text{cond.}} = \tau \frac{dA_{\text{cond.}}}{dt} \tag{14}$$

We next ask, "What is the rate of generation of interfacial surface?" The mechanical energy stability criterion of burnout provides the basis for answering the question. The theory, as articulated for pool boiling burnout by Lienhard and Hasan (1979), says that the rate of creation of interfacial surface should equal the rate at which vapor kinetic energy leaves the heater. Thus

$$\sigma \frac{dA_{\text{cond.}}}{dt} = \frac{1}{2} u_g^2 (\rho_g \bar{u}_g A_{\text{heater}}) \tag{15}$$

where $\bar{u}_g$ is the average velocity of vapor leaving the heater

$$\bar{u}_g \equiv q_{\text{max,sat}}/\rho_g h_{fg} \tag{16}$$

We also note that

$$u_g = \bar{u}_g (A_{\text{heater}}/A_{\text{jet}}) \tag{17}$$

Combining equations (10), (11), (15), and (17) we obtain

$$\frac{dA_{\text{cond.}}}{dt} \propto \frac{\rho_g u_g^3}{\sigma} A_{\text{jet}} \propto \frac{\sigma^{3/4}}{\rho_g^{1/2}[g(\rho_f - \rho_g)]^{1/4}} A_{\text{jet}} \tag{18}$$

[1] We assume some familiarity with the hydrodynamic theory of burnout on the part of the reader. We refer those unfamiliar with the theory to extensive reviews by Lienhard and Dhir (1973) and by Witte and Lienhard (1985).

Table 1 Average measured values of q_{max} in saturated liquids

Liquid	R′	q_{max} (MW/m^2)	$\frac{q_{max}}{q_{max,Sun}}$
Acetone	0.1515	0.494	1.06
	0.1651	0.487	1.08
	0.2015	0.466	1.09
	0.2412	0.457	1.08
Isopropanol	0.1513	0.525	0.92
	0.1642	0.509	0.94
	0.1956	0.471	0.93
	0.2346	0.435	0.91
Methanol	0.1565	0.765	1.05
	0.1590	0.744	1.06
	0.1987	0.699	1.06
	0.2385	0.659	1.06
Freon 113	0.1985	0.285	1.18
	0.2480	0.265	1.20
	0.3115	0.237	1.13
	0.3725	0.219	1.10

Finally we combine equations (6), (9), (10), (11), (12), (14), and (18) with equation (13). The result contains a factor of A_{jet}/A_{heater} in it, and we note that Sun and Lienhard found this factor to depend weakly on R'. The resultant substitutions therefore yield

$$\frac{q_{max,sub}}{q_{max}} = 1 + f(R')\mathrm{Ja}/\mathrm{Pe}^{1/4} \tag{19}$$

where q_{max} may represent either Sun's prediction or the actual measured value of q_{max} in a saturated liquid, and where Pe is an effective Peclet number

$$\mathrm{Pe} \equiv \frac{\sigma^{3/4}}{\alpha[g(\rho_f - \rho_g)]^{1/4}\rho_g^{1/2}} \tag{20}$$

The data for the region of low subcooling are plotted in accordance with equation (19) in Fig. 8. There are three difficulties involved with this plot. The first arises in normalizing the ordinate. We discovered in the course of this work that equation (8) systematically underpredicts the saturated data for acetone by about 8 percent, those for methanol by about 6 percent, and those for Freon-113 by about 16 percent. It overpredicts the data for isopropanol by about 7 percent. Closer scrutiny made it clear that these systematic differences among the various fluids was responsible for most of the ±20 percent deviation of the data that Sun originally reported for his prediction, as well. We have therefore used the average measured q_{max} values (instead of the prediction) to normalize the ordinate in Fig. 8. These values are listed in Table 1.

The second difficulty is that of specifying which of the three regions of subcooling a given data point falls in. We discuss this difficulty after we present the three correlations.

The third difficulty – that of specifying the function $f(R')$ – conveniently vanishes. The process of least-squares correlation revealed that this function was weakly enough dependent on R' to be represented as the constant 4.28. Consequently equation (19) reduces to

$$\frac{q_{max,sub}}{q_{max}} = 1 + 4.28\ \mathrm{Ja}/\mathrm{Pe}^{1/4} \tag{21}$$

where q_{max} is the experimentally determined value[2] from Table 1.

[2]We also correlated these results using the q_{max} value predicted by Sun and Lienhard to normalize equations (19) and (21). The resulting $f(R')$ was still a constant but somewhat higher – 5.66 – and the rms deviation increased to ±10.2 percent. These changes reflected the small systematic inconsistencies of equation (6) mentioned above. When one does not have a measured value of q_{max} he may use equation (6) and the constant 5.66.

Equation (21) represents the available data within an rms error of ±5.95 percent.

The Region of Intermediate Subcooling. The photographs make it clear that the low subcooling mechanism is not appropriate to the vapor escape process in the moderately subcooled region. The jets and columns vanish in this range of ΔT_{sub} as bubbles grow and condense in a region that is increasingly restricted to the neighborhood close to the cylinder. Without jets and columns, we must then ask what sort of instability now causes burnout.

A closer study of the photographs in both this (and this highly subcooled region as well) reveals intense bubble growth and condensation action near the surface.[3] Consequently, there is fairly limited liquid-solid contact around the heater, and the liquid immediately outside this highly active vapor bubble layer is saturated.

One may thus imagine that the cylinder has a radius larger than R by the thickness of the bubble layer, with heat transfer occurring by *natural convection* from the saturated liquid to the surrounding subcooled liquid. Normally, natural convection would not be terribly effective; however in this case the no-slip condition (between the saturated interface and the bubble layer) is largely removed *by* the bubble layer. We therefore believe that, in this region, burnout occurs when the efficient phase-change process in the bubble layer reaches the limit of heat that can be removed by the not-quite-as-efficient natural convection process outside the vapor layer.

If heat transfer is determined in this way, the dimensional functional equation for $q_{max,sub}$ is then

$$q_{max,sub} = f(\Delta T_{sub}, R_{eff}, g, \beta, k, \alpha, \nu) \tag{22}$$

where β is the coefficient of thermal expansion of the liquid, ν is the kinetic viscosity, and R_{eff} is the sum of the cylinder radius and one departing bubble diameter. We use the Fritz (1937) departing bubble diameter (for saturated pool boiling) and obtain

$$R_{eff} = R(1 + 0.02\theta/R') \tag{23}$$

where the second term represents the Fritz radius.[4] Equation (22) has eight variables in four dimensions and thus reduces to four dimensionless groups

$$\frac{q_{max,sub}R_{eff}}{k\Delta T_{sub}} = f\left(\frac{gR_{eff}^3}{\alpha\nu},\ \beta\Delta T_{sub},\ \mathrm{Pr}\right) \tag{24}$$

We do not know what functional form these groups should take, and therefore look first for a simple power law relation. In doing this we assume that the primary independent variable is the combination of the three terms on the right that we call the Rayleigh number Ra, and that the Prandtl number Pr is not important beyond its role in Ra. However, correlation reveals that the independent influence of the term $\beta\Delta T_{sub}$ cannot be ignored as it can in many cases of single-phase natural convection. When we correlate the existing data using such a relationship, we obtain

$$\mathrm{Nu} = 28 + 1.50\mathrm{Ra}^{1/4}/(\beta\Delta T_{sub})^{7/8} \tag{25}$$

where the Nusselt number for this case is defined as

$$\mathrm{Nu} \equiv \frac{q_{max,sub}(2R_{eff})}{k\Delta T_{sub}} \tag{26}$$

and the Rayleigh number is

[3]This action is undoubtedly coupled with mass transfer *through* the bubbles, as postulated by Edwards and Snyder (1954) (see, e.g., Snyder and Robin (1968).

[4]The factor of 0.02 in this relation is Fritz's original constant. We had first expected that it would change in the present situation, and allowed it to be determined by least-squares correlation in the subsequent calculations. To our surprise, this procedure yielded the Fritz constant exactly.

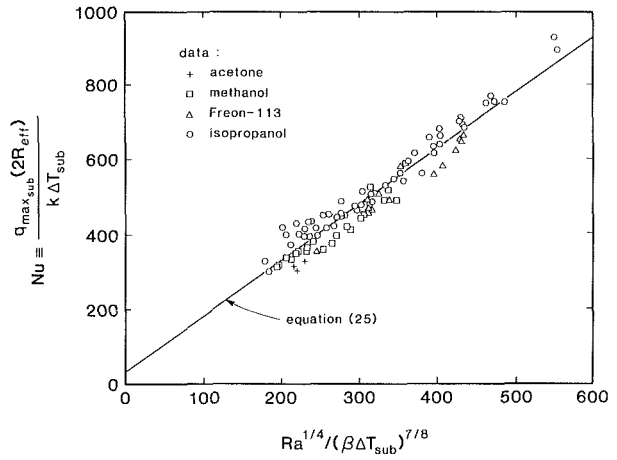

Fig. 9 Correlation of $q_{max,sub}$ data in the region of moderate subcooling in accordance with equation (25)

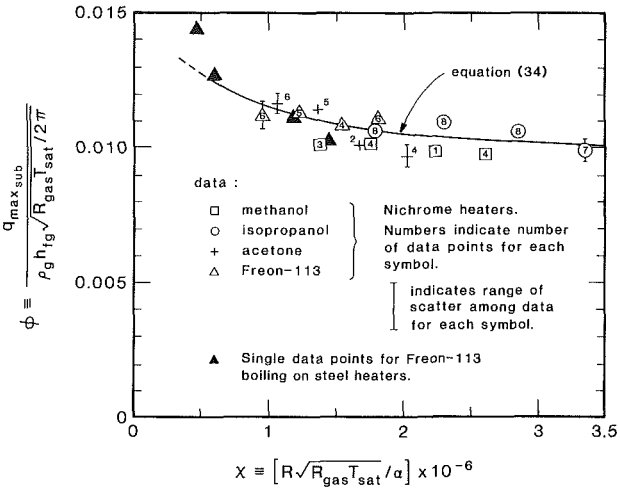

Fig. 10 Correlation of $q_{max,sub}$ data in the region of high subcooling in accordance with equation (34)

$$Ra \equiv \frac{g\beta\Delta T_{sub}(2R_{eff})^3}{\alpha\nu} \tag{27}$$

We also note that the familiar 1/4 power exponent of Ra in equation (25) is the result of the correlation and it was *not assumed*. It, and the $-7/8$ exponent of $(k\Delta T_{sub})$, were both obtained beyond two-decimal-place accuracy by correlation.

The use of equation (25) requires values of the retreating contact angle θ, which enters both Nu and Ra through R_{eff} (recall equation (23).) We used the tilting plate method to measure θ for each of the liquids, at its saturation temperature, on clean nichrome. For acetone, isopropanol, methanol, and Freon-113, respectively, we obtained $\theta = 12$, 18, 15, and 24 deg.

Equation (25) is plotted with all of the available data for the moderately subcooled region in Fig. 9. It represents the data accurately within an rms error of ± 7.06 percent.

The Region of High Subcooling. In the third regime of boiling, the boiling configuration is still similar to that in the range of moderate subcooling. Rapidly growing and collapsing bubbles form and reform a thin structure of liquid-vapor interfaces in which there occurs rapid transient conduction related to repeated contacts with the heater surface. The maximum heat fluxes in this regime of high subcooling are very high – typically three times the saturated values – yet they are no longer dependent on ΔT_{sub}.

The fact that these heat fluxes have reached a ΔT_{sub}-independent limit calls for a new mechanism of boiling, one that occurs when the phase-change heat transfer process can no longer keep up with natural convection. We note that Schrage (1953) pointed out that the absolute limit of a phase-change heat flux was the limit set by the effusion of molecules in one direction from an interface. He noted that this heat flux is approximated within a few percent by

$$q_{mol.eff.} = \rho_g h_{fg}\sqrt{R_{gas}T_{sat}/2\pi} \tag{28}$$

where R_{gas} is the ideal gas constant on a unit mass basis.

This is an ideal limit that cannot ever be reached in any but the most idealized system. However, the actual limit reached in a real process should be related to this limit.[5] Thus we define the fraction of this limit reached in an experiment,

$$\phi \equiv \frac{q_{max,sub}}{q_{mol.eff.}} \tag{29}$$

The data come very close to defining the same fraction ϕ – slightly in excess of 0.01 – for all of the fluids investigated. However, the data reveal that ϕ deviates upward for the smaller wires. There is clearly an influence of geometric scale that vanishes for the larger heaters. The relevant scale parameter in this process must be a transient conduction length, probably one that is related to the transient heating of liquid in the structure of the changing liquid-vapor interface. (This presumption is checked experimentally below.) We accordingly expect ϕ to depend on the heater radius R, the thermal diffusivity of the liquid α, and an appropriate time scale for the problem. The available time scale in this situation is the time required for molecules to flow over the characteristic distance R. Thus we write

$$\phi = \phi\left(\alpha, R, \frac{R}{\sqrt{R_{gas}T_{sat}}}\right) \tag{30}$$

These four variables are expressed in just two dimensions so equation (30) can be rearranged into a relation between two dimensionless groups

$$\phi = \phi(\chi) \tag{31}$$

where the new group χ takes the form of a Peclet number. To avoid confusion with the previously defined Pe, we call it χ.

$$\chi \equiv R(R_{gas}T_{sat})^{1/2}/\alpha \tag{32}$$

Those of the experimental data (shown in Figs. 3-6) that belong to the highly subcooled regime are plotted in Fig. 10 on ϕ versus χ coordinates. Four additional $q_{max,sub}$ data were obtained using steel heaters with a thermal diffusivity three times that of nichrome. The steel heater data correlate very closely with the nichrome data when they are plotted on the coordinates required by equation (31). Therefore we are confident that our selection of the conduction length based on the liquid diffusivity was appropriate.

The data suggest a correlation of the form

$$\phi = a + be^{c\chi} \tag{33}$$

A least-squares fit of this form yields

$$\phi = 0.01 + 0.0047\exp(-1.11 \times 10^{-6}\chi) \tag{34}$$

which represents the data with an rms deviation of 6.82 percent.

Discussion

On Determining the Region in Which a Given Data Point Will Fall. A serious, and essentially unresolved, problem with the three predictions is that of determining which of them is appropriate to a heater of given size in a given liquid at a given ΔT_{sub}. Figure 11 is a typical plot of raw data – data for 1.04 mm dia heaters in methanol. It also includes the three

[5] This idea is developed further by Gambill and Lienhard (1986).

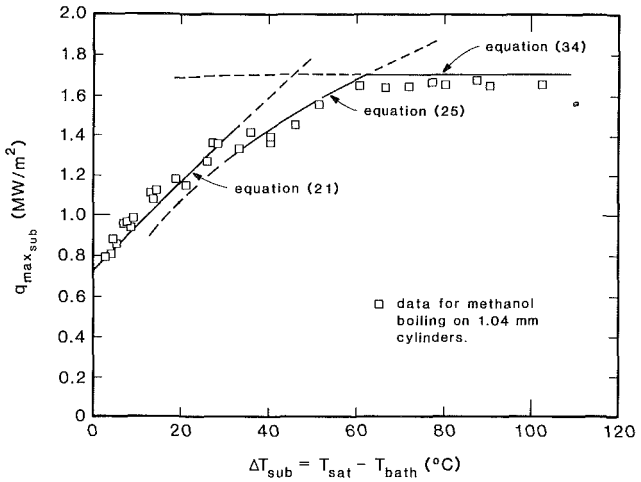

Fig. 11 Comparison of the data with the three predictions for methanol boiling on 1.04-mm-dia cylinders

predictions for the three regions, equations (21), (25), and (34). This plot dramatizes the difficulty we face.

One would want the three regions to be delineated by the intersections of the three correlating equations. However, in some cases the low and moderate subcooling region curves intersect and in some cases they do not. In Fig. 11 they do not, and the data clearly jump from the low ΔT_{sub} prediction to the moderate ΔT_{sub} prediction at about 30°C. We do not yet know what factors determine where this jump occurs.

We used the following procedure to identify the appropriate region for each data point. We first guessed the region on the basis of Figs. 3–6. Then we made preliminary correlations of the data and generated plots similar to those in Fig. 11. Next we judged which points lay in which region by looking at each point in relation to the predictions. Finally, we made new correlations based on these decisions. After about three such iterations no further changes were required.

The results obtained for acetone in this process exhibited a trend different from that shown in Fig. 11. The low and moderate ΔT_{sub} predictions intersected at a very small value of ΔT_{sub} as shown in Fig. 12. The acetone data (for all but the smallest heaters) failed to deviate from the low ΔT_{sub} prediction until they reached the high ΔT_{sub} limit.

The resulting boundary between the moderate and high subcooling regions is clearly defined by the single intersection between equations (25) and (34). When equations (21) and (25) intersect, the left-hand point of intersection does not locate the transition between the regions of low and moderate subcooling and we have no situation in which the right hand intersection occurs in the range of interest. All cases of transition from low to moderate ΔT_{sub} behavior occurred at a seemingly arbitrary point.

Comparison of the Present Correlations With Literature Data. Certain of the existing data sets are incompletely reported, and many of the other sets reflect system variables that are inconsistent with the present models. Our models apply only to *pool* boiling on *"large" isothermal* cylinders.

All three of our correlation equations are restricted to burnout on cylinders for which R' is greater than about 0.1. It was demonstrated by Bakhru and Lienhard (1972) that the hydrodynamic burnout processes are completely destroyed as R' falls below 0.1, because capillary forces then dominate the vapor escape. Many of the extant data lie in this range, and none of them can be compared with our correlations.

Some of the extant data for $q_{max,sub}$ were obtained by keeping the liquid subcooled with a superposed liquid flow across the cylinder. Subsequent studies of flow boiling burnout have shown that such data were, in fact, strongly influenced by the

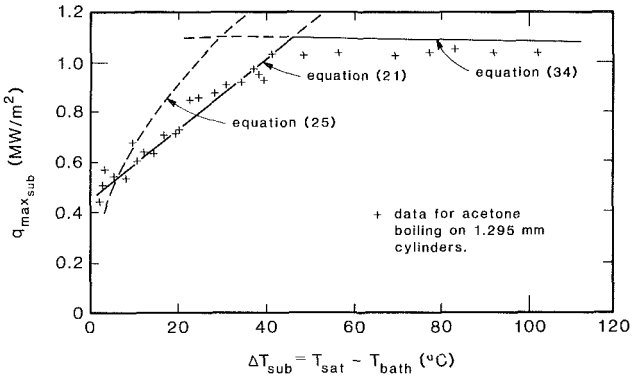

Fig. 12 Comparison of the data with the three predictions for acetone boiling on 1.3-mm-dia cylinders

superposed flow, and cannot be compared with a pool boiling correlation.

Finally, our moderate and high subcooling correlations are based on a uniform-wall-temperature assumption. Several of the extant $q_{max,sub}$ data were obtained on thin-walled, high-thermal-resistance tubes (Ivey and Morris used such heaters).

Therefore, the only significant surviving data set that we are aware of, with which we can compare our results, are the Ivey and Morris data for water in the region of low subcooling. The line through the center of these data is shown in Fig. 8. (The scatter of these data about the line shown is approximately the same as ours.)

This *ex post facto* comparison is almost perfect despite the fact that it involves a liquid – water – not involved in the present correlation. This data set extends to a subcooling of 70°C and it compares well with equation (21) over the entire range. Furthermore, Ivey and Morris' photographs show that the jets-and-columns structure is more or less preserved at least to $\Delta T_{sub} = 61$°C.

At high subcooling, the Ivey–Morris data substantially exceed the limit set by equation (34). Since their experiments involved a constant wall heat flux, they probably caused boiling contact to be maintained over the entire cylinder surface. In our experiments, contact is probably localized at the bottom of the heater.

A Note on the Function: $q_{max,sub}(\Delta T_{sub})$. For many years the common wisdom has been that $q_{max,sub}$ varies directly as ΔT_{sub}. This linearity has been roughly borne out by existing data sets and models. The present study shows that

- The relation is linear in the region of low subcooling.
- $q_{max,sub}$ varies approximately as $(\Delta T_{sub})^{3/8}$ in the region of moderate subcooling except as it is modified by the strong temperature dependence of the thermal properties.
- In the region of high subcooling, $q_{max,sub}$ shows no dependence on ΔT_{sub} except for a small influence of physical property variations.

The previous experimental studies could not reveal these latter two regimes because, without a large number of data, tight control of all variables, and a wide range of ΔT_{sub} they simply were not evident. Kutateladze, for example, failed to discriminate influences of heater size, or even to report diameters. His data might actually have reached into the high subcooling region, but not far enough to make the actual trend apparent.

Conclusions and Open Issues

1 We have obtained what we believe to be the most comprehensive set of subcooled q_{max} data yet developed, and they reveal that there are three regions of subcooled burnout behavior.

2 In the region of lowest subcooling, burnout occurs as a consequence of the conventional hydrodynamic instability, but $q_{max,sub}$ is augmented by the extra vapor that must be generated to satisfy condensation on the jet walls. Equation (21), based on this model, represents the data within an rms error of 5.85 percent.

3 In the region of moderate subcooling, burnout occurs when the nucleate boiling process supplies heat to the saturated outer edge of the bubble layer faster than natural convection can remove it. Equation (25), based on this model, represents the data within an rms error of 7.02 percent.

4 In the region of high subcooling, burnout occurs when the nucleate boiling process itself is limited by molecular effusion and fails to provide energy as rapidly as it can be removed by natural convection. Equation (34), based on this model, represents the data with an rms error of 6.82 percent.

5 Each correlation represents the data within about twice the probable error estimate. All are restricted to $R' > 0.1$ and the moderate and high subcooling correlations are applicable only to isothermal cylinders.

6 Additional experiments aimed at diagnosing components of the present models are needed. This is particularly true of the convective or "moderately subcooled" region.

7 The most serious unresolved issue in this study is that of specifying, *a priori*, which region is appropriate for a given ΔT_{sub} in a given liquid and on a heater of a given size.

8 Subcooled burnout on uniform-wall-heat-flux cylinders should be studied both experimentally and analytically.

Acknowledgments

The initial work on the design of this experiment was done in 1980–81 by Dr. S. M. Liu while she was on leave from National Taiwan University. This work has received support under NSF Grant No. MEA-8218708.

References

Bakhru, N., and Lienhard, J. H., 1972, "Boiling From Small Cylinders," *Int. J. Heat Mass Transfer*, Vol. 15, No. 11, pp. 2011–2025.

Edwards, D. K., 1954, "The Role of Interphase Mass Transfer in the Mechanism of Nucleate Boiling," Master's Thesis, Mech. Engr. Dept., University of California, Berkeley, CA.

Elkassabgi, Y., May 1986, "The Peak Pool Boiling Heat Flux From Horizontal Cylinders in Subcooled Liquids," Doctoral Dissertation, Mech. Engr. Dept., Univ. of Houston, Houston, TX.

Fritz, W., 1937, "Maximum Volume of Vapor Bubbles," *Z. für Physik*, Vol. 36, pp. 379–384.

Gambill, W. R., and Lienhard, J. H., 1986, "An Upper Bound for the Boiling Heat Flux," ASME-JSME Thermal Engineering Joint Conference, Honolulu, HI, Mar. 22–27, 1986.

Ivey, H. J., and Morris, D. J., 1962, "On the Relevance of the Vapour-Liquid Exchange Mechanism for Sub-cooled Boiling Heat Transfer at High Pressure," UKAEA Report No. AEEW-R 137.

Ivey, H. J., and Morris, D. J., 1966, "Critical Heat Flux of Saturation and Subcooled Pool Boiling in Water at Atmospheric Pressure," *Proc. 3rd Int. Heat Transfer Conf.*, Vol. III, Chicago, IL, Aug. 10, 1966, pp. 129–142.

Kutateladze, S. S., 1951, "Hydrodynamic Theory of Changes in the Boiling Process Under Free Convection Conditions," *Izv. Akad. Nauk. SSSR, Otd. Tekh. Nauk.*, No. 4, p. 529.

Kutateladze, S. S., and Schneiderman, L. L., 1953, "Experimental Study of Influence of Temperature of Liquid on Change in the Rate of Boiling," USAEC Rept, AEC tr. 3405, pp. 95–100.

Lienhard, J. H., and Dhir, V. K., 1973, "Extended Hydrodynamic Theory of the Peak and Minimum Pool Boiling Heat Fluxes," NASA CR-2270.

Lienhard, J. H., and Hasan, M. M., 1979, "On Predicting Boiling Burnout Wtih the Mechanical Energy Stability Criterion," ASME JOURNAL OF HEAT TRANSFER, Vol. 101, No. 2, pp. 276–9.

Lienhard, J. H., and Witte, L. C., 1985, "An Historical Review of the Hydrodynamic Theory of Boiling," *Chem. Engr. Revs.*, Vol. 3, Nos. 3 and 4, pp. 187–280.

Schrage, R. W., 1953, *Interphase Mass Transfer*, Columbia University Press, New York, Chap. II.

Snyder, N. W., and Robin, T. T., 1968, "Mass-Transfer Model in Subcooled Nucleate Boiling," ASME-AIChE Heat Transfer Conf., Philadelphia, PA, Aug. 11–14, 1968, Paper No. 68-HT-51.

Sun, K. H., and Lienhard, J. H., 1970, "The Peak Pool Boiling Heat Flux on Horizontal Cylinders," *Int. J. Heat Mass Transfer*, Vol. 13, pp. 1425–1439.

Zuber, N., Tribus, M., and Westwater, J. W., 1963, "The Hydrodynamic Crisis in Pool Boiling of Saturated and Subcooled Liquids," *International Developments in Heat Transfer*, No. 27, ASME, New York, pp. 230–236.

B. J. Huang
Professor.

R. Zelaya
Graduate Assistant.

Department of Mechanical Engineering,
National Taiwan University,
Taipei, Taiwan 10764

Heat Transfer Behavior of a Rectangular Thermosyphon Loop

The thermal performance of a rectangular thermosyphon loop was studied. The analysis, using a one-dimensional approximation, the conventional friction factor, and an empirical correlation for the overall heat transfer in the cooler, was shown to be able to predict accurately the loop performance at steady state or approaching steady state, if the effective length was used to replace the geometric length in the calculation of loop friction. The steady-state natural circulation flow solution obtained was shown to be a function of a dimensionless group PY *or* $(NuGr/Pr)$ Y *and agrees very well with the experimental results.*

Introduction

The performance of natural circulation loops or thermosyphon loops has been extensively studied because its understanding is very important in the design of solar thermosyphon collectors, reactor emergency cooling systems, and other industrial equipment.

Theoretical analysis of the loop performance is very complicated due to the coupling between the momentum and energy transport. It has been argued that the disagreement between analyses and experiments arises mainly from the adoption of the conventional friction factor correlation (Creveling et al., 1975; Bau and Torrance, 1981a), one-dimensional approximation (Mertol et al., 1982; Zvirin et al., 1981) and convective heat transfer correlations (Bau and Torrance, 1981a; Zvirin et al., 1981) in the analysis. Recent studies were thus centered around these topics.

For the sake of simplification, the loops studied were always in some simple configuration such as two vertical branches with a point heat source at the bottom and a point heat sink at the top (Keller, 1966; Welander, 1967; Zvirin and Greif, 1979), circular toroidal loop heated uniformly over the lower half and cooled over the upper half through a constant wall temperature or an annular heat exchanger (Creveling et al., 1975; Damerell and Schoenhals, 1979; Greif et al., 1979; Mertol et al., 1981; Mertol et al., 1983; Mertol and Greif, 1982; Lavine et al., 1986), U-shaped open loops heated symmetrically or asymmetrically (Torrance, 1979; Bau and Torrance, 1981a; Bau and Torrance, 1981b), closed loops with heating leg and cooling jacket (Zvirin et al., 1981; Zvirin and Rabinoviz, 1982), or a rectangular thermosyphon loop with heating in the bottom horizontal part by a uniform-temperature heat source and cooling in the top horizontal part by a uniform-temperature heat sink (Chen, 1985).

It can be seen from these investigations that the performance of the loop varies extensively from one loop geometry to another and with different operating conditions. In addition, it has been frequently stated that the friction factor as well as the convective heat transfer correlations in a natural circulation loop are different from the conventional ones for straight pipes, and a modification based on the experimental data is thus needed such that the one-dimensional approximation can be valid (Creveling et al., 1975; Bau and Torrance, 1981a, Zvirin et al., 1981). This was ascribed to the multidimensional or secondary flow effect and natural convection, which were analytically verified recently by Lavine et al. (1986) using a three-dimensional analysis.

In general, the overall loop friction comes from two sources: first, the wall friction within the straight pipe sections, and second, the eddy or form losses due to the bends, fittings in the loop, or loop curvature. Multidimensional effects near the curved part of the loop may be propagated and enhanced and affect the loop friction as the ratio of diameter to length (D/L) becomes larger or the radius of curvature of the loop is small. Thus, the conventional friction factor correlation for one-dimensional straight pipe flow needs to be modified if it is to be applied to a curved loop. Modification to the convective heat transfer correlations in the loop is required as well because the combined natural and forced-convection effect is involved.

In the present paper, a rectangular loop, which can closely emulate a solar thermosyphon collector or a reactor core cooling system, was studied. The loop consists of a partly heated vertical leg at one side and a partly cooled vertical leg at the other side. The heating is furnished directly by a constant and uniform heat flux in the heater section, which can be provided by some means such as a solar collector or a nuclear core in practice. The cooling is provided with a cooling jacket with coolant flow to remove heat from the loop (see Fig. 1). For this rectangular loop, the secondary flow effect is probably small and an analysis was performed in the present study using the one-dimensional approximation and the conventional friction factor for a straight pipe. Measurements of the temperature distribution along the loop in an experimental loop were then made during the transient and steady states and were compared with the analysis.

One-Dimensional Analysis

As shown in Fig. 1, it is assumed that a constant and uniform heat flux q is supplied in the heater section, while heat is removed from the loop in the cooler section.

To facilitate the analysis, viscous dissipation, axial conduction, and heat loss from the loop to the ambient were neglected. The one-dimensional approximation and constant properties (except for the use of Boussinesq approximation for the density) were used. It was further assumed that the cooler is composed of a heat exchanger with coolant flow in the upward direction (see Fig. 1) and the heater and the cooler are all well insulated so that there is no heat loss to the ambient.

Since the coolant flow rate in the cooler is usually very high in practice, it can be assumed that the temperature of the coolant varies linearly along the flow direction. It was further assumed that the heat transfer direction inside the cooler is from the loop fluid having a mean temperature $\bar{T}$ to the coolant flow having a mean temperature $\bar{T}_c$.

In practice, the wall shear force may be greater than in a straight pipe, due to eddy or form losses in fittings, valves, and curved parts of the loop. To account for this, an "effective length" L_{ec} was used, which is the sum of the geometric

Contributed by the Heat Transfer Division for publication in JOURNAL OF HEAT TRANSFER. Manuscript received by the Heat Transfer Division October 15, 1986. Keywords: Heat Pipes and Thermosyphons, Modeling and Scaling.

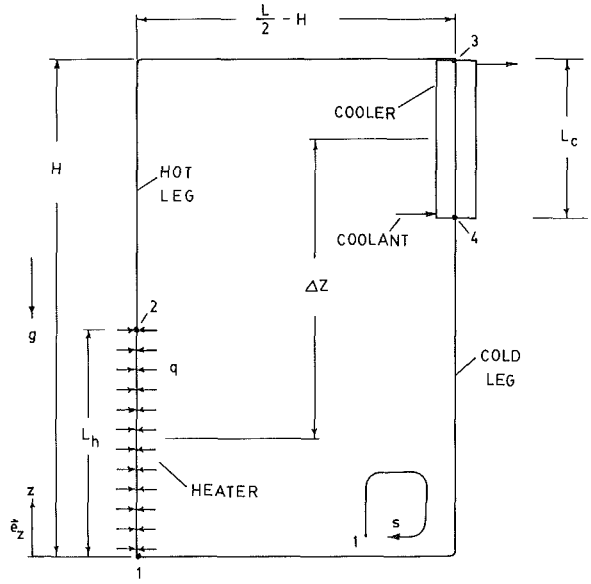

Fig. 1 Schematic diagram of a thermosyphon loop

length of the loop L and the "equivalent length" L_e responsible for the loop friction other than the straight-pipe shear friction τ_w, i.e., $L_{ec} = L + L_e$. Therefore, when taking the integral of the momentum equation around the loop, the shear force term should be taken along the effective length L_{ec}.

Applying a momentum and energy balance to the loop and the cooler and noting that the shear force relation $\tau_w = f \rho_r V^2$, the nondimensional differential equations are obtained (see Nomenclature)

$$\frac{dv}{d\tau} + 4\,(L_{ec}/D)\,f\,v^2 = \mathrm{St}^* \int \theta dx \mathbf{e}_z \cdot \mathbf{e}_s \tag{1}$$

$$\frac{\partial\theta}{\partial\tau} + v\frac{\partial\theta}{\partial x} = \begin{cases} \dfrac{4\ \mathrm{St}^*}{D/L}, & 0 \le x \le L_h/L \quad (2) \\ -\dfrac{4\ \mathrm{St}^*}{D/L}\,(\theta - \theta_c), & 1/2 \le x \le 1/2 + L_c/L \quad (3) \\ 0, \quad \text{otherwise} & (4) \end{cases}$$

$$\frac{L_c/L}{2v_c}\frac{d\bar{\theta}_c}{d\tau} + (1+\sigma)\bar{\theta}_c = \sigma\bar{\theta} + \theta_{c,i} \tag{5}$$

where St* is the Stanton number defined as

$$\mathrm{St}^* = \frac{U}{\rho_r C_p V_r} = \frac{U^3}{qLg\beta\,(\rho_r C_p)^2} \tag{6}$$

V_r is a reference velocity defined as

$$V_r = \frac{qLg\beta\rho_r C_p}{U^2} \tag{7}$$

Steady-State Solutions

By solving equation (2) with vanishing time derivative terms, a steady-state linear temperature solution is obtained in the heater

$$\theta_{ss} = \theta_{1ss} + \frac{4\ \mathrm{St}^*}{v_{ss}(D/L)}x, \qquad 0 \le x \le L_h/L \tag{8}$$

Similarly, solution of equation (3) yields an exponential distribution in the cooler section

$$\theta_{ss} = (\theta_{3ss} - \bar{\theta}_{css})\,\exp\left[\frac{-4\ St^*}{v_{ss}(D/L)}\,(x - 1/2)\right] + \bar{\theta}_{css},$$
$$\text{for } 1/2 \le x \le 1/2 + L_c/L \tag{9}$$

Equation (4) gives a uniform temperature solution for the insulated parts of the loop, i.e., $\theta_{1ss} = \theta_{4ss}$ and $\theta_{2ss} = \theta_{3ss}$ (see Fig. 1). Here, a characteristic temperature difference of the loop can be defined and determined from equation (8)

$$\Delta\theta_{ss} \equiv \theta_{3ss} - \theta_{4ss} = \theta_{2ss} - \theta_{1ss} = \frac{4\mathrm{St}^*\,(L_h/L)}{v_{ss}(D/L)} \tag{10}$$

The temperature distributions solved previously can then be substituted into the integral term of the momentum equation (1), to yield

$$\frac{(L_{ec}/L)}{(L_h/L)\mathrm{St}^{*2}} f\,v_{ss}^3 + \frac{D/L}{4\mathrm{St}^*}\frac{L_h}{L}\,v_{ss} = \frac{(L_c/L)}{\exp\left[\dfrac{4(L_c/L)\mathrm{St}^*}{(D/L)v_{ss}}\right] - 1} + \frac{H}{L} - \frac{L_h}{2L} \tag{11}$$

Nomenclature

C_p = specific heat, kJ/kg°C
D = inside diameter of the loop, m
D_1 = inner diameter of cooling jacket, m
$\mathbf{e}_s$ = unit vector in the s direction
$\mathbf{e}_z$ = unit vector in the upward direction
Gr = Grashof number defined in heater = $D^3\rho_r^2 g\beta\,(T_w - T_b)/\mu^2$
Gr_c = Grashof number defined in cooler = $D^3\rho_r^2 g\beta\,(T_{bc} - T_{wc})/\mu^2$
g = acceleration of gravity = 9.81 m/s²
H = height of the loop, m
h = convective heat transfer coefficient of loop fluid in heater, W/m²°C
h_i = convective heat transfer coefficient of loop fluid in cooler, W/m²°C
h_o = convective heat transfer coefficient in coolant flow, W/m²°C
k = thermal conductivity of loop fluid, W/m°C
k_t = thermal conductivity of loop wall, W/m°C
L = total geometric length of the loop, m
L_c = length of cooler, m
L_h = length of heater, m
m_c = mass flow rate of coolant, kg/s
Nu = Nusselt number defined in heater ≡ hD/k
Nu_c = Nusselt number defined in cooler ≡ h_iD/k
$\overline{\mathrm{Nu}}$ = overall Nusselt number defined for cooler ≡ UD/k
P = dimensionless parameter defined in equation (15)
Pr = Prandtl number of loop fluid = $\mu C_p/k$
Q = total heating rate in heater, W
Q_c = total cooling rate in cooler, W
q = heat flux per unit heated area in heater, W/m²
Re = Reynolds number of circulating flow = $\rho_r DV/\mu$
St* = Stanton number defined in equation (6)
s = spatial coordinate running around the loop, m
T = fluid temperature, °C
ΔT = temperature drop of loop

Solving the above algebraic equation, the circulating velocity of the thermosyphon loop at steady state can be obtained. An approximate equation of the steady-state circulating velocity similar to equation (11), however, can be found by assuming a linear temperature distribution in the loop fluid through the cooler. This is a reasonable approximation in many cases (although not during the startup period). In this case, equations (1)–(5) can be easily solved for steady-state conditions to yield

$$v_{ss}^3 = \frac{\mathrm{St}^{*2}(\Delta Z/L)(L_h/L)}{f(L_{ec}/L)} \tag{12}$$

where $\Delta Z = H - (L_h + L_c)/2$, which is the relative height between the cooler and the heater.

Here, a conventional correlation for frictional factor at steady state is used, which is in the form $f = a/\mathrm{Re}_{ss}^b$, where Re_{ss} is the Reynolds number defined at steady state, i.e., $\mathrm{Re}_{ss} = \rho_r D V_{ss}/\mu$, and a and b are equal to 0.03955 and 0.25, respectively, for turbulent flow, and 8 and 1, respectively, for laminar flow (Fox and McDonald, 1978). Substituting this into equation (12), it can be shown that in the following relations, the characteristic parameter PY is obtained. For laminar flow

$$\mathrm{Re}_{ss} = (PY/8)^{1/2} \tag{13}$$

For turbulent flow

$$\mathrm{Re}_{ss} = (PY/0.03955)^{4/11} \tag{14}$$

where P is a dimensionless parameter related to the heating rate q, which is defined as

$$P \equiv \frac{\rho_r^2 g \beta D^4 q}{\mu^3 C_p} \tag{15}$$

Y is a geometric dimensionless parameter defined as

$$Y \equiv \frac{(\Delta Z/L)(L_h/L)}{(D/L)(L_{ec}/L)} \tag{16}$$

It is shown from equations (13) and (14) that the dimensionless group PY determines the steady-state natural circulation flow. Similarly, combining equations (13) and (14) with (10) and (12) and noting that $\mathrm{St}^* = (1/P)(D/L)(\overline{\mathrm{Nu}}/\mathrm{Pr})^3$, where $\overline{\mathrm{Nu}}$ is the cooler overall Nusselt number defined as UD/k, the characteristic temperature difference of the loop is obtained:

For laminar flow:

$$\Delta\theta_{ss} = \frac{4(\overline{\mathrm{Nu}}/\mathrm{Pr})(L_h/L)}{(PY/8)^{1/2}(D/L)} \tag{17}$$

For turbulent flow:

$$\Delta\theta_{ss} = \frac{4(\overline{\mathrm{Nu}}/\mathrm{Pr})(L_h/L)}{(PY/0.03955)^{4/11}(D/L)} \tag{18}$$

It should be noted here that the use of equation (12) in arriving at equations (17) and (18) implies that the temperature distribution of the loop fluid in the cooler is assumed to be linear. It is shown from equations (17) and (18) that the dimensionless parameters PY, $\overline{\mathrm{Nu}}/\mathrm{Pr}$, L_h/L, and D/L determine the steady-state temperature distribution.

For laminar flow, equations (13) and (17) show that the steady-state flow of the loop, V_{ss}, is proportional to the 1/2 power of the heating rate q and relative height ΔZ. The steady-state temperature difference of the loop ΔT_{ss} $(= T_{3ss} - T_{4ss} = T_{2ss} - T_{1ss} = q\Delta\theta_{ss}/U)$ is proportional to the 1/2 power of the heating rate q and the effective length L_{ec}, but inversely proportional to the 1/2 power of the relative height ΔZ. This conclusion coincides with that of Zvirin et al. (1981) and Uhlemann and Bansal (1985).

For turbulent flow, equation (14) shows that the steady-state flow V_{ss} is proportional to the 4/11 power of q and ΔZ. The steady-state temperature difference ΔT_{ss} is proportional to the 4/11 power of L_{ec}, but inversely proportional to the 7/11 power of q and the 4/11 power of ΔZ, as shown by equation (18).

Experimental Investigation

1 Experimental Setup. In the present study, an experimental loop was constructed and measurements were made to study the steady and transient natural circulation phenomena and determine the overall heat transfer coefficient U in the cooler that is to be used in the analysis.

The heating of the loop is provided directly by a constant and uniform heat flux by an evenly wound electrical heating ribbon attached tightly on the heater surface. The cooling is provided by the cooling jacket using water as the coolant to remove heat from the loop. The vertical cooler of the loop was

Nomenclature (cont.)

fluid in cooler $\equiv T_3 - T_4$, °C
T_b = bulk temperature of loop fluid in heater, °C
T_{bc} = bulk temperature of loop fluid in cooler, °C
T_w = loop wall temperature in heater, °C
T_{wc} = loop wall temperature in cooler, °C
$\bar{T}$ = mean fluid temperature in cooler $= (T_3 + T_4)/2$, °C
$\bar{T}_c$ = mean coolant temperature in cooler $= (T_{c,i} + T_{c,o})/2$, °C
$T_{c,i}$ = inlet temperature of coolant, °C
$T_{c,o}$ = outlet temperature of coolant, °C
t = time, s
U = overall heat transfer coefficient of cooler, W/m²°C
V = fluid velocity, m/s
V_r = reference velocity defined in equation (7), m/s
v = dimensionless velocity $\equiv V/V_r$
x = dimensionless spatial coordinate running around the loop $\equiv s/L$
Y = dimensionless parameter defined in equation (16)
ΔZ = relative height between heater and cooler $\equiv H - (L_h + L_c)/2$
β = thermal expansion coefficient, °C⁻¹
θ = dimensionless temperature of loop fluid $\equiv (T - T_r)/(q/U)$
$\theta_{c,i}$ = $\equiv (T_{c,i} - T_r)/(q/U)$
$\bar{\theta}$ = dimensionless mean loop fluid temperature in cooler $\equiv (\bar{T} - T_r)/(q/U)$
$\bar{\theta}_c$ = dimensionless mean temperature of coolant $\equiv (\bar{T}_c - T_r)/(q/U)$
μ = viscosity of loop fluid, kg/m s
ρ = density, kg/m³
σ = a parameter used in equation (5) $\equiv \pi D L_c U/2 m_c C_p$
τ = dimensionless time $\equiv V_r t/L$

Subscripts

c = coolant fluid; cooler
r = reference state
ss = steady state
ssi = steady state property at location i, i = 1,2,. . .

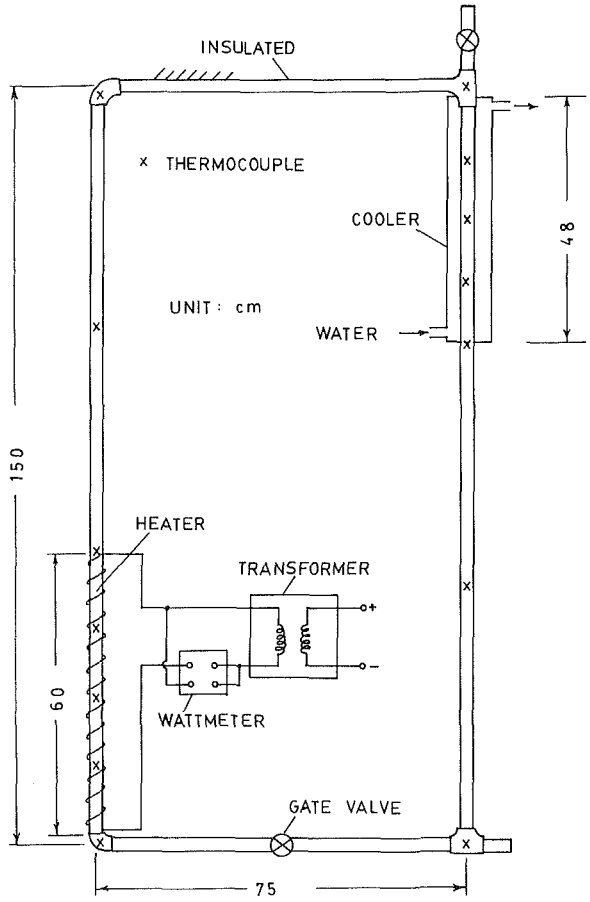

Fig. 2 Configuration of the experimental loop

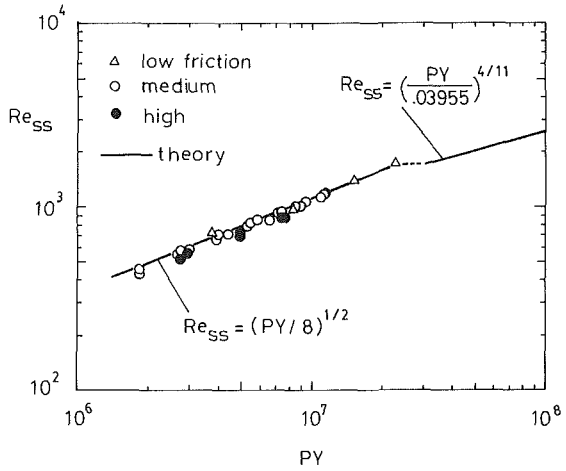

Fig. 3 Measurements of steady-state natural circulation flow

designed as a double-pipe heat exchanger consisting of an annular stainless-steel jacket with coolant flowing in the upward direction, as schematically shown in Fig. 2.

The loop was made of stainless steel in a rectangular shape with a 2.8-cm inside diameter and a height of 150 cm. The lengths of the cooling tube L_c and the heating section L_h are 48 and 60 cm, respectively, and the total loop length is 450 cm with $L/D = 160.7$. The relative height between the cooler and the heater measured from their centers, ΔZ, is 96 cm.

Water was the loop fluid. The electrical heat was supplied to the heater through a variable transformer (range: 0-1500 W) and was measured by a wattmeter. To reduce the heat loss to the ambient, the heater was insulated by 5-cm-thick calcium silicate. To prevent heat loss, fiberglass insulation was installed over the outside surface of the cooler and the connecting pipes. The total heat loss was found to be approximately 10 percent of the total heat input, which was determined by measuring the heat input power in the heater and the cooling rate in the cooler.

To measure the temperature distribution, 14 T-type thermocouples were installed along the centerline of the loop (Fig. 2) and were recorded by a HP-3054DL data logger with uncertainties of ± 0.6°C. To determine the total cooling rate in the cooler, Q_c, the coolant mass flow rate was measured by a rotameter with an uncertainty of ±0.003 kg/s. To overcome the difficulty in measuring the small temperature difference of the coolant flow across the cooling jacket, a HP 2804 quartz thermometer that gives an uncertainty of ± 0.001°C in a direct measurement of temperature difference was used to measure the coolant temperature drop across the cooling jacket so that the total cooling rate Q_c could be accurately determined to within ± 5 percent error.

The loop friction as well as loop circulation rate could be varied by adjusting a gate valve installed in the loop to produce three effective lengths, L_{ec} = 12.1, 24.6, and 37.0 m, which were estimated from conventional piping equations and referred to as low, medium, and high loop frictions, respectively. This estimation is believed to have an uncertainty of ± 10 percent. The total heating rate in the heater was adjusted from 225 to 1400 W and this made most of the circulating flows laminar in the experiments. Experiments at higher heating rate (> 1600 W) will easily cause vaporization in the loop and thus were not performed. The present experiment was run for three coolant flowrates: 10, 20, and 29 liter/min, which are in the turbulent flow regime with Reynolds numbers ranging from 2400 to 7000.

2 Measurement of Steady-State Natural Circulation Flow. The natural circulation flow at steady state Re_{ss} can be found by measuring the total cooling rate Q_c and the temperature drop of loop fluid in the cooler ΔT_{ss} $(= T_{3ss} - T_{4ss})$ and the following equation derived from an energy balance of the cooler:

$$Re_{ss} = \frac{4Q_c}{\pi D \mu C_p \Delta T_{ss}} \tag{19}$$

The parameter P appearing in equations (13) and (14) can be experimentally determined by measuring the heating flux q in the heater and using equation (15). The experimental data can then be presented in terms of PY and Re_{ss} so that a comparison with the theoretical analysis can be made. It should be noted here that the cooling rate Q_c measured in the cooler was about 10 percent less than the total heating rate Q_h measured in the heater due to the heat loss from the loop. Therefore, the experimental data of Re_{ss} were probably underestimated by an amount of less than 10 percent relative to the measurements of P, say, a fewer precent. Nevertheless, it is seen from Fig. 3 that the theoretical prediction for the steady-state natural circulation flow, using the present one-dimensional approximation, equation (13), is very accurate indeed. This indicates that one-dimensional analysis is appropriate for a rectangular thermosyphon loop in which the effect of secondary motion is negligible for small D/L, as used in the present experiment.

It is worthwhile noting that the parameter P defined in equation (15) can be written in terms of the Nusselt number of the heater and the Grashof and Prandtl numbers (Gr and Pr)

$$P = \mathrm{NuGr/Pr} \tag{20}$$

In this case, equations (13) and (14) can be treated as a theoretical convective heat transfer correlation for the rectangular thermosyphon loop and can be converted into the form

$$(\mathrm{NuGr/Pr})Y = \begin{cases} 8\ \mathrm{Re}_{ss}^2, & \text{for laminar flow} \\ 0.03955\ \mathrm{Re}_{ss}^{11/4} & \text{for turbulent flow} \end{cases} \quad (21)$$

It can be seen, from this relation, that the convective heat transfer correlation in a natural circulation loop is characterized by the dimensionless group $(\mathrm{NuGr/Pr})Y$ in which the effective length L_{ec} and other geometric lengths of the loop are included in Y.

It is very interesting that equation (21) is identical with the correlation derived theoretically by Holman and Boggs (1960) except the total geometric length of the loop is replaced by the effective length L_{ec} in the present correlation. Holman and Boggs derived their correlation using a simple momentum and energy balance for single-phase flow in a natural circulation loop. This correlation had already been justified by experiments using Freon-12 as the loop fluid.

Holman and Boggs' experimental loop had large curvatures at the top and the loop corners. The form loss of the loop was thus probably small as compared with that of the present loop so that the effective length can be approximated by the total geometric length, i.e., $L_{ec} \approx L$. This may explain why the effect of form losses in the loop friction was not observed in their experiments.

By equation (21), the experimental result of the present study shown in Fig. 3 is equivalent to a convection correlation for a heated upward flow in a natural circulation loop.

3 Determination of Overall Coefficient U. The overall heat transfer coefficient of the cooler U can be computed by the relation, according to the definition $Q_c = U\pi DL_c(\bar{T} - \bar{T}_c)$

$$U = \frac{1}{\dfrac{1}{h_i} + \dfrac{D \ln (D_1/D)}{2k_t} + \dfrac{1}{h_o}\dfrac{D}{D_1}} \quad (22)$$

To reduce the uncertainties in the calculation of h_i and h_o, an empirical correlation for U was derived in the present study. Here, Q_c, $\bar{T}$, and $\bar{T}_c$ were directly measured in the experiment and U was computed by the relation $U = Q_c/\pi DL_c(\bar{T} - \bar{T}_c)$.

For the laminar circulating flows as in the present experiments, it can be assumed that the thermal resistance due to the loop wall is relatively small as compared with the convective resistances and is thus negligible. Therefore, the correlation $\overline{\mathrm{Nu}} = f(\mathrm{Re}_{ss}, \mathrm{Re}_c) = f(PY, \mathrm{Re}_c)$ can be used, where the last equality is based on equations (20) and (21), $\overline{\mathrm{Nu}} = UD/k$, and Re_c is the Reynolds number of the coolant flow.

It was found from the experiment (Fig. 4) that for the loop tested at steady state

$$\overline{\mathrm{Nu}} = c\,E^d, \text{ for } 2400 < \mathrm{Re}_c < 7000 \quad (23)$$

where $E \equiv 7.0\ PY$; $c = 2.357 \times 10^{10}\ \mathrm{Re}_c^{-3.263} + 0.501$; $d = 0.159 + 1.74 \times 10^{-5}\ \mathrm{Re}_c - 1.16 \times 10^{-9}\ \mathrm{Re}_c^2$. This correlation was then used in the numerical analysis of the loop performance later on.

4 Loop Performance Measurements. The steady-state performance was measured using the experimental loop. Figure 5 shows that the measured temperature differences ΔT_{ss} $(= T_{3ss} - T_{4ss})$ are in good agreement with the analysis and vary with the 1/2 power of the heating rate as expected from equation (17). (This is because all the experiments are in the laminar regime.) The larger errors for the case of high loop friction are probably due to the uncertainties in estimating the effective length.

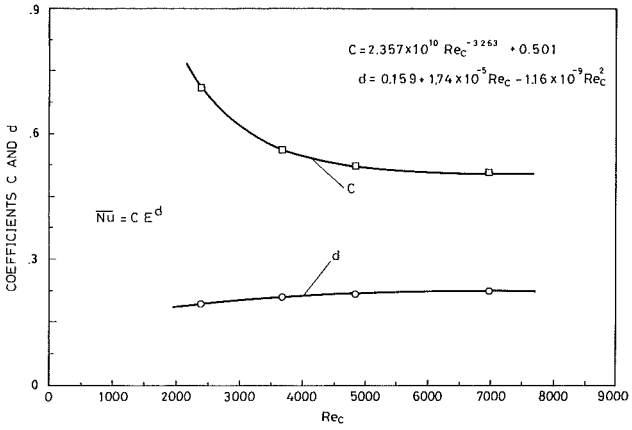

Fig. 4 Coefficients *c* and *d* for overall heat transfer in the cooler

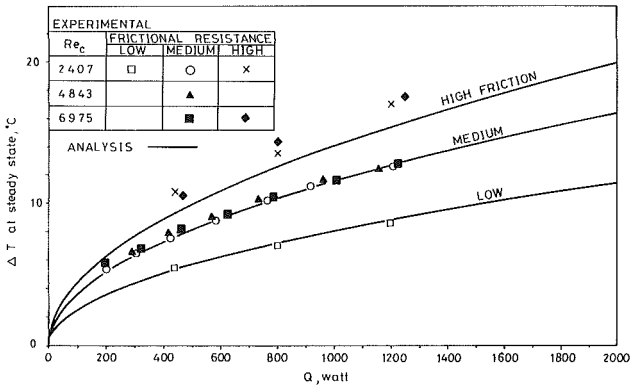

Fig. 5 Steady-state results

For the transient performance, solving equations (1)–(5) numerically with the initial conditions of rest states can give transient-state solutions. The solution procedure is difficult partly due to the coupling between the equations, but mainly due to the nonlinear properties of the time-variant frictional factor f and the time-variant overall heat transfer coefficient U, which are complex functions of the instantaneous circulating velocity.

For simplification, it was assumed that the time variation of the circulating velocity is very slow so that a quasi-steady approximation holds. Hence, the frictional factor can be calculated by using the Fanning friction factor. In addition, the overall heat transfer coefficient U in the cooler was assumed to be time-invariant and the value at steady-state was used. The numerical solutions with constant coefficients were then carried out using 90 fixed grids along the loop. The analytical solutions as well as the transient measurements are presented in Figs. 6–11.

It is interesting to note that the analytical results coincide fairly well with the measurements of temperature distribution after 6 min from startup (see Figs. 6 and 9). The inaccurate analysis during the starting periods is mainly due to the time delay of the heating process in the heater. Usually it took several minutes for heat transfer from the electric heater to the loop fluid to reach steady heating during the experiments. This apparently violates the initial and boundary conditions of the governing equations and may cause serious errors during startup. Another possible factor causing this error is the time-variant nature of the combined convection and overall heat transfer coefficients in the cooler in the transient process. Recall that a constant value at steady state was used as an approximation. This approximation holds soon after startup,

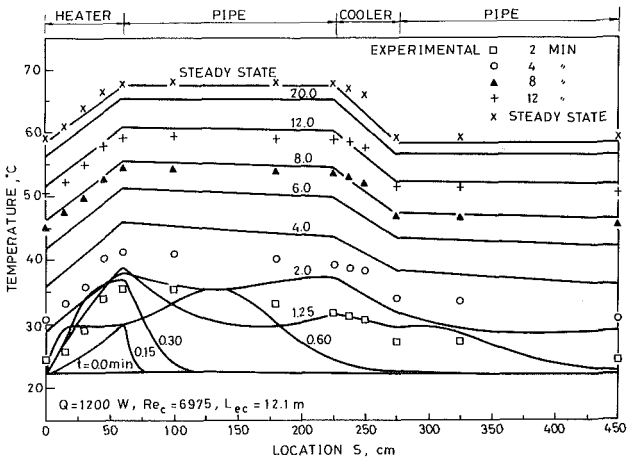

Fig. 6 Transient temperature distributions

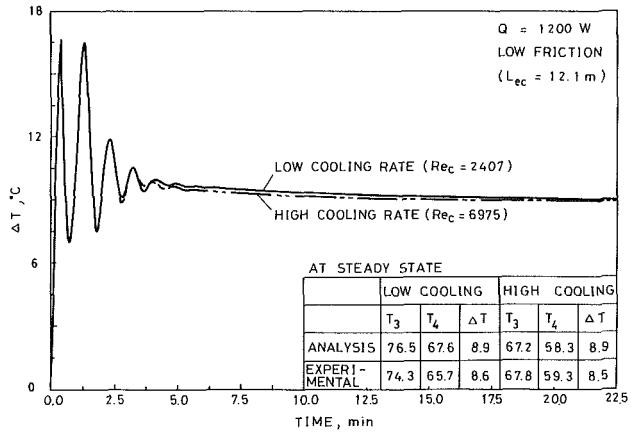

Fig. 7 Temperature difference under transient conditions

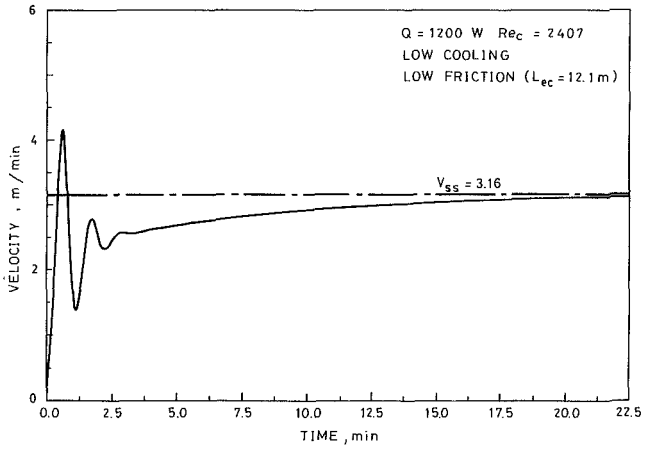

Fig. 8 Transient velocity solution

since the circulating velocity reaches about 80 percent of the steady-state value in 5 min from startup (see Figs. 8 and 11).

It also can be seen from Figs. 7 and 10 that very good agreement between analysis and experiments at steady state can be obtained for the temperature differences $\Delta T\,(=T_3-T_4)$, with the largest error occurring for the high friction case.

It can be seen from the analysis that oscillations in temperature and velocity occur during the starting period as shown in Figs. 7, 8, 10, and 11. This oscillation phenomenon is similar to that of a damped spring-mass system. In fact, the high inertia force induced by heating and cooling during the startup is always retarded by the loop friction induced by flow

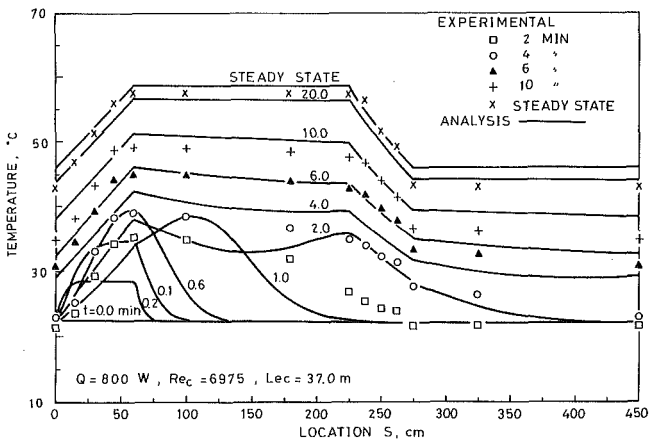

Fig. 9 Transient temperature distributions

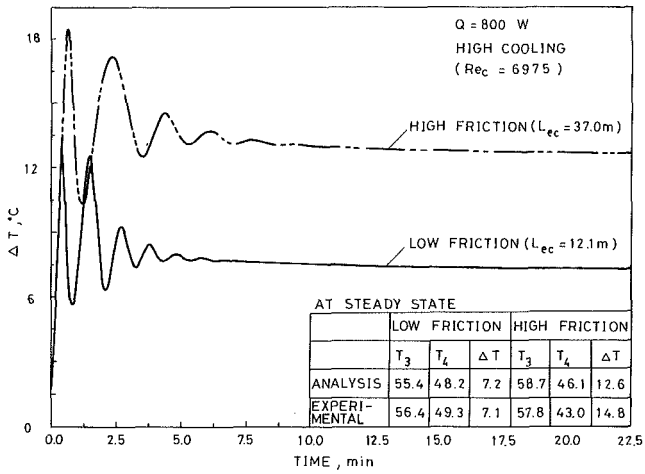

Fig. 10 Temperature difference under transient conditions

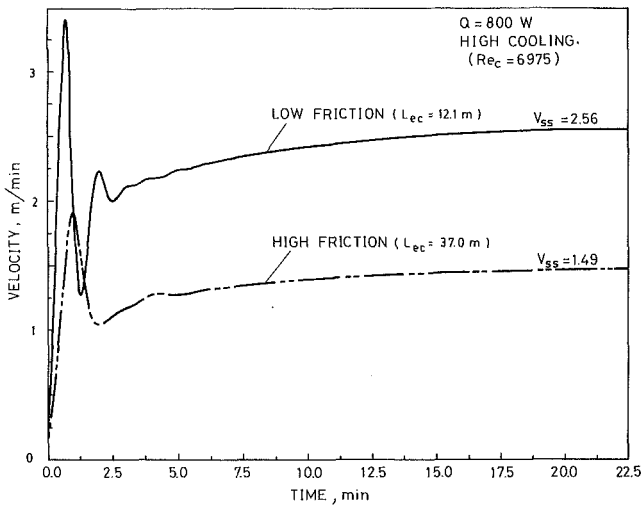

Fig. 11 Transient velocity solution

circulation; therefore a velocity as well as a temperature oscillation takes place. This oscillation will finally be damped out and a steady-state performance will be achieved, if the loop is stable. If the loop is unstable or oscillatory, the oscillation will be aggravated or continued forever. This is referred to as instability and is not studied here.

Since it was very difficult to control the boundary and initial conditions of the experiments to those required in the analysis,

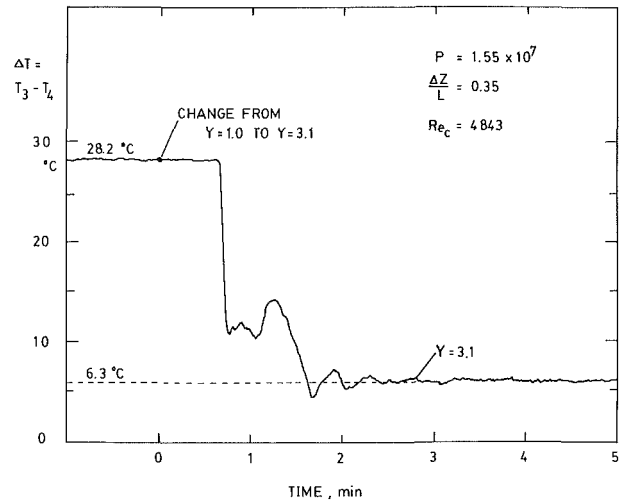

Fig. 12 Oscillation phenomenon of thermosyphon loop during startup

the oscillation phenomenon cannot be directly observed from the transient data presented in Figs. 6 and 9. However, if a step change is suddenly applied to the loop, which is operating at a steady state, the oscillatory phenomena can be observed. A particular experiment was thus purposely conducted in the present study to see this oscillatory phenomenon.

Since the HP 3497 data logger used in the previous experiments cannot read the temperatures continuously, the temperature difference ΔT was directly measured by a pair of T-type thermocouples and recorded by a continuous recorder. It can be seen from Fig. 12 that the temperature drop ΔT across the cooler starts to oscillate as the loop friction or the effective length L_{ec} was suddenly reduced by quickly opening the gate valve in the loop at time zero. (This corresponds to a sudden increase of Y.) A time delay of about 0.8 min was first observed, which was apparently due to propagation of the temperature signal from the heater to the cooler.

It seems that the first period of the oscillation was distorted. This probably resulted from flow transition since the flow is finally in transition regime (with Reynolds number around 2000), as can be seen from Fig. 3 or equation (14). No analytical results, however, can be used to compare with these experimental data during transient period since the transient analysis in the present study was performed with initial state of zero motion only.

Finally, it should be emphasized here that all the transient processes discussed above finally approach stable flows. This is due to the fact that, for all the given operating conditions, the disturbance will be damped out and a stable and steady flow will finally occur. Although unstable flow may occur under certain circumstances, the present study has shown that the one-dimensional analysis always guarantees accurate results as the flow reaches or approaches steady state.

Conclusions

The thermal performance of a rectangular thermosyphon loop was studied using a one-dimensional approximation and the conventional friction factor correlation. However, the effective length was used to replace the geometric length in the calculation of loop friction in order to account for the form frictional loss of the loop. A correlation for the overall heat transfer in the cooler was experimentally determined and used in the analysis. The solution for steady-state natural circulation flow found in the present study is shown to be a function of a dimensionless group PY or $(\mathrm{NuGr/Pr})Y$ and agrees very well with the experimental results. The comparison of the experimental measurements of steady-state temperature differences and transient temperature distributions with the analysis has shown that the present analysis can accurately predict the loop performance at steady state or approaching steady state. The effect of secondary motion in the loop appears to be negligible for the present experimental loop, which has a low D/L ratio (1/160.7). An oscillatory phenomenon of the loop performance in a step response, which is qualitatively consistent with the transient analysis, was also experimentally observed in the present study. More research on the effect of D/L as well as the oscillation phenomena during transient periods is still needed in order to understand further the limitations of the one-dimensional approximation and the instability of the loop.

Acknowledgments

The present study was supported by the National Science Council of the Republic of China through Grant No. NSC73-0401-E002-08.

References

Bau, H. H., and Torrance, K. E., 1981a, "Transient and Steady Behavior of an Open, Symmetrically-Heated, Free Convection Loop," *International Journal of Heat and Mass Transfer*, Vol. 24, pp. 597-609.

Bau, H. H., and Torrance, K. E., 1981b, "On the Stability and Flow Reversal of an Asymmetrically Heated Open Convection Loop," *J. Fluid Mech.*, Vol. 106, pp. 417-433.

Chen, K., 1985, "On the Oscillatory Instability of Closed-Loop Thermosyphons," ASME JOURNAL OF HEAT TRANSFER, Vol. 107, pp. 826-832.

Churchill, S. W., 1977, "Friction-Factor Equation Spans All Fluid-Flow Regimes," *Chemical Engineering*, pp. 91-92.

Creveling, H. F., De Paz, J. F., Baladi, J. Y., and Schoenhals, R. J., 1975, "Stability Characteristics of a Single-Phase Free Convection Loop," *J. Fluid Mech.*, Vol. 67, pp. 65-84.

Damerell, P. S., and Schoenhals, R. J., 1979, "Flow of a Toroidal Thermosyphon With Angular Displacement of Heated and Cooled Sections," ASME JOURNAL OF HEAT TRANSFER, Vol. 101, pp. 672-676.

Eckert, E. R. G., and Diaguila, A. J., 1954, "Convective Heat Transfer for Mixed, Free and Forced Flow Through Tubes," *Trans. ASME*, Vol. 76, pp. 497-505.

Fox, R. W., and McDonald, A. T., 1978, *Introduction to Fluid Mechanics*, Wiley, New York.

Greif, R., Zvirin, Y., and Mertol, A., 1979 "The Transient and Stability Behavior of a Natural Convection Loop," ASME JOURNAL OF HEAT TRANSFER, Vol. 101, pp. 684-688.

Holman, J. P., and Boggs, J. H., August 1960, "Heat Transfer to Freon 12 Near the Critical State in a Natural Circulation Loop," ASME JOURNAL OF HEAT TRANSFER, Vol. 88, pp. 221-226.

Keller, J. B., 1966, "Periodic Oscillations in a Model of Thermal Convection," *Journal of Fluid Mech.*, Vol. 26, pp. 599-606.

Lavine, A. S., Greif, R., and Humphrey, J. A. C., 1986, "Three-Dimensional Analysis of Natural Convection in a Toroidal Loop: Effect of Tilt Angle," ASME JOURNAL OF HEAT TRANSFER, Vol. 108, pp. 796-805.

McAdams, W. H., 1954, *Heat Transmission*, McGraw-Hill, New York.

Mertol, A., Greif, R., and Zvirin, Y., 1981, "The Transient, Steady State and Stability Behavior of a Thermosyphon With Throughflow," *International Journal of Heat and Mass Transfer*, Vol. 24, pp. 621-633.

Mertol, A., Greif, R., and Zvirin, Y., 1982, "Two Dimensional Study of Heat Transfer and Fluid Flow in a Natural Convection Loop," ASME JOURNAL OF HEAT TRANSFER, Vol. 104, pp. 508-514.

Mertol, A., and Greif, R., 1982, "Study of a Thermosyphon With a Counter-Flow Heat Exchanger," *Proceedings of 7th International Heat Transfer Conference*, Munich, Federal Republic of Germany, Sept. 6-10, Vol. 2, pp. 239-244.

Torrance, K. E., 1979, "Open-Loop Thermosyphons With Geological Applications," ASME JOURNAL OF HEAT TRANSFER, Vol. 101, pp. 677-683.

Uhlemann, R., and Bansa, N. K., 1985, "Side-by-Side Comparison of a Pressurized and a Nonpressurized Solar Water Heating Thermosyphon System," *Solar Energy*, Vol. 34, No. 4/5, pp. 317-328.

Welander, P., 1967, "On the Oscillatory Instability of a Differentially Heated Fluid Loop," *Journal of Fluid Mech.*, Vol. 29, pp. 17-30.

Zvirin, Y., and Greif, R., 1979, "Transient Behavior of Natural Circulation Loops: Two Vertical Branches With Point Heat Source and Sink," *International Journal of Heat and Mass Transfer*, Vol. 22, pp. 499-504.

Zvirin, Y., Jeuck, P. R., Sullivan, C. W., and Duffey, R. B., 1981, "Experimental and Analytical Investigation of a Natural Circulation System With Parallel Loops," ASME JOURNAL OF HEAT TRANSFER, Vol. 103, pp. 645-652.

Zvirin, Y., and Rabinoviz, Y., 1982, "On the Behavior of Natural Circulation Loops With Parallel Channels," *Seventh International Heat Transfer Conference*, Munich, Federal Republic of Germany, Vol. 2, pp. 299-304.

A. E. Ruggles
Department of Mechanical Engineering, Aeronautical Engineering & Mechanics.

R. T. Lahey, Jr.
Department of Nuclear Engineering & Engineering Physics.
Fellow ASME

D. A. Drew
Department of Mathematical Sciences.

H. A. Scarton
Department of Mechanical Engineering, Aeronautical Engineering & Mechanics.
Mem. ASME

Rensselaer Polytechnic Institute, Troy, NY 12180-3590

An Investigation of the Propagation of Pressure Perturbations in Bubbly Air/Water Flows

Dispersion and attenuation was measured for standing waves in a vertical waveguide filled with a bubbly air/water mixture. The propagation speed of pressure pulses was also measured. The data were compared with a two-fluid model for a range of values of the virtual volume coefficient, C_{VM}. *The experimentally determined* C_{VM} *was found to be a function of global void fraction* ($\langle\alpha\rangle$). *Moreover it was noted that this* C_{VM} *was less strongly related to void fraction than those proposed by Zuber (1964) and Van Wijngaarden (1976).*

Introduction

The virtual volume coefficient C_{VM} is important in the proper representation of interfacial momentum transfer in a two-fluid model of two-phase flow (Drew et al., 1979). The functional relationship of the virtual volume coefficient to other pertinent flow characteristics such as global void fraction $\langle\alpha\rangle$ and phase distribution has been the subject of prior research. Zuber (1964) and Van Wijngaarden (1976) have proposed theoretical models for the dependence of the virtual volume coefficient C_{VM} on global void fraction $\langle\alpha\rangle$ for bubbly flows:

$$C_{VM} = C_{VM_0}\left[\frac{1+2\langle\alpha\rangle}{1-\langle\alpha\rangle}\right] \qquad \text{(Zuber, 1964)} \qquad (1)$$

$$C_{VM} = C_{VM_0}[1+2.78\langle\alpha\rangle] \qquad \text{(Van Wijngaarden, 1976)} \quad (2)$$

where $C_{VM_0} = 0.5$, for a spherical bubble. Previous data indicated that the virtual volume coefficient increases with void fraction (Mokeyev, 1964; Henry et al., 1971; Chernyy et al., 1979; Kuo, 1979), which is consistent with the behavior of these models. A set of more definitive data is presented in which careful control was exercised over all potentially important flow characteristics. These data have been used in conjunction with a two-fluid model to establish an empirical relationship between C_{VM} and $\langle\alpha\rangle$ of the form

$$C_{VM} = 0.5[1+12\langle\alpha\rangle^2], \quad (\langle\alpha\rangle) < 20 \text{ percent} \qquad (3)$$

This relationship predicts a weaker increase in C_{VM} with $\langle\alpha\rangle$ than the theoretical models of equations (1) and (2).

Two-Fluid Model. A two-fluid model was used to predict the measured data. This model was developed for a dispersed bubbly air/water flow (Cheng et al., 1983; Ruggles, 1987). Models for bubble dynamics, viscous flow effects, and interfacial heat transfer are included. The interfacial heat transfer model of Cheng (1985) implies that the gas phase follows a polytropic process, making a transition from adiabatic to isothermal behavior as the excitation frequency decreases. This behavior is important to predict properly the sound propagation speeds at frequencies far below bubble resonance, where these data were taken. The two-fluid model will now be summarized.

The gas continuity equation is

$$\rho_g\frac{\partial\alpha}{\partial t} + \alpha\frac{\partial\rho_g}{\partial t} + \rho_g u_g\frac{\partial\alpha}{\partial z} + \alpha\left[\rho_g\frac{\partial u_g}{\partial z} + u_g\frac{\partial\rho_g}{\partial z}\right] = 0 \qquad (4a)$$

where for an ideal gas

$$\frac{\partial\rho_g}{\partial t} = \frac{\rho_g}{p_g}\frac{\partial p_g}{\partial t} - \frac{\rho_g}{h_g}\frac{\partial h_g}{\partial t}$$

and

$$\frac{\partial\rho_g}{\partial z} = \frac{\rho_g}{p_g}\frac{\partial p_g}{\partial z} - \frac{\rho_g}{h_g}\frac{\partial h_g}{\partial z}$$

The liquid continuity equation is

$$-\rho_l\frac{\partial\alpha}{\partial t} + (1-\alpha)\left[\beta_l\frac{\partial p_l}{\partial t} + \phi_l\frac{\partial h_l}{\partial t}\right] - \rho_l u_l\frac{\partial\alpha}{\partial z} + (1-\alpha)\left[u_l\beta_l\frac{\partial p_l}{\partial z} + u_l\phi_l\frac{\partial h_l}{\partial z} + \rho_l\frac{\partial u_l}{\partial z}\right] = 0 \qquad (4b)$$

where

$$\beta_l = \frac{\partial\rho_l}{\partial p_l}\bigg|_{h_l} \qquad (4c)$$

and

$$\phi_l = \frac{\partial\rho_l}{\partial h_l}\bigg|_{p_l} \qquad (4d)$$

The gas phase momentum equation is

$$\rho_g\left[\frac{\partial u_g}{\partial t} + u_g\frac{\partial u_g}{\partial z}\right] + \frac{\partial p_g}{\partial z} - \rho_g g\cos\theta + F_D + F_{VM} + F_R + F_B = 0 \qquad (5a)$$

and the liquid phase momentum equation is

$$(1-\alpha)\rho_l\left[\frac{\partial u_l}{\partial t} + u_{l0}\frac{\partial u_l}{\partial z}\right] + (1-\alpha)\frac{\partial p_l}{\partial z} + \frac{\partial\alpha}{\partial z}(p_{l_i} - p_l) - (1-\alpha)g\rho_l\cos\theta - \alpha[F_D + F_{VM} + F_R + F_B] + F_W = 0 \qquad (5b)$$

where

F_D ≡ the drag force
$F_{VM} \triangleq \rho_l C_{VM} a_{VM}$ = virtual mass force
F_R ≡ radial reaction force due to bubble radius variations
F_B ≡ Basset force
F_W ≡ wall shear force

Contributed by the Heat Transfer Division and presented at the ASME Winter Annual Meeting, Anaheim, California, December 1986. Manuscript received by the Heat Transfer Division October 27, 1986. Keywords: Multiphase Flows.

The difference between the liquid pressure at the interface p_{l_i}, and the average liquid pressure p_l, can be derived from an inviscid flow analysis of the fluid surrounding a pulsating and translating bubble as

$$(p_{l_i}-p_l)=\rho_l\left[R_b\left(\frac{D_g^2R_b}{Dt^2}\right)+\frac{3}{2}\left(\frac{D_gR_b}{Dt}\right)^2-\frac{1}{4}(u_g-u_l)^2\right] \tag{6}$$

The form of the radial reaction force F_R also comes from this analysis as

$$F_R=\frac{3}{R_b}C_{VM}\rho_l(u_g-u_l)\frac{D_gR_b}{Dt} \tag{7}$$

and in this study the virtual mass acceleration a_{VM} was given by

$$a_{VM}=\left[\frac{\partial u_g}{\partial t}+u_g\frac{\partial u_g}{\partial z}\right]-\left[\frac{\partial u_l}{\partial t}+u_l\frac{\partial u_l}{\partial z}\right]\triangleq\frac{D_gu_g}{Dt}-\frac{D_lu_l}{Dt} \tag{8}$$

Since the purpose of this study was to investigate the propagation of pressure perturbations in air/water mixtures, the gas phase energy equation was not used in its normal form. Rather, the problem of the dynamics of an individual gas bubble in a liquid medium was solved explicitly to relate the gas enthalpy and bubble radius to the liquid pressure and enthalpy. This analysis results in (Cheng, 1985)

$$\frac{D_g^2R_b}{Dt^2}+2\beta\frac{D_gR_b}{Dt}+\omega_n^2R_b+\frac{p_l}{\rho_lR_b}=0 \tag{9a}$$

where

$$\beta=\beta_{VIS}+\beta_{TH}+\beta_{AC}+\beta_{COM}+\beta_{BL} \tag{9b}$$

and

$$\omega_n^2=\omega_{VIS}^2+\omega_{TH}^2+\omega_{AC}^2+\omega_{COM}^2+\omega_{BL}^2 \tag{9c}$$

The terms contributing to the damping coefficient β, and the reasonant frequency ω_n, are due to liquid viscosity (VIS), interfacial heat transfer (*TH*), acoustic scattering (*AC*), liquid compressibility (COM), and bullk liquid viscosity (*BL*), respectively.

Finally, the liquid phase thermal energy equation is given by

$$(1-\alpha)\rho_l\left[\frac{\partial h_l}{\partial t}+u_l\frac{\partial h_l}{dz}\right]-(1-\alpha)\left[\frac{\partial p_l}{\partial t}+u_l\frac{\partial p_l}{dz}\right]-u_lF_w-[q_{l_i}''/L_s]=0 \tag{10}$$

where $1/L_s$ is the interfacial area density.

Equations (3)–(10) can be written in matrix form as

$$\underline{\underline{A}}\frac{\partial\underline{\psi}}{\partial t}+\underline{\underline{B}}\frac{\partial\underline{n}}{\partial z}=\underline{\underline{C}}\underline{\psi} \tag{11}$$

where

$$\underline{\psi}=\left[\alpha, p_l, u_g, u_l, h_l, R_b, \frac{D_gR_b}{Dt}\right]^T \tag{12}$$

Equation (11) was perturbed as follows:

$$[\underline{\underline{A}}_0+\delta\underline{\underline{A}}]\left[\frac{\partial\delta\underline{\psi}}{\partial t}\right]+[\underline{\underline{B}}_0+\delta\underline{\underline{B}}]\left[\frac{\partial\underline{\psi}_0}{\partial z}+\frac{\partial\delta\underline{\psi}}{\partial z}\right]=[\underline{\underline{C}}_0+\delta\underline{\underline{C}}][\underline{\psi}_0+\delta\underline{\psi}] \tag{13}$$

The steady-state equation describing the unperturbed two-phase flow is given by

$$\underline{\underline{B}}_0\frac{\partial\underline{\psi}_0}{\partial z}=\underline{\underline{C}}_0\underline{\psi}_0$$

Assuming that the spatial derivatives of the steady-state solution are of order δ, the linearized equation set describing the response of the system to small perturbations is given by

$$\underline{\underline{A}}_0\frac{\partial\delta\underline{\psi}}{\partial t}+\underline{\underline{B}}_0\frac{\partial\delta\underline{\psi}}{\partial z}=\underline{\underline{C}}_0'\delta\underline{\psi} \tag{15}$$

where

$$\underline{\underline{C}}_0'=\underline{\underline{C}}_0+\left.\frac{\partial\underline{\underline{C}}}{\partial\underline{\psi}}\right|_0\underline{\psi}_0$$

The perturbation of the state variables can be introduced in the form

$$\delta\underline{\psi}=\underline{\psi}'e^{i(kz-\omega t)} \tag{16}$$

Combining equations (15) and (16) we obtain the algebraic equation

Nomenclature

a_{VM} = virtual mass acceleration
B_l = coefficient of volumetric expansion for a liquid
$C_{2\phi}$ = speed of propagation of pressure perturbations in a two-phase mixture
C_{VM} = virtual volume coefficient
c_p = constant pressure specific heat capacity
c_v = constant volume specific heat capacity
$\frac{D_g(\,)}{Dt}$ = material derivative $=\frac{\partial(\,)}{\partial t}+u_g\frac{\partial(\,)}{\partial z}$
f = frequency
F = force
g = gravitational acceleration
H_{i0} = interfacial heat transfer coefficient
h = enthalpy
i = imaginary number $\sqrt{-1}$
k = wavenumber
$1/L_S$ = interfacial area density
p = pressure
q_{ki}'' = interfacial heat transfer rate
R = radius
T = temperature
t = time
u = velocity
v = specific volume
z = axial location
α = void fraction
β_l = equation (4*c*)
β = equation (9*b*)
η = attenuation coefficient
θ = angle of inclination of flow from vertical, or phase angle (equation (24))
λ = wavelength
μ = dynamic viscosity
ρ = density
σ = surface tension
ϕ_l = equation (4*d*)
ω = angular frequency

Subscripts

b = bubble
2ϕ = two-phase
g = gas
i = interfacial
l = liquid
0 = equilibrium value
p = pressure
VM = virtual mass

Symbols

$(\bar{\ })$ = effective value
$\langle\ \rangle$ = area averaging over the flow area
$\delta(\ )$ = perturbation
$(\ )^T$ = transpose of an array

$$\{\underline{\underline{A}}_0(\underline{\psi})[-i\omega]+\underline{\underline{B}}_0(\underline{\psi})[ik]-\underline{\underline{C}}_0'(\underline{\psi})\}\underline{\psi}'=0 \tag{17}$$

Equation (17), in conjunction with the requirement that $\underline{\psi}'$ be finite, implies a dispersion relationship of the form

$$\det\{(\omega/k)\underline{\underline{A}}_0-\frac{i}{k}\underline{\underline{C}}_0'-\underline{\underline{B}}_0\}=0 \tag{18}$$

The dispersion relation gives seven wavenumbers for each value of angular frequency ω. Five of the seven roots have celerities typical of convective velocities of the liquid and vapor phase, u_l and u_g. Unfortunately, the wavelengths associated with these roots are too short to allow the two-fluid medium to be treated as a continuum when frequencies go above 10-20 Hz. Furthermore, four of these roots are highly attenuated. The remaining two roots travel at celerities typical of the so-called "speed of sound" in the two-phase medium. One of these roots has a positive real part (i.e., it travels downwind, in the positive z direction). The other has a negative real part and travels in the negative z direction. These two roots have velocities that vary in absolute value by a small amount associated with some two-phase convective velocity. The difference between these two roots has been used to predict the sonic velocity ($c_{2\phi}$):

$$c_{2\phi}=\frac{|[\omega/\mathrm{Re}(k)]_p^+-[\omega/\mathrm{Re}(k)]_p^-|}{2} \tag{19a}$$

and the spatial attenuation coefficient (η),

$$\eta=\omega\mathrm{Im}[(\omega/k)_p^-]^{-1} \tag{19b}$$

The propagation speeds and attenuation of pressure perturbations were measured for standing waves in a bubbly air/water flow with the global void fraction $\langle\alpha\rangle$ varying from 0.5 percent to 18 percent and the bubble radii, R_b varying from 0.5 mm to 2.5 mm. Frequencies were varied from 20 Hz to 200 Hz to allow measurement of the dispersion and attenuation curves for each flow situation. All standing wave measurements were taken with no liquid flow. The standing wave dispersion and attenuation data were compared with two-fluid model predictions for a range of values of the virtual volume coefficient. The value of C_{VM} giving agreement with a given data set was then chosen as the appropriate value.

Propagation speeds were also measured for pressure pulses. These measurements were performed for the same flow situations as the standing wave data, with the addition of varying the superficial liquid velocity from 0.0 m/s to 1.0 m/s. The pressure pulse propagation velocity data was compared with the nonlinear two-fluid model given by equation (11). To determine the pulse propagation speeds, the eigenvalues of the system were determined from (Ruggles et al., 1987)

$$\det[\underline{\underline{A}}-\xi\underline{\underline{B}}]=0 \tag{20a}$$

where

$$\mathrm{Re}[\xi_j]=\left(\frac{dz}{dt}\right)_j^{-1} \tag{20b}$$

The roots of equation (20a) behave similarly to those of equation (18). However, only the root with the negative real part, ξ_p^-, was used to predict the pulse propagation speeds. The pressure data were compared to the two-fluid model using a range of values for C_{VM}. The value of C_{VM} producing agreement with the data was chosen as the appropriate value for that flow situation.

Standing Wave Measurements

The apparatus used for the standing wave measurements is shown in Fig. 1. The waveguide used to generate the standing wave pattern was constructed from 63.5 mm i.d., 76.2 mm o.d., stainless steel tube 2 m long. This tube was fitted with three side-mounted pressure transducers and a hydrophone mounted on a traversing mechanism. Sinusoidal pressure

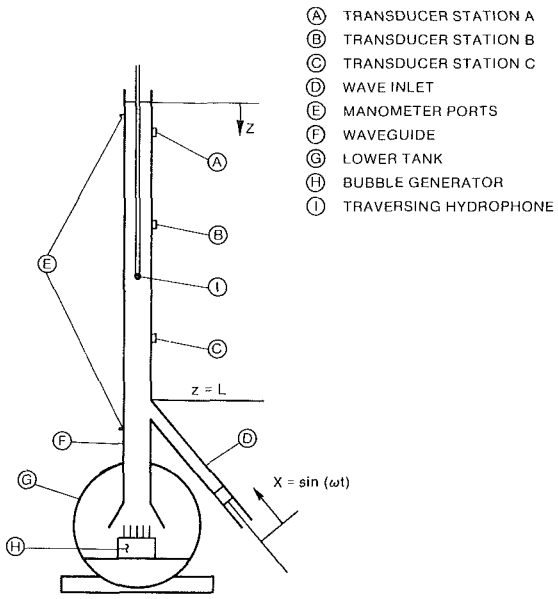

Fig. 1 Measurement system for sound propagation in a bubbly air/water mixture

oscillations were introduced through a side port, using an electromechanical shaker and piston arrangement. An isolation system prevented sound energy from the shaker and piston from entering the waveguide walls and disturbing the side-mounted transducers. An air cushion isolated the entire wave guide and lower plenum from laboratory floor vibrations.

Air bubbles were introduced in the lower plenum using one of four banks of hypodermic needles. The bubble radius produced by each needle was inferred through the measurement of the volume flow rate through the individual needles and measurement of the corresponding bubble departure frequency. Bubble radii were also measured directly using high-speed photographic techniques. The distribution of bubble radii was measured for several air flow rates for each bank. The values of bubble radius for data taken in the region where $\langle\alpha\rangle$ was less than 7 percent were determined as described above. In addition, subsequent experiments were performed using a clear acrylic section having quick-closing valves. This section replaced the waveguide in the neighborhood of side-mounted transducer B. For runs having finite $\langle j_l\rangle$, the global void fraction was measured by simultaneously closing the quick-closing valves. This avoided errors in trying to infer $\langle\alpha\rangle$ from measurements of the hydrostatic head. High-speed photographs of the flow were also taken to allow the bubble size distribution to be determined. These observations accounted for any bubble coalescence that occurred at the higher void fractions.

The propagation speed is also very sensitive to uncertainties in the measured void fraction. This is especially true for void fraction less than 3 percent. One of three manometers was used to measure the variation in hydrostatic pressure due to void fraction. The first of these measured global void fraction $\langle\alpha\rangle$ from 0.000 to 1.000 percent, the second measured $\langle\alpha\rangle$ from 1.00 to 8.00 percent, and the third measured $\langle\alpha\rangle$ from 8.0 to 20.0 percent. Three manometers were necessary to provide sufficient range and accuracy in the measurement of void fraction.

The propagation speed and attenuation of the pressure perturbations associated with standing waves were measured using three independent techniques. In the first of these techniques the hydrophone was traversed through the wave guide while the locations and amplitudes of the pressure nodes and antinodes were recorded. The propagation speed and attenua-

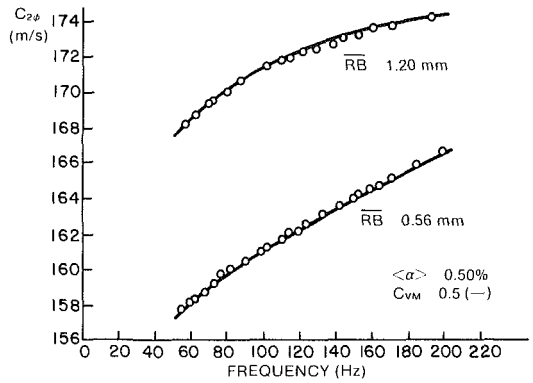

Fig. 2 Propagation speed versus frequency

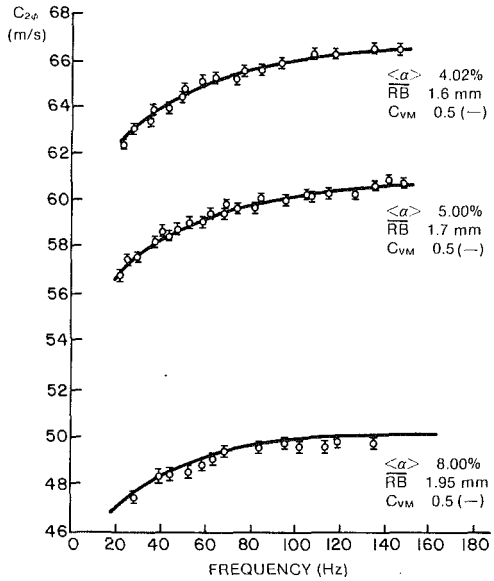

Fig. 3 Propagation speed versus frequency

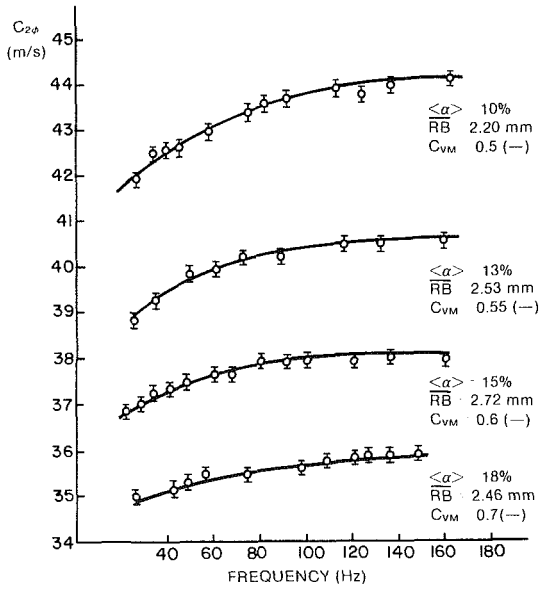

Fig. 4 Propagation speed versus frequency

tion could then be calculated since the distance between nodes is half of the wavelength λ. That is

$$c_{2\phi} = \lambda f \tag{21a}$$

$$\eta = \left(\frac{4\pi}{\lambda}\right) \sinh^{-1} \frac{|\delta p_{\min}(n+1)| - |\delta p_{\min}(n)|}{2\,|\delta p_{\max}(n+1/2)|} \tag{21b}$$

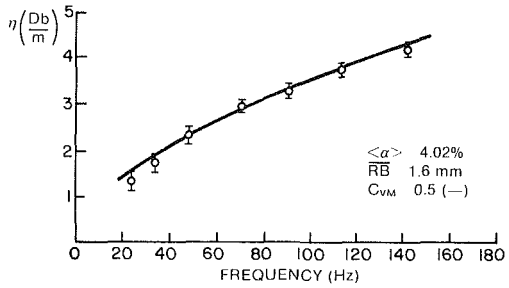

Fig. 5 Attenuation versus frequency

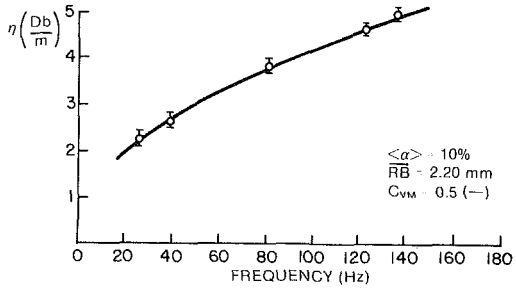

Fig. 6 Attenuation versus frequency

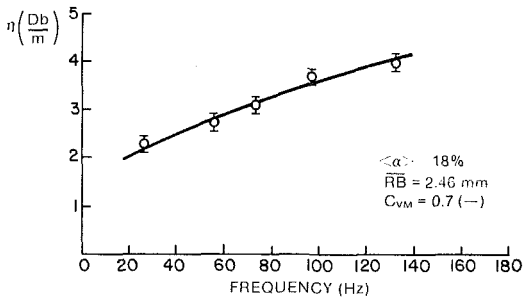

Fig. 7 Attenuation versus frequency

where n is the node number, counting from the top of the waveguide. The frequency f of the standing wave was measured using a Tektronix 7854 digital oscilloscope with a waveform calculator.

The second measurement technique used the root-mean-square pressure amplitude readings, δp_{RMS}, from the three side-mounted transducers to infer the wavelength and attenuation of the standing wave. That is,

$$\frac{\delta p_{\mathrm{RMS}}}{|A^+|} = 2e^{-\eta l}\left[\cosh^2(\eta l) - \cosh^2\left(\frac{2\pi}{\lambda} l\right)\right]^{1/2} \tag{22a}$$

where from Fig. 1 the distance from the free surface is

$$l = L - z \tag{22b}$$

and A^+ is the amplitude of the upward traveling wave at $z = L$.

The third measurement technique involved varying the frequency until a pressure node was situated over one of the side-mounted transducers. This indicated that an integral number of half-wavelengths existed between the transducer and the bubbly air/water interface with the ambient. The number of half-wave lengths was then measured using the traversing hydrophone and the propagation speed was calculated using equation (21a). These redundant measurement techniques were used to assure accuracy of the data and to verify that the presence of the traversing hydrophone did not affect the data.

An error analysis was performed using standard propagation of error techniques. The measurement uncertainties are given along with representative standing wave data in Figs. 2-7. The agreement between the model and the data is seen to be excellent.

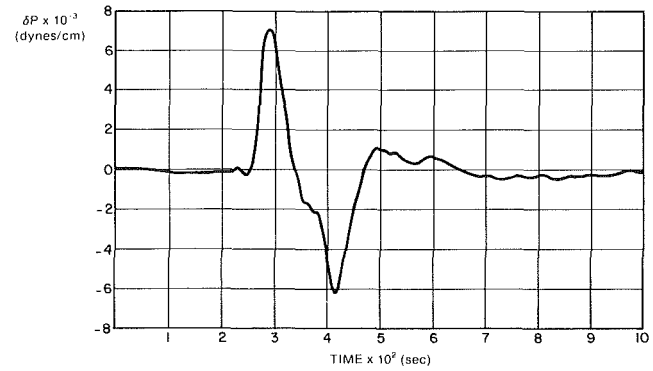

Fig. 8 Pressure pulse (typical)

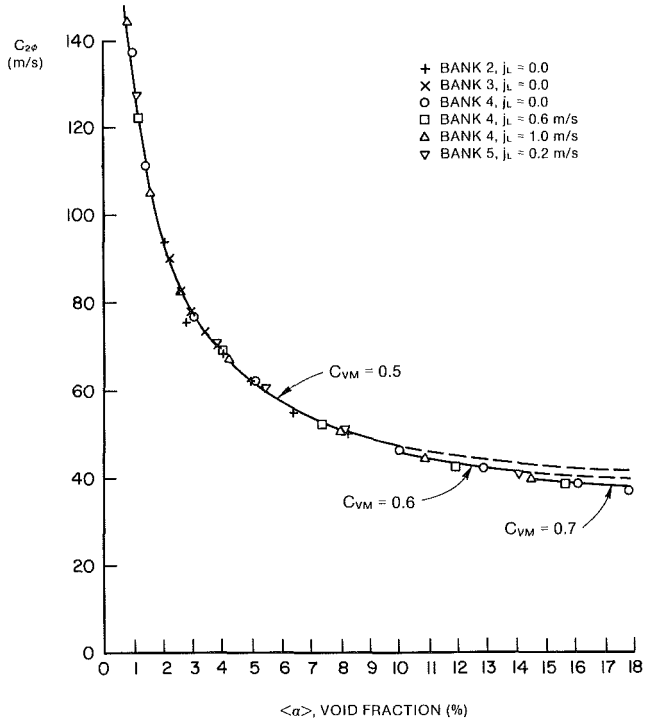

Fig. 9 Pressure pulse propagation speed versus global void fraction

Pressure Pulse Measurements

The apparatus used to take the pressure pulse propagation speed measurements was identical to that in Fig. 1. The pressure pulses were introduced by driving the electromechanical shaker with a square-wave generator. The upper end of the waveguide was connected to a separation tank and the lower plenum was fitted with a metered water flow to facilitate variation of the superficial liquid velocity, $\langle j_l \rangle$.

A typical pressure pulse is given in Fig. 8 as it appeared at the lower transducer station of Fig. 1. It was noted that the pressure pulses exhibited some attenuation as they passed the upper transducer stations. However, no distortion of pulse shape or steepening of the forward edge was observed.

Pressure pulse speed measurements were made using two independent techniques. The first of these was a time-of-flight method. This technique used a Tektronix 7854 digital oscilloscope with the peak positive pressure chosen as the discrete time feature of each pulse. The second pressure pulse speed measurement technique involved taking the slope of the phase versus frequency plot from the cross power spectral density (CPSD) function between a lower and upper side-mounted transducer set (Bendat, 1971). This slope can be related to the propagation speed of a pulse by noting that (Kosaly et al., 1981)

$$\delta\underline{\psi}(z, t) = \delta\underline{\psi}\left(t - \frac{z}{v}\right) \tag{23}$$

If we Fourier transform equation (23) to the frequency domain

$$\delta\underline{\psi}(\omega, z) = e^{i\left[\frac{\omega z}{v} + \theta\right]} |\delta\underline{\psi}(\omega)| \tag{24}$$

where θ is the phase angle of the frequency component ω. The CPSD may be written as

$$\begin{aligned} \text{CSPD}(\omega) &= \delta\underline{\psi}(\omega, z_1)\delta\underline{\psi}^*(\omega, z_2) \\ &= e^{-\frac{\omega}{v}(z_2 - z_1)} |\delta\underline{\psi}(\omega)|^2, \quad z_1 \le z_2 \end{aligned} \tag{25}$$

This indicates that the phase of the CPSD of a propagation perturbation is locally linear with frequency; thus the slope of the CPSD phase angle versus frequency plot yields

$$\text{Slope} = \frac{(z_2 - z_1)}{v} = \frac{d\theta}{d\omega}$$

In our case, $v = c_{2\phi}$, $z_2 = z_{\text{lower}}$ and $z_1 = z_{\text{upper}}$; thus we have

$$c_{2\phi} = [(z_{\text{lower}} - z_{\text{upper}})360 \text{ deg}]\left(\frac{d\theta}{df}\right)^{-1} \tag{26}$$

The CPSDs were calculated using a Hewlett-Packard 3562A dynamic signal analyzer. This technique proved a useful independent verification that the time-of-flight method accurately indicated the propagation speed.

The pressure pulse propagation data taken in this study are presented in Fig. 9.

Discussion of Results

The standing wave dispersion data given in Fig. 2 clearly show the strong dependence of the propagation speed of pressure perturbations on bubble radius. This effect is due to the dependence of the propagation speed on the interfacial heat transfer between the two phases. The larger bubbles have less interfacial area available for heat transfer and thus exhibit a more nearly adiabatic process, and thus a greater celerity. It can also be noted that celerity increases with frequency. Indeed, more time exists for heat transfer at the lower frequencies, thus promoting a more nearly isothermal process and a lower celerity.

The pulse data given in Fig. 9 illustrate the strong dependence in two-phase pulse propagation speed with void fraction in the region of low void fraction. The pulse propagation speed data given here are consistent with, but more tightly controlled than, those of other researchers (e.g., Hall, 1971). Unfortunately, the pulse data still contain too much scatter to discern a clear dependence of the pulse propagation speed on bubble radius, as predicted by the two-fluid model.

Figure 10 gives the values of the virtual volume coefficient C_{VM} that produced agreement between the predictions of the two-fluid model and the data. Uncertainty in the values of C_{VM} are due to two sources, the measurement uncertainty in the values of sound speed, and the uncertainty in the predicted values of sound speed due to uncertainties in the measured flow state used as input to the model. Both contributions were calculated using standard propagation-of-error techniques. Variation in the value of C_{VM} results in a total upward or downward shift of the attenuation or sound speed versus frequency curve. Thus the shape of the curve is primarily due to the heat transfer model, while the position of the curve is governed by the selected value of C_{VM}. Significantly, the agreement between the measured and predicted values is con-

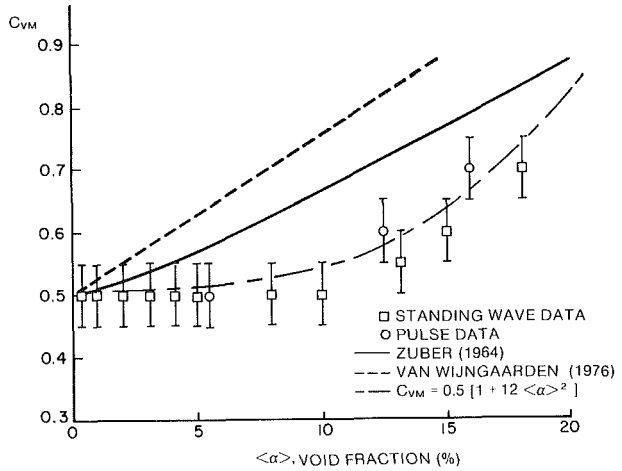

Fig. 10 Virtual mass coefficient versus global void fraction

sistent for all frequencies measured, indicating that the heat transfer model is in good order.

An empirical fit to the predicted values of C_{VM} in Fig. 10 gives

$$C_{VM} = 0.5[1 + 12\langle\alpha\rangle^2] \qquad (\langle\alpha\rangle \leq 20 \text{ percent}) \qquad (25)$$

It is interesting to note that the measured variation of the virtual volume coefficient with void fraction is significantly less than that predicted by the models of Zuber (1964) and Van Wijngaarden (1976). The fact that the value of C_{VM_0} was 0.5 may have caused some of this discrepancy. This choice of C_{VM_0} in equations (1) and (2) is only appropriate for spherical bubbles. Bubbles of radius exceeding 1.5 mm were not spherical in this experiment.

Conclusions

The data presented represent a significant improvement over previous experiments where acoustic pressure propagation in bubbly air/water flows was measured (e.g., Hall, 1971; Silberman, 1957; Carstensen et al., 1947). The precision of the data allows the verification of constitutive laws governing both heat and momentum transfer between the phases. Significantly, an empirical relationship is developed for the virtual volume coefficient C_{VM}, as a function of global void fraction $\langle\alpha\rangle$. This is a valuable relationship in the modeling of flow transients where interfacial momentum transfer effects are important.

References

Bendat, J. S., and Pierson, A. G., 1971, *Random Data: Analysis and Measurements Procedures*, Wiley-Interscience, New York.

Carstensen, E. L., and Foldy, L. L., 1947, "Propagation of Sound Through a Liquid Containing Bubbles," *J. Acoust. Soc. Am.*, Vol. 19, No. 3, pp. 481–501.

Cheng, L-Y., Drew, D. A., and Lahey, R. T., Jr., 1983, "An Analysis of Wave Dispersion, Sonic Velocity, and Critical Flow in Two-Phase Mixtures," NUREG CR/3372, July.

Cheng, L.-Y., Drew, D. A., and Lahey, R. T., Jr., 1985, "An Analysis of Wave Propagation in Bubbly Two-Component Two-Phase Flow," ASME JOURNAL OF HEAT TRANSFER, Vol. 107, pp. 402–408.

Chernyy, I. M., and Srebnyuk, S. M., 1979, "Phase Slip in a Flow of a Gas-Liquid Mixture," *Fluid Mechanics—Soviet Research*, Vol. 8, No. 3, pp. 86–92.

Drew, D., Cheng, L., and Lahey, R. T., Jr., 1979, "The Analysis of Virtual Mass Effects in Two-Phase Flow," *Int. Journal of Multiphase Flow*, Vol. 5, pp. 233–242.

Hall, P., 1971, "The Propagation of Pressure Waves and Critical Flow in Two-Phase Mixtures," Ph.D., Thesis, Heriot-Watt University, Edinburgh, Great Britain.

Henry, R. E., Grolmes, M. A., and Fauske, H. K., 1971, "Pressure Pulse Propagation in Two-Phase One- and Two-Component Mixtures," ANL-7792.

Kosaly, G., Albrecht, R. W., Crowe, R. D., and Dailey, D. J., 1981, "Neutronic Response to Two-Phase Flow in a Nuclear Reactor," SMORN-III, Tokyo, Japan, Oct. 26–30.

Kuo, J. T., 1979, "Interphase Momentum Transfer in the Flow of Bubbles Through Nozzles," EPRI NP-980.

Mokeyev, Yu. G., 1977, "Effect of Particle Concentration on Their Drag and Induced Mass," *Fluid Mech. Soviet Research*, Vol. 6, p. 161.

Ruggles, A. E., 1987, "An Experimental and Analytical Investigation of the Propagation of Pressure Perturbations in Bubbly Air/Water Flows," Ph.D., Thesis, Rensselaer Polytechnic Institute, Troy, NY.

Ruggles, A. E., Drew, D. A., and Lahey, R. T., Jr., 1987, "The Relationship Between Standing Waves, Pressure Pulse Propagation and Critical Flow Rate in Two-Phase Mixtures," *Waves in Multiphase Systems*, ASME Symposium Volume, 24th ASME/AIChE National Heat Transfer Conference, Pittsburgh, PA, Aug.

Silberman, E., 1957, "Sound Velocity and Attention in Bubbly Mixtures Measured in Standing Wave Tubes," *J. Acoust. Soc. Am.*, Vol. 19, pp. 925–933.

Van Wijngaarden, L., 1976, "Hydrodynamic Interaction Between Gas Bubbles in Liquid," *Journal of Fluid Mechanics*, Vol. 77, Part 1, pp. 27–44.

Zuber, N., 1964, "On the Dispersed Two-Phase Flow on the Laminar Flow Regime," *Chemical Engineering Science*, Vol. 19, p. 897.

Rapid, Steady-State Measurement of the Effective Diffusion Coefficient of Gases in Closed-Cell Foams

A. G. Ostrogorsky[1]

L. R. Glicksman

Department of Mechanical Engineering,
Massachusetts Institute of Technology,
Cambridge, MA 02139

A rapid steady-state technique was developed to measure the effective permeability and diffusion coefficients of closed-cell foam insulation. To test the new technique, N_2 data were first obtained by the long-term steady-state technique, and then reproduced ten times faster by the rapid steady-state technique. By using the new technique, reference values of effective diffusion coefficients of N_2, O_2, and Fluorocarbon 11 in closed-cell polyurethane foams were obtained at different temperatures. Data for Fluorocarbon 11 were obtained 30 times faster than data could be obtained by long-term steady-state tests.

To estimate when steady-state has been achieved, the transient diffusion equation was solved, and the solution was given in the form of a chart. The time needed to achieve steady-state mass flux in a foam sample was found to depend strongly on the ratio of the partial pressures imposed on the surface of a tested sample. By use of the solution, the value of the foam effective diffusion coefficient can be obtained before steady-state conditions are achieved within the sample.

Introduction

Buildings and appliances are frequently insulated with closed-cell foams made of polymers such as polyurethane. Closed-cell foams have the lowest conductivity of any insulation material currently available, other than vacuum insulation systems.

Heat is transferred through closed-cell foam insulation by conduction through the solid polymer making up the cell structure, conduction through the gas within the cells, and by thermal radiation (Schuetz and Glicksman, 1984). Because of the small cell size, there is no convective heat transfer. At least 50 percent of the total heat is transferred by conduction through the gas, so it is advantageous to have a low-conductivity gas inside of the foam, for example Fluorocarbon (R11). The total conductivity of new closed-cell polyurethane foam is only 2/3 of the conductivity of stagnant air. It is 1/2 the conductivity of glass fiber insulation, allowing buildings with conventional construction practices to approach superinsulation values.

The increase of foam conductivity with age occurs as air components diffuse into the foam while Fluorocarbon vapor diffuses out. This effect is known as the aging effect. Air components diffuse much faster than Fluorocarbon vapor, so that the aging process can be divided into two stages: the diffusion of the air components, which last typically 1 year for a 2.5-cm-thick unfaced sample, and diffusion of Fluorocarbon 11, which lasts approximately 20 times longer.

The diffusion of the air components into the foam increases the foam conductivity by about 60 percent. The diffusion of the Fluorocarbon 11 out of the foam increases the conductivity of the foam by another 50 percent of the initial value.

To quantify the aging rate of closed-cell foam, a test called the accelerated aging test is presently performed by industry (Federal Register, 1979). A fresh foam sample is kept for 90 to 180 days at 60°C (140°F). This temperature increases the rate of the diffusion process, although the exact increase for different gas components is not well known. The overall foam thermal conductivity is measured before and after the accelerated aging. Foams having a smaller increase in the thermal conductivity in this test are assumed to age more slowly over their entire life. The accelerated aging test quantifies the foam resistance to aging, and therefore enables industry to distinguish foams with good and bad aging properties. Still it has several major disadvantages:

- it does not give any insight into the physics of the aging process;
- it is unclear whether the foams have reached their ultimate age values at the end of the accelerated aging test;
- the increase of the diffusion rate with temperature is different for N_2, O_2, CO_2, and R11. Consequently, it is difficult to relate the aging that occurred during the accelerated test to the aging that would occur in different operating conditions. Accelerated aging is done at isothermal conditions; in actual practice, foams are subjected to temperature gradients;
- during accelerated aging tests the composition and the conductivity of the gas mixture inside the foam is not known. Therefore it is impossible to extrapolate the results of an accelerated aging test if the foam has not completely aged;
- the test is too lengthy to enable fast feed-back between production conditions and quality of the foam.

Because of the above deficiencies of the accelerated aging tests, industry at present is not able to determine and guarantee the properties of closed-cell foams over their lifetime.

If the effective diffusion coefficients of Fluorocarbon 11 and air components are determined, they can be used in the transient diffusion equation to predict the change of the gas composition with time in foams. The gas composition can be related to the effective conductivity of the foam. The effective foam diffusion coefficient can be measured, or it can be modeled based on knowledge of the foam geometry and permeability of the solid polymer cell walls (Ostrogorsky et al., 1986).

The diffusion of gas molecules in a closed-cell foam is characterized by conduction (permeation) and storage of gas molecules. The ratio of these two transport properties defines the third transport property, the foam effective diffusion coefficient

[1] Presently at Mechanical Engineering Department, Columbia University, 220 Mudd Building, New York, NY 10027.

Contributed by the Heat Transfer Division and presented at the ASME Winter Annual Meeting, New Orleans, LA, December 1984. Manuscript received by the Heat Transfer Division May 9, 1986. Keywords: Instrumentation, Mass Transfer, Thermophysical Properties.

Table1 Published data on the foam effective diffusion coefficient at room temperature

DENSITY kg/m^3	D_{02} 10^{-8}[cm^2/s]	D_{N2} 10^{-8}[cm^2/s]	D_{R11} 10^{-8}[cm^2/s]	Reference	Test Technique*
33.5	200.0	100.0	3.0	Ball (1970)	5
35.2	11.2	6.3	0.225	Norton (1967)	2
28.5	4.85	1.05	0.013	Brandreth (1980)	1
35.2	-	-	0.042	Norton (1982)	4
24.5(MDI)	196.2	-	-	Lee (1983)	3
25.6(TDI)	147.6	-	-	Lee (1983)	3
20.7(TDI)	76.8	-	-	Reitz (1983)	3
28.3(MDI)	119.0	-	-	Reitz (1983)	3
30.4(MDI)	193.0	-	-	Reitz (1983)	3
24.9(TDI)	123.3	-	-	Booth (1985)	3
31.8(MDI)	132.0	-	-	Booth (1985)	3
29.2(MDI)	118.5	-	-	Booth (1985)	3
25.2(MDI)	46.8	7.6	.22 to .57	Present work	6

* Test Technique:

1 Stored plugs of foam for various times and measured transient change of gas composition by gas chromatography

2 Measured effusion from the plugs by mass spectrometry

3 Permeability coefficient was measured

4 Film data and a model

5 Thermal conductivity was measured

6 Permeability coefficient was measured by rapid steady-state technique.

$$D_{\text{eff}} = Pe_{\text{eff}}/S_{\text{eff}} \tag{1}$$

where the effective capacity of the foam to store gas molecules per unit of foam volume and unit of gas partial pressure can be referred to as the effective solubility coefficient S_{eff}. The effective foam permeability coefficient Pe_{eff} is defined through the relationship

$$J_{m,\,ss} = Pe_{\text{eff}}(p_2 - p_1)/L \tag{2}$$

where p_2 and p_1 are the partial pressure of the gas imposed on the surfaces of a foam slab having thickness L.

Measurements of mass transport properties are carried out by two basic methods (*Encylopedia of Polymer Science and Technology*, 1968): transmission methods and sorption-desorption methods. In the sorption-desorption methods the solubility coefficient is usually obtained from the equilibrium sorption value. For example, the change of weight of the sample is often measured. The transient sorption or desorption rate gives the diffusion coefficient.

In the transmission methods a partial pressure gradient is applied across the sample. The gradient can be applied with or without a total pressure difference across the sample. The permeation rate can be measured by different methods, such as a volumetric measurement, a pressure measurement, gas chromatography, mass spectroscopy or others (*Encylopedia of Polymer Science and Technology*, 1968). From the permeation rate, the diffusion coefficient can be computed.

By volume, the solid occupies only about 2 percent of the foam. Because of that, the storage of the gases in the solid can be neglected compared to the storage in the cells unless the solubility of the gas in the solid is much higher than in the voids. It has been shown (Norton, 1967) that more than 98 percent of air components is stored in the cells (voids), while it is uncertain how much of the fluorocarbon can be dissolved in the solid. If the solubility of gases in the solid is neglected, the foam capacity to store gases (effective solubility coefficent) can be accurately computed by making use of the ideal gas law (Ostrogorsky et al., 1986). Consequently, one needs to measure only one transport property: the foam permeability coefficient or the foam diffusion coefficient; the third property can be computed from equation (1).

Transient measurements are faster than steady-state measurements, which is an advantage since gas diffusion is a very slow process. Generally, transient methods are considered to be less accurate. For example, it is more difficult to maintain thermal equilibrium during a transient measurement then during a steady-state measurement. Transient methods have several disadvantages when applied to closed-cell foams:

- Since only a relatively thin surface layer of foam takes part in the transient process, it is unclear how well the continuum assumption can be applied to one or two cell layers, and
- the surface of a foam sample is usually damaged by cutting and has many open cells. The open cells change the solid-to-gas ratio inside the surface layer and increase the sorption-desorption area. This area is difficult to determine.

The published data of foam effective diffusion coefficients are given in Table 1. Since diffusion is a very slow process, most of the data were obtained by a transient or indirect measurement. Especially slow is the diffusion of Fluorocarbon 11 and N_2. The large spread of the data obtained by transient or indirect measurement implies that measurement of the diffusion coefficient in closed-cell foams require different, more accurate measuring methods than the methods used up to present.

The steady-state permeability measurement requires a linear partial pressure profile of a specific gas species under test. The time needed to develop the steady-state profile depends on the foam diffusion coefficient.

The data presented later in this paper show that at room temperature the time needed to develop a steady-state partial pressure profile in a 1-cm-thick foam sample is approximately: 10 years for R11, 100 days for N_2, 20 days for O_2, and 5 days for CO_2.

Up to the present very few data of the foam diffusion coefficient have been obtained by permeability measurements because of the long time needed to achieve steady state. Reitz (1983) obtained permeability data for O_2 and CO_2, while Lee

Nomenclature

A = area, cm^2
D = diffusion coefficient, cm^2/s
E = energy of activation, J
Fo = Fourier number
J_m = mass flux, $\text{cm}^3_{\text{STP}}/\text{cm}^2$-s; cm^3_{STP} = mass of gas in 1 cm^3 at standard temperature and pressure
L = thickness, cm
P = partial pressure of gas species, atm
Pe = permeability coefficient, cm^3_{STP}/cm-s-atm
Pe_0 = reference value of Pe, cm^3_{STP}/cm-s-atm
R = gas constant, J/kg-K
S = solubility, $\text{cm}^3_{\text{STP}}/\text{cm}^3$-atm
T = temperature, K
t = time, s

Subscripts

eff = effective
i = initial
ss = steady state
STP = standard temperature and pressure
t = transient
2 = high-pressure side
1 = low-pressure side

Superscripts

* = dimensionless form

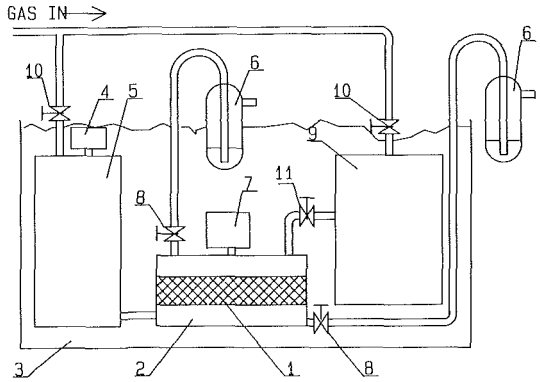

Fig. 1 Schematic diagram of the apparatus for rapid steady-state measurement of the foam effective diffusion coefficient: (1) foam sample; (2) permeability cell; (3) constant temperature bath; (4) pressure transducer; (5) high-pressure tank; (6) oil traps; (7) pressure transducer; (8) valve; (9) low-pressure tank; (10) valves; (11) valve

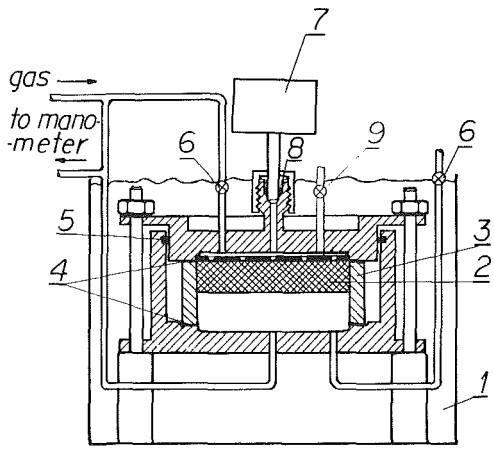

Fig. 2 Apparatus for foam permeability tests: (1) constant temperature bath; (2) foam sample; (3) stainless-steel ring; (4) indium gaskets; (5) O ring; (6) valves; (7) pressure transducer; (8) indium O ring; (9) valve

et al. (1983) and Booth et al. (1985) obtained data for O_2, as shown in Table 1. The foam permeability data are converted to diffusion coefficients by assuming gas is only stored in the cell voids and a negligible amount is dissolved in the solid. For the slowly diffusing gases, R11 and N_2, foam permeability data have not been published up to the present. However, the diffusion of R11 and N_2 has a major effect on the foam aging since concentration of the O_2 and CO_2 in the foam cells is low. The scatter in the data is due in part to the tests on different density foams; the primary cause of the scatter is experimental uncertainties.

In the present research, the steady-state permeation rate was selected as the most accurate method to measure the foam effective diffusion coefficient. To speed up the data-taking process, an innovative method to develop the steady-state profile inside foam samples rapidly was developed. The method enables faster development of the steady-state partial pressure profile by one to two orders of magnitude compared to the presently used steady-state methods.

To avoid the error due to transient diffusion during steady-state measurements, one needs to know the time needed to achieve steady state. For heat transfer steady-state measurements, Shirtliffe (1973) has analyzed the needed settling time. He computed and plotted the error due to neglect of the remaining transient effect.

In the present research, we have related the transient mass flux to the diffusion coefficient without introducing an error by using the analytical solution of the transient transfer process. The analytical solution contains an infinite series while the diffusion coefficient is given implicitly.

Since a transient measurement is less accurate than a steady-state measurement, all data reported in the present research were obtained by measurement of the steady-state flux, while the transient solution was used to estimate the effective diffusion coefficient and check whether steady state was achieved.

Apparatus for Rapid Steady-State Measurement of Foam Effective Diffusivity

The diffusion coefficients of gases in closed-cell polyurethane foams are strongly temperature dependent. The foam permeability coefficient was found to follow an Arrhenius-type equation (Reitz, 1984; Ostrogorsky and Glicksman, 1986)

$$Pe_{\text{eff}} = Pe_0 \exp(-E/RT) \tag{3}$$

where Pe_0 is a reference value of Pe, R is the gas constant, T is the temperature, and E is the energy of activation. The effective solubility has an inverse linear temperature dependence, which comes from the ideal gas law (Ostrogorsky et al., 1986)

$$S_{\text{eff}} = T_{\text{STP}}/T \quad [\text{cm}^3_{\text{STP}}/\text{cm}^3 - \text{atm}] \tag{4}$$

where T_{STP} is the standard temperature, 298 K. By combining equations (1) and (4) one obtains

$$D_{\text{eff}} = Pe_{\text{eff}}(T/T_{\text{STP}}) \tag{5}$$

When the temperature increases by 50°C, from 25 to 75°C, the diffusion coefficient of the air components, measured in the present study, increases by a factor of approximately 6, 8, and 10 for CO_2, O_2, and N_2, respectively. The present technique makes use of the increase of the diffusion coefficient with temperature to shorten the time to achieve steady-state conditions. The sample is maintained at high temperature until a linear concentration distribution is established across the sample. The temperature is then lowered to the test condition while maintaining the same concentration gradient.

The experimental apparatus, which makes use of the high value of the diffusion coefficient at elevated temperatures, is shown in Fig. 1. The main part of the rapid steady-state apparatus consists of the foam permeability cell, Fig. 2, used in the long-term steady-state permeability measurements (Ostrogorsky et al., 1986).

The permeation rate is determined by measuring the pressure increase in the low-pressure (upper) plenum of the permeability cell. The pressure increase was measured by a Validyne AP10 absolute pressure transducer and a Validyne DP15 differential pressure transducer. Validyne DP15, used in the long-term steady-state measurements, was found to be sensitive to barometric pressure changes and was replaced by the Validyne AP10 during the rapid steady-state measurements. The AP10 transducer features all-welded construction and very low internal volume (65 mm^3). The pressure range of the transducer is 140,000 Pa. The volume change in the upper plenum due to diaphragm movement is only 3.6×10^{-3} mm^3. At room temperature and steady-state conditions, only 1 h is needed to obtain a pressure increase of N_2 at 25°C, sufficient to measure accurately the slope of the pressure increase (20 min are needed at 50°C).

The volumetric inflow was related to the pressure increase in the upper plenum by the following calibration procedure: The gas supply tube line is removed, and valve 9 (in Fig. 2) is replaced by a high precision bore, 0.5 mm i.d. capillary tube. A slug of isobutyl methyl ketone is next forced into the capillary tube by means of a hypodermic needle. As the slug length is increased up to 20 cm the pressure change in the

plenum is recorded. The slug volume is equal to the volume inflow into the plenum. Small corrections are needed to account for the volume of the capillary tube, which is typically equal to several percent of the volume of the upper plenum.

The whole apparatus shown in Fig. 1 was made out of materials used in high vacuum applications, having very low vapor pressure and diffusion coefficients much lower than the foam D_{eff}. The foam sample, 75 mm in diameter, usually 10 mm thick, was fixed to a stainless steel mounting ring by DER 331 epoxy (Allied Resin Corporation), which has very low vapor pressure. The mounting ring was sealed to the permeability cell with indium gaskets. The connecting tubes were welded to the cell from the gas side, to eliminate the surface that can trap gas and to aid in cell cleaning.

To reduce the contamination of the surface in contact with gases, the parts of the permeability cell in contact with the gas were rinsed with trichloroethylene, acetone, and ethyl alcohol; cleaned ultrasonically; and dried in an oven at about 100°C.

To detect possible leakage paths, and ensure that the outgassing is much smaller than the measured permeation rate, an impermeable stainless steel plate was used in the cell instead of the sample. Special care was devoted to ensure that no open paths (pores) exist in the foam sample and the epoxy used to fix the sample to the stainless steel mounting ring. Pores large compared to the mean free path of air molecules are easy to detect: pressure difference imposed across the sample causes, without a time lag, a bulk flow several orders of magnitude higher than the permeation rates. Diffusion through pores having diameters smaller than the mean free path of air molecules, known as Knudsen diffusion, is much more difficult to detect. When pores smaller than the mean free path of air molecules are present, permeability of the foam is weakly dependent on both temperature and the test gas (i.e., N_2, O_2, and CO_2 permeate with approximately the same rate and do not follow the Arrhenius relation). Therefore, the presence of the "small" pores can be detected only after a sample has been tested with different gasses and/or at different temperatures (Ostrogorsky et al., 1986; Fox, 1986).

The gas volume on the low-pressure side was minimized to reduce the influence of temperature. To ensure thermal equilibrium, the cell was submerged in a constant temperature bath. The temperature of the water bath was controlled to within ± 0.03°C while the temperature in the room was controlled within ± 0.1°C.

Several additional components were added to the initial design of the permeability apparatus to enable rapid development of the partial pressure steady state profile. The high and the low-pressure sides of the permeability cell were connected to tanks having very large volumes (1000 cm^3) compared to the volume of the gas that permeates through the foam sample during the tests (several mm^3).

Measuring Method

A partial pressure difference of one gas species, typically 1 atm, is imposed on the boundaries of the foam sample being tested.[2] The sample is flushed under a pressure difference and elevated temperature to develop a linear steady-state partial pressure profile inside the sample.[3] At the same time, the other gases that might be present in the foam cells due to previous tests or aging are eliminated from the sample and the apparatus. During flushing, the metering valve 11 allows a very low flow rate. To estimate the time needed to eliminate the other gases by flushing one should assume constant initial partial pressure inside the foam. By flushing, zero partial pressure is imposed on both boundaries. Then because of the analogy between the mass and heat transfer, the outgassing time can be estimated from charts developed for transient heat conduction in solids (Heisler charts, Carslaw and Jaeger, 1959).

When the linear steady-state profile is established and the other gases are eliminated, valves 8 and 10, shown on Fig. 1, are closed. By closing valves 8 and 10, the foam sample is isolated from the barometric pressure variations in the environment and from the pressure variations in the gas supply due to the regulators. The permeability cell is connected to the low-pressure tank (i.e., valve 11 is opened). Note that in the tanks, partial pressure is equal to the total pressure since only one gas species is present. In the foam cells, in addition to the air components, fluorocarbon vapor is usually present. Fluorocarbon diffuses much more slowly than the air components and therefore does not introduce a significant error in the measurement.

The temperature of the bath is changed (reduced) to the temperature at which the measurement at Pe_{eff} is to be conducted. Before the measurement, complete thermal equilibrium has to be achieved. Measurements of the pressure change in the upper plenum indicate that thermal equilbrium in the apparatus is achieved within an hour.

According to the ideal gas law, the partial pressure inside the closed-foam cells will change with the change of temperature. Simultaneously, the partial pressure inside the closed tanks will also change, governed by the ideal gas law. For the same temperature change the partial pressure in the tanks will match the partial pressure of the gas in the surface cells of the foam. Therefore, the continuity of the partial pressure is preserved across the foam surface.

During the thermal transient, very low temperature gradients can be expected across the foam sample, causing small deviations from a linear partial pressure profile. These deviations will not permanently alter the developed linear partial pressure profile since the deviations are at least two orders of magnitude smaller than the imposed partial pressure difference. In addition the thermal diffusivity of the foams is four to six orders of magnitude larger than the diffusivity for mass transfer so that thermal equilibrium can be quickly established before the mass transfer is measured at the new temperature level.

The thermal conductivity of the solid polymer is much higher than the thermal conductivity of the gas within the closed cells. Therefore, even if substantial temperature gradients were imposed across the foam sample, the temperature difference across cell walls typically 0.5 μm thick would be negligible. Because of that, mass transfer due to temperature gradients (Soret diffusion) would not influence the foam aging during operation.

To measure the volumetric flow rate through the foam sample, the plenum is isolated from the reservoir by closing valve 11 (Fig. 1). The plenum has a very small volume (5 cm^3) so that the pressure increase in the low-pressure plenum due to the volumetric inflow through the foam sample can be measured and related to the permeability and diffusion coefficients (equations (2) and (1)).

The temperature is changed to another level with the low-pressure plenum connected to the reservoir (valve 11 in Fig. 1 is open). Again, in the present design of the permeability cell, the linearity of the steady-state concentration profile will not be perturbed by the temperature change and data can be taken as soon as thermal equilibrium is achieved.

[2] In Ostrogorsky et al.(1986) and Ostrogorsky and Glicksman (1986) we have shown experimentally that the mass flux through a polyurethane foam sample is proportional to the applied partial pressure difference. Consequently, Pe_{eff} is independent applied partial pressure difference.

[3] At 75°C the N_2 linear steady-state profile is established approximately ten times faster than at room temperature (25°C), while at 125°C, it is established 100 times faster than at room temperature.

Prediction of the Time Needed to Achieve Steady State by Transient Measurement of the Foam Diffusion Coefficient

To perform an accurate measurement, steady-state mass transfer must be achieved before the data are taken or the temperature level changes. The time needed to develop a steady-state partial pressure profile can be found from the solution to the partial differential equation, which describes the transient diffusion inside a foam slab.

The foam samples have the shape of a right cylinder with a height much smaller than the diameter. The ends of the cylinder are exposed to constate partial pressures p_1 and p_2, respectively; the side of the cylinder is impermeable. Therefore the sample can be modeled as an infinite slab (Fig. 3).

We first wish to find the unsteady partial pressure in the sample when the initial partial pressure inside the foam sample is taken to be constant or equal to zero. The transient diffusion of each gas species can be considered independent of the other species in the foam. At $t>0$, constant, unequal partial pressures are imposed on the two boundaries. The formulation of the problem in terms of partial pressures relative to the initial partial pressure is

$$\partial p/\partial t = D_{\text{eff}}\partial^2 p/\partial x^2 = (Pe_{\text{eff}}/S_{\text{eff}})\partial^2 p/\partial x^2 \tag{6}$$

$$p(x, 0)=0, \quad p(0, t)=p_1, \quad p(L, t)=p_2$$

From the solution to equation (6), the transient partial pressure is equal to (Carslaw and Jaeger, 1959)

$$p(x, t)=p_1+(p_2-p_1)x/L+2/\pi\sum_{n=1}^{\infty}[(p_2\cos(n\pi)-p_1)/n]$$
$$\sin(n\pi x/L)\exp(-n^2\pi^2 D_{\text{eff}}t/L^2) \tag{7}$$

The measured mass flux (transient or steady state) is equal to

$$J_{m,tr}=Pe_{\text{eff}}[\partial p_i/\partial x]_{x=0} \tag{8}$$

where $[\partial p_i/\partial x]_{x=0}$ is the transient slope of the partial pressure at the low-pressure side of the foam surface. If steady state has not been achieved, this slope will not be equal to the linear steady-state slope and equation (2) gives an erroneous permeability coefficient.

The measured flux at $x=0$ can be obtained by combining equations (7), (1), and (8) to obtain

$$J_{m,tr}=(Pe_{\text{eff}}/L)\{(p_2-p_1)+2\sum_{n=1}^{\infty}(p_2\cos(n\pi)-p_1)$$
$$\exp[-n^2\pi^2 Pe_{\text{eff}}t/(S_{\text{eff}}L^2)]\} \tag{9}$$

We wish to find the unknown permeability Pe_{eff} by measuring $J_{m,tr}$ at $x=0$. The known (measured) quantities in equation (9) are: transient flux, time, solubility S_{eff}, thickness L, and partial pressures p_1 and p_2. These six known quantities and the unknown permeability coefficient Pe can be rearranged in the three nondimensional groups

$$p^*=p_1/p_2 \tag{10}$$

$$\text{Fo}=D_{\text{eff}}t/L^2=Pe_{\text{eff}}t/(S_{\text{eff}}L^2) \tag{11}$$

and $J_{m,ss}$, defined by the equation (2).

Note that both Fo and $J_{m,ss}$ contain the permeability coefficient and therefore can not be computed ($J_{m,ss}$ cannot be measured since steady state has not been established at the time of the measurement). By dividing $J_{m,ss}$ by Fo, we obtain the nondimensional group where all the quantities are known

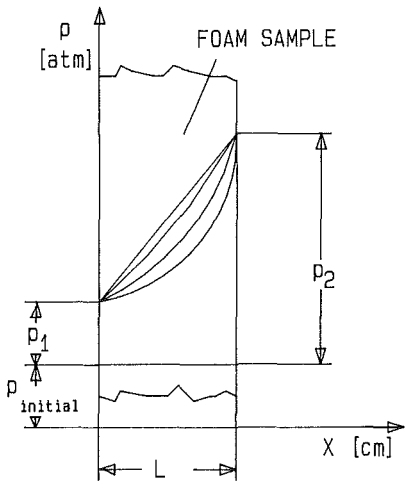

Fig. 3 Initial and boundary conditions imposed on a foam sample during permeability tests

$$(J_{m,ss}/\text{Fo})=S_{\text{eff}}(L/t)(p_2-p_1) \tag{12}$$

$(J_{m,ss}/\text{Fo})$ is used to nondimensionalize the transient flux as

$$J^*_{m,\text{Fo}}=J_{m,tr}/(J_{m,ss}/\text{Fo}) \tag{13}$$

or, by substituting equations (9) and (12) into (13)

$$J^*_{m,\text{Fo}}=\text{Fo}\left[1+2\sum_{n=1}^{\infty}(\cos(n\pi)-p^*)\exp(-n^2\pi^2\text{Fo})/(1-p^*)\right] \tag{14}$$

where only Fo contains the unknown transport coefficient Pe_{eff} (or D_{eff}).

Equation (14) relates Fo to p^* and $J^*_{m,\text{Fo}}$ implicitly. $J_{m,\text{Fo}}{}^*$ is plotted in Fig. 4 against Fo with p^* as parameter.

To use the chart in Fig. 4, $J_{m,tr}$, t, p_1, p_2, and L, are measured and the solubility S_{eff} is computed from equation (4). Next, $p^*=p_1/p_2$, $J_{m,ss}/\text{Fo}$ is found from equation (12) and $J^*_{m,\text{Fo}}$ from equation (13). Fo is obtained from Fig. 4. Finally, the permeability and the diffusion coefficient can be computed

$$Pe_{\text{eff}}=\text{Fo}S_{\text{eff}}\text{L}^2/t \tag{15}$$

$$D_{\text{eff}}=\text{Fo}L^2/t \tag{16}$$

The results shown on Fig. 4 permit permeability measurements to be made before steady state has been achieved.

The linear steady-state partial profile is achieved when $J^*_{m,\text{Fo}}$ is equal to Fo (equation (14)). Note that the steady-state condition requires not only a linear partial pressure gradient of the test gas but also elimination of other gases that might be present due to previous tests or aging. Since fluorocarbon has such a low diffusion rate, it will not contribute significant errors to the tests of other gases.

Results and Discussion

The measured values of the effective permeability coefficients of CO_2, O_2, N_2, and R11 obtained at different temperatures are shown in Fig. 5 and Table 2. The values of the effective diffusion coefficient are also given in Table 2. For air components, each data point plotted represents at least three separate measurements. The error in the cell calibration is estimated to be 10 percent. Measurement of the sample thickness, and measurement of the imposed partial pressure difference, account each for another 5 percent error in the ab-

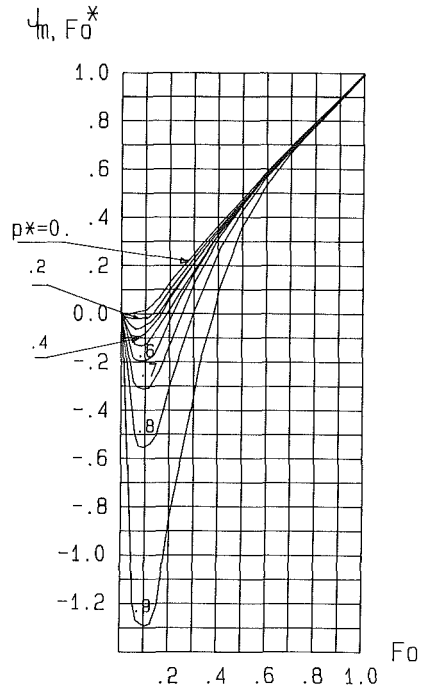

Fig. 4 Chart for transient measurement of the foam diffusion coefficient and time needed to achieve steady state ($J^*_{m,Fo}$ is defined by equation (14), $p^* = p_1/p_2$; $Fo = D_{eff}t/L^2$)

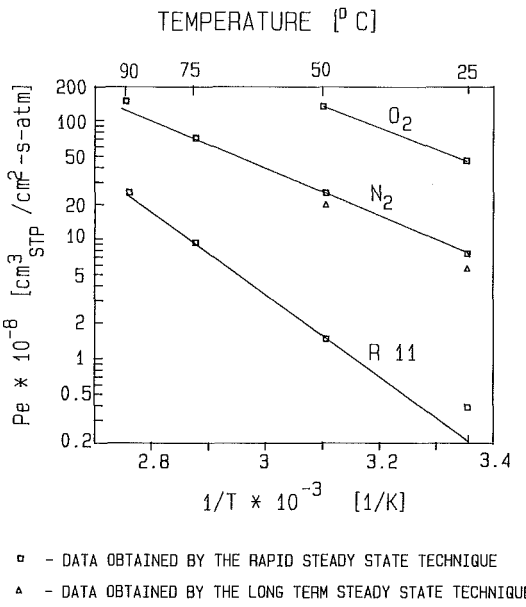

Fig. 5 Permeability coefficient as a function of temperature obtained by rapid and by long-term steady-state technique

solute value of Pe_{eff}. The reproducibility of the data depends on the permeation rate of the tested gas. With the present cell design we are able to reproduce the permeability coefficient of N_2 within ±2 percent or better.

When the rapid steady-state technique was not used, about 120 days were needed to obtain a steady-state linear profile with N_2 at 25°C, while about 40 days are needed at 50°C. The measurement of Pe_{eff} was next repeated with the rapid steady-state method. Steady-state was obtained in 13 days at 75°C. After that the temperature was changed within several hours to 50, 25, and 90°C, respectively, and Pe_{eff} was measured at each temperature level. Note that the data obtained with the

Table 2 Foam permeability and diffusion coefficient measured by the rapid and long-term steady-state technique (polyurethane, MDI type foam sample, density—25.2 kg/m^3)

Permeability Coefficient, $Pe_{eff}=J_{m,ss}L/(P_2-P_1)$, 10^{-8}[cm_{STP}^3/cm-s-atm]:

Temp.	Pe_{CO2}**	Pe_{O2}	Pe_{N2}	Pe_{N2}**	Pe_{R11}
25°C	202.0	46.8	7.6	6.0	0.23 to 0.57*
50°C	488.0	134.0	24.3	19.0	1.6
75°C	-	-	70.8		9.6
90°C			166.0		24.3

Diffusion Coefficient, $D_{eff}=Pe_{eff}(T/298),10^{-8}$[$cm^2$/s]:

Temp.	D_{CO2}**	D_{O2}	D_{N2}	D_{N2}**	D_{R11}
25°C	202.0	46.8	7.6	6.0	0.23 to 0.57
50°C	529.0	145.0	26.3	20.6	1.7
75°C	-	-	82.7		11.2
90°C	-	-	202.0		29.6

*Extrapolation of data at 50°C and 90°C yields the value .20x10^{-8}[cm_{STP}^3/cm-s-atm]

**Measured by the long-term steady-state technique; all other data are obtained by the rapid steady-state technique.

rapid steady-state technique follow the Arrhenius-type temperature dependence and are in good agreement with the data obtained by developing steady-state at room temperature and at 50°C. The 22 percent difference in Pe_{eff} is possibly caused by the use of two different pressure transducers (DP 15 and AP 10), which were calibrated separately.

The rapid steady-state method has enabled data with Fluorocarbon 11 to be obtained. A 1-cm-thick foam sample was kept for 100 days at 90°C, which is equivalent to about 3000 days at room temperature. To obtain accurate data, measurements were repeated at different temperatures for about 30 days. At least eight measurements were made at each temperature level. At 90°C the maximum deviation from the mean was ±9 percent. At 25°C the mean deviation was ±42 percent. The percentage deviation at 25°C is higher because the magnitude of the permeability is much lower than the magnitude at 90°C. The larger deviations between experimental results reflect errors inherent in measurements made at these extremely low permeation rates. Also, if any significant portion of R11 is retained in the solid polymer and subsequently vaporizes when the temperature level is changed it will cause errors in the rapid steady-state results.

Due to the increase in the diffusion coefficient with temperature, the rapid steady-state technique for the polyurethane closed-cell foams is an order of magnitude faster than the long-term steady-state technique. Compared to the accelerated aging tests (thermal conductivity measurements) performed at 140°F, the long-term steady-state permeability tests performed at the same temperature are faster by a factor of 6.3 and 25. The foam sample in the permeability cell is only 1 cm thick, whereas the foam panels used in the accelerated aging tests range from 2.54 to 5.1 cm thick. The characteristic time of diffusion is inversely proportional to the square of the sample thickness.

The highest temperature that foam can be exposed to limits the amount of test acceleration obtained at elevated temperatures. After the foam sample was kept at 90°C for 100

days, exposed to a pressure difference of 60,500 Pa (8.5 psia) of Fluorocarbon 11, its thickness decreased to 1/2 of the initial valve although the cell walls were not damaged. Tests repeated at different times at 90°C did not indicate any increase of permeability with time. Since the number of cell walls, not the distance between them, determines the resistance to permeation, the steady-state results obtained are still valid. However, the effective diffusion coefficient of the foam should be based on the original foam thickness.

The strong dependence between the ratio of the pressures at the two boundaries, p^*, and the time needed to achieve steady-state is shown in Fig. 4. For $p^* = 0$, $J^*_{m,\mathrm{Fo}}$ is never negative, while for $p^* = 0.9$, $J^*_{m,\mathrm{Fo}}$ is negative up to $\mathrm{Fo} = 0.038$. For $p^* = 0.2$, $J^*_{m,\mathrm{Fo}}$ approaches Fo (i.e., steady-state $J^*_{m,\mathrm{Fo}}$) for $\mathrm{Fo} = 0.4$, while $\mathrm{Fo} = 0.7$ is needed for $p^* = 0.9$. This indicates that it is advantageous to have p^* as small as possible during the measurement. As p^* approaches 1, it takes a longer time to approach steady-state, and the mass flux is small and difficult to measure.

Conclusions

An innovative experimental technique that enables rapid achievement of steady-state conditions in closed-cell foam samples was developed. By using this technique, the permeability of closed cell polyurethane foam can be measured 10–30 times faster than with presently used techniques. The amount of test acceleration is limited by the highest temperature that the foam can tolerate.

By using the rapid steady-state technique, permeability and diffusivity data were obtained for O_2, N_2, and Fluorocarbon 11 at different temperatures. The relatively low reproducibility of the Fluorocarbon 11 data is believed to be caused by the limitations of the equipment rather than by theoretical limitations of the technique.

The N_2 data obtained by the rapid steady-state technique were compared to the N_2 data at 25 and 50°C obtained by the long-term steady-state technique. Reasonable agreement was observed.

The analytical solution of the transient diffusion that occurs in foam samples during permeability tests was developed and plotted in the form of a convenient chart. From this chart, the foam effective permeability and diffusion coefficient can be obtained from the measurement of the transient mass flux, i.e., before steady-state is reached. From the same chart, the time needed to achieve steady-state can be determined both at high temperatures when the rapid steady-state technique is used to develop the steady-state profile, or at room temperature when the long-term steady-state technique is used.

References

Ball, G. W., Hurd, R., and Walker, M. G., 1970, "The Thermal Conductivity of Rigid Urethane Foams," *Journal of Cellular Plastics*, Vol. 6, pp. 66–76.

Booth, L. D., 1986, The Dow Chemical Company, Personal Communication.

Booth, L. D., and Lee, W. M., 1985, "Effects of Polymer Structure on K-Factor Aging of Polyurethane Foam," *Journal of Cellular Plastics*, Vol. 21, pp. 26–30.

Brandreth, D. A., and Ingersole, H. G., 1980, "Accelerated Aging of Rigid Polyurethane Foam," *Journal of Cellular Plastics*, Vol. 16, pp. 235–238.

Carslaw, H. S., and Jaeger, J. C., 1959, *Conduction of Heat in Solids*, 2nd ed., Oxford University Press, pp. 99–100.

Encyclopedia of Polymer Science and Technology, 1968, Vol. 9, Wiley, New York, pp. 794–807.

Federal Register, 1979, Part III, Vol. 44, No. 167, Aug. 27, pp. 50218–50245.

Fox, T. J., 1986, "Aging in Closed-Cell Phenolic Foam," S. M. Thesis, Department of Mechanical Engineering, Massachusetts Institute of Technology, Cambridge, MA.

Lee, W. M., and Brown, C. N., 1983, "Gas Permeability Determination in Urethane Foams," *Journal of Thermal Insulation*, Vol. 6, pp. 285–289.

Norton, F. J., 1967, "Thermal Conductivity and Life Polymer Foams," *Journal of Cellular Plastics*, Vol. 3, pp. 23–36.

Norton, F. J., 1982, "Diffusion of Chlorofluorocarbon Gases in Polymer Films and Foams," *Journal of Plastics*, Vol. 18, pp. 300–318.

Ostrogorsky, A. G., and Glicksman, L. R., 1986, "Aging of Polyurethane Foams: the Influence of Gas Diffusion on Thermal Conductivity," ORNL/SUB/84-9009/2.

Ostrogorsky, A. G., Glicksman, L. R., and Reitz, D., 1986, "Aging of Polyurethane Foams," *International Journal of Heat and Mass Transfer*, Vol. 29, pp. 1169–1175.

Reitz, D. W., 1983, "A Basic Study of Gas Diffusion in Foam Insulation," S. M. Thesis, Department of Mechanical Engineering, Massachusetts Institute of Technology, Cambridge, MA.

Schuetz, M. A., and Glicksman, L. R., 1984, "Basic Study of Heat Transfer Through Foam Insulation," *Journal of Cellular Plastics*, Vol. 20, pp. 114–121.

Shirtliffe, C. J., 1973, "Establishing Steady-State Thermal Conditions in Flat Slab Specimens," ASTM Special Technical Publication, No. 544, pp. 13–33.

Journal of Heat Transfer

Technical Notes

This section contains shorter technical papers. These shorter papers will be subjected to the same review process as that for full papers.

A Note on Prandtl's Transposition Theorem

L. S. Yao[1]

1 Introduction

Given a solution of the boundary-layer equations for a two-dimensional, steady incompressible flow, Prandtl (1938) showed that additional solutions can be derived by a simple transformation. This is the well-known *Prandtl's transposition theorem*. The gist of the theorem is that the flow is displaced by the amount of the vertical displacement of an irregular solid surface, and the vertical component of the velocity is adjusted according to the slope of the surface (see equation (1)). The form of the boundary-layer equations is invariant under the transformation, and the surface conditions can therefore be applied on a transformed *flat* surface. This allows the boundary conditions to be easily incorporated into any numerical method. Due to its universality, simplicity, and immediate applicability to problems, Prandtl's theorem is still frequently applied today, almost fifty years after it was first introduced.

Glauert (1957) extended the theorem to unsteady and three-dimensional boundary layers. He also explicitly pointed out that it allows the normal displacement of the solid surface to be, at most, the order of the boundary-layer thickness, say $0(\epsilon)$. Only for such a small displacement can the boundary-layer solution for the surface be obtained by adopting the original inviscid-flow solution. By a comparison of various viscous terms and by restricting them to be no larger than $0(\epsilon)$, Glauert concluded that the typical distance for a change of the solid geometry along the flow direction must be larger than $0(\epsilon^{1/2})$, a distance intermediate between the length of the body and the thickness of the boundary layer. In other words, $\Delta_x \le 0(\epsilon^{1/2})$ and $\Delta_{xx} \le 0(1)$, where $y=\Delta(x)$ denotes the irregular solid surface (see Fig. 1), and the subscript x denotes derivatives.

In section 2, Prandtl's theorem is rederived for a *finite* solid-surface displacement Δ. Even though the derivation extends the theorem out of the context originally intended by Prandtl, it is indeed more convenient to solve the resulting equations numerically in the transformed coordinates (Yao, 1980, 1983). Furthermore, if Δ is small, Prandtl's theorem represents the leading-order solution of the extended theorem, which is shared by a class of geometries. The details of the individual geometries are needed only for the higher-order solutions.

Since Prandtl's coordinates are not orthogonal in physical space, the derivation shows that the normal pressure gradient, which is small and can be neglected across the boundary layer, has a leading-order effect in the axial momentum equation expressed in Prandtl's coordinates. This explains why the *correct* form of the boundary-layer equations in Prandtl's coordinates can only be derived from the Navier-Stokes equations, as demonstrated in this note, and cannot be obtained by the transformation of the boundary-layer equations in other coordinates as has been commonly done in the past.

2 Derivation

A two-dimensional flow model, shown in Fig. 1, is used to extend Prandtl's transposition theorem. Its further extension to three-dimensional flows is straightforward. The Navier-Stokes and energy equations in Prandtl's coordinates are

$$u_x + v_y = 0$$

$$uu_x + vu_y = -p_x + \Delta_x p_y + \theta + \epsilon^2[u_{xx} + (1+\Delta_x^2)u_{yy} - 2\Delta_x u_{xy} - \Delta_{xx}u_y]$$

$$uv_x + vv_y + \Delta_{xx}u^2 = \Delta_x p_x - (1+\Delta_x^2)p_y - \Delta_x^\theta + \epsilon^2[v_{xx} + (1+\Delta_x^2)v_{yy} - 2\Delta_x v_{xy} - \Delta_{xx}v_y + \Delta_{xxx}u + 2\Delta_{xx}u_x - 2\Delta_x\Delta_{xx}u_y]$$

$$u\theta_x + v\theta_y = \frac{\epsilon^2}{\mathrm{Pr}}[\theta_{xx} + (1+\Delta_x^2)\theta_{yy} - 2\Delta_x\theta_{xy} - \Delta_{xx}\theta_y] \qquad (1)$$

where the dimensionless variables are defined as

$$\begin{aligned} x &= (\bar{x}+L)/L,\ y=(\bar{y}-\bar{\Delta})/L \ \text{(coordinates)} \\ u &= \bar{u}/U_\infty,\ v=(\bar{v}-\Delta_x\bar{u})/U_\infty \ \text{(velocities)} \\ p &= (\bar{p}-\bar{p}_\infty)/\rho U_\infty^2 \ \text{(pressure)} \\ \theta &= (T-T_\infty)/(T_w-T_\infty) \ \text{(temperature)} \\ \epsilon^{-2} &= \mathrm{Re}=U_\infty L/\nu \ \text{(for a forced flow)} \\ \epsilon^{-4} &= \mathrm{Gr}=\beta g(T_w-T_\infty)L^3/\nu^2 \ \text{(for natural convection)} \\ \Delta &= \bar{\Delta}/L \end{aligned} \qquad (2)$$

L is the distance from the leading edge of the body, and the subscript denotes partial differentiation. The gravitational acceleration is denoted by g, the thermal conductivity is k, the Prandtl number is $\mathrm{Pr}=\nu/\alpha$, the thermal diffusivity is α, the kinematic viscosity is ν, the density is ρ, and the thermal expansion coefficient is β. For a forced flow, U_∞ is the characteristic velocity. For a natural-convection boundary layer, $U_\infty = \mathrm{Gr}^{1/2}\nu/L$. The buoyancy forces are represented by θ in equation (1), and should be set to zero for an isothermal flow.

[1]Department of Mechanical and Aerospace Engineering, Arizona State University, Tempe, AZ 85287.

Contributed by the Heat Transfer Division for publication in the JOURNAL OF HEAT TRANSFER. Manuscript received by the Heat Transfer Division March 19, 1987. Keywords: Forced Convection, Modeling and Scaling.

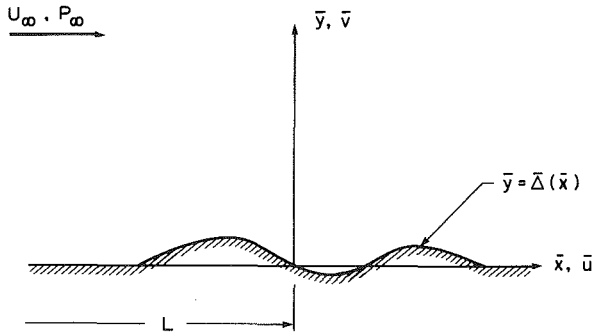

Fig. 1 Two-dimensional flow model and coordinates

In the limit $\epsilon \to 0$, equation (1) models inviscid flows. These equations become invariant under the transformation if Δ, Δ_x, and Δ_{xx} also approach zero in the limit $\epsilon \to 0$. If the height of the displacement is $0(\epsilon^n)$ and its axial extent is $0(\epsilon^m)$, then this limit requires

$$m < n/2 \tag{3}$$

where m and n are positive. If we restrict the height of the displacement to about the thickness of the boundary layer, then equation (3) coincides with Glauert's restriction. In general, equation (3) is a less restrictive condition than that due to Glauert. For certain practical problems, Δ is usually much smaller than the boundary-layer thickness, but the axial extent of the solid surface displacement is also small. Consequently, this leads to large Δ_x and Δ_{xx}, and equation (3) is not satisfied. This is why equation (1) provides a more convenient set of starting equations for perturbation solutions.

For a thin boundary layer, the normal coordinate and velocity are scaled as

$$r = y/\epsilon \quad \text{and} \quad \hat{v} = \bar{v}/\epsilon. \tag{4}$$

Consequently, equation (1) becomes

$$u_x + \hat{v}_r = 0 \tag{5a}$$

$$uu_x + \hat{v}u_r = -p_x + \epsilon^{-1}\Delta_x p_r + \theta + (1+\Delta_x^2)u_{rr} + 0(\epsilon) \tag{5b}$$

$$\Delta_{xx}u^2 = \Delta_x(p_x - \theta) - \epsilon^{-1}(1+\Delta_x^2)p_r + 0(\epsilon) \tag{5c}$$

$$u\theta_x + \hat{v}\theta_r = \frac{1}{\mathrm{Pr}}(1+\Delta_x^2)\theta_{rr} \tag{5d}$$

Equation (5c) clearly indicates that the pressure gradient across the boundary layer is $0(\epsilon)$ and can be neglected. However, it has a leading-order effect in the axial momentum equation. The elimination of p_r between equations (5b) and (5c) and the neglect of small terms yields

$$uu_x + \hat{v}u_r + \frac{\Delta_x\Delta_{xx}}{1+\Delta_x^2}u^2 = \frac{-1}{1+\Delta_x^2}(p_x - \theta) + (1+\Delta_x^2)u_{rr} \tag{6}$$

It is easy to see that equation (6) reduces to the original form of the boundary-layer equation in the limit $\epsilon \to 0$ if the surface displacement satisfies condition (3). The third term of equation (6) represents the effect of *centrifugal* force and is the most important curvature effect. Including terms associated with the details of the surface geometry, equation (6) is the boundary-layer equations for a curved surface. In fact, Prandtl's coordinates are *body-fitted coordinates*. The topological meaning of equation (6) is clear: A surface can be constructed if its location, slope, and curvature are known. The no-slip surface condition originally applied at $\bar{y} = \bar{\Delta}$ is now applied at $r = 0$.

It is worthwhile to note that a perturbation solution for a small Δ can be readily obtained from equations (2) and (6) by expanding the solution in powers of Δ for both the inviscid and boundary-layer flows. Since the leading-order governing equations are independent of Δ and its derivatives, their solutions do not explicitly depend on the geometry. This shows that the original form of Prandtl's theorem is valid only as the leading-order solution. One additional advantage of such a series solution is that the boundary conditions are applied *exactly* on the solid surface in Prandtl's coordinates; therefore, it can provide a more accurate result than the Stokes series, as demonstrated in the solution for heat conduction in eccentric annuli [see Appendix of Yao (1980)].

References

Glauert, M. B., 1957, "A Boundary Layer Theorem, With Applications to Rotating Cylinders," *J. Fluid Mech.*, Vol. 2, p. 89.

Prandtl, L., 1938, "AurBerechung der Grenzchichten," *Z. angew. Math. Mech.*, Vol. 18, p. 77; also in: *Laminar Boundary Layers*, L. Rosenhead, ed., Clarendon Press, Oxford, 1963, p. 211.

Yao, L. S., 1980, "Analysis of Heat Transfer in Slightly Eccentric Annuli," ASME JOURNAL OF HEAT TRANSFER, Vol. 102, p. 279.

Yao, L. S., 1983, "Natural Convection Along a Vertical Wavy Surface," ASME JOURNAL OF HEAT TRANSFER, Vol. 105, p. 465.

Free Convection Between Vertical Plates With Periodic Heat Input

C. Y. Wang[1]

Nomenclature

- a = thermal diffusivity
- A = steady velocity profile
- B = unsteady velocity profile
- F = steady temperature profile
- g = gravitational acceleration
- G = unsteady temperature profile
- h = gap half-width
- k = thermal conductivity
- K = constant defined by equation (23)
- L = height of channel
- Pr = Prandtl number
- q_1 = steady heat input
- q_2 = amplitude of unsteady heat input
- S, St = Strouhal number = $h^2\omega/\nu$
- t = time
- T = temperature
- T_1 = steady temperature on wall
- T_2 = unsteady temperature amplitude on wall
- u = vertical velocity
- x = vertical coordinate
- y = horizontal coordinate
- z = $(1 + i)/\sqrt{2}$
- α = a constant; its fourth power is the normalized vertical temperature gradient
- β = coefficient of thermal expansion
- γ = const
- δ = const
- η = y/h
- λ = constant defined by equation (27)
- Λ = modified channel Rayleigh number = $2h^5g\beta q_1/L\nu ak$
- μ_1, μ_2 = constants defined by equation (24)
- ν = kinematic viscosity
- ρ = density
- ω = frequency

[1]Michigan State University, East Lansing, MI 48824; Mem. ASME.

Contributed by the Heat Transfer Division for publication in the JOURNAL OF HEAT TRANSFER. Manuscript received by the Heat Transfer Division May 5, 1987. Keywords: Electronic Equipment, Natural Convection, Transient and Unsteady Heat Transfer.

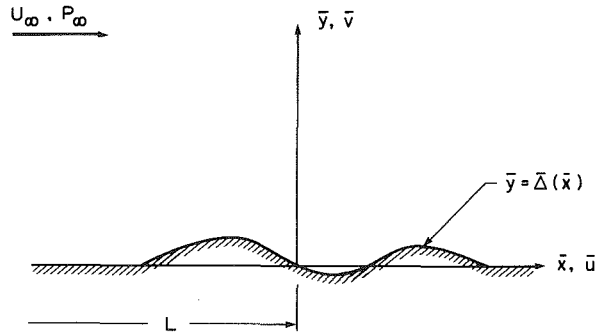

Fig. 1 Two-dimensional flow model and coordinates

In the limit $\epsilon \to 0$, equation (1) models inviscid flows. These equations become invariant under the transformation if Δ, Δ_x, and Δ_{xx} also approach zero in the limit $\epsilon \to 0$. If the height of the displacement is $0(\epsilon^n)$ and its axial extent is $0(\epsilon^m)$, then this limit requires

$$m < n/2 \tag{3}$$

where m and n are positive. If we restrict the height of the displacement to about the thickness of the boundary layer, then equation (3) coincides with Glauert's restriction. In general, equation (3) is a less restrictive condition than that due to Glauert. For certain practical problems, Δ is usually much smaller than the boundary-layer thickness, but the axial extent of the solid surface displacement is also small. Consequently, this leads to large Δ_x and Δ_{xx}, and equation (3) is not satisfied. This is why equation (1) provides a more convenient set of starting equations for perturbation solutions.

For a thin boundary layer, the normal coordinate and velocity are scaled as

$$r = y/\epsilon \quad \text{and} \quad \hat{v} = \bar{v}/\epsilon. \tag{4}$$

Consequently, equation (1) becomes

$$u_x + \hat{v}_r = 0 \tag{5a}$$

$$uu_x + \hat{v}u_r = -p_x + \epsilon^{-1}\Delta_x p_r + \theta + (1+\Delta_x^2)u_{rr} + 0(\epsilon) \tag{5b}$$

$$\Delta_{xx}u^2 = \Delta_x(p_x - \theta) - \epsilon^{-1}(1+\Delta_x^2)p_r + 0(\epsilon) \tag{5c}$$

$$u\theta_x + \hat{v}\theta_r = \frac{1}{\mathrm{Pr}}(1+\Delta_x^2)\theta_{rr} \tag{5d}$$

Equation (5c) clearly indicates that the pressure gradient across the boundary layer is $0(\epsilon)$ and can be neglected. However, it has a leading-order effect in the axial momentum equation. The elimination of p_r between equations (5b) and (5c) and the neglect of small terms yields

$$uu_x + \hat{v}u_r + \frac{\Delta_x\Delta_{xx}}{1+\Delta_x^2}u^2 = \frac{-1}{1+\Delta_x^2}(p_x - \theta) + (1+\Delta_x^2)u_{rr} \tag{6}$$

It is easy to see that equation (6) reduces to the original form of the boundary-layer equation in the limit $\epsilon \to 0$ if the surface displacement satisfies condition (3). The third term of equation (6) represents the effect of *centrifugal* force and is the most important curvature effect. Including terms associated with the details of the surface geometry, equation (6) is the boundary-layer equations for a curved surface. In fact, Prandtl's coordinates are *body-fitted coordinates*. The topological meaning of equation (6) is clear: A surface can be constructed if its location, slope, and curvature are known. The no-slip surface condition originally applied at $\bar{y} = \bar{\Delta}$ is now applied at $r = 0$.

It is worthwhile to note that a perturbation solution for a small Δ can be readily obtained from equations (2) and (6) by expanding the solution in powers of Δ for both the inviscid and boundary-layer flows. Since the leading-order governing equations are independent of Δ and its derivatives, their solutions do not explicitly depend on the geometry. This shows that the original form of Prandtl's theorem is valid only as the leading-order solution. One additional advantage of such a series solution is that the boundary conditions are applied *exactly* on the solid surface in Prandtl's coordinates; therefore, it can provide a more accurate result than the Stokes series, as demonstrated in the solution for heat conduction in eccentric annuli [see Appendix of Yao (1980)].

References

Glauert, M. B., 1957, "A Boundary Layer Theorem, With Applications to Rotating Cylinders," *J. Fluid Mech.*, Vol. 2, p. 89.

Prandtl, L., 1938, "AurBerechung der Grenzchichten," *Z. angew. Math. Mech.*, Vol. 18, p. 77; also in: *Laminar Boundary Layers*, L. Rosenhead, ed., Clarendon Press, Oxford, 1963, p. 211.

Yao, L. S., 1980, "Analysis of Heat Transfer in Slightly Eccentric Annuli," ASME JOURNAL OF HEAT TRANSFER, Vol. 102, p. 279.

Yao, L. S., 1983, "Natural Convection Along a Vertical Wavy Surface," ASME JOURNAL OF HEAT TRANSFER, Vol. 105, p. 465.

Free Convection Between Vertical Plates With Periodic Heat Input

C. Y. Wang[1]

Nomenclature

a = thermal diffusivity
A = steady velocity profile
B = unsteady velocity profile
F = steady temperature profile
g = gravitational acceleration
G = unsteady temperature profile
h = gap half-width
k = thermal conductivity
K = constant defined by equation (23)
L = height of channel
Pr = Prandtl number
q_1 = steady heat input
q_2 = amplitude of unsteady heat input
S, St = Strouhal number = $h^2\omega/\nu$
t = time
T = temperature
T_1 = steady temperature on wall
T_2 = unsteady temperature amplitude on wall
u = vertical velocity
x = vertical coordinate
y = horizontal coordinate
z = $(1 + i)/\sqrt{2}$
α = a constant; its fourth power is the normalized vertical temperature gradient
β = coefficient of thermal expansion
γ = const
δ = const
η = y/h
λ = constant defined by equation (27)
Λ = modified channel Rayleigh number = $2h^5g\beta q_1/L\nu ak$
μ_1, μ_2 = constants defined by equation (24)
ν = kinematic viscosity
ρ = density
ω = frequency

[1]Michigan State University, East Lansing, MI 48824; Mem. ASME.

Contributed by the Heat Transfer Division for publication in the JOURNAL OF HEAT TRANSFER. Manuscript received by the Heat Transfer Division May 5, 1987. Keywords: Electronic Equipment, Natural Convection, Transient and Unsteady Heat Transfer.

Introduction

Electric and electronic panels are often cooled by free convection. In some cases the current is periodic due to on-off control mechanisms or due to partially rectified a-c voltage. Periodic heat input of a single vertical plate with no edges was investigated by Menold and Yang (1962) and Schetz and Eichhorn (1962). Others have studied the effect on boundary layer development, also on a single plate (Chung and Anderson, 1961; Nanda and Sharma, 1963; Kelleher and Yang, 1968; Yang et al., 1974; Muhuri and Gupta, 1979). The present note addresses the fully developed convection between two periodically heated parallel plates. Fully developed flow, occurring at small Rayleigh numbers (Bar-Cohen and Rohsenow, 1984), is becoming more common due to the trend in miniaturization of the panels.

Prescribed Temperature

Let the temperature be $T_1 + T_2 \cos \omega t$ on the walls. Since fully developed flow is independent of x, the problem is linear. We separate steady and unsteady parts as follows:

$$u = \frac{\beta g h^2}{\nu}[(T_1 - T_0)A(\eta) + T_2 B(\eta)e^{i\omega t}] \quad (1)$$

$$T = T_0 + (T_1 - T_0)F(\eta) + T_2 G(\eta)e^{i\omega t} \quad (2)$$

Upon substitution into the usual Boussinesq equations we find

$$F'' = 0, \quad A'' + F = 0, \quad F(\pm 1) = 1, \quad A(\pm 1) = 0 \quad (3)$$

$$G'' = i\mathrm{StPr}G = 0, \quad B'' - i\mathrm{St}B = -G, \quad G(\pm 1) = 1,$$

$$B(\pm 1) = 0 \quad (4)$$

where St is the Strouhal number. The solutions are

$$F = 1, \quad A = \frac{1}{2}(1 - \eta^2) \quad (5)$$

$$G = \frac{\cosh(z\sqrt{\mathrm{StPr}}\,\eta)}{\cosh(z\sqrt{\mathrm{StPr}})} \quad (6)$$

$$B = \frac{i}{\mathrm{St}(\mathrm{Pr}-1)}\left[\frac{\cosh(z\sqrt{\mathrm{StPr}}\,\eta)}{\cosh(z\sqrt{\mathrm{StPr}})} - \frac{\cosh(z\sqrt{\mathrm{St}}\,\eta)}{\cosh(z\sqrt{\mathrm{St}})}\right], \quad \mathrm{Pr} \neq 1 \quad (7)$$

$$B = \frac{iz}{2\sqrt{\mathrm{St}}\cosh(z\sqrt{\mathrm{St}})}[\eta \sinh(z\sqrt{\mathrm{St}}\,\eta) - \tanh(z\sqrt{\mathrm{St}})\cosh(z\sqrt{\mathrm{St}}\,\eta)], \quad \mathrm{Pr} = 1 \quad (8)$$

Figure 1 shows the real and imaginary parts of $G(\eta)$ for various St and Pr = 0.7 (air). The unsteady temperature profile is

$$\mathrm{Re}(T_2 G e^{+i\omega t}) = T_2[\mathrm{Re}\ G(\eta)\cos \omega t - Im\ G(\eta)\sin \omega t] \quad (9)$$

For large St (high frequency) the boundary layer character is evident. Figure 2 shows the induced unsteady velocity distribution. The unsteady velocity diminishes to zero for large St.

Prescribed Heat Flux

Let the heat flux on the walls be $q_1 + q_2 \cos \omega t$. We assume a solution of the form

$$u = \frac{h^3 g\beta}{k\nu}\left[\frac{q_1}{\alpha^4}A(\eta) + q_2 B(\eta)e^{i\omega t}\right] \quad (10)$$

$$T = T_0 + \frac{a\nu}{h^4 g\beta}\alpha^4 x + \frac{h}{k}[q_1 F(\eta) + q_2 G(\eta)e^{i\omega t}] \quad (11)$$

$$P = P_0 + \frac{\rho\nu a}{2h^4}\alpha^4 x(x - L) \quad (12)$$

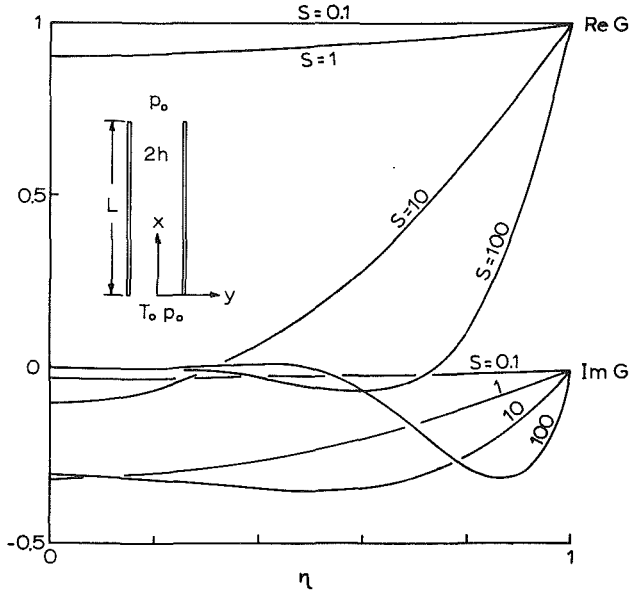

Fig. 1 The unsteady temperature profile $G(\eta)$. The real part is in phase and the imaginary part is 90 deg out of phase. Case with prescribed wall temperature.

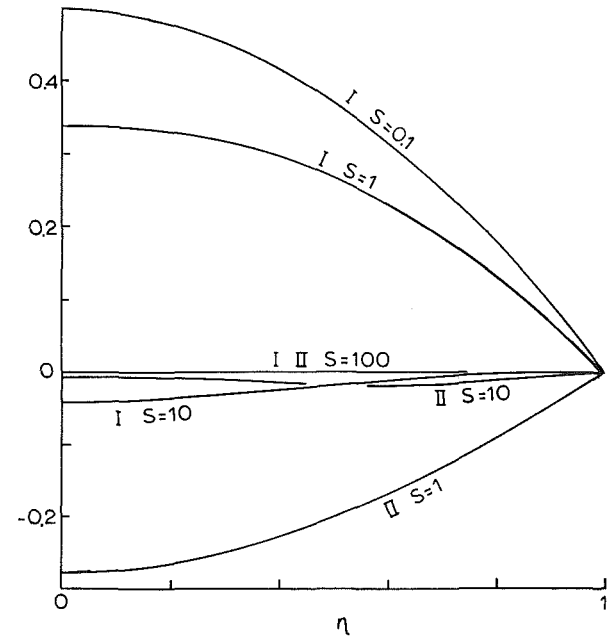

Fig. 2 Unsteady velocity profile $B(\eta)$, case with prescribed wall temperature, I = Re(B), II = $Im(B)$

The linear term x of the temperature and the quadratic term of the pressure are characteristics of uniformly heated ducts. The Boussinesq equations yield

$$F'' = A, \quad \alpha^{-4}A'' = -F - \alpha^4/\Lambda, \quad F'(\pm 1) = \pm 1,$$

$$A(\pm 1) = 0 \quad (13)$$

$$G'' - i\mathrm{StPr}G = \alpha^4 B, \quad B'' - i\mathrm{St}B = -G, \quad G'(\pm 1) = \pm 1,$$

$$B(\pm 1) = 0 \quad (14)$$

where $\Lambda \equiv 2h^5 g\beta q_1/L\nu ak$ is a modified channel Rayleigh number. Another relation is needed to determine the constant α, where α^4 denotes the normalized axial temperature gradient. Since the fluid is rising due to heat input, we require the mean temperature to be T_0 at the bottom at $x = 0$

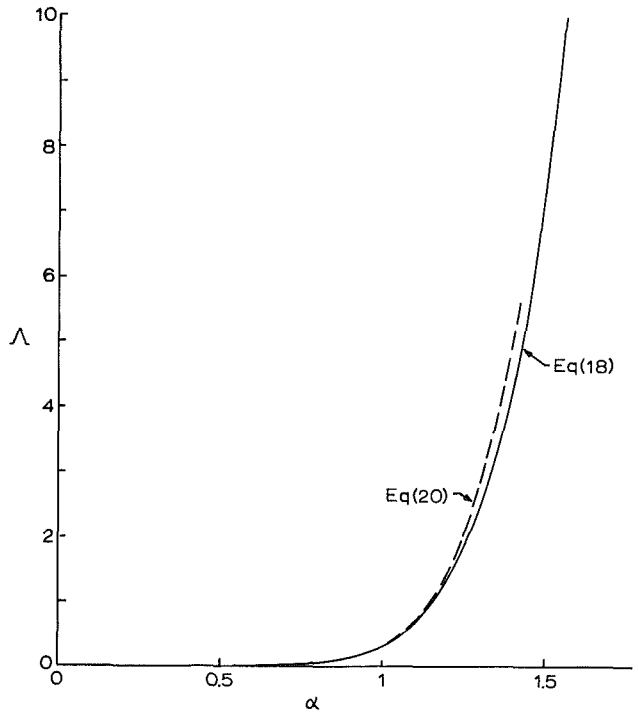

Fig. 3 Modified Rayleigh number Λ as function of $\alpha = [h^4 g\beta \partial T/\partial x/a\nu]^{1/4}$; dashed line is the asymptotic approximation

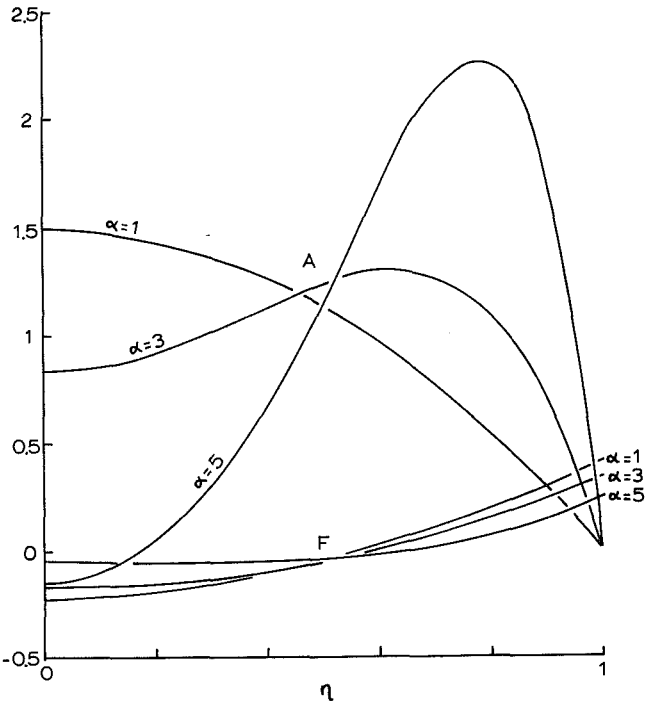

Fig. 4 Steady velocity $A(\eta)$ and temperature profile $F(\eta)$, case with prescribed wall heat flux

$$\int_{-1}^{1} F(\eta)\,d\eta = 0 \tag{15}$$

After some work, the solutions to equations (13) are

$$A(\eta) = \frac{-\alpha Im\left[\dfrac{\cosh(\alpha z\eta)}{\cosh(\alpha z)}\right]}{\mathrm{Re}[z\tanh(\alpha z)]} \tag{16}$$

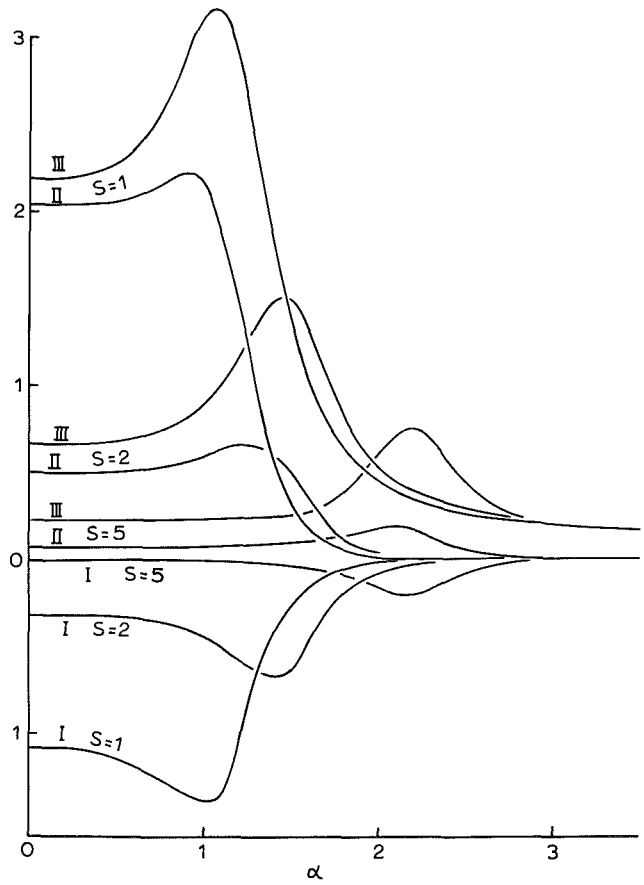

Fig. 5 Amplitude of unsteady velocity I = |B(0)|, and unsteady temperature II = |G(0)|, III = |G(1)|, as a function of α, case with prescribed heat flux

$$F(\eta) = \frac{-\alpha^4}{\Lambda} + \frac{\mathrm{Re}\left[\dfrac{\cosh(\alpha z\eta)}{\cosh(\alpha z)}\right]}{\alpha\,\mathrm{Re}[z\tanh(\alpha z)]} \tag{17}$$

$$\Lambda = \alpha^6 \mathrm{Re}[z\tanh(\alpha z)]/\mathrm{Re}\left[\frac{\tanh(\alpha z)}{z}\right] \tag{18}$$

This universal relationship between the normalized mean temperature gradient α and the modified Rayleigh number Λ is plotted in Fig. 3. We see Λ increases rapidly with α only when $\alpha > 1$. For small α we find

$$A(\eta) \sim \frac{3}{2}(1-\eta^2),\quad F(\eta) \sim -\frac{9}{40} + \frac{3}{4}\eta^2 - \frac{1}{8}\eta^4 \tag{19}$$

$$\Lambda \sim \frac{\alpha^3}{3} \tag{20}$$

Figure 4 shows the steady velocity profile equation (16), and the steady temperature profile equation (17).

The unsteady problem is more difficult. In equations (14) we set

$$G = \gamma e^{\mu\eta},\quad B = \delta e^{\mu\eta} \tag{21}$$

For nontrivial γ and δ the eigenvalues are

$$\mu^2 = \frac{i}{2}[\mathrm{St}(\mathrm{Pr}+1) \pm K] \tag{22}$$

where

$$K \equiv \sqrt{\mathrm{St}^2(\mathrm{Pr}-1)^2 + 4\alpha^4} > 0 \tag{23}$$

We denote

$$\mu_1 \equiv z\sqrt{\frac{\mathrm{St}(\mathrm{Pr}+1)+K}{2}}, \quad \mu_2 \equiv z\sqrt{\frac{\mathrm{St}(\mathrm{Pr}+1)-K}{2}} \tag{24}$$

The solution for B, satisfying the boundary conditions, is

$$B = \lambda\left[\frac{\cosh(\mu_1\eta)}{\cosh(\mu_1)} - \frac{\cosh(\mu_2\eta)}{\cosh(\mu_2)}\right] \tag{25}$$

Thus

$$G = \lambda\left[(i\mathrm{St}-\mu_1^2)\frac{\cosh(\mu_1\eta)}{\cosh(\mu_1)} - (i\mathrm{St}-\mu_2^2)\frac{\cosh(\mu_2\eta)}{\cosh(\mu_2)}\right] \tag{26}$$

The boundary conditions on $G'(1)$ give

$$\lambda = \frac{1}{(i\mathrm{St}-\mu_1^2)\mu_1\tanh(\mu_1) - (i\mathrm{St}-\mu_2^2)\mu_2\tanh(\mu_2)} \tag{27}$$

Three nondimensional parameters α, Pr, and St govern the unsteady universal functions $B(\eta)$ and $G(\eta)$. The amplitudes of the oscillations $|B(0)|$, $|G(0)|$, $|G(1)|$ are shown in Fig. 5 for Pr = 0.7. It is seen that the amplitude decreases with increased frequency St. For given St the amplitude increases to a maximum, then decreases to zero as α is further increased.

Discussion

Is it possible to superpose solutions? For the case of prescribed surface temperature, the fact that equations (3) and (4) are linear and homogeneous implies superposition is indeed possible, i.e., the sum of two solutions is another solution. However, equation (13), in the case of prescribed heat flux, is linear but nonhomogeneous. This shows the steady flow and temperature fields $A(\eta)$ and $F(\eta)$ cannot be superposed due to the nonzero axial temperature gradient. On the other hand, for given *steady* temperature gradient, the unsteady oscillatory field can be superposed since equations (14) are linear and homogeneous. Thus any periodic unsteady effect can be decomposed into its Fourier components.

The forms of our equations (10)–(12) lead to nondimensional universal equations (13) and (14). Also equation (10), containing the given heat flux q_1, q_2, assures a global heat balance. Thus α is obtained from the mean temperature T_0 at $x = 0$. Of course, the field is not fully developed at $x = 0$; however, experiments show the entrance effect is negligible for low to moderate Rayleigh numbers (Bar-Cohen and Rohsenow, 1984).

Although a Nusselt number for the steady state is well defined, its meaning for the unsteady variation is less clear. Following Menold and Yang (1962) and Schetz and Eichhorn (1962), our results are presented in terms of velocity and temperature profiles.

We conclude the following. For low frequencies the effect on the unsteady flow is large, and in phase with the oscillatory temperature or heat input. For high frequencies the effect diminishes to zero. In general the flow and temperature are complicated functions of the Prandtl number, Strouhal number, and indirectly, the Rayleigh number. A "quasi-steady" approach, i.e., frequency low enough that the steady-state solution can be used at any instance, is adequate only at very low Strouhal numbers (less than 0.1); otherwise the analytical solutions presented in this paper should be used.

References

Bar-Cohen, A., and Rohsenow, W. M., 1984, "Thermally Optimum Spacing of Vertical Natural Convection Cooled, Parallel Plates," ASME JOURNAL OF HEAT TRANSFER, Vol. 106, pp. 116–123.

Chung, P. M., and Anderson, A. D., 1961, "Unsteady Laminar Free Convection," ASME JOURNAL OF HEAT TRANSFER, Vol. 83, pp. 473–478.

Kelleher, M. D., and Yang, K. T., 1968, "Heat Transfer Response of Laminar Free-Convection Boundary Layers Along a Vertical Heated Plate to Surface-Temperature Oscillations," *ZAMP*, Vol. 19, pp. 31–44.

Menold, E. R., and Yang, K. T., 1962, "Asymptotic Solutions for Unsteady Laminar Free Convection on a Vertical Plate," ASME *Journal of Applied Mechanics*, Vol. 29, pp. 124–126.

Muhuri, P. K., and Gupta, A. S., 1979, "Free Convection Boundary Layer on a Flat Plate Due to Small Fluctuations in Surface Temperature," *ZAMM*, Vol. 59, pp. 117–121.

Nanda, R. J., and Sharma, V. P., 1963, "Free Convection Laminar Boundary Layers in Oscillatory Flow," *Journal of Fluid Mechanics*, Vol. 15, pp. 419–428.

Schetz, J. A., and Eichhorn, R., 1962, "Unsteady Natural Convection in the Vicinity of a Doubly Infinite Vertical Plate," ASME JOURNAL OF HEAT TRANSFER, Vol. 84, pp. 334–338.

Yang, J. W., Scaccia, C., and Goodman, J., 1974, "Laminar Natural Convection About Vertical Plates With Oscillatory Surface Temperature," ASME JOURNAL OF HEAT TRANSFER, Vol. 96, pp. 9–14.

Correlations for Mixed Convection Flows Across Horizontal Cylinders and Spheres

B. F. Armaly,[1] T. S. Chen,[1] and N. Ramachandran[2]

Nomenclature

d = diameter of cylinder or sphere
g = gravitational acceleration
Gr_d = Grashof number $= g\beta(T_w - T_\infty)d^3/\nu^2$
$\bar{h}$, $\bar{h}_F$ = average heat transfer coefficients for mixed and pure forced convection, respectively
k = thermal conductivity
$\overline{\mathrm{Nu}}_d$ = mixed convection average Nusselt number $= \bar{h}d/k$
$\overline{\mathrm{Nu}}_{dF}$ = forced convection average Nusselt number $= \bar{h}_F d/k$
Pr = Prandtl number $= \nu/\alpha$
Re_d = Reynolds number $= u_\infty d/\nu$
T_f = film temperature $= (T_w + T_\infty)/2$
T_w = wall temperature
T_∞ = free-stream temperature
u_∞ = free-stream velocity
α = thermal diffusivity
β = volumetric coefficient of thermal expansion
ν = kinematic viscosity

Introduction

Mixed convection in air flow across horizontal cylinders and spheres has been studied both analytically and experimentally by many investigators, covering various ranges of Reynolds and Grashof numbers of practical interest. Nusselt number results have been presented either in graphic forms or in various equation forms that are generally not convenient for use. In this note, an attempt is made to summarize the analytical and experimental results of several representative studies for these two flow configurations in simple correlation equations that can be employed in heat transfer calculations. It is noted that similar correlation equations for cylinders and spheres have been proposed by Churchill (1983) for various

[1]Professor, Department of Mechanical & Aerospace Engineering, University of Missouri—Rolla, Rolla, MO 65401; Fellow ASME.

[2]Presently at USRA, NASA/MSFC, Huntsville, AL 35806; Assoc. Mem. ASME.

Contributed by the Heat Transfer Division for publication in the JOURNAL OF HEAT TRANSFER. Manuscript received by the Heat Transfer Division July 8, 1987. Keywords: Forced Convection, Mixed Convection, Natural Convection.

We denote

$$\mu_1 \equiv z\sqrt{\frac{\mathrm{St}(\mathrm{Pr}+1)+K}{2}}, \quad \mu_2 \equiv z\sqrt{\frac{\mathrm{St}(\mathrm{Pr}+1)-K}{2}} \tag{24}$$

The solution for B, satisfying the boundary conditions, is

$$B = \lambda\left[\frac{\cosh(\mu_1\eta)}{\cosh(\mu_1)} - \frac{\cosh(\mu_2\eta)}{\cosh(\mu_2)}\right] \tag{25}$$

Thus

$$G = \lambda\left[(i\mathrm{St}-\mu_1^2)\frac{\cosh(\mu_1\eta)}{\cosh(\mu_1)} - (i\mathrm{St}-\mu_2^2)\frac{\cosh(\mu_2\eta)}{\cosh(\mu_2)}\right] \tag{26}$$

The boundary conditions on $G'(1)$ give

$$\lambda = \frac{1}{(i\mathrm{St}-\mu_1^2)\mu_1\tanh(\mu_1) - (i\mathrm{St}-\mu_2^2)\mu_2\tanh(\mu_2)} \tag{27}$$

Three nondimensional parameters α, Pr, and St govern the unsteady universal functions $B(\eta)$ and $G(\eta)$. The amplitudes of the oscillations $|B(0)|$, $|G(0)|$, $|G(1)|$ are shown in Fig. 5 for Pr = 0.7. It is seen that the amplitude decreases with increased frequency St. For given St the amplitude increases to a maximum, then decreases to zero as α is further increased.

Discussion

Is it possible to superpose solutions? For the case of prescribed surface temperature, the fact that equations (3) and (4) are linear and homogeneous implies superposition is indeed possible, i.e., the sum of two solutions is another solution. However, equation (13), in the case of prescribed heat flux, is linear but nonhomogeneous. This shows the steady flow and temperature fields $A(\eta)$ and $F(\eta)$ cannot be superposed due to the nonzero axial temperature gradient. On the other hand, for given *steady* temperature gradient, the unsteady oscillatory field can be superposed since equations (14) are linear and homogeneous. Thus any periodic unsteady effect can be decomposed into its Fourier components.

The forms of our equations (10)–(12) lead to nondimensional universal equations (13) and (14). Also equation (10), containing the given heat flux q_1, q_2, assures a global heat balance. Thus α is obtained from the mean temperature T_0 at $x = 0$. Of course, the field is not fully developed at $x = 0$; however, experiments show the entrance effect is negligible for low to moderate Rayleigh numbers (Bar-Cohen and Rohsenow, 1984).

Although a Nusselt number for the steady state is well defined, its meaning for the unsteady variation is less clear. Following Menold and Yang (1962) and Schetz and Eichhorn (1962), our results are presented in terms of velocity and temperature profiles.

We conclude the following. For low frequencies the effect on the unsteady flow is large, and in phase with the oscillatory temperature or heat input. For high frequencies the effect diminishes to zero. In general the flow and temperature are complicated functions of the Prandtl number, Strouhal number, and indirectly, the Rayleigh number. A "quasi-steady" approach, i.e., frequency low enough that the steady-state solution can be used at any instance, is adequate only at very low Strouhal numbers (less than 0.1); otherwise the analytical solutions presented in this paper should be used.

References

Bar-Cohen, A., and Rohsenow, W. M., 1984, "Thermally Optimum Spacing of Vertical Natural Convection Cooled, Parallel Plates," ASME JOURNAL OF HEAT TRANSFER, Vol. 106, pp. 116–123.

Chung, P. M., and Anderson, A. D., 1961, "Unsteady Laminar Free Convection," ASME JOURNAL OF HEAT TRANSFER, Vol. 83, pp. 473–478.

Kelleher, M. D., and Yang, K. T., 1968, "Heat Transfer Response of Laminar Free-Convection Boundary Layers Along a Vertical Heated Plate to Surface-Temperature Oscillations," *ZAMP*, Vol. 19, pp. 31–44.

Menold, E. R., and Yang, K. T., 1962, "Asymptotic Solutions for Unsteady Laminar Free Convection on a Vertical Plate," ASME *Journal of Applied Mechanics*, Vol. 29, pp. 124–126.

Muhuri, P. K., and Gupta, A. S., 1979, "Free Convection Boundary Layer on a Flat Plate Due to Small Fluctuations in Surface Temperature," *ZAMM*, Vol. 59, pp. 117–121.

Nanda, R. J., and Sharma, V. P., 1963, "Free Convection Laminar Boundary Layers in Oscillatory Flow," *Journal of Fluid Mechanics*, Vol. 15, pp. 419–428.

Schetz, J. A., and Eichhorn, R., 1962, "Unsteady Natural Convection in the Vicinity of a Doubly Infinite Vertical Plate," ASME JOURNAL OF HEAT TRANSFER, Vol. 84, pp. 334–338.

Yang, J. W., Scaccia, C., and Goodman, J., 1974, "Laminar Natural Convection About Vertical Plates With Oscillatory Surface Temperature," ASME JOURNAL OF HEAT TRANSFER, Vol. 96, pp. 9–14.

Correlations for Mixed Convection Flows Across Horizontal Cylinders and Spheres

B. F. Armaly,[1] T. S. Chen,[1] and N. Ramachandran[2]

Nomenclature

d	=	diameter of cylinder or sphere
g	=	gravitational acceleration
Gr_d	=	Grashof number $= g\beta(T_w - T_\infty)d^3/\nu^2$
$\bar{h}$, $\bar{h}_F$	=	average heat transfer coefficients for mixed and pure forced convection, respectively
k	=	thermal conductivity
$\overline{\mathrm{Nu}}_d$	=	mixed convection average Nusselt number $= \bar{h}d/k$
$\overline{\mathrm{Nu}}_{dF}$	=	forced convection average Nusselt number $= \bar{h}_F d/k$
Pr	=	Prandtl number $= \nu/\alpha$
Re_d	=	Reynolds number $= u_\infty d/\nu$
T_f	=	film temperature $= (T_w + T_\infty)/2$
T_w	=	wall temperature
T_∞	=	free-stream temperature
u_∞	=	free-stream velocity
α	=	thermal diffusivity
β	=	volumetric coefficient of thermal expansion
ν	=	kinematic viscosity

Introduction

Mixed convection in air flow across horizontal cylinders and spheres has been studied both analytically and experimentally by many investigators, covering various ranges of Reynolds and Grashof numbers of practical interest. Nusselt number results have been presented either in graphic forms or in various equation forms that are generally not convenient for use. In this note, an attempt is made to summarize the analytical and experimental results of several representative studies for these two flow configurations in simple correlation equations that can be employed in heat transfer calculations. It is noted that similar correlation equations for cylinders and spheres have been proposed by Churchill (1983) for various

[1]Professor, Department of Mechanical & Aerospace Engineering, University of Missouri—Rolla, Rolla, MO 65401; Fellow ASME.

[2]Presently at USRA, NASA/MSFC, Huntsville, AL 35806; Assoc. Mem. ASME.

Contributed by the Heat Transfer Division for publication in the JOURNAL OF HEAT TRANSFER. Manuscript received by the Heat Transfer Division July 8, 1987. Keywords: Forced Convection, Mixed Convection, Natural Convection.

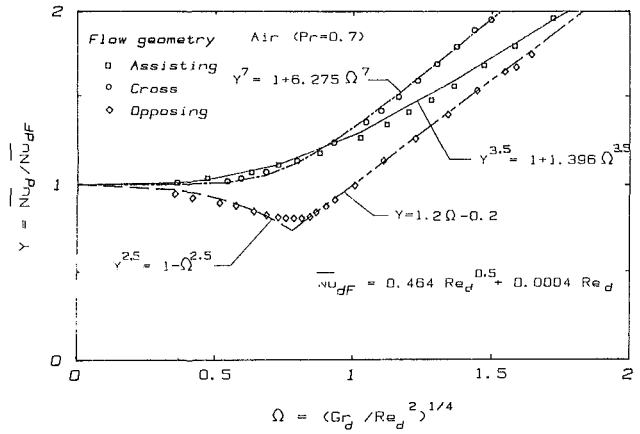

Fig. 1 Measured (Oosthuizen and Madan, 1970, 1971) and correlated average Nusselt numbers for air flow, Pr = 0.7, across isothermal horizontal cylinders ($10^2 < Re_d < 3 \times 10^3$ and $2.5 \times 10^4 < Gr_d < 3 \times 10^5$)

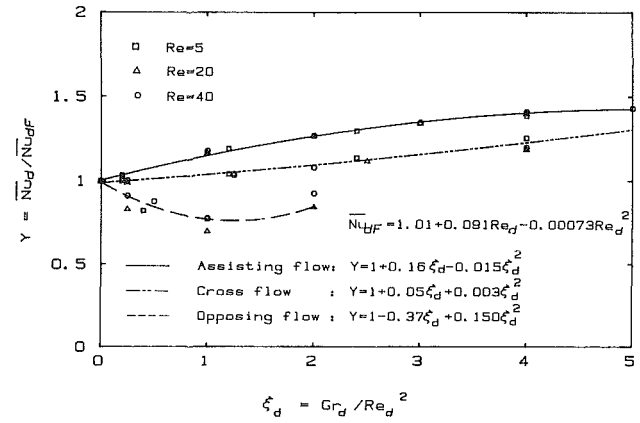

Fig. 2 Predicted (Badr, 1983, 1983) and correlated average Nusselt numbers for air flow, Pr = 0.7, across isothermal horizontal cylinders ($1 < Re_d < 60$ and $0 < Gr_d < 7200$).

Prandtl numbers, and a large scatter of experimental data is found along his correlation equations. The present correlation equations are for air flow and in some regions are more accurate in predicting measured results (an improvement of more than 10 percent) than those presented by Churchill (1983).

Correlations

(A) Horizontal Cylinders in Crossflow. Measurements and predictions of average mixed convection Nusselt numbers for horizontal cylinders in cross air flow (Pr = 0.7) have been reported by Oosthuizen and Madan (1970, 1971), Badr (1983, 1984), Hatton et al. (1970), and Nakai and Okazaki (1975a), among others, for assisting flow (in which the forced flow is in the same direction as the buoyancy force), opposing flow (in which the forced flow is exactly in the opposite direction to the buoyancy force), and cross flow, covering a wide range of Reynolds and Grashof numbers. These results for the various Reynolds and Grashof number ranges can be correlated in simple equation forms.

Measurements by Oosthuizen and Madan (1970, 1971) for isothermal horizontal cylinders in air cover the flow regime of $10^2 < Re_d < 3 \times 10^3$ and $2.5 \times 10^4 < Gr_d < 3 \times 10^5$. Their average Nusselt number results can be correlated by the following equations:

For assisting flow ($\phi = 0$ *deg*)

$$\overline{Nu}_d/\overline{Nu}_{dF} = [1 + 1.396\Omega^{3.5}]^{1/3.5} \tag{1}$$

For cross flow ($\phi = 90$ *deg*):

$$\overline{Nu}_d/\overline{Nu}_{dF} = [1 + 6.275\Omega^7]^{1/7} \tag{2}$$

For opposing flow ($\phi = 180$ *deg*):

$$\overline{Nu}_d/\overline{Nu}_{dF} = [1 - \Omega^{2.5}]^{1/2.5}, \qquad \Omega < 0.7 \tag{3}$$

and

$$\overline{Nu}_d/\overline{Nu}_{dF} = 1.2\Omega - 0.2, \qquad \Omega > 0.7 \tag{4}$$

In equations (1)–(4), the average Nusselt number for pure forced convection is given by

$$\overline{Nu}_{dF} = 0.464\,Re_d^{0.5} + 0.0004\,Re_d \tag{5}$$

and

$$\Omega = (Gr_d/Re_d^2)^{1/4} \tag{6}$$

with $Gr_d = g\beta(T_w - T_\infty)d^3/\nu^2$ and $Re_d = u_\infty d/\nu$. In addition, it is noted that all fluid properties are evaluated at the film temperature $T_f = (T_w + T_\infty)/2$. A comparison between the measured results and the correlations is illustrated in Fig. 1.

Analytical results for flow across isothermal horizontal cylinders in fluids of Pr = 0.7 have been reported by Badr (1983, 1984) for the domain of $1 < Re_d < 60$ and $0 < Gr_d < 7200$. His average Nusselt number results can be correlated by the following relations:

For assisting flow ($\phi = 0$ *deg*):

$$\overline{Nu}_d/\overline{Nu}_{dF} = 1 + 0.16\xi_d - 0.015\,\xi_d^2 \tag{7}$$

For cross flow ($\phi = 90$ *deg*):

$$\overline{Nu}_d/\overline{Nu}_{dF} = 1 + 0.05\xi_d - 0.003\,\xi_d^2 \tag{8}$$

For opposing flow ($\phi = 180$ *deg*):

$$\overline{Nu}_d/\overline{Nu}_{dF} = 1 - 0.37\xi_d + 0.150\,\xi_d^2 \tag{9}$$

In equations (7)–(9)

$$\xi_d = Gr_d/Re_d^2 \tag{10}$$

and the average Nusselt number for pure forced convection is correlated as

$$\overline{Nu}_{dF} = 1.01 + 9.1 \times 10^{-2} Re_d - 7.3 \times 10^{-4} Re_d^2 \tag{11}$$

A comparison between the above correlations and the calculated results can be found in Fig. 2.

Measurements of the average Nusselt numbers for electrically heated horizontal cylinders in air by Hatton et al. (1970) cover the flow domain of $10^{-2} < Re_d < 40$ and $10^{-3} < Gr_d < 10$. Their measured results have been well correlated by the equation

$$\overline{Nu}_d\,(T_f/T_\infty)^{-0.154} = 0.384 + 0.581 R_f^{0.439} \tag{12}$$

where

$$R_f = Re_d[1 + 2.06(Gr_d Pr)^{0.418}\cos\phi/Re_d + 1.06(Gr_d Pr)^{0.836}/Re_d^2]^{1/2} \tag{13}$$

and T_f is the film temperature at which the fluid properties were evaluated. The angle ϕ is measured from the vertically upward direction of the forced flow (with $\phi = 0$, 90, and 180 deg for assisting, cross, and opposing flows, respectively). Equation (12) correlates the experimental data well for all forced flow directions except for the opposing flow case in the region of $0.25 < (Gr_d Pr)^{0.418}/Re_d < 2.5$ where the deviations between the measured and the correlated results exceed 10 percent.

Analysis and measurements of the average Nusselt number for mixed convection air flow across horizontal wires of length-diameter ratios $2 \times 10^4 < L/d < 2.5 \times 10^4$ were reported by Nakai and Okazaki (1975a) for the domain of very low Reynolds and Grashof numbers, with $10^{-3} < Re_d < 10^{-1}$ and $10^{-6} < Gr_d < 6.5 \times 10^{-5}$ (i.e., a creeping flow). Their measured results can be correlated by the following equations:

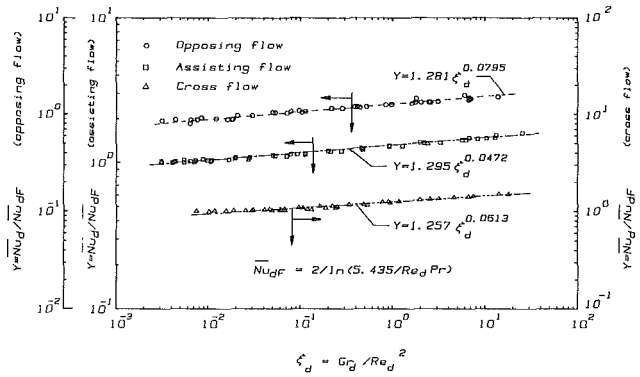

Fig. 3 Measured (Nakai and Okazaki, 1975a) and correlated average Nusselt numbers for air flow, Pr = 0.7, across isothermal horizontal wires ($10^{-3} < Re_d < 10^{-1}$ and $10^{-6} < Gr_d < 6.5 \times 10^{-5}$)

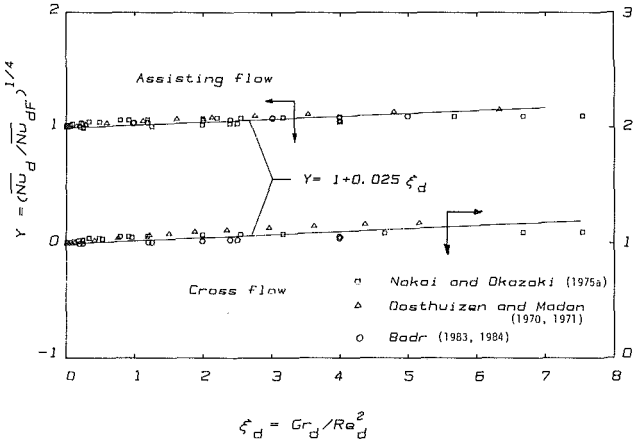

Fig. 4 A comparison of average Nusselt numbers between measured/predicted values and a single correlation equation for air flow, Pr = 0.7, across isothermal horizontal cylinders

For assisting flow ($\phi = 0$ deg):

$$\overline{Nu}_d/\overline{Nu}_{dF} = 1.295\xi_d^{0.0472} \tag{14}$$

For cross flow ($\phi = 90$ deg):

$$\overline{Nu}_d/\overline{Nu}_{dF} = 1.257\xi_d^{0.0613} \tag{15}$$

For opposing flow ($\phi = 180$ deg):

$$\overline{Nu}_d/\overline{Nu}_{dF} = 1.281\xi_d^{0.0795} \tag{16}$$

In equations (14)–(16), $\xi = Gr_d/Re_d^2$, as given by equation (10), and the pure forced convection average Nusselt number is given by Nakai and Okazaki (1975b) as

$$\overline{Nu}_{dF} = 2/\ln[5.453/(PrRe_d)] \tag{17}$$

The correlation equations (14)–(16) are in excellent agreement with the measured data, as can be seen from Fig. 3. The fluid properties are evaluated at the film temperature T_f, except for Gr_d, in which the properties are based on the free-stream temperature.

It is of practical interest to combine the separate correlation equations for assisting and cross flows covering the different Re_d and Gr_d ranges into a single correlation equation for both flows. This can be readily accomplished. Equations (1), (7), and (14) for the former and equations (2), (8), and (15) for the latter are thus cast into a single correlation equation in the form

$$(\overline{Nu}_d/\overline{Nu}_{dF})^{1/4} = 1 + 0.025\xi_d \tag{18}$$

where $\xi_d = Gr_d/Re_d^2$ as before and the $\overline{Nu}_{Fd}$ expression comes from equation (5), (11), or (17), depending on the ranges of Re_d and Gr_d. Equation (18) correlates well with available

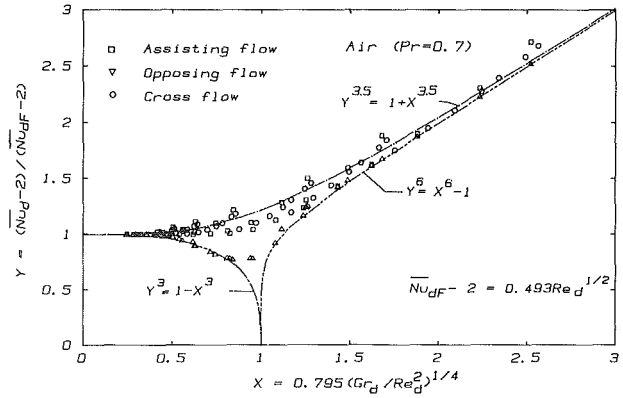

Fig. 5 Measured (Yuge, 1960) and correlated average Nusselt numbers for air flow, Pr = 0.7, across isothermal spheres ($3.5 < Re_d < 5.9 \times 10^3$ and $1 < Gr_d < 10^5$)

analytical results of Badr (1983, 1984) and experimental data of Oosthuizen and Madan (1970, 1971) and of Nakai and Okazaki (1975a, 1975b) and is accurate to within 6 percent for the assisting flow and to within 8 percent for the cross flow, as can be seen from Fig. 4. However, for better accuracy, it is recommended that the individual correlation equations for the various ranges of Re_d and Gr_d be adopted.

As mentioned in the introduction, the correlation equations proposed by Churchill (1983) display a large scatter in the data and hence are not as accurate as the correlations presented in this note. For example, for the case of assisting flow from an isothermal horizontal cylinder, Churchill's (1983) general correlation has an error of 15.3 percent for the average Nusselt number in comparison to the data of Oosthuizen and Madan (1970) for $Gr_d = 1 \times 10^5$ and $Re_d = 1.445 \times 10^2$. The present correlation predicts the average Nusselt number to within 1.57 percent error for the same experimental parameters.

(B) Spheres in Crossflow. Mixed convection flow across spheres exhibits features similar to those of horizontal cylinders in crossflow. Measurements of the average Nusselt numbers for spheres in mixed convection air flow ($Pr = 0.7$) were reported by Yuge (1960) for assisting, opposing, and cross flows in the domain where $3.5 < Re_d < 5.9 \times 10^3$ and $1 < Gr_d < 10^5$. His measured results can be correlated by the following expressions:

For both assisting and cross flows ($\phi = 0$ and 90 deg):

$$(\overline{Nu}_d - 2)/(\overline{Nu}_{dF} - 2) = [1 + (0.795\Omega)^{3.5}]^{1/3.5} \tag{19}$$

For opposing flow ($\phi = 180$ deg):

$$(\overline{Nu}_d - 2)/(\overline{Nu}_{dF} - 2) = [1 - (0.795\Omega)^3]^{1/3} \tag{20}$$

when $0.795\,\Omega < 1$ and

$$(\overline{Nu}_d - 2)/(\overline{Nu}_{dF} - 2) = [(0.795\Omega)^6 - 1]^{1/6} \tag{21}$$

when $0.795\Omega > 1$.

In equations (19)–(21), $\Omega = (Gr_d/Re_d^2)^{1/4}$ as defined by equation (6) and

$$\overline{Nu}_{dF} - 2 = 0.493\,Re_d^{1/2} \tag{22}$$

for pure forced convection. In the correlations, all fluid properties are evaluated at the film temperature T_f. A reasonably good agreement exists between the measured results and the correlations, as can be seen from Fig. 5.

Conclusion

In this note, correlation equations for mixed convection flows across horizontal cylinders and spheres in air are presented for various ranges of Reynolds and Grashof numbers. These correlation equations can be readily employed to calculate the average Nusselt numbers for the two flow configurations at different flow domains. The correlations are

seen to agree well with experimental data. A single correlation equation for cylinders in both assisting and cross flows that covers the entire range of Reynolds and Grashof numbers is also presented.

Acknowledgments

This study was supported in part by a research grant from the National Science Foundation (NSF MEA 83-00785).

References

Badr, H. M., 1983, "A Theoretical Study of Laminar Mixed Convection From a Horizontal Cylinder in a Cross Stream," *International Journal of Heat and Mass Transfer*, Vol. 26, pp. 639–653.

Badr, H. M., 1984, "Laminar Combined Convection From a Horizontal Cylinder—Parallel and Contra Flow Regimes," *International Journal of Heat and Mass Transfer*, Vol. 27, pp. 15–27.

Churchill, S. W., 1983, "Combined Free and Forced Convection Around Immersed Bodies," in: *Heat Transfer Handbook*, Chap. 2.5.9, Hemisphere, Washington, DC.

Hatton, A. P., James, D. D., and Swire, H. W., 1970, "Combined Forced and Natural Convection With Low-Speed Air Flow Over Horizontal Cylinders," *Journal of Fluid Mechanics*, Vol. 42, pp. 17–31.

Nakai, S., and Okazaki, T., 1975a, "Heat Transfer From a Horizontal Circular Wire at Small Reynolds and Grashof Numbers—II. Mixed Convection," *International Journal of Heat and Mass Transfer*, Vol. 18, pp. 397–413.

Nakai, S., and Okazaki, T., 1975b, "Heat Transfer From a Horizontal Circular Wire at Small Reynolds and Grashof Numbers—I. Pure Convection," *International Journal of Heat and Mass Transfer*, Vol. 18, pp. 387–396.

Oosthuizen, P. H., and Madan, S., 1970, "Combined Convective Heat Transfer From Horizontal Cylinders in Air," ASME JOURNAL OF HEAT TRANSFER, Vol. 92, pp. 194–196.

Oosthuizen, P. H., and Madan, S., 1971, "The Effect of Flow Direction on Combined Convective Heat Transfer From Cylinders to Air," ASME JOURNAL OF HEAT TRANSFER, Vol. 93, pp. 240–242.

Yuge, Y., 1960, "Experiments on Heat Transfer From Spheres Including Combined Natural and Forced Convection," ASME JOURNAL OF HEAT TRANSFER, Vol. 82, pp. 214–220.

Heat Transfer About a Vertical Permeable Membrane

M. Kaviany[1]

Nomenclature

- $\mathrm{Bi} = h\delta/k_e$ = Biot number
- $c = [g\beta(T_h - T_c)/4\nu^2]^{1/4}$, $\mathrm{m}^{-3/4}$
- f = related to stream function
- h = local heat transfer coefficient, $\mathrm{W/m^2\text{-}K}$
- $\mathrm{Gr}_x = g\beta(T_h - T_c)x^3/\nu^2$ = Grashof number
- k = thermal conductivity, W/m-K
- $\mathrm{Nu}_x = hx/k_f$ = Nusselt number
- $\mathrm{Pe} = v_w\delta/\alpha_e$ = Peclet number
- $\mathrm{Pr} = \nu/\alpha_f$ = Prandtl number
- q_T = local net heat flux, $\mathrm{W/m^2}$
- Q_T = total net heat flow, W
- $\mathrm{Re} = v_w\delta/\nu$ = Reynolds number
- u, v = vertical and horizontal components of velocity, m/s
- v_w = seepage velocity, m/s
- x, y = coordinate axes in the vertical and horizontal directions, m
- $X, Y = x/\delta, y/\delta$
- α = thermal diffusivity, $\mathrm{m^2/s}$
- β = volumetric thermal expansion coefficient, 1/K
- δ_1, δ_2 = boundary layer thicknesses, m
- δ = membrane thickness, m
- $\Delta = \delta/L$ = dimensionless membrane thickness
- $\eta = cy/x^{1/4}$ = similarity variable
- $\theta = (T - T_c/(T_h - T_c)$ = dimensionless temperature
- $\kappa = k_e/k_f$
- ν = kinematic viscosity, $\mathrm{m^2/s}$
- $\xi = v_w x/2^{3/2}\,\nu\mathrm{Gr}_x^{1/2}$ = expansion variable
- ρ = density, $\mathrm{kg/m^3}$

Superscripts

- $\bar{}$ = integrated over L; $\bar{Q}_T = \frac{1}{L}\int_0^L Q_T dx$
- 0 = zeroth-order
- 1 = first-order

Subscripts

- 1, 2 = hot, cold fluid
- L = based on L
- c = critical
- e = effective
- f = fluid
- x, y, η = x, y, η derivatives

1 Introduction

The natural convection heat transfer about both sides of vertical walls without any seepage has been studied (Lock and Ko, 1973; Anderson and Bejan, 1980; Viskanta and Lankford, 1981; Sparrow and Prakash, 1981) and the effects of the wall thickness and thermal conductivity on the local and average heat transfer rates have been determined. Viskanta and Lankford (1981) have concluded that in predicting the heat transfer rate through the wall, for low-thermal-conductivity walls the a priori unknown wall surface temperatures can be estimated as the arithmetic average of the reservoir temperatures without loss of accuracy (for most practical situations). Sparrow and Prakash (1981) treated the surface temperature as variable but used the local temperature along with the available isothermal boundary-layer analysis for determination of the local heat transfer rate and found this to be reasonable at relatively low Grashof numbers.

In this study the heat transfer rate between two reservoirs of different temperatures connected in part through a permeable membrane is analyzed. Rather than solving the complete problem numerically for the three domains (fluid–wall–fluid), the available results on the effects of suction and blowing on the natural convection boundary layer are used in an analysis of the membranes with low thermal conductivity and small seepage velocities, which are characteristic of the membranes considered. This will lead to rather simple expressions for the determination of the heat transfer rate. Figure 1 gives a schematic diagram of the problem considered.

2 Analysis

2.1 Fluids. The presence of suction and blowing is accommodated using the first-order expansion solution given by Sparrow and Cess (1961), which uses a perturbation parameter

$$\xi = \frac{v_w x}{2^{3/2}\nu\mathrm{Gr}_x^{1/4}} = \frac{\mathrm{Re}\; x/\delta}{2^{3/2}\mathrm{Gr}_x^{1/4}} \tag{1}$$

[1]Department of Mechanical Engineering and Applied Mechanics, The University of Michigan, Ann Arbor, MI 48109.

Contributed by the Heat Transfer Division for publication in the JOURNAL OF HEAT TRANSFER. Manuscript received by the Heat Transfer Division June 25, 1987. Keywords: Conjugate Heat Transfer, Modeling and Scaling, Natural Convection.

seen to agree well with experimental data. A single correlation equation for cylinders in both assisting and cross flows that covers the entire range of Reynolds and Grashof numbers is also presented.

Acknowledgments

This study was supported in part by a research grant from the National Science Foundation (NSF MEA 83-00785).

References

Badr, H. M., 1983, "A Theoretical Study of Laminar Mixed Convection From a Horizontal Cylinder in a Cross Stream," *International Journal of Heat and Mass Transfer*, Vol. 26, pp. 639–653.

Badr, H. M., 1984, "Laminar Combined Convection From a Horizontal Cylinder—Parallel and Contra Flow Regimes," *International Journal of Heat and Mass Transfer*, Vol. 27, pp. 15–27.

Churchill, S. W., 1983, "Combined Free and Forced Convection Around Immersed Bodies," in: *Heat Transfer Handbook*, Chap. 2.5.9, Hemisphere, Washington, DC.

Hatton, A. P., James, D. D., and Swire, H. W., 1970, "Combined Forced and Natural Convection With Low-Speed Air Flow Over Horizontal Cylinders," *Journal of Fluid Mechanics*, Vol. 42, pp. 17–31.

Nakai, S., and Okazaki, T., 1975a, "Heat Transfer From a Horizontal Circular Wire at Small Reynolds and Grashof Numbers—II. Mixed Convection," *International Journal of Heat and Mass Transfer*, Vol. 18, pp. 397–413.

Nakai, S., and Okazaki, T., 1975b, "Heat Transfer From a Horizontal Circular Wire at Small Reynolds and Grashof Numbers—I. Pure Convection," *International Journal of Heat and Mass Transfer*, Vol. 18, pp. 387–396.

Oosthuizen, P. H., and Madan, S., 1970, "Combined Convective Heat Transfer From Horizontal Cylinders in Air," ASME JOURNAL OF HEAT TRANSFER, Vol. 92, pp. 194–196.

Oosthuizen, P. H., and Madan, S., 1971, "The Effect of Flow Direction on Combined Convective Heat Transfer From Cylinders to Air," ASME JOURNAL OF HEAT TRANSFER, Vol. 93, pp. 240–242.

Yuge, Y., 1960, "Experiments on Heat Transfer From Spheres Including Combined Natural and Forced Convection," ASME JOURNAL OF HEAT TRANSFER, Vol. 82, pp. 214–220.

Heat Transfer About a Vertical Permeable Membrane

M. Kaviany[1]

Nomenclature

- $\mathrm{Bi} = h\delta/k_e$ = Biot number
- $c = [g\beta(T_h - T_c)/4\nu^2]^{1/4}$, $\mathrm{m}^{-3/4}$
- f = related to stream function
- h = local heat transfer coefficient, $\mathrm{W/m^2\text{-}K}$
- $\mathrm{Gr}_x = g\beta(T_h - T_c)x^3/\nu^2$ = Grashof number
- k = thermal conductivity, W/m-K
- $\mathrm{Nu}_x = hx/k_f$ = Nusselt number
- $\mathrm{Pe} = v_w\delta/\alpha_e$ = Peclet number
- $\mathrm{Pr} = \nu/\alpha_f$ = Prandtl number
- q_T = local net heat flux, $\mathrm{W/m^2}$
- Q_T = total net heat flow, W
- $\mathrm{Re} = v_w\delta/\nu$ = Reynolds number
- u, v = vertical and horizontal components of velocity, m/s
- v_w = seepage velocity, m/s
- x, y = coordinate axes in the vertical and horizontal directions, m
- $X, Y = x/\delta, y/\delta$
- α = thermal diffusivity, $\mathrm{m^2/s}$
- β = volumetric thermal expansion coefficient, 1/K
- δ_1, δ_2 = boundary layer thicknesses, m
- δ = membrane thickness, m
- $\Delta = \delta/L$ = dimensionless membrane thickness
- $\eta = cy/x^{1/4}$ = similarity variable
- $\theta = (T - T_c/(T_h - T_c)$ = dimensionless temperature
- $\kappa = k_e/k_f$
- ν = kinematic viscosity, $\mathrm{m^2/s}$
- $\xi = v_w x/2^{3/2}\,\nu\mathrm{Gr}_x^{1/2}$ = expansion variable
- ρ = density, $\mathrm{kg/m^3}$

Superscripts

- $\bar{}$ = integrated over L; $\bar{Q}_T = \frac{1}{L}\int_0^L Q_T dx$
- 0 = zeroth-order
- 1 = first-order

Subscripts

- 1, 2 = hot, cold fluid
- L = based on L
- c = critical
- e = effective
- f = fluid
- x, y, η = x, y, η derivatives

1 Introduction

The natural convection heat transfer about both sides of vertical walls without any seepage has been studied (Lock and Ko, 1973; Anderson and Bejan, 1980; Viskanta and Lankford, 1981; Sparrow and Prakash, 1981) and the effects of the wall thickness and thermal conductivity on the local and average heat transfer rates have been determined. Viskanta and Lankford (1981) have concluded that in predicting the heat transfer rate through the wall, for low-thermal-conductivity walls the a priori unknown wall surface temperatures can be estimated as the arithmetic average of the reservoir temperatures without loss of accuracy (for most practical situations). Sparrow and Prakash (1981) treated the surface temperature as variable but used the local temperature along with the available isothermal boundary-layer analysis for determination of the local heat transfer rate and found this to be reasonable at relatively low Grashof numbers.

In this study the heat transfer rate between two reservoirs of different temperatures connected in part through a permeable membrane is analyzed. Rather than solving the complete problem numerically for the three domains (fluid–wall–fluid), the available results on the effects of suction and blowing on the natural convection boundary layer are used in an analysis of the membranes with low thermal conductivity and small seepage velocities, which are characteristic of the membranes considered. This will lead to rather simple expressions for the determination of the heat transfer rate. Figure 1 gives a schematic diagram of the problem considered.

2 Analysis

2.1 Fluids. The presence of suction and blowing is accommodated using the first-order expansion solution given by Sparrow and Cess (1961), which uses a perturbation parameter

$$\xi = \frac{v_w x}{2^{3/2}\nu\mathrm{Gr}_x^{1/4}} = \frac{\mathrm{Re}\; x/\delta}{2^{3/2}\mathrm{Gr}_x^{1/4}} \tag{1}$$

[1]Department of Mechanical Engineering and Applied Mechanics, The University of Michigan, Ann Arbor, MI 48109.

Contributed by the Heat Transfer Division for publication in the JOURNAL OF HEAT TRANSFER. Manuscript received by the Heat Transfer Division June 25, 1987. Keywords: Conjugate Heat Transfer, Modeling and Scaling, Natural Convection.

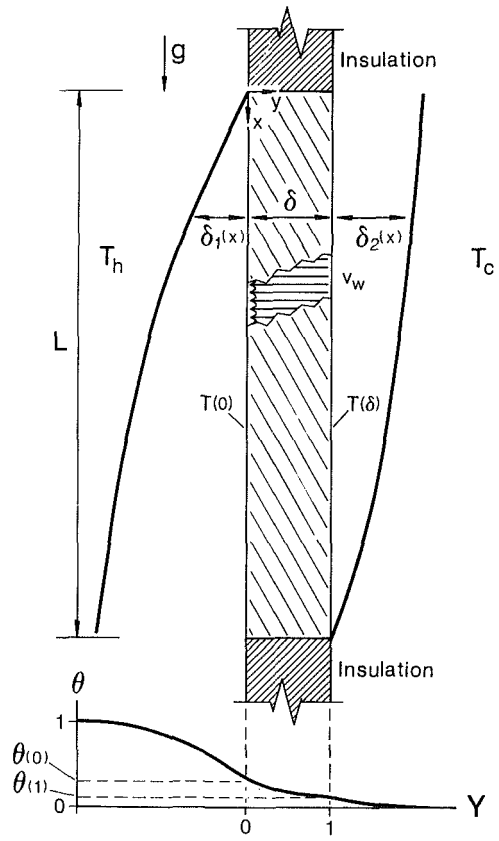

Fig. 1 Schematic of the problem considered

The expansions used are

$$\theta = \sum_{i=0}^{\infty} \theta_i \xi^i,$$

and

$$f = \sum_{i=0}^{\infty} f_i \xi^i.$$

Their results for Pr = 0.72 (which was reproduced for validation) and those obtained numerically here (using a modified Runge–Kutta method) for other Prandtl numbers are given in Table 1. The dimensionless local heat transfer rate is

$$\mathrm{Nu}_x = -\frac{\mathrm{Gr}_x^{1/2}}{2^{1/2}}\left[\theta_\eta^0(0) + \theta_\eta^1(0)\ \frac{\mathrm{Re}\ x/\delta}{2^{3/2}\mathrm{Gr}^{1/4}}\right] = \frac{hx}{k_f} \tag{2}$$

2.2 Membrane. For a prescribed and uniform seepage velocity the energy equation is

$$\mathrm{Pe}\theta_Y = \theta_{YY} + \Delta^2\theta_{XX} \tag{3}$$

For values of $\Delta^2 \ll 1$, the last term makes a negligible contribution and is omitted. The thermal boundary conditions at any vertical position x are continuity of temperature and heat flux. By applying equation (2) for the interfacial heat flux, we have

$$\mathrm{Nu}_{x,1}\ \frac{\delta k_{f,1}}{x k_e}[1-\theta(0)] = \mathrm{Bi}_1[1-\theta(0)] = -\theta_Y(0) \tag{4}$$

$$\mathrm{Nu}_{x,2}\ \frac{\delta k_{f,2}}{x k_e}\ \theta(1) = \mathrm{Bi}_2\theta(1) = -\theta_Y(1) \tag{5}$$

where k_e is the effective stagnant thermal conductivity of the porous medium and is usually determined experimentally. The solution is

Table 1 Numerical results for suction or blowing

Pr	$\theta_\eta^0(0)$	$f_{\eta\eta}^0(0)$	$\theta_\eta^1(0)$	$f_{\eta\eta}^1(0)$
0.1	−0.2315	0.8559	0.2043	−0.9967
0.72	−0.5044	0.6759	1.401	−0.3175
1.0	−0.5670	0.6421	1.931	−0.1583
10	−1.169	0.4193	18.40	1.664
100	−2.191	0.2520	180.4	6.724

$$\theta(Y) = \frac{e^{\mathrm{Pe}Y} - e^{\mathrm{Pe}}\left(\dfrac{\mathrm{Pe}}{\mathrm{Bi}_2}+1\right)}{1 - e^{\mathrm{Pe}} - \mathrm{Pe}\left(\dfrac{1}{\mathrm{Bi}_1}+\dfrac{e^{\mathrm{Pe}}}{\mathrm{Bi}_2}\right)} \tag{6}$$

and the two derivatives appearing in equations (4) and (5) are

$$\theta_Y(0) = \frac{\mathrm{Pe}}{1 - e^{\mathrm{Pe}} - \mathrm{Pe}\left(\dfrac{1}{\mathrm{Bi}_1}+\dfrac{e^{\mathrm{Pe}}}{\mathrm{Bi}_2}\right)} \tag{7}$$

$$\theta_Y(1) = e^{\mathrm{Pe}Y}\theta_Y(0) \tag{8}$$

2.3 System. The local surface temperatures, $\theta(0)$ and $\theta(1)$, and the local heat transfer coefficients, Bi_1 and Bi_2, are not known a priori and must be determined by trial and error. The four equations needed for this determination are equations (4), (5) and equation (2) written for the two sides. The final forms of these four equations are

$$\mathrm{Bi}_1 + \frac{\mathrm{Pe}}{[1-\theta(0)]\left[1 - e^{\mathrm{Pe}} - \mathrm{Pe}\left(\dfrac{1}{\mathrm{Bi}_1}+\dfrac{e^{\mathrm{Pe}}}{\mathrm{Bi}_2}\right)\right]} = 0 \tag{9a}$$

$$\mathrm{Bi}_2 + \frac{\mathrm{Pe}\ e^{\mathrm{Pe}}}{\theta(1)\left[1 - e^{\mathrm{Pe}} - \mathrm{Pe}\left(\dfrac{1}{\mathrm{Bi}_1}+\dfrac{e^{\mathrm{Pe}}}{\mathrm{Bi}_2}\right)\right]} = 0 \tag{9b}$$

$$\frac{\mathrm{Bi}_1\kappa_1}{\Delta} + \frac{\mathrm{Gr}_{L,1}^{1/4}}{2^{1/2}}\left(\frac{x}{L}\right)^{-1/4}[1-\theta(0)]^{1/4}\left[\theta_\eta^0(0) + \theta_\eta^1(0)\ \frac{\mathrm{Re}}{\Delta\ 2^{3/2}\mathrm{Gr}_{L,1}^{1/4}\left(\dfrac{x}{L}\right)^{3/4}[1-\theta(0)]^{1/4}}\right] = 0 \tag{9c}$$

$$\frac{\mathrm{Bi}_2\kappa_2}{\Delta} + \frac{\mathrm{Gr}_{L,2}^{1/4}}{2^{1/2}}\left(1-\frac{x}{L}\right)^{-1/4}\theta(1)^{1/4}\left[\theta_\eta^0(0) - \theta_\eta^1(0)\ \frac{\mathrm{Re}}{\Delta\ 2^{3/2}\mathrm{Gr}_{L,2}^{1/4}\left(1-\dfrac{x}{L}\right)^{3/4}\theta(1)^{1/4}}\right] = 0 \tag{9d}$$

Note that equation (9*c*) is written for blowing and equation (9*d*) for suction.

2.4 Seepage Velocity for a Nearly Adiabatic Wall. The dimensionless local net heat flux to the cold reservoir is

$$q_T = [\mathrm{Pe} + \mathrm{Bi}_2(x)]\theta(1) \tag{10}$$

and for zero local net heat transfer it is required that

$$\mathrm{Pe} = -\mathrm{Bi}_2(x) \tag{11}$$

This condition requires that the thermal energy arriving in the

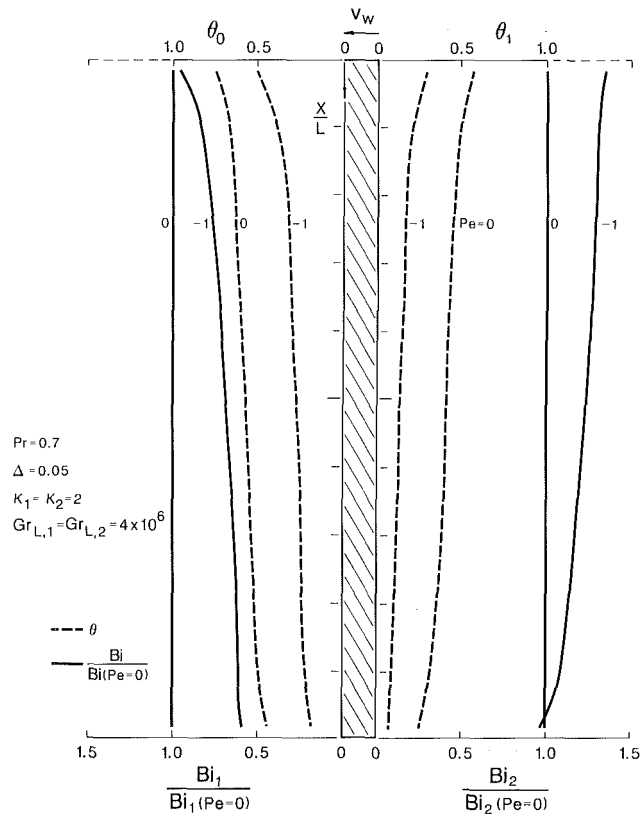

Fig. 2 Variations of temperature and normalized heat transfer coefficient on both sides of the membrane

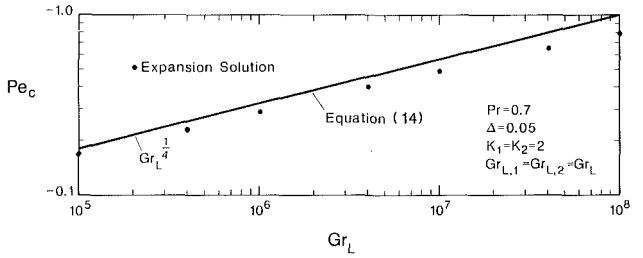

Fig. 3 Comparison between the result of thin membrane approximation (equation (14)) and the result of the more rigorous prediction (equations (9*a–d*) and (12))

boundary layer of the cold reservoir be returned through seepage.

In light of the uniform seepage velocity considered and the vertical nonuniformity of Bi_2, an average seepage velocity resulting in an adiabatic condition along the entire length of the membrane does not exist. As an approximation, a uniform seepage velocity is defined as

$$Pe_c\int_0^1\theta(1)d(x/L)\equiv-\int_0^1 Bi_2(x)\theta(1)d(x/L) \tag{12}$$

Note that this averaging of the heat flow is not physically achievable, because over a portion of the wall it requires seepage heat flow in excess of that conducted through the wall. For a more accurate analysis of the adiabatic wall, variable seepage velocities such as those given by Vedhanayagam et al. (1980) must be considered.

3 Results and Discussion

3.1 Vertical Temperature Distribution. In order to assess the extent of vertical variations in $\theta(0)$, $\theta(1)$, Bi_1, and Bi_2, the case of presence of a gas (at near standard conditions) on both sides of a low-conductivity membrane has been considered. Figure 2 gives the results for $\Delta = 0.05$, $\kappa_1 = \kappa_2 = 2$, and $Gr_{L,1} = Gr_{L,2} = 4 \times 10^6$. The uniform seepage is in the negative y direction, i.e., $Pe \leq 0$. For $Pe = 0$, it is expected that the temperature drop across the membrane $\theta(0) - \theta(1)$ will be nearly uniform along most of the membrane, except at the ends (at the leading edge of each boundary layer), where it becomes large. This trend is found in Fig. 2 for $Pe = 0$. The results also show that except for these leading edge portions, the temperature along either side of the membrane is nearly uniform. For seepage occurring counter to the temperature gradient (i.e., $Pe < 0$) on the left-hand side, the blowing causes a thickening of the boundary layer and the local Biot number becomes smaller than its $Pe = 0$ counterpart. The vertical variation in the normalized Bi_1 shows a similar trend with the maximum reduction in the normalized Biot number occurring at the trailing edge. An opposite trend is found for the suction on the right-hand side of the membrane. Again, except for the small segments near the ends the quantitites of interest, i.e., $\theta(0)$, $\theta(1)$, normalized Bi_1 and Bi_2, are nearly uniform. Note that both Bi_1 and Bi_2 vary along the wall and based on the results given in Fig. 2 their variations are similar to those for the case of $Pe = 0$ (i.e., h decreases in proportion to the 1/4 power of the distance from the leading edge).

3.2 Critical Seepage Velocity. The dimensionless, total heat flow is the integral of equation (10) over the entire length, i.e.,

$$\bar{Q}_T=\int_0^1(Pe+Bi_2)\theta(1)d(x/L) \tag{13}$$

Figure 3 shows the variation in Pe_c with respect to Gr_L ($= Gr_{L,1} = Gr_{L,2}$) for the system considered in Fig. 2. The symbols are for the solutions to equations (9*a–d*). Also shown is an approximation based on neglecting the effect of suction on Bi_2 and taking $\theta(1) = 0.5$. This approximation is obtained by integration of equation (9*d*) and gives

$$-Pe_c=Bi_{2,c}=-\frac{4}{3}\frac{\Delta}{\kappa_2}\frac{\theta_\eta^0(0)}{2^{1/2}}(0.5)^{1/4}Gr_{L,2}^{1/4} \tag{14}$$

or

$$v_{w,c}=0.79\frac{\alpha_f}{L}\theta_\eta^0(0)Gr_{L,2}^{1/4} \tag{15}$$

As is evident, for relatively small values of $Gr_{L,2}$, good agreement exists between this approximation and the results based on the inclusion of the effect of Pe on $\theta(1)$ and Bi(2). As $Gr_{L,2}$ increases these effects become significant and equation (14) becomes less accurate. In general, for accurate estimates of Pe_c, equations (9*a–d*), which include the effects of suction or blowing and heat conduction in the membrane, should be solved simultaneously.

References

Anderson, R., and Bejan, A., 1980, "Natural Convection on Both Sides of a Vertical Wall Separating Fluids at Different Temperature," ASME JOURNAL OF HEAT TRANSFER, Vol. 102, pp. 630–635.

Lock, G. S. H., and Ko, R. S., 1973, "Coupling Through a Wall Between Two Free Convective Systems," *Int. J. Heat Mass Transfer*, Vol. 16, pp. 2087–2096.

Sparrow, E. M., and Cess, R. D., 1961, "Free Convection With Blowing or Suction," ASME JOURNAL OF HEAT TRANSFER, Vol. 83, pp. 387–389.

Sparrow, E. M., and Prakash, C., 1981, "Interaction Between Internal Natural Convection in an Enclosure and an External Natural Convection Boundary-Layer Flow," *Int. J. Heat Mass Transfer*, Vol. 24, pp. 895–907.

Vedhanayagam, M., Altenkrich, R. A., and Eichhon, R., 1980, "A Transformation of the Boundary Layer Equations for Free Convection Past Vertical Flat Plate With Arbitrary Blowing and Wall Temperature Variations," *Int. J. Heat Mass Transfer*, Vol. 23, pp. 1286–1288.

Viskanta, R., and Lankford, D. W., 1981, "Coupling of Heat Transfer Between Two Natural Convection Systems Separated by a Vertical Wall," *Int. J. Heat Mass Transfer*, Vol. 24, pp. 1171–1177.

Free Convection in a Heat-Generating Porous Medium in a Finite Vertical Cylinder

W. E. Stewart, Jr.[1] and C. L. G. Dona[1]

Nomenclature

c_p = bulk specific heat
d = diameter of sphere
g = gravitational acceleration
H = height of cylinder
k_m = bulk thermal conductivity
Nu = Nusselt number = $\dfrac{\Delta T_0}{\Delta T}$
$\bar{P}$ = dimensional pressure
$\dot{q}'''$ = uniform heat generation rate per unit volume
r = radial coordinate direction
R = radius of cylinder
Re = Reynolds number = $v_z\, d/\nu_f$
Ra = modified Rayleigh number
t = time
T = temperature
T_∞ = isothermal boundary temperature
v_r = radial velocity
v_z = axial velocity
z = axial coordinate direction
α = $k_m/(\rho c_p)_f$
β = coefficient of thermal expansion $= 1/T_\infty$
ϵ = porosity
θ = dimensionless temperature = $(T-T_\infty)/(\dot{q}'''RH/k_m)$
κ = bulk permeability
μ = dynamic viscosity
ν_f = kinematic viscosity of fluid $= \mu_\infty/\rho_\infty$
ρ = density
σ = $(\rho c_p)_m/(\rho c_p)_f$
ϕ = volume-averaged temperature difference $= T_{\text{avg}} - T_\infty$
ϕ_0 = volume-averaged temperature difference assuming conduction only
ψ = stream function
$(\rho c_p)_m$ = mean bed value = $(1-\epsilon)(\rho c_p)_s + \epsilon(\rho c_p)_f$

Superscripts

$\bar{}$ = dimensional quantity

Subscripts

f = fluid
m = mean value
∞ = boundary value

[1]Energy Research Laboratory, Department of Mechanical and Aerospace Engineering, University of Missouri–Kansas City, Truman Campus, Independence, MO 64050.

Contributed by the Heat Transfer Division and presented at the ASME/JSME Thermal Engineering Joint Conference, Honolulu, Hawaii, March 1987. Manuscript received by the Heat Transfer Division November 10, 1986. Keywords: Natural Convection, Porous Media.

Introduction

Fluid currents formed in a fluid-saturated porous medium during convective heat transfer have many important applications, such as oil and gas production, cereal grain storage, geothermal energy, and porous insulation. This investigation considers the numerical solution of the steady-state streamlines and isotherms formed by the convective and conduction heat transfer in an air–solid porous medium in an enclosed, short, vertical cylinder. The porous medium is considered to be generating heat uniformly throughout its volume.

Hardee and Nilson (1977) investigated internal heat generation in porous media in rectangular and cylindrical enclosures, where the vertical walls and bottoms were insulated and the tops were held at a constant temperature. They found the temperature difference across the porous bed agreed well with the experimental work of Buretta and Berman (1976) and Elder (1967).

Beukema et al. (1982) were concerned with a situation similar to that considered here, modeling the heat transfer in stored food products. They determined numerically and experimentally the heat transfer characteristics of a rectangular parallelepiped with all surfaces isothermal, filled with a model porous medium material that had a heat capacity and dimensions similar to those of agricultural products. The convective heat transfer was monitored by following the steady-state profile of dimensionless temperature along the central vertical axis with varying heat generation rates.

Gartling (1980) analytically solved the temperature and flow patterns of a heat-generating fluid in a right cylinder with isothermal sides. As the Rayleigh number was increased, the maximum temperature moved off the centerline of the cylinder. The flow patterns remained single cell up to a Rayleigh number of 1.4×10^5. Between Ra = 1.4×10^5 and Ra = 2.85×10^5, a second flow cell formed at the upper centerline.

The situation considered here is a vertical cylinder containing an internally heat-generating porous medium. The cylinder side and top are isothermal and at the same temperature. The bottom surface of the cylinder is adiabatic. These boundary conditions simulate those occurring in a food storage bin with its bottom insulated by the ground and the top and side remaining at the ambient temperature. For the fluid, the thermophysical properties of air are used and for the porous medium a range of thermophysical properties typical of food products (Beukema et al., 1983; Thompson et al., 1971; Sinha and Muir, 1973; Patterson et al., 1971) is used.

Numerical Model

The system modeled is a vertical right circular cylinder of radius R and height H. The cylinder was assumed to be filled with spheres having bulk thermophysical properties typical of agricultural products. The fluid and solid were assumed to be in thermal equilibrium. Using the Boussinesq approximation and the stream function ψ in the Darcy equation, with the nondimensional terms

$$r=\bar{r}/R,\quad z=\bar{z}/R,\quad \psi=\bar{\psi}/(\alpha R),\quad \theta=(T-T_\infty)/(\dot{q}'''RH/k_m),$$
$$\text{and } t=\alpha\bar{t}/R^2$$

results in the single nondimensional energy equation

$$\sigma\frac{\partial\theta}{\partial t}+\frac{1}{r}\frac{\partial\psi}{\partial z}\frac{\partial\theta}{\partial r}-\frac{1}{r}\frac{\partial\psi}{\partial r}\frac{\partial\theta}{\partial z}=\frac{1}{r}\frac{\partial}{\partial r}\left(r\frac{\partial\theta}{\partial r}\right)+\frac{\partial^2\theta}{\partial z^2}+\frac{R}{H} \tag{1}$$

where $\sigma=(\rho c_p)_m/(\rho c_p)_f$.

The nondimensional momentum equation becomes

$$\frac{\partial}{\partial r}\left(\frac{1}{r}\frac{\partial \psi}{\partial r}\right)+\frac{\partial}{\partial z}\left(\frac{1}{r}\frac{\partial \psi}{\partial z}\right)$$

$$=-\frac{g_z\beta\kappa\dot{q}'''R^2H}{\nu_f\alpha k_m}\frac{\partial\theta}{\partial r} \tag{2}$$

The coefficient of $\partial\theta/\partial r$ is the Rayleigh number

$$\mathrm{Ra}=\frac{g_z\beta\kappa(\dot{q}''')R^2H}{\nu_f\,\alpha k_m} \tag{3}$$

The boundary conditions assumed were an isothermal cylinder side and top and an adiabatic cylinder bottom. Stream function values at the cylinder surfaces and axial centerline were set equal to zero, which allowed for slip flow to occur at all surfaces. Thus, the boundary conditions and initial condition for equation (1) are

$$\theta(1,\ z,\ t)=0$$
$$\theta(r,\ H/R,\ t)=0$$
$$\partial\theta(r,\ 0,\ t)/\partial z=0$$
$$\partial\theta(0,\ z,\ t)/\partial r=0$$
$$\theta(r,\ z,\ 0)=0$$

and the boundary conditions for equation (2) are

$$\psi(r,\ 0,\ t)=0$$
$$\psi(r,\ H/R,\ t)=0$$
$$\psi(1,\ z,\ t)=0$$
$$\psi(0,\ z,\ t)=0$$

The Nusselt number was defined similarly to Tveitereid (1967) as

$$\mathrm{Nu}=\frac{\phi_0}{\phi} \tag{4}$$

where ϕ is the volume-averaged mean temperature difference between the porous medium in the cylinder and the boundary temperature and ϕ_0 is the temperature difference in the case of pure conduction.

Equations (1) and (2) were expressed in transient, finite difference form and ψ and θ solved for explicitly, for $H/R = 2$. Equation (1) was used to obtain θ, which were then substituted into equation (2) to obtain new ψ values. This process was continued until the θ and ψ values reached equilibrium. Equilibrium was defined as the point where the temporal change in θ was less than 10^{-6} times the value of θ. If the $(\partial\psi/\partial z)$ $(\partial\theta/\partial r)$ and $(\partial\psi/\partial r)$ $(\partial\theta/\partial z)$ terms in equation (2) are expressed by the combined central, upwind difference scheme proposed by Patankar (1981), the Nusselt number, θ, and ψ values obtained by using central differencing differ by less than 0.1 percent from those obtained by upwind differencing, but the scheme is sometimes unstable. For simplicity and stability, upwind differencing was used for the calculations where convection was present and central differencing was used to calculate the temperature difference expected if conduction was the only mode of heat transfer. A grid size of 31 × 61 was used. Larger grid sizes showed that the Nusselt number results changed less than 1 percent with a doubling of the grid size.

Discussion and Results

As expected from the definition of the Rayleigh number, convection increased with increasing heat generation rate and permeability and decreased with increasing bulk thermal conductivity and outside boundary temperature. The results of Nu for thirty simulations of Ra are shown in Fig. 1.

The effect of a different porosity at the boundaries (boundary effects) was tested by calculating a boundary cell porosity of 0.524 by assuming a stacked sphere arrangement at the cylinder wall and top surface. This compares to a value of 0.43, which was used for the remainder of the cylinder and all other simulations. New values of bulk thermal conductivity, heat capacity, density, and permeability were calculated from the new porosity and used for the boundary cell on the cylinder side and top. The grid size was expanded to 91 × 181, where the cell width was equivalent to approximately two sphere diameters and the cell boundary volume at the top and side of the cylinder was approximately 2.5 percent of the total cylinder volume. The Nusselt numbers resulting from the inclusion of the increased boundary layer porosity were within 1 percent of the Nusselt numbers obtained in the previous cases, where no changes in porosity were assumed at the boundary.

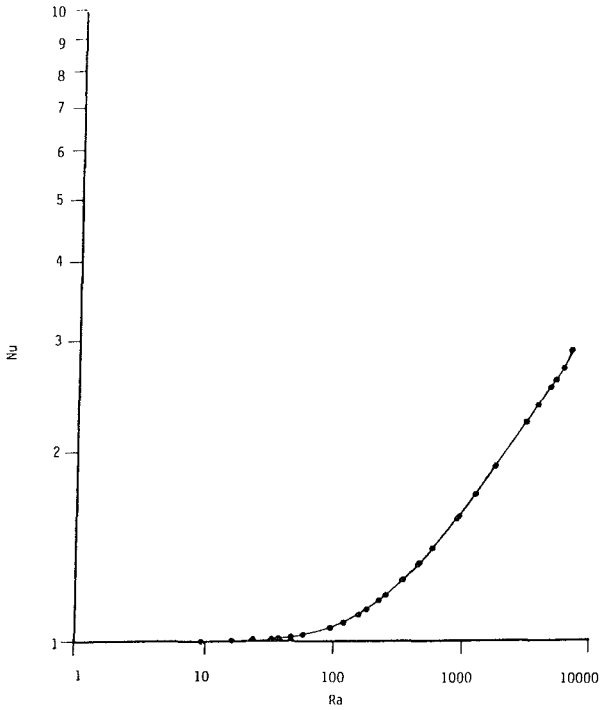

Fig. 1 Nusselt number results for the range of Rayleigh numbers investigated

At Ra = 221.9 the maximum temperature (37.9°C for $T_\infty = 21.°C$) moves off the bottom of the cylinder. The isotherms become compressed near the top of the cylinder and skewed from the horizontal direction. The streamline center moves upward from the conduction solution (Stewart and Dona, 1986), indicating the rising center of air movement and the shifting upward of the maximum temperature.

As Rayleigh number increases the isotherms are further compressed on both the top and side of the cylinder. The isotherms also become more skewed out toward the cylinder side. The streamline center correspondingly moves upward and outward. The maximum temperature in the cylinder at Ra = 1775 was 100°C for T_∞ = 10°C.

As the center of air movement continues to move outward with increasing Rayleigh number, the velocity of the air at the centerline decreases. At approximately Ra = 6700, the velocity at the top center of the cylinder slows enough so the buoyancy forces overcome the inertial forces. As the maximum temperature in the cylinder moves off the center axis (Fig. 2), the cooler, more dense air near the upper centerline of the cylinder begins to move downward in the opposite direction of the air being carried upward in the main convection cell. This results in the formation of multicellular, reverse flow near the centerline (Fig. 3). The maximum internal temperature was 240°C for T_∞ = 33°C.

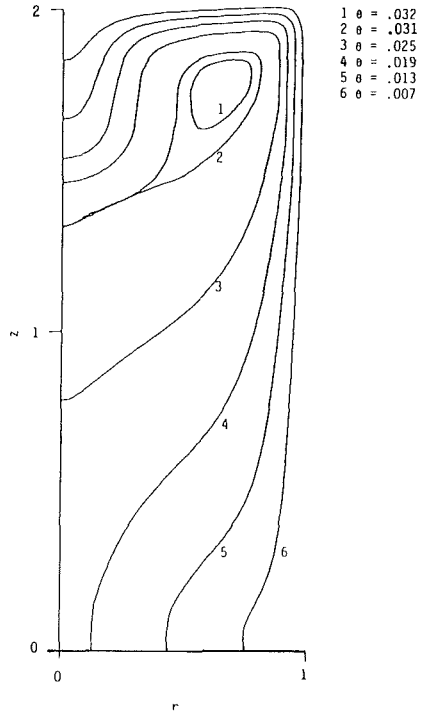

Fig. 2 Dimensionless isotherms for Ra = 6717

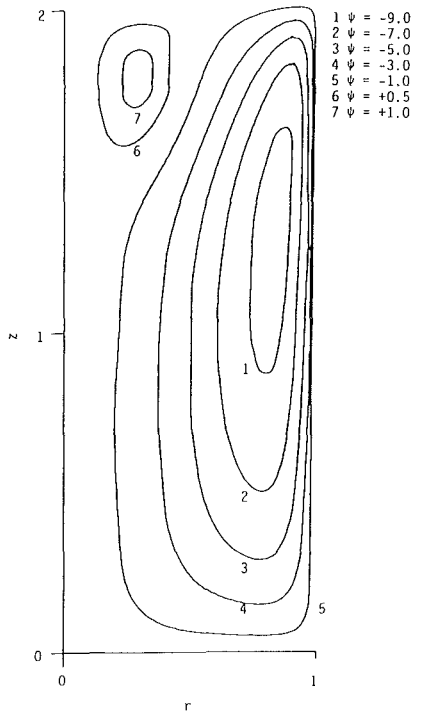

Fig. 3 Dimensionless streamlines for Ra = 6717

The results presented here do not include inertia effects. Different inertia expressions have been suggested as modifications to the Darcy flow equations. Drew and Segal (1971) have proposed a $V\Delta V$ term while Irmay (1958), working with packed beds, has proposed a term of the form $V|V|$. Irmay's general equations have been extended by Patterson et al. (1971) specifically to packed beds of corn. Their formulation is used here to evaluate the relative importance of the inertia effects.

The equation of Patterson et al. (1971) for the pressure drop through packed beds of biological products is of the form

$$\Delta P = Au + Bu^2 \tag{5}$$

where

$$A = k_E\, 150\, \frac{(1-\epsilon)^2}{\epsilon^3}\, \mu\, \frac{h}{d^2}$$

$$B = k_E\, 1.75\, \frac{1-\epsilon}{\epsilon^3}\, \frac{h}{d}\, \rho_f$$

ΔP = pressure drop across the bed

h = bed height

k_E = Ergun product constant

u = velocity

The Darcy flow velocity term Au in equation (5) predominates at low velocities. As the velocity increases, the Bu^2 term becomes more significant, and it predominates for higher velocities.

To evaluate the relative importance of excluding the inertia forces from equations (3) and (4), average values of axial velocities in the cell nearest the side boundary were calculated. This cell was used because the radial velocity at the cylinder sides is small, thus approximating one-dimensional flow. The velocity at the side boundary is also the largest in magnitude anywhere in the cylinder, resulting in potentially the greatest effect due to neglect of inertia terms.

These average velocities were used to calculate Reynolds numbers and ratios of Bu^2 to Au terms for different Rayleigh numbers. For Re $<$ 1 (Ra $<$ 457), the ratio Bu^2/Au is 0.02 or less. For 1 $<$ Re $<$ 10 (Ra = 7000) the magnitude of Bu^2/Au ranged from approximately 2 percent to 15 percent. These results agree qualitatively with Irmay's (1971) predictions of the Bu^2 term being negligible for Re $<$ 1 but becoming significant for Re $>$ 1.

The accuracy of the numerical method was assessed by performing an energy balance on the whole cylinder, to see if the heat loss through the boundaries equaled the total heat generated. For seven simulations between Ra = 53 and Ra = 7400, the differences between heat loss at the boundary and the total heat generated varied between 1.7 percent at Ra = 53 and 7.1 percent at Ra = 1052. These heat balance results show reasonable numerical accuracy.

Conclusions

Numerical results have been obtained using the Darcy formulation for a fluid-saturated heat-generating porous medium contained in a finite vertical cylinder over a range of modified Rayleigh numbers. The stream function formulation of the governing equations was solved using the explicit transient, finite difference technique. Compression of isotherms near the top and side of the cylinder occurred as Rayleigh number increased. Single-cell flow occurred until a Rayleigh number of approximately 7×10^3 was reached, whereupon a smaller, reverse flow region formed near the centerline. This flow transition was accompanied by the movement of the maximum cylinder temperature off the cylinder centerline. Convection increased with increasing heat generation rate and permeability and decreased with increasing bulk thermal conductivity and boundary temperatures.

References

Beukema, K. J., Bruin, S., and Schenk, J., 1983, "Three-Dimensional Natural Convection in a Confined Porous Medium With Internal Heat Generation," *International Journal Heat Mass Transfer*, Vol. 26, pp. 451–458.

Elder, J. W., 1967, "Steady Free Convection in Porous Media Heated From Below," *Journal Fluid Mechanics*, Vol. 27, pp. 29–48.

Drew, D., and Segel, L., 1971, "Averaged Equations for Two Phase Flow," *Studies Appl. Math.*, Vol. 39, pp. 205–215.

Gartling, D. K., 1980, "A Finite Element Analysis of Volumetrically Heated

Fluids in an Axisymmetric Enclosure," *Proceedings, 3rd International Conference on Finite Elements in Flow Problems*, D. H. Norrie, ed., pp. 174–182.

Hardee, H. C., and Nilson, R. H., 1977, "Natural Convection in Porous Media With Heat Generation," *Nuclear Science and Engineering*, Vol. 63, pp. 119–132.

Irmay, S., 1958, "On the Theoretical Derivation of Darcy and Forchheimer Formulae," *Trans. Am. Geophys. Un.*, Vol. 39, pp. 702–706.

Patankar, S. V., 1981, *Numerical Heat Transfer and Fluid Flow*, McGraw-Hill-Hemisphere, New York.

Patterson, R. J., Bakker-Arkema, F. W., and Bickert, W. G., 1971, "Static Pressure Airflow Relationships in Packed Beds of Granular Biological Materials Such as Grain-II," *Trans. Am. Soc. Agric. Engrs.*, Vol. 14, pp. 172–174, 178.

Sinha, R. N., and Muir, W. F., eds., 1973, "Grain Storage: Part of a System," *AVI*, Westport, CT.

Stewart, W. E., Jr., and Dona, C. L. G., 1986, "Low Rayleigh Number Flow in Heat Generating Porous Media," *Int. Comm. Heat and Mass Transfer*, Vol. 13, pp. 281–294.

Thompson, T. L., Villa, L. G., and Cross, O. E., 1971, "Simulated and Experimental Performance of Temperature Control System for Chilled High Moisture Grain Storage," *Trans. Am. Soc. Agric. Engrs.*, pp. 554–559.

Melting of a Solid in Porous Medium Induced by Free Convection of a Warm Dissimilar Fluid

M. Kazmierczak,[1] D. Sadowski,[1] and D. Poulikakos[1]

Nomenclature

c = heat capacity
f = function of the similarity variable
g = gravitational acceleration
k = effective thermal conductivity
K = permeability
L = latent heat of fusion
M = melting parameter, equation (23)
Nu = Nusselt number, equation (26)
P = dimensionless group, equation (25)
q'' = heat transfer rate
Q = dimensionless group, equation (24)
Ra_a = Rayleigh number in the ambient fluid, equation (12)
Ra_m = Rayleigh number in the melt, equation (4)
T = temperature
u = velocity component in the x direction
v = velocity component in the y direction
x = coordinate parallel to the melting front, Fig. 1
x_* = coordinate parallel to the melt/ambient interface, Fig. 1
y = coordinate normal to the melting front
α = effective thermal diffusivity
β_a = coefficient of thermal expansion of the ambient fluid
γ = inclination angle, Fig. 1
δ = melt layer thickness
η = similarity variable
θ = dimensionless temperature
μ = fluid dynamic viscosity
ν = fluid kinematic viscosity
ρ = fluid density
ψ = stream function

Subscripts

a = pertaining to the ambient fluid
$a\infty$ = pertaining to the region of the ambient fluid outside the thermal boundary layer
m = denoting the melt layer
$m\delta$ = denoting the edge of the melt layer ($y = \delta$)
ms = denoting the melting front ($y = 0$)
0 = denoting the region of the solid far from the melting front

[1]Department of Mechanical Engineering, University of Illinois at Chicago, Chicago, IL 60680.

Contributed by the Heat Transfer Division for publication in the JOURNAL OF HEAT TRANSFER. Manuscript received by the Heat Transfer Division February 13, 1987. Keywords: Phase-Change Phenomena, Porous Media.

1 Introduction

Buoyancy-driven flow from a vertical flat plate in porous medium was investigated first by Cheng and Minkowycz (1977). Their results were extended later to the case of cold water natural convection by Ramilison and Gebhart (1980). In two recent studies Epstein and Cho (1976) and Kazmierczak et al. (1986) studied theoretically the effect of forced and natural convection, respectively, on the phenomenon of melting from a flat plate embedded in porous medium.

The present study pertains to a different class of melting problems in porous medium. Unlike the above studies where both the solid and the liquid phase are of the same substance, here melting from a vertical flat plate is initiated by a warm fluid that is dissimilar to the solid phase it surrounds. Therefore, the liquid in the melt layer is dissimilar to the warm liquid outside the melt layer. Of particular interest to the present study is the case where the density difference between the melt and the ambient fluid is considerably greater than that caused by thermal expansion. Hence, the buoyancy force responsible for the motion in the melt layer originates from differences in material densities and not, as is customarily assumed, from temperature differences. Regarding the warm ambient fluid responsible for the initiation and continuation of the melting phenomenon, it is assumed that the temperature gradients existing in the vicinity of the interface between the ambient fluid and the melt region drive a natural convection flow inside the ambient fluid near the melt/ambient fluid interface. This flow is taken into account and its effect on the melting phenomenon is thoroughly investigated. The main application of the basic research reported in this paper is in geophysical heat transfer where melting of the type studied here may occur, resulting in the spreading of pollutants.

2 Mathematical Model

Figure 1 depicts the melting of a vertical surface in porous medium when the melt and the warm ambient fluid are dissimilar. It is assumed that the melt density is considerably

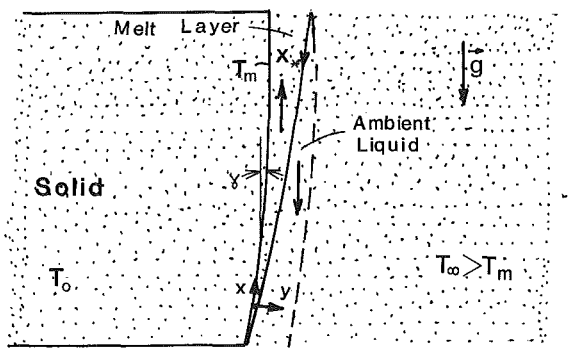

Fig. 1 Schematic of melting of a flat vertical plate in a porous medium saturated with a dissimilar fluid

Fluids in an Axisymmetric Enclosure," *Proceedings, 3rd International Conference on Finite Elements in Flow Problems*, D. H. Norrie, ed., pp. 174–182.

Hardee, H. C., and Nilson, R. H., 1977, "Natural Convection in Porous Media With Heat Generation," *Nuclear Science and Engineering*, Vol. 63, pp. 119–132.

Irmay, S., 1958, "On the Theoretical Derivation of Darcy and Forchheimer Formulae," *Trans. Am. Geophys. Un.*, Vol. 39, pp. 702–706.

Patankar, S. V., 1981, *Numerical Heat Transfer and Fluid Flow*, McGraw-Hill-Hemisphere, New York.

Patterson, R. J., Bakker-Arkema, F. W., and Bickert, W. G., 1971, "Static Pressure Airflow Relationships in Packed Beds of Granular Biological Materials Such as Grain-II," *Trans. Am. Soc. Agric. Engrs.*, Vol. 14, pp. 172–174, 178.

Sinha, R. N., and Muir, W. F., eds., 1973, "Grain Storage: Part of a System," *AVI*, Westport, CT.

Stewart, W. E., Jr., and Dona, C. L. G., 1986, "Low Rayleigh Number Flow in Heat Generating Porous Media," *Int. Comm. Heat and Mass Transfer*, Vol. 13, pp. 281–294.

Thompson, T. L., Villa, L. G., and Cross, O. E., 1971, "Simulated and Experimental Performance of Temperature Control System for Chilled High Moisture Grain Storage," *Trans. Am. Soc. Agric. Engrs.*, pp. 554–559.

Melting of a Solid in Porous Medium Induced by Free Convection of a Warm Dissimilar Fluid

M. Kazmierczak,[1] D. Sadowski,[1] and D. Poulikakos[1]

Nomenclature

c = heat capacity
f = function of the similarity variable
g = gravitational acceleration
k = effective thermal conductivity
K = permeability
L = latent heat of fusion
M = melting parameter, equation (23)
Nu = Nusselt number, equation (26)
P = dimensionless group, equation (25)
q'' = heat transfer rate
Q = dimensionless group, equation (24)
Ra_a = Rayleigh number in the ambient fluid, equation (12)
Ra_m = Rayleigh number in the melt, equation (4)
T = temperature
u = velocity component in the x direction
v = velocity component in the y direction
x = coordinate parallel to the melting front, Fig. 1
x_* = coordinate parallel to the melt/ambient interface, Fig. 1
y = coordinate normal to the melting front
α = effective thermal diffusivity
β_a = coefficient of thermal expansion of the ambient fluid
γ = inclination angle, Fig. 1
δ = melt layer thickness
η = similarity variable
θ = dimensionless temperature
μ = fluid dynamic viscosity
ν = fluid kinematic viscosity
ρ = fluid density
ψ = stream function

Subscripts

a = pertaining to the ambient fluid
$a\infty$ = pertaining to the region of the ambient fluid outside the thermal boundary layer
m = denoting the melt layer
$m\delta$ = denoting the edge of the melt layer ($y = \delta$)
ms = denoting the melting front ($y = 0$)
0 = denoting the region of the solid far from the melting front

1 Introduction

Buoyancy-driven flow from a vertical flat plate in porous medium was investigated first by Cheng and Minkowycz (1977). Their results were extended later to the case of cold water natural convection by Ramilison and Gebhart (1980). In two recent studies Epstein and Cho (1976) and Kazmierczak et al. (1986) studied theoretically the effect of forced and natural convection, respectively, on the phenomenon of melting from a flat plate embedded in porous medium.

The present study pertains to a different class of melting problems in porous medium. Unlike the above studies where both the solid and the liquid phase are of the same substance, here melting from a vertical flat plate is initiated by a warm fluid that is dissimilar to the solid phase it surrounds. Therefore, the liquid in the melt layer is dissimilar to the warm liquid outside the melt layer. Of particular interest to the present study is the case where the density difference between the melt and the ambient fluid is considerably greater than that caused by thermal expansion. Hence, the buoyancy force responsible for the motion in the melt layer originates from differences in material densities and not, as is customarily assumed, from temperature differences. Regarding the warm ambient fluid responsible for the initiation and continuation of the melting phenomenon, it is assumed that the temperature gradients existing in the vicinity of the interface between the ambient fluid and the melt region drive a natural convection flow inside the ambient fluid near the melt/ambient fluid interface. This flow is taken into account and its effect on the melting phenomenon is thoroughly investigated. The main application of the basic research reported in this paper is in geophysical heat transfer where melting of the type studied here may occur, resulting in the spreading of pollutants.

2 Mathematical Model

Figure 1 depicts the melting of a vertical surface in porous medium when the melt and the warm ambient fluid are dissimilar. It is assumed that the melt density is considerably

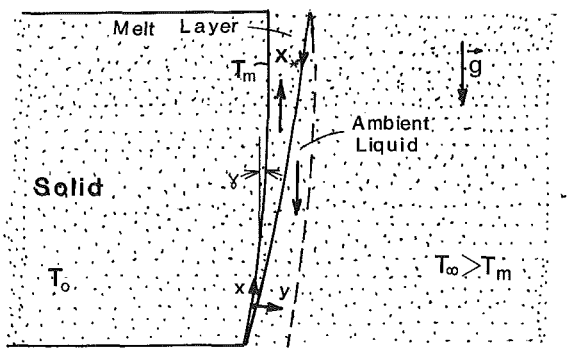

Fig. 1 Schematic of melting of a flat vertical plate in a porous medium saturated with a dissimilar fluid

[1]Department of Mechanical Engineering, University of Illinois at Chicago, Chicago, IL 60680.

Contributed by the Heat Transfer Division for publication in the JOURNAL OF HEAT TRANSFER. Manuscript received by the Heat Transfer Division February 13, 1987. Keywords: Phase-Change Phenomena, Porous Media.

smaller than the ambient fluid density. This accounts for the upward motion of the melt layer. On the other hand, the temperature of the ambient fluid in the vicinity of the melt layer is affected by the melting phenomenon. This cooling effect results in a downward moving, temperature-driven, natural convection boundary layer in the ambient fluid near its interface with the melt layer. Fingering between the two counterflowing layers is not likely to occur because of the large density difference between the two fluids. This point has been proven experimentally and theoretically for the counterpart of this problem in classical fluids (Chen et al., 1986).

To model fluid flow problems in porous media, volumetrically averaged equations are customarily used. This approach will be adopted here, as well. Hence, the moving interface phenomenon of the present problem is similar to the same phenomenon evolving in a continuum medium (melting in classical fluids, for example). The governing equations in the melt region and in the ambient fluid are based on the Darcy flow model (Cheng, 1979). This model works well within its range of validity and has been used extensively for modeling boundary layer flows in porous media with considerable success. However, it is worth recognizing that when dealing with a sparsely packed porous matrix, taking into account the macroscopic shear yields a better approximation of the near-wall region. Our work pertains to a densely packed porous matrix. In addition, no solid wall is present causing imperfections in the packing of the porous medium. Our model simulates the movement of the melting interface in a uniform, solid, densely packed porous matrix.

Several assumptions are made to establish mathematical tractability in the problem. First, since the solid boundary is gradually receding, the coordinate system (Fig. 1) should be time dependent. However, in the limit of slow melting rate, it is reasonable to consider the melting process as quasi-steady. Similar assumptions in melting problems have been adopted by Epstein and Cho (1976a, b), Roberts (1958), and Chen et al. (1986). Second, boundary layer flow and heat transfer are assumed to take place in both fluids. Third, the curvature of the melting interface as well as of the ambient fluid/melt interface is neglected in the manner proposed successfully by Chen et al. (1986), Epstein and Cho (1976a, b), and Taghavi-Tafreshi and Dhir (1982). To this end the inclination angle γ (Fig. 1) is assumed to be small, hence, $\cos\gamma \approx 1 + 0(\gamma^2)$. Fourth, the Boussinesq approximation is used to describe the temperature-driven natural convection process in the ambient fluid. Fifth, the volume change effect is neglected.

With the help of the above assumptions, the mathematical model of the problem accepts a similarity solution. Since the Darcy flow model and the volumetrically averaged energy equation are used frequently in porous media convection studies and since the details of the similarity solution procedure are described in the above-mentioned references, here we show only the final similarity equations and boundary and matching conditions.

For the melt region the following variables are introduced:

$$\eta_m = \mathrm{Ra}_m^{1/2}\frac{y}{x} \tag{1}$$

$$\psi_m = \alpha_m \mathrm{Ra}_m^{1/2} f_m(\eta_m) \tag{2}$$

$$\theta_m = \frac{T_m - T_{ms}}{T_{a\infty} - T_{ms}} \tag{3}$$

where the Rayleigh number Ra_m and the stream function ψ_m are defined as

$$\mathrm{Ra}_m = \frac{K(\rho_{a\infty} - \rho_m)gx}{\mu_m \alpha_m} \tag{4}$$

$$u_m = \frac{\partial \psi_m}{\partial y} \tag{5}$$

$$v_m = -\frac{\partial \psi_m}{\partial x} \tag{6}$$

The quantities η_m and θ_m are the similarity variable and the dimensionless temperature in the melt layer respectively, and $f_m(\eta_m)$ is a function of η_m related to the stream function through equation (2). Based on the above definitions, the transformed momentum and energy equations in the melt layer read

$$f_m' = 1 \tag{7}$$

$$\theta_m'' = -\frac{1}{2} f_m \theta_m' \tag{8}$$

The primes denote differentiation with respect to η_m. The similarity transformation for the ambient fluid boundary layer is based on the following functions:

$$\eta_a = \mathrm{Ra}_a^{1/2}\frac{y-\delta}{x_*} \tag{9}$$

$$\psi_a = \alpha_a \mathrm{Ra}_a^{1/2} f_a(\eta_a) \tag{10}$$

$$\theta_a = \frac{T_a - T_{a\infty}}{T_{ms} - T_{a\infty}} \tag{11}$$

where the Rayleigh number for the ambient fluid is

$$\mathrm{Ra}_a = \frac{Kg\beta_a(T_{a\infty} - T_{ms})x_*}{\nu_a \alpha_a} \tag{12}$$

The notation used in equations (9)–(11) is identical to that used in the melt layer with the subscript a denoting the ambient fluid. The similarity equations for the ambient fluid are

$$f_a' = \theta_a \tag{13}$$

$$\theta_a'' = -\frac{1}{2} f_a \theta_a' \tag{14}$$

The primes in the above equations denote differentiation with respect to η_a. To complete the similarity transformation, the boundary and matching conditions are written in terms of the similarity functions as well

$\eta_m = 0$

$$\theta_m = 0 \tag{15}$$

$$f_m + 2M\theta_m' = 0 \tag{16}$$

$$\theta_m' = \frac{\eta_{m\delta}}{2M} \tag{17}$$

$\eta_m = \eta_{m\delta}$

$$\theta_a = 1 - \theta_m \tag{18}$$

$$\theta_a' = -P\,\theta_m' \tag{19}$$

and $\eta_a = 0$

$$f_a = \frac{Q}{P}\,\theta_a\,\eta_{m\delta} \tag{20}$$

$\eta_a \to \infty$

$$f_a' = 0 \tag{21}$$

$$\theta_a = 0 \tag{22}$$

No details on the boundary and matching conditions are given here for brevity. The physical meaning of these conditions has been discussed in Kazmierczak and Poulikakos (1987), Epstein and Cho (1976a, b), and Taghavi-Tafreshi and Dhir (1982a, b).

Three new dimensionless groups appeared in the similarity equations and are defined as follows:

$$M = \frac{c_m(T_{a\infty} - T_{ms})}{L + C_s(T_{ms} - T_o)} \tag{23}$$

$$Q = \frac{k_m}{k_a} \tag{24}$$

$$P = \left[\frac{\rho_{a\infty} - \rho_m}{\rho_{a\infty}\beta_a(T_{a\infty} - T_{ms})}\,\frac{\mu_a}{\mu_m}\,\frac{\rho_m}{\rho_a}\,\frac{c_m}{c_a}\,\frac{k_m}{k_a}\right]^{1/2} \tag{25}$$

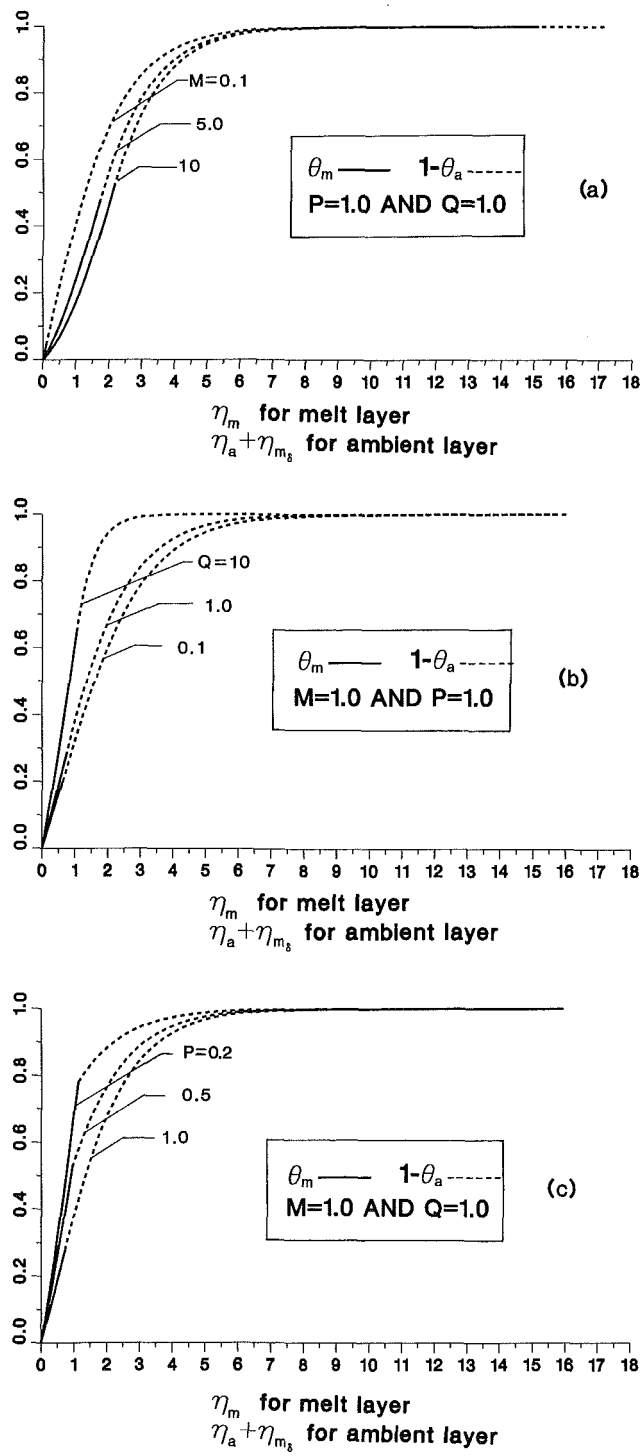

Fig. 2 Temperature variation across the two layers: (*a*) effect of *M*, (*b*) effect of Q, (*c*) the effect of *P*

Physically the first parameter represents the strength of the melting phenomenon and the second parameter the ratio of effective thermal conductivities in the melt and in the ambient fluid. The third parameter involves ratios of several properties in the melt and in the ambient fluid. Note that in the limit of no melting, $M \to 0$, $P \to 1$, $Q \to 1$.

The numerical solution of equations (7), (8), (13), (14), (15)–(22) is obtained with the help of a shooting scheme involving the fourth-order Runge–Kutta method (Ferziger, 1981). At first, $\theta_m'(0)$ is guessed. Based on this guess $f_m(0)$ is obtained from equation (16) and $\eta_{m\delta}$ from equation (17). Next, the numerical integration of equations (7) and (8) is performed starting at $\eta_m = 0$ and ending at $\eta_m = \eta_{m\delta}$. Using the calculated values for θ_m and θ_m' at $\eta_{m\delta}$, the matching conditions (18)–(20) yield θ_a, θ_a', and f_a at $\eta_a = 0$ (or $\eta_m = \eta_{m\delta}$). This information makes possible the numerical integration of equations (13) and (14) from $\eta_a = 0$ to $\eta_a \to \infty$. At the edge of the ambient fluid boundary layer, conditions (21) and (22) are checked. The guessed value of θ_m' (0) is continuously adjusted and the entire process described above is repeated until these conditions are satisfied.

The heat transfer results of this study are reported with the help of the local Nusselt number, defined as

$$\mathrm{Nu} = \frac{q'' x}{(T_{a\infty} - T_{ms}) k_m} = \theta_m'(0)\ \mathrm{Ra}^{1/2} \tag{26}$$

3 Results and Discussion

The main results of this study document the temperature field and heat transfer inside the two boundary layers. We chose to report temperature profiles in the following manner: Both the temperature variation in the melt and in the ambient were reported in the same graph. Solid lines were used for the melt and dashed lines for the ambient fluid. The abscissa for the melt is η_m and for the fluid $\eta_{m\delta} + \eta_a$. Note that since $\eta_a = 0$ at the interface, the above decision was necessary to avoid discontinuities in the numbers of the abscissa scale. Finally, to report a dimensionless temperature variation that is qualitatively similar to the real temperature variation we plotted the quantity $1 - \theta_a$ for the ambient fluid instead of the quantity θ_a. From equations (3) and (11) it can be easily deduced that θ_m and $1 - \theta_a$ are the results of the same nondimensionalization (by using the same reference quantities) of the real temperatures in the melt and in the ambient regions.

Figures 2(*a*) shows the effect of the parameter M on the temperature variation in the system. Increasing M increases the thickness of the melt layer. This result makes sense physically and is readily explained with the help of the definition of M (equation (23)). Increasing M implies the presence of warmer ambient fluid or smaller latent heat or fusion. Both these factors enhance the melting phenomenon and yield a thicker melt layer. An increase in the temperature difference across the melt layer is also observed as M increases.

Next, the effect of the parameter Q on the temperature distribution in the system is illustrated (Fig. 2*b*). Increasing Q appears to increase the thickness of the melt layer as well as the temperature difference across the layer. An additional fact that is obvious in Fig. 2(*b*) is that increasing Q yields a steeper temperature gradient at the wall. This effect is the opposite of what was observed in Fig. 2(*a*), where increasing M decreased the wall temperature gradient.

The impact of the parameter P on the temperature distribution is illustrated in Fig. 2(*c*). The parameter P affects the temperature field in a different manner from parameters M and Q. Increasing P yields a thinner melt layer and considerably decreases the temperature difference across the melt layer. This behavior is exactly the opposite from what was discussed in connection with the parameter Q.

Attention is next shifted to discussion of results pertaining to the heat transfer at the melting front. Figure 3(*a*) shows the effect of M on local heat transfer rate. The solid lines are for a fixed value of Q and different values of P and the dashed lines for a fixed value of P and different values of Q. Except for large values of Q ($Q = 5$, 10) it appears that Nu decreases as the melting parameter increases. It is worth noting that in the limit of no melting ($M = 0$, $P = Q = 1$) the well-known value of $\mathrm{Nu}/\mathrm{Ra}^{1/2}$ obtained by Cheng and Minkowycz (1977) is approached. Increasing P for fixed Q significantly decreases the heat transfer for all values of M. Increasing Q for fixed P, on the other hand, increases the heat transfer. An important

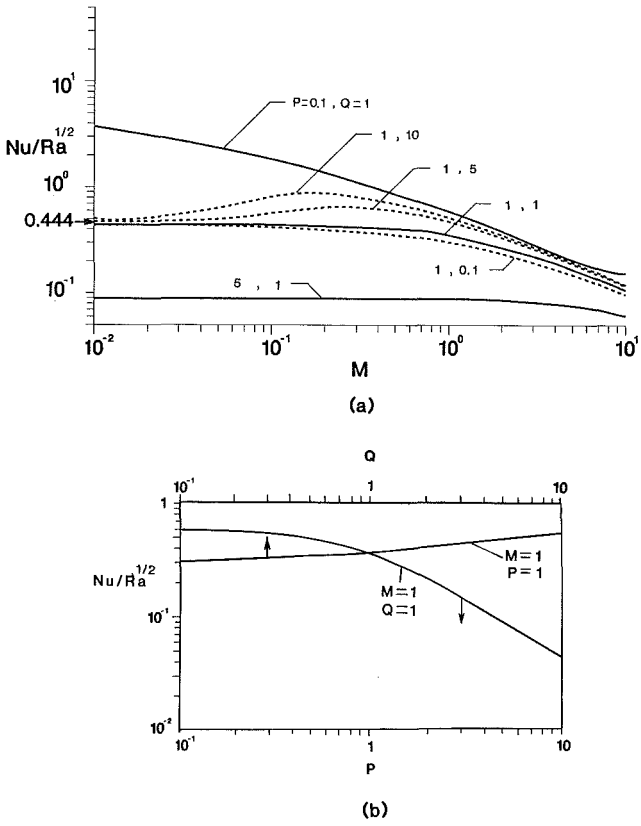

Fig. 3 (*a*) Effect of M on Nu; (*b*) effect of Q and P on Nu

result is that for large values of Q the dependence of Nu on M becomes nonmonotonic. As M increases, Nu increases until a maximum is reached, after which Nu decreases. This maximum shifts to the left as Q increases. From a physical standpoint this result means that if the effective thermal conductivity in the melt is large relative to the effective thermal conductivity in the ambient fluid, an optimum melting rate exists that maximizes the heat transfer at the melting front.

The parameters Q and P affect Nu in opposite ways (Fig. 3*b*). Increasing Q increases Nu while increasing P decreases Nu. The effect of Q is weak. For values of Q less than unity Nu is practically independent of Q.

4 Concluding Remarks

In this paper, the problem of melting of a vertical flat surface in porous medium initiated by a warm dissimilar fluid was investigated. The driving mechanism of the flow in the melt was dominated by the density difference between the melt and the ambient fluid. The flow in the ambient fluid was a natural convection boundary layer driven by thermal buoyancy, in counterflow with the melt.

The main results of this study provided information regarding the temperature distribution in the melt and in the ambient fluid and the heat transfer at the melting front. It was found that increasing the melting parameter M generally decreases the heat transfer in the melting front except for large values of Q. In this case the dependence of Nu on M was nonmonotonic and featured a maximum. This maximum occurred at smaller values of M as Q increased. The dependence of Nu on Q was weak. Increasing Q increased Nu. Finally, increasing the parameter P reduced the heat transfer at the melting front.

Acknowledgment

Support for this research provided by NSF through grant number CBT-8451144 is greatly appreciated.

References

Chen, M. M., Farhadieh, R., and Baker, L., Jr., 1986, "On Free Convection Melting of a Solid Immersed in a Hot Dissimilar Fluid," *Int. J. Heat Mass Transfer*, Vol. 29, pp. 1087–1093.

Cheng, P., and Minkowycz, W. J., 1977, "Free Convection About a Vertical Flat Plate Embedded in a Saturated Porous Medium With Application to Heat Transfer From a Dike," *J. Geophys. Res.*, Vol. 82, pp. 2040–2044.

Cheng, P., 1979, "Heat Transfer in Geothermal Systems," *Advances in Heat Transfer*, Vol. 14, pp. 1–105.

Epstein, M., and Cho, D. H., 1976a, "Melting Heat Transfer in Steady Laminar Flow Over a Flat Plate," ASME JOURNAL OF HEAT TRANSFER, Vol. 98, pp. 531–533.

Epstein, M., and Cho, D. H., 1976b, "Laminar Film Condensation on a Vertical Melting Surface," ASME JOURNAL OF HEAT TRANSFER, Vol. 98, pp. 108–113.

Ferziger, J. H., 1981, *Numerical Methods for Engineering Applications*, Wiley, New York.

Kazmierczak, M., Poulikakos, D., and Pop, I., 1986, "Melting From a Flat Plate Embedded in a Porous Medium in the Presence of Steady Natural Convection," *Numerical Heat Transfer*, Vol. 10, pp. 571–581.

Ramilison, J. M., and Gebhart, B., 1980, "Buoyancy Induced Transport in Porous Media Saturated With Pure or Saline Water at Low Temperatures," *Int. J. Heat Mass Transfer*, Vol. 23, pp. 1521–1531.

Roberts, A. L., 1958, "On the Melting of a Semi-infinite Body Placed in a Warm Stream of Air," *Journal of Fluid Mechanics*, Vol. 4, pp. 505–528.

Taghavi-Tafreshi, K., and Dhir, V. K., 1982a, "Analytical and Experimental Investigation of Simultaneous Melting-Condensation on a Vertical Wall," ASME JOURNAL OF HEAT TRANSFER, Vol. 104, pp. 24–33.

Taghavi-Tafreshi, K., and Dhir, V. K., 1982b, "Shape Change of an Initially Vertical Wall Undergoing Condensation Driven Melting," ASME JOURNAL OF HEAT TRANSFER, Vol. 105, pp. 235–240.

A Note on the Scale Analysis of Phase Change Problems

A. Moutsoglou[1]

The scaling technique used extensively by Bejan (1984) is applied to a phase change problem recently investigated by Cheung (1987). The scaling methodology is a speedy, approximate way of performing a parametric study within an order of magnitude of accuracy. Such a study is presented in this note for examining the growth of a solidified freeze-coat layer on the surface of a chilled continuous plate moving steadily through a quiescent warm liquid. Cheung (1987) studied this problem via a similarity analysis by a combined analytical-computational scheme. His results are utilized as a basis for comparison with the predictions of the present scale analysis.

A schematic of the system configuration is illustrated in Fig. 1. The continuous plate moving steadily with a velocity U issues into a quiescent liquid through a slit ($x=0$). The plate is prechilled and enters the liquid bath at a temperature T_{wi} below the freezing point of the liquid T_f. The temperature of the ambient liquid bath is $T_\infty > T_f$. As indicated in Fig. 1, $\delta(x)$ and $\delta_T(x)$ are, respectively, the velocity and thermal boundary layer thicknesses of the fluid, which moves in the direction of the motion of the plate. The thickness of the freeze coat that forms as the liquid solidifies on the plate surface is denoted by $s(x)$. The determination of the axial variation of $s(x)$ represents the main objective of this note. Finally, $p(x)$ denotes the heat diffusion penetration depth in the thick plate.

Analytical Model

With the coordinate frame fixed at the slit, the governing equations based on the assumptions stated in Cheung have the following form:

[1]Department of Mechanical Engineering, South Dakota State University, Brookings, SD 57007.

Contributed by the Heat Transfer Division for publication in the JOURNAL OF HEAT TRANSFER. Manuscript received by the Heat Transfer Division January 13, 1987. Keywords: Materials Processing and Manufacturing Techniques, Modeling and Scaling, Phase-Change Phenomena.

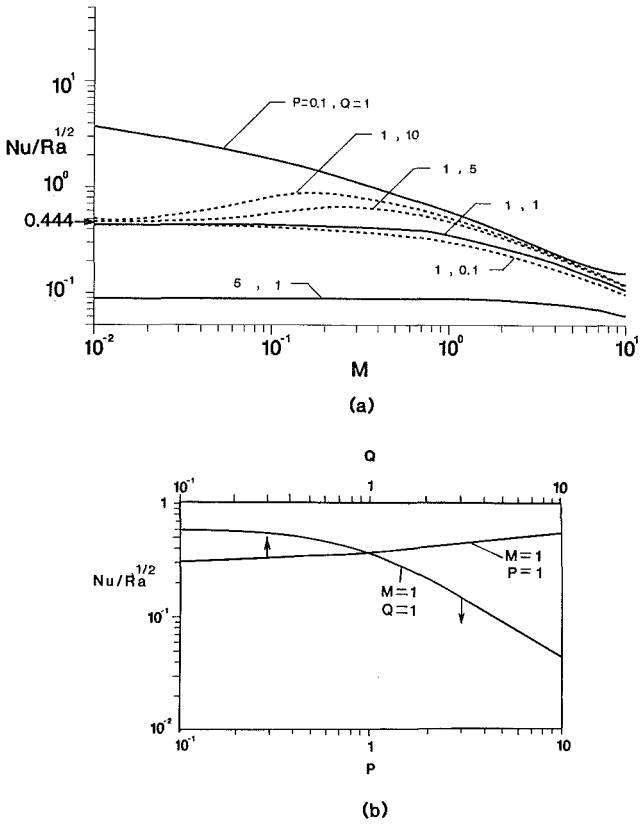

Fig. 3 (*a*) Effect of M on Nu; (*b*) effect of Q and P on Nu

result is that for large values of Q the dependence of Nu on M becomes nonmonotonic. As M increases, Nu increases until a maximum is reached, after which Nu decreases. This maximum shifts to the left as Q increases. From a physical standpoint this result means that if the effective thermal conductivity in the melt is large relative to the effective thermal conductivity in the ambient fluid, an optimum melting rate exists that maximizes the heat transfer at the melting front.

The parameters Q and P affect Nu in opposite ways (Fig. 3*b*). Increasing Q increases Nu while increasing P decreases Nu. The effect of Q is weak. For values of Q less than unity Nu is practically independent of Q.

4 Concluding Remarks

In this paper, the problem of melting of a vertical flat surface in porous medium initiated by a warm dissimilar fluid was investigated. The driving mechanism of the flow in the melt was dominated by the density difference between the melt and the ambient fluid. The flow in the ambient fluid was a natural convection boundary layer driven by thermal buoyancy, in counterflow with the melt.

The main results of this study provided information regarding the temperature distribution in the melt and in the ambient fluid and the heat transfer at the melting front. It was found that increasing the melting parameter M generally decreases the heat transfer in the melting front except for large values of Q. In this case the dependence of Nu on M was nonmonotonic and featured a maximum. This maximum occurred at smaller values of M as Q increased. The dependence of Nu on Q was weak. Increasing Q increased Nu. Finally, increasing the parameter P reduced the heat transfer at the melting front.

Acknowledgment

Support for this research provided by NSF through grant number CBT-8451144 is greatly appreciated.

References

Chen, M. M., Farhadieh, R., and Baker, L., Jr., 1986, "On Free Convection Melting of a Solid Immersed in a Hot Dissimilar Fluid," *Int. J. Heat Mass Transfer*, Vol. 29, pp. 1087–1093.

Cheng, P., and Minkowycz, W. J., 1977, "Free Convection About a Vertical Flat Plate Embedded in a Saturated Porous Medium With Application to Heat Transfer From a Dike," *J. Geophys. Res.*, Vol. 82, pp. 2040–2044.

Cheng, P., 1979, "Heat Transfer in Geothermal Systems," *Advances in Heat Transfer*, Vol. 14, pp. 1–105.

Epstein, M., and Cho, D. H., 1976a, "Melting Heat Transfer in Steady Laminar Flow Over a Flat Plate," ASME JOURNAL OF HEAT TRANSFER, Vol. 98, pp. 531–533.

Epstein, M., and Cho, D. H., 1976b, "Laminar Film Condensation on a Vertical Melting Surface," ASME JOURNAL OF HEAT TRANSFER, Vol. 98, pp. 108–113.

Ferziger, J. H., 1981, *Numerical Methods for Engineering Applications*, Wiley, New York.

Kazmierczak, M., Poulikakos, D., and Pop, I., 1986, "Melting From a Flat Plate Embedded in a Porous Medium in the Presence of Steady Natural Convection," *Numerical Heat Transfer*, Vol. 10, pp. 571–581.

Ramilison, J. M., and Gebhart, B., 1980, "Buoyancy Induced Transport in Porous Media Saturated With Pure or Saline Water at Low Temperatures," *Int. J. Heat Mass Transfer*, Vol. 23, pp. 1521–1531.

Roberts, A. L., 1958, "On the Melting of a Semi-infinite Body Placed in a Warm Stream of Air," *Journal of Fluid Mechanics*, Vol. 4, pp. 505–528.

Taghavi-Tafreshi, K., and Dhir, V. K., 1982a, "Analytical and Experimental Investigation of Simultaneous Melting-Condensation on a Vertical Wall," ASME JOURNAL OF HEAT TRANSFER, Vol. 104, pp. 24–33.

Taghavi-Tafreshi, K., and Dhir, V. K., 1982b, "Shape Change of an Initially Vertical Wall Undergoing Condensation Driven Melting," ASME JOURNAL OF HEAT TRANSFER, Vol. 105, pp. 235–240.

A Note on the Scale Analysis of Phase Change Problems

A. Moutsoglou[1]

The scaling technique used extensively by Bejan (1984) is applied to a phase change problem recently investigated by Cheung (1987). The scaling methodology is a speedy, approximate way of performing a parametric study within an order of magnitude of accuracy. Such a study is presented in this note for examining the growth of a solidified freeze-coat layer on the surface of a chilled continuous plate moving steadily through a quiescent warm liquid. Cheung (1987) studied this problem via a similarity analysis by a combined analytical-computational scheme. His results are utilized as a basis for comparison with the predictions of the present scale analysis.

A schematic of the system configuration is illustrated in Fig. 1. The continuous plate moving steadily with a velocity U issues into a quiescent liquid through a slit ($x=0$). The plate is prechilled and enters the liquid bath at a temperature T_{wi} below the freezing point of the liquid T_f. The temperature of the ambient liquid bath is $T_\infty > T_f$. As indicated in Fig. 1, $\delta(x)$ and $\delta_T(x)$ are, respectively, the velocity and thermal boundary layer thicknesses of the fluid, which moves in the direction of the motion of the plate. The thickness of the freeze coat that forms as the liquid solidifies on the plate surface is denoted by $s(x)$. The determination of the axial variation of $s(x)$ represents the main objective of this note. Finally, $p(x)$ denotes the heat diffusion penetration depth in the thick plate.

Analytical Model

With the coordinate frame fixed at the slit, the governing equations based on the assumptions stated in Cheung have the following form:

[1]Department of Mechanical Engineering, South Dakota State University, Brookings, SD 57007.

Contributed by the Heat Transfer Division for publication in the JOURNAL OF HEAT TRANSFER. Manuscript received by the Heat Transfer Division January 13, 1987. Keywords: Materials Processing and Manufacturing Techniques, Modeling and Scaling, Phase-Change Phenomena.

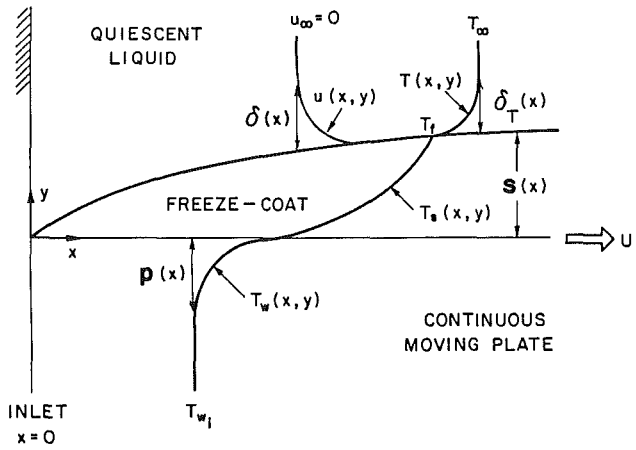

Fig. 1 Schematic and coordinate system

Liquid Boundary Layer Region; $x \geq 0$, $y \geq s(x)$

$$\frac{\partial u}{\partial x} + \frac{\partial v}{\partial y} = 0 \tag{1}$$

$$\frac{\partial}{\partial x}(u^2) + \frac{\partial}{\partial y}(uv) = \nu \frac{\partial^2 u}{\partial y^2} \tag{2}$$

$$\frac{\partial}{\partial x}(uT) + \frac{\partial}{\partial y}(vT) = \alpha \frac{\partial^2 T}{\partial y^2} \tag{3}$$

$$u = 0, \quad T = T_\infty > T_f \qquad \text{at } x = 0 \tag{4a}$$

$$u = U, \quad v = 0, \quad T = T_f \qquad \text{at } y = s(x) \tag{4b}$$

$$u \to 0 \text{ as } y \to s(x) + \delta(x), \qquad T \to T_\infty \text{ as } y \to s(x) + \delta_T(x) \tag{4c}$$

Freeze-Coat Region; $x \geq 0$, $0 \leq y \leq s(x)$

$$\rho_s C_{ps} U \frac{\partial T_s}{\partial x} = k_s \frac{\partial^2 T_s}{\partial y^2} \tag{5}$$

$$s = 0 \qquad \text{at } x = 0 \tag{6a}$$

$$T_s = T_w, \quad k_s \frac{\partial T_s}{\partial y} = k_w \frac{\partial T_w}{\partial y} \qquad \text{at } y = 0 \tag{6b}$$

$$T_s = T_f, \quad \rho_s U h_{if} \frac{ds}{dx} = k_s \frac{\partial T_s}{\partial y} - k \frac{\partial T}{\partial y} \qquad \text{at } y = s \tag{6c}$$

Plate Region; $x \geq 0$, $y \leq 0$

$$\rho_w C_{pw} U \frac{\partial T_w}{\partial x} = k_w \frac{\partial^2 T_w}{\partial y^2} \tag{7}$$

$$T_w = T_{wi} < T_f \qquad \text{at } x = 0 \tag{8a}$$

$$T_w = T_s, \quad k_w \frac{\partial T_w}{\partial y} = k_s \frac{\partial T_s}{\partial y} \qquad \text{at } y = 0 \tag{8b}$$

$$T \to T_{wi} \quad \text{as } y \to -p(x) \tag{8c}$$

It is noted that the normal velocity of the liquid at the solidification surface, due to volumetric changes upon freezing, is not accounted for in this analysis.

Scale Analysis

The governing system of equations (1)–(8) is solved approximately by the scale analysis. The analysis differs in a way from that described by Bejan (1984); here the scaling is done on the integral form of the governing differential equations rather than on the equations themselves. Such a procedure seems to be more direct and yields coefficients associated with the scaled terms.

Integrating the momentum equation (2) over the flow boundary layer thickness $\delta(x)$, and utilizing the flow boundary conditions (4*a*, *b*) results in

$$\rho \frac{d}{dx} \int_{s(x)}^{s+\delta} u^2 dy + \rho \frac{ds}{dx} U^2 = -\mu \frac{\partial u}{\partial y}\bigg|_{y=s(x)} \tag{9}$$

Scaling the above equation yields

$$\rho \frac{U^2}{2} \frac{\delta}{x} + \rho \frac{s}{x} U^2 \sim \mu \frac{U}{\delta} \tag{10}$$

or

$$\frac{\delta}{x} \sim \sqrt{\frac{2}{\mathrm{Re}_x} + \frac{s^2}{x^2}} - \frac{s}{x} \tag{11}$$

To estimate the thermal boundary layer thickness $\delta_T(x)$, the integral form of the energy equation (3) is employed

$$\frac{d}{dx} \int_{s(x)}^{s+\delta_T} u(T - T_\infty) dy + U \frac{ds}{dx}(T_f - T_\infty) = -\alpha \frac{\partial T}{\partial y}\bigg|_{y=s(x)} \tag{12}$$

For fluids with $\delta >> \delta_T$ or $\mathrm{Pr} >> 1$, $u \sim U$ inside the thermal boundary layer, and the scale analysis gives

$$\frac{U}{2} \frac{\delta_T}{x} + U \frac{s}{x} \sim \frac{\alpha}{\delta_T} \tag{13}$$

or

$$\frac{\delta_T}{x} \sim \sqrt{\frac{2}{\mathrm{Re}_x \mathrm{Pr}} + \frac{s^2}{x^2}} - \frac{s}{x} \qquad \text{for } \mathrm{Pr} >> 1 \tag{14}$$

This is in agreement with the Nusselt number trends for continuous moving surfaces reported by Erickson et al. (1966) when s is set to zero.

For fluids with $\delta_T >> \delta$ or $\mathrm{Pr} << 1$, the integral vanishes for $y > \delta$ as the velocity vanishes. Thus, inside the flow boundary layer $T \sim T_f$, and the scale analysis yields

$$\frac{U}{2} \frac{\delta}{x} + U \frac{s}{x} \sim \frac{\alpha}{\delta_T} \tag{15}$$

or

$$\frac{\delta_T}{x} \sim \frac{2}{\mathrm{Re}_x \mathrm{Pr}} \frac{1}{\frac{\delta}{x} + 2\frac{s}{x}} \tag{16}$$

Combining with equation (11) one obtains

$$\frac{\delta_T}{x} \sim \frac{2}{\mathrm{Re}_x \mathrm{Pr}} \frac{1}{\sqrt{\frac{2}{\mathrm{Re}_x} + \frac{s^2}{x^2}} + \frac{s}{x}} \qquad \text{for } \mathrm{Pr} << 1 \tag{17}$$

In order to estimate the freeze-coat thickness $s(x)$, the integral form of equation (5) is considered

$$\rho_s C_{ps} U \int_0^{s(x)} \frac{\partial T_s}{\partial x} dy = k_s \frac{\partial T_s}{\partial y}\bigg|_{s(x)} - k_s \frac{\partial T_s}{\partial y}\bigg|_0 \tag{18}$$

Using the Leibnitz rule, and substituting for the two conduction terms from equations (6*c*) and (6*b*), respectively, one can rewrite equation (18) as follows:

$$\rho_s C_{ps} U \frac{d}{dx} \int_0^{s(x)} T_s dy - \rho_s C_{ps} U T_f \frac{ds}{dx} = \rho_s U h_{if} \frac{ds}{dx} + k \frac{\partial T}{\partial y}\bigg|_{s(x)} - k_w \frac{\partial T_w}{\partial y}\bigg|_0 \tag{19}$$

Equation (19) is then scaled to give

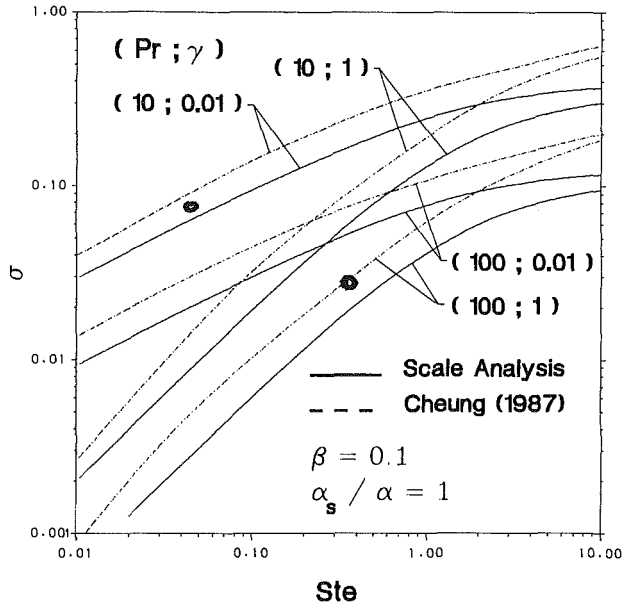

Fig. 2 Freeze-coat thickness versus Stefan number, $\alpha_s/\alpha = 1$, $\beta = 0.1$

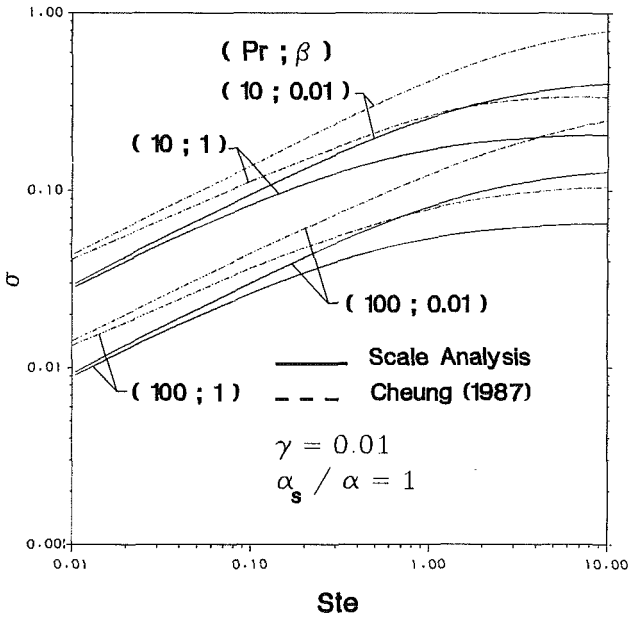

Fig. 3 Freeze-coat thickness versus Stefan number, $\alpha_s/\alpha = 1$, $\gamma = 0.01$

$$\rho_s C_{ps} U \frac{(T_{w0} - T_f)}{2} \frac{s}{x} \sim \rho_s U h_{if} \frac{s}{x} + \frac{k}{\delta_T}(T_\infty - T_f) - k_w \frac{T_{w0} - T_{wi}}{p} \tag{20}$$

where $T_{w0}(x)$ is the surface temperature of the plate at $y = 0$.

In a similar manner, the integral form of the energy equation for the plate, equation (7), can be expressed by

$$\rho_w C_{pw} U \frac{d}{dx} \int_0^{-p(x)} T_w dy + \rho_w C_{pw} U T_{wi} \frac{dp}{dx} = -k_w \frac{\partial T_w}{\partial y}\bigg|_{y=0} \tag{21}$$

and the scaled form as

$$-\rho_w C_{pw} U \frac{(T_{w0} - T_{wi})}{2} \frac{p}{x} \sim -k_w \frac{(T_{w0} - T_{wi})}{p} \tag{22}$$

From equation (22), the heat diffusion penetration depth in the plate is given as

$$p(x) \sim \sqrt{\frac{2\alpha_w x}{U}} \tag{23}$$

The variation of the surface temperature of the plate is estimated from the scaling of equation (8*b*)

$$k_w \frac{T_{w0} - T_{wi}}{p} \sim k_s \frac{T_f - T_{w0}}{s} \tag{24}$$

Substituting equation (23) into (24) and solving for T_{w0} one gets

$$T_{w0}(x) \sim \frac{T_f + \frac{k_w}{k_s}\left(\frac{U}{2\alpha_w x}\right)^{1/2} s T_{wi}}{1 + \frac{k_w}{k_s}\left(\frac{U}{2\alpha_w x}\right)^{1/2} s} \tag{25}$$

Finally, an estimate of the dimensionless freeze-coat thickness σ may be obtained by substituting equations (14) or (17), (23), and (25) into (20) and rearranging

$$\frac{1}{2} \frac{\sigma^2}{2^{1/2}\mathrm{Pr}^{-1/2}\left(\frac{\alpha_s}{\alpha}\right)^{1/2}\gamma + \sigma} + \frac{\sigma}{\mathrm{Ste}} \sim -\beta \frac{\alpha_s}{\alpha} \frac{1}{\sqrt{2\mathrm{Pr} + \sigma^2\mathrm{Pr}^2} - \sigma\mathrm{Pr}} + \frac{\alpha_s}{\alpha} \frac{1}{\mathrm{Pr}} \frac{1}{2^{1/2}\mathrm{Pr}^{-1/2}\left(\frac{\alpha_s}{\alpha}\right)^{1/2}\gamma + \sigma} \tag{26}$$

where the thermal boundary layer thickness δ_T for high Prandtl number fluids was chosen from equation (14).

The dimensionless parameters appearing in equation (26) are defined as

$\sigma = \frac{s}{x}\mathrm{Re}_x^{1/2}$: dimensionless freeze-coat thickness

$\mathrm{Re}_x = \frac{Ux}{\nu}$: Reynolds number

$\mathrm{Pr} = \frac{\nu}{\alpha}$: Prandtl number

$\mathrm{Ste} = \frac{C_{ps}(T_f - T_{wi})}{h_{fi}}$: Stefan number

$\beta = \frac{k(T_\infty - T_f)}{k_s(T_f - T_{wi})}$: liquid superheat parameter

$\gamma = \left(\frac{k_s \rho_s C_{ps}}{k_w \rho_w C_{pw}}\right)^{1/2}$: thermal ratio between freeze coat and plate

$\frac{\alpha_s}{\alpha}$: thermal diffusivity ratio between freeze coat and fluid

Equation (26) is of the form

$$\sigma \sim F(\mathrm{Pr}, \mathrm{Ste}, \beta, \gamma, \alpha_s/\alpha) \tag{27}$$

The scale analysis produced the same five parameters for the dependence of the freeze-coat thickness as those of Cheung, except that the density ratio ρ_s/ρ due to volumetric changes has been neglected in the present study.

Results

To assess the accuracy of the scale analysis employed in this note, the dimensionless freeze-coat thickness σ, estimated from equation (26), is plotted in Figs. 2 and 3, and compared with the results of Cheung, who obtained the freeze-coat thickness from an accurate analytical-computational scheme based on a similarity transformation. The data of Cheung, plotted in Figs. 2 and 3 in this note, are from Figs. 5 and 6 in his paper.

Figures 2 and 3 indicate that the scale analysis successfully predicts the functional dependence of the freeze-coat thickness on the various parameters implied by equation (27). As the physical trends have been discussed adequately by Cheung, only the accuracy of the procedure is further elaborated herein. As seen from the figures, the scale analysis consistently underpredicts the freeze-coat thickness. However, as can be attested from the figures, the accuracy of the scale analysis does not seem to depend strongly on the relative magnitude of the controlling parameters. Thus, in Fig. 2, which is for liquid superheat parameter $\beta = 0.1$, the scale analysis results seem to be shifted by about 30 percent down from those of Cheung, for Stefan numbers up to around 3 for both Prandtl numbers of 10 and 100, and thermal property ratios γ of 0.01 and 1. As the scale analysis results level off faster than those of Cheung, the shift is about 40 percent at Stefan numbers of 10. The corresponding shift in Fig. 3, which is for thermal property ratio $\gamma = 0.01$, is also about 30 percent up to Stefan numbers of 1, but increases again at Stefan numbers of 10 to about 50 and 40 percent, respectively, for liquid superheat parameters β of 0.01 and 1.

Conclusions

The scale analysis is applied to the integral form of the equations that govern the growth of a solidified freeze-coat layer. As little as the effort involved in employing the scaling technique is, it provides satisfactory estimates as evidenced from the present comparison. Finally, a noteworthy benefit of the scale analysis in phase change problems is that it provides the dimensionless parameters pertinent in similarity analyses.

References

Bejan, A., 1984, *Convection Heat Transfer*, Wiley-Interscience, New York.

Cheung, F. B., 1987, "The Thermal Boundary Layer on a Continuous Moving Plate With Freezing," *AIAA Journal of Thermophysics and Heat Transfer*, Vol. 1, No. 4, pp. 335-342.

Erickson, L. E., Cha, L. C., and Fan, L. T., 1966, "The Cooling of a Moving Continuous Flat Sheet," *Heat Transfer*, AIChE Chemical Engineering Progress Symposium Series, Vol. 62, Los Angeles, pp. 157-165.

Scales of Melting in the Presence of Natural Convection in a Rectangular Cavity Filled With Porous Medium

P. Jany[1] and A. Bejan[2]

Introduction

The problem of heat transfer during melting and solidification is relevant in numerous technical applications, for example, in the areas of thermal energy storage, food treatment, soil and groundwater physics, and the design of heat pump heat exchangers buried in the ground. Mathematical solutions based on the pure conduction model have been possible since Stefan's studies last century. Considerably more challenging is the problem of melting and solidification in the presence of convection. The effect of natural convection flow in the melt has been investigated extensively during the last two decades. Experimental work (Rieger et al., 1983; Ho and Viskanta, 1984; Bénard et al., 1985; and references therein) as well as numerical simulations (Ho and Viskanta, 1984; Bénard et al., 1985; Sparrow et al., 1977; Okada, 1984; Gadgil and Gobin, 1984; and references therein) demonstrated that natural convection can have a strong effect on heat transfer rates and on the melting front shape.

Equally relevant to the technological areas mentioned in the preceding paragraph is the phenomenon of phase change in a fluid-porous medium. In a recent paper Aung and Yener (1985) identified this topic as one important unsolved problem, and recommended its future study. Indeed, during the present study we were able to find only a few papers concerning phase change processes in porous media. Freezing has been studied experimentally (Weaver and Viskanta, 1986a; Weaver, 1985; and references therein) and analytically (Weaver amd Viskanta, 1985) by means of a pure heat conduction model. Similarity solutions for the melting process along a flat plate have been developed by considering also the effect of forced convection (Epstein and Cho, 1976; Reid, 1978) and the effect of natural convection (Kazmierczak et al., 1986). Melting in both a horizontal and a vertical cylindrical capsule (Weaver and Viskanta, 1986b) and melting around a horizontal pipe (Okada and Fukumoto, 1982) have been investigated experimentally and analytically.

The present note focuses on the basic problem of melting in a rectangular porous domain heated from the side. The main features of the heat transfer phenomenon are anticipated on the basis of scale analysis. These predictions are later compared with results from a numerical finite-difference simulation.

Problem Statement

A rectangular cavity of length L and height H with impermeable walls is filled with porous medium and solid phase change material. This system is initially at the fusion temperature T_f. All the walls are insulated except the left vertical wall, which, starting at $t = 0$, is heated and maintained at a higher temperature, $T_w > T_f$. If the natural circulation in the domain occupied by liquid phase change material is neglected, the heat transfer solution is the same as in the Stefan problem (Carslaw and Jaeger, 1959)

$$S(\mathrm{Fo}) = 2C\mathrm{Fo}^{1/2} \tag{1}$$

$$\mathrm{Nu}(\mathrm{Fo}) = \frac{1}{\pi^{1/2}\mathrm{erf}(C)}\,\mathrm{Fo}^{-1/2} \tag{2}$$

in which C is the root of the equation

$$\frac{C\,\mathrm{erf}(C)}{\exp(-C^2)} = \frac{\mathrm{Ste}}{\pi^{1/2}} \tag{3}$$

In this solution S represents the horizontal distance measured from the melting front to the heated wall, divided by H. The Nusselt number Nu is based on H, and follows from the integration of the temperature gradients along the heated wall, $\mathrm{Nu} = [-1/(T_w - T_f)]\int_0^H (\partial T/\partial x)_w dy$, where x and y are the horizontal and vertical coordinates, respectively. The dimensionless time Fo and the Stefan number are defined as

$$\mathrm{Fo} = t\,\frac{\alpha}{H^2} \tag{4}$$

$$\mathrm{Ste} = \frac{c_p(T_w - T_f)}{\phi \Delta h} \tag{5}$$

In these definitions t denotes the time, α the thermal diffusivity, c_p the isobaric specific heat, ϕ the porosity, and Δh the latent heat of fusion. The pure conduction solution (1)-(3)

[1]NATO Postdoctoral Fellow, Department of Mechanical Engineering and Materials Science, Duke University, Durham, NC 27706.

[2]Professor, Department of Mechanical Engineering and Materials Science, Duke University, Durham, NC 27706. Fellow ASME.

Contributed by the Heat Transfer Division for publication in the JOURNAL OF HEAT TRANSFER. Manuscript received by the Heat Transfer Division January 13, 1987. Keywords: Natural Convection, Phase-Change Phenomena, Porous Media.

Results

To assess the accuracy of the scale analysis employed in this note, the dimensionless freeze-coat thickness σ, estimated from equation (26), is plotted in Figs. 2 and 3, and compared with the results of Cheung, who obtained the freeze-coat thickness from an accurate analytical-computational scheme based on a similarity transformation. The data of Cheung, plotted in Figs. 2 and 3 in this note, are from Figs. 5 and 6 in his paper.

Figures 2 and 3 indicate that the scale analysis successfully predicts the functional dependence of the freeze-coat thickness on the various parameters implied by equation (27). As the physical trends have been discussed adequately by Cheung, only the accuracy of the procedure is further elaborated herein. As seen from the figures, the scale analysis consistently underpredicts the freeze-coat thickness. However, as can be attested from the figures, the accuracy of the scale analysis does not seem to depend strongly on the relative magnitude of the controlling parameters. Thus, in Fig. 2, which is for liquid superheat parameter $\beta = 0.1$, the scale analysis results seem to be shifted by about 30 percent down from those of Cheung, for Stefan numbers up to around 3 for both Prandtl numbers of 10 and 100, and thermal property ratios γ of 0.01 and 1. As the scale analysis results level off faster than those of Cheung, the shift is about 40 percent at Stefan numbers of 10. The corresponding shift in Fig. 3, which is for thermal property ratio $\gamma = 0.01$, is also about 30 percent up to Stefan numbers of 1, but increases again at Stefan numbers of 10 to about 50 and 40 percent, respectively, for liquid superheat parameters β of 0.01 and 1.

Conclusions

The scale analysis is applied to the integral form of the equations that govern the growth of a solidified freeze-coat layer. As little as the effort involved in employing the scaling technique is, it provides satisfactory estimates as evidenced from the present comparison. Finally, a noteworthy benefit of the scale analysis in phase change problems is that it provides the dimensionless parameters pertinent in similarity analyses.

References

Bejan, A., 1984, *Convection Heat Transfer*, Wiley-Interscience, New York.

Cheung, F. B., 1987, "The Thermal Boundary Layer on a Continuous Moving Plate With Freezing," *AIAA Journal of Thermophysics and Heat Transfer*, Vol. 1, No. 4, pp. 335-342.

Erickson, L. E., Cha, L. C., and Fan, L. T., 1966, "The Cooling of a Moving Continuous Flat Sheet," *Heat Transfer*, AIChE Chemical Engineering Progress Symposium Series, Vol. 62, Los Angeles, pp. 157-165.

Scales of Melting in the Presence of Natural Convection in a Rectangular Cavity Filled With Porous Medium

P. Jany[1] and A. Bejan[2]

Introduction

The problem of heat transfer during melting and solidification is relevant in numerous technical applications, for example, in the areas of thermal energy storage, food treatment, soil and groundwater physics, and the design of heat pump heat exchangers buried in the ground. Mathematical solutions based on the pure conduction model have been possible since Stefan's studies last century. Considerably more challenging is the problem of melting and solidification in the presence of convection. The effect of natural convection flow in the melt has been investigated extensively during the last two decades. Experimental work (Rieger et al., 1983; Ho and Viskanta, 1984; Bénard et al., 1985; and references therein) as well as numerical simulations (Ho and Viskanta, 1984; Bénard et al., 1985; Sparrow et al., 1977; Okada, 1984; Gadgil and Gobin, 1984; and references therein) demonstrated that natural convection can have a strong effect on heat transfer rates and on the melting front shape.

Equally relevant to the technological areas mentioned in the preceding paragraph is the phenomenon of phase change in a fluid-porous medium. In a recent paper Aung and Yener (1985) identified this topic as one important unsolved problem, and recommended its future study. Indeed, during the present study we were able to find only a few papers concerning phase change processes in porous media. Freezing has been studied experimentally (Weaver and Viskanta, 1986a; Weaver, 1985; and references therein) and analytically (Weaver amd Viskanta, 1985) by means of a pure heat conduction model. Similarity solutions for the melting process along a flat plate have been developed by considering also the effect of forced convection (Epstein and Cho, 1976; Reid, 1978) and the effect of natural convection (Kazmierczak et al., 1986). Melting in both a horizontal and a vertical cylindrical capsule (Weaver and Viskanta, 1986b) and melting around a horizontal pipe (Okada and Fukumoto, 1982) have been investigated experimentally and analytically.

The present note focuses on the basic problem of melting in a rectangular porous domain heated from the side. The main features of the heat transfer phenomenon are anticipated on the basis of scale analysis. These predictions are later compared with results from a numerical finite-difference simulation.

Problem Statement

A rectangular cavity of length L and height H with impermeable walls is filled with porous medium and solid phase change material. This system is initially at the fusion temperature T_f. All the walls are insulated except the left vertical wall, which, starting at $t = 0$, is heated and maintained at a higher temperature, $T_w > T_f$. If the natural circulation in the domain occupied by liquid phase change material is neglected, the heat transfer solution is the same as in the Stefan problem (Carslaw and Jaeger, 1959)

$$S(\mathrm{Fo}) = 2C\mathrm{Fo}^{1/2} \tag{1}$$

$$\mathrm{Nu}(\mathrm{Fo}) = \frac{1}{\pi^{1/2}\mathrm{erf}(C)}\,\mathrm{Fo}^{-1/2} \tag{2}$$

in which C is the root of the equation

$$\frac{C\,\mathrm{erf}(C)}{\exp(-C^2)} = \frac{\mathrm{Ste}}{\pi^{1/2}} \tag{3}$$

In this solution S represents the horizontal distance measured from the melting front to the heated wall, divided by H. The Nusselt number Nu is based on H, and follows from the integration of the temperature gradients along the heated wall, $\mathrm{Nu} = [-1/(T_w - T_f)]\int_0^H (\partial T/\partial x)_w dy$, where x and y are the horizontal and vertical coordinates, respectively. The dimensionless time Fo and the Stefan number are defined as

$$\mathrm{Fo} = t\,\frac{\alpha}{H^2} \tag{4}$$

$$\mathrm{Ste} = \frac{c_p(T_w - T_f)}{\phi \Delta h} \tag{5}$$

In these definitions t denotes the time, α the thermal diffusivity, c_p the isobaric specific heat, ϕ the porosity, and Δh the latent heat of fusion. The pure conduction solution (1)-(3)

[1]NATO Postdoctoral Fellow, Department of Mechanical Engineering and Materials Science, Duke University, Durham, NC 27706.

[2]Professor, Department of Mechanical Engineering and Materials Science, Duke University, Durham, NC 27706. Fellow ASME.

Contributed by the Heat Transfer Division for publication in the JOURNAL OF HEAT TRANSFER. Manuscript received by the Heat Transfer Division January 13, 1987. Keywords: Natural Convection, Phase-Change Phenomena, Porous Media.

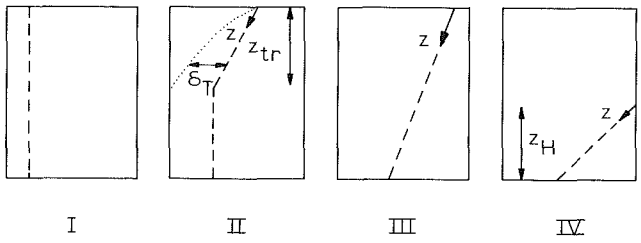

Fig. 1 Four-regime model for scale analysis

breaks down as the natural convection effect in the melt becomes significant, that is when the Rayleigh number Ra_* increases

$$Ra_* = \frac{Kg\beta H(T_w - T_f)}{\alpha\nu} \tag{6}$$

Here K stands for permeability, g for gravitational acceleration, β for thermal expansion coefficient, and ν for kinematic viscosity. The heat transfer scales of the natural convection-melting phenomenon are derived in the next section.

Scale Analysis

In the present problem it is convenient to identify first the four regimes I-IV whose main characteristics are sketched in Fig. 1. The "conduction" regime (I) is ruled by pure thermal diffusion and covered by the exact solution given in equations (1)–(3). The "transition" regime (II) is where the flow carves its own convection-dominated zone in the upper part of the liquid region, while the lower part remains ruled by conduction. The "convection" regime (III) begins when the convection-dominated zone of the preceding regime fills the entire height H. Finally, the arrival of the liquid–solid interface at the right vertical wall marks the beginning of the "variable-height" regime (IV).

Transition Regime. The scales of regimes I and II become apparent if we focus on the transition regime II, where z_{tr} is the height of the convection-dominated upper zone. The boundary layer thickness scale in this upper zone is (e.g., Bejan, 1984, p. 392)

$$\delta_T \sim z_{tr}\left(Ra_* \frac{z_{tr}}{H}\right)^{-1/2} \tag{7}$$

The convection-dominated zone is such that at its lower extremity δ_T is of the same order as the width of the conduction-dominated zone of height $(H - z_{tr})$, in other words

$$z_{tr}\left(Ra_* \frac{z_{tr}}{H}\right)^{-1/2} \sim H(\text{Ste Fo})^{1/2} \tag{8}$$

which means

$$z_{tr} \sim H\, Ra_*\, \text{Ste Fo} \tag{9}$$

The scale of the overall Nusselt number is obtained by adding the conduction heat transfer integrated over the height $(H - z_{tr})$ to the convection heat transfer integrated over the upper portion of height z_{tr}. The result is

$$\text{Nu} \sim (\text{Ste Fo})^{-1/2} + Ra_*(\text{Ste Fo})^{1/2} \tag{10}$$

or, in terms of the average melting front location,

$$S_{av} \sim (\text{Ste Fo})^{1/2} + Ra_*(\text{Ste Fo})^{3/2} \tag{11}$$

S_{av} is the average dimensionless thickness of the melt zone of height H: $S_{av} = \int_0^1 S d(y/H)$, where y is the vertical coordinate. The transition regime II expires when z_{tr} becomes of order H in equation (9), i.e., at a time of order

$$(\text{Ste Fo})_{II} \sim Ra_*^{-1} \tag{12}$$

The most striking feature of this first set of scaling results is the Nu minimum revealed by equation (10). Setting $\partial \text{Nu}/\partial(\text{Ste Fo}) = 0$, we find that the Nu minimum occurs at a time of order

$$(\text{Ste Fo})_{\min} \sim Ra_*^{-1} \tag{13}$$

and that the minimum Nusselt number scale is

$$\text{Nu}_{\min} \sim Ra_*^{1/2} \tag{14}$$

Convection Regime. In this regime the heat transfer and the melting front advance are controlled by the two thermal resistances of thickness δ_T

$$\text{Nu} \sim \int_0^H \delta_T^{-1} dz \sim Ra_*^{1/2} \tag{15}$$

$$S_{av} \sim Ra_*^{1/2}\text{Ste Fo} \tag{16}$$

The convection regime begins at a time of order $\text{Ste Fo} \sim Ra_*^{-1}$, equations (12) and (13), and expires when the melting front reaches the right wall.

Variable-Height Regime. From this time on the height of the liquid–solid interface (z_H) decreases steadily until the solid region disappears entirely. Therefore, even though the liquid-saturated region remains in the convection regime, the vertical length scale in the "effective" Rayleigh number that drives this circulation decreases with time.

We solve for the Nu scale by combining the average melting front position during regime IV

$$S_{av} \sim \frac{L}{H}\left(1 - \frac{1}{2}\frac{z_H}{H}\right) \tag{17}$$

with $dS_{av}/d(\text{Ste Fo}) \sim \text{Nu}$ and

$$\text{Nu} \sim \left(\frac{z_H}{H} Ra_*\right)^{1/2}, \quad (z_H < H) \tag{18}$$

The resulting Nu scale is

$$\text{Nu} \sim Ra_*^{1/2} - \left(\frac{L}{H}\right)^{-1} Ra_*\text{Ste Fo} \tag{19}$$

The average melting front position model (1) is based on the assumption that the base of the solid region always has a length of order L.

The variable-height regime begins at the end of the convection regime III, at a time of order

$$(\text{Ste Fo})_{III} \sim \frac{L}{H} Ra_*^{-1/2} \tag{20}$$

Numerical Results

The governing equations for the conservation of mass, momentum, and energy in the melt as well as the energy-balance condition for the moving solid–liquid interface were solved numerically. The numerical procedure was based on the following assumptions: (*i*) two-dimensional flow, (*ii*) the Darcy flow model for the liquid-saturated part of the system, (*iii*) local thermodynamic equilibrium between (isotropic) porous medium and phase change material, (*iv*) constant thermophysical properties except the density in the buoyancy term (the Boussinesq approximation), and (*v*) negligible volume change during the phase change process. Additionally, the movement of the interface was assumed slow compared with the scales of the fluid flow (small Ste numbers). According to this "quasi-stationary front" approximation the motion of the interface is determined, among other things, by a state of steady natural convection in the melted region.

The physical domain occupied by the melt was transformed analytically into a rectangular solution domain (see, for in-

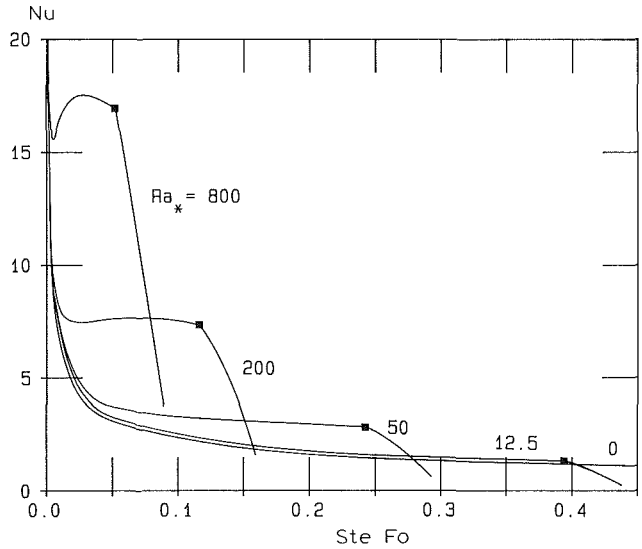

Fig. 2 The Nusselt number as a function of time and Rayleigh number; $L/H = 1$

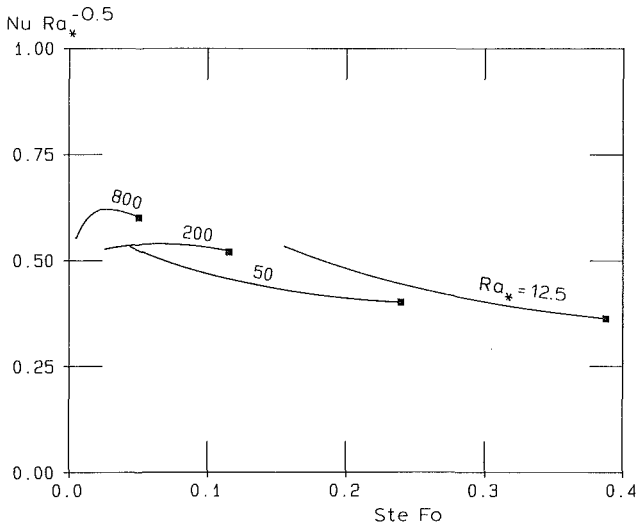

Fig. 3 The Nusselt number scaling law $Nu \sim Nu_*^{1/2}$ in regime III; $L/H = 1$

stance, Okada, 1984). All the terms that were generated by this transformation were taken into acount in the numerical formulation of the problem. The governing equations were solved using staggered grids and the control volume formulation, as proposed by Patankar (1980). All the terms producing heat fluxes were approximated by the power law scheme. Source terms were linearized using the centered difference approximation. The solution method was an "alternative direction implicit" procedure which allows twofold application of the fast and effective Thomas algorithm at every iteration step. The initial stages of the phenomenon were described by the pure conduction solution (1)–(3).

A grid system of 41 × 41 nodal points was chosen as a tradeoff between accuracy, numerical stability, and computation time. For example, one accuracy test consisted of comparing the Nu_{min} values corresponding to $Ra_* = 200$. Increasing the fineness of the grid in the sequence (11×11, 21×21, 31×31, 41×41, 51×51, 61×61) yielded a respective sequence of relative Nu_{min} values (0.956, 0.977, 0.988, 0.994, 0.997, 1.000) and a sequence of relative computational times (0.002, 0.02, 0.10, 0.26, 0.55, 1.000). Each melting run was divided approximately into 100 time steps. The computational times depended on Ra_* and L/H; they were of the order of 5000

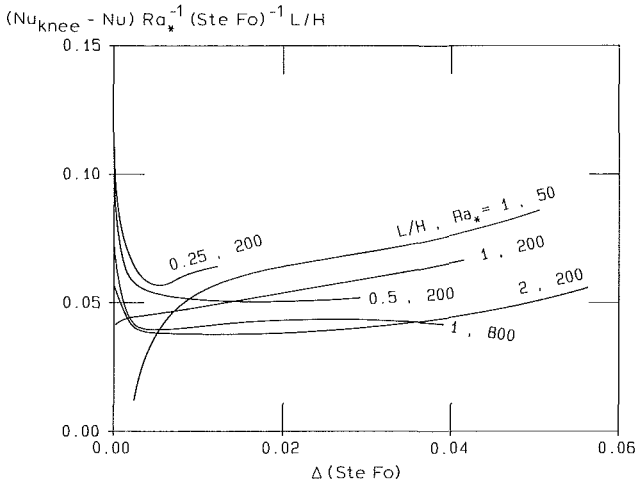

Fig. 4 The Nusselt number scaling law for regime IV

CPU on an IBM 3081 computer. More details concerning the numerical formulation and solution can be found in the original full-length paper version of this note (Jany and Bejan, 1987).

One sample of the numerical results is exhibited in Fig. 2, which shows the Nusselt number versus time (Ste Fo) for different Rayleigh numbers and $L/H = 1$. The square symbol marked on each curve represents the first arrival of the liquid–solid interface at the right vertical wall ("knee point"). This figure shows that the Nusselt number departs significantly from the pure conduction solution ($Ra_* = 0$) as the Rayleigh number increases above approximately 50. At Ra_* values of order 200 and higher, the Nu (Ste Fo) curve has a minimum at "short times," i.e., before the melting front reaches the right wall. This minimum is explained by the scale analysis outlined in the preceding section. Consider then the numerical values calculated for the ratio on $Nu_{min}/Ra_*^{1/2}$

$$\begin{aligned} Nu_{min}/Ra_*^{1/2} &= 0.549 \text{ for } Ra_* = 1200 \\ Nu_{min}/Ra_*^{1/2} &= 0.548 \text{ for } Ra_* = 800 \\ Nu_{min}/Ra_*^{1/2} &= 0.543 \text{ for } Ra_* = 400 \\ Nu_{min}/Ra_*^{1/2} &= 0.526 \text{ for } Ra_* = 200 \end{aligned} \tag{21}$$

The constancy of the numerical $Nu_{min/Ra_*^{1/2}}$ ratio validates the scaling law (14).

The scaling law (15) for the convection regime (III) is tested in Fig. 3, which shows that in the Ra_* domain 12.5–800 the $Nu/Ra_*^{1/2}$ ratio is consistently of order 0.5 during the convection regime. Interesting is that the value of $Nu/Ra_*^{1/2}$ is extremely close to what we expect in the convection regime in a rectangular porous medium, namely, 0.577 (Weber, 1975). In other words, the fact that the phase change deforms the right boundary of the liquid–solid interface has only the minor effect retained in the undulations of the $Nu/Ra_*^{1/2}$ curves of Fig. 3.

Finally, in the variable-height regime (IV) the departure of the Nusselt number from the convection regime plateau ($Nu_{knee} - Nu$) should scale as Ra_* Ste Fo H/L, equation (19). This idea is tested in Fig. 4, where the abscissa shows the time counted after the knee point, Δ(Ste Fo). It is clear that the order of magnitude of the ratio $(Nu_{knee} - Nu)/(Ra_*$ Ste Fo $H/L)$ is sufficiently insensitive to large variations in (Ste Fo), Ra_*, and L/H.

Conclusion

The presented study and its numerical counterpart (Jany and Bejan, 1987) documented the phenomenon of melting in a

rectangular confined porous medium saturated with phase change material. The effect of natural convection was found to be qualitatively similar to what is observed during melting in cavities without porous materials. The main features of the phenomenon were explained on the basis of scale analysis. It was shown that the melting of the entire phase change material passes through a sequence of four regimes (Fig. 1), and that each regime has its own Nusselt number and melting front location scaling rules.

The high-Ra relationship between Nusselt number and time, for example, shows first a decreasing trend (regime I), a minimum (regime II), a plateau (regime III) and, finally, a decreasing trend en route to the disappearance of the solid region which had been serving as heat sink (regime IV). Put together, these trends account for the "van der Waals"-type curves of Nu versus time seen here in Fig. 2 and in analogous studies of melting without a porous matrix (Jany and Bejan, 1988).

Acknowledgments

This study was conducted during Peter Jany's visit as a NATO Postdoctural Fellow at Duke University. The financial support received from NATO through the "Deutscher Akademischer Austausch Dienst" (DAAD) is greatfully acknowledged. Adrian Bejan's research was supported by the Electric Power Research Institute Contract No. RP 8006-4 under the management of Dr. Jong H. Kim.

References

Aung, W., and Yener, Y., 1985, "Research Directions in Natural Convection," *Natural Convection—Fundamentals and Applications*, S. Kakac, W. Aung, and R. Viskanta, eds., Hemisphere, Washington, DC, pp. 1155–1171.

Bejan, A., 1984, *Convection Heat Transfer*, Wiley, New York.

Bénard, C, Gobin, D., and Martinez, F., 1985, "Melting in Rectangular Enclosures: Experiments and Numerical Simulations," ASME JOURNAL OF HEAT TRANSFER, Vol. 107, pp. 794–803.

Carslaw, H. S., and Jaeger, J. C., 1959, *Conduction of Heat in Solids*, Oxford University Press, pp. 282–296.

Epstein, M., and Cho, D. H., 1976, "Melting Heat Transfer in Steady Laminar Flow Over a Flat Plate," ASME JOURNAL OF HEAT TRANSFER, pp. 531–533.

Gadgil, A., and Gobin, D., 1984, "Analysis of Two-Dimensional Melting in Rectangular Enclosures in Presence of Convection," ASME JOURNAL OF HEAT TRANSFER, Vol. 106, pp. 20–26.

Ho, C.-J., and Viskanta, R., 1984, "Heat Transfer During Melting From an Isothermal Vertical Wall," ASME JOURNAL OF HEAT TRANSFER, Vol. 106, pp. 12–19.

Jany, P., and Bejan, A., 1987, "Melting in the Presence of Natural Convection in a Rectangular Cavity Filled with Porous Medium," Report DU-AB-4, Department of Mechanical Engineering and Materials Science, Duke University, Durham,. NC.

Jany, P., and Bejan, A., 1988, "Scaling Theory of Melting With Natural Convection in an Enclosure," *Int. J. Heat Mass Transfer*, Vol. 31, in press.

Kazmierczak, M., Poulikakos, D., and Pop , I., 1986, "Melting From a Flat Plate Embedded in Porous Medium in the Presence of Steady Natural Convection," *Numerical Heat Transfer*, Vol. 10, pp. 571–581.

Okada, M., 1984, "Analysis of Heat Transfer During Melting From a Vertical Wall," *Int. J. Heat Mass Transfer*, Vol. 27, pp. 2057–2066.

Okada, M., and Fukumoto, T., 1982, "Melting Around a Horizontal Pipe Embedded in a Frozen Porous Medium," *Trans. Japan Soc. Mech. Engrs.*, Vol. 48B, pp. 2041–2049 [in Japanese].

Patankar, S. V., 1980, *Numerical Heat Transfer and Fluid Flow*, Hemisphere, Washington, DC.

Reid, R. L., 1978, "Integral Methods for the Melting of Permafrost by Groundwater Flow," *AIChE Symposium Series*, pp. 265–270.

Rieger, H., Projahn, U., Bareiss, M., and Beer, H., 1983, "Heat Transfer During Melting Inside a Horizontal Tube," ASME JOURNAL OF HEAT TRANSFER, Vol. 105, pp. 226–234.

Sparrow, E. M., Patankar, S. V., and Ramadhyani, S., 1977, "Analysis of Melting in the Presence of Natural Convection in the Melt Region," ASME JOURNAL OF HEAT TRANSFER, Vol. 99, pp. 520–526.

Weaver, J. A., 1985, "Solid-Liquid Phase Change Heat Transfer in Porous Media," MSME Thesis, Purdue University, West Lafayette, IN.

Weaver, J. A., and Viskanta, R., 1985, "Freezing of Liquid Saturated Porous Media," *Heat Transfer in Porous Media and Particulate Flows*, L. S. Yao et al., eds., ASME, HTD-Vol. 46, pp. 1–8.

Weaver, J. A., and Viskanta, R., 1986a, "Freezing of Water-Saturated Porous Media in a Rectangular Cavity," *Int. Comm. Heat Mass Transfer*, Vol. 13, pp. 245–252.

Weaver, J. A., and Viskanta, R., 1986b, "Melting of Frozen, Porous Media Contained in a Horizontal or a Vertical, Cylindrical Capsule," *Int. J. Heat Mass Transfer*, Vol. 29, pp. 1943–1951.

Weber, J. E., 1975, "The Boundary Layer Regime for Convection in a Vertical Porous Layer," *Int. J. Heat Mass Transfer*, Vol. 18, pp. 569–573.

Beam Expansion and Focusing Effects on Evaporative Laser Cutting

S. Biyikli[1] and M. F. Modest[2]

Nomenclature

c = specific heat
F_o = laser flux at center of beam in the focal plane
h_{ig} = heat of sublimation
$\mathbf{i}, \mathbf{j}, \mathbf{k}$ = unit vector in x, y, z directions
k = thermal conductivity
$\mathbf{n}$ = unit vector normal to the groove
N_e = evaporative loss number
N_k = conduction loss number
N_w = beam focusing number
N_λ = beam divergence number
R = effective laser beam radius
R_o = laser beam radius at focal plane
s, S = groove depth
$S_{\max}$ = maximum groove depth
$S_\infty(\eta)$ = established groove cross section
T_{ev} = evaporation temperature
T_∞ = ambient temperature
u = laser scanning speed
U = nondimensional scanning speed
w = distance between the focal plane and surface
x, y, z = Cartesian coordinates
α = absorptivity
θ = nondimensional temperature
ξ, η, ζ = nondimensional x, y, z coordinates
ρ = density

Introduction

In recent years there has been a considerable increase in the use of high-power lasers as a tool for material processing, such as welding, trimming, scribing, cutting, etc. [1]. Material processing is achieved by evaporating material with a focused Gaussian laser beam as a heat source. A Gaussian laser beam at TEM_{00} mode is focused by a lens through which the laser beam passes and behind which it converges to a minimum beam waist around the focal point of the lens. With this concentrated energy at the focal point of the lens it is possible to heat, melt, and vaporize any known material. Investigations in the area of laser material processing have treated cases with and without phase change, and a variety of irradiation or source conditions have been studied both theoretically and experimentally. Thermal models may be divided into two main categories: (*i*) models with detailed treatment of thermal conduction (e.g., [2]) and (*ii*) models where details of phase transition (melting, vaporization) are considered [3–6].

[1]Department of Mechanical Engineering, University of Southern California, Los Angeles, CA 90089-1453.

[2]Department of Mechanical Engineering, The Pennsylvania State University, University Park, PA 16802.

Contributed by the Heat Transfer Division and presented at the ASME-JSME Thermal Engineering Joint Conference, Honolulu, Hawaii, March 22–27, 1987. Manuscript received by the Heat Transfer Division November 21, 1986. Keywords: Evaporation, Laser Processing, Materials Processing and Manufacturing Processes.

rectangular confined porous medium saturated with phase change material. The effect of natural convection was found to be qualitatively similar to what is observed during melting in cavities without porous materials. The main features of the phenomenon were explained on the basis of scale analysis. It was shown that the melting of the entire phase change material passes through a sequence of four regimes (Fig. 1), and that each regime has its own Nusselt number and melting front location scaling rules.

The high-Ra relationship between Nusselt number and time, for example, shows first a decreasing trend (regime I), a minimum (regime II), a plateau (regime III) and, finally, a decreasing trend en route to the disappearance of the solid region which had been serving as heat sink (regime IV). Put together, these trends account for the "van der Waals"-type curves of Nu versus time seen here in Fig. 2 and in analogous studies of melting without a porous matrix (Jany and Bejan, 1988).

Acknowledgments

This study was conducted during Peter Jany's visit as a NATO Postdoctural Fellow at Duke University. The financial support received from NATO through the "Deutscher Akademischer Austausch Dienst" (DAAD) is greatfully acknowledged. Adrian Bejan's research was supported by the Electric Power Research Institute Contract No. RP 8006-4 under the management of Dr. Jong H. Kim.

References

Aung, W., and Yener, Y., 1985, "Research Directions in Natural Convection," *Natural Convection—Fundamentals and Applications*, S. Kakac, W. Aung, and R. Viskanta, eds., Hemisphere, Washington, DC, pp. 1155–1171.

Bejan, A., 1984, *Convection Heat Transfer*, Wiley, New York.

Bénard, C, Gobin, D., and Martinez, F., 1985, "Melting in Rectangular Enclosures: Experiments and Numerical Simulations," ASME JOURNAL OF HEAT TRANSFER, Vol. 107, pp. 794–803.

Carslaw, H. S., and Jaeger, J. C., 1959, *Conduction of Heat in Solids*, Oxford University Press, pp. 282–296.

Epstein, M., and Cho, D. H., 1976, "Melting Heat Transfer in Steady Laminar Flow Over a Flat Plate," ASME JOURNAL OF HEAT TRANSFER, pp. 531–533.

Gadgil, A., and Gobin, D., 1984, "Analysis of Two-Dimensional Melting in Rectangular Enclosures in Presence of Convection," ASME JOURNAL OF HEAT TRANSFER, Vol. 106, pp. 20–26.

Ho, C.-J., and Viskanta, R., 1984, "Heat Transfer During Melting From an Isothermal Vertical Wall," ASME JOURNAL OF HEAT TRANSFER, Vol. 106, pp. 12–19.

Jany, P., and Bejan, A., 1987, "Melting in the Presence of Natural Convection in a Rectangular Cavity Filled with Porous Medium," Report DU-AB-4, Department of Mechanical Engineering and Materials Science, Duke University, Durham,. NC.

Jany, P., and Bejan, A., 1988, "Scaling Theory of Melting With Natural Convection in an Enclosure," *Int. J. Heat Mass Transfer*, Vol. 31, in press.

Kazmierczak, M., Poulikakos, D., and Pop , I., 1986, "Melting From a Flat Plate Embedded in Porous Medium in the Presence of Steady Natural Convection," *Numerical Heat Transfer*, Vol. 10, pp. 571–581.

Okada, M., 1984, "Analysis of Heat Transfer During Melting From a Vertical Wall," *Int. J. Heat Mass Transfer*, Vol. 27, pp. 2057–2066.

Okada, M., and Fukumoto, T., 1982, "Melting Around a Horizontal Pipe Embedded in a Frozen Porous Medium," *Trans. Japan Soc. Mech. Engrs.*, Vol. 48B, pp. 2041–2049 [in Japanese].

Patankar, S. V., 1980, *Numerical Heat Transfer and Fluid Flow*, Hemisphere, Washington, DC.

Reid, R. L., 1978, "Integral Methods for the Melting of Permafrost by Groundwater Flow," *AIChE Symposium Series*, pp. 265–270.

Rieger, H., Projahn, U., Bareiss, M., and Beer, H., 1983, "Heat Transfer During Melting Inside a Horizontal Tube," ASME JOURNAL OF HEAT TRANSFER, Vol. 105, pp. 226–234.

Sparrow, E. M., Patankar, S. V., and Ramadhyani, S., 1977, "Analysis of Melting in the Presence of Natural Convection in the Melt Region," ASME JOURNAL OF HEAT TRANSFER, Vol. 99, pp. 520–526.

Weaver, J. A., 1985, "Solid-Liquid Phase Change Heat Transfer in Porous Media," MSME Thesis, Purdue University, West Lafayette, IN.

Weaver, J. A., and Viskanta, R., 1985, "Freezing of Liquid Saturated Porous Media," *Heat Transfer in Porous Media and Particulate Flows*, L. S. Yao et al., eds., ASME, HTD-Vol. 46, pp. 1–8.

Weaver, J. A., and Viskanta, R., 1986a, "Freezing of Water-Saturated Porous Media in a Rectangular Cavity," *Int. Comm. Heat Mass Transfer*, Vol. 13, pp. 245–252.

Weaver, J. A., and Viskanta, R., 1986b, "Melting of Frozen, Porous Media Contained in a Horizontal or a Vertical, Cylindrical Capsule," *Int. J. Heat Mass Transfer*, Vol. 29, pp. 1943–1951.

Weber, J. E., 1975, "The Boundary Layer Regime for Convection in a Vertical Porous Layer," *Int. J. Heat Mass Transfer*, Vol. 18, pp. 569–573.

Beam Expansion and Focusing Effects on Evaporative Laser Cutting

S. Biyikli[1] and M. F. Modest[2]

Nomenclature

c = specific heat
F_o = laser flux at center of beam in the focal plane
h_{ig} = heat of sublimation
$\mathbf{i}, \mathbf{j}, \mathbf{k}$ = unit vector in x, y, z directions
k = thermal conductivity
$\mathbf{n}$ = unit vector normal to the groove
N_e = evaporative loss number
N_k = conduction loss number
N_w = beam focusing number
N_λ = beam divergence number
R = effective laser beam radius
R_o = laser beam radius at focal plane
s, S = groove depth
$S_{\max}$ = maximum groove depth
$S_\infty(\eta)$ = established groove cross section
T_{ev} = evaporation temperature
T_∞ = ambient temperature
u = laser scanning speed
U = nondimensional scanning speed
w = distance between the focal plane and surface
x, y, z = Cartesian coordinates
α = absorptivity
θ = nondimensional temperature
ξ, η, ζ = nondimensional x, y, z coordinates
ρ = density

Introduction

In recent years there has been a considerable increase in the use of high-power lasers as a tool for material processing, such as welding, trimming, scribing, cutting, etc. [1]. Material processing is achieved by evaporating material with a focused Gaussian laser beam as a heat source. A Gaussian laser beam at TEM_{00} mode is focused by a lens through which the laser beam passes and behind which it converges to a minimum beam waist around the focal point of the lens. With this concentrated energy at the focal point of the lens it is possible to heat, melt, and vaporize any known material. Investigations in the area of laser material processing have treated cases with and without phase change, and a variety of irradiation or source conditions have been studied both theoretically and experimentally. Thermal models may be divided into two main categories: (*i*) models with detailed treatment of thermal conduction (e.g., [2]) and (*ii*) models where details of phase transition (melting, vaporization) are considered [3–6].

[1]Department of Mechanical Engineering, University of Southern California, Los Angeles, CA 90089-1453.

[2]Department of Mechanical Engineering, The Pennsylvania State University, University Park, PA 16802.

Contributed by the Heat Transfer Division and presented at the ASME-JSME Thermal Engineering Joint Conference, Honolulu, Hawaii, March 22–27, 1987. Manuscript received by the Heat Transfer Division November 21, 1986. Keywords: Evaporation, Laser Processing, Materials Processing and Manufacturing Processes.

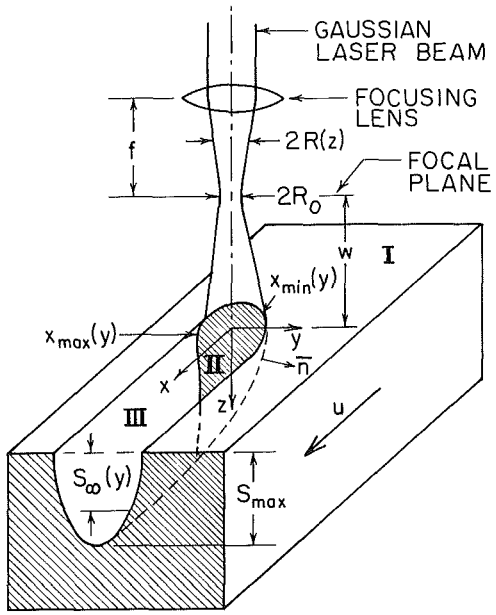

Fig. 1 Cross-sectional view of laser evaporation setup and regimes

Most of the analytical models reported in the literature assumed parallel laser beams, which is a reasonable assumption only when there is no focusing of the beam, or when the focal length of the lens is many times the depth of the groove. In practical applications, material processing is achieved by melting or evaporating material with a Gaussian laser beam, which is focused by a lens to a small spot size around its focal point in order to increase the intensity of the laser beam. The radius of the focused beam waist and subsequent expanison of the beam depend on the characteristics of the laser beam as well as the type of lens being used. Both beam waist and expansion rate have profound effects on the size and shape of the laser cuts. Bar-Isaac and Korn [7] used a three-dimensional moving heat source model to describe the effect of a focused laser beam in the drilling process. They studied the effects of changing focal position of the beam on the motion of the evaporation surface. In the present work, evaporative cutting of a semi-infinite material with a moving, focused continuous-wave laser is considered. The effect of focusing parameters, such as position of lens focal point above or below the surface, minimum beam radius, and beam divergence rate are investigated.

Theoretical Analysis

In order to develop a mathematical model the physical description of the problem is given as follows: A focused Gaussian laser beam strikes the surface of an opaque semi-infinite material moving in the x direction with constant velocity, as shown in Fig. 1. There are three different regimes on the surface of the material. Regime I is that part of the surface that is still too far away to have reached evaporation temperature or too far away on the side to ever reach evaporation; Regime II is the area close to the beam center where evaporation takes place; and finally, Regime III is that part of the surface where evaporation has been completed. The heat transfer model is developed by using the following assumptions, for which a detailed discussion of their implications has been given in Modest and Abakians [6]:

1 The solid moves at constant velocity.

2 The solid is isotropic with constant thermal properties.

3 The material is opaque, i.e., the laser beam does not penetrate appreciably into the medium, with constant absorptivity.

4 Change of phase of the medium from solid to vapor occurs in one step at a single evaporation temperature.

5 The evaporated material does not interfere with the laser beam reaching the surface.

6 Multiple reflections of laser radiation within the groove are neglected.

By using these assumptions and a similar derivation developed by Modest and Abakians [6], the heat transfer model is governed by the following equation:

$$\rho c u \frac{\partial T}{\partial x} = k \nabla^2 T \tag{1}$$

subject to the boundary conditions

$$x \to \pm\infty,\ y \to \pm\infty:\ T \to T_\infty$$

where T is the temperature in the material, and u is the velocity in the x direction. The boundary condition at the surface is obtained from an energy balance on a surface element. Modest and Abakians [6] showed that the influence of convection and radiation losses on groove depth and shape is small and for that reason it is assumed here that heat losses to the outside are negligible. The boundary condition at the surface is then

$$z = s(x, y): \quad \alpha(\mathbf{n}\cdot\mathbf{F}) = -h_{ig}\rho u(\mathbf{n}\cdot\mathbf{i}) - k(\mathbf{n}\cdot\nabla T) \tag{2}$$
$$T = T_{ev} \text{ if } \mathbf{n}\cdot\mathbf{i} < 0 \quad \text{(evaporation zone)}$$

where $\mathbf{F}$ is the laser beam intensity, $\mathbf{n}$ is the unit surface normal pointing into the medium, α is surface absorptivity, h_{ig} is heat of sublimation, and s is the local groove depth. An expression for the laser beam radius $R(z)$ is given by Self [8] as

$$R(z) = R_o\left[1 + \left(\frac{w+z}{\pi R_0^2/\lambda}\right)^2\right]^{1/2} \tag{3}$$

where w is the distance between the focal plane of the lens and the material surface (positive for a focal plane above the surface), λ is the wavelength of the laser, and R_o is the effective laser beam radius at the focal plane. Since laser power for the expanding laser beam must be conserved (no matter what shape surface the beam may strike), the beam intensity may be expressed as

$$\mathbf{F}(x, y, z) = (\mathbf{k} + \tan\theta\cos\phi\mathbf{i} + \tan\theta\sin\phi\mathbf{j})F_o \times \frac{R_o^2}{R^2(z)} e^{-(x^2+y^2)/R^2(z)} \tag{4}$$

where $F_o = P/\pi R_o^2$ is the flux density of the laser beam at the beam center, P is the laser power, $\mathbf{i}$, $\mathbf{j}$, and $\mathbf{k}$ are unit vectors in the x, y, and z directions, θ is the angle between a laser ray and the z axis, and ϕ is the azimuthal angle for the ray measured from the x axis in the x–y plane. Subsituting the laser beam intensity and the surface normal into equation (2) produces nonlinear partial differential equations with surface temperature and groove depth as unknowns [6]. These equations are nondimensionalized by introducing the following variables and parameters:

$$\xi = x/R_o,\quad \eta = y/R_o,\quad \zeta = z/R_o,\quad \Gamma = R/R_o$$
$$S = s(x, y)/R_o,\quad \Theta = (T - T_\infty)/(T_{ev} - T_\infty)$$
Evaporative loss number $N_e = \rho u h_{ig}/\alpha F_o$
Conduction loss number $N_k = k(T_{ev} - T_\infty)/R_o\alpha F_o$ (5)
Nondimensional scanning speed $U = \rho c u R_o/k$
Beam divergence number $N_\lambda = \lambda/\pi R_o$
Beam focusing number $N_w = w/R_o$

The above model is solved by using the following additional assumptions;

7 The diffusion term may be replaced by one-dimensional diffusion in the normal direction, i.e., $\nabla^2\theta \simeq \partial^2\theta/\partial n^2$, where n

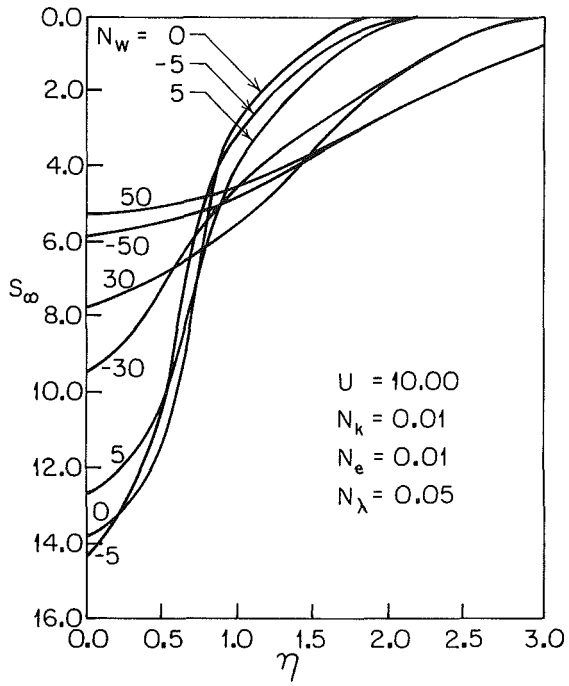

Fig. 2 Effect of focal positions on the groove cross section

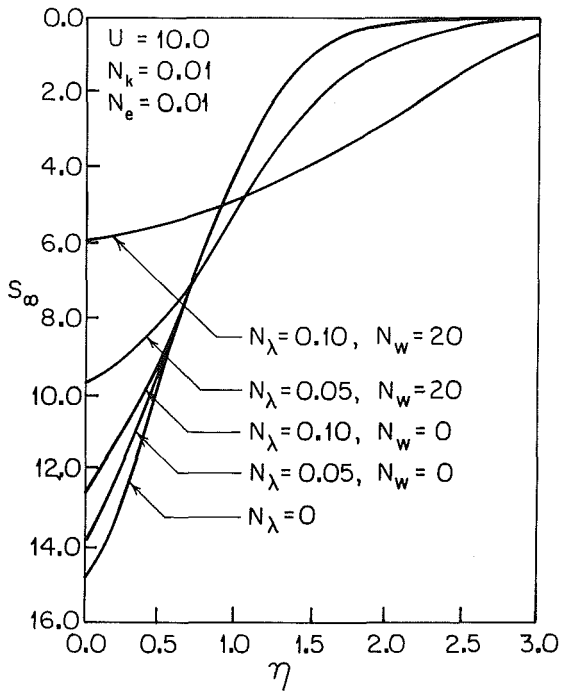

Fig. 3 Effect of beam divergence on the groove cross section

is the distance along the vector **n**, and the conduction equation can be solved by an integral method. With these simplifications and nondimensional variables, the governing equations for different regimes are solved in a similar fashion as described by Modest and Abakians [6].

Discussion of Results

When a beam is focused by a lens, the resulting beam waist and subsequent expansion of the beam depend on the characteristics of the laser beam as well as the type of lens being used. The nondimensional beam divergence number N_λ shows the rate of beam expansion, and N_w indicates the position of the beam waist relative to the solid surface.

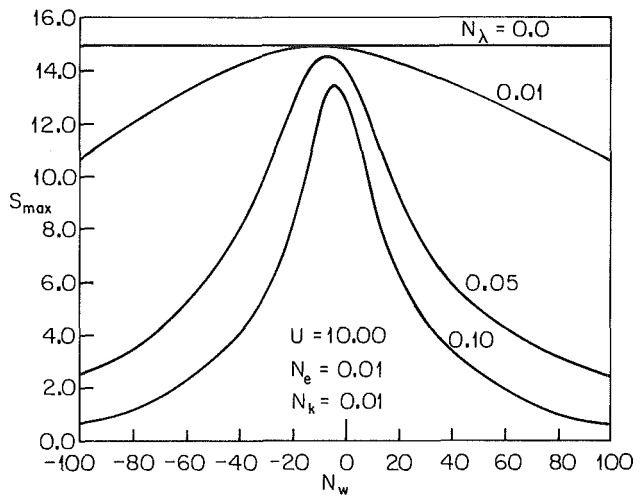

Fig. 4 Variation of maximum groove depth as a function of beam focusing number and beam expansion rate

The influence of beam waist position on fully developed groove shape and depth is shown in Fig. 2. It is observed that the depth of the cuts increases and passes through a maximum when the beam is focused slightly inside the material. This type of behavior has also been observed by Bar-Isaac and Korn [7] for laser drilling. When the focal point is moved farther into the material the groove becomes shallower. The increase in groove depth by focusing the beam slightly inside the material is apparently due to better average focusing of the laser energy, hence utilizing the energy more efficiently for evaporation rather than for conduction. Further moving the focal point into the material diverges the beam in the evaporating zone and increases the conduction losses. When the focal plane is moved up from the surface of the material the groove gets shallower and wider, since the laser energy is less concentrated everywhere within the evaporation zone.

The effect of the beam expansion rate on the size and shape of fully developed grooves is depicted in Figs. 3 for different beam divergence numbers N_λ. With increasing beam divergence the groove depth decreases somewhat since the beam expands beyond the focal point resulting in unconcentrated laser energy for deep grooves. In practice, large beam divergence numbers correspond to short focal length lenses. The decrease in depth is rather minor if the beam is well focused, but can be very substantial if the beam is poorly focused.

As shown in Fig. 2, the depths of the grooves pass through a maximum when the beam is focused slightly inside the material. The variation of fully developed maximum groove depth as a function of beam focusing number is shown in Fig. 4 for different beam expansion rates. Maximum groove depth for parallel beams ($N_\lambda = 0$) is, of course, constant for all values of beam focusing numbers. In practice, parallel beams coming from a laser are unfocused and, therefore, have large beam diameters depending on the laser characteristics and are rarely strong enough to cause evaporation. In order to evaporate a material these beams need to be focused to a small diameter, thus the parallel beam in Fig. 4 corresponds to an ideal beam, which has a diameter equal to the diameter of a focused beam at the focal plane, showing a case of a lens with an infinite focal length. Using a lens with a shorter focal length increases the beam divergence and, thus, reduces the groove depth.

It was seen in Figs. 2 and 4 that the groove obtains a maximum depth when focused slightly inside the medium. This does not necessarily mean, however, that the material removal rate also has a maximum when the beam is focused inside the medium, as seen from Fig. 5. In this figure the removal rate is

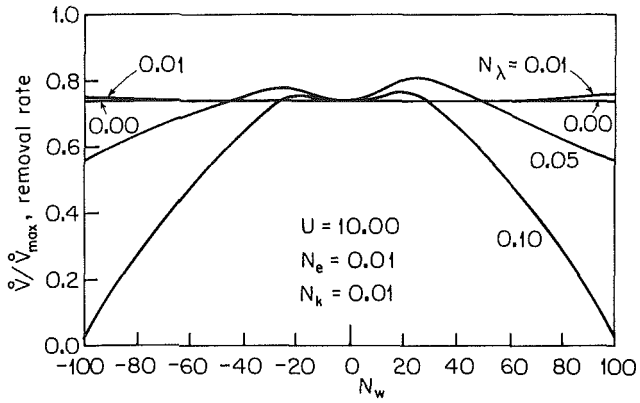

Fig. 5 Material removal rate as a function of beam focusing number

nondimensionalized by the theoretical maximum, i.e., the material removal in the absence of conduction losses:

$$\dot{V}/\dot{V}_{\max} = \frac{2}{\pi}(N_e + UN_k)\int_0^\infty S_\infty(\eta)d\eta \qquad (6)$$

As expected, the removal rate drops off rapidly for laser beams with their focal points far above or below the surface. In the vicinity of $N_w = 0$ the removal rate is relatively flat with a slight minimum for small negative N_w. Thus it is seen that achieving a deeper groove has its price: A deeper groove has steeper walls with larger total surface area, resulting in larger conduction losses. The observation of a maximum removal rate for a beam focused above the surface has been made experimentally by Wallace [9], who investigated laser shaping of ceramics.

It is interesting to note that it is possible to achieve higher material removal rates for a diverging beam ($N_\lambda > 0$) than for a parallel beam for a few focal point positions above and below the surface. This may be explained by looking at the beam intensity hitting the groove surface, equation (4): For a steep surface the vertical component of the flux onto the wall becomes quite small, so that the contribution of the small radial intensity component (nonexistent for parallel beams) becomes very important.

Conclusions

A heat transfer model for evaporative cutting of a semi-infinite body with a moving continuous wave laser has been developed and solved numerically to investigate the effects of beam focusing and expansion on the size and shape of a groove. It was seen that the depth of the grooves increases and passes through a maximum when the beam is focused slightly inside the material. The groove depth decreases when the beam is focused above the surface of the material. Thus, the groove depths can be increased by using lenses with long focal lengths. Longer focal length lens give larger minimum beam radii at the focal plane, but with a lower beam divergence rate. On the other hand, maximum removal rates are obtained for beams with appreciable divergence rates focused slightly above the surface.

Acknowledgments

Support for this work under the National Institute of Arthritis, Diabetes, Digestive and Kidney Diseases, Grant No. AM30240, is gratefully acknowledged.

References

1 Shkarofsky, I. P., "Review on Industrial Applications of High Power Laser Beams III," *RCA Review*, Vol. 36, 1975, pp. 338-368.

2 Modest, M. F., and Abakians, H., "Heat Conduction in a Moving Semi-infinite Solid Subjected to Pulsed Laser Irradiation," ASME JOURNAL OF HEAT TRANSFER, Vol. 108, 1986, pp. 597-601.

3 Rogerson, J. E., and Chayt, G. A., "Total Melting Time in the Ablating Slab Problem," *J. of Applied Physics*, Vol. 42, 1971, pp. 2711-2713.

4 von Allmen, M., "Laser Drilling Velocity in Metals," *J. of Applied Physics*, Vol. 47, 1976, pp. 5460-5463.

5 Mazumder, J., and Steen, W. M., "Heat Transfer Model for CW Laser Material Processing," *J. of Applied Physics*, Vol. 51(2), 1980, pp. 941-947.

6 Modest, M. F., and Abakians, H., "Evaporative Cutting of a Semi-infinite Body With a Moving CW Laser," ASME JOURNAL OF HEAT TRANSFER, Vol. 108, 1986, pp. 602-607.

7 Bar-Isaac, C., and Korn, U., "Moving Heat Source Dynamics in Laser Drilling Process," *Appl. Phys.*, Vol. 3, 1974, pp. 45-54.

8 Self, A. S., "Focusing of Spherical Gaussian Beams," *Applied Optics*, Vol. 22, No. 5, 1983, pp. 658-661.

9 Wallace, R. J., "A Study of the Shaping of Hot Pressed Silicon Nitride With a High Power CO_2 Laser," Ph.D. Dissertation, University of Southern California, Los Angeles, CA, 1983.

Boiling Incipience in Plane Rotating Water Films

I. Mudawwar[1] and M. A. El-Masri[2]

Nomenclature

a = centrifugal acceleration = $\omega^2 R$
g = gravitational acceleration
h = single-phase convective heat transfer coefficient = $q/(T_w - T_{sat})$
h^* = dimensionless heat transfer coefficient = $(h\,\nu_l^{2/3})/(k_l a^{1/3})$
h_{fg} = latent heat of vaporization
k = thermal conductivity
k_s = wall roughness
Pr = Prandtl number
q = wall heat flux
q_i = incipient heat flux
$\tilde{q}_i$ = incipient heat flux defined in equation (6)
R = radius of rotation
Re = film Reynolds number = $4\Gamma/\mu_l$
T = temperature
y_{lam} = thickness of the laminar sublayer
β = dimensionless film thickness = $\delta\, a^{1/3}/\nu_l^{2/3}$
Γ = mass flow rate per unit film width
ΔT_{sat} = wall superheat = $T_w - T_{sat}$
δ = film thickness
μ = dynamic viscosity
ν = kinematic viscosity
ρ = density
σ = surface tension
τ_w = wall shear stress
ω = rotational speed
$\tilde{\omega}$ = rotation number = $\omega R^2/\nu_l$

Subscripts

l = liquid
sat = saturated
v = vapor
w = wall

[1]School of Mechanical Engineering, Purdue University, W. Lafayette, IN 47907.

[2]Department of Mechanical Engineering, Massachusetts Institute of Technology, Cambridge, MA 02139.

Contributed by the Heat Transfer Division for publication in the JOURNAL OF HEAT TRANSFER. Manuscript received by the Heat Transfer Division August 4, 1987. Keywords: Boiling, Evaporation, Rotating Flows.

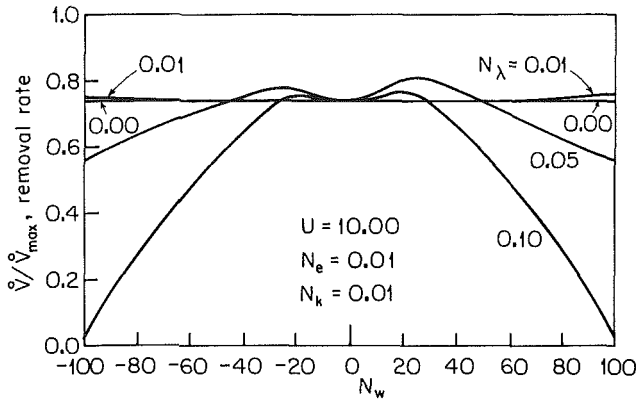

Fig. 5 Material removal rate as a function of beam focusing number

nondimensionalized by the theoretical maximum, i.e., the material removal in the absence of conduction losses:

$$\dot{V}/\dot{V}_{\max} = \frac{2}{\pi}(N_e + UN_k)\int_0^\infty S_\infty(\eta)d\eta \qquad (6)$$

As expected, the removal rate drops off rapidly for laser beams with their focal points far above or below the surface. In the vicinity of $N_w = 0$ the removal rate is relatively flat with a slight minimum for small negative N_w. Thus it is seen that achieving a deeper groove has its price: A deeper groove has steeper walls with larger total surface area, resulting in larger conduction losses. The observation of a maximum removal rate for a beam focused above the surface has been made experimentally by Wallace [9], who investigated laser shaping of ceramics.

It is interesting to note that it is possible to achieve higher material removal rates for a diverging beam ($N_\lambda > 0$) than for a parallel beam for a few focal point positions above and below the surface. This may be explained by looking at the beam intensity hitting the groove surface, equation (4): For a steep surface the vertical component of the flux onto the wall becomes quite small, so that the contribution of the small radial intensity component (nonexistent for parallel beams) becomes very important.

Conclusions

A heat transfer model for evaporative cutting of a semi-infinite body with a moving continuous wave laser has been developed and solved numerically to investigate the effects of beam focusing and expansion on the size and shape of a groove. It was seen that the depth of the grooves increases and passes through a maximum when the beam is focused slightly inside the material. The groove depth decreases when the beam is focused above the surface of the material. Thus, the groove depths can be increased by using lenses with long focal lengths. Longer focal length lens give larger minimum beam radii at the focal plane, but with a lower beam divergence rate. On the other hand, maximum removal rates are obtained for beams with appreciable divergence rates focused slightly above the surface.

Acknowledgments

Support for this work under the National Institute of Arthritis, Diabetes, Digestive and Kidney Diseases, Grant No. AM30240, is gratefully acknowledged.

References

1 Shkarofsky, I. P., "Review on Industrial Applications of High Power Laser Beams III," *RCA Review*, Vol. 36, 1975, pp. 338–368.

2 Modest, M. F., and Abakians, H., "Heat Conduction in a Moving Semi-infinite Solid Subjected to Pulsed Laser Irradiation," ASME JOURNAL OF HEAT TRANSFER, Vol. 108, 1986, pp. 597–601.

3 Rogerson, J. E., and Chayt, G. A., "Total Melting Time in the Ablating Slab Problem," *J. of Applied Physics*, Vol. 42, 1971, pp. 2711–2713.

4 von Allmen, M., "Laser Drilling Velocity in Metals," *J. of Applied Physics*, Vol. 47, 1976, pp. 5460–5463.

5 Mazumder, J., and Steen, W. M., "Heat Transfer Model for CW Laser Material Processing," *J. of Applied Physics*, Vol. 51(2), 1980, pp. 941–947.

6 Modest, M. F., and Abakians, H., "Evaporative Cutting of a Semi-infinite Body With a Moving CW Laser," ASME JOURNAL OF HEAT TRANSFER, Vol. 108, 1986, pp. 602–607.

7 Bar-Isaac, C., and Korn, U., "Moving Heat Source Dynamics in Laser Drilling Process," *Appl. Phys.*, Vol. 3, 1974, pp. 45–54.

8 Self, A. S., "Focusing of Spherical Gaussian Beams," *Applied Optics*, Vol. 22, No. 5, 1983, pp. 658–661.

9 Wallace, R. J., "A Study of the Shaping of Hot Pressed Silicon Nitride With a High Power CO_2 Laser," Ph.D. Dissertation, University of Southern California, Los Angeles, CA, 1983.

Boiling Incipience in Plane Rotating Water Films

I. Mudawwar[1] and M. A. El-Masri[2]

Nomenclature

a = centrifugal acceleration = $\omega^2 R$
g = gravitational acceleration
h = single-phase convective heat transfer coefficient = $q/(T_w - T_{sat})$
h^* = dimensionless heat transfer coefficient = $(h\,\nu_l^{2/3})/(k_l a^{1/3})$
h_{fg} = latent heat of vaporization
k = thermal conductivity
k_s = wall roughness
Pr = Prandtl number
q = wall heat flux
q_i = incipient heat flux
$\tilde{q}_i$ = incipient heat flux defined in equation (6)
R = radius of rotation
Re = film Reynolds number = $4\Gamma/\mu_l$
T = temperature
y_{lam} = thickness of the laminar sublayer
β = dimensionless film thickness = $\delta\, a^{1/3}/\nu_l^{2/3}$
Γ = mass flow rate per unit film width
ΔT_{sat} = wall superheat = $T_w - T_{sat}$
δ = film thickness
μ = dynamic viscosity
ν = kinematic viscosity
ρ = density
σ = surface tension
τ_w = wall shear stress
ω = rotational speed
$\tilde{\omega}$ = rotation number = $\omega R^2/\nu_l$

Subscripts

l = liquid
sat = saturated
v = vapor
w = wall

[1]School of Mechanical Engineering, Purdue University, W. Lafayette, IN 47907.

[2]Department of Mechanical Engineering, Massachusetts Institute of Technology, Cambridge, MA 02139.

Contributed by the Heat Transfer Division for publication in the JOURNAL OF HEAT TRANSFER. Manuscript received by the Heat Transfer Division August 4, 1987. Keywords: Boiling, Evaporation, Rotating Flows.

Introduction

Knowledge of heat transfer in rotating liquid films is of paramount importance for evaluating the thermal efficiency of gas turbines with water-cooled blades. Centrifugal forces constitute the primary driving forces for liquids flowing in radial rotating channels. Coriolis forces, on the other hand, tend to thin out the flow in the form of a film that covers one side of the channel. Fully developed motion of the film is determined by a balance between centrifugal and shear forces. Thus, rotating film motion resembles that of a free-falling gravity-driven film since both are characterized by a balance between shear and body forces. However, Coriolis forces can strongly influence interfacial waves and turbulent velocity fluctuations of rotating films. This is evident from the results of Kirkpatrick (1980), who compared film thickness measurements for the cases of free-falling and rotating films. His data indicate profound waviness at higher Reynolds numbers for the case of gravity-driven films. On the other hand, interfacial waves in rotating films were found to stabilize at Reynolds numbers in excess of 8000.

This paper focuses on the effects of Coriolis forces and wall roughness on the convective heat transfer coefficient and the incipient boiling heat flux in thin rotating films.

Experimental System

The experimental apparatus used in the present work has been described in detail in the previous paper by Mudawwar et al. (1985). As shown in Fig. 1, the primary rotating system consisted of a 34.30 cm o.d. aluminum disk on which the test channel was mounted. The disk was flanged to the end of a stainless shaft and rotated at speeds up to 1775 rpm by a 7.5 hp motor equipped with a continuous full-range speed controller. A stationary vessel surrounding the rotating disk (not shown in the figure) provided accurate pressure control over the range 1.0–5.41 atm. The deionized water was preheated by external electric heaters before entering the shaft. Another stagnation preheater was installed inside the rotating disk to overcome heat losses from the water to the shaft. The flow was forced through a nozzle into the surface of the preheater. During operation, stagnation preheater power was increased until the saturation temperature was reached. The saturated water was collected inside a spiral pocket and diverted by centrifugal forces into the radial test channel. Radial film flow was established by a nozzle-shaped injection plate. The film was thinned by centrifugal forces to approximately 0.04 mm at the surface of the test heater, the center of which was located 13.0 cm from the shaft axis. The heating module consisted of a nichrome ribbon sandwiched between boron nitride plates and covered with a copper plate, which transferred the heat to the liquid film. Electric power was supplied across the terminals of the ribbon and dissipated to the film over a 12×6.35 mm^2 heat transfer area.

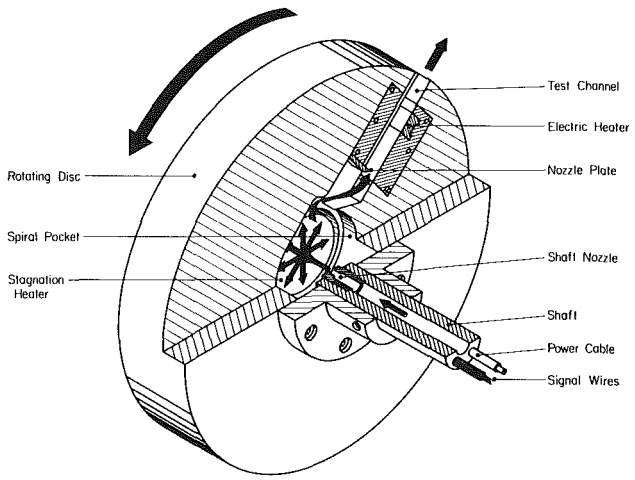

Fig. 1 Sectional diagram of the rotating test section

Results and Discussion

Heat transfer data for rotating films were obtained in the form of boiling curves for a wide range of rotational speeds (ω = 500–1775 rpm), pressures (p = 1.0–5.41 atm), and film Reynolds numbers (Re = 7.1×10^3 – 60.7×10^3). Figure 2 shows heat transfer results for several flow rates and a/g = 146. At low pressures the critical heat flux occurred after a relatively small range of boiling heat flux. For a fixed mass flow rate and centrifugal acceleration, higher pressures considerably increased the critical heat flux. Higher acceleration levels increased both the critical heat flux and the heat transfer coefficient prior to boiling.

Following earlier studies (Chun and Seban, 1971) on gravity-driven films, the film thickness δ and the single-phase convective heat transfer coefficient h can be correlated in the following manner:

$$\beta = \frac{\delta\, a^{1/3}}{\nu_l^{2/3}} = f(\mathrm{Re}) \tag{1}$$

$$h^* = \frac{h\, \nu_l^{2/3}}{k_l\, a^{1/3}} = f(\mathrm{Re},\ \mathrm{Pr}_l) \tag{2}$$

where

$$\mathrm{Re} \equiv \frac{4\Gamma}{\mu_l} \tag{3}$$

However, disagreements between free-falling and rotating film thickness correlations have been reported by Kirkpatrick (1980), who failed to develop an empirical equation for his rotating film data according to equation (1). Furthermore, single-phase heat transfer data obtained in the present study were much greater than predicted by Chun and Seban's correlation for free-falling films (i.e., $a = g$) undergoing interfacial evaporation. A possible explanation for the significant difference between gravity-driven and rotating film correlations is the strong influence of Coriolis forces (and possibly wall roughness) on single-phase convection in the film.

Thus, equations (1) and (2) can be modified for rotating films by accounting for Coriolis force effects. That is,

$$\beta = f(\mathrm{Re},\ \hat{\omega}) \tag{4}$$

$$h^* = f(\mathrm{Re},\ \mathrm{Pr}_l,\ \hat{\omega}) \tag{5}$$

The correlation given in Fig. 3 has the same Prandtl number exponent as Chun and Seban's correlation for free-falling films, and possesses an accuracy of ± 30 percent.

From the analysis of Hsu and Graham (1961), Han and Griffith (1965), and Bergles and Rohsenow (1964), nucleation is believed to commence on a heating surface when the liquid surrounding a growing bubble exceeds the temperature of its outer surface. In the presence of a wide range of cavity sizes, nucleation of a hemispherical bubble within a superheated wall layer characterized by a linear temperature distribution is determined by the following equation:

$$\bar{q}_i = \frac{8 T_{\mathrm{sat}} \sigma}{k_l \rho_v h_{fg}}\, h^2 \tag{6}$$

The experimental results for the incipient boiling heat flux in rotating films are compared in Fig. 4 to equation (6). The ratio $q_i/\bar{q}_i$ is far from unity for most of the operating conditions. Such inconsistencies have been attributed by many researchers to the condition of the boiling surface. If the boiling surface is very smooth, for example, equation (6) can be in great error since nucleation can be totally suppressed. Davis

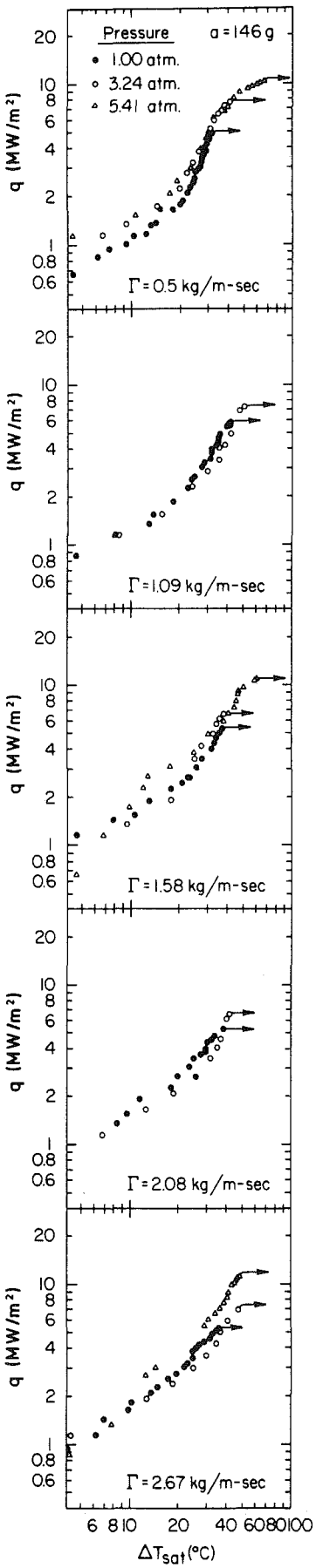

Fig. 2 Boiling heat transfer data for $a/g = 146$

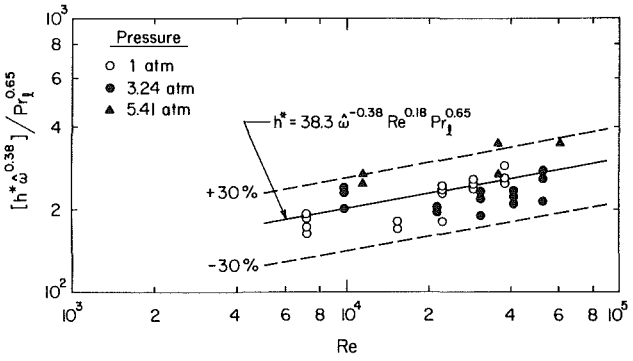

Fig. 3 Variation of the dimensionless single-phase evaporation heat transfer coefficient with Reynolds number and rotation number

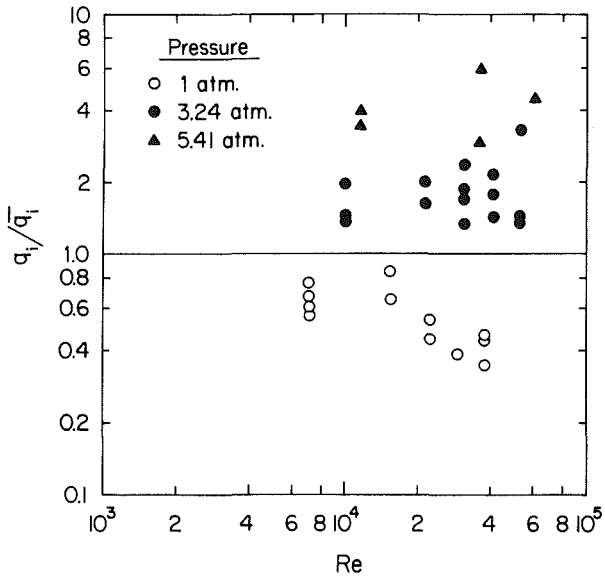

Fig. 4 Comparison between experimental incipient heat flux data and equation (6)

and Anderson (1966) modified equation (6) to account for the characteristics of the boiling surface. Nevertheless, their model was also based on the assumption of linear temperature distribution in the vicinity of the wall. Thus the validity of equation (6) is dependent on the existence of a laminar sublayer within the thermal boundary layer. In the range of operating conditions of the rotating water film data (Pr ≈ 1) of the present study, the thickness (y_{lam}) of the laminar sublayer can be approximated by

$$\frac{y_{lam}\sqrt{\frac{\tau_\omega}{\rho_l}}}{\nu_l} = 5 \tag{7}$$

For a fully developed rotating film, equation (7) reduces to

$$\frac{y_{lam}}{\delta} = \frac{5}{\beta^{1.5}} \tag{8}$$

The surface can be considered hydraulically smooth or rough depending on the ratio of the wall roughness k_s to the thickness of the laminar sublayer. That is,

$$\text{smooth surface: } \frac{k_s}{\delta} < \frac{5}{\beta^{1.5}} \tag{9}$$

$$\text{rough surface: } \frac{k_s}{\delta} > \frac{70}{\beta^{1.5}} \tag{10}$$

Thus equation (6) can only be valid if the condition of equation (9) is satisfied. By comparison with our rotating film data, the smooth wall condition corresponds to $k_s < 1$ μm (based on the rotating film thickness data of Kirkpatrick, 1980). Since the heat transfer surface was fabricated by milling, most of the data were found to fall in the roughness range corresponding to equation (10).

Conclusions

This study has focused on boiling heat transfer to thin rotating water films. The primary objective was to study the effects of pressure, centrifugal acceleration, and flow rate on boiling incipience. The primary conclusions are as follows:

1 Acceleration increased the convective heat transfer coefficient prior to boiling and delayed boiling incipience.

2 Coriolis forces play a significant role in rotating film convective processes. Prior to boiling, these forces influence the turbulent velocity fluctuations within the film as well as the stability of the free film interface.

3 Rotating films are typically very thin, and as such, wall roughness is believed to destroy the laminar portion of the thermal boundary layer. Thus, common incipient boiling models based on the existence of a linear temperature profile in the vicinity of the heated surface should be avoided if the surface fails to satisfy the smoothness condition of equation (9). The present data also indicate the existence of a different mechanism for boiling incipience that may be the result of turbulent exchange of heat between the wall and the bulk of the film rather than molecular diffusion.

References

Bergles, A. E., and Rohsenow, W. M., 1964, "The Determination of Forced Convection Surface-Boiling Heat Transfer," ASME JOURNAL OF HEAT TRANSFER, Vol. 86, pp. 365-372.

Chun, K. R., and Seban, R. A., 1971, "Heat Transfer to Evaporating Liquid Films," ASME JOURNAL OF HEAT TRANSFER, Vol. 93, pp. 391-396.

Davis, E. J., and Anderson, G. H., 1966, "The Incipience of Nucleate Boiling in Forced Convection Flow," *AIChE Journal*, Vol. 12, pp. 774-780.

Han, C. Y., and Griffith, P., 1965, "The Mechanisms of Heat Transfer in Nucleate Pool Boiling. Part I: Bubble Initiation, Growth and Departure," *International Journal of Heat and Mass Transfer*, Vol. 8, pp. 887-904.

Hsu, Y. Y., and Graham, R. W., 1961, "Analytical and Experimental Study of Thermal Boundary Layer and Ebullition Cycle," NASA Technical Note TNO-594.

Kirkpatrick, A. T., 1980, "Wave Mechanics of Inclined and Rotating Liquid Films," Ph.D. Thesis, Department of Mechanical Engineering, Massachusetts Institute of Technology, Cambridge, MA.

Mudawwar, I. A., El-Masri, M. A., Wu, C. S., and Ausman-Mudawwar, J. R., 1985, "Boiling Heat Transfer and Critical Heat Flux in High-Speed Rotating Liquid Films," *International Journal of Heat and Mass Transfer*, Vol. 28, pp. 795-806.

Limits to Critical Heat Flux Enhancement in a Liquid Film Falling Over a Structured Surface That Simulates a Microelectronic Chip

T. A. Grimley,[1,2] I. Mudawwar,[1] and F. P. Incropera[1]

Nomenclature

L = length of heater
q = heat flux based on the total base area of the enhanced surface
q_M = critical heat flux (CHF) based on the total base area of the enhanced surface
T = temperature
ΔT_{sat} = wall superheat at the base of the enhanced surface = $T_w - T_{sat}$
ΔT_{sub} = inlet subcooling = $T_{sat} - T_{in}$
U = mean inlet velocity
δ = film inlet thickness

Subscripts

in = inlet
sat = saturated
sub = subcooled
w = wall

[1]School of Mechanical Engineering, Purdue University, West Lafayette, IN 47907.

[2]Fluid and Thermal Systems Group, Southwest Research Institute, San Antonio, TX 78284.

Contributed by the Heat Transfer Division for publication in the JOURNAL OF HEAT TRANSFER. Manuscript received by the Heat Transfer Division May 6, 1987. Keywords: Boiling, Electronic Equipment, Evaporation.

Introduction

The combination of increasing power densities and stringent surface temperature constraints for microelectronic components has stimulated interest in cooling by means of pool boiling in a dielectric liquid. However, although dielectric fluorocarbons such as FC-72 (manufactured by 3M) are highly compatible with electronic components, small thermal conductivities and latent heats make them poor heat transfer fluids. Moreover, pool boiling studies concerned with CHF enhancement (Bergles and Chyu, 1982; Marto and Lepere, 1982) have shown that significant hysteresis (temperature overshoot) at the inception of boiling may violate component temperature limitations.

More recently, the falling liquid film has been considered as a means of enhancing the performance of dielectric coolants by controlling boiling hysteresis and increasing the critical heat flux (CHF). From experimental studies performed for a gravity-driven liquid (FC-72) film flowing over a smooth surface (Mudawwar et al., 1987), the ability to suppress hysteresis was demonstrated, and the trend of increasing CHF with decreasing heater length was determined. However, even for the smallest heater length of the study (L = 12.7 mm), CHF values were not much higher than those associated with pool boiling.

To determine whether structured surfaces could be used to substantially extend CHF, Grimley et al. (1987) performed experiments for a thin film of FC-72 falling over a 63.5-mm-long surface with either longitudinal microfins or microstuds. Although both the microfin and microstud surfaces enhanced nucleate boiling heat transfer relative to a smooth surface, only the microfin surface provided significant enhancement of CHF. CHF was observed to be due to dryout of a thin subfilm, which remained on the boiling surface after the bulk of the fluid in the falling film had separated due to intense vapor generation. It was argued that the microfins extended CHF by allowing surface tension forces to maintain the liqud film on the surface more effectively and by inhibiting the lateral spread of dry patches after film separation. In contrast, the microstud surface acted to break up the film, thereby hastening film separation and decreasing CHF. In addition, it was found that CHF could be enhanced by subcooling the liquid or by installing a louvered flow deflector a short distance from the heated surface. While subcooling decreased the intensity of vapor effusion by supplying the heated surface with liquid of reduced temperature, the deflector inhibited film separation.

On the basis of the foregoing results, it is known that CHF in a falling liquid film may be enhanced by reducing the length of the heated surface, machining longitudinal grooves in the surface, shrouding the surface with a louvered flow deflector, or subcooling the liquid. However, experiments have yet to be performed in which these effects are considered collectively in

Thus equation (6) can only be valid if the condition of equation (9) is satisfied. By comparison with our rotating film data, the smooth wall condition corresponds to $k_s < 1$ μm (based on the rotating film thickness data of Kirkpatrick, 1980). Since the heat transfer surface was fabricated by milling, most of the data were found to fall in the roughness range corresponding to equation (10).

Conclusions

This study has focused on boiling heat transfer to thin rotating water films. The primary objective was to study the effects of pressure, centrifugal acceleration, and flow rate on boiling incipience. The primary conclusions are as follows:

1 Acceleration increased the convective heat transfer coefficient prior to boiling and delayed boiling incipience.

2 Coriolis forces play a significant role in rotating film convective processes. Prior to boiling, these forces influence the turbulent velocity fluctuations within the film as well as the stability of the free film interface.

3 Rotating films are typically very thin, and as such, wall roughness is believed to destroy the laminar portion of the thermal boundary layer. Thus, common incipient boiling models based on the existence of a linear temperature profile in the vicinity of the heated surface should be avoided if the surface fails to satisfy the smoothness condition of equation (9). The present data also indicate the existence of a different mechanism for boiling incipience that may be the result of turbulent exchange of heat between the wall and the bulk of the film rather than molecular diffusion.

References

Bergles, A. E., and Rohsenow, W. M., 1964, "The Determination of Forced Convection Surface-Boiling Heat Transfer," ASME JOURNAL OF HEAT TRANSFER, Vol. 86, pp. 365-372.

Chun, K. R., and Seban, R. A., 1971, "Heat Transfer to Evaporating Liquid Films," ASME JOURNAL OF HEAT TRANSFER, Vol. 93, pp. 391-396.

Davis, E. J., and Anderson, G. H., 1966, "The Incipience of Nucleate Boiling in Forced Convection Flow," *AIChE Journal*, Vol. 12, pp. 774-780.

Han, C. Y., and Griffith, P., 1965, "The Mechanisms of Heat Transfer in Nucleate Pool Boiling. Part I: Bubble Initiation, Growth and Departure," *International Journal of Heat and Mass Transfer*, Vol. 8, pp. 887-904.

Hsu, Y. Y., and Graham, R. W., 1961, "Analytical and Experimental Study of Thermal Boundary Layer and Ebullition Cycle," NASA Technical Note TNO-594.

Kirkpatrick, A. T., 1980, "Wave Mechanics of Inclined and Rotating Liquid Films," Ph.D. Thesis, Department of Mechanical Engineering, Massachusetts Institute of Technology, Cambridge, MA.

Mudawwar, I. A., El-Masri, M. A., Wu, C. S., and Ausman-Mudawwar, J. R., 1985, "Boiling Heat Transfer and Critical Heat Flux in High-Speed Rotating Liquid Films," *International Journal of Heat and Mass Transfer*, Vol. 28, pp. 795-806.

Limits to Critical Heat Flux Enhancement in a Liquid Film Falling Over a Structured Surface That Simulates a Microelectronic Chip

T. A. Grimley,[1,2] I. Mudawwar,[1] and F. P. Incropera[1]

Nomenclature

L = length of heater
q = heat flux based on the total base area of the enhanced surface
q_M = critical heat flux (CHF) based on the total base area of the enhanced surface
T = temperature
ΔT_{sat} = wall superheat at the base of the enhanced surface = $T_w - T_{sat}$
ΔT_{sub} = inlet subcooling = $T_{sat} - T_{in}$
U = mean inlet velocity
δ = film inlet thickness

Subscripts

in = inlet
sat = saturated
sub = subcooled
w = wall

[1]School of Mechanical Engineering, Purdue University, West Lafayette, IN 47907.

[2]Fluid and Thermal Systems Group, Southwest Research Institute, San Antonio, TX 78284.

Contributed by the Heat Transfer Division for publication in the JOURNAL OF HEAT TRANSFER. Manuscript received by the Heat Transfer Division May 6, 1987. Keywords: Boiling, Electronic Equipment, Evaporation.

Introduction

The combination of increasing power densities and stringent surface temperature constraints for microelectronic components has stimulated interest in cooling by means of pool boiling in a dielectric liquid. However, although dielectric fluorocarbons such as FC-72 (manufactured by 3M) are highly compatible with electronic components, small thermal conductivities and latent heats make them poor heat transfer fluids. Moreover, pool boiling studies concerned with CHF enhancement (Bergles and Chyu, 1982; Marto and Lepere, 1982) have shown that significant hysteresis (temperature overshoot) at the inception of boiling may violate component temperature limitations.

More recently, the falling liquid film has been considered as a means of enhancing the performance of dielectric coolants by controlling boiling hysteresis and increasing the critical heat flux (CHF). From experimental studies performed for a gravity-driven liquid (FC-72) film flowing over a smooth surface (Mudawwar et al., 1987), the ability to suppress hysteresis was demonstrated, and the trend of increasing CHF with decreasing heater length was determined. However, even for the smallest heater length of the study (L = 12.7 mm), CHF values were not much higher than those associated with pool boiling.

To determine whether structured surfaces could be used to substantially extend CHF, Grimley et al. (1987) performed experiments for a thin film of FC-72 falling over a 63.5-mm-long surface with either longitudinal microfins or microstuds. Although both the microfin and microstud surfaces enhanced nucleate boiling heat transfer relative to a smooth surface, only the microfin surface provided significant enhancement of CHF. CHF was observed to be due to dryout of a thin subfilm, which remained on the boiling surface after the bulk of the fluid in the falling film had separated due to intense vapor generation. It was argued that the microfins extended CHF by allowing surface tension forces to maintain the liqud film on the surface more effectively and by inhibiting the lateral spread of dry patches after film separation. In contrast, the microstud surface acted to break up the film, thereby hastening film separation and decreasing CHF. In addition, it was found that CHF could be enhanced by subcooling the liquid or by installing a louvered flow deflector a short distance from the heated surface. While subcooling decreased the intensity of vapor effusion by supplying the heated surface with liquid of reduced temperature, the deflector inhibited film separation.

On the basis of the foregoing results, it is known that CHF in a falling liquid film may be enhanced by reducing the length of the heated surface, machining longitudinal grooves in the surface, shrouding the surface with a louvered flow deflector, or subcooling the liquid. However, experiments have yet to be performed in which these effects are considered collectively in

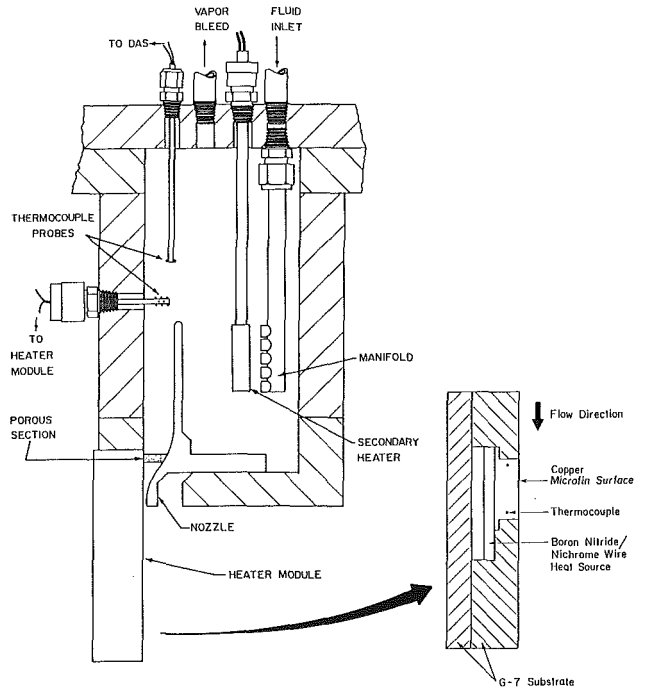

Fig. 1 Schematic of heater module and flow supply chamber

order to establish upper limits for CHF enhancement. Hence, the purpose of this study has been to determine boiling characteristics for a subcooled film of FC-72 falling over a short microfinned surface with an attached flow deflector. Experiments have been performed for a 12.7-mm-long by 25.4-mm-wide microfinned surface and for subcooling in the range from 0 to 14°C. The length of the heater is representative of microelectronic chip sizes.

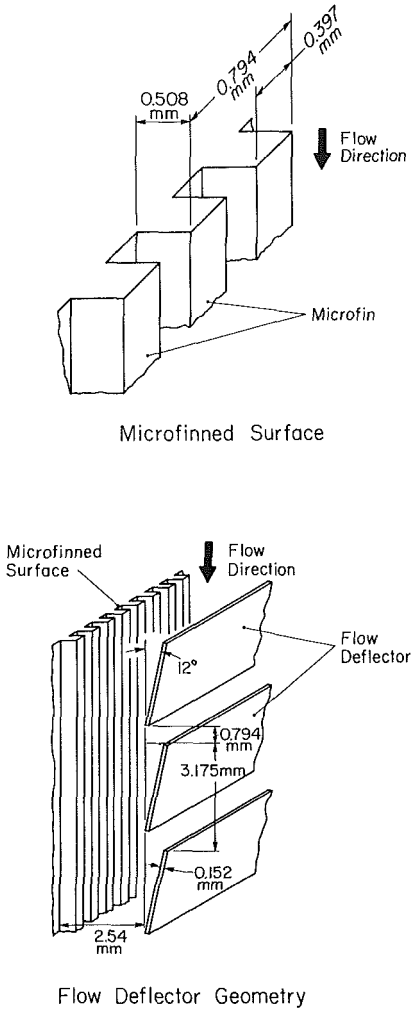

Fig. 2 Microfin surface geometry with flow deflector

Experimental System

As shown in Fig. 1, the gravity-driven liquid film was supplied to a heater module by a nozzle attached to the base of a fluid containment chamber. The thickness of the film was controlled by adjusting the nozzle position, and a porous plate upstream of the nozzle provided sufficient back pressure to fill the chamber with fluid. The upper edge of the heater was located at the nozzle exit. The heater module consisted of an oxygen-free copper block, which was pressed against a nichrome wire heat source in a G-7 fiberglass substrate. The nichrome wire was wound along grooves machined in one of two adjoining boron nitride (BN) plates, while very fine BN powder was used to minimze the thermal contact resistance between the BN plates and at the interface between the heat source and copper block. A conduction analysis of the heater module indicated that heat losses to the surroundings were less than 2 percent of the power input. Temperature measurements made at upstream and downstream locations in the copper block indicated longitudinal variations of less than 0.5°C, thereby permitting the assumption of isothermal surface conditions.

As shown in Fig. 2, the microfin geometry consists of 0.508-mm-high by 0.397-mm-wide fins spaced on 0.797 mm centers machined into the copper block. Prior to use, the surface was cleaned with acetone, blown dry with nitrogen, and mounted in the insulating substrate with the fins aligned in the flow direction. The base of the fins was flush with the surface of the substrate. The deflector was formed from 0.152-mm-thick brass stock into which louvers were formed by cutting 0.794 mm slots spaced on 31.75 mm centers. The webs were then bent approximately 12 deg, and the deflector was mounted 2.54 mm from the base of the boiling surface. Since the deflector was not in good thermal contact with the boiling surface, it served to modify the separated flow of the film, rather than to act as an extended surface.

Fluid was supplied to the test chamber by a closed-loop fluid delivery system constructed of stainless steel and compatible plastics. To insure high fluid purity, the FC-72 was degassed in a charging system connected to the fluid delivery system. The fluid delivery system was then charged by evacuating it to 500 μm before allowing the FC-72 to be flashed from the charging system. During operation, control was maintained over the film velocity, the film thickness, the fluid temperature upstream of the heater module, and the chamber pressure. Subcooling was quantified in terms of the difference between the saturated temperature corresponding to the test chamber pressure (T_{sat}) and the fluid inlet temperature (T_{in}). System details are provided elsewhere (Grimley et al., 1987). At atmospheric pressure T_{sat} = 56°C for FC-72.

Once the desired pressure, temperature, and film conditions were established, power was applied to the heat source. Boiling curves were generated by increasing the power to the heater module in discrete steps and then waiting for steady-state conditions. When steady-state was reached, the pressure, temperatures, power, and flow rate were recorded by an HP3054 data acquisition system. As CHF was approached, the magnitude of the power increment was decreased to reduce uncertainty in the reported value of CHF. CHF was detected by a rapid surge in the boiling surface temperature.

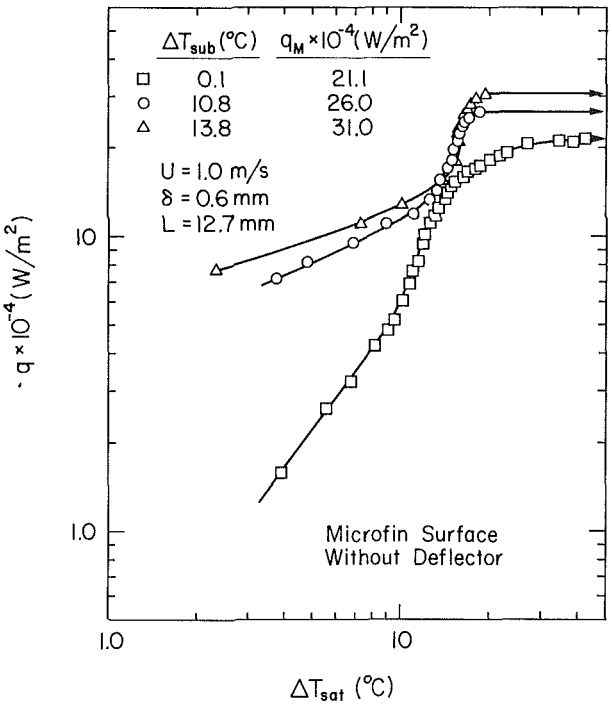

Fig. 3 Effect of subcooling on the boiling curve for the microfin surface without the flow deflector

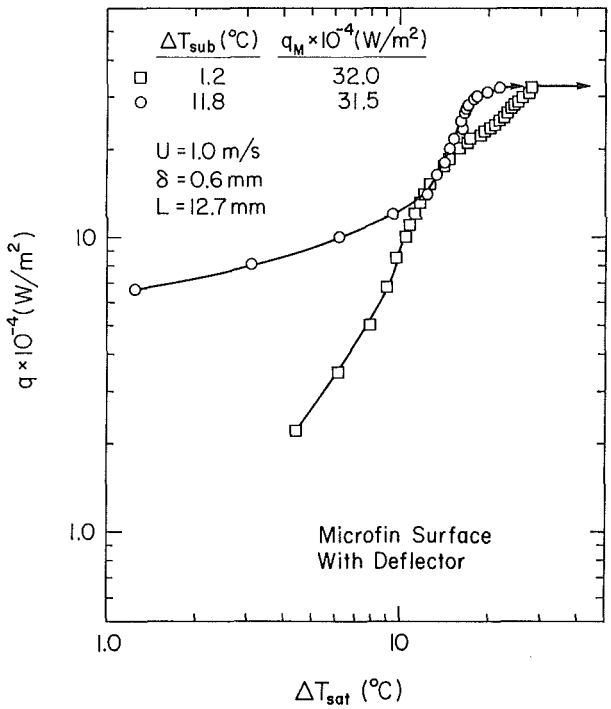

Fig. 4 Effect of subcooling on the boiling curve for the microfin surface with the flow deflector

Experimental Results

The results are presented in the form of boiling curves that plot the average heat flux q as a function of the temperature difference, $\Delta T_{sat} = (T_w - T_{sat})$. All experiments were performed with an average film velocity of $U = 1.0$ m/s and a film thickness of $\delta = 0.6$ mm.

For saturated conditions ($\Delta T_{sub} = 0$), the boiling process was similar to that previously described (Grimley et al., 1987; Mudawwar et al., 1987). Nucleation first occurred near the lower edge of the heated surface between the microfins. As the heat flux was increased, nucleation sites became active in the upstream region and nucleation patches formed across the span of the heater. The nucleation patches coalesced and the void fraction increased in the flow direction. For saturated conditions, film separation occurred near the lower edge of the heater when the void fraction became too large to maintain a continuous liquid film on the heated surface. When the bulk of the film separated, a thin sublayer remained on the surface and was visible between the microfins. CHF occurred when non-rewetting dry patches formed in the sublayer.

Without the flow deflector, the effect of subcooling on the boiling curve is shown in Fig. 3. The large convection coefficient associated with the upstream region of the 12.7 mm heater delayed boiling incipience to $q \approx 12$ W/cm^2, which is approximately three times larger than that required for a 63.5-mm-long heater (Grimley et al., 1987). CHF corresponded to $q_M = 21.1$ W/cm^2 for saturated conditions, which is approximately 30 percent larger than that obtained for a smooth surface of the same length (Mudawwar et al., 1987). In contrast Grimley et al. (1987) had previously found a 50 percent increase in CHF when microfins were used with a 63.5-mm-long heater. Hence, the effectiveness of the microfin surface is diminished by a reduction in the heater length. As shown in Fig. 3, in addition to increasing the value of CHF, subcooling reduced the temperature difference at the onset of CHF. The surface temperature was reduced from approximately 97°C for the saturated condition to about 78°C for the subcooled conditions. As for the long heater (Grimley et al., 1987), subcooling delayed nucleation and inhibited bubble growth once nucleation had occurred. However, for the short heater, bubble growth was inhibited to a greater degree and CHF occurred without significant film separation.

The fact that CHF occurred without significant film separation suggests that a different CHF mechanism exists for highly subcooled films. Although the wall temperature exceeds the saturation temperature, the bulk of the film remains subcooled, thereby inhibiting the growth of bubbles produced at the wall and reducing the downstream void fraction. CHF could then occur when the heat flux is large enough to generate a thin vapor blanket at the wall, for which the attendant void fraction is not large enough to cause significant film separation.

Figure 4 shows boiling curves obtained with the deflector and the liquid film at nearly saturated conditions and 11.8°C subcooling. For saturated conditions, CHF occurred at $q_M = 32$ W/cm^2, which is a 50 percent increase relative to the value obtained without the deflector. This increase was similar to the 44 percent increase that occurred for the 63.5 mm heater (Grimley, 1987). Moreover, interaction of the film with the deflector was similar to that observed for the 63.5 mm heater. Initially, the film flowed over the heater without contacting the deflector. As the heat flux was increased, nucleation occurred and the film thickened, allowing the outer surface of the film to contact the deflector. At higher fluxes, bubbles vented between the louvers and an increasing fraction of the film flowed outside the deflector. The contact point moved upstream until it approached the top of the heater, and enough pressurization occurred to project a liquid stream away from the deflector.

As shown in Fig. 4, CHF showed no improvement when subcooling was used in combination with the deflector. The boiling curve did change, however, and the temperature difference at the onset of CHF was reduced. Subcooling delayed the onset of backflow over the deflector to $q \approx 29$ W/cm^2, in contrast to 12 W/cm^2 for saturated conditions. The fact that backflow was delayed to more than 90 percent of CHF indicates that, as in the absence of the deflector, CHF for the subcooled conditions was not accompanied by significant

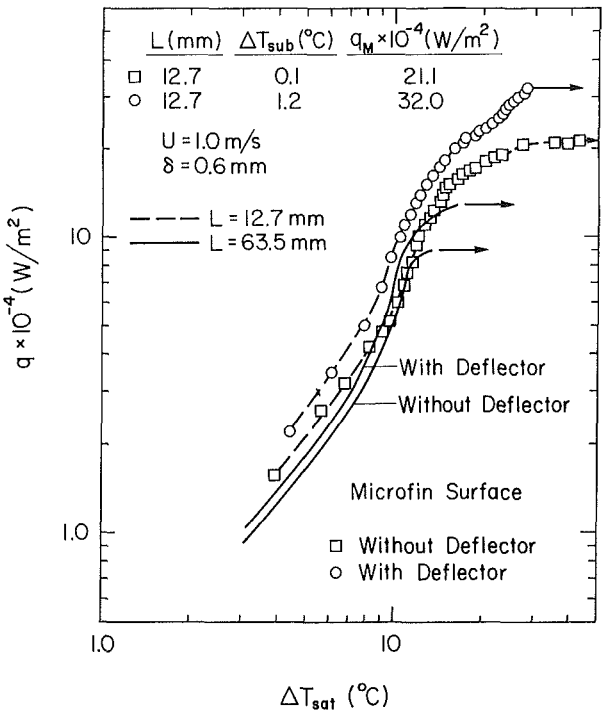

Fig. 5 Comparison of boiling curves for different heater lengths with and without flow deflector (liquid film is at or near saturated conditions)

separation. Because subcooling reduced film separation, the combination of the flow deflector and subcooling did not increase the value of CHF relative to that corresponding to use of the deflector with a saturated film.

Figure 5 compares boiling curves for 12.7 and 63.5-mm-long heaters with and without flow deflection. Although larger heat fluxes may be achieved with the short heater, the surface temperature at the onset of CHF is also considerably larger for the short heater. For applications with low surface temperature limits, flow deflection or subcooling may therefore be required to reduce the surface temperature.

Conclusions

This study has focused on boiling heat transfer from a vertically mounted, structured surface to a falling liquid film of FC-72. The primary objective was to study the cumulative effect of a small heater length, microfins, liquid subcooling, and a louvered flow deflector on the critical heat flux. The primary conclusions are as follows:

1 The 12.7-mm-long microfinned surface enhanced CHF relative to a smooth surface of equal length and a microfinned surface that was five times longer.

2 Subcooling increased CHF and decreased the temperature difference at the onset of CHF. The effect of subcooling on CHF was less pronounced for the 12.7-mm-long heater than for a 62.5-mm-long heater.

3 For subcooled conditions on the short heater, CHF occurred without significant film separation.

4 Although the louvered flow deflector enhanced CHF for saturated conditions, no improvement was found when subcooling was used in combination with the deflector.

5 CHF may be improved by a combination of reduced heater length, subcooling, and flow deflection, but the effects are not independent and superposition does not apply. For a 12.7-mm-long heater and film velocities typical of passive or semi-passive electronic cooling systems, it appears that the combination of microfins, subcooling and a flow deflector cannot enhance CHF much above 30 W/cm^2.

In summary the concept of boiling in a falling film is attractive for cooling electronic components by virtue of its suppression of the hysteresis phenomenon and its compatibility with passive or semi-passive flow arrangements. Morever, significant enhancement may be achieved by using microfinned surfaces in combination with liquid subcooling or a flow deflector to achieve critical heat fluxes as large as 30 W/cm^2 for FC-72 and a 12.7-mm-long heater. However, unless the film is supplied to relatively large extended surfaces to increase the heat transfer area, it is unlikely that existing or future augmentation schemes will render the concept suitable for dissipating the large fluxes (> 100 W/cm^2) projected for VLSI devices.

Acknowledgments

Support of this work by the IBM corporation is gratefully acknowledged.

References

Bergles, A. E., and Chyu, M. C., 1982, "Characteristics of Nucleate Boiling From Porous Metallic Coatings," ASME JOURNAL OF HEAT TRANSFER, Vol. 104, pp. 279–285.

Grimley, T. A., Mudawwar, I. A., and Incropera, F. P., 1987, "Flowing Fluorocarbon Liquid Films Using Structured Surfaces and Flow Deflectors," *International Journal of Heat and Mass Transfer*, in press.

Marto, P. J., and Lepere, V. J., 1982, "Pool Boiling Heat Transfer From Enhanced Surfaces to Dielectric Fluids," ASME JOURNAL OF HEAT TRANSFER, Vol. 104, pp. 292–299.

Mudawwar, I. A., Incropera, T. A., and Incropera, F. P., 1987, "Boiling Heat Transfer and Critical Heat Flux in Liquid Films Falling on Vertically Mounted Heat Sources," *International Journal of Heat and Mass Transfer*, Vol. 30, pp. 2083–2095.